Twelfth Symposium

NAVAL HYDRODYNAMICS

BOUNDARY LAYER STABILITY AND TRANSITION
SHIP BOUNDARY LAYERS AND PROPELLER HULL INTERACTION
CAVITATION
GEOPHYSICAL FLUID DYNAMICS

NATIONAL ACADEMY OF SCIENCES

MBL/WHOI
0 0301 0002225 7

Twelfth Symposium

NAVAL HYDRODYNAMICS

Boundary Layer Stability and Transition
Ship Boundary Layers and Propeller Hull Interaction
Cavitation
Geophysical Fluid Dynamics

sponsored by the
OFFICE OF NAVAL RESEARCH
the
DAVID W. TAYLOR NAVAL SHIP RESEARCH AND DEVELOPMENT CENTER
and the
NAVAL STUDIES BOARD
of the
NATIONAL RESEARCH COUNCIL

MARINE
BIOLOGICAL
LABORATORY
LIBRARY
WOODS HOLE, MASS.
W. H. O. I.

NATIONAL ACADEMY OF SCIENCES
Washington, DC 1979

Partial support for the publication of these Proceedings was provided by the Office of Naval Research of the Department of the Navy. The content does not necessarily reflect the position or the policy of the Navy, the U.S. Government, or the National Academy of Sciences and no endorsement should be inferred.

ISBN 0-309-02896-5

Library of Congress Catalog Card No. 79-53803

Available from:

Office of Publications
National Academy of Sciences
2101 Constitution Avenue, N.W.
Washington, D.C. 20418

Printed in the United States of America

PROGRAM COMMITTEE

George F. Carrier, Chairman, *Harvard University*

William E. Cummins, Vice Chairman, *David W. Taylor Naval Ship Research and Development Center*

Ralph D. Cooper, *Office of Naval Research*

Stanley W. Doroff, *Office of Naval Research*

Lee. M. Hunt, *National Research Council*

Wen Chin Lin, *David W. Taylor Naval Ship Research and Development Center*

Justin H. McCarthy, Jr., *David W. Taylor Naval Ship Research and Development Center*

Vincent J. Monacella, *David W. Taylor Naval Ship Research and Development Center*

SYMPOSIUM AIDES

Marguerite A. Bass
Yetta S. Hassin
Office of Naval Research

Lavern Powell
David W. Taylor Naval Ship Research and Development Center

Bernice P. Hunt
Joyce L. Wright
National Academy of Sciences

Grace Masuda
Institute of Medicine

Hope M. Bell
Doris E. Bouadjemi
Beatrice Bretzfield
Mary G. Gordon
Virginia A. Harrison
Debra A. Tidwell
Eva F. Tully
National Research Council

Preface

The Twelfth Symposium on Naval Hydrodynamics was held at Washington, D.C., during the period 5-9 June 1978 under the joint sponsorship of the Office of Naval Research, the David W. Taylor Naval Ship Research and Development Center, and the National Academy of Sciences.

The technical program of the Symposium consisted of eight sessions equally apportioned among the following four subjects of great current interest in the general field of naval hydrodynamics: (1) boundary layer stability and transition, (2) ship boundary layers and propeller hull interaction, (3) cavitation, and (4) geophysical fluid dynamics. Tours of the hydrodynamic research facilities of the David W. Taylor Naval Ship Research and Development Center and of Hydronautics, Inc., were also included in the technical program.

It is interesting to recal that the National Academy of Sciences was a cosponsor of the First and Second Symposia in this series which were held respectively in 1956 and 1958. It is a great pleasure to acknowledge once again the invaluable assistance of the Academy in launching these Symposia and in establishing the high standards of quality and style for them by which we are guided, even to this day.

Similarly, the David W. Taylor Naval Ship Research and Development Center has played an important role in the series of Symposia on Naval Hydrodynamics from their very inception. Scientists and engineers from the Center have presented outstanding scientific papers at each of the Symposia and have, in addition, participated in an informal manner in the planning of many of the earlier ones.

For these reasons the Office of Naval Research is especially pleased and honored at the opportunity presented by the cosponsorship of this Twelfth Symposium to renew and continue the fruitful collaboration with its old scientific allies. We are deeply grateful for their generous assistance in the past and present, and look forward with confidence to their continued support in the future.

Of the seemingly endless list of people who contributed in large and small ways to the planning and organizing of the Twelfth Symposium the following deserve special recognition: Professor George F. Carrier of Harvard University and the Naval Studies Board of the National Research Council, who served as chairman of the Program and Organizing Committee; Dr. William E. Cummins of the David W. Taylor Naval Ship Research and Development Center, who served as vice-chairman of the Committee, and his colleagues from the Center, Dr. Wen Chin Lin, Mr. Justin H. McCarthy, Jr. and Mr Vincent J. Monacella, who served on the Committee; Mr. Lee M. Hunt of the Naval Studies Board, who served on the Committee and who, with the able assistance of Miss Virginia A. Harrison, personally carried out the multitude of detailed arrangements required for the success of the Symposium; and Dr. Nelson T. Grisamore of the National Academy of Sciences, who edited these Proceedings.

A special note of appreciation is extended to Mr. Phillip Eisenberg, President of Hydronautics, Inc., for his delightful after-dinner talk at the Symposium Banquet and for the tour of Hydronautics, Inc., which he graciously arranged for the participants of the Symposium.

To all of these, and many more, the Office of Naval Research is forever indebted.

Ralph D. Cooper
Office of Naval Research

Contents

Preface v

Ralph D. Cooper

Introductory Address 1

Courtland D. Perkins

Introductory Address 3

Robert K. Geiger

Introductory Address 5

Myron V. Ricketts

SESSION I: BOUNDARY LAYER STABILITY AND TRANSITION

Stability and Transition Investigations Using the Navier-Stokes Equations 9

Hermann F. Fasel

The Physical Processes Causing Breakdown to Turbulence 22

M. Gaster

The Instability of Oscillatory Boundary Layers 25

Christian von Kerczek

Heated Boundary Layers 33

Eli Reshotko

Discussion 48

SESSION II: BOUNDARY LAYER STABILITY AND TRANSITION

Nonparallel Stability of Two-Dimensional Heated Boundary Layer Flows 53

N. M. El-Hady and A. H. Nayfeh

Three-Dimensional Effects in Boundary Layer Stability 63

Leslie M. Mack

Experiments on Heat-Stabilized Laminar Boundary Layers in a Tube 77

Steven J. Barker

Some Effects of Several Freestream Factors on Cavitation Inception on Axisymmetric Bodies 86

Edward M. Gates and Allan J. Acosta

Discussion 109

SESSION III: SHIP BOUNDARY LAYERS AND PROPELLER HULL INTERACTION

Calculation of Thick Boundary Layer and Near Wake of Bodies of Revolution by a Differential Method 115

Virenda C. Patel and Yu-Tai Lee

Stern Boundary-Layer Flow on Axisymmetric Bodies 127

Thomas T. Huang, Nicholas Santelli, and Garnell Belt

Theoretical Computation and Model and Full-Scale Correlation of the Flow at the Stern of a Submerged Body 158

A. W. Moore and C. B. Wills

Experimental and Theoretical Investigation of Ship Boundary Layer and Wake 169

Shuji Hatano, Kazuhiro Mori, and Takio Hotta

A General Method for Calculating Three-Dimensional Laminar and Turbulent Boundary Layers on Ship Hulls 188

Tuncer Cebeci, K. C. Chang, and Kalle Kaups

Study on the Structure of Ship Vortices Generated by Full Sterns 209

Hiraku Tanaka and Takayasu Ueda

SESSION IV: SHIP BOUNDARY LAYERS AND PROPELLER HULL INTERACTION

Wake Scale Effects on a Twin-Screw Displacement Ship 225

Arthur M. Reed and William G. Day, Jr.

Influence of Propeller Action on Flow Field Around a Hull 248

Shunichi Ishida

Prediction Of the Velocity Field in Way of the Ship Propeller 265

I. A. Titov, A. F. Poostoshniy, and O. P. Orlov

Recent Theoretical and Experimental Developments in the Prediction of Propeller Induced Vibration Forces on Nearby Boundaries 278

Bruce D. Cox, William S. Vorus, John P. Breslin, and Edwin P. Rood

A Determination of the Free Air Content and Velocity in Front of the "Sydney-Express" Propeller in Connection with Pressure Fluctuation Measurements 300

Andreas P. Keller and Ernst A. Weitendorf

Discussion 319

SESSION V: CAVITATION

Pressure Fields and Cavitation in Turbulent Shear Flows 327

Roger E. A. Arndt and William K. George

Secondary Flow Generated Vortex Cavitation 340

Michael L. Billet

On the Linearized Theory of Hub Cavity with Swirl 348

G. H. Schmidt and J. A. Sparenberg

Unsteady Cavitation on an Oscillating Hydrofoil 362

Young T. Shen and Frank B. Peterson

Cavitation on Hydrofoils in Turbulent Shear Flow 385

Hitoshi Murai, Akio Ihara, and Yasuyuki Tsurumi

Scale Effects on Propeller Cavitation Inception 400

G. Kuiper

Discussion 426

SESSION VI: CAVITATION

A Holographic Study of the Influence of Boundary Layer and Surface Characteristics on Incipient and Developed Cavitation on Axisymmetric Bodies 433

J. H. J. van der Meulen

Mechanism and Scaling of Cavitation Erosion 452

Hiroharu Kato, Toshio Maeda, and Atsushi Magaino

Experimental Investigations of Cavitation Noise 470

Göran Bark and Willem B. van Berlekom

Cavitation Noise Modelling at Ship Hydrodynamic Laboratories 494

G. A. Matveyev and A. S. Gorshkoff

Fluid Jets and Fluid Sheets: A Direct Formulation 500

P. M. Naghdi

Discussion 516

SESSION VII: GEOPHYSICAL FLUID DYNAMICS

The Boussinesq Regime for waves in a Gradually Varying Channel 523

John W. Miles

Study on Wind Waves as a Strongly Nonlinear Phenomenon 529

Yoshiaki Toba

An Interaction Mechanism betwee Large and Small Scales for Wind-Generated Water Waves 541

Marten Landahl, Sheila Widnall, and Lennart Hultgren

Preliminary Results of Some Stereophotographic Sorties Flown Over the Sea Surface 555

L. H. Holtuijsen

Gerstner Edge Waves in a Stratified Fluid Rotating about a Vertical Axis 570

Eric Mollo-Christensen

The Origin of the Oceanic Microstructure 574

Grigoriy I. Barenblatt and Andrei S. Monin

SESSION VIII: GEOPHYSICAL FLUID DYNAMICS

The Rise of a Strong Inversion Caused by Heating at the Ground 585

Robert R. Long and Lakshmi H. Kantha

Laboratory Models of Double-Diffusive Processes in the Ocean 596

J. Stewart Turner

Buoyant Plumes in a Transverse Wind 607

Chia-Shun Yih; Appendix by J. P. Benqué

Internal Waves 618

O. M. Phillips

Breaking Internal Waves in Shear Flow 623

S. A. Thorpe

LIST OF PARTICIPANTS 629

Introductory Address

Dr. Courtland D. Perkins
President, National Academy of Engineering

On behalf of the National Academy of Engineering and the National Academy of Sciences it is my distinct pleasure and privilege to welcome you to our Nation's Capitol, to the home of both Academies, and to the Twelfth Symposium on Naval Hydrodynamics.

We have welcomed the opportunity to join with the Office of Naval Research and the David W. Taylor Naval Ship Research and Development Center in organizing and hosting the Twelfth Symposium in this distinguished series of meetings.

We have, as a matter of fact, a special interest in the continuing success of the series since we cosponsored the First and Second Symposia with the Office of Naval Research in 1956 and 1958. Therefore, it is as gratifying for us as it must be for the Office of Naval Research to find that the international community of fluid dynamics and related specialties continues to find these meetings a unique forum for the exchange of research results and the discussion of problem areas of concern to both military and commercial activities.

The interest and the involvement of the Academies in naval science and engineering, of course, has a much longer history. After a careful reading of the early history of the National Academy of Sciences, one is persuaded that the Academy would not have come into being in 1863 had it not been for the carefully laid plan and persuasive arguments of the Navy's Chief of Navigation, Commodore Charles Henry Davis. One is further impressed by the fact that perhaps a quarter of those who signed the Academy's Charter were affiliated with the Navy in one way or another. And it is significant that the first five studies conducted by the fledgling Academy were requested by the Navy. In case some of you may be interested, these were:

On Protecting the Bottom of Iron Vessels
On Magnetic Deviation in Iron Ships
On Wind and Current Charts
Sailing Directions
On the Explosion On the United States Steamer CHENANGO

I don't want to leave you with the impression that the Academy worked only on naval problems during the 1863-65 period. We did another study entitled "On the Question of Tests for the Purity of Whiskey" --an investigation undoubtedly stimulated by President Lincoln's remark that he wished he could supply all his generals with whatever it was that General Ulysses S. Grant was drinking.

I have taken this short detour through some early Academy history, not so much to demonstrate our own long and continuous interest in naval science and engineering but to recognize the important role played by the Navy in supporting science and engineering throughout its 200-year history. Over the past 32 years the Office of Naval Research has continued that tradition by serving as a model for enlightened government support of basic research.

On a more personal note may I conclude by saying that as a former professor of aeronautical engineering at Princeton University your technical program is of special interest to me. Therefore, I wish you an interesting and productive meeting. We are pleased that you have chosen to meet at our institution, and the staff we have assembled to support you is available to assure that your stay is a pleasant one.

Introductory Address

Rear Admiral Robert K. Geiger, USN
Chief, Office of Naval Research

On behalf of the Office of Naval Research I would like to extend a sincere welcome to all the participants of the Twelfth Symposium on Naval Hydrodynamics.

I wish to express my thanks to the National Academy of sciences for its assistance and role as a host and cosponsor of the Symposium through its National Research Council.

Thanks are also due to the third member of the triumvirate of cosponsors of this, the Twelfth Symposium on Naval Hydrodynamics, namely the David W. Taylor Naval Ship Research and Development Center, known more familiarly to most of us old-timers as the David Taylor Model Basin and often referred to affectionately as DTMB. This facility has been a major contributor to the scientific program of each of the Symposia in this series, as a glance at the proceedings of any of the Symposia will confirm. I am happy to say that the present meeting is no exception and that it is again well represented on the technical program. However, this is the first time that it has participated as a cosponsor and I am especially pleased to acknowledge the invaluable assistance that our old colleague and ally in the field of naval hydrodynamics research has rendered in the organization and management of the present Symposium.

The first two Symposia of this series were held in 1956 and 1958 and were also sponsored by the Office of Naval Research and the National Academy of Sciences. Many of the guiding principles that govern the organization of the Symposia in this series were established in these first meetings. For example, the selection of a limited number of central themes of timely naval hydrodynamic interest upon which to focus the technical program of the meeting was introduced in the Second Symposium.

From the very beginning, the international aspects of the Symposia were emphasized through the invitation of speakers from all over the world wherever outstanding research in naval hydrodynamics was going on. Starting with the Third Symposium, the international aspects were strengthened by locating the meetings outside the United States and cosponsoring them with relevant organizations in host countries.

The list of such meetings includes Symposia held in the Netherlands, Norway, Italy, France, and England, and we hope to continue this pattern into the future as long as the series of Symposia continue to provide a useful forum for the exchange of valuable information on results of advanced research in the field of naval hydrodynamics.

I am gratified to see so many representatives of several countries in addition to the United States, and the number of technical papers presented by internationally known authorities in fluid dynamics and related fields.

For the Navy, progress in hydrodynamics research has become increasingly urgent. The Navy must find ways to discover and correct the problems that a new design may run into before reaching the point of full-scale sea trials.

Since the sea is the Navy's business and we have been involved in it a long time, we are expected to know it well. Only investigators like yourselves are aware of how limited is our knowledge of the forces that impact on a buoyant body propelled through the water. As much as our understanding has increased, we know we have much more to learn. This information can only be obtained through the arduous bit-by-bit process of basic research, such as you gentlemen pursue.

Today our nation is faced with the dilemma that we must plan types of ships that are radically different in design from anything in the past. At the same time, these ships must be inexpensive to operate and maintain in addition to satisfying our traditional standards.

The results of the research that will be reported at this Symposium should help us move toward that formidable goal. It is clear that all of you here today are dedicated scientists, so I do not need to urge you to keep pressing forward in your search for solutions to the frustrating problems in hydrodynamics. I would like to stress, however, that you maintain strong lines of communication so that as many people as possible can benefit when you inevitably succeed in your endeavors.

Best wishes for a successful symposium.

Introductory Address

Captain Myron V. Ricketts, USN
Commander, David W. Taylor
Naval Ship Research and Development Center

We at the David W. Taylor Naval Ship Research and Development Center are both pleased and proud to join with the Office of Naval Research and the National Academy of Sciences in sponsoring the Twelfth Symposiumon Naval Hydrodynamics. While not a sponsor of the four earlier symposia held in Washington, the Center was directly and indirectly involved with all of the previous meetings. Of the forty-one papers to be presented at the present Symposium, five are authored by Center researchers, roughly the same number of papers given by Center authors at earlier symposia. In addition, much of the other U.S. research to be presented in papers to this Symposium was supported by the U.S. Navy's General Hydrodynamics Research Program which the Center has administered for nearly thirty years.

It is worthy to note that this year's conference is directed mainly at the underlying physics of hydrodynamic processes. The papers are of quite a fundamental nature, perhaps more so than was true of many of the earlier symposia. The Symposium topics are of immense importance to both the merchant ship and naval communities: *Boundary Layer Stability and Transition* because of their relationship to vehicle drag, cavitation inception, and flow noise; *Ship Boundary Layers and Propeller/Hull Interaction* because a need to accurately predict vehicle drag, propulsive efficiency, and vibration; *Cavitation*, a very major cause of erosion, vibration, and noise; and finally, *Geophysical Fluid Dynamics* which describes the environment in which ocean systems must operate. Each topic area is a subject of current and lively interest and has witnessed remarkable advances over the past few years.

The very high quality of the research papers to be presented this week is typical of previous Naval Hydrodynamics Symposia and has earned for the series the reputation of being the preeminent international conferences on ship hydrodynamics. Each symposium has constituted an exceedingly valuable open forum which promotes national and international ties and dialogues between researchers in the field of hydrodynamics.

I would like to close by saying that my Center's namesake, Admiral David W. Taylor, the U.S. pioneer hydrodynamicist and foremost naval architect, introducer to the U.S. of towing tanks, water tunnels, transformer of empiricism to scientific methods, would be very pleased to be associated with the Twelfth Symposium on Naval Hydrodynamics. On Wednesday we look forward to welcoming you on a tour of the hydrodynamic facilities at the Center. You will see work in progress at our rotating arm facility, seakeeping basin, towing tanks and turning basin, and at our largest cavitation tunnel. Best wishes for a very successful conference.

Session I

BOUNDARY LAYER STABILITY AND TRANSITION

PHILLIP. S. KLEBANOFF
Session Chairman
National Bureau of Standards
Washington, D.C.

Stability and Transition Investigations Using the Navier-Stokes Equations

Hermann F. Fasel
Universität Stuttgart
Stuttgart, Federal Republic of Germany

SUMMARY

With this paper an attempt is made to review the stability and transition simulations, performed at the University of Stuttgart, which are based on finite-difference solutions of the Navier-Stokes equations. Research in this area has demonstrated that implicit finite-difference methods for the solution of the complete Navier-Stokes equations for unsteady, two-dimensional, incompressible flows can be successfully applied to investigations of hydrodynamic stability and to certain aspects of transition. This approach of numerically solving the partial differential equations describing the underlying flow mechanisms promises to be a valuable aid in transition research. In particular, this concept may prove to be especially rewarding for investigations of aspects of stability and transition which as yet are not feasible with other theoretical models.

There are two main reasons for the attractiveness of this approach: Firstly, no assumptions whatsoever have to be made concerning the basic flow field under investigation. Thus, for example, all possible effects resulting from the growth of a boundary layer in downstream direction can be included in such investigations. Even strongly converging or diverging flows, or flows with separation and/or reattachment can be studied. Secondly, no restrictions have to be made concerning amplitude and form of the disturbances which are injected into the flow. Therefore, using larger disturbance amplitudes certain nonlinear effects of the amplification process can be readily investigated.

The major aspects of this approach will be discussed in this paper. Emphasis will be placed not only on conveying the advantages of such investigations but also on elaborating the difficulties and shortcomings of such numerical simulations. Finally, a conjecture concerning the course of future developments will be attempted.

1. INTRODUCTION

The phenomena occurring in transition from laminar to turbulent flow have been the subject of intensive research ever since the discovery that these two entirely different states of flow exist. From all the research efforts basically only one universally-accepted theoretical concept evolved, namely, linear stability theory, verified experimentally by the famous experiments of Schubauer and Skramstad (1943).

However, experimental evidence has also shown that linear stability theory is only applicable for one 'special' transition process, namely, transition initiated by the presence of very small disturbances in the flow. In this case a substantial portion of the entire transition process is indeed well described by this theory, i.e. the amplification of two-dimensional disturbance waves (the so-called Tollmien-Schlichting waves) can be predicted adequately. But even for this special transition process, triggered by small disturbances, linear stability theory is inadequate in the description and investigation of the mechanisms that follow the growth of Tollmien-Schlichting waves, and which finally cause the breakdown to fully turbulent flow. Nevertheless, due to the relative success of the linear stability theory and its impressive experimental verification, the vast majority of theoretical transition investigations were, and still are, based on stability theory concepts, thus constantly improving and perfecting this theory.

The inherent shortcomings of this concept nontheless (such as being applicable only when transition is initiated by small disturbances, or that certain assumptions concering the basic and disturbance flow have to be made to keep the resulting equations tractible) led to a search for other means to investigate transition. One of the more promising concepts that has emerged in recent years is based on direct numerical solutions of the complete partial differential equations that describe the flow phenomena arising in the transition process. This approach became feasible with the rapid progress in the development of large, high-speed digital computers.

The main difficulties here arise from the fact that these flow phenomena can be adequately represented only when the complete Navier-Stokes equations (or certain modifications thereof) are used. Thus, this approach requires the solution of the Navier-Stokes equations for strongly time-varying flow fields, due to the highly unsteady nature of the transition processes. Additionally, complications increase because the numerical solutions have to yield reliable results for relatively high Reynolds numbers (higher than the critical Reynolds number) to allow onset of transition. For a numerical solution procedure it is therefore necessary to allow for adequate resolution of the large temporal and spatial gradients resulting from the occurrence of thin time-varying fluid layers with large gradients close to solid walls.

The development of finite-difference methods, which are applicable for such complex, unsteady flow phenomena as those occuring in laminar turbulent transition, is associated with numerous difficulties which will be elaborated upon in this paper. Because of these difficulties relatively few previous attempts based on such an approach became known. Reasonably successful earlier investigations of this kind (based also on finite-difference solutions) are reported, for example, for incompressible flows in a boundary layer [De Santo and Keller, (1962)], for Poiseuille and plane Poiseuille flow [Dixon and Hellums (1967), Crowder and Dalton (1971)] and for a compressible boundary-layer flow [Nagel (1967)]. These earlier attempts clearly demonstrated the usefulness and potential of such investigations. However, due either to insuffcient resolution of the resulting gradients and/or assumptions made concerning the basic or disturbance flows, or to shortcomings of the difference methods used, the results of these calculations were more of a qualitative nature. Therefore, relatively little information could be gained concerning the various phenomena arising in the laminar-turbulent transition process.

Some years ago, a research effort was initiated at the University of Stuttgart aiming at the development of numerical methods for the solution of the Navier-Stokes equations which would be applicable for detailed investigations of various aspects of stability and of phenomena occurring in transition. To date, an effective implicit finite-difference method has evolved for the calculation of unsteady, two-dimensional incompressible flows. The applicability of the numerical method to investigate stability and two-dimensional transition phenomena has been demonstrated by realistic simulations of Tollmien-Schlichting waves. Detailed results of these calculations are discussed elsewhere [Fasel (1976)]. With calculations involving large amplitude disturbances [Fasel et al. (1977)] it was additionally shown that numerical simulations using the implicit difference method yield results which enable insight into certain nonlinear mechanisms of the transition process.

In this paper the major aspects of the numerical approach using finite-difference methods will be reviewed and the present state of the developments discussed. Emphasis will be placed on the advantages of the numerical approach in general and on directional options chosen for the present method. Special attention will also be focused on the difficulties and limitations of such simulations.

2. SELECTION OF THE INTEGRATION DOMAIN

For a numerical solution of the Navier-Stokes equations using finite-difference techniques a finite domain in which the equations are being solved has to be specified. The selection of the integration domain determines the nature of a physical flow problem to be simulated, because the boundary conditions required along the boundaries of this domain determine to a large degree the solution within the domain. For reasons of simplicity, in the present studies only rectangular domains of the x,y plane were considered as depicted schematically in Figures 1 and 2 with the direction of the basic, undisturbed flow being in the x-direction. Rectangular domains allow relatively easy application of difference methods by using simple rectangular meshes. For example the rectangular domain may be a section of a boundary-layer flow on a semi-infinite flat plate (Figure 1) or a section of a flow between two parallel plates (Figure 2).

In selecting the integration domain one has to consider that boundary conditions must be found for the 'artificial' boundaries B-C in Figures 1 and 2 and additionally for C-D in Figure 1. These conditions should allow physically meaningful solutions in the finite domain, i.e. solutions that would be obtained if the domain were not made finite by means of these artificial boundaries. Due to the spatially elliptic (in x,y) character of the Navier-Stokes equations application of finite-difference methods requires boundary conditions on all boundaries of the x,y domain. Of course, in a mathematical sense the equations are parabolic because of the time derivative (See section 3). Selection of boundary conditions for boundaries representing solid walls (such as A-B in Figures 1 and 2 and C-D in Figure 2) generally creates no additional difficulty although consistent implementation in the numerical scheme is frequently difficult to achieve. Also, free stream boundaries such as C-D in Figure 1 for the boundary-layer flow can be handled in satisfactory fashion (see Section 4).

However, the upstream (A-D) and to a larger extent the downstream (B-C) boundary require special considerations because the specific treatment of these boundaries determines the approach to be taken in a prospective stability and transition simulation. In selecting the boundary conditions

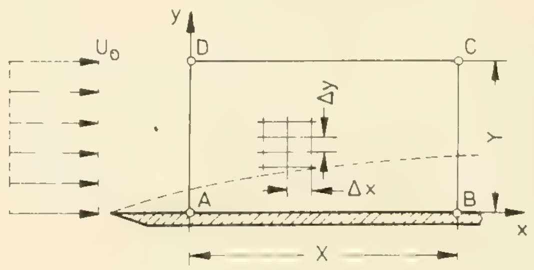

FIGURE 1. Integration domain for boundary layer on flat plate.

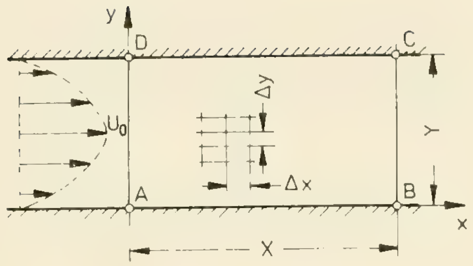

FIGURE 2. Integration domain for plane Poiseuille flow.

there are basically two different approaches which lead to entirely different conceptions of the transition simulation:

1) Use of periodicity conditions at the upstream (A-D) and downstream (B-C) boundary, i.e. corresponding disturbance quantities are equal at the two boundaries for all times.

Here it is assumed that flow phenomena are spatially periodic in downstream direction where the integration domain X contains integer multiples of the spatial wavelength. When the spatial development is forced to be periodic, the flow responds with a temporal development. Thus, with this arrangement the temporal reaction of the flow to an initial disturbance (at t=0) of the flow field can be studied. This case corresponds in linear stability theory to an eigenvalue problem with wave number α real and frequency β complex ($\beta=\beta_r+i\beta_i$), i.e. amplification in time. Figure 3, for example, shows a typical result of a finite-difference calculation based on such an approach for a plane Poiseuille flow [Bestek and Fasel (1977)]. Plotted here is a time signal for a case which is unstable according to linear stability theory. The flow is only disturbed once at t=0. After a certain time span, where considerable reorganization of the disturbance flow takes place, the disturbances assume a periodic character with a slight amplification in time-direction.

The Navier-Stokes calculation for this approach may be conceived as a means of solving the eigenvalue problem as in linear stability theory, with α and Reynolds number given and obtaining the frequency β_r, amplification rate β_i, and the amplitude distribution of the distrubance flow. Of course these answers could be obtained with considerably less effort from linear stability analysis. The advantage of this present approach is, however, that it can be easily extended to investigations of certain nonlinear effects by merely increasing the amplitude level of the initial disturbances [see, for example, George and Hellums (1972)]. An equivalent study of nonlinear effects formulated as an eigenvalue problem in a stability theory analysis would, on the other hand, become considerably more involved.

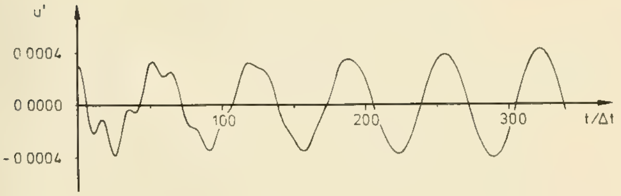

FIGURE 3. Temporal development of u'-disturbance at $y/\Delta y = 3$ for initially disturbed flow (small amplitude); spatially periodic case (plane Poiseuille flow).

A major drawback of this first approach is, however, that it is pratically only applicable for basic flows that do not vary in downstream direction (parallel flows), because only then is the periodicity assumption for the disturbance flow a realistic one. Thus, strictly speaking, boundary-layer flows could not be treated in this manner since they are basically (although very mildly) non-parallel. It has been shown that non-parallel effects can have a strong influence on the stability characteristics of this flow [Gaster (1974), Saric et al. (1977)].

A second, perhaps even more serious disadvantage of this model is that the disturbance development in downstream direction cannot be investigated. As observed in numerous laboratory experiements the phenomena of transition are not periodic in space but rather are inherently space dependent. The disturbance flow may vary rapidly in downstream direction. This space dependency of the transition process does not only occur for flows where the basic flow is already dependent on the downstream location. It also occurs when the basic flow does not vary in downstream direction, as was impressively demonstrated experimentally by Nishioka et al. (1975) for the parabolic profiles of plane Poiseuille flow between parallel plates. Thus, this model is not suitable for realistic studies of transition phenomena.

However, finite difference simulations based on this approach become considerably less involved and are less costly in practical execution than for the second approach discussed subsequently. The former approach is therefore applicable for fundamental investigations of various unresolved questions in hydrodynamic stability (such as certain nonlinear effects) or for preliminary studies of flow simulations based on the approach discussed below.

2) At the upstream boundary, time-dependent disturbances are introduced. Use of boundary conditions at the downstream boundary which allow downstream propagation of the spatial disturbance waves.

This second approach differs entirely in concept from the first one. Here, the reaction of the flow field to the disturbances introduced at the upstream boundary is of interest, particularly the spatial developments of the ensuing disturbance waves. In contrast to the previous approach, this case corresponds in stability theory to an eigenvalue problem with α complex ($\alpha=\alpha_r+i\alpha_i$) and β real. A typical result for a boundary-layer flow of a calculation based on this concept is shown in Figure 4. Plotted is the disturbance variable u' (velocity component in x-direction) versus the downstream coordinate x. The downstream development of the disturbance (in this case amplification) may be clearly observed. Thus, this approach enables the calculation of the spatial reaction of the flow to upstream disturbances, and therefore realistic simulations of space-dependent transition phenomena

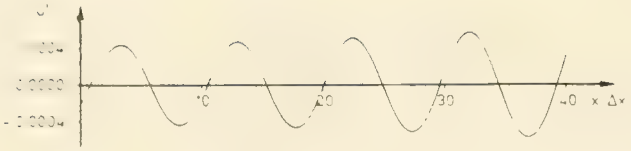

FIGURE 4. Downstream development of u'-disturbance at y/Δy = 3 for boundary-layer flow disturbed periodically (small amplitude) at upstream boundary.

as observed in laboratory experiments should be possible.

For example, realistic numerical simulations of Tollmien-Schlichting waves (as observed in the Schubauer and Skramstad experiments) can be performed by using at the upstream boundary A-D periodic disturbances as produced by a vibrating ribbon in the physical experiments. If the location of A-D is considered to be somewhat downstream of the ribbon in the real experiments, eigenfunctions of linear stability theory may be conveniently used to disturb the flow in the numerical simulation. It was shown that the disturbance flow somewhat downstream of the ribbon is well described by linear stability theory when amplitudes are small.

The disadvantage of the second approach is that the development of numerical methods to solve the resulting mathematical problem is considerably more difficult than in the first approach. Although in a strict mathematical sense both problems represent mixed initial-boundary-value problems, the main difference between the two concepts is that the first approach results in a predominantly initial value problem, where the temporal evolution of an initially disturbed flow field is calculated.

The second concept leads to a predominantly boundary-value problem where the spatial reaction of the flow field (which is also time-dependent, of course) to disturbances introduced on the left boundary is to be calculated. In the latter case difficulties arise from the necessity of finding adequate downstream boundary conditions which allow unhindered passage of the disturbance waves propagating downstream, and properly implementing them into the numerical method. Since the aim of this research effort is directed toward realistic simulations of transition phenomena, emphasis in the development of finite-difference methods was placed on methods that were applicable to solving the mathematical problem resulting from the latter approach. The remainder of the discussions in this paper are therefore also based on this concept.

3. FORMULATIONS OF NAVIER-STOKES EQUATIONS FOR NUMERICAL METHODS

The Navier-Stokes equations can be cast into various forms to be used as basis for a finite-difference method. Each formulation has its inherent advantages and disadvantages. The decision in favour of a particular formulation has to be governed by the physical flow problem to be investigated and by the difference scheme finally used. In most cases, and also particularly for the present investigations, such a decision is difficult to make beforehand. Extensive preliminary numerical experiments are necessary before a decision can be made in favour of a particular formulation.

For two-dimensional, incompressible flows the stream-function-vorticity formulation is most widely used in numerical fluid dynamics. It is also a possible choice for the present investigations. It consists of the vorticity-transport equation

$$\frac{\partial \omega}{\partial t} + u\frac{\partial \omega}{\partial x} + v\frac{\partial \omega}{\partial y} = \frac{1}{Re}\Delta\omega \quad , \qquad (1)$$

and a Poisson equation for the stream function

$$\Delta\psi = \omega \quad , \qquad (2)$$

where Δ is the Laplace operator, ω is defined as

$$\omega = \frac{\partial u}{\partial y} - \frac{\partial v}{\partial x} \quad , \qquad (3)$$

and the stream function as

$$\frac{\partial \psi}{\partial y} = u \quad , \quad \frac{\partial \psi}{\partial x} = -v \qquad (4)$$

With this definition of the stream function the continuity condition

$$\frac{\partial u}{\partial x} + \frac{\partial v}{\partial y} = 0 \qquad (5)$$

is satisfied for the continuum equations, however, not necessarily for the discretized equations. All variables in Eqs. (1) to (5) are dimensionless; they are related to their dimensional counterparts, denoted by bars, as follows

$$x = \frac{\bar{x}}{L} \, , \; y = \frac{\bar{y}}{L} \, , \; u = \frac{\bar{u}}{U_0} \, , \; v = \frac{\bar{v}}{U_0} \, , \; t = \frac{\bar{t}U_0}{L},$$

$$\omega = \frac{\bar{\omega}L}{U_0} \, , \; Re = \frac{U_0 L}{\bar{\nu}} \, , \; \psi = \frac{\bar{\psi}}{U_0 L} \, ,$$

where L is a characteristic length, U_0 a reference velocity and Re a Reynolds number (ν kinematic viscosity). Thus this formulation represents a system of two partial differential equations, each of second order, for the unknown variables ω and ψ because u and v in Eq. (1) can be eliminated using Eq. (4).

A variation of this formulation is the so-called conservative form for which the vorticity-transport equation

$$\frac{\partial\omega}{\partial t} + \frac{\partial(u\omega)}{\partial x} + \frac{\partial(v\omega)}{\partial y} = \frac{1}{Re}\Delta\omega \qquad (6)$$

is used instead of Eq. (1). With this formulation conservation of vorticity is guaranteed for the continuum equations.

A second formulation of the governing equations also consists of a vorticity-transport equation (1) or (6). However, instead of the Poisson equation, (2), for ψ, two Poisson equations for the velocity components u and v are used

$$\left\{ \begin{aligned} \Delta u &= \frac{\partial \omega}{\partial y} \quad , \\ \Delta v &= -\frac{\partial \omega}{\partial x} \quad , \end{aligned} \right. \qquad (7)$$

which can be derived from the definition of vorticity, (3), using the continuity equation, (5). This system of partial differential equations for the ω,u,v formulation is of higher order than the ω,ψ system. The higher order allows less restrictive boundary conditions which is advantageous in applications to transition simulations as discussed in Section 4.

A third form of the governing equations is the so-called primitive variable formulation with the two momentum equations

$$\left\{\begin{aligned} &\frac{\partial u}{\partial t} + u\frac{\partial u}{\partial x} + v\frac{\partial u}{\partial y} = -\frac{\partial p}{\partial x} + \frac{1}{Re}\,\Delta u, \\ &\frac{\partial v}{\partial t} + u\frac{\partial v}{\partial x} + v\frac{\partial v}{\partial y} = -\frac{\partial p}{\partial y} + \frac{1}{Re}\,\Delta v, \end{aligned}\right. \qquad (8)$$

(where $p = \bar{p}/\bar{\rho}U_0^2$, with density $\bar{\rho}$) and a Poisson equation for the pressure

$$\Delta p = 2\,\frac{\partial u}{\partial x}\,\frac{\partial v}{\partial y} - 2\,\frac{\partial v}{\partial x}\,\frac{\partial u}{\partial y}\;, \qquad (9)$$

which is derived from Eq. (8) using the continuity Eq. (5).

There is also a conservative form of the primitive variable formulation (conserving momentum)

$$\left\{\begin{aligned} &\frac{\partial u}{\partial t} + \frac{\partial (u^2)}{\partial x} + \frac{\partial (uv)}{\partial y} = -\frac{\partial p}{\partial x} + \frac{1}{Re}\,\Delta u\;, \\ &\frac{\partial v}{\partial t} + \frac{\partial (uv)}{\partial x} + \frac{\partial (v^2)}{\partial y} = -\frac{\partial p}{\partial y} + \frac{1}{Re}\,\Delta v\;, \end{aligned}\right. \qquad (10)$$

and a Poisson equation in a now different form

$$\Delta p = -\frac{\partial^2 (u^2)}{\partial x^2} - 2\,\frac{\partial^2 (uv)}{\partial x \partial y} - \frac{\partial^2 (v^2)}{\partial y^2} - \frac{\partial D}{\partial t} + \frac{1}{Re}\,\Delta D, \quad (11)$$

with the so-called dilation term

$$D = \frac{\partial u}{\partial x} + \frac{\partial v}{\partial y} \qquad (12)$$

The absence of the dilation terms in a Poisson equation for the pressure may cause nonlinear numerical instability, which can be avoided when such terms are retained (Harlow and Welch, 1965).

Conservative versus Nonconservative Formulation for Use in Transition Studies

The evaluation of the relative merits of conservative formulations over non-conservative ones is a widely investigated subject in numerical fluid dynamics [Roache (1976), Fasel (1978)]. Nevertheless, satisfactory answers have not yet been found except for compressible flows for which conservative formulations are obviously advantageous. One argument in favour of conservative formulations is that better accuracy can be obtained. However, for incompressible flow problems there are several examples contradicting this claim. When evaluating possible advantages of a conservative formulation one has to keep in mind that the respective quantities (such as vorticity in the ω,ψ or ω,u,v formulation or momentum for the u,v,p formulation) are initially only conserved for the continuum equations. The conservation property may be carried over to the discretized equations only if certain difference approximations (in this case, central differences) are used. For the implementation of the boundary conditions it is frequently very difficult or sometimes impossible to employ such difference approximations required to maintain the conservation properties for the discretized equations.

For the present investigations, comparison calculations during the early stage of the development of the numerical method have shown that, for the ω,ψ or ω,u,v systems, almost equivalent accuracy can be obtained with either formulation. Because the conservative formulation leads to a somewhat slower solution algorithm for the solution of the difference equations, preference was given therefore to a non-conservative formulation.

Vorticity Transport (ω,ψ or ω,u,v) versus Primitive Variable (u,v,p) Formulation

In reviewing literature on numerical simulations of viscous incompressible flows it is noticeable that formulations involving a vorticity-transport equation, rather than the primitive variable formulation, are preferred. The unpopularity of the u,v,p system is a result of numerable unsuccessful attempts in applying it to calculations of viscous incompressible flows. Although a few successful applications based on the u,v,p system are reported in more recent literature, there are still serious arguments against its use for stability and transition simulations. Difficulties result from problems associated with the use of a Poisson equation for the pressure. This equation is often a source of numerical instabilities, possibly due to difficulties of properly implementing the boundary conditions for pressure into the numerical scheme. Although the numerical instabilities could be brought under control, at least to a degree, (for example by introducing the dilation terms in Eq. 11) so that solutions could be obtained for steady flow problems, the inherent inclination of this formulation to numerical instability still prohibits its use for transition simulations. Frequently numerical solutions based on this system are of a slightly oscillatory nature (although amplitudes are extremely small) and therefore interaction with oscillations of the physically meaningful disturbances as occurring in transition studies cannot be avoided.

For these reasons finite-difference methods devised for investigations of stability and transition are based on the equations in vorticity transport form, i.e. either on the ω,ψ system (Eqs. 1 and 2) or the ω,u,v system (Eqs. 1 and 7). Nevertheless current efforts are also directed toward development of difference methods based on the equations in primitive-variable formulation. Emphasis is placed on extreme numerical stability in order to make this method also applicable for stability and transition studies. The continuing attraction of the equations in primitive-variable form results from the fact that, for the three-dimensional case, fewer fields of variables have to be stored than for a vorticity-transport formulation. For the three-dimensional case, storage requirements are an order of magnitude even more critical than for the two-dimensional calculations.

Use of Navier-Stokes Equations for the Disturbance Flow

For stability and transition simulations, the dependent variables, which appear in the different formulations of the Navier-Stokes equations discussed previously, are those of the total flow, that is, including both the basic and the disturbance flow. There is an alternate approach, namely, to decompose the total flow into the basic flow and a disturbance flow such that

$$u=U+u' \ , \ v=V+v' \ , \ p=P+p' \ , \ \psi=\Psi+\psi' , \ \omega=\Omega+\omega' , \quad (13)$$

where the prime indicates the variables of the disturbance flow and the capital letters denote those of the basic flow. Substituting relationships (13) into various forms of the Navier-Stokes equations, it is possible to rewrite the equations with the disturbance variables as dependent variables. Several terms involving only the basic flow can be dropped, assuming the basic flow satisfies the Navier-Stokes equations.

The aspect of directly solving the equations for the disturbance variables is an attractive one, since it is the disturbance conditions that are of interest when performing numerical stability and transition studies. For this reason this approach has probably been preferred in earlier attempts. It also allows for detailed investigations of the effects of the nonlinear (convective) terms because, in a difference method based on this form, the 'linearization' can be conveniently switched on or off.

A careful evaluation of this form of equations, however, reveals that it also has some major disadvantages. The equations in disturbance form contain several additional terms (involving disturbance terms with terms of the basic flow) which are not present in a corresponding formulation for the total flow. Thus, in finite-difference solutions additional numerical operations are required. A more serious disadvantage is that, because of the additional terms involving the basic flow, the basic flow quantities have to be kept in fast-access computer storage to be readily accessible for the numerical operations in order to avoid excessive computation times. On the other hand, using the equations for the total flow the basic flow quantities are not directly involved in the solution algorithm. In this case they are only required for analysis and better respresentation of the results (for example to determine the disturbance quantities). For this purpose they can be stored in mass storage of lower speed accessibility.

The availability of sufficient fast-access storage is, even with the latest computer generation, still a critical limitation for such numerical investigations of stability and transition. For large scale simulations involving large numbers of grid points, use of the disturbance formulation is prohibitive. For this reason, for the present research effort, use of the equations for the total flow variables was generally preferred instead of the disturbance formulation. However, the basic solution algorithm of the definite-difference method was developed such that it is applicable with only minor modifications for either formulation.

4. BOUNDARY AND INITIAL CONDITIONS

The selection of adequate boundary conditions and the practical implementation into a finite-difference scheme represents one of the major difficulties in the development of a finite-difference model applicable for stability and transition studies. Difficulties arise from the necessity that boundary conditions, selected and implemented along the artificial boundaries (see Section 2) for the finite integration domain, have to enable solutions that would be identical to solutions if the governing equations were solved in the infinite domain. There is, of course, no way of checking this because solutions for the infinite domain are not available. This indicates that, for selecting boundary conditions, it is necessary to rely on experience, intuition, and test calculations.

For practical reasons the boundary conditions at these artificial boundaries have to be such that physically meaningful results can be obtained with a relatively small integration domain. The number of grid points, and therefore computer storage and amount of numerical operations required for a numerical solution, is directly dependent on the size of the integration domain. Thus, only with a relatively small domain may the computational costs of numerical simulations be kept within acceptable limits. This aspect is of particular importance during the testing phases of the numerical methods.

There are also other difficulties resulting from the complicated nature of the governing equations. For the nonlinear systems of governing equations in the formulations of Section 3 it is not yet possible to decide if a given problem consisting of the governing equations and a set of boundary conditions is well-posed in the sense of Hadamard (1952). Moreover, it is not obvious whether Hadamard's postulates for a well-posed problem are adequate to include physically meaningful solutions only. Additional difficulties may arise because finite-difference methods frequently require more boundary conditions than would be needed for the original differential formulation if exact solutions were possible [Richtmyer and Morton (1967)]. From numerical experimentation with model equations simpler than the full Navier-Stokes equations it is known that these additional 'numerical' boundary conditions are often a source of numerical instabilities possibly caused by certain inconsistencies. Therefore, one is confronted with the delicate task of selecting and implementing the extra conditons (where it is normally not known a priori which conditions are the extra ones) in such a way that the numerical stability of an otherwise stable method would not be adversely affected.

Initial Conditions

When the simulation of space dependent transition phenomena is of interest as in the present investigation the reaction of the flow to disturbances introduced at the upstream boundary has to be calculated. In this case one may assume an undisturbed flow as initial condition at t=0 enabling the disturbance waves introduced for t>0 to propagate downstream into an undisturbed flow field. Denoting the undisturbed flow field with capital letters the initial conditions for the ω,ψ system can be written as

$$\begin{cases} \omega(x,y,0) = \Omega(x,y) \quad , \\ \psi(x,y,0) = \Psi(x,y) \quad , \end{cases} \tag{14}$$

and for the ω,u,v system

$$\begin{cases} \omega(x,y,0) = \Omega(x,y) \quad , \\ u(x,y,0) = U(x,y) \quad , \\ v(x,y,0) = V(x,y) \quad , \end{cases} \tag{15}$$

The undisturbed flow field is obtained by solving the Navier-Stokes equations for the steady flow. Of course, for the flow between two parallel plates the Poiseuille profiles already represent exact solutions of the Navier-Stokes equations and can therefore be used directly. For the boundary-layer flow a solution has to be calculated numerically by solving the Navier-Stokes equations without the unsteady term $\partial\omega/\partial t$ in Eq. (1). The argument could be raised that in this case Blasius profiles could be used instead. The differences between the Blasius solution and a numerical Navier-Stokes solution are indeed very small. Nevertheless, for investigations with very small disturbance amplitudes, the differences can be of the same order of magnitude as the disturbances themselves and therefore the transient character of the flow could become considerably distorted. The boundary conditions used for the calculation of the undisturbed, basic flow are discussed subsequently in connection with the conditions used for the calculation of the unsteady, disturbed flow.

Boundary Conditions

At solid walls (non-permeable, no-slip), such as boundary A-B of Figure 1 or A-B and C-D of Figure 2, the velocity components vanish

$$u=0 \quad , \quad v=0 \quad , \quad U=0 \quad , \quad V=0 \quad . \tag{16}$$

The vorticity-transport formulations (the u,v,p formulation will not be discussed further) require special treatment for the vorticity calculation at the walls. For the ω,ψ formulation vorticity can be calculated from the relationship

$$\omega = \frac{\partial^2\psi}{\partial y^2} \tag{17}$$

derived from Eq. (2); for the ω,u,v formulation either

$$-\frac{\partial\omega}{\partial x} = \frac{\partial^2 v}{\partial y^2} \tag{18}$$

derived from Eq. (7b) or

$$\omega = \frac{\partial u}{\partial y} \tag{19}$$

resulting from Eq. (3) can be used. Equations (17)-(19) are applicable for the calculation of both the steady, undisturbed and the unsteady, disturbed flow.

At the upstream boundary A-D the disturbances are introduced by superimposing onto the profiles of a basic, undisturbed flow (denoted by subscript B; for example, Blasius profiles or Poiseuille profiles could be used for the cases considered in Figures 1 and 2) so-called perturbation functions which are dependent on y and t only. Thus for the ω,ψ formulation we have

$$\begin{cases} \omega(0,y,t) = \omega_B(y) + P_\omega(y,t) \quad , \\ \psi(0,y,t) = \psi_B(y) + P_\psi(y,t) \end{cases} \tag{20}$$

and for the ω,u,v formulation

$$\begin{cases} \omega(0,y,t) = \omega_B(y) + P_\omega(y,t) \quad , \\ u(0,y,t) = u_B(y) + P_u(y,t) \quad , \\ v(0,y,t) = v_B(y) + P_v(y,t) \quad . \end{cases} \tag{21}$$

For the calculation of the steady, undisturbed flow field the perturbation functions in Eqs. (20) and (21) of course vanish. For simulations of Tollmien-Schlichting waves, for example, the perturbation functions are periodic in time where amplitude distributions (or so-called perturbation profiles) as obtained from linear stability theory can be used.

The freestream boundary C-D (Figure 1) for the boundary-layer flow is an artificial boundary and requires special considerations as discussed in Section 2. For both the calculation of the steady flow and the unsteady, disturbed flow, vorticity is assumed zero ($\omega'=\Omega=0$). For boundary-layer type flows, vorticity for both basic and disturbance flow (when disturbances are introduced within the boundary layer) decays rapidly away from the wall and is practically zero at a distance of two δ (δ boundary layer thickness) from the wall.

For the calculation of the steady flow using the ω,u,v system suitable conditions for C-D are

$$U = U_{fs}(x) \tag{22}$$

where the freestream velocity $U_{fs}(x)$ may be specified according to the downstream pressure variation of the boundary layer flow. A condition for the v component can be derived from the continuity equation, (5), using Eq. (22)

$$\frac{\partial v}{\partial y} = -\frac{dU_{fs}(x)}{dx} \quad . \tag{23}$$

For the ω,ψ system a condition equivalent to Eq. (22) can be used

$$\frac{\partial\psi}{\partial y} = U_{fs}(x) \quad . \tag{24}$$

The ψ',u',v' disturbances decay relatively slowly in direction normal to the wall. For example, for Tollmien-Schlichting waves the ψ' or v' amplitude at $6\delta^*$, (for $Re^*=630$, based on displacement thickness δ^*) may still be close to 50% of the maximal amplitude. Therefore Dirichlet conditions ($u'=v'=\psi'=0$) could only be used if the freestream boundary were very far, for example $50\delta^*$, from the wall.

This would be impractical due to the excessive amounts of grid points required. On the other hand, the conditions given below allow a relatively small integration domain in y-direction. They only postulate that the disturbances decay asymtotically in y-direction. For the ω,ψ formulation such a condition is

$$\frac{\partial \psi'}{\partial y} = -\alpha\psi' \quad , \tag{25}$$

and for the ω,u,v formulation

$$\left\{ \begin{aligned} \frac{\partial u'}{\partial y} &= -\alpha u' \quad , \\ \frac{\partial v'}{\partial y} &= -\alpha v' \quad , \end{aligned} \right. \tag{26}$$

where α is the local wave number of the resulting disturbance waves. Test calculations have shown that with the conditions (25) or (26), together with the Dirichlet-type vorticity condition discussed previously, physically meaningful results can be obtained when the integration domain in y-direction includes only two to three boundary-layer thicknesses.

Selection and implementation of the boundary conditions at the downstream boundary B-C represents a very difficult task. These boundary conditions have to enable propagation of disturbances right through this boundary, where any effects causing even the slightest wave reflection have to be avoided. The conditions found most satisfactory in this respect are for the ω,ψ formulation

$$\left\{ \begin{aligned} \frac{\partial^2\omega'}{\partial x^2} &= -\alpha^2\omega' \quad , \\ \frac{\partial^2\psi'}{\partial x^2} &= -\alpha^2\psi' \quad , \end{aligned} \right. \tag{27}$$

and for the ω,u,v formulation

$$\left\{ \begin{aligned} \frac{\partial^2\omega'}{\partial x^2} &= -\alpha^2\omega' \quad , \\ \frac{\partial^2 u'}{\partial x^2} &= -\alpha^2 u' \quad , \\ \frac{\partial^2 v'}{\partial x^2} &= -\alpha^2 v' \quad . \end{aligned} \right. \tag{28}$$

Numerical experiments with conditions (27) and (28) have shown that physically reasonable results are already possible when, for periodic upstream disturbance input, the length of the integration domain includes only three to four wavelengths.

For the calculation of the steady flow (for the boundary-layer flow, for example) boundary conditions which are compatible with those of the unsteady calculations are for the ω,ψ system

$$\frac{\partial^2\Omega}{\partial x^2} = 0 \quad , \quad \frac{\partial^2\Psi}{\partial x^2} = 0 \quad , \tag{29}$$

and for the ω,u,v system

$$\frac{\partial^2\Omega}{\partial x^2} = 0 \quad , \quad \frac{\partial^2 U}{\partial x^2} = 0 \quad , \quad \frac{\partial^2 V}{\partial x^2} = 0 \quad .$$

The boundary conditions Eqs. (27) or Eqs. (28) for the downstream boundary [also Eqs. (25) and (26) for the free stream boundary] can be derived assuming neutral, periodic behaviour of the disturbance flow. However, extensive test calculations have shown that use of such conditions does not enforce a strict periodic behaviour of the disturbance flow near these boundaries. Rather, these conditions allow damping or amplification of the disturbances even on these boundaries themselves. These conditions have also proven to be applicable for calculations with periodic disturbance input of large amplitudes as well as for non-periodic disturbance input (random disturbances, for example) [see Fasel et al. (1977)].

For cases where α is not known a priori it can be determined interatively. Starting with an initial guess $\alpha_0(x)$ (α is generally a function of x, of course, although for the derivation of the boundary conditions it was assumed constant to arrive at simple relationships) an improved $\alpha(x)$ can be determined from the resulting disturbance waves developing in the integration domain. Even with relatively crude initial guesses $\alpha_0(x)$ (for example $\alpha_0=0$) this interation loop converges rapidly, and for practical purposes two or three iterations are sufficient.

There is no formal difference between the boundary conditions (27) and (28) used for the ω,ψ and ω,u,v formulation, respectively. Both sets of conditions specify relationships for the second derivatives in the disturbance variables. Nevertheless a subtle difference does exist. Condition (27) for ψ' implies that (due to the definition of ψ, Eq. 4b) for v' a relationship involving the first derivative is prescribed

$$\frac{\partial v'}{\partial x} = -\alpha^2\psi' \quad . \tag{31}$$

This is obviously more restrictive than condition (28c) where for v' a second derivative is prescribed. For small periodic disturbances the two sets of conditions lead to practically the same results, although the results with the ω,ψ system, together with conditions (27), exhibit subtle irregularities near the downstream boundary for the waves propagating through this boundary. The ω,u,v system, together with conditions (28), however become superior to the ω,ψ system with conditions (27) when larger disturbance amplitudes are involved. In this case, reflection-type phenomena can be observed in increasing manner at the downstream boundary for the ω,ψ system. For the investigation of the effects of a backward-facing step on transition [Fasel et al. (1977)] the small vortices traveling downstream are caught at the downstream boundary when the ω,ψ system and conditions (27) are used, rendering the numerical results worthless. Using conditions (28) with the ω,u,v system, on the other hand, allows smooth passage of these vortices through that boundary.

For these reasons conditions (28), in connection with the ω,u,v system, have proven to be the best choice so far in properly treating the downstream boundary. The relatively small upstream influence of these conditions can be best demonstrated with typical results from test calculations. Figure 5 for example, shows a comparison of the disturbance variable u' for calculations with small periodic disturbances where first in Eqs. (28) an adequate value for α (α=35.6, obtained from linear stability

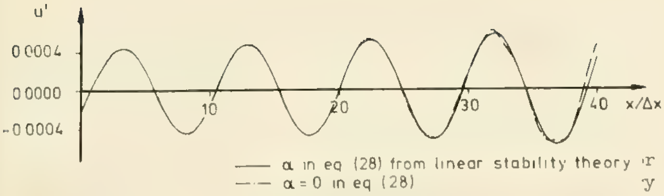

FIGURE 5. Downstream development of u'-disturbance at $y/\Delta y = 3$ for different boundary conditions at the downstream boundary (boundary layer on a flat plate).

theory) was used while for the other calculation α was simply set zero. It is obvious that even with the poor value for α the upstream influence is restricted to a region of approximately one wavelength, while the disturbance further upstream is practically unaffected. This relatively minor upstream influence can also be observed in Figure 6 where the amplification curves (for the maximum of u') are compared for the two cases. The disturbance amplification further than one wavelength upstream is practically unaffected by the value used for α in Eqs. (28).

5. NUMERICAL METHOD

A numerical method for transition studies has to generally allow for numerical solutions of a boundary-value problem for the calculation of the steady flow, i.e. solution of Eqs. (1) and (2) or Eqs. (1) and (7) (without $\partial\omega/\partial t$ in Eq. 1) with appropriate boundary conditions discussed in Section 4. Further the solution of a mixed initial-boundary-value problem for the calculation of the unsteady flow is required, i.e. solution of Eqs. (1) and (2) or Eqs. (1) and (7) with the boundary conditions for the unsteady, disturbed flow and initial conditions discussed in Section 4. The partial differential equations are of fourth order for the ω,ψ formulation and of even higher order for the ω,u,v-system. For both formulations the governing equations are elliptic for the calculation of the steady flow and parabolic for the unsteady flow. In this paper the discussion is restricted to application of finite-difference methods for the solution of the mathematical problems posed.

A difference method for investigations of hydrodynamic stability and transition phenomena has to meet a number of requirements in order to ensure success. Some of the requirements deemed most important in this context are as follows:

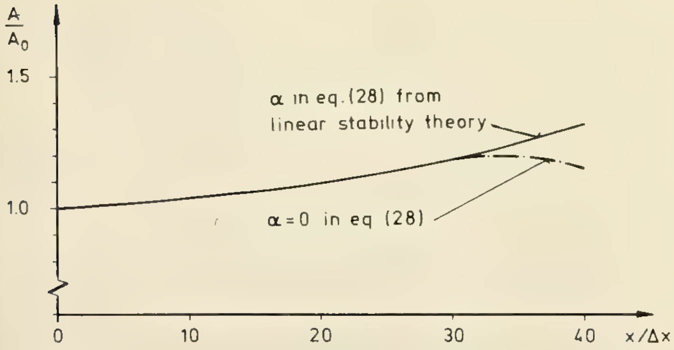

FIGURE 6. Amplification curves for maximum of u' for different boundary conditions at the downstream boundary (boundary layer on flat plate).

(i) Stability, convergence

Rigorous mathematical proofs of (numerical) stability and convergence for nonlinear problems as difficult as the one at hand have not been accomplished as yet. For the present investigation, however, stability of the numerical method is of fundamental importance. Numerical instability is frequently exhibited in form of oscillations which would be hardly discernible from the physically meaningful oscillations caused by introduced forced perturbations. Hence, a prospective difference method has to be highly stable, even for relatively large Reynolds numbers.

In general, for transition studies of the kind considered in this paper convergence is also quite serious. Convergence is not necessarily guaranteed if for a properly posed problem the numerical scheme is stable and consistent as is the case for linear partial differential equations of second order [Lax's equivalence theorem, see Richtmyer and Morton (1967)]. However, experimenting first with small periodic disturbances one can at least empirically check the convergence behaviour of the numerical method by comparing calculations for various grid sizes with linear-stability-theory results and experimental measurements. Then for other disturbance inputs, such as large amplitude periodic disturbances, one hopes that the convergence characteristics do not change significantly.

(ii) Accuracy of second order

For these investigations at least second-order accuracy of the numerical method (i.e. the truncation error of the difference analogue to the governing equations, initial and boundary conditions at least of second order) is required to exclude or minimize undesirable non-physical effects, such as artificial viscosity, when mesh intervals of practical sizes are used.

(iii) Realistic resolution of the transient character of unsteady flow fields

Transition phenomena are of highly unsteady nature, with the time-dependent behaviour of the flow being of special interest. Thus, the difference method has to be such that realistic resolution of the transient character of such flow fields is possible. Therefore truly second-order accuracy is also desirable for the time derivative.

(iv) Efficiency with respect to computational speed and required fast-access storage capacity

Numerical solutions of the complete Navier-Stokes equations for unsteady flows at high Reynolds numbers require numerous time-consuming numerical operations. Therefore computers with large, fast-access computer storage capacity, reaching even the limits of modern computer systems, are necessary. A prospective difference method for transition simulations has to be extremely efficient, i.e. maximizing computational speed and minimizing required computer storage capacity as much as possible, in order to be capable at all of undertaking investigations of this nature with the computers available today.

Of the requirements discussed here, numerical stability is the most stringent one and hence has to be given most consideration. For this reason only implicit methods are suitable. Implicit methods are generally much more stable than their implicit counterparts. For the adequate resolution of the large gradients, resulting from the strongly time-dependent flow fields to be investigated, relatively small spatial intervals Δx and Δy are required. Using explicit methods this could lead to excessively small time-steps required to maintain numerical stability. For example, using an explicit counterpart to the present implicit method, the time-step, according to a linearized stability analysis, would have to be more than 100 times smaller for a practical calculation than when using the corresponding implicit scheme. To satisfy requirement *(iv)* attention has to be given to making the implicit difference method extremely efficient and also to meeting the other requirements discussed previously.

Experimentation with various implicit difference schemes suggested that 'fully' implicit schemes are the most promising for transition studies. 'Fully' implicit means that all difference approximations and nodal values for the approximation of governing equations and boundary conditions are taken at the most recent time-level. For our fully implicit method three time-levels are employed to obtain a truncation error of second order for the time derivative $\partial\omega/\partial t$ in Eq. (1).

For all space derivatives, central difference approximations with second-order truncation error are employed. The implementation of the boundary conditions into the numerical scheme requires special care so that overall second-order accuracy can be maintained.

This implicit scheme leads to two systems of equations for the ω,ψ formulation and to three systems of equations for the ω,u,v formulation. These systems of equations can be solved by iteration. Because of the retention of full implicity the equation system resulting from the vorticity-transport equation is coupled with the Poisson equation systems via the nonlinear convection terms. It is additionally coupled with the systems resulting from the Poisson equations via the calculation of the wall vorticity from Eq. (17) for the ω,ψ formulation and from either Eqs. (18) or (19) for the ω,u,v formulation.

A very effective solution algorithm based on line-iteration has been developed for our method for this coupled system. It is discussed elsewhere in more detail [Fasel (1978)]. This solution algorithm has shown to be equally effective when the basic equations are transformed to allow for a variable mesh in the physical plane such as, for example, to concentrate grid points close to walls where high gradients are expected. Overrelaxation to accelerate convergence can be easily implemented as has been done for several calculations [Fasel et al. (1977)]. Another advantage is that the solution algorithm is readily exchangeable to be applied for both the governing equations in ω,ψ and ω,u,v formulation. This has been successfully exploited in the investigations of the effects of a backward-facing step on transition. In this study both formulations were used in the integration domain; the ω,ψ formulation was used in the region containing the corners of the step which can be treated more conveniently with this formulation. For the domain bounded by the downstream boundary the ω,u,v formulation was applied, because it allows use of less restrictive boundary conditions as discussed in Section 4.

The effectiveness of this solution algorithm can be best judged by presenting a typical computation time for a practical calculation. For a periodically disturbed flow with small disturbance amplitudes, using a 35 x 41 grid and calculating 260 time-steps, the required CPU time on a CDC 6600 is about five minutes, including the calculation of the steady flow. This is relatively little, considering that the flow is disturbed at every-time level and that full implicity is retained in the numerical method.

6. NUMERICAL RESULTS

The implicity difference method which we have developed has been subjected to crucial test calculations to verify its applicability to investigations of stability and transition. First, the reaction of the boundary-layer on a flat plate to periodic disturbances of small amplitudes was investigated in detail. It was demonstrated that the spatial propagation of Tollmien-Schlichting waves could be simulated where comparison of the numerical calculations with results of linear stability theory and laboratory measurements showed good agreement. Results of such calculations for the numerical method based on the ω,u,v formulation are presented and discussed elsewhere [Fasel (1976)].

The usefulness of the numerical simulations for the investigation of two-dimensional, nonlinear effects was demonstrated by calculating the reaction of a boundary-layer flow to periodic disturbances of larger amplitudes. Investigating the propagation of spatially growing or decaying disturbance waves in a plane Poiseuille flow (both in the linear and nonlinear regime) verified that the numerical method is not limited to boundary-layer flows but rather that it is equally applicable to other flows of importance. Finally, numerical investigations of of transition phenomena in the presence of a two-dimensional roughness element (backward-facing step) showed that simulations with this numerical model allow insight into processes which may possibly be important for understanding certain transition mechanisms. Results of this investigation and of the investigations mentioned before are discussed in another paper [Fasel et al. (1977)].

Because the purpose of this paper is to review main aspects of numerical transition simulations, emphasis here is not on conveying new results or details of numerical calculations. Rather, results presented here are intended to be of exemplary nature and were selected in order to clearly demonstrate essential aspects of such simulations and to show what can be expected from such numerical calculations.

The drawings in Figures 7 and 8 should facilitate an evaluation of the potential of such numerical simulations, and, of course, also point out possible disadvantages and limitations. Figures 7 and 8 show results for a boundary-layer flow on a flat plate, disturbed at the upstream boundary with small periodic disturbances. This case is particularly suitable for demonstration purposes. The ensuing

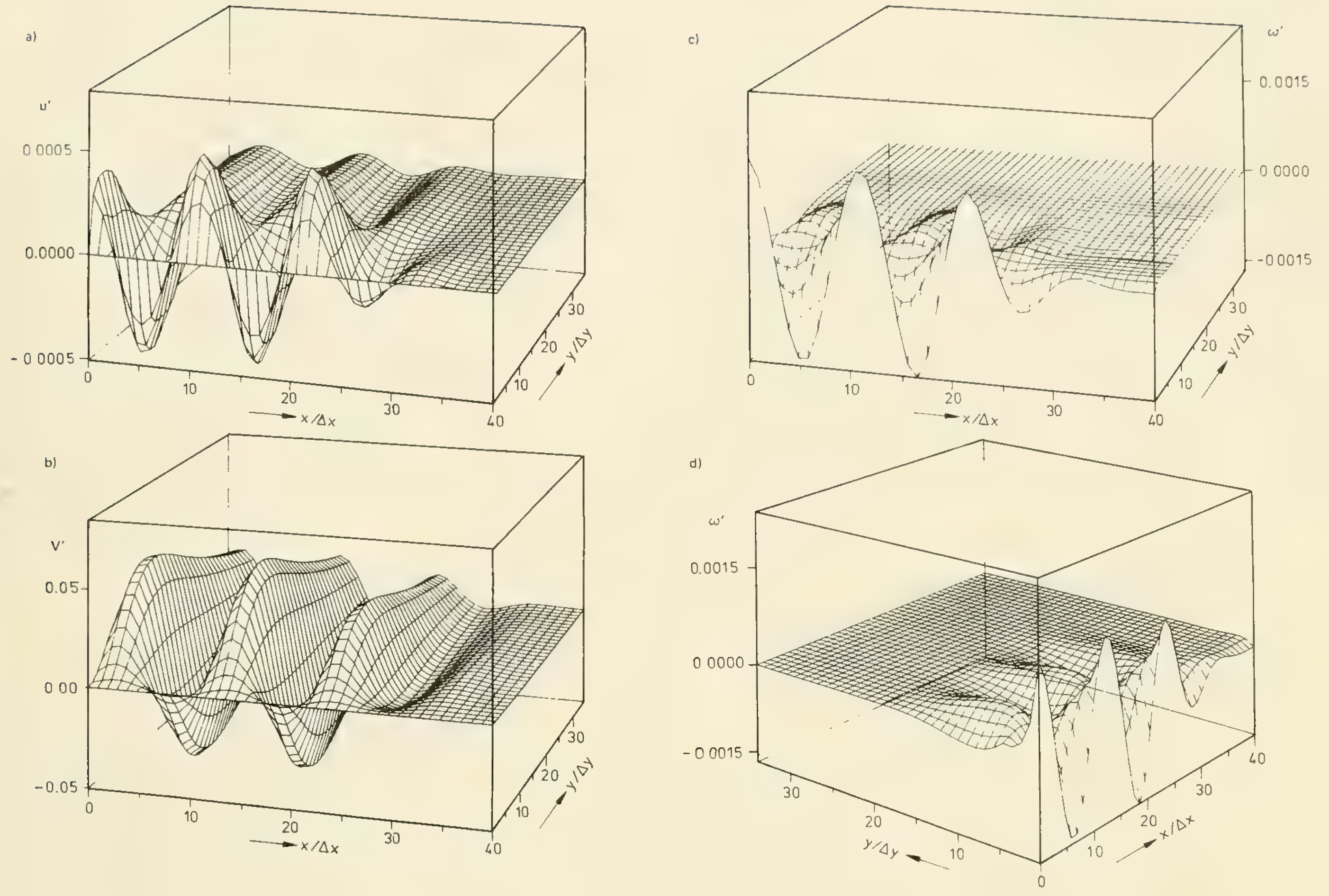

FIGURE 7. Disturbance variables versus x/Δx and y/Δy (perspective representation) at t/Δt = 80; a) u', b) v', c) ω', d) ω' (different view).

Tollmien-Schlichting waves that can be studied from such calculations are thoroughly investigated, experimentally as well as theoretically, and the results of these calculations are therefore more intelligible than those of more complicated phenomena of transition.

For these calculations, based on the ω,u,v formulation, the Reynolds number at the upstream boundary is Re*=630. For the periodic disturbance input, for which perturbation profiles of linear stability theory are used, the frequency parameter (defined as $F=10^4\bar{\beta}\bar{\nu}/U_0^2$, with disturbance frequency $\bar{\beta}$) is F=1.3. In this case the flow is unstable according to linear stability theory (the location of the left boundary corresponds to a point on the neutral curve) and therefore the disturbances should become amplified in downstream direction. For the calculations an equi-distant grid with 35 points in y-direction and 41 points in x-direction was used.

In Figures 7 and 8 the function values of the disturbance flow (obtained by subtracting the quantities of the basic flow from those of the total flow) are plotted for all three fields of variables u',v',ω', for which the total flow variables are directly obtained from the numerical calculations. To allow simultaneous representation of the function values at all grid points a perspective representation was chosen where the function values are plotted versus the downstream coordinate x/Δx and the coordinate normal to the wall y/Δy. These perspective representations allow the best possible qualitative survey of the large amount of data obtained from such calculations.

In Figure 7 the disturbance variables u',v',ω' are plotted for a time instance of t=80Δt, which corresponds to a time of two time periods after initiation of the disturbances at the upstream boundary. In Figures 7a, 7b, and 7c the view is in the direction away from the wall, looking slightly in upstream direction. In Figure 7d the view is also in the direction away from the wall, looking now, however, downstream. From these figures the propagation of the disturbance waves into the undisturbed flow field can be clearly observed.

Figure 8 shows the corresponding drawings for the three variables u',v',ω' at a time instance of t=250Δt, that is, more than two time periods after the disturbance wave reached the downstream boundary. These plots demonstrate that the downstream boundary conditions work properly. Obviously, the waves can smoothly pass through this boundary, causing no noticeable reflections. Even after hundreds of time-steps the flow at and near this boundary maintains its time-periodic character and therefore the state of the disturbance flow as represented in Figure 8 would repeat itself periodically if the calculations were continued for further time-steps.

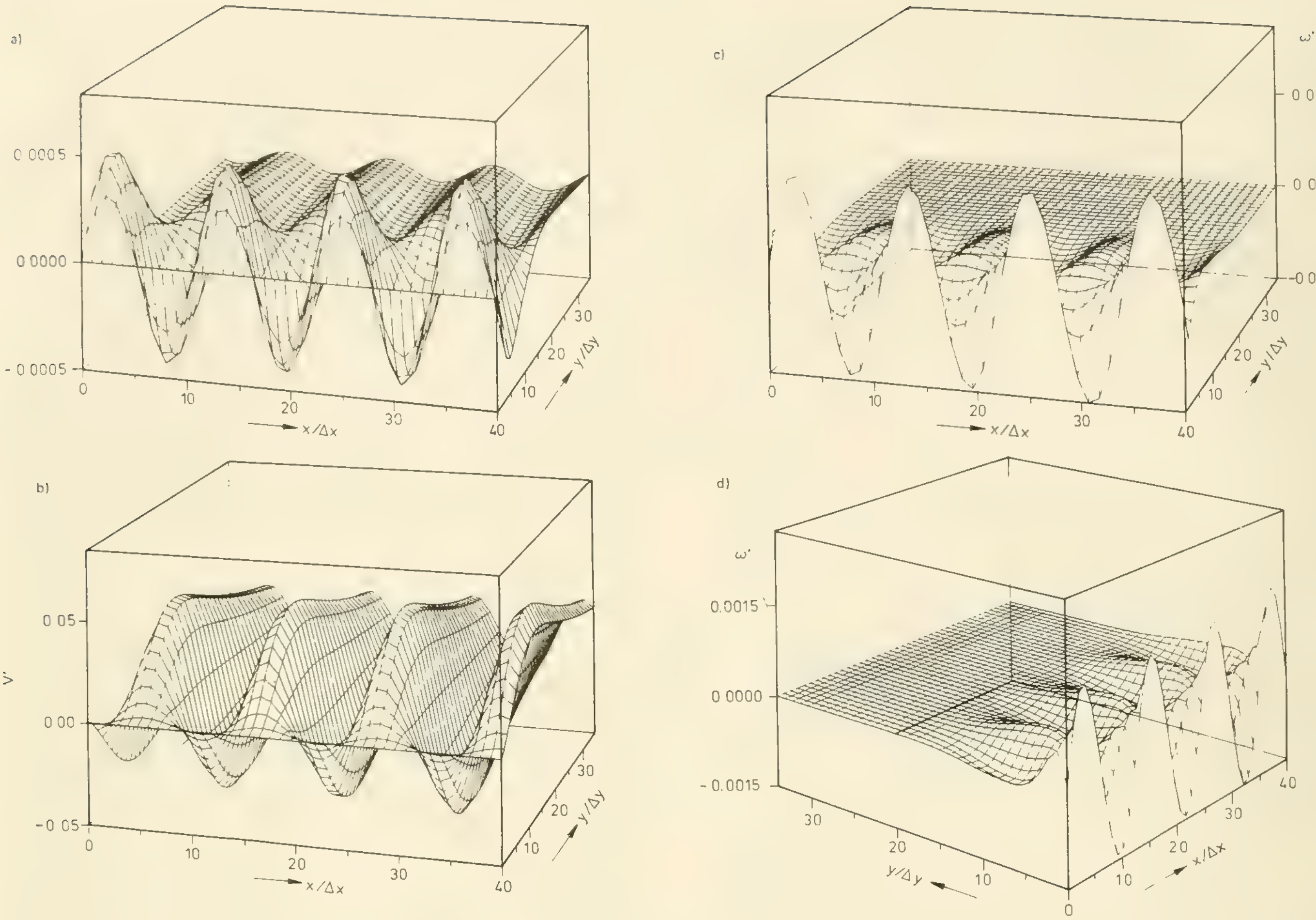

FIGURE 8. Disturbance variables versus x/Δx and y/Δy (perspective representation) at t/Δt = 250; a) u', b) v', c) ω', d) ω' (different view).

In Figures 7 and 8 the large gradients normal to the wall of the u' and ω' disturbances become clearly visible (for ω' this can be best observed from Figures 7d and 8d) while v' changes more gradually. The large gradients observable in these results indicate already the major difficulties and limitations in numerical simulations of transition phenomena. In a numerical solution method these large gradients have to be adequately resolved to obtain meaningful representation of essential physical phenomena. For nonlinear disturbance waves resulting from disturbance input with larger amplitudes [Fasel et al. (1977)] or for other more complicated transition phenomena the gradients may become even considerably larger. Using finite-difference methods of a given accuracy (for example, second order as for the present method) better resolution can only be achieved by using additional grid points. This, however, leads to ever larger equation systems the sizes of which are limited by computer storage capacity and computation time.

Some help can be expected from employing variable mesh systems allowing allocation of more grid points closer to walls, where the gradients are largest, and using fewer points further away where gradients are small. This can be best achieved using coordinate transformations for which test calculations have shown that sizable savings in the number of grid points, and also in computation time, are possible to achieve accuracy comparable with calculations in an equidistant grid. Additional improvement may be expected from application of higher-order accurate difference schemes (higher than second order) which are presently in the state of development and about to be used in our numerical method.

The results shown in Figures 7 and 8 also unveil the considerable potential and advantages of such numerical simulations. The finite-difference solutions produce a bulk of data, i.e. the values of the variables directly involved in the solution procedure are obtained for all grid points and for all time-levels that are calculated. The data can be conveniently stored on mass storage devices, such as magnetic tape (used for the present calculations, for example). The data stored can be processed immediately or at any later data to obtain any specific information desired, or to produce additional data that might be deemed necessary for a more detailed evaluation of particular flow phenomena. For example, they can be used to obtain frequency spectra, Reynolds stresses, energy balances, amplitude distributions, or to produce contour plots (equivorticity lines, stream lines) etc. Another positive side of such numerical simulations is that if the data would be destroyed or lost, they could be reproduced identically, which would be hardly possible in comparable laboratory experiments.

7. CONCLUDING REMARKS

The objective of the present review was to discuss possible approaches to numerical simulations of stability and transition based on numerical solutions of the Navier-Stokes equations using finite-difference methods. The approach, allowing investigations of spatially propagating disturbance waves, mainly elaborated upon in this paper, appears most promising for realistic numerical investigations of physical phenomena occurring in transition. The immense amount of reproducible data obtained from such calculations allows detailed information of any part of the flow field which may be helpful to gain insight into essential mechanisms occurring in transition.

The restriction of the numerical model to two-dimensional flows has also a positive side. With this model truly two-dimensional numerical experiments can be performed while in laboratory experiments it is always difficult to completely exclude unwanted three-dimensional effects. Of course the later stages of transition are inherently three-dimensional in nature and therefore for a study of these later developments a three-dimensional model would be desirable.

The main difficulties and limitations of such simulations result from the large gradients which occur in the transition process. For adequate resolution of the large gradients which become even larger for more complicated phenomena, increasing numbers of grid points are required which may lead to excessive requirements of computer storage and computation time.

In spite of these difficulties the number of numerical simulations of transition, similar to the approach discussed in this paper, is likely to increase due to the enormous potential inherent in such investigations. Emphasis will probably be on the development of difference methods with higher accuracy which are applicable for such studies. Additionally, increasing use of numerical methods other than finite-difference methods is likely, such as spectral methods or finite-element methods. Finally, with continuing progress in the development to high-speed digital computers, detailed quantitative investigations of three-dimensional transition phenomena will probably become feasible in the near future.

This research is supported by the Deutsche Forschungsgemeinschaft, Bonn-Bad Godesberg, contract Ep 5/7.

REFERENCES

Bestek, H., and H. Fasel (1977). Ein numerisches Verfahren zur Untersuchung angefachter, kleiner Störungen bei der ebenen Poiseuille-Strömung. Paper presented at the GAMM-Meeting 1977 in Copenhagen/Denmark. To be published in *ZAMM 58* (1978).

Crowder, H. J., and C. Dalton (1971). On the stability of Poiseuille flow in a pipe. *J. Comp. Phys. 7,* 12.

De Santo, D. F., and H. B. Keller (1962). Numerical studies of transition from laminar to turbulent flow over a flat plate. *J. Soc. Ind. Appl. Math. 10,* 569.

Dixon, T. N., and J. D. Hellums (1967). A study on stability and incipient turbulence in Poiseuille and plane-Poiseuille flow by numerical finite-difference simulation. *AIChE J. 13,* 866.

Fasel, H. (1976). Investigation of the stability of boundary layers by a finite-difference model of the Navier-Stokes equations. *J. Fluid Mech. 78,* 355.

Fasel, H., H. Bestek, and R. Schefenacker (1977). Numerical simulation studies of transition phenomena in incompressible, two-dimensional flows. Proc. *AGARD Conf. on Laminar-Turbulent Transition,* Lyngby, Denmark 1977. AGARD-CP-224, Paper No. 14.

Fasel, H. (1978). Recent developments in the numerical solution of the Navier-Stokes equations and hydrodynamic stability problems. *Proc. VKI-Lecture Series "Computational Fluid Dynamics",* March 13-17, Brussels, Belgium.

Gaster, M. (1974). On the effects of boundary-layer growth on flow stability. *J. Fluid Mech. 66,* 465.

George, W. D., and J. D. Hellums (1972). Hydrodynamic stability in plane Poiseuille flow with finite amplitude disturbances. *J. Fluid Mech. 51,* 687.

Hadamard, J. (1952). *Lectures on Cauchy's Problem in Linear Partial Differential Equations.* Dover.

Harlow, F. H., and J. E. Welch (1965). Numerical calculation of time-dependent viscous imcompressible flow of fluid with free surface. *Phys. Fluids 8,* 2182.

Nagel, A. L. (1967). Compressible boundary layer stability by time-integration of the Navier-Stokes equations. *Boeing Scientific Research Laboratores, Flight Sciences Report No. 119.*

Nishioka, M., S. Iida, and Y. Ichikawa (1975). An experimental investigation of the stability of plane Poiseuille flow. *J. Fluid Mech. 72,* 731.

Richtmyer, R. D., and K. W. Morton (1967). *Difference Methods for Initial Value Problems.* Interscience Publishers, Second Edition, New York.

Roache, P. J. (1976). *Computational Fluid Dynamics.* Hermosa Publishers, Albuquerque.

Saric, W. S., and A. H. Nayfeh (1977). Nonparallel stability of boundary layers with pressure gradients and suction. *Proc. AGARD Conf. on Laminar-Turbulent Transition,* Lyngby, Denmark 1977. AGARD-CP-224, Paper No. 6.

The Physical Processes Causing Breakdown to Turbulence

M. Gaster
National Maritime Institute
Teddington, England

I want to present some recent experimental observations that provide further insight into the physical processes that occur in the transition from a laminar to a turbulent boundary layer. We know that external disturbances, such as free-stream turbulence and sound, excite small pertubations in the laminar flow, and that under certain conditions these may develop downstream in the form of growing wave trains. At low pertubation levels these unstable travelling waves are adequately described by the linearised equations of motion. Measurements on weak artificially excited waves have, by and large, provided excellent confirmation of linear theory. Far downstream the amplitudes of the pertubation velocities will, however, become too large for the neglect of the non-linear terms to be valid, and a non-linear description of the motion is necessary. Even in the relatively simple situation of the constrained parallel Poiseuille flow, which has been extensively studied, the non-linear theories so far developed can only weakly describe non-linear events, and even then the computations are very involved. These non-linear theoretical models are nevertheless very helpful in describing the various interactions between the fundamental, its harmonics, and the mean flow, but they cannot go far toward providing a model of the process of breakdown to turbulence, nor are they intended for that purposes.

Non-linear analyses have been concerned mostly with the evolution of purely periodic wave trains. In the case of linear problems it is quite proper to consider any disturbance in terms of its Fourier elements. Knowledge of the behaviour of purely periodic wave trains enables more complex disturbances to be described. Unfortunately this is not the case when the disturbance is non-linear, and the welcome simplification obtained by breaking down a problem into harmonics is no longer valid. When the initial disturbances arise from natural rather random stimuli the linear wave train will initially consist of a band of unstable waves. After some amplification a slowly modulated almost sinusoidal oscillation will inevitably develop. When the selective amplification is very large, as is the case in many boundary layer flows, the modulations are slow, and it does not seem too much of an idealisation to treat the non-linear problems analytically as if it were a purely regular wave train. It turns out, however, that the degree of modulation does not have to be large for its influence on the Reynolds stresses and thus the 'mean motion' to be very significant. In a typical experiment on a laminar boundary layer over a flat plate in a low turbulence wind tunnel one finds that the instability waves are modulated sufficiently to influence the transition process. It is found, for example, that breakdown to turbulence occurs violently and in a random manner quite unlike the type of breakdown that is observed in controlled periodic wave trains. Measurements on isolated wave packets also show the effect that modulation of the wave train has on transition, but in a more controlled way.

Previously reported measurements [Gaster and Grand (1975)] on artifically excited wave packets showed consistent and quite well defined deviations from the structure predicted by linear theory. Since the maximum level of the velocity fluctuations measured lay below that for which significant non-linearity is exhibited by regular periodic wave trains, the reason for this behaviour was at that time unclear. In the experiments only one level of input excitation was used and so there was no direct way of assessing the importance of the non-linear terms. These experiments have been repeated at the National Maritime Institute with various levels of input excitation and it has now been conclusively established that the previously observed warping of wave fronts and the non-Gaussian character of some of the hot-wire signal envelopes arose from non-linearity. This behaviour can best be illustrated by showing a comparison of the hot-wire signals that arise: (a) with a sinusoidal input, and (b) a pulsed input. As in the previous series of experiments the boundary layer flow was excited by an acoustic device mounted in a recess on the reverse side of the flat plate. A small hole through the plate provided the necessary fluid dynamic coupling at a point on the boundary of the working face. Figure 1 shows a set of hot-wire anemometer records taken with the probe mounted just outside the boundary layer one metre downstream of the leading edge. The exciter was driven sinusoidally at four different amplitude levels increasing from (i) to (iv). The velocity fluctuations appear to be regular and show no harmonic or other distortion until the level of turbulence intensity exceeded 1% peak-to-peak of the free-stream velocity (see iv). Exciting the flow with isolated pulses on other hand, produces a somewhat different picture. Figure 2 again contains four hot-wire records obtained with different levels of drive applied impulsively. At the lowest level shown the signal consists of a smooth roughly Gaussian packet of ripples, but even a small increase in driving amplitude produces a clearly discernible distortion to this signal. These distortions are similar to those obtained in the earlier experiments quoted. As the amplitude is further increased the signal becomes increasingly distorted until at some level a secondary burst of relatively high frequency oscillations appears. It should be remarked that the amplitude scaling on both Figures 1 and 2 are identical, showing that non-linear effects occur at much lower amplitudes for the impulsively applied disturbance than for a periodic one. In these particular experiments it appears that non-linearity becomes apparent in the hot-wire signal at a peak to peak amplitude of only 1/5th that for a continuous wave train.

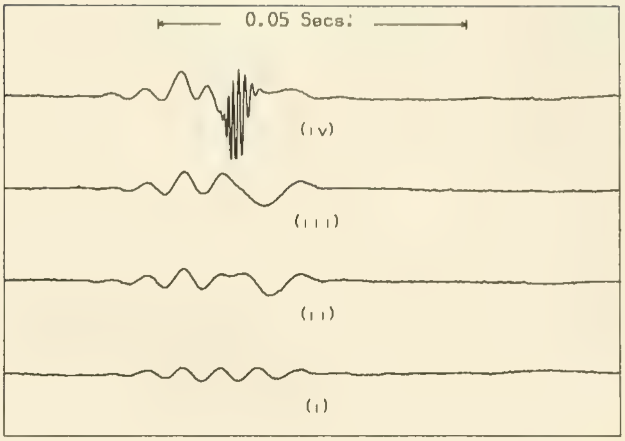

FIGURE 2. Hot-wire signals from pulsed excitation.

The high frequency oscillation appears to be associated with a steep shear layer that forms within the velocity profile momentarily as the wave packets sweep past the measuring station. These shear layers initially appear on either side of the centre line, and not surprisingly therefore the peak levels of the high frequency secondary oscillation also arise off centre at roughly these locations. The high frequency waves grow rapidly with downstream distance, initially developing exponentially but later the growth levels off. At that stage the filtered secondary wave packets were observed to distort in a way reminiscent of the primary wave packet. It was therefore conjectured that there might be yet a further level of instability on the secondary wave oscillations when these became sufficiently large. Just two days before leaving for this meeting this idea was tested. Hot-wire signals from appropriate regions of the flow were filtered to see whether there was any signal above the frequency of the secondary oscillations. When the secondary wave amplitude was large, a burst of high frequency oscillations could be seen on the oscilloscope. Figure 3 shows the result of applying a high-pass filter, set to pass above 2 kHz, to such a hot-wire anemometer signal. The time scale of this record is considerably expanded compared with that of Figures 1 and 2, and shows that the oscillation frequency in the burst was around 5 kHz. The basic primary wave packet of roughly 150 Hz developed over 1 m before breaking and supporting a secondary burst of 1 kHz. This secondary instability grew in amplitude to levels large enough to indicate the influence of non-linearities in a distance of roughly 4 cm. The tertiary mode of 5 kHz detected at this stage seems likely to grow even more rapidly. One can only presume that further stages in this evolutionary process are inhibited by viscosity.

These experiments on the non-linear wave packet and its breakdown to turbulence are as yet incomplete and it is my purpose here to indicate only the

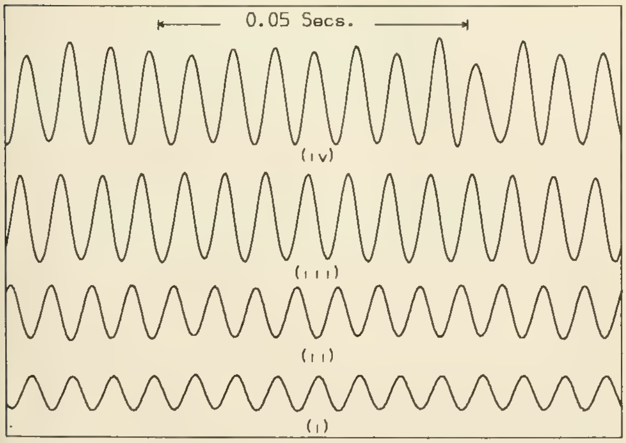

FIGURE 1. Hot-wire signals from sinusoidal excitation.

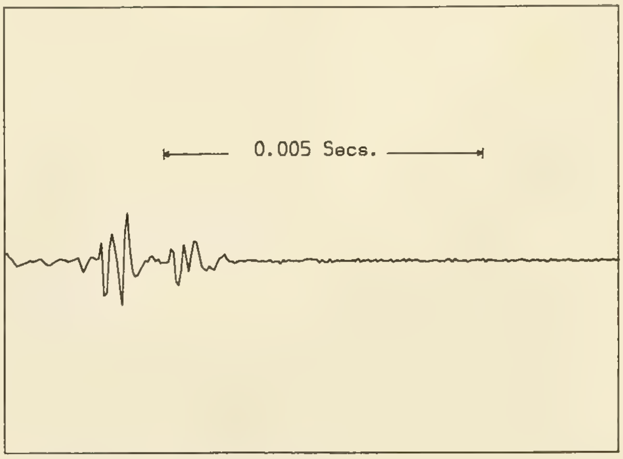

FIGURE 3. High frequency burst.

most important features of the process. Firstly, a clear demonstration of the difference between a purely periodic wave train and a modulated train as far as the level at which non-linear effects occur is presented. The local breakdown observed in the wave packet case is similar to that observed in the breakdown of the modulated wave trains that arise from natural random excitations. Secondary breakdown does of course also occur on large enough periodic waves, but modulation seems to cause this phenomenon to take place at somewhat lower levels of primary disturbance and in a slightly different form. The artifically driven wave packet embodies some of the most important features found in naturally occurring waves, and since they can be generated in a controlled manner the effects can be quantified. It is essential to understand this process if one is going to make estimates of where transition occurs on the basis of the amplitudes of instability waves calculated from linear theory. At present, most prediction methods rely solely on the intensity of the most unstable wave. This is clearly inadequate as breakdown is also dependent on the modulation of the wave train, and consequently the bandwidth of the amplified part of the spectrum must also be taken into account in some way yet to be established.

Secondly, the transition from regular waves to turbulence appears to occur through a cascade process. The stresses induced by a modulated wave train cause steep shear layers to form in the boundary layer. These support instabilities of higher frequencies and shorter wavelengths than the waves that caused the distortions, and these grow to large amplitudes in appropriately shorter distances. This process must at some stage be tempered by viscosity, but in these experiments three levels of instability have been so far detected. The lowest frequency motion was artifically excited by the input pulse, while the two successviely higher frequencies were excited by random turbulence in the flow at the particular location in space and time where local instabilities existed. The development of a fine scale structure is thus a local, almost explosive, phenomenon. Such a cascade breakdown process provides the necessary mechanism for the generation of fine scale motions that arise in a fully turbulent flow.

REFERENCE

Gaster, M., and I. Grant (1975). An Experimental Investigation of the Formation and Development of a Wave Packet in a Laminar Boundary Layer, *Proc. R. Soc. Lond. A 347*, 253-269.

The Instability of Oscillatory Boundary Layers

Christian von Kerczek
David W. Taylor Naval Ship Research and Development Center, Bethesda, Maryland

ABSTRACT

The instability of the two-dimensional flat plate oscillatory boundary layer induced by a stream with velocity $U_0 + U_1 \cos \omega t$ is considered. The velocity amplitudes, U_0 and U_1, are constants and U_1/U_0 is assumed to be small. The instability of this oscillatory boundary layer is analyzed by a time-dependent linear parallel flow instability theory. The change of the Tollmien-Schlichting growth rates due to the imposed oscillations are computed to second order in U_1/U_0. It is found that for imposed oscillation frequencies in the range of the Tollmien-Schlichting frequencies of the underlying Blasius flow, the boundary layer is stabilized by the oscillations of the external flow.

1. INTRODUCTION

In this paper, we study the instability of the two-dimensional oscillatory laminar boundary layer which forms on a flat plate that is exposed to a stream with a velocity, $U_0 + U_1 \cos \omega t$, perpendicular to the plate's leading edge. The velocity amplitudes, U_o and U_1, are constants, ω is the angular frequency of the oscillation, and t denotes time. The considerations of the instability of oscillatory flows has become an important field of research in recent years and has been reviewed by Davis (1976). The particular class of problems concerned with the instability and laminar-turbulent transition of oscillatory boundary layers has been reviewed by Loehrke, Morkovin, and Fejer (1975). The latter review indicates that very few studies of instability and transition have focused directly on the subject of oscillatory boundary layers. Such studies that have concentrated on oscillatory boundary layers have been mainly experimental investigations which were restricted to low frequency oscillations compared to the oscillation frequency of unstable Tollmien-Schlichting waves. The only analytical work concerning the instability of oscillatory boundary layers has been the quasi-steady analysis of Obremski and Morkovin (1969) which was aimed at these low frequency cases.

The study of the instability of oscillatory boundary layers has technological as well as fundamental importance. Examples of a fundamental nature for which the study of the instability of oscillatory flows may have relevance are the problems of how ambient disturbances affect the instability of the underlying steady boundary layer. Specific examples might be the effects of ambient acoustic waves or ambient turbulence on steady boundary layer instability. The problem of the effects of ambient turbulence on the instability of a steady boundary layer probably is not completely accessible by the theory of the instability of oscillatory boundary layers. However, a sufficiently complex, but organized, ambient oscillation may be adequate for duplicating some aspects of the effects of ambient turbulence on steady boundary layer instability. We are hopeful that this may be the case because of similar phenomena in the field of nonlinear ordinary differential equations. The study of the instability of forced periodic solutions of nonlinear ordinary differential equations has furnished a much richer class of phenomena than the corresponding study of the instability of only the steady solutions of these equations [see, for example, Hayashi (1964); in particular, the results for the forced van der Pol equation, pp. 286-300].

In the present study, we focus on the very simple oscillatory boundary layer that was described earlier. The purely oscillatory part of this boundary layer is approximated by the oscillatory Stokes layer which has no spatial structure in the plane of the plate, i.e., it is an exactly parallel flow. Thus, this model problem may be too simple to reveal any particularly important features of realistic ambient disturbances. However, the model problem is a good starting point and serves as a basis on which to develop the appropriate methods of analysis for the instability of oscillatory flows. We will be concerned mainly with moderate and high frequency oscillations comparable to the oscillation frequencies of unstable Tollmien-Schlichting waves. Thus, a direct comparison of our results with the low-frequency experimental results cited by Loerke, Morkovin, and Fejer (1975) will not be possible.

The method used here for analyzing the instability of the oscillatory boundary layer is a combination numerical and perturbation method [Yakubovich and Starzhinskii (1975)]. In this method, the changes in the amplification rates of the free disturbances of the underlying steady boundary layer are computed as perturbation series in the amplitude parameter, U_1/U_o, for any positive value of the frequency, ω. Certain resonant and combination frequencies are of particular interest. The numerical method used here to evaluate the perturbation series allows the efficient and easy generation of many terms of the series.

The plan of this paper is as follows: In Section 2, we formulate the basic flow whose instability is to be examined along with the associated theory instability problem. Section 3 outlines the solution method. Section 4 discussed the numerical results. Some concluding remarks concerning the instability of womewhat more complex oscillatory boundary layers are contained in Section 5.

2. INSTABILITY THEORY

The basic flow field whose instability is to be investigated is the oscillatory boundary layer formed on a flat plate in a unidirectional stream with speed $U_o + U_1 \cos \omega t$ perpendicular to the leading edge of the plate and parallel to its plane. Let the cartesian coordinate frame (x,y,z) be placed with its origin in the leading edge of the plate, the x-axis pointing downstream parallel to the plate, the y-axis perpendicular to the plane of the plate and the z-axis pointing in the spanwise direction. For values of the parameter, $(w\omega/U_o) >> 1$, the ratio, $\beta_1 = \bar{\delta}/\delta_S$, of the boundary layer thickness, $\bar{\delta} = \sqrt{x\nu/U_o}$, to the oscillatory Stokes layer thickness, $\delta_S = \sqrt{2\nu/\omega}$, is large and the oscillatory boundary layer resulting for small values of $\Delta = U_1/U_o$ can be approximated well [see Ackerberg and Phillips (1972)] by the sum of the Blasius profile $U_B(y)$ [see Rosenhead (1963), p. 225] and the Stokes layer profile $U_S(y, t)$ [Rosenhead (1963), p. 381].

Let us scale the x- and y-coordinates by the local value of the displacement thickness

$$\delta_* = 1.7208 \sqrt{x\nu/U_o} \qquad (1)$$

Then the transverse coordinate, η, is defined by $\eta \equiv y/\delta_*$ and $x' = x/\delta_*$. The time scale is δ_*/U_o so that dimensionless time is $t' = tU_o/\delta_*$ and henceforth the primes will be dropped. Then the basic oscillatory boundary layer profile is given approximately by

$$U(\eta,t) = f_B(\eta) + \Delta \mathrm{Re}\left[(1-e^{-(1+i)\beta\eta})e^{i\Omega t}\right] \qquad (2)$$

where $f_B(\eta)$ is the Blasius profile, $\beta = \delta_*/\delta_S$, $\Omega = \omega\delta_*/U_o = 2\beta^2/R_{\delta_*}$, and $R_{\delta*} = U_o\delta_*/\nu$.

We shall consider the instability of the basic flow (2) in a similar manner to the standard two-dimensional linear instability theory for steady boundary layers. In particular, the quasi-parallel temporal instability theory as outlined by Rosenhead (1963) is followed. The restriction to two-dimensional disturbances can be justified based on an extended version of Squires' theorem [see von Kerczek and Davis (1974)]. The perturbation velocities (u,v) are determined from the stream function, $\psi(x,\eta,t) = \varphi(\eta,t)e^{i\alpha x}$:

$$u = -\mathrm{Re}\frac{\partial\psi}{\partial\eta} = -\mathrm{Re}\frac{\partial\varphi}{\partial\eta}e^{i\alpha x},$$
$$v = \mathrm{Re}\frac{\partial\psi}{\partial x} = \mathrm{Re}\, i\alpha\varphi e^{i\alpha x}. \qquad (3a,b)$$

The disturbance equation for the perturbation velocities is then given by

$$\frac{\partial}{\partial t}\pounds\varphi = \frac{1}{R_{\delta_*}}\pounds^2\varphi + i\alpha\left(U\pounds\varphi - \frac{\partial^2 U}{\partial\eta^2}\varphi\right) \qquad (4)$$

where $\pounds \equiv \partial^2/\partial\eta^2 - \alpha^2$, $i = \sqrt{-1}$, Re(a) denotes the real part of a, and α is the wave number of the sinusoidally varying disturbance in the x-direction. The boundary conditions are

$$\varphi = \frac{\partial\varphi}{\partial\eta} = 0, \text{ at } \eta = 0 \qquad (5a)$$

and

$$\varphi,\ \frac{\partial\varphi}{\partial\eta} \to 0 \text{ as } \eta \to \infty. \qquad (5b)$$

By analogy with Floquet theory for ordinary differential equations with periodic coefficients [Coddington and Levinson (1958)], we seek solutions of (4) and (5) in the form

$$\varphi = g(\eta,t)\ e^{\lambda t} \qquad (6)$$

where $g(\eta,t)$ is a periodic function of t with period $2\pi/\Omega$. This is a reasonable choice of solution because we are mainly interested in the oscillation induced changes of the principal disturbance mode of the Blasius flow. The principal disturbance mode of Blasius flow has multiplicity one.

We shall adopt in this study an absolute definition of instability which requires that some measure of the disturbance amplitude becomes infinite as $t \to \infty$. If the amplitude remains bounded as $t \to \infty$, then the flow is defined to be stable to infinitesimal disturbances. However, we must keep in mind that the local instantaneous amplitude may be important in this linear theory because a disturbance may be transiently so large (but bounded) that the linear instability theory is no longer valid. Furthermore, the instantaneous magnitude as a multiple of the initial magnitude of the disturbance is an important quantity for assessing the likelihood of transition from laminar to turbulent flow. Thus we shall consider in detail the gross amplification rate G of a disturbance which we define by

$$G \equiv \frac{1}{e_T}\frac{de_T}{dt} \qquad (7)$$

where e_T is the total energy of the disturbance defined by

$$e_T \equiv \frac{\alpha}{2\pi} \int_0^\infty \int_0^{2\pi/\alpha} (u^2 + v^2) dx d\eta \qquad (8)$$

Then the relative amplification ratio, e_{T_1}/e_{T_2}, of a disturbance as it grows during the time interval from t_0 to t_1 can be shown to be

$$\frac{e_{T_1}}{e_{T_0}} = \frac{I(t_1)}{I(t_0)} \exp \left(2 \int_{t_0}^{t_1} \lambda_r dt \right) \qquad (9)$$

$$I(t) \equiv \int_0^\infty \left(\left|\frac{\partial g}{\partial \eta}\right|^2 + \alpha^2 |g|^2 \right) d\eta \qquad (10)$$

and $\lambda_r = \mathrm{Re}(\lambda)$.

Since the disturbance energy propogates down the boundary layer at the group velocity, c_g [see Gaster (1962)] one can compute the relative amplification ratio, e_{T_1}/e_{T_0}, by calculating the integral in the exponential function of Eq. (9) over the spatial interval, x_0 to x_1, using the transformation, $dx = c_g dt$.

3. SOLUTION OF THE DISTRUBANCE EQUATION

Solutions of Eq. (4) in the form (6) can be obtained as a series in Δ,

$$\varphi = (g_0 + \Delta g_1 + \ldots) e^{(\lambda_0 + \sigma_1 \Delta + \ldots)t} \qquad (11)$$

where each term of (11) can be evaluated by solving appropriate perturbation equations obtained by substituting (11) into (4) and (5). Such perturbation equations are basically inhomogeneous unsteady Orr-Sommerfeld equations and must be solved numerically. Our approach is equivalent to this except we reverse the procedure by first executing a numerical procedure which reduces the Eqs. (4) and (5) to a system of ordinary differential equations in time. These are easily solved by perturbation theory to as high an order as desired.

Let us first expand the function φ in the Chebyshev series

$$\varphi(y,t) = \sum_{n=1}^{N} a_n(t) T_{n-1}(y) \qquad (12)$$

where the $T_n(y) = \cos^{-1}(n \cos y)$, $n = 0,1,\ldots$are the Chebyshev polynomials of the first kind and where we have mapped the interval, $\eta \varepsilon [0,\eta_\infty]$, onto $y \varepsilon [-1,1]$. Then we use the τ-method as described by Orszag (1971) to obtain the system of ordinary differential equations

$$Q \frac{d\bar{a}}{dt} = \frac{1}{R_{\delta_*}} (P + i\alpha J)\, \bar{a} + i\alpha\Delta V \bar{a} \qquad (13)$$

where Q,P,J and V are (N-4)x(N-4) term matrices and $\bar{a} = (a_1,\ldots,a_{N-4})^\dagger$. The dagger (†) superscript denotes the transpose of a vector or matrix. The coefficients, $a_{N-3},\ldots,a_N$, are determined by the boundary conditions once $\bar{a}$ is known. The matrices, Q,P,J, and V, are the respective representations of the operators, $\pounds, \pounds^2, (f_B \pounds - \partial^2 f_B/\partial y^2)$ and $(\mathcal{S} - \partial^2 \mathcal{S}/\partial y^2)$, together with the boundary conditions (6) in the space, φ_N, whose basis is the first N Chebyshev polynomials, $T_0,\ldots, T_{N-1}$ [Orszag (1971)]. The function, $\mathcal{S}$, is the Stokes layer profile.

$$\mathcal{S} = \mathrm{Re}\left[(1 - e^{-(1+i)\beta\eta}) e^{i\Omega t}\right]. \qquad (14)$$

Note that the matrices, Q,P, and J, are real constant matrices and V is real and time periodic and of the form

$$V = V^{(1)} e^{i\Omega t} + V^{(-1)} e^{-i\Omega t} \qquad (15)$$

where $V^{(1)}$ and $V^{(-1)}$ are constant matrices.

The matrix, Q, is invertable so that we can multiply (13) by Q^{-1} to get

$$\frac{d\bar{a}}{dt} = \frac{1}{R_{\delta_*}} (P' + i\alpha J')\bar{a} + i\alpha\Delta V'\bar{a} \qquad (16)$$

where $P' = Q^{-1}P$ etc.; henceforth we shall dispense with the primes in (16)

The perturbation procedure is most easily and illuminatingly carried out by transforming (16) so that the matrix, $(P+i\alpha J)/R_{\delta_*}$, is in diagonal form. That is we will be working directly in the (approximate) eigenspace of the steady Orr-Sommerfeld equation for Blasius flow. Suppose that the invertible matrix, B, transforms $(P+i\alpha J)/R_{\delta_*}$ into diagonal form. Then let

$$\bar{a} = B\bar{b} \qquad (17)$$

and substitute (17) into (16) and left-multiply by B^{-1}. Then

$$\frac{d\bar{b}}{dt} = D\bar{b} + \Delta E\bar{b} \qquad (18)$$

where

$$D = B^{-1} \frac{1}{R_{\delta_*}} (P + i\alpha J) B = \lceil \lambda_1, \ldots, \lambda_{N-4} \rfloor \qquad (19a)$$

$$E = +i\alpha B^{-1} V B \equiv E^{(1)} e^{i\Omega t} + E^{(-1)} e^{-i\Omega t} \qquad (19b)$$

and the notation, $\lceil d_1, \ldots, d_n \rfloor$, stands for a diagonal matrix of order n.

The problem is now to find solutions of (18) in the form

$$\bar{b}(t) = \bar{z}(t) e^{\lambda t} \qquad (20)$$

where $\bar{z}(t+2\pi/\Omega) = \bar{z}(t)$. We are mainly interested in perturbations of magnitude Δ of the steady flat-plate disturbance mode which becomes unstable far downstream of the leading edge. This mode is associated with one of the eigenvalues of D, say λ_ρ, which for values of x between the two values, $x_0 < x_1$, satisfies $\mathrm{Re}\lambda_\rho > 0$. It is known that $\lambda\rho$ is a simple eignevalue [see Mack (1976)] so that a solution of the form (20) can be expanded as

$$\bar{z}(t) = \bar{z}_o(t) + \Delta\bar{z}_1(t) + \Delta^2\bar{z}_2(t) +\ldots \qquad (21a)$$

$$\lambda = \lambda_\rho + \Delta\sigma_1 + \Delta^2\sigma_2 +\ldots. \qquad (21b)$$

Substituting these two expansions into (20) and (18) and equating the terms of equal order in Δ yields the set

$$\frac{d\bar{z}_o}{dt} - (D-\lambda_\rho I)\bar{z}_o = 0 \qquad (22)$$

$$\frac{d\bar{z}_1}{dt} - (D-\lambda_\rho I)\bar{z}_1 = (E-\sigma_1 I)\bar{z}_o \qquad (23)$$

$$\frac{d\bar{z}_2}{dt} - (D-\lambda\rho I)\bar{z}_2 = (E-\sigma_1 I)\bar{z}_1 - \sigma_2\bar{z}_o \qquad (24)$$

etc.

Note that the constant coefficient matrix of these equations is

$$D - \lambda_\rho I = \ulcorner\gamma_1,\ldots,\gamma_{N'}\lrcorner$$

where $\gamma_j \equiv \lambda_j - \lambda_\rho, j = 1,\ldots, N' = N - 4$.

The only $2\pi/\Omega$ periodic solution that is possible for Eq. (22) when $(\lambda_j-\lambda_\rho)\neq\pm m\Omega$ for $m = 0,1,2,\ldots$ and $j \neq \rho$ is the solution

$$\bar{z}_o = c(\delta_{\rho j})^\dagger \qquad (25)$$

where $\delta_{\rho j}$ is the Kronecker delta and c is an arbitrary complex constant. This statement is merely a restatement of the fact that the eigenfunction corresponding to the eigenvalue, λ_ρ, is the ρ-th column of matrix B, i.e., the least stable eigenmode of the underlying steady Blasius flow.

Since the solution (20) requires that $\bar{z}(t)$ be periodic with period $2\pi/\Omega$ in t, we shall need the inner product $<\bar{f},\bar{g}>$ defined by

$$<\bar{f},\bar{g}> = \frac{\Omega}{2\pi}\int_0^{2\pi/\Omega}\sum_{j-1}^{N'} f_j g_j{}^* dt. \qquad (26)$$

where the asterisk superscript denotes the complex conjugate. We shall also need the adjoint eigenfunction of Eq. (22) that corresponds to the eigenvalue, $\gamma_\rho = 0$, and that is $2\pi/\Omega$ periodic in t. This eigenfunction is

$$\bar{y}_o = d(\delta_{\rho j})^\dagger. \qquad (27)$$

For convenience we normalize $\bar{z}_o$ and $\bar{y}_o$ so that

$$<\bar{z}_o,\bar{y}_o> = 1$$

by setting $c = d = 1$.

The solution of any one of the equations in the set (23), (24), etc. is obtained from the solution of the previous member, by the application of the Fredholm Alternative and the requirement that these solutions are unique, i.e., they do not contain multiples of the eigensolution of Eq. (22) and are $2\pi/\Omega$ periodic in time. All of the equations of the set (23), (24) etc. have the form

$$\frac{d\bar{z}_j}{dt} - (D-\lambda_\rho I)\bar{z}_j = \bar{h}(t) \qquad (28)$$

where $\bar{h}(t)$ is a periodic vector function, which has a Fourier series representation of the form

$$\bar{h}(t) = \sum_{k=-\infty}^{\infty}\bar{h}_k e^{ik\Omega t} \qquad (29)$$

where $\bar{h}_k$ are constant vectors and the ρ-th component, $h_{o\rho}$ of $\bar{h}_o$, is zero. (This property is enforced by the solution procedures.)

Then, application of the Fredholm Alternative for solving (28) yields the requirement that

$$<\bar{h}(t),\bar{y}_o> = 0 \qquad (30)$$

Assuming condition (30) to hold (this will be achieved by properly selecting the σ_j's), the general solution, $\bar{z}_j$, can be written as

$$\bar{z}_j = \exp[(D-\lambda_\rho I)t] \times$$

$$\left\{\bar{\xi}_o + \int_0^t \exp[-(D-\lambda_\rho I)s]\bar{h}(s)ds\right\} \qquad (31)$$

Equation (31) is easily evaluated because

$$\exp[(D-\lambda_\rho I)t] = \ulcorner e^{\gamma_1 t},\ldots,e^{\gamma_{N'}t}\lrcorner \qquad (32)$$

Equation (32) is the main reason for diagonalizing the matrix, $(1/R_{\delta_*})(P+i\alpha J)$. It makes evaluation of the exponential matrix and the integral of Eq. (31) trivial. Thus, by evaluating Eq. (31), and requiring that $\bar{z}_j(t)$ be unique and $2\pi/\Omega$ periodic in t, values for the constant vector, $\bar{\xi}_0$, are obtained which eliminate all the non-$2\pi/\Omega$ periodic functions from (31). The result of these calculations is

$$\bar{z}_j(t) = \sum_{k=-\infty}^{\infty}\left(\frac{h_{k\ell}}{ik\Omega-\gamma_\ell}\right)^\dagger e^{ik\Omega t} \qquad (33)$$

The solution procedure then is to apply Eqs. (30) and (33) to each of the Eqs. (23), (24) etc. in sequence starting with (23). These calculations have been programmed and are quite easily performed. (Our program does these calculations to the 7th order term, but more terms can be easily incorporated.) We are mainly interested in the first two perturbation terms which result in

$$\sigma_1 = 0;\ \bar{z}_1(t) = \bar{\zeta}^{(1)}e^{i\Omega t} + \bar{\zeta}^{(-1)}e^{-i\Omega t} \qquad (34)$$

where

$$\bar{\zeta}^{(1)} = \left(\frac{E^{(1)}_{j\rho}}{i\Omega-\gamma_j}\right)^\dagger, \qquad (35a)$$

$$\bar{\zeta}^{(-1)} = \left(\frac{-E_{j\rho}^{(-1)}}{i\Omega+\gamma_j} \right)^{\dagger} , \qquad (35b)$$

and

$$\sigma_2 = \sum_{j=1}^{N'} (E_{\rho j}^{(1)} \zeta_j^{(-1)} + E_{\rho j}^{(-1)} \zeta_j^{(1)}) , \qquad (36a)$$

$$\bar{z}_2(t) = \bar{\eta}^{(2)} e^{2i\Omega t} + \bar{\eta}^{(o)} + \bar{\eta}^{(-2)} e^{-2i\Omega t} , \qquad (36b)$$

where

$$\bar{\eta}^{(2)} = \left(\frac{\sum_{j=1}^{N'} (E_{\ell j}^{(1)} \zeta_j^{(1)}}{2i\Omega-\gamma_\ell} \right)^{\dagger} , \qquad (37a)$$

$$\bar{\eta}^{(o)} = \left(\left(\sum_{j=1}^{N'} (E_{\ell j}^{(1)} \zeta_j^{(-1)} + E_{\ell j}^{(-1)} \zeta_j^{(1)}) - \sigma_2 \delta_{\rho\ell} \right) / (-\gamma_\ell) \right)^{\dagger} , \qquad (37b)$$

$$\bar{\eta}^{(-2)} = \left(\frac{\sum_{j=1}^{N'} E_{\ell j}^{(-1)} \zeta_j^{(-1)}}{-2i\Omega-\gamma_\ell} \right)^{\dagger} . \qquad (37c)$$

We note that the order Δ perturbation, σ_1, of the eigenvalue λ_ρ is zero so that the long-term effect of a flow oscillation with amplitude Δ is only of order Δ^2. However, the short-term effect is still of order Δ because the eigenfunction, $\bar{z}_1(t)$, appears in the term I(t) in the relative amplification ratio, e_{T_1}/e_{T_0}, given by Eq. (9). In fact, the structure of the matrix, E, is such that all values of σ_j with odd indices are zero and λ has an expansion in even powers of Δ about the simple eigenvalue, λ_ρ. This can be surmized easily from the fact that the phase of the imposed oscillatory part of the boundary layer flow should not play a role in the modifications of the eigenvalue, λ_ρ. Furthermore, note that the solutions, $\bar{z}_1(t)$ and $\bar{z}_2(t)$, exhibit clearly the possible effects, at second order, of certain resonant couplings. None of the denominators in (35) and (37) are zero because $\gamma_j \neq \pm ik\Omega$ for any integer values of j or k; hence these solutions are uniformly valid for any positive value of the frequency, Ω. It is possible, however, that at resonant frequencies such as at $\Omega = \pm \mathcal{I}m(\gamma_\mu)$, the value of σ_2 will have a relative maximum. Of particular importance is that in the low frequency limit, $\Omega \to 0$, the σ_j's may be singular. The lower values of Ω will be an important consideration and will be discussed in detail in the next section.

4. NUMERICAL RESULTS AND DISCUSSION

Before describing the computational results that have been obtained, we emphasize that in this work the instability of the oscillatory boundary layer as a whole is being compared to the instability of the underlying steady Blasius boundary layer. However, it is easier to describe this comparison in the terminology of the oscillatory forcing of the Blasius boundary layer instability. For example, if the oscillatory boundary layer is less stable than the steady boundary layer by itself, then we describe this situation as one in which the imposed oscillations tend to destabilize the steady flow.

The first set of calculations were made to test for resonant interactions at second order in Δ. By consulting the solutions (35) and (36), it can be seen that the mean effect of the imposed oscillations on the eigenvalue, λ_ρ, is manifested by the term, σ_2. There are two types of resonances possible. The first type is the "harmonic parametric resonance" which corresponds to values of Ω given by $\omega_\rho/\Omega = 1/2, 1, 2, \ldots$ where ω_ρ is the response frequency of the disturbance, $\omega_\rho = \mathcal{I}m\lambda_\rho$. The second type of resonance is the "combination resonance" corresponding to values of Ω given by $\mathcal{I}m (i\Omega \pm \gamma_j) = 0$ (note the denominators of solution 35). Figure 1 shows the computational results at certain frequencies Ω in the range, $1 \leq \omega_\rho/\Omega \leq 3$. It can be seen that the imposed oscillations stabilize the flow. Figure 1 shows that no resonance effects are predicted at either $\omega_\rho/\Omega = 1,2,3$, or at $\omega_\rho/\Omega = 1.417$ and 1.74, which correspond to the two possible combination resonances in the frequency range shown. This lack of resonance effect results mainly because the external free stream oscillations induce a significant amount of oscillatory vorticity inside the boundary layer only in a region very close to the wall. This can be seen by examination of the Stokes layer profile (14) where the exponential factor has a vertical decay constant, β, which is equal to about 5 in the range of frequencies considered. The main fluctuations of the disturbance velocity are concentrated at the mean critical layer, $\eta_c \approx 0.5$ [where η_c is given by $c_r = f_B(\eta_c)$ and c_r is the mean phase velocity of the disturbance].

Thus, instead of the Stokes layer interacting directly with the disturbance of the underlying steady boundary layer at the level, η_c, where most of the disturbance energy is being produced, it is confined mainly to the wall region where it cannot be very effective. Furthermore, the Stokes layer lacks a spatial structure in the x-direction that can match in some way the spatial structure of the

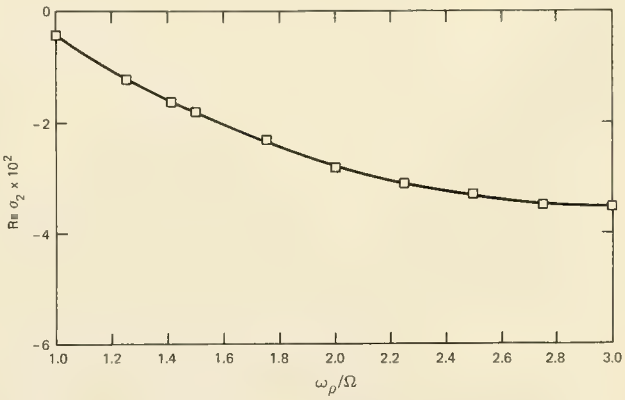

FIGURE 1. The growth rate perturbation Re σ_2 for α = 0.15. $R_{\delta*}$ = 1128 (on the neutral curve) $\omega_f = \omega_\rho / R_{\delta*}$ = 0.43×10^{-4}.

disturbance mode. It is notable that the imposed oscillations have an increased stabilizing effect as Ω decreases (ω_ρ/Ω increases). This increased stabilizing effect can be expected for two reasons. The first reason is found in the solution (35) which shows that the terms,

$$E_{\rho\rho}^{(1,-1)}(\pm i\Omega-\gamma_\rho),$$

may become unbounded if

$$E_{\rho\rho}^{(1)} \text{ or } E_{\rho\rho}^{(-1)}$$

remains bounded as $\Omega \to 0$, because $\gamma_\rho = 0$. Secondly, it can be seen in the Stokes layer profile (14) that the oscillations of the boundary layer become more effective in penetrating up to the critical layer when Ω decreases (i.e., β also decreases since

$$\beta = \sqrt{\Omega R_{\delta_*}/2}).$$

However, we cannot use the present parallel flow-model at very low frequencies because in one period, $2\pi/\Omega$, of the imposed oscillation, a disturbance will propogate down the boundary layer a distance, δx, that is too large for the parallel flow assumption to hold (i.e., constant boundary layer properties in the x-direction). For example, the change, $\delta R_{\delta *}$, in the displacement thickness Reynolds number, R_{δ_*}, over the distance, δx, (near the values of α = 0.15 and R_{δ_*} = 1200) is given approximately by

$$\delta R_{\delta_*} \approx 3.5N/\omega_\rho \qquad (38)$$

where $N = \omega_\rho/\Omega$. Thus, in the range of values of α and $R_{\delta *}$ of our calculations $\delta R_{\delta *} \simeq 70$ N so that for N = 3, $\delta R_{\delta *}$ is nearly 20 percent of the value of $R_{\delta *}$. Under the circumstance, the parallel flow approximation is only roughly valid. Nevertheless, the values of $\delta R_{\delta *}$ as a fraction of $R_{\delta *}$ decrease as one goes downstream of the neutral curve for fixed values of the frequency ratio, ω_ρ/Ω. Thus, the parallel flow approximation improves as one follows a constant frequency disturbance downstream of the neutral point.

The second set of calculations that were performed was for the amplification of a fixed frequency disturbance propogating down the oscillatory boundary layer. Two values of ω_ρ/Ω, equal to 2 and 3, were chosen for illustration. The disturbance examined is an unstable Tollmien-Schlichting wave of constant absolute frequency $\omega_f = \omega_\rho/R_{\delta *} = 0.43 \times 10^{-4}$ along the constant frequency line $\alpha = 0.00133\ R_{\delta *}$. This disturbance first begins to grow in the steady boundary layer at the values of α = 0.15, $R_{\delta *}$ = 1128, and ceases to grow at about the values of α = 0.3 and $R_{\delta *}$ = 2255. The disturbance trajectory $\alpha = 0.00133\ R_{\delta *}$ passes nearly through the point in the α, $R_{\delta *}$ plane of maximum rate of amplification.

Figure 2 shows the values of $\text{Re}\sigma_2$ obtained for the growing Tollmien-Schlichting wave along the trajectory, $\alpha = 0.00133\ R_{\delta *}$, at the two different values ω_ρ/Ω = 2 and 3. An interesting feature of the results in Figure 2 is that $|\text{Re}\sigma_2|$ increases with $R_{\delta *}$ although the quantity β also increases which would seem to indicate further decoupling of the oscillatory Stokes layer (14) from the disturbance oscillations. Presumably, the values of $|\text{Re}\sigma_2|$ decrease as $R_{\delta *}$ becomes sufficiently large for then β also becomes so large that the Stokes layer will almost completely disappear. It can be seen in Figure 2 that the stabilization of the boundary layer can be substantial for the value of ω_ρ/Ω = 3 and at the larger values of $R_{\delta *}$.

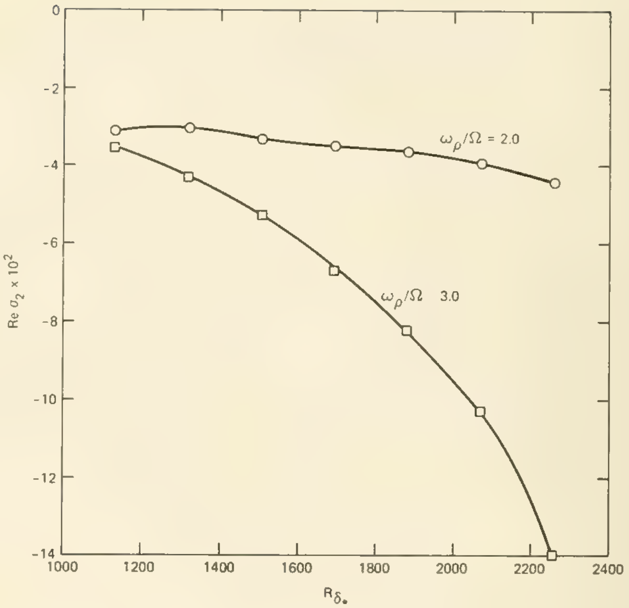

FIGURE 2. Growth rate perturbation Re σ^2 along α = 0.00133 $R_{\delta *}$.

Figure 3 shows the values of $\text{Re}\lambda = \text{Re}\lambda_\rho + \Delta^2\text{Re}\sigma_2$ for the value of Δ = 0.1 and the three values of ω_ρ/Ω = 0,2, and 3. (ω_ρ/Ω = 0 is equivalent to Δ = 0). The total effect of the imposed oscillations with Δ = 0.1 is not very substantial at the value, ω_ρ/Ω = 2, but at the value of ω_ρ/Ω = 3, the stabilization of the flow is significant. We note that an oscillation amplitude of Δ = 0.1 is a rather large value at the frequencies considered here and would require a large amount of power to achieve in an experimental test facility such as a wind tunnel unless the mean flow is very slow.

The rates of amplification shown in Figure 3 can be summed according to formula (9) to obtain the relative amplification ratio, e_{T_1}/e_{T_0}. One can show that

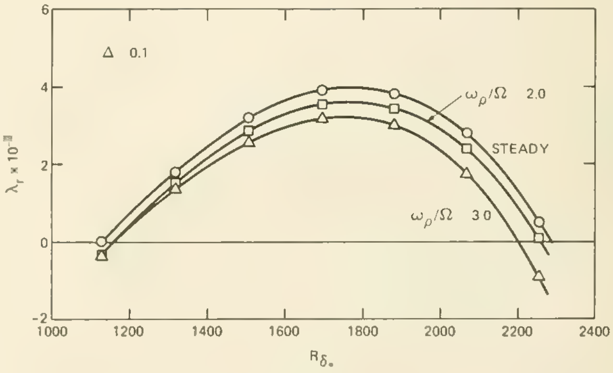

FIGURE 3. The amplification rate λ_r along the trajectory α = 0.00133 $R_{\delta *}$.

$$J \equiv 2 \int_{t_0}^{t_1} \mathrm{Re}\lambda dt$$
$$= 0.676 \int_{R_{\delta_{*0}}}^{R_{\delta_{*1}}} (\mathrm{Re}\lambda/c_g) dR_{\delta_*} \qquad (39)$$

where $R_{\delta_{*0}}$ and $R_{\delta_{*1}}$ are the values of R_{δ_*} at the locations of the disturbance at the times, t_0 and t_1, respectively. The value of c_g, the group velocity, along the trajectory $\alpha = 0.00133\ R_{\delta_*}$, was computed to be about 0.356. We neglected the $O(\Delta^2)$ modification of c_g due to the imposed oscillations. This modification of c_g is $O(10^{-3})$ and thus does not affect the integral, J, in a substantial way. From the results shown in Figure 3, one obtains (by a trapezoidal rule integration), the values of $J \approx 11, 8.7$, and 6.3 for $\omega_\rho/\Omega = 0, 2$, and 3 respectively. The integral I(t) of (10) is evaluated by certain sums and products of the vector components of the solutions, (35) and (37). We omit the details. The resulting expression for I(t), to second order in Δ, has the following form

$$I(t) = A_1 + A_2\Delta^2 + \Delta(B_1\cos\Omega t + B_2\sin\Omega t)$$
$$+ \Delta^2(C_1\cos 2\Omega t + C_2\sin 2\Omega t) \qquad (40)$$

where $A_1 > 0, A_2, B_1, B_2, C_1$ and C_2 are real numbers that depend on the Reynolds number, R_{δ_*}. These coefficients have been computed along the disturbance trajectory, $\alpha = 0.00133\ R_{\delta_*}$ and are plotted in Figure 4. By using the values of A_2, B_1, B_2, C_1 and C_2 from Figure 4 ($A_1 \equiv 1.0$ by suitable normalization) in Eq. (40) for the value of $\Delta = 0.1$ one finds that

$$0.5 < \frac{I(t)}{I(t_0)} < 2$$

at all the values of Reynolds number, R_{δ_*}, for which the disturbance grows. It is customary to assess the overall growth of a disturbance by considering the natural logarithm of the amplification ratio, e_T/e_{T_0}. From (9) we have

$$\ln \frac{e_T}{e_{T_0}} = \ln \frac{I(t)}{I(t_0)} + J$$

and one can see that although the term, $\ln I(t)/I(t_0)$, contributes an oscillatory factor to $\ln e_T/e_{T_0}$ (recall that, by following the disturbance down the plate, $t \propto R_{\delta_*}$) this contribution is minor relative to the maximum value attained by J. Thus it can be seen that the major effect of the parallel free stream oscillations is to reduce the mean growth rate of the unstable disturbances. This effect is small for small values of Δ but can be significantly large at such large values of Δ as $\Delta > 0.1$. We note that typical free stream turbulence rarely has a velocity magnitude as large as 10 percent of the mean free stream speed.

Experimental results on the effects of parallel free stream oscillation on the instability and transition of the flat plate boundary layer are reviewed by Loehrke, Morkovin and Fejer (1975). However, we shall not make any comparison with their experiments because these were for very low frequency oscillations ($\omega_\rho/\Omega \approx 10$) for which our parallel flow instability theory is of doubtful applicability. An appropriate analytical instability theory for comparison with these experiments is a quasi-steady and parallel flow theory [see Obremski and Morkovin (1969)].

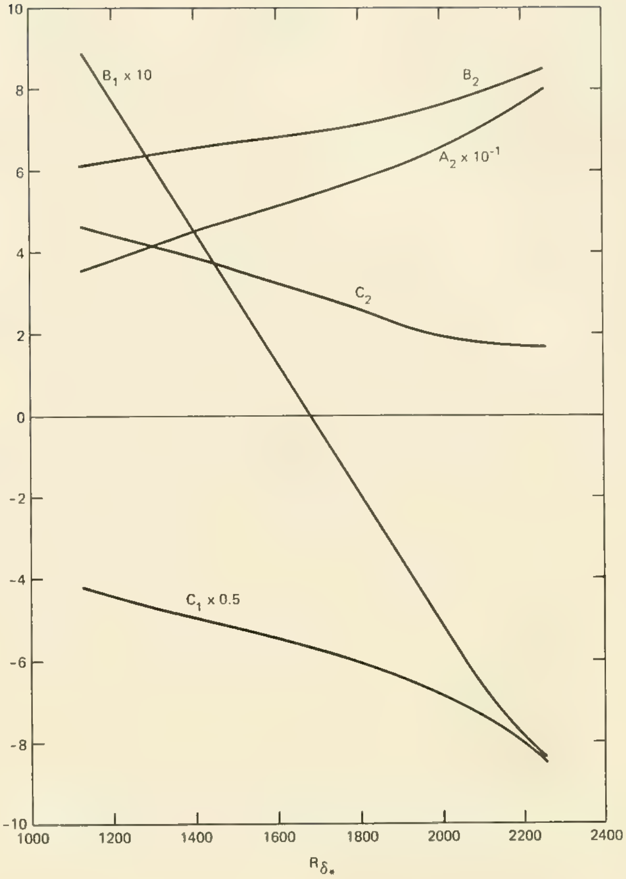

FIGURE 4. The coefficients of I(t) along $\alpha = 0.00133\ R_{\delta_*}$, $\omega_\rho/\Omega = 3$.

5. CONCLUDING REMARKS

Our main result is that the parallel free stream oscillations, which manifest themselves in the Blasius boundary layer as a Stokes layer, lead to a mean stabilization of the flow. This stabilization is very weak except for oscillation amplitudes that are at least near 10 percent of the mean free stream speed. Precise experimental data on the effects of such oscillations on Blasius boundary layer instability is not available in the frequency range considered in this work. However, the results are in accord with transition data for oscillatory pipe flows. Sarpkaya (1966) has shown experimentally that transition is delayed substantially when harmonic axial oscillations are superimposed on steady pipe flow. Furthermore, von Kerczek and Davis (1975) have shown that the oscillatory Stokes layer by itself is very stable, probably at all Reynolds numbers, so that one might conjecture that if the Stokes layer begins to dominate the boundary layer (which occurs for low frequencies Ω and large amplitudes Δ), then the Blasius boundary layer can be stabilized by these oscillations. However, the Stokes layer stability is very sensitive to extraneous effects such as streamline curvature. For instance, experiments show that transition of plane Stokes layers occurs at Stokes layer Reynolds numbers, R_{st}, (where $R_{st} = \Delta R_{\delta_*}/\beta$) on the order of 500 [see Li (1954)]. However, if a slight amount of streamline curvature exists, as would occur in Stokes layers induced on the bottom of a water channel supporting free-surface gravity waves [see Collins (1963)], the *transition* Reynolds number is reduced to about 160. Thus, the effect on the instability of the Blasius boundary layer of free stream oscillations with a spatial structure such as $U_o + U_1\cos(kx-\omega t)$ can be expected to be different from the parallel flow oscillations considered above.

It is well known that ambient turbulence tends to promote laminar to turbulent transition of the boundary layer. Thus, if some oscillatory boundary layer does in fact properly model certain features of the interaction of the ambient turbulence with the underlying steady boundary layer then it is to be expected that such a oscillatory boundary layer is less stable than the underlying steady boundary layer. Although the present numerical results show only a stabilizing effect for the type of oscillation considered, as inferred above there is reason to believe that a more complex form of oscillation of the boundary layer can be destabilizing. The theory of the instability of forced oscillatory boundary layers provides an alternative point of view from that of Rogler and Reshotko (1974) and Mack (1975) on the role of the interaction of free-stream disturbances with Tollmien-Schlichting waves.

ACKNOWLEDGEMENT

This work was supported by the Naval Sea Systems Command.

REFERENCES

Ackerberg, R. C., and J. H. Phillips, (1972). The Unsteady Laminar Boundary Layer on a Semi-Infinite Flat Plate Due to Small Fluctuations in the Magnitude of the Free Stream Velocity. *J. Fluid Mechanics, 51,* 137-157.

Coddington, E. A., and N. Levinson, (1955). *The Theory of Ordinary Differential Equations,* McGraw-Hill, New York.

Collins, J. I. (1963). Inception of Turbulence at the Bed under Periodic Gravity Waves. *J. Geophysical Res., 68,* 6007-6014.

Craik, A. D. D., (1971). Nonlinear Resonant Instability in Boundary Layers. *J. Fluid Mechanics, 50,* pp. 393-413.

Davis, S. H., (1976). The Stability of Time-Periodic Flows. *Annual Review of Fluid Mechanics, 8,* 57-74.

Gaster, M., (1963). A Note on the Relation Between Temporarily-Increasing and Spatially-Increasing Disturbances in Hydrodynamic Stability. *J. Fluid Mechanics, 14,* 222-224.

Hayashi, C., (1964). *Nonlinear Oscillations in Physical Systems,* McGraw-Hill Book Co., New York.

Kerczek, C. von, and S. H. Davis, (1974). Linear Stability Theory of Oscillatory Stokes Layers, *J. Fluid Mechanics, 62,* 753-773.

Li, H., (1954). *Tech. Mem. 47, Beach Erosion Board,* U.S. Army Corps of Engineers, Washington, D.C.

Loehrke, R. I., M. V. Morkovin, and A. A. Fejer (1975). Transition in Nonreversing Oscillating Boundary Layers, *Transactions ASME, J. Fluid Engineering, 97,* 534-549.

Mack, L. M. (1975). Linear Stability Theory and the Problem of Supersonic Boundary-Layer Transition, *AIAA J.,* 13, 278-289.

Mack, L. M., (1976). A Numerical Study of the Temporal Eigenvalue Spectrum of the Blasius Boundary Layer, *J. Fluid Mechanics, 73,* 497-520.

Obremski, H. J. and M. V. Morkovin, (1969). Application of Quasi-Steady Stability Model to Periodic Boundary-Layer Flows, *AIAA J., 7,* 1298-1301.

Orszag, S. A., (1971). Accurate Solution of the Orr-Sommerfeld Stability Equation, *J. Fluid Mechanics, 50,* 689-703.

Rogler, H. L. and E. Reshotko, (1975). Disturbances in a Boundary Layer Introduced by a Low Intensity Array of Vortices, *SIAM J. Appl. Math., 28,* 431-462.

Rosenhead, L., (1963). *Laminar Boundary Layers,* Oxford.

Sarpkaya, T., (1966). Experimental Determination of the Critical Reynolds Number for Pulsating Poiseuille Flow, *Trans. ASME, J. Basic Engineering, 88,* 589-598.

Yakubovich, V. A. and V. M. Starzhinskii, (1975). *Linear Differential Equations with Periodic Coefficients,* Translated from the Russian by D. Lauvish, John Wiley & Sons.

Heated Boundary Layers

Eli Reshotko
Case Western Reserve University
Cleveland, Ohio

ABSTRACT

Heating the walls on which laminar boundary layers develop in water can delay their transition to turbulent flow and lead to significant drag reduction. This paper describes the work done over the last several years at Case Western Reserve University in examining the bases and consequences of the heating phenomenon. Included are theoretical and experimental studies of the stability of heated water boundary layers for both uniform and non-uniform wall temperature distributions, and experimental study of the effect of heating on laminar separation and a quantitative assessment of the prospective drag reduction on underwater vehicles.

1. INTRODUCTION

It was noted many years ago in experiments at low subsonic speeds [Frick and McCullough (1942), Liepmann and Fila (1947)] that the transition location of the flat plate boundary layer in air is advanced as a result of plate heating. Based on this observation it had long been suspected that heating would have the opposite effect in water, namely that it would delay the onset of transition. This is because heating in water reduces the viscosity near the wall resulting in a fuller, more stable velocity profile for a flat plate than the Blasius profile. Cooling in water (and heating in air) on the other hand tends to give an inflected velocity profile which is less stable than the Blasius profile.

These suspicions remained untested until confirmed by the analysis of Wazzan, Okamura, and Smith (1968, 1970). These results triggered a significant activity in the United States to determine whether wall heating could realistically be used as a technique for drag reduction. A portion of this effort was undertaken at Case Western Reserve University (CWRU) under the joint auspices of the Office of Naval Research and the General Hydrodynamics Research Program of the David W. Taylor Naval Ship Research and Development Center. The CWRU effort has been both analytical and experimental and is ongoing. This paper will review the results to date of the CWRU activity and indicate current and future directions.

2. ANALYSIS OF THE STABILITY OF HEATED WATER BOUNDARY LAYERS

The analysis of Wazzan et al. (1968, 1970) considers the stability characteristics of the boundary layer to be governed by the disturbance vorticity equation including consideration of viscosity variations in the basic flow but ignoring temperature fluctuations and the coupled viscosity fluctuations. The disturbance differential equation consists of the fourth-order Orr-Sommerfeld operator augmented by some lower order terms and is as follows:

$$(\bar{U}-c)(\phi''-\alpha^2\phi) - U''\phi = -\frac{i}{\alpha R}[\mu(\phi^{iv} - 2\alpha^2\phi'' + \alpha^4\phi) + 2\bar{\mu}'(\phi''' - \alpha^2\phi) + \bar{\mu}''(\phi'' + \alpha^2\phi)] \qquad (1)$$

with boundary conditions

$$\phi(0) = \phi'(0) = \phi(\infty) = \phi'(\infty) = 0 \qquad (2)$$

The analysis of Lowell and Reshotko (1974) on the other hand is based on the following coupled sixth-order system of vorticity and energy disturbance equations:

$$
\begin{aligned}
&(\bar{U}-c)[(\bar{\rho}\phi)'' - \alpha^2(\bar{\rho}\phi)] - \bar{U}''(\bar{\rho}\phi) + i[r(\bar{U}-c)^2]' \\
&= -\frac{i}{\alpha R}\Bigg\{ \mu\Bigg(\left[\frac{1}{\bar{\rho}}(\bar{\rho}\phi)'\right]''' - 2\alpha^2\left[\frac{1}{\bar{\rho}}(\bar{\rho}\phi)'\right]' + \alpha^4\phi \\
&\qquad + \alpha^2\left[\frac{\rho'}{\bar{\rho}}\phi\right]'\Bigg) + 2\bar{\mu}'\Bigg(\left[\frac{1}{\bar{\rho}}(\bar{\rho}\phi)'\right]'' \\
&\qquad - \alpha^2\left[\frac{1}{\bar{\rho}}(\bar{\rho}\phi)'\right]\Bigg) + \bar{\mu}''\Bigg(\left[\frac{1}{\bar{\rho}}(\bar{\rho}\phi)'\right]' + \alpha^2\phi\Bigg)\Bigg\} \\
&\qquad - \frac{1}{\alpha R}\Bigg\{\Bigg(m\bar{U}' - \bar{\mu}[\frac{r(\bar{U}-c)}{\bar{\rho}}]'\Bigg)'' \\
&\qquad + \alpha^2\Bigg(m\bar{U}' - \bar{\mu}\left[\frac{r(U-c)}{\bar{\rho}}\right]'\Bigg) \\
&\qquad + 2\alpha^2\Bigg(\bar{\mu}\left[\frac{r(\bar{U}-c)}{\bar{\rho}}\right]\Bigg)'\Bigg\} \qquad (3)
\end{aligned}
$$

$$
\begin{aligned}
\bar{c}_p[i(\bar{U}-c)\tau + (\bar{\rho}\phi)\bar{T}] = \frac{1}{\alpha RPr}\Bigg\{&[(\bar{\rho}\bar{k})\tau' + \bar{\rho}\kappa\bar{T}']' \\
&- \frac{\alpha^2}{\bar{\rho}^2}(\bar{\rho}\bar{k})\tau\Bigg\} \qquad (4)
\end{aligned}
$$

with boundary conditions

$$
\begin{aligned}
\phi(0) &= \phi'(0) = \tau(0) = 0 \\
\phi(\infty) &= \phi'(\infty) = \tau(\infty) = 0
\end{aligned} \qquad (5)
$$

In equations (3) and (4) all properties of the basic flow are variable. The quantities r, m, and κ are the density, viscosity, and thermal conductivity fluctuation amplitudes respectively and the coupling comes about through the viscosity fluctuations that are directly related to the temperature fluctuations.

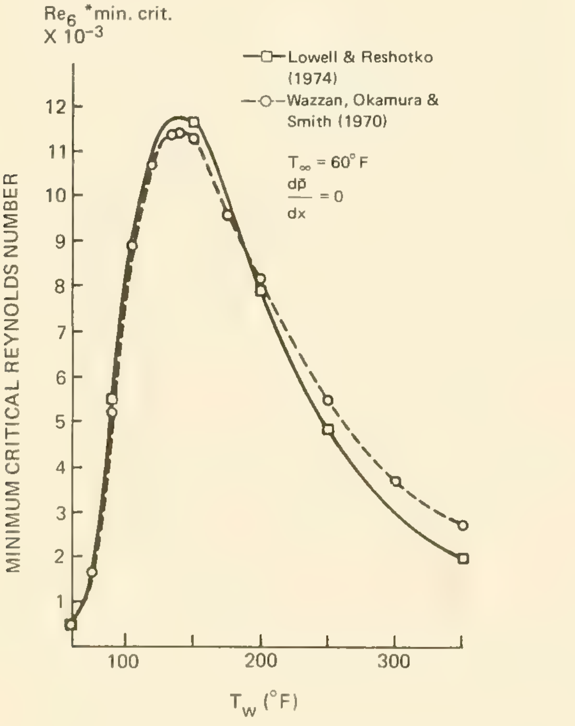

FIGURE 1. Effect of wall temperature on minimum critical Reynolds number ,[from Lowell and Reshotko (1974)].

The results of these two analyses for the minimum critical Reynolds number with wall heating are shown in Fig. 1. The curves are very much alike. Furthermore, the neutral stability characteristics and the growth rates as calculated in the aforementioned analyses are sufficiently close so that there is no important quantitative difference between the two. The coupling of vorticity and temperature fluctuations through the viscosity seems therefore to be rather weak.

As is seen in Figure 1, both sets of calculations predict significant boundary layer stabilization (increased minimum critical Reynolds number, decreased disturbance amplification rates, etc.) with moderate heating, but display a maximum and subsequent decrease as the wall to free-stream temperature difference is further increased. The significant stabilization indicated for overheats of up to 40°C (∿70°F) prompted a study of the possible drag reduction due to heating to see if this drag reduction technique was in fact worth pursuing further.

3. DRAG REDUCTION IN WATER BY HEATING

It is shown in this section that significant reductions of drag are available to water vehicles with on-board propulsion system is discharged through heating the laminar flow portion of the hull. The analysis is as follows [following Reshotko (1977)]:

For a vehicle with an on-board propulsion system

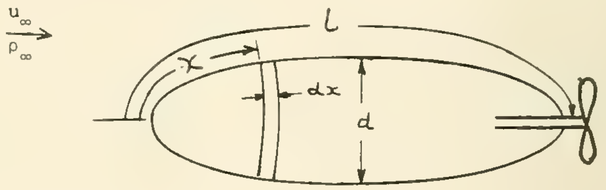

the friction drag is

$$D_F = q\left[\int_0^{x_{tr}} c_{f\ell}\ wdx + \int_{x_{tr}}^{L} c_{ft}\ wdx\right] \qquad (6)$$

where q is the dynamic pressure, $c_{f\ell}$ and c_{ft} are respectively the laminar and turbulent friction coefficients, wdx is the area element at length x, L is the vehicle length, and x_{tr} is the transition location.

The total drag can be written

$$D = D_F(D/D_F) \qquad (7)$$

where D/D_F is the ratio of total to friction drag. For an axisymmetric body this ratio is a function of the fineness ratio of the configuration.

Hoerner (1958) suggests that

$$D/D_F = 1 + 1.5(\frac{d}{L})^{3/2} + \ldots \qquad (8)$$

The drag power can then be written

$$P_D = Du_\infty = q\ u_\infty(D/D_F)(C_{DF}A) \qquad (9)$$

where $[C_{DF}A]$ is the quantity in brackets in equation (1).

The power available for heating is related to the thermal efficiency of the power plant as follows:

$$P_A = \left(\frac{P_D}{\eta_{th}} - P_D\right)\eta_{eff} = P_D\left(\frac{1}{\eta_{th}} - 1\right)\eta_{eff} \tag{10}$$

where η_{eff} is the effectiveness of transmitting the reject heat to the water in the desired manner.

If one considers heating only the laminar portion of the hull then the power required to accomplish such heating is

$$P_H = \rho_\infty u_\infty c\Delta T \int_o^{x_{tr}} c_{h\ell}\, wdx \tag{11}$$

where c is the specific heat of water, $c_{h\ell}$ is the laminar Stanton number for the heated boundary layer at $\Delta T = T_w - T_\infty$.

Applying the available heating power P_A to the laminar portion of the flow, $(P_A = P_H)$, after some simplification yields

$$\left[1 + \frac{\int_{x_{tr}}^{L} c_{ft}\, wdx}{\int_o^{x_{tr}} c_{f\ell}\, wdx}\right] = \frac{c\Delta T}{u_\infty^2}\,\frac{\left[\dfrac{\int_o^{x_{tr}} c_{h\ell}\, wdx}{\int_o^{x_{tr}} \frac{c_{f\ell}}{2}\, wdx}\right]}{\left[\dfrac{D}{D_F}\left(\dfrac{1}{\eta_{th}} - 1\right)\eta_{eff}\right]} \tag{12}$$

The left side is the ratio of overall friction drag to the laminar friction drag and is configuration dependent. The right side depends on the dimensionless ratio $c\Delta T/u_\infty^2$ and on the bracketed parameter in the denominator related to the amount of reject heat that can be transferred to the boundary layer. The bracketed parameter in the numerator is a Reynolds analogy factor which is configuration dependent. In order to close the calculation, a relation is needed between ΔT and transition Reynolds number $Re_{x_{tr}}$ which is also dependent on configuration.

Example - The Flat Plate

In order to quantitatively evaluate the prospective drag reduction due to heating, it is necessary to choose a particular configuration. The flat plate is chosen because of its great simplicity and because some information on transition with surface heating is available. The results should be representative of what can be obtained for slender shapes having pressure gradients that are not too large.

For a flat plate (w = const)

$$\int_0^{x_{tr}} c_{f\ell}\, dx = 1.328\,\frac{x_{tr}}{\sqrt{Re_{x_{tr}}}} \tag{13}$$

$$\int_{x_{tr}}^{L} c_{ft}\, dx = 0.074\left(\frac{L}{Re_L^{1/5}} - \frac{x_{tr}}{Re_{x_{tr}}^{1/5}}\right)$$

and by Reynolds analogy

$$c_{h_\ell} = \frac{c_{f\ell}}{2}\, Pr^{-2/3} \tag{14}$$

Thus for the case of the flat plate, Eq. (12) becomes

$$\left[1 + \frac{0.074}{1.328}\left(\frac{Re_L^{4/5} - Re_{x_{tr}}^{4/5}}{Re_{x_{tr}}^{1/2}}\right)\right] = \frac{c\Delta T}{u_\infty^2}\,\frac{Pr^{-2/3}}{\left\{\dfrac{D}{D_F}\left(\dfrac{1}{\eta_{th}} - 1\right)\eta_{eff}\right\}} \tag{15}$$

The left side of equation (15) is the ratio of overall friction drag to laminar friction drag for a flat plate.

The variation of transition Reynolds number $Re_{x_{tr}}$ with overheat ΔT depends on the choice of transition criterion. A criterion that has been shown to give plausible trends is the e^9 criterion of Smith and Gamberoni (1956) and Van Ingen (1956). For low speed flows, these authors correlated transition Reynolds number over plates, wings, and bodies with the amplitude ratio using linear stability theory of the most unstable frequency from its neutral point to the transition point. They found that the transition Reynolds number $Re_{x_{tr}}$ as predicted by assuming an amplification factor of e^9 was seldom in error by more than 20%. Wazzan et al. (1970) have calculated and presented such a curve for heated flat plates in water a portion of which is shown in Figure 2. Although not quite shown on the figure, $Re_{x_{tr}}$ reaches a maximum value of about 260×10^6 at an overheat of about 43°C. The most recent data of Barker (1978) taken in a constant-diameter pipe are shown on this figure as well. Barker obtains a considerable increase of transition Reynolds number with heating in the entrance flow boundary layers and his data attests

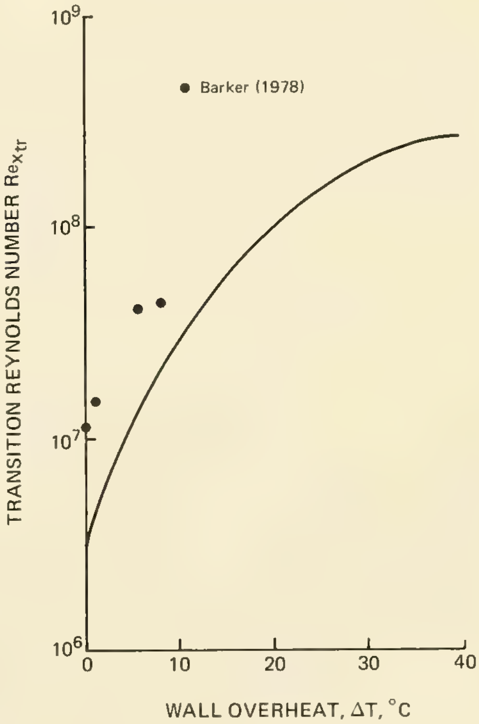

FIGURE 2. Variation of transition Reynolds number for a flat plate with uniform wall overheat according to an "e^9" transition criterion, T_∞ = 60°F.

to the reasonability of the assumed transition schedule with overheat.

Drag reduction calculations have been performed for plate speeds up to 24.4 m/sec (80 fps), for plate lengths of 3.05 m (10 ft), 15.24 m (50 ft). 30.48 m (100 ft), 152.4 m (500 ft), and 304.8 m (1000 ft), and for values of $[\frac{D}{D_F}(\frac{1}{\eta_{th}} - 1)\eta_{eff}]$ of 2,5, and 9. Since the product $D\eta_{eff}/D_F$ might be very close to unity, one may view the aforementioned values of the "efficiency factor" $[\frac{D}{D_F}(\frac{1}{\eta_{th}} - 1)\eta_{eff}]$ as approximately corresponding to $\eta_{th} = 0.33, 0.17,$ and 0.10 respectively.

Results are presented in Figure 3 for the case of an efficiency factor of 5($\eta_{th} \simeq 0.17$). Shown in Figure 3 are $D/D_{\Delta T=0}$, the ratio of the drag with heating to that without using the reject heat for drag reduction purposes, the corresponding laminar fraction of the plate x_{tr}/L, the wall temperature rise of the laminar region, and finally the ratio of the computed drag with heating to that for fully laminar flow over the entire plate.

Generally speaking the drag reduction becomes noticable as speeds exceed 10 m/sec (∿20 knots). Although the drag ratio is not a strong function of length, the overheat in the laminar region increases quite significantly with vehicle length. For $\eta_{th} \simeq 0.17$ (Figure 3), drag reduction of about 60% are atainable for vehicle speeds of 25 m/sec (∿50 knots) but the vehicle is far from full laminarization. The variation of drag ratio with η_{th} is shown in Figure 4 for selected cases. The lower the thermal efficiency, the larger the drag reduction and vice-versa. The indication from the calculations is that full laminarization can be obtained in a number of cases (Figure 4) but only if η_{th} gets below about 0.03. Since the e^9 transition curve (Figure 2) has a maximum value of $Re_{x_{tr}}$ below 3×10^8, vehicles with length Reynolds numbers above 3×10^8 cannot be completely laminarized.

For a plate of given length at a prescribed speed, the fuel consumption (proportional to D/η_{th}, the slope of a line through the origin in Figure 4) increases as η_{th} is reduced. But it is far below that of the unheated plate.

Real Configurations

Real vehicle configurations involve additional factors not considered in this flat-plate calculation. Favorable pressure gradient, for example, can be very effective in delaying transition while regions of adverse gradient are otherwise. Non-uniform longitudinal heating distributions can result in a more optimal use of the available heat. Effects

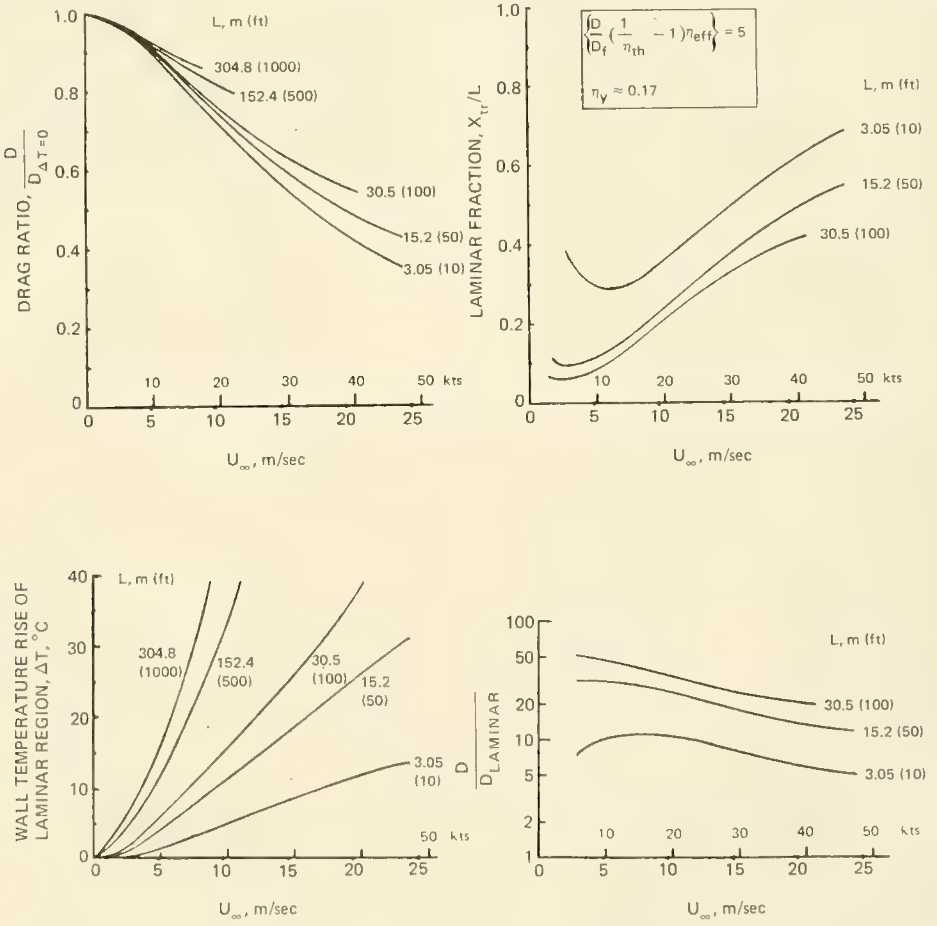

FIGURE 3. Drag reduction by use of reject heat of propulsion system for transition delay. $\left[\frac{D}{D_F}(\frac{1}{\eta_{th}} - 1)\eta_{eff}\right] = 5$, ($\eta_{th} \simeq 0.17$).

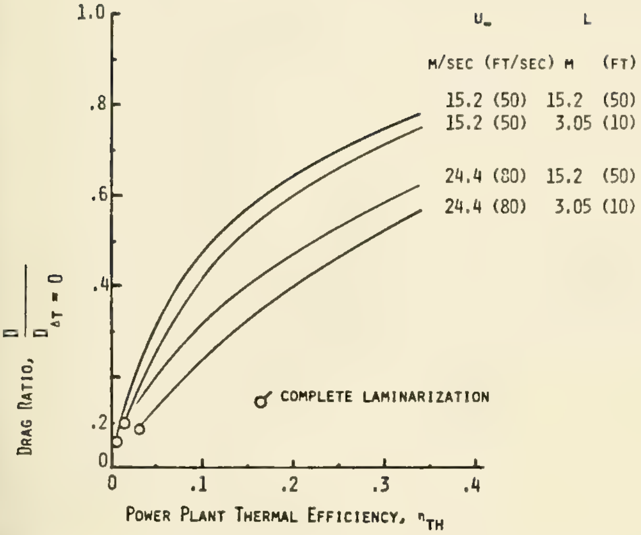

FIGURE 4. Effect of thermal efficiency of propulsive power plant on drag reduction.

of surface roughness on transition are possibly more pronounced for heated surfaces than for unheated. These factors are presently being studied both experimentally and analytically by a number of investigators for the purpose of obtaining an objective evaluation of the practical capabilities of this relatively simple and readily available means of drag reduction. The related experimental investigations done at CWRU will be described in the next two sections.

4. STABILITY EXPERIMENTS IN WATER

The first experimental study of flat plate boundary-layer stability in air was by Schubauer and Skramstad (1948) who used hot wire anemometry to measure the growth characteristics of sinusoidal velocity disturbances introduced into the boundary layer by a vibrating ribbon. Ross et al.(1970) repeated the Schubauer and Skramstad experiment to obtain data for comparison with improved numerical solutions of the Orr-Sommerfeld equation. Similar stability experiments have been performed in water by Wortmann (1955) and Nice (1973). The results of these experiments are in agreement with the numerical solutions of the Orr-Sommerfeld equation except near the minimum critical Reynolds number, where the departure from parallel-flow theory seemingly results from the breakdown of the parallel flow assumption. Among the attempts to correct the parallel-flow formulation, those of Bouthier (1972, 1973) and Saric and Nayfeh (1975, 1977) using the method of multiple scales yield numerical results which display the best agreement with experimental results.

A natural extension of the above work is in the investigation of factors which can increase boundary layer stability. As indicated earlier, one of these factors is wall heating in water. The objective of the experimental work done at CWRU was to see if the predicted increase in stability due to heating is in fact realized. To this end the stability of flat plate boundary layer was investigated on both a heated and unheated plate. For the heated plate, the case of uniform wall temperature may be more interesting from an engineering viewpoint. For example, since the portion of the plate upstream of the minimum critical point of the unheated plate is stable without heating, why not begin heating at the minimum critical point and use more advantageously, the power that would have gone to heating the leading edge region?

To systematize the approach to the problem, two types of nonuniform wall temperature distributions were studied: step changes in wall temperature of magnitude ΔT occuring at a location x_s; and power law wall temperature distributions of the form $T_w(x)-T_\infty = Ax^n$ for n both positive and negative. The temperature T_∞ is that of the external stream. In order to isolate the effect of the parameters, n and x_s, on the boundary layer stability, one of two quantities must be held fixed - either the total heating power put into the plate, Q_{total}, or the local wall temperature difference at some reference location $T_w(x_{ref})-T_\infty$. Since heat losses from the test plate used in this experiment could not be accurately measured, the total heating power put into the plate could not be related to the total convective heat transfer to the boundary layer. Therefore the wall temperature difference at x_{ref}, $T_w(x_{ref})-T_\infty$, was held constant as n and x were varied, with x_{ref} chosen in the region in which stability measurements were performed.

Experiment

The experiment was performed in a low turbulence water tunnel which has a test section 15.5 in. long, 9 in. wide, and 6 in. high. The free stream turbulence intensity in the test section is 0.1 - 0.2% for free stream velocities $u_e \leq 11$ ft/sec.

The flat aluminum test plate, which is 13.6 in. long, 9 in. wide, and 0.625 in. thick is suspended from a frame which fits the top of the test section as shown in Figure 5. The origin of the coordinate system is located at the leading edge. The x-coordinate is the running length measured in the streamwise direction, y is measured normal to the surface, and z is the spanwise coordinate measured from the plate centerline. The rounded leading edge (1/32 inch radius) is located 0.425 in. below the top of the test section, thus forming a slot which spans the top of the test section. The turbulent wall boundary layer of the water tunnel is removed by suction through this slot. Suction is adjusted so as to locate the flow stagnation point at a stable position just downstream of the leading edge on the test side of the plate. A laminar boundary layer then develops along the plate starting from the stagnation point location.

Plate heating is provided by eleven electric heating elements positioned as shown in Figure 5. Plate surface temperature is monitored by eleven thermistors imbedded in the surface of the plate along the centerline. However, because of the large temperature gradients which occur in the plate, the thermistors do not yield an accurate indication of the plate surface temperature. The surface temperature is determined from boundary layer temperature profiles measured with a hot-film anemometer operating as a resistance thermometer.

The pressure distribution on the plate surface in both the spanwise and streamwise direction is

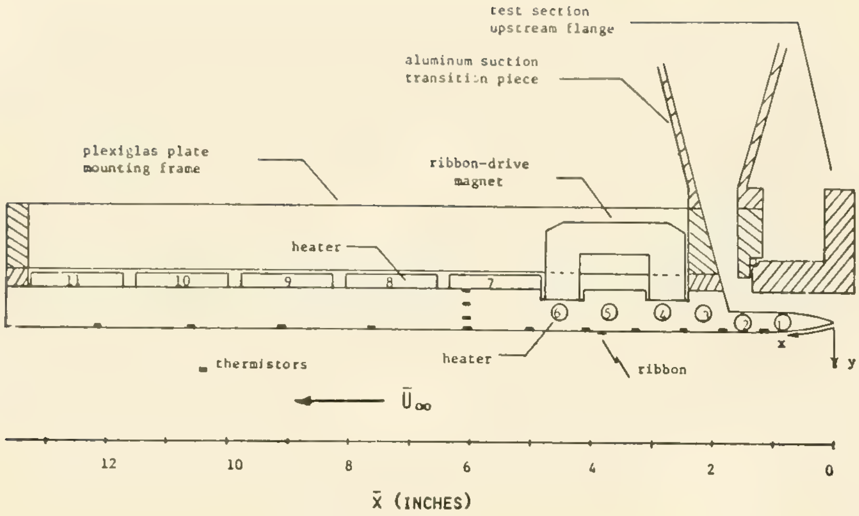

FIGURE 5. Test plate installation.

monitored using static pressure taps in conjunction with a manometer board. Artificial velocity disturbances are introduced into the boundary layer with a phosphorbronze ribbon 0.001 in. thick and 0.125 in. wide which is stretched across the plate surface 3.75 inches behind the leading edge. Ribbon vibration is achieved by passing a sinusoidal current through the ribbon in the z-direction in the presence of a magnetic field maintained by horseshoe magnets located on top of the plate.

A traversing mechanism located in the water tunnel diffuser downstream of the test section is used to position hot-film anemometer probes in the x and y direction for boundary layer profile measurements. The z-position of the probes is fixed at the plate centerline.

Temperature measurements in the thermal boundary layer are made with a DISA 55D01 anemometer and a 55F19 hot-film boundary layer probe operated in the constant current mode as a resistance thermometer. This unit is calibrated against the free stream temperature measured by thermistors extending into the free stream through the side walls of the test section. Boundary layer velocity measurements are made with a DISA hot-film system consisting of two 55F19 probes, a 11M01 constant temperature anemometer equipped with a 55M14 temperature compensated bridge, a linearizer, r.m.s. voltmeter, and d.c. voltmeter. The system is calibrated against the velocity measured by a pitot-static tube located in the center of the test section. A General Radio 1900-A wave analyzer is used to measure the r.m.s. amplitude of the anemometer signal resulting from ribbon-generated disturbances in the boundary layer.

The mean velocity profile is measured at x = 5.5 inches, which is the center of the region in which disturbance growth rates are measured. This position is also the value of x_{ref}, the point at which the local wall temperature is held constant as the temperature distribution parameters n and x_s are varied. The displacement thickness, δ^*, is determined by plotting the mean profile and using a polar planimeter to graphically perform the integration

$$\delta^* = \sqrt{\frac{\nu x}{u_e}} \int_0^\infty \left(1 - \frac{u}{u_e}\right) d\eta, \quad \text{where } \eta = y\sqrt{u/\nu x}$$

Since the maximum wall temperature difference used in the present work is $T_w - T_\infty = 8°F$, the error incurred by using the incompressible formulas given here to calculate δ^* and η is only about 0.1%. All experimental results reported below are therefore based on the incompressible forms of δ^* and η. The Reynolds number, $R_{\delta^*} = u_e\delta^*/\nu$, is formed using the kinematic viscosity evaluated at the free stream temperature.

For a fixed Reynolds number and ribbon frequency, the ribbon-generated disturbance amplitude is measured at five stations spaced 0.25 in. apart between x = 5 inches and x = 6 inches. In this region the pressure gradient is small (Falkner-Skan $\beta < 0.02$) and there is no interaction between the ribbon-generated disturbance and the natural disturbances present in the boundary layer. The disturbance amplitude recorded at each station is the peak amplitude, defined as $A(x) = [u'(\eta,x)/u_e]_{max}$, found by searching through the boundary layer in the y-direction. The spatial disturbance growth rate is then calculated from the slope $(dA/dx)\big|_{x=5.5''}$ of a polynomial-curve fit of the A(x) data. By repeating the above process for several different frequencies the growth rate vs. frequency characteristics of the boundary layer are determined for a fixed Reynolds number and temperature distribution.

All stability measurements reported here for non-uniform wall temperature distributions were performed near $R_{\delta^*} = 800$. At Reynolds numbers higher than 800 the ribbon-generated disturbances become more difficult to follow since background noise levels in the boundary layer increase with Reynolds number. At Reynolds numbers lower than 800 the disturbance growth rates are already small for uniform wall temperature in the range $3°F \leq T_w(x) - T_\infty \leq 8°F$, and measurement of the decreased growth rates resulting from non-uniform wall temperature distribution is subject to large relative errors.

Results and Discussion

Uniform Wall Temperature Distributions

The Mean Flow - A comparison between heated and unheated mean velocity profiles measured under identical flow conditions is shown in Figure 6 together with the calculated unheated profile obtained using Lowell's (1974) program for $\beta = -0.0036$, which is the measured β for the case shown. For $\eta > 6$ the measured velocity is uniform to within 1%. The unheated boundary layer thickness for this case is $\delta = 0.066$ inches (η=6.3). Note that velocities measured in the region $\eta < 0.75$ are consistently higher than would be expected from the straight-line nature of the velocity profile in this region. These velocities may be subject to wall interference effects due to the size of the hot-film probe relative to the boundary layer. At the last measured point, $\eta \simeq 0.5$, the prongs of the hot-film probe touch the wall. The probe prong diameter is 0.010 inches (η=0.95 in the present case), while the sensing element diameter is 0.003 inches (η=0.29). The discrepancy shown in Figure 6 between measured and calculated profiles for $T_w - T_\infty = 0$ may be due to the integrated effect of the upstream pressure distribution on the measured profile. Note that the difference between the heated and unheated velocity profiles is within experimental error. The heated profile is slightly fuller than the unheated profile in agreement with Lowell's numerical solutions of the variable fluid property boundary layer equations. The calculated ratio of $\delta^*_{heated}/\delta^*_{unheated}$ for this case is 0.968 while the measured ratio is 0.967.

Mean temperature profiles measured at varying values of $T_w - T_\infty$ and R_{δ^*} are compared to Lowell's (1974) solution of the boundary layer energy equation in Figure 6. Note that the thermal boundary layer thickness is smaller than the velocity boundary layer thickness by approximately the ratio $\delta_T/\delta_u = Pr^{-1/3} = 0.54$, where the Prandtl number of water is taken as 6.3 at T_∞ = 75°F. Further details concerning the mean flow field may be found in Strazisar (1975).

The Disturbance Flow Field - While the CWRU Water Tunnel has a relatively low turbulence level of 0.1% to 0.2%, this is still much higher than Ross et al. (1970) in air. It has nevertheless been ascertained by Strazisar (1975) that the present ribbon-generated disturbances do not interact with disturbances of other frequencies present in the tunnel turbulence and furthermore display the linearity required in order that the disturbances be considered "infinitesimal".

The development of ribbon-generated disturbances just downstream of the ribbon is investigated to insure that the disturbances develop fully before reaching the station where growth rates are first measured, namely x = 5 inches. Figure 7 shows the results for a decaying disturbance with $\omega_r = 138 \times 10^{-6}$, $R_{\delta^*} = 601$ at x - 5.5 inches. The dimensionless frequency ω_r is defined $\omega_r = (2\pi f)\nu/u_e^2$ where f is the ribbon frequency. (The experimental lower branch neutral point at $R_{\delta^*} = 601$ is at $\omega_r = 150 \times 10^{-6}$.) Points in the region $\eta < 0.75$ are shown as broken symbols due to possible interference effects because of probe proximity to the wall. The disturbance amplitude distribution through the boundary layer attains its final shape at x = 4.5 inches but the peak amplitude rises between x = 4.0 and x = 4.5 inches. Downstream of x = 4.5 inches both the shape and peak amplitude of the disturbance display expected behavior as seen by comparison with the calculated eigenfunction for this frequency and Reynolds number obtained using Lowell's (1974) program. Since the measured wavelength of this disturbance is 0.66 inches the appropriate disturbance eigenfunction is seemingly established in less than 1-1/2 wave lengths.

A measured disturbance temperature amplitude distribution is compared with the corresponding numerical solution in Figure 7. The calculated distribution is scaled by equalizing the area under the measured and calculated distributions in the region $0.75 < \eta < 3$. The shape of the disturbance temperature amplitude distribution is also found to be virtually independent of the disturbance frequency at a fixed R_{δ^*}.

Disturbance Growth Rates - Measured disturbance growth rates as a function of frequency for uniform wall temperature are shown in Figure 8 for $R_{\delta^*} = 800$. The dimensionless spatial growth rate

$$-\alpha_i = \frac{1}{A}\frac{dA}{dx}\frac{\delta^*}{R_{\delta^*}}$$

where A is the amplitude of the disturbance at the particular frequency under consideration. The solid lines in Figure 8 are curves faired through the measured points. The curve through the circular symbols is for the unheated plate. It is evident that with increased heating of the plate, the growth rates progressively decrease and the range of disturbance frequencies receiving amplification is diminished. Similar behavior is indicated at other Reynolds numbers as well.

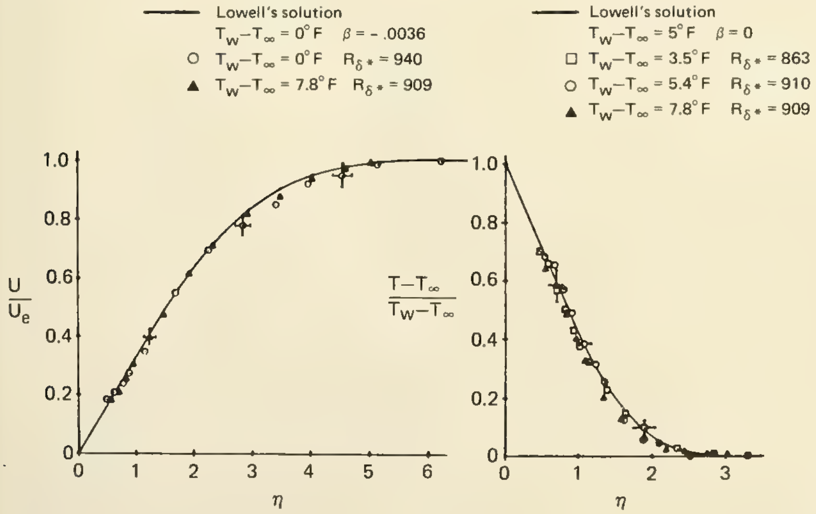

FIGURE 6. Mean velocity and temperature profiles for uniform wall heating.

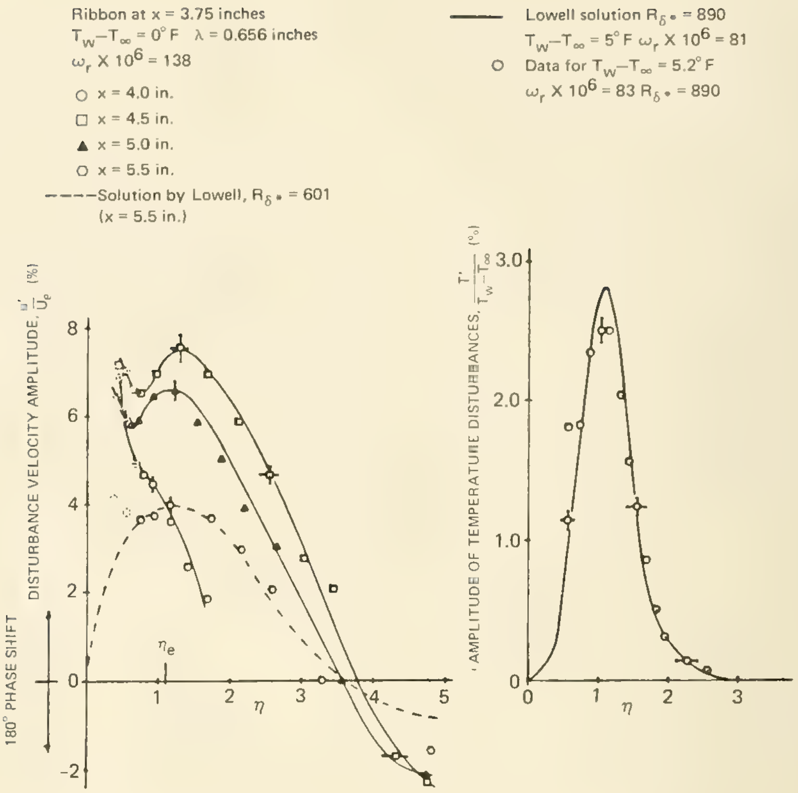

FIGURE 7. Velocity and temperature fluctuation amplitudes in the boundary layer.

Neutral Stability - For reference, the neutral stability results for the unheated plate will be presented first. Neutral points obtained in the present experiment are plotted together with those from prior investigations in Figure 9. The solid line in Figure 9 is the non-parallel flow solution of Saric and Nayfeh (1975) while the dashed line is the corresponding parallel flow solution of the Orr-Sommerfeld equation. Lower branch neutral points in the region $R_{\delta *} < 500$, $\omega_r < 210 \times 10^{-6}$ are denoted by bars in the present work because distinct neutral points could not be identified. Experimental results indicate that a neutral point lies somewhere in the barred region at each disturbance frequency considered. The present results are in agreement with the experimental results of Ross et al. (1970), Schubauer and

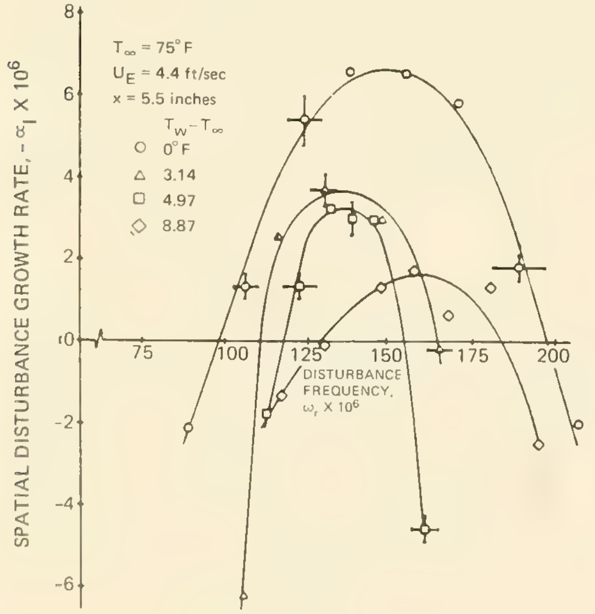

FIGURE 8. Measured disturbance growth characteristics for uniform wall temperature distributions, $Re_{\delta *}$ = 800.

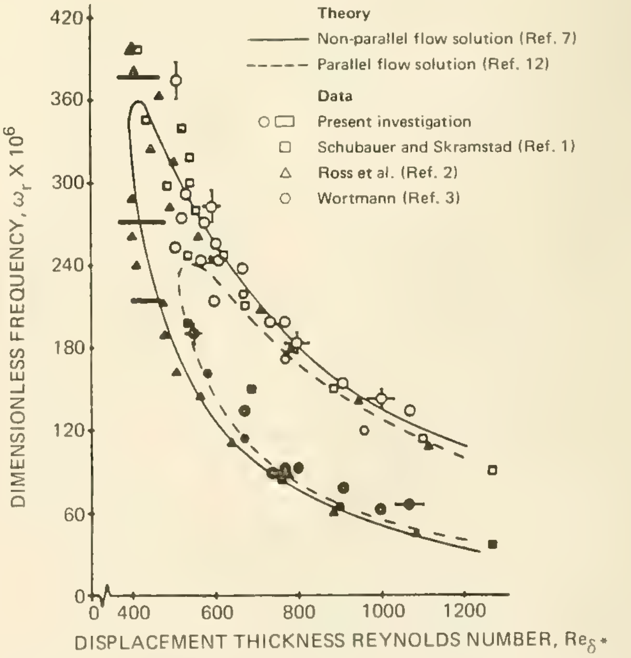

FIGURE 9. Neutral stability results for the unheated plate. (Solid symbols denote lower branch points, open symbols denote upper branch points).

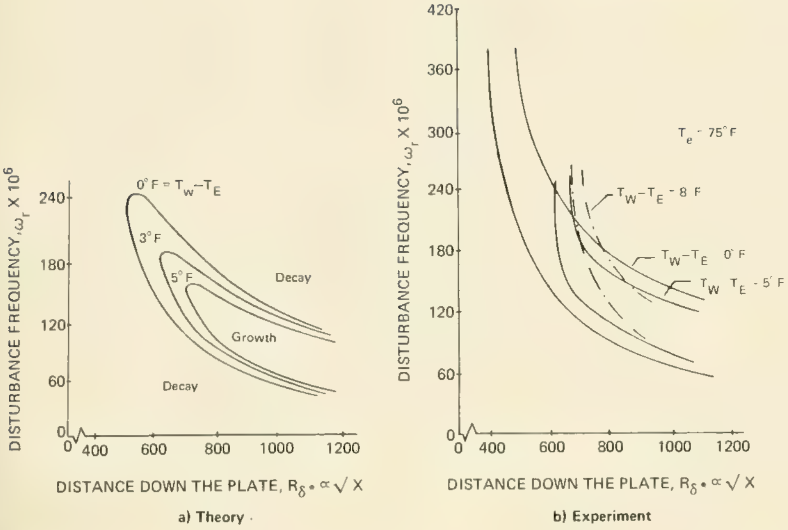

a) Theory

b) Experiment

FIGURE 10. Neutral stability characteristics for uniform wall temperature. $T_\infty = 75°F$.

Skramstad (1948), and Wortmann (1955), and provide further verification of the departure from parallel-flow solutions in the region $R_{\delta^*} < 500$. The agreement obtained allows one to proceed to the case of the heated plate with some credibility.

Experimentally determined neutral curves in the (ω_r, R_{δ^*}) plane for nominal uniform wall temperature differences of $T_W - T_\infty = 0,5,8°F$ are compared to the parallel flow results of Lowell (1974) in Figure 10. The experimental results are curves faired through the measured neutral points, which have not been shown for the sake of clarity. Comparison between the calculated parallel-flow results and experiment indicates that the departures between the two found near $(R_{\delta^*})_{\text{min.crit}}$ for the unheated case persist in the heated cases. It is readily seen that with increases in $T_W - T_\infty$, $(R_{\delta^*})_{\text{min.crit}}$ increases and also the range of frequencies receiving amplification decreases. Note that while the theoretical neutral curves according to Lowell's parallel flow calculation nest within each other, this does not happen experimentally until R_{δ^*} exceeds 860.

Predicted and measured values of $(R_{\delta^*})_{\text{min.crit}}$ are compared in Figure 11. The measured rate of increase in $(R_{\delta^*})_{\text{min.crit}}$ compares favorably with that predicted by Lowell (1974) and by Wazzan et al. (1970). Over the range of values of $T_W - T_\infty$ covered by the present work it is conjectured that the non-parallel flow nature of the boundary layer serves to reduce the value of $(R_{\delta^*})_{\text{min.crit}}$ by about 120 units from that predicted for parallel flow. This reduction seems independent of the level of wall heating. A more complete description of these results ig given in Strazisar, Reshotko, and Prahl (1977).

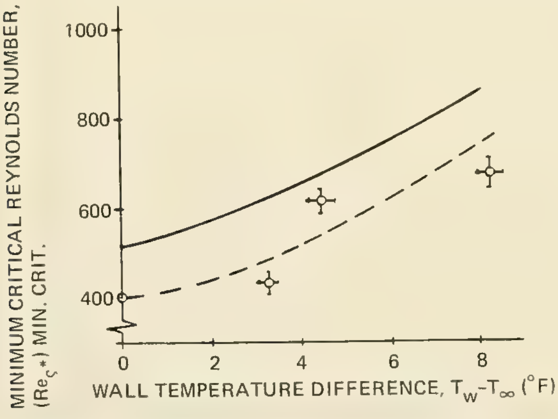

FIGURE 11. Effect of heating on minimum critical Reynolds number.

Non-Uniform Wall Temperature Distributions

As indicated earlier, the two types of non-uniform wall temperature distributions studied are a) the power-law type in which $(T_W - T_\infty) = Ax^n$ and b) step changes in wall temperature of magnitude $\Delta T = T_W - T_\infty$ occuring at location x_s. In the discussions that follow, n is the exponent of the power-law wall temperature distribution and $s = x_s/x_{ref}$ is the fraction of the distance to the measuring station ($x_{ref} = 5.5$ inches) at which the step change in wall temperature is located.

The Mean Flow - Mean velocity profiles for varying values of n, s and $T_W(x_{ref}) - T_\infty$ are compared to the Blasius profile in Figure 12. The discrep-

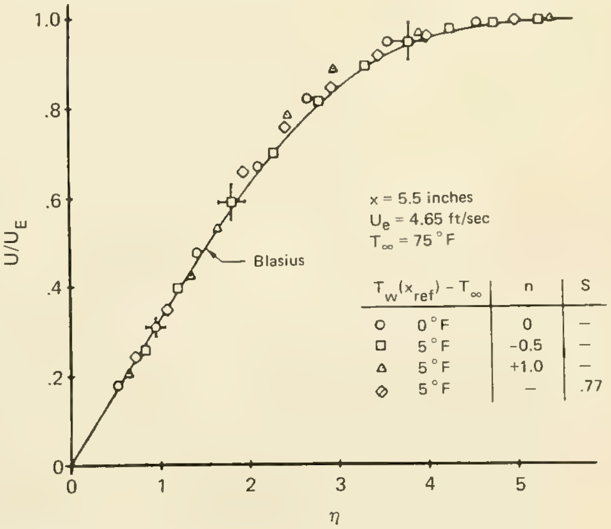

FIGURE 12. Mean velocity profiles for varying wall temperature distributions.

ancy between the unheated profile and the Blasius solution may be due to small pressure gradient effects.

Mean temperature profiles and wall temperature distributions measured for values of $T_w(x_{ref})-T_\infty \approx 5°F$ are compared to relevant solutions of the boundary layer equations in Figure 19. These similar solutions were obtained by Runge-Kutta integration of the coupled momentum and energy equations assuming variable viscosity and thermal conductivity. Their development is not shown here. The error bars shown in Figure 13 represent the maximum measurement error. Agreement between the measured and predicted profiles is reasonable considering the fact that the wall temperature cannot be monitored or maintained near the leading edge due to equipment limitations. The thermal boundary layer near the leading edge is too thin to make temperature profile measurements with the hot film practical. The first indication of the wall temperature is thus provided by the thermistor imbedded in the plate surface at x = 1.2". The heater nearest the leading edge is located at 0.71" < x < 0.96". The actual wall temperature thus rises in some unknown manner from $T_w-T_\infty = 0$ at the leading edge to a value near the desired local wall temperature at x - 0.71". These limitations are more severe for increasingly negative values of n, which require large temperature differences near the leading edge, and may be the cause of the discrepancy between theory and experiment seen in Figure 13 for the attempted n = -0.5 profile.

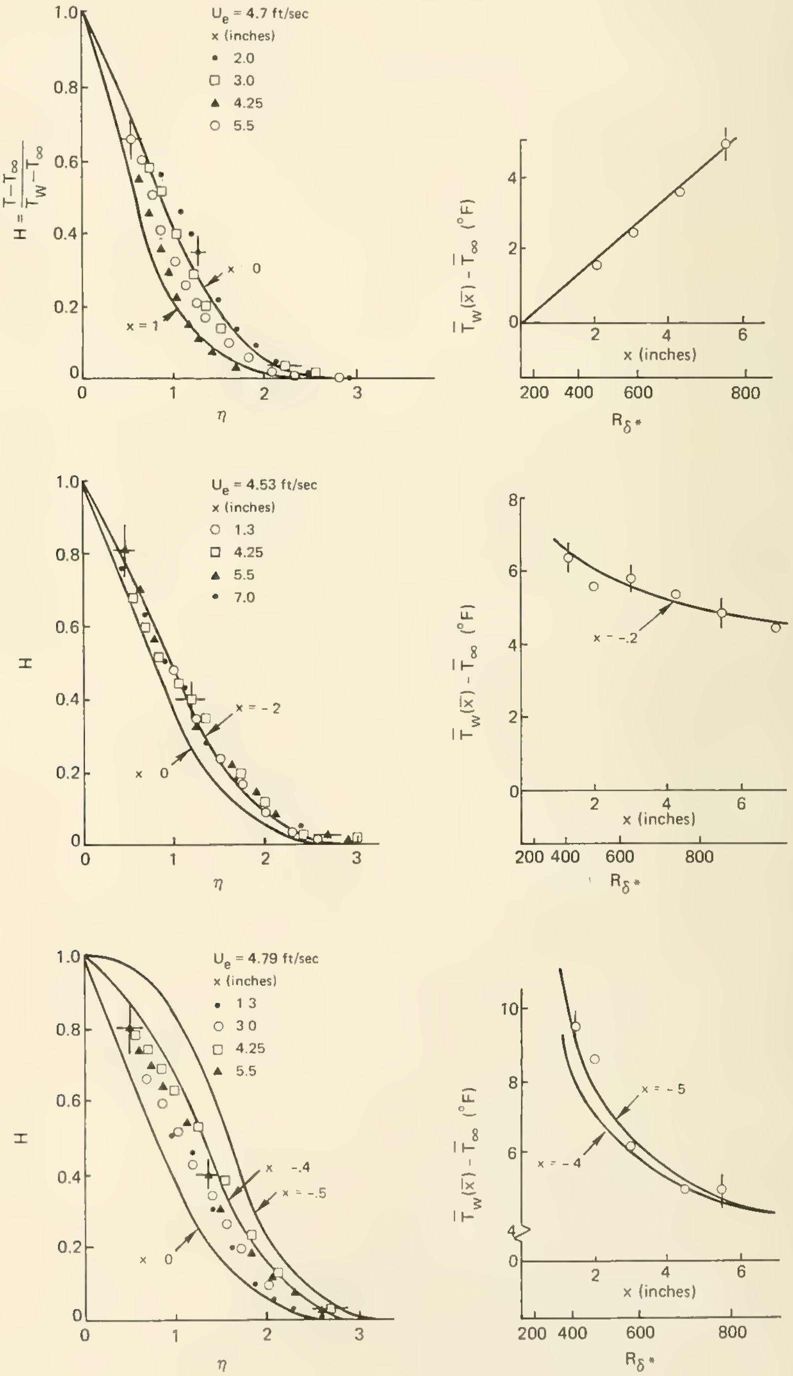

FIGURE 13. Mean temperature profiles for power law wall temperature distributions, $T_w(x) - T_\infty = Ax^n$.

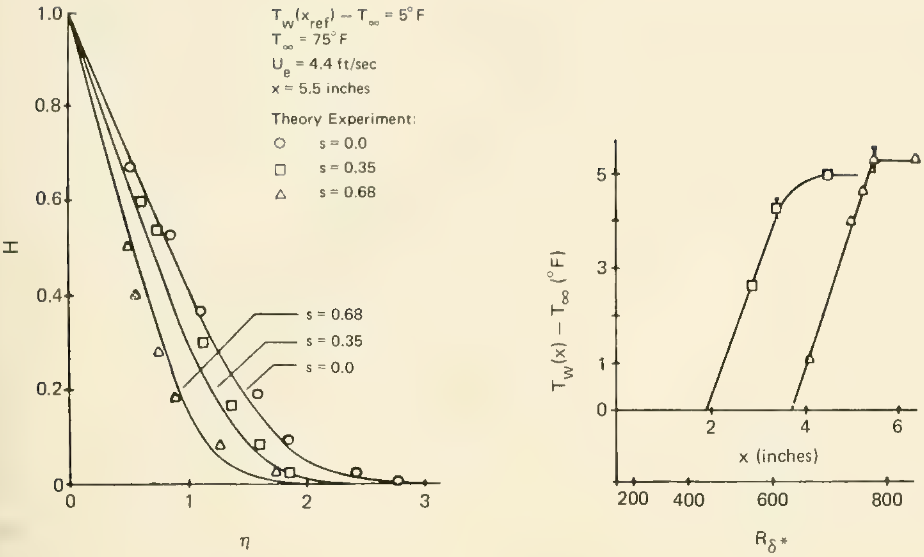

FIGURE 14. Mean temperature profiles at x = 5.5" for step changes in wall temperature.

Temperature profiles measured at $x_{ref} = 5.5"$ for several values of $S = x_s/x_{ref}$, with $\Delta T = 5°F$, are compared to analytic results in Figure 14. The actual wall temperature does not undergo a steep step change due to conduction of heat through the plate upstream of the first heater used in each case. As a result there is not a unique value of x_s, the step change "location". For purposes of comparison solutions were obtained to the constant property energy equation assuming that the temperature profile developed entirely within the linear portion of the velocity profile. This is a reasonable assumption for the Prandtl number of water. Comparison of the measured profiles with these approximate step change solutions indicates that the best agreement between theory and experiment results when x_s is taken as the x-location at which the wall temperature first begins to rise above the free stream temperature. The choice of x_s is used in all of the results reported herein.

The agreement between measured and predicted temperature profiles shown in Figures 13 and 14 for $T_w(x_{ref})-T_\infty = 5°F$ is typical of that obtained at local wall temperature differences of 3°F and 8°F as well.

Disturbance Growth Rates - Disturbance growth rate characteristics for vaying values of n at a fixed Reynolds number near $R_{\delta *} = 800$ with $T_w(x_{ref}) - T_\infty = 5°$, are shown in Figure 15. The unheated case is included for reference. The curves shown are faired through the measured (α_i, ω_r) points, which are not shown for the sake of clarity. For n = +1.0 the maximum disturbance growth rate is greater than that for n=0 at a given value of $T_w(x_{ref})-T_\infty$, and the band of amplified disturbance frequencies moves to a higher frequency range. Similar results are obtained for $T_w(x_{ref})-T_\infty = 3°F$ and 5°F.

Disturbance growth rates vs. frequency for various values of s, with $\Delta T = 5°F$ are shown in Figure 16 at a nominal Reynolds number of $R_{\delta *} = 800$. The unheated case is included for reference and measured points (α_i, ω_r) are once again not plotted for the sake of clarity. The case s = 0 corresponds

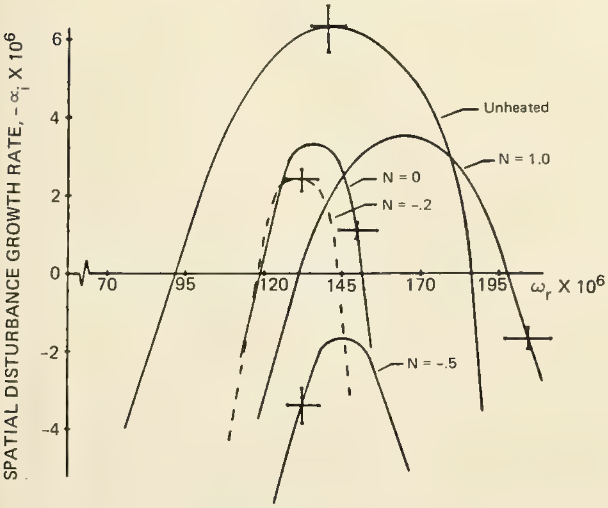

FIGURE 15. Measured disturbance growth characteristics for power law wall temperature distributions $T_w(x) - T_\infty = Ax^n$, $R_{\delta *} = 800$.

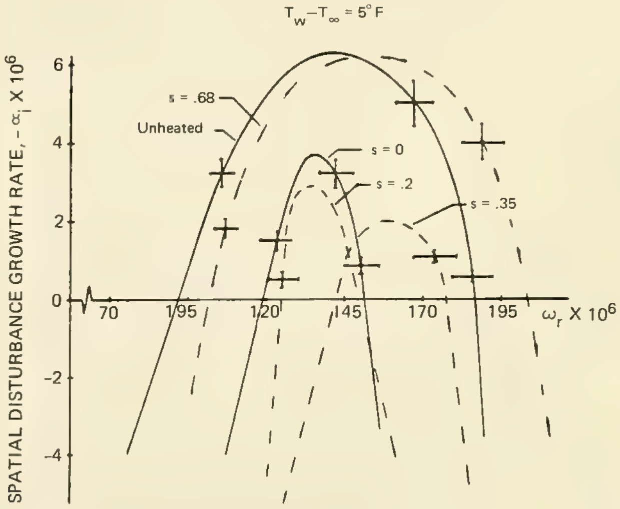

FIGURE 16. Measured growth characteristics for a step change increase in wall temperature, $R_{\delta *} = 800$.

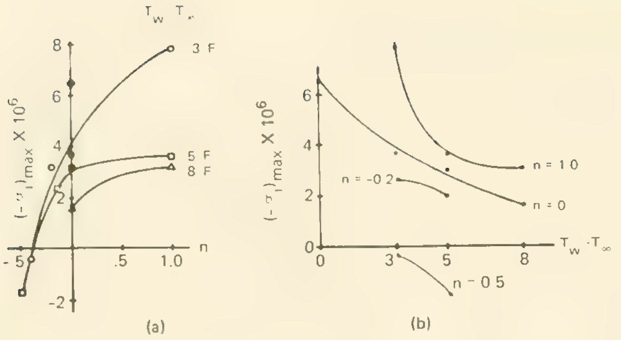

FIGURE 17. Maximum growth rates for power law wall temperature distributions, $T_w(x) - T_\infty = Ax^n$, $R_{\delta^*} \approx 800$.

to uniform wall heating beginning at the leading edge while the case s = 1 corresponds to a step change in temperature occurring at the measuring station $x_{ref} = 5.5$ inches. The peak disturbance growth rate displays a minimum as s increases for each value of ΔT considered here. The band of amplified disturbance frequencies also moves toward a higher frequency range as s increases.

Disturbance growth rate behavior as a function of wall temperature distribution is summarized in Figures 17 and 18, where $(-\alpha_i)_{max}$ is defined as the maximum disturbance growth rate for a given value of $T_w(x_{ref})-T_\infty$ at fixed values of n is shown in Figure 17b. We see that positive exponents can result in large disturbance growth rates at low wall heating levels. At higher levels of wall heating the relative reduction in $(-\alpha_i)_{max}$ between any two temperature levels is greatest as n decreases.

The variation of $(-\alpha_i)_{max}$ with s at values of $\Delta T = 3°F$ and 5°F is shown in Figure 18. The minimum in $(-\alpha_i)_{max}$ at each wall heating level occurs near the minimum critical Reynolds number of the unheated boundary layer. The measured value of $(R_{\delta^*})_{min.crit}$ for $\Delta T = 0$ is 400, which corresponds to s = 0.25 in Figure 18, while the predicted parallel flow value of $(R_{\delta^*})_{min.crit} = 520$ for $\Delta T = 0$ corresponds to s = 0.42.

An attempt was made to use the program of Lowell and Reshotko (1974) to solve the parallel-flow spatial stability problem for power law, wall temperature distributions since the solution scheme allows the mean flow solution to be read directly into the coefficient matrix of the disturbance growth rate at a fixed frequency and Reynolds number is a minimum for n=0, and increases by maximum of 12% for values of n in the range $-1/2 \le n \le 1$. This behavior, which is not consistent with the experimental results, may be due to the fact that significant changes in wall temperature and therefore in the velocity and temperature distributions are taking place over one or two wave-lengths in violation of the parallel-flow assumptions. It is felt that a proper multiple scales formulation of the stability problem, which takes into account the rather rapid variation of wall temperature with x, is required to properly assess the present results for power-law and step function wall temperature variations. The results for non-uniform wall temperature distributions are given in more detail in the paper by Strazisar and Reshotko (1978).

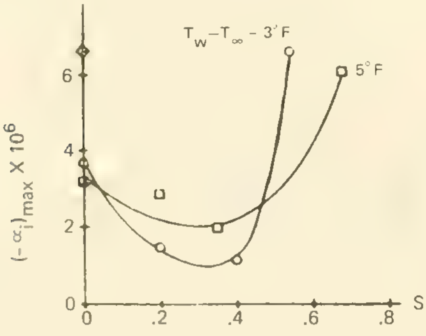

FIGURE 18. Maximum growth rates for step change increases in wall temperature.

5. EFFECT OF WALL HEATING ON SEPARATION

An underwater vehicle is basically a body of revolution having generally favorable pressure gradients forward of the maximum diameter and adverse pressure gradients downstream of the maximum diameter. If laminar flow can be maintained all the way to the adverse pressure gradient region then the boundary layer will be very easily separated unless measures are taken to delay such separation.

An obvious way to delay separation is by suction. This however involves the complexities of suction slots, internal ducting and later discharge of the flow removed from the vehicle boundary layer. A "cleaner" possibility for separation delay if it in fact would work is heating.

Wazzan et al. (1970) showed that heating can cause a separating profile to fill out significantly. Figure 19 indicates that for a Falkner-Skan $\beta = -0.1988$, an overheat of 90°F, converts a separating profile to one having the shape factor of a Blasius boundary layer. This motivated our proposal to investigate experimentally the potential effect of heating on delay of laminar separation. Subsequent calculations by Aroesty and Berger (1975) using an

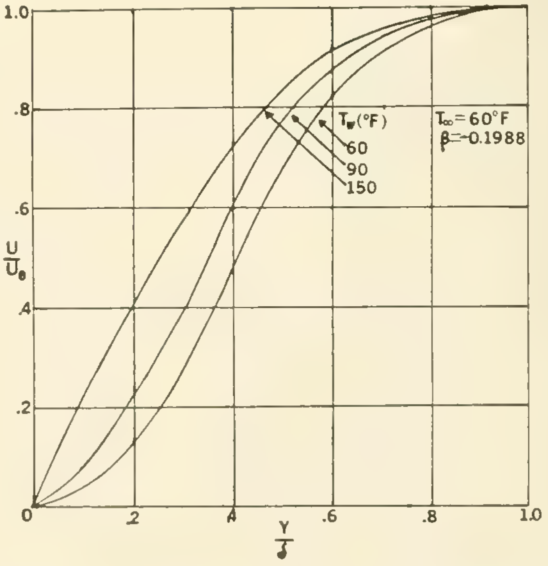

FIGURE 19. Velocity profiles at various wall temperatures for $\beta = -0.1988$ [Wazzan et al. (1970)].

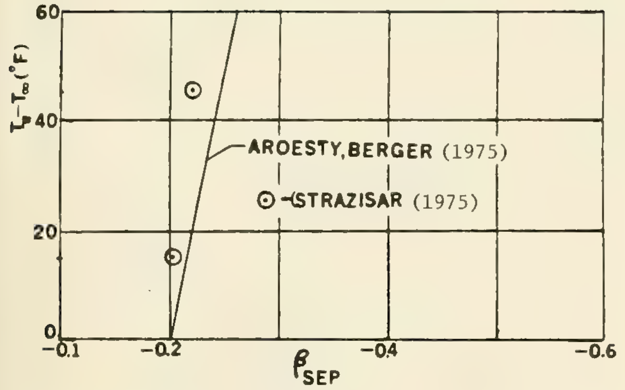

FIGURE 20. Effect of overheat on Falkner-Skan separation parameter.

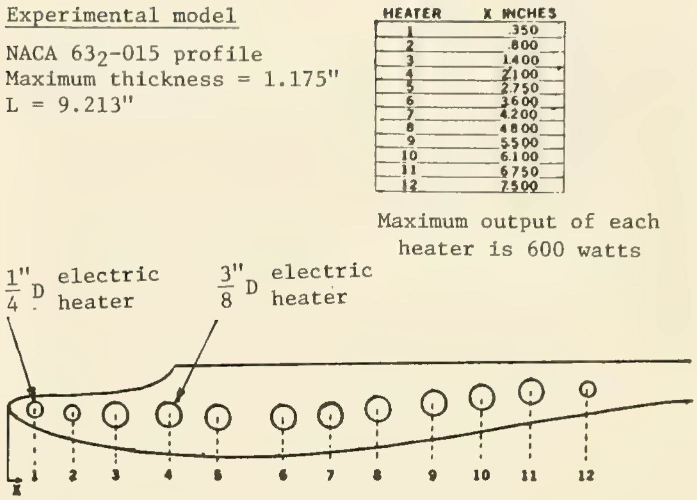
Experimental model
NACA 63_2-015 profile
Maximum thickness = 1.175"
L = 9.213"
Maximum output of each heater is 600 watts
$\frac{1"}{4}$ D electric heater
$\frac{3"}{8}$ D electric heater
X
1
2
3
4
5
6
7
8
9
10
11
12

HEATER	X INCHES
1	.350
2	.800
3	1.400
4	2.100
5	2.750
6	3.600
7	4.200
8	4.800
9	5.500
10	6.100
11	6.750
12	7.500

FIGURE 22. Location of rod heaters in experimental model.

approximate procedure showed that despite the large changes in profile shown in Figure 19, the value of β at separation did not change very much with heating (Figure 20). This was confirmed as also shown on Figure 20 by exact calculations of Strazisar (1975) using Lowell's (1974) program. The question of the length retardation of separation on a real configuration nevertheless remained an open one.

Experiment

This experiment was also performed in the CWRU Low Turbulence Water Tunnel described in Section 4 using a specially designed two-dimensional model having an NACA 63_2-015 profile. The model (Figure 21) is designed as part of the upper wall of the test section of the water tunnel. The boundary layer developing on the upper wall of the nozzle is removed through a scoop with the bleed rate adjusted so that the stagnation streamline is straight and steady. Rod heaters (Figure 22) are provided over the length of boundary layer development. The tests were conducted at rather low unit Reynolds numbers so as to promote laminar flow in the separation region and to minimize the power needed for large temperature differences. The electric heaters distributed through the plate provide wall temperatures of the order of 60°F above the free-stream fluid temperature in the region of separation. Wall temperature distributions are shown in Figure 23.

The separation behavior was determined by combinations of the following indicators: 1) indication of separation by visual observations of a dye stream injected along the surface through static pressure holes, 2) location of separation indicated by the static pressure distribution along the plate, and 3) use of hot film anemometry to measure boundary layer velocity profiles.

As with many water flow facilities, results are dependent on the state of cleanliness of the experimental equipment. In particular, the velocity profiles were affected by the condition of the airfoil surface and the screens in the settling chamber. Even when the screens and airfoil surface were relatively clean, there was some scatter in the level of the boundary layer shape parameter as evidenced by the results for the unheated airfoil. The effects of heating on shape factor displayed consistent trends that were generally independent of facility condition. The experimental setup, procedures and measurement systems are described in detail by Timbo and Prahl (1977).

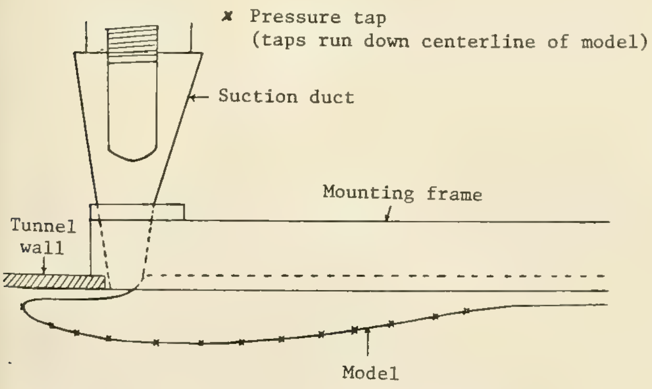

FIGURE 21. Model as mounted in water tunnel.

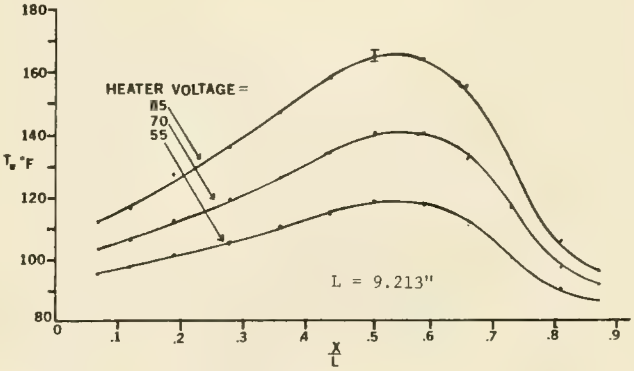

FIGURE 23. Surface temperature distributions, T_∞ = 70°F.

Results

When dye was injected into the boundary layer through the pressure taps along the centerline of the airfoil, it usually did not all move directly upstream on the centerline. Some of the dye moved initially spanwise and then upstream. Regardless of the path of the dye, its motion was never steady. When the airfoil surface was polished and the most accessible of the screens in the settling chamber cleaned, the most forward upstream position of the dye on the unheated airfoil was 4.1 inches (x/L = 0.45). With heating, the patter of upstream dye flow remained indistinguishable from the unheated case. Thus for the wall overheats tested, up to 80°F measured at x = 4.01" (x/L = 0.44 in Figure 23), there was no separation delay discernable using the dye injection method.

In looking at pressure distributions, separation is identified as the point where the experimental pressure distribution departs from the theoretical recompression distribution on the aft portion of the airfoil. The pressure taps will not indicate a separated boundary layer unless there is continuous separation at the tap's position. Thus unless the upstream motion of the dye is very steady, which is usually not the case, the position of separation as determined by the most upstream penetration of dye is consistently farther upstream than indicated by pressure distributions.

The separation point by examination of pressure distributions on unheated airfoil occurs at x≈4.9" (x/L = 9.53). This is close to the location x = 5" predicted for separation using the Thwaites method. Heating, as reported by Timko and Prahl (1977), caused no significant alteration in the pressure distributions and so again one cannot point to any delay of separation by heating from these data.

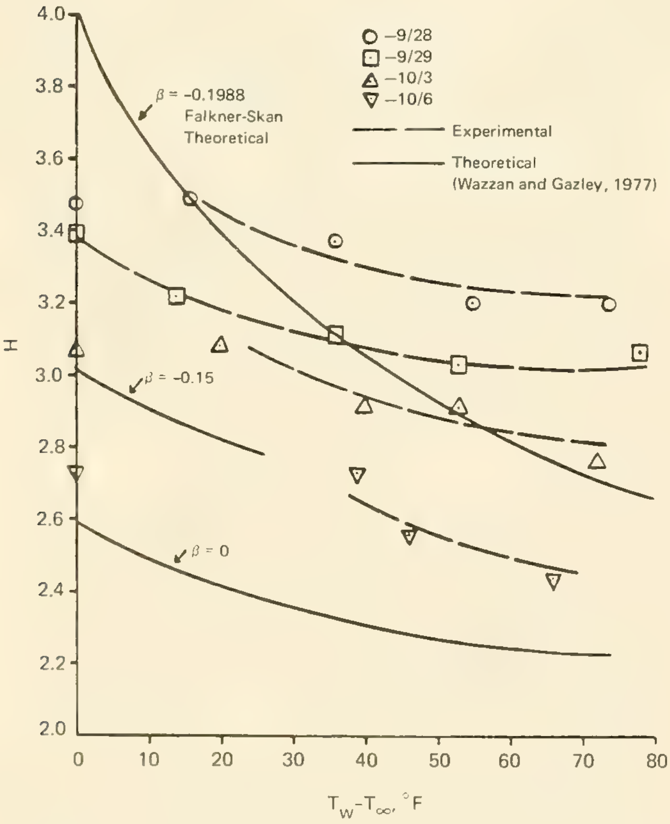

FIGURE 24. Variation of shape factor H with wall heating.

Since the first two indicators showed negligible shift of separation with heating, the boundary layer velocity profiles were measured in some detail at a point upstream of separation with and without heating. Figure 24 shows the results for boundary layer shape factor at a station 3.88" downstream of the leading edge. Heating causes a reduction in shape factor from the unheated value. The unheated profiles correspond to $-0.17 \lesssim \beta \lesssim -0.15$ and the slight reduction in shape factor with heating is in accordance with expectation from the similar solutions of Wazzan and Gazley (1977). Despite these shape factor reductions the profiles are changing so rapidly with longitudinal distance (hence the scatter in Figure 24) that the separation location is hardly affected.

Thus for the amounts of wall heating employed in this study the separation point does not move noticeably from its unheated position. This in a sense confirms the results of Aroesty and Berger (1975) and of Strazisar (1975) (Figure 20) which show the theoretical insensitivity of the value of β at separation to heating.

6. CONCLUDING REMARKS

The studies to date reported herein together with those of Wazzan et al. (1970, 1977), Barker (1978) and others are such as to justify further investigation of the various elements of the heating phenomenon. Among the factors affecting the practical application of heating is the combined effect of heating and roughness on stability and transition. The work of Kosecoff, Ko, and Merkle (1976) suggests that the roughness effect is due to the instability of the mean profile as distorted by the roughness. An alternative view being investigated at CWRU is that the roughness introduces disturbances into the boundary layer that may subsequently be amplified by the Tollmien-Schlichting mechanism. In this view the wavelength of the roughness is important as well as its height. An experiment has been planned that will map out the mean and disturbance flow-fields in the vicinity of roughness elements so that the relevant mechanism can be identified. This will provide a fluid mechanic characterization of roughness and help in further assessment of the effects of roughness on transition of heated water boundary layers. With further attention given also to heat exchanger design propulsion system, and fabrication techniques, there are promising prospects for the achievement of drag reduction by heating in water.

ACKNOWLEDGEMENTS

The author wishes to acknowledge the participation of the following colleagues in the effort reported in this paper: Dr. J. M. Prahl, Dr. M. Nice, Dr. R. L. Lowell, Dr. A. Strazisar, and Mr. M. Timko. All of us are grateful for the sponsorship of the work by the Fluid Dynamics Program of the Office of Naval Research and by the General Hydrodynamics Research Program of the David W. Taylor Naval Ship Research and Development Center.

REFERENCES

Aroesty, J., and S. A. Berger, (1975). Controlling the Separation of Laminar Boundary Layers in Water: Heating and Suction. *Report R-1789-ARPA, RAND Corp.*

Barker, S. J. (1978). Pipe Flow Experiments at Large Reynolds Numbers. *Proc. 12th Symposium on Naval Hydrodynamics.*

Bouthier, M. (1972). Stabilite lineaire des ecoulements presques paralleles. *J. de Mecanique, 11,* No. 4, 599-621.

Bouthier, M. (1973). Stabilite lineaire des ecoulements presques paralleles. II. La couche limite de Blasium. *J. de Mecanique, 12,* 75-95.

Frick, C. W., Jr., and G. B. McCullough, (1942). Tests of a Heated Low Drag Airfoil. *NACA ARR.*

Hoerner, S. F. (1958). *Fluid Dynamic Drag.* 2nd. edition.

Kosecoff, M. A., D. R. S. Ko, and C. L. Merkle, (1976). An Analytical Study of the Effect of Surface Roughness on the Stability of a Heated Water Boundary Layer. *Physical Dynamics, Inc. Report PDT-76-131.*

Liepmann, H. W., and G. H. Fila, (1947). Investigations of Effects of Surface Temperature and Single Roughness Elements on Boundary Layer Transition. *NACA Rept. 890.*

Lowell, R. L., and E. Reshotko, (1974). Numerical Study of the Stability of a Heated Water Boundary Layer. *Report FTAS/TR-73-95, Case Western Reserve University.*

Nice, M. L.,(1973). Experimental Study of the Stability of a Heated Water Boundary Layer. Ph.D. Dissertation, Case Western Reserve University. (Also Nice, M. L., and J. M. Prahl. *Report FTAS/TR-73-93, Case Western Reserve University.*

Reshotko, E. (1977). Drag Reduction in Water by Heating. Proceedings. *2nd International Conference on Drag Reduction.* Cambridge, Sept. BHRA, Paper E2.

Ross, J. A., F. H. Barnes, J. G. Burns, and M. A. S. Ross, (1970). The Flat Plate Boundary Layer, Part 3, Comparison of Theory with Experiments. *J. Fluid Mech., 43,* 819-832.

Saric, W. S., and A. H. Nayfeh, (1975). Non-Parallel Stability of Boundary Layer Flows. *Physics of Fluids, 18,* 945-950.

Saric, W. S., and A. H. Nayfeh, (1975). Non-Parallel Stability of Boundary Layers with Presure Gradients and Suction. Paper No. 6, *AGARD Conference on Laminar-Turbulent Transition, AGARD CP-224.*

Schubauer, G. S., and H. K. Skramstad, (1948). Laminar Boundary Layer Oscillations and Transition on a Flat Plate. *NACA Report 909.*

Smith, A. M. O., and N. Gamberoni, (1956). Transition, Pressure Gradient and Stability Theory. *Report EF 26388, Douglas Aircraft Co.*

Strazisar, A. J., (1975). Experimental study of the Stability of Heated Laminar Boundary Layers in Water. Ph.D. Dissertation, Case Western Reserve University. (Also, Strazisar, A. J., J. M. Prahl, and E. Reshotko. *Report FTAS/TR-75-113, Case Western Reserve University,* September 1975).

Strazisar, A., (1975). Private communication.

Strazisar, A. J., E. Reshotko, and J. M. Prahl, (1977). Experimental study of the stability of heated laminar boundary layers in water. *J. Fluid Mech., 83,* Pt. 2, 225-247.

Strazisar, A. and E. Reshotko, (1977). Stability of Heated Laminar Boundary Layers in Water. *AGARD Conference on Laminar-Turbulent Transition, AGARD-CP-224,* Paper No. 10.

Strazisar A., and E. Reshotko, (1978). Stability of Heated Laminar Boundary Layers in Water with Non-Uniform Surface Temperature. *Physics of Fluids, 21.*

Timko, M., and J. M. Prahl, (1977). Experimental Study of the Effect of Wall Heating on the Separation of a Laminar Boundary Layer in Water. *Report FTAS/TR-77-135, Case Western Reserve University.*

Van Ingen, J. L., (1956). A Suggested Semi-Empirical Method for the Calculation of the Boundary Layer Transition Region. *Report VTH-74, Dept. of Aero. Eng'g., University of Technology, Delft.*

Wazzan, A. R., T. T. Okamura, and A. M. O. Smith, (1968). Spatial and Temporal Stability Charts for the Falkner-Skan Boundary Layer Profiles. *Douglas Aircraft Co, Report No. DAC-6708.*

Wazzan, A. R., T. T. Okamura, and A. M. O. Smith, (1970). The Stability and Transition of Heated and Cooled Incompressible Laminar Boundary Layers. *Proc. 4th Int. Heat Transfer Conf., 2, FC 1.4, Elsevier,* (ed. U. Grigull and E. Hahne).

Wazzan, A. R., and C. Gazley, Jr., (1977). The Combined Effects of Pressure Gradient and Heating on the Stability and Transition of Water Boundary Layers. *Proceedings 2nd Int. Conf. on Drag Reduction,* Cambridge, Sept. 1977, Paper E3.

Wortmann, F. X., (1955). Untersuching instabiler Grenzschictschwingingen in einem Wasserkanan mit der Tellurmethode. *50 Jahre Grenzschichtforschuug.* Friedr. Vieweg and Sogn, Braunschweig, (ed. H. Gortler and W. Tollmien).

Discussion

CARL GAZLEY, Jr.

Several of us* at Rand and UCLA have made a series of computations which serve to illuminate some of the experiments described by Professor Reshotko. His experiments with non-uniform wall temperature distribution indicate the sensitivity of the boundary-layer stability to the way the surface temperature changes with distance along the plate. For the power-law variation, $\Delta T = Ax^n$, Reshotko's experiments for $\Delta T < 8°F$ appear to indicate decreased stability and increased amplification rates as the experiment n decreases toward zero. Our computations indicate the same trend at low temperature differences, but also show a reversal at a temperature difference of about 20°F with an increasing stability with increasing n above this ΔT. In fact, very large increases occur for a ΔT above 30°.

Our results were obtained both by exact numerical techniques based on the Orr-Sommerfeld equation [Wazzan and Gazley (1978)] and by a modifiaction of the Dunn-Lin approximation [Aroesty et al. (1978)]. The results for flat-plate flow in terms of the minimum critical Reynolds number based on displacement thickness are shown in Figures 1 and 2 for values of n = 1 and 2 as a function of the local temperature difference. The modified Dunn-Lin approximation is seen to agree remarkably well with the exact computations. More extensive results of that approximation are shown in Figure 3 for values of n ranging from zero to 2. For temperature differences above about 30°F, the advantageous effects of an increasing temperature difference are seen to be very large.

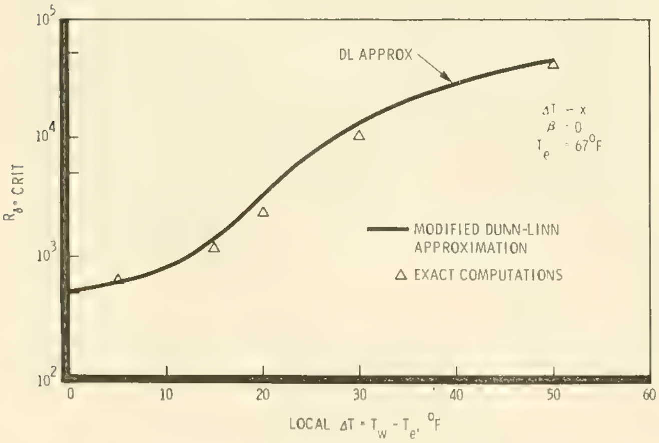

FIGURE 1. Variation of critical Reynolds Number with local temperature difference. Flat plate with linear increase of temperature difference.

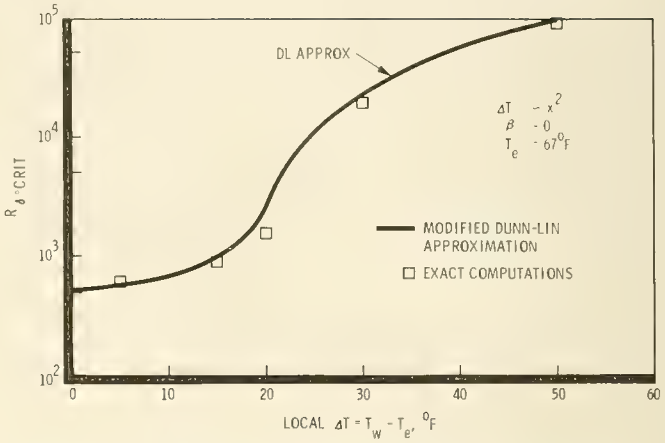

FIGURE 2. Variation of critical Reynolds Number with local temperature difference. Flat plate with temperature difference increasing with the square of distance.

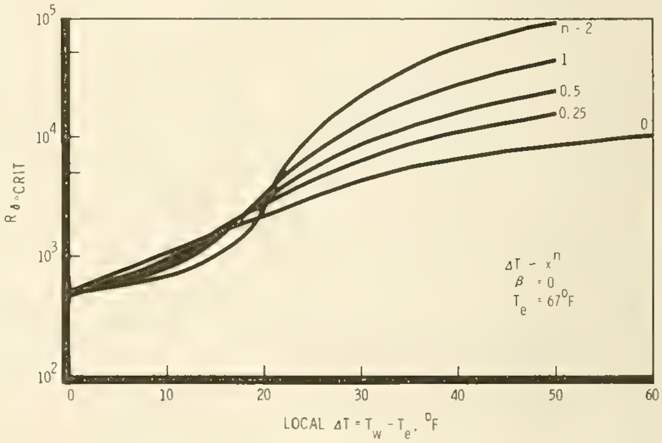

FIGURE 3. Variation of Critical Reynolds Number with local temperature difference for several surface-temperature distributions.

REFERENCES

Wazzan, A. R., and C. Gazley, Jr. (1978). The Combined Effects of Pressure Gradient and Heating on the Stability and Transition of Water Boundary Layers. *The Rand Corporation, R-2175-ARPA.*

Aroesty, J., et al. (1978). Simple Relations for the Stability of Heated Laminar Boundary Layers in Water: Modified Dunn-Lin Method.

---

*J. Aroesty, C. Gazley, Jr., G. M. Harpole, W. S. King, and A. R. Wazzan

Author's Reply

ELI RESHOTKO

Dr. Gazley and his colleagues have long been interested and active in the topic of heated boundary layers and his comments on the consequences of power-law temperature distributions are greatly appreciated.

Let me first restate our experimental results. Referring to Figure 17 of the paper, our experiments for ΔT < 8°F appear to indicate decreased amplification rates as the exponent n decreases toward zero and in fact for some range of negative values of n, the disturbances become damped. In the temperature range ΔT < 8°F, neither our calculations (cited in the paper) nor Gazley's give any basis for this experimental result.

Nayfeh and El-Hady (private communication) have recently pointed out that water boundary layers with non-isothermal walls cannot have similar boundary layer solutions because of the variable properties of water. They show that if one first calculates the non-similar boundary layer profiles expected at the measuring station of the Strazisar-Reshotko experiments and then analyzes the stability of these profiles, the resulting growth rates are qualitatively in accord with the Strazisar-Reshotko results as shown in the figure below supplied to me by Professor Nayfeh. Note in the figure that as n decreases, the growth rates also decrease, and although the calculated maximum growth rates are not negative for the non-parallel calculations with n = -0.5, they are very close to zero. This trend is opposite to what was obtained for the stability of similar boundary layer mean profiles.

Nayfeh and El-Hady's calculations do not go beyond ΔT = 8°F. But I believe that they have made their point that when studying the stability of water boundary layers with power-law or other non-isothermal wall temperature distributions, one must analyze the stability of the appropriate non-similar boundary layer profiles in order to obtain even the correct qualitative trends. Therefore I believe that the results presented by Dr. Gazley in his comment must be reexamined.

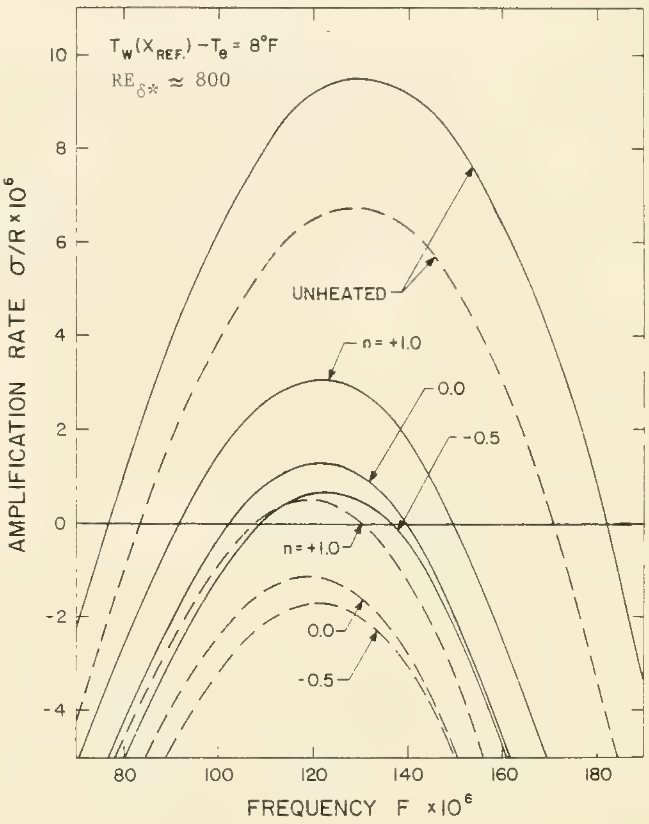

Effect of power law wall heating on stability of non-similar water boundary layer. ---- parallel, —— non-parallel. $\sigma = \text{Im}(\alpha_o + \varepsilon\alpha_1)$ where α_o is the quasi-parallel amplification rate and $\varepsilon\alpha_1$ is the non-parallel contribution.

Session II

BOUNDARY LAYER STABILITY AND TRANSITION

KARL WIEGHARDT
Session Chairman
University of Hamburg
Hamburg, Federal Republic of Germany

Nonparallel Stability of Two-Dimensional Heated Boundary Layer Flows

N. M. El-Hady and A. H. Nayfeh
Virginia Polytechnic Institute and State University, Blacksburg, Virginia

ABSTRACT

The method of multiple scales is used to analyze the linear-nonparallel stability of two-dimensional heated liquid boundary layers. Included in the analysis are disturbances due to velocity, pressure, temperature, density, and transport properties, as well as variations of the liquid properties with temperature. An equation is derived for the modulation of the wave amplitude with streamwise distance. Although the analysis is applicable to both uniform and nonuniform wall heating, numerical results are presented only for the uniform heating case. The numerical results are in good agreement with the experimental results of Strazisar, Reshotko, and Prahl.

1. INTRODUCTION

It is generally accepted that the instability of small amplitude disturbances in a laminar boundary layer is an integral part of the transition process. Significant changes in the boundary layer stability characteristics can be achieved by utilizing different factors, such as pressure gradients, suction, injection, compliant boundaries, and heating or cooling of the boundary layer.

Surface heating in a liquid boundary layer can be utilized to yield a mean velocity profile which is more stable than the Blasius profile. The reason is that heat transfer alters the shape of the boundary-layer temperature profile which in turn alters the velocity profile through the viscosity-temperature dependence. The effect of wall heating on the stability of boundary layers in water was investigated by Wazzan et al. (1968, 1970). They included the variation of the viscosity with temperature through the thermal boundary layer. They obtained a modified Orr-Summerfeld equation. However, they did not include temperature fluctuations in the disturbance flowfield. Their results show that while cooling the wall has a destabilizing effect on the flow, moderate heating has a strong stabilizing effect. Lowell (1974) reformulated the problem by adding fluctuations for the temperature, density, and transport properties. The results of Lowell did not vary appreciably from those of Wazzan et al. (1970).

The presently available analyses (Wazzan et al. and Lowell) for the stability of heated boundary layers in water are all parallel flow analyses. The results of the parallel stability analyses do not agree with available experimental results. Strazisar et al. (1975, 1977) performed experiments on the stability of boundary layers on both unheated and uniformly heated flat plates. These experiments confirmed the increased stability resulting from wall heating in water. Strazisar and Reshotko (1977) extended their experiments to cases of nonuniform surface heating in the form of power-law temperature distributions; that is, $T_w(x) - T_e = Ax^n$. Their results are given only for a displacement thickness Reynolds number $R^* = 800$ and indicate that, for a given level of wall heating, cases with $n < 0$ have the lowest growth rates. Strazisar and Reshotko (1977) found that applying Lowell's analysis (1974) to the case of power-law temperature distributions yielded results that did not agree with the experimental results.

In this paper, we use the method of multiple scales (1973) to analyze the linear, nonparallel stability of two-dimensional boundary layers in water on a flat plate, taking into account uniform as well as nonuniform wall heating. We include disturbances in the temperature, density, and transport properties of the liquid in addition to disturbances in the velocities and pressure. However, we present numerical results only for the case of uniform wall heating and compare our results with the experimental data of Strazisar et al. (1975, 1977). When the variation of the temperature, thermodynamic, and transport properties are neglected, the present solution reduces to those of

Bouthier (1973), Nayfeh, Saris, and Mook (1974), Gaster (1974), and Saric and Nayfeh (1975, 1977).

The formulation of the problem and method of solution is taken in the next section, the solution of the first-order problem is given in Section 3, the solution of the second-order problem is given in Section 4, the mean flow is discussed in Section 5, and the numerical results and their comparison with the experimental data of Strazisar et al. (1975, 1977) is given in Section 6.

2. PROBLEM FORMULATION AND METHOD OF SOLUTION

The present study is concerned with the two-dimensional, nonparallel stability of two-dimensional, viscous, heat conducting liquid boundary layers to small amplitude disturbances. The analysis takes into account variations in the fluid properties but neglects buoyancy, dissipation, and expansion energies. All fluid properties are assumed to be known functions of the temperature alone.

Dimensionless quantities are introduced by using a suitable reference length L* and the freestream values as reference quantities, where the star denotes dimensional quantities.

To study the linear stability of a mean boundary-layer flow, we superpose a small time-dependent disturbance on each mean flow, thermodynamic, and trasport quantity. Thus, we let

$$\hat{q}(x,y,t) = Q_0(x,y) + q(x,y,t) \qquad (1)$$

where $Q_0(x,y)$ is a mean steady quantity and $q(x,y,t)$ is an unsteady disturbance quantity. Here, q stands for the streamwise and transverse velocity components u and v, the temperature T, the pressure p, the density ρ, the specific heat c_p, the viscosity μ, and the thermal conductivity κ. Substituting Eq. (1) into the Navier-Stokes and energy equations, subtracting the mean quantities and linearizing the resulting equations in the q's, we obtain the following disturbance equation:

$$\frac{\partial \rho}{\partial t} + \frac{\partial}{\partial x}(\rho_0 u + \rho U_0) + \frac{\partial}{\partial y}(\rho_0 v + \rho V_0) = 0 \qquad (2)$$

$$\begin{aligned}
&\rho_0\left(\frac{\partial u}{\partial t} + U_0\frac{\partial u}{\partial x} + u\frac{\partial U_0}{\partial x} + V_0\frac{\partial u}{\partial y} + v\frac{\partial U_0}{\partial y}\right) \\
&+ \rho\left(U_0\frac{\partial U_0}{\partial x} + V_0\frac{\partial U_0}{\partial y}\right) \\
&= -\frac{\partial p}{\partial x} + \frac{1}{R}\left\{\frac{\partial}{\partial x}\left[\mu_0\left(r\frac{\partial u}{\partial x} + s\frac{\partial v}{\partial y}\right)\right.\right. \\
&\qquad \left. + \mu\left(r\frac{\partial U_0}{\partial x} + s\frac{\partial V_0}{\partial y}\right)\right] \\
&\qquad + \frac{\partial}{\partial y}\left[\mu_0\left(\frac{\partial u}{\partial y} + \frac{\partial v}{\partial x}\right)\right. \\
&\qquad \left.\left. + \mu\left(\frac{\partial U_0}{\partial y} + \frac{\partial V_0}{\partial x}\right)\right]\right\} \qquad (3)
\end{aligned}$$

$$\begin{aligned}
&\rho_0\left(\frac{\partial v}{\partial t} + U_0\frac{\partial v}{\partial x} + u\frac{\partial V_0}{\partial x} + V_0\frac{\partial v}{\partial y} + v\frac{\partial V_0}{\partial y}\right) \\
&+ \rho\left(U_0\frac{\partial V_0}{\partial x} + V_0\frac{\partial V_0}{\partial y}\right) \\
&= -\frac{\partial p}{\partial y} + \frac{1}{R}\left\{\frac{\partial}{\partial x}\left[\mu_0\left(\frac{\partial u}{\partial y} + \frac{\partial v}{\partial x}\right)\right.\right. \\
&\qquad \left. + \mu\left(\frac{\partial U_0}{\partial y} + \frac{\partial V_0}{\partial x}\right)\right] \\
&\qquad + \frac{\partial}{\partial y}\left[\mu_0\left(r\frac{\partial v}{\partial y} + s\frac{\partial u}{\partial x}\right)\right. \\
&\qquad \left.\left. + \mu\left(r\frac{\partial V_0}{\partial y} + s\frac{\partial U_0}{\partial x}\right)\right]\right\} \qquad (4)
\end{aligned}$$

$$\begin{aligned}
&\rho_0\left[\frac{\partial T}{\partial t} + u\frac{\partial T_0}{\partial x} + U_0\frac{\partial T}{\partial x} + v\frac{\partial T_0}{\partial y} + V_0\frac{\partial T}{\partial y}\right] \\
&+ \left(\rho_0\frac{c_p}{c_{p_0}} + \rho\right)\left[U_0\frac{\partial T_0}{\partial x} + V_0\frac{\partial T_0}{\partial y}\right] \\
&= \frac{1}{RPr_e c_{p_0}}\left\{\frac{\partial}{\partial x}\left(\kappa_0\frac{\partial T}{\partial x} + \kappa\frac{\partial T_0}{\partial x}\right)\right. \\
&\qquad \left. + \frac{\partial}{\partial y}\left(\kappa_0\frac{\partial T}{\partial y} + \kappa\frac{\partial T_0}{\partial y}\right)\right\} \qquad (5)
\end{aligned}$$

$$\rho,\ \mu,\ \kappa,\ c_p = \text{functions } (T) \qquad (6)$$

Here, c_{p_0} is the liquid specific heat at constant pressure, $R = \rho_e^* U_e^* L^*/\mu_e^*$ is the Reynolds number and $Pr_e = c_{pe}^* \mu_e^*/\kappa_e^*$ is the freestream Prandtl number. Moreover,

$$r = \frac{2}{3}(e + 2), \quad s = \frac{2}{3}(e - 1),$$

$$h = \frac{1}{3}(1 + 2e), \quad \lambda = \frac{2}{3}\mu(e-1) \qquad (7)$$

where e is the ratio of the second to the first viscosity coefficients (e = 0 is the Stokes assumption).

The problem is completed by the specification of the boundary conditions; they are

$$u = v = T = 0 = \text{at } y = 0 \qquad (8)$$

$$u,v,T \to 0 \quad \text{as} \quad y \to \infty \qquad (9)$$

We restrict our analysis to mean flows which are slightly nonparallel; that is, the transverse velocity component is small compared with the streamwise velocity component. This condition demands all mean flow variables to be weak functions of the streamwise position. These assumptions are expressed mathematically by writing the mean flow variables in the form

$$U_0 = U_0(x_1,y), \quad V_0 + \epsilon\tilde{V}_0(x_1,y),$$

$$P_0 = P_0(x_1), \quad T_0 = T_0(x_1,y)$$

$$\rho_0 = \rho_0(x_1,y), \quad c_{p_0} = c_{p_0}(x_1,y),$$

$$\mu_0 = \mu_0(x_1,y), \quad \kappa_0 = \kappa_0(x_1,y) \qquad (10)$$

where $x_1 = \epsilon x$ with ε being a small dimensionless parameter characterizing the nonparallelism of the mean flow. In what follows, we drop the caret from V_0.

To determine an approximate solution to Eqs. (2)-(10), we use the method of multiple scales [Nayfeh (1973)] and seek a first-order expansion for the eight dependent disturbance variables u, v, p, T, ρ, c_p, μ and κ in the form of a traveling harmonic wave; that is, we expand each disturbance flow quantity in the form

$$q(x_1,y,t,) = [q_1(x_1,y) + \varepsilon q_2(x_1,y) + \ldots]\exp(i\theta) \tag{11}$$

where

$$\frac{\partial\theta}{\partial x} = \alpha_0(x_1), \quad \frac{\partial\theta}{\partial t} = -\omega \tag{12}$$

For the case of spatial stability, α_0 is the complex wavenumber for the quasi-parallel flow problem and ω is the disturbance frequency which is taken to be real.

Substituting Eqs. (11) and (12) into Eqs. (2)-(10), transforming the time and the spatial derivatives from t and x to θ and x_1, and equating the coefficients of ε^0 and ε on both sides, we obtain problems describing the q_1 and q_2 flow quantities. These problems are referred to as the first- and second-order problems and they are solved in the next two sections.

3. THE FIRST-ORDER PROBLEM

Substituting Eqs. (11) and (12) into Eqs. (2)-(10) and equating the coefficients of ε^0 on both sides, we obtain the following

$$L_1(u_1,v_1,p_1,T_1) = i\alpha_0[\rho_0 u_1 + (U_0 - \frac{\omega}{\alpha_0})\rho_1] + \frac{\partial}{\partial y}(\rho_0 v_1) = 0 \tag{13}$$

$$\begin{aligned}
L_2(u_1,v_1,p_1,T_1) &= \left[i\rho_0\alpha_0\left(U_0 - \frac{\omega}{\alpha_0}\right) + \frac{r}{R}\mu_0\alpha_0^2\right]u_1 + \left(\rho_0\frac{\partial U_0}{\partial y}\right. \\
&\quad \left. - \frac{i}{R}\frac{\partial\mu_0}{\partial y}\alpha_0\right)v_1 + i\alpha_0 p_1 - \frac{T_1}{R}\frac{\partial}{\partial y}\left(\frac{d\mu_0}{dT_0}\frac{\partial U_0}{\partial y}\right) \\
&\quad - \frac{1}{R}\frac{\partial\mu_0}{\partial y}\frac{\partial u_1}{\partial y} - \frac{ih}{R}\mu_0\alpha_0\frac{\partial v_1}{\partial y} \\
&\quad - \frac{1}{R}\frac{d\mu_0}{dT_0}\frac{\partial U_0}{\partial y}\frac{\partial T_1}{\partial y} - \frac{1}{R}\mu_0\frac{\partial^2 u_1}{\partial y^2} = 0
\end{aligned} \tag{14}$$

$$\begin{aligned}
L_3(u_1,v_1,p_1,T_1) &= \left[i\rho_0\alpha_0\left(U_0 - \frac{\omega}{\alpha_0}\right) + \frac{1}{R}\mu_0\alpha_0^2\right]v_1 \\
&\quad - \frac{is}{R}\alpha_0\frac{\partial\mu_0}{\partial y}u_1 - \frac{i}{R}\alpha_0\frac{d\mu_0}{dT_0}\frac{\partial U_0}{\partial y}T_1 \\
&\quad - \frac{ih}{R}\mu_0\alpha_0\frac{\partial u_1}{\partial y} - \frac{r}{R}\frac{\partial\mu_0}{\partial y}\frac{\partial v_1}{\partial y} \\
&\quad + \frac{\partial p_1}{\partial y} - \frac{r}{R}\mu_0\frac{\partial^2 v_1}{\partial y^2} = 0
\end{aligned} \tag{15}$$

$$\begin{aligned}
L_4(u_1,v_1,p_1,T_1) &= \left[i\rho_0\alpha_0\left(U_0 - \frac{\omega}{\alpha_0}\right) + \frac{1}{RPr_e c_{p_0}}\left(\kappa_0\alpha_0^2 - \frac{\partial^2\kappa_0}{\partial y^2}\right)\right]T_1 \\
&\quad + \rho_0\frac{\partial T_0}{\partial y}v_1 - \frac{2}{RPr_e c_{p_0}}\frac{\partial\kappa_0}{\partial y}\frac{\partial T_1}{\partial y} \\
&\quad - \frac{1}{RPr_e c_{p_0}}\kappa_0\frac{\partial^2 T_1}{\partial y^2} = 0
\end{aligned} \tag{16}$$

The boundary conditions are:

$$u_1 = v_1 = T_1 = 0 \quad \text{at } y = 0 \tag{17}$$

$$u_1,\ v_1,\ T_1 \to 0 \quad \text{as } y \to \infty \tag{18}$$

Equations (13) - (18) constitute an eigenvalue problem, which is solved numerically. It is convenient to express it as a set of six first-order equations by introducing the new variables z_{1n} defined by

$$z_{11} = u_1, \quad z_{12} = \frac{\partial u_1}{\partial y}, \quad z_{13} = v_1,$$

$$z_{14} = p_1, \quad z_{15} = T_1, \quad z_{16} = \frac{\partial T_1}{\partial y} \tag{19}$$

Then, Eqs. (13)-(18) can be rewritten in the compact form

$$\frac{\partial z_{1i}}{\partial y} - \sum_{j=1}^{6} a_{ij}z_{1j} = 0 \text{ for } i = 1,2..,6 \tag{20}$$

$$z_{11} = z_{13} = z_{15} = 0 \quad \text{at } y = 0 \tag{21}$$

$$z_{11},\ z_{13},\ z_{15} \to 0 \quad \text{as } y \to \infty \tag{22}$$

where the a_{ij} are the elements of a 6 × 6 variable-coefficient matrix. The nineteen nonzero elements of this matrix are listed in Appendix I.

We solve this eigenvalue problem by using SUPORT [Scott and Watts (1977)]. To set up the numerical problem, we first replace the boundary conditions (22) by a new set at $y = \tilde{y}$ where $\tilde{y}$ is a convenient location outside the boundary layer. Outside the boundary layer, the mean flow is independent of y and the coefficients a_{ij} are constants. Hence, the general solution of Eqs. (20) can be expressed in the form

$$z_{1i} = \sum_{j=1}^{6} \Lambda_{ij}c_j\exp(\lambda_j y) \text{ for } i = 1,2,\ldots,6 \tag{23}$$

where the λ_j are the eigenvalues of the matrix $[a_{ij}]$, the Λ_{ij} are the corresponding eigenvectors and the c_j are arbitrary constants. The real parts of three of the λ_j are negative, while the real parts of the remaining λ_j are positive. Let us order these eignevalues so that the real parts of λ_1, λ_2, and λ_3 are negative. Then, the boundary condition (22) demands that c_4, c_5 and c_6 are zero. To set up this condition for SUPORT, we first solve Eqs. (23) for the $c_j\exp(\lambda_j y)$ and obtain

$$c_j\exp(\lambda_j y) = \sum_{i=1}^{6} b_{ij}z_{1i} \text{ for } j = 1,2,\ldots,6 \tag{24}$$

where the matrix $[b_{ij}]$ is the inverse of $[\Lambda_{ij}]$. Setting $c_4 = c_5 = c_6 = 0$ in Eq. (24) leads to

$$\sum_{i=1}^{6} b_{ij} z_{1i} = 0 \text{ for } j = 4,5, \text{ and } 6 \text{ at } y = \tilde{y} \tag{25}$$

where the b_{ij} are the elements of a 3 × 6 constant-coefficient matrix.

Using Eqs. (25) as the boundary condition at $y = \tilde{y}$ and guessing a value for α_0, we use SUPORT to integrate Eqs. (20) from $y = \tilde{y}$ to $y = 0$ and attempt to satisfy the boundary conditions (21). If the guessed value for α_0 is the correct eigenvalue, the three boundary conditions will be satisfied. In general, the guessed value is not the correct value and the boundary conditions at the wall are not satisfied. A Newton-Raphson procedure is used to update the value of α_0 and the integration is repeated until the wall-boundary conditions are satisfied to within a prescribed accuracy. This leads to a value for α_0 and a further integration of Eqs. (20) leads to a solution that can be expressed in the form

$$z_{1i} = A(x_1)\zeta_i(x_1,y) \text{ for } i = 1,2,\ldots,6 \tag{26}$$

where A is still an undetermined function at this level of approximation. It is determined by imposing a solvability condition at the next level of approximation.

4. THE SECOND-ORDER PROBLEM

With the solution of the first-order problem given in Eq. (26), the second-order problem becomes

$$\frac{\partial z_{2i}}{\partial y} - \sum_{j=1}^{6} a_{ij} z_{2j}$$

$$= G_i \frac{dA}{dx_1} + F_i A \text{ for } i = 1,2,\ldots,6 \tag{27}$$

$$z_{21} = z_{23} = z_{25} = 0 \quad \text{at } y = 0 \tag{28}$$

$$z_{21}, z_{23}, z_{25} \to 0 \quad \text{as } y \to \infty \tag{29}$$

where the G_i and F_i are known functions of the ζ_i, α_0 and the mean flow quantities. They are defined in Appendix II.

Since the homogeneous parts of Eqs. (27)-(29) are the same as Eqs. (20)-(22) and since the latter have a nontrivial solution, the inhomogeneous Eqs. (27)-(29) have a solution if, and only if, a solvability condition is satisfied. In this case the solvability condition demands the inhomogeneities to be orthogonal to every solution of the adjoint homogeneous problem; that is,

$$\int_0^\infty \sum_{i=1}^{6} \left[G_i \frac{dA}{dx_1} + F_i A \right] W_i \, dy = 0 \tag{30}$$

where the $W_i(x_1,y)$ are the solutions of the adjoint homogeneous problem corresponding to the eigenvalue α_0. Thus, they are the solutions of

$$\frac{\partial W_i}{\partial y} + \sum_{j=1}^{6} a_{ji} W_j = 0 \text{ for } i = 1,2,\ldots,6 \tag{31}$$

$$W_2 = W_4 = W_6 = 0 \quad \text{at } y = 0 \tag{32}$$

$$W_2, W_4, W_6 \to 0 \quad \text{as } y \to \infty \tag{33}$$

Substituting for the G_i and F_i from Appendix II into Eq. (30), we obtain the following equation for the evolution of the amplitude A:

$$\frac{1}{A}\frac{dA}{dx_1} = i\alpha_1(x_1) \tag{34}$$

where

$$i\alpha_1 = -\int_0^\infty \sum_{j=1}^{6} F_j W_j \, dy \Bigg/ \int_0^\infty \sum_{j=1}^{6} G_j W_j \, dy \tag{35}$$

The solution of Eq. (34) can be written as

$$A = A_0 \exp[i\varepsilon \int \alpha_1(x_1) dx] \tag{36}$$

where A_0 is a constant of integration.

To determine $\alpha_1(x_1)$, we need to evaluate $d\alpha_0/dx_1$ and the $\partial\zeta_i/\partial x_1$. To accomplish this, we differentiate Eqs. (20)-(22) with respect to x_1 and obtain

$$\frac{\partial}{\partial y}\left(\frac{\partial \zeta_i}{\partial x_1}\right) = \sum_{j=1}^{6} a_{ij}\left(\frac{\partial \zeta_j}{\partial x_1}\right)$$

$$+ G_i \frac{d\alpha_0}{dx_1} + H_i \text{ for } i = 1,2,\ldots,6 \tag{37}$$

$$\frac{\partial \zeta_1}{\partial x_1} = \frac{\partial \zeta_3}{\partial x_1} = \frac{\partial \zeta_5}{\partial x_1} = 0 \text{ at } y = 0 \tag{38}$$

$$\frac{\partial \zeta_1}{\partial x_1}, \frac{\partial \zeta_3}{\partial x_1}, \frac{\partial \zeta_5}{\partial x_1} \to 0 \text{ as } y \to \infty \tag{39}$$

The initial conditions for the computational procedures are chosen to exclude any multiple of the homogeneous solution. The H_i are known functions of ζ_i, α_0 and the mean flow quantities and their derivatives; they are given by

$$H_i = \sum_{j=1}^{6} \zeta_j \frac{\partial a_{ij}}{\partial x_1}\bigg|_{\alpha_0} \text{ and}$$

$$G_i = \sum_{j=1}^{6} \zeta_j \frac{\partial a_{ij}}{\partial x_1} \text{ for } i = 1,2,\ldots,6 \tag{40}$$

Using the solvability condition of Eqs. (37)-(39), we find that

$$\frac{d\alpha_0}{dx_1} = - \int_0^\infty \sum_{i=1}^{6} H_i W_i dy \int_0^\infty \sum_{i=1}^{6} G_i W_i dy \qquad (41)$$

Therefore, to the first approximation

$$z_1 = A_0 \zeta(x_1,y) \exp[i \int (\alpha_0 + \varepsilon\alpha_1) dx - i\omega t] + O(\varepsilon) \quad (42)$$

where the z_1 are related to the disturbance variables by Eq. (19) and the constant A_0 is determined from the initial conditions. It is clear from Eq. (42) that, in addition to the dependence of the eigensolutions on x, the eigenvalue α_0 is modified by $\varepsilon\alpha_1$. The present solution reduces to those obtained by Nayfeh, Saric, and Mook (1974) and Saric and Nayfeh (1975) for the case of nonheat conducting flows.

5. THE MEAN FLOW

For flows whose thermodynamic and transport properties are functions of temperature, the two-dimensional boundary-layer equations for a zero-pressure gradient are

$$\frac{\partial}{\partial x^*} (\rho^* u^*) + \frac{\partial}{\partial y^*} (\rho^* v^*) = 0 \qquad (43)$$

$$\rho^* u^* \frac{\partial u^*}{\partial x^*} + \rho^* v^* \frac{\partial u^*}{\partial y^*} = \frac{\partial}{\partial y^*} (\mu^* \frac{\partial u^*}{\partial y}) \qquad (44)$$

$$\rho^* u^* c_p^* \frac{\partial T^*}{\partial x^*} + \rho^* v^* c_p^* \frac{\partial T^*}{\partial y^*} = \frac{\partial}{\partial y} (\kappa^* \frac{\partial T^*}{\partial y^*}) \qquad (45)$$

The temperature dependence of ρ and μ couples the momentum and the energy equations. Note that buoyancy and viscous dissipation effects are neglected.

Although the stability analysis is applicable to any wall temperature variations, we present stability results for the case of constant wall temperature for which the flow is self similar. Thus, we introduce the transformation.

$$\eta = \frac{\sqrt{R_x}}{x^*} \int_0^{y^*} \rho dy^* \qquad (46)$$

where R_x is the freestream x-Reynolds number defined by

$$R_x = \rho_e^* U_e^* x^* / \mu_e^* \qquad (47)$$

Introducing this transformation in Eqs. (43)-(45) and solving the continuity equations for v, we transform the original set of partial-differential equations into the following set of ordinary-differential equations:

$$\frac{\partial}{\partial \eta} (\rho\mu \frac{\partial u}{\partial \eta}) + g \frac{\partial u}{\partial \eta} = 0 \qquad (48)$$

$$\frac{\partial}{\partial \eta} (\rho\kappa \frac{\partial T}{\partial \eta}) + Pr_e c_p g \frac{\partial T}{\partial \eta} = 0 \qquad (49)$$

where

$$g(\eta) = \frac{1}{2\rho} \int_0^{\eta} \rho u d\eta \qquad (50)$$

Note that all fluid properties are made dimensionless by using their freestream values.

Equations (48)-(50) are supplemented by the following boundary conditions:

$$u = 0,\ T = T_w^*/T_e^* \text{ and } g = 0 \text{ at } \eta = 0 \qquad (51)$$

$$u \to 1 \text{ and } T \to 1 \qquad \text{as } \eta \to \infty \qquad (52)$$

where the subscript w denotes wall values. Equations (48)-(52) are numerically integrated by using Runge-Kutta and Adams-Moulten integration techniques with the liquid thermodynamic and transport properties computed at each integration step. All numerical results presented here are for water; the dependence of its thermodynamic and transport properties on the temperature is given in Appendix III.

6. ANALYTICAL RESULTS AND COMPARISON WITH EXPERIMENTS

Although the analysis is applicable to both uniform and nonuniform wall heating, results are presented only for the case of uniform wall heating for which the mean flow is self similar.

The only available experimental results for the stability of uniformly heated boundary-layer flows are those of Strazisar et al. (1975, 1977). Using a water tunnel, they introduced disturbances by vibrating a ribbon and measured the response by using a temperature compensated hot-film anemometry. They used the r.m.s. of the stream-wise component of the disturbance velocity, u, to calculate the growth rates. They determined the growth rate as a function of frequency at different Reynolds numbers.

For a parallel mean flow, $\alpha_1 = 0$, α_0 and A are constants, and the ζ_n are function of y only. Hence, one can unambiguously define the growth rate σ of the distrubance as the imaginary part of $\overline{\alpha}_0$; that is,

$$\sigma = - \operatorname{Im}(\alpha_0) \qquad (53)$$

This definition is equivalent to

$$\sigma = \operatorname{Re} (\frac{\partial}{\partial x} \ell n u) = \operatorname{Re}(\frac{\partial}{\partial x} \ell n v) =$$

$$\operatorname{Re} (\frac{\partial}{\partial x} \ell n p) = \operatorname{Re}(\frac{\partial}{\partial x} \ell n T) \qquad (54)$$

On the other hand, for a nonparallel mean flow, $\alpha_1 \neq 0$, A and α_0 are functions of x, and the ζ_n are functions of both x and y. Thus, if one generalizes (53) to take into account $\varepsilon\alpha_1$, one obtains

$$\sigma = - \operatorname{Im}(\alpha_0 + \varepsilon\alpha_1) \qquad (55)$$

which is not equivalent to (54). Moreover, the quantity α_1 and hence σ depend on the normalization of the ζ_n because part of the ζ_n can be absorbed in

A and α_1. If one generalizes the definition (54) and uses (42), one obtains

$$\sigma = -\,\mathrm{Im}(\alpha_0 + \epsilon\alpha_1) + \epsilon\mathrm{Re}\left(\frac{\partial}{\partial x}\,\ln\zeta_n\right) \qquad (56)$$

Thus, the growth rate in (56) depends on the choice of ζ_n because the axial and transverse variations of the ζ_n are not the same. Since the ζ_n are functions of both y and x, one may term a stable flow unstable or vice versa.

Since there are many possible definitions of the growth rate in a nonparallel flow, one should be careful in comparing analytical and experimental results. Saric and Nayfeh (1975, 1977) found that the best correlation between the nonparallel theory and available experimental data for the Blasius flow is obtained if one uses the definition (55). In this paper, we compare the definitions (55) and (56) evaluated at the value η where ζ_1 is a maximum.

Figure 1 shows the variation of the calculated disturbance growth rates σ/R with frequency $FR=\omega/R$ for $T_w-T_e = 0$, 3,5, and 8°F and for the displacement thickness Reynolds number $R^* = 800$. This range of T_w-T_e is chosen for comparison with the existing experimental results. The growth rate is calculated by using the definition (55) and by normalizing ζ_1 so that $\zeta_1 \to \exp(-\alpha_0 y)$ as $y \to \infty$. This figure indicates that the disturbance growth rate decreases with increasing T_w-T_e. The maximum growth rate is reduced by approximately 56% by increasing the wall temperature by 5°F. The maximum growth rate is very small when the wall temperature is increased by 8°F at $R^* = 800$. Figure 1 shows that the range of unstable frequencies decreases with increasing T_w-T_e.

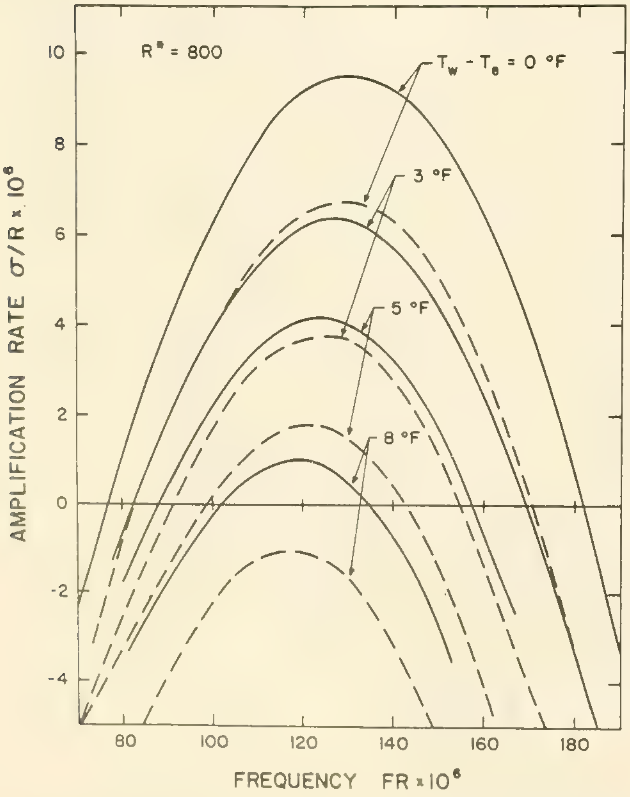

FIGURE 1. The variation of the spatial growth rate with frequency for varying wall temperatures at $R^* = 800$. ——— Nonparallel, ----- Parallel.

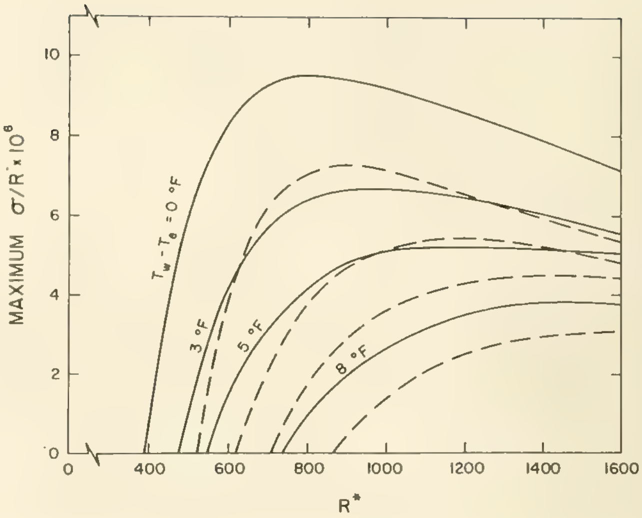

FIGURE 2. The variation of the maximum growth rate with streamwise position for varying wall temperatures. ——— Nonparallel, ----- Parallel.

Figure 2 shows the variation of the maximum growth rate obtained from our analysis with T_w-T_e. It shows that the maximum growth rate decreases with increasing wall temperature at all Reynolds numbers.

Figures 1 and 2 show a comparison between the growth rates based on the parallel, (53), and nonparallel, (55), stability theories. The nonparallel maximum growth rates are approximately 30% larger than the parallel ones. Moreover, the nonparallel critical Reynolds number is approximately 20% lower than the parallel one for all the values of T_w-T_e considered as shown in Figure 2.

Figures 3a-3d show comparisons of the experimental growth rates of Strazisar et al. and the nonparallel growth rates defined by (53), (55) and (56) for different values of T_w-T_e and different values of R*. These figures show good agreement between the growth rate defined by (55) and the experimental results, in contrast with the parallel theory which underpredicts the experimental results by large amounts. Moreover, including the distortion of the eigenfunction with streamwise position in the definition of the growth rate yields a growth rate that is very close to the parallel one and hence underpredicts the experimental results by large amounts.

7. CONCLUSION

The method of multiple scales is used to analyze the linear nonparallel stability of two-dimensional liquid boundary layers on a flat plate for the cases of uniform and nonuniform wall heatings. We include disturbances in the temperature, density, thermodynamic, and transport properties of the liquid in addition to disturbances in the velocities and pressure. The growth rates calculated from nonparallel results without including the distortion of the eigenfunction with streamwise position are in good agreement with the experimental results of Strazisar et al. (1975, 1977). The nonparallel results show that wall heating in water has a stabilizing effect on the flow; there is a decrease in the disturbance growth rates, a decrease in the range of unstable frequencies and an increase in the critical Reynolds number.

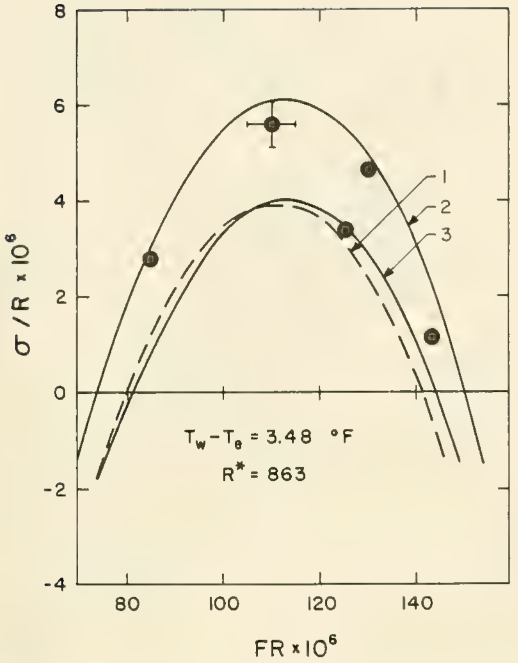

FIGURE 3a. Comparison of the analytical and the experimental spatial growth rates for various displacement thickness Reynolds numbers and wall temperatures. Experiments, Strazisar et al. (1975, 1977), 1) $\sigma = \mathrm{Im}(\alpha_0)$, 2) $\sigma = -\mathrm{Im}(\alpha_0 + \varepsilon\alpha_1)$, 3) $\sigma = -\mathrm{Im}(\alpha_0 + \varepsilon\alpha_1) + \frac{\varepsilon}{|\zeta_1|} \frac{\partial|\zeta_1|}{\partial x_1}$.

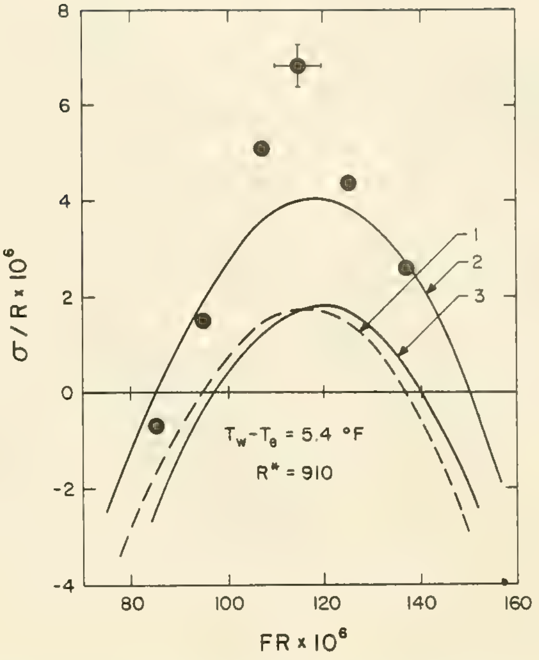

FIGURE 3c. Comparison of the analytical and the experimental spatial growth rates for various displacement thickness Reynolds numbers and wall temperatures. Experiments, Strazisar et al. (1975, 1977), 1) $\sigma = -\mathrm{Im}(\alpha_0)$, 2) $\sigma = -\mathrm{Im}(\alpha_0 + \varepsilon\alpha_1)$, 3) $\sigma = -\mathrm{Im}(\alpha_0 + \varepsilon\alpha_1) + \frac{\varepsilon}{|\zeta_1|} \frac{\partial|\zeta_1|}{\partial x_1}$.

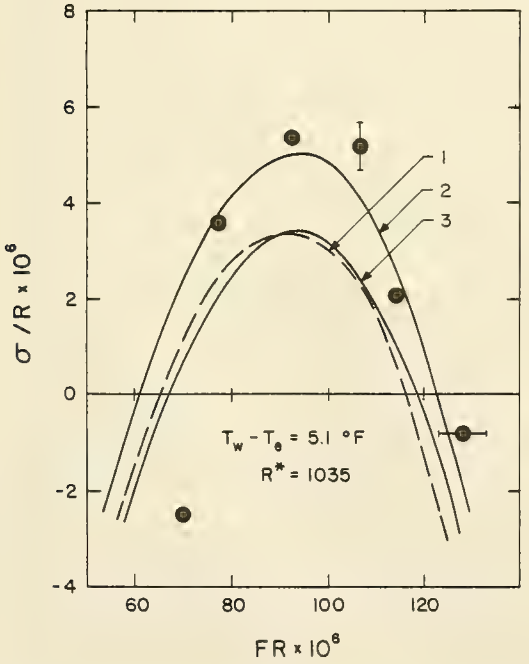

FIGURE 3b. Comparison of the analytical and the experimental spatial growth rates for various displacement thickness Reynolds numbers and wall temperatures. Experiments, Strazisar et al. (1975, 1977), 1) $\sigma = \mathrm{Im}(\alpha_0)$, 2) $\sigma = -\mathrm{Im}(\alpha_0 + \varepsilon\alpha_1)$, 3) $\sigma = -\mathrm{Im}(\alpha_0 + \varepsilon\alpha_1) + \frac{\varepsilon}{|\zeta_1|} \frac{\partial|\zeta_1|}{\partial x_1}$.

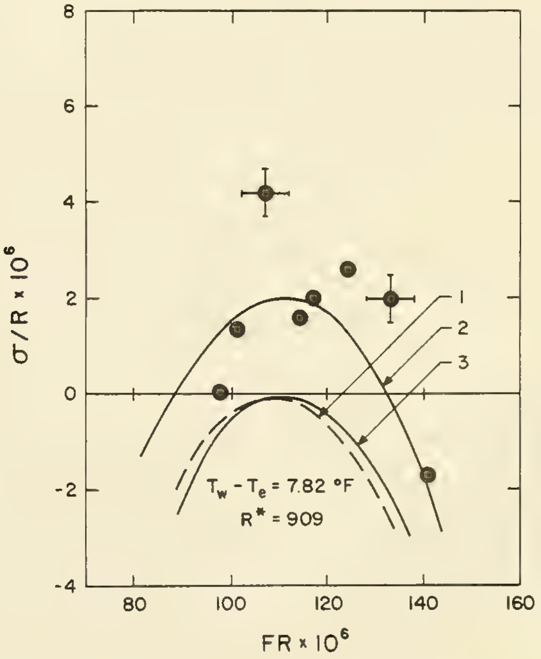

FIGURE 3d. Comparison of the analytical and the experimental spatial growth rates for various displacement thickness Reynolds numbers and wall temperatures. Experiments, Strazisar et al. (1975, 1977), 1) $\sigma = -\mathrm{Im}(\alpha_0)$, 2) $\sigma = -\mathrm{Im}(\alpha_0 + \varepsilon\alpha_1)$, 3) $\sigma = -\mathrm{Im}(\alpha_0 + \varepsilon\alpha_1) + \frac{\varepsilon}{|\zeta_1|} \frac{\partial|\zeta_1|}{\partial x_1}$.

ACKNOWLEDGMENT

The authors are indebted to Dr. W. S. Saric for many valuable comments. This work was supported by the NASA Langley Research Center Under Grant No. NSG 1255.

REFERENCES

Bouthier, M. (1973). Stabilité linéaire des écoulements presque paralléles. *J. de Mécanique 12,* 75.

Gaster, M. (1974). On the effects of boundary-layer growth on flow stability. *J. Fluid Mech. 66,* 465.

Lowell, R. S. (1974). Numerical study of the stability of a heated water boundary layer, Ph.D. dissertation, Case Western Reserve University; also, *Dept. Fluid, Thermal, and Aerospace Sci., Case Western Reserve Univ., Rep. FTAS/TR-73-93.*

Nayfeh, A. H. (1973). *Perturbation Methods.* Wiley, New York, Chap. 6.

Nayfeh, A. H., W. S. Saric, and D. T. Mook (1974). Stability of nonparallel flows. *Arch. Mech. 26,* 401.

Saric, W. S., and A. H. Nayfeh (1975). Nonparallel stability of boundary layer flows, *Phys. Fluids 18,* 945.

Saric, W. S., and A. H Nayfeh (1977). Nonparallel stability of boundary layers with pressure gradients and suction. *AGARD Conference Proceedings No. 224, Laminar-Turbulent Transition,* Paper No. 6.

Scott, M. R., and H. A. Watts (1977). SUPORT-A computer code for two-point boundary value problems via orthonormalization. *SIAM J. Num. Anal. 14,* 40.

Strazisar, A. J., and E. Reshotko (1977). Stability of heated laminar boundary layers in water with non-uniform surface temperature, *AGARD Conference No. 224, Laminar-Turbulent Transition,* Paper No. 10.

Strazisar, A. J., J. M. Prahl, and E. Reshotko (1975). Experimental study of stability of heated laminar boundary layers in water, *Dept. Fluid, Thermal and Aerospace Sci., Case Western Reserve Univ., Rep. FTAS/TR-75-113.*

Strazisar, A. J., E. Reshotko, and J. M. Prahl (1977). Experimental study of stability of heated laminar boundary layers in water. *J. Fluid Mech. 83,* 225.

Wazzan, A. R., T. T. Okamura, and A. M. O. Smith (1968). The stability of water flow over heated and cooled flat plates. *J. Heat. Trans. 90,* 109.

Wazzan, A. R., T. T. Okamura, and A. M. O. Smith (1970). The stability and transition of heated and cooled imcompressible boundary layers, *Proceedings, 4th International Heat Transfer Conference,* ed. Grigall U. and E. Hahne, Amsterdam.

APPENDIX I

$$a_{12} = 1$$

$$a_{21} = \frac{i\rho_0\alpha_0 R}{\mu_0}\left(U_0 - \frac{\omega}{\alpha_0}\right) + \alpha_0^2$$

$$a_{22} = -\frac{1}{\mu_0}\frac{\partial\mu_0}{\partial y}$$

$$a_{23} = \frac{\rho_0 R}{\mu_0}\frac{\partial U_0}{\partial y} - i\alpha_0\left(\frac{1}{\mu_0}\frac{\partial\mu_0}{\partial y} - \frac{h}{\rho_0}\frac{\partial\rho_0}{\partial y}\right)$$

$$a_{24} = \frac{i\alpha_0 R}{\mu_0}$$

$$a_{25} = -\frac{h\alpha_0^2}{\rho_0}\frac{d\rho_0}{dT_0}\left(U_0 - \frac{\omega}{\alpha_0}\right) - \frac{1}{\mu_0}\frac{\partial}{\partial y}\left(\frac{d\mu_0}{dT_0}\frac{\partial U_0}{\partial y}\right)$$

$$a_{26} = -\frac{1}{\mu_0}\frac{d\mu_0}{dT_0}\frac{\partial U_0}{\partial y}$$

$$a_{31} = -i\alpha_0$$

$$a_{33} = -\frac{1}{\rho_0}\frac{\partial\rho_0}{\partial y}$$

$$a_{34} = -\frac{i\alpha_0}{\rho_0}\frac{d\rho_0}{dT_0}\left(U_0 - \frac{\omega}{\alpha_0}\right)$$

$$a_{41} = -\frac{i\alpha_0\mu_0}{R}\left(\frac{2}{\mu_0}\frac{\partial\mu_0}{\partial y} - \frac{r}{\rho_0}\frac{\partial\rho_0}{\partial y}\right)$$

$$a_{42} = -\frac{i\alpha_0\mu_0}{R}$$

$$a_{43} = \frac{\alpha_0\mu_0}{R}\left\{-\alpha_0 - \frac{r}{\alpha_0\mu_0\rho_0}\frac{\partial\mu_0}{\partial y}\frac{\partial\rho_0}{\partial y} - \frac{r}{\alpha_0\rho_0}\left[\frac{\partial^2\rho_0}{\partial y^2} - \frac{2}{\rho_0}\left(\frac{\partial\rho_0}{\partial y}\right)^2\right]\right.$$
$$\left. - \frac{i\rho_0 R}{\mu_0}\left(U_0 - \frac{\omega}{\alpha_0}\right)\right\}$$

$$a_{45} = \frac{i\alpha_0\mu_0}{R}\left\{\frac{1}{\mu_0}\frac{d\mu_0}{dT_0}\frac{\partial U_0}{\partial y} - \frac{r}{\mu_0\rho_0}\frac{d\rho_0}{dT_0}\frac{\partial\mu_0}{\partial y}\left(U_0 - \frac{\omega}{\alpha_0}\right)\right.$$
$$\left. - \frac{r}{\rho_0}\left[\frac{d\rho_0}{dT_0}\frac{\partial U_0}{\partial y} + \left(U_0 - \frac{\omega}{\alpha_0}\right)\left(\frac{\partial}{\partial y}\frac{d\rho_0}{dT_0} - \frac{2}{\rho_0}\frac{d\rho_0}{dT_0}\frac{\partial\rho_0}{\partial y}\right)\right]\right\}$$

$$a_{46} = -\frac{i\alpha_0\mu_0 r}{R\rho_0}\frac{d\rho_0}{dT_0}\left(U_0 - \frac{\omega}{\alpha_0}\right)$$

$$a_{56} = 1$$

$$a_{63} = \frac{RPr_e c_{p_0}\rho_0}{\kappa_0}\frac{\partial T_0}{\partial y}$$

$$a_{65} = \frac{iRPr_e c_{p_0}\alpha_0\rho_0}{\kappa_0}\left(U_0 - \frac{\omega}{\alpha_0}\right) + \alpha_0^2 - \frac{1}{\kappa_0}\frac{\partial^2\kappa_0}{\partial y^2}$$

$$a_{66} = -\frac{2}{\kappa_0}\frac{\partial\kappa_0}{\partial y}$$

APPENDIX II

$$G_1\frac{dA}{dx_1} + F_1 A = 0$$

$$G\frac{dA}{dx_1} + F_2 A = -\frac{ih\alpha_0}{\rho_0}I_m - \frac{R}{\mu_0}I_x$$

$$G_3\frac{dA}{dx_1} + F_3 A = \frac{1}{\rho_0}I_m$$

$$G_4\frac{dA}{dx_1} = F_4 A = \frac{r}{R}\frac{\mu_0}{\rho_0}\left(\frac{1}{\mu_0}\frac{\partial\mu_0}{\partial y} - \frac{2}{\rho_0}\frac{\partial\rho_0}{\partial y}\right)I_m + \frac{r}{R}\frac{\mu_0}{\rho_0}\frac{\partial}{\partial y}I_m + I_y$$

$$G_5\frac{dA}{dx_1} + F_5 A = 0$$

$$G_6\frac{dA}{dx_1} + F_6 A = -\frac{RPr_e c_{p_0}}{\kappa_0}I_e$$

where

$$I_m = -\left\{\rho_0\zeta_1 + U_0\frac{d\rho_0}{dT_0}\zeta_5\right\}\frac{dA}{dx_1} - \left\{\frac{\partial\rho_0}{\partial x_1}\zeta_1 + \rho_0\frac{\partial\zeta_1}{\partial x_1} + \left[\frac{d\rho_0}{dT_0}\left(\frac{\partial U_0}{\partial x_1} + \frac{\partial V_0}{\partial y}\right)\right.\right.$$
$$\left.\left. + U_0\frac{\partial}{\partial x_1}\left(\frac{d\rho_0}{dT_0}\right) + V_0\frac{\partial}{\partial y}\left(\frac{d\rho_0}{dT_0}\right)\right]\zeta_5 + U_0\frac{d\rho_0}{dT_0}\frac{\partial\zeta_5}{\partial x_1} + V_0\frac{d\rho_0}{dT_0}\frac{\partial\zeta_5}{\partial y}\right\}A$$

$$I_x = \left\{\left(\frac{2ir}{R}\mu_0\alpha_0 - \rho_0 U_0\right)\zeta_1 + \frac{1}{R}\frac{\partial\mu_0}{\partial y}\zeta_3 + \frac{h}{R}\mu_0\frac{\partial\zeta_3}{\partial y} - \zeta_4\right\}\frac{dA}{dx_1}$$
$$+ \left\{\left[\frac{ir}{R}\left(\mu_0\frac{d\alpha_0}{dx_1} + \alpha_0\frac{\partial\mu_0}{\partial x_1}\right) - \rho_0\frac{\partial U_0}{\partial x_1}\right]\zeta_1 + \left(\frac{2ir}{R}\mu_0\alpha_0 - \rho_0 U_0\right)\frac{\partial\zeta_1}{\partial x_1}\right.$$

continued on page 62

$$- \rho_0 V_0 \zeta_2 + \frac{s}{R} \frac{\partial \mu_0}{\partial x_1} \frac{\partial \zeta_3}{\partial y} + \frac{h}{R} \mu_0 \frac{\partial}{\partial x_1} (\frac{\partial \zeta_3}{\partial y}) + \frac{1}{R} \frac{\partial \mu_0}{\partial y} \frac{\partial \zeta_3}{\partial x_1} - \frac{\partial \zeta_4}{\partial x_1}$$

$$+ [\frac{i}{R} \alpha_0 \frac{d\mu_0}{dT_0} (r \frac{\partial U_0}{\partial x_1} + s \frac{\partial V_0}{\partial y}) - \frac{d\rho_0}{dT_0} (U_0 \frac{\partial U_0}{\partial x_1} + V_0 \frac{\partial U_0}{\partial y})]\zeta_5 \Bigg\} A$$

$$I_y = \Bigg\{ \frac{s}{R} \frac{\partial \mu_0}{\partial y} \zeta_1 + \frac{h}{R} \mu_0 \zeta_2 + (\frac{2i}{R} \mu_0 \alpha_0 - \rho_0 U_0)\zeta_3 + \frac{1}{R} \frac{d\mu_0}{dT_0} \frac{\partial U_0}{\partial y} \zeta_5 \Bigg\} \frac{dA}{dx_1}$$

$$+ \Bigg\{ \frac{s}{R} \frac{\partial \mu_0}{\partial y} \frac{\partial \zeta_1}{\partial x_1} + \frac{1}{R} \frac{\partial \mu_0}{\partial x_1} \zeta_2 + \frac{h}{R} \mu_0 \frac{\partial \zeta_2}{\partial x_1} + [\frac{i}{R} (\mu_0 \frac{d\alpha_0}{dx_1} + \alpha_0 \frac{\partial \mu_0}{\partial x_1})$$

$$- \rho_0 \frac{\partial V_0}{\partial y}]\zeta_3 - \rho_0 V_0 \frac{\partial \zeta_3}{\partial y} + (\frac{2i}{R} \mu_0 \alpha_0 - \rho_0 U_0) \frac{\partial \zeta_3}{\partial x_1} + \frac{1}{R} [h \frac{d\mu_0}{dT_0} \frac{\partial}{\partial x_1} \times$$

$$(\frac{\partial U_0}{\partial y}) + \frac{\partial U_0}{\partial y} \frac{\partial}{\partial x_1} (\frac{d\mu_0}{dT_0}) + r \frac{d\mu_0}{dT_0} \frac{\partial^2 V_0}{\partial y^2} + (r \frac{\partial V_0}{\partial y} + s \frac{\partial U_0}{\partial x_1}) \frac{\partial}{\partial y} (\frac{d\mu_0}{dT_0})]\zeta_5$$

$$+ \frac{1}{R} \frac{d\mu_0}{dT_0} \frac{\partial U_0}{\partial y} \frac{\partial \zeta_5}{\partial x_1} + \frac{1}{R} \frac{d\mu_0}{dT_0} (r \frac{\partial V_0}{\partial y} + s \frac{\partial U_0}{\partial x_1})\zeta_6 \Bigg\} A$$

$$I_e = \Bigg\{ (\frac{2i}{RPr_e c_{p_0}} \alpha_0 \kappa_0 - \rho_0 U_0)\zeta_5 \Bigg\} \frac{dA}{dx_1} - \Bigg\{ \rho_0 \frac{\partial T_0}{\partial x_1} \zeta_1 - [\frac{i}{RPr_e c_{p_0}} \times$$

$$(\alpha_0 \frac{d\kappa_0}{dT_0} \frac{\partial T_0}{\partial x_1} + \kappa_0 \frac{d\alpha_0}{dx_1} + \alpha_0 \frac{\partial \kappa_0}{\partial x_1}) - (\frac{d\rho_0}{dT_0} + \frac{\rho_0}{c_{p_0}} \frac{dc_{p_0}}{dT_0})(U_0 \frac{\partial T_0}{\partial x_1}$$

$$+ V_0 \frac{\partial T_0}{\partial y})]\zeta_5 + (\frac{2i}{RPr_e c_{p_0}} \alpha_0 \kappa_0 - \rho_0 U_0) \frac{\partial \zeta_5}{\partial x_1} - \rho_0 V_0 \zeta_6 \Bigg\} A$$

APPENDIX III

The variation of the water thermodynamic and transport properties with temperature is given by

$$\rho^* = 1 - \frac{(T^* - 3.9863)^2 (T^* + 288.9414)}{508929.2\ (T^* + 68.12963)} + 0.011445 \exp(- \frac{374.3}{T^*})$$

ρ^* in gm/mℓ, T^* in °C.

$$\mathrm{Log}(\frac{1.002}{\mu^*}) = \frac{1.37023(T^* - 20) + 8.36 \times 10^{-4}(T^* - 20)^2}{109 + T^*}$$

μ^* in Cp, T^* in °C

$$\kappa^* = - 9.901090 + 0.1001982T^* - 1.873892 \times 10^{-4} T^{*2}$$
$$+ 1.039570 \times 10^{-7} T^{*3}$$

κ^* in m watts $\mathrm{cm}^{-1} K^{-1}$, T^* in °K

$$c_p^* = 2.13974 - 9.68137 \times 10^{-3} T^* + 2.68536 \times 10^{-5} T^{*2}$$
$$- 2.42139 \times 10^{-8} T^{*3}$$

c_p^* in cal $g_m^{-1} K^{-1}$, T^* in °K

A discussion of the sources and accuracy of these formulas can be found in Lowell (1974).

Three-Dimensional Effects in Boundary Layer Stability

Leslie M. Mack
California Institute of Technology
Pasadena, California

SUMMARY

Most work in linearized boundary-layer stability theory has been carried out either on the basis of two-dimensional mean flow and plane wave disturbances with the wavenumber in the flow direction, or, for a more general case, by a transformation of the equations to two-dimensional form. This procedure can obscure important physical aspects of wave propagation in two space dimensions. In this paper the stability equations are retained in three-dimensional form throughout. A method for treating spatially amplifying disturbances with a complex group velocity is adopted and applied first to oblique waves in a two-dimensional boundary layer, and then to the two-parameter yawed Falkner-Skan boundary layers. One parameter is the spanwise to chordwise velocity. For boundary layers with small crossflow, the maximum amplification rate with respect to frequency is calculated as a function of flow angle for waves whose normal is aligned with the flow. Next, the minimum critical Reynolds number of zero-frequency crossflow instability is obtained for both large and small pressure gradients, and finally the instability properties of two particular boundary layers with crossflow instability are determined for all unstable frequencies.

1. INTRODUCTION

Most work in linearized boundary-layer stability theory has been restricted to two-dimensional mean flows, and, for these flows, even further restricted to plane-wave disturbances with the wave normal in the flow direction.* The latter restriction is normally justified by reference to the theorem of Squire (1933), which states that in a two-dimensional incompressible boundary layer, the minimum critical Reynolds number is given by a two-dimensional wave. Even though the most unstable wave at a given Reynolds number is two dimensional in accordance with the theorem, the most unstable wave of a particular frequency can well be three dimensional. Furthermore, the unstable three-dimensional waves can have phase orientation angles (the angle between the local freestream direction and the wave normal) up to almost 80°. Any method for the estimation of transition that is based on stability theory must take this large range of unstable three dimensional waves into account. For a supersonic two-dimensional boundary layer, even the most unstable plane wave at a given Reynolds number is three dimensional. The two-dimensional waves become of little importance as the Mach number increases above one until the hypersonic regime is reached, where a two-dimensional second-mode wave is the most unstable.

When we turn to three-dimensional boundary layers, there are no two-dimensional waves, but the transformation of Stuart [Gregory et al. (1955)] reduces the three-dimensional temporal stability problem to a series of two-dimensional problems. That is, the temporal amplification rate can be obtained by solving a two-dimensional problem for the boundary-layer profile in the direction of the wave normal. This approach was carried through numerically by Brown (1961) for the rotating disk and a limited number of swept-wing boundary layers. When the same approach is applied to the spatial theory, it leads to complex velocity profiles and loses much of its utility except as a computational device.

Instead of trying to make a two-dimensional world out of a three-dimensional world, it might as well be accepted that boundary-layer instability is inherently three dimensional, even with two-dimensional mean flow, and to formulate the instability problem directly as three dimensional [Mack, (1977); this paper will be referred to as M77]. A transformation of the dependent variables reduces the order of the incompressible eigenvalue problem from sixth to fourth order, but the velocity profiles and wave parameters are not transformed. This approach is equally valid for the temporal and spatial theories, but for the latter a growth direction must be assigned before eigenvalues can be computed. In M77 this direction was taken equal to the direction of the real part of the group velocity and numerical results were obtained for two-dimensional incompressible and compressible flat-plate boundary layers and for the rotating disk boundary layer.

---

*Such a wave is called two-dimensional because it has only two disturbance velocity components. All other plane waves have three velocity components in any coordinate system, and are called three dimensional.

In the present paper, a theoretical presentation is given in Section 2 to justify the use of a spatial mode whose direction of growth is determined by the complex group velocity. In Section 3, some results concerning three-dimensional spatial waves in the Blasius boundary layer are given as an example. In Section 4, we adapt the family of yawed-wedge three-dimensional boundary layers [Cooke (1950)] for use in stability calculations. In Section 5, under Boundary Layers with Small Crossflow, we consider the effect of the flow angle (the angle between the local potential-flow direction and the direction of the pressure gradient) on the maximum amplification rate for small pressure gradients. Next, in Section 5 we take up crossflow instability and determine the critical Reynolds number for several combinations of pressure gradient and flow angle. We then obtain the maximum amplification rate and instability boundaries of all unstable frequencies as a function of the wavenumber vector for a favorable pressure-gradient boundary layer which is unstable at low Reynolds numbers only because of crossflow instability. Finally, in the last part of Section 5, we repeat the latter calculation for an adverse pressure-gradient boundary layer with crossflow instability at a Reynolds number where the boundary layer is unstable even without crossflow instability. In all of the examples, only the amplification rate is calculated, and on the basis of locally uniform flow. No results concerning wave amplitude are given, although in Section 2, we make use of a simple wave amplitude equation in order to properly define the spatial amplification rate.

2. THREE DIMENSIONAL STABILITY THEORY

Formulation and Transformations

The linearized, incompressible, parallel-flow, dimensionless Navier-Stokes equations for the elementary modes

$$\begin{pmatrix} u(x,y,z,t) \\ v(x,y,z,t) \\ w(x,y,z,t) \\ p(x,y,z,t) \end{pmatrix} = \begin{pmatrix} f(y) \\ \phi(y) \\ h(y) \\ \pi(y) \end{pmatrix} \exp[i(\alpha x + \beta z - \omega t)], \qquad (1)$$

where u,v,w are the velocity fluctuations and p is the pressure fluctuation, can be reduced to (M77)

$$Z_1' = Z_2',$$

$$Z_2' = [\alpha^2 + \beta^2 + iR(\alpha U + \beta W - \omega)]Z_1 + (\alpha U' + \beta W')RZ_3 + i(\alpha^2 + \beta^2)RZ_4, \qquad (2)$$

$$Z_3' = -iZ_1$$

$$Z_4' = -\frac{i}{R}Z_2 - \left[i(\alpha U + \beta W - \omega) + \frac{\alpha^2 + \beta^2}{R}\right]Z_3,$$

for the determination of the eigenvalues. The primes refer to differentiation with respect to y, and the dependent variables are

$$Z_1(y) = \alpha f(y) + \beta h(y),\ Z_3(y) = \phi(y),$$

$$Z_4(y) = \pi(y).$$

There are two additional uncoupled equations for h(y). In Eqs. (2), α and β are the complex wavenumber components in the x and z directions, ω is the complex frequency, U and W are the mean velocity components in the x and z directions, and R is the Reynolds number $U_p^*L^*/\nu^*$, where the velocity scale U_p^* is the potential velocity and L^* is a suitable length scale. Asterisks refer to dimensional quantities. The modes in Eq. (1) can be termed plane waves in the x,z plane because of the phase function, even though there is a modal structure in the y direction.

The boundary conditions are

$$Z_1(0) = 0 \quad , \quad Z_3(0) = 0 \ , \qquad (3)$$
$$Z_1(y) \to 0 \quad , \quad Z_3(y) \to 0 \quad \text{as } y \to \infty .$$

If we choose x to be the direction of the local potential flow, then z is the crossflow direction and

$$U(y) \to 1 \ , \quad W(y) \to 0 \quad \text{as } y \to \infty .$$

Thus U(y) is the mainflow velocity profile; W(y) is the crossflow profile.

In the temporal stability theory, α and β are real, and Eqs. (2) can be reduced to two-dimensional form in two different ways. The first transformation is

$$\tilde\alpha = (\alpha^2 + \beta^2)^{\frac{1}{2}} \ , \ \tilde U = U + \frac{\beta}{\alpha} W, \qquad (4)$$
$$\tilde\alpha \tilde R = \alpha R \ , \quad \tilde\omega/\tilde\alpha = \omega/\alpha.$$

When W = 0, this is the transformation of Squire (1933). It relates the eigenvalues of a three-dimensional wave of frequency ω in a velocity profile (U,W) at Reynolds number R to the eigenvalues of a two-dimensional wave of frequency $\omega/\cos\psi$ in a velocity profile $U + W\tan\psi$ at Reynolds number $R\cos\psi$, where

$$\psi = \tan^{-1}(\beta/\alpha)$$

is the phase orientation angle.

The second transformation,

$$\tilde\alpha = (\alpha^2 + \beta^2)^{\frac{1}{2}} \ , \quad \tilde\alpha \tilde U = \alpha U + \beta W,$$
$$\tilde R = R \quad , \quad \tilde\omega = \omega \ ,$$

is that of Stuart [Gregory et al. (1955)]. It relates the eigenvalues of a three-dimensional wave of frequency ω in a velocity profile (U,W) at Reynolds number R to the eigenvalues of a two-dimensional wave of the same frequency in a velocity profile $U\cos\psi + W\sin\psi$ at the same Reynolds number. The Squire transformation is most useful for a two-dimensional boundary layer because the velocity profile is unchanged. Thus all eigenvalues of three-dimensional waves can be obtained from known eigenvalues of two-dimensional waves with no additional calculations. In a three-dimensional boundary layer, the velocity profile must change and the Stuart transformation is preferred because the frequency can remain fixed at a given Reynolds number as the phase orientation angle ψ is varied.

Spatial Stability Theory

Statement of the Problem

In the spatial stability theory, α and β are complex and ω is real. Neither transformation is of much utility except when

$$\alpha_i/\beta_i = \alpha_r/\beta_r. \tag{6}$$

When (6) is not satisfied, $\tilde{\alpha}$ is complex, and in the Squire transformation both $\tilde{R}$ and $\tilde{\omega}$ are also complex as well as $\tilde{U}$ for a three-dimensional boundary layer. In the Stuart transformation, $\tilde{U}$ is complex for all boundary layers. With complex quantities, we might as well deal directly with (2), as these equations have already been reduced to fourth order and nothing is to be gained from an additional transformation. There only remains the question, to be answered later in this Section, of whether any use can be made of the simplification offered by (6).

It is convenient to define a real wavenumber vector

$$\vec{k} = (\alpha_r, \beta_r),$$

and a real spatial amplification rate vector

$$\vec{\sigma} = (-\alpha_i, -\beta_i),$$

in place of the complex vector $\vec{k} - i\vec{\sigma}$. The magnitudes of the vectors are k and σ, and their directions are given by the two angles

$$\psi = \tan^{-1}(\beta_r/\alpha_r), \quad \bar{\psi} = \tan^{-1}(\beta_i/\alpha_i).$$

Equation (6) is now seen to be a statement that $\vec{k}$ and $\vec{\sigma}$ are parallel ($\bar{\psi} = \psi$). Plane waves with $\bar{\psi} \neq \psi$ have been termed inhomogeneous by Landau and Lifshitz (1960).

The solution of the eigenvalue problem set up by (2) and (3) gives the complex dispersion relation

$$\omega = \Omega(\vec{k}, \vec{\sigma}, x, z).$$

Even with ω, x and z fixed, there remain four real wave parameters: k, ψ, σ and $\bar{\psi}$. Only two of these can be determined in a single eigenvalue calculation, e.g., k and σ with ψ and $\bar{\psi}$ specified. The angle ψ can be considered an independent variable on the same basis as the frequency. The problem is to choose $\bar{\psi}$. What we are looking for is a single spatial mode which serves the same purpose as a two-dimensional spatial mode in a two-dimensional boundary layer, where it represents the wave produced by a stationary harmonic source. The amplification rate of this mode is used as a measure of the relative instability of different velocity profiles, and its amplitude can be applied to the transition problem.

Introduction of an Amplitude Equation

In order to describe wave propagation in the nonuniform medium of the boundary layer, equations are needed for the wave amplitude and the change in the wavenumber vector in addition to the dispersion relation. Even though no amplitude calculations are included in this paper, a consideration of the amplitude equation will help us select $\bar{\psi}$.

In a nonuniform medium the elementary modes (1) are not general enough and must be replaced by

$$u(x,y,z,t) = A(x,z,t)\exp[\sigma(\bar{\psi})\bar{x}]f(y)\exp[i(\alpha_r x + \beta_r z - \omega t)]. \tag{7}$$

In this, the exponential amplitude factor has been written separately in terms of the spatial amplification rate $\sigma(\bar{\psi})$. This amplification rate is the magnitude of $\vec{\sigma}(\vec{k}, \bar{\psi}, \omega, x, z)$ considered as a function of k, ψ, ω, x, z with a fixed value of $\bar{\psi}$. Each $\bar{\psi}$ defines a coordinate

$$x = \cos\bar{\psi}\ x + \sin\bar{\psi}\ z$$

along which the wave growth is directed.

Nayfeh et al. (1978) have derived an equation for the amplitude factor $A(x,z,t)$ on the basis of the multiple scales technique, with A considered to be a slowly varying function of x,z,t, as are α, β, ω and $f(y)$. In a uniform medium, and with A independent of time, their equation reduces to

$$C_x \frac{\partial A}{\partial x} + C_z \frac{\partial A}{\partial z} = 0, \tag{8}$$

where $\vec{C} = (C_x, C_z)$ is the (complex) group velocity. We may note that (8) is also obtained from

$$\frac{\partial A^2}{\partial t} + (\nabla.\vec{C})A^2 = 0, \tag{9}$$

which is the energy conservation equation of Whitham's theory (1974). Davey (1972) has applied (9) to non-conservative wave motion in a two-dimensional mean flow, and refers to the amplitude function A as a pseudo amplitude, or the 'dispersive part' of the amplitude.

Spatial Mode - Real Group Velocity

We restrict ourselves first to the case of $\vec{C}$ real and define the orthogonal coordinates

$$\bar{x}_{gr} = \cos\bar{\psi}_{gr}\ x + \sin\bar{\psi}_{gr}\ z, \tag{10a}$$

$$\bar{z}_{gr} = -\sin\bar{\psi}_{gr}\ x + \cos\bar{\psi}_{gr}\ z, \tag{10b}$$

where

$$\bar{\psi}_{gr} = \tan^{-1}(C_z/C_x).$$

The angle $\bar{\psi}_{gr}$ defines the direction of the characteristic coordinate $\bar{x}_{gr}$, which is identical to a group velocity trajectory, and A is constant along each characteristic according to (8).

The amplitude portion of (7) is now

$$\hat{a}(x,z) = A(\bar{z}_{gr})\exp[\sigma(\bar{\psi})\bar{x}], \tag{11}$$

and (7) can be interpreted as a certain type of solution for a uniform medium when A is variable, provided only that A is constant along a characteristic. A knowledge of A along some initial curve completely specifies $\hat{a}$ along the characteristics of A, and the characteristics of A are also the characteristics of $\hat{a}$. Therefore we can write (11) as

$$\hat{a}(\bar{x}_{gr}) = \hat{a}_o(\bar{z}_{gr})\exp(\sigma_{gr}\bar{x}_{gr}), \tag{12}$$

where (10) has been used to eliminate $\bar{x}$ and

$$\sigma_{gr} = \sigma(\bar{\psi})\cos(\bar{\psi}-\bar{\psi}_{gr}). \tag{13}$$

Consequently, (7) becomes

$$u(x,y,z,t) = \hat{a}_o(\bar{z}_{gr})\exp(\sigma_{gr}\bar{x}_{gr})f(y)\exp[i(\alpha_r x + \beta_r z - \omega t)]. \tag{14}$$

If $\hat{a}_o$ is a constant everywhere, the spatial mode (14) represents a physical wave in the entire x,z plane that could be produced by a particular stationary harmonic line source in a uniform medium. If $\hat{a}_o$ is constant only along a characteristic, we have a form of ray theory, and (14) in turn applies only along a characteristic (ray). In other words, x and z are constrained to follow the characteristic. The latter viewpoint is more useful for a general, nonuniform boundary layer, and also applies to a stationary harmonic line source in a uniform boundary layer when the locus and amplitude distribution of the source are arbitrary.

Equation (13) was derived in M77 from a generalized Gaster relation between temporal and spatial amplification rates. Its meaning can best be seen from Figure 1, where the constant amplitude lines for the two growth directions $\bar{\psi}_{gr}$ and $\bar{\psi}$ are shown. These lines are normal to the direction of growth, just as the constant phase lines are normal to the direction of the wavenumber vector. A certain growth along $\bar{x}_{gr}$ in distance $\Delta\bar{x}_{gr}$ requires the amplification rate along $\bar{x}$ to be $1/\cos(\bar{\psi}-\bar{\psi}_{gr})$ larger than the amplification rate along $\bar{x}_{gr}$ to yield the same growth along $\bar{x}$ in the shorter distance $\Delta x = \Delta\bar{x}_{gr}\cos(\bar{\psi}-\bar{\psi}_{gr})$. It is this relationship between $\sigma(\bar{\psi})$ and σ_{gr} that is expressed by (13). For a fixed orientation of the constant amplitude lines normal to $\bar{x}_{gr}$, the growth in different directions follows the usual vector law with the amplification rate in direction $\bar{\psi}_1$ given by

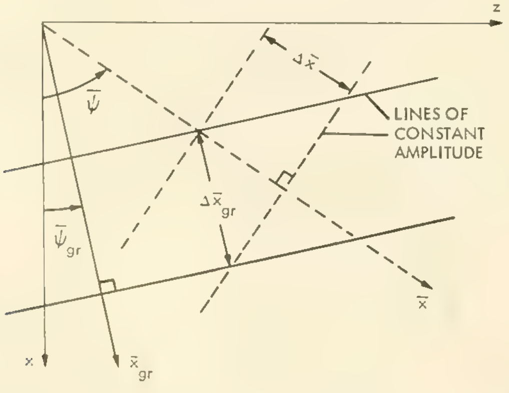

FIGURE 1. Wave growth in direction $\bar{x}_{gr}$ as described by constant amplitude lines normal to $\bar{x}_{gr}$ and to $\bar{x}$.

$$\sigma(\bar{\psi}_1) = \sigma_{gr}\cos(\bar{\psi}_1 - \bar{\psi}_{gr}).$$

We can use (13) to (a) determine σ_{gr} from $\sigma(\bar{\psi})$ provided $\bar{\psi}_{gr}$ is known; (b) determine $\bar{\psi}$ if two neighboring values of $\sigma(\bar{\psi})$ are known; and (c) answer the question left open previously of whether we can make use of the simplification in the spatial theory afforded by (6). The latter is easily done. With (6), the transformation (5) applies to spatial waves and gives

$$-\alpha_i = \sigma(\psi)\cos\psi. \tag{15a}$$

With $\bar{\psi} = \psi$, (13) relates $\sigma(\psi)$ to $-\alpha_i$ by

$$\begin{aligned} -\alpha_i &= \sigma_{gr}\cos\bar{\psi}_{gr} \\ &= [\sigma(\psi)\cos\psi](1 + \tan\psi\tan\bar{\psi}_{gr})\cos^2\bar{\psi}_{gr}. \end{aligned} \tag{15b}$$

It is evident from this expression that (6) is valid only for $\bar{\psi}_{gr} = 0$ (or $\psi = \bar{\psi}_{gr}$). However, $\sigma(\psi)$ can be used to calculate σ_{gr}, if $\bar{\psi}_{gr}$ is known, on the same basis as any other $\sigma(\bar{\psi})$. This procedure is obviously to be avoided when the direction of $\vec{k}$ is perpendicular to that of $\vec{\sigma}$.

Spatial Mode - Complex Group Velocity

With a complex dispersion relation, the group velocity, defined as

$$\vec{C} = \left(\frac{\partial\omega}{\partial\alpha}, \frac{\partial\omega}{\partial\beta}\right) \tag{16}$$

is also complex. For pure temporal or spatial modes, $\vec{C}$ is real only at points of maximum amplification rate. Consequently, it is important to know how the complex $\vec{C}$ affects the preceding analysis. With C_x and C_z complex, (8) is no longer hyperbolic, as pointed out by Nayfeh et al. (1978). However, it is still possible to proceed by defining a real characteristic in the three-dimensional space $(x_r + ix_i, z)$. Such a technique was used in a different context by Garabedian and Lieberstein (1958).

The complex vector group velocity is conveniently described in terms of a complex magnitude and a complex angle by writing

$$C_x = C\cos\bar{\psi}_g, \quad C_z = C\sin\bar{\psi}_g, \tag{17a}$$

where

$$C = \left(C_x^2 + C_z^2\right)^{\frac{1}{2}} \tag{17b}$$

is the complex magnitude, and

$$\bar{\psi}_g = \bar{\psi}_{gr} + i\bar{\psi}_{gi} \tag{17c}$$

is the complex angle.

The complex counterparts of (10) are

$$\bar{x}_g = \cos\bar{\psi}_g\,x + \sin\bar{\psi}_g\,z,$$

$$\bar{z}_g = -\sin\bar{\psi}_g\,x + \cos\bar{\psi}_g\,z,$$

With $x = x_r + ix_i$, and $\bar{x}_g$ required to be real,

$$x_i = \tanh\bar{\psi}_{gi}(\tan\bar{\psi}_{gr}\, x_r - z),$$

and

$$\bar{x}_g = \cosh\bar{\psi}_{gi}\left(\bar{x}_{gr} - \tan\bar{\psi}_{gr}\tanh^2\bar{\psi}_{gi}\,\bar{z}_{gr}\right).$$

With $\bar{x}_g$ real, the analysis for real $\vec{C}$ applies and gives for the now complex amplitude along the real characteristic,

$$\hat{a}(\bar{x}_g) = \hat{a}(\bar{z}'_{gr})\exp[\sigma(\bar{\psi})\cos(\bar{\psi} - \bar{\psi}_g)\bar{x}_g]. \qquad (18)$$

This expression differs from (12) in that $\bar{\psi}_g$ is complex, $\bar{x}_{gr}$ has been replaced by $\bar{z}_g$ and $\bar{z}_{gr}$ (orthogonal to $\bar{x}'_{gr}$, see below).

We define

$$\bar{x}'_{gr} = \bar{x}_{gr} - \tan\bar{\psi}_{gr}\tanh^2\bar{\psi}_{gi}\,\bar{z}_{gr} \qquad (19a)$$

as the characteristic coordinate in the physical plane to replace $\bar{x}_{gr}$. The angle between $\bar{x}'_{gr}$ and $\bar{x}_{gr}$ is given by

$$\tan(\bar{\psi}'_{gr} - \bar{\psi}_{gr}) = -\tan\bar{\psi}_{gr}\tanh^2\bar{\psi}_{gi}. \qquad (19b)$$

We can now write the complex amplitude (18) as

$$\hat{a}(\bar{x}_g) = \hat{a}_0(\bar{z}'_{gr})\exp\left\{\sigma(\bar{\psi})\left[\cos(\bar{\psi} - \bar{\psi}_{gr})\cosh^2\bar{\psi}_{gi} + i\sin(\bar{\psi} - \bar{\psi}_{gr})\cosh\bar{\psi}_{gi}\sinh\bar{\psi}_{gi}\right]\bar{x}'_{gr}\right\}. \qquad (20)$$

The real part of the exponential factor defines the spatial amplification rate along $\bar{x}'_{gr}$ to be

$$\sigma = \sigma(\bar{\psi})\cos(\bar{\psi} - \bar{\psi}_{gr})\cosh^2\bar{\psi}_{gi}. \qquad (21a)$$

This expression differs from its real counterpart (13), aside from the factor $\cosh^2\psi_{gi}$, in that here $\bar{\psi}_{gr}$ is the real part of the complex angle $\bar{\psi}_g$ and not the angle formed by the real parts of C_x and C_z. When $\bar{\psi} = \bar{\psi}_{gr}$,

$$\sigma = \sigma_{gr}\cosh^2\psi_{gi}, \qquad (21b)$$

and, unlike σ_{gr}, σ is not directly calculable as an eigenvalue. The imaginary part of the exponential factor of (20) gives the phase difference between the elementary mode growing along $\bar{x}$ and the spatial mode (20) growing along $\bar{x}'_{gr}$. The phase difference can be written as

$$\bar{\alpha}'_{gr} - \bar{\alpha}(\bar{\psi}) = \sigma(\bar{\psi})\sin(\bar{\psi} - \bar{\psi}_{gr})\cosh\bar{\psi}_{gi}\sinh\bar{\psi}_{gi}, \qquad (22)$$

where $\bar{\alpha}$ is the wavenumber component in the $\bar{x}'_{gr}$ direction. We can now write the complex $\vec{C}$ counterpart to the pure spatial mode (14) as

$$u(x,y,z,t) = \hat{a}_0(\bar{z}'_{gr})\exp(\sigma\bar{x}'_{gr})\, f(y)$$
$$\exp\left\{i\left(\alpha_r x + \beta_r z + \left[\bar{\alpha}'_{gr} - \bar{\alpha}(\bar{\psi})\right]\bar{x}'_{gr} - \omega t\right)\right\}. \qquad (23)$$

With (23) we have arrived at the spatial mode that will be used for the numerical calculations to follow. The amplitude growth is along $\bar{x}'_{gr}$ with magnitude σ given by (21b). The eigenvalues are preferably computed with $\psi = \psi_{gr}$, but as ψ_{gr} is generally not known in advance, or for computational convenience, they can be computed at a neighboring ψ and σ obtained from (21a). If $\bar{\psi}$ is sufficiently close to ψ_{gr}, the phase shift given by (22) is negligible and the orientation angle ψ is unaffected by the transformation.

If $\bar{\psi}_g$ were independent of $\bar{\psi}$, both (14) and (23) would also be expected to be independent of $\bar{\psi}$. However, as $\bar{\psi}$ departs from $\bar{\psi}_{gr}$, $\sigma(\bar{\psi})$ becomes large and the evaluation of the complex derivatives in (16) takes place in a region of the complex α and β planes well removed from the points which give $\bar{\psi}_{gr}$. The same difficulty exists in making comparisons between temporal and spatial amplification rates. Although the elementary modes with arbitrary $\bar{\psi}$ are available for the solution of an initial value problem by superposition, we give physical significance here only to the special spatial mode with $\bar{\psi} = \bar{\psi}_{gr}$. All of the other spatial modes, as well as the combined temporal/spatial modes with α,β,ω all complex, do not enter the present analysis except for computational purposes.

OBLIQUE WAVES IN A TWO-DIMENSIONAL BOUNDARY LAYER

Numerical Example of Transformation Formulas

We shall first discuss the transformations from three- to two-dimensional form and then the transformation between a spatial mode with arbitrary growth direction and the mode with growth direction ψ_{gr}. A single numerical example for the Blasius boundary layer will suffice. We use the conventional dimensionless frequency parameter $F = \omega^*\nu^*/U_1^{*2}$, and choose the length scale to be $L^* = (x^*\nu^*/U_1^*)^{1/2}$. With this choice, the Reynolds number appearing in (2) is $R = (U_1^*\,x^*/\nu^*)^{1/2}$. The subscript 1 refers to freestream conditions.

For $F = 0.2225 \times 10^{-4}$, $R = 1600$ and $\psi = 50°$, a direct calculation of the eigenvalues with (6), i.e., $\bar{\psi} = 50°$, or the completely equivalent two-dimensional calculations with either the Squire or Stuart transformations, gives

$$k = 0.1671, \; \sigma(\psi) = 4.119 \times 10^{-3}.$$

Application of the wavenumber transformation rule in (4) and (5) gives

$$\alpha_r = 0.1074, \; -\alpha_i = 2.648 \times 10^{-3}.$$

for the complex wavenumber in the x direction.

If $\bar{\psi}_{gr}$ is computed in the neighborhood of $\bar{\psi} = 50°$ from (13) by means of the assumption that σ_{gr} is independent of $\bar{\psi}$ and with the frequency held constant, we find

$$\bar{\psi}_{gr} = 9.39°$$

to be an approximate value for the real part of the complex angle of the group velocity vector. (If the wavenumber is held constant, $\bar{\psi}_{gr} = 8.80°$; a value closer to the angle formed by the real parts of C_x and C_z.) The eigenvalues of the ψ - 50° wave with $\psi = 9.39°$ are

$$k = 0.1669, \; \sigma_{gr} = 3.127 \times 10^{-3},$$

and in the x direction

$$\alpha_r = 0.1073, -\alpha_i = 3.085 \times 10^{-3}.$$

The eigenvalues computed with (6) differ from these values in the fourth decimal place, which means that α_i has an unacceptable error of 16.5%, an error which can also be calculated directly from (15b). Consequently, this example reiterates that (6), or the real Squire and Stuart transformations, can only be used if $\bar{\psi}_{gr} = 0$ (or $\bar{\psi} = \bar{\psi}_{gr}$).

For the check of the transformation of an elementary spatial mode with growth direction $\bar{x}$ to the 'physical' mode with growth direction $\bar{x}_{gr}$, we start by calculating the eigenvalues as a function of $\bar{\psi}$ for $0 < \bar{\psi} < 95°$ and the same F, R and ψ as in the previous example. In addition, we calculate the complex group velocity by evaluating the complex derivatives of (2) from central differences for increments in α_r, β_r of ±0.001 about the calculated α_r, β_r at each ψ. The real and imaginary parts of the complex angle $\bar{\psi}_g$ are listed in columns 2 and 3 of Table 1. The angle $\bar{\psi}'_{gr}$ of the growth direction $\bar{x}'_{gr}$, as obtained from (19b), is listed in Column 4. Eigenvalues were computed as a function of $\bar{\psi}$ with $\psi = 50°$ by integrating (2), starting at $y/L = 8.0$, with a fourth-order Runge-Kutta integration and 80 equal integration steps. The results are listed in columns 5 and 6.

If (13) with $\bar{\psi}_{gr} \doteq \tan^{-1}(C_{zr}/C_{xr})$ is applied to the $\sigma(\bar{\psi})$ given in column 6, a nearly constant σ_{gr} is obtained out to about $\bar{\psi} = 60°$. For $\bar{\psi} > 60°$, σ_{gr} decreases steadily, and at $\bar{\psi} = 95°$ it is 21% lower than the σ_{gr} for $\bar{\psi} = \bar{\psi}_{gr}$. Columns 7 and 8 give the angle ψ and wavenumber k for $\bar{\psi} = \bar{\psi}_{gr}$ as calculated from the phase-shift formula (22) of the transformation for complex group velocity. The corresponding amplification rate, as calculated from (21a), is listed in column 9. Comparisons of directly computed eigenvalues with these k and σ are provided in the last two columns. Column 10 lists the eigenvalue k computed for the $\bar{\psi}_{gr}$ of column 2 and the ψ of column 7. Column 11 lists the amplification rate σ obtained from the eigenvalue σ_{gr} accompanying k and from (21b).

We see that the transformation formulas work quite well out to $\bar{\psi} = 60°$, where the difference between columns 9 and 11 is 0.13%. The change of the σ in column 9 with $\bar{\psi}$ is only about half of the change given by the transformation with real group velocity and the correct $\bar{\psi}_{gr}$ given by C_{xr} and C_{zr}. In this particular example, at least, the smallest change of σ with $\bar{\psi}$ is found if (13) is used with $\bar{\psi}_{gr}$ also computed from (13) on the basis of two neighboring values of $\sigma(\bar{\psi})$ obtained with the frequency held constant and σ_{gr} assumed to be independent of $\bar{\psi}$. The conclusion to be drawn is that in order to obtain the desired spatial amplification rate σ as defined by (21b), $\sigma(\bar{\psi})$ may be computed at some convenient $\bar{\psi}$ which can differ from the correct $\bar{\psi}_{gr}$ by as much as 40° or 50°, but should be as close as possible. Only later, after $\bar{\psi}_{gr}$ and $\bar{\psi}_{gi}$ are know, is $\sigma(\bar{\psi})$ converted to σ by the transformation formulas. Almost any of the methods discussed above for applying the transformations gives acceptable numerical accuracy.

Effect of Obliqueness Angle on Instability

The frequency $F = 0.2225 \times 10^{-4}$ used in the examples of the previous Section is the most unstable frequency at R = 1600, and the maximum amplification rate for this frequency occurs for $\psi = 0°$. The distribution of σ with ψ is shown in Figure 2 for this frequency and $F \times 10^4 = 0.280$, 0.1490 and 0.1008. The latter two frequencies are the most unstable for $\psi = 60°$ and 75°, respectively. They have their peak amplification rates, not for $\psi = 0°$, but for $\psi = 34.4°$ and 61.8°, respectively. These results demonstrate that although the maximum amplification rate at a given Reynolds number with respect to both frequency and orientation occurs for a two-dimensional wave, the maximum amplification rate with respect to orientation of given frequency occurs for a three-dimensional wave if the frequency is less than the most unstable frequency.

The envelope curve formed by the individual frequency curves is also shown in Figure 2. This curve gives σ_{max}, the maximum amplification rate with respect to frequency, as a function of ψ. The envelope curve emphasizes the wide range of unstable orientations in a two-dimensional boundary layer. It can be seen that σ_{max} is not reduced to one-half

TABLE 1 Numerical check of spatial-mode transformation for complex group velocity. R = 1600, $F = 0.2225 \times 10^{-4}$, $\psi = 50°$.

$\bar{\psi}$	$\bar{\psi}_{gr}$	$\bar{\psi}_{gi}$	$\bar{\psi}'_{gr}$ (19b)	k eig., $\psi = 50°$	$\sigma(\bar{\psi}) \times 10^3$	ψ (22)	k (22)	$\sigma \times 10^3$ (21a)	k eig., ψ of C7, $\bar{\psi} = \bar{\psi}_{gr}$	$\sigma \times 10^3$
1	2	3	4	5	6	7	8	9	10	11
0	9.23	-4.03	9.18	0.1668	3.171	49.99	0.1669	3.145	0.1669	3.146
9.21	9.21	-4.02	9.16	0.1669	3.127	50.00	0.1669	3.143	0.1669	3.143
30.0	9.16	-4.02	9.11	0.1670	3.340	50.02	0.1669	3.137	0.1669	3.138
60.0	9.08	-4.00	9.04	0.1672	4.928	50.06	0.1670	3.122	0.1670	3.126
90.0	8.67	-3.88	8.63	0.1687	19.66	50.30	0.1677	2.977	0.1676	3.060
95.0	8.36	-3.63	8.33	0.1710	46.04	50.66	0.1688	2.710	0.1686	2.957

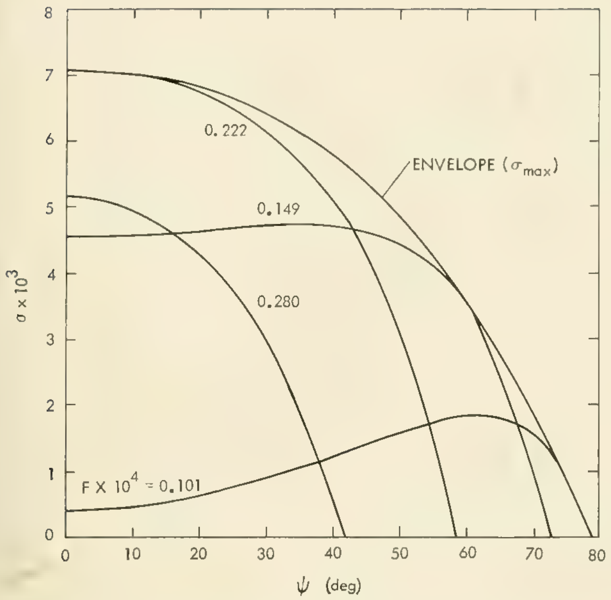

FIGURE 2. Amplification rate as function of ψ for four frequencies. Blasius boundary layer, R = 1600.

of its two-dimensional value until ψ has increased to 60°. With unstable waves for $-79° < \psi < 79°$, a consideration of only the two-dimensional wave gives an incomplete picture of the instability of the boundary layer.

THREE-DIMENSIONAL FALKNER-SKAN BOUNDARY LAYERS

In order to study the influence of three dimensionality in the mean flow on boundary-layer stability, it is necessary to have a family of boundary-layers where the magnitude of the crossflow can be varied in a systematic manner. The two-parameter yawed-wedge flows introduced by Cooke (1950) are suitable for this purpose. One parameter is the usual Falkner-Skan dimensionless pressure gradient; the other is the ratio of the spanwise and chordwise velocities. A combination of the two parameters makes it possible to simulate simple planar three-dimensional boundary layers.

The inviscid velocity in the plane of the wedge and normal to the leading edge is

$$U^*_{c_1} = C^*(x^*_c)^m ,$$

where the wedge angle is $(\pi/2)\,\beta_h$ and $\beta_h = 2m/(m+1)$. We shall refer to this velocity as the chordwise velocity. The velocity parallel to the leading edge, or spanwise velocity is

$$W^*_{s_1} = \text{const.}$$

The subscript 1 refers to the local freestream. For this inviscid flow, the boundary-layer equations in the x_c direction, as shown by Cooke (1950), reduce to

$$f''' + ff'' + \beta_h \left[\left(\frac{m+1}{2} \right) - f'^2 \right] = 0.$$

This equation is the usual Falkner-Skan equation for a two-dimensional boundary layer, and is independent of the spanwise flow. The dependent variable $f(\eta)$ is related to the dimensionless chordwise velocity by

$$U_c = \frac{U^*_c}{U^*_{c_1}} = \left(\frac{2}{m+1} \right) f'(\eta) \quad ,$$

and the independent variable is the similarity variable

$$\eta = y^* \left(\frac{U^*_{c_1}}{\nu^* x^*_c} \right)^{1/2} ,$$

where x^*_c is measured normal to the leading edge. Once $f(\eta)$ is known, the flow in the spanwise direction z^*_s is obtained from

$$g'' + fg' = 0 ,$$

where

$$W_s = \frac{W^*_s}{W^*_{s_1}} = g(\eta) .$$

Both $f'(\eta)$ and $g(\eta)$ are zero at $\eta = 0$ and approach unity as $\eta \to \infty$. Tabulated values of $g(\eta)$ for a few values of β_h may be found in Rosenhead (1963, p. 470).

The final step is to use $f'(\eta)$ and $g(\eta)$ to construct the mainflow and crossflow velocity components needed for the stability equations. A flow geometry appropriate to a swept back wing is shown in Figure 3. There is no undisturbed freestream for a Falkner-Skan flow, but such a direction is assumed and a yaw, or sweep, angle ψ_{sw} is defined with respect to it. The local freestream, or potential flow, is at an angle ψ_p with respect to the undisturbed freestream. It is the potential flow that defines the x,z coordinates of the stability equations. The angle of the potential flow with respect to the chord is

$$\theta = \tan^{-1} \left(\frac{W^*_{s_1}}{U^*_{c_1}} \right),$$

and θ is related to ψ_{sw} and ψ_p by

$$\theta = \psi_{sw} + \psi_p .$$

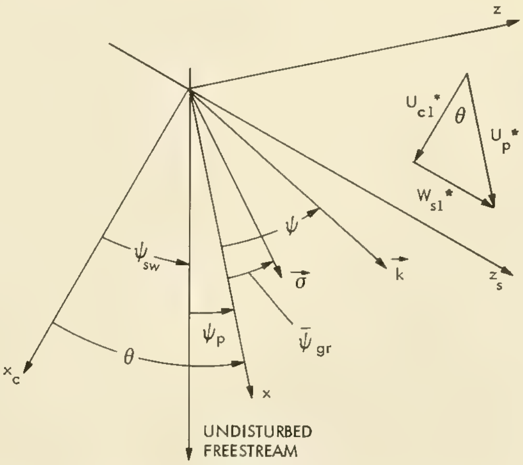

FIGURE 3. Diagram of coordinate systems used for Falkner-Skan-Cooke boundary layers.

With the local potential velocity, $U_p^* = (U_{c1}^{*2} + W_{s1}^{*2})^{1/2}$, as the reference velocity, the dimensionless mainflow and crossflow velocity components are

$$U(\eta) = f'(\eta)\cos^2\theta + g(\eta)\sin^2\theta, \qquad (24a)$$

$$W(\eta) = \left[-f'(\eta) + g(\eta)\right]\cos\theta\,\sin\theta\ . \qquad (24b)$$

These velocity profiles are defined by β_h, which fixes $f'(\eta)$ and $g(\eta)$, and the angle θ. We note from (24b) that for a given pressure gradient all crossflow profiles have the same shape; only the magnitude of the crossflow velocity changes with the flow direction. In contrast, according to (24a), the mainflow profiles change shape as θ varies. For $\theta = 0$, $U(\eta) = f'(\eta)$; for $\theta = 90°$, $U(\eta) = g(\eta)$; for $\theta = 45°$, the two functions make an equal contribution.

When the velocity profiles (24) are used directly in the stability relations, (2), the velocity and length scales of the equations must be the same as in (24). This identifies the velocity scale as U_p^*, the length scale as

$$L^* = \left[\nu^* x_c^* / U_{c_1}^*(x_c^*)\right]^{1/2} ,$$

and the Reynolds number $U_p^* L^*/\nu^*$ as

$$R \doteq R_c/\cos\theta \quad ,$$

where $R_c = \left[U^*_{c_1}(x^*_c)x^*_c)\nu^*\right]^{1/2}$ is the square root of the Reynolds number along the chord. For positive pressure gradients ($m > 0$), $\theta = 90°$ at $x = 0$ and $\theta \to 0°$ as $x \to \infty$; for adverse pressure gradients ($m < 0$), $\theta = 90°$ at $x = 0$ and $\theta \to 0°$ as $x \to \infty$; for adverse pressure gradients ($m < 0$), $\theta = 0°$ at $x = 0$ and $\theta \to 90°$ as $x \to \infty$. The Reynolds number R_c is zero at $x = 0$ for all pressure gradients, as is R with one important exception. The exception is where $m = 1$ ($\beta_h = 1$) is the stagnation-point solution; here it is the attachment-line solution. In the vicinity of $x = 0$, the chordwise velocity is

$$U^*_{c_1} = x^*_c\,(dU^*_{c_1}/dx^*_c)_{x=0} .$$

The potential velocity along the attachment line is W^*_{s1}, and the Reynolds number is

$$R(x{=}0) = W^*_{s1} \Big/ \left[\nu^*(dU^*_{c1}/dx^*_c)_{x=0}\right],$$

a non-zero value.

For the purposes of this paper, θ may be regarded as a free parameter, and the velocity profiles (24) used at any Reynolds number. However, for the flow over a given wedge, θ can be set arbitrarily at only one Reynolds number. If θ_{ref} is θ at $R_c = (R_c)_{ref}$, the θ at any other R_c is given by

$$\tan\theta = \tan\theta_{ref}\ \left[(R_c)_{ref}/R_c\right]^{m/(m+1)},$$

For $m \ll 1$, the dependence on R_c is so weak that θ is constant almost everywhere. One way of choosing $(R_c)_{ref}$ within the context of Figure 3 is to make it the chord Reynolds number where $\psi_p = 0$; i.e., the local potential flow is in the direction of the undisturbed freestream. Then θ_{ref} is equal to the yaw angle ψ_{sw}.

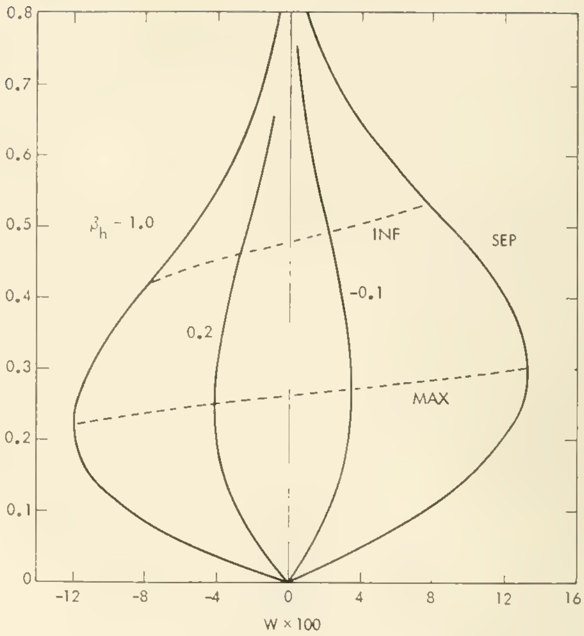

FIGURE 4. Four crossflow velocity profiles, Falkner-Skan-Cooke boundary layers. INF, inflection point; MAX, maximum crossflow; SEP, separation pressure gradient (β_h = -0.1988377).

Figure 4 shows the crossflow velocity profiles for $\theta = 45°$ and four values of β_h. The inflection point and point of maximum crossflow velocity (W_{max}) are also noted on the figure. In Figure 5, W_{max} for $\theta = 45°$ is given as a function of β_h from near separation to $\beta_h = 1.0$. The crossflow velocity for any other flow angle is obtained by multiplying the W_{max} of the figure by $\cos\theta\sin\theta$. The maximum crossflow velocity of 0.133 is generated by the separation profiles rather than by the stagnation profiles, where $W_{max} = 0.120$. However, W_{max} varies rapidly with β_h in the neighborhood of separation, as do all other boundary-layer parameters, and for $\beta_h = -0.190$, W_{max} is only 0.102.

The function $g(\eta)$ is only weakly dependent on

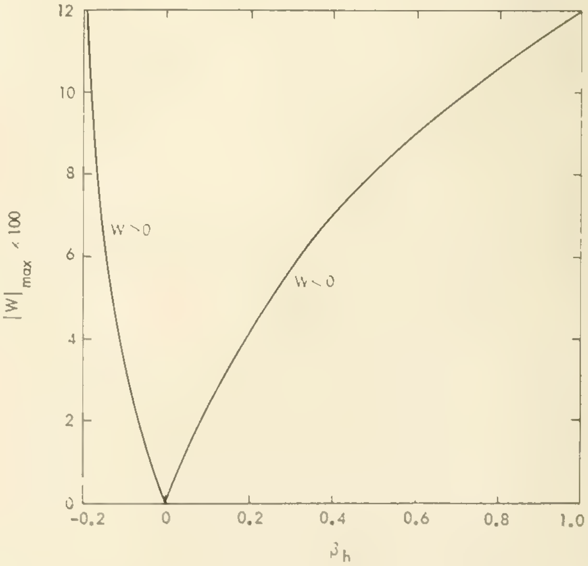

FIGURE 5. Effect of pressure gradient on maximum crossflow, Falkner-Skan-Cooke boundary layers.

TABLE 2. Properties of three-dimensional Falkner-Skan-Cooke boundary layers.

β_h	θ	η_δ	$\eta_\delta{}^*$	H	W_{max}	$\bar{W}$	ε_{inf}	η_{inf}
SEP	2.2	8.238	3.495	4.024	0.0102	0.00476	0.487	4.306
	5.0	8.236	3.489	4.010	0.0231	0.01077	1.100	
	10.0	8.229	3.466	3.959	0.0455	0.02123	2.156	
	40.0	8.095	3.075	3.280	0.1310	0.06214	5.709	
	45.0	8.058	2.986	3.167	0.1330	0.06339	5.696	
	50.0	8.017	2.897	3.064	0.1310	0.06274	5.516	
-0.10	45.0	6.522	1.985	2.698	0.0349	0.01619	1.498	3.213
-0.02	45.0	6.098	1.763	2.609	0.0058	0.00267	0.249	2.940
0.02	45.0	5.931	1.682	2.578	-0.0054	-0.00248	-0.232	2.835
0.04	45.0	5.854	1.646	2.564	-0.0104	-0.00480	-0.449	2.787
0.10	45.0	5.646	1.551	2.529	-0.0239	-0.01094	-1.029	2.659
0.20	45.0	5.348	1.424	2.482	-0.0423	-0.01924	-1.823	2.478
1.0	2.4	3.143	0.6496	2.227	-0.0100	-0.00503	-0.406	1.524
	10.0	3.196	0.6603	2.226	-0.0410	-0.02021	-1.669	
	40.0	3.574	0.8050	2.275	-0.1181	-0.05204	-5.129	
	45.0	3.621	0.8378	2.301	-0.1191	-0.05217	-5.291	
	50.0	3.661	0.8706	2.332	-0.1181	-0.05081	-5.295	
	55.0	3.695	0.9024	2.366	-0.1127	-0.04804	-5.135	
	80.0	3.791	1.0153	2.524	-0.0410	-0.01704	-1.987	
	87.6	3.799	1.0260	2.542	-0.0100	-0.00416	-0.489	

β_h, and, unlike $f'(\eta)$, never has an inflection point even for an adverse pressure gradient. Indeed it remains close to the Blasius profile in shape, as underlined by a shape factor H (ratio of displacement to momentum thickness) that only changes from 2.703 to 2.539 as β_h goes from -0.1988377 (separation) to 1.0 (stagnation). The weak dependence of $g(\eta)$ on β_h was first pointed out by Rott and Crabtree (1952), and made the basis of an approximate method for calculating boundary layers on yawed cylinders. For our purposes, it allows some of the results of the stability calculations to be anticipated. For waves with the wavenumber vector aligned with the local potential flow, we can expect the amplification rate to vary smoothly from its value for a two-dimensional Falkner-Skan flow to a value not too far from Blasius as θ goes from zero to 90°.

The stability results in the next section will be presented in terms of the Reynolds number R and the similarity length scale L*. In order that the results may be converted to the length scales of the boundary-layer thickness, displacement thickness and momentum thickness, Table 2 lists the dimensionless quantities $\eta_\delta = \delta/L^*$, $\eta_\delta{}^* = \delta^*/L^*$ and $H = \eta_\delta{}^*/\eta_\theta$ of the mainflow profile for several combinations of β_h and θ. Also listed are W_{max}, the average crossflow velocity $\bar{W} = (\int W d\eta)/\eta_\delta$, the deflection angle of the streamline at the inflection point, ε_{inf}, and the location of the inflection point, η_{inf}. The quantity η_δ is defined as the point where $U = 0.999$.

STABILITY OF FALKNER-SKAN-COOKE BOUNDARY LAYERS

Boundary Leyers with Small Crossflow

In a two-dimensional boundary layer, the most unstable wave is two dimensional. Therefore, we can expect that in three-dimensional boundary layers with small crossflow the most unstable wave will have its wavenumber vector nearly aligned with the local potential flow, and we can restrict ourselves to waves with $\psi = 0°$ for the purpose of determining the maximum amplification rate. With the temporal stability theory, this procedure is equivalent to studying the two-dimensional instability of the mainflow profile, but is only approximately so in the spatial theory unless $\bar{\psi}_{gr} = 0°$. As $\bar{\psi}_{gr}$ is usually small for $\bar{\psi} = 0°$, even with large crossflow, we may also view the $\psi = 0°$ spatial results as a measure of the instability of the mainflow profile.

In order to place the three-dimensional effects in context, it is helpful to first consider a small deviation in the assumed pressure gradient on the maximum amplification rate of two-dimensional Falkner-Skan profiles. Figure 6 shows the maximum spatial amplification rate (with respect to frequency) as a function of Reynolds number for Blasius flow and for $\beta_h = \pm 0.02$. What is noteworthy about these results is the magnitude of the shift in σ_{max} for what are quite small pressure gradients. It is evident that an experiment intended to measure amplification rates in a Blasius boundary layer to within an accuracy of 10% is required to maintain an exceptional uniformity in the flow.

The effect of the flow angle θ on the maximum spatial amplification rate of the waves with $\psi = 0°$ is shown in Figure 7 for $\beta_h = \pm 0.02$ and two Reynolds numbers. In these calculations, ψ_{gr} and ψ_{gi} were both taken equal to zero. The amplification rate σ_{max} is expressed as a ratio to the Blasius value $(\sigma_b)_{max}$ shown in Figure 6. It will be recalled that with $\beta_h = 0$, $g(\eta) = f(\eta)$, and the velocity profile remains the Blasius function for all flow angles. The effect of a non-zero flow angle with $\beta_h \neq 0$ is destabilizing for a favorable pressure gradient, and stabilizing for an adverse pressure gradient. Consequently, it reduces the pressure-gradient effect shown in Figure 6. The reason for this result is easy to understand by reference to (24). We have already pointed out in Section 4 that the spanwise velocity profile $g(\eta)$

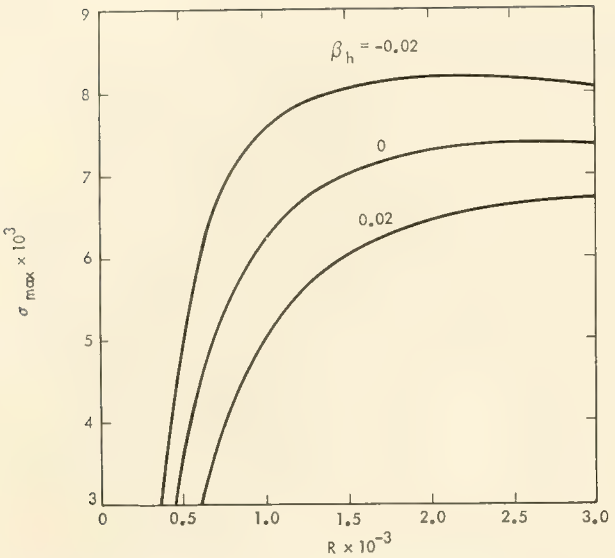

FIGURE 6. Effect of small pressure gradients on the maximum amplification rate with respect to frequency for two-dimensional Falkner-Skan boundary layers.

is always close to the Blasius function. Thus as the flow angle increases from zero the amplification rate must change from the two-dimensional Falkner-Skan value at $\theta = 0°$ to a value not far from Blasius at $\theta = 90°$.

As discussed in Section 4, the only physically meaningful flow with $\theta = 90°$ and a non-zero Reynolds number is the attachment-line flow ($\beta_h = 1.0$). For all other values of β_h, R at this flow angle must be either zero ($\beta_h > 0$) or infinite ($\beta_h < 0$). With $\beta_h = 1.0$ and $R = 1000$ ($R = 404.2$, where R_θ is the momentum-thickness Reynolds number), $\sigma_{max}/(\sigma_b)_{max} = 0.766$. The minimum critical Reynolds number of this profile is $(R_\theta)_{cr} = 268$ (the parallel-flow Blasius value is 201), yet turbulent bursts have been observed as low as $R_\theta = 250$ for small disturbances by Poll (1977).

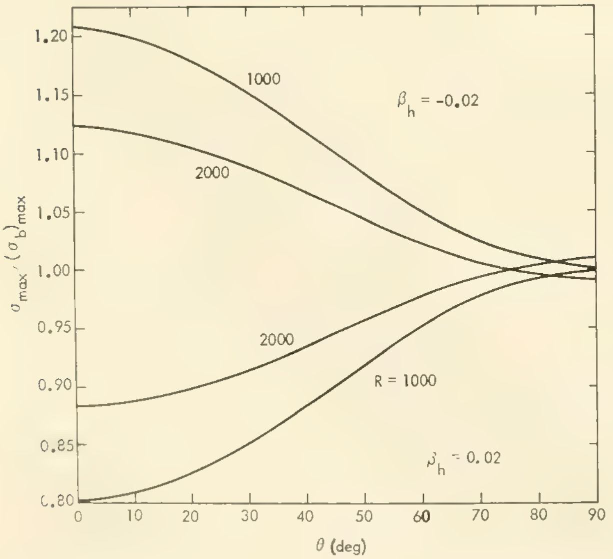

FIGURE 7. Effect of flow angle on the maximum amplification rate with respect to frequency of $\psi = 0°$ waves for two boundary layers with small crossflow at two Reynolds numbers.

We must still show that the waves with $\psi = 0°$ properly represent the maximum instability of three-dimensional profiles with small crossflow. For this purpose a calculation was made of σ as a function of ψ for $\beta_h = -0.02$, $\theta = 45°$, $R = 1000$ and $F = 0.4256 \times 10^{-4}$, the most unstable frequency for $\psi = 0°$ at this Reynolds number. It was found that the crossflow indeed introduces an asymmetry into the distribution of σ with ψ, and the maximum of σ is located at $\psi = -6.2°$ rather than at 0°. However, this maximum value differs from the σ_{max} of Figure 7 by only 0.7%. It was also determined that $\bar{\psi}_{gr} = -0.04°$ and $\bar{\psi}_{gi} = -0.3°$ (approximately) for $\psi = 0°$, which justifies taking both of these quantities zero in all of the $\psi = 0°$ calculations.

Crossflow Instability

Minimum Critical Reynolds Number of Steady Disturbances

The instability that is unique to three-dimensional boundary layers is called crossflow instability. It was discovered experimentally by Gray (1952) and later given a detailed theoretical explanation by Stuart in Gregory et al. (1955). This instability arises from the inflection point of the crossflow velocity profile. As explained by Stuart, there is a particular direction close to the crossflow direction for which the mean velocity at the inflection point of the resultant velocity profile is zero. Consequently, at sufficiently large Reynolds numbers unstable steady disturbances exist which have their constant phase lines nearly aligned with the potential flow.

Although crossflow instability is by no means restricted to steady disturbances, these disturbances do make a convenient starting point for our investigation. The reason is that a suitable initial guess for the angle ψ, which must be known rather accurately for the eigenvalue search procedure to converge, is given by

$$\psi = (\beta_h/|\beta_h|)\ (\pi/2 - |\varepsilon|_{inf}),$$

where ε_{inf} is the streamline deflection angle listed in Table 2. It turns out that this value is within a fraction of a degree of the angle of the most unstable wavenumber. There is no such convenient rule for the wavenumber itself, but the inverse of η_{inf}, the location of the inflection point in the similarity coordinate, or better still $0.9/\eta_{inf}$, is usually an adequate enough initial guess to ensure rapid convergence to an eigenvalue.

As the crossflow is a maximum at $\theta = 45°$ for a given β_h, we can expect the crossflow instability to also be a maximum near this angle. Figure 8 shows the minimum critical Reynolds number R_{cr} at $\theta = 45°$ for the zero-frequency disturbances as a function of β_h. For comparison, R_{cr} of the two-dimensional Falkner-Skan profiles, as computed by Wazzan et al. (1968), is also given. For adverse pressure gradients, the steady disturbances become unstable at Reynolds numbers well above the R_{cr} of the two-dimensional profiles. On the contrary, for $\beta_h > 0.07$ the reverse is true, and for most pressure gradients in this range the steady disturbances become unstable at much lower Reynolds numbers than the two-dimensional R_{cr} (for $\beta_h = 1.0$, the two-

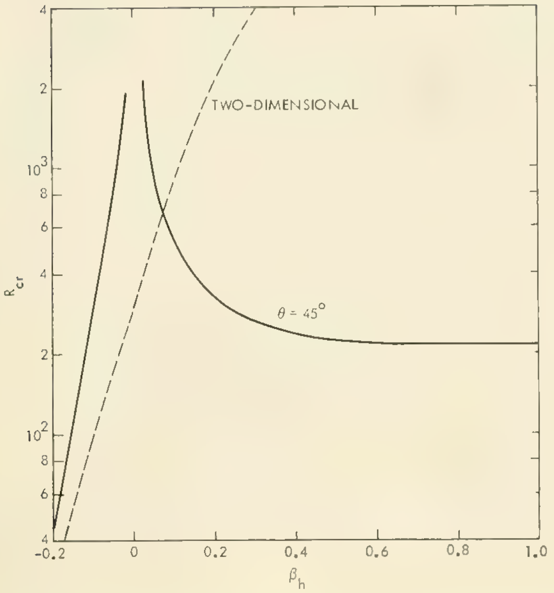

FIGURE 8. Minimum critical Reynolds number as function of pressure gradient: ——, steady disturbances, Falkner-Skan-Cooke boundary layers with $\theta = 45°$; ---, two-dimensional Falkner-Skan boundary layers [from Wazzan et al. (1968)].

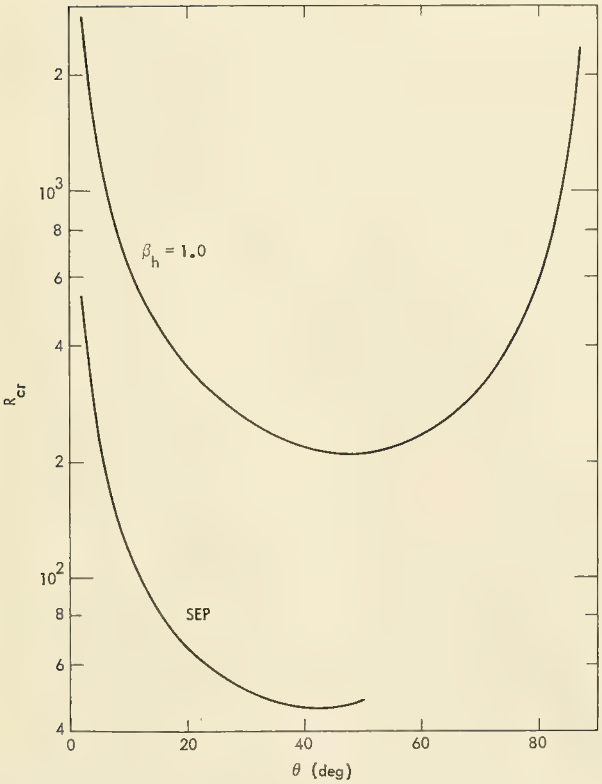

FIGURE 9. Effect of flow angle on minimum critical Reynolds number of steady disturbances for $\beta_h = 1.0$ and separation boundary layers.

TABLE 3. Wave parameters at minimum critical Reynolds number of steady disturbances.

β_h	θ	R_{cr}	k_{cr}	ψ_{cr}	$(\bar{\psi}_{gr})_{cr}$
SEP	2.2	535	0.213	-89.41	0.2
	5.0	237	0.213	-88.68	0.4
	10.0	121	0.215	-87.44	0.9
	40.0	46.5	0.230	-83.54	3.0
	45.0	46.7	0.230	-83.57	3.0
	50.0	48.4	0.231	-83.81	3.0
-0.10	45.0	276	0.295	-88.42	0.9
-0.02	45.0	1885	0.310	-89.74	0.2
0.02	45.0	2133	0.322	89.76	-0.1
0.04	45.0	1129	0.327	89.53	-0.2
0.10	45.0	527	0.339	88.93	-0.6
0.20	45.0	328	0.358	88.12	-1.1
1.00	2.4	2755	0.553	89.60	-0.3
	10.0	671	0.547	88.33	-1.1
	40.0	219	0.545	84.88	-3.4
	45.0	212	0.540	84.70	-3.5
	50.0	212	0.540	84.70	-3.5
	55.0	218	0.538	84.85	-3.3
	80.0	563	0.532	88.00	-1.5
	87.6	2325	0.532	89.51	-0.3

dimensional R_{cr} is 19,280 compared to $R_{cr} = 212$ for zero-frequency crossflow instability).

The distribution of R_{cr} with θ is shown in Figure 9 for $\beta_h = 1.0$ over the complete range of θ, and for the separation profiles ($\beta_h = -0.1988377$) over the range $0° < \theta < 50°$. Near $\theta = 0°$ and $90°$, R_{cr} is very sensitive to θ; near, but not precisely at, $\theta = 45°$ R_{cr} has a minimum. This minimum occurs close to the maximum of $|\varepsilon|_{inf}$ (cf. Table 2), which, unlike W_{max}, is not symmetrical about $\theta = 45°$. Table 3 lists the critical wave parameters for a few combinations of β_h and θ. The extensive computations needed to fix these parameters precisely were not carried out in most cases, and so the values in the Table are not exact. The listed $\bar{\psi}_{gr}$ was obtained from (13); $\bar{\psi}_{gi}$ was not calculated.

Boundary Layer with Crossflow Instability Only

As an example of a boundary layer which is unstable at low Reynolds number only as a result of crossflow instability, we select $\beta_h = 1.0$ and $\theta = 45°$, and present results for the complete range of unstable frequencies. Although this pressure gradient can only occur at an attachment line, Figure 8 leads us to expect that all profiles with a strong favorable pressure gradient will have similar results. For this type of profile, the minimum critical Reynolds number of the least stable frequency is very close to the R_{cr} of Figure 7. We therefore choose a Reynolds number well above R_{cr} where the instability is fully developed.

Figure 10 provides a summary of the stability characteristics at $R = 400$. For a given frequency, the eignevalue $\sigma(\psi)$ can be computed as a function of either k or ψ, with the other parameter given as the second eigenvalue. For strictly crossflow instability, k is the more suitable independent variable as ψ can have an extremum in the unstable region. All unstable eigenvalues of a given frequency with a specified increment in k were calculated in a single computer run with $\bar{\psi}_{gr} = 0°$, and then corrected to an approximate $\bar{\psi}_{gr}(k)$ obtained from (13) with constant wavenumber. A least-squares curve fit to $\sigma(k)$ provided σ_{max}, to maximum spatial amplification rate with respect to the vector wavenumber, and k_{max} and ψ_{max}, the magnitude and direction of the wavenumber of σ_{max}.

Figure 10a gives σ_{max} as a function of the dimensionless frequency F, and also shows the portion of the ψ-F plane for which there is instability. The unstable region is enclosed between the curves marked ψ_U and ψ_L. These curves represent either neutral stability points or extrema of ψ.

The corresponding wavenumber magnitudes are shown in Figure 10b. The negative frequencies signify that with ψ taken to be continuous through F = 0, the phase velocity changes sign. If we choose ψ so that the wavenumber and phase velocity are both positive, then it is ψ that changes sign at F = 0. Consequently, there are two groups of positive unstable frequencies with quite different phase orientations. The first group, which includes the peak amplification rate, is oriented anywhere from 5° to 31° (clockwise) from the direction opposite to the crossflow direction. The second group is oriented close to the crossflow direction itself.

All of the unstable frequencies have in common that the direction of growth is within a few degrees of the potential-flow direction. The angle $\bar{\psi}_{gr}$ of ψ_{max}, as computed from (13), is negative and has its largest magnitude of just under 6° near $F = -0.60 \times 10^{-4}$. Orientations other than ψ_{max} can have growth directions further removed from the flow direction.

Boundary Layers with both Crossflow and Mainflow Instability

As an example of a boundary layer which has both crossflow and mainflow instability at low Reynolds numbers, we select $\beta_h = -0.10$ and $\theta = 45°$. In contrast to the previous case, the steady disturbances do not become unstable until a Reynolds number, R = 276, where the peak amplification rate is already 7.35×10^{-3}. [For $\beta_h = -0.10$ and $\theta = 0°$ $\sigma_{max} = 11.0 \times 10^{-3}$ at $F = 2.2 \times 10^{-4}$ according to Wazzan et al. (1968)]. The distribution of σ with ψ is shown in Figure 11 for $F = 2.2 \times 10^{-4}$, a frequency close to the most unstable frequency of $F = 2.1 \times 10^{-4}$. We see that with a maximum crossflow velocity of 0.0349 (cf. Table 2), the distribution of σ about $\psi = 0°$ is markedly asymmetric, and the maximum amplification rate of 7.31×10^{-3} is located at $\psi = -29.4°$ rather than near zero. This asymmetry was barely perceptible for the small crossflow boundary layers of Figure 7 where the crossflow is only one-sixth as large. The σ at $\psi = 0°$ of Figure 11 (5.82×10^{-3}) is close to σ_{max} with respect to frequency of the $\psi = 0°$ waves (5.91×10^{-3}). Since this value is 20% below the peak amplification rate, the $\psi = 0°$ waves are no longer adequate to represent the maximum instability as with small crossflow boundary layers. Figure 11 also gives the distribution with ψ of k and $\bar{\psi}_{gr}$. The latter quantitiy was obtained from (13) with constant wavenumber, and we see that it remains within ± 7.5° of the potential-flow direction throughout the unstable region.

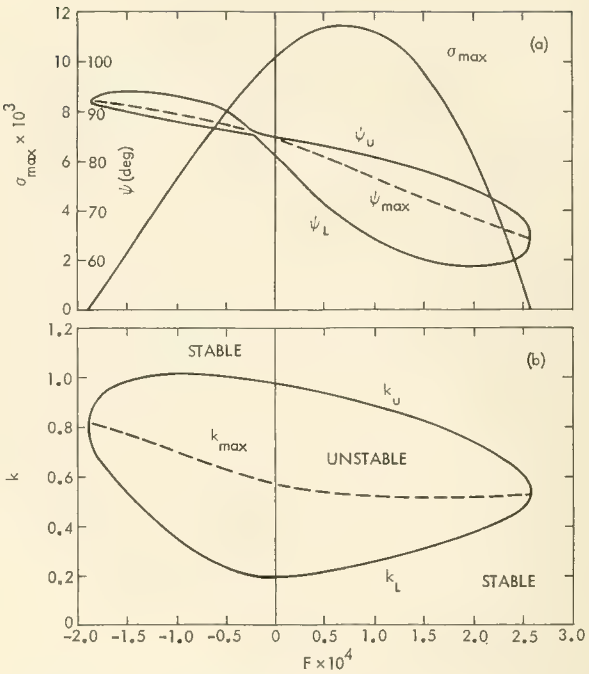

FIGURE 10. Instability properties of $\beta_h = 1.0$, $\theta = 45°$ Falkner-Skan-Cooke boundary layer at R = 400. (a) maximum amplification rate with respect to wavenumber and unstable ψ - F region; (b) unstable k-F region.

Because R = 276 is the minimum critical Reynolds number of the steady disturbances, the unstable region terminates in a neutral stability point at F = 0. We are particularly interested here in Reynolds numbers where F = 0 is also unstable, and as an example, Figure 12 gives results for all unstable frequencies at R = 555. Figure 12a shows σ_{max} as a function of F (here, as in Figure 10, σ_{max} is the maximum with respect to k), as well as the unstable region of the k-F plane; the unstable region of the ψ-F plane appears in Figure 12b. These two unstable regions are quite different from those of Figure 10 where there is only crossflow instability. The negative frequencies do resemble those of Figure 10 in that the unstable range of ψ is small, of k is large, and with ψ defined so that F > 0, the orientations are close to the crossflow direction. However, for the higher frequencies, which are by far

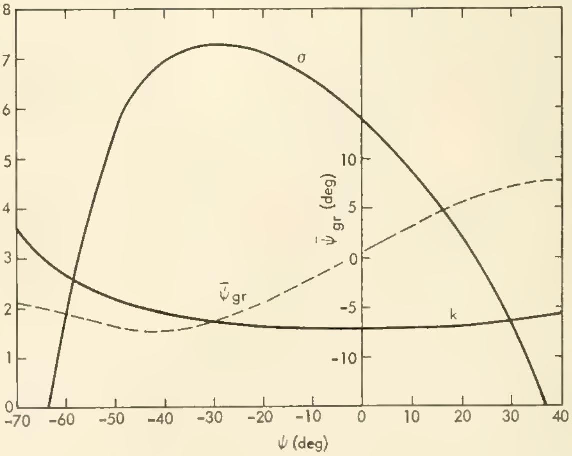

FIGURE 11. Effect of wavenumber angle on σ, k and $\bar{\psi}_{gr}$ for $\beta_h = -0.10$, $\theta = 45°$ Falkner-Skan-Cooke boundary layer at R = 276. $F = 2.2 \times 10^{-4}$.

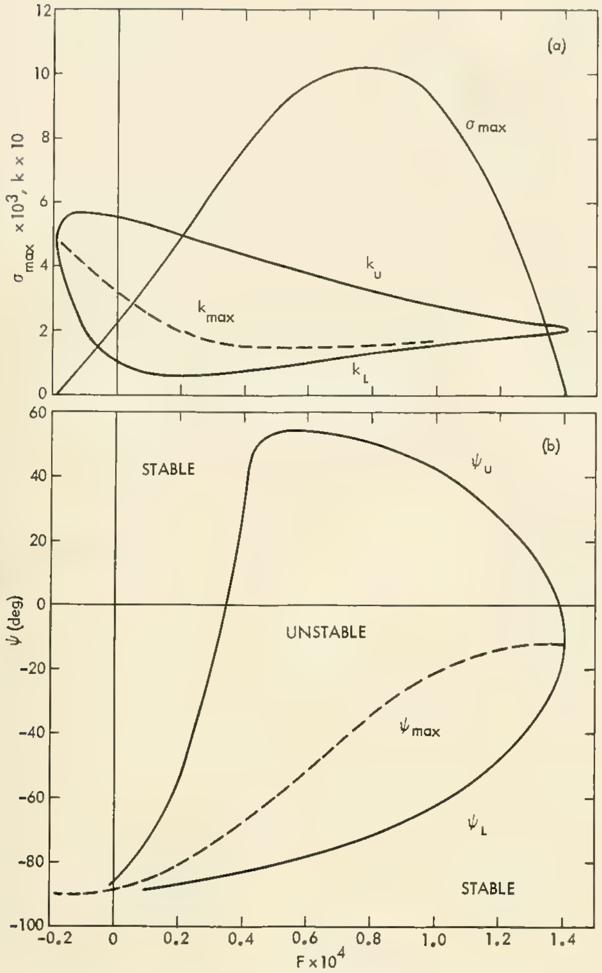

FIGURE 12. Instability properties of $\beta_h = -0.10$, $\theta = 45°$ Falkner-Skan-Cooke boundary layer at $R = 555$. (a) maximum amplification rate with respect to wavenumber and unstable k-F region; (b) unstable ψ-F region.

the most unstable, the unstable regions of Figure 12 bear more of a resemblance to those of a two-dimensional boundary layer than to Figure 10. The main differences from the two-dimensional case are the asymmetry about $\psi = 0°$ already noted in Figure 11, the one-sidedness of ψ_{max}, and, for $F < 0.4 \times 10^{-4}$, the replacement of a lower cutoff frequency for instability by a rapid shift with decreasing frequency to waves oriented opposite to the crossflow direction and which are unstable down to zero frequency. The instability shown in Figure 12 represents primarily an evolution of the small crossflow boundary layers of Figure 7 to larger crossflow. Only the frequencies, say $|F| < 0.2 \times 10^{-4}$, have to do with the pure crossflow instability of Figure 10. For frequencies near 0.4×10^{-4}, ψ varies little with k in one part of the unstable region, as with crossflow instability; in the other part, as with mainflow instability, the opposite is true. This behavior becomes more pronounced at high Reynolds numbers.

CONCLUDING REMARKS

All of the numerical results that have been presented stem from the viewpoint adopted in Section 2 that useful information concerning three-dimensional boundary-layer stability can be obtained from particular pure spatial modes just as with two-dimensional boundary layers. Arguments were given to support using the modes whose growth direction is determined from (17) or, more exactly, from (19b). A transformation (21a), was derived to enable the use of waves with an arbitrary growth direction in calculating eigenvalues. The transformation used in the temporal theory to reduce the three-dimensional problem to a two-dimensional probelm in the direction of the wavenumber vector was shown to apply to spatial modes only when this direction is close to the correct growth direction, or the latter is the same as the potential-flow direction ($\bar{\psi}_{gr} = 0°$).

The waves which have their wavenumber vector aligned with the local potential flow ($\psi = 0°$ when the x axis of the mean-flow coordinate sytem is also in the flow direction) always have their growth direction very close to the potential-flow direction. If the crossflow is small, the maximum amplification rate of the $\psi = 0°$ waves is almost identical to the maximum amplification rate of the three-dimensional boundary layer. Consequently, if we are only interested in establishing the maximum amplification rate of a small crossflow boundary layer, it can be obtained from the mainflow profile alone. We used this approach to obtain the effect of the flow (yaw) angle on the instability of the Falkner-Skan-Cooke yawed-wedge boundary layers for small pressure gradients, and found that yaw reduces both the stabilizing effect of a favorable pressure gradient and the destabilizing effect of an adverse pressure gradient.

With moderate or large crossflow, crossflow instability, which arises from the inflection point of the crossflow velocity profile, is present and can destabilize a boundary layer at low Reynolds numbers which would otherwise be stable. As befits the name, the unstable waves have their wavenumber vectors oriented near the crossflow (or opposite) direction. Also the instability covers a wide band of unstable frequencies (including zero) and wavenumbers. The growth direction of all unstable waves is still near the potential-flow direction. If the mainflow profile is also unstable, then the unstable frequencies near zero act as with pure crossflow instability and the higher frequencies as with pure mainflow instability. Intermediate frequencies have the latter behavior for small wavenumbers, and the former for large wavenumbers.

The results demonstrate why crossflow is more of a problem for the maintenance of laminar flow with strong favorable pressure gradients than with adverse pressure gradients. In the former case, crossflow provides a powerful instability mechanism even when the mainflow profile is stable; in the latter, the crossflow only increases the amplification rate over that of an already unstable mainflow profile. This increase is about 50% for the $\theta = 45°$ separation boundary layer.

ACKNOWLEDGMENT

This paper represents the results of one phase of research carried out at the Jet Propulsion Laboratory, California Institute of Technology under Contract No. NAS7-100 sponsored by the National Aeronautics and Space Administration. Financial support is gratefully acknowledged from the Tactical Technology Office, Defense Advanced Research Projects Agency, and from Langley Research Center.

REFERENCES

Brown, W. B. (1961). A stability criterion for three-dimensional laminar boundary layers. *Boundary Layer and Flow Control, Vol. 2,* G. V. Lachmann, ed., Pergamon Press, New York, pp. 913-923.

Cooke, J. C. (1950). The boundary layer of a class of infinite yawed cylinders. *Proc. Camb. Phil. Soc. 46,* 645.

Davey, A. (1972). The propagation of a weak nonlinear wave. *J. Fluid Mech. 53,* 769.

Grabedian, P. R., and H. M. Lieberstein (1958). On the numerical calculation of detached bow shock waves in hypersonic flow. *J. Aero. Sci. 25,* 109.

Gray, W. E. (1952). The nature of the boundary layer at the nose of a swept back wing, Unpublished work Min. Aviation, London.

Gregory, N., J. T. Stuart, and W. S. Walker (1955). On the stability of three-dimensional boundary layers with application to the flow due to a rotating disk. *Phil. Trans. Roy. Soc. London A248,* 155.

Landau, L. D., and E. M. Lifshitz (1960). *Electrodynamics of Continuous Media,* Pergamon Press, New York, p. 263.

Mack, L. M. (1977). Transition prediction and linear stability theory. *Laminar-Turbulent Transition, AGARD Conference Proceedings No. 224,* pp. 1-1 to 1-22.

Nayfeh, A. H., A Padhye, and W. S. Saric (1978). The relation between temporal and spatial stability in three-dimensional flows, AIAA Paper, to be presented.

Poll, D. I. A. (1977). Leading edge transition on swept wings. *Laminar-Turbulent Transition, AGARD Conference Proceedings No. 224,* 21-1 to 21-11.

Rosenhead, L. (1963). *Laminar Boundary Layers,* Oxford Univ. Press.

Rott, N., and L. F. Crabtree (1952. Simplified laminar boundary layer calculations for bodies of revolution and for yawed wings. *J. Aero. Sci. 19,* 553.

Squire, H. B. (1933). On the stability for three-dimensional disturbances of viscous fluid flow between parallel walls. *Proc. Roy. Soc. London A142,* 621.

Wazzan, A. R., T. T. Okamura, and A. M. O. Smith (1968). Spatial and temporal stability charts for the Falkner-Skan boundary-layer profiles. *McDonnell Douglas Report No. DAC-67086,* Long Beach, Calif.

Whitham, G. B. (1974). *Linear and Nonlinear Waves,* Wiley-Interscience, New York.

Experiments on Heat-Stabilized Laminar Boundary Layers in a Tube

Steven J. Barker
Poseidon Research and University*
of California at Los Angeles

ABSTRACT

There has been considerable recent interest in the stabilization of water boundary layers by wall heating. Calculations based upon linear stability theory have predicted transition Reynolds numbers as high as 2×10^8 for a zero pressure gradient boundary layer over a heated wall. The flow tube experiment described in this paper was intended to investigate these predictions. The test boundary layer develops on the inside of a cylindrical tube, 0.1 m in diameter and 6.1 m in length. The displacement thickness is small relative to the tube radius under nearly all operating conditions. The tube is heated by electrical heaters on the outside wall. The location of transition can be determined by a heat flux measurement, by flush-mounted hot film probes, or by flow visualization at the tube exit.

A transition Reynolds number of 10^7 can be obtained without heat, which shows that free stream turbulence and other perturbations are well controlled. At 7°C wall overheat, a transition Reynolds number of 42×10^6 has been obtained, which is at least as high as the prediction for that overheat. However, as temperature is further increased there have been no additional increases in transition Reynolds number, which is in contradiction to the theory.

Possible reasons for the differences between theory and experiment have also been investigated. New test section exits have been developed to determine the effects of downstream boundary conditions upon the flow. An instrumented section has been used to measure detailed velocity profiles in the boundary layer, and determine intermittency as a function of azimuthal angle. From these measurements we can evaluate the possibility of buoyancy-generated instabilities in the tube. Future tests will also investigate the influence of free stream turbulence, streamwise vorticity in the boundary layer, and wall temperature variations.

1. INTRODUCTION

Numerical calculations such as those of Wazzan, Okamura, and Smith (1968, 1970) have predicted large increases in the transition Reynolds numbers of water boundary layers with the addition of wall heating. The stabilizing mechanism is the decrease in fluid viscosity near the wall resulting from the heating. This increases the negative curvature of the velocity profile, making the flow more stable to small disturbances. The present study is an experimental investigation of these predictions, using the boundary layer developing on the inside wall of a cylindrical tube. This boundary layer is thin relative to the tube diameter, so that it approximates a boundary layer over a flat plate.

The numerical predictions of Wazzan et al. are based on two-dimensional, linear stability theory. The mean flow is assumed plane and parallel, and the superimposed small disturbance is described by a stream function,

$$\psi(x,y,t) = \phi(y) \exp i\alpha(x-ct) \qquad (1)$$

Here $\phi(y)$ is the disturbance amplitude, α is the wavenumber and is assumed real, and c is the wave velocity which may be complex. The imaginary part of c determines whether the disturbance is temporally amplified or damped. If we substitute this stream function into the Navier-Stokes equations and linearize, taking account of the variation of viscosity μ with distance from the wall y, we find

$$(U - c)(\phi'' - \alpha^2\phi) - U''\phi = \frac{-i}{\alpha Re}[\mu(\phi'''' - 2\alpha^2\phi'' + \alpha^4\phi) + 2\mu'(\phi''' - \alpha^2\phi') + \mu''(\phi'' + \alpha^2\phi)] \qquad (2)$$

---

*This work was performed by the Marine Systems Division of Rockwell International, and Poseidon Research. It was sponsored by the Defense Advanced Research Projects Agency.

In this equation, $U(x)$ is the external flow velocity and Re is the Reynolds number based upon free stream velocity U_∞ and boundary layer thickness δ. This is known as the "modified Orr-Sommerfeld equation," the variable viscosity terms.

Wazzan et al. have solved Eq. (2) numerically for the boundary layer over a heated flat plate, using velocity profiles generated by the method of Kaups and Smith (1967). The solutions determine the critical Reynolds number, which is the lowest Reynolds number at which any disturbance has a positive amplification rate. The last step of the calculation is to relate the critical Reynolds number to the transition Reynolds number, using the "e to the ninth" criterion of A. M. O. Smith (1957). According to this empirical criterion, transition occurs when the most unstable disturbance has grown to e^9 (which is 8,103) times its original amplitude. The linear theory is used in calculating the growth of the disturbance to this amplitude.

Strasizar, Prahl, and Reshotko (1975) have measured growth rates of disturbances generated by a vibrating ribbon in a heated boundary layer. They found neutral stability curves and were able to determine critical Reynolds numbers for wall overheats of up to 5°F (2.8°C). They found that in this range of overheats the critical Reynolds numbers are in reasonable agreement with the theoretical predictions. These experiments were performed at moderate Reynolds numbers and did not yield data on transition or on stability at higher overheats.

The results of the Wazzan et al. calculations predict that the transition Reynolds number of a zero pressure gradient boundary layer should increase with wall temperature up to about 70°F (39°C) of overheat if the free stream temperature is 60°F (16°C). At that overheat, the transition Reynolds number should be in excess of 2×10^8 (based upon distance from the leading edge). Thus the experiment designed to investigate these predictions must be able to generate a very high Reynolds number boundary layer while maintaining low free stream disturbance levels. The wall should be very smooth and its temperature must be precisely controlled. These are the chief considerations that led to the experimental geometry described below.

2. EXPERIMENTAL APPARATUS

Configuration

A facility in which water is recirculated through the test section was not used for two reasons. (1) Heat is continuously added to the test section so that a recirculating experiment would require some sort of heat exchanger. (2) The free stream turbulence level in the test section must be less than 0.05 percent, which has previously been difficult to achieve in a recirculating water facility. The experiment must then be of the "blow-down" type, in which water is removed from one reservoir and discharged into another. Run times of more than twenty minutes are desired, which requires large reservoirs. This led to the selection of the Colorado State University Engineering Research Center as the site of the experiment. Here the water supply is Horsetooth Reservoir, which provides water to the laboratory through a 0.6 m diameter pipe at a total pressure of 6.8×10^5 N/m^2 (100 lb/in.^{2}). The discharge runs into a smaller lake below the laboratory. At the maximum flow rate of this experiment (200 liters/sec), the run time is effectively unlimited.

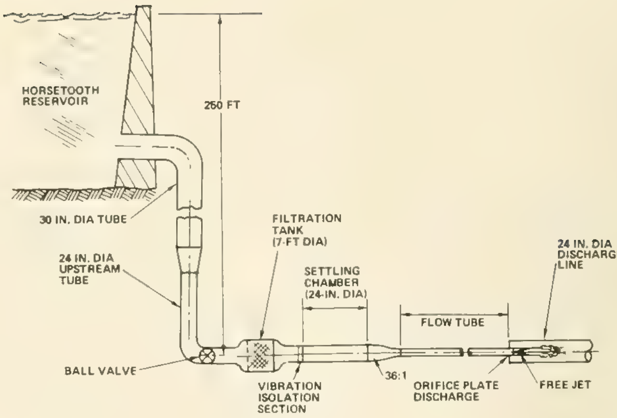

FIGURE 1. Experimental geometry.

The flow tube apparatus consits of a settling chamber for turbulence management, a contraction section, a test section and various types of instrumentation described below. A diagram of the experimental geometry is shown in Figure 1.

Settling Chamber

The inside diameter of the settling chamber is 0.6 m, the same as that of the supply line from the reservoir. The test section is 0.102 m in diameter, so that the contraction ratio is 35:1. The settling chamber is made up of four separable sections, as shown in Figure 2. The sections are made of fiberglass to avoid heat transfer through the walls, and their total length is 3.35 m. Each end of each section is counter-bored to hold a 0.15 m long aluminum cylinder with a 1.3 cm wall thickness. Each cylinder will hold one or more turbulence manipulators, including screens, porous foam, or honeycomb material. This design allows the settling chamber to be assembled in different configurations, so that it can be optimized experimentally.

The details of the design and optimization of the turbulence management system have been reported separately [Barker (1978)]. The configuration shown in Fibure 2 was arrived at after a great deal of testing. There is a considerable body of literature on the subject of turbulence management, and this provided some guidelines for the optimization of the present system. The most detailed recent study is that of Loehrke and Nagib (1972), who measured mean velocity and turbulence level downstream of various turbulence manipulators. Further recommendations for the construction of a turbulence management system have been given by Corrsin (1963), Bradshaw (1965), and Lumley and McMahon (1967).

At the downstream end of the settling chamber is an additional 0.30 m long section containing porous wall boundary layer suction. Hot film anemometer surveys in the settling chamber have shown that at test section velocities above 9 m/sec (0.26 m/sec in the settling chamber) the boundary layer becomes turbulent before the flow enters the contraction. A thin turbulent boundary layer entering the strong favorable pressure gradient of the contraction

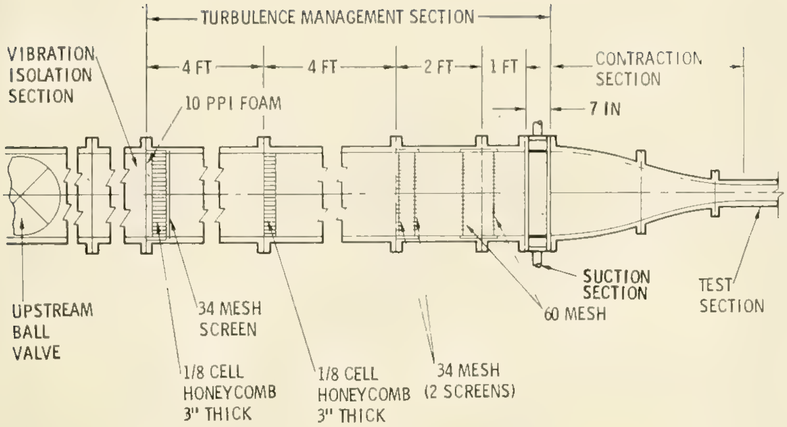

FIGURE 2. Schematic of turbulence management system.

section will tend to "relaminarize," as described by Launder (1964) and Back et al. (1969). However, this would leave us with unknown initial conditons at the entrance to the test section. Therefore we have added the suction section to completely remove the turbulent boundary layer. This section has a 0.1 m length of porous wall surrounded by an annular plenum chamber. The suction flow from the plenum is controlled by a valve and a Venturi meter. At each test section velocity above 9 m/sec, the suction flow is adjusted to the minimum value necessary to remove the turbulent boundary layer at the contraction entrance.

Contraction and Test Section

The 35:1 contraction was designed by a potential flow calculation using the method of Chmielewski (1974). The length to diameter ratio of the contraction was chosen by balancing the effect of relaminarization with that of the Goertler instability in the concave-curved portion. A careful study of these two effects led to a length to diameter ratio of 2.25, which made the contraction 1.37 m long. The contraction was constructed in two sections: a fiberglass upstream half and an aluminum downstream half. The joint between the two sections is in the region of greatest favorable pressure gradient, and has no measurable step across it.

Recent velocity measurements in the test section (discussed below) have led to the design and construction of a new contraction section to replace the original one. The new contraction will have an annular bleed flow surrounding an entrance section which is all convex. In this way the concave-curved wall, which can produce Goertler vortices, will be avoided entirely. Results using this new contraction will soon be available.

The flow tube test section is 6.4 m in length and 0.102 m in diameter, with a 2.5 cm wall thickness. It is made of aluminum, and the inside wall has been polished to a surface roughness of less than 10^{-7} m RMS (4 micro-inches). Surface waviness has been measured as less than one part per thousand for wavelengths less than 2 cm. The tube has been optically aligned on site so that it is straight to within less than 0.018 cm over its entire length. The outside wall is covered with electrical band heaters, which are connected together in groups covering about 0.30 m of length. Each heater group is servocontrolled by a system which maintains a preset temperature on a thermocouple located near the inside tube wall. In this way the inside wall temperature can be controlled independently of flow velocity, and different variations of temperature along the tube length can be studied.

To avoid tripping the boundary layer, no penetrations of the inside wall are allowed except at the downstream end. The only instrumentation in the test section is an array of thermocouples within the wall, spaced along the tube length. At each location, there is one thermocouple on the outside surface and one in a small hole drilled to within 0.15 cm of the inside surface. The temperature difference between the two thermocouples determines the heat flux through the wall at a particular location. Since heat flux increases by a factor of about ten at the transition point, these temperature measurements should provide a good transition indicator. A total of 53 thermocouple voltages are digitized and recorded.

During the earlier experiments, there was a single hot film anemometer probe at the downstream end of the test section. This probe was located within the boundary layer and was used to indicate intermittency only. In the more recent measurements, a new instrumented section has been developed and installed on the downstream end of the test section. This section is 0.61 m long and its inside diameter matches that of the test section to within 2×10^{-5} m. Two types of measurement can be made in the instrumented section. Very small Pitot tubes can be used to traverse the boundary layer and measure mean velocity profiles, and flush mounted hot films can determine intermittency at various locations.

Since the boundary layer is typically less than 0.5 cm thick, the Pitot tubes must be very small. The one being used at present has a cross-section of 0.013×0.076 cm. The smaller dimension is oriented in the direction perpendicular to the wall. The tube is traversed from the wall to the free stream by a micrometer, which can position it with an uncertainty of ±0.002 cm. In addition, the entire central portion of the tube can be rotated in the azimuthal direction so that the Pitot tube can be traversed about the circumference of the test section. The azimuthal rotation can be performed while the experiment is running.

The hot film anemometers in the instrumented section are all mounted flush with the wall to avoid tripping the boundary layer. The Pitot tubes are removed from the section while hot film measurements are being made. The films are used only to determine intermittency, hence they are not calibrated. There are eight hot film locations--two streamwise separated stations each having four probes at different azimuthal angles. All eight outputs can be displayed simultaneously on oscilloscope traces or recorded on a photographic strip-chart recorder.

A high static pressure must be maintained in the test section to avoid possible cavitation or outgassing from heated walls. Therefore the pressure loss for controlling the flow velocity is located at the downstream end of the experiment. Originally, a set of sharp-edged orifice plates was used on the end of a 1 m long extension tube added to the test section. Concern over possible upstream influence of the disturbances generated at the orifice plate led to the development of a smooth contraction section for the downstream end. With the smooth contraction, it is possible to maintain laminar flow all the way to the exit of the experiment, and thus determine transition by flow visualization in the exit jet. In addition, a "plug nozzle" has been developed, which consists of a strut-supported central cone which can be moved in and out of the end of the test section. This adjustable exit valve permits us to vary the test section static pressure independently of flow velocity while maintaining laminar flow all the way to the exit. With any of these possible exit conditions, the test section velocity can be determined from the test section static pressure and the known discharge coefficient of the nozzle.

3. RESULTS

Free Stream Turbulence

Mean and fluctuating velocities were measured in the settling chamber by a cylindrical hot film anemometer. The probe penetrated the settling chamber wall 0.1 m downstream of the boundary layer suction section, and could be traversed from the wall to the centerline. Mean velocities and turbulence levels were measured at many points, and turbulence spectra were measured at two or three points for each flow condition. In addition, a 1.2 m long instrumented straight tube could be substituted for the 6.4 m test section. This short tube contained a Pitot tube, accelerometers, and hot film probes. The unheated transition Reynolds number was measured in the 1.2 m tube for each settling chamber configuration. This Reynolds number varied from 800,000 for the empty settling chamber with no turbulence manipulators to 5.0 × 10^6 for the "best" configuration. This configuration (shown in Figure 2) includes one piece of porous foam, two sections of honeycomb, and four screens. The last screen is located 0.3 m upstream of the beginning of the contraction, and has a mesh of 24 per cm. All screens in the settling chamber have more than 55 percent open area, in accordance with the findings of Bradshaw (1965).

Detailed results of the velocity measurements in the settling chamber have been reported separately [Barker (1978)], and are only summarized here. At test section velocities less than 9 m/sec, the settling chamber boundary layer remains laminar and the only effect of the suction is to make it thinner. The turbulence level is about 0.07 percent at all distances from the wall for the configuration of Figure 2. At higher velocities the turbulence level near the wall reaches 3 or 4 percent with no suction, but remains 0.07 percent at distances from the wall greater than 2 cm. As the suction flow rate is increased, the mean velocity profile shows thinning of the boundary layer and the turbulence level near the wall drops rapidly. At the optimum suction rate, the highest turbulence level near the wall in the settling chamber is about 0.4 percent. The suction has no measurable effect upon the mean velocity profile or turbulence level more than 2 cm from the wall.

The settling chamber velocity measurements and the unheated transition Reynolds numbers indicate that the turbulence management system is performing well. If the turbulence level reduction through the contraction is proportional to the square root of the contraction ratio [Pankhurst and Holder (1952)], then the turbulence level in the test section should be about 0.01 percent. This is lower than the turbulence level recorded in most wind tunnels, and certainly lower than any previously reported water tunnel.

Transition Reynolds Numbers

Figure 3 shows measured transition Reynolds numbers as a function of wall overheat for the uniform wall temperature case. The results on the upper curve were obtained with the smooth, laminar flow nozzle at the downstream end of the test section, using flow visualization at the exit to determine transition. The water temperature was approximately 50°F (10°C) during these tests. Note that the transition Reynolds number rapidly increases with wall temperature up to 10°F (6°C) wall overheat, at which it has reached a value of 42 × 10^6. This represents a factor of four increase in transition Reynolds number for a relatively small heat input. However, above 10°F there are no further increases in transition Reynolds number, while the theory predicts that it should increase up to about 60°F (33°C) overheat. Previously published results [Barker and Jennings (1977)] have shown that varying the wall temperature distribution does not change

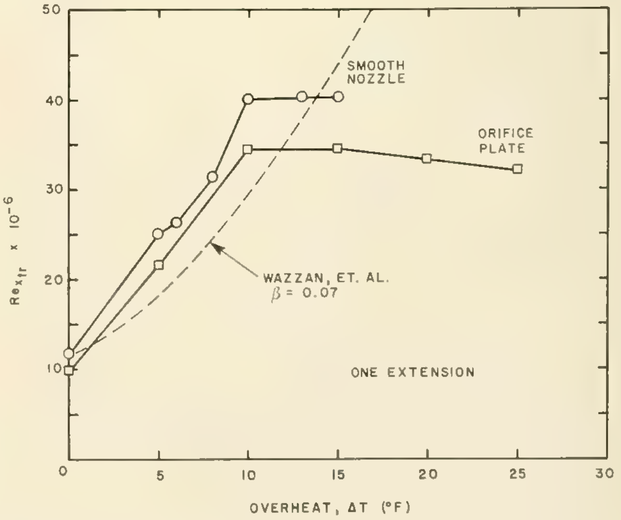

FIGURE 3. Transition Reynolds numbers measured at exit: one extension tube.

this result. In fact, uniform wall temperature has produced the largest transition Reynolds numbers to date. The primary difference between the results shown here and those published previously is that the present experimental curve reaches the limit Reynolds number of 42×10^6 at a lower overheat than before. This change is attributed to the improvement of the exit conditons with the development of the laminar flow nozzle.

All of the data of Figure 3 were taken by maintaining laminar flow over the full length of the tube and observing transition at the exit. If the flow velocity is increased further, so that the transition region moves upstream in the test section, the measured transition Reynolds numbers are much lower. In addition, there is a hysteresis effect when transition is allowed to move more than about 1 m upstream from the exit. That is, to restore fully laminar flow over the full tube length the velocity must be reduced to a value lower than that which previously yielded fully laminar flow. This hysteresis may be a phenomenon which is accentuated by the flow tube geometry. The free stream in the flow tube is confined by the boundary layer, so that the boundary layer can influence the free stream once it becomes turbulent. This free stream influence could propagate upstream, which has led to conjecture about disturbances from the test section exit affecting the transition Reynolds number.

To test this hypothesis of downstream disturbances affecting transition Reynolds number, a separate study has been conducted to determine the dependence of transition upon the tube exit geometry. As discussed above, there are three types of exit nozzle available: orifice plates, the smooth contraction, and the plug valve. In addition, the length of unheated tube between the heated test section and the exit can be varied from zero to 3.7 m in increments of 1.22 m. For each configuration, transition can be determined either at the exit itself or at the end of the heated section. Transition at the exit is easily determined by flow visualization, as shown in Figure 4. This photograph of the smooth exit contraction shows laminar flow (4a) and turbulent flow (4b), both at a length Reynolds number of approximately 40×10^6. In Figure 4a, note the glassy region very near the exit, which soon becomes milky in appearance as the air-water shear layer undergoes transition. The longitudinal streaks in Figure 4a are appraently due to Goertler vortices generated in the concave part of the smooth exit contraction. They are not seen with the plug valve exit, which has no concave region.

The data of Figure 3 are for one 1.22 m extension section on the end of the heated section, followed by either the smooth contraction or the orifice plate. Transition is measured at the exit in either case. Note that the transition Reynolds numbers with the orifice plate exit are about 20 percent lower than with the smooth contraction, showing a definite effect of the exit condition. Figure 5 shows the same comparison with 2.44 m of unheated extension tube between the test section and exit. Here we see a much larger difference between results with the orifice and with the smooth contraction. The smooth contraction transition Reynolds numbers are nearly the same as with 1.22 m of extension tube, while the orifice Reynolds numbers have dropped almost by a factor of two. Clearly the effect of the exit condition upon transition Reynolds

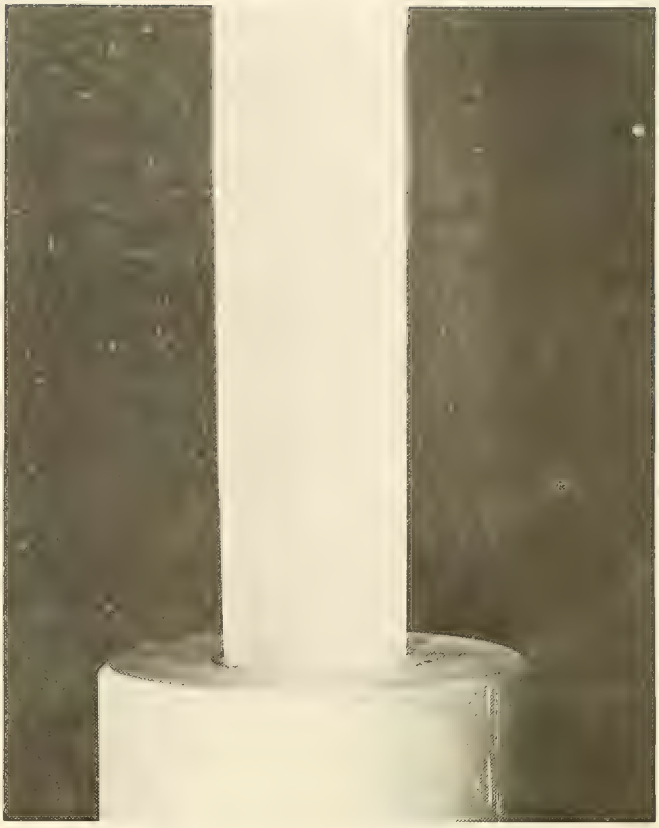
FIGURE 4a. Exit jet from smooth nozzle: laminar boundary layer.

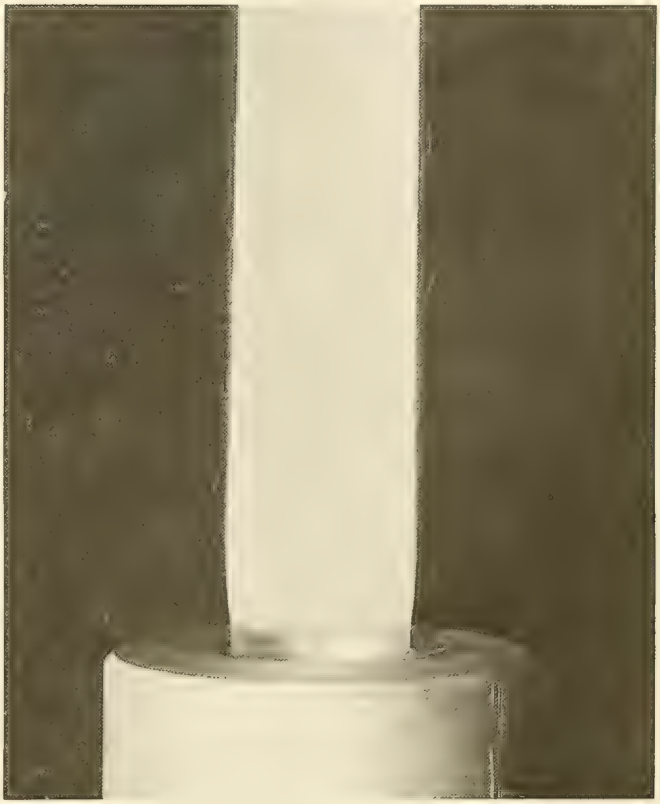
FIGURE 4b. Exit jet from smooth nozzle: turbulent boundary layer.

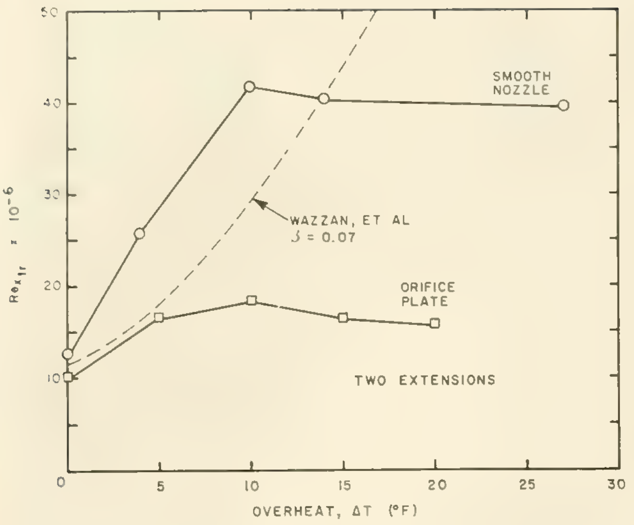

FIGURE 5. Transition Reynolds numbers measured at exit: two extension tubes.

number is far more pronounced here than for the shorter extension tube length. The most reasonable explanation of this lies in the fact that in the second case the boundary layer has passed over a much longer region of unheated wall, which should have a destabilizing effect. This less stable boundary layer is then more sensitive to external perturbations such as the disturbances created by the orifice plate exit.

As the extension tube length is increased still further, the transition Reynolds numbers obtained with the smooth contraction begin to decrease. Apparently the destabilizing effect of the long unheated wall is felt even with the low disturbance exit condition. These results indicate that, under some conditions, a moderate length of unheated wall can be used downstream with no measurable reduction of transition Reynolds number.

When transition is determined at a distance of 1.4 m upstream of the exit rather than at the exit nozzle itself, the influence of the exit condition is greatly diminished. Taking the case of the 2.44 m unheated extension as an example, there is a factor of 2.3 difference in the maximum transition Reynolds number obtained with the orifice and with the smooth contraction when transition is measured at the exit (Figure 5). However, when transition is measured 1.4 m upstream of the exit, the corresponding difference is only 15 percent in Reynolds number. Clearly the disturbances present at the exit nozzle can affect the transition process if it occurs near the nozzle, but this influence diminishes rapidly as transition moves upstream of the exit. Since the highest transition Reynolds numbers have consistently been obtained with laminar flow over the full length of the tube, most future measurements will be made using one of the two laminar flow exit conditions.

Although it is difficult to assess uncertainties in transition Reynolds number in this experiment, some effort should be made. Results for the highest transition Reynolds numbers exhibit a large amount of scatter, but most of this can now be attributed to variations in the free stream particulate content. The purity of the water supply varies considerably with weather conditions at the site, and these changes in purity have been directly correlated with changes in transition Reynolds number. Under the most adverse conditions, this effect has reduced the maximum transition Reynolds number to less than 15×10^6 (compared with 42×10^6 for "clean" water). If we compare results that were obtained during periods of relatively high water purity, the standard deviation in transition Reynolds number is about 10 percent of the mean.

This extreme sensitivity of the results to water purity was quite unexpected, and an effort has been made to improve the water quality by filtering upstream of the settling chamber. Measurements of the particle concentration spectrum have been made using a Coulter Counter, and some of the results are shown in Figure 6. The bands on this figure indicate the typical ranges of concentration that are obtained in the present experiments, as well as in the NSRDC towing basin and the ocean. Note that the flow tube particle spectrum has a steeper slope than either the ocean or the tow basin, which implies that for particle sizes greater than 10 μ, the flow tube water is much cleaner than the other two. The filtration system presently used in the flow tube effectively removes all particles larger than 100 μ.

The reason for the strong sensitivity of results to relatively minor contamination of the water supply is not understood at present. The most likely mechanism seems to be a slight increase in wall roughness due to the adhesion of particles to the wall. Whatever the mechanism, this effect will clearly be of importance in hydrodynamic applications.

Comparison with Theory

Wazzan et al. (1970) have presented numerically predicted transition Reynolds numbers for heated

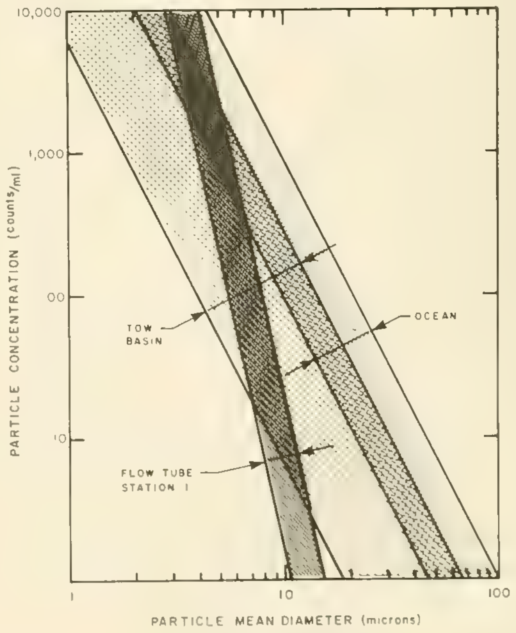

FIGURE 6. Particle concentration spectra: flow tube, NSRDC towing basin, and open ocean.

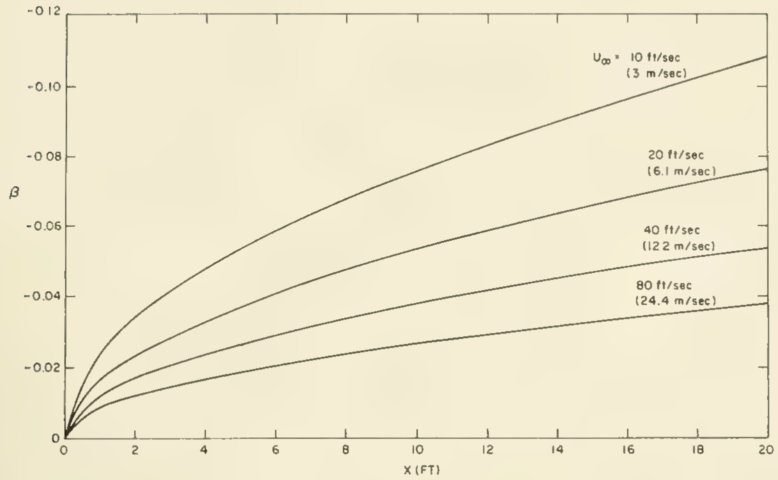

FIGURE 7. β versus x for several values of U_∞.

wall boundary layers with zero pressure gradient. More recently, similar calculations have been performed for boundary layers in favorable pressure gradient flows. Before comparing the flow tube results with such predictions we should estimate the favorable pressure gradient produced by the boundary layer displacement effect in the tube. The most common way to characterize streamwise pressure gradient in a boundary layer is by the similarity parameter β [Schlichting (1968)]. For the general class of wedge flows, the external velocity U is given by $U = Cx^m$, and the parameter β is then $2m/(m + 1)$. Both m and β are constants in any wedge flow, and are equal to zero for the zero pressure gradient boundary layer. We have calculated approximate local values of β in the flow tube, using the Blasius growth law for the boundary layer displacement thickness:

$$\delta^* = 1.72(\nu x/U_\infty)^{\frac{1}{2}} \qquad (3)$$

(The calculation can be iterated to include the effect of pressure gradient upon δ^*, but the difference is negligible.) The resulting values of β as a function of x at several values of U_∞ are shown in Figure 7. β is proportional to the square root of x, and thus has its largest value at the downstream end of the tube.

Figures 3 and 5, which show transition Reynolds numbers versus overheat for the flow tube, also include the theoretical predictions of Wazzan et al. (1970) for a β of 0.07. This represents an approximate average of β in the tube for the velocity range of interest. (Calculations using exact β values from the tube will be done in the near future.) Note that the experimental results lie near or even above the $\beta = 0.07$ prediction for overheats from zero to 13°F (7°C). At this point the experimental curve quite suddenly levels out, while the predicted curve continues to rise at an increasing slope. The predicted curve reaches its maximum at a Reynolds number of about 250×10^6 (near 45°C overheat), while the experiment has never yielded more than 42×10^6.

There are several possible reasons for the disagreement between theory and experiment at the higher overheats. (1) The theory does not account for the destabilizing effects of density stratification, which will become increasingly important as overheat is increased. Buoyancy effects may destabilize the flow in three distinct ways: (a) the bottom of the tube wall is subject to thermal convection rolls, similar in form to the Goertler instability; (b) the side wall boundary layer will experience a cross-flow due to the rising fluid near the wall; and (c) the top wall boundary layer will grow in thickness faster than normal because of the fluid rising up from the sides. (2) The theory neglects the effects of temperature and viscosity fluctuations upon the growth of the velocity fluctuations. There is evidence that this is a reasonable approximation. (3) The theory relies upon the e^9 transition criterion, which may become increasingly incorrect at higher overheats. This criterion has never before been applied to boundary layers with inhomogeneous physical properties. There is a large distance between the minimum critical point in the boundary layer and the predicted transition point using e^9. It is questionable whether the region of linear growth can extend over such a large range of Reynolds numbers. (4) Wall roughness is not accounted for in the theory, and the importance of roughness will increase with wall heating (and with increased velocity) due to the thinning of the boundary layer. Roughnesses that are insignificant at zero or low overheat may become important as overheat increases.

Velocity Profile Measurements

In view of the differences between experimental results and computed transition Reynolds numbers, measurements have been made of boundary layer velocity profiles in the flow tube to try to establish the mechanism of transition. If the buoyancy effects described above are in fact significant, they should produce measurable deviations from axisymmetry in the mean velocity profiles. In addition, they might cause transition to occur earlier on the top, side, or bottom wall, depending upon which mechanism is predominant. We therefore, designed the instrumented section (described above) to be installed on the downstream end of the 6.1 m test section. This contains Pitot tubes for mean velocity measurements and flush mounted hot film probes for intermittency measurements. The instrumented section has been very successful in measuring mean velocity profiles in the flow tube. Figure 8 shows a typical measured profile that has been

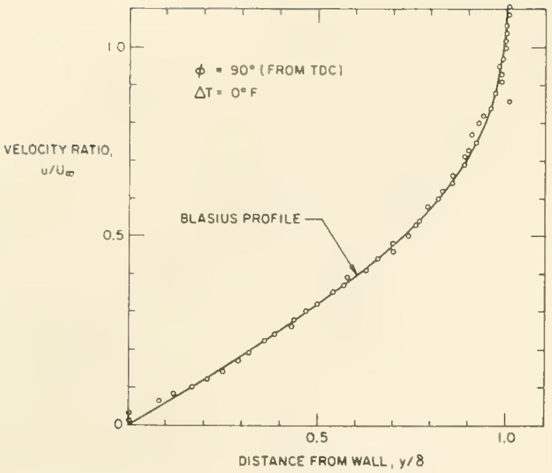

FIGURE 8. Normalized velocity profile with zero overheat, compared with Blasius profile.

normalized and plotted with a curve representing the Blasius profile for a zero pressure gradient boundary layer. Actually, the agreement shown here is better than it should be due to the positive β of the flow tube boundary layer.

The most surprising result that has been obtained with the instrumented section is the large deviation from axisymmetry in the profiles, even with no wall heat. Figure 9 shows a plot of δ* (displacement thickness), θ (momentum thickness), and H (shape factor) versus azimuthal angle φ for no wall heat at a free stream velocity of 1.60 m/sec. The dashed lines indicate the calculated values for β = 0 and β = 0.16, which is the value of β at the downstream end of the test section. The variations in δ* and θ are more than 50 percent, which was totally unexpected. Figure 10 shows an azimuthal velocity profile, that is, u versus φ at a fixed y. Here we see that the departure from axisymmetry is wave-like in nature, and that significant changes in velocity occur over a 15° change in φ.

This behavior suggests that the asymmetries may be caused by streamwise vortices within the boundary layer, which would have a cross-stream length scale on the order of the boundary layer thickness. Such vortices could be caused by the Goertler instability in the contraction section, as described above. To test this hypothesis, a new contraction section is presently being built which will avoid the Goertler instability entirely. This new contraction will have a fully convex inlet section surrounded by an annular bleed flow. All fluid from the settling chamber boundary layer will be removed by the bleed flow.

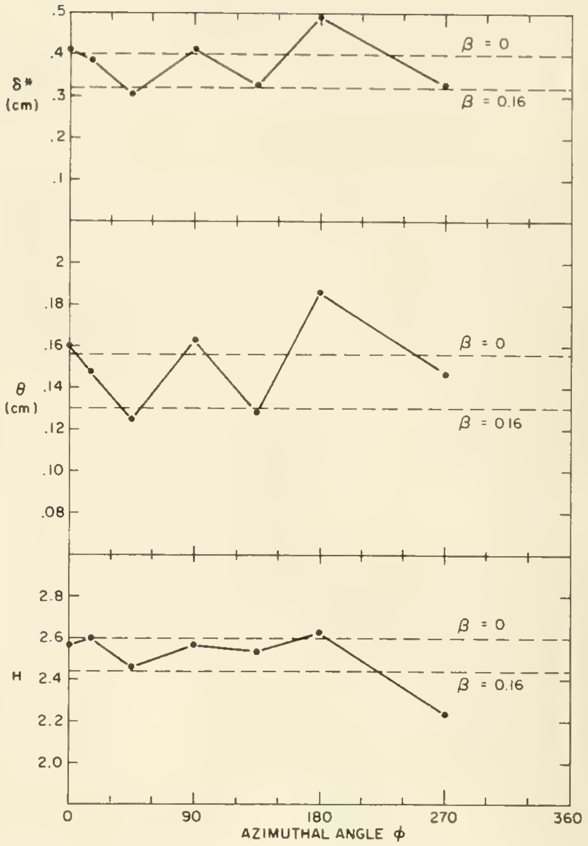

FIGURE 9. Displacement thickness, momentum thickness, and shape factor vs. azimuthal angle for zero overheat, U_∞ = 155 cm/sec.

Variations in mean velocity profiles due to heating have in fact been measured, but they are small relative to the changes with azimuthal angle shown in Figures 9 and 10. The shape factor H tends to decrease with increasing overheat as expected. However, no firm evidence of buoyancy-driven instabilities has yet been seen, even at low flow velocities and high overheats.

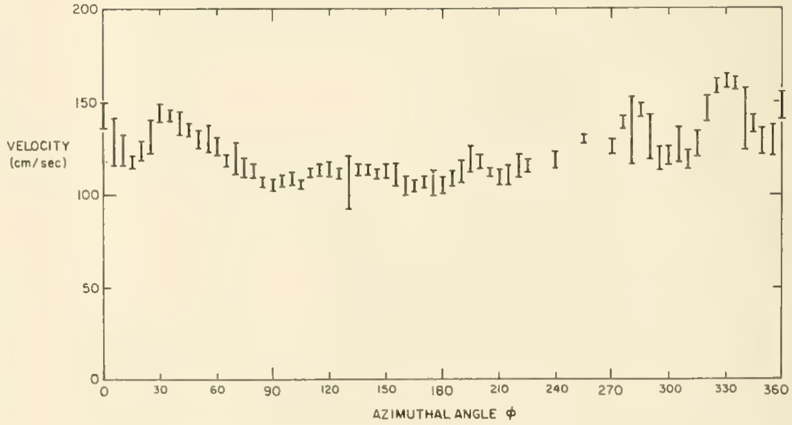

FIGURE 10. Velocity, u, vs. azimuthal angle, φ, at y = 0.51 cm ([illegible] in.).

4. CONCLUSIONS

The flow tube experiment has already demonstrated that wall heating can have a significant effect upon transition Reynolds numbers in water boundary layers. Although the maximum transition Reynolds number of 42 × 10^6 is well below the predicted maximum, this value has been obtained with only 7°C wall overheat. The unheated transition Reynolds number of 10^7 shows that disturbances are well controlled in the experiment.

Possible causes for the differences between the predicted and realized transition Reynolds numbers at higher overheats are still under investigation. Preliminary results from the instrumented section indicate that buoyancy-driven instabilities are not a significant factor. However, major deviations from boundary layer axisymmetry have been observed even with no wall heat. These perturbations of the unheated flow could themselves have an effect upon transition Reynolds numbers. This is particularly true if the actual disturbances are Goertler vortices, because these vortices would increase in strength with increasing flow velocity. Since the transition length is fixed at the end of the tube in this experiment, transition Reynolds number will be directly proportional to velocity. Thus the Goertler vortices could impose a limit in transition Reynolds number if they begin to dominate the transition process above some critical flow velocity. This hypothesis will be tested by the installation of the new contraction section, which eliminates the possibility of Goertler vortex formation.

ACKNOWLEDGMENT

The author wishes to acknowledge the participation and support of the Marine Systems Division of Rockwell International, and in particular Mr. Douglas Gile. In addition, the author acknowledges the Defense Advanced Research Projects Agency, who sponsored this research.

REFERENCES

Back, L. H., R. F. Cuffel, and P. F. Massier (1969). *AIAA Journal, 7,* 4; 730.

Barker, S. J., and C. Jennings (1977). The effect of wall heating on transition in water boundary layers. *Proc. of NATO-AGARD Symposium on Laminar-Turbulent Transition,* Copenhagen, 19-1.

Barker, S. J. (1978). Turbulence Management in a High Speed Water Flow Facility. Submitted to ASME.

Bradshaw, P. (1965). *J. Fluid Mech., 22* pt. 4, 679.

Chmielewski, G. E. (1974). *J. Aircraft, 11,* 8; 435.

Corrsin, S. (1963). Turbulence: Experimental methods, in *Handbuch der Physik, 8,* pt. 2, 523.

Kaups, K., and A. M. O. Smith (1967). The laminar boundary layer in water with variable properties. *Proc. ASME-AIChE Heat Transfer Conf.,* Seattle, Wash.

Launder, B. E. (1964). Laminarization of the Turbulent Boundary Layer by Acceleration, *M. I. T. Gas Turbine Lab Report 77.* Cambridge, Mass.

Loehrke, R. I., and H. M. Nagib (1972). *Experiments on Management of Free-Stream Turbulence.* NATO-AGARD Report 598.

Lumley, J. L., and J. F. McMahon (1967). *Trans. ASME,* D, *89,* 764.

Schlichting, H. (1968). *Boundary Layer Theory,* McGraw-Hill, New York.

Smith, A. M. O. (1957). Transition, pressure gradient, and stability theory, *Proc. 9th Int. Congress on Appl. Mech., 4,* 234, Brussels.

Spangler, J. G., and C. S. Wells (1968). *AIAA Journal, 6,* 3; 543.

Strasizar, A., J. M. Prahl, and E. Reshotko (1975). Experimental Study of Heated Laminar Boundary Layers in Water, *Case Western Reserve Univ., Dept. of Fluid, Thermal, and Aerospace Science Report FT AS/TR-75-113.*

Wazzan, A. R., T. T. Okamura, and A. M. O. Smith (1968). *Trans. ASME,* C, *90,* 109.

Wazzan, A. R., T. T. Okamura, and A. M. O. Smith (1970). The stability and transition of heated and cooled incompressible boundary layers. *Proc. 4th Int. Heat Transfer Conf.,* Paris.

Some Effects of Several Freestream Factors on Cavitation Inception of Axisymmetric Bodies

Edward M. Gates
University of Alberta
Edmonton, Canada

Allan J. Acosta
California Institute of Technology
Pasadena, California

ABSTRACT

Some of the effects of freestream turbulence and a dilute polymer solution on the fully wetted flow and the subsequent cavitation inception has been investigated for three different bodies. Two of these bodies possess a laminar separation and one does not. In the fully wetted investigation the flow on one of the bodies was found to be insensitive to the present disturbances whereas the other two were found by comparison to be very sensitive. Although there is a pronounced "suppression" of inception by the polymer, it seems clear that the effects observed are due primarily to the change in the real fluid features of the flow past the bodies themselves and not to an intrinsic cavitation process. There appeared to be no special polymer effect, insofar as cavitation is concerned, on the body not having a laminar separation, confirming the results of van der Meulen. Due to practical limitations the effects of turbulence per se on inception could not be separately evaluated.

The inception index on all bodies was found to be greatly dependent on the distribution of nuclei within the water tunnel. For those cases in which a turbulent transition was established well upstream, travelling bubbles were a common form of cavitation observed on all test bodies. The number of these cavitation events were so few, however, that in one test facility having a resorber, it was just as likely for an attached cavity to form as it was to observe a travelling bubble. In both cases the inception index was far below the customary minimum pressure coefficient reference value. Nuclei counts made with the aid of holograms reveal significantly fewer microbubbles within the flow of this test facility than in those not having a resorber.

1. INTRODUCTION

Our understanding of the details of the process of cavitation inception (and thus our ability to scale laboratory results to prototype conditions) is far from complete [e.g. Acosta and Parkin (1975), Morgan and Peterson (1977)]. This lack of understanding is well illustrated by our ability to do no more than indicate reasons which are believed to be responsible for the large variations in the results of the ITTC comparative test series [Lindgren and Johnsson (1966), Johnsson (1969)]. These results, some of which are presented in Figures 1 and 2, did, however, prompt a considerable amount of effort to investigate more systematically the factors influencing cavitation inception. In particular there are three areas in which there have been significant developments: (i) the influence of viscous effects on inception, (ii) the discovery that in some situations the presence of drag-reducing polymers in the water cause a suppression of the inception index, and (iii) the development of equipment to accurately measure freestream nuclei populations.

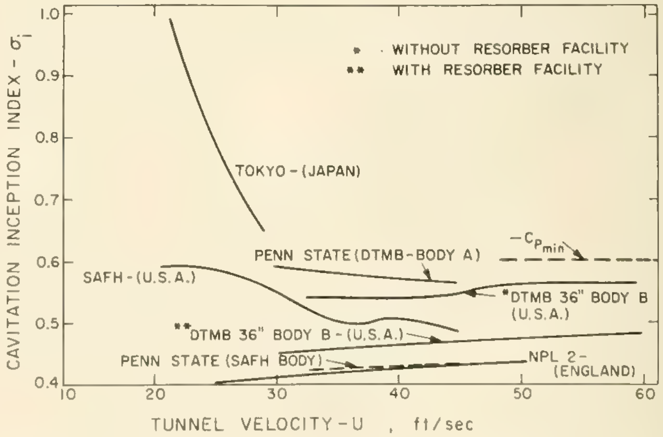

FIGURE 1. Results of the comparative inception test on a modified ellipsoidal headform sponsored by the International Towing Tank Conference, Lindgren and Johnsson (1966).

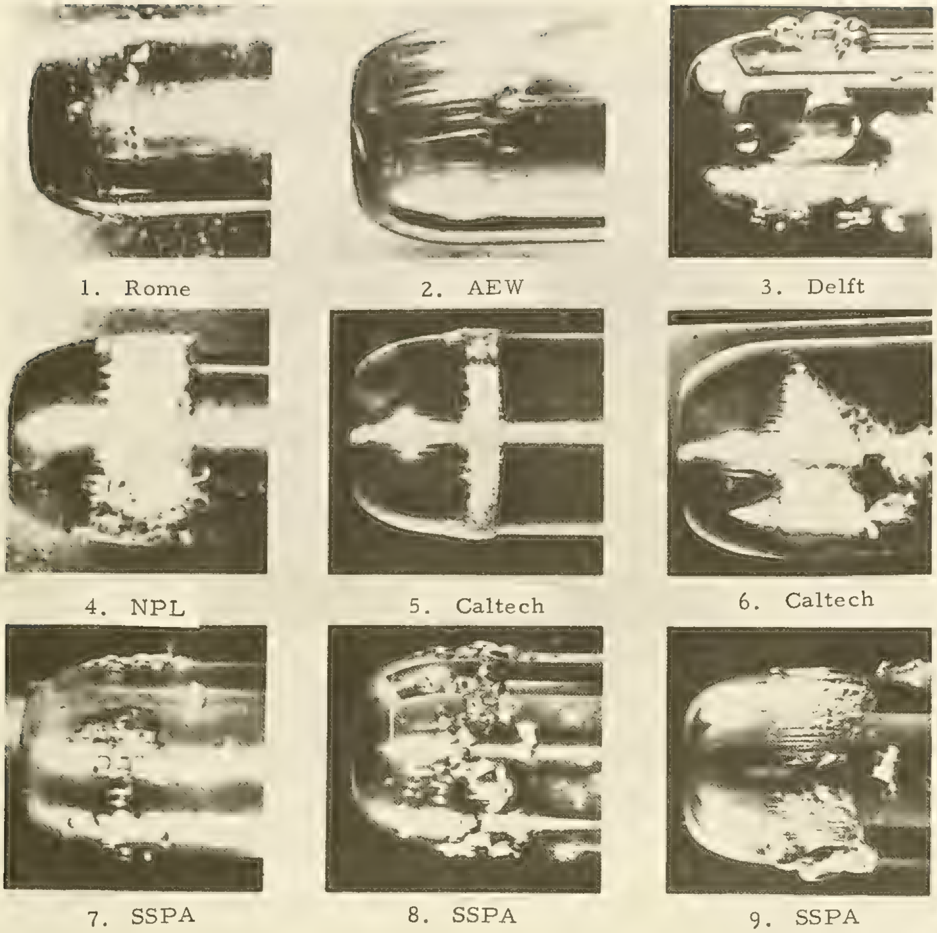

1. Rome 2. AEW 3. Delft 4. NPL 5. Caltech 6. Caltech 7. SSPA 8. SSPA 9. SSPA

FIGURE 2. Photographs of different types of cavitation observed in the ITTC tests, Lindgren and Johnsson (1966).

Viscous Effects

Parkin and Kermeen (1953) appear to be the first investigators to appreciate the influence of the boundary layer on the inception process. However, even though their interpretations of the experimental results were used in many subsequent inception theories [e.g. van der Walle (1962), Holl and Kornhauser (1969) to name only two] further experimental investigations of these viscous effects were carried out only much later.

Among these, Arakeri and Acosta (1963), by using the schlieren flow visualization technique, were able to observe cavitation inception within the structure of the flow. A primary feature of the flow observed by them was a laminar separation in which the cavitation was seen to occur first. There was further some suggestion by them that the laminar-to-turbulent transition itself may promote cavitation, perhaps through a mechanism similar to that for inception in turbulent pipe flow [Arndt and Daily (1969)]. In any case, it should be expected then, that any factor which could influence the presence of separation or even transition may also influence the inception of cavitation. One such well-known factor is freestream turbulence. [For recent accounts of these effects on transition see, e.g., Spangler and Wells (1968), Hall and Gibbings (1972), and Mack (1977)]. Unfortunately, the measurement of turbulence in water is more difficult than its aerodynamic counterpart and, until recent times, there has been no great demand for determining the freestream turbulence in water tunnels. For reference we tabulate in Table I the turbulence levels for a few water tunnels for which this information is available (12th ITTC Cavitation Committee).

Polymer Effects

It was inevitable that the much-heralded, drag-reducing polymer solutions would be the subject of cavitation experiments also. Very early in the course of this work Hoyt (1966) and Ellis et al. (1970) found that the inception index was reduced by as much as a factor of two for hemisphere-nosed bodies. There was, furthermore, a pronounced change in the physical appearance of the cavitation, once it was well developed, as subsequently illustrated by the beautiful photographs of Brennan (1970). Two possible explanations for the cavitation-suppression effect were then advanced: in the first, it was speculated that the dynamics of individual bubbles were changed by the presence of the polymer, and in the second, it was assumed that the basic viscous flow about the model was altered by the presence of the polymer. Ting and Ellis (1974) could find no difference in the collapse time of spark-generated bubbles in either water or polymer solutions weakening the idea that the bubble mechanics are important for this process. Later, however, Holl and co-workers (1974) in commenting on experiments

TABLE I Turbulence Levels in Some Water Tunnels

Ottawa, Canada	0.75%	ORL Pennsylvania State, USA	0.8%
Kriloff No. 2 Leningrad, USSR	0.4%	HSWT California Institute of Technology, USA	0.25%
NPL No. 1 Feltham, UK	0.5%	LTWT California Institute of Technology, USA (present work)	0.05% to 3.75%
MIT Massachusetts, USA	0.77%		
6" Tunnel Minnesota, USA	0.8%		

carried out at the Garfield Thomas Water Tunnel (GTWT) noted that there appeared to be no laminar separation on a hemisphere nose body when polymer was added to the water, but no direct flow visualization was done. Later van der Meulen (1976) verified this speculation with the clever use of schlieren holography to observe simultaneously the viscous flow and cavitation inception on a 10 mm diameter hemisphere nose body. His results showed clearly that when polymer was injected into the boundary layer that the laminar separation was removed. van der Meulen suggested that the polymer removed the separation by causing an early transition to a turbulent non-separating boundary layer. He then attributed the suppression effect to the removal of the large pressure fluctuations associated with the transition zone of the free shear layer [Arakeri (1975)].

Freestream Nuclei

It is generally accepted that inception begins at the nuclei in the liquid and that there are two sources for these nuclei--the test body surface and the incoming flow. At one time "surface nuclei" received considerable attention [e.g. Acosta and Hamaguchi (1967), Holl and Treaster (1966), Holl (1968), Peterson (1968) and van der Meulen (1972)]. While on the one hand it was shown that under certain circumstances, but not in normal cavitation testing, surface nuclei could exert a controlling influence upon inception. It seemed evident on the other hand from the results of the ITTC tests that freestream nuclei were the more important. Further, the development of the concepts of cavitation event counting [Schiebe (1966)] in conjunction with Johnson and Hsieh's (1966) trajectory calculations, the idea of "cavitation susceptibility" [Schiebe (1972)] and the development of equipment to measure freestream nuclei populations have led to more interest in the influence of freestream nuclei versus surface nuclei. In particular, the experiments of Keller (1972) have prompted considerable interest in measuring and relating freestream nuclei populations to inception.

Morgan (1972) has reviewed the various types of instruments available for measuring freestream nuclei populations and Peterson et al. (1975) have made an experimental comparison of three of these, namely; light scattering, microscopy, and holography. At the moment holography seems the best in that no "calibration" is required, a permanent record is obtained, a large volume is sampled, and, as Peterson observed, one can determine if the nuclei are solid particles or micro-bubbles.

There is seen to be ample reason then to pursue these various freestream factors in inception research. Two are primarily fluid-dynamic in nature and of these the questions concerning freestream turbulence levels are of historic interest in fluid mechanics and naval architecture. The cavitation nuclei however are directly involved in the cavitation inception process and the recent experimental progress cited above make one hope for a more quantitative predictive ability than in the past insofar as inception is concerned. The present work is in the mainstream of these observations; briefly we report on observations made in two different flow facilities having widely different freestream nuclei distributions on identical bodies. In one of these, the freestream turbulence level is varied over nearly a factor of 100 (but not in a condition of cavitation then) and we confirm and extend the observations of van der Meulen on the polymer effect. Schlieren photography is extensively used to visualize thermal boundary layers on the test bodies used and in-line holography is used to determine nuclei populations in the working section.

Before discussing these effects we should comment briefly on the means used for the determination of the actual inception observation. A standard procedure has been to observe the test body under stroboscopic light and to say that inception occurs when macroscopic cavities or bubbles become visible on the model. However, this method is observer-dependent and the trend now is to use cavitation-event counters free of human judgment. Ellis et al. (1970) and Keller (1972) have developed optical techniques which count interruptions of light beams which are adjusted to graze the model surface where inception has been observed to occur. Peterson (1972), Brockett (1972), and Silberman et al. (1973) have also determined inception acoustically by locating a hydrophone inside the test model. There are problems of identifying the types and location of the cavitation phenomena occurring with these "events." Aside from the question of technique, there is also the question of selecting appropriate threshold levels at which an event becomes countable and also the event rate at which inception is defined to occur. At present there is no universal agreement of just what these values should be.

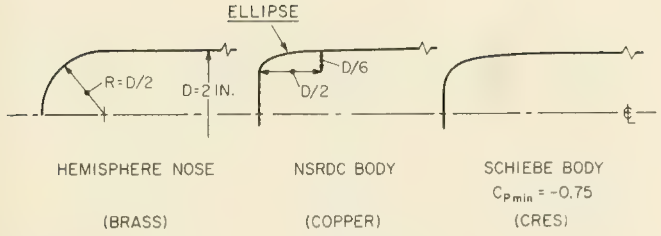
ELLIPSE
R=D/2
D=2 IN.
D/6
D/2
℄
HEMISPHERE NOSE
(BRASS)
NSRDC BODY
(COPPER)
SCHIEBE BODY
$C_{P_{min}} = -0.75$
(CRES)

FIGURE 3. Definition of test models.

2. EXPERIMENTAL EQUIPMENT AND METHODS

Test Models

Three axisymmetric test models were used in the present experiments: a brass hemisphere nose, a copper modified ellipsoidal (or NSRDC) body, and a stainless steel standard headform from the Schiebe series with a minimum pressure coefficient (C_{pmin}) of -0.75. The hemisphere nose and Schiebe bodies were fabricated specifically for these tests, whereas the NSRDC body is the same as that used by Brockett (1972) and Arakeri (1976). Each body is 5.08 cm in diameter and has a 0.423 cm diameter hole at the stagnation point for polymer injection. No quantitative measure of surface roughness was made, but each model was highly polished [a highly polished surface typically has a 0.1×10^{-7}m rms finish, Beckwith and Buck (1961)]. The model geometries are shown in Figure 3.

The models were supported by a two-bladed sting in the LTWT and by a three-bladed sting in the HSWT with the nose of the model being about six body diameters upstream of the sting in each case. Misalignment from the geometric tunnel center-line in both the LTWT and HSWT was measured to be about 0.2°.

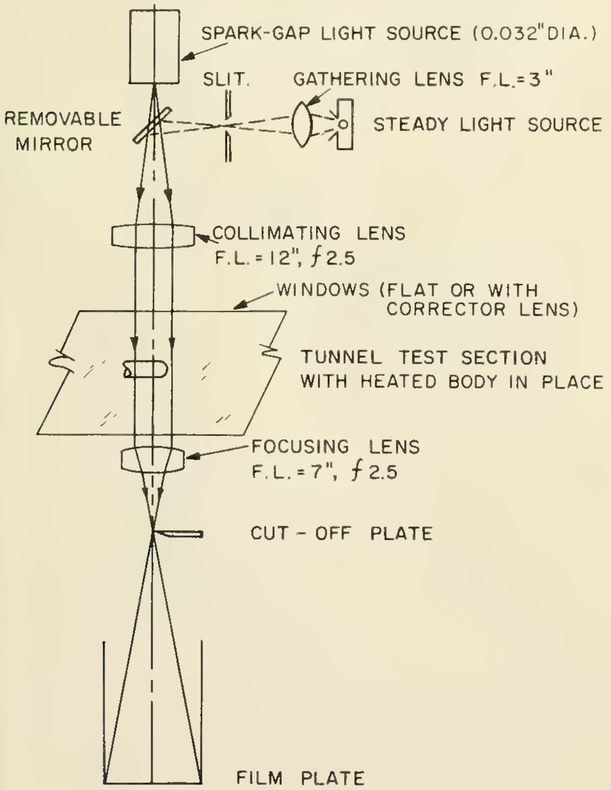
SPARK-GAP LIGHT SOURCE (0.032" DIA.)
SLIT
GATHERING LENS F.L.=3"
REMOVABLE MIRROR
STEADY LIGHT SOURCE
COLLIMATING LENS F.L.=12", ƒ2.5
WINDOWS (FLAT OR WITH CORRECTOR LENS)
TUNNEL TEST SECTION WITH HEATED BODY IN PLACE
FOCUSING LENS F.L.=7", ƒ2.5
CUT-OFF PLATE
FILM PLATE

FIGURE 4. Schematic diagram of flow visualization system.

Flow Visualization

Thermal boundary layers in the viscous flow past the test model were observed by schlieren photography. The particular schlieren configuation used is shown schematically in Figure 4 and is essentially the same as that used by Arakeri (1973). Also following Arakeri, the prerequisite density gradient was produced by heating the body with internal cartridge type electric heaters. An example schlieren photograph obtained using this system is presented in Figure 5.

Water Tunnel

The two facilities used in the present experiments were the High Speed Water Tunnel (HSWT) and the

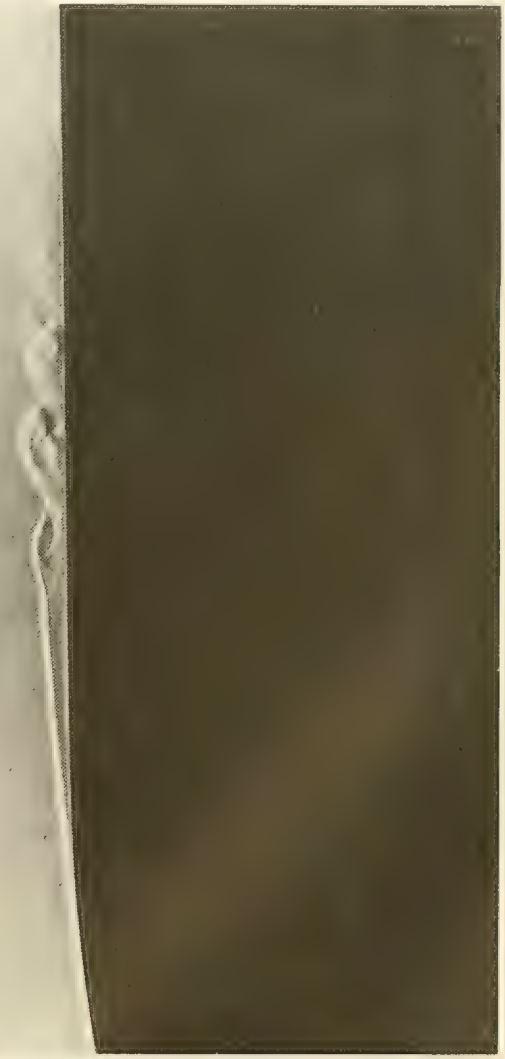

FIGURE 5. A schlieren photograph of a 5 cm diameter hemisphere showing laminar separation and turbulent reattachment at a body Reynolds number of 2.6×10^5. The maximum height of the separated region is about 2 mm.

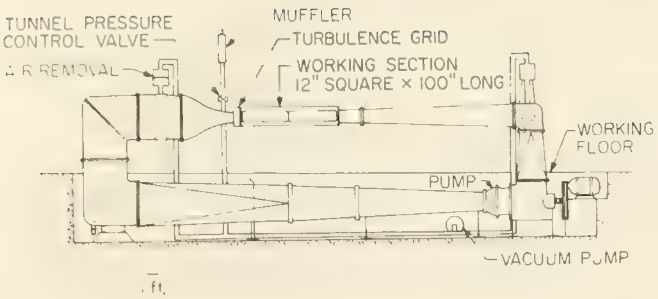
TUNNEL PRESSURE CONTROL VALVE
AIR REMOVAL
MUFFLER
TURBULENCE GRID
WORKING SECTION 12" SQUARE × 100" LONG
WORKING FLOOR
PUMP
VACUUM PUMP
ft.

FIGURE 6. Diagram of the Low Turbulence Water Tunnel (LTWT).

Low Turbulence Water Tunnel (LTWT) both at the California Institute of Technology. Since the HSWT has been described in detail elsewhere [see Knapp et al. (1948) or Knapp, Daily, and Hammit (1970)], it will only be noted here that one, it has a resorber and two, the freestream turbulence level has been measured to be about 0.2 percent by Professor S. Barker. The LTWT [Vanoni et al. (1950)] is also a closed loop recirculating tunnel; but, as can be seen in Figure 6, it has no resorber. In this facility the maximum test section velocity and minimum cavitation number are approximately 8 meters per second and 0.3 respectively. The unique feature of the LTWT is that the freestream turbulence level in the test section can be varied from a very low value (for water tunnels) of 0.05 percent to a high value of 3.6 percent. The low turbulence level is obtained by use of small turning vanes in each elbow of the circuit, a very gradual diffuser (included angle is 3°13'), a nozzle with a 16:1 contraction ratio, and by turbulence damping screens and honeycombs in the "stagnation" section of the tunnel just upstream of the nozzle. The configuration of screens and honeycombs which produces the 0.05 percent turbulence level is shown schematically in Figure 7 (with the exception that no turbulence generating grid is installed) and is based upon the results of Loehrke and Nagib's (1972) report.

By inserting different turbulence generating grids into the tunnel circuit the turbulent intensity can be gradually increased from 0.05 to approximately 3.6 percent. The description of these grids is as follows:

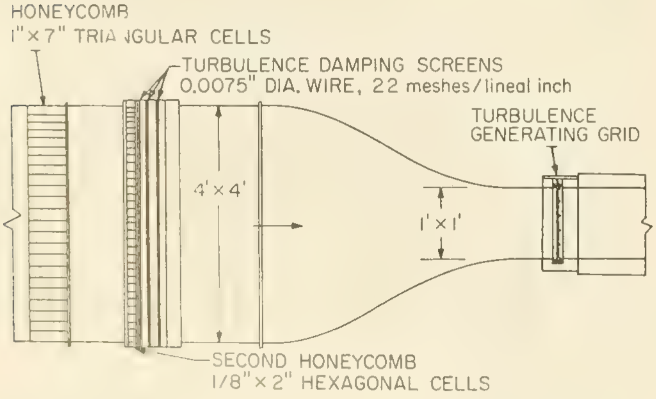
HONEYCOMB
1"×7" TRIANGULAR CELLS
TURBULENCE DAMPING SCREENS
0.0075" DIA. WIRE, 22 meshes/lineal inch
TURBULENCE GENERATING GRID
4'×4'
1'×1'
SECOND HONEYCOMB
1/8"×2" HEXAGONAL CELLS

FIGURE 7. Sketch of LTWT contraction nozzle showing the turbulence manipulators.

grid No. 1: 12.7mm diameter bars with 50.8mm mesh
grid No. 2: 6.35mm diameter bars with 25.4mm mesh
grid No. 3: three 25.4mm diameter horizontal bars on 76.2mm centers
grid No. 4: 0.635mm diameter fishing line with 19.05mm mesh

Grids 1, 2, and 4 are located at the entrance to the test section as is shown in Figure 7 (the distance from these grids to the test model is approximately 1.2 meters). Grid No. 3 is located in the "stagnation" section immediately after the final turbulence damping screen. Grid No. 3 has this particular configuration because (after much trial and error) it was found to produce a turbulence level which is close to the levels measured in a number of other facilities--see Table 1.

A DISA constant temperature anemometer was used to measure the turbulence levels in the test section. The probe was a wedge-shaped hot film type and was firmly mounted on the tunnel center-line at the model position (1.2 meters from the test section entrance). The results of these measurements have been summarized in Figure 8.

Polymer Injection System

The injection approach of introducing the polymer into the boundary layer versus filling the tunnel with a polymer solution (polymer ocean) was chosen. After considering a number of injection configurations [Wu (1971)] it was decided to follow van der

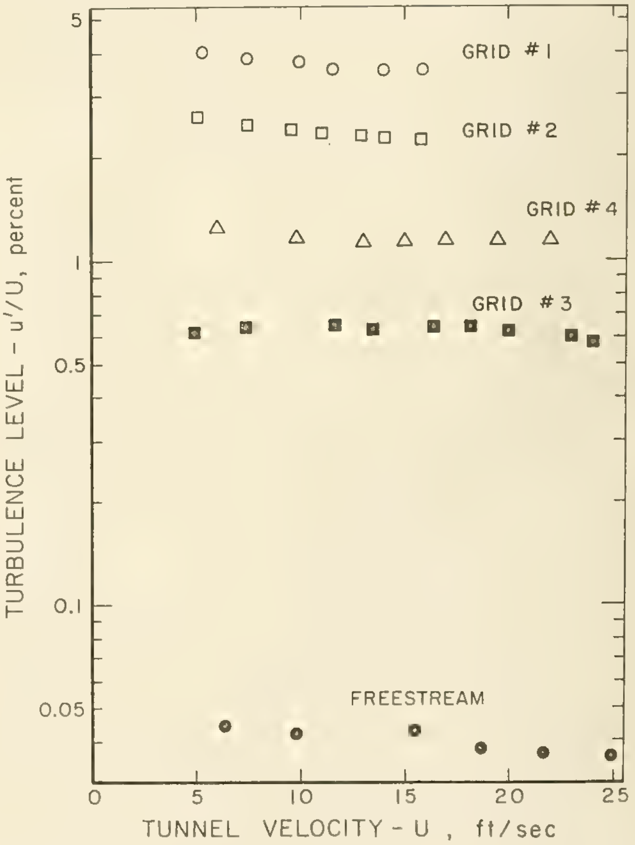

FIGURE 8. Summary of turbulence intensity measurements in the LTWT.

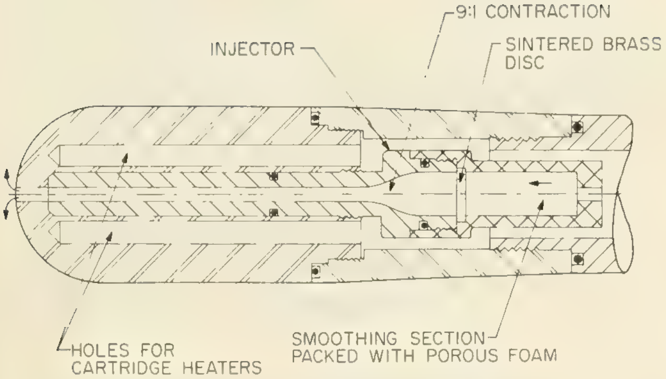
9:1 CONTRACTION
INJECTOR
SINTERED BRASS DISC
HOLES FOR CARTRIDGE HEATERS
SMOOTHING SECTION PACKED WITH POROUS FOAM

FIGURE 9. Cross-section of injector used for these polymer experiments. The body diameter is 5 cm.

Meulen's (1973) example and inject the polymer into the boundary layer through a hole at the stagnation point. To do this an injector was designed to introduce the polymer into the boundary layer without also introducing disturbances. The injector is shown schematically in Figure 9 assembled inside the hemisphere nose body and consists of first a settling chamber 12.7mm in diameter and 31.75mm long. This section was packed with porous plastic foam held in place by a sintered brass disc. The purpose of this section is to disperse the jet entering the injector and provide a smooth flow into the 9:1 contraction which follows. After the smooth contraction there is a tube with a length to diameter ratio of 22 and this tube ends at the surface of the model.

To minimize polymer degradation, the polymer solutions were "pushed" through the injector from a reservoir by using compressed air instead of a pump. A check with a turbulent flow rheometer [the same one as used by Debrule (1972)] showed degradation of the polymer after it passed through the injection system to be minimal. Preliminary tests were carried out with water as the injectant to ensure that the injection process itself was not responsible for any observed changes in the flow. Results of these tests for the NSRDC body are presented in Figure 10 and show that even at an injection rate of three to ten times higher than actually used with polymer solutions no differences are detectable from the no-injection case.

Nuclei Counter

Nuclei distributions were deduced from holograms of the test fluid. The experimental apparatus and method is much the same as used by Peterson (1972), Feldberg and Shlemenson (1973) and is described in detail in Gates and Bacon (1978). Essentially it is a two-step image forming process. In the first step, a hologram of a sample volume of the water in the tunnel test section is recorded on a special high resolution film by a "holocamera." In the second step, the developed hologram is reconstructed producing a three dimensional image of the original volume which can be probed at the investigator's leisure. The holocamera and reconstruction system are shown schematically in Figure 11 and 12 respectively.

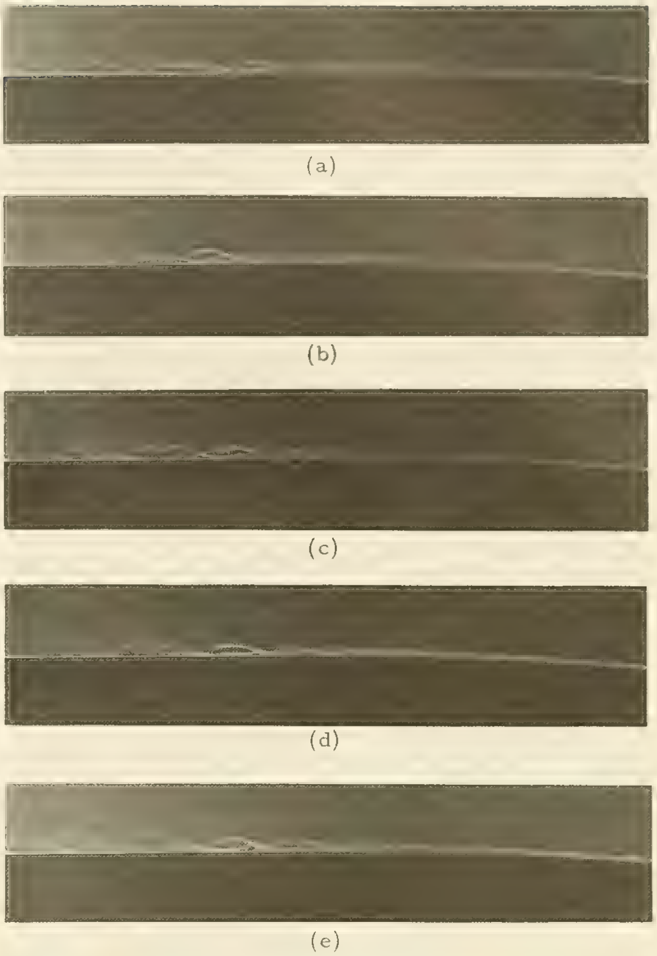
(a)
(b)
(c)
(d)
(e)

FIGURE 10. Schlieren photographs showing the effect of injecting water on the NSRDC body at a body Reynolds number of 3.2×10^5, (a) injection rate = 0 mℓ/sec, (b) 1.8 mℓ/sec, (c) 3.6 mℓ/sec, (d) 6.6 mℓ/sec, (e) 9.8 mℓ/sec. No effect is observed.

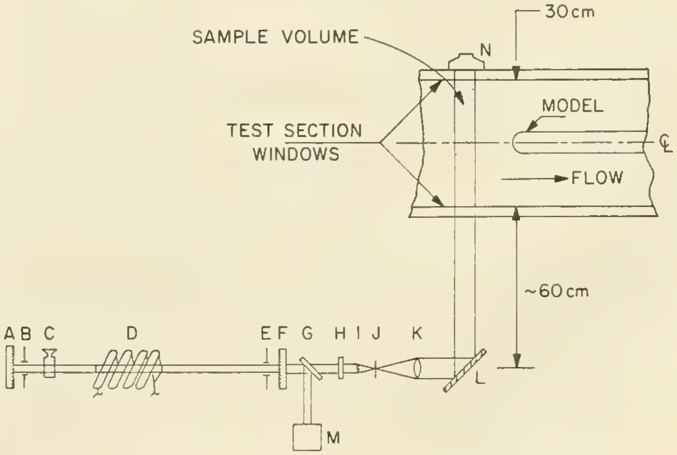

FIGURE 11. Diagram of the holocamera; (a) dielectric mirror, (b) iris, (c) dye-quench cell, (d) ruby-flash lamp assembly, (e) iris, (f) dielectric mirror, (g) beam splitter, (h) neutral density filter, (i) beam expander lens, (j) 25μ pinhole, (k) collimating lens, (l) front surface mirror, (m) p.i.n. diode, (n) film pack.

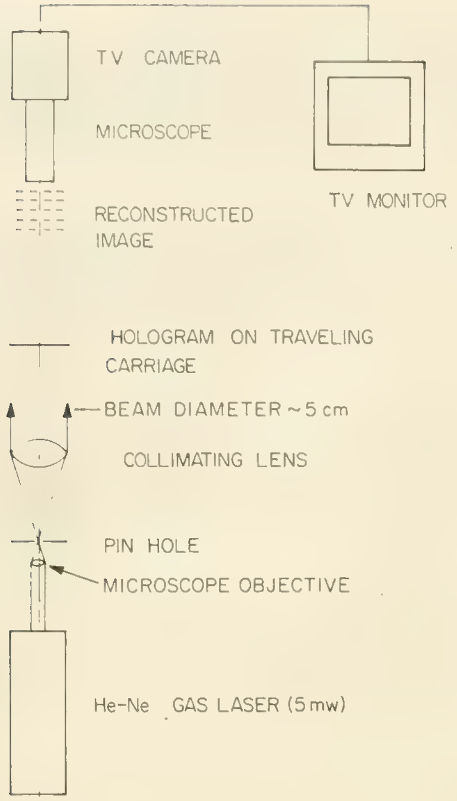

FIGURE 12. Arrangements to reconstruct and read the holograms.

3. GENERAL EXPERIMENTAL PROCEDURES

Before any experiments were carried out, the water in each facility was de-aerated to reduce the number of freestream air bubbles produced in the tunnel circuit. This was of particular importance in the LTWT which has no resorber. During the present tests the air content in the LTWT was typically between 7 - 8ppm whereas in the HSWT it was between 9 - 10ppm (air content levels were measured with a van Slyke blood gas analyzer). At these air contents there were *very* few macroscopic air bubbles visible in the flow approaching the model in the HSWT (as will be seen later). However, in the LTWT there were always many macroscopic air bubbles easily visible in the approaching flow.

In a typical cavitation test in the LTWT, the tunnel velocity and polymer injection rate (if any) were first adjusted to the desired values. Inception was then obtained by reducing as rapidly as possible the tunnel static pressure until the presence of cavitation was visually observed on the model under stroboscopic illumination. At the point of inception, a schlieren photograph, a hologram, the tunnel velocity, and the tunnel static pressure were recorded simultaneously. Each test had to take less than forty seconds since by that time the abundant supply of cavitation bubbles generated at the pump would reach the test section and dramatically change the freestream conditions. After each test, the tunnel pressure was raised to about one atmosphere and the tunnel allowed to circulate for five minutes. This recess between each test was required to let the ruby laser cool down and also to let the freestream bubbles go back into solution or rise to the high points in the tunnel circuit.

The same general test procedure was used in the HSWT except for small differences in pressure measurement. However, *desinent* cavitation observations were also made in this facility. All holograms made in the HSWT were done without the model in place but at conditions of velocity and pressure at which inception had been observed to occur.

4. PRESENTATION AND DISCUSSION OF FULLY WETTED RESULTS

Freestream Turbulence Levels

Observations

The influence of gradually increasing freestream turbulence level upon the viscous flow about each test body is illustrated in the sequences of schlieren photographs presented in Figures 13 through 15. In each sequence of photographs the test body is seen in silhouette and the flow is from right to left. The magnification is such that the surface length shown in these photographs is

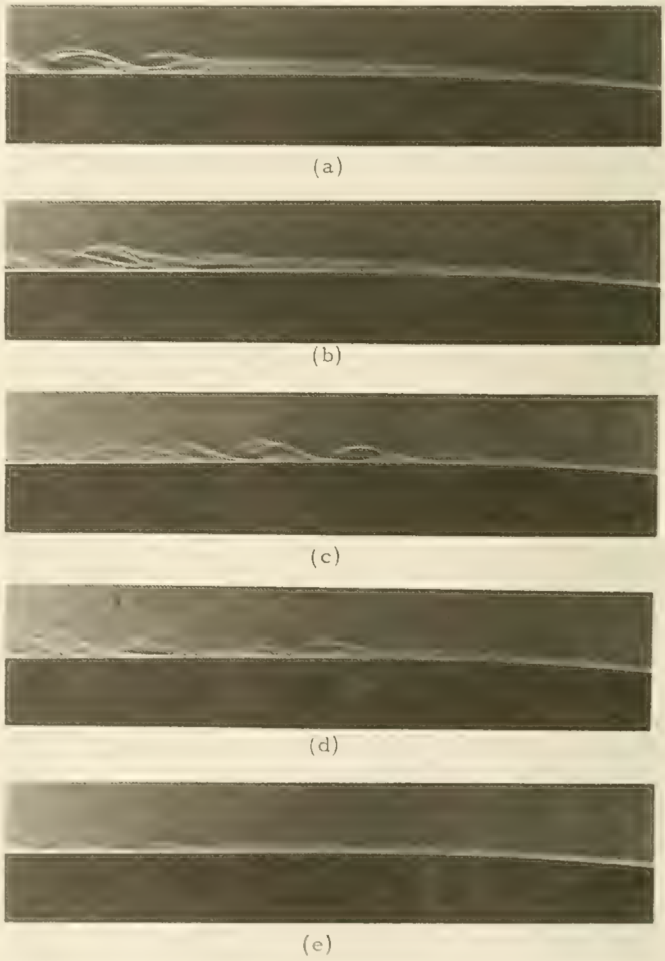
(a)
(b)
(c)
(d)
(e)

FIGURE 13. The effect of freestream turbulence level on the flow past the NSRDC body (the flow is right to left) at a body Reynolds number of 1.6×10^5: (a) $u'/v = 0.05$ percent, (b) 0.65, (c) 1.1, (d) 2.3, (e) 3.6 percent.

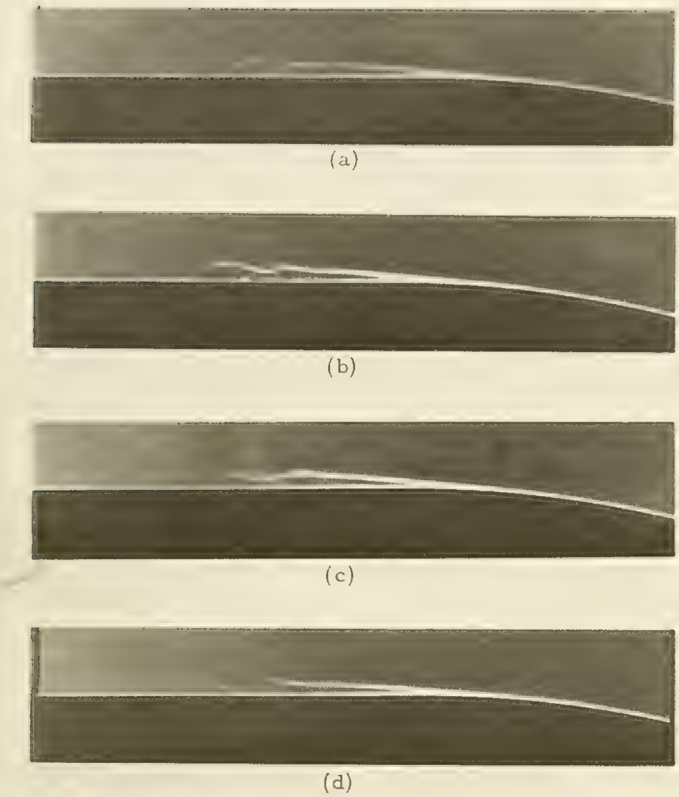

FIGURE 14. The effect of freestream turbulence level on the flow past the hemisphere body at a body Reynolds number of 2.6 × 10^5. (Same turbulence values as in Figure 13.)

approximately 10mm. As can be seen in the first photograph of each of Figures 13 and 14, the NSRDC and the hemisphere nose bodies respectively have a laminar separation. Transition on these bodies occurs on the resulting free shear layer and the flow subsequently reattaches as a turbulent boundary layer. With increasing turbulence intensities the point of transition on the NSRDC body moved upstream on the free shear layer. As the position of transition moved forward, the size of the separation bubble decreased until finally it disappeared when the position of transition and separation coincided. Once the point of transition moved upstream of the point of separation, no further observations of the thermal boundary layer could be made with the present schlieren system. Unlike the NSRDC model, the increasing turbulence level seemed to have no effect upon the viscous flow about the hemisphere nose body--as can readily be seen in Figure 14. This rather surprising result will be returned to later.

As is shown in the first photograph of Figure 15, the Schiebe body has no laminar separation and transition occurs on the model surface rather than on a free shear layer. With increasing freestream turbulence level two effects were noted; first, as can be seen in Figure 15, the position of transition moves substantially upstream and secondly, the appearance of the disturbance appears to change. This change is not quite so evident in only a few pictures, but we believe we observe more-or-less periodic and highly amplified boundary layer waves in Figure 15a and even b. However, for the higher turbulence levels frequent "bursts" interspersed with a periodic phenomenon seemed to be more common. A random collection of schlieren photographs of the same body (Figure 16) at an intermediate turbulence level shows these various forms more clearly.

Discussion

To quantify the effects of turbulence level, the position, length, and maximum height of the separation bubble were measured for the NSRDC and hemisphere nose bodies. For the Schiebe body, which has no separation, the position of transition was recorded--the position of transition being defined as that point at which the first noticeable disturbance occurs in the laminar boundary layer. These quantities are defined in Figure 17 and were measured directly from the negatives of the schlieren photographs with the aid of a scale or reference

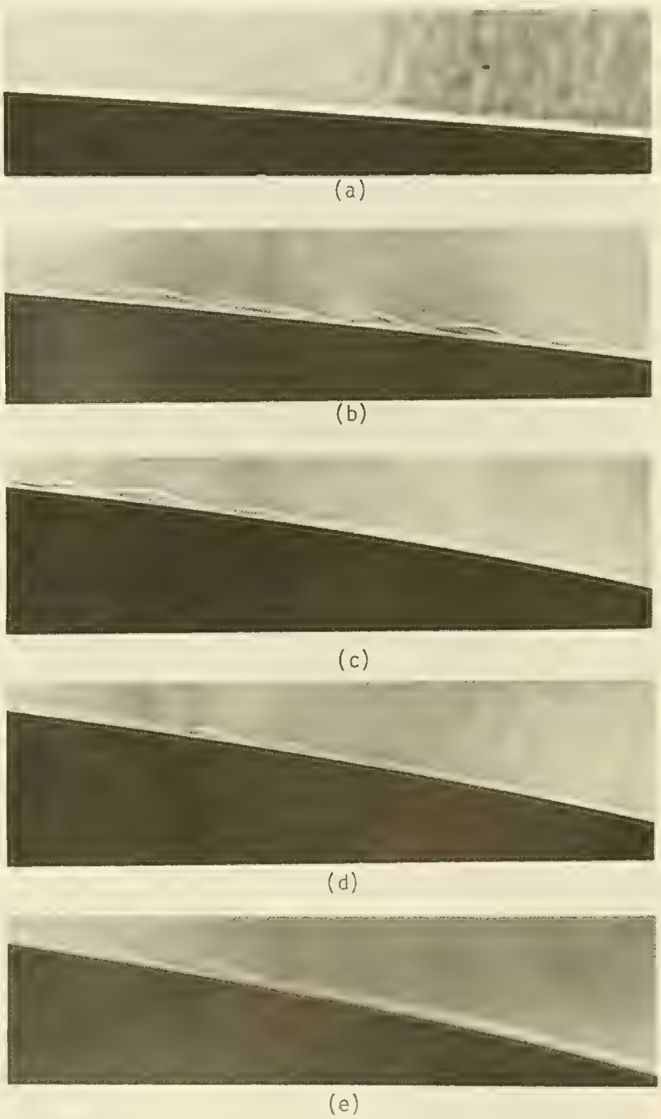

FIGURE 15. The effect of freestream turbulence level on the flow past the Schiebe body at a body Reynolds number of 2.5 × 10^5. The turbulence levels are those in figure 13 and the regions shown are at arc-length diameter ratios of (a) 0.82-1.07, (b) 0.76-1.01, (c) 0.60-0.85, (d) 0.61-0.86, (e) 0.47-0.63.

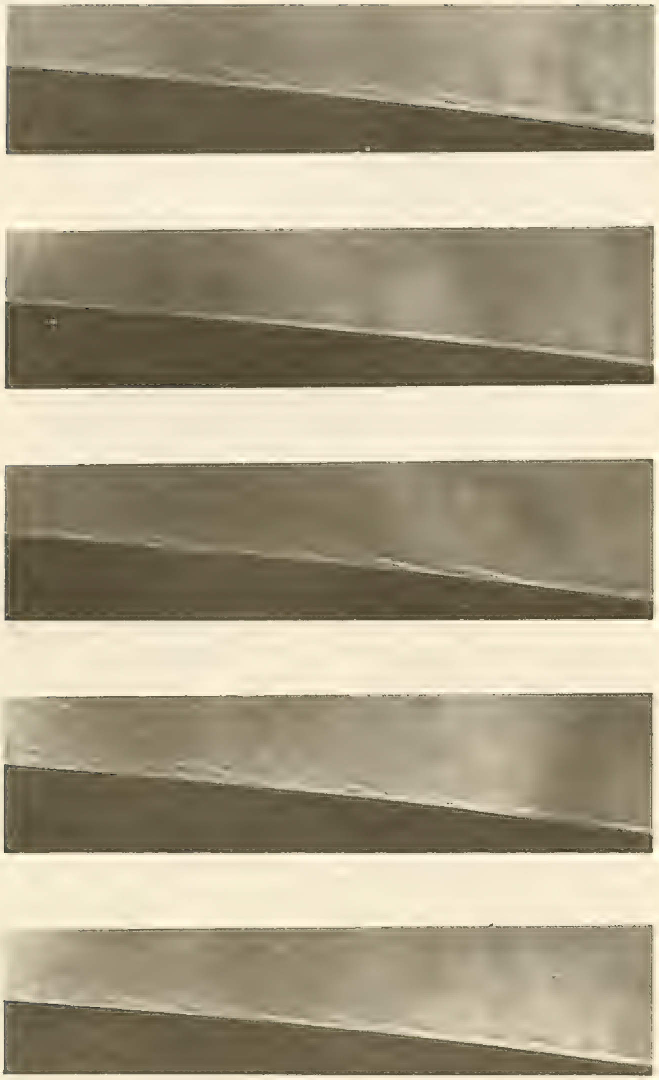

FIGURE 16. Random photographs of the flow past the Schiebe body at a Reynolds number of 3.4 × 10^5 with background turbulence level of 1.1 percent. The region shown covers the arc length diameter ratio of 0.68 to 0.93.

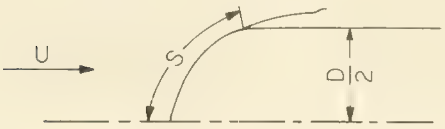

(a) POSITION OF LAMINAR SEPARATION OR TRANSITION WHICHEVER IS APPLICABLE

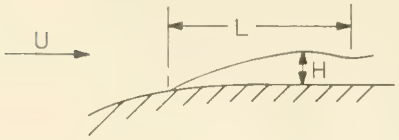

(b) LENGTH AND HEIGHT OF SEPARATED REGION

FIGURE 17. Definition sketch of separation location.

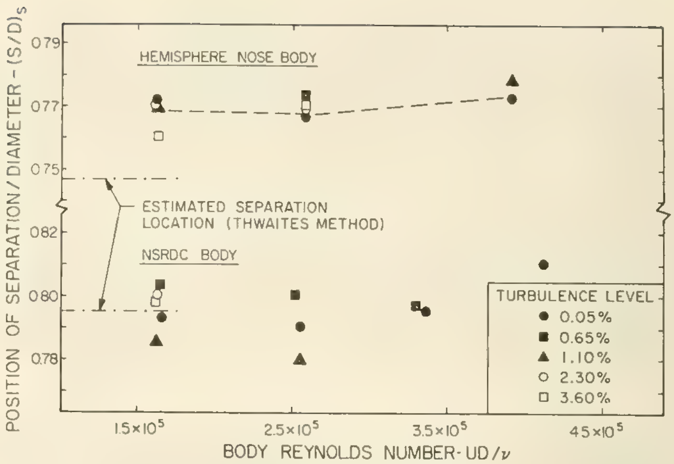

FIGURE 18. Observed separation locations as a function of turbulence level for two bodies.

negative. Note that the position of transition on the free shear layer coincides with the definition of the end of the separated bubble.

Each of these measured quantities was nondimensionalized by dividing by the body diameter and are plotted versus the body Reynolds number with the freestream turbulence level as a parameter in Figures 18 through 21. For the NSRDC body, Figure 19 shows that the size of the separation bubble decreases with increasing velocity and turbulence level--the critical Reynolds number being reduced from a value of greater than 4 × 10^5 at 0.05 percent to near 2.5 × 10^5 at 3.6 percent. As was expected from the schlieren photographs of the hemisphere nose (Figure 14), Figure 20 shows the length of the separation bubble is independent of turbulence level but decreases with increasing velocity. Finally, Figure 21 shows that as with the NSRDC body, the position of transition on the Schiebe body moves forward with increasing velocity and turbulence intensity.

The most startling result of the above tests was the insensitivity of the boundary layer on the hemisphere nose to the present disturbances imposed by the freestream turbulence. Hall and Gibbings

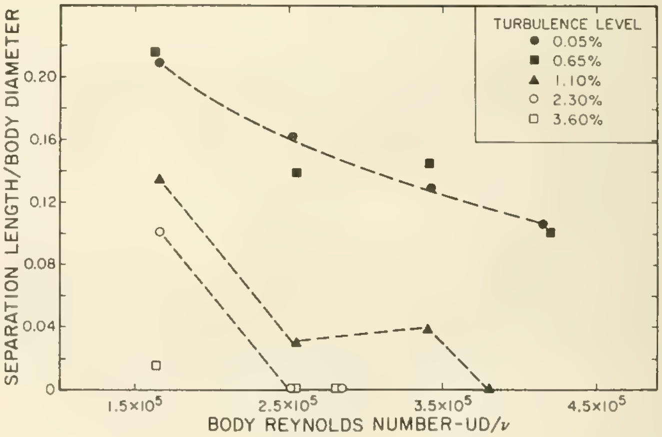

FIGURE 19. The length of the separated region as a function of freestream turbulence level for the NSRDC body.

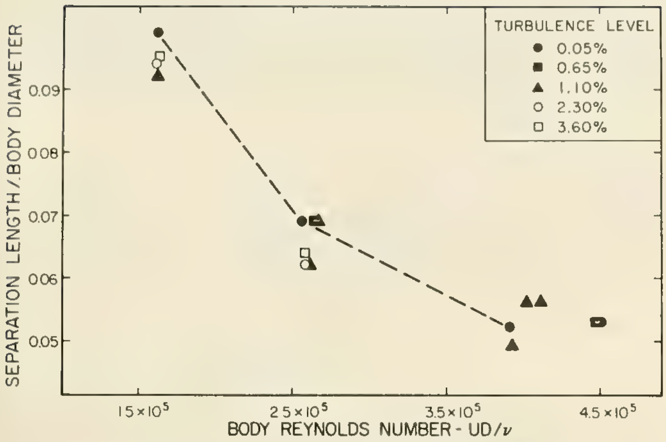

FIGURE 20. The length of the separated region as a function of freestream turbulence level for the hemisphere body.

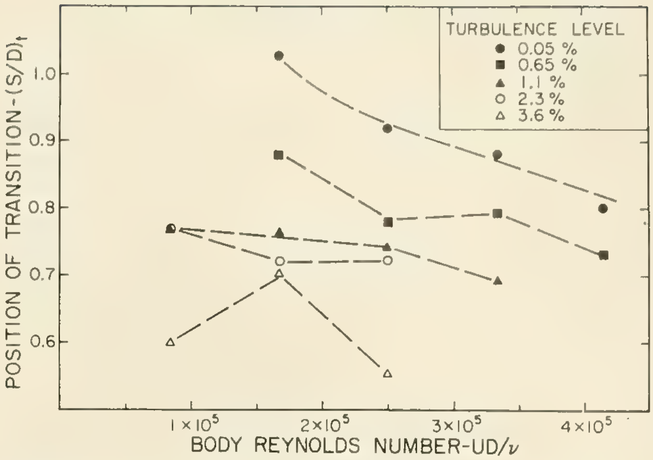

FIGURE 21. The location of transition on the Schiebe body as a function of turbulence level.

(1972) have summarized the available experimental data and semi-empirical correlations at that time for the combined effects of pressure gradient and freestream turbulence level upon transition. However, this correlation does not predict an insensitivity to increasing turbulence levels. No doubt this discrepancy is related to the question of how the freestream disturbances are assumed to interact with the boundary layer. For example, van Driest and Blumer (1963) accounted for the effect of freestream turbulence by using Taylor's assumption that the unsteady perturbation induced instantaneous variations in the velocity gradient. But, as just noted, this type of correlation did not work. Later, Spangler and Wells (1968) demonstrated that not only the intensity, but also the energy spectrum and the nature of the disturbance must be taken into consideration. Reshotko (1976) and Mack (1977) have re-emphasized Spangler and Wells' conclusions and pointed out the lack of understanding of the interaction mechanism between the freestream disturbance and the boundary layer* is one of the major obstacles in the consistent prediction of transition. Thus, although the effect of freestream turbulence on these bodies cannot be predicted with confidence, we at least may offer some speculation based on these ideas to explain the behavior on the hemisphere nose body.

It is readily possible using the approximate method of transition prediction suggested by Jaffe et al. (1970) in conjunction with the stability charts for the Falkner-Skan profiles computed by Wazzan et al. (1968b) to determine the critical frequency, or most unstable frequency for growth, for each body at a number of velocities. These estimates are presented in Table 2. We then estimate with the aid of measured energy spectra of grid generated turbulence, Tsuji (1956) that there is approximately sixty times as much energy available in the freestream at the critical frequency of the NSRDC body than there is at the critical frequency of the hemisphere nose body. Furthermore, the distance from the position of neutral stability to the position of separation is only 0.07 diameters on the hemisphere nose model whereas on the NSRDC body it is 0.40 diameters. Thus on the NSRDC body not only is there considerable more energy available at the critical frequency, but there is also more opportunity for disturbances to grow than for the hemisphere nose body. This same trend is also found for the Schiebe body at the low turbulence levels. The critical frequencies are even less than those of the NSRDC model (Table 2). There is, therefore, more energy available at those frequencies than even on the NSRDC model. Finally, the distance from the position of neutral stability to transition is between 0.40 to 0.60 diameters--much the same as for the NSRDC model.

We find it somewhat reasonable then, in retrospect, for the hemisphere body to be found insensitive, in the present experiments, to the freestream disturbances. Regrettably, the present visual observations are not sufficiently quantitative to shed light on this basic problem of boundary layer receptivity to external disturbances and their subsequent growth into turbulence.

By using an oil film technique, Brockett (1972) found the NSRDC model to have a critical velocity of 2.8 meters per second at 20°C and Peterson (1972) reports 4.2 meters per second at 10°C in the NSRDC 12-inch water tunnel. The *same* body in the HSWT was found to have a critical velocity of about 9.2 meters per second and it was observed to be above 7.6 meters per second in the LTWT at 0.05 percent turbulence level. To reduce the value of the critical velocity to 4 meters per second in the LTWT required a 316 percent turbulence level, which is as can be seen from Table 1 a very high value for a water tunnel test section. (Initially it was thought unlikely that the disturbance level in the NSRDC facility is this high. However, after inspecting a drawing of the facility [Figure 2.3 pg. 26, Knapp et al. (1970)] such a high level does not seem so unlikely.) However, in this as well as in most water tunnel facilities the energy spectrum is not known, forestalling therefore a direct comparison of transition phenomena.

The present observations of transition on the Schiebe body at the lowest turbulence level are compared with calculations of Wazzan* and experi-

---

*This is the concept of boundary layer receptivity developed by M. V. Morkovin [see the review of Reshotko (1976)].

*Private communication.

TABLE II Approximate Critical Boundary Layer Frequencies for Several Bodies

Re_D	Hemisphere Nose (Hz)	NSRDC (Hz)	Schiebe (Hz)
1.67×10^5	1070	670	--
2.50×10^5	1800	1060	350
3.33×10^5	2140	1780	650
4.17×10^5	3350	2100	1200

ments of van der Meulen (1976) in Figure 22. There is good agreement of the experimental results and also with Wazzan's e^9 calculations.

Polymer Injection

Observations

The influence of gradually increasing the injection rate of the polymer solution upon the basic flow about each test body is illustrated in the sequences of schlieren photographs in Figures 23 through 25. In Figure 23(a) the maximum height of the separation bubble is 0.5mm and on the hemisphere nose body in 24(a) the maximum bubble height is 0.25mm. Unlike the freestream turbulence level, the presence of polymer in the boundary layer was found to influence the basic viscous flow on *all* the test models. As can be seen in the schlieren photographs, as the polymer injection rate was increased the position of transition moved upstream in each case. For the NSRDC and hemisphere nose models a critical injection rate was reached at which the positions of transition and separation coincided and the laminar separation was eliminated. At injection rates above this critical value the position of transition appeared to move further upstream, but with the limited resolution of the present schlieren system, these poisitions could not be accurately determined.

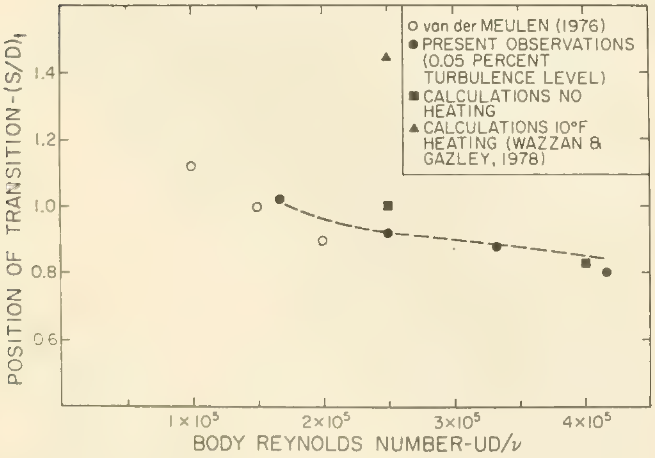

FIGURE 22. Comparison of transition observations on the Schiebe body.

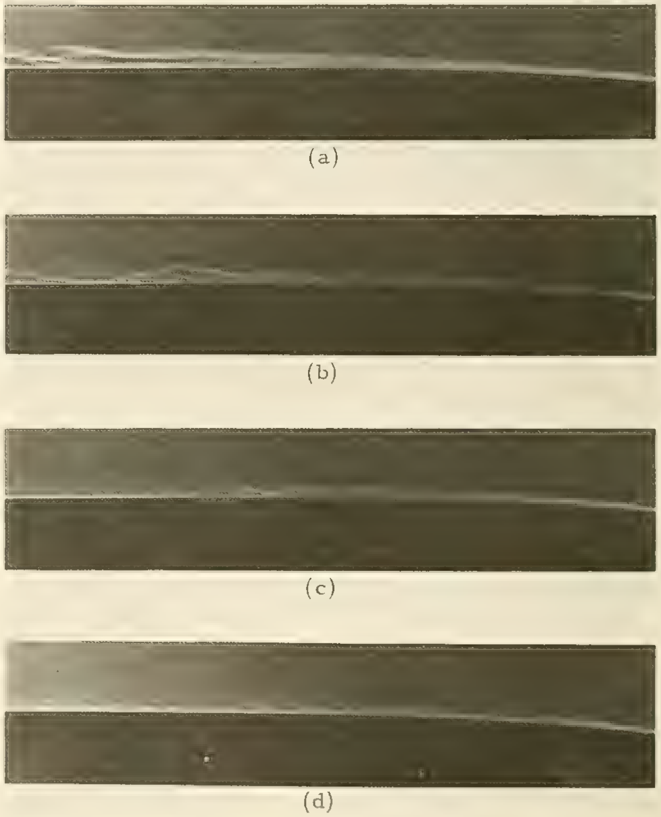

FIGURE 23. Flow past the NSRDC body with injection of 500 wppm Polyox (WSR 301) at a Reynolds number of 1.6×10^5: (a) no injection; (b) 0.1 mℓ/sec, $G = 0.5 \times 10^{-6}$; (c) 0.3 mℓ/sec, $G = 1.5 \times 10^{-6}$; (d) 0.5 mℓ/sec, $G = 2.5 \times 10^{-6}$. G is the dimensionless polymer injection rate.

Discussion

It would seem desirable to normalize somehow the injection rate of polymer fluid. We have chosen to do this by dividing the mass flux of polymer

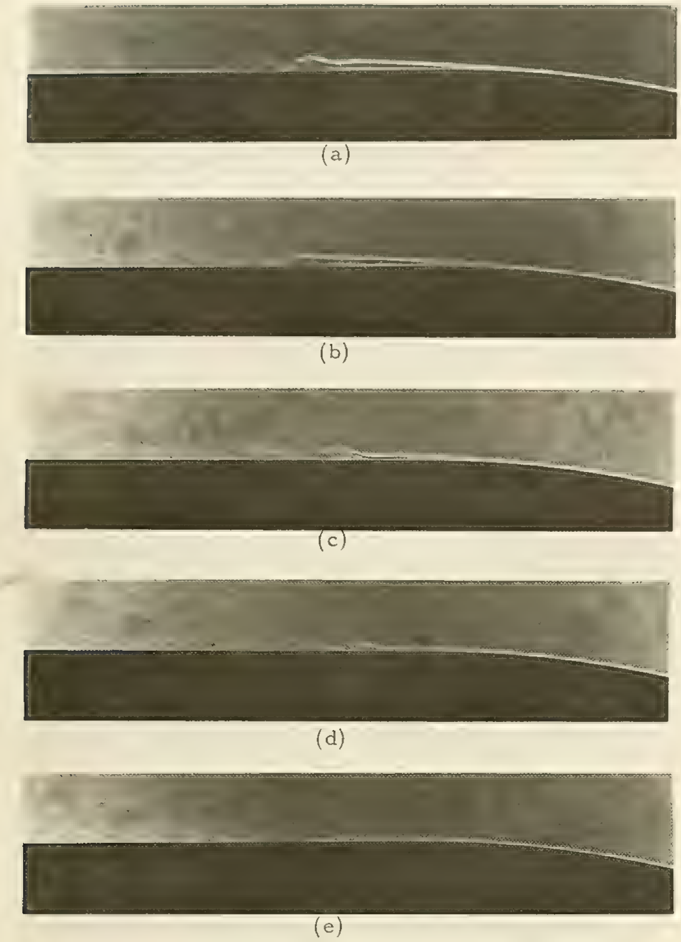

(a)

(b)

(c)

(d)

(e)

FIGURE 24. Flow past the hemisphere body with injection of 100 wppm Polyox at a Reynolds number of 3.9×10^5. The dimensionless injection values are: (a) G = 0, no injection, (b) 0.5×10^{-6}, (c) 1.1×10^{-6}, (d) 1.7×10^{-6}, (e) 2.9×10^{-6}.

material by the mass flux of the boundary layer displacement flow. Although this is an arbitrary normalization, in the present experiments the displacement effect of the injectant fluid was always much less than the boundary layer displacement thickness, δ_t. Thus we define a quantity G

$$G \equiv \frac{cQ}{\pi D V_\infty \delta_{ts}}$$

where c is the polymer concentration (weight basis) in the injectant Q the volume flow rate of injectant (basically the same fluid as the test medium) with D and V_∞ being the body diameter and tunnel velocity respectively. For the NSRDC and hemisphere models δ_{ts} was calculated at the position of the laminar separation whereas for the Schiebe body it was arbitrarily calculated at S/D = 1.00. The present results, so normalized, are presented in Figures 26, 27, and 28. As with the freestream turbulence level, no change in the position of separation on the NSRDC and hemisphere nose models was observed when polymer was injected into the boundary layer.

The results of the experiments show the presence of very small quantities of Polyox to be destabilizing to the laminar boundary layers on the present test models. This destabilization effect has been observed before: in fully developed cavity flows past spheres and cylinders Brennen (1970) observed distortions in the cavity surface and separation line due to the presence of polymer. Brennan attributed the changes in cavity appearance to a polymer induced instability in the wetted surface flow on the headform. Sarpkaya (1973, 1974) investigated the flow of dilute polymer solutions about cylinders and several airfoils and also explained his observations by suggesting a polymer induced instability in the laminar boundary layer. Some later experiments by Tagori et al. (1974) support some of Sarpkaya's speculation for one of the airfoils.

A destabilizing effect is rather contrary to the general impression obtained from the available literature on the effects of drag-reducing polymers on fluid friction [see for example Hoyt (1972)]. We were unable however, to find in the available literature any satisfactory explanation of the effect on transition of the polymer fluids.

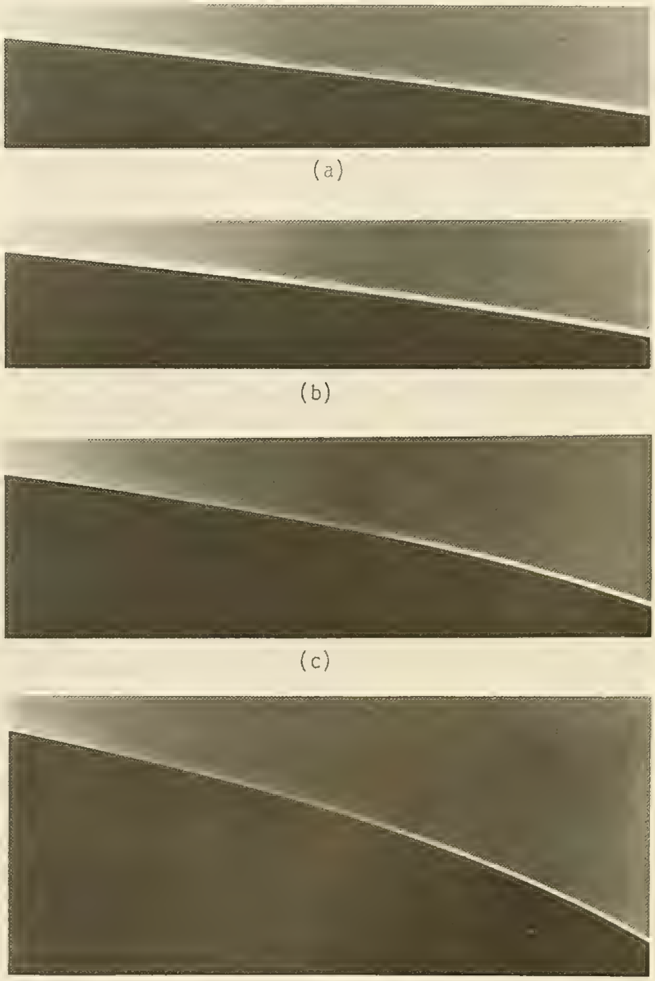

(a)

(b)

(c)

FIGURE 25. Flow past the Schiebe body at a Reynolds number of 4.2×10^5 with injection of 500 wppm Polyox. The dimensionless injection parameters are, (a) G = 0, (b) 2.3×10^{-6}, (c) 1.5×10^{-5}, (d) 2.9×10^{-5}. Each frame is 0.2 body diameters in length and they are centered at arc length ratios of 0.82, 0.75, 0.6, 0.53, respectively.

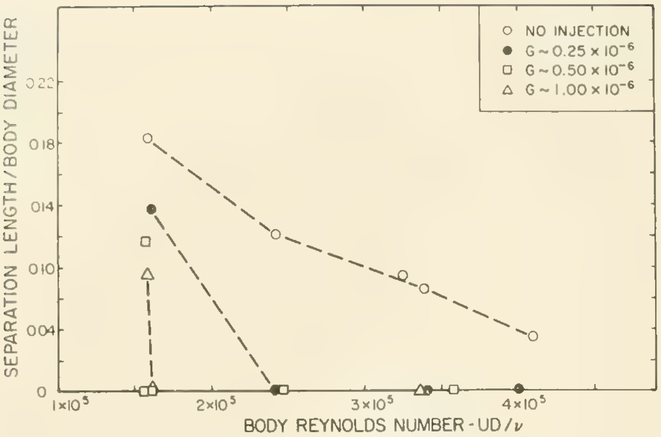

FIGURE 26. The length of the laminar separation as a function of polyox injection on the NSRDC body.

Comparison of Present Results with those of van der Meulen

van der Meulen (1976) has studied the influence of dilute polymer solutions (Polyox, WSR 301) upon the fully-wetted flow and cavitation inception for a hemisphere nose body and was the first, to our knowledge, to observe the Schiebe body ($C_{p_{min}}$ = -0.75). He also was the first to inject the polymer solution at the stagnation point. To observe the flow on the test models, van der Meulen used pulsed ruby laser holography. However, to make the flow visible a salt was added to the polymer solution. In his case the injectant was a 2 percent salt--500wppm Polyox solution.

On the hemisphere nose body he observed that the injection of the salt-polymer solution eliminated the laminar separation and he further speculated that the polymer caused an early transition to a turbulent non-separating boundary layer. On the Schiebe body, which has no laminar separation, the laminar to turbulent transition point was found to move upstream of the no-injection position. The present results for this body are seen to agree qualitatively with those of van der Meulen (Figure 28), although the deduced injection rates of the latter are rather larger. Even though freestream conditions of these two tests may not quite be the same, it is evident because of the nearly one order of magnitude change in Reynolds number that the polymer fluid is the chief agent of boundary layer instability.

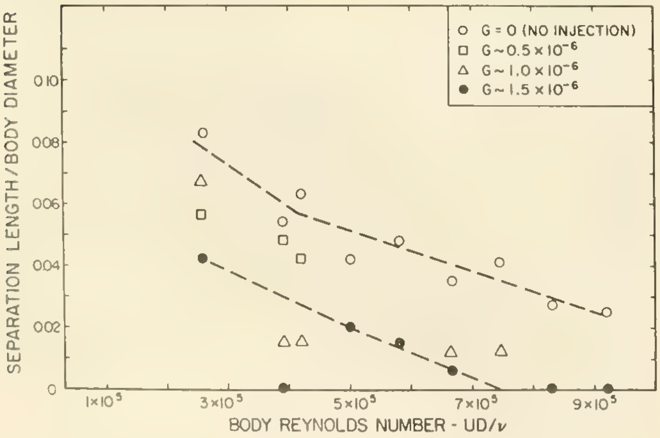

FIGURE 27. The length of the laminar separation as a function of polyox injection on the hemispehre nose body.

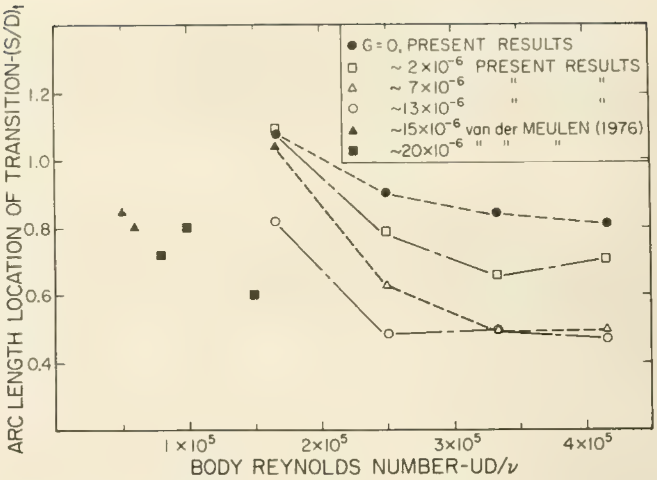

FIGURE 28. The position of transition on the Schiebe body as a function of polymer injection.

5. EFFECT OF FLOW VISUALIZATION ON TRANSITION

It is now well documented that heating a laminar water boundary layer, tends to stabilize it [see for example Wazzan et al. (1968a, 1970)]. This point was further discussed with reference to the hemisphere and ITTC test bodies by Arakeri and Acosta (1973) who concluded that for the separating flows of these bodies, the effect of heating was on the order of only a few percent. Since the heating rate and velocity ranges are similar in the present experiments, it is expected that the influence of heating on the hemisphere and NSRDC bodies is not significant. However, there is some question as to the influence of heating on the non-separating flow on the Schiebe body. Shown in Figure 22 are averaged observed values of the position of transition calculated by Wazzan with and without wall heating. First, it can be seen that there is good agreement between Wazzan's calculation for an unheated boundary layer with e^9 amplification and the observed position of transition. However, the point to be noted is that (with a wall temperature 10°F above the ambient water temperature) these same calculations predict a 40 percent delay in transition at $Re_D = 2.5 \times 10^5$. This would suggest that wall heating is important although not perhaps sufficient to alter major trends in the present experiments. There is however the qualification that the calculation assumes a constant wall temperature while this is not the actual case.

An attempt to measure the actual wall temperature was made by installing six thermocouples near the surface of the model at positions of S/D = 0.4, 0.6, 0.8, 1.0, 1.2, 1.4. The position of neutral stability on this body is S/D = 0.37 and the average position of transition varied from S/D = 1.0 to S/D = 0.8. Since it is the heating in the boundary layer prior to transition that is of importance, the values of the wall temperatures at S/D = 0.4, 0.6, 0.8, 1.0 were of the most interest. The total heat flux was set at 250 watts (about 3W/cm^2) at which the schlieren effect was observable. The wall temperatures were then measured at increasing values of velocity. It was found that the maximum wall temperature between S/D = 0.4 and 1.0 varied from 3°C to 5°C above the ambient temperature. However, it must be emphasized that these are very conservative values since the thermocouples are actually somewhat below the surface in a region of a high temperature gradient. When this gradient is accounted for our estimate of the surface excess temperature is from 1-3°C, a smaller but not negligible amount. van der Meulen avoided the temperature effect by injecting a two percent salt solution. On the whole this method and the present one agree quite favorably (Figure 22). There is, however, the possibility of instability via a destabilizing density gradient. This point was addressed experimentally and in Figure 29 matched pairs of schlieren photographs, without and with salt injection are presented. It was found that although the appearance of the transition changed markedly the location of transition did not change significantly.

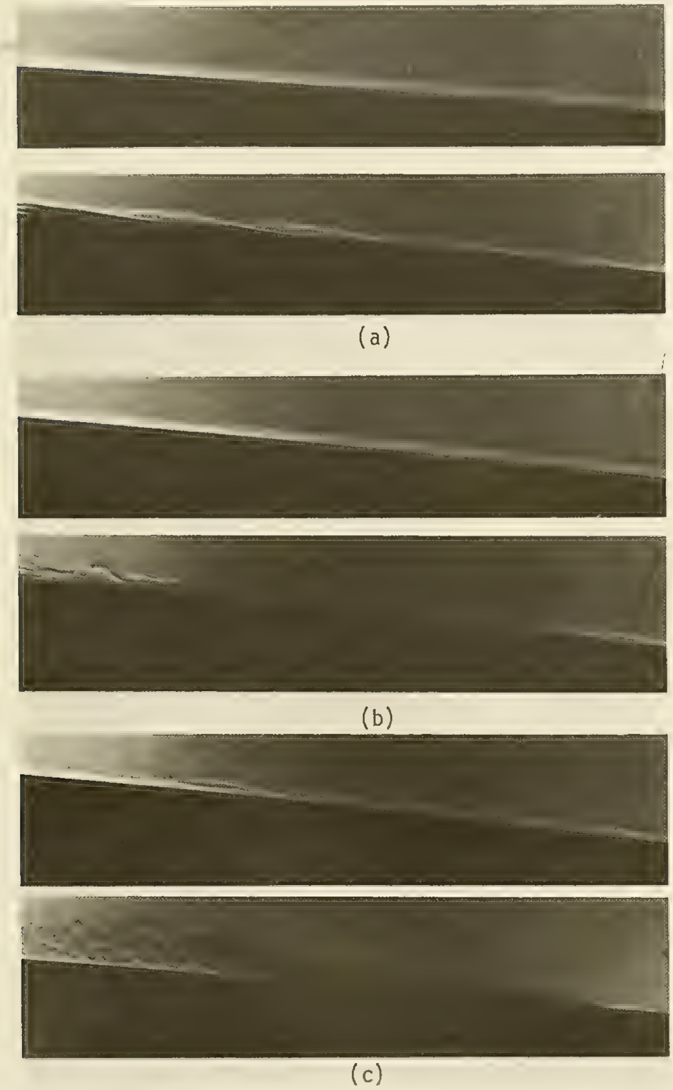
(a)

(b)

(c)

FIGURE 29. Schlieren photographs of the Schiebe body with and without salt water injection. The top photograph of each group is without injection; the bottom photograph shows the injection of MgSO$_4$ solution having a specific gravity of 1.02. The Reynolds number is 1.67×10^5 in (a), 2.50×10^5 in (b), and 3.33×10^5 in (c).

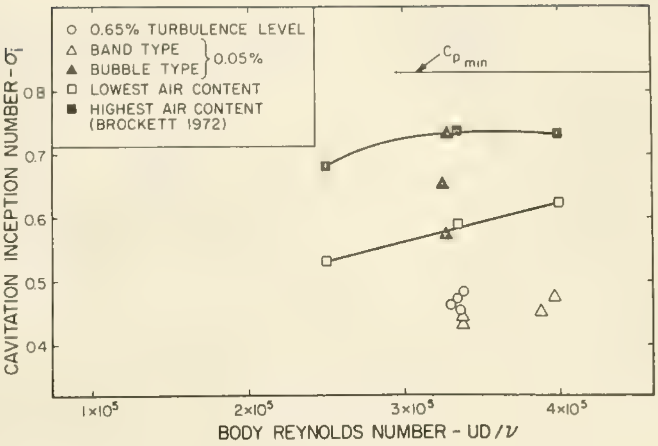

FIGURE 30. Cavitation inception on the NSRDC body.

6. PRESENTATION OF CAVITATION INCEPTION RESULTS

Freestream Turbulence Level

The data on the influence of freestream turbulence level upon cavitation inception is limited because of the low maximum water speed in the LTWT of about 8m/s but more importantly because the turbulence generating grids located at the entrance to the test section cavitated themselves before the test models did. Consequently, only the 0.05 and 0.65 percent turbulence level configurations could be used. The NSRDC body was the only one to be so investigated. Some of these inception data are summarized in Figure 30 where they are compared with Brockett's (1972) data. Inception on the NSRDC body was always of the band type which occurred suddenly without any precursor bubble type cavitation. As can be seen in Figure 30, inception occurred at the same value of the inception index for both turbulence levels, but as illustrated in Figure 31 the subsequent developed cavitation was much less steady at the higher turbulence intensity.

The Effects of Polymer Solutions

Hemisphere Nose Body

The type of cavitation and the value of the inception index were found to be strongly dependent on the amount of polymer present in the boundary layer. For a fixed polymer solution concentration and freestream velocity the following changes in inception were observed to take place: at zero injection rate, incipient band type cavitation as illustrated in Figure 32(a) always occurred. At injection rates less than the critical value (the injection rate at which the separation would disappear), band type inception still occurred but as can be seen in Figure 32(b) the surface of the developed cavitation

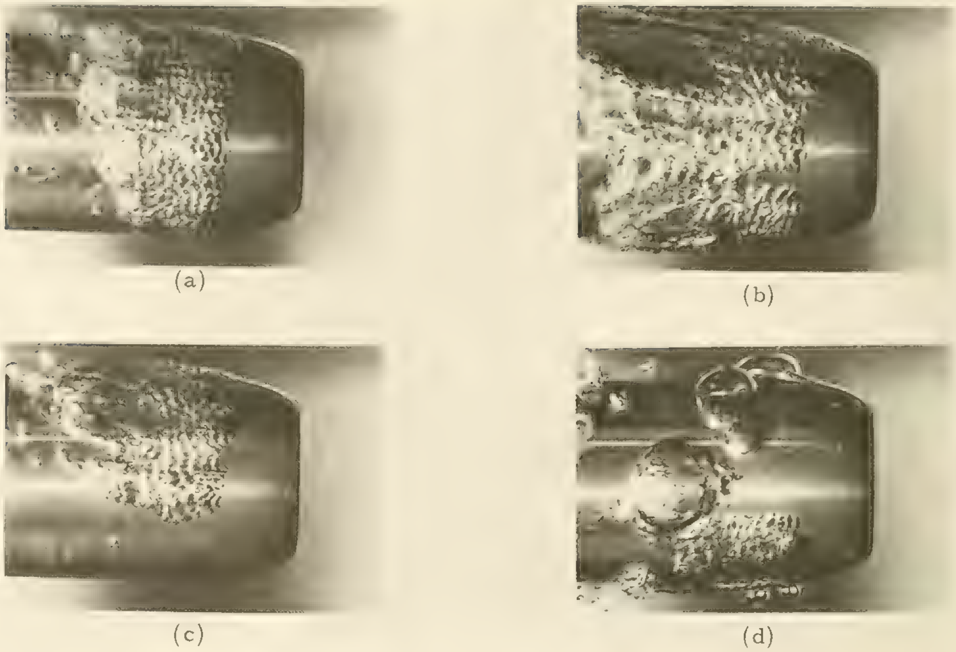

(a) (b) (c) (d)

FIGURE 31. The physical appearance of cavitation on the NSRDC body at two turbulence levels in the LTWT. The Reynolds number is 3.4×10^5. In (a) the turbulence level is 0.05 percent and the cavitation index is 0.44. The turbulence level in the remaining photographs is 0.65 percent and the cavitation index is about 0.35 for all cases.

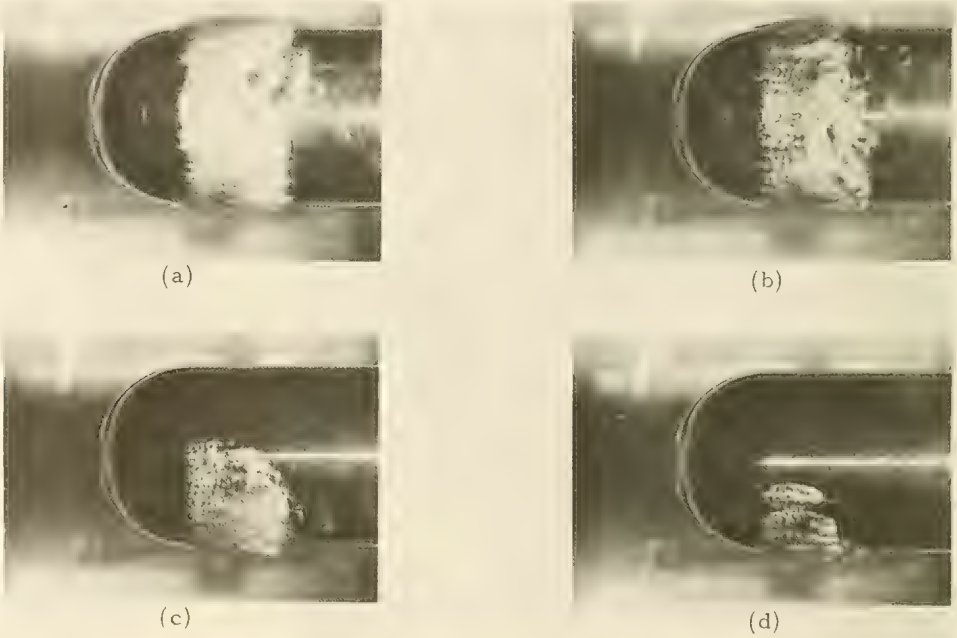

(a) (b) (c) (d)

FIGURE 32. In these photographs 500 wppm of polyox solution is injected at the nose of the hemisphere body. The cavitation index is 0.59, and the Reynolds number is 6.7×10^5 (HSWT). The dimensionless injection rate, G, is zero in (a) 1.9×10^{-6} in (b), 4.4×10^{-6} in (c), and $5.24 \cdot 10^{-6}$ in (d). In many instances the attached cavitation would disappear.

has a definite wave structure and the separation line has become very irregular. Inspection of Schlieren photographs of the fully wetted flow at this injection rate showed that the position of transition on the free shear layer had moved upstream from the no injection case and that the separation region was smaller in size. With a further increase in the injection rate to near critical values, different types of cavitation were observed depending upon the facility. In the HSWT, band type inception would occur intermittently in patches with irregular separation lines and surfaces as is shown in Figure 32(c), (d). At injection rates above the critical value, the same type of behavior took place, but with the flow altering between fully wetted and patchy band type cavitation more rapidly. A decrease in the cavitation number at this injection rate would make the cavitation more "violent," but no steady attached cavitation could be obtained. At these near-and-above critical injection rates the fully wetted observations showed the laminar separation had been eliminated with only an occasional short reappearance. That is, the flow in the region of interest was almost always turbulent. If then the injection rate was suddenly reduced to zero, a large steady cavity would quickly form on the body.

In the LTWT the same sequence of cavitation events with increasing injection rates would occur as in the HSWT. However, near and above critical injection rates, travelling bubble and band type cavitation would occur simultaneously, unlike the HSWT where no bubble type cavitation was observed.

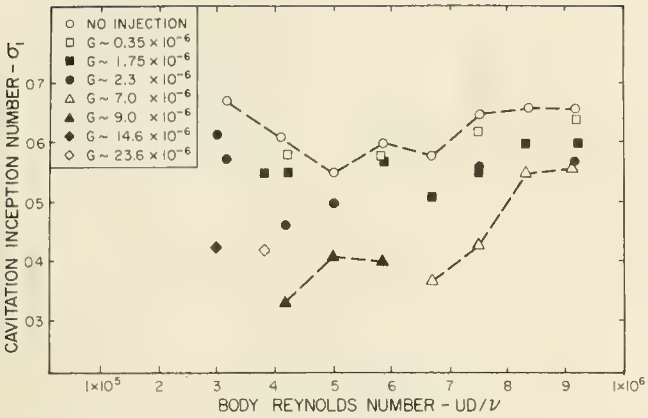

FIGURE 33. Cavitation inception with polymer injection on the hemisphere body.

This difference will be discussed later. These inception data have been summarized in Figure 33.

NSRDC Body

The NSRDC body was tested only in the LTWT and it too was observed to go through a sequence of cavitation development similar to that of the hemisphere nose body in the LTWT; namely, that the injection of polymer at sub-critical rates changed the original band type inception to simultaneously occurring intermittent band and travelling bubble type inception. At above critical injection rates the intermittency became more rapid but still no steady attached cavitation could be obtained. Examples of these types of cavitation are shown in Figure 34. Notice in particular Figure 34(d) where only one cavitation bubble is visible at a cavitation number of 0.34. Values of the inception index versus body Reynolds number are presented in Figure 35.

Schiebe Body

The Schiebe body was tested in both the LTWT and the HSWT, but the influence of polymer was only studied in the LTWT. Again as for the hemisphere nose body, the type of cavitation depended upon the facility. In the LTWT, travelling bubble type inception always occurred and the presence of polymer was found to have *no* significant effect on either the type of cavitation or the inception index. Lowering of the tunnel pressure below the inception value produced a steady, attached cavity of the type normally associated with the presence of a laminar separation. On the other hand, in the HSWT, travelling bubble type cavitation events were extremely rare. Inception occurred with the sudden appearance of an unsteady attached cavity occasionally preceded by one or two travelling bubble events. Examples of these types of cavitation on the Schiebe body are given in Figure 36 and a summary of the inception data is given in Figure 37. A unique location of inception could not be accurately determined in either facility for this body.

7. DISCUSSION

Freestream Turbulence Level

The main purpose of the investigation of freestream turbulence level upon cavitation inception was to determine if it could be a contributing factor to the differences in cavitation results on identical bodies tested in different facilities. In particular, could the differences in cavitation inception on the *same* NSRDC test body between the CIT HSWT and the NSRDC 12-inch tunnel be explained by different

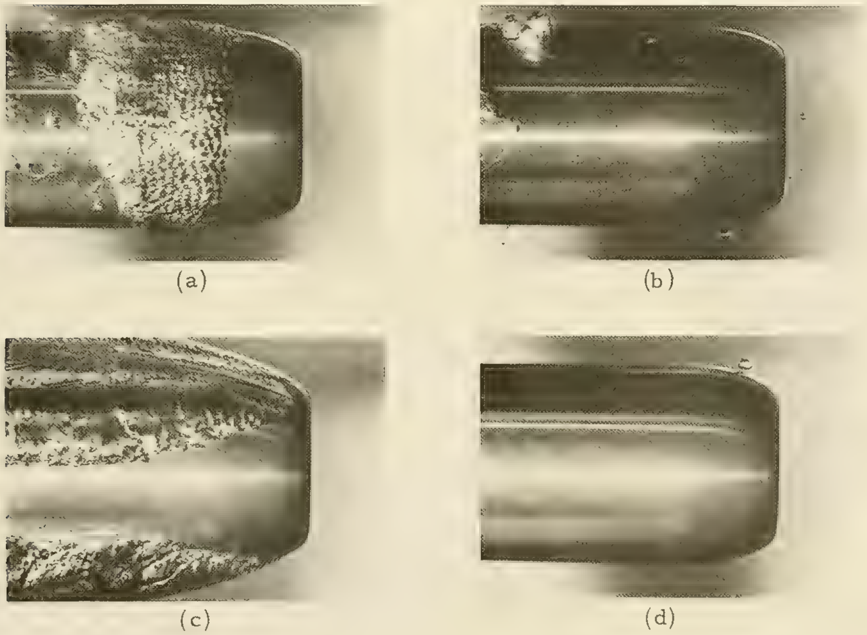
(a) (b)

(c) (d)

FIGURE 34. The physical appearance of cavitation on the NSRDC body at a Reynolds number of 3.4×10^5 in the LTWT with (a) no injection, (b) $G = 3.4 \times 10^{-7}$, cavitation index = 0.45 [same as in (a)], (c) 3.4×10^{-7}, cavitation index = 0.34, and (d) 7.1×10^{-6} at the same index!

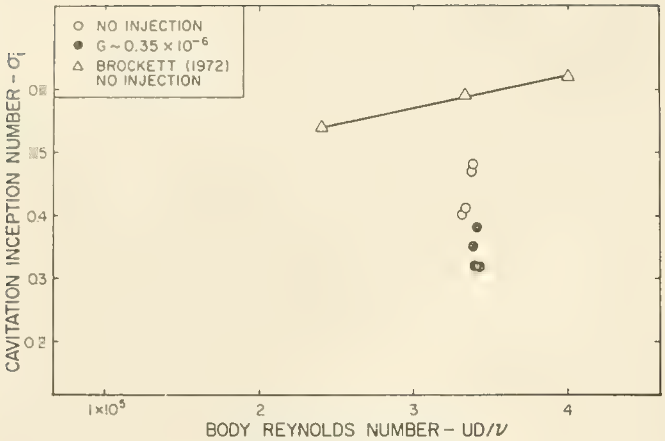

FIGURE 35. Cavitation suppression by polymer injection on the NSRDC body.

turbulence levels? From the proceeding discussion of the fully wetted results it appears that the differences in observed critical Reynolds numbers are probably due to a higher turbulence level in the NSRDC facility. It follows then that the differences in the *type* of inception for velocities less than 30 feet per second can be explained in terms of the different viscous flows. However, we still need to account for the different freestream populations of nuclei, the subject of the next section.

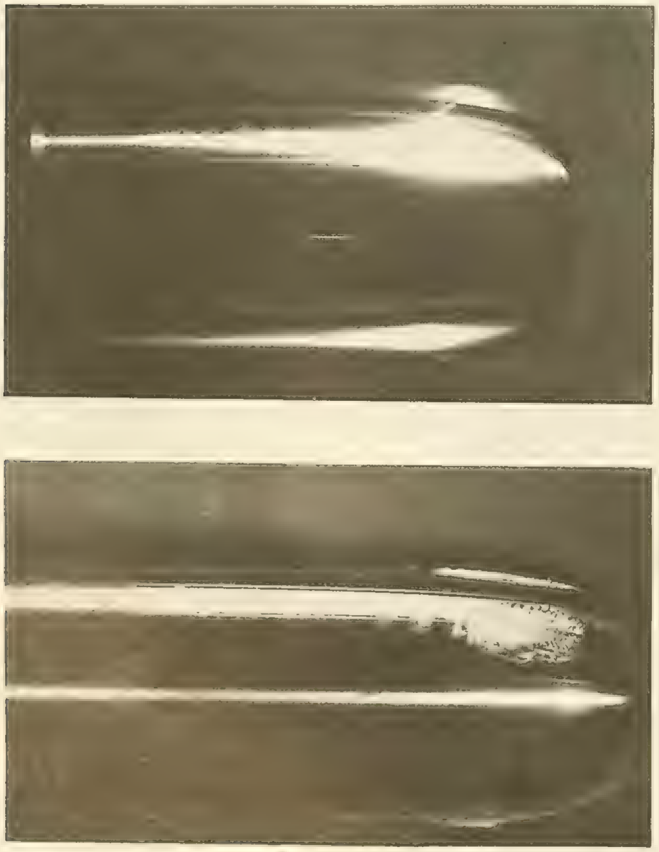

FIGURE 36. Photographs of cavitation on the (same) Schiebe body in the LTWT (upper picture) at a cavitation index of 0.52 and in the HSWT at an index of 0.41. The flow speeds are 7.3 and 14 m/s, respectively.

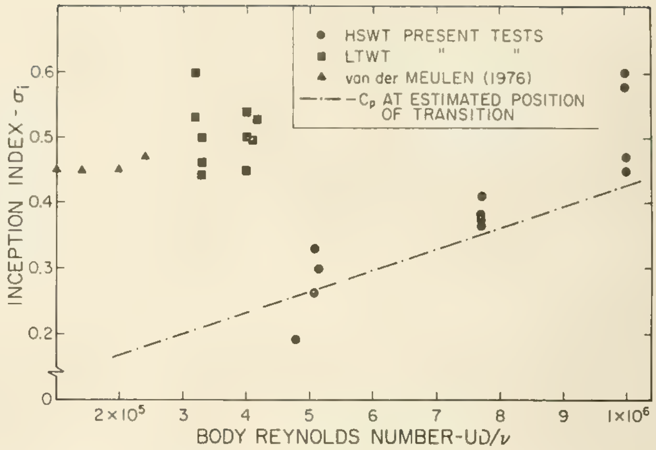

FIGURE 37. Cavitation inception on the Schiebe body in three different facilities.

Polymer Injection

Some inception data for the hemisphere nose body with polymer injections are given in Figure 38 as a function of the injection rate for two concentrations. The *same* data have been replotted in Figure 39 against the non-dimensional injection parameter G. It can readily be seen that the two curves have collapsed onto one. A similar happy result was found when the dimensions of the laminar separation bubble on the hemisphere nose body were plotted versus the parameter G. These correlations of the inception index and separation bubble dimensions with G implies that the polymer "effectiveness" is proportional only to the amount present within the boundary layer, here taken to be the displacement thickness.

For the NSRDC and hemisphere nose bodies it can be seen that increasing amounts of polymer in the boundary layer produce an increasing suppression

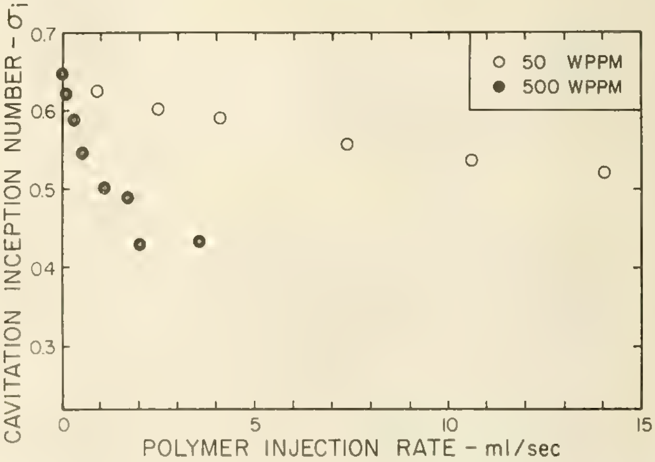

FIGURE 38. Cavitation index with polymer injection on the hemisphere body at a Reynolds number of 7.5×10^5.

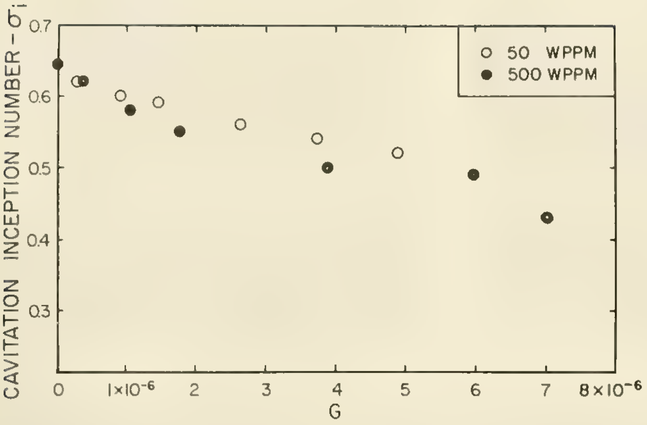

FIGURE 39. The data of figure 38 replotted against the dimensionless injection parameter G.

of cavitation index. There is a limit, however, beyond which no further increase in cavitation suppression occurs. In the present experiments on the hemisphere nose body this limiting value of G is approximately 7×10^{-6} which also coincides with the removal of the laminar separation. These results and others are summarized in Figure 40 where the maximum percent reduction in cavitation index has been plotted versus the Reynolds number. These include the "polymer ocean" results of Baker et al. (1973), Holl et al. (1974), and Ellis et al. (1970). However, the information from their reports is limited and all that can be said is that they give values approximately the same as those noted in the present case. The agreement is believed to be reasonably good for experiments of this type insofar as the maximum effect goes. We presume that similar effects in "ocean" experiments could be achieved at much smaller concentrations if the G parameter has significance.

During their cavitation tests Baker and Holl noted a change in the appearance of the developed cavitation. From photographic observations of these changes they speculated that the cavitation attenuation was due to a "flow reorientation in the region of the laminar separation bubble." They further suppose [Arndt et al. (1975)] that the amount of attenuation might depend on a Deborah number, TV_∞/δ_S, where T is the molecular relaxation time of the molecule, V_∞ the freestream velocity, and δ_S is the boundary layer displacement thickness at separation. It now seems clearly established in our opinion, that the overall gross effect caused by the polymer in the flow about these bodies is a removal of the laminar separation by stimulation of transition and that this is indeed the origin of the flow "reorientation" noted by Baker and Holl. Presumably, the molecular relaxation time has an important role in boundary layer stability, but as yet this appears to be unknown; it may be that the parameter proposed by Arndt is important for some laminar flows with separation (as it is indeed for the flow about a circular cylinder), but we think not in the context of the present experiments.

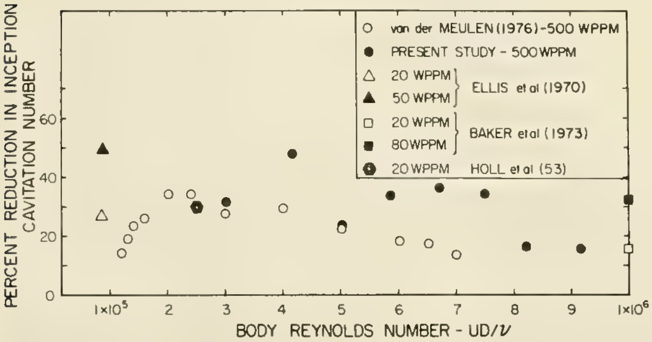

FIGURE 40. Maximum cavitation inception index suppression by polyox WSR 201 on the hemisphere nose. The Ellis and Baker results are for polymer "oceans."

Since the suppression of cavitation upon these bodies is a result of the elimination of the laminar separation by the polymer it is worthwhile to compare the present results with those in which the separation is eliminated by another method. Arakeri and Acosta (1976) carried out a series of tests with a hemisphere nose body and an ITTC body using boundary layer trips to reduce the critical Reynolds number in the HSWT. It was, briefly, found that with the trip present and at velocities above the new critical velocity, the occurrence of cavitation was significantly suppressed, and that at higher velocities the tunnel would choke from the model support before the body could be made to cavitate! The present polymer tests show a very similar large effect on inhibiting cavitation but not quite as dramatic as the tripped tests.

8. FREESTREAM NUCLEI AND CAVITATION INCEPTION

Some Observations in the LTWT

As will be recalled from the description of the LTWT, this facility has no resorber which necessitated cavitation data acquisition before pump-generated bubbles entered the test section. On a number of occasions the cavitation on the NSRDC and hemisphere bodies was deliberately maintained and the pump-generated gas bubbles allowed to pass through the test section. As the number of free gas bubbles increased, the initially-occurring band type cavitation was gradually destroyed and replaced by travelling bubble type cavitation. An alternative procedure was to lower tunnel static pressure so that the cavitation number had a value below $-C_{P\min}$ but above the inception value and again allow the pump-generated bubbles to accumulate. The body would then eventually cavitate with inception then always being of the travelling bubble type. Schlieren observations of the basic viscous flow on the hemisphere nose were made at these gradually increasing freestream bubble populations and nuclei populations were measured when band type inception occurred and when this above deliberately-promoted bubble type inception occurred. The schlieren observations show (see Figure 41) that as the number of freestream nuclei increased, the laminar separation on the hemisphere nose became unsteady and was finally greatly diminished if not eliminated. Thus, in effect, the free-stream bubbles serve to trip the boundary layer.

Nuclei populations obtained when band type inception occurred ($\sigma_i = 0.44$) are shown with distributions obtained when deliberately promoted travelling bubble inception occurred ($\sigma_i = 0.58$, 0.73) in Figure 42. As can be seen in this figure, for

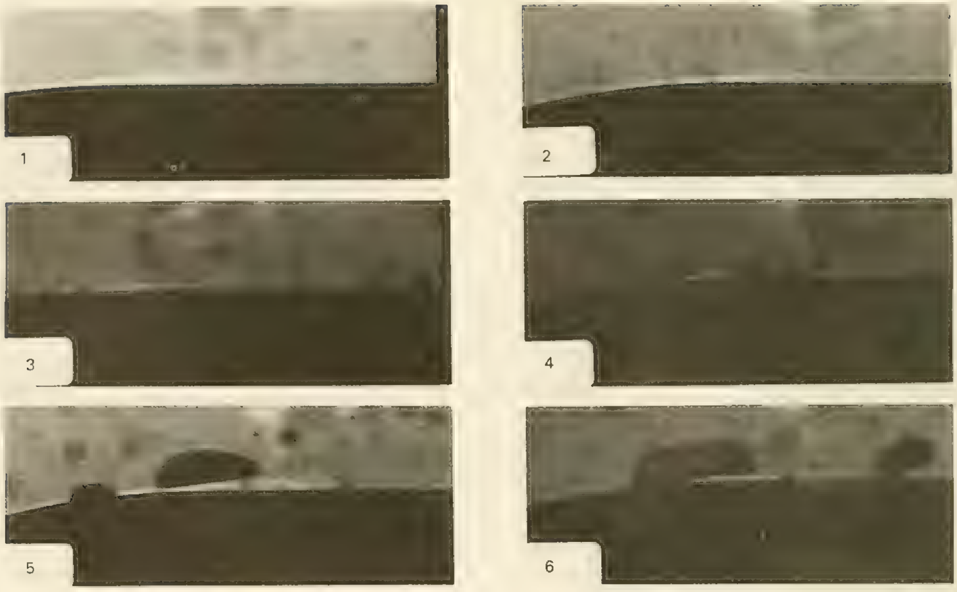

FIGURE 41. Flow past the hemisphere nose with many freestream bubbles showing boundary layer stimulation.

nuclei with radii less than 100 microns all the distributions are essentially the same whereas for nuclei greater than 100 microns radius the bubble-type inception distributions have many more nuclei than the band type inception distributions. Thus it seems possible that in facilities with many macroscopic freestream gas bubbles, the normally occurring laminar separation on some bodies can be eliminated. The subsequent cavitation index and form of cavitation should then be controlled by the nuclei population.

If so, the experiments on the NSRDC body at that facility and those tests on the same body in the LTWT, when bubble type inception was deliberately promoted, should be very similar. This is, in fact, the case as the inception numbers are more-or-less the same. Beyond that, nuclei distributions are known for the two tests [Peterson (1972) and Figure 42] so that, following the philosophy of Silberman et al. (1974), it is possible to estimate the number of "cavitable" nuclei per unit volume for each experimental point. A rough estimate of the number of travelling cavitation events can be easily made if we take Johnson and Hsieh's (1966) "capture" radius of 0.01 body radius to determine the flux of fluid through the cavitating region. These data, calculated and measured events are tabulated in Table 3. Peterson measured the event rate acoustically and chose one event/sec as the threshold level because of the agreement with a "visual" inception estimate. (Only the visual estimate was made in the LTWT.)

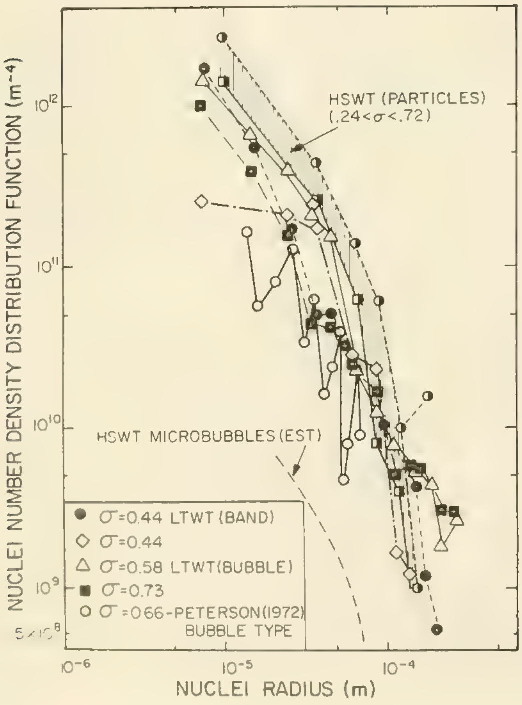

FIGURE 42. Nuclei distributions measured by holography in the LTWT (all microbubbles) and in the HSWT (essentially only solid particles).

Observation in the HSWT

On the whole, the agreement of observations and event rates is satisfactory and it seems clear in this circumstance that viscous effects are not of primary importance and that travelling bubble cavitation, the type studied by the St. Anthony Falls group, is the prevalent form. But, on all of the bodies studied we have seen different forms of cavitation occur, when separation was not present, if the number of freestream nuclei is very small, as it is presumably in the California Institute of Technology HSWT and other resorber facilities. Then, even on the Schiebe body we see attached forms of cavitation at inception (see Figure 36) at very low inception indices with only rare occurrences of travelling bubble cavitation [see also Arakeri et al. (1976)]. In these circumstances the fluid and the nuclei that it contains pass through regions of some tension (up to about 1/2 at m in the HSWT). It is conceivable then that the substantial pressure fluctuations in transition regions [Huang and Hannon (1975)] can initiate cavitation. This is the rationale for Arakeri's (1975) inception-transition pressure coefficient correlation. Values of $-c_{ptr}$

TABLE III CAVITATION EVENT RATES

Facility	Model Mat'l.	σ_1	U_∞ (ft/sec)	R_c (microns)	Cavitatable Nuclei/cm^3 (est)	Calculated Events/sec	Measured Events per sec
NSRDC	CU	0.62	29.86	12	0.5	0.9	1.0
	CU	0.66	29.86	15	1.8	3.2	1.0
	AU-Plated	0.65	29.86	14	2.1	3.8	1.0
	DELRIN	0.69	29.86	18	0.5	0.9	1.0
	DELRIN	0.71	29.86	21	2.4	4.3	1.0
LTWT	CU	0.58	20.15	21	8.9	10.7	--
	CU	0.64	20.10	29	2.0	2.4	--
	CU	0.66	20.15	32	0.9	1.1	--
	CU	0.73	20.25	58	1.7	2.0	--

are also shown for the Schiebe body in Figure 37; again the correlation is suggestive but not conclusive.

Further evidence of the difference between a resorber facility and a recirculating tunnel is given by the nuclei distributions of the flow in the California Institute of Technology HSWT. These data are averaged in the graph of Figure 42. Following Peterson (1972) it is possible to distinguish particulate matter from gaseous microbubbles down to about 10 micrometers. Thus we identify solid particulates on the one hand and microbubbles on the other. All of the nuclei reported in Figure 42 for the LTWT are microbubbles. It is significant that the HSWT shows a very similar distribution of *solid particulates,* but very few microbubbles. In about ten holograms made of the HSWT flow, within the various sample volumes that were counted, about 100 particles/cm^3 on the average were found. However, of these, *less* than one on the average was a microbubble, too few even to hazard a guess as to the distribution. This finding certainly tends to explain the experimental trends in this facility if it is assumed (as appears evident) that the solid particulates do not act as nucleating sources.

In closing this section we have perhaps come full circle in inception research to re-emphasize the important role of the cavitation nuclei. The influence of laminar inception on cavitation is now much clearer as are the effects of the processes that cause stimulation of the boundary layer. If there are many nuclei present (so that a large tension on the body does not exist prior to cavitation) it is likely that travelling bubble cavitation will predominate, then the notion of a "standard body" to deduce cavitation susceptibility appears to be useful. However, with only a few nuclei other more complex forms of cavitation are seen at inception.

Comparison of Nuclei Distributions

Data from several other investigations, reduced to the number density distribution function, N(R), by the following approximation

$$N\left(\frac{R_1 + R_2}{2}\right) = \frac{\text{number of nuclei per unit with radii between } R_1 \text{ and } R_2}{(R_2 - R_1)}$$

are shown in Figure 43. A tabulation of the measuring techniques and test conditions for each investigation is given in Table 4. All the data have approximately the same slope, but the values of the distribution function can differ by several orders of magnitude, i.e., although the nuclei population changed by several orders of magnitude, the distribution of the nuclei sizes remains constant. The large differences in populations is undoubtedly a consequence of the large variation in conditions which existed in the water when the data was collected and is no doubt one of the contributing factors to the lack of repeatability seen in cavitation tests.

A goal of cavitation research is to be able to predict the inception of cavitation and thus be able to scale laboratory results to prototype conditions. It is interesting then to compare nuclei populations in water tunnels to those in the ocean. Medwin acoustically measured bubble populations in the ocean near Monterey, California, and in Figure 43 two of his measured distributions are presented. The summer distribution agrees reasonably well with the distributions obtained under cavitating conditions in strongly deaerated water. However, in the LTWT there are considerably more bubbles than found in the ocean for radii greater than about 30

TABLE IV COMPARISON OF NUCLEI MEASUREMENTS

Investigator	Measuring Technique	Facility	Conditions at time of Measurement
Gavrilov (1970)	Acoustic	--	Standing tap water
Peterson et al (1975)	Light Scattering Holography Microscopy	Water Tunnel at TDF	At inception on 50 mm diameter NSRDC body $\sigma=0.49$
Arndt & Keller (1976)	Light Scattering	Water Tunnel at NSMB	Cavitation tests on a sharp edged disc. Air contents: 6.3 and 12.5 ppm
Keller & Weitendorf (1976)	Light Scattering	Water Tunnel at Hamburg Model Basin	Propeller test, gassed water, Air content: ~30 ppm
Medwin (1977)	Acoustic	Monterey Bay, California	Various depths and seasons
Peterson (1974)	Coulter Counter	Santa Catalina Channel California	Various depths
U.S. Navy (Naval Ocean System Center, San Diego, California. Courtesy Dr. T. Lang)	Coulter Counter	San Diego Bay and offshore	Various depths
Present Tests	Holography	LTWT	Air content ~ 7 ppm, $\sigma=0.44$

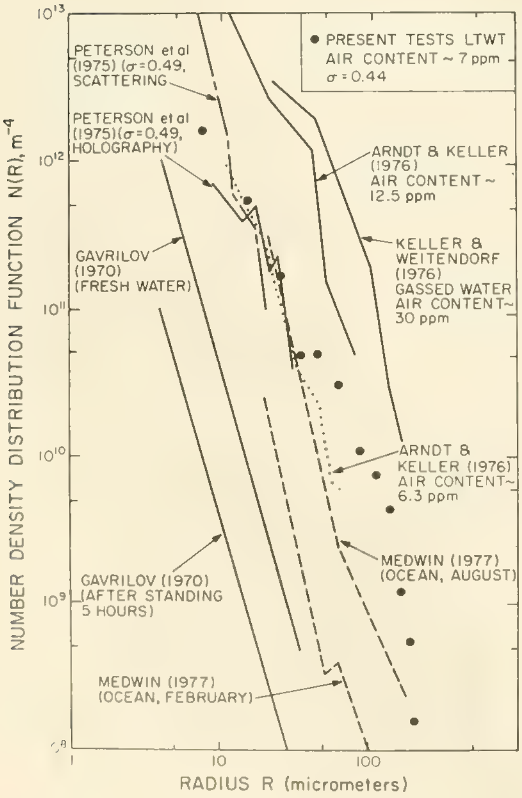

FIGURE 43. Nuclei distributions from various sources.

micrometers. Further, in the winter the measured bubble population in the ocean is one order of magnitude less than in the summer. We see then it is actually possible for laboratory facilities to have much higher nuclei populations than actually occur in the ocean. Medwin concludes interestingly that the microbubbles had a biological as well as physical origin because the concentration of bubbles increased with depth. This observation is perhaps of importance for the Coulter Counter measurements of Peterson (1974) and Lang (1977). The particulates measured there, although thought to be of organic material, may actually also contain some gas. Finally, it is amazing to observe the wide range of applicability of fairly simple power laws for particulate and microbubble populations.

9. CONCLUSIONS

It is clear that the onset of cavitation and its physical appearance at this onset can be greatly affected by freestream turbulence and the presence of minute amounts of long chain polymer solutes. The present results support the conclusion that these effects are indirect insofar as cavitation goes and that the primary effect is on the viscous flow past the test body. The polymer solutions in particular promote an early boundary layer transition which forestalls the presence of laminar separation much as does boundary layer stimulation by freestream turbulence or trips. It follows that cavitation on bodies not having laminar separation should not be much affected by freestream turbulence or polymer solutions. This appears to be the case if the test medium has "many" freestream nuclei so that travelling bubble cavitation is predominant. However, if only a few nuclei are present, attached forms of cavitation occur at inception even on nonseparating bodies. From recent nuclei measurements in the ocean it appears that some test facilities may have too many nuclei and others possibly too few.

ACKNOWLEDGMENTS

This work was supported by the Department of the Navy, Office of Naval Research under Contract N00014-76-C-0156 (in part) and by the Naval Sea Systems Command, General Hydromechanics Research Program, administered by the David W. Taylor Naval Ship Research and Development Center under Contract N00014-75-C-0378. This assistance is gratefully acknowledged. Special thanks are due to Mrs. Barbara Hawk for manuscript preparation and to Joseph Katz and David Faulkner for their painstaking efforts in hologram analysis. Finally we thank Professor M. Morkovin for his careful and helpful review of the manuscript.

REFERENCES

Acosta, A. J., and H. Hamaguchi (1967). Cavitation inception on the ITTC standard headform. *Hydrodynamics Laboratory, Report No. E-149.1, California Institute of Technology.*

Acosta, A. J., and B. R. Parkin (1975). Cavitation inception--A selective review, *J. Ship Res., 19,* 4; 193-205.

Arakeri, V. H., and A. J. Acosta (1973). Viscous effects in inception of cavitation on axisymmetric bodies. *J. Fluids Eng. 95,* Ser. 1, 4; 519-528.

Arakeri, V. H. (1975). A note on the transition observations on an axisymmetric body and some related fluctuating wall pressure measurements. *J. Fluids Eng., 97,* Ser. 1, 1; 82-87.

Arakeri, V. H., and A. J. Acosta (1976). Cavitation inception observations on axisymmetric bodies at supercritical Reynolds numbers. *J. Ship Res., 20,* 1; 40-50.

Arndt, R. E. A., M. L. Billet, J. W. Holl, and C. B. Baker (1975). A note on the inhibition of cavitation in dilute polymer solutions. *App. Res. Lab. Tech. Memo. 75-285, The Penn. State Univ.*

Arndt, R. E. A. and J. W. Daily (1969). Cavitation in turbulent boundary layers. *Cavitation State of Knowledge,* ASME; 64-86.

Arndt, R. E. A. and A. P. Keller (1976). Free gas content effects on cavitation inception and noise in a free shear flow; Two phase flow and cavitation in power generation systems. *IAHR Symp. Grenoble,* March 16, 1976.

Baker, C. B., R. E. A. Arndt, and J. W. Holl (1973). Effect of various concentrations of WSR-301 polyethylene oxide in water upon the cavitation performance of 1/4-inch and 2-inch hemispherical nosed bodies. *App. Res. Lab. Tech. Memo. 73-257, The Penn. State Univ.*

Beckwith, T. G., and N. L. Buck (1961). *Mechanical Measurements.* Addison-Wesley, Reading, Mass.

Brennen, C. (1970). Some cavitation experiments with dilute polymer solutions. *J. of Fluid Mech., 44,* part 1; 51-63.

Brockett, T. (1972). Some environmental effects on headform cavitation inception. *NSDRC Rep. 3974.*

Cavitation Committee (1969). Summary of replies to questionnaire on water tunnel methods. *12th ITTC.*

Debrule, P. M. (1972). Friction and heat transfer coefficients in smooth and rough pipes with dilute polymer solutions. *Ph.D. Dissertation, California Institute of Technology.*

Ellis, A. T., J. G. Waugh, and R. Y. Ting (1970). Cavitation suppression and stress effects in high-speed flows of water with dilute macromolecular additives. *J. of Basic Eng.,* Sept.; 459-466.

Feldberg, L. A., and K. T. Shlemenson (1973). The holographic study of cavitation nuclei. *Discussion to Proc. IUTAM Symp. on Nonsteady Flow of Water at High Speeds.* Leningrad, USSR (English version; Moscow 1973); 106-111.

Gates, E. M., and J. Bacon (1978). Determination of cavitation nuclei distributions by holography. *J. Ship Res. 22,* 1; 29-31.

Gavrilov, L. R. (1970). Free gas content of a liquid and acoustical techniques for its measurement. *Sov. Phys-Acoustics, 15,* 3; 285-295.

Hall, D. J., and J. C. Gibbings (1972). Influence of stream turbulence and pressure gradient upon boundary layer transition. *J. of Mech. Eng. Sci., 14,* 2; 134-146.

Holl, J. W., and A. L. Treaster (1966). Cavitation hysteresis. *J. of Basic Eng., Trans. ASME,* Ser. D, *88,* 1; 199-212.

Holl, J. W. (1968). Sources of cavitation nuclei. Pres. at the 15th *Amer. Towing Tank Conf.,* Ottawa, Canada.

Holl, J. W., and A. L. Kornhauser (1969). Thermodynamic effects on desinent cavitation on hemispherical nosed bodies in water of temperatures from 80 degrees F to 260 degrees F. Pres. at the *Joint Conf. of App. Mech. and Fluids Eng. Divisions,* ASME, Northwestern Univ. ASME paper No. 69-FE-1.

Holl, J. W., R. E. A. Arndt, M. L. Billet, and C. B. Baker (1974). Cavitation research at the Garfield Thomas Water Tunnel. *App. Res. Lab. Tech. Memo. 74-62, The Penn. State Univ.*

Hoyt, J. W. (1966). Effects of High-polymer solutions on a cavitating body. *Proc. 11th ITTC, Tokyo.*

Hoyt, J. W. (1972). The effects of additives on fluid friction. *J. of Basic Eng.,* June; 258-285.

Huang, T. T., and D. E. Hannan (1975). Pressure fluctuations in the regions of flow transitions. *DTNSRDC Rep. 4723.*

Jaffe, N. A., T. T. Okamura, and A. M. O. Smith (1970). Determination of spatial amplification factors and their application to predicting transition. *AIAA J., 8,* 2; 301-308.

Johnson, Jr., V. E., and T. Hsieh (1966). The influence of the trajectories of gas nuclei on cavitation inception. *6th Symp. on Nav. Hydro.*

Johnsson, C. A. (1969). Cavitation inception on headforms, further tests. *12th ITTC,* Rome; 381-392.

Keller, A. P. (1972). The influence of the cavitation nucleus spectrum on cavitation inception, investigated with a scattered light counting method. *J. of Basic Eng.,* Dec.; 917-925.

Knapp, R. T., J. Levy, J. P. O'Neill, and F. B. Brown (1948). The Hydrodynamics Laboratory of the California Institute of Technology. *Trans. ASME, 70*; 437-457.

Knapp, R. T., J. W. Daily, and F. G. Hammitt (1970). *Cavitation.* McGraw-Hill, New York.

Lang, T. G., (1977). Naval Ocean Systems, Private Comm.

Lindgren, H., and C. A. Johnsson (1966). Cavitation inception on head forms ITTC comparative experiments. *Pub. of the Swedish State Shipbuilding Exper. Tank, No. 58.* (Also presented at the 11th ITTC Tokyo, 1966).

Loehrke, R. I., and H. M. Nagib (1972). Experiments on management of freestream turbulence. *AGARD Rep. No. 598.*

Mack, L. M. (1977). Transition and laminar instability. *J. P. L. Pub. 77-15.*

Medwin, H. (1970). In situ acoustic measurements of bubble populations in coastal ocean waters. *J. Geophys. Res. 75*, 599-611.

Medwin, H. (1977). In situ acoustic measurements of microbubbles at sea. *J. Geophys. Res. 82*, 6, 921-976.

Morgan, W. B. (1972). Air content and nuclei measurements. *13th ITTC, Rep. of Cavitation Comm.*

Morgan, W. B., and F. B. Peterson (1977). Cavitation inception. *18th Amer. Tow. Tank Conf.*, U.S. Naval Acad., Annapolis, Md.

Parkin, B. R., and R. W. Kermeen (1953). Incipient cavitation and boundary layer interaction on a streamlined body. *Hydro. Lab. Rep. E-35.2, California Institute of Technology.*

Peterson, F. B. (1968). Cavitation originating at liquid-solid interfaces. *NSDRC Rep. 2799.*

Peterson, F. B. (1972). Hydrodynamic cavitation and some considerations of the influence of free gas content. *9th Symp. on Naval Hydro.*

Peterson, F. B., F. Danel, A. Keller, and Y. Lecoffe (1975). Determination of bubble and particulate spectra and number density in a water tunnel with three optical techniques. *14th ITTC.*

Peterson, L. L., (1974). The propagation of sunlight and the size distribution of suspended particles in a municipally polluted ocean water. *Ph.D. Thesis, California Institute of Technology.*

Reshotko, E. (1976). Boundary-layer stability and transition. *Ann. Rev. of Fluid Mech., 8*; 311-349.

Sarpkaya, T., P. G. Rainey, and R. E. Kell (1973). Flow of dilute polymer (Polyox WSR-301) solutions about circular cylinders. *J. of Fluid Mech., 57*; 177-208.

Sarpkaya, T. (1974). On the performance of hydrofoils in dilute Polyox solutions. *Int'l. Conf. on Drag-Reduction,* Churchill Coll., Cambridge, England, 4-6 Sept.

Schiebe, F. R. (1966). Cavitation occurrence counting--a new technique in inception research. *Cavitation Forum, ASME,* N.Y., 8-9.

Schiebe, F. R. (1972). Measurement of the cavitation susceptibility of water using standard bodies. *St. Anthony Falls Hyd. Lab. Project Rep. No. 118, Univ. of Minn.*

Silberman, E., F. Schiebe, and E. Mrosla (1973). The use of standard bodies to measure the cavitation strength of water. *St. Anthony Falls Hyd. Lab., Rep. No. 141, Univ. of Minn.*

Spangler, J. G., and C. S. Wells, Jr. (1968). Effects of freestream disturbances on boundary layer transition. *AIAA J., 6;* 543-545.

Tagori, T., K. Masunaga, H. Okamoto, and M. Suzuki (1974). Visualization of flow of dilute polymer solutions around two-dimensional hydrofoils. *2nd Symp. of Flow Visualization*, Univ. of Tokyo, July; 83-88.

Ting, R. Y., and A. T. Ellis (1974). Bubble growth in dilute polymer solutions. *Physics of Fluids, 17*, 7; 1461-1462.

Tsuji, H. (1956). Experimental studies on the spectrum of isotropic turbulence behind two grids. *J. of Phys. Soc. of Japan, 11*, 10; 1096-1104.

van der Meulen, J. H. J. (1972). Cavitation on hemispherical nosed teflon bodies. *Int'l. Shipbuilding Prog., 19*, 218; 333-341.

van der Meulen, J. H. J. (1973). Cavitation suppression by polymer injection. *ASME Cavitation and Polyphase Flow Forum,* N.Y.; 48.

van der Meulen, J. H. J. (1976). A holographic study of cavitation on axisymmetric bodies and the influence of polymer additives. *Doctoral Thesis, Netherlands Ship Model Basin.*

van der Walle, F. (1962). On the growth of nuclei and the related scaling factors in cavitation inception. *4th Symp. on Naval Hydro.*

van Driest, E. R., and C. B. Blumer (1963). Boundary layer transition: freestream turbulence and pressure gradient effects. *AIAA J., 1,* 6; 1303-1306.

Vanoni, V. A., E. Hsu, and R. W. Davies (1950). Dynamics of particulate matter in fluid suspensions. *Hydro. Lab. Rep. No. 71.1a, California Institute of Technology.*

Wazzan, A. R., T. T. Okamura, and A. M. O. Smith (1968a). The stability of water flow over heated and cooled flat plates. *J. of Heat Transfer,* Feb.; 109-114.

Wazzan, A. R., T. T. Okamura, and A. M. O. Smith (1968b). Spatial and temporal stability charts for the Falkner-Skan boundary layer profiles. *D.A.C. rep. 67086, McDonnell Douglas Corp.*

Wazzan, A. R., G. Keltner, T. T. Okamura, and A. M. O. Smith (1972). Spatial stability of stagnation water boundary layer with heat transfer. *Physics of Fluids, 15*, 12; 2114-2118.

Wazzan, A. R., C. Gazley, Jr. (1978). The combined effects of pressure gradient and heating on the stability and transition of water boundary layers. *Rand Rept. R-2175-ARPA.*

Wu, J. (1971). Some techniques of ejecting additive solutions for drag reduction. *Hydronautics Technical Rept. 7101-1.*

Additional Reference*

van Ingen, J. L. (1977). "Transition, pressure gradient, suction, separation and stability theory," paper 20 *AGARD proc. CP-224.*

---

[*] Suggested by Professor M. V. Morkovin

Discussion

M. A. WEISSMAN

My question was "What is your definition of growth rate?" This is quite a crucial point, for in comparing theory to experiment, we must make sure that we are comparing like to like.

The meaning of growth rate for nonparallel flow is not obvious. Let us consider El-Hady and Nayfeh's lowest order solution (Eq. 42):

$$z_1 = A_0 \zeta(x_1, y) \exp[i\int(\alpha_0 + \varepsilon\alpha_1)dx - i\omega t] \qquad (1)$$

The downstream growth of the magnitude of this function is not purely contained in the expotential factor. The change in the eigenfunction, ζ, with x_1 also contributes to "growth." In fact, a complete definition of growth would be

$$G = \frac{1}{|z_1|}\frac{\partial |z_1|}{\partial x}$$

which reduces to

$$G = \hat{\alpha}_0 + \varepsilon\hat{\alpha}_1 + \frac{1}{|\zeta|}\frac{\partial|\zeta|}{\partial x_1} \qquad (2)$$

using (1), where it is understood that $\hat{\alpha}_0$ and $\hat{\alpha}_1$ are the negative and imaginary parts of α_0 and α_1. [Bouthier (1972), Gaster (1974), and Eagles and Weissman (1975)].

Equation 2 shows that the growth rate is actually a function of y. (It is also a function of the flow quantity under consideration, see the above mentioned references.) However, if we agree to measure the growth rate at a particular y-position and if the eigenfunction is normalized at that position (so that $\partial|\zeta|/\partial x_1 = 0$ at that position), then the influence of the changing eigenfunction on growth rate will disappear (for this particular definition of growth rate). The poit is that $\hat{\alpha}_1$ is not uniquely defined; it depends on the normalization used for ζ. [This can also be seen from examination of the equation defining α_1, Eq. 35]. The authors have neglected to explain what their normalization was.

REFERENCES

Eagles, P. M., and M. A. Weissman (1975). On the Stability of Slowly Varying Flow. *J. Fluid. Mech. 69*, 241-262.

Author's Reply

ALI H. NAYFEH

The growth rate in a parallel flow can be unambiguously defined, but it cannot be unambiguously defined in a nonparallel flow. Because the eigenfunctions are functions of y as well as x, Saric and Nayfeh (1977) note that stable flows may be termed unstable and vice versa. Saric and Nayfeh (1977) discussed in great detail the different possible definitions of the growth rate and compared these definitions with all available experimental data for the Blasius flow. They found that all the experimental data (neutral curves or growth rates) obtained at the values of η for which $|u|$ has a maxima can be correlated with the nonparallel results if the growth rate is defined as in (55). For the heated liquid problem, we arrived at the same conclusion. Including the distortion of the eigenfunction with the streamwise position, the definition, (56), underpredicts the growth by large amounts.

Discussion

G. CHAHINE and D. H. FRUMAN

The question of whether polymer solutions affect cavitation inception through changes of the flow structure or through the inhibition of bubble growth has been the subject of much controversy. In this excellent paper the authors seem to adhere to the first school of thought and disregard the second. We think that there is ample evidence of the profound flow changes introduced by the ejected polymers to support, at least partially, their contention. However, evidence also exists showing that the onset of acoustically generated cavitation is delayed by the presence of minute amounts of polymers and asbestos fibers [Hoyt (1977)]. also, in investigating the behavior of spark-generated bubbles in the vicinity of a solid wall, the discussers have observed significant changes being promoted by the presence of the polymers.

Figure 1 shows the geometric dimensions that have been considered in the analysis of the bubble behavior. The displacement of point A, where the re-entering jet originates, divided by the maximum lateral dimension of the bubble, R_{cmax}, is plotted in Figure 2 as a function of the dimensionless time parameter, t/τ_R, and the parameter, η, which is the ratio between R_{cmax} and ℓ, the distance between the center of the spherical initial bubble and the wall. As shown, the polymer solution has a retarding effect on the re-entering jet. This effect increases with increasing η [Chahine and Fruman (1979)]. Together with results shown in Hoyt, our data further confirm that, in the absence of flow, bubble behavior is affected by the intrinsic properties of dilute polymer solutions.

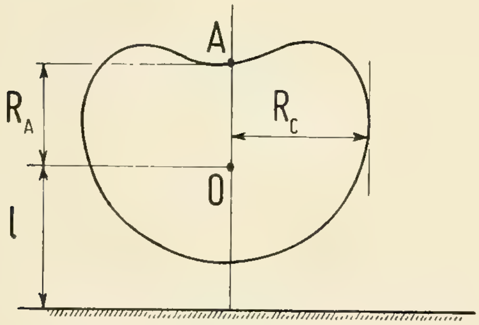

FIGURE 1

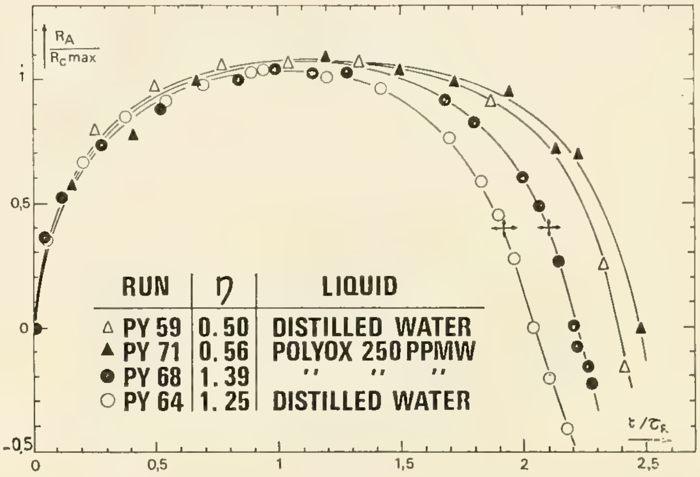

FIGURE 2

REFERENCES

Hoyt, J. W., (1977). Cavitation in Polymer Solutions and Fiber Suspensions. *Cavitation and Polyphase Flow Forum, ASME.*

Chahine, G. L., and D. H. Fruman (1979). Dilute Polymer Solution Effects on Bubble Growth and Collapse. *Physics of Fluids.*

Authors' Reply

EDWARD M. GATES and ALLAN J. ACOSTA

Messrs. Chahine and Fruman have raised the question of the relative importance of polymer-induced changes in bubble growth versus induced changes in the flow structure with regard to the suppression of cavitation. Although both experimental [Ellis and Ting (1970); Chahine and Fruman[1] (1979)] and theoretical [Street (1968); Fogler and Goddard (1970)] work demonstrate that in "no-flow" situations the growth and collapse rates in polymer solutions are different than those in pure water, the magnitude and sense (Street predicts an increase in bubble growth rate) of the changes are open to question. On the other hand, the results of Hoyt (1976), Brennen (1970), van der Meulen (1976), and the present work show drag-reducing polymers have a very dramatic effect upon the flow structure in jets and axisymmetric bodies. The authors believe that in the present work the influence of these profound flow alterations predominate over any influence of modified bubble dynamics as nicely shown by them as evidenced by the following observations:

First, it was observed in the LTWT that cavitation inception on the non-separating Schiebe body was not influenced by viscous considerations and was of the travelling bubble type. In this situation we would expect that if the polymer effect upon bubble dynamics was significant, it should be well illustrated under these circumstances. However, we (like van der Meulen) observed no change in either the cavitation index or the appearance of the cavitation at inception. Second, on the hemisphere nose and NSRDC bodies a similarly large suppression of the inception index was obtained by Arakeri and Acosta (1976) through the elimination of the laminar separation by a mechanical boundary layer trip - a situation for which there is no change of bubble dynamics.

From these observations we infer that the influence of the polymer on cavitation inception is dominated by changes in the flow structure rather than modified bubble dynamics. However, in "non-flow" sitations it must be assumed that modified bubble dynamics are responsible for the observed changes and the work of Messrs. Chahine and Fruman is a useful addition to this area of study.

REFERENCES

[1] See Reference from Chahine and Fruman discussion.

Street, J. R., (1968). The Rheology of Phase Growth in Elastic Liquids. *Trans. Soc. Rheol., 12, p. 103.*
Fogler, H. S., and J. D. Goddard (1970). Collapse of Spherical Cavities in Viscoelastic Fluids. *Physics of Fluids, 13, (5), pp. 1135-1141.*
Hoyt, J. W., (1976). Effect of Polymer Additives on Jet Cavitation. *Journal of Fluids Engineering, Trans. ASME, March, pp. 106-112*

Session III

SHIP BOUNDARY LAYERS AND PROPELLER HULL INTERACTION

PETER N. JOUBERT
Session Chairman
University of Melbourne
Melbourne, Australia

Calculation of Thick Boundary Layer and Near Wake of Bodies of Revolution by a Differential Method

V. C. Patel and Y. T. Lee
The University of Iowa
Iowa City, Iowa

ABSTRACT

The differential equations of the thick axisymmetric turbulent boundary layer and wake are solved using a finite-difference method. The equations include longitudinal and transverse surface curvature terms as well as the static-pressure variation across the boundary layer and wake. Closure of the mean-flow equations is affected by a rate equation for the Reynolds stress deduced from the turbulent kinetic-energy equation. The results of the method are compared with the two sets of data obtained at the Iowa Institute of Hydraulic Research from experiments in the tail region of a modified spheroid and low-drag body of revolution, and also with the predictions of a simple integral approach proposed earlier. It is shown that the differential approach is superior, provided due account is taken of the normal pressure variation and the direct influence of the extra rates of strain, associated with the longitudinal and transverse surface curvatures, on the length scale of the turbulence.

1. INTRODUCTION

In the absence of flow separation, the boundary layer on a pointed-tailed body of revolution continues to grow in thickness up to the tail. Over the rear quarter of the length of a typical body, the boundary layer thickness becomes large enough to invalidate the assumptions of conventional thin boundary-layer theory. The measurements of Patel, Nakayama, and Damian (1974) on a modified spheroid as well as those of Patel and Lee (1977) on a low-drag body indicate that the breakdown of thin boundary layer approximations is manifested by several concurrent flow features, namely (a) the boundary layer thickness is no longer small compared with the local transverse and longitudinal radii of surface curvature, (b) the velocity component normal to the wall is not small, (c) the pressure is not constant across the boundary layer, and (d) the pressure distribution on the body surface does not conform with that predicted by potential flow theory, as a consequence of the interaction between the thick boundary layer and the external inviscid flow. These features have been recognized in the development of the simple integral method of Patel (1974) for the calculation of a thick axisymmetric boundary layer, and later on, in the formulation of the interaction scheme of Nakayama, Patel, and Landweber (1976a,b) which attempted to couple the boundary layer, the near wake and the external inviscid flow by means of successive iterations. Although the overall iteration scheme proved to be quite successful, the treatment of the boundary layer using the integral method, and particularly its extension to calculate the near wake, required many assumptions which remain untested. The purpose of the present work was therefore to develop a more rational procedure in which the differential equations of the thick boundary layer and the near wake are solved by means of a numerical method, since it appeared that such a procedure would provide not only a more reliable vehicle for the extension of the boundary layer solution into the wake, but also yield the detailed information on the velocity profiles required for the interaction calculations. This paper describes the new differential method and evaluates its performance relative to the integral method as well as the available experimental information.

2. DIFFERENTIAL EQUATIONS AND TURBULENCE MODEL

In the (x,y,ϕ) coordinate system shown in Figure 1, x and y are distances measured along and normal to the body surface, respectively, and ϕ is the azimuthal angle. As shown by Patel (1973) and Nakayama, Patel, and Landweber (1976b), the momentum equations of a thick axisymmetric turbulent boundary layer may be written

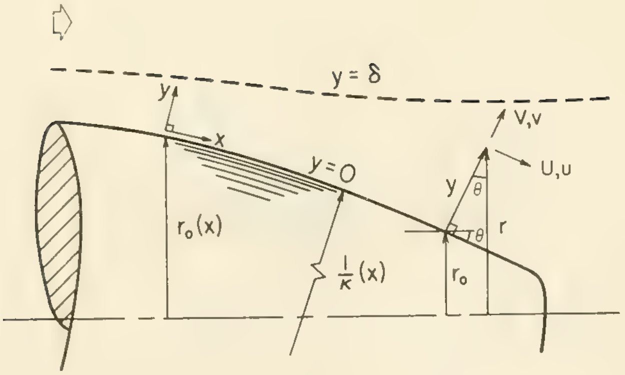

FIGURE 1. Coordinate system and notation.

$$\frac{U}{h_1}\frac{\partial U}{\partial x}+V\frac{\partial U}{\partial y}+\frac{\kappa}{h_1}UV+\frac{1}{\rho h_1}\frac{\partial p}{\partial x}-\frac{1}{rh_1}\frac{\partial}{\partial y}\left(\frac{h_1 r\tau}{\rho}\right)=0 \qquad (1)$$

$$\frac{U}{h_1}\frac{\partial V}{\partial x}+V\frac{\partial V}{\partial y}-\frac{\kappa}{h_1}U^2+\frac{1}{\rho}\frac{\partial p}{\partial y}=0 \qquad (2)$$

and the continuity equation is

$$\frac{\partial}{\partial x}(Ur)+\frac{\partial}{\partial y}(rh_1V)=0 \qquad (3)$$

U and V are the components of mean velocity in the x and y directions, respectively; $h_1 = 1 + \kappa y$, κ being the longitudinal surface curvature; $\tau = -\rho uv + \mu\, \partial U/\partial y$, where ρ is density, μ is viscosity and $-\rho uv$ is the Reynolds stress; $r = r_o + y \cos\theta$ is the radial distance measured from the body axis, θ being the angle between the tangent to the surface and the axis of the body; and p is the static pressure. These equations resulted from order of magnitude considerations and an examination of the data from the modified spheroid experiments of Patel, Nakayama, and Damian (1974). Specifically, from Eq. (2) we note that the static pressure varies across the boundary layer and that the gradient of the pressure in the direction normal to the surface is associated primarily with the curvature of the mean streamlines.

Equations (1), (2), and (3) also apply to the wake, with $\kappa = 0$ and $\theta = 0$ (i.e., $r = y$). In place of the no-slip boundary conditions on the body surface, however, the conditions on the wake centerline are $\partial U/\partial y = 0$ and $\tau = 0$.

If the Reynolds stress is determined by a one-equation model using the turbulent kinetic-energy equation, as proposed by Bradshaw, Ferriss, and Atwell (1967), then the appropriate closure equation for the flow outside the viscous sublayer and the blending zone is

$$\frac{1}{2a_1}\left\{\frac{U}{h_1}\frac{\partial\tau}{\partial x}+V\frac{\partial\tau}{\partial y}\right\}-\tau\left\{\frac{\partial u}{\partial y}-\kappa U\right\}+\frac{1}{r}\frac{\partial}{\partial y}\left\{rG\frac{\tau}{a_1^{3/2}}\sqrt{\frac{\tau_{max}}{\rho}}\right\}+\frac{1}{\ell}\frac{\tau^{3/2}}{\rho^{1/2}}=0 \qquad (4)$$

where a_1 is a constant (=0.15), G is a diffusion function and ℓ is a length-scale function identified with the usual mixing length. G and ℓ are assumed to be universal functions of y/δ, where δ is the boundary layer thickness. The particular forms of these functions proposed by Bradshaw et al. (1967) for a thin boundary layer have gained wide acceptance and have proved adequate for the prediction of a variety of boundary layers developing under the influence of different pressure gradients and upstream history. In the adoption of this closure model for the treatment of thick boundary layers and wakes, however, it is necessary to consider the influence of transverse and longitudinal surface curvatures on the turbulence.

Figure 2 shows the conventional transverse and longitudinal curvature parameters for the modified spheroid and low-drag body [Patel and Lee (1977)]. The ratio of the boundary-layer thickness to the transverse radius of curvature, δ/r_o, is seen to be more than twice as large in the latter case as in the former. In both cases, however, δ/r_o is less than 0.4 up to X/L = 0.75, so that the boundary layers may be regarded as thin up to that station. Over the rear one-quarter of the body length, the influence of transverse curvature would prevail not only through the geometrical terms in the momentum and continuity equations but also through any direct effect on the turbulence. The precise nature of the latter is not known at the present time since the turbulence is also affected by the longitudinal curvature of the streamlines associated with the curvature of the surface as well as the curvature induced by the rapid thickening of the boundary layer over the tail.

The longitudinal surface curvature parameter $\kappa\delta$ is seen to be quite different for the two bodies. In the case of the modified spheroid, the curvature is convex up to X/L = 0.933 and zero thereafter, while that of the low-drag body is initially convex and becomes concave for X/L > 0.772. Several recent studies with nominally two-dimensional thin

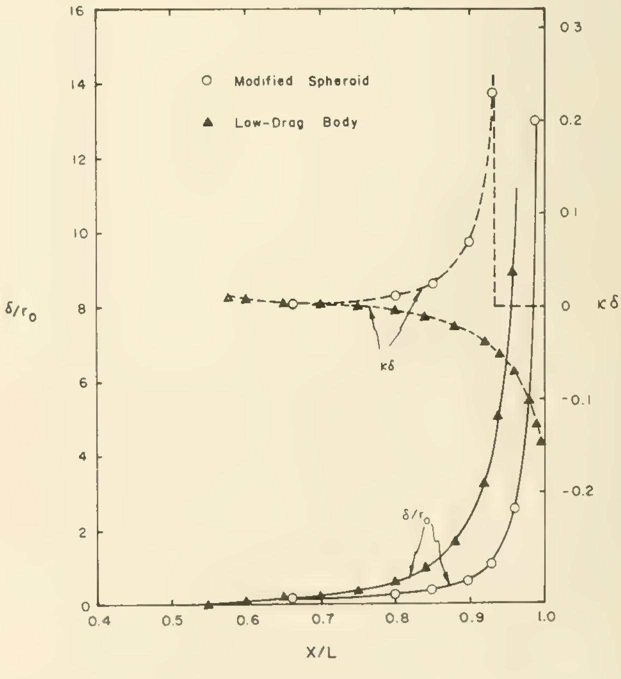

FIGURE 2. Ratios of boundary-layer thickness to the longitudinal and transverse radii of surface curvature.

turbulent boundary layers [Bradshaw (1969, 1973), So and Mellor (1972, 1973, 1975), Meroney and Bradshaw (1975); Ramaprian and Shivaprasad (1977); Shivaprasad and Ramaprian (1977)] have indicated that even mild ($\kappa\delta \sim 0.01$) longitudinal surface curvature exerts a dramatic influence on the turbulence structure. In particular, it is noted that quantities such as the mixing length ℓ, the structure parameter $a_1 = -\overline{uv}/q^2$ and the shear-stress correlation coefficient $\overline{uv}/(\sqrt{\overline{u^2}}\ \sqrt{\overline{v^2}})$ are influenced markedly, and experiments indicate that convex streamline curvature leads to a reduction in these, whereas concave curvature has an opposite effect. The turbulence measurements on the modified spheroid and the low-drag body appear to confirm these observatons although the relative influence of longitudinal streamline curvature and transverse surface curvature could not be separated readily.

Bradshaw (1973) has argued that whenever a thin turbulent shear layer experiences an extra rate of strain, i.e., in addition to the usual $\partial U/\partial y$, the response of the turbulence parameters is an order of magnitude greater than one would expect from an observation of the appropriate extra terms in the mean-flow equations of momentum and continuity. For THIN shear layers and SMALL extra rates of strain he proposed a simple linear correction for the length scale of the turbulence, viz.

$$\frac{\ell}{\ell_o} = 1 + \frac{\alpha e}{\partial U/\partial y} \tag{5}$$

where ℓ_o is the length scale with the usual rate of strain, $\partial U/\partial y$, ℓ is the length scale with the extra rate of strain, e, and α is a constant of the order of 10. For the axisymmetric boundary layer being considered here, there are two extra rates of strain:

$$e_\ell = -\frac{\kappa U}{1 + \kappa y} \tag{6}$$

due to the longitudinal curvature, and

$$e_t = \frac{U}{1 + \kappa y}\frac{1}{r}\frac{\partial r}{\partial x} = \frac{U}{r}\frac{dr_o}{dx} \tag{7}$$

due to the convergence or divergence of the streamlines (in planes parallel to the surface) associated with the changes in the transverse curvature. The former is a shearing strain while the latter is a plain strain, and it is not certain whether the two effects can be added simply in using Eq. (5) as recommended by Bradshaw (1973). If this is the case, however, we would expect a greater reduction in ℓ in the tail region of the modified spheroid, where κ is positive and dr_o/dx is negative, than on the low-drag body, where κ becomes negative and would therefore tend to offset the influence of the negative dr_o/dx. Although the available data appear to bear this out to some extent, a direct comparison between Eqs. (5), (6), and (7) and the data was not attempted, especially in view of Bradshaw's [Bradshaw and Unsworth (1976)] assertion that Eq. (5) should be used in conjunction with a simple rate equation which accounts for the upstream extra rate-of-strain history. He proposes

$$\frac{\ell}{\ell_o} = 1 + \frac{\alpha e_{eff}}{\partial U/\partial y} \tag{8}$$

and

$$\frac{d}{dx}(e_{eff}) = \frac{e - e_{eff}}{10\delta} \tag{9}$$

where e is the actual rate of strain, e_{eff} is its effective value and 10δ represents the "lag length" over which the boundary layer responds to a change in e. In order to determine the merit of this proposal, it is of course necessary to incorporate it in an actual calculation and make a comparison between the predictons and measurement. Such an attempt has been made here.

The functions ℓ_o and G used in the present study are shown in Figure 3. For the wake calculation, the linear variation of ℓ_o in the wall region is replaced by the constant value of 0.09, as shown by the dotted line in the figure. The local distribution of the length scale, ℓ, is thus given by Eqs. (6) through (9) while the diffusion function, G, and the structure parameter, a_1, retain their thin-boundary-layer values.

3. SOLUTION OF THE DIFFERENTIAL EQUATIONS

A numerical method available for the solution of equations corresponding to (1), (3), and (4) for a thin two-dimensional boundary layer was modified to introduce the longitudinal- and transverse-curvature terms. Instead of incorporating the y-momentum, Eq. (2), into the solution procedure, however, changes were made such that a prescribed variation, across the boundary layer, of the pressure gradient $\partial p/\partial x$ could be used. This implies that the pressure field is known a priori. The solution of Eqs. (1), (3), and (4) together with Eqs. (6), (7), (8), and (9) can then be obtained through step-by-step integration by marching downstream from some initial station where the velocity and shear-stress profiles are prescribed. A staggered mesh, explicit numerical scheme, similar to that used by Nash (1969), was used to integrate the equations in the domain between the first mesh point away from the surface (or the wake centerline) to some distance, typically 1.25 δ, outside the boundary layer and the wake. The fifteen mesh points across the boundary layer are distributed

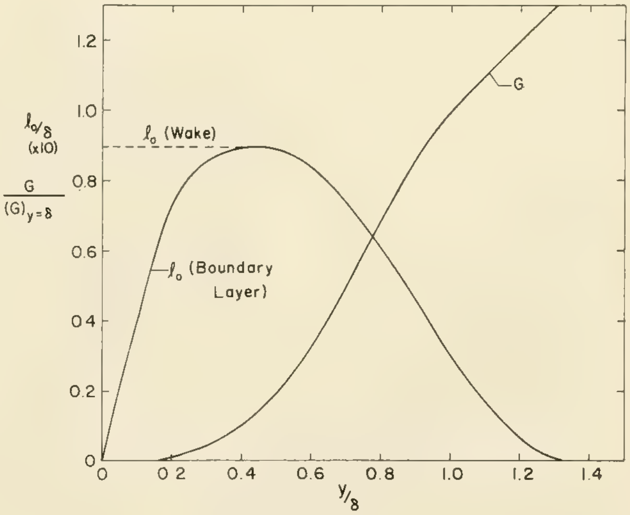

FIGURE 3. Distributions of empirical functions, ℓ_0 and G.

non-uniformly to provide a greater concentration near the wall and the wake centerline. Instead of carrying out the integration of the equations up to the wall, i.e., through the viscous sublayer and the blending zone, the numerical solution at the first mesh point, located in the fully turbulent part of the boundary layer, is matched to the wall using the law of the wall. In the extension of the method to the wake, the matching between the first mesh point and the wake centerline is accomplished by using the conditions $\partial U/\partial y = 0$ and $\tau = 0$ on the centerline. The main differences between the boundary layer and wake calculation procedures are therefore the treatment of the flow between the first mesh point and the wall or the wake centerline, and the change in ℓ_o at the tail. Note that the local value of ℓ in the boundary layer as well as the wake is different from ℓ_o due to the lag, Eq. (8). The length scale recovers the reference distribution ℓ_o asymptotically in the far wake. Since the near wake data from the low-drag body indicated that most of the adjustment from the boundary layer to the far wake is accomplished over roughly five initial wake thicknesses, the lag length for the wake calculation was taken to be 5 δ, rather than 10 δ used for the boundary-layer calculation on the basis of Bradshaw's (1973) suggestion. Since the extra rates of strain vanish at the tail ($\kappa = 0$, $dr_o/dx = 0$), the length scale approaches the ℓ_o distribution at about five wake radii downstream of the tail.

Preliminary calculations performed with the differential method described above quickly indicated that the extra rates of strain in both experiments were much larger than those examined by Bradshaw (1973) in support of the linear length-scale correction formula of Eq. (8). In fact, the use of the linear formula led to a rapid decrease in ℓ and indicated almost total destruction of the Reynolds stress across the boundary layer in the tail region and the near wake. In view of this, recourse was made to a non-linear correction formula in the form

$$\frac{\ell}{\ell_o} = \{1 - \frac{\alpha e_{eff}}{\partial U/\partial y}\}^{-1} \qquad (8a)$$

which reduces to the linear one, Eq. (8), for small extra rates of strain. Equations (1), (3), and (4), together with (6), (7), (8a), and (9), were then solved with the following inputs:

A: the measured wall pressure distribution C_{pw} (i.e., no normal pressure variation) and $\ell(y/\delta) = \ell_o(y/\delta)$
B: the measured C_{pw} with $\ell(y/\delta)$ corrected for only the longitudinal curvature ($e = e_\ell$)
C: the measured C_{pw} with $\ell(y/\delta)$ corrected for only the streamline convergence ($e = e_t$)
D: as above, but with $e = e_\ell + e_t$
E: using $e = e_\ell + e_t$ in Eqs. (8a) and (9), and a variable $\partial p/\partial x$ across the boundary layer evaluated by assuming a linear variation in p from $y = 0$ to $y = \delta$ and using the measured values of C_{pw}, $C_{p\delta}$ and δ.

Thus, case A corresponds to an axisymmetric boundary layer with thin, two-dimensional boundary-layer physics. The other cases enable the evaluation of the relative influence of the extra rates of strain as well as the static pressure variation through the boundary layer. The calculations were started with the velocity and shear-stress profiles measured at X/L = 0.662 on the modified spheroid and at X/L = 0.601 on the low-drag body.

4. COMPARISONS WITH EXPERIMENT

The major results of the calculations are summarized in Figure 4(a-k) for the low-drag body and in Figure 5(a-h) for the modified spheroid. However, in the latter case the calculations are restricted to the boundary layer since detailed measurements were not made in the wake. Both figures contain comparisons between the experimental and calculated velocity, shear-stress, and mixing-length profiles at a few representative axial stations as well as the development of the integral parameters, $\bar{\delta}_2$, Δ_2, $\bar{H}$, H, and C_f, with axial distance. These parameters are defined by

$$\bar{\delta}_1 = \int_0^\delta (1 - \frac{U}{U_\delta})\,dy, \quad \bar{\delta}_2 = \int_0^\delta \frac{U}{U_\delta}\,dy, \quad \bar{H} = \bar{\delta}_1/\bar{\delta}_2 \qquad (10)$$

$$\Delta_1 = \int_0^\delta (1 - \frac{U}{U_\delta})\,r\,dy, \quad \Delta_2 = \int_0^\delta \frac{U}{U_\delta}(1 - \frac{U}{U_\delta})\,r\,dy,$$

$$H = \Delta_1/\Delta_2 \qquad (11)$$

and

$$C_f = \frac{\tau_w}{\frac{1}{2}\rho U_\delta^2} \qquad (12)$$

Where U_δ is the velocity component at the edge of the boundary layer and wake ($y = \delta$), tangent to the body surface for the boundary layer and parallel

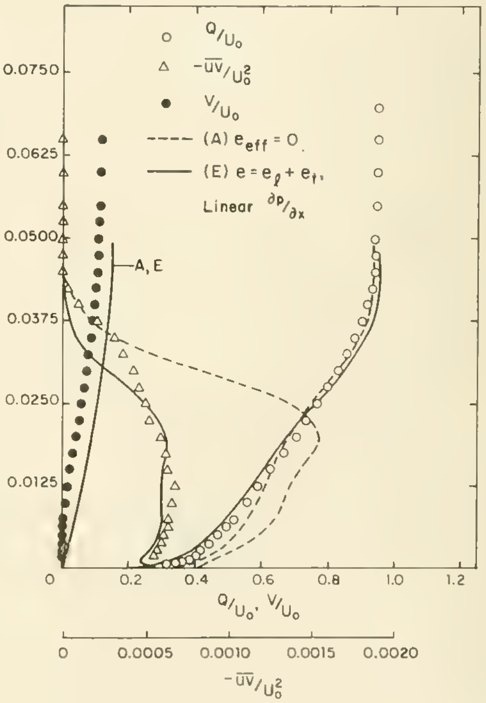

FIGURE 4(a). Comparison of measurements with the solution of the differential equations, low-drag body. Velocity and shear stress profiles at X/L = 0.920.

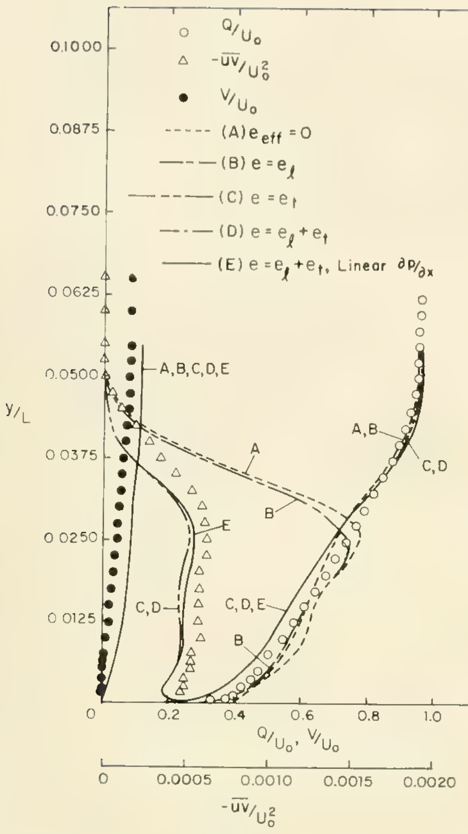

FIGURE 4(b). Velocity and shear stress profiles at X/L = 0.960.

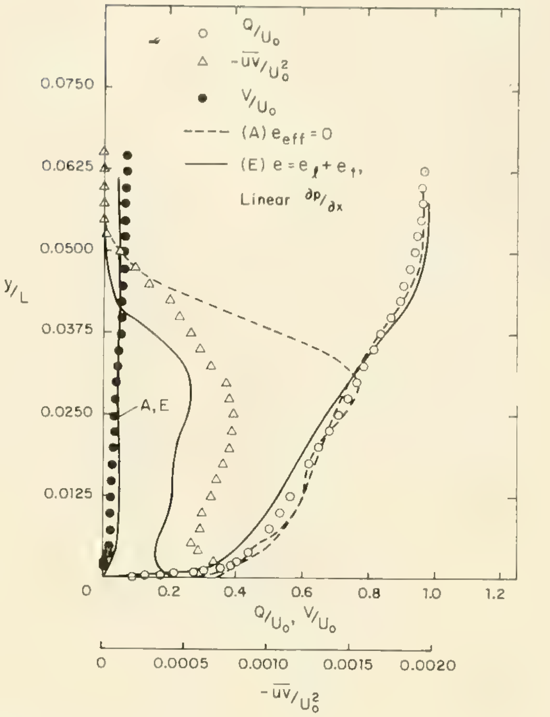

FIGURE 4(c). Velocity and shear stress profiles at X/L = 1.000.

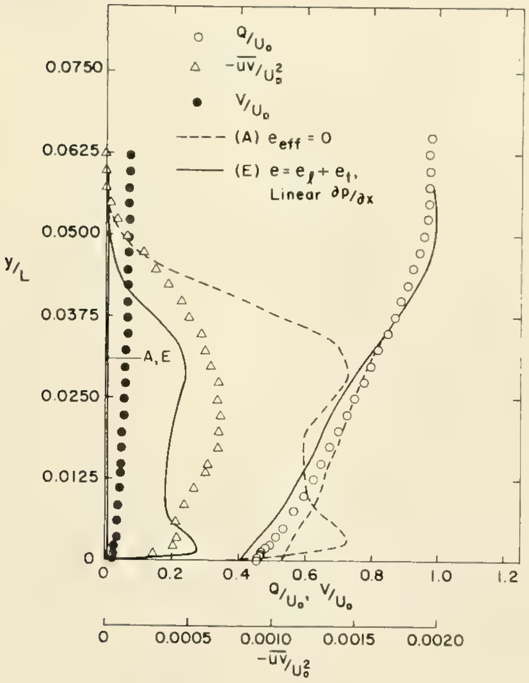

FIGURE 4(d). Velocity and shear stress profiles at X/L = 1.06.

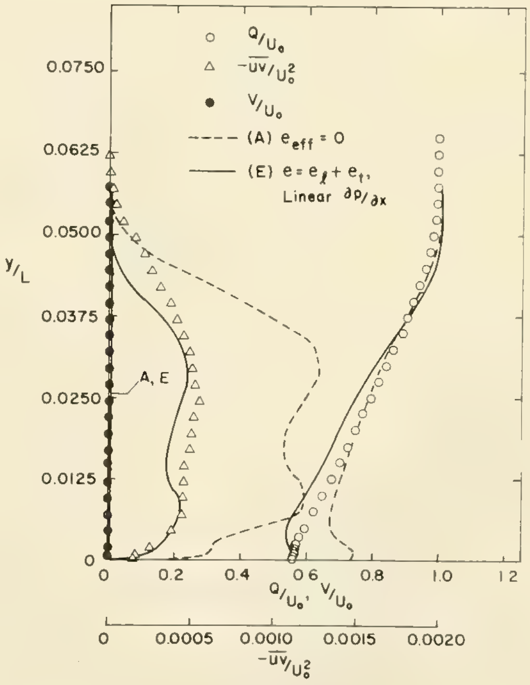

FIGURE 4(e). Velocity and shear stress profiles at X/L = 1.20.

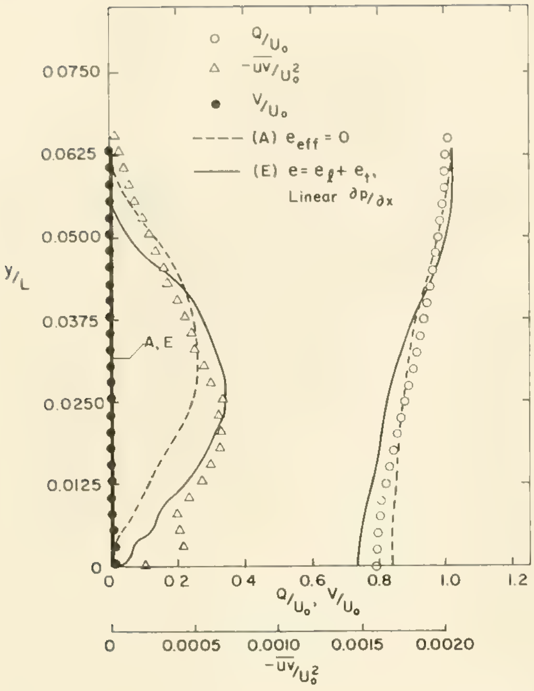

FIGURE 4(f). Velocity and shear stress profiles at X/L = 2.472.

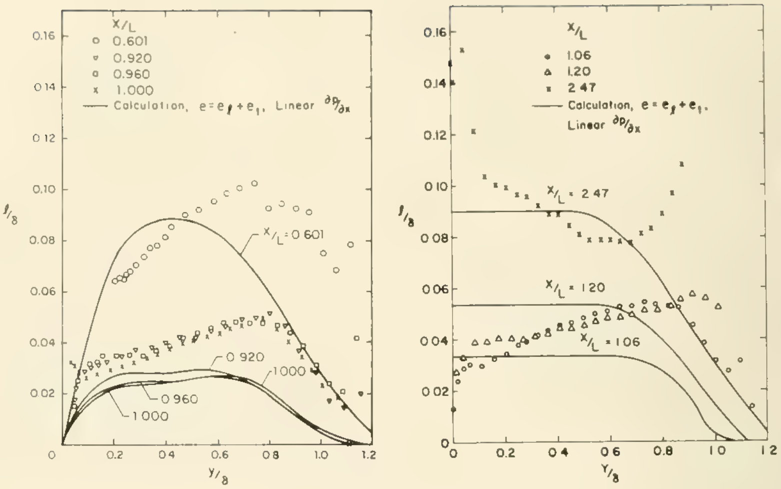

FIGURE 4(g). Mixing length profiles.

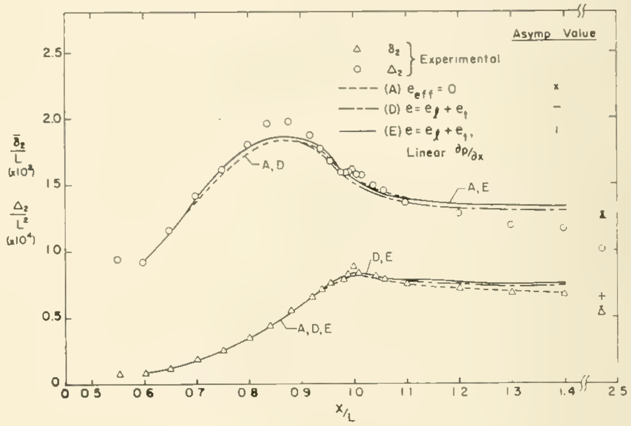

FIGURE 4(i). Planar and axisymmetric momentum deficits.

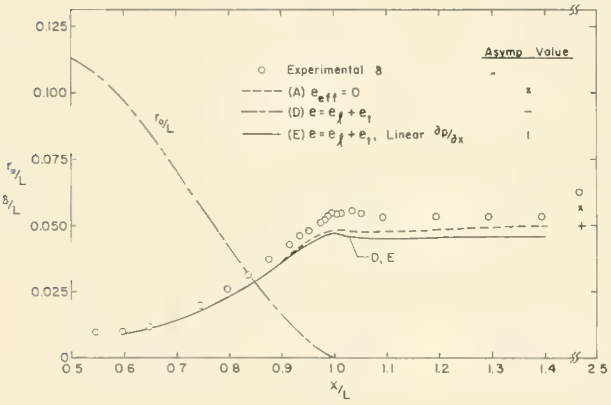

FIGURE 4(h). Boundary layer and wake thickness.

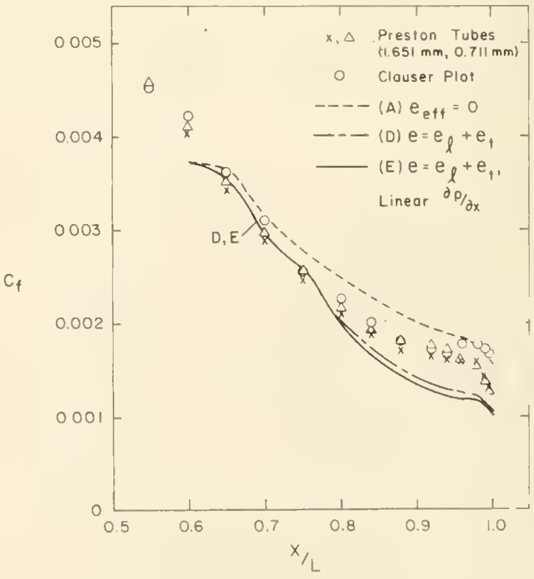

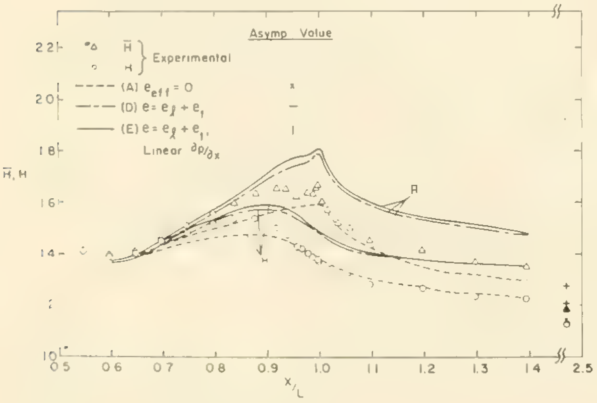

FIGURE 4(j). Shape parameters.

FIGURE 4(k). Wall shear stress.

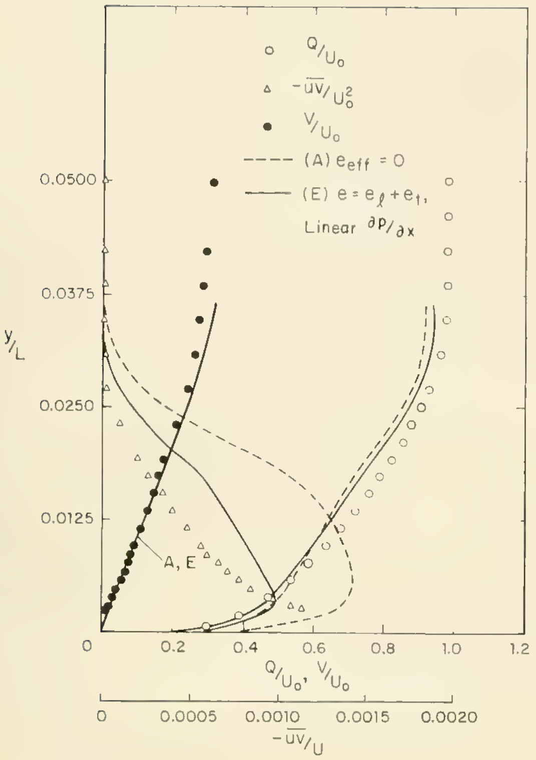

FIGURE 5. Comparison of measurements with the solution of the differential equations, modified spheroid.
(a) Velocity and shear stress profiles at X/L = 0.930.

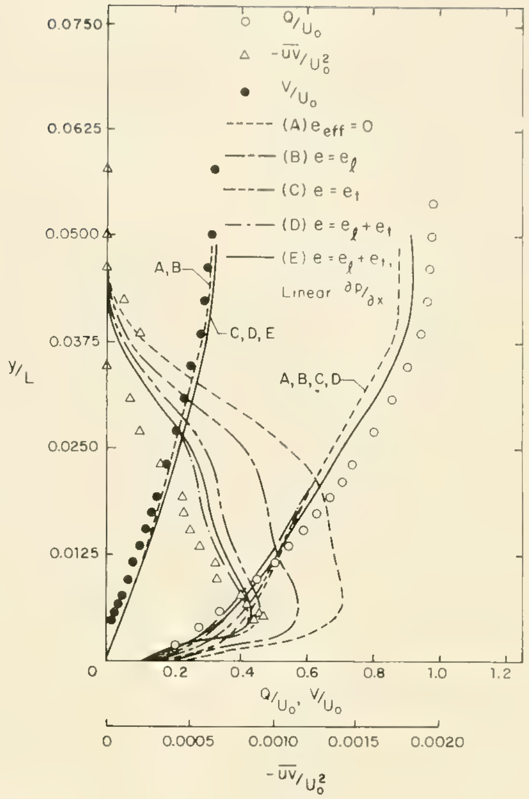

FIGURE 5(b). Velocity and shear stress profiles at X/L = 0.960.

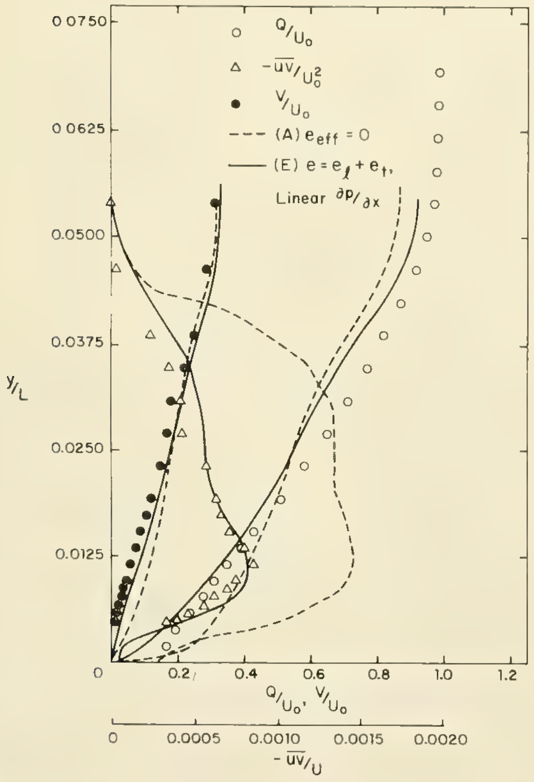

FIGURE 5(c). Velocity and shear stress profiles at X/L = 0.990.

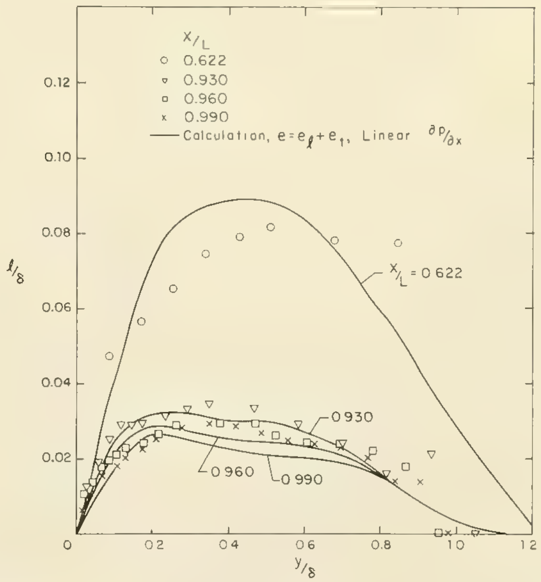

FIGURE 5(d). Mixing length profiles.

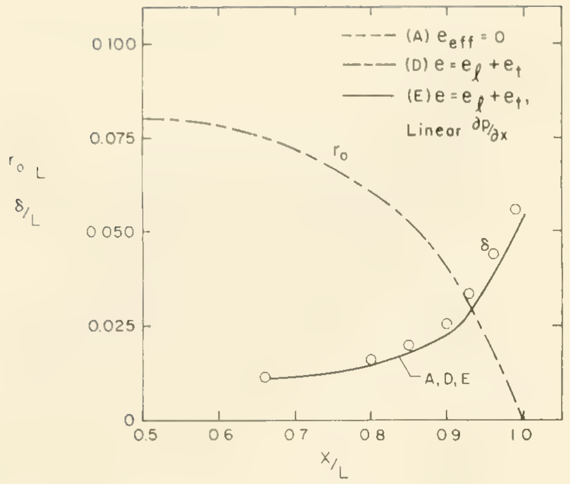

FIGURE 5(e). Boundary layer thickness.

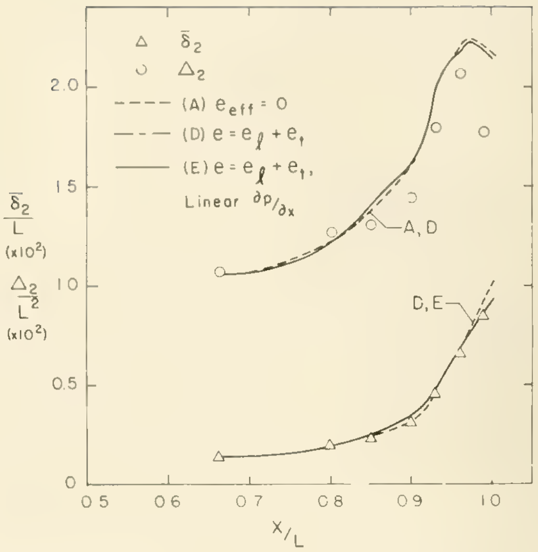

FIGURE 5(f). Planar and axisymmetric momentum deficits.

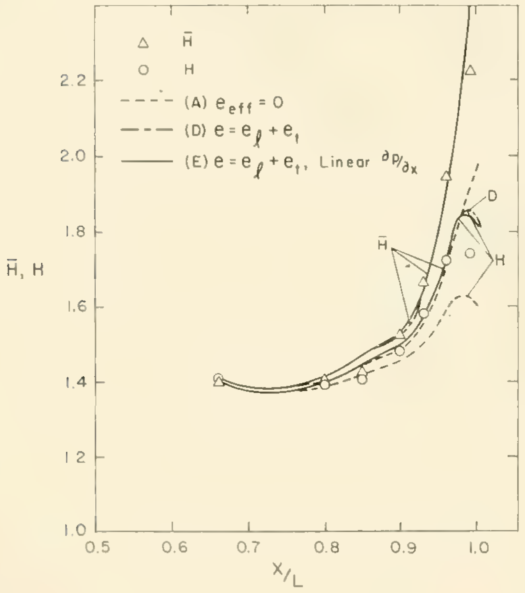

FIGURE 5(g). Shape parameter.

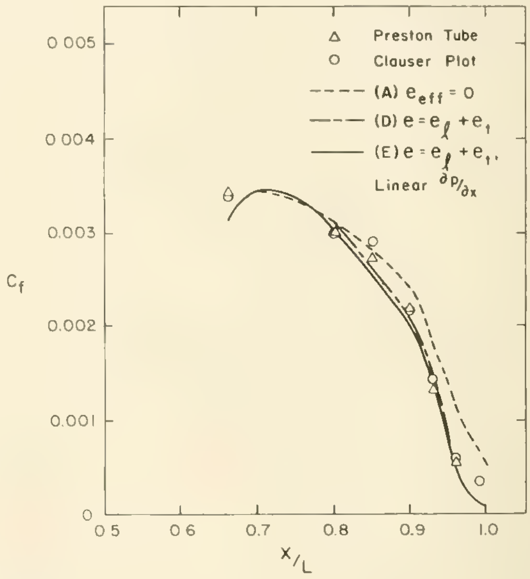

FIGURE 5(h). Wall shear stress.

to the axis for the wake. In the interest of clarity, the results of all the calculations (cases A through E) are shown only at one axial station (Figure 4b and 5b), those at other stations being qualitatively similar.

Considering the most detailed figures, 4b and 5b, first, it is clear that the predictions are rather poor when the length scale, ℓ, is assumed to be the same as that in a thin boundary layer (case A). This is particularly evident in the prediction of the shear-stress profiles across the boundary layer and the near wake. Incorporation of the correction to ℓ to account for the extra rate of strain due to longitudinal curvature (case B) leads to a marginal improvement in the case of the low-drag body and a dramatic improvement for the modified spheroid. This is to be expected in view of the grossly different surface curvature histories of the two bodies as noted earlier (Figure 2). Nevertheless, it is clear that this correction by itself is not sufficient to account for the differences between the data and the calculations with thin boundary-layer turbulence models (case A). The application of the correction for the extra rate of strain due to the transverse curvature (case C) appears to account for a major portion of these differences for both bodies. The influence of transverse curvature is in fact seen to be somewhat larger for the low-drag body as would be expected from the fact that δ/r_o is greater in that case (Figure 2). The simple addition of the effects of the two rates of strain (case D) leads to a significant improvement in the prediction of both the velocity profiles and the shear stress profiles. The incorporation of a variable pressure gradient across the boundary layer (case E), which is an attempt to account for the normal pressure gradients, appears to make a significant improvement in the prediction of the velocity profile in the case of the modified spheroid, but its influence is small, and confined to the outer part of the boundary layer, in the case of the low-drag body.

Examination of the velocity and shear-stress profiles at several axial stations shown in Figures 4a-f and 5a-c suggests that the incorporation of the non-linear length-scale correction of Eq. (8a), the associated rate Eq. (9) and the static-pressure variation in the equations of the thick boundary layer, which already include the direct longitudinal and transverse curvature terms, leads to satisfactory overall agreement with the data for both bodies. It is particularly noteworthy that the velocity and shear stress distributions in the far wake ($X/L = 2.472$) of the low-drag body are predicted with good accuracy. The level of agreement can obviously be improved further by appropriate modifications in the empirical functions in the turbulent kinetic-energy equation and changes in the lag-length used in the length-scale equation. The predictions of the shear stress profiles are consistent with those of the mixing-length distributions shown in Figures 4g and 5e insofar as lower shear stresses correspond to an over correction in the mixing length. These comparisons provide further insight into the manner in which the length scale must be modified to improve the correlation between the calculation method and experiment. It is apparent that the consistent discrepancy between the calculated and measured velocity and shear-stress profiles near the outer edge of the boundary layer and wake stems from a poor representation of the length scale distribution.

It is interesting to note that, for both bodies the calculation precedure predicts normal components of mean velocity which are of the same order of magnitude as those measured. The relatively close agreement between the predictions and experiment for both components of velocity is perhaps a good indication of the axial symmetry achieved in the experiments. The large values of the normal velocity and the influence of static pressure variation noted above would appear to indicate that incorporation of the y-momentum equation in the calculation procedure would be worthwhile. Note that this has been avoided in the present calculations by using the measured pressure distributions at the surface and the outer edge of the boundary layer.

Finally, the comparisons made in Figures 4 (i-k) and 5 (e-h) with respect to the integral parameters show several interesting and consistent features. It is observed that the prediction of the physical thickness of the boundary layer and the wake is insensitive to the changes in ℓ as well as the inclusion of static pressure variation. The under estimation of the thickness is associated with the discrepancy, noted earlier, in the velocity profile near the outer edge of the boundary layer and wake. The planar momentum thickness $\bar{\delta}_2$ and the momentum-deficit area Δ_2 are also insensitive to changes in ℓ. The variation of static pressure across the boundary layer appears to make a small but noticeable contribution to the development of Δ_2 in both cases. However, it is not large enough to account for the differences between the calculations and experiment. The predictions of the shape parameters, $\bar{H}$ and H, presented in Figures 4j and 5g, appear to be satisfactory, especially in view of the rather large scale of the plots. Nevertheless, there is a systematic difference between the data and the calculation in the tail region and wake of the low-drag body. As indicated earlier, this can be improved by modifications in the empirical functions and the lag length. The predictions of the wall shear stress, shown in Figures 4k and 5h, indicate that the present method gives acceptable results for both bodies.

5. COMPARISONS WITH THE INTEGRAL APPROACH

An integral method for the calculation of a thick axisymmetric boundary layer was described by Patel (1974) and its extension to the wake was proposed by Nakayama, Patel, and Landweber (1976b). A few possible improvements in this method were examined recently relative to the description of the velocity profiles in the near wake and these are discussed by Patel and Lee (1977). The most recent version of this method has been used here to calculate the development of the boundary layer and the wake of the low-drag body in order to assess its performance relative to the experimental data (which were not available at the time the method and its extension were proposed) and the more elaborate differential method.

The results of the calculations are shown in Figure 6. It is seen that the performance of the integral method is comparable with that of the differential method (compare Figures 4h-k with 6a-d) with respect to the prediction of the boundary layer up to the tail. The prediction of the near wake is, however, distinctly inferior to that of the differential method, particular with respect to the physical thickness δ and momentum deficit area Δ_2. The main conclusion to emerge from these calculations is that the integral method is capable of giving a good overall description of the flow features with considerably less computing effort. The differential approach is to be preferred, however, since it affords the opportunity for further refinement and gives greater details which may be necessary for many applications. A more thorough discussion of the integral method and its shortcomings is given in Patel and Lee (1977).

6. CONCLUSIONS

From the present solutions of the differential equations, using the (one-equation) turbulent kinetic-energy model of Bradshaw, Ferriss, and Atwell (1967), it is clear that methods developed for thin shear layers cannot be relied upon to predict the behavior of the thick boundary layer and wake of a body of revolution. Although these calculations have demonstrated that the boundary-layer calculation can be readily extended to the wake and that a fairly satisfactory prediction procedure can be developed by incorporating ad hoc corrections to the model for the extra rates of strain, along the lines recommended by Bradshaw (1973), it is indeed surprising that such modifications, proposed originally for small extra rates of strain and thin shear layers, work so well for the two bodies which are substantially different in shape. In keeping with recent trends in the formulation of turbulence models, one inquires whether thick axisymmetric boundary layers and near wakes ought to be treated by the so-called two-equation models. From the rapid changes in the mixing-length indicated by

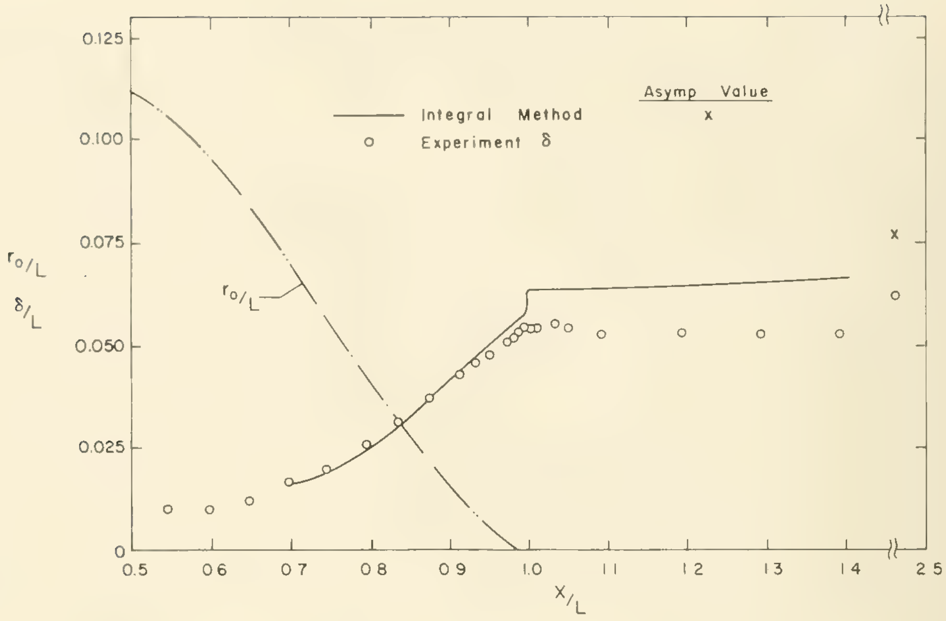

FIGURE 6. Comparison of experiments with the solution of the integral equations, low-drag body. (a) Boundary layer and wake thickness.

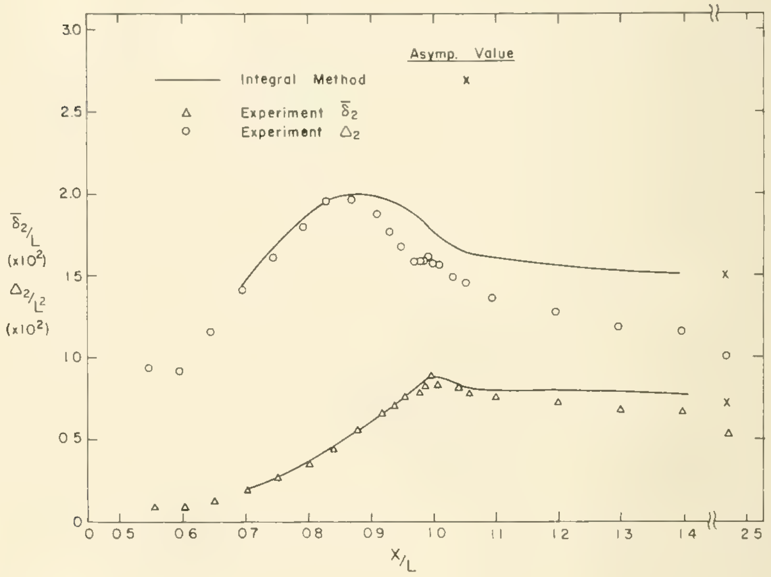

FIGURE 6(b). Planar and axisymmetric momentum deficits.

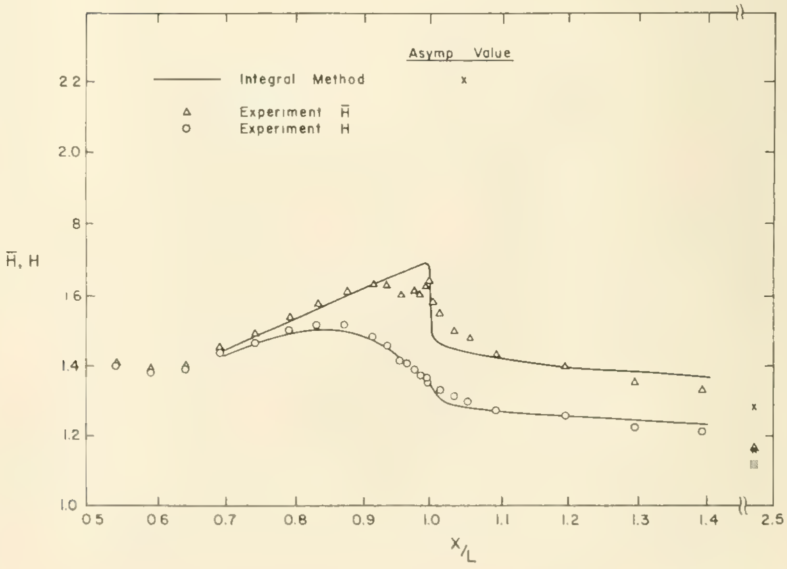

FIGURE 6(c). Shape parameter.

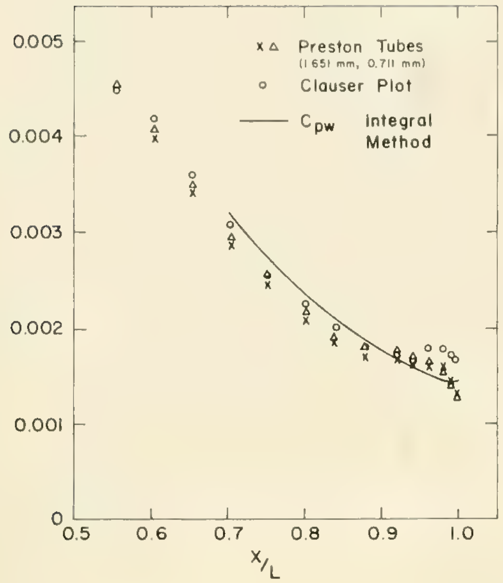

FIGURE 6(d). Wall shear stress.

the data, this would appear to be desirable since it would provide an extra equation for the length-scale of the turbulence in addition to that for its intensity. This would also enable the incorporation of the variations in the structure parameter, a_1, observed in the experiments. However, the recent work of Launder, Priddin and Sharma (1977) and Chambers and Wilcox (1977) indicates that even two-equation models, at least of the type available at the present time, require further modifications to account for the extra rates of strain stemming from such effects as streamline curvature, streamline convergence, and rotation, two of which are present in the case examined here.

In addition to the problem of turbulence models, the thick boundary layer and the near wake contain the complication of normal pressure gradients. The available data show that there exist substantial variations of static pressure across the boundary layer. The calculations presented here as well as those performed with the integral method by Patel and Lee (1977), suggest that the influence of the normal pressure gradients on the development of the boundary layer and the near wake is not negligible although it is masked by the rather major effects of the transverse and longitudinal surface curvatures on the turbulence. If normal pressure variations are to be taken into account in a method based on the differential equations, it is necessary to include the y-momentum equation in the solution procedure and regard the pressure as an additional unknown. This is perhaps best accomplished by means of an iterative scheme such as that proposed by Nakayama, Patel, and Landweber (1976a,b), although other possibilities can be explored. In view of the success of the present differential method, it is proposed to incorporate the present method in this iterative scheme, in place of the integral method, to study the viscous-inviscid interaction in the tail region in greater detail.

The representative calculations presented in Section 5 demonstrate the overall reliability of the simple integral method of Patel (1974) for the prediction of the thick boundary layer. Its extension to the wake is not altogether satisfactory and this is attributed largely to the lack of a systematic procedure for the description of the velocity profiles in the near wake. This method is ideally suited, however, for rapid calculations to determine the state of the boundary layer in the tail region for certain applications.

ACKNOWLEDGMENTS

This research was carried out under the sponsorship of the Naval Sea Systems Command, General Hydro-Mechanics Research Program, Sub-project SR023 01 01, administered by the David W. Taylor Naval Ship Research and Development Center, Contract N00014-75-C-0273. The authors acknowledge the assistance of Professor B. R. Ramaprian through several stimulating discussions on the influence of longitudinal surface curvature on turbulent boundary layers.

REFERENCES

Bradshaw, P. (1969). The Analogy Between Streamline Curvature and Buoyancy in Turbulent Shear Flow. *J. Fluid Mech. 36*, 177.

Bradshaw, P. (1973). Effects of Streamline Curvature on Turbulent Flow. *AGARDograph No. 169*.

Bradshaw, P., and K. Unsworth (1976). Computation of Complex Turbulent Flows, in Reviews of Viscous Flows. *Proceedings of the Lockheed-Georgia Company Symposium*, 448.

Bradshaw, P., D. H. Ferriss, and N. P. Atwell (1967). Calculation of Boundary Layer Development Using the Turbulent Energy Equation. *J. Fluid Mech. 28*, 593.

Chambers, T. L., and D. C. Wilcox (1977). Critical Examination of Two-Equation Turbulence Closure Models for Boundary Layers. *AIAA Journal 15*, 6; 821.

Launder, B. E., C. H. Priddin, and B. I. Sharma (1977). The Calculation of Turbulent Boundary Layers on Spinning and Curved Surfaces. ASME, *J. Fluids Engineering 99*, No. 1, 231. See also discussions by P. Bradshaw and G. Mellor, (1977), ASME, *J. Fluids Engineering 99*, 2; 435.

Meroney, R. N., and P. Bradshaw (1975). Turbulent Boundary Layer Growth Over Longitudinally Curved Surfaces. *AIAA Journal 13*, 1448.

Nakayama, A., V. C. Patel, and L. Landweber (1976a). Flow Interaction Near the Tail of a Body of Revolution, Part I: Flow Exterior to Boundary Layer and Wake. ASME, *J. Fluids Engineering 98*, 531.

Nakayama, A., V. C. Patel, and L. Landweber (1976b). Flow Interaction Near the Tail of a Body of Revolution, Part II: Iterative Solution for Flow Within and Exterior to Boundary Layer and Wake. ASME, *J. Fluids Engineering 98*, 538.

Nash, J. F. (1969). The Calculation of Three-Dimensional Turbulent Boundary Layers in Incompressible Flow. *J. Fluid Mech. 37*, 625.

Patel, V. C. (1973). On the Equations of a Thick Axisymmetric Turbulent Boundary Layer. *Iowa Institute of Hydraulic Research, IIHR Report No. 143*.

Patel, V. C. (1974). A Simple Integral Method for the Calculation of Thick Axisymmetric Turbulent Boundary Layers. *The Aeronautical Quarterly 25*, 47.

Patel, V. C., and Y. T. Lee (1977). Thick Axisymmetric Turbulent Boundary Layer and Near Wake of a Low Drag Body of Revolution. *Iowa Institute of Hydraulic Research, IIHR Report No. 210*.

Patel, V. C., A. Nakayama, and R. Damian (1974). Measurements in the Thick Axisymmetric Turbulent Boundary Layer Near the Tail of a Body of Revolution. *J. Fluid Mech. 63*, 345.

Ramaprian, B. R., and B. G. Shivaprasad (1977). Mean Flow Measurements in Turbulent Boundary Layers Along Mildly-Curved Surfaces. *AIAA Journal 15*, 189.

Shivaprasad, B. G., and B. R. Ramaprian (1977). Some Effects of Longitudinal Wall-Curvature on Turbulent Boundary Layers. *Proceedings of Symposium on Turbulent Shear Flows*, Penn State University, 9.21.

So, R. M. C., and G. L. Mellor (1972). An Experimental Investigation of Turbulent Boundary Layers Along Curved Surfaces. *NASA-CR-1940*.

So, R. M. C., and G. L. Mellor (1974). Experiment on Convex Curvature Effects in Turbulent Boundary Layers. *J. Fluid Mech. 60*, 43.

So, R. M. C., and G. L. Mellor (1975). Experiment on Turbulent Boundary Layers on Concave Wall. *The Aeronautical Quarterly 26*, 35.

Stern Boundary-Layer Flow on Axisymmetric Bodies

T. T. Huang, N. Santelli, and G. Belt
David W. Taylor Naval Ship Research and Development Center, Bethesda, Maryland

ABSTRACT

Measurements of static pressure distributions, mean velocity profiles, and distributions of turbulence intensities and Reynolds stress were made across the stern boundary-layers on two axisymmetric bodies. In order to avoid tunnel blockage, the entire afterbody was placed in the open-jet test section of the DTNSRDC Anechoic Wind Tunnel. The numerical iteration scheme which uses the boundary layer and open wake displacement body is found to model satisfactorily the interaction between the thick stern boundary layer and the external potential flow. The measured static pressure distributions across the entire stern boundary layer and the near wake are predicted well by potential flow computations for the displacement bodies. The measured distributions of mean velocity and eddy viscosity over the stern, except in the tail region ($X/L > 0.90$), are also well-predicted when the Douglas CS differential boundary-layer method is used in conjunction with the inviscid pressure distribution on the displacement body. However, the measured distributions of turbulence intensity, eddy viscosity, and mixing-length parameters in the tail region are found to be much smaller than those of a thin boundary layer. An approximate similarity characteristic for the thick axisymmetric stern boundary layer is obtained when the mixing-length parameters in the tail region are normalized by the square-root of the boundary-layer cross-sectional area instead of the boundary-layer thickness.

1. INTRODUCTION

Many single-screw ship propellers operate inside of thick stern boundary layers. An accurate prediction of velocity inflow to the propeller is essential to meet the ever-increasing demand for improving propeller performance. Huang et al. (1976) used a Laser Doppler Velocimeter (LDV) to measure the velocity profiles on axisymmetric models with and without a propeller in operation. The measured difference between these velocity profiles has provided the necessary clues to formulate an inviscid interaction theory for propellers and thick boundary layers. An iterative scheme was employed to compute the velocity profiles of the thick axisymmetric boundary layer. In this approach, the initial boundary-layer computation proceeds making use of the potential-flow pressure distribution on the body [Hess and Smith (1966)]. The flow calculations are then repeated for a modified body and wake geometry, by adding the computed local displacement thickness as suggested by Preston (1945) and Lighthill (1958). Potential-flow methods are then used to compute the pressure distribution around the modified body and the boundary-layer calculations are repeated using the new pressure distribution. The basic iterative scheme is continued until the pressure distributions on the body from two successive approximations agree to within a given error criterion (1 percent).

The Douglas CS differential boundary-layer method [Cebeci and Smith (1974)], modified to properly acacount for the effects of transverse curvature, was used to calculate the boundary-layer over the axisymmetric body. The integral wake relations given by Granville (1958) were used to calculate the displacement thickness in the wake. In the stern/near-wake region ($0.95 \leq X/L \leq 1.05$), where X is the axial distance from the nose and L is the total length, a fifth-degree polynomial was used, with the constants determined by the condition that the thickness, slope, and curvature be equal to those calculated by the boundary-layer method at $X/L = 0.95$ and by the integral wake relations at $X/L = 1.05$. Comparison with experimental results of Huang et al. (1976) show that the potential-flow/boundary-layer interaction computer program predicts accurate values of pressure, shear stress, and velocity profiles over the forward 90 percent of the bodies, where the boundary layers are thin compared with the radii of the bodies. Over the last 10 percent of body length, the measured shear stress and velocity profiles became smaller than those predicted by the theory. These differences are more noticeable over the last 5 percent of the body length where the boundary-layer thicknesses are greater than the radii of the bodies, especially for fuller sterns.

In order to examine the thick stern boundary-layer properties in detail, it is necessary to measure the distributions of static pressure, turbulence intensities and Reynolds stress across the thick stern boundary layer. The magnitudes of the eddy viscosity and the mixing-length parameter were determined and compared with those obtained for thin boundary layers. It is found that the eddy viscosity and the mixing length for thick boundary layers are smaller than those of thin boundary layers. An improvement to the Douglas CS differential method can be made by modifying the mixing-length model in the tail region. The distributions of measured static pressure, which were found to be nonuniform across the thick stern boundary layers and near wake, can be approximated very well by potential flow computations for the displacement bodies. The gross curvature effects of the mean streamlines on the static pressure distributions outside the displacement surface are represented very well by those of the potential-flow streamlines of the fictitious displacement body. Thus, the nonuniform static pressure distributions across the thick stern boundary layer can be interpreted mainly as an inviscid phenomenon and can be assumed to have little effect on the stern boundary-layer development.

Two axisymmetric bodies without flow separation, Afterbodies 1 and 2 of Huang et al. (1976), were chosen for this investigation. Their geometric simplicity offers considerable experimental and computational convenience in treating fundamental aspects of thick stern boundary layers. Afterbody 1 is a fine convex stern while Afterbody 2 is a full convex stern.

In the following discussion, the experimental techniques and geometries of the model are given in detail. The measurements of mean velocities, turbulence intensities, and Reynolds stresses were analyzed to obtain eddy viscosity and mixing length. The application of the present results to improvement of the accuracy of boundary-layer computations over the entire stern is outlined.

2. WIND TUNNEL AND MODELS

The experimental investigation was conducted in the wind tunnel of the DTNSRDC anechoic flow facility.

TABLE 1 - Offsets for Model 1

X/L	Y/L	Y/R	X/L	Y/L	Y/R	X/L	Y/L	Y/R
0.0000	0.0000	0.0000	.2684	.0456	1.0000	.7363	.0427	.9382
.0050	.0100	.2193	.2783	.0456	1.0000	.7477	.0421	.9235
.0099	.0142	.3118	.2883	.0456	1.0000	.7553	.0416	.9127
.0149	.0175	.3835	.2982	.0456	1.0000	.7666	.0408	.8951
.0199	.0202	.4441	.3082	.0456	1.0000	.7780	.0399	.8755
.0249	.0227	.4975	.3181	.0456	1.0000	.7856	.0392	.8615
.0298	.0248	.5454	.3280	.0456	1.0000	.7970	.0382	.8387
.0348	.0268	.5891	.3380	.0456	1.0000	.8045	.0375	.8225
.0398	.0287	.6291	.3479	.0456	1.0000	.8159	.0363	.7963
.0447	.0303	.6659	.3579	.0456	1.0000	.8273	.0350	.7679
.0497	.0319	.7000	.3678	.0456	1.0000	.8349	.0341	.7477
.0547	.0333	.7315	.3777	.0456	1.0000	.8462	.0326	.7155
.0596	.0347	.7607	.3877	.0456	1.0000	.8576	.0310	.6807
.0646	.0359	.7877	.3976	.0456	1.0000	.8652	.0299	.6560
.0696	.0370	.8126	.4076	.0456	1.0000	.8765	.0281	.6167
.0746	.0381	.8355	.4175	.0456	1.0000	.8841	.0268	.5889
.0795	.0390	.8567	.4274	.0456	1.0000	.8955	.0248	.5445
.0845	.0399	.8760	.4374	.0456	1.0000	.9069	.0226	.4970
.0895	.0407	.8936	.4473	.0456	1.0000	.9144	.0211	.4633
.0944	.0414	.9097	.4573	.0456	1.0000	.9245	.0189	.4147
.0994	.0421	.9241	.4672	.0456	1.0000	.9344	.0166	.3636
.1044	.0427	.9371	.4771	.0456	1.0000	.9443	.0140	.3078
.1093	.0432	.9486	.4871	.0456	1.0000	.9513	.0122	.2673
.1143	.0437	.9587	.4970	.0456	1.0000	.9563	.0108	.2380
.1193	.0441	.9676	.5070	.0456	1.0000	.9612	.0095	.2080
.1243	.0444	.9752	.5169	.0456	1.0000	.9642	.0087	.1900
.1292	.0447	.9816	.5268	.0456	1.0000	.9662	.0081	.1778
.1342	.0450	.9869	.5368	.0456	1.0000	.9682	.0076	.1669
.1392	.0452	.9912	.5467	.0456	1.0000	.9692	.0074	.1619
.1441	.0453	.9945	.5567	.0456	1.0000	.9702	.0072	.1571
.1491	.0454	.9969	.5666	.0456	1.0000	.9722	.0068	.1489
.1541	.0455	.9986	.5765	.0456	1.0000	.9732	.0066	.1453
.1590	.0448	.9836	.5865	.0456	1.0000	.9751	.0063	.1393
.1640	.0456	1.0000	.5964	.0456	1.0000	.9771	.0062	.1364
.1690	.0456	1.0000	.6064	.0456	1.0000	.9791	.0059	.1293
.1740	.0456	1.0000	.6188	.0456	.9999	.9811	.0056	.1222
.1789	.0456	1.0000	.6264	.0455	.9997	.9831	.0053	.1165
.1839	.0456	1.0000	.6378	.0455	.9988	.9851	.0050	.1107
.1889	.0456	1.0000	.6454	.0455	.9977	.9871	.0048	.1051
.1938	.0456	1.0000	.6567	.0453	.9952	.9881	.0046	.1018
.1988	.0456	1.0000	.6681	.0452	.9915	.9901	.0043	.0951
.2087	.0456	1.0000	.6757	.0450	.9883	.9920	.0040	.0880
.2187	.0456	1.0000	.6871	.0448	.9823	.9940	.0036	.0782
.2286	.0456	1.0000	.6984	.0444	.9748	.9960	.0028	.0625
.2366	.0456	1.0000	.7060	.0441	.9690	.9980	.0019	.0413
.2485	.0456	1.0000	.7174	.0437	.9588	1.0000	0.0000	0.0000
.2584	.0456	1.0000	.7250	.0433	.9511			

The wind tunnel has a 2.44 m by 2.44 m closed-jet test section, followed by a 7.16 m by 7.16 m open-jet test section. The length of the open-jet section is 6.40 m. The maximum air speed which can be achieved is 61 m/sec; in the present experiments, the velocity of the wind tunnel was held constant at 30.48 m/sec. The measured ambient turbulence level in the open-jet test section without the model in place was 0.1 percent. Integration of the measured noise spectrum levels in the open-jet test section, over the frequency range of 0 to 10,000 Hz, indicated that the typical background acoustic noise at 30.48 m/sec was around 93 db re 0.0002 dyn/cm^2. These levels of ambient turbulence and acoustic noise were considered low enough so as not to unfavorably affect the measurements of boundary-layer characteristics.

Two axisymmetric convex afterbodies without stern separation were used for the present experimental investigation. Their afterbody length/diameter ratios (L_A/D) were 4.308 and 2.247. The detailed offsets for Models 1 and 2 are given in Tables 1 and 2. Each afterbody was connected to a parallel middle body of length L_M and an existing streamlined forebody with a bow-entrance length diameter ratio (L_E/D) of 1.82. The total length of each model (L) is fixed at a constant value of 3.066 m. The diameter of the parallel middle body (r_{max}) is 27.94 cm. The common forebody and a portion of the parallel were constructed of wood. The afterbody and the remaining portions of the parallel middle body were constructed of molded fiberglass; specified profile tolerances were held to less than ±0.4 mm, all imperfections were removed, meridians were faired, and the fiberglass was polished to a 0.64-micron rms surface finish. The tail ends of the afterbody were shaped to accommodate the hub of an existing propeller. This modification caused a considerable change of body curvature in the region of $X/L \geq 0.96$. However, as will be seen later, the thicknesses of the boundary layer in this region are much larger than the local radii of the body. This deficiency does not cause serious degradation of boundary-layer flow at that point.

The model was supported by two streamlined struts separated by roughly one-third of the model length. The upstream strut had a 15 cm chord and the downstream strut a 3 cm chord. The disturbances generated by the supporting struts were within the region below the horizontal centerplane. Prior to the experiments, pressure taps and Preston tubes were used to check the axisymmetric characteristics of the stern flow at X/L = 0.90, 0.95, and 0.98. The circumferential variations of pressure and surface shear stress on the upper half of the two afterbodies at these three locations were within two percent. All the final measurements were made in each body's vertical centerplane along the upper meridian where there was little extraneous effect

TABLE 2 - Offsets for Model 2

X/L	Y/L	Y/R	X/L	Y/L	Y/R	X/L	Y/L	Y/R
0.0000	0.0000	0.0000	.2684	.0456	1.0000	.7363	.0456	1.0000
.0050	.0100	.2193	.2783	.0456	1.0000	.7477	.0456	1.0000
.0099	.0142	.3118	.2883	.0456	1.0000	.7553	.0456	1.0000
.0149	.0175	.3836	.2982	.0456	1.0000	.7666	.0456	1.0000
.0199	.0202	.4443	.3082	.0456	1.0000	.7780	.0456	1.0000
.0249	.0227	.4975	.3181	.0456	1.0000	.7856	.0456	1.0000
.0298	.0249	.5455	.3280	.0456	1.0000	.7952	.0456	1.0000
.0348	.0268	.5891	.3380	.0456	1.0000	.8050	.0455	.9996
.0398	.0287	.6291	.3479	.0456	1.0000	.8147	.0454	.9959
.0447	.0303	.6659	.3579	.0456	1.0000	.8245	.0450	.9871
.0497	.0319	.7000	.3678	.0456	1.0000	.8342	.0443	.9723
.0547	.0333	.7316	.3777	.0456	1.0000	.8459	.0431	.9452
.0593	.0347	.7606	.3877	.0456	1.0000	.8556	.0417	.9153
.0646	.0359	.7877	.3976	.0456	1.0000	.8654	.0400	.8789
.0696	.0370	.8126	.4076	.0456	1.0000	.8751	.0381	.8364
.0746	.0381	.8357	.4175	.0456	1.0000	.8849	.0359	.7881
.0795	.0390	.8566	.4274	.0456	1.0000	.8946	.0335	.7349
.0845	.0399	.8761	.4374	.0456	1.0000	.9044	.0309	.6775
.0895	.0407	.8937	.4473	.0456	1.0000	.9141	.0281	.6162
.0944	.0414	.9097	.4573	.0456	1.0000	.9239	.0251	.5514
.0994	.0421	.9241	.4672	.0456	1.0000	.9336	.0220	.4840
.1044	.0427	.9372	.4771	.0456	1.0000	.9453	.0182	.3993
.1093	.0432	.9487	.4871	.0456	1.0000	.9512	.0162	.3557
.1143	.0437	.9588	.4970	.0456	1.0000	.9570	.0142	.3111
.1193	.0441	.9677	.5070	.0456	1.0000	.9609	.0128	.2808
.1243	.0444	.9751	.5169	.0456	1.0000	.9648	.0114	.2501
.1292	.0447	.9817	.5268	.0456	1.0000	.9662	.0109	.2383
.1342	.0450	.9869	.5368	.0456	1.0000	.9682	.0101	.2221
.1392	.0452	.9913	.5467	.0456	1.0000	.9692	.0098	.2145
.1441	.0453	.9945	.5567	.0456	1.0000	.9702	.0094	.2055
.1491	.0454	.9969	.5666	.0456	1.0000	.9722	.0087	.1901
.1541	.0455	.9987	.5765	.0456	1.0000	.9732	.0083	.1818
.1590	.0455	.9996	.5865	.0456	1.0000	.9751	.0075	.1654
.1640	.0456	1.0000	.5964	.0456	1.0000	.9771	.0068	.1490
.1690	.0456	1.0000	.6064	.0456	1.0000	.9791	.0060	.1309
.1740	.0456	1.0000	.6188	.0456	1.0000	.9811	.0056	.1222
.1789	.0456	1.0000	.6264	.0456	1.0000	.9831	.0053	.1165
.1839	.0456	1.0000	.6378	.0456	1.0000	.9851	.0050	.1108
.1889	.0456	1.0000	.6454	.0456	1.0000	.9871	.0048	.1052
.1938	.0456	1.0000	.6567	.0456	1.0000	.9881	.0046	.1019
.1988	.0456	1.0000	.6681	.0456	1.0000	.9901	.0043	.0951
.2087	.0456	1.0000	.6757	.0456	1.0000	.9920	.0040	.0879
.2187	.0456	1.0000	.6871	.0456	1.0000	.9940	.0036	.0781
.2286	.0456	1.0000	.6984	.0456	1.0000	.9960	.0029	.0626
.2386	.0456	1.0000	.7060	.0456	1.0000	.9980	.0019	.0412
.2485	.0456	1.0000	.7174	.0456	1.0000	1.0000	0.0000	0.0000
.2584	.0456	1.0000	.7250	.0456	1.0000			

from the supporting strut. One half of the model length protruded from the closed-jet working section of the wind tunnel into the open-jet test section. The ambient static pressure coefficients across and along the entire open-jet chamber (7.16 × 7.16 × 6.4 m) were found to vary less than 0.3 percent of dynamic pressure. The tunnel blockage and the longitudinal pressure gradient along the tunnel length were almost completely removed by testing the afterbody in the open-jet test section.

The location of boundary-layer transition from laminar to turbulent flow was artifically induced by a 0.61 mm diameter trip wire located at $X/L = 0.05$. When the flow was probed with a hot-wire, the trip wire was found to effectively stimulate the flow at a location 1 cm downstream from the wire. As a result of the parasitic drag of the wire, the boundary layer can be theoretically considered to become turbulent at a virtual origin upstream of the trip wire. This virtual origin for the turbulent flow is defined such that the sum of the laminar frictional drag from the body nose to the trip wire, the parasitic drag of the trip wire, and the turbulent frictional drag after the trip wire equals the sum of the laminar frictional drag from the nose to the virtual origin and the turbulent frictional drag from the virtual origin to the after end of the model [McCarthy et al. (1976)]. The location of the virtual origin on the forebody with a 0.61 mm trip wire at $X/L = 0.05$ was found to be at $X/L = 0.015$ for a length Reynolds number of 5.9×10^6. The location of transition in the mathematical model for the present boundary-layer calculation is specified at this virtual origin. The length Reynolds number based on the distance from the trip wire to the end of the parallel middle body is larger than for 4×10^6 for the two afterbodies. It can be assumed that a fully established axisymmetric turbulent boundary layer exists at the beginning of the afterbody and that the trip wire has no peculiar effect on the boundary-layer characteristics of the stern.

3. INSTRUMENTATION

A 1.83-cm Preston tube was taped to the stern at successively further aft locations in order to measure the shear stress distribution along the upper meridian of each stern. The Preston tube used was calibrated in a 2.54-cm water pipe flow facility described by Huang and von Kerczek (1972). Pressure taps (0.8 mm diameter) were used to measure steady pressures at the same locations as the Preston tubes. The taps were connected by "Tygon" plastic tubes to a scanning valve located inside the model. The output tube from the scanning valve was run from the model through the supporting strut to a precision pressure transducer located on the quiescent floor of the open-jet chamber. The pressure transducer was a Validyne Model DP 15-560 designed for measuring low pressure up to $\pm 1.4 \times 10^4$ dyn/cm^2 (±0.2 psi). The zero-drift, linearity, and hysteresis of this transducer system were carefully checked and the overall accuracy was found to be within 0.5 percent of the dynamic pressure.

A Prandtl type pitot-static pressure probe of 3.125-mm diameter with four equally spaced holes located at three diameters aft of the nose was used to measure static pressure across the boundary layer. The yaw sensitivity of the static pressure probe was examined by yawing the probe in the freestream. It was found that the measured static pressure was insensitive to the probe angle up to 5° yaw. The response of measured static pressure to probe angle was nearly a cosine function of yaw angle for yaw angles less than 15°. The static pressure probe was aligned parallel to the model axis for all of the static pressure measurements. The local angles between the resultant velocity of the boundary-layer flow and probe axis were found to be less than 15° (5° for most cases). The maximum static pressure coefficient in the boundary layer was less than 0.2. Thus, the error in the measured static pressure caused by not aligning the probe with the local flow was less than 0.8 percent of the dynamic pressure.

The mean axial and radial velocity components and the Reynolds stress were measured by a TSI, Inc. Model 1241 "X" wire. The probe elements were 0.05 mm in diameter with a sensing length of 1.0 mm. The spacing between the two cross elements is 1.0 mm. A two-channel TSI Model 1050-1 hot-wire anemometer and linearizer were used. The "X" wire, together with temperature compensated probes, were calibrated at the factory and supplied with their individual linearization polynomial coefficients. This eliminated the time-consuming linearization process. The frequency response of the anemometer system claimed by the manufacturer is dc to 200 kHz. Calibration of the "X" wire was made before and after each set of measurements. It was found that this hot-wire anemometer system had a ±0.5 percent accuracy (±0.15 m/s accuracy at the free stream velocity of 30.5 m/sec) during the entire experiment. The accuracy of cross-flow velocity measurements by the cross wire was estimated by yawing the cross-wire in the free stream. It was found that the accuracy of the measured cross-flow velocities was about one percent of the free stream velocity.

The linearized signals were fed into a Time/Data Model 1923-C Real-Time analyzer. Both channels of analog signal were digitized at a rate of 80 points per second for ten seconds. These data were immediametely analyzed by a computer code to obtain the individual components of mean velocity, turbulence fluctuation, and Reynolds stress on a real time basis.

A traversing system enclosed in a 15 cm chord, streamlined strut was used to support both the static pressure probe and the cross-wire probe. The traversing system was mounted either on an I-beam along the axis of the lower floor of the open-jet chamber or on the ceiling of the closed-jet section. The combination of these two mounting arrangements allowed the measurements to be made at any axial location along the stern and up to 50 percent of the body length downstream from the aft end of the body. Positioning of the traversing system was achieved by manual adjustment in the axial direction and by remote control in the radial direction. The total radial traverse of the probe was 25 cm. The radial position of the probe was monitored by a potentiometer to with a ±0.01 mm accuracy.

4. COMPARISON OF EXPERIMENTAL AND THEORETICAL RESULTS

In the following, the experimental results for the thick stern boundary layers are presented and compared with theoretical results. The theories used in the comparison are the Douglas CS differential boundary-layer method in conjunction with the displacement body concept. The iteration procedures for numerical computation are given by Huang et al. (1976). In this investigation, the displacement body concept for solving the interaction between the thick stern boundary layer and potential flow will be examined and an eddy-viscosity model will be evaluated.

Measured and Computed Pressure and Shear Stress Distributions

Significant improvement in the accuracy of measuring surface pressure and shear stress have been made by using a precision pressure transducer. The present results are more reliable than the earlier results of Huang et al. (1976), although the differences are small.

The measured and computed values of the pressure coefficient, $C_p = 2(p - p_o)/\rho U_o^2$, are compared in Figure 1 for Afterbody 1 and in Figure 2, for Afterbody 2; p is the local static pressure, ρ is the mass density of the fluid, U_o is the free-stream velocity and p_o is the ambient pressure (the quiescent chamber static pressure of the open-jet section). The pressure coefficients computed on the displacement body were carried radially back to the hull surface and the radial distribution of pressure at a given axial station was assumed to be a constant between the hull surface and the fictitious displacement surface. The maximum error in the static pressure associated with this assumption is less than two percent of the dynamic pressure (next section). The agreement between theory and measurement is excellent for both afterbodies. The results suggest that the displacement body concept as used by Huang et al. (1976) permits accurate computation of the pressure distribution on the stern.

The measured and computed distributions of local shear stress, C_τ, are compared in Figure 3. The agreement between theory and measurement is also very good for both afterbodies except for $x/L > 0.95$ where the measured values of C_τ are lower than the computed values.

Measured and Computed Static Pressure Distribution

The measured and computed static pressure coefficients for Afterbody 1 are compared in Figure 4 at various locations across the stern boundary layer and in Figure 5 for the near wake. Figures 6 and 7 show the comparisons for Afterbody 2. The off-body option of the Douglas potential-flow computer code was used to compute the static pressure distributions off the displacement body. As can be seen in Figures 4 through 7, the computed static pressure distributions across the entire stern boundary layer and near wake mostly agree well with the measured static pressure distributions. The discrepancy between the measured and computed values of C_p is in general less than 0.01 which is about the accuracy of the measurement.

As will be seen later, both displacement bodies are convex from the parallel middle body up to $X/L = 0.91$ and become concave downstream from $X/L > 0.91$. However, the actual afterbodies are convex all the way up to $X/L = 0.96$. The measured values of C_p shown in Figures 4 through 7 increase with radial distance for $X/L < 0.91$, indicating that the mean streamlines are convex; and measured values of C_p decrease with radial distance for $X/L > 0.91$,

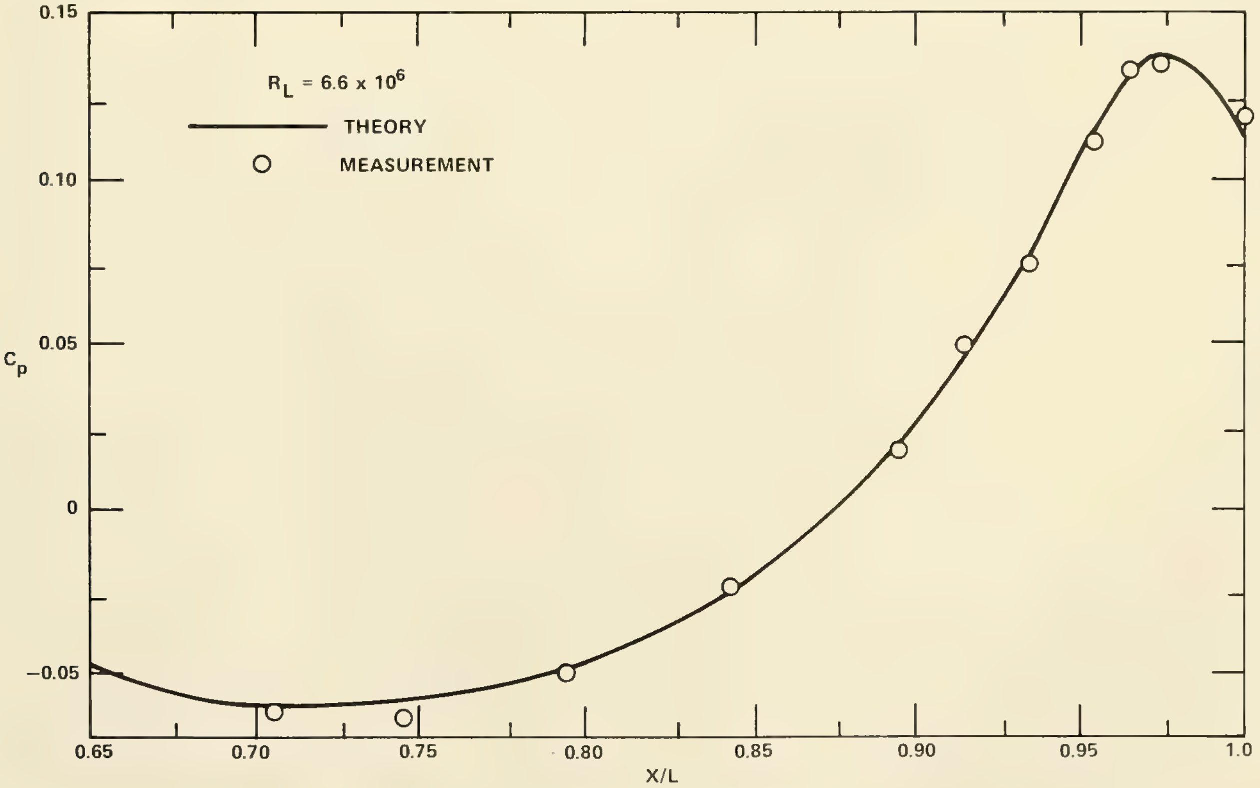

FIGURE 1. Computed and measured stern pressure distribution on afterbody 1.

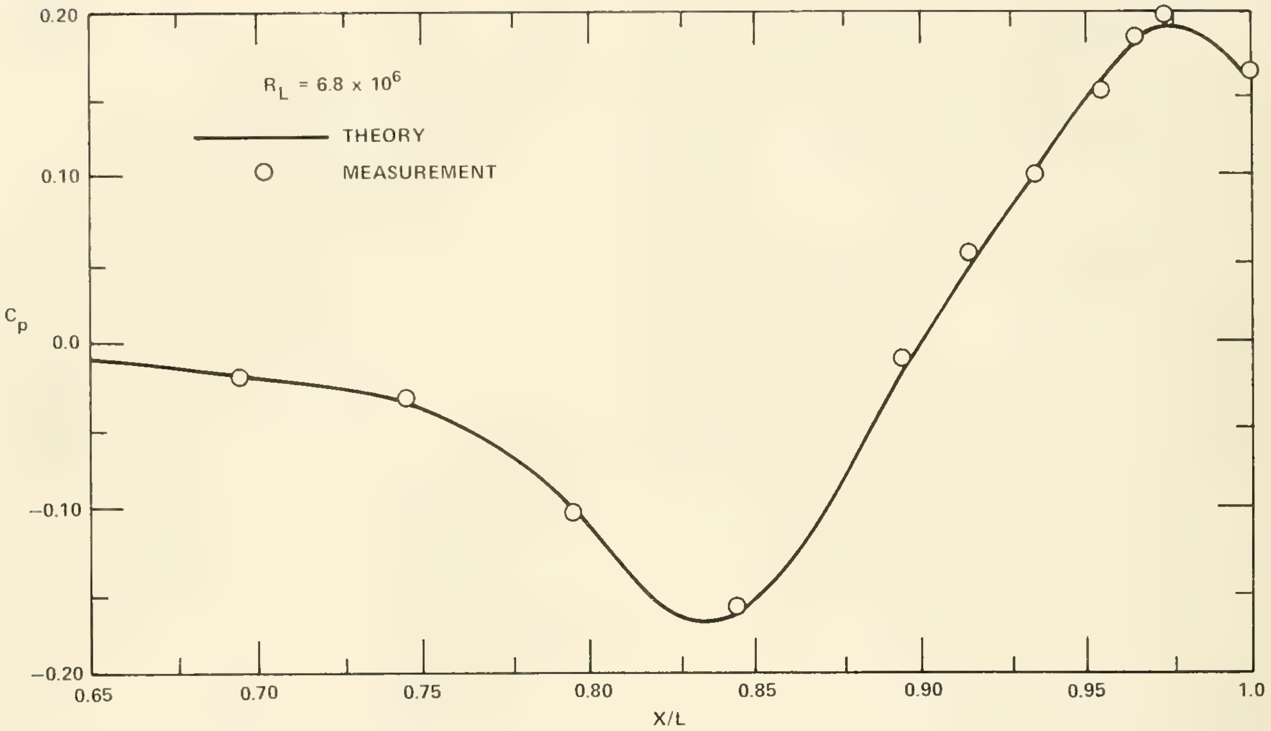

FIGURE 2. Computed and measured stern pressure distribution on afterbody 2.

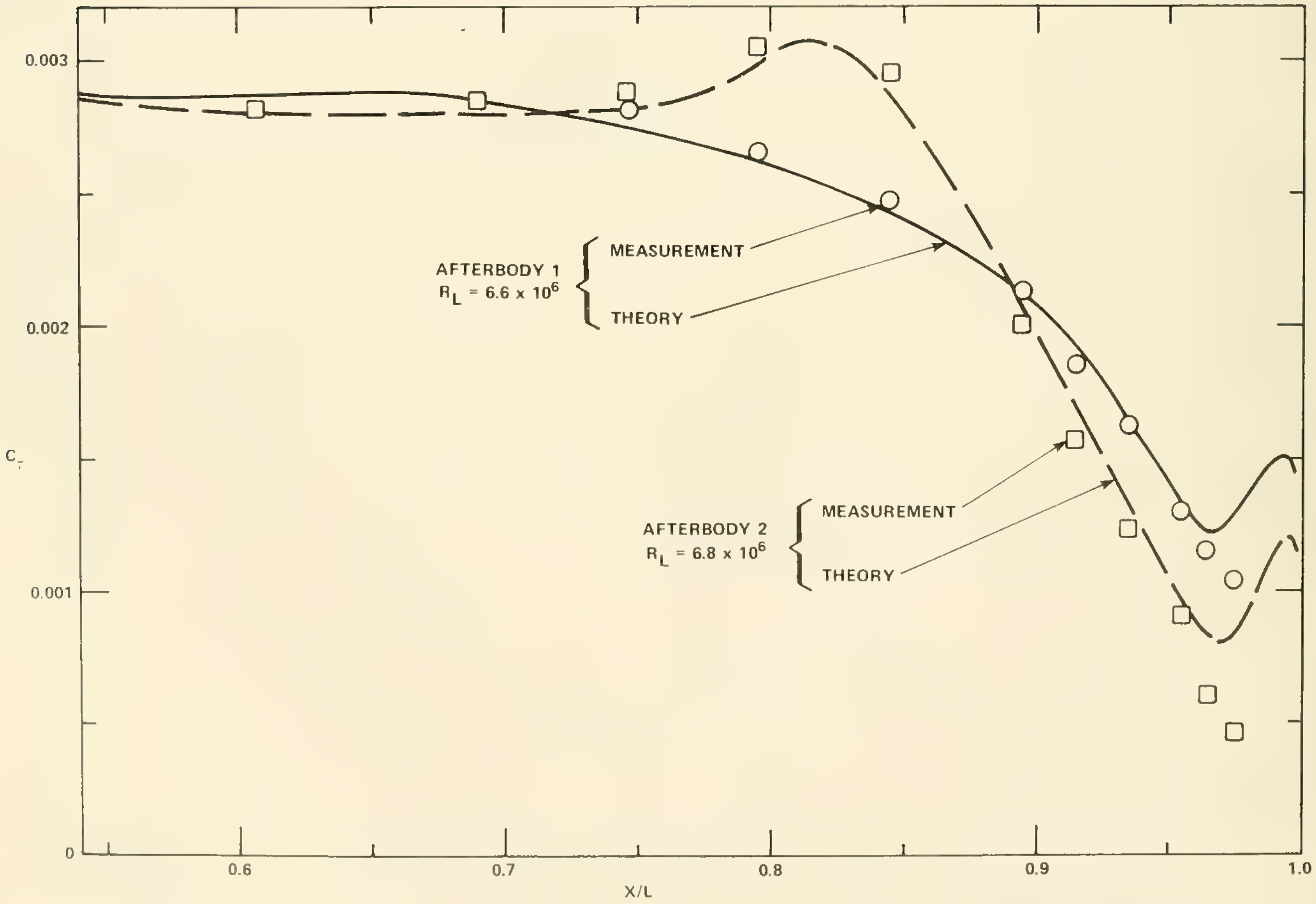

mputed and measured shear stress distribution on afterbodies 1 and 2.

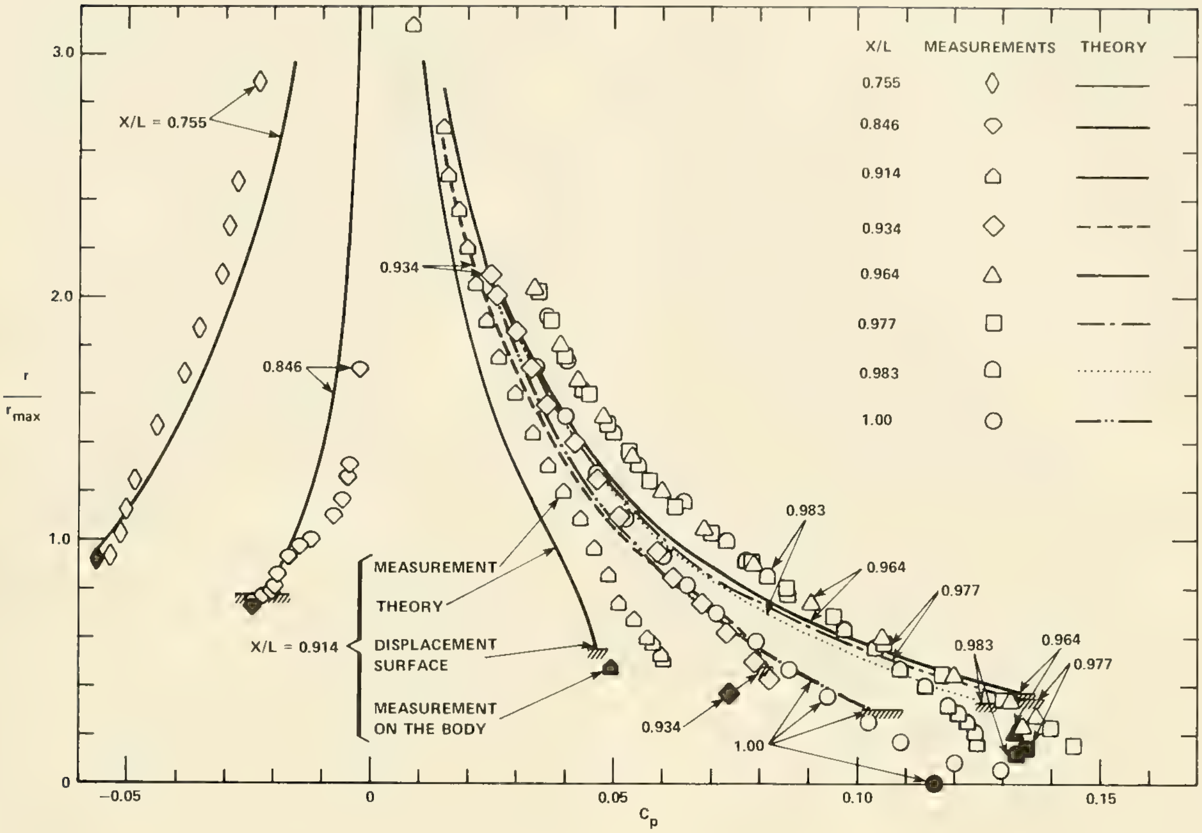

FIGURE 4. Computed and measured static pressure distributions across stern boundary layer of afterbody 1.

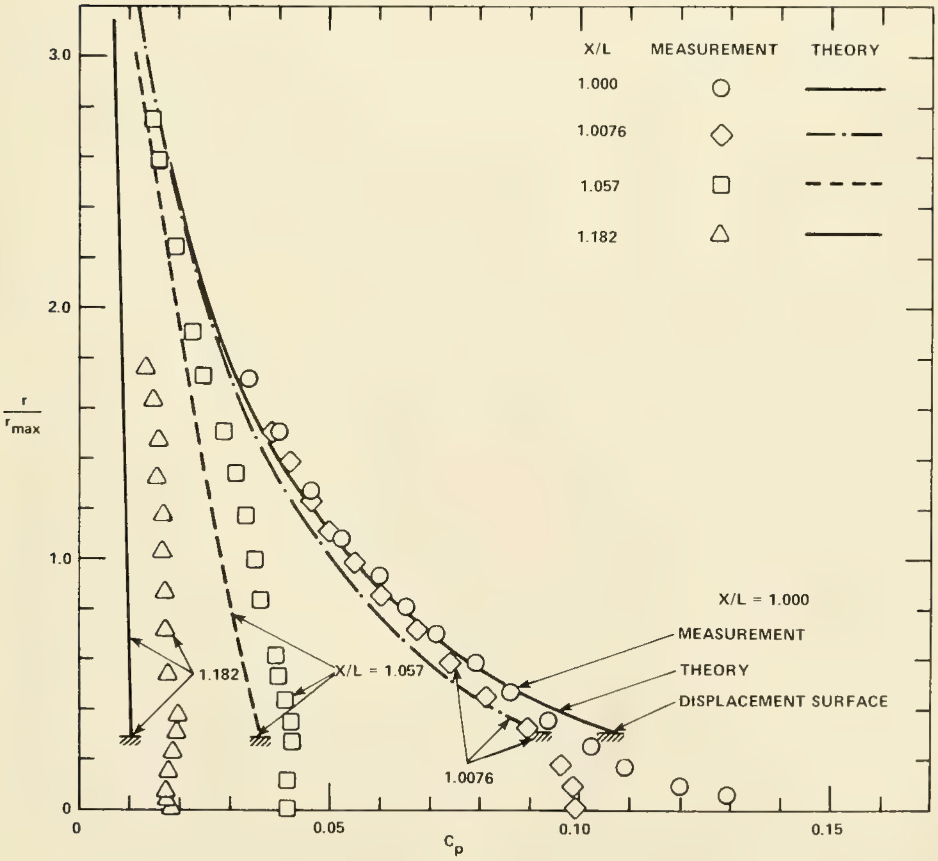

FIGURE 5. Computed and measured static pressure distributions across near wake of afterbody 1.

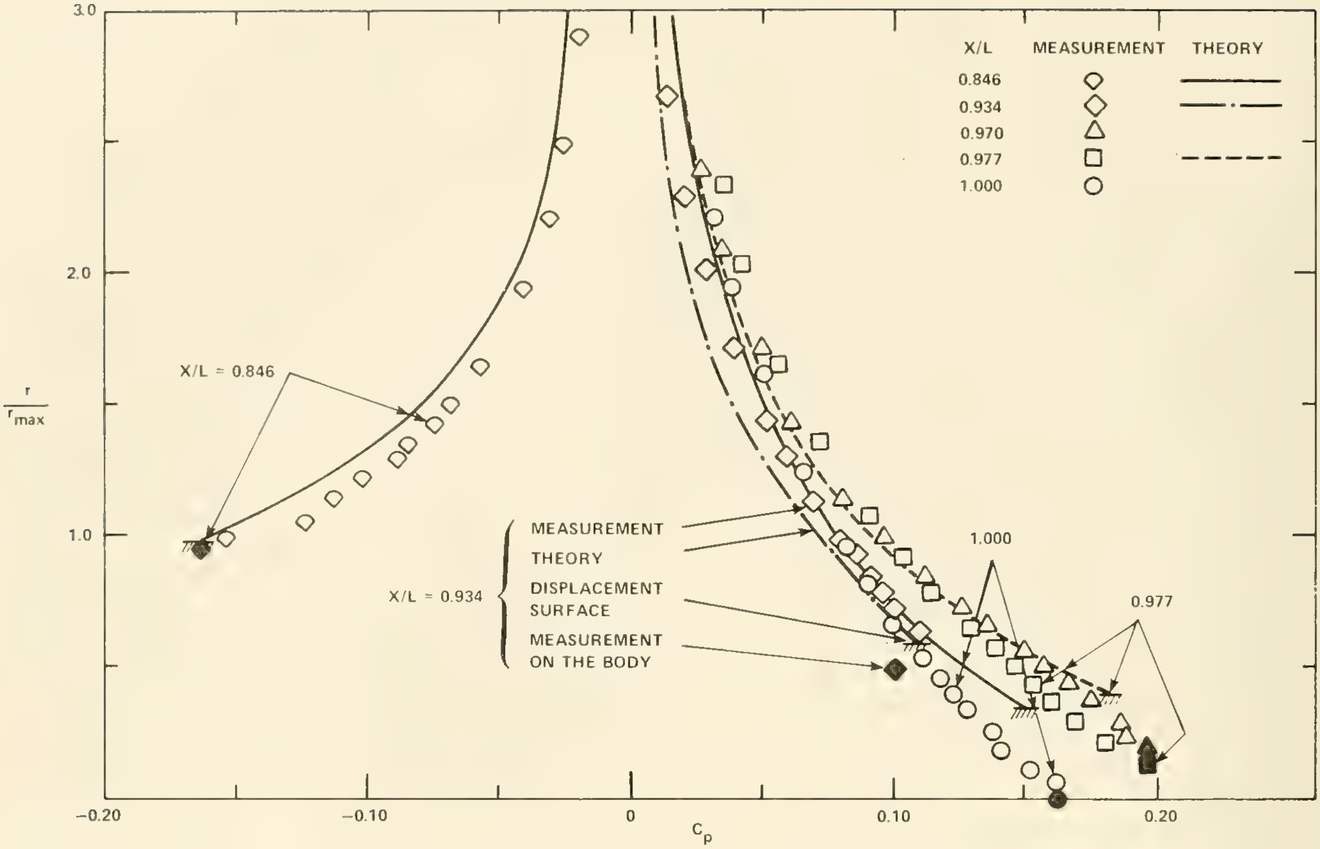

FIGURE 6. Computed and measured static pressure distributions across stern boundary layer of afterbody 2.

indicating that the mean streamlines are concave. Thus, the curvatures of the mean streamlines are more closely related to the curvatures of the displacement body than the actual body. The close agreement between the computed and measured static pressure distributions again supports the displacement body concept for computing the potential flow outside of the displacement surface.

5. MEASURED AND COMPUTED MEAN VELOCITY PROFILE

The incompressible steady continuity and momentum equations for thin axisymmetric turbulent boundary layers are

$$\partial(ru_s)/\partial s + \partial(rv_n)/\partial n = 0 \tag{1}$$

and

$$\begin{aligned} & u_s \partial u_s/\partial s + v_n \partial u_s/\partial n \\ & = -dp/\rho ds + \partial[r(\nu\partial u_s/\partial n)\overline{-u_s'v_n'}]/r\partial n \\ & u_s(s,0) = v_n(s,0) = 0 \text{ at } n = 0 \end{aligned} \tag{2}$$

where

$$r(s,n) = r_o(s,n) + n\cos\alpha$$

$$\alpha = \tan^{-1}(dr_o/dx)$$

r_o is the body radius; x is the axial distance; u_s and v_n are the mean velocity components respectively parallel to and normal to the meridan of the body (s and n directions); ν is the kinematic viscosity of the fluid; $\overline{-u_s'v_n'}$ is the Reynolds stress; and u_s' and v_n' are the velocity fluctuations in the s and n directions respectively. The Douglas CS method assumes that the Reynolds stress depends upon the local flow parameters only, e.g.,

$$\overline{-u_s'v_n'} = \begin{Bmatrix} \varepsilon_i \\ \varepsilon_o \end{Bmatrix} \frac{\partial u_s}{\partial s} \quad \begin{matrix} \text{for } o \leq n \leq n_c \\ \\ \text{for } n_c \leq n \leq \delta \end{matrix} \tag{3}$$

where $\varepsilon_i = \ell^2 \dfrac{r}{r_o} \dfrac{\partial u_s}{\partial n}$ (eddy viscosity in the inner region)

$$\varepsilon_o = 0.0168\,\gamma_{tr} \int_o^\infty (U_e - u_s)\,dn = 0.0168\, U_e\, \delta_p^*\, \gamma_{tr},$$

(eddy viscosity in the outer region),

$$\ell = 0.4\, r_o \ln\left(\frac{r}{r_o}\right) \left\{1 - \exp\left[-\frac{r_o}{A} \ln\left(\frac{r}{r_o}\right)\right]\right\},$$

(mixing-length parameter in the inner region),

$$A = 26\,\nu\left(\frac{\tau_w}{\rho}\right)^{-\frac{1}{2}}$$, (Van Driest's damping factor),

$$\delta_\rho^* = \int_0^\delta \left(1 - \frac{u_s}{U_e}\right) dn, \quad \text{[displacement thickness (planar definition)]}$$

$$\gamma_{tr} \cong \left[1 + 5.5 \left(\frac{n}{\delta}\right)^6\right]^{-1}, \quad \text{(intermittency factor)},$$

$$\delta \simeq \delta_{995}, \quad \text{(boundary-layer thickness)},$$

$$\tau_w, \quad \text{(wall shear stress)},$$

U_e is the potential-flow velocity used in the boundary-layer calculations, and at y_c, ε_i is equal to ε_o. A computer code to solve for the values u_s/U_e and v_n/U_e has been developed by Cebeci and Smith (1975) using Keller's numerical box scheme.

The velocity components measured in the present investigation are u_x and v_r, the components in the axial and the radial directions of the axisymmetric body. The computed values of u_x and v_r are given by

$$\frac{u_x(r)}{U_o} = \frac{u_s(n)}{U_e}\frac{U_e}{U_o}\cos\alpha - \frac{v_n(n)}{U_e}\frac{U_e}{U_o}\sin\alpha, \tag{4}$$

$$\frac{v_r(r)}{U_o} = \frac{u_s(n)}{U_e}\frac{U_e}{U_o}\sin\alpha + \frac{v_n(n)}{U_e}\frac{U_e}{U_o}\cos\alpha, \tag{5}$$

where u_s/U_e and v_n/U_e are computed by the CS method. The potential-flow pressure is assumed to be constant between the body surface and the displacement surface and is equal to the pressure p_d computed on the displacement body. The value of U_e used in Eqs. (4) and (5) is equal to $\sqrt{1 - p_d}$ and U_e is assumed to be parallel to the body surface.

The displacement-body concept can be used to improve the computed values of u_x and v_r outside of the displacement surface of thick boundary layers, e.g.,

$$\frac{u_x(r)}{U_o} = \frac{u_s(n)}{U_p\cos(\theta-\alpha)}\frac{U_p\cos(\theta-\alpha)}{U_o}\cos\alpha - \frac{v_n(n)}{U_p\sin(\theta-\alpha)}\frac{U_p\sin(\theta-\alpha)}{U_o}\sin\alpha, \tag{6}$$

$$\frac{v_r(n)}{U_o} = \frac{u_s(n)}{U_p\cos(\theta-\alpha)}\frac{U_p\cos(\theta-\alpha)}{U_o}\sin\alpha + \frac{v_n(n)}{U_p\sin(\theta-\alpha)}\frac{U_p\sin(\theta-\alpha)}{U_o}\cos\alpha, \tag{7}$$

where the variation of the inviscid static pressure,

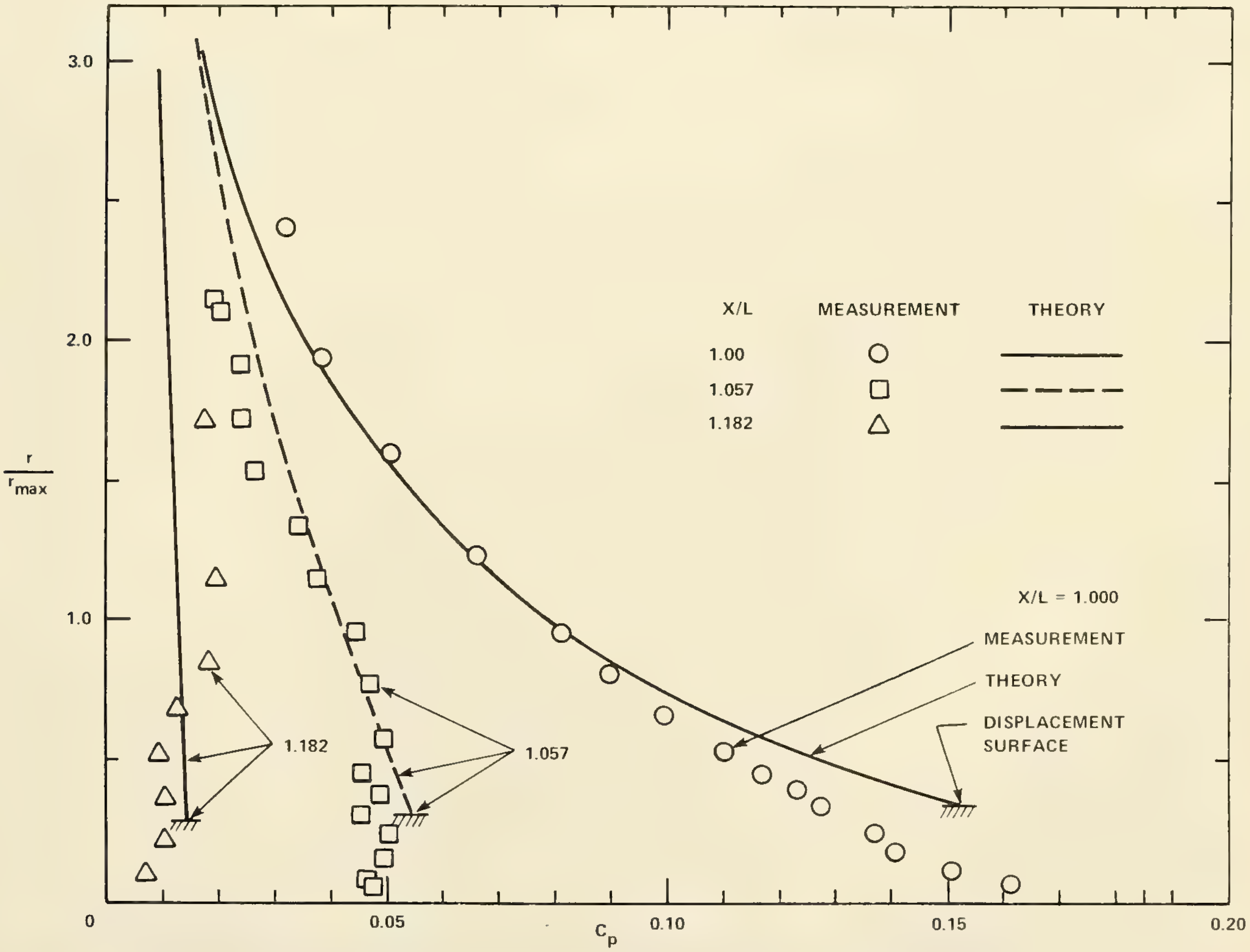

FIGURE 7. Computed and measured static pressure distributions across near wake of afterbody 2.

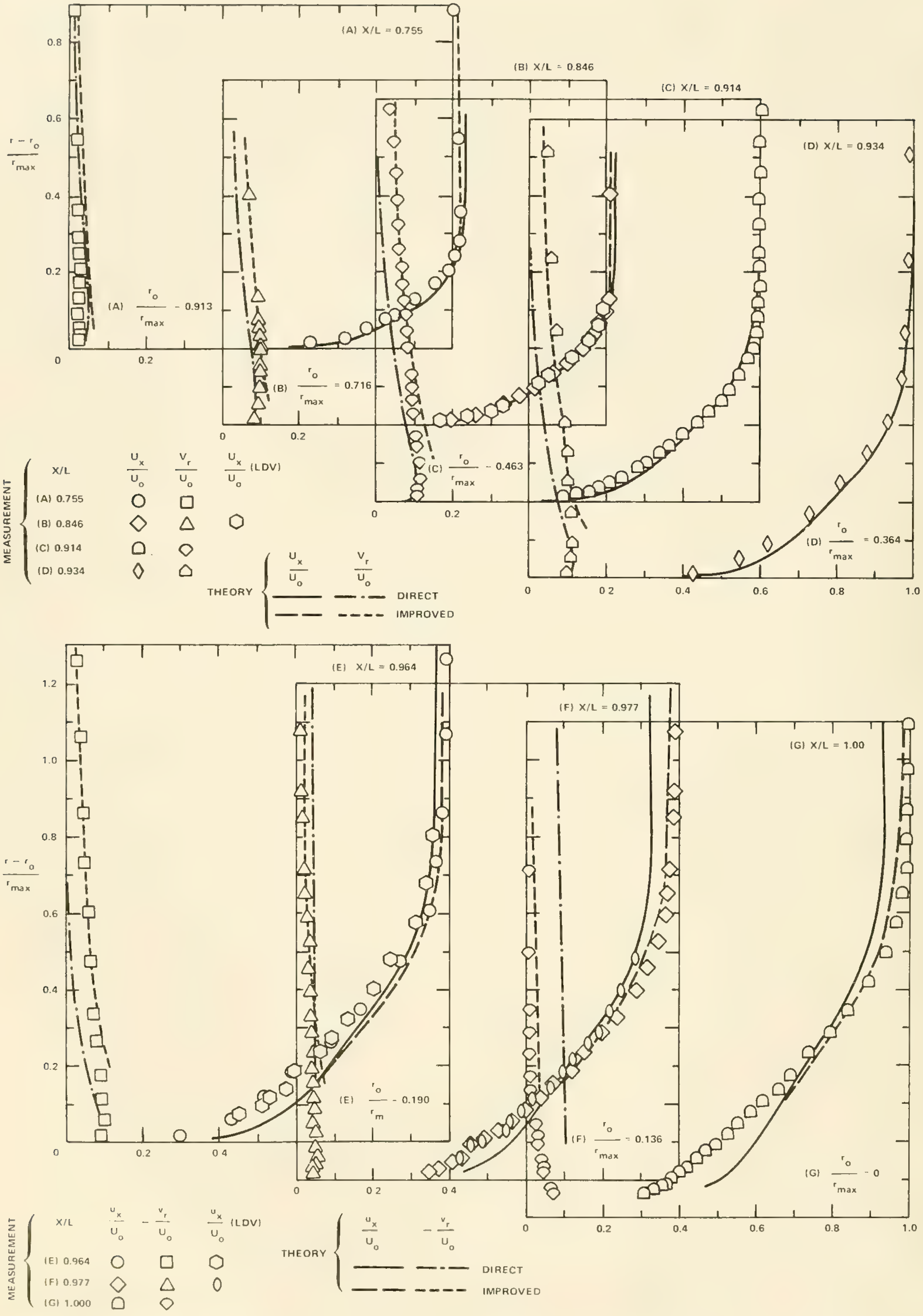

[illegible] Computed and measured mean axial and radial velocity distributions across stern boundary [illegible]

$C_p(r)$, across the thick boundary layer is expressed in terms of the inviscid resultant velocity U_p [$U_p(r) = \sqrt{1 - C_p(r)}$] and θ is the angle between the inviscid resultant velocity U_p and body axis (θ is positive when U_p is directed away from the axis). In the first improvement the values $u_s/(U_p\cos(\theta-\alpha))$ are taken as the computed values of $f' = u_s/U_e$ in the CS method with U_e equal to the inviscid resultant velocity on the displacement body. At the edge boundary layer, the value of $u_s(U_p\cos(\theta-\alpha))$ is equal to 1.0. The value of $v_n/(U_p\sin(\theta-\alpha))$ is also equal to 1.0 since the boundary-layer-induced normal velocity is assumed to be equal to the inviscid normal velocity of the displacement body at that point [Lighthill (1958)]. The theoretical proof for an axisymmetric body has not been worked out in the literature and will not be given here. However, the validity of the assumption will be borne out by the experimental measurements of v_r. Therefore, Eqs. (6) and (7) reduce to the proper limit at the edge of the boundary layer, e.g.,

$$\frac{u_x(r=\delta_r)}{U_o} = \frac{U_\delta}{U_o}\cos\theta, \qquad (8)$$

$$\frac{v_r(r=\delta_r)}{U_o} = \frac{U_\delta}{U_o}\sin\theta, \qquad (9)$$

which are the inviscid axial and radial velocity components of the displacement body, where $U_\delta = \sqrt{1 - C_p(r = \delta_r)}$. Outside of the boundary layer, Eqs. (8) and (9) are also valid so long as the local inviscid values of U_p and θ for the displacement body are used. The improved values in Eqs. (6) and (7) account for the variation of the inviscid static pressure and potential-flow vector across the thick boundary layer and make appropriate use of the results of the CS method. As already noted, the variation of static pressure computed across the boundary layer outside of the displacement surface agrees quite well with the experimental results.

Figure 8 shows the comparison of the mean axial and radial velocity profiles at several axial stations on Afterbody 1, and Figure 9 shows the measured axial velocity profiles across the near wake of Afterbody 1. The theoretical results at X/L = 1.00 were calculated at X/L = 0.998. Figures 10 and 11 show comparisons of the measured and computed velocity profiles for Afterbody 2. The mean axial and radial velocity components u_x and v_r were measured by a cross-wire probe and the experimental accuracy of measurements of u_x/U_o and v_r/U_o were respectively about 0.5 percent and 1.0 percent.

As shown in Figures 8 and 10, the theoretically computed velocities, which account for the variation of static pressure distribution across the thick boundary layer, agree better with the measured axial and radial profiles outside of the displacement surface. These results suggest that a simple improvement of the existing boundary-layer computation method can be made for the thick stern boundary

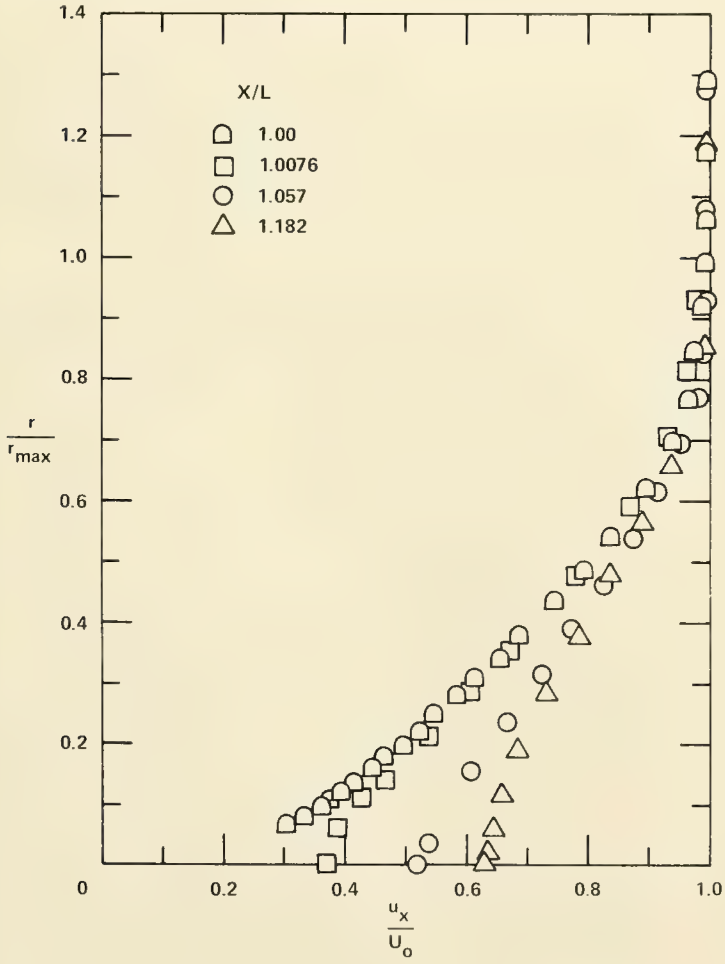

FIGURE 9. Measured mean axial velocity distributions across near wake of afterbody 1.

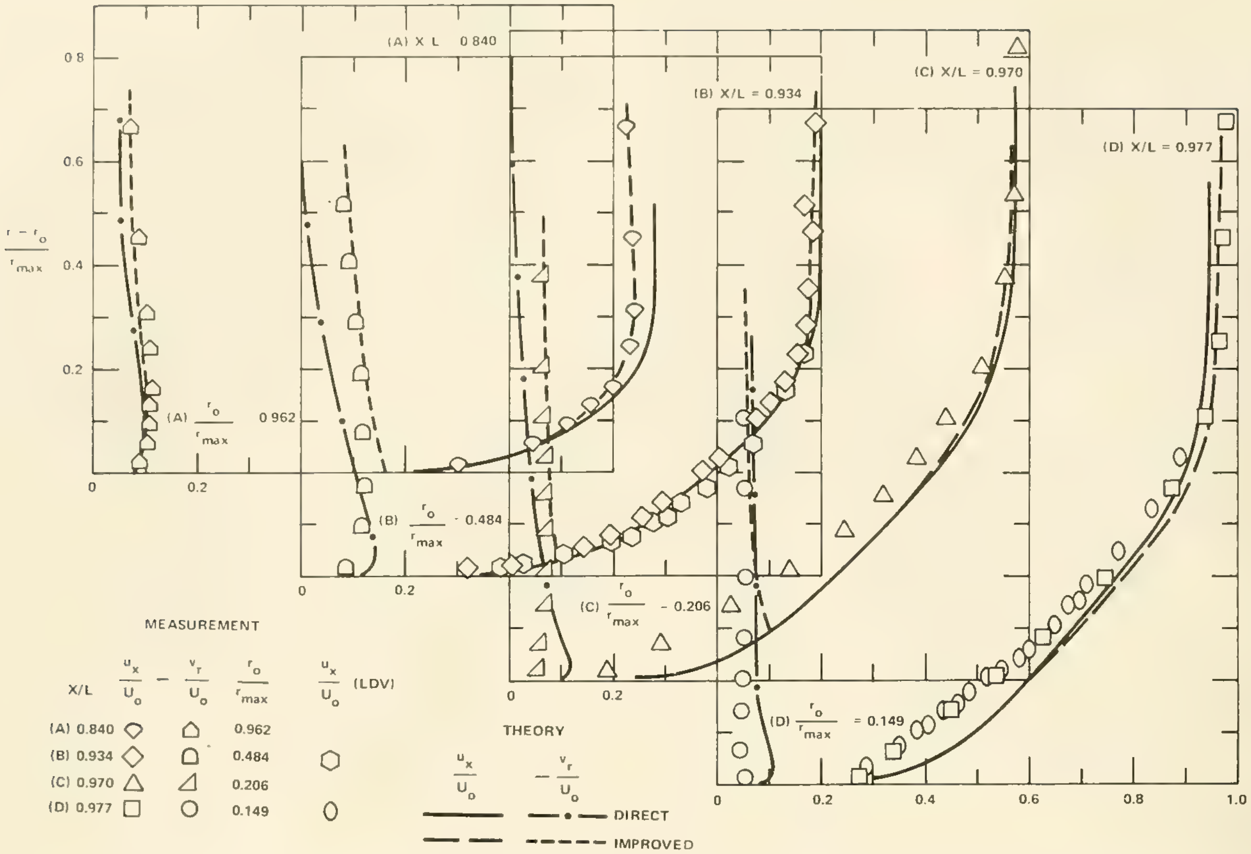

FIGURE 10. Measured and computed mean axial and radial velocity distributions across stern boundary layer of afterbody 2.

layer by means of the displacement body concept. However, it is important to point out that the measured axial velocity profiles in the inner region are in general smaller than the theoretical values. The eddy viscosity model plays an important role in this region; therefore, it is essential to examine the eddy viscosity model used for computing the thick stern boundary layer. Figures 8 and 10 also show the comparison of the axial velocities measured by the cross-wire and by LDV (Huang et al., 1976). The agreement is very good inside the boundary layer. However, due to the artifical seeding of oil mist required for the LDV, the axial velocities near the edge of the boundary layer measured by LDV are smaller than that by the cross-wire.

6. COMPARISON OF MEASURED AND COMPUTED INTEGRAL PARAMETERS

The integral parameters are derived from the measured velocity distribution. The two-dimensional displacement thickness is defined as

$$\delta_p^* = \int_0^{\delta_r} \left[1 - \frac{u_x(r)}{U_x(r)} \right] dr \quad , \tag{10}$$

where δ_r is the boundary thickness measured radially normal to the body axis and $U_x(r)$ is the value of the axial component of inviscid flow velocity computed about the displacement body. The value of $U_x(r)$ is computed by the potential-flow method except inside of the displacement surface where it is assumed that $U_x(r) = U_x(r_d)$ with r_d being the radius of the displacement surface. The boundary-layer thickness δ_r is defined at the radial position where the measured value of $u_x(r)$ equals 0.995 $U_x(r)$. It is difficult to obtain δ_r precisely since the accuracy of the u_x/U_o measurement is only about 0.005. Nevertheless, the overall accuracy of the values of δ_r estimated in the present investigation is about 10 percent.

A measure of the mass-flux deficit in the thick axisymmetric boundary layer is defined by

$$\Lambda = \int_{r_o}^{r_o+\delta_r} \left[1 - \frac{u_x(r)}{U_x(r)} \right] r dr = \int_{r_o}^{r_o+\delta_r^*} r dr \tag{11}$$

where r_o is the local body radius and δ_r^* is the axisymmetric displacement thickness. Thus, the axisymmetric displacement thickness becomes

$$\frac{r_o + \delta_r^*}{r_{max}} = \sqrt{\left(\frac{r_o}{r_{max}}\right)^2 + 2 \frac{\Lambda}{r_{max}^2}} \tag{12}$$

where r_{max} is the maximum radius of the body.

The displacement body in the present investigation is defined by $r_d = \delta_r^* + r_o$ rather than the planar definition, $r_d = \delta_p^* + r_o$. Similarily, a measure of the momentum-flux deficit is defined by

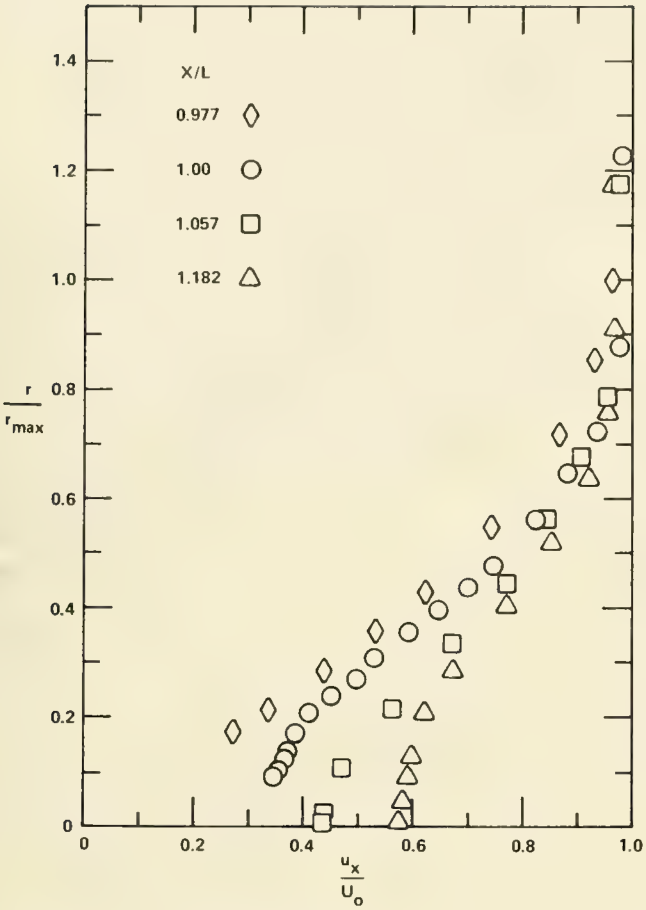

FIGURE 11. Measured mean axial velocity distributions across near wake of afterbody 2.

$$\Omega = \int_{r_o}^{r_o+\delta_r} r \left[1 - \frac{u_x(r)}{U_x(r)} \right] \frac{u_x(r)}{U_x(r)} \; rdr \qquad (13)$$

The measured and computed values of δ_r^* and δ_r are shown in Figure 12 for Afterbody 1 and in Figure 13 for Afterbody 2. The measured values of δ_r^* and δ_r for $X/L > 0.90$ are slightly larger than the computed values for both bodies.

The transverse curvatures of the boundary-layer flow with respect to the body radius, $(r_o + \delta_r^*)/r_o$ and $(r_o + \delta_r)/r_o$, are also shown in Figures 12 and 13. A drastic increase of the values of $(r_o + \delta_r^*)/r_o$ and $(r_o + \delta_r)/r_o$ occurs at $X/L = 0.9$, indicating the important effect of transverse curvature on the stern. The longitudinal curvature of the body is denoted by $K_o = (d^2r_o/dx^2)\ [1 + (dr_o/dx^2)]^{-3/2}$ and the longitudinal curvature of the displacement body is denoted by $K_d = (d^2r_d/dx^2)\ [1 + (dr_d/dx)^2]^{-3/2}$. A positive sign for K_o or K_d indicates concave surface. The values of $K_o r_{max}$ and $K_d r_{max}$ are shown in Figures 12 and 13. There is a significant difference between K_o and K_d in the thick boundary layer region. In each case, the curvature of the displacement body is convex up to $X/L = 0.92$, then changes to concave and remains concave throughout the entire thick boundary-layer and near-wake region. The curvature of the body surface is convex up to $X/L = 0.96$. As already shown in Figures 4 and 6, the measured distributions of static pressure and hence the curvatures of the mean streamlines are much more closely related to the displacement body than to the actual body. The magnitudes of the maximum concave and convex radii of curvature of the displacement bodies are estimated to be 8 r_{max} and 30 r_{max} for Afterbody 1 (Figure 12) and 7 r_{max} and 8 r_{max} for Afterbody 2 (Figure 13), respectively. The magnitudes of the radii of curvature of the mean streamlines outside of the displacement body are expected to be larger than 10 r_{max}.

7. MEASURED TURBULENCE CHARACTERISTICS

The cross-wire probe was used to measure the turbulence characteristics in the thick boundary layer. The measured Reynolds stresses and the measured mean velocity profiles were used to obtain eddy viscosity and mixing length.

Measured Reynolds Stresses

The turbulence characteristics in the thick boundary layer can be represented by the distributions of Reynolds stresses, namely, $\overline{-u'v'}$, u'^2, v'^2, and w'^2, where u', v', and w' are the turbulence fluctuations in the axial, radial, and azimuthal directions, respectively. Figures 14 and 15 show the measured distribution of Reynolds stress $\overline{-u'v'}/U_o^2$ and three components of turbulence intensity at several axial locations along the two afterbodies. In general, for a given location, the intensity of the axial turbulence-velocity component has the highest value and the intensity of the radial component has the smallest value. The degree of anisotropy decreases as the stern boundary layer becomes thicker. Furthermore, the increased boundary-layer thickness is accompanied by a reduction of turbulence intensities and a more uniform distribution of turbulence intensities in the inner region. The variation along the body of the radial location of the maximum values of the measured Reynolds stress $\overline{-u'v'}/U_o^2$ layer is small. The spatial resolution of the cross-wire probe is not fine enough to measure the Reynolds stress distributions in the inner region when the boundary layer is thin. As the stern boundary layer increases in thickness, the location of maximum Reynolds stress moves away from the wall (Figures 14 and 15). The values of Reynolds stress $\overline{-u'v'}$ decrease quickly from the maximum value to zero at the edge of the boundary layer. As shown in Figures 14 and 15, the shape of the Reynolds stress distribution curves in the outer region is quite similar for all the thick boundary layers. It is interesting to note that the shapes of the Reynolds stress distributions in the inner regions are different from those measured in the wake at $X/L = 1.057$ and 1.182 (Figures 14 and 15); this is a typical characteristic of a developing wake [Chevray (1968)]. The Reynolds stresses experience a drastic reduction in magnitude near the edge of the boundary layer.

A turbulence structure parameter defined by $a_1 = \overline{-u'v'}/q^2$, where $q^2 = u_1'^2 + v_1'^2 + w'^2$, is of interest. The measured distributions of a_1 are shown in Figure 16. Most thin boundary layer data show that a_1 is almost constant ($a_1 \doteq 0.15$) between 0.05 and 0.8δ. The present thick stern axisymmetric data shown in Figure 16 indicate that a_1 is almost constant up to 0.6 δ_r, and the magnitudes of a_1

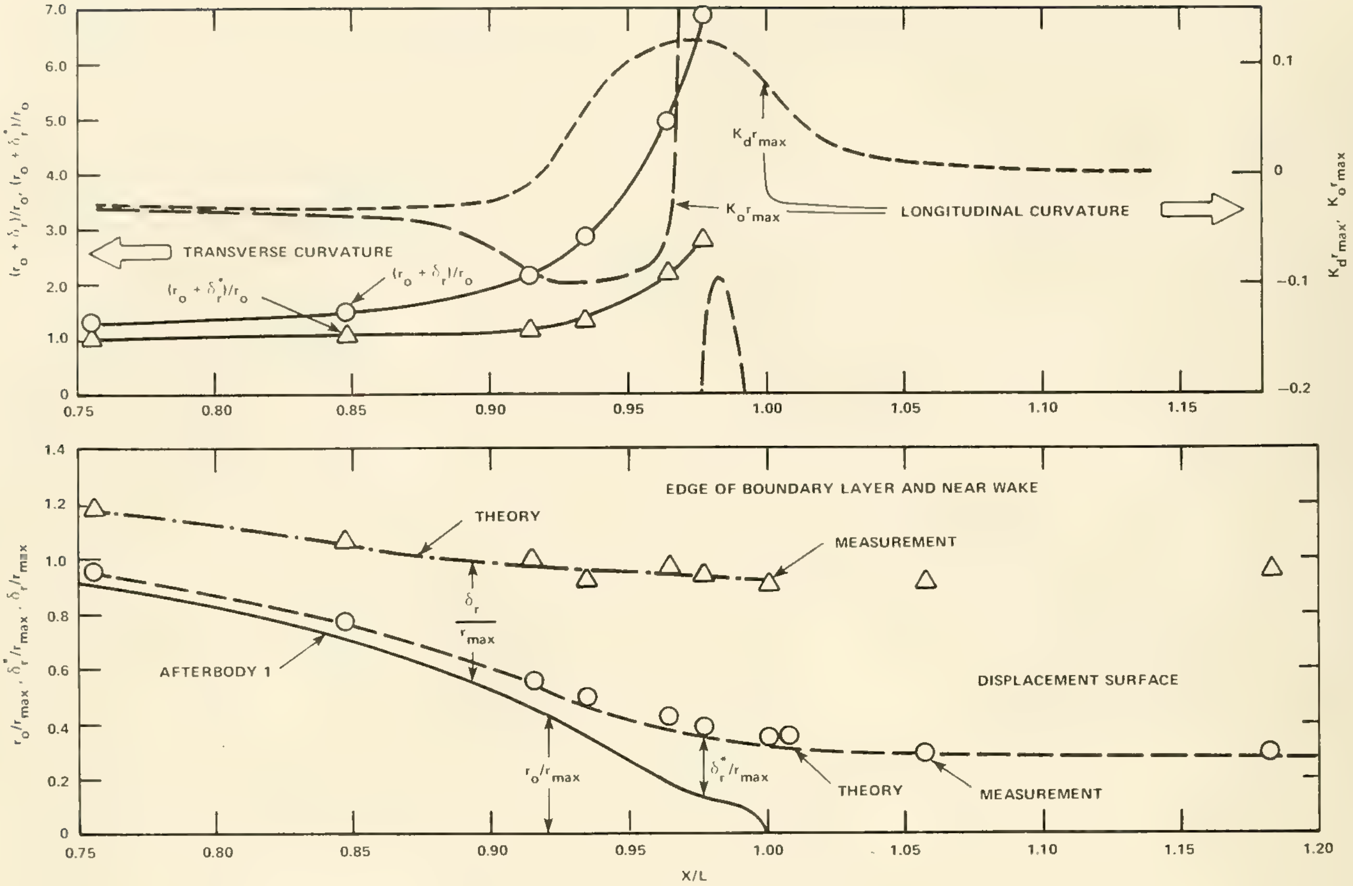

FIGURE 12. Transverse and longitudinal curvature parameters for afterbody 1.

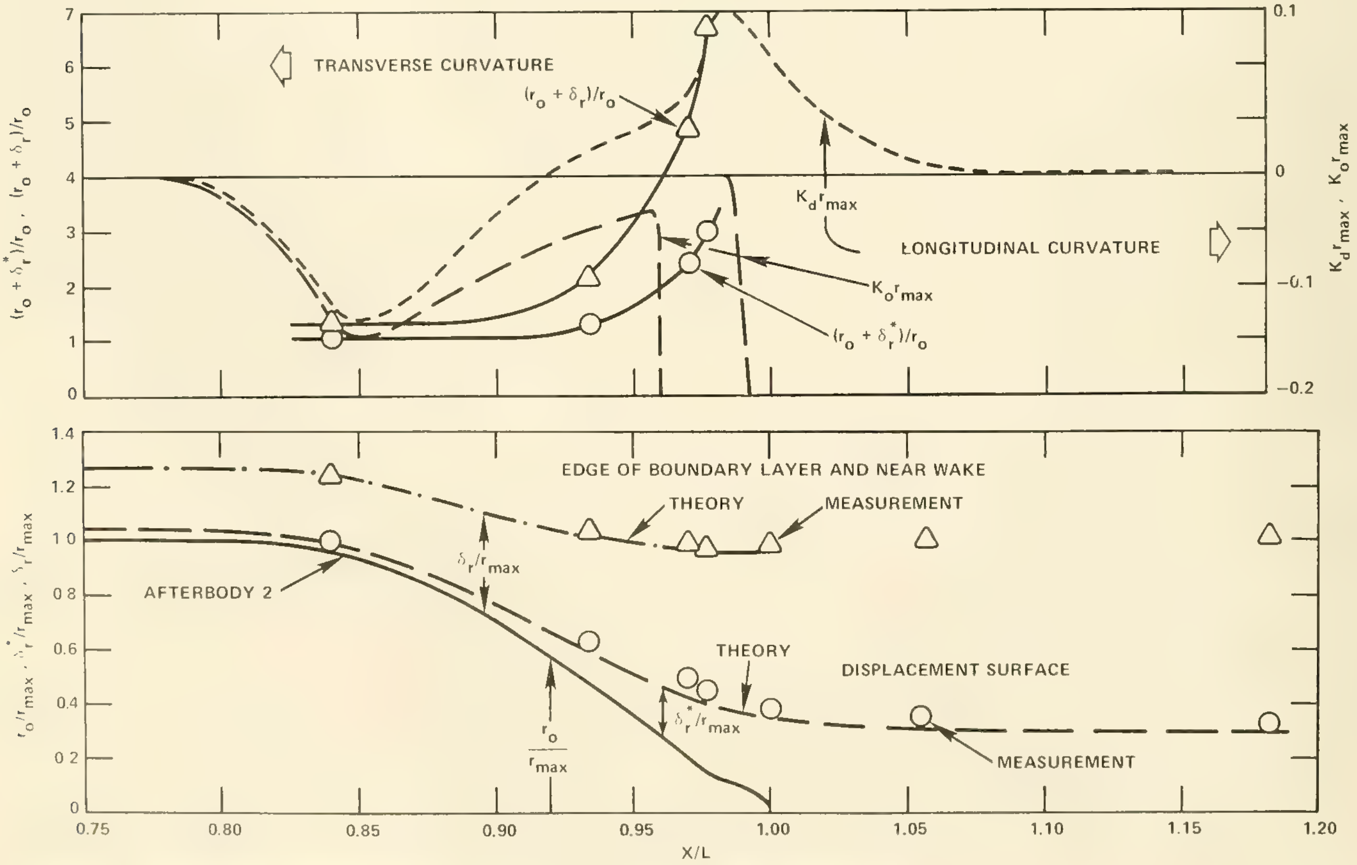

[illegible] [illegible] [illegible] curvature parameters for afterbody [illegible]

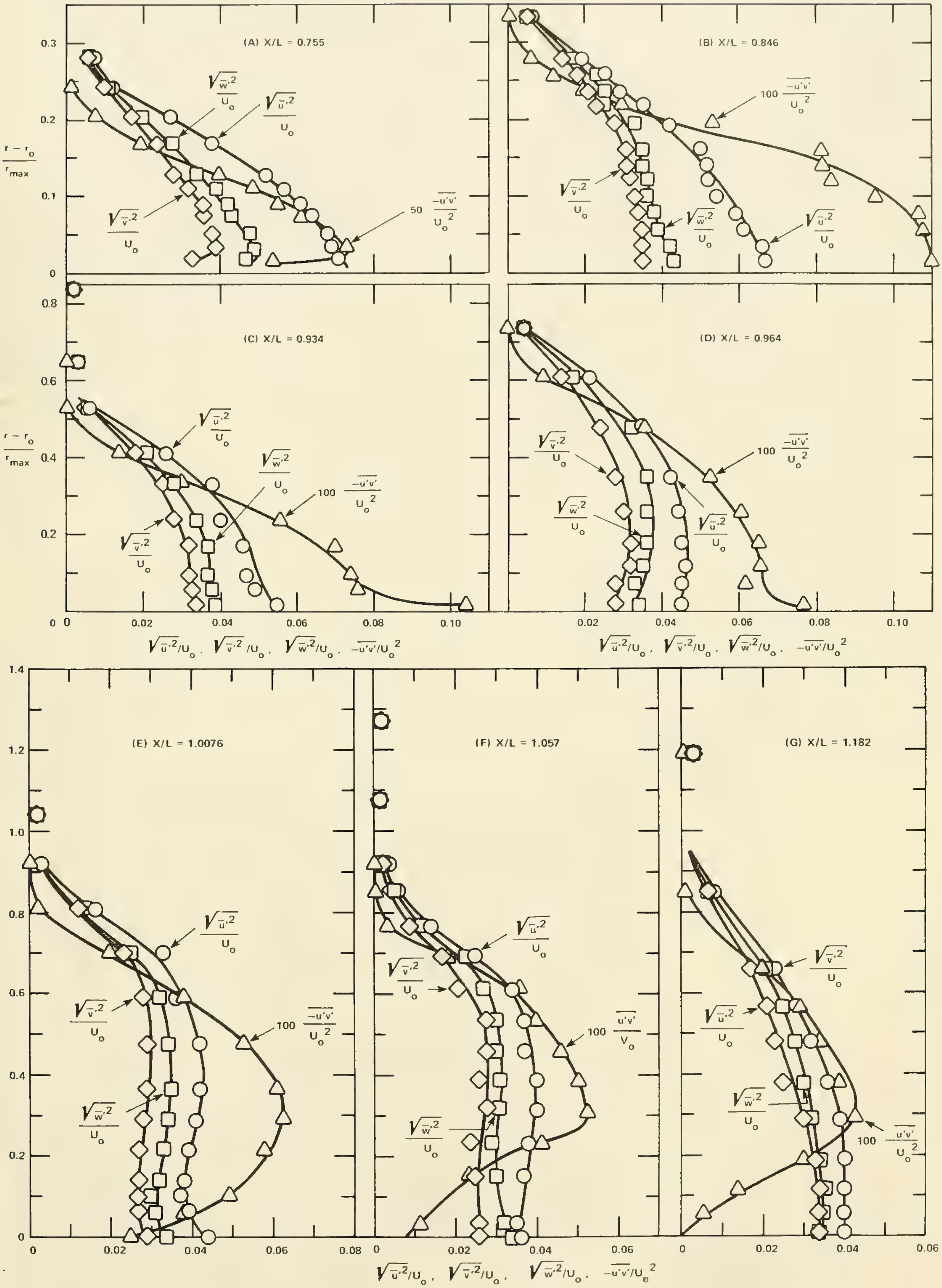

FIGURE 14. Measured distributions of Reynolds stresses for afterbody 1.

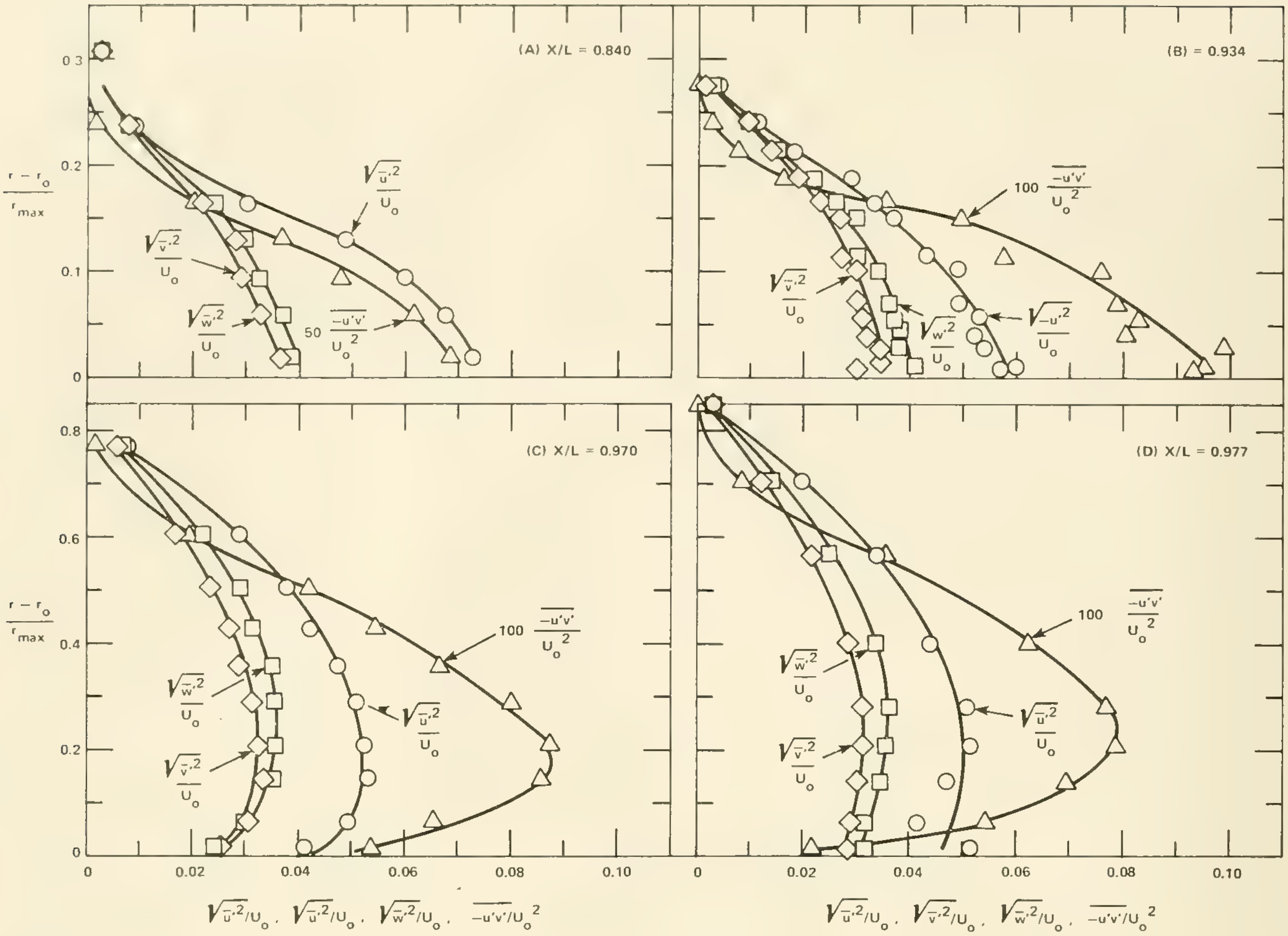

FIGURE 15. Measured distributions of Reynolds stresses for afterbody 2.

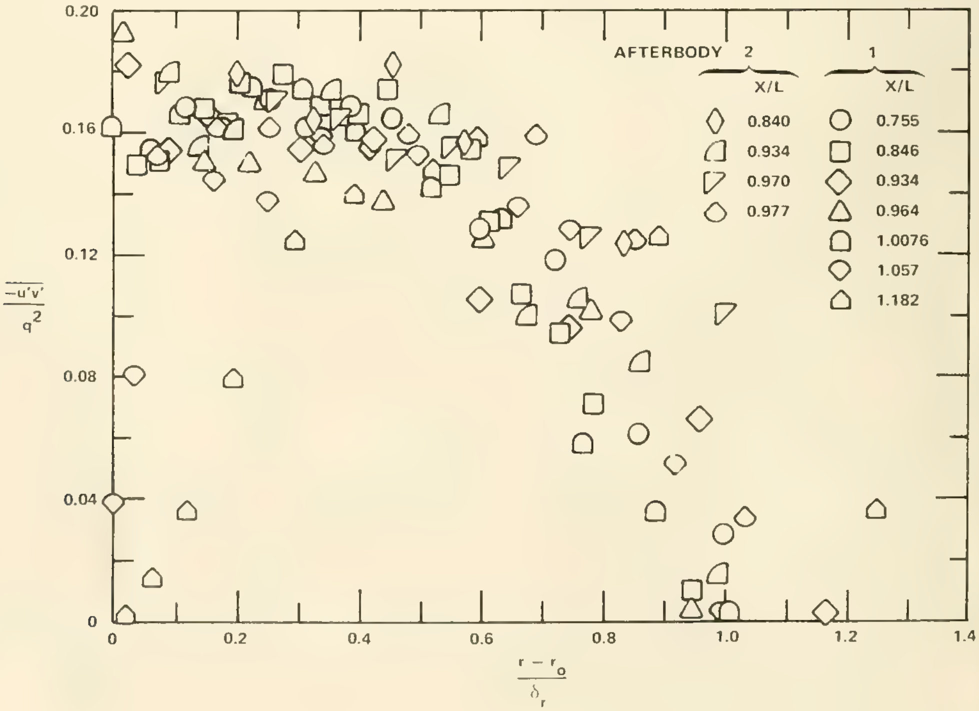

[illegible]

decrease toward the edge of the boundary layer. The values of a_1 also decrease in the inner region of wake at X/L = 1.057 and 1.182 of Afterbody 1. It should be pointed out that the measured values of q^2 contain the free-stream turbulence fluctuation, no attempt having been made to remove the free-stream turbulence fluctuation from the measured values of q^2. The measured reduction of a_1 near the outer edge of the boundary layer is in part caused by the larger contribution of the free-stream turbulence to q^2 than to $\overline{-u'v'}$. Nevertheless, the measured values of the turbulence structure parameter a_1 are quite constant across the inner portion of the boundary layer where the effect of free-stream turbulence is small.

Eddy Viscosity and Mixing Length

The measured distributions of shear stress $\overline{-u'v'}$ and mean velocity gradient, $\partial u_x/\partial r$, were used to calculate the variations of eddy viscosity and mixing length across the thick stern boundary layers according to the following definitions

$$\overline{-u'v'} = \varepsilon \frac{\partial u_x}{\partial r} \qquad (14)$$

and

$$\overline{-u'v'} = \ell^2 \left| \frac{\partial u_x}{\partial r} \right| \frac{\partial u_x}{\partial r} \qquad (15)$$

The experimentally-determined distributions of eddy viscosity, $\varepsilon/U_\delta \delta_p{}^*$, are shown in Figure 17 for Afterbody 1 and in Figure 18 for Afterbody 2, where U_δ is the potential-flow velocity at the edge of the boundary layer and $\delta_p{}^*$ is the displacement thickness (based on the planar definition, Eq. 10). Figures 19 and 20 show the experimentally-determined distributions of mixing length ℓ/δ_r for the afterbodies, where δ_r is the boundary-layer thickness measured normal to the body axis. As shown in Figures 19 and 20, the measured distributions of eddy viscosity agree resonably well with the eddy-viscosity model of Cebeci and Smith (1974, Eq. 3) when the boundary layers are thin. However, as the stern boundary layer thickens, the measured values of $\varepsilon/U_\delta \; \delta_p{}^*$ in the thick stern boundary layers are only about 1/6 of the values for thin boundary layers given by the Cebeci and Smith model (1974). The measured distributions of mixing length shown in Figures 19 and 20 also agree quite well with the thin boundary layer results of Bradshaw, Ferriss, and Atwell (1967). Again as the boundary thickens, the measured values of ℓ/δ_r reduce drastically. The values of ℓ/δ_r in the thick stern boundary layers are only about 1/3 of those of the thin boundary layers. Similar reductions of eddy viscosity and mixing length in thick stern boundary layers were also measured by Patel et al. (1974, 1977).

As the axisymmetric boundary layer thickens in the stern region, the boundary layer thickness δ_r and the displacement thickness $\delta_p{}^*$ increase drastically. However, the values of eddy viscosity and mixing length do not have enough time to respond to this change. Therefore, neither the eddy viscosity model of Cebeci and Smith (1974), nor the mixing length results of Bradshaw, Ferriss, and Atwell (1967) can be applied to the thick stern boundary layer.

8. TURBULENCE MODELS

In most works, the basic assumption made in the differential methods for calculating turbulent boundary layers is that the mixing length or eddy viscosity is uniquely related to the mean velocity gradient and the boundary-layer thickness parameter at a given location. So long as the boundary layer is thin and the change in boundary-layer properties due to the pressure gradient is gradual, this simple assumption is know to be satisfactory [see e.g., Cebeci and Smith (1974)]. When the past history of boundary layer characteristics is important, Brad-

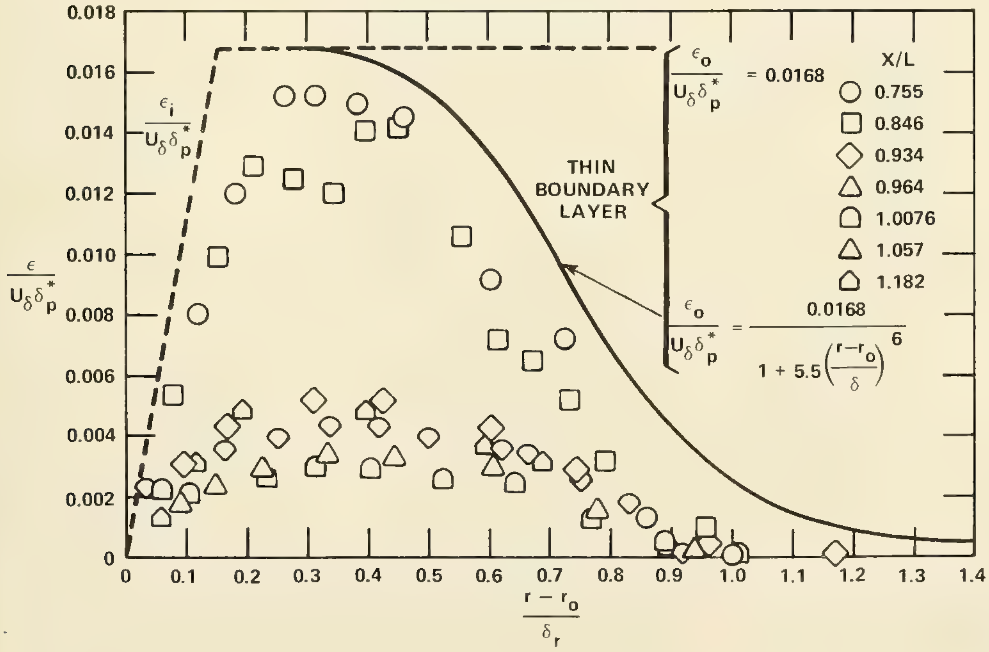

FIGURE 17. Measured distributions of eddy viscosity for afterbody 1.

shaw et al. (1967) argue that the turbulence energy equation can be used to model the memory effect. In order to determine the rate of change of turbulent intensity along a mean streamline, three assumptions have to be made: namely, that turbulence intensity is directly proportional to the local Reynolds stress, $a_1 = \overline{-u'v'}/q^2 = 0.15$; that the dissipation rate is determined by the local Reynolds stress and a length scale depending on n/δ; and the energy diffusion is directly proportional to the local Reynolds stress with a factor depending on the mixing value of Reynolds stress. On the basis of thin boundary-layer data two empirical functions for the last two assumptions were proposed by Bradshaw et al. (1967). The first assumption, $\ell/\delta = f_1\ (n/\delta)$, was found not to be applicable to the present thick axisymmetric stern boundary layers. The deviation of the apparent mixing length along the curved boundary from that of a thin flat boundary was also noted and discussed by Bradshaw (1969). A simple linear correction to the length scale of the turbulence by the extra rate of strain was made by Bradshaw (1973). The extension of this concept has just been made for the thick axisymmetric boundary layer by Patel et al. (1978).

It is important to note that the boundary-layer thickness of a typical axisymmetric body increases drastically at the stern. Most of the rapid change takes place within a streamwise distance of a few boundary-layer thicknesses. Most of the empirical functions for solving the turbulence energy equa-

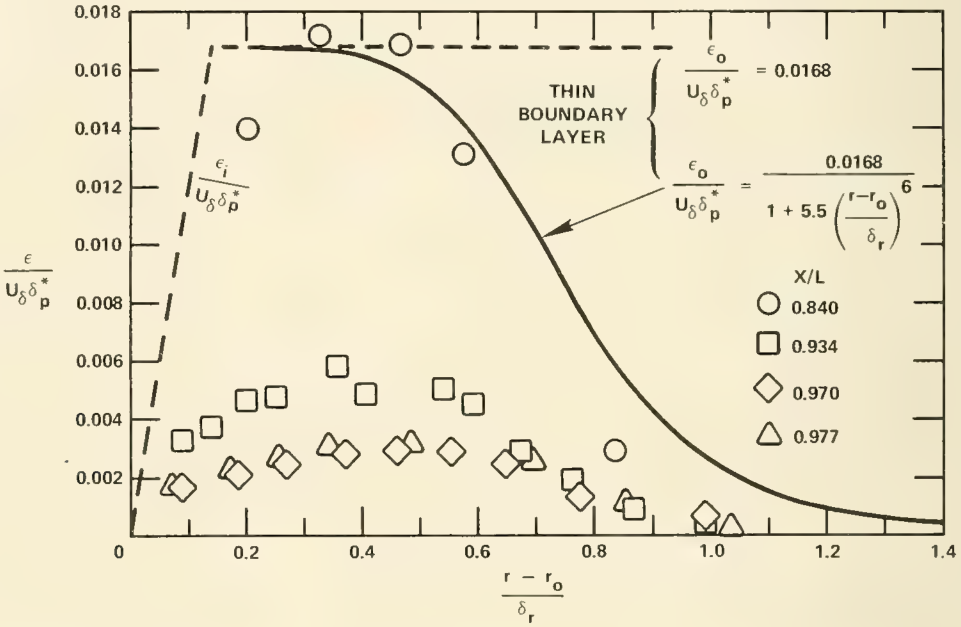

FIGURE 18. Measured distributions of eddy viscosity for afterbody 2.

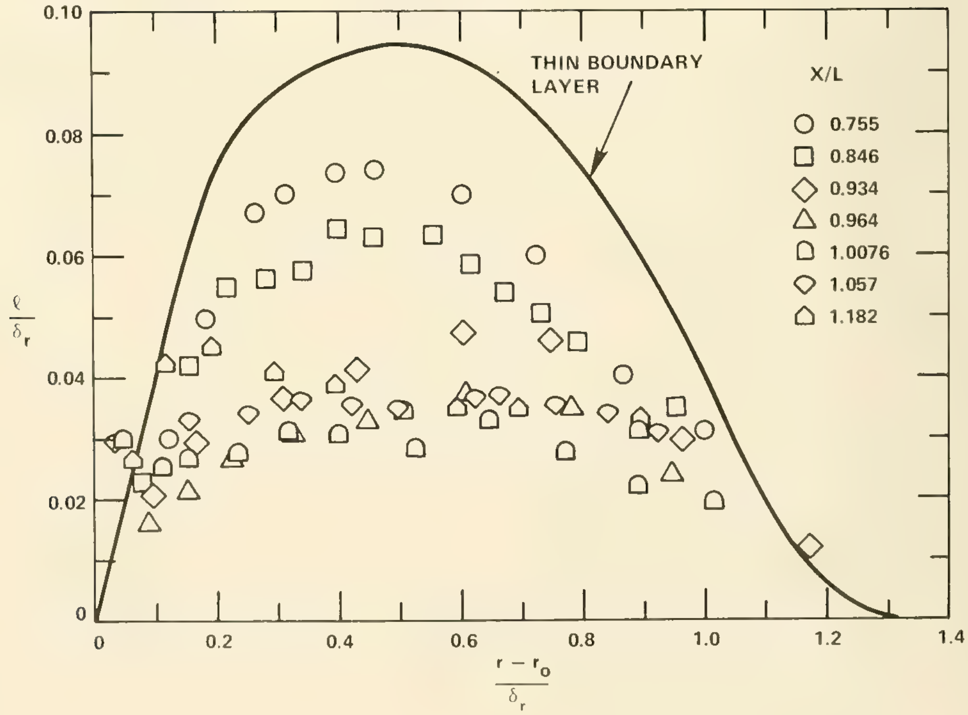

[illegible] distribu- [illegible]

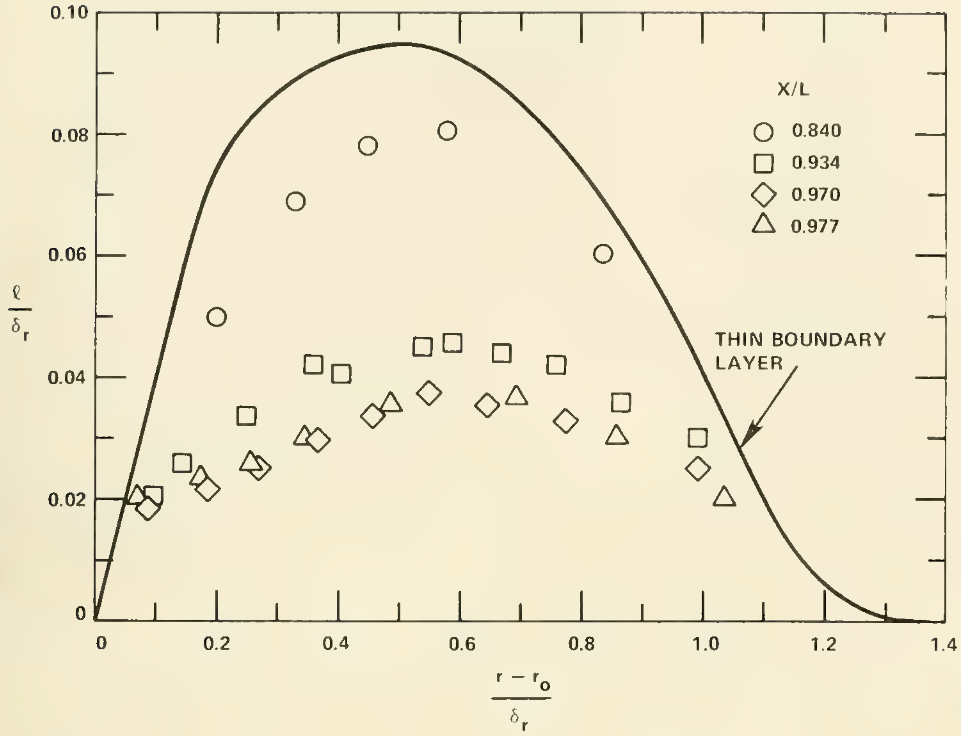

FIGURE 20. Measured distributions of mixing length for afterbody 2.

tion will undergo rapid changes in basic forms. The one known for certain is the empirical function for mixing length. Therefore, it may be difficult to compute the rate of change of the turbulence energy or the extra rate of strain in the region.

Fortunately the present measured distributions of Reynolds stresses shown in Figures 14 and 15 are quite similar in the outer region and differences appear in the inner region where the turbulence is reduced in intensity and more homogeneous. In such an axisymmetric flow configuration, the characteristic length scale is more closely related to the entire turbulence annulus between the body surface and the edge of the boundary layer rather than the radial distance between the two. Therefore, we propose that the mixing length of an axisymmetric turbu-length boundary layer is proportional to the square root of this area when the thickness increases drastically at the stern:

$$\ell \sim \sqrt{(r_o + \delta_r)^2 - r_o^2}$$

In order to examine this simple hypothesis, the present measured values of $\ell/\sqrt{(r_o + \delta_r)^2 - r_o^2}$ together with the data of Patel et al. (1974, 1977) are shown in Figure 21. The solid line is the best fit of the present data. The present values of ℓ are slightly greater than those for Patel's modified spheroid (1974) and are slightly lower than those for Patel's low-drag body (1977). The data in Figure 21 support this simple hypothesis although the data are quite scattered due to large variations of stern configurations and Reynolds number, and probable measuring errors.

The existing thin turbulent boundary-layer differential methods can be applied to the forward portion of the axisymmetric body up to the station where the boundary layer thickness increases to about 20 percent of the body radius. Further downstream, the apparent mixing length of the thick axisymmetric stern boundary layer (ℓ) can be roughly approximated by the mixing length for a thin flat boundary layer (ℓ_o) by

$$\frac{\ell}{\ell_o} = \frac{\sqrt{(r_o + \delta_r)^2 - r_o^2}}{3.33\delta_r} \qquad (16)$$

which is the solid line of Figure 21. At the aft end of the stern r_o is zero and the value of ℓ/ℓ_o is 1/3.33. This simple approximation of the mixing length for thick axisymmetric stern turbulent boundary layers can be incorporated into most existing differential methods. As noted earlier, the measured axial velocities inside the thick boundary layer (especially in the inner region) are smaller than the computed values (Figures 8 and 10). The present CS method overestimates the magnitude of eddy viscosity (Eq. 3) for the thick stern boundary layer. While the mixing length approximations obtained in the present investigation can be incorporated into the CS method to predict more accurately the thick stern boundary-layer velocities, further refinement of the theoretical methods is desirable.

9. CONCLUSIONS

In this paper, we have described recent experimental investigations of the thick turbulent boundary layers on two axisymmetric sterns without shoulder flow separation. A comprehensive set of boundary layer measurements, including mean and turbulence velocity profiles and static pressure distributions, are presented. Two major conclusions can be drawn:

The Lighthill/Preston displacement body concept has been proven experimentally to be an efficient and accurate tool for treating the viscid and in-

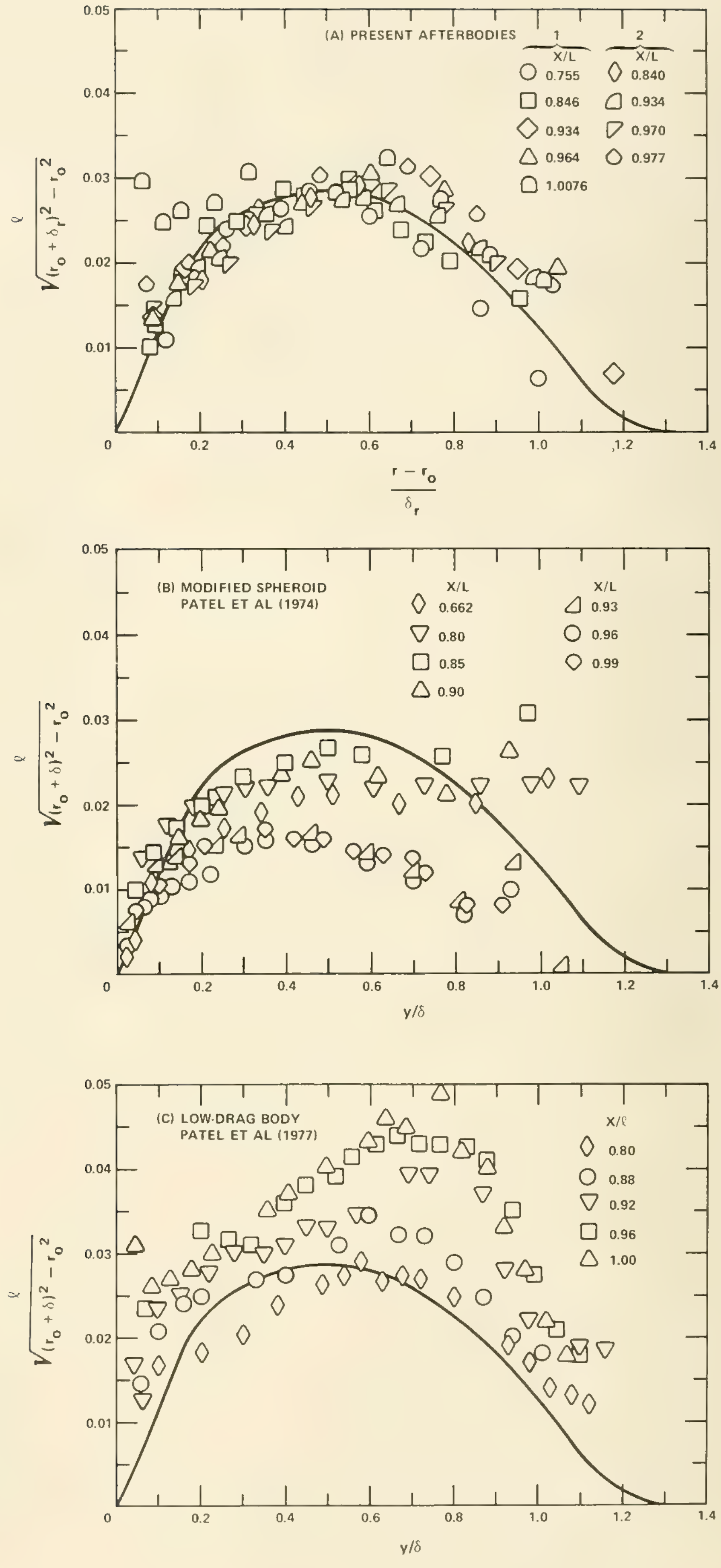

Fig. [illegible] Similarity concept for the mixing length of thick axisymmetric stern turbulent boundary layers.

viscid stern flow interation on axisymmetric bodies. The measured static pressure distributions on the body and across the entire thick boundary layer and wake were predicted by the displacement body method to an accuracy within one percent of dynamic pressure. Theoretical predictions of the measured axial and radial velocity profiles outside the displacement surface were improved significantly when the variations of the static pressure and radial velocity of the displacement body were incorporated into the computation.

Neither the measured values of eddy viscosity nor mixing length were found to be proportional to the local displacement thickness or the local boundary-layer thickness of the thick axisymmetric boundary layer. As the boundary layer thickens rapidly at the stern, the turbulence characteristics in the outer region remain quite similar but the turbulence reduces its intensity and becomes more uniformly distributed in the inner region. The measured mixing length of the thick axisymmetric stern boundary layer was found to be proportional to the square root of the area of the turbulent annulus between the body surface and the edge of boundary layer. This simple similarity hypothesis can be incorporated into existing differential boundary-layer computation methods.

ACKNOWLEDGMENT

The work reported herein was funded under the David W. Taylor Naval Ship R&D Center's Independent Research Program, Program Element Number 61152N, Project Number ZR 000 01.

REFERENCES

Bradshaw, P., D. H. Ferriss, and N. P. Atwell (1967). Calculation of boundary layer development using the turbulent energy equation. *J. Fluid Mech., 28,* 593-616.

Bradshaw, P. (1969). The analogy between streamline curvature and buoyancy in turbulent shear flow. *J. Fluid Mech., 36,* 177-191.

Bradshaw, P. (1973). Effects of streamline curvature on turbulent flow, *AGARDograph* No. 169.

Cebeci, T., and A. M. O. Smith (1974). *Analysis of turbulent boundary layers.* Academic Press, New York.

Chevray, R. (1968). The turbulent wake of a body of revolution, ASME. *J. of Basic Engineering, 90,* 275-284.

Granville, P.S. (1953). The calculation of the viscous drag of bodies of revolution. *David Taylor Model Basin Report 849.*

Hess, J. L., and A. M. O. Smith (1966). Calculation of potential flow about arbitrary bodies. *Progress in Aeronautical Sciences, Vol. 8,* Pergamon Press, New York, Chapter 1.

Huang, T. T., and C. H. von Kerczek (1972). Shear stress and pressure distribution on a surface ship model: theory and experiment. *Ninth ONR Symposium on Naval Hydrodynamics,* Paris; available in U.S. Government Printing Office, ACR-203-Vol. 2, 1963-2010.

Huang, T. T. et al. (1976). Propeller/stern/boundary-layer interaction on axisymmetric bodies: theory and experiment. *David Taylor Naval Ship Research and Development Center Report 76-0113.*

Lighthill, M. J. (1958). On displacement thickness. *J. Fluid Mech., 4,* 383-392.

McCarthy, J. H., J. L. Power, and T. T. Huang (1976). The roles of transition, laminar separation, and turbulence stimulation in the analysis of axisymmetric body drag. *Eleventh ONR Symposium on Naval Hydrodynamics,* London; Published by Mechanical Engineering Publications Ltd., London and New York.

Patel, V. C., A. Nakayama, and R. Damian (1974). Measurements in the thick axisymmetric turbulent boundary layer near the tail of a body of revolution. *J. Fluid Mech., 63,* 345-362.

Patel, V. C., Y. T. Lee, and O. Guven (1977). Measurements in the thick axisymmetric turbulent boundary layer and the near wake of a low-drag body of revolution. *Symposium on Turbulent Shear Stress,* Pennsylvania State University, University Park, pp.9.29-9.36.

Patel, V. C. and Y. T. Lee (1978). Calculation of thick boundary layer and near wake of bodies of revolution by a differential method. *ONR Twelfth Symposium on Naval Hydrodynamics,* (This Volume, Section III).

Preston, J. H. (1945). The effect of the boundary layer and wake on the flow past a symmetrical aerofoil at zero incidence; Part I, the velocity distribution at the edge of, and outside the boundary layer and wake. *ARC R&M 2107.*

APPENDIX

The raw data and derived results of the present experiments are tabulated in the following so that they can be used independently by other investigators. Table 3 shows the measured pressure and shear stress coefficients on Afterbodies 1 and 2. Tables 4 and 5 provide the measured static pressure coefficients across the stern boundary layers and near wakes of Afterbodies 1 and 2, respectively. Tables 6 and 7 contain the values of measured mean axial and radial velocities, three components of turbulence fluctuations, and Reynolds stresses across the boundary layer and near wake of Afterbodies 1 and 2, respectively. The experimentally derived data on eddy viscosity, mixing length, planar and axisymmetric displacement thickness, and boundary layer thickness are also given.

TABLE 3 - Measured Pressure and Shear Stress Coefficients on Afterbodies 1 and 2

AFTERBODY 1, $R_L = 6.6 \times 10^6$				AFTERBODY 2, $R_L = 6.8 \times 10^6$			
$\frac{X}{L}$	$\frac{r_o}{r_{max}}$	C_p	C_τ	$\frac{X}{L}$	$\frac{r_o}{r_{max}}$	C_p	C_τ
0.7060	0.9690	-0.062	-	0.6000	1.0000	-0.013	0.00281
0.7455	0.9267	-0.064	0.00281	0.7000	1.0000	-0.024	0.00284
0.7952	0.8423	-0.050	0.00265	0.7455	1.0000	-0.035	0.00288
0.8449	0.7192	-0.024	0.00248	0.7952	1.0000	-0.106	0.00305
0.8946	0.5480	+0.018	0.00213	0.8449	0.9476	-0.160	0.00295
0.9145	0.4633	+0.050	0.00185	0.8946	0.7349	-0.010	0.00200
0.9344	0.3636	+0.074	0.00163	0.9145	0.6137	+0.053	0.00156
0.9543	0.2396	+0.112	0.00130	0.9344	0.4834	+0.090	0.00123
0.9642	0.1900	+0.133	0.00115	0.9543	0.3317	+0.170	0.00090
0.9741	0.1394	+0.135	0.00104	0.9642	0.2547	+0.183	0.00060
1.0000	0.0000	+0.116	-	0.9741	0.1740	+0.198	0.00046
				1.0000	0.0000	+0.185	-

TABLE 4 - Measured Static Pressure Coefficients Across Stern Boundary Layer and Near Wake of Afterbody 1

x/L = 0.7553			x/L = 0.9144			x/L = 0.9344			x/L = 0.9642		
$\frac{r}{r_{max}}$	$\frac{r-r_o}{r_{max}}$	C_p	$\frac{r}{r_{max}}$	$\frac{r-r_o}{r_{max}}$	C_p	$\frac{r}{r_{max}}$	$\frac{r-r_o}{r_{max}}$	C_p	$\frac{r}{r_{max}}$	$\frac{r-r_o}{r_{max}}$	C_p
0.9127	0	-0.0560	0.4633	0	0.050	0.3636	0	0.0740	0.1900	0	0.133
0.9345	0.0218	-0.0530	0.4997	0.0364	0.0604	0.4214	0.0578	0.0821	0.2209	0.0309	0.1344
1.0283	0.1156	-0.0510	0.5181	0.0548	0.0604	0.4981	0.1345	0.0791	0.2536	0.0636	0.1370
1.1298	0.2171	-0.0500	0.5508	0.0875	0.0587	0.6102	0.2466	0.0674	0.3260	0.1360	0.1318
1.2392	0.3265	-0.0480	0.5892	0.1259	0.0570	0.7253	0.3617	0.0682	0.4397	0.2497	0.1202
1.4736	0.5609	-0.0434	0.6687	0.2054	0.0546	0.8375	0.4739	0.0624	0.5945	0.4045	0.1050
1.6767	0.7640	-0.0380	0.7397	0.2764	0.0514	0.9497	0.5861	0.0593	0.7408	0.5508	0.0907
1.8720	0.9593	-0.0350	0.8519	0.3886	0.0492	1.0989	0.7353	0.0518	0.8942	0.7042	0.0791
2.0908	1.1781	-0.0302	0.9670	0.5037	0.0464	1.2509	0.8873	0.0471	1.0448	0.8548	0.0686
2.2861	1.371	-0.0287	1.0835	0.6202	0.0434	1.4000	1.0364	0.0421	1.1939	1.0039	0.0604
2.4736	1.5609	-0.0270	1.1957	0.7324	0.0400	1.5563	1.1927	0.0368	1.3416	1.1516	0.0540
2.8798	1.9671	-0.0226	1.3093	0.8460	0.0370	1.7054	1.3418	0.0333	1.4993	1.3093	0.0482
3.2783	2.3438	-0.0214	1.4386	0.9753	0.0338	1.8546	1.4910	0.0305	1.6485	1.4585	0.0430
3.7079	2.7952	-0.0197	1.5906	1.1273	0.0301	2.0066	1.6430	0.0264	1.7976	1.6076	0.0393
4.3251	3.4124	-0.0158	1.7426	1.2792	0.0269	2.0904	1.7268	0.0256	2.0334	1.8434	0.0338
			1.8931	1.4298	0.0241	3.0227	2.6591	0.0133	3.9287	3.7387	0.0095
			2.0451	1.5418	0.0221	3.3580	2.9943	0.0114	4.1063	3.9163	0.0084
			2.1971	1.7338	0.0206	3.6960	3.3324	0.0099	4.2966	4.1066	0.0077
			2.3491	1.8858	0.0183	4.0355	3.6719	0.0079	4.9429	4.7529	0.0052

TABLE 4 (Continued)

x/L = 0.9771

$\frac{r}{r_{max}}$	$\frac{r-r_o}{r_{max}}$	C_p
0.1364	0	0.135
0.1600	0.0236	0.1441
0.2324	0.0960	0.1400
0.3447	0.2083	0.1293
0.4569	0.3205	0.1172
0.5748	0.4384	0.1058
0.6827	0.5464	0.0950
0.7949	0.6586	0.0856
0.9057	0.7693	0.0781
1.0251	0.8887	0.0705
1.1373	1.0009	0.0628
1.2466	1.1102	0.0574
1.3645	1.2281	0.0536
1.4796	1.3432	0.0490
1.5918	1.4555	0.0450
1.7395	1.6031	0.0406
1.8901	1.7537	0.0374
2.0137	1.8773	0.0350

x/L = 0.9830

$\frac{r}{r_{max}}$	$\frac{r-r_o}{r_{max}}$	C_p
0.1164	0	0.133
0.1278	0.0114	0.1250
0.1647	0.0483	0.1249
0.2031	0.0867	0.1241
0.2471	0.1307	0.1224
0.2826	0.1662	0.1211
0.3153	0.1989	0.1189
0.3892	0.2728	0.1142
0.4659	0.3495	0.1090
0.5412	0.4248	0.1036
0.6136	0.4972	0.0974
0.7684	0.6520	0.0858
0.8437	0.7273	0.0817
0.9162	0.7998	0.0774
0.9914	0.8750	0.0735
1.1463	1.0299	0.0650
1.2968	1.1804	0.0555
1.4431	1.3267	0.0505
1.5966	1.4802	0.0441
1.7343	1.6179	0.0409

x/L = 0.8462

$\frac{r}{r_{max}}$	$\frac{r-r_o}{r_{max}}$	C_p
0.7155	0	-0.0240
0.7450	0.0295	-0.0239
0.7620	0.0466	-0.0213
0.7791	0.0636	-0.0200
0.8018	0.0864	-0.0193
0.8217	0.1063	-0.0193
0.8572	0.1418	-0.0189
0.8572	0.1801	-0.0183
0.9297	0.2142	-0.0163
0.9694	0.2540	-0.0142
1.0092	0.2938	-0.0118
1.0873	0.3719	-0.0071
1.1598	0.4443	-0.0054
1.2322	0.5168	-0.0045
1.3061	0.5906	-0.0040
1.3785	0.6631	-0.0030
1.7000	0.9945	-0.0020

x/L = 1.00

$\frac{r}{r_{max}}$	C_p
0.061	0.1295
0.098	0.1209
0.172	0.1092
0.249	0.1022
0.361	0.0940
0.477	0.0865
0.587	0.0796
0.702	0.0716
0.814	0.0656
0.928	0.0604
1.081	0.0527
1.273	0.0464
1.455	0.0406
1.724	0.0344

x/L = 1.0076

$\frac{r}{r_{max}}$	C_p
0	0.0995
0.099	0.0987
0.192	0.0963
0.327	0.0897
0.453	0.0815
0.585	0.0740
0.720	0.0677
0.855	0.0604
0.980	0.0553
1.116	0.0503
1.247	0.0465
1.382	0.0426
1.511	0.0387
1.724	0.0344

x/L = 1.057

$\frac{r}{r_{max}}$	C_p
0	0.0418
0.057	0.0413
0.152	0.0411
0.247	0.0426
0.344	0.0424
0.433	0.0415
0.527	0.0400
0.616	0.0396
0.831	0.0364
1.000	0.0353
1.169	0.0333
1.342	0.0316
1.511	0.0293
1.724	0.0249
1.900	0.0230
2.240	0.0195
2.580	0.0168
2.750	0.0150

x/L = 1.182

$\frac{r}{r_{max}}$	C_p
0	0.0181
0.036	0.0174
0.074	0.0172
0.149	0.0178
0.224	0.0189
0.303	0.0194
0.387	0.0196
0.561	0.0180
0.716	0.0176
0.864	0.0170
1.018	0.0170
1.168	0.0170
1.318	0.0160
1.464	0.0160
1.621	0.0150
1.756	0.0140

TABLE 5 - Measured Static Pressure Coefficients Across Stern Boundary Layer and Near Wake of Afterbody 2

x/L = 0.8400			x/L = 0.9336			x/L = 0.9702		
$\frac{r}{r_{max}}$	$\frac{r-r_o}{r_{max}}$	C_p	$\frac{r}{r_{max}}$	$\frac{r-r_o}{r_{max}}$	C_p	$\frac{r}{r_{max}}$	$\frac{r-r_o}{r_{max}}$	C_p
0.9855	0.0236	-0.1550	0.5112	0.0273	0.1194	0.2419	0.0364	0.1884
1.0536	0.0918	-0.1252	0.5850	0.1011	0.1183	0.2930	0.0875	0.1854
1.1417	0.1799	-0.1140	0.6348	0.1509	0.1103	0.3754	0.1699	0.1740
1.2141	0.2523	-0.1030	0.7214	0.2375	0.1006	0.4379	0.2324	0.1654
1.2937	0.3319	-0.0903	0.7768	0.2929	0.0953	0.5061	0.3006	0.1563
1.3406	0.3788	-0.0858	0.8450	0.3611	0.0907	0.5686	0.3631	0.1482
1.4173	0.4555	-0.0755	0.9330	0.4491	0.0847	0.6623	0.4568	0.1342
1.4968	0.5350	-0.0697	0.9856	0.5017	0.0794	0.7262	0.5207	0.1252
1.6374	0.6756	-0.0594	1.1319	0.6480	0.0686	0.8541	0.6486	0.1110
1.9357	0.9739	-0.0422	1.2995	0.8156	0.0583	0.9961	0.7906	0.0957
2.2085	1.2466	-0.0316	1.4359	0.9520	0.0508	1.1467	0.9412	0.0804
2.4926	1.5307	-0.0267	1.7100	1.2261	0.0381	1.4393	1.2338	0.0604
2.8860	1.9242	-0.0207	2.0055	1.5216	0.0282	1.7177	1.5122	0.0488
			2.2938	1.8099	0.0198	2.0941	1.8886	0.0340
			2.6745	2.1906	0.0127	2.4038	2.1983	0.0247

x/L = 0.9771			x/L = 1.000		x/L = 1.057		x/L = 1.182	
$\frac{r}{r_{max}}$	$\frac{r-r_o}{r_{max}}$	C_p	$\frac{r}{r_{max}}$	C_p	$\frac{r}{r_{max}}$	C_p	$\frac{r}{r_{max}}$	C_p
0.1672	0.0182	0.1576	0.0600	0.1609	0.0412	0.0471	0	0.0004
0.2112	0.0622	0.1632	0.1111	0.1505	0.0467	0.0467	0.0426	0.0067
0.2893	0.1403	0.1637	0.1836	0.1402	0.0492	0.0492	0.2102	0.0095
0.3589	0.2099	0.1600	0.2475	0.1362	0.0503	0.0503	0.3722	0.0099
0.4328	0.2838	0.1518	0.3356	0.1271	0.0447	0.0447	0.5313	0.0090
0.5038	0.3548	0.1454	0.3995	0.1224	0.0484	0.0484	0.6889	0.0120
0.5763	0.4273	0.1379	0.4648	0.1166	0.0450	0.0450	0.8523	0.0179
0.6501	0.5011	0.1284	0.5444	0.1099	0.0493	0.0493	1.1250	0.0191
0.7922	0.6432	0.1142	0.6736	0.0991	0.0462	0.0462	1.7159	0.0172
0.9257	0.7767	0.1030	0.8214	0.0895	0.0439	0.0439		
1.0720	0.9230	0.0895	0.9591	0.0806	0.0368	0.0368		
1.3533	1.2043	0.0712	1.2404	0.0654	0.0340	0.0340		
1.6516	1.5026	0.0551	1.6069	0.0501	0.0260	0.0260		
2.0308	1.8818	0.0409	1.9506	0.0378	0.0234	0.0234		
2.3348	2.1858	0.0336	2.2148	0.0314	0.0232	0.0232		
					0.0198	0.0198		
					0.0181	0.0181		

TABLE 6 - Measured Mean and Turbulence Velocity Characteristics for Afterbody 1

$x/L = 0.755$, $r_o/r_{max} = 0.9127$ $\tan\alpha = -0.0671$

$\frac{r-r_o}{r_{max}}$	$\frac{u_x}{U_o}$	$\frac{v_r}{U_o}$	$\frac{\sqrt{\overline{u'^2}}}{U_o}$	$\frac{\sqrt{\overline{v'^2}}}{U_o}$	$\frac{\sqrt{\overline{w'^2}}}{U_o}$	$100\frac{-\overline{u'v'}}{U_o^2}$	$\frac{-\overline{u'v'}}{q^2}$	$\frac{r-r_o}{\delta_r}$	$\frac{\varepsilon}{U_\delta \delta_p^*}$	$\frac{\ell}{\delta_r}$	$\frac{\ell}{\sqrt{(r_o+\delta_r)^2-r_o^2}}$
0.018	0.627	-0.016	0.071	0.033	0.047	0.108	0.130	0.064			
0.034	0.719	-0.018	0.069	0.039	0.049	0.146	0.168	0.121	0.0080	0.030	0.011
0.051	0.771	-0.019	0.068	0.038	0.048	0.136	0.162	0.182	0.0120	0.049	0.018
0.074	0.820	-0.019	0.064	0.036	0.043	0.123	0.170	0.264	0.0152	0.067	0.024
0.089	0.846	-0.019	0.061	0.036	0.042	0.110	0.162	0.318	0.0152	0.070	0.025
0.110	0.881	-0.019	0.057	0.032	0.039	0.0969	0.167	0.393	0.0149	0.073	0.026
0.129	0.908	-0.019	0.052	0.030	0.036	0.0809	0.165	0.460	0.0145	0.078	0.028
0.169	0.951	-0.020	0.038	0.024	0.032	0.0389	0.128	0.604	0.00911	0.070	0.026
0.203	0.983	-0.020	0.027	0.017	0.018	0.0159	0.118	0.725	0.0072	0.060	0.022
0.241	1.003	-0.019	0.012	0.010	0.011	0.0022	0.061	0.861	0.00125	0.040	0.015
0.280	1.015	-0.017	0.007	0.006	0.006	0.0004	0.024	1.00	0.00017	0.030	0.0011
0.361	1.020	-0.016	0.003	0.003	0.003	0.00005	0.019	1.29			
0.545	1.010	-0.012	0.002	0.002	0.002	-					
0.884	1.000	-0.006	0.002	0.002	0.002	-					
1.793	1.000	-0.003	0.002	0.002	0.002	-					

$$\frac{\delta_p^*}{r_{max}} = 0.0426, \quad \frac{\delta_r^*}{r_{max}} = 0.0444, \quad \frac{\delta_r}{r_{max}} = 0.280$$

$x/L = 0.846$, $r_o/r_{max} = 0.7155$, $\tan\alpha$ -0.1343

$\frac{r-r_o}{r_{max}}$	$\frac{u_x}{U_o}$	$\frac{v_r}{U_o}$	$\frac{\sqrt{\overline{u'^2}}}{U_o}$	$\frac{\sqrt{\overline{v'^2}}}{U_o}$	$\frac{\sqrt{\overline{w'^2}}}{U_o}$	$100\frac{-\overline{u'v'}}{U_o^2}$	$\frac{-\overline{u'v'}}{q^2}$	$\frac{r-r_o}{\delta_r}$	$\frac{\varepsilon}{U_\delta \delta_p^*}$	$\frac{\ell}{\delta_r}$	$\frac{\ell}{\sqrt{(r_o+\delta_r)^2-r_o^2}}$
0.0145	0.593	-0.078	0.067	0.035	0.043	0.113	0.149	0.0414			
0.0280	0.660	-0.082	0.066	0.035	0.042	0.110	0.150	0.0800	0.00536	0.0226	0.0100
0.0543	0.731	-0.090	0.061	0.035	0.039	0.108	0.167	0.155	0.0099	0.042	0.0186
0.0760	0.771	-0.091	0.059	0.034	0.038	0.107	0.176	0.217	0.0128	0.0548	0.0243
0.0984	0.806	-0.093	0.054	0.033	0.036	0.0955	0.179	0.281	0.0124	0.0563	0.0249
0.1200	0.840	-0.093	0.052	0.032	0.036	0.0840	0.167	0.343	0.0119	0.0574	0.0254
0.1381	0.864	-0.094	0.052	0.031	0.035	0.082	0.167	0.395	0.0140	0.0647	0.0287
0.1600	0.890	-0.093	0.050	0.031	0.035	0.0815	0.174	0.457	0.0142	0.063	0.0279
0.1950	0.931	-0.093	0.042	0.028	0.033	0.0533	0.146	0.557	0.0106	0.0642	0.0285
0.2163	0.951	-0.093	0.035	0.023	0.025	0.0294	0.129	0.618	0.00718	0.0585	0.0258
0.2350	0.965	-0.091	0.029	0.021	0.025	0.0196	0.107	0.671	0.00512	0.0540	0.0239
0.2560	0.975	-0.089	0.026	0.018	0.023	0.0118	0.094	0.731	0.00518	0.0502	0.0223
0.2770	0.991	-0.087	0.019	0.014	0.017	0.0095	0.071	0.791	0.00317	0.0454	0.0201
0.3341	1.003	-0.084	0.005	0.005	0.006	0.00045	0.046	0.955	0.00053	0.0351	0.0156
0.6040	1.002	-0.063	0.003	0.002	0.002	0.00002					
1.2915	1.000	-0.036	0.002	0.002	0.002	0					
2.0018	1.000	-0.024	0.002	0.002	0.002	0					

$$\frac{\delta_p^*}{r_{max}} = 0.0489, \quad \frac{\delta_r^*}{r_{max}} = 0.0521, \quad \frac{\delta_r}{r_{max}} = 0.35$$

TABLE 6 - Continued

$x/L = 0.934$, $r_o/r_{max} = 0.364$, $\tan\alpha$ -0.2440

$\frac{r-r_o}{r_{max}}$	$\frac{u_x}{U_o}$	$\frac{v_r}{U_o}$	$\frac{\sqrt{\overline{u'^2}}}{U_o}$	$\frac{\sqrt{\overline{v'^2}}}{U_o}$	$\frac{\sqrt{\overline{w'^2}}}{U_o}$	$100\frac{\overline{-u'v'}}{U^2_o}$	$\frac{\overline{-u'v'}}{q^2}$	$\frac{r-r_o}{\delta_r}$	$\frac{\varepsilon}{U_\delta \delta_p^*}$	$\frac{\ell}{\delta_r}$	$\frac{\ell}{\sqrt{(r_o+\delta_r)^2-r_o^2}}$
0.0127	0.425	-0.096	0.055	0.034	0.039	0.104	0.182	0.023			
0.0511	0.541	-0.104	0.049	0.033	0.038	0.0759	0.154	0.0929	0.00302	0.0207	0.0135
0.0909	0.613	-0.105	0.047	0.032	0.037	0.0740	0.161	0.165	0.00424	0.0294	0.0193
0.1704	0.727	-0.103	0.047	0.032	0.036	0.0700	0.154	0.310	0.00517	0.0369	0.0242
0.2360	0.805	-0.097	0.040	0.028	0.034	0.0556	0.157	0.429	0.00513	0.0411	0.0270
0.3309	0.884	-0.091	0.038	0.025	0.028	0.0300	0.105	0.602	0.00413	0.045	0.0295
0.4105	0.931	-0.087	0.026	0.018	0.021	0.0139	0.096	0.746	0.00287	0.0460	0.0302
0.5284	0.964	-0.076	0.007	0.006	0.007	0.00088	0.066	0.961	0.000465	0.0296	0.0194
0.6477	0.974	-0.066	0.003	0.003	0.003	0.00002	0.003	1.178	0.0000277	0.0120	0.0079
0.8366	0.982	-0.055	0.003	0.002	0.002	0.00003					
1.1093	0.989	-0.044	0.002	0.002	0.002						
1.4470	0.993	-0.034	0.002	0.002	0.002						
1.7926	0.997	-0.028	0.002	0.002	0.002						
2.1803	1.000	-0.024	0.002	0.002	0.002						

$$\frac{\delta_p^*}{r_{max}} = 0.1064, \quad \frac{\delta_r^*}{r_{max}} = 0.1251, \quad \frac{\delta_r}{r_{max}} = 0.55$$

$x/L = 0.964$, $r_o/r_{max} = 0.190$, $\tan\alpha = -0.2770$

$\frac{r-r_o}{r_{max}}$	$\frac{u_x}{U_o}$	$\frac{v_r}{U_o}$	$\frac{\sqrt{\overline{u'^2}}}{U_o}$	$\frac{\sqrt{\overline{v'^2}}}{U_o}$	$\frac{\sqrt{\overline{w'^2}}}{U_o}$	$100\frac{\overline{-u'v'}}{U_o^2}$	$\frac{\overline{-u'v'}}{q^2}$	$\frac{r-r_o}{\delta_r}$	$\frac{\varepsilon}{U_\delta \delta_p^*}$	$\frac{\ell}{\delta_r}$	$\frac{\ell}{\sqrt{(r_o+\delta_r)^2-r_o^2}}$
0.0145	0.294	-0.085	0.045	0.028	0.034	0.0767	0.193	0.0186			
0.0700	0.428	-0.093	0.045	0.028	0.033	0.0615	0.158	0.0897	0.00176	0.0160	0.0131
0.1168	0.509	-0.086	0.046	0.032	0.035	0.0654	0.150	0.150	0.00232	0.0212	0.0174
0.1751	0.586	-0.083	0.045	0.032	0.036	0.0651	0.150	0.224	0.00286	0.0262	0.0215
0.2589	0.682	-0.075	0.044	0.030	0.036	0.0605	0.146	0.332	0.00336	0.0308	0.253
0.3469	0.768	-0.069	0.042	0.028	0.036	0.0528	0.137	0.445	0.00323	0.0328	0.0269
0.4748	0.868	-0.061	0.035	0.024	0.032	0.0354	0.125	0.609	0.00299	0.0371	0.0304
0.6069	0.936	-0.055	0.021	0.014	0.017	0.00968	0.106	0.778	0.00145	0.0349	0.0286
0.7361	0.964	-0.047	0.004	0.004	0.004	0.00090	0.005	0.944	0.000304	0.0237	0.0194
0.8654	0.978	-0.041	0.003	0.003	0.003	0.00004	0.014	1.109			
1.0671	0.988	-0.035	0.002	0.002	0.002	0.00002	0.016	1.368			
1.2674	0.994	-0.029	0.002	0.002	0.002	0.00003					
1.4719	0.997	-0.026	0.002	0.002	0.002	0.00002					
1.6793	0.991	-0.022	0.002	0.002	0.002						
1.881	0.996	-0.020	0.002	0.002	0.002						
2.1893	0.998	-0.018	0.002	0.002	0.002						

$$\frac{\delta_p^*}{r_{max}} = 0.1858, \quad \frac{\delta_r^*}{r_{max}} = 0.2343, \quad \frac{\delta_r}{r_{max}} = 0.78$$

TABLE 6 - (Continued)

$x/L = 1.0076,\ r_o/r_{max} = 0.$

$\frac{r}{r_{max}}$	$\frac{u_x}{U_o}$	$\frac{v_r}{U_o}$	$\frac{\sqrt{\overline{u'^2}}}{U_o}$	$\frac{\sqrt{\overline{v'^2}}}{U_o}$	$\frac{\sqrt{\overline{w'^2}}}{U_o}$	$100\frac{-\overline{u'v'}}{U_o^2}$	$\frac{-\overline{u'v'}}{q^2}$	$\frac{r-r_o}{\delta_r}$	$\frac{\varepsilon}{U_\delta \delta_p^*}$	$\frac{\ell}{\delta_r}$
0	0.368	-0.059	0.044	0.029	0.034	0.0251	0.162	0		
0.061	0.385	-0.053	0.039	0.027	0.031	0.0385	0.154	0.067	0.00219	0.0296
0.101	0.426	-0.047	0.037	0.027	0.030	0.0495	0.165	0.111	0.00209	0.0248
0.139	0.462	-0.043	0.038	0.027	0.032	0.0524	0.164	0.153	0.00227	0.0262
0.213	0.535	-0.037	0.039	0.027	0.033	0.0580	0.174	0.234	0.00248	0.0272
0.288	0.607	-0.020	0.041	0.028	0.034	0.0625	0.173	0.316	0.00292	0.0309
0.365	0.670	-0.010	0.042	0.029	0.035	0.0610	0.159	0.401	0.00285	0.0305
0.477	0.781	-0.005	0.042	0.029	0.034	0.0530	0.141	0.524	0.00246	0.0282
0.589	0.871	-0.005	0.036	0.028	0.032	0.0380	0.130	0.647	0.00239	0.0325
0.702	0.929	-0.004	0.033	0.023	0.025	0.0106	0.057	0.771	0.00105	0.0275
0.811	0.961	-0.004	0.016	0.012	0.013	0.0020	0.035	0.891	0.00038	0.0208
0.923	0.977	-0.004	0.004	0.003	0.003	0.0009	0.027	1.014	0.000207	0.0182
1.040	0.993	-0.004	0.002	0.002	0.002	0.0002				

$$\frac{\delta_p^*}{r_{max}} = 0.243, \quad \frac{\delta_r^*}{r_{max}} = 0.350, \quad \frac{\delta_r}{r_{max}} = 0.91$$

$x/L = 1.057,\ r_o/r_{max} = 0$

$\frac{r}{r_{max}}$	$\frac{u_x}{U_o}$	$\frac{v_r}{U_o}$	$\frac{\sqrt{\overline{u'^2}}}{U_o}$	$\frac{\sqrt{\overline{v'^2}}}{U_o}$	$\frac{\sqrt{\overline{w'^2}}}{U_o}$	$100\frac{-\overline{u'v'}}{U_o^2}$	$\frac{-\overline{u'v'}}{q^2}$	$\frac{r-r_o}{\delta_r}$	$\frac{\varepsilon}{U_\delta \delta_p^*}$	$\frac{\ell}{\delta_r}$
0	0.519	-0.049	0.036	0.026	0.034	0.0117	0.038	0	-	-
0.034	0.538	-0.043	0.035	0.026	0.032	0.0235	0.080	0.037	0.00236	0.0293
0.152	0.609	-0.024	0.037	0.025	0.030	0.0416	0.144	0.165	0.00351	0.0328
0.232	0.667	-0.015	0.038	0.024	0.029	0.0493	0.137	0.252	0.00396	0.0340
0.311	0.722	-0.010	0.040	0.028	0.031	0.0527	0.158	0.338	0.00438	0.0364
0.388	0.774	-0.006	0.040	0.026	0.031	0.0505	0.156	0.422	0.00420	0.0357
0.460	0.824	-0.004	0.037	0.026	0.031	0.0460	0.152	0.500	0.00394	0.0350
0.573	0.894	-0.004	0.037	0.028	0.030	0.0400	0.132	0.622	0.00357	0.0364
0.614	0.916	-0.004	0.034	0.021	0.027	0.0353	0.135	0.667	0.00336	0.0370
0.693	0.952	-0.004	0.025	0.017	0.023	0.0186	0.129	0.753	0.00255	0.0357
0.770	0.981	-0.003	0.018	0.011	0.015	0.00569	0.098	0.837	0.00104	0.0341
0.847	0.989	-0.003	0.004	0.003	0.003	0.00033	0.051	0.921	0.00029	0.0305
0.923	0.991	-0.003	0.003	0.002	0.002	0.00010	0.024	1.003	0.000323	-
1.077	0.991	-0.002	0.002	0.002	0.002	0.00007	-	1.171		-
1.276	0.993	-0.002	0.002	0.002	0.002	0.00005	-			-
1.459	0.994	-0.002	0.002	0.002	0.002	0				
1.697	0.998	-0.002	0.002	0.002	0.002	0				

$$\frac{\delta_p^*}{r_{max}} = 0.1754, \quad \frac{\delta_r^*}{r_{max}} = 0.2921, \quad \frac{\delta_r}{r_{max}} = 0.92$$

TABLE 6 - (Continued)

$x/L = 1.182$, $r_o/r_{max} = 0$

$\frac{r}{r_{max}}$	$\frac{u_x}{U_o}$	$\frac{v_r}{U_o}$	$\frac{\sqrt{\overline{u'^2}}}{U_o}$	$\frac{\sqrt{\overline{v'^2}}}{U_o}$	$\frac{\sqrt{\overline{w'^2}}}{U_o}$	$100\frac{\overline{-u'v'}}{U_o^2}$	$\frac{\overline{-u'v'}}{q^2}$	$\frac{r-r_o}{\delta_r}$	$\frac{\varepsilon}{U_\delta \delta_p^*}$	$\frac{\ell}{\delta_r}$
0.020	0.632	-0.010	0.040	0.034	0.034	0	0	0.021		
0.058	0.644	-0.008	0.040	0.034	0.035	0.0055	0.0138	0.061	0.00120	0.0263
0.114	0.659	-0.005	0.040	0.034	0.035	0.0140	0.035	0.120	0.00305	0.042
0.186	0.683	-0.006	0.040	0.033	0.034	0.0303	0.079	0.196	0.00482	0.045
0.283	0.732	-0.004	0.039	0.030	0.032	0.0428	0.124	0.298	0.00516	0.0406
0.377	0.785	-0.003	0.036	0.025	0.030	0.0390	0.138	0.397	0.00470	0.0386
0.479	0.837	-0.003	0.032	0.023	0.028	0.0340	0.146	0.504	0.00385	0.0339
0.564	0.890	-0.003	0.028	0.021	0.025	0.0290	0.157	0.594	0.00365	0.0348
0.658	0.937	-0.002	0.023	0.017	0.021	0.0200	0.159	0.693	0.00302	0.0347
0.848	0.991	-0.002	0.010	0.009	0.009	0.0033	0.025	0.893	0.00117	0.0328
1.189	0.995	-0.002	0.003	0.002	0.002	0.00006	0.035	1.252	-	
1.641	0.995	-0.001	0.002	0.002	0.002	0.00004	-			
2.162	0.995	-0.001	0.002	0.002	0.002	0	-			

$$\frac{\delta_p^*}{r_{max}} = 0.1543, \quad \frac{\delta_r^*}{r_{max}} = 0.2832, \quad \frac{\delta_r}{r_{max}} = 0.95$$

$x/L = 0.914$, $r_o/r_{max} = 0.9145$

$\frac{r-r_o}{r_{max}}$	$\frac{u_x}{U_o}$	$-\frac{v_r}{U_o}$
0.0042	0.448	0.085
0.0136	0.482	0.091
0.0213	0.520	0.101
0.0280	0.552	0.096
0.0392	0.574	0.104
0.0500	0.598	0.107
0.0700	0.639	0.112
0.0907	0.675	0.108
0.1100	0.706	0.111
0.1307	0.734	0.103
0.1479	0.761	0.106
0.1772	0.796	0.099
0.2058	0.833	0.096
0.2344	0.864	0.093
0.2687	0.894	0.091
0.2980	0.919	0.089
0.3324	0.941	0.088
0.3782	0.964	0.085
0.4067	0.979	0.082
0.4475	0.984	0.078
0.4876	0.987	0.074
0.5276	0.990	0.069
0.5677	0.992	0.067
0.6142	0.992	0.063
0.6599	0.992	0.059
0.7229	0.993	0.054
0.7915	0.994	0.052
0.8609	0.995	0.047
0.9417	0.995	0.043
1.0275	0.998	0.041
1.1369	1.000	0.032
1.2971	1.001	0.032
1.4522	1.003	0.027
1.6474	1.004	0.024
1.8770	1.004	0.005

$$\frac{\delta_p^*}{r_{max}} = 0.0772, \quad \frac{\delta_r^*}{r_{max}} = 0.0875$$

$$\frac{\delta_r}{r_{max}} = 0.54 \qquad \tan\alpha = -0.2094$$

$x/L = 0.977$, $r_o/r_{max} = 0.1364$

$\frac{r-r_o}{r_{max}}$	$\frac{u_x}{U_o}$	$-\frac{v_r}{U_o}$
0.0073	0.318	0.033
0.0128	0.334	0.039
0.0183	0.345	0.041
0.0238	0.360	0.046
0.0349	0.381	0.042
0.0459	0.400	0.047
0.0624	0.428	0.055
0.0845	0.459	0.045
0.1011	0.483	0.049
0.1294	0.524	0.049
0.1514	0.555	0.035
0.1845	0.595	0.045
0.2176	0.634	0.044
0.2563	0.676	0.040
0.2901	0.713	0.036
0.3328	0.748	0.033
0.3839	0.796	0.035
0.4287	0.837	0.033
0.4949	0.884	0.030
0.5563	0.915	0.028
0.6225	0.947	0.029
0.6894	0.960	0.025
0.7501	0.962	0.020
0.8170	0.976	0.019
0.9494	0.982	0.016
1.0218	0.984	0.013
1.1770	0.988	0.012
1.2487	0.989	0.011
1.3253	0.991	0.009
1.3984	0.991	0.009
1.4756	0.993	0.007
1.5474	0.994	0.006
1.6253	0.994	0.006
1.7026	0.995	0.005
1.7743	0.995	0.005

$$\frac{\delta_p^*}{r_{max}} = 0.1866, \quad \frac{\delta_r^*}{r_{max}} = 0.2469$$

$$\frac{\delta_r}{r_{max}} = 0.80 \qquad \tan\alpha = -0.1036$$

$x/L = 1.000$, $r_o/r_{max} = 0$

$\frac{u_x}{U_o}$	$-\frac{v_r}{U_o}$
0.303	0.063
0.321	0.062
0.332	0.055
0.340	0.054
0.350	0.052
0.360	0.050
0.375	0.045
0.396	0.042
0.412	0.041
0.442	0.031
0.470	0.029
0.493	0.025
0.524	0.023
0.556	0.022
0.584	0.019
0.613	0.005
0.652	0.008
0.688	0.007
0.744	0.006
0.794	0.006
0.839	0.005
0.893	0.005
0.939	0.006
0.965	0.006
0.976	0.005
0.991	0.005
0.991	0.005
0.995	0.003
0.995	0.003
0.998	0.003
0.996	0.002
0.997	0.002
1.000	0.000
1.000	0.000

$$\frac{\delta_p^*}{r_{max}} = 0.2393, \quad \frac{\delta_r^*}{r_{max}} = 0.2478$$

$$\frac{\delta_r}{r_{max}} = 0.90$$

TABLE 7 - Measured Mean and Turbulence Velocity Characteristics for Afterbody 2

$x/L = 0.840$, $r_o/r_{max} = 0.9618$ $\tan\alpha = -0.1047$

$\frac{r-r_o}{r_{max}}$	$\frac{u_x}{U_o}$	$\frac{v_r}{U_o}$	$\frac{\sqrt{\overline{u'^2}}}{U_o}$	$\frac{\sqrt{\overline{v'^2}}}{U_o}$	$\frac{\sqrt{\overline{w'^2}}}{U_o}$	$100\frac{-\overline{u'v'}}{U_o^2}$	$\frac{-\overline{u'v'}}{q^2}$	$\frac{r-r_o}{\delta_r}$	$\frac{\varepsilon}{U_\delta \delta_p^*}$	$\frac{\ell}{\delta_r}$	$\frac{\ell}{\sqrt{(r_o+\delta_r)^2-r_o^2}}$
0.018	0.703	-0.091	0.0723	0.0364	0.0387	0.1366	0.169	0.064			
0.058	0.8444	-0.109	0.0676	0.0328	0.0368	0.1234	0.176	0.204	0.0140	0.05	0.0180
0.0935	0.9096	-0.106	0.0600	0.0320	0.0340	0.0950	0.164	0.328	0.0172	0.0697	0.0250
0.1304	0.956	-0.112	0.0487	0.0286	0.0293	0.0738	0.182	0.458	0.0169	0.0780	0.0280
0.1645	0.9911	-0.115	0.0402	0.0213	0.0240	0.0411	0.155	0.577	0.0131	0.0809	0.0291
0.2380	1.037	-0.110	0.010	0.0091	0.0092	0.0033	0.123	0.836	0.0029	0.0623	0.0224
0.3094	1.042	-0.103	0.0031	0.0025	0.0025	-	-	1.086	-	-	
0.4500	1.038	-0.089	0.0025	0.002	0.002	-	-				
0.6659	1.028	-0.073	0.002	0.002	0.002	-					
1.1602	1.013	-0.051	0.002	0.002	0.002	-					
1.7668	1.004	-0.038	0.002	0.002	0.002	-					

$$\frac{\delta_p^*}{r_{max}} = 0.0357, \quad \frac{\delta_r^*}{r_{max}} = 0.0371, \quad \frac{\delta_r}{r_{max}} = 0.285$$

$x/L = 0.9336$, $r_o/r_{max} = 0.4839$ $\tan\alpha = -0.3216$

$\frac{r-r_o}{r_{max}}$	$\frac{u_x}{U_o}$	$\frac{v_r}{U_o}$	$\frac{\sqrt{\overline{u'^2}}}{U_o}$	$\frac{\sqrt{\overline{v'^2}}}{U_o}$	$\frac{\sqrt{\overline{w'^2}}}{U_o}$	$100\frac{-\overline{u'v'}}{U_o^2}$	$\frac{-\overline{u'v'}}{q^2}$	$\frac{r-r_o}{\delta_r}$	$\frac{\varepsilon}{U_\delta \delta_p^*}$	$\frac{\ell}{\delta_r}$	$\frac{\ell}{\sqrt{(r_o+\delta_r)^2-r_o^2}}$
0.0102	0.3206	-0.088	0.0569	0.030	0.035	0.093	0.173	0.0182			
0.02	0.402	-0.091	0.060	0.035	0.041	0.095	0.179	0.0357			
0.055	0.546	-0.115	0.0541	0.0343	0.038	0.0990	0.178	0.098	0.00322	0.0205	0.0124
0.079	0.598	-0.117	0.052	0.032	0.038	0.0801	0.154	0.141	0.00366	0.0260	0.0157
0.112	0.652	-0.119	0.053	0.031	0.037	0.0824	0.160	0.20	0.00459	0.0322	0.0195
0.140	0.6955	-0.122	0.049	0.030	0.036	0.0785	0.170	0.250	0.00469	0.0336	0.0203
0.201	0.776	-0.121	0.049	0.030	0.033	0.0759	0.173	0.359	0.00575	0.0420	0.0254
0.228	0.8063	-0.119	0.043	0.027	0.030	0.0575	0.165	0.407	0.00478	0.0401	0.0243
0.300	0.878	-0.115	0.037	0.026	0.030	0.0495	0.165	0.539	0.00499	0.0451	0.0273
0.330	0.903	-0.113	0.032	0.023	0.025	0.0352	0.153	0.589	0.00423	0.0454	0.0275
0.375	0.930	-0.110	0.029	0.019	0.022	0.0167	0.099	0.670	0.00284	0.0442	0.0268
0.427	0.9524	-0.104	0.018	0.014	0.015	0.0078	0.105	0.763	0.00185	0.0421	0.0255
0.483	0.970	-0.094	0.011	0.010	0.000	0.0027	0.084	0.863	0.00092	0.0355	0.0215
0.555	0.984	-0.090	0.004	0.002	0.003	0.0007	0.014	0.991	0.00039	0.0299	0.0181
0.660	0.995	-0.085	0.002	0.002	0.002	-	-	1.179	-	-	
0.9273	1.000	-0.070	0.002	0.002	0.002	0	-	1.656	-	-	
1.340	1.000	-0.052	0.002	0.002	0.002			2.393			

$$\frac{\delta_p^*}{r_{max}} = 0.1126, \quad \frac{\delta_r^*}{r_{max}} = 0.1296, \quad \frac{\delta_r}{r_{max}} = 0.560$$

TABLE 7 - (Continued)

$x/L = 0.970$, $r_o/r_{max} = 0.2055$ $\tan\alpha$ -0.4077

$\frac{r-r_o}{r_{max}}$	$\frac{u_x}{U_o}$	$\frac{v_r}{U_o}$	$\frac{\sqrt{\overline{u'^2}}}{U_o}$	$\frac{\sqrt{\overline{v'^2}}}{U_o}$	$\frac{\sqrt{\overline{w'^2}}}{U_o}$	$100\frac{\overline{-u'v'}}{U_o^2}$	$\frac{\overline{-u'v'}}{q^2}$	$\frac{r-r_o}{\delta_r}$	$\frac{\varepsilon}{U_\delta \delta^*_p}$	$\frac{\ell}{\delta_r}$	$\frac{\ell}{\sqrt{(r_o+\delta_r)^2-r_o^2}}$
0.0182	0.1878	-0.0563	0.0411	0.0244	0.241	0.0531	0.185	0.023			
0.0679	0.2885	-0.0618	0.0495	0.0304	0.030	0.0756	0.177	0.087	0.00166	0.0182	0.0147
0.1432	0.4251	-0.0701	0.0531	0.0333	0.0352	0.0850	0.164	0.184	0.00209	0.0215	0.0174
0.2099	0.5365	-0.0729	0.0524	0.0324	0.0359	0.0872	0.171	0.269	0.00244	0.0248	0.0201
0.2881	0.6423	-0.0741	0.0510	0.0314	0.0355	0.0800	0.165	0.369	0.00278	0.9295	0.0238
0.3577	0.7203	-0.0724	0.0479	0.0290	0.0354	0.0666	0.152	0.459	0.00287	0.0334	0.0270
0.4287	0.7813	-0.0729	0.0421	0.0271	0.0315	0.0545	0.156	0.550	0.00289	0.0372	0.0301
0.504	0.8377	-0.0704	0.0379	0.0232	0.0290	0.0420	0.149	0.646	0.00243	0.0357	0.0229
0.6034	0.9090	-0.0678	0.0287	0.0168	0.0219	0.0199	0.126	0.774	0.00154	0.0326	0.0264
0.7724	0.9560	-0.0626	0.008	0.007	0.007	0.00173	0.107	0.990	0.000339	0.0250	0.0202
0.9301	0.9701	-0.0559	0.002	0.002	0.002	-		-			
1.2185	0.9800	-0.0474	0.002	0.002	0.002						
1.5764	0.9897	-0.0401	0.002	0.002	0.002						
2.1858	0.9994	-0.0302	0.002	0.002	0.002						

$$\frac{\delta^*_p}{r_{max}} = 0.239, \quad \frac{\delta^*_r}{r_{max}} = 0.289, \quad \frac{\delta_r}{r_{max}} = 0.78$$

$x/L = 0.977$, $r_o/r_{max} = 0.149$ $\tan\alpha = -0.3901$

$\frac{r-r_o}{r_{max}}$	$\frac{u_x}{U_o}$	$\frac{v_r}{U_o}$	$\frac{\sqrt{\overline{u'^2}}}{U_o}$	$\frac{\sqrt{\overline{v'^2}}}{U_o}$	$\frac{\sqrt{\overline{w'^2}}}{U_o}$	$100\frac{\overline{-u'v'}}{U_o^2}$	$\frac{\overline{-u'v'}}{q^2}$	$\frac{r-r_o}{\delta_r}$	$\frac{\varepsilon}{U_\delta \delta^*_p}$	$\frac{\ell}{\delta_r}$	$\frac{\ell}{\sqrt{(r_o+\delta_r)^2-r_o^2}}$
0.0164	0.2741	-0.515	0.0313	0.0175	0.0230	0.0219	0.121				
0.0632	0.3400	-0.0443	0.0416	0.0289	0.0319	0.0544	0.152	0.077	0.00174	0.0206	0.0176
0.1399	0.442	-0.0446	0.0471	0.0301	0.0344	0.0692	0.161	0.171	0.00225	0.0236	0.0202
0.2081	0.5363	-0.0499	0.0515	0.0314	0.0354	0.0788	0.161	0.254	0.00265	0.0260	0.0223
0.2806	0.6259	-0.0513	0.0509	0.0317	0.0364	0.0770	0.156	0.342	0.00308	0.0306	0.0262
0.3970	0.7300	-0.0527	0.0442	0.0287	0.0339	0.0625	0.159	0.484	0.00319	0.0356	0.0305
0.5675	0.8700	-0.0532	0.0339	0.0219	0.0250	0.0355	0.157	0.692	0.00250	0.0367	0.0314
0.7039	0.9340	-0.0511	0.0200	0.012	0.014	0.00868	0.124	0.858	0.00114	0.0300	0.0257
0.8488	0.9624	-0.0483	0.003	0.003	0.003	0.000417	0.033	1.035	0.000137	0.0201	0.0172
1.0576	0.9699	-0.0426	0.002	0.002	0.002						
1.2749	0.9729	-0.0372	0.002	0.002	0.002						
1.5519	0.9769	-0.0330	0.002	0.002	0.002						
2.1826	0.9898	-0.0263	0.002	0.002	0.002						

$$\frac{\delta^*_p}{r_{max}} = 0.233, \quad \frac{\delta^*_r}{r_{max}} = 0.294, \quad \frac{\delta_r}{r_{max}} = 0.82$$

TABLE 7 - (Concluded)

x/L = 1.000

$\frac{r}{r_{max}}$	$\frac{u_x}{U_o}$
0.089	0.3460
0.102	0.3605
0.123	0.3705
0.135	0.3755
0.169	0.3885
0.204	0.4110
0.238	0.4520
0.279	0.4975
0.307	0.5300
0.353	0.5965
0.393	0.6475
0.434	0.7020
0.474	0.7485
0.561	0.8235
0.646	0.8850
0.722	0.9325
0.877	0.9700
1.227	0.9825
1.692	0.9970
2.037	1.0025
2.265	1.0025

$$\frac{\delta_p^*}{r_{max}} = 0.2836$$

$$\frac{\delta_r^*}{r_{max}} = 0.3780$$

$$\frac{\delta_r}{r_{max}} = 0.96$$

x/L = 1.057

$\frac{r}{r_{max}}$	$\frac{u_x}{U_o}$
0.000	0.4336
0.026	0.4440
0.105	0.4712
0.216	0.5623
0.333	0.6729
0.442	0.7723
0.560	0.8488
0.675	0.9088
0.786	0.9595
1.171	0.9819
1.659	0.9856
2.151	0.9893

$$\frac{\delta_p^*}{r_{max}} = 0.2315$$

$$\frac{\delta_r^*}{r_{max}} = 0.3550$$

$$\frac{\delta_r}{r_{max}} = 1.00$$

x/L = 1.182

$\frac{r}{r_{max}}$	$\frac{u_x}{U_o}$
0.000	0.5760
0.040	0.5850
0.085	0.5942
0.124	0.6006
0.203	0.6216
0.281	0.6764
0.398	0.7715
0.519	0.8538
0.637	0.9211
0.752	0.9581
0.904	0.9670
1.172	0.9780
1.644	0.9887
2.174	0.9988

$$\frac{\delta_p^*}{r_{max}} = 0.1880$$

$$\frac{\delta_r^*}{r_{max}} = 0.3248$$

$$\frac{\delta_r}{r_{max}} = 1.02$$

Theoretical Computation and Model and Full-Scale Correlation of the Flow at the Stern of a Submerged Body

A. W. Moore
Admiralty Marine Technology Establishment
Teddington, England

C. B. Wills
Admiralty Marine Technology Establishment
Haslar, England

©British Crown Copyright 1979.

ABSTRACT

This paper describes an empirical method devised for modifying measurements made at a propeller position at the rear of unpowered bodies such that the flow at the same position on a full-scale self-propelled body may be predicted.

A boundary layer calculation procedure for estimating boundary-layer velocity profiles at the tail region of a body of revolution is discussed, and the inclusion of a simple representation of a propeller is described. Comparisons between velocities measured at Reynolds numbers of order 10^6 and calculated velocities show reasonable correlation both for unpowered and for powered bodies of revolution. It is shown how the results of boundary-layer velocity calculations are used to derive a method for modifying flow measurements at model scale to represent full-scale flow over the propeller disc area. Comparisons are made between predictions based on this method and measurements on powered and unpowered bodies at high and low Reynolds numbers.

1. INTRODUCTION

For many applications a self-propelled marine vehicle has a propeller fitted at the rear of the body where it gains in propulsive performance and in cavitation performance by operating in the relatively slow moving fluid in the hull boundary layer. It follows that a fundamental requirement for propeller design is a knowledge of the boundary layer flow at the propeller position. This information is not usually known since there are no theoretical methods presently available for calculating the boundary flow at the rear of a powered asymmetric body with appendages. An estimate of the required flow field can be obtained from measurements at model scale but as the Reynolds number based on model length is considerably lower than the full-scale value, it is necessary to make some modification to the measurements to simulate the effect of a thinner boundary layer at full scale. If the flow field is measured on an unpowered model, as is often the case, further modification is required to allow for flow acceleration due to the propeller.

This paper describes an approximate method which has been developed for estimating corrections required to flow measurements on unpowered bodies. A boundary layer calculation procedure is briefly outlined and then compared with data from tests on axisymmetric bodies at low Reynolds numbers and non axisymmetric bodies at both low and high Reynolds numbers.

2. BOUNDARY LAYER CALCULATION

The method is based on the work of Myring (1973) and only a brief outline is presented herein. An iterative scheme is adopted in which a boundary layer calculation is done for a given pressure distribution over the body and a potential flow calculation is done to calculate the pressure distribution over the body with boundary layer displacement thickness added. In the boundary layer calculation procedure, an integral method is used in which the laminar flow region is calculated using the method of Luxton and Young (1962) and the turbulent flow is calculated using a method similar to that due to Head (1960). The transition point must be specified and it is assumed that momentum area and a shape parameter are continuous at transition.

An important feature in Myring's method is his treatment of the turbulent boundary layer in the region of the tail. The usual boundary layer assumptions become invalid in this region where the ratio of boundary layer thickness to body radius tends to infinity so Myring defines a momentum area and a displacement area which overcomes the problem and which reduce respectively to body radius times momentum thickness and body radius times displacement thickness far from the tail where boundary layer thickness is small. A conventional momentum integral equation is derived in terms of the defined parameters and this is solved using an empirical relationship for skin friction coefficient which assumes that wall shear-stress does not change sign. Therefore the method is only applicable to bodies on which the boundary layer remains attached. It is also assumed that the variation of static pressure across the boundary layer is negligible. This latter assumption has been found to be incorrect for bodies with blunt tails (i.e., cone angles greater than 30°) and an empirical modification has been made based on the work of Patel (1974) who developed independently a method which is similar to Myring's but which recognises the importance of static pressure variation. The modification introduced in the present method is that the predicted velocity distribution along the body is changed empirically in the tail region, the change being related to differences between measured and predicted velocity distributions at the rear of a given body with a blunt stern. It has been found that this modification results in improved correlation between measured and predicted boundary layer velocity profiles.

A simple actuator disc representation of a propeller has now been included in the potential flow part of the calculation in order to give a first approximation to the acceleration effects on the flow caused by the action of the propeller.

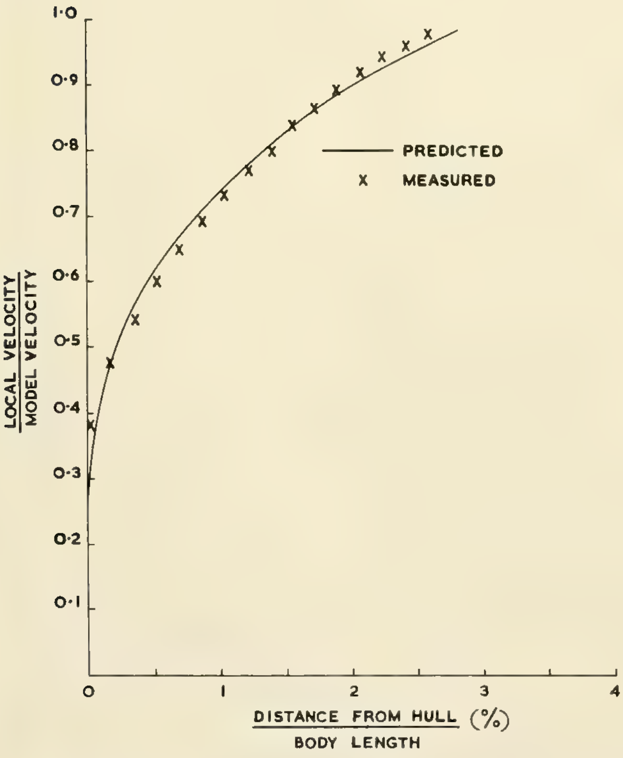

FIGURE 1. Measured and predicted velocities 0.96L from the bow of a body of revolution with tail cone angle of 26°.

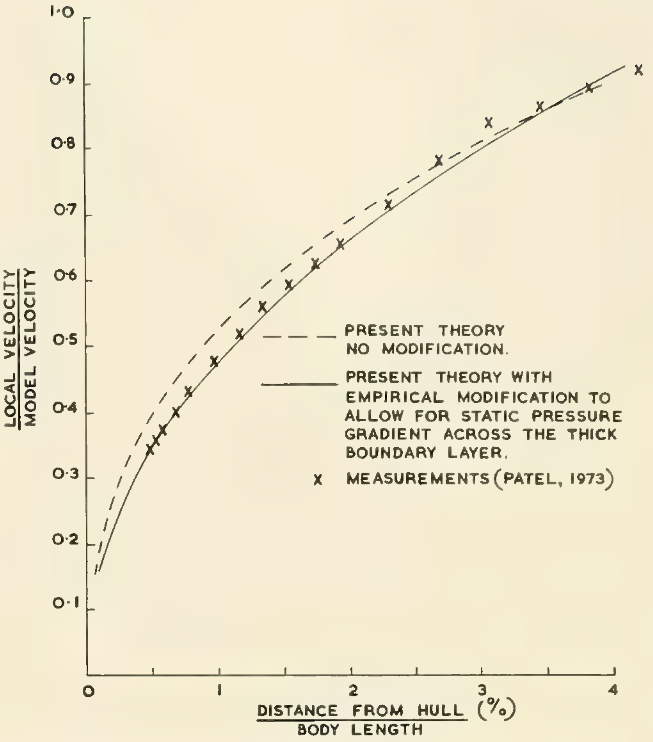

FIGURE 2. Measured and predicted velocities 0.96L from the bow of a body of revolution with blunt stern [Patel (1973)].

3. RESULTS AT LOW REYNOLDS NUMBER ON AXISYMMETRIC BODIES

Comparison between Predicted and Measured Results

The main interest in the present work is in the prediction of boundary layer velocity profiles in the tail region of a body and the results presented in this section relate to model measurements under conditions giving a Reynolds number based on model length from 1×10^6 to 6×10^6.

The velocity measurements shown in Figure 1 were made at a station 0.96 L from the bow of a body of revolution of length L and having a relatively fine stern (cone angle 26°). The measurements are of total velocity whereas the calculation method gives values of velocity component parallel to the hull. The theoretical curve in Figure 1 is obtained by applying a small correction to the calculated velocities to allow for the difference between local flow angle and hull angle. It can be seen that the resulting predicted curve gives values to within 4% of the measured velocities. Detailed measurements at the rear of a body of revolution having a blunt stern have been reported by Patel et al. (1973) and results for a station 0.96 L from the bow are shown in Figure 2. The broken line is the theoretical boundary layer profile predicted from Myring's method with no allowance for static pressure variation across the boundary layer. This curve is significantly different from the measured velocities which are more than 10% less than predicted values in the inner part of the boundary layer. Correlation between measured and predicted results is improved when the empirical modification allowing for static pressure variation has been made and the resulting curve is seen in Figure 2 to be in better agreement with the measurements.

Theoretical results obtained with the simple representation of a propeller included in the method indicate that the propeller can produce large local changes in the boundary layer flow. An example for which measurements are also available is shown in Figure 3 where results are presented for various stations along a body of revolution having a fine tail and contra-rotating propellers. The measurements are of total velocity and were made with rakes of probes fixed to the body, the rake at the forward propeller plane being removed when the propeller was fitted. The velocity profiles on the unpowered body are well predicted except close to the tail where boundary layer separation appears to be present: it is noted earlier that the calculation procedure will not predict separation. The changes produced by the propellers are in surprisingly good agreement with predicted changes considering that an actuator disc representation of the propellers has been adopted. The velocities in a region close to the hull are under-predicted at the two rearmost stations and at the station very close to the tail the velocities near to the edge of the boundary layer are also underpredicted. Apart from these discrepancies the effect of the propeller is well represented.

Velocity profiles close to the propeller plane with and without propeller operating have been reported by Huang (1976). A typical example is shown in Figure 4 where it can be seen that the Myring theoretical prediction for the unpowered body gives velocities which tend to be too low. Nevertheless the discrepancy is less than 4% of the measured values.

Reliability of Harmonic Analyses of Measured Flow Fields

The comparisons between theoretical prediction and measurement indicate that the calculation method gives a good approximation to velocity profiles measured on powered and unpowered bodies of revolution. The method is not expected to predict velocities to better than 4% in absolute terms but this is satisfactory for the purpose of deriving a simple means for modifying model measurements to represent full-scale values. It is required to obtain a representative flow field over the propeller disc area and an essential starting point is to have reliable model data not only in the sense that velocities can be measured accurately at a given point, but also that, if a Fourier analysis is made of the velocities measured during one revolution at a given radius, then a good approximation to the magnitudes of wake harmonics is

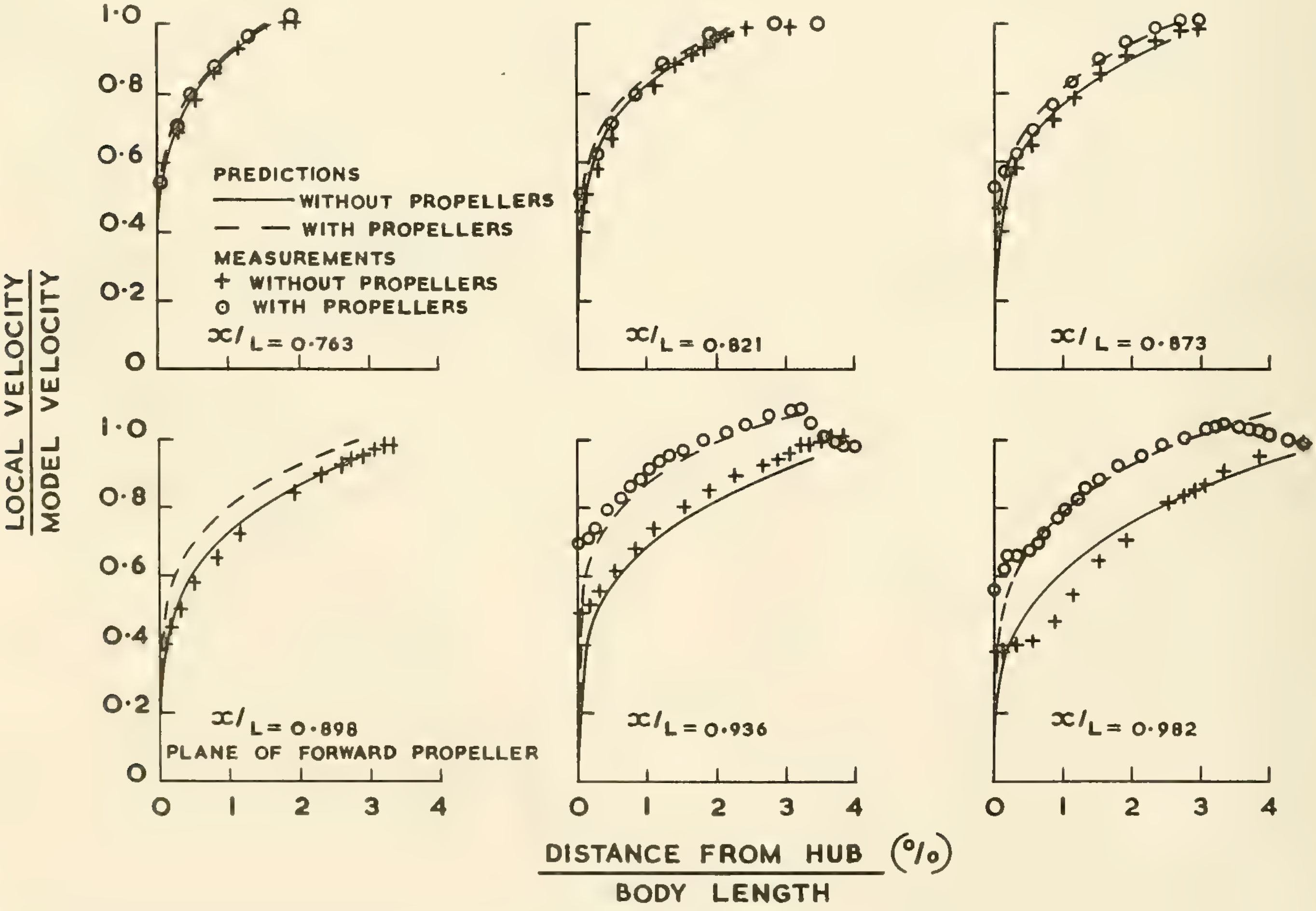

FIGURE 3. Velocity predictions and measurements on a torpedo-like body.

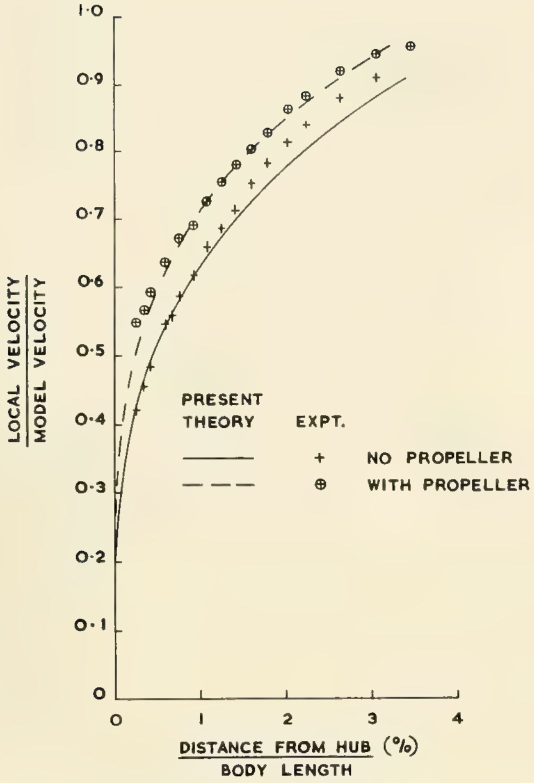

FIGURE 4. Velocity profiles immediately ahead of the propeller DTNSRDC body 5225-1 [Huang (1976)].

obtained. This information is relevant to the estimation of unsteady forces generated by a propeller. Some tests have been made in a wind tunnel to assess the reliability of model measurements at a typical propeller position on a three dimensional body. Inflow non-uniformity was introduced by fitting four struts to the body and the velocity field was measured by a single traversable pitot-static prove with head 1.5 mm in diameter. Measurements at a given radius were made on different runs with incremental steps of 1°, 2°, and 3° in the circumferential position of the probe and 10 repeat runs were made with 3° incremental steps. A Fourier analysis of each set of results was made and the harmonic spectra are summarised in Figure 5. It can be seen that the standard deviations in the magnitudes of wake harmonics are quite small showing that misleading information concerning the relative magnitudes of different wake harmonics would not be obtained on any one run. The differences in magnitudes from the runs with 1°, 2°, and 3° steps in probe position are also quite small in general although a few wake harmonics, such as 11, do show significant changes. No consistent trend is observed in comparing amplitudes at low harmonic number but at harmonic numbers greater than 25 the amplitudes obtained from the run with 1° steps tend to be higher than those from other runs, the implication being that choosing a coarser step size has resulted in a small loss in accuracy.

The amplitudes of wake harmonics at harmonic numbers greater than 20 are small (less than 0.005 times tunnel speed) except for harmonic numbers which are multiples of 4. These higher values are associated with the wakes from the four struts which each produce a 'trough' in the measured flow field. The high harmonic amplitudes at high harmonic numbers implies a possible inaccuracy in results from a Fourier analysis based on the finite number of measured points. This was investigated theoretically by assuming an idealised wake defect giving a triangular waveform as indicated in Figure 6. The number of wake defects and wake width could be varied and for each assumed flow field an exact Fourier analysis was obtained analytically and the results were compared with similar analyses determined numerically with the waveform described at discrete points as specified in the measurements. Figure 7 shows results obtained with 4 narrow wake defects and 120 points specifying the velocity profile. Two wake widths are considered; when maximum wake width is 9° harmonics above 20 are in reasonable agreement with the exact solution although harmonics below 20 are too low; when wake width is reduced to 4½° the amplitude of harmonics from the exact solution falls slowly with increasing harmonic number whereas the amplitudes determined numerically show no reduction in amplitude. In this case, where points are specified every 3° and the width of each wake defect is only 4½°, 'aliasing' in the numerical results is not unexpected. Such pitfalls in numerical analysis are well known and Manley (1945) shows that erroneous values in analyses of the type described above might be expected at harmonic numbers given by (N-jK) where N is the number of specified points, K the number of wake defects and j is an integer. A parametric study for triangular waveforms in

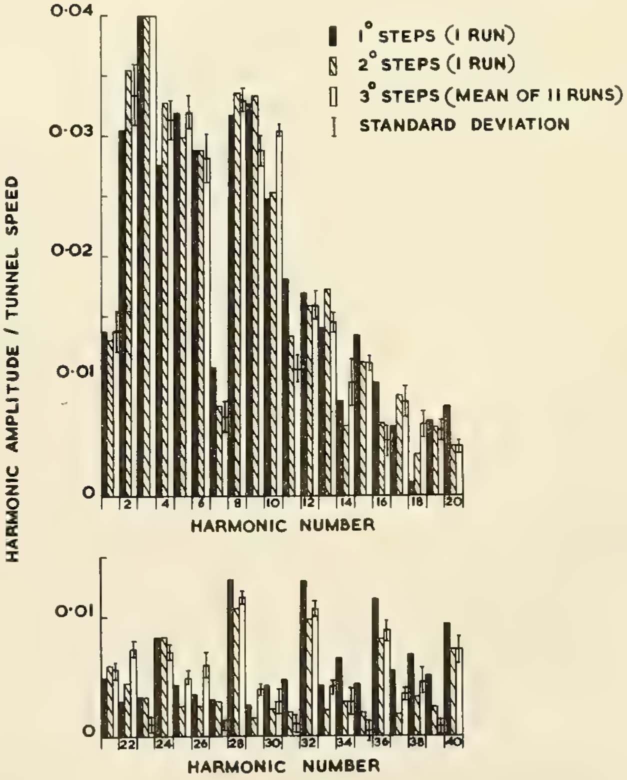

FIGURE 5. Harmonic analysis of different measurements of a non-uniform flow field.

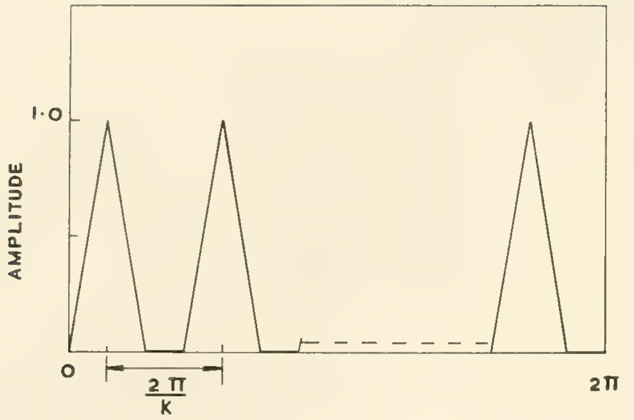

FIGURE 6. Theoretical representation of wake defects in the flow field.

which N, K, and wake width were varied showed that, in general, errors did not become significant until wake width was less than twice the angular spacing of the specified points, i.e., 720°/N.

4. USE OF THE PREDICTION METHOD IN PROPELLER DESIGN

A knowledge of the flow in the region of a propeller is required first, in order to design it, and second, to estimate its performance characteristics. The former requires an estimate of the unpowered mean velocity through the propeller position together with the radial variation of mean circumferential velocity. Of the latter, the prediction of unsteady propeller forces in particular also requires the detail wake structure at the propeller position in the powered condition.

The theoretical boundary layer prediction method outlined in Section 2 cannot be used directly to predict the above wake information for practical vehicle configurations because of limitations such as its restriction to unappended bodies of revolution. However, it can be employed indirectly by using the method to predict the changes from model testing conditions to full-scale vehicle conditions and then applying these scale effects to available model data.

The procedure adopted for the predictions discussed in the following section was to replace the non symmetric, appended vehicle by an equivalent body of revolution. Powered and unpowered boundary layer predictions were then carried out and, by assuming a simple power law for the boundary layer velocity profile, the mean circumferential velocities were determined for the equivalent model and full-scale bodies. In this way it was possible to estimate at any position the scale effect upon the unpowered wakes, the propeller induction effects, and any combination of the two. These effects were then applied to all the measured unpowered model data to give predictions of both model and full-scale powered wakes for comparison with measured data.

5. COMPARISON BETWEEN PREDICTED AND MEASURED RESULTS ON NON-SYMMETRIC BODIES

As part of a programme to investigate the effects of scaling and propeller induction on wakes, experiments have been carried out on two practical vehicle forms covering a range of Reynolds numbers, based on body length, from approximately 1×10^7 to 6×10^8. The two vehicles concerned were propelled by a single centre line propeller and were fitted with a set of cruciform after-control surfaces just ahead of the propeller. The afterbody form was axisymmetric in both cases, one vehicle having a fine stern (vehicle A) and the other a blunt stern (vehicle B).

The low Reynolds number data were obtained in the ship tanks at AMTE (Haslar) using small conventional pitot static tubes. For body A, measurements were made at a position 26 percent of the local control surface chord aft of the control surface trailing edge. This corresponded to 28 percent of the propeller diameter forward of the propeller. The measurements were made at 2° intervals over an angle of approximately 90° centred on one control surface, and at radial distances from the body surface of 12.5 percent and 25 percent of the propeller radius. For body B, data were obtained 24 percent of the local control surface chord aft of the control surface trailing edge, corresponding to 22 percent of the propeller diameter forward of the propeller. In this case 6 pitot static tubes were used covering a range of radial distances from the hull of 12.5 percent to 65 percent of the propeller radius.

The high Reynolds number data were obtained from trials carried out at sea on vehicle A using 5 con-

(a) N = 120, K = 4, WAKE WIDTH 9°.

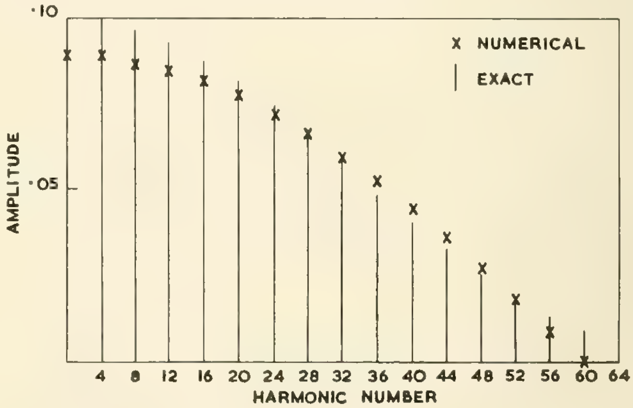

(b) N = 120, K = 4, WAKE WIDTH 4½°.

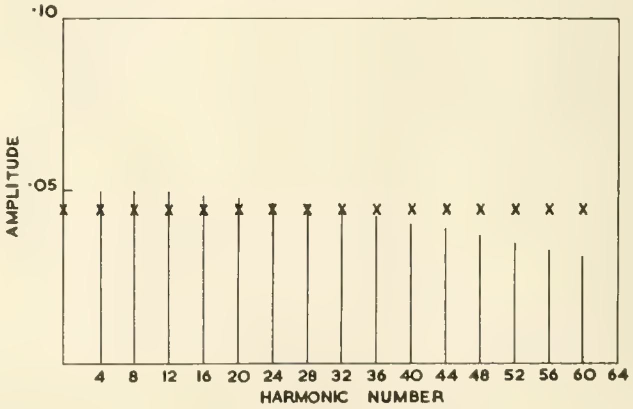

FIGURE 7. Comparison between an exact Fourier analysis of the theoretical velocity profile and a numerical analysis of the same profile specified at a discrete number of points.

ventional pitot static tubes at each of the above radial positions.

The high Reynolds number measurements could only be carried out at self-propulsion conditions. However, the model experiments in the ship tank were run over a range of propulsion conditions, the model speed, propeller rpm, and resistance being recorded.

Analysis of Experimental Data

The low Reynolds number results for vehicle A are presented in Figures 8 and 9 while the equivalent high Reynolds number trail data is given in Figure 10. For body B the available data is restricted to that obtained in the low Reynolds number ship tank tests and the results are presented in Figures 11 to 13. For the sake of brevity the velocity profiles given in Figures 11 to 13 have been limited to those for alternate measurement radii.

It can be shown that the propeller diffusion ratio, defined as the ratio of the mean velocity through the propeller to the unpowered mean wake velocity through the propeller position, can be obtained from the propeller thrust or hull resistance together with the mean volumetric wake and thrust deduction. Thus, using the model powered and unpowered resistance measurements and values of wake and thrust deduction obtained from previous model tests, the propeller diffusion ratio has been calculated for the model propulsion conditions pertaining during the experiments. Similar calculations have been carried out for the sea trial conditions using data obtained from previous propulsion trials. The results of these analyses are given on Figures 8 to 13, and also in Table 1 which summarises the experimental and trial conditions.

The velocities just ahead of the propeller have been averaged at each radius to give the variation of the mean circumferential velocities with diffusion ratio presented in Figures 14 and 15. In an attempt to quantify the secondary flow component in the above velocity profiles the ratio of the mean peak velocity to the mean minimum velocity has been evaluated and plotted in Figures 16 and 17. The normal parameter used to specify the velocity defect, namely the ratio of the minimum velocity in the 'trough' to the mean velocity at the edge of the 'trough' is given in Figures 16 and 18. No values are given for the inner radius on body B because, as can be seen from Figure 11, the wake defect is not clearly defined at this position. The latter parameter is also compared in Figure 19 with an empirical relationship based on two-dimensional data [e.g., Raj (1973)].

The results of using the Myring based boundary layer prediction method as described in Section 4 for the powered model and trial conditions are also plotted in Figures 14 to 18.

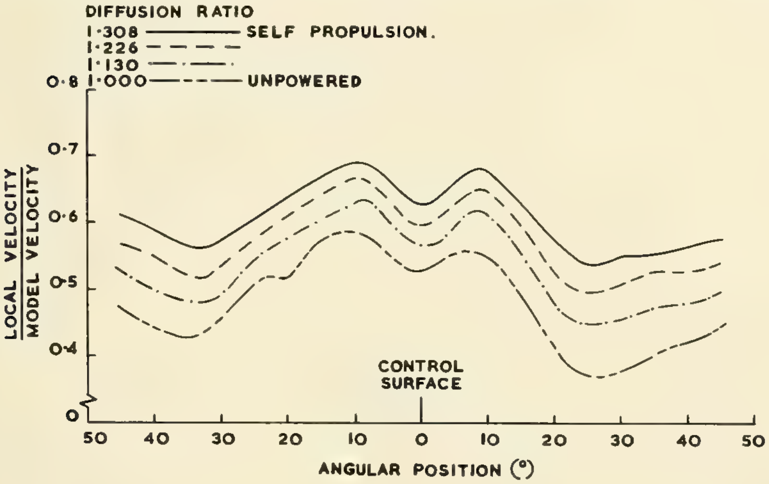

FIGURE 8. Vehicle A model velocity profiles at position 12.5 percent of propeller radius from the hull.

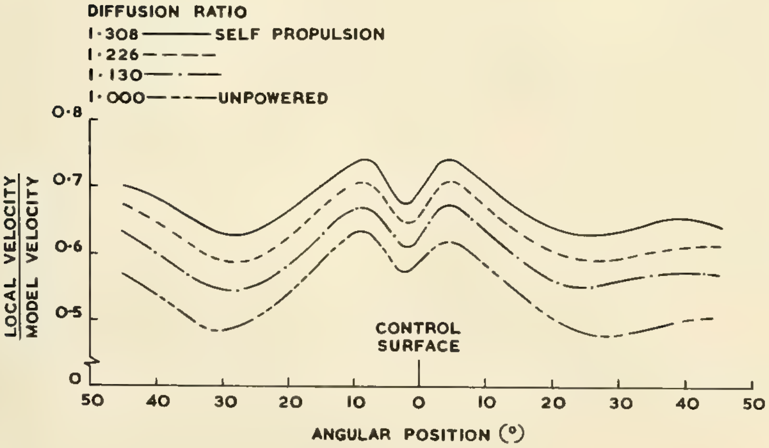

FIGURE 9. Vehicle A model velocity profiles at position 25 percent of propeller radius from the hull.

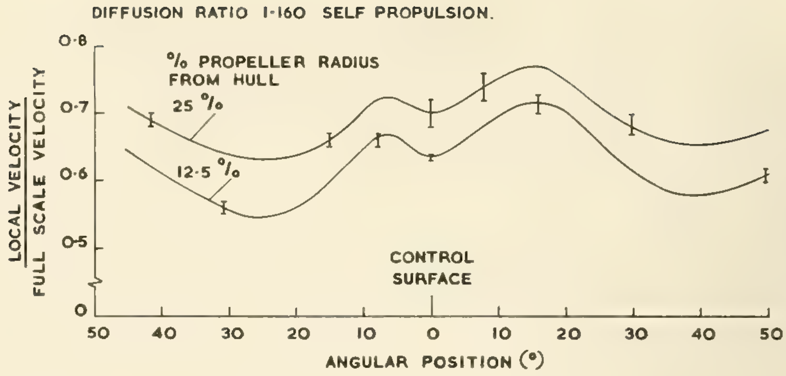

FIGURE 10. Vehicle A full-scale velocity profiles 12.5 percent and 25 percent of propeller radius from the hull.

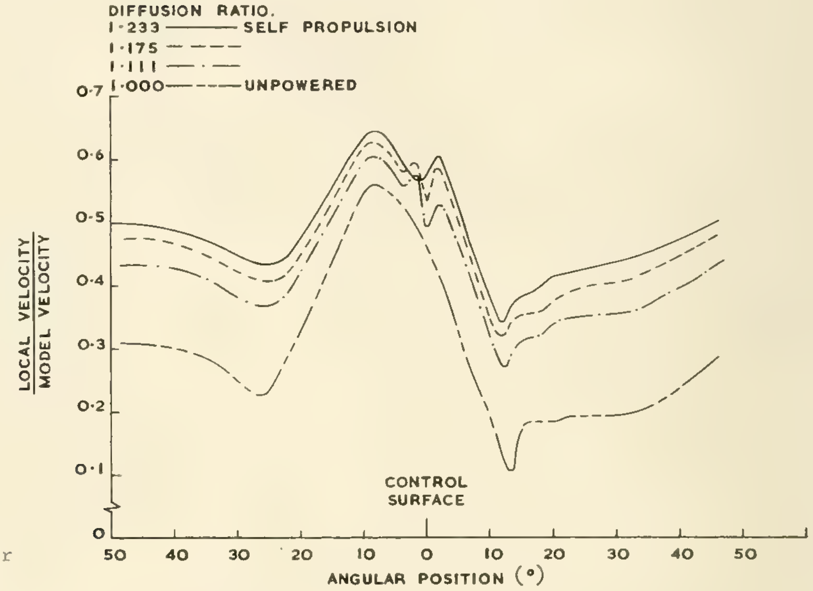

FIGURE 11. Vehicle B model velocity profiles at position 12.5 percent of propeller radius from the hull.

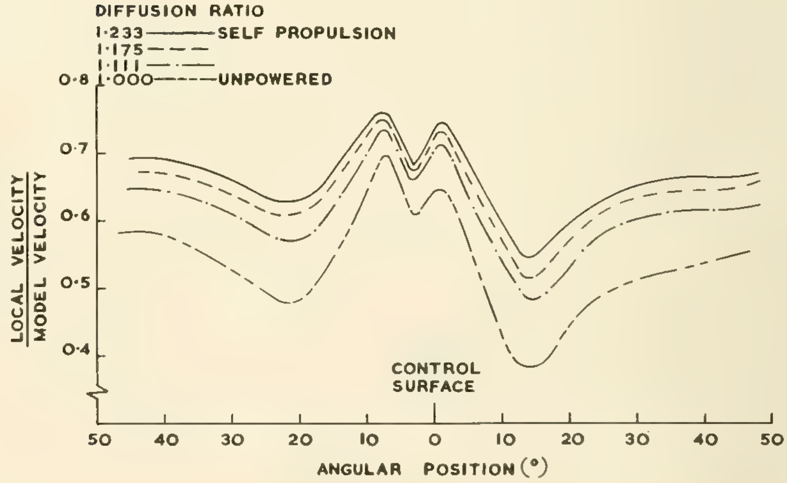

FIGURE 12. Vehicle B model velocity profiles at position 33.5 percent of propeller radius from the hull.

Discussion of Measured Data

It is clear from Figure 16 that the relative magnitude of the velocity defect at the two radii considered on vehicle A is virtually unaffected by the propeller, and is subject to only a very small scale effect. The latter gives rise to a reduction in the depth of the velocity defect between the model and full-scale equivalent to an increase of between 1 percent and 3 percent in the ratio of minimum velocity in the 'trough' to the mean velocity at the edge of the 'trough'. It can be seen from Figure 19 that for vehicle A the actual values of the velocity defect are considerably lower than predicted by the empirical relationship derived from two-dimensional test results. This is not

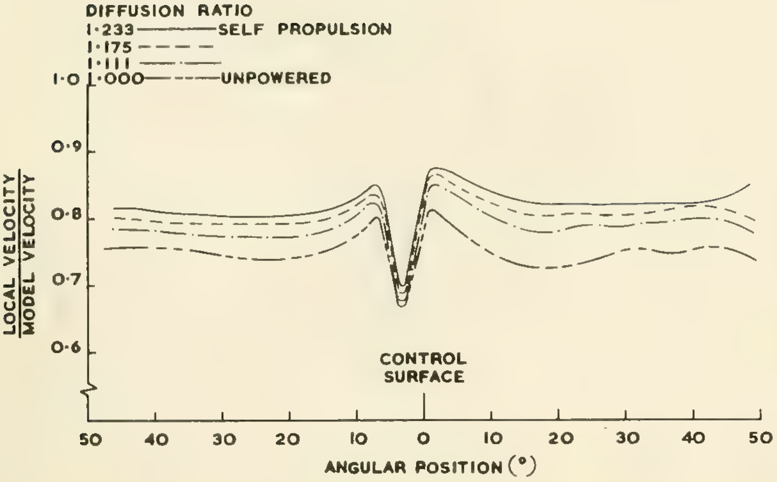

FIGURE 13. Vehicle B model velocity profiles at position 54.5 percent of propeller radius from the hull.

surprising since the two radii concerned are close to the hull and the velocity defect is developing in a complex three-dimensional flow field influenced by the secondary flow and this is possibly leading to a more rapid mixing of the flow. The results obtained over a much larger distance from the hull on vehicle B support the above hypothesis since it can be seen from Figures 18 and 19 that as the distance from the hull increases the magnitude of the wake defect increases and approaches the two-dimensional value. The model results for vehicle B shown in Figure 18 tend, in general, to indicate a small increase in the depth of the wake defect as the propeller diffusion ratio increases. The maximum value of this increase in the wake defect, between the model self-propelled and unpowered condition, is only of the order of 3 percent. This change is somewhat surprising since the propeller produces a favourable pressure gradient aft of the control surfaces, and on the evidence of two-dimensional data this would be expected to reduce the wake defect.

In contrast to the velocity defect the secondary flow can be seen from Figures 16 and 17 to be significantly reduced by the presence of the propeller, this reduction becoming larger as the diffusion ratio increases. Additionally, at equal propeller diffusion ratio, the full-scale secondary flow is significantly less than measured on the model. From the data obtained on vehicle A (Figures 14 and 16) it can be seen that, comparing the results at model and full-scale self-propulsion conditions, the magnitude of the secondary flow and the mean circumferential velocity at the two radii considered agree to within 2 percent and 3 percent respectively. Although comparison between the velocity profiles is difficult because of the non-symmetry of the trial data, Figures 1 to 3 indicate that at these conditions there is also reasonable agreement between the velocity profiles. These results indicate a possible condition for similar

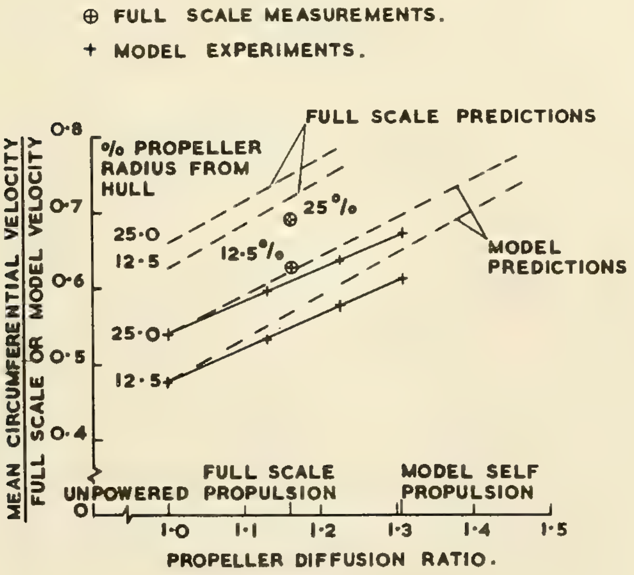

FIGURE 14. Mean circumferential velocity in the measuring plane for vehicle A.

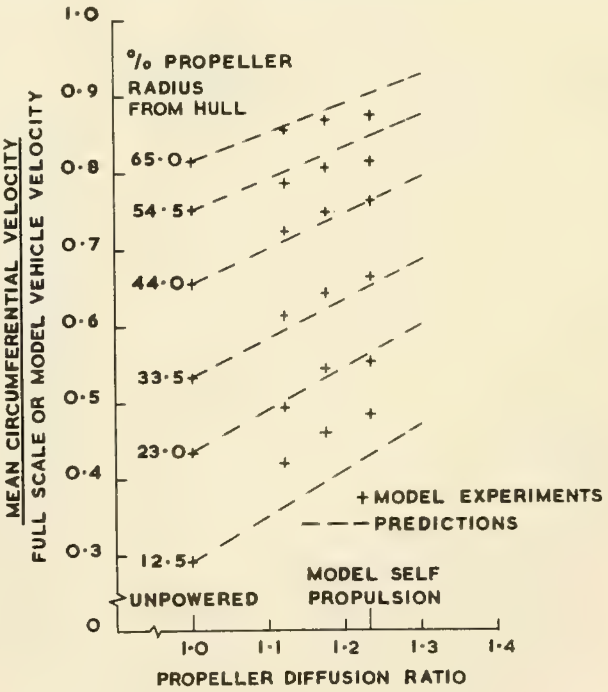

FIGURE 15. Mean circumferential velocity in the measuring plane for vehicle B.

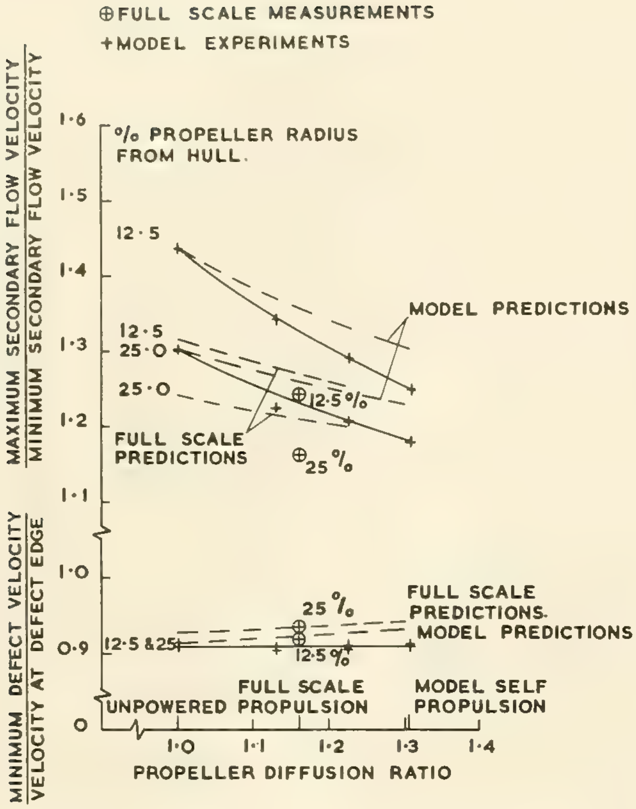

FIGURE 16. Relative magnitude of the secondary flow and velocity defect for vehicle A.

inflow to the propeller at model and full-scale; however, it should not be regarded as a general conclusion on the basis of this one experiment. Additionally although the propeller inflow may be similar at self-propulsion the propeller thrust loading, as indicated by the diffusion ratio, will be different.

Comparison between the wake defect and secondary flow model measurements for the two vehicles (Figures 16 to 18) show generally similar magnitudes for the former, but a much larger secondary flow in the case of the body with the fuller afterbody. The latter effect can also be seen in the velocity profiles given in Figures 8 and 11.

Comparison between Predicted and Measured Results

It can be seen from Figure 14 that the mean circumferential velocity predictions for the powered model of vehicle A are always higher than measured. The maximum differences occur at model self-propulsion conditions and are 7 percent and 4 percent for the positions 12.5 percent and 25 percent of the propeller radius from the hull respectively. Both the measured data and the predicted velocities can be seen to vary linearly with propeller diffusion ratio. For the blunter stern, Figure 15 indicates that for radial positions between 23 percent and 44 percent of the propeller radius from the hull the predictions of mean circumferential velocity are generally in good agreement with the measured data. For the two outer radii the predictions tend to be high as in the case for body A, the maximum errors at model self-propulsion being of the order of 4 percent. However, for the innermost radial position, the powered predictions are up to 14 percent below the measured values. It is apparent for Figure 15 that, in contrast to the other radii, the model results for this position are not linear with propeller diffusion ratio because of the low velocity obtained in the unpowered condition. Since the measured data was linear at a similar radial position for body A this suggests that the poor powered prediction of velocity for body B is due to the low unpowered velocity measurement which is used as the datum for the prediction. This low measured velocity may be the result of flow separation on the vehicle with the blunt afterbody which is suppressed by the favourable pressure gradient produced when the propeller is operating.

Comparison between the full-scale and predicted mean circumferential velocities in Figure 14 show the latter to be less accurate than for the model case, the predicted values being 15 percent and 9 percent high for the inner and outer positions respectively. However, correlation of propulsion data from sea trials and model experiments on vehicle A suggest an equivalent full-scale hull Reynolds number of one-tenth of the true value and

TABLE 1 Experimental and Trial Conditions

Vehicle	Conditions	Hull Reynolds Number	Diffusion Ratio	Remarks
A	Model	1.3×10^7	1.308	Self propulsion
			1.226	
			1.130	
A	Trial	5.5×10^8	1.160	Self propulsion
B	Model	1.2×10^7	1.233	Self propulsion
			1.175	
			1.111	

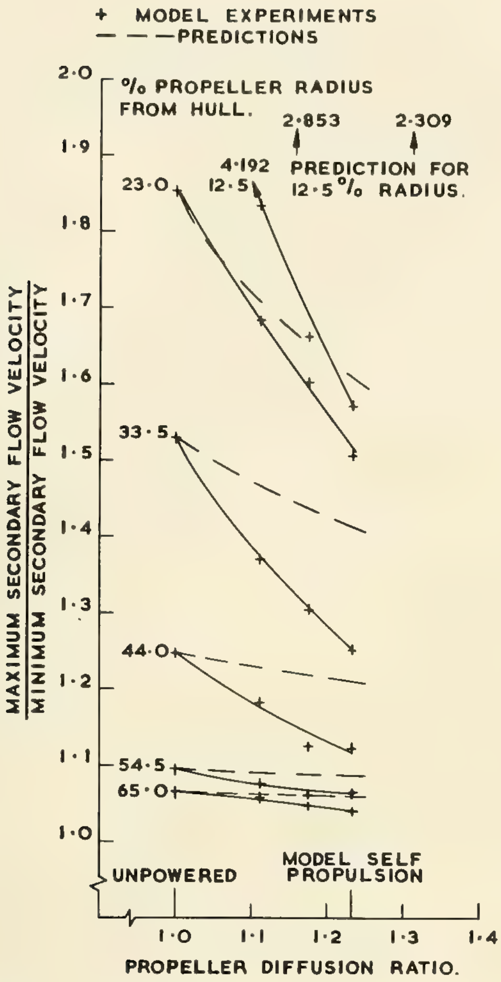

FIGURE 17. Relative magnitude of the secondary flow for vehicle B.

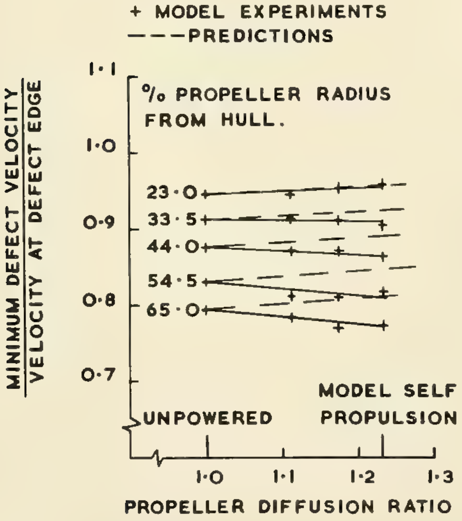

FIGURE 18. Relative magnitude of the velocity defect for vehicle B.

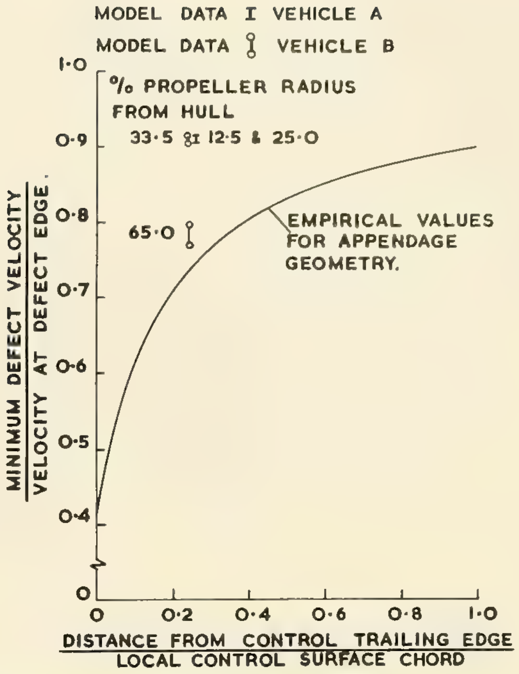

FIGURE 19. Variation of model velocity defect with distance from the control surface.

if this is used for the predictions the above differences become + 1 percent and - 2 percent respectively. Thus the speed trial and full-scale wake data become compatible and both suggest a scale effect on the flow velocity for the vehicle A with the finer stern much smaller than predicted. This may be due to the fact that the full-scale vehicle is hydraulically rough at all but the very lowest speeds while the prediction method assumes hydraulically smooth conditions.

The process of adding the predicted mean circumferential velocity changes to all measured velocities are described in Section 4 naturally leads to a change in the ratios used herein to describe the relative magnitudes of the velocity defect and secondary flow. For the velocity defect Figures 16 and 18 show that the predicted magnitude decreases slightly with increasing diffusion ratio such that at model self-propulsion the relative magnitudes are 3 percent higher than measured for body A and up to 6 percent for body B. The predicted relative magnitude of the wake defect at the full scale condition is within 2 percent of that measured, although as already noted the absolute velocities are 15 percent and 9 percent higher than measured. The use of a smaller scaling effect based on the equivalent Reynolds number discussed above would slightly reduce the above error in predicted velocity defect.

The predicted relative magnitude of the secondary flow can be seen from Figures 16 and 17 to decrease with increasing diffusion ratio but at a slower rate than actually measured on the models. Thus, the propeller is having an influence on the development of the secondary flow in addition to the simple change in relative magnitude arising from the propeller induced velocity. It is clear that at model conditions, the difference between the measured and predicted secondary flow is much greater for the blunter afterbody form of vehicle

B. At model self-propulsion conditions these differences are up to 5 percent for vehicle A but 60 percent for vehicle B. The secondary flow prediction for the full-scale conditions on body A given in Figure 16 can again be seen to be higher than the measured values but only by up to 4 percent at the two radii considered. In this case the use of a smaller scaling effect would lead to higher predicted values such that the differences between these and the measured values would increase to the order of 6 percent.

The above results show that the agreement between the measured and predicted data has been limited and further work is required before the proposed scaling method can be regarded as satisfactory. The principal requirement is for further high Reynolds number data and it is proposed to obtain this by additional full-scale trials, together with experiments on models in a compressed air wind tunnel.

6. CONCLUSIONS

An integral boundary-layer calculation method for bodies of revolution is shown to give a good prediction of boundary layer velocity profile for attached flows in the tail region of a body.

Inclusion of a simple actuator disc representation of a propeller in the calculation method gives a reasonable first approximation to the effect of a propeller on the flow.

Comparison between results from Fourier analyses of measurements from runs repeated a number of times and of measurements made with different incremental steps in probe position indicates that wake harmonics can be determined reliably from measurements at model scale.

Fourier analyses of idealised velocity profiles representing wake defects in an otherwise uniform flow field have been obtained analytically. Comparison between these results and numerical harmonic analyses of the same profile specified at a discrete number of points shows no significant differences in the amplitudes of wake harmonics at high harmonic number provided that the width of the wake is not too small.

The measurements presented herein indicate that the velocity defect produced behind a control surface is only slightly affected by either the presence of a propeller aft of the control surface, or by the change in Reynolds number from model to full-scale.

Near the hull, where the flow is influenced by secondary flow effects, the velocity defect behind a control surface is much smaller than predicted from two-dimensional data. For positions outside the influence of the secondary flow the velocity defect approaches the two-dimensional value.

The velocity defect is of a similar order of magnitude for the two bodies examined. However, the secondary flow effects are significantly larger for the vehicle with the blunter stern.

The secondary flow produced by the interaction of a control surface with the hull boundary layer is reduced significantly by the presence of a propeller aft of the control surface, and from model to full-scale conditions. This reduction increases with increasing propeller diffusion ratio.

By using the unpowered model measurements as datum it has been possible to predict the model powered mean circumferential velocities to within 4 percent for radial positions from the hull greater than 12.5 percent of the propeller radius. At this radius itself, the predictions are within 7 percent for the finer stern model and 14 percent for the fuller stern; however, the latter may be due to separation effects which are not taken into account in the prediction method.

Predictions of the mean circumferential velocity at the full-scale conditions for the vehicle with the finer stern are high by up to 15 percent. If the ship prediction is made at a reduced Reynolds number suggested by speed trial results the predictions come within 2 percent. Predictions of the powered velocity defect are within 6 percent for model conditions and 2 percent for ship conditions, the latter figure applying to either the true or reduced full-scale Reynolds number. Predictions of the model powered secondary flow are within 5 percent for the body with the finer stern, but up to 60 percent for the fuller form. However, for the full-scale conditions obtained on the finer stern the predictions are within 4 percent at the true Reynolds number, and 6 percent at the reduced value.

A practical method of estimating propeller induction and wake scaling effects has been proposed and demonstrated to give limited agreement with model and full-scale data. Further experimental data are required to refine the method and to this end high Reynolds number model experiments are planned to be carried out in a compressed air wind tunnel, and further full-scale trials scheduled.

REFERENCES

Head, M. R. (1960). Entrainment in the turbulent boundary layer. *British ARC, R & M 3152.*

Huang, T. T., S. Santelli, H. T. Wang, and N. C. Groves. (1976). Propeller/stern/boundary-layer interaction on axisymmetric bodies: theory and experiment. *DTNSRDC Rep 76-0113.*

Luxton, R. E., and A. D. Young. (1962). Generalised methods for the calculation of the laminar compressible boundary layer characteristics with heat transfer and non-uniform pressure distribution. *British ARC, R & M 3233.*

Manley, R. G. (1945). *Waveform analysis.* Chapman and Hall, London.

Myring, D. F. (1973). The profile drag of bodies of revolution in subsonic axisymmetric flow. RAE TR 72234. (Unpublished).

Patel, V. C. (1974). A simple integral method for the calculation of thick axisymmetric turbulent boundary layers. *Aeronautical Quarterly, 15,* Pt. 1.

Patel, V. C., A. Nakayama, and R. Damian. (1973). An experimental study of the thick turbulent boundary layer near the tail of a body of revolution. *Iowa Institute of Hydraulic Research Report, 142.*

Raj, R., and B. Lakshminarayana. (1973). Characterisics of the wake behind a cascade of airfoils. *J. Fluid Mechs, 61,* Pt. 4.

Experimental and Theoretical Investigation of Ship Boundary Layer and Wake

Shuji Hatano, Kazuhiro Mori and Takio Hotta
Hiroshima University, Hiroshima, Japan

ABSTRACT

Characteristics of the boundary layer and wake flow of ships are investigated experimentally and attempts are made to estimate their velocity distributions.

Boundary layer characteristics, before the onset of separation, are studied; a three-dimensional boundary layer calculation is carried out by the integral method, while examining the boundary layer assumptions and the validity of auxiliary equations by direct measurements of velocity and static pressure profiles in boundary layer as well as skin friction distribution on hull surface.

Assuming that the wake is the domain of influence of the boundary layer and consists of three sub-regions, i.e., vorticity diffusion region, separated retarding region, and viscous sublayer, different governing equations for each sub-region are derived by local asymptotic expansions.

Velocity distribution in the vorticity diffusion region is estimated in two steps: first, vorticity distribution is found by solving the vorticity diffusion equation, then velocity distribution is calculated from the obtained vorticity distribution by invoking Biot-Savart's law.

Satisfactory agreements are attained between calculations and measurements both for boundary layer and wake.

1. INTRODUCTION

Introductory Remarks

The prediction of the viscous flow field around ship hulls, boundary layer on the hull surface, and the wake, is one of the most important problems in ship hydrodynamics. Important design-conditions, such as estimations of viscous resistance or wake distribution on a propeller disk, are all closely connected with this problem. Instabilities of ship maneuvering and propeller-excited-vibrations are also presently urgent problems in practice; they are also fundamentally connected with the viscous

Calculations of a ship boundary layer have been carried out by many investigators during the last decade; e.g., Uberoi (1969), Gadd (1970), Webster and Huang (1970), Hatano et al. (1971), Himeno and Tanaka (1973), and Larsson (1975). They have solved boundary layer equations in integral forms. Cebeci et al. (1975), as well as Soejima and Yamazaki (1978), has tried to solve them by the finite-difference method.

Such remarkable progress in ship boundary layer calculations are mainly due to studies of two-dimensional boundary layers and to the use of high speed computers. Though some of them yield good results, an absence of experimental examination of boundary layer assumptions or auxiliary equations can be found when applying them to shiplike bodies. Experimental examinations are very important because most of auxiliary equations are derived from two-dimensional experiments.

On the other hand, as to the ship wake, many experimental studies have been carried out not only for ship models but also for full scale ships, e.g., Yokoo et al., (1971) and Hoekstra, (1975) mainly discussed the prediction of full scale wake characteristics based on model wake survey.

Rational theoretical studies are still more important. As to theoretical studies of wake, we must retreat to problems of flow behind rather simple obstacles like flat-plates, circular cylinders, or bodies of revolution. Even in such cases, most treatments are based on potential theory such as free-streamline theory or cavity-flow theory, reviewed by Wu, (1972). However, because vorticities existing within wakes are mainly generated in boundary layers of hull surfaces and shed into wakes viscously and convectively through separations, the prediction of wake flow should be treated in close relation to boundary layer flow.

The previous works by Hatano et al., (1975, 1977), were carried out from this standpoint. But they are only the beginning of research on ship wakes and many future problems were pointed out, especially requirements for further experimental studies.

The present authors are firmly convinced that, for such viscous flow problems, marriages of experimental and theoretical studies are primarily important in order to make further progress. Because of this, the present paper is divided into two parts; experimental studies on ship boundary layers and wakes (Section 2 and 4), and theoretical studies and numerical calculations (Section 3 and 5).

Coordinate Systems and Models Used

Two coordinate systems are employed throughout the present paper. One is the right-hand linear coordinate system, O-xyz, whose origin is at midship and on the waterplane and the oncoming flow, U_0, is in the x-direction. The other is the streamline coordinate, $x_1x_2x_3$; the curves of constant x_2 coincide with potential flow streamlines on hull surface and x_3 is normal direction to hull surface (Figure 1).

All quantities are dimensionless by half ship length ℓ $(=L/2)$, ship speed U_0, and fluid density ρ, unless specified in another form.

For the present research three ship models, GBT-125, GBT-30, and MS-02 were used whose body plans with potential streamlines and principal dimensions are shown in Figure 2 and Table 1.

GBT-125 and GBT-30 are practical tanker ship models, similar in geometry to each other. GBT-125 is a double model and was used under submerged conditions for studies of boundary layer flow. MS-02, which was used for the studies of wake flow, has a rather simple stern form; the framelines are elliptic and given by the equation,

$$\left(\frac{y}{y_0}\right)^2 + \left(\frac{z}{d}\right)^2 = 1 , \quad x \geq a \ (a=0.4) \tag{1}$$

where

$$y_0 = b_0 \left[1-\left(\frac{x-a}{1-a}\right)^{0.7}\right] , \tag{2}$$

and b_0 is the half breadth of the waterplane at $x = 0.4$ (S.S.3) and d is the draft. The remainder, $(x \leq 0.4)$, has a practical hull form. This is because the practical stern form produces a very complicated stern flow, e.g., an intensive longitudinal vortex, not suitable for the present investigations.

Experiments were carried out in the circulating water channel and the towing tank of Hiroshima University.

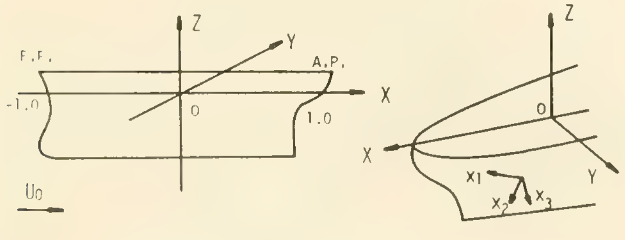

FIGURE 1. Coordinate systems.

TABLE 1 PRINCIPAL DIMENSIONS OF MODELS

	GBT-125	GBT-30	MS-02
L	$1.250^{(m)}$	$3.000^{(m)}$	$3.000^{(m)}$
B	.193	.462	.485
d	.065	.157	.165
C_b	.836	.836	.768

NOTATION

L, ℓ	ship model length and half length
b	ship model breadth
C_b	block coefficient of the ship model
d	ship model draft
ρ	density
ν	kinematic coefficient of viscosity
ν_e	eddy viscosity coefficient
g	gravity acceleration
U_0	velocity of oncoming flow, ship speed
F_n	Froude number $=U_0/\sqrt{gL}$
R_e	Reynolds number $=U_0L/\nu$
ε	small parameter for asymptotic expansions $= R_e^{-1/8}$
x,y,z	orthogonal linear coordinates
x_1,x_2,x_3	orthogonal curvilinear coordinates
ξ,η,ζ	distances along x_1,x_2,x_3 coordinates
h_1,h_2,h_3	corresponding metric coefficients
K_1,K_2	convergences defined by $K_1 = -\frac{1}{h_1h_2}\frac{\partial h_2}{\partial x_1}$, $K_2 = -\frac{1}{h_1h_2}\frac{\partial h_1}{\partial x_2}$
$\tilde{\xi},\tilde{\eta},\tilde{\zeta}$ $\tilde{\xi},\tilde{\eta},\hat{\zeta}$ $\tilde{\xi},\tilde{\eta},\zeta^*$	normalized distances for vorticity diffusion region, separated retarding region, and viscous sublayer respectively
q	velocity vector
q_v	viscous part of velocity vector
u,v,w	velocity components in x,y,z directions excluding uniform flow
q_1,q_2,q_3	mean velocity components in x_1,x_2,x_3 directions
q_1',q_2',q_3'	fluctuating velocity components in x_1,x_2,x_3 directions
U_e	resultant velocity at boundary layer edge
U_1,V_1,W_1	velocity components at boundary layer edge in x_1,x_2,x_3 directions
$\tilde{u}_0,\tilde{u}_i,\tilde{v}_i,\tilde{w}_i$ $\hat{u}_i,\hat{v}_i,\hat{w}_i$ u_i^*,v_i^*,w_i^* $(i=1,2,...)$	asymptotic terms of normalized mean velocity for vorticity diffusion region, separated retarding region, and viscous sublayer region
$\hat{u}_i',\hat{v}_i',\hat{w}_i'$ $(i=1,2,...)$	asymptotic terms of normalized fluctuating velocity for separated retarding region
ω	vorticity vector
$\omega_x,\omega_y,\omega_z$	vorticity components in x,y,z directions
$\omega_1,\omega_2,\omega_3$	vorticity components in x_1,x_2,x_3 directions
$\tilde{\omega}_{\xi}i,\tilde{\omega}_{\eta}i,\tilde{\omega}_{\zeta}i$ $(i=1,2,...)$	asymptotic terms of normalized vorticity for vorticity diffusion region
p	pressure

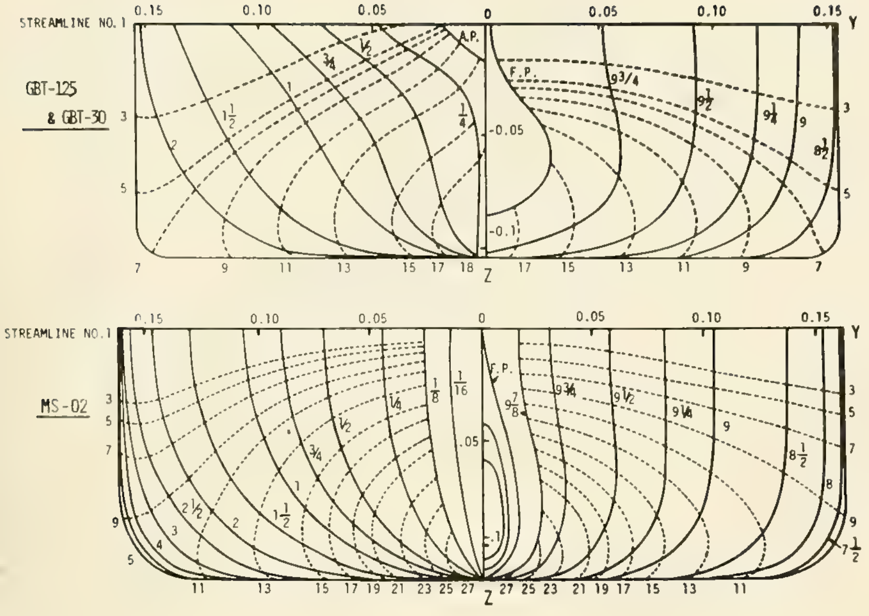

FIGURE 2. Body plans and potential flow streamlines of models.

p_∞	pressure far upstream
C_p	pressure coefficient $=(p-p_\infty)/\frac{1}{2}\rho U_0^2$
$p_i(i=1,2,\ldots)$	asymptotic terms of normalized pressure
δ	boundary layer thickness
$\delta_1^*,\delta_2^*,\theta_{11}$ $\theta_{21},\theta_{12},\theta_{22}$	three-dimensional boundary layer thickness parameters defined by Eqs. (5), (19)
H	shape factor of streamwise velocity profile $=\delta_1^*/\theta_{11}$
β	angle between surface streamline and external streamline direction, positive in x_2 direction
n	index for power-law velocity profile
g_1,g_2	parameter for wake part of wall-wake law in q_1, q_2 components
κ,B	coefficients of wall-wake law
f_0,f_1	wall and wake functions of wall-wake law defined by Eq. (10)
τ_w	resultant skin friction
τ_{w1},τ_{w2}	components of skin friction in x_1 and x_2 directions
u_τ	friction velocity
F	entrainment function
Γ_a	parameter for separation
x_s,x_r	positions of onset of separation and reattachment
V	integral region for induced velocity
∇	gradient vector
O( )	symbol of orders $f=O(\varepsilon)$; $\lim_{\varepsilon\to 0}\frac{f}{\varepsilon}=M$ (M:constant)

2. EXPERIMENTAL STUDIES ON BOUNDARY LAYER

Kinds of Experiments and Measuring Techniques

In order to examine the boundary layer assumptions and the validity of semi-empirical equations in case of ship-like bodies, the following kinds of experiments were carried out [Hatano et al., (1978)].

Static pressure measurements on hull surface

Static pressure holes of 0.6mm were arranged on the hull surface along streamlines and the static pressure was measured by towing ahead and astern.

Static pressure measurements in boundary layer

Static pressure in the boundary layer was measured by using a static pressure tube. It is 1.2mm in diameter with two 0.4mm ϕ holes on diametrically opposite sides. A traverser with a micrometer was used to move the probe normal to the hull surface. The preliminary experiments showed that the static pressure was free from incident flows whose attack angles were less than 20°.

Velocity measurements in boundary layer

A total head probe, made from hypodermic tubing of outside diameter 0.28mm and 2.7mm respectively, was mounted on the traverser. Total pressure was measured after locating flow directions by yawing the directionally-sensitive hot film probe. Using the measured static pressure, velocity was estimated and decomposed into streamwise and crossflow components.

Local skin friction measurements

Local skin friction on the hull surface was measured directly by a floating-element type friction meter [Hotta, (1975)]. The floating element is 14mm in diameter with gaps of 0.05mm to the mounting case and balanced by electromagnetic force.

All experiments described above were carried out using the GBT-125 under submerged conditions at a depth of about 6 times the draft of the model. The Reynolds number was kept constant at 10^6.

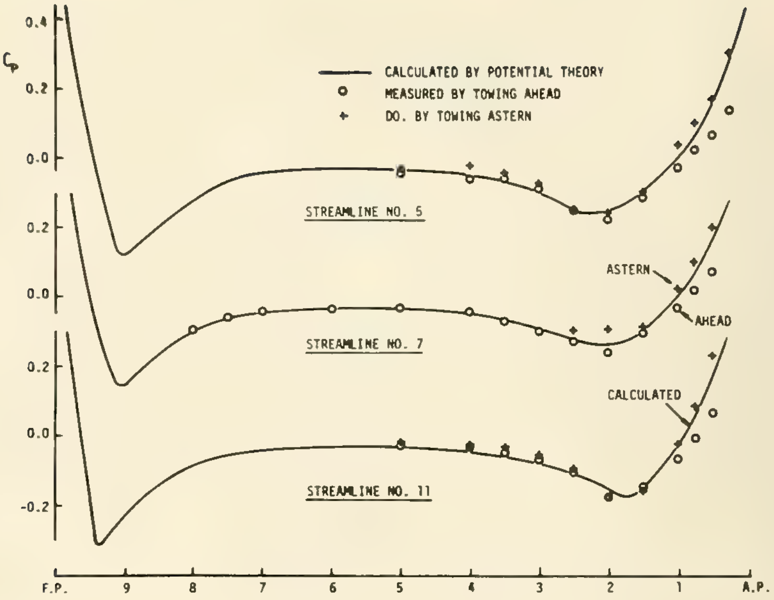

FIGURE 3. Static pressure distribution on the hull surface (GBT-125).

Experimental Examinations of Boundary Layer Assumptions and Semi-Empirical Equations

Boundary Layer Assumptions

The usual first approximate calculations of the boundary layer were carried out under the assumption that the static pressure is constant across boundary layers and is equal to the inviscid flow pressure. These assumptions are open to experimental examination when the boundary layer thickness is not thin, especially in the case of ship-like bodies.

Static pressure distributions on the hull surface along streamline Nos. 5, 7, and 11 are shown in Figure 3 with calculated potential flow pressures. Potential flow calculations were carried out by the well-known surface-source method [Hess and Smith, (1962)] representing the hull by 254 × 2 small rectilinear panels. Static pressures while being towed onward are in good agreement with those calculated, except near the stern, where pressure has not recovered and is slightly low. However, towing astern shows good agreements even near the stern. This means that displacement effects of the boundary layer are appreciable near the stern.

Figure 4 shows static pressure profiles in the boundary layer*. It was observed that pressure profiles are almost constant across the boundary layer except for some positions where the pressure is monotonically increasing or decreasing in that normal direction. The tendencies of increments are significant at S.S.1½ or S.S.1¼ of streamline No. 11. This can be referred to the centrifugal force due to the small radii of curvature of the bilge keel. On the other hand, a decrease can be found for all the streamlines at S.S.½ or S.S.¼, which may be the effect of separation. (As described later, flow can be assumed to have separated near S.S.½.) There the concept of boundary layer itself should be discarded.

It can be safely pointed out that the pressure-

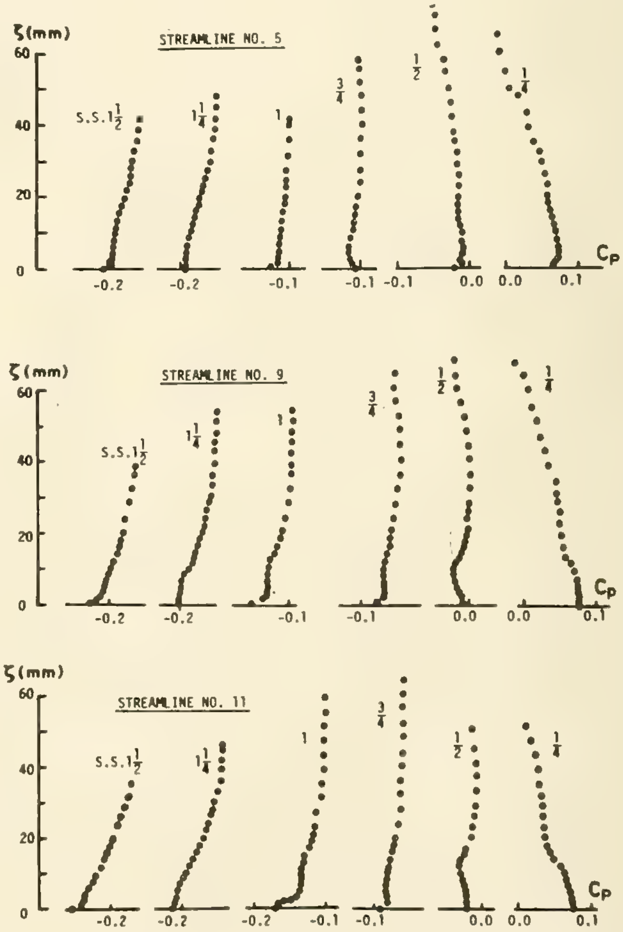

FIGURE 4. Static pressure profiles in the boundary layer (GBT-125).

*Static pressure on the hull surface does not agree with that of Figure 3. While the measurements whose results are shown in Figure 3 were carried out in the towing tank, those shown in Figure 4 were in the circulating water channel. The discrepancies are all due to this difference in experimental conditions; the cross section of the circulating water channel is restricted to 1200mm × 820mm and pressure is underestimated.

constant assumption can be employed unless the radii of curvature are not significantly small; the displacement effects are important near the stern and should be taken into account in higher order calculations [Hatano and Hotta (1977)].

Velocity Profiles

In order to calculate the boundary layer equations by an integral method it is convenient to represent velocity profiles by analytical functions which include several parameters.

The most commonly used formulae are based on a 1/n-power law and on a wall-wake law. The former has a definite merit of simplicity. The latter, developed by Coles (1956), has more freedom than the 1/n-power law and can be expected to represent velocity profiles more exactly.

Mager's expression is well known as the three-dimensional velocity profile model based on a 1/n-power law, Mager (1951). He gave the streamwise and crossflow velocity profiles as

$$q_1/U_e = \left(\frac{\zeta}{\delta}\right)^{1/n}, \tag{3}$$

$$q_2/U_e = \tan\beta \left(\frac{\zeta}{\delta}\right)^{1/n} \left(1-\frac{\zeta}{\delta}\right)^2 \tag{4}$$

where n is a variable parameter.

If velocity profiles are represented by Eqs. (3) and (4), the boundary layer thickness-parameters δ_1^*, θ_{11} and shape factor H are

$$\delta_1^* = \frac{1}{U_e}\int_0^\delta (U_1 - q_1)d\zeta = \frac{1}{n+1}\delta\ ,$$

$$\theta_{11} = \frac{1}{U_e^2}\int_0^\delta q_1(U_1 - q_1)d\zeta = \frac{n}{(n+1)(n+2)}\delta, \tag{5}$$

$$H = \frac{\delta_1^*}{\theta_{11}} = \frac{n+2}{n}$$

and Eqs. (3) and (4) can be written in other forms,

$$q_1/U_e = \left[\frac{\zeta}{\theta_{11}}\frac{H-1}{H(H+1)}\right]^{\frac{H-1}{2}} \tag{6}$$

$$q_2/U_e = \tan\beta\left[\frac{\zeta}{\theta_{11}}\frac{H-1}{H(H+1)}\right]^{\frac{H-1}{2}}\left[1-\frac{\zeta}{\theta_{11}}\frac{H-1}{H(H+1)}\right]^2 . \tag{7}$$

If θ_{11} and δ_1^* are integrated and β is determined from measured velocity profiles, then velocity profiles represented by Mager's model can be calculated from Eqs. (6) and (7) and can be compared with the measured profiles.

Figure 5 shows the comparisons of them. It can be safely pointed out that Mager's model is employ-

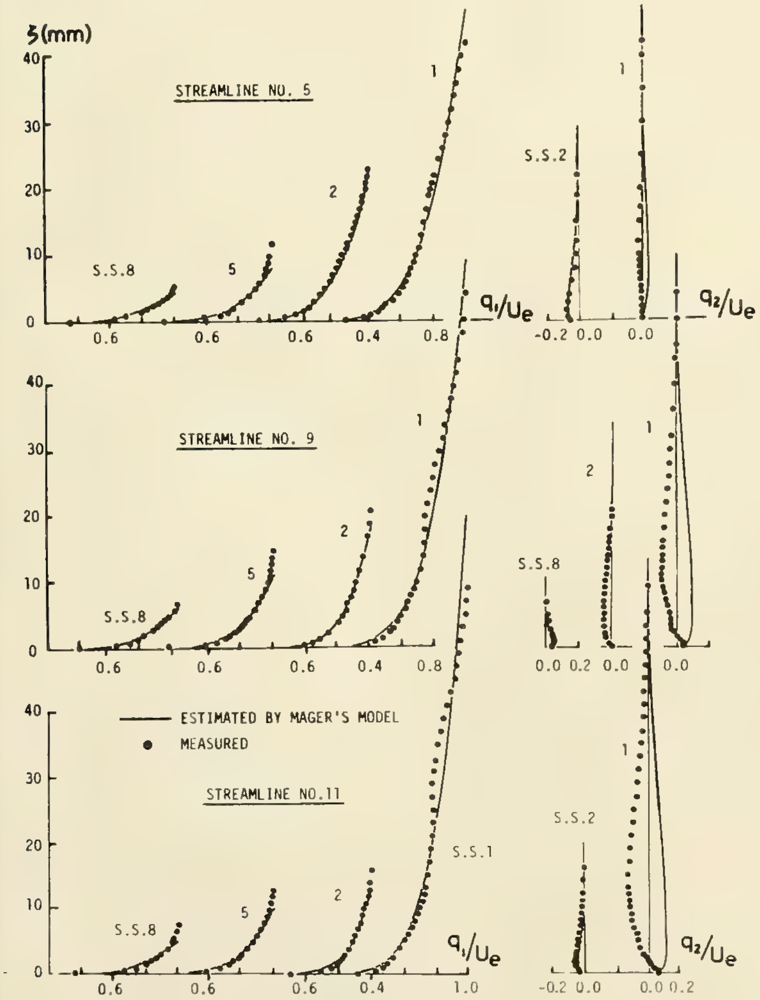

FIGURE 5. Velocity profiles represented by Mager's model.

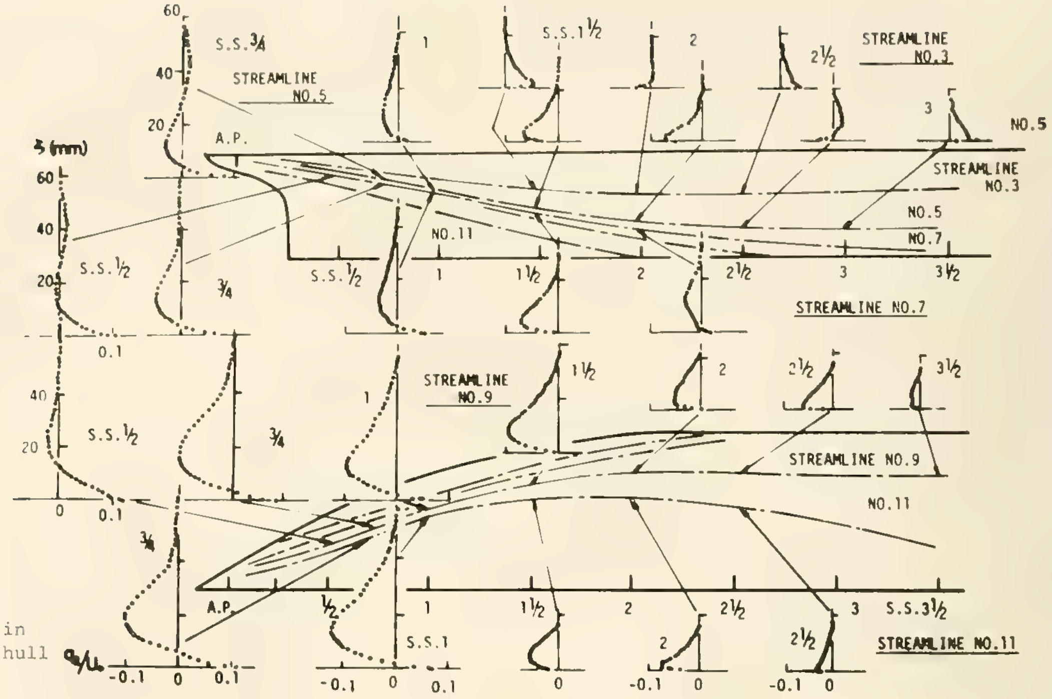

FIGURE 6. Crossflow profiles in the boundary layer on the AFT hull surface (GBT-125).

able for the velocity profiles of ship-like bodies as far as streamwise components.

Figure 6 shows crossflow profiles measured on aft parts of a model. As easily observed, there are some profiles which have reverse type (S-shaped) profiles. For most of remaining parts, the crossflow angles are very small and do not show reverse type profiles. Because Eq. (4) has only one inflection point, such S-shaped profiles can not be represented by it.

To represent even reverse crossflows, more general polynomial expressions are proposed [e.g., Eichelbrenner (1973), Okuno (1977)]. However, they require additional equations or boundary conditions and it is reported they do not always yield improvements [Okuno (1977)]. This is because the crossflow does not always have such universal profiles near the stern.

On the other hand, the three-dimensional velocity profiles based on Coles' wall-wake law can be represented by

$$q_1/U_e = \frac{u_\tau}{U_e} f_0\left(\frac{u_\tau \zeta}{\nu}\right)\cos\beta + g_1 f_1\left(\frac{\zeta}{\delta}\right) , \quad (8)$$

$$q_2/U_e = \frac{u_\tau}{U_e} f_0\left(\frac{u_\tau \zeta}{\nu}\right)\sin\beta + g_2 f_1\left(\frac{\zeta}{\delta}\right) , \quad (9)$$

where

$$f_0\left(\frac{u_\tau \zeta}{\nu}\right) = \frac{1}{\kappa}\log_{10}\left(\frac{u_\tau \zeta}{\nu}\right) + B , \quad (10)$$

$$f_1\left(\frac{\zeta}{\delta}\right) = \frac{1}{2}\left[1-\cos\left(\pi\frac{\zeta}{\delta}\right)\right] ,$$

and

$$u_\tau = (\tau_w/\rho)^{1/2}. \quad (11)$$

g_1, g_2 are variable parameters, for wake parts, u_τ is the friction velocity, and κ, B are constants.

f_1 given by Eq. (10) is called the wake function. Figure 7 shows the existence of such parts in case of ship-like bodies also. Velocity profiles deviate from linearity when approaching the outer edge of the boundary layer. Velocity profiles, represented by Eqs. (8) and (9), are compared with measured profiles. Here parameters g_1 and g_2 are determined by the condition that q_1 equals U_e and q_2 equals zero at the boundary and u_τ is determined by a least-squares fit to the measured profiles. The values of Clauser, 5.6 and 4.9, were used for $1/\kappa$ and B respectively. Good reproductions are examined except crossflow representations.

As to crossflow profiles, the situation is not much improved from Mager's model; reverse crossflow observed in experiments can also not be represented by the wall-wake law. The finite-difference method may be a possible step toward representation of any type of velocity profiles.

Local Skin Friction

In the case of turbulent flow, most of the friction is due to the turbulence (Reynolds' stress). For this reason it is necessary to introduce additional equations to determine it in closed form.

Ludwieg and Tillmann's semi-empirical equation for the skin friction [Ludwieg and Tillmann (1949)] is most commonly used; it is

$$\tau_{w1}/\rho U_e^2 = 0.123\times 10^{-0.678H}\left(\frac{U_e\theta_{11}}{\nu}\right)^{-0.268} \quad (12)$$

Because Eq. (12) is obtained from two-dimensional experiments, the validity should be examined when applied to three-dimensional flow.

When Coles' wall-wake law is employed for the velocity profile, the skin friction can be deter-

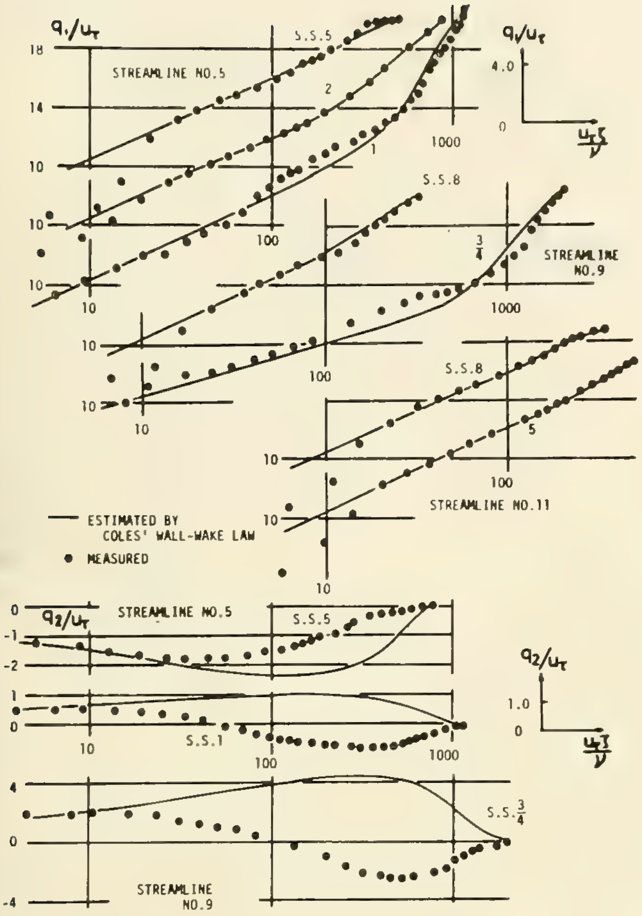

FIGURE 7. Velocity profiles represented by Cole's wall-wake law.

mined from the friction velocity. But it should also be examined experimentally.

In Figure 8, three kinds of experimental values of skin friction are compared along streamline Nos. 9, 11, and 18; directly measured values, those obtained from Ludwieg-Tillmann's formula, Eq. (12), and those from friction velocity, Eq. (11). For estimations of the latter two values, measured velocity profiles are invoked. Calculated results are also shown here for later discussions.

The values of Ludwieg-Tillmann's formula produce fairly good agreements with those directly measured, which implies that Ludwieg-Tillmann's expression is also good for three-dimensional flow.

Entrainment Equation

In streamline coordinates, the continuity equation is given by

$$\frac{\partial}{\partial x_1}(q_1h_2) + \frac{\partial}{\partial x_2}(q_2h_1) + h_1h_2\frac{\partial}{\partial x_3}q_3 = 0. \qquad (13)$$

Integrating with respect to x_3, from zero to δ, gives

$$\frac{\partial}{h_1\partial x_1}(\delta-\delta_1^*) - \frac{\partial\delta_2^*}{h_2\partial x_2}$$

$$= F - (\delta-\delta_1^*)\left\{\frac{1}{h_1h_2}\frac{\partial h_2}{\partial x_1} + \frac{1}{U_e h_1}\frac{\partial Ue}{\partial x_1}\right\} \qquad (14)$$

where F is the entrainment function given by

$$F = U_1\frac{\partial\delta}{h_1\partial x_1} + V_1\frac{\partial\delta}{h_2\partial x_2} - W_1 . \qquad (15)$$

Equation (14) is often used as the third (auxiliary) equation when the boundary layer calculation is carried out by the integral method. Here, F should also be given in someway in closed form.

In two-dimensional flow, Eq. (14) is reduced to

$$F = \frac{1}{U_e}\frac{d}{dx_1}[U_e(\delta-\delta_1^*)]. \qquad (16)$$

Head (1960) gave a relationship between F and $(\delta-\delta_1^*)/\theta_{11}(\equiv H_{\delta-\delta_1^*})$ which was examined by two-dimensional experiments.

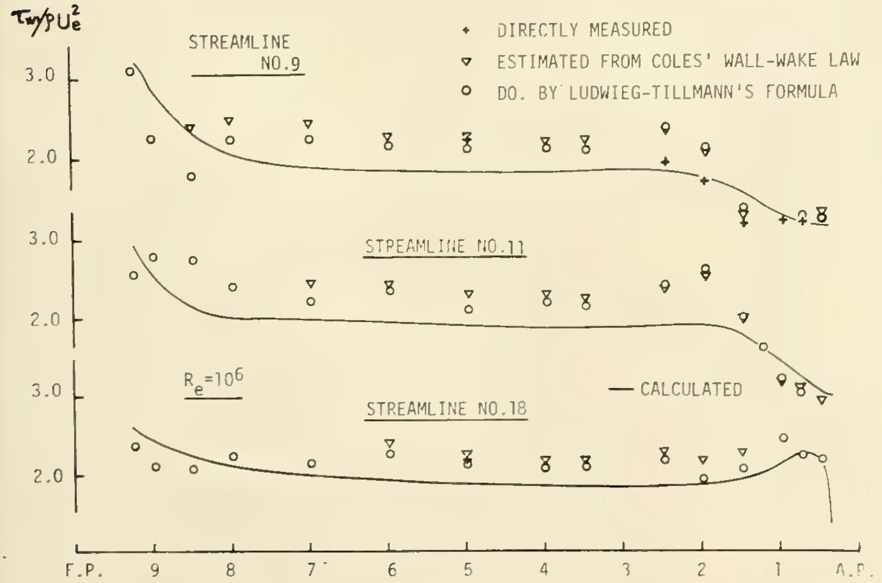

FIGURE 8. Comparisons of local skin friction (GBT-125).

Introducing an assumption that the entrainment equation of three-dimensional flow is related exclusively to the streamwise quantities, Cumpsty and Head (1967) employed the Head's entrainment function for three-dimensional boundary layer calculations. This is of course open to criticism.

In Figure 9, Head's entrainment function and experimental values, obtained from Eq. (14), invoking measured velocity profiles, are compared. It can be mentioned that Head's function gives rather good mean lines both in relation to $H_{\delta-\delta_1^*}$ - H and F-$H_{\delta-\delta_1^*}$. The values of $H_{\delta-\delta_1^*}$ are not fairly related to H in the fore part, where laminar flow may still exist, and neither F to $H_{\delta-\delta_1^*}$ in the aft part. The former does not seriously effect F. We should bear in mind here that the determination of boundary layer thicknesses is not clear in the three-dimensional case and accurate estimations of their derivatives are very difficult.

Himeno and Tanaka (1973) used the moment of momentum equation as the third equation instead. In this case, assumptions for the Reynolds' stress are also required and significant improvements are not always found.

Summarizing the above discussions it can be safely concluded that the integral method, where either Mager's model or the wall-wake law is used for velocity profile, Ludwieg-Tillmann's equation for skin friction, and entrainment equation for auxiliary equation, is expected to yield meaningful results. Moreover, it can be also pointed out that improvements can be attained when the second order approximation for the static pressure is taken into account near the stern. However, in the region where reverse crossflows or large crossflow angles exist, although the boundary layer assumption is not violated, the integral method is no more available.

BOUNDARY LAYER CALCULATIONS

According to the preceding conclusions, boundary layer calculations were carried out by the integral method and compared with experimental results.

Basic Equations and Auxiliary Equations

The integrated boundary layer equations are given in streamline coordinates by

$$\frac{\partial\theta_{11}}{\partial\xi} + \frac{\partial\theta_{12}}{\partial\eta} + (H+2)\frac{\theta_{11}}{U_e}\frac{\partial U_e}{\partial\xi} - K_1(\theta_{11}-\theta_{22})$$

$$= \tau_{w1} / \rho U_e^2 \quad , \tag{17}$$

$$\frac{\partial\theta_{21}}{\partial\xi} + \frac{\partial\theta_{22}}{\partial\eta} + \frac{2\theta_{21}}{U_e}\frac{\partial U_e}{\partial\eta} + \frac{\theta_{11}}{U_e}\frac{\partial U_e}{\partial\eta}(H+1+\frac{\theta_{12}}{\theta_{11}})$$

$$- 2K_1\theta_{21} = \tau_{w2} / \rho U_e^2 \ , \tag{18}$$

where θ_{11}, θ_{12}, θ_{21}, and θ_{22} are momentum thickness parameters defined by

$$U_e^2\ \theta_{11} = \int_0^\delta q_1(U_1-q_1)d\zeta \ ,$$

$$U_e^2\ \theta_{12} = \int_0^\delta q_2(U_1-q_1)d\zeta \ ,$$

$$U_e^2\ \theta_{21} = \int_0^\delta q_1(V_1-q_2)d\zeta \ ,$$

$$U_e^2\ \theta_{22} = \int_0^\delta q_2(V_1-q_2)d\zeta \ . \tag{19}$$

The entrainment equation is employed as the third equation;

$$\frac{\partial}{\partial\xi}(\delta-\delta_1^*) - \frac{\partial}{\partial\eta}\delta_2^* = F - (\delta-\delta_1^*)(-K_1+\frac{1}{U_e}\frac{\partial U_e}{\partial\xi}) . \tag{20}$$

For the function F, the relation of Head is used, which has already been examined.

If Mager's velocity profiles are employed here, boundary layer thickness parameters are given using θ_{11}, H and β,

$$\theta_{21} = \theta_{11}E(H)\tan\beta \ , \ \theta_{22} = \theta_{11}C(H)\tan^2\beta \ ,$$

$$\theta_{12} = \theta_{11}J(H)\tan\beta \ , \ \delta_2^* = \theta_{11}D(H)\tan\beta \ ,$$

$$\delta-\delta_1^* = \theta_{11}N(H) \ , \tag{21}$$

where

$$C(H) = -\frac{24}{(H-1)(H+2)(H+3)(H+4)} \ ,$$

$$D(H) = -\frac{16H}{(H-1)(H+3)(H+5)} \ ,$$

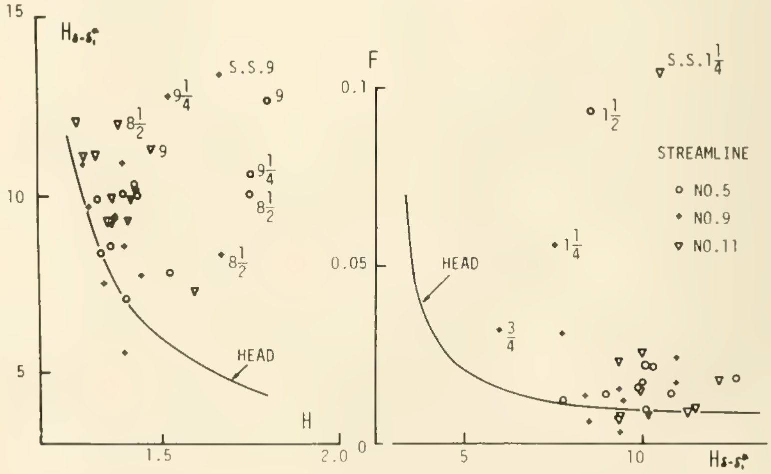

FIGURE 9. Comparison of Head's entrainment function with experiments.

$$E(H) = -\frac{2}{(H-1)(H+2)} \quad ,$$

$$J(H) = E(H) - D(H) \quad ,$$

$$N(H) = \frac{2H}{H-1} \equiv H_{\delta-\delta_1^*} \quad . \qquad (22)$$

Then Eqs. (17), (18), and (20) are reduced to simultaneous differential equations in $\partial\theta_{11}/\partial\xi$, $\partial H/\partial\xi$, and $\partial\beta/\partial\xi$;

$$a_i\frac{\partial\theta_{11}}{\partial\xi} + b_i\frac{\partial H}{\partial\xi} + c_i\frac{\partial\beta}{\partial\xi} = d_i \qquad (i=1,2,3) \qquad (23)$$

where

$$a_1 = 1, \quad b_1 = 0, \quad c_1 = 0,$$

$$d_1 = -J\tan\beta\frac{\partial\theta_{11}}{\partial\eta} - J'\theta_{11}\tan\beta\frac{\partial H}{\partial\eta} - J\theta_{11}\sec^2\beta\frac{\partial\beta}{\partial\eta} - (H+2)\frac{\theta_{11}}{U_e}\frac{\partial U_e}{\partial\xi} + K_1\theta_{11}(1-C\tan^2\beta) + \tau_{w1} / \rho U_e^2 \quad ,$$

$$a_2 = E\tan\beta, \quad b_2 = E'\theta_{11}\tan\beta, \quad c_2 = E\theta_{11}\sec^2\beta,$$

$$d_2 = -2E\tan\beta\frac{\theta_{11}}{U_e}\frac{\partial U_e}{\partial\xi} - C\tan^2\beta\frac{\partial\theta_{11}}{\partial\eta} - C'\theta_{11}\tan^2\beta\frac{\partial H}{\partial\eta} - 2C\theta_{11}\tan\beta\sec^2\beta\frac{\partial\beta}{\partial\eta} - (1+H+C\tan^2\beta)K_2\theta_{11} + 2K_1E\theta_{11}\tan\beta + \tau_{w1} / \rho U_e^2\tan\beta \quad ,$$

$$a_3 = N, \quad b_3 = N'\theta_{11}, \quad c_3 = 0, \qquad (24)$$

$$d_3 = D\tan\beta\frac{\partial\theta_{11}}{\partial\eta} + D'\theta_{11}\tan\beta\frac{\partial H}{\partial\eta} + D\theta_{11}\sec^2\beta\frac{\partial\beta}{\partial\eta} + F - N\theta_{11}\left(-K_1 + \frac{1}{U_e}\frac{\partial U_e}{\partial\xi}\right) \quad ,$$

(The ' means differentiation with respect to H.)

If Ludwieg-Tillmann's skin friction formula, Eq. (12), is used, all the coefficients of Eq. (24) are known at earlier ξ coordinate.

This formulation is the same as that of Cumpsty and Head (1967).

Numerical Calculations and Discussions

Numerical calculations were carried out for GBT-125 at $R_e=10^6$. First, 18 streamlines were traced interpolating the 254 × 2 descrete values of velocity, obtained by the surface source method, and x_1 coordinates were determined.

The differentials with respect to η were numerically determined along the η axis which was defined by bending short segments orthogonally to the x_1 axis. This is the main difference from Cumpsty-Head's original calculations. For such calculations as $\partial U_e/\partial\eta$, $\partial\theta_{11}/\partial\eta$, and so on, the differentials with respect to η should be carried out as carefully as possible. Most numerical errors stem from these terms.

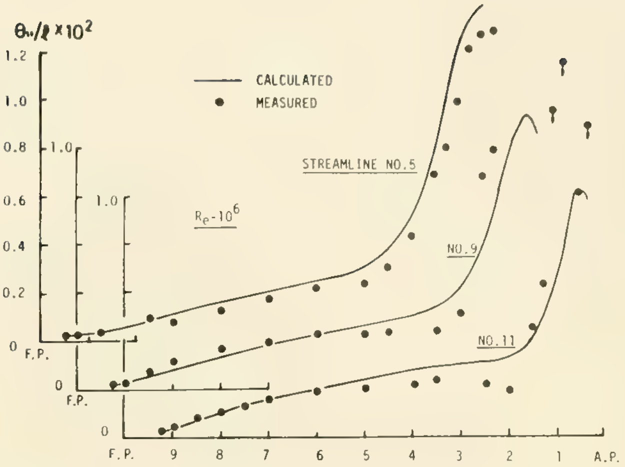

FIGURE 10. Comparisons of momentum thickness (GBT-125).

0.5×10^{-4}, 1.4, and 0.0 were used for the initial values of θ_{11}, H and β at S.S. 9¼(x=-0.85). These values were obtained from Buri's two-dimensional formula assuming the flow is turbulent just from F.P. (see Figure 1). Fortunately they do not seriously affect the calculations.

About 200 steps were taken and Eq. (23) is integrated with respect to ξ by Lunge-Kutta-Gill's method (five points for each step).

In Figures 10, 11, and 12, calculated results of θ_{11}, H, and β along typical streamline Nos. 5, 9, and 11 are shown along with experimental results. The skin friction is shown in Figure 8. Streamline No. 5 generates a simple, quasi-two-dimensional curve on the hull surface and it may be expected the flow can be truly represented by the present framework. On the other hand streamline No. 11 passes through a region where the boundary layer is rather thin and also through a bilge corner where pressure increments were observed.

The experimental values of the streamwise momentum thickness, θ_{11}, of streamline No. 11 were much greater than those calculated around S.S.1. This discrepancy can be related to the fact that S.S.1 of streamline No. 11 corresponds to the position

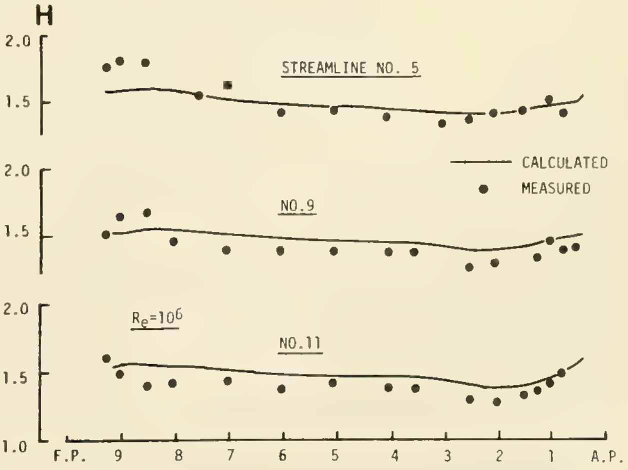

FIGURE 11. Comparisons of shape factor (GBT-125).

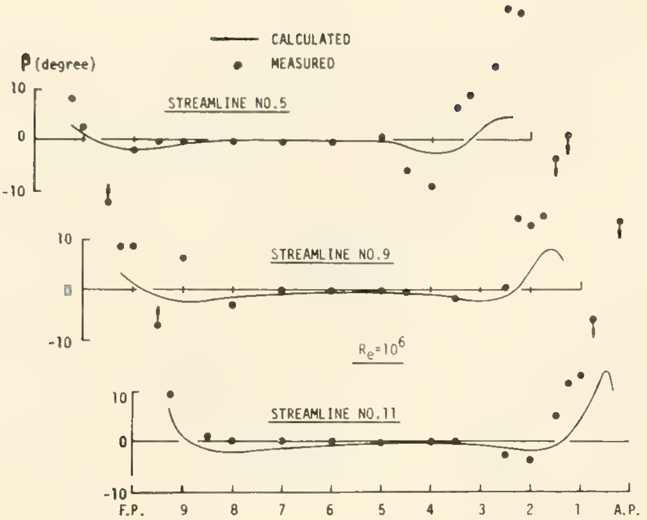

FIGURE 12. Comparisons of crossflow angle (GBT-125).

just behind the bilge keel and the occurrence of bilge separation can be suspected.

Shape factor H, in every case, does not vary significantly and agreements between calculations and measurements are good except near the stern. There, as shown in comparisons of β, large crossflow angles existed and the present scheme can not be employed here.

It is interesting that large crossflow angles can also be observed in experiments near the bow. They create a suspicion of the occurrence of bow-bilge separation.

Skin friction τ_{w1} shows also good agreement. It is observed that both experimental and calculated values do not decrease. This suggests three-dimensional separation differs a little from that of two-dimensional where skin frictions vanish.

As a whole, it can be safely concluded that, except near the stern, calculated results show good agreements with measured as far as integral quantities like θ_{11} or H. It can be also concluded that the present scheme, using integrated mementum boundary layer equations as governing equations, can be appreciated in spite of its brevity.

EXPERIMENTAL STUDIES ON BOUNDARY LAYER SEPARATION AND WAKE

Kinds of Experiments and Measuring Techniques

The characteristics of separation and separated flow of ship-like bodies are dim. Experiments may throw light upon them. In order to discuss the characteristics of separation and separated flow, the following experiments were carried out in addition to the previous experiments. All experiments were carried out with MS-02 and experiments (c) and (d) used GBT-30 also. Experiments were executed at the speeds of $F_n=0.1525$ ($R_e \doteq 2.17\times10^6$) and $F_n=0.16$ ($R_e \doteq 2.38\times10^6$) for MS-20 and GBT-30 respectively.

Flow Observations

Planting twin tufts on the hull surface, flow directions near the stern were observed by a submerged camera; one tuft was just on hull surface and the other was 22mm off, normal from surface.

Free-surface flow around the ship stern was also observed in relation to the separated flow by the aluminium powder method.

Velocity Measurements in Separated Flow Region

Velocity in the separated region was measured using a hot film anemometer. The probe is a conical type, 2mm in diameter. One horizontal plane of z=-0.02 was covered where framelines are almost vertical. Because the probe was set parallel to the uniform flow, the velocity is not quantitatively accurate.

Velocity Measurements in Wake

Two five-hole pitot tubes were used for velocity measurements in the wake; 8mm-diameter tube for MS-02 and 10mm-diameter tube for GBT-30. For estimations of vorticity, measurements were carried out on three-dimensional lattice-points spaced 0.025, 0.015, and 0.015 in x, y, and z directions respectively.

Vorticity Estimations in Wake

The vorticity can be estimated by differentiating the measured velocity distributions;

$$\omega_x = \frac{\partial w}{\partial y} - \frac{\partial v}{\partial z}, \quad \omega_y = \frac{\partial u}{\partial z} - \frac{\partial w}{\partial x}, \quad \omega_z = \frac{\partial v}{\partial x} - \frac{\partial u}{\partial y}. \tag{25}$$

The differentials were obtained numerically by three-point approximation.

Discussions on Boundary Layer Separation and Wake Flow

Boundary Layer Flow near Separation

Figure 13 shows flow directions near the stern of MS-02 obtained by the twin tufts method.

It was observed that, very near A.P., both tufts are drooping. This means that the velocity is almost dead; in other words, separation has occurred.

On the remaining parts, the outer tufts show almost the same direction as the calculated potential flow direction; on the other hand the inner tufts differ greatly from them and produce large crossflow angles. A reference to the surface pressure distribution gives a clear explanation that flow near the hull surface, whose velocity is very low, cannot make further steps against the pressure increments and change direction suddenly from the external streamwise direction toward the low-pressure regions. Significant occurrences of shear flow and generation of vortices are assumed which correspond to beginnings of three-dimensional separation.

The above situation can be understood more clearly from velocity profiles in the boundary layer near separation. Figure 14 shows the velocity profiles of GBT-125 along streamline Nos. 5, 9, and 11. A sudden large crossflow occurs near S.S.½ for all the streamlines and, correspondingly, the streamwise velocity profile also changes. The

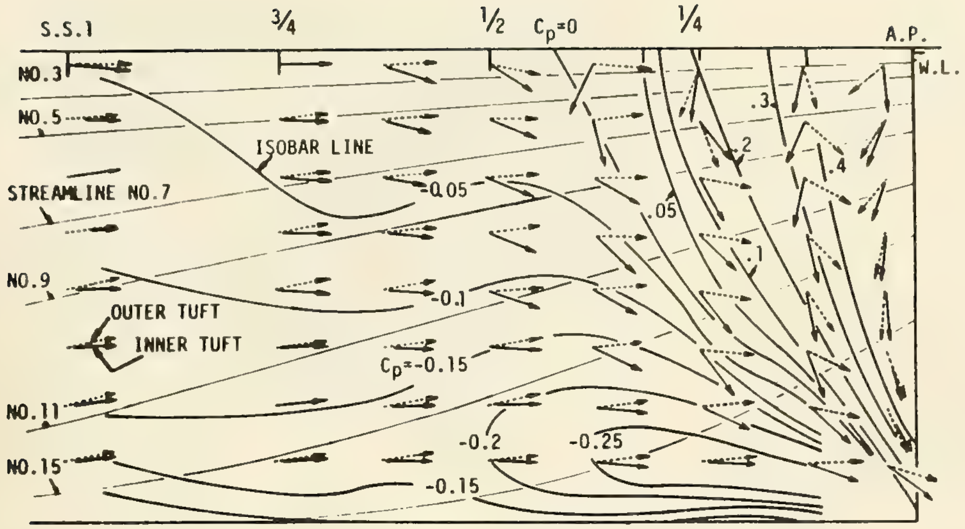

FIGURE 13. Flow directions near stern and isobar lines (MS-02).

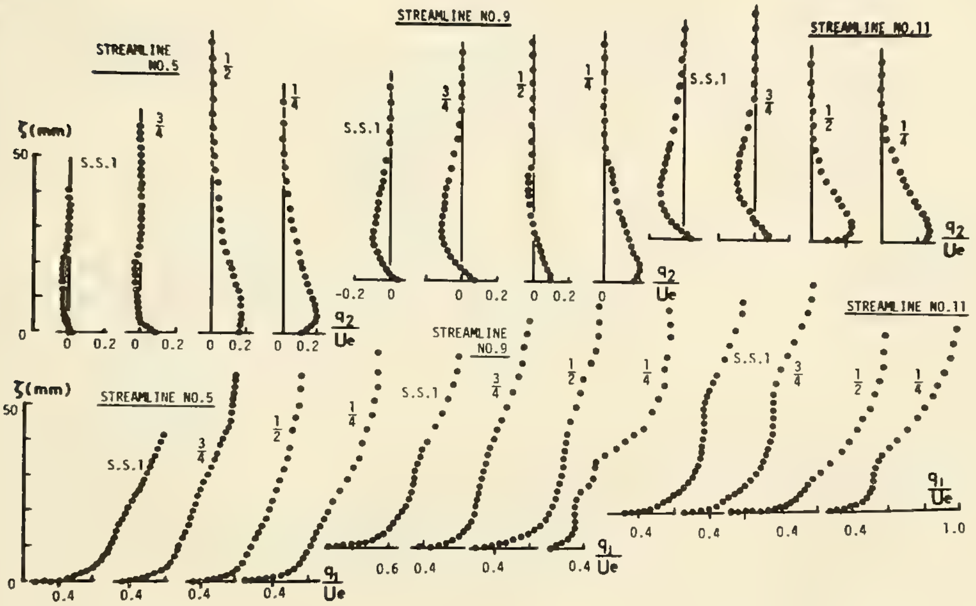

FIGURE 14. Velocity profiles in boundary layer near the stern (GBT-125).

maximum crossflow velocity amounts to about half of the streamwise velocity.

Such behaviors of flow near the stern are not in the category of boundary layer flow, therefore, boundary layer calculations should be stopped and another treatment employed.

Criterion for Boundary Layer Separation

It is necessary to introduce some criterion for boundary layer separation in order to change the governing equations from boundary layer to some others.

There are many criteria mainly for two-dimensional separation [e.g., Chang (1970)].

A parameter, Γ_a, defined by

$$\Gamma_a = -U_e \frac{\partial U_e}{\partial \xi} \frac{\theta_{11}}{\tau_{w1}} , \qquad (26)$$

is proposed.

The proposal is based on the experimental facts that the beginning of three-dimensional boundary layer separation is closely related to the pressure gradients, as discussed in the previous section, and that boundary layer flow, such as with large momentum thickness and small skin friction, can no longer exist. Therefore, flows with large values of Γ_a cannot exist in real flow in the sense of boundary layer flow. On the other hand, if the boundary layer assumptions are kept, the calculated values of Γ_a can increase without any upper bound.

Figure 15 shows Γ_a obtained by the boundary layer calculations and from experiments. The calculated values get increasingly large approaching the stern, but experimental values do not and they seem to have some upper bound.

The value of $\Gamma_a = 20$ is reasonable as a criterion for separation, because, as shown in Figure 14, large crossflow angles were observed near x=0.9 (S.S.½) and the onset of separation is suspected.

Of course, more experimental data are necessary for the present discussion and further experimental

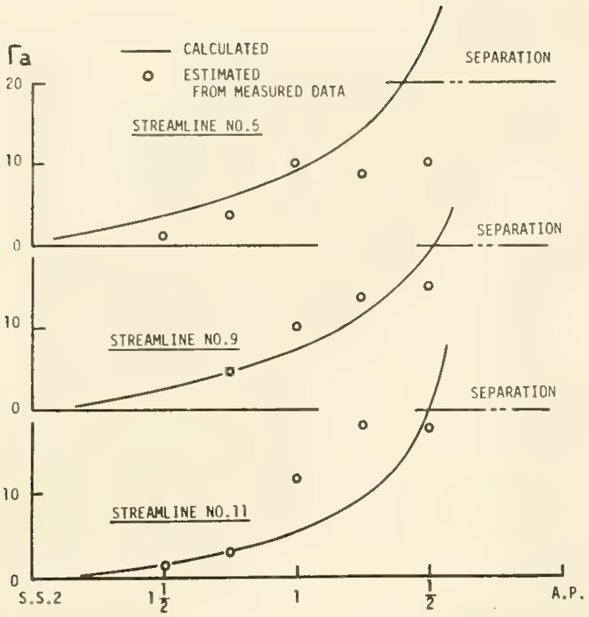

FIGURE 15. Criterion for separation.

and theoretical studies may give a firmer foundation for the present criterion.

Flow Field after Occurrence of Separation

Once separation has occurred, the flow field differs greatly from the unseparated boundary layer flow. The existence of the dead region, pointed out in the previous section, is one phenomena.

Figure 16 shows velocity profiles, after the occurrence of separation, measured by the hot film anemometer. The bars in the figure represent fluctuations in velocity. The region where the velocity fluctuates so intensively and is very low consists of a characteristic thin layer, a separated retarding region. It can be definitely distinguished from the outer part where the flow does not differ greatly from the unseparated flow. The newly-generated vortex is confined to this region.

Figure 17 is free-surface flow of MS-02. It shows more clearly the existence of the above mentioned, separated retarding region. The dividing streamline can be observed which coincides with the border line of the separated retarding region.

In the case of practical ship forms, we have not enough information as to whether or not such regions exist. But from the velocity profiles of GBT-125 (Figure 14), their existence can be supposed in those cases also.

According to the present experimental studies, it is implied that any single approximate equation of the Navier-Stokes equation completely governs the flow field near the stern.

Eddy Viscosity Coefficient in Wake

In order to predict turbulent terms in the Navier-Stokes equation, there is a concept of eddy viscosity. It is based on an idea that momentum loss due to turbulence can be represented by momentum loss due to friction and the coefficient is constant as to positions and directions. According to this assumption, the Navier-Stokes equation is written,

$$q.\nabla\omega_x - \omega.\nabla q = \nu_e\nabla^2\omega_x, \qquad (27)$$

where ν_e is the eddy viscosity coefficient.

Equation (27) is a kind of diffusion equation with ν_e the diffusivity coefficient. It can be determined experimentally; substituting the measured values of velocity and vorticity into Eq. (27) leaves only ν_e as an unknown.

Using experimental data of the GBT-30, covering $1.08 \leq x \leq 1.16$, ν_e is determined by the least-square method. The estimated values of ν_e are not unique; they differ slightly for each direction, 2.7×10^{-4}, 2.4×10^{-4}, and 1.6×10^{-4} for ω_x, ω_y, and ω_z. The mean value is 2.2×10^{-4}, and consequently the equivalent Reynolds number, based on the eddy viscosity, is about 1/300 of the real Reynolds number.

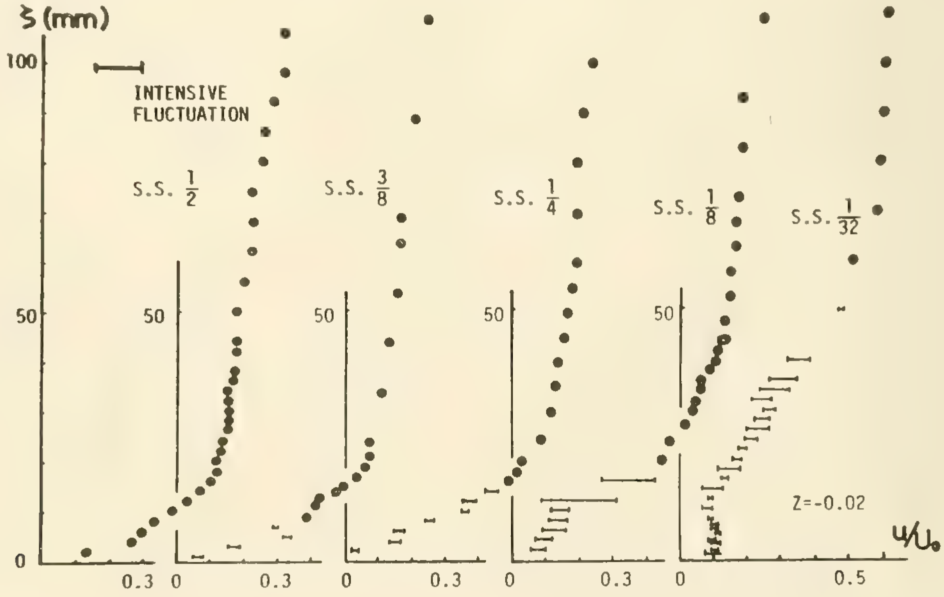

FIGURE 16. Velocity profiles near the separation position (MS-02).

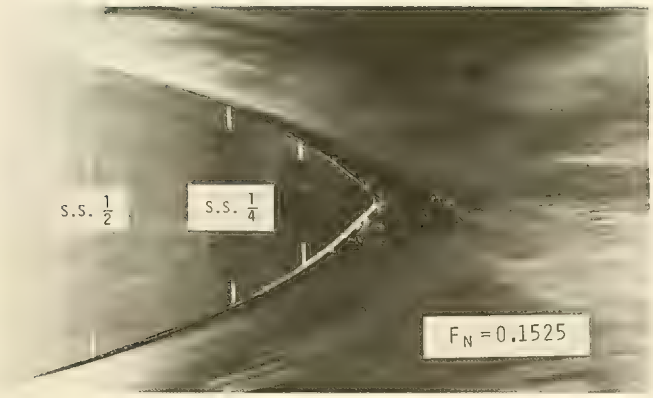

FIGURE 17. Free-surface flow near the stern (MS-02).

Subdivision of the Flow Field

It has been made clear by experimental studies that the separated flow has at least two, quite different viscous regions where no single approximate equation of Navier-Stokes equation seems to be valid for both. It can be proposed to subdivide the flow field near the stern into five regions as shown in Figure 18; potential flow region, boundary layer region, vorticity diffusion region, separated retarding region, and viscous sublayer region.

Their characteristics are as follows.

Potential flow region:

The region where the viscous term can be wholly neglected and only displacement effects should be taken into account.

Boundary layer region:

The region where the boundary layer assumption is valid and the backward influence of separation can be neglected.

Vorticity diffusion region:

The region where the vorticity, which has been generated in the boundary layer, is diffused convectively and viscously. No vorticity is newly generated in this region. Because the dividing streamline is a kind of free-streamline, the pressure on it might be constant.

Separated retarding region:

The region where the velocity is very small and the turbulence is intensive. Because even a recirculating flow can be observed, the governing equation for this region should be an elliptic type.

Viscous sublayer region:

This is the very thin layer region which just adheres to the hull surface. The molecular viscosity is predominant and the velocity profile should satisfy the no-slip condition on the hull surface.

CALCULATION OF VELOCITY DISTRIBUTIONS IN THE SHIP'S WAKE

Approximation of Navier-Stokes Equation by Local Asymptotic Expansion

In order to get appropriate approximations of the Navier-Stokes equation for each region, local asymptotic expansions of relevant quantities are made, using small parameter ε defined by

$$\varepsilon = R_e^{-1/8} \quad . \tag{28}$$

The quantity ε, was first introduced by Stewartson (1969) and ε << 1 in case of a large Reynolds number.

If the x_3 coordinate can be assumed to be linear, i.e.,

$$h_3 = 1, \tag{29}$$

the continuity equation and Reynolds equations are written in streamline coordinates as follows.

$$\frac{\partial q_1}{h_1 \partial x_1} + \frac{\partial q_2}{h_2 \partial x_2} + \frac{\partial q_3}{\partial x_3} - K_1 q_1 - K_2 q_2 = 0 \tag{30}$$

$$\frac{q_1}{h_1}\frac{\partial q_1}{\partial x_1} + \frac{q_2}{h_2}\frac{\partial q_1}{\partial x_2} + q_3 \frac{\partial q_1}{\partial x_3} - K_2 q_1 q_2 + K_1 q_2^2$$
$$= -\frac{\partial}{h_1 \partial x_1}\left(\frac{p}{\rho} + q_1'^2\right) - \frac{\partial}{h_2 \partial x_2} q_1' q_2'$$
$$- \frac{\partial}{\partial x_3} q_3' q_1' + 2K_2 q_1' q_2' + K_1 (q_1'^2 - q_2'^2)$$
$$+ \frac{\nu}{h_2}\left\{\frac{\partial}{\partial x_3}(h_2 \omega_2) - \frac{\partial \omega_3}{\partial x_2}\right\} \tag{31}$$

$$\frac{q_1}{h_1}\frac{\partial q_2}{\partial x_1} + \frac{q_2}{h_2}\frac{\partial q_2}{\partial x_2} + q_3 \frac{\partial q_2}{\partial x_3} + K_2 q_1^2 - K_1 q_1 q_2$$
$$= -\frac{\partial}{h_2 \partial x_2}\left(\frac{p}{\rho} + q_2'^2\right) - \frac{\partial}{\partial x_3} q_2' q_3' - \frac{\partial}{h_1 \partial x_1} q_1' q_2'$$
$$- K_2 (q_1'^2 - q_2'^2) + 2K_1 q_1' q_2'$$
$$+ \frac{\nu}{h_1}\left[\frac{\partial \omega_3}{\partial x_1} - \frac{\partial}{\partial x_3}(h_1 \omega_1)\right] \tag{32}$$

$$\frac{q_1}{h_1}\frac{\partial q_3}{\partial x_1} + \frac{q_2}{h_2}\frac{\partial q_3}{\partial x_2} + q_3 \frac{\partial q_3}{\partial x_3} = -\frac{\partial}{\partial x_3}\left(\frac{p}{\rho} + q_3'^2\right)$$
$$- \frac{\partial}{h_1 \partial x_1} q_1' q_3' - \frac{\partial}{h_2 \partial x_2} q_2' q_3' + K_1 g_1' g_3' + K_2 q_2' q_3'$$
$$+ \frac{\nu}{h_1 h_2}\left[\frac{\partial}{\partial x_2}(h_1 \omega_1) - \frac{\partial}{\partial x_1}(h_2 \omega_2)\right] \tag{33}$$

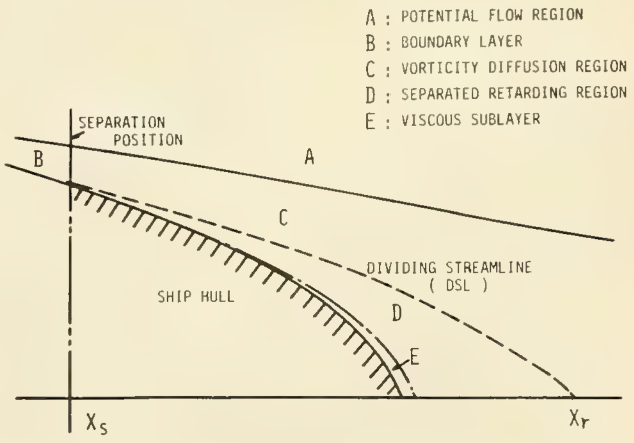
A : POTENTIAL FLOW REGION
B : BOUNDARY LAYER
C : VORTICITY DIFFUSION REGION
D : SEPARATED RETARDING REGION
E : VISCOUS SUBLAYER
SEPARATION POSITION
B
A
C
SHIP HULL
DIVIDING STREAMLINE (DSL)
D
E
X_s
X_r

FIGURE 18. Subdivision of separated flow field near the stern.

where ω_1, ω_2, ω_3 are the components of vorticity given by

$$\omega_1 = \frac{\partial q_3}{h_2\partial x_2} - \frac{\partial q_2}{\partial x_3},$$

$$\omega_2 = \frac{\partial q_1}{\partial x_3} - \frac{\partial q_3}{h_1\partial x_1}, \tag{34}$$

$$\omega_3 = \frac{\partial q_2}{h_1\partial x_1} - \frac{\partial q_1}{h_2\partial x_2} + K_2q_1 - K_1q_2.$$

and they satisfy

$$\nabla\cdot\omega = 0. \tag{35}$$

In the reduction of Eqs. (31, 32, 33) from the Navier-Stokes equation, conventional predictions for turbulent components are used; the velocity is assumed to consist of time-averaged terms and fluctuating terms.

On the other hand, if the constant eddy viscosity can be assumed, the following equations are derived directly from Navier-Stokes equation;

$$\frac{\partial}{h_2\partial x_2}(\omega_1q_2-\omega_2q_1) + \frac{\partial}{\partial x_3}(\omega_1q_3-\omega_3q_1)$$

$$= \nu_e\left[\left(\frac{1}{h_2^2}\frac{\partial^2}{\partial x_2^2} + \frac{\partial^2}{\partial x_3^2}\right)\omega_1 - \frac{\partial}{h_1\partial x_1}\left(\frac{\partial\omega_2}{h_2\partial x_2} + \frac{\partial\omega_3}{\partial x_3}\right)\right.$$

$$\left. - \frac{\partial}{h_2\partial x_2}(K_2\omega_1-K_1\omega_2) - K_2\frac{\partial\omega_2}{h_1\partial x_1} + K_{22}\frac{\partial\omega_1}{h_2\partial x_2}\right], \tag{36}$$

$$\frac{\partial}{h_1\partial x_1}(\omega_2q_1-\omega_1q_2) + \frac{\partial}{\partial x_3}(\omega_2q_3-\omega_3q_2)$$

$$= \nu_e\left[\left(\frac{1}{h_1^2}\frac{\partial^2}{\partial x_1^2} + \frac{\partial^2}{\partial x_3^2}\right)\omega_2 - \frac{\partial}{h_2\partial x_2}\left(\frac{\partial\omega_1}{h_1\partial x_1} + \frac{\partial\omega_3}{\partial x_3}\right)\right.$$

$$\left. - \frac{\partial}{h_1\partial x_1}(K_1\omega_2-K_2\omega_1) - K_1\frac{\partial\omega_1}{h_2\partial x_2} + K_{11}\frac{\partial\omega_2}{h_1\partial x_1}\right], \tag{37}$$

$$\left(K_1 - \frac{\partial}{h_1\partial x_1}\right)(\omega_1q_3-\omega_3q_1) + \left(K_2 - \frac{\partial}{h_2\partial x_2}\right)(\omega_2q_3-\omega_3q_2)$$

$$= \nu_e\left[\left(\frac{1}{h_1^2}\frac{\partial^2}{\partial x_1^2} + \frac{1}{h_2^2}\frac{\partial^2}{\partial x_2^2}\right)\omega_3 - \frac{\partial}{\partial x_3}\left(\frac{\partial\omega_1}{h_1\partial x_1} + \frac{\partial\omega_2}{h_2\partial x_2}\right)\right.$$

$$+ \frac{\partial}{\partial x_3}(K_1\omega_1+K_2\omega_2) - (K_1-K_{11})\frac{\partial\omega_3}{h_1\partial x_1}$$

$$\left. - (K_2-K_{22})\frac{\partial\omega_3}{h_2\partial x_2}\right]. \tag{38}$$

where

$$K_{11} = -\frac{1}{h_1^2}\frac{\partial h_1}{\partial x_1}, \quad K_{22} = -\frac{1}{h_2^2}\frac{\partial h_2}{\partial x_2}. \tag{39}$$

Vorticity Diffusion Region (C-region)

For the vorticity diffusion region, the constant eddy viscosity is assumed.

Introducing non-dimensional curvilinear small line segments $\partial\tilde{\xi}$, $\partial\tilde{\eta}$, and $\partial\tilde{\zeta}$, we represent the differentiations

$$\frac{\partial}{h_1\partial x_1} = \frac{1}{L\varepsilon}\frac{\partial}{\partial\tilde{\xi}}, \quad \frac{\partial}{h_2\partial x_2} = \frac{1}{L\varepsilon}\frac{\partial}{\partial\tilde{\eta}},$$

$$\frac{\partial}{\partial x_3} = \frac{1}{L\varepsilon^2}\frac{\partial}{\partial\tilde{\zeta}} \tag{40}$$

Here we assume the derivatives by new variables are all $0(1)$, i.e.,

$$\frac{\partial}{\partial\tilde{\xi}} = 0(1), \quad \frac{\partial}{\partial\tilde{\eta}} = 0(1), \quad \frac{\partial}{\partial\tilde{\zeta}} = 0(1). \tag{41}$$

The origin of the new variables coincides with that of $0\text{-}x_1x_2x_3$ but $\tilde{\xi}=0$ corresponds to the position of separation.

We tentatively assume that the asymptotic series for velocity and vorticity of C-region have the following forms;

$$q_1/U_0 = \tilde{u}_0(\tilde{\xi},\tilde{\eta},\tilde{\zeta}) + \varepsilon u_1(\tilde{\xi},\tilde{\eta},\tilde{\zeta}) + \varepsilon^2\tilde{u}_2(\tilde{\xi},\tilde{\eta},\tilde{\zeta}) + \ldots,$$

$$q_2/U_0 = \varepsilon\tilde{v}_1(\tilde{\xi},\tilde{\eta},\tilde{\zeta}) + \varepsilon^2\tilde{v}_2(\tilde{\xi},\tilde{\eta},\tilde{\zeta}) + \ldots,$$

$$q_3/U_0 = \varepsilon^2\tilde{w}_1(\tilde{\xi},\tilde{\eta},\tilde{\zeta}) + \varepsilon^3\tilde{w}_2(\tilde{\xi},\tilde{\eta},\tilde{\zeta}) + \ldots,$$

$$\frac{\omega_1}{U_0/L} = \frac{1}{\varepsilon}\tilde{\omega}_{\xi_1}(\tilde{\xi},\tilde{\eta},\tilde{\zeta}) + \tilde{\omega}_{\xi_2}(\tilde{\xi},\tilde{\eta},\tilde{\zeta}) + \ldots,$$

$$\frac{\omega_2}{U_0/L} = \frac{1}{\varepsilon^2}\tilde{\omega}_{\eta 1}(\tilde{\xi},\tilde{\eta},\tilde{\zeta}) + \frac{1}{\varepsilon}\tilde{\omega}_{\eta 2}(\tilde{\xi},\tilde{\eta},\tilde{\zeta}) + \ldots,$$

$$\frac{\omega_3}{U_0/L} = \frac{1}{\varepsilon}\tilde{\omega}_{\xi 1}(\tilde{\xi},\tilde{\eta},\tilde{\zeta}) + \tilde{\omega}_{\xi_2}(\tilde{\xi},\tilde{\eta},\tilde{\zeta}) + \ldots. \tag{43}$$

All the quantities appearing in Eqs. (42) and (43) are assumed to be $0(1)$.

Moreover, we introduce non-dimensional variables k_1, k_2, k_{11}, k_{22} by

$$k_1 = L\cdot K_1, \quad k_2 = L\cdot K_2, \quad k_{11} = L\cdot K_{11},$$

$$k_{22} = L\cdot K_{22}, \tag{44}$$

whose orders are $0(1)$ for all the regions.

Substituting Eqs. (40), (42), and (43) into Eq. (30) and Eq. (35), we get as leading terms,

$$\frac{\partial\tilde{u}_0}{\partial\tilde{\xi}} = 0, \tag{45}$$

$$\frac{\partial\tilde{\omega}_{\eta 1}}{\partial\eta} + \frac{\partial\tilde{\omega}_{\xi 1}}{\partial\tilde{\zeta}} = 0, \tag{46}$$

and into Eqs. (36, 37, 38) we get,

$$\frac{\partial}{\partial\tilde{\eta}}(\tilde{\omega}_{\eta 1}\tilde{u}_0) + \frac{\partial}{\partial\tilde{\zeta}}(\tilde{\omega}_{\zeta 1}\tilde{u}_0) = 0, \tag{47}$$

$$\frac{1}{\varepsilon^3}\frac{\nu_e}{U_0L}\frac{\partial^2\tilde{\omega}_{\eta 1}}{\partial\tilde{\zeta}^2} - \frac{\partial}{\partial\tilde{\xi}}(\tilde{\omega}_{\eta 1}\tilde{u}_0) = 0, \tag{48}$$

$$\frac{1}{\varepsilon^3}\frac{\nu_e}{U_0L}\frac{\partial^2\tilde{\omega}_{\zeta 1}}{\partial\tilde{\zeta}^2} - \frac{\partial}{\partial\tilde{\xi}}(\tilde{\omega}_{\zeta 1}\tilde{u}_0) = 0. \tag{49}$$

In order for the viscous diffusion term to exist, ν_e/U_0L should be at least $0(\varepsilon^3)$.

We have obtained four equations, Eqs. (46-49), for three unknowns, $u_0, \tilde{\omega}_{\eta 1}$, and $\tilde{\omega}_{\zeta 1}$, but it can be easily shown that one of them is not independent.

Changing variables back into the original ones, we get, as the governing equations for C-region,

$$\frac{\partial}{h_2 \partial x_2}(\omega_2 q_1) + \frac{\partial}{\partial x_3}(\omega_3 q_1) = 0 \quad , \tag{50}$$

$$\nu_e \frac{\partial^2 \omega_2}{\partial x_3^2} - \frac{\partial}{h_1 \partial x_1}(\omega_2 q_1) = 0 \quad , \tag{51}$$

$$\nu_e \frac{\partial^2 \omega_3}{\partial x_3^2} - \frac{\partial}{h_1 \partial x_1}(\omega_3 q_1) = 0 \quad . \tag{52}$$

The terms of order $O(1/\varepsilon^2)$ are neglected in the above equations.

Separated Retarding Region (D-region)

Introducing normalized variables, $\tilde{\xi}$, $\tilde{\eta}$, $\hat{\zeta}$ for the separated retarding region in the same manner, the orders of differentiation are assumed,

$$\frac{\partial}{h_1 \partial x_1} = \frac{1}{L}\frac{\partial}{\varepsilon \partial \tilde{\xi}} \quad , \quad \frac{\partial}{h_2 \partial x_2} = \frac{1}{L}\frac{\partial}{\varepsilon \partial \tilde{\eta}}$$
$$\frac{\partial}{\partial x_3} = \frac{1}{L}\frac{\partial}{\varepsilon^3 \partial \hat{\zeta}} \quad , \tag{53}$$

$$\frac{\partial}{\partial \tilde{\xi}} = O(1) \quad , \quad \frac{\partial}{\partial \tilde{\eta}} = O(1) \quad , \quad \frac{\partial}{\partial \hat{\zeta}} = O(1) \quad . \tag{54}$$

Velocity and pressure are assumed to be expanded asymptotically,

$$q_1/U_0 = \varepsilon(\hat{u}_1 + \hat{u}_1') + \varepsilon^2(\hat{u}_2 + \hat{u}_2') + \dots \quad ,$$
$$q_2/U_0 = \varepsilon(\hat{v}_1 + \hat{v}_1') + \varepsilon^2(\hat{v}_2 + \hat{v}_2') + \dots \quad , \tag{55}$$
$$q_3/U_0 = \varepsilon^3(\hat{w}_1 + \hat{w}_1') + \varepsilon^4(\hat{w}_2 + \hat{w}_2') + \dots \quad ,$$

$$(p - p_\infty)/\rho U_0^2 = \varepsilon p_1 + \varepsilon p_2 + \dots \quad , \tag{56}$$

where $\hat{u}_1, \hat{u}_2, \dots$ are all time-averaged variables and $\hat{u}_1', \hat{u}_2', \dots$ are fluctuating. Here the fluctuating terms of pressure are omitted because they do not appear in the basic equations.

The vorticity can be also expanded asymptotically,

$$\frac{\omega_1}{U_0/L} = -\frac{1}{\varepsilon^2}\frac{\partial \hat{v}_1}{\partial \hat{\zeta}} - \frac{1}{\varepsilon}\frac{\partial \hat{v}_2}{\partial \hat{\zeta}} + O(1) \quad ,$$
$$\frac{\omega_2}{U_0/L} = \frac{1}{\varepsilon^2}\frac{\partial \hat{u}_1}{\partial \hat{\zeta}} + \frac{1}{\varepsilon}\frac{\partial \hat{u}_2}{\partial \hat{\zeta}} + O(1) \quad ,$$
$$\frac{\omega_3}{U_0/L} = \frac{\partial \hat{v}_1}{\partial \tilde{\xi}} - \frac{\partial \hat{u}_1}{\partial \tilde{\eta}} + O(\varepsilon) \quad . \tag{57}$$

Under these assumptions, the leading terms of the continuity equation are written,

$$\frac{\partial \hat{u}_1}{\partial \tilde{\xi}} + \frac{\partial \hat{v}_1}{\partial \tilde{\eta}} + \frac{\partial \hat{w}_1}{\partial \hat{\zeta}} = 0 \quad , \tag{58}$$

and the governing equations are

$$\begin{aligned}
&\hat{u}_1\frac{\partial \hat{u}_1}{\partial \tilde{\xi}} + \hat{v}_1\frac{\partial \hat{u}_1}{\partial \tilde{\eta}} + \hat{w}_1\frac{\partial \hat{u}_1}{\partial \hat{\zeta}} \\
&+ \varepsilon\Big[\frac{\partial}{\partial \tilde{\xi}}(\hat{u}_1\hat{u}_2) + (\hat{v}_1\frac{\partial}{\partial \tilde{\eta}} + \hat{w}_1\frac{\partial}{\partial \hat{\zeta}})\hat{u}_2 + (\hat{v}_2\frac{\partial}{\partial \tilde{\eta}} + \hat{w}_2\frac{\partial}{\partial \hat{\zeta}})\hat{u}_1 \\
&\qquad -k_2\hat{u}_1\hat{v}_1 + k_1\hat{v}_1^2\Big] \\
&= -\frac{1}{\varepsilon}\frac{\partial p_1}{\partial \tilde{\xi}} - \Big[\frac{\partial}{\partial \tilde{\xi}}(p_2 + \hat{u}_1'^2) + \frac{\partial}{\partial \tilde{\eta}}(\hat{u}_1'\hat{v}_1') + \frac{\partial}{\partial \hat{\zeta}}(\hat{u}_1'\hat{w}_1')\Big] \\
&\quad -\varepsilon\Big[\frac{\partial}{\partial \tilde{\xi}}(p_3 + 2\hat{u}_1'\hat{u}_2') + \frac{\partial}{\partial \tilde{\eta}}(\hat{u}_1'\hat{v}_2' + \hat{u}_2'\hat{v}_1') \\
&\quad + \frac{\partial}{\partial \hat{\zeta}}(\hat{u}_1'\hat{w}_2' + \hat{u}_2'\hat{w}_1') - 2k_2\hat{u}_1'\hat{v}_1' - k_1(\hat{u}_1'^2 - \hat{v}_1'^2)\Big] \\
&\quad + \frac{1}{\varepsilon^6}\frac{\nu}{U_0 L}\frac{\partial^2 \hat{u}_1}{\partial \hat{\zeta}^2} + O(\varepsilon^2)
\end{aligned} \tag{59}$$

$$\begin{aligned}
&\hat{u}_1\frac{\partial \hat{v}_1}{\partial \tilde{\xi}} + \hat{v}_1\frac{\partial \hat{v}_1}{\partial \tilde{\eta}} + \hat{w}_1\frac{\partial \hat{v}_1}{\partial \hat{\zeta}} \\
&+ \varepsilon\Big[\frac{\partial}{\partial \tilde{\eta}}(\hat{v}_1\hat{v}_2) + (\hat{u}_1\frac{\partial}{\partial \tilde{\xi}} + \hat{w}_1\frac{\partial}{\partial \hat{\zeta}})v_2 + (\hat{u}_2\frac{\partial}{\partial \tilde{\xi}} + \hat{w}_2\frac{\partial}{\partial \hat{\zeta}})\hat{v}_1 \\
&\qquad +k_2\hat{u}_1^2 - k_1\hat{u}_1\hat{v}_1\Big] \\
&= -\frac{1}{\varepsilon}\frac{\partial p_1}{\partial \tilde{\eta}} - \Big[\frac{\partial}{\partial \tilde{\xi}}(\hat{u}_1'\hat{v}_1') + \frac{\partial}{\partial \tilde{\eta}}(p_2 + \hat{v}_1'^2) + \frac{\partial}{\partial \hat{\zeta}}(\hat{v}_1'\hat{w}_1')\Big] \\
&\quad -\varepsilon\Big[\frac{\partial}{\partial \tilde{\xi}}(\hat{u}_1'\hat{v}_2' + \hat{u}_2'\hat{v}_1') + \frac{\partial}{\partial \tilde{\eta}}(p_3 + 2\hat{v}_1'v_2') \\
&\quad + \frac{\partial}{\partial \hat{\zeta}}(\hat{v}_1'\hat{w}_2' + \hat{v}_2'\hat{w}_1') + k_2(\hat{u}_1'^2 - \hat{v}_1'^2) - 2k_1\hat{u}_1'\hat{v}_1'\Big] \\
&\quad + \frac{1}{\varepsilon^6}\frac{\nu}{U_0 L}\frac{\partial^2 \hat{v}_1}{\partial \hat{\zeta}^2} + O(\varepsilon^2) \quad ,
\end{aligned} \tag{60}$$

$$\frac{\partial p_1}{\partial \hat{\zeta}} + \varepsilon\frac{\partial p_2}{\partial \hat{\zeta}} + O(\varepsilon^2) = 0. \tag{61}$$

The leading terms of Eqs. (59, 60, 61) yield

$$p_1(\tilde{\xi}, \tilde{\eta}, \hat{\zeta}) = \text{const.} \tag{62}$$

Equation (62) means that the pressure is constant throughout the present region as far as $O(\varepsilon)$ is concerned.

Now the second terms of Eqs. (58, 59, 60) yield

$$\begin{aligned}
\hat{u}_1\frac{\partial \hat{u}_1}{\partial \tilde{\xi}} + \hat{v}_1\frac{\partial \hat{u}_1}{\partial \tilde{\eta}} + \hat{w}_1\frac{\partial \hat{u}_1}{\partial \hat{\zeta}} &= -\frac{\partial}{\partial \tilde{\xi}}(p_2 + \hat{u}_1'^2) \\
&\quad - \frac{\partial}{\partial \tilde{\eta}}(\hat{u}_1'\hat{v}_1') - \frac{\partial}{\partial \hat{\zeta}}(\hat{u}_1'\hat{w}_1') \quad ,
\end{aligned} \tag{63}$$

$$\begin{aligned}
\hat{u}_1\frac{\partial \hat{v}_1}{\partial \tilde{\xi}} + \hat{v}_1\frac{\partial \hat{v}_1}{\partial \tilde{\eta}} + \hat{w}_1\frac{\partial \hat{v}_1}{\partial \hat{\zeta}} &= -\frac{\partial}{\partial \tilde{\xi}}(\hat{u}_1'\hat{v}_1') \\
&\quad - \frac{\partial}{\partial \tilde{\eta}}(p_2 + \hat{v}_1'^2) - \frac{\partial}{\partial \hat{\zeta}}(\hat{v}_1'\hat{w}_1') \quad ,
\end{aligned} \tag{64}$$

$$\frac{\partial p_2}{\partial \hat{\zeta}} = 0 \quad . \tag{65}$$

In the above equations, the molecular viscosity disappears but its effects are still existing indirectly through turbulence.

Equation (65) gives the so-called boundary layer approximation. But because cross terms of fluctuating components exist in Eqs. (63) and (64), they do not always yield the same type as boundary layer equations which can not predict the recirculating flow observed in experiments.

Viscous Sublayer (E-region)

In the viscous sublayer, E-region, the no-slip condition must be satisfied on the hull surface. Here the intensity of turbulence may be very small and all the turbulent terms in the Reynolds equations vanish infinitesimally.

The following asymptotic expansions are assumed from the Blasius solution.

$$q_1/U_0 = \varepsilon u_1^* + \varepsilon^2 u_2^* + \dots ,$$
$$q_2/U_0 = \varepsilon v_1^* + \varepsilon^2 v_2^* + \dots , \qquad (66)$$
$$q_3/U_0 = \varepsilon^4 w_1^* + \varepsilon^5 w_2^* + \dots ,$$

where the orders of each term are all O(1).

The derivatives are represented by

$$\frac{\partial}{h_1 \partial x_1} = \frac{1}{L}\frac{\partial}{\varepsilon \partial \tilde{\xi}} \;, \quad \frac{\partial}{h_2 \partial x_2} = \frac{1}{L}\frac{\partial}{\varepsilon \partial \tilde{\eta}} \;,$$

$$\frac{\partial}{\partial x_3} = \frac{1}{L}\frac{\partial}{\varepsilon^4 \partial \zeta^*} \;, \qquad (67)$$

and their orders are

$$\frac{\partial}{\partial \tilde{\xi}} = O(1) \quad , \quad \frac{\partial}{\partial \tilde{\eta}} = O(1) \quad , \quad \frac{\partial}{\partial \zeta^*} = O(1) \quad . \qquad (68)$$

Substituting the above assumptions into Eqs. (31, 32, 33), the leading terms are obtained as follows in original variables;

$$q_1 \frac{\partial q_1}{h_1 \partial x_1} + q_2 \frac{\partial q_1}{h_2 \partial x_2} + q_3 \frac{\partial q_1}{\partial x_3}$$
$$= -\frac{1}{\rho}\frac{\partial p}{h_1 \partial x_1} + \nu \frac{\partial^2 q_1}{\partial x_3^2} \quad , \qquad (69)$$

$$q_1 \frac{\partial q_2}{h_1 \partial x_1} + q_2 \frac{\partial q_2}{h_2 \partial x_2} + q_3 \frac{\partial q_2}{\partial x_3}$$
$$= -\frac{1}{\rho}\frac{\partial p}{h_2 \partial x_2} + \nu \frac{\partial^2 q_2}{\partial x_3^2} \quad , \qquad (70)$$

$$\frac{\partial p}{\partial x_3} = 0 \quad . \qquad (71)$$

The continuity equation is

$$\frac{\partial q_1}{h_1 \partial x_1} + \frac{\partial q_2}{h_2 \partial x_2} + \frac{\partial q_3}{\partial x_3} = 0. \qquad (72)$$

Here the quantities of $O(\varepsilon^2)$ are omitted.

These are the boundary layer equations themselves. They must be matched with the solution for the D-region in quite the same manner as the conventional method of boundary layer calculation.

The following matching conditions should be satisfied when governing equations are solved.

(i) for upstream;

$$\lim_{\tilde{\xi} \to -\infty} \tilde{u}_0(\tilde{\xi},\tilde{\eta},\tilde{\zeta}) = u_B, \quad \lim_{\tilde{\xi} \to -\infty} \tilde{v}_1(\tilde{\xi},\tilde{\eta},\tilde{\zeta}) = v_B,$$

$$\lim_{\tilde{\xi} \to -\infty} \tilde{w}_1(\tilde{\xi},\tilde{\eta},\tilde{\zeta}) = w_B \qquad (73)$$

where u_B, v_B, and w_B are the velocity components in the boundary layer in the x_1, x_2, x_3 directions respectively.

(ii) far from the hull surface; the solutions should be matched to the solution of the A-region, potential flow.

(iii) between the C- and D-region;

$$\tilde{u}_0(\tilde{\xi},\tilde{\eta},0) = 0 \;, \quad \tilde{u}_1(\tilde{\xi},\tilde{\eta},0) =$$
$$\lim_{\hat{\zeta} \to \infty} \left[\hat{u}_1(\tilde{\xi},\tilde{\eta},\hat{\zeta}) - \hat{\zeta}\frac{\partial}{\partial \tilde{\zeta}} \tilde{u}_0(\tilde{\xi},\tilde{\eta},\tilde{\zeta}) \Big|_{\tilde{\zeta}=0} \right] \;, \qquad (74)$$

$$\tilde{v}_1(\tilde{\xi},\tilde{\eta},0) = \lim_{\hat{\zeta} \to \infty} \hat{v}_1(\tilde{\xi},\tilde{\eta},\hat{\zeta}) \quad , \qquad (75)$$

$$\tilde{w}_1(\tilde{\xi},\tilde{\eta},0) = 0 \;, \quad \tilde{w}_2(\tilde{\xi},\tilde{\eta},0) =$$
$$\lim_{\hat{\zeta} \to \infty} \left[\hat{w}_1(\xi,\eta,\zeta) - \hat{\zeta}\frac{\partial}{\partial \tilde{\zeta}} \tilde{w}_1(\tilde{\xi},\tilde{\eta},\tilde{\zeta}) \Big|_{\tilde{\zeta}=0} \right] , \qquad (76)$$

(iv) between the D- and E-region;

$$\hat{u}_1(\tilde{\xi},\tilde{\eta},0) = \lim_{\zeta^* \to \infty} u_1^*(\tilde{\xi},\tilde{\eta},\tilde{\zeta}^*) \quad , \qquad (77)$$

$$\hat{v}_1(\tilde{\xi},\tilde{\eta},0) = \lim_{\zeta^* \to \infty} v_1^*(\tilde{\xi},\tilde{\eta},\tilde{\zeta}^*) \quad , \qquad (78)$$

$$\hat{w}_1(\tilde{\xi},\tilde{\eta},0) = 0 \quad , \quad \hat{w}_2(\tilde{\xi},\tilde{\eta},0) =$$
$$\lim_{\zeta^* \to \infty} \left[w_1^*(\tilde{\xi},\tilde{\eta},\zeta^*) - \zeta^* \frac{\partial}{\partial \hat{\zeta}} \hat{w}_1(\tilde{\xi},\tilde{\eta},\hat{\zeta}) \Big|_{\hat{\zeta}=0} \right] . \qquad (79)$$

The governing equations for the D-region do not close. Some auxiliary equations are required, but this problem is left for future work.

Numerical Calculations for the C-Region

To solve the derived equations analytically is almost impossible; this is because not only are the equations non-linear but also the hull surface, where the boundary conditions are prescribed, is very complicated in geometry. Instead, they must be solved numerically. But it may be still more difficult because the calculation should be carried out for all the regions at the same time in order to satisfy the matching conditions. However, this difficulty can be removed by an iteration method; the surface consisting of dividing streamlines (DSL) is given a priori in the beginning as the intermediate region between C- and D-regions where the matching is carried out. Of course the surface of DSL can be obtained finally as a solution of the flow field, but the assumption of DSL makes it possible to solve the governing equations in every region almost independently and it is expected that repeated iterations may bring forth a reasonable solution.

The flow in the C-region can be determined by taking a new streamline coordinate system $0\text{-}x_1x_2x_3$, where the x_1-axis coincides with DSL and the x_3-axis is normal to the DSL surface.

By the finite-difference scheme, Eqs. (48) and (49) are transformed into tridiagonal linear equations for $k \geq 2$;

$$\omega_2(i,j,k-1) - 2C(i,j,k)\omega_2(i,k,k) + \omega_2(i,j,k+1)$$

$$= A_2(i,j,k) \quad , \tag{80}$$

$$\omega_3(i,j,k-1) - 2C(i,j,k)\omega_3(i,j,k) + \omega_3(i,j,k+1)$$

$$= A_3(i,j,k) \quad , \tag{81}$$

where $\omega_2(i,j,k)$ etc. denote those values at $x_1=x_{1i}$, $x_2=x_{2j}$, and $x_3=x_{3k}$,

$$C(i,j,k) = 1 + \frac{\Delta\zeta^2}{\nu_e\Delta\xi} q_1(i,j,k) \quad ,$$

$$A_2(i,j,k) = -\,\omega_2(i-1,j,k-1) +$$

$$2\omega_2(i-1,j,k)\left[1 - \frac{\Delta\zeta^2}{\nu_e\Delta\xi} q_1(i-1,j,k)\right] - \omega_2(i-1,j,k+1),$$

$$A_3(i,j,k) = -\,\omega_3(i-1,j,k-1) +$$

$$2\omega_3(i-1,j,k)\left[1 - \frac{\Delta\zeta^2}{\nu_e\Delta\xi} q_1(i-1,j,k)\right] - \omega_3(i-1,j,k+1), \tag{82}$$

and $\Delta\xi$, $\Delta\zeta$ are short segments in the x_1, x_3 directions.

Equations (80) and (81) can be solved by the forward marching procedure if the velocity profile of q_1 is given at the separation position. Here the value of vorticity at k=1, on DSL, is made equal to that at k=2.

Once the vorticity distributions are obtained throughout, the boundary layer and wake, say V, velocity distributions can be calculated as induced velocity of vorticity by invoking Biot-Savart's law;

$$q_v(x,y,z) = \nabla \times \frac{1}{4\pi} \iiint_V \left(\frac{\omega'}{r} - \frac{\omega_1'}{r_1}\right) dx'dy'dz'$$

where ω_1' is the mirror image of ω' whose components are ω_x, ω_y, $-\omega_z$ and

$$r^2 = (x-x')^2 + (y-y')^2 + (z-z')^2 \ ,$$

$$r_1^2 = (x-x')^2 + (y-y')^2 + (z+z')^2 \ . \tag{84}$$

Because Eq. (83) gives the viscous component of velocity, the potential component should be added to q_v.

In the present calculation, DSL is determined from experiments for the first iteration; it consists of line segments, departing at $x_s=0.9$ and reattaching at $x_r=1.1$ (see Figure 18). The streamwise velocity q_1 in Eq. (82) is given by a quadratic function of ζ which is equal to U_1 at the outer edge and to 2/3 U_1 on DSL. The integral intervals for x and ζ are 0.005 and 0.0025 respectively.

In order to obtain the velocity distributions at x=1.025, the region covering from x=0.8 to x=1.4 is integrated in Eq. (83). Here, 300-times molecular kinematic viscosity is used as ν_e.

The boundary layer and the potential flow calculations are carried out in the same manner as in Section 3.

In Figure 19, typical calculated results of the first iteration for MS-02 are shown compared with experiments. The ship speed is $F_n=0.1525$ and the corresponding equivalent Reynolds number is about 8700. Here the calculations for the D- and E-regions have not been carried out; therefore both regions are excluded from the vorticity-integrating region V.

Satisfactory results are obtained, as far as C-region is concerned, especially in u and w. The velocity v is always underestimated, in other words, overestimated in the negative direction; this may

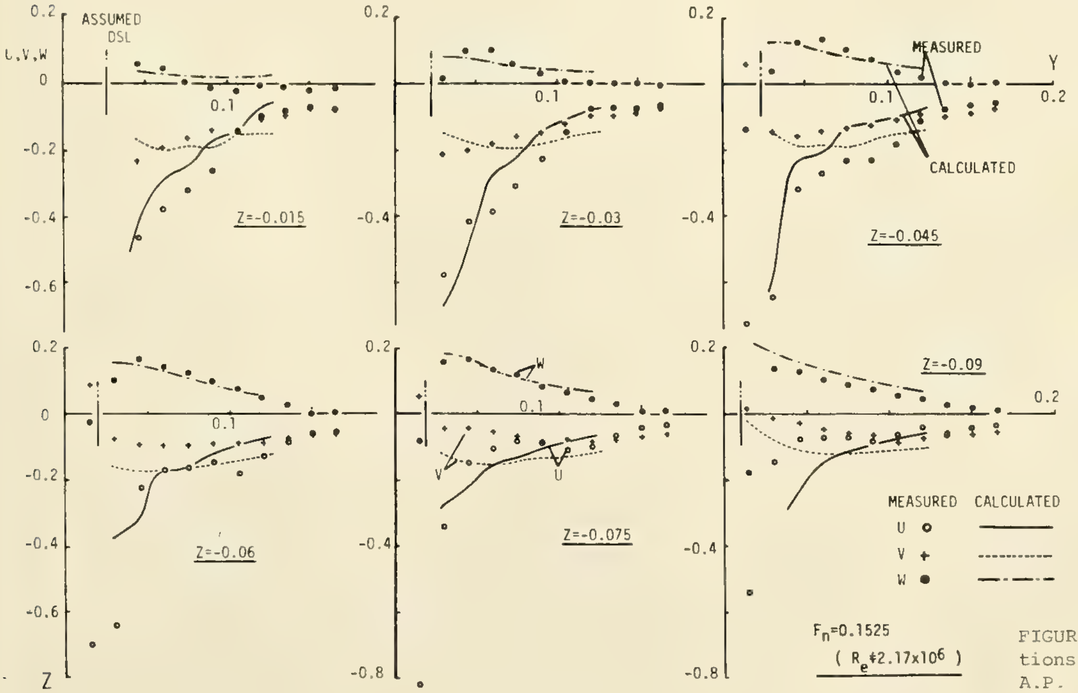

FIGURE 19. Velocity distributions in wake at (1/8)L AFT from A.P. (MS-02).

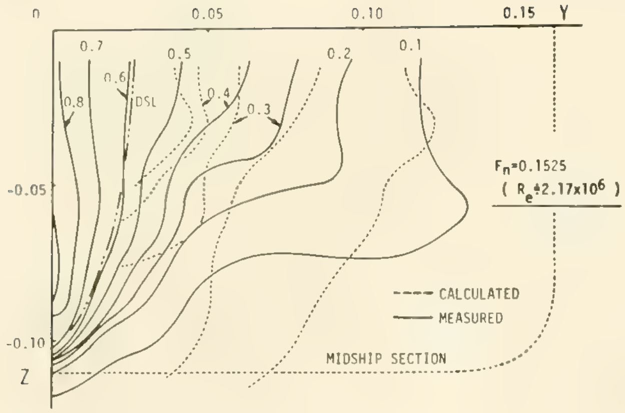

FIGURE 20. Wake distribution at (1/8)L AFT from A.P. (MS-02).

be because in the present calculations the potential components are determined with no attention to displacement effects.

Figure 20 shows the calculated wake distribution compared with measured. They do not always produce quantitative agreement with each other, but complimental uses of the present calculations with model-wake survey may offer a useful method for the prediction of full scale wake characteristics.

It is expected that much further improvement can be attained by taking into account the D- and E-regions.

CONCLUSION

The flow characteristics of boundary layers and wakes of ship-like bodies are discussed. The following remarks can be mentioned as conclusions;

(i) The pressure-constant assumption of boundary layer is a good approximation except near the ship stern or bilge keel where there is a small radius of curvature. The pressure does not recover near the stern because of the displacement effects of the boundary layer.

(ii) Most commonly used semi-empirical equations for velocity profiles, skin friction, and entrainment can be safely employed in case of ship-like bodies, but the functional expression for crossflow in boundary layer has a certain limit for large or reverse crossflows.

(iii) The integral method of boundary layer calculation may be carried out more effectively by a hybrid use of integral and finite-difference methods.

(iv) The three-dimensional boundary layer separation is closely related to pressure distribution on the hull surface. Its initiation is referred to the occurrence of large crossflow.

(v) The eddy viscosity coefficient is about 300-times the molecular one, in the ship's wake.

(vi) The separated flow region has sub-regions which have different characteristics and no single approximate equation of Navier-Stokes equation is valid uniformly for all regions.

(vii) The local asymptotic expansion method is promising for the separated flow. Further experimental investigations as to turbulence are necessary.

ACKNOWLEDGMENT

The assistance of graduate students of the Faculty of Engineering of Hiroshima University, who participated in carrying out experiments and numerical calculations, is cordially appreciated.

REFERENCE

Cebeci, T., K. Kaups, and J. Ramsey (1975). Calculations of Three-Dimensional Boundary Layer on Ship Hulls. *Proc. of First Intern. Conf. on Numerical Ship Hydro.*, 409.

Chang, P. K. (1970). *Separation of Flow*, Pergamon Press Ltd., Oxford, pp. 139.

Coles, D. (1956). The law of the wake in the turbulent boundary layer, *J. of Fluid Mech. 1*, 191.

Cumpsty, N. A., and M. R. Head (1967). The Calculation of Three-Dimensional Turbulent Boundary Layers, Part 1: Flow over the Rear of an Infinite Swept Wing. *Aero nautical Quart. 18*, 55.

Eichelbrenner, E. A. (1973). Three-Dimensional Boundary Layers. *Annual Review of Fluid Mech. 5*, M. Van Dyke, and W. G. Vincenti, ed., pp. 339-360.

Gadd, G. E. (1970). The Approximate Calculation of Turbulent Boundary Layer Development on Ship Hulls. *Trans. RINA 113*, 59.

Hatano, S., M. Nakato, T. Hotta, and S. Matsui (1971). Calculation of Ship Frictional Resistance by Three-Dimensional Boundary Layer Theory. *J. of Soc. of Nav. Arch. of Japan 130*, 1. (*Selected Papers from J. of Soc. of Nav. Arch. 11*, 12.)

Hatano, S., K. Mori, M. Fukushima, and R. Yamazaki (1975). Calculation of Velocity Distributions in Ship Wake. *J. of Soc. of Nav. Arch. of Japan 138*, 54; Hatano, S., K. Mori, and T. Suzuki (1977). 2nd Report, *Do., 141*, 10.

Hatano, S., and T. Hotta (1977). A Second Order Calculation of Three-Dimensional Turbulent Boundary Layer. *Naval Architecture and Ocean Engineering 15*, 1.

Hatano, S., K. Mori, and T. Hotta (1978). Experiments of Ship Boundary Layer Flows and Considerations on Assumptions in Boundary Layer Calculation. *Trans. of The West-Japan Soc. of Nav. Arch. 56* (to be published).

Head, M. R. (1958). Entrainment in the Turbulent Boundary Layer. *Aeronautical Res. Council Rep. and Mem. 3152.*

Hess, J. L., and A. M. O. Smith (1962). Calculation of Non-Lifting Potential Flow about Arbitrary Three-Dimensional Bodies. *Rep. No. E. S. 40622 Douglas Aircraft Co., Inc.*.

Himeno, Y., and I. Tanaka (1973). An Integral Method for Predicting Behaviors of Three-Dimensional Turbulent Boundary Layers on Ship Surfaces. *J. of The Kansai Soc. of Nav. Arch., Japan 147*, 61.

Hoekstra, M. (1975). Prediction of Full Scale Wake Characteristics Based on Model Wake Survey. *Intern. Shipbuilding Progress 22*, 204.

Hotta, T. (1975). A New Skin Friction Meter of Floating-Element Type and the Measurements of Local Shear Stress. *J. of the Soc. of Nav. Arch. of Japan 138*, 74.

Larsson, L. (1975). A Calculation Method for Three-Dimensional Turbulent Boundary Layers on Shiplike Bodies. *Proc. of First Intern. Conf. on Numerical Ship Hydro.*, 385.

Ludwieg, H., and W. Tillmann (1949). Untersuchungen über die Wandschubspannung in Turbulenten Reibungsschichten. *Ing. Arch. 17*, 288.

Mager, A. (1952). Generalization of boundary layer momentum integral equations to three-dimensional flows including those of rotating systems. *NACA Rep. 1067.*

Okuno, T. (1977). Distribution of Wall Shear Stress and Cross Flow in Three-Dimensional Turbulent Boundary Layer on Ship Hull. *Nav. Arch. and Ocean Eng. 15,* 10.

Stewartson, K. (1969). On the flow near the trailing edge of a flat plate II. *Mathematika 16,* 106.

Uberoi, S. B. S. (1969). Viscous Resistance of Ships and Ship Models. *Hydro-og Aerodynamisk Laboratorium Rep. Hy-13.*

Webster, W. C., and T. T. Huang (1970). Study of the Boundary Layer on Ship Forms. *Jour. of Ship Res. 14.* 153.

Yokoo, K., H. Takahashi, M. Nakato, Y. Yamazaki, H. Tanaka, and T. Ueda (1971). Comparison of Wake Distributions Between Ship and Models. *J. of Soc. of Nav. Arch. of Japan 130, 41.* (*Selected Papers from J. of Soc. of Nav. Arch. 11,* 25.)

A General Method for Calculating Three-Dimensional Laminar and Turbulent Boundary Layers on Ship Hulls

Tuncer Cebeci, K. C. Chang, and Kalle Kaups
Douglas Aircraft Company,
Long Beach, California

ABSTRACT

A general method for representing the flow properties in the three-dimensional boundary layers around ship hulls of arbitrary shape is described. It makes use of an efficient two-point finite-difference scheme to solve the boundary-layer equations and includes an algebraic eddy-viscosity représentation of the Reynolds-stress tensor. The numerical method contains novel and desirable features and allows the calculation of flows in which the circumferential velocity component contains regions of flow reversal across the boundary layer. The inviscid pressure distribution is determined with the Douglas-Neumann method which, if necessary, can conveniently allow for the boundary-layer displacement surface. To allow its application to ships, and particularly to those with double-elliptic and flat-bottomed hulls, a nonorthogonal coordinate system has been developed and is shown to be economical, precise, and comparatively easy to use. Present calculations relate to zero Froude number but they can readily be extended to include the effects of a water wave and the local regions of flow separation which may stem from bulbous-bow geometries.

1. INTRODUCTION

A general method for determining the local flow properties and the overall drag on ship hulls is very desirable and particularly so with the present need to conserve energy resources. It is difficult to achieve for a number of reasons including the turbulent nature of the three-dimensional boundary layer, the complexity and wide range of geometrical configurations employed, the possibility of local regions of separated flow, and the existence of the free surface. In addition, and although these difficulties may be overcome in total or in part, the resulting calculation method must have the essential features of generality, efficiency and accuracy.

The purpose of this paper is to describe a general method which is capable of representing the flow properties in the boundary layer around ship hulls of arbitrary shape. It is based on the general method of Cebeci, Kaups, and Ramsey (1977), developed for calculating three-dimensional, compressible laminar and turbulent boundary layers on arbitrary wings and previously proved to satisfy the requirements of numerical economy and precision. To allow its application to ships in general, and to double-elliptic and flat-bottomed hulls in particular, an appropriate coordinate system has been developed. Previously described coordinate systems, for example a streamline system such as that of Lin and Hall (1966) or the orthogonal arrangement of Miloh and Patel (1972) are limited in their applicability and the present nonorthogonal arrangement is similar to that of Cebeci, Kaups, and Ramsey (1977).

The numerical procedure for solving the three-dimensional boundary-layer equations makes use of Keller's two-point finite-difference method (1970) and Cebeci and Stewartson's procedure (1977) in computing flows in which the transverse velocity component contains regions of reverse flow. This is in contrast to previous investigations, for example those of Lin and Hall (1966) and Gadd (1970), which are limited either to zero crossflow or to a unidirectional and small crossflow. It is also in contrast to the previous methods of Chang and Patel (1975) and Cebeci and Chang (1977) which did not have a good and reliable procedure for computing the flow in which the transverse velocity component contained flow reversal.

In representing turbulent flow by time-averaged equations, a turbulence model is required and an algebraic eddy-viscosity formulation, similar to that of Cebeci, Kaups, and Ramsey (1977), is used. This is in contrast to the two-equation approach which Rastagi and Rodi (1978) have applied to three-dimensional boundary layers and which, in principle, should be better able to represent flows which are far from equilibrium. The previous comparisons presented in Cebeci (1974, 1975) demonstrated that the present eddy-viscosity model allows excellent agreement between measurements and calculations but did not include comparison with the three-dimensional boundary-layer measurements of Vermeulen (1971). Since this data includes a strongly adverse-pressure gradient case which allows a stringent test of the present model, corresponding calculations and comparisons are reported.

The calculation method is described in detail in the following section which states the three-dimensional, boundary-layer equations in curvilinear, nonorthogonal coordinates and describes and discusses the required initial conditions, turbulence model, and transformations in separate subsections. Section 3 is devoted to the coordinate system which is an essential feature of the present method. The numerical method is discussed briefly in Section 4 and calculated results are presented in Section 5 which includes comparisons with the measurements of Vermeulen (1971) and demonstrations of the ability of the method to represent the geometry of different hull configurations and to result in realistic velocity and drag characteristics. Summary conclusions are presented in Section 6.

2. BASIC EQUATIONS

Boundary-Layer Equations

The governing boundary-layer equations for three-dimensional incompressible laminar and turbulent flows in a curvilinear nonorthogonal coordinate system are given by:

Continuity Equation

$$\frac{\partial}{\partial x}(uh_2\sin\theta) + \frac{\partial}{\partial z}(wh_1\sin\theta) + \frac{\partial}{\partial y}(vh_1h_2\sin\theta) = 0 \qquad (1)$$

x-Momentum Equation

$$\frac{u}{h_1}\frac{\partial u}{\partial x} + \frac{w}{h_2}\frac{\partial u}{\partial z} + v\frac{\partial u}{\partial y} - K_1u^2\cot\theta + K_2w^2\csc\theta + K_{12}uw$$

$$= -\frac{\csc^2\theta}{h_1}\frac{\partial}{\partial x}\left(\frac{P}{\rho}\right) + \frac{\cot\theta\csc\theta}{h_2}\frac{\partial}{\partial z}\left(\frac{p}{\rho}\right)$$

$$+ \frac{\partial}{\partial y}\left(\nu\frac{\partial u}{\partial y} - \overline{u'v'}\right) \qquad (2)$$

z-Momentum Equation

$$\frac{u}{h_1}\frac{\partial w}{\partial x} + \frac{w}{h_2}\frac{\partial w}{\partial z} + v\frac{\partial w}{\partial y} - K_2w^2\cot\theta + K_1u^2\csc\theta + K_{21}uw$$

$$= \frac{\cot\theta\csc\theta}{h_1}\frac{\partial}{\partial x}\left(\frac{P}{\rho}\right) - \frac{\csc^2\theta}{h_2}\frac{\partial}{\partial z}\left(\frac{p}{\rho}\right)$$

$$+ \frac{\partial}{\partial y}\left(\nu\frac{\partial w}{\partial y} - \overline{v'w'}\right) \qquad (3)$$

Here, h_1 and h_2 are the metric coefficients and they are, in general, functions of x and z; that is,

$$h_1 = h_1(x,z); \qquad h_2 = h_2(x,z) \qquad (4)$$

Also, θ represents the angle between the coordinates x and z. The parameters K_1 and K_2 are known as the geodesic curvatures of the curves z = const and x = const, respectively. They are given by

$$K_1 = \frac{1}{h_1h_2\sin\theta}\left[\frac{\partial}{\partial x}(h_2\cos\theta) - \frac{\partial h_1}{\partial z}\right],$$

$$K_2 = \frac{1}{h_1h_2\sin\theta}\left[\frac{\partial}{\partial z}(h_1\cos\theta) - \frac{\partial h_2}{\partial x}\right] \qquad (5)$$

The parameters K_{12} and K_{21} are defined by

$$K_{12} = \frac{1}{\sin\theta}\left[-\left(K_1 + \frac{1}{h_1}\frac{\partial\theta}{\partial x}\right) + \cos\theta\left(K_2 + \frac{1}{h_2}\frac{\partial\theta}{\partial z}\right)\right] \qquad (6a)$$

$$K_{21} = \frac{1}{\sin\theta}\left[-\left(K_2 + \frac{1}{h_2}\frac{\partial\theta}{\partial z}\right) + \cos\theta\left(K_1 + \frac{1}{h_1}\frac{\partial\theta}{\partial x}\right)\right] \qquad (6b)$$

For an orthogonal system $\theta = \pi/2$ and the parameters K_1, K_2, K_{12}, and K_{21}, reduce to

$$K_1 = -\frac{1}{h_1h_2}\frac{\partial h_1}{\partial z}, \qquad K_2 = -\frac{1}{h_1h_1}\frac{\partial h_2}{\partial x} \qquad (7)$$

$$K_{12} = -K_1 \qquad K_{21} = -K_2 \qquad (8)$$

At the edge of the boundary layer, (2) and (3) reduce to

$$\frac{u_e}{h_1}\frac{\partial u_e}{\partial x} + \frac{w_e}{h_2}\frac{\partial u_e}{\partial z} - K_1u_e^2\cot\theta + K_2w_e^2\csc\theta + K_{12}u_ew_e$$

$$= -\frac{\csc^2\theta}{h_1}\frac{\partial}{\partial x}\left(\frac{P}{\rho}\right) + \frac{\cot\theta\csc\theta}{h_2}\frac{\partial}{\partial z}\left(\frac{P}{\rho}\right) \qquad (9)$$

$$\frac{u_e}{h_1}\frac{\partial w_e}{\partial x} + \frac{w_e}{h_2}\frac{\partial w_e}{\partial z} - K_2w_e^2\cot\theta + K_1u_e^2\csc\theta + K_{21}u_ew_e$$

$$= \frac{\cot\theta\csc\theta}{h_1}\frac{\partial}{\partial x}\left(\frac{P}{\rho}\right) - \frac{\csc^2\theta}{h_2}\frac{\partial}{\partial z}\left(\frac{P}{\rho}\right) \qquad (10)$$

The boundary conditions for Eqs. (1) to (3) are:

$$y = 0: \qquad u,v,w = 0 \qquad (11a)$$

$$y = \delta: \qquad u = u_e(x,z),\ w = w_e(x,z) \qquad (11b)$$

Initial Conditions

The solution of the system given by (1) to (3), subject to (11), requires initial conditions on two planes intersecting the body along coordinate lines. In general, the construction of these initial conditions for three-dimensional flows on arbitrary bodies such as ship hulls is difficult due to the variety of bow shapes, which may be extensive and complicated. For this reason, assumptions are necessary in order to start the calculations.

In our study we choose the inviscid dividing streamline on which $\partial p/\partial z = 0$ to be one of the initial data line (see Figure 1). In the case of rectilinear motion of a ship, this streamline runs along the plane of symmetry. Because of symmetry conditions, w and $\partial p/\partial z$ are zero on this line causing (3) to become singular. However, differentiation with respect to z yields a nonsingular equation. After performing the necessary differentiation for the z-momentum equation and taking advantage of appropriate symmetry conditions, we can write the so-called longitudinal attachment-line equations as:

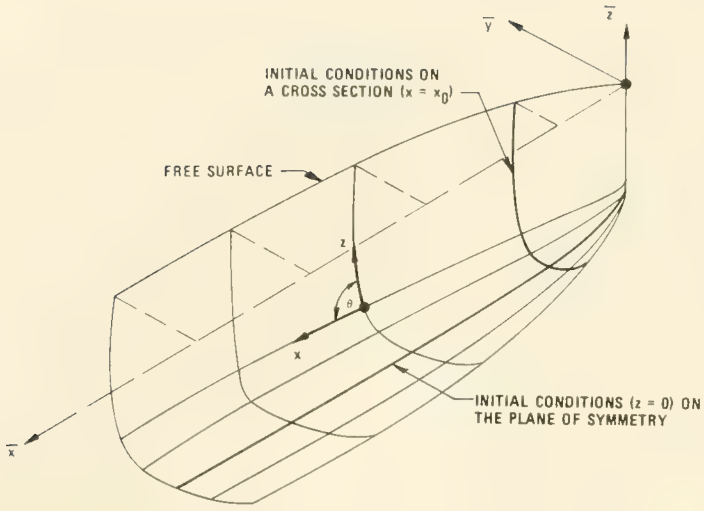
$\bar{y}$
$\bar{z}$
INITIAL CONDITIONS ON A CROSS SECTION ($x = x_0$)
FREE SURFACE
z
θ
x
INITIAL CONDITIONS ($z = 0$) ON THE PLANE OF SYMMETRY
$\bar{x}$

FIGURE 1. The nonorthogonal coordinate system and the initial data lines for the ship hull.

Continuity Equation

$$\frac{\partial}{\partial x}(uh_2\sin\theta) + h_1\sin\theta w_z + \frac{\partial}{\partial y}(vh_1h_2\sin\theta) = 0 \qquad (12)$$

x-Momentum Equation

$$\frac{u}{h_1}\frac{\partial u}{\partial x} + v\frac{\partial u}{\partial y} - \cot\theta K_1u^2$$

$$= \frac{u_e}{h_1}\frac{\partial u_e}{\partial x} - K_1u_e^2\cot\theta + \frac{\partial}{\partial y}\left(\nu\frac{\partial u}{\partial y} - \overline{u'v'}\right) \qquad (13)$$

z-Momentum Equation

$$\frac{u}{h_1}\frac{\partial w_z}{\partial x} + \frac{w_z^2}{h_2} + v\frac{\partial w_z}{\partial y} + K_{21}uw_z$$

$$= \frac{u_e}{h_1}\frac{\partial w_{ze}}{\partial x} + \frac{w_{ze}^2}{h_2} + K_{21}u_ew_{ze} + \frac{\partial}{\partial y}\left(\nu\frac{\partial w_z}{\partial y} - (\overline{w'v'})_z\right) \qquad (14)$$

Where $w_z = \partial w/\partial z$ and $(\overline{w'v'})_z = \partial(\overline{w'v'})/\partial z$. These equations are subject to the following boundary conditions:

$$y = 0: \qquad u = v = w_z = 0 \qquad (15a)$$

$$y = \delta: \qquad u = u_e,\ w_z = w_{ze} \qquad (15b)$$

The other initial data should be selected near the bow of the ship along the line perpendicular to the z = const coordinate (see Figure 1). However, because of the variety of possible bow shapes, approximations are necessary. For a simple, smooth bow section, where curvatures are small and no separation is expected, the flow along the initial line can be successfully assumed to be two-dimensional without pressure gradient, and the governing two-dimensional equations for a flat plate are solved. However, for most general merchant ships, the bow section is complicated and flow separation and reattachment are expected because of large curvature variations and adverse pressure gradients; as a consequence, the boundary-layer calculations can only be performed downstream of the attachment line (or point) where turbulent flow is presumed (since it is unlikely that the flow remains laminar after separation and reattachment with high Reynolds number). Generation of the initial data for turbulent flows is much more involved if there are no experimental data available. It requires sound mathematical and physical judgment and tedious trial-and-error efforts. We shall discuss this aspect of the problem later in the paper.

Turbulence Model

For turbulent flows, it is necessary to make closure assumptions for the Reynolds stresses, $-\rho\overline{u'v'}$ and $-\rho\overline{v'w'}$. In our study, we satisfy the requirement by using the eddy-viscosity concept and relate the Reynolds stresses to the mean velocity profiles by

$$-\overline{u'v'} = \varepsilon_m\frac{\partial u}{\partial y}, \qquad -\overline{v'w'} = \varepsilon_m\frac{\partial w}{\partial y} \qquad (16)$$

We use the eddy-viscosity formulation of Cebeci (1974), and define ε_m by two separate formulas. In the inner region, ε_m is defined as

$$(\varepsilon_m)_i = L^2\left[\left(\frac{\partial u}{\partial y}\right)^2 + \left(\frac{\partial w}{\partial y}\right)^2 + 2\cos\theta\left(\frac{\partial u}{\partial y}\right)\left(\frac{\partial w}{\partial y}\right)\right]^{1/2} \qquad (17)$$

where

$$L = 0.4\, y\,[1 - \exp(-y/A)] \qquad (18a)$$

$$A = 26\,\frac{\nu}{u_\tau}, \qquad u_\tau = \left(\frac{\tau_{tw}}{\rho}\right)^{1/2} \qquad (18b)$$

$$\tau_{tw} = \mu\left[\left(\frac{\partial u}{\partial y}\right)_w^2 + \left(\frac{\partial w}{\partial y}\right)_w^2 + 2\cos\theta\left(\frac{\partial u}{\partial y}\right)_w\left(\frac{\partial w}{\partial y}\right)_w\right]^{1/2} \qquad (18c)$$

In the outer region ε_m is defined by the following formula

$$\varepsilon_m = 0.0168\left|\int_0^\infty (u_{te} - u_t)\,dy\right| \qquad (19)$$

where

$$u_{te} = (u_e^2 + w_e^2 + 2u_ew_e\cos\theta)^{1/2} \qquad (20a)$$

$$u_t = (u^2 + w^2 + 2uw\cos\theta)^{1/2} \qquad (20b)$$

The inner and outer regions are established by the continuity of the eddy-viscosity formula.

Transformation of the Basic Equations

The boundary-layer equations can be solved either in physical coordinates or in transformed coordinates. Each coordinate system has its own advantage. In three-dimensional flows, the computer time and storage required is an important factor. The transformed coordinates are then favored because the coordinates allow larger steps to be taken in the longitudinal and transverse directions.

We define the transformed coordinates by

$$x = x,\ z = z,\ d\eta = \left(\frac{u_e}{\nu s_1}\right)^{1/2} dy,\ s_1 = \int_0^x h_1 dx \qquad (21)$$

and introduce a two-component vector potential such that

$$u h_2 \sin\theta + \frac{\partial\psi}{\partial y}, \qquad w h_1 \sin\theta = \frac{\partial\phi}{\partial y} \tag{22a}$$

$$v h_1 h_2 \sin\theta = -\left(\frac{\partial\psi}{\partial x} + \frac{\partial\phi}{\partial x}\right) \tag{22b}$$

where ψ and ϕ are defined as

$$\psi = (\nu s_1 u_e)^{\frac{1}{2}} h_2 f(x,z,\eta) \sin\theta \tag{23a}$$

$$\phi = (\nu s_1 u_e)^{\frac{1}{2}} (u_{ref}/u_e) h_1 g(x,z,\eta) \sin\theta \tag{23b}$$

and u_{ref} is some reference velocity.

Using these transformations and the relations given by (9), (10), and (11), we can write the x-momentum and z-momentum equations for the general case as:

x-Momentum

$$(bf'')' + m_1 ff'' - m_2 (f')^2 - m_5 f'g'$$

$$+ m_6 f''g - m_8 (g')^2 + m_{11}$$

$$= m_{10}\left(f' \frac{\partial f'}{\partial x} - f'' \frac{\partial f}{\partial x}\right) + m_7 \left(g' \frac{\partial f'}{\partial z} - f'' \frac{\partial g}{\partial z}\right) \tag{24}$$

z-Momentum

$$(bg'')' + m_1 fg'' - m_4 f'g' - m_3 (g')^2 + m_6 gg''$$

$$- m_9 (f')^2 + m_{12}$$

$$= m_{10}\left(f' \frac{\partial g'}{\partial x} - g'' \frac{\partial f}{\partial x}\right) + m_7 \left(g' \frac{\partial g'}{\partial z} - g'' \frac{\partial g}{\partial z}\right) \tag{25}$$

and their boundary conditions as

$$\eta = 0: \quad f = f' = g = g' = 0;$$

$$\eta = \eta_\infty, \quad f' = 1, \quad g' = w_e/u_{ref} \tag{26}$$

Here primes denote differentiation with respect to η, and

$$f' = \frac{u}{u_e}, \quad g' = \frac{w}{u_{ref}}, \quad b = 1 + \varepsilon_m^+, \quad \varepsilon_m^+ = \frac{\varepsilon_m}{\nu} \tag{27}$$

The coefficients m_1 to m_{12} are given by

$$m_1 = \frac{1}{2}\left(1 + \frac{s_1}{h_1 u_e} \frac{\partial u_e}{\partial x}\right) + \frac{s_1}{h_1 h_2 \sin\theta} \frac{\partial}{\partial x} (h_2 \sin\theta)$$

$$m_2 = \frac{s_1}{h_1 u_e} \frac{\partial u_e}{\partial x} - s_1 K_1 \cot\theta, \quad m_3 = -s_1 K_2 \frac{u_{ref}}{u_e} \cot\theta$$

$$m_4 = s_1 K_{21}, \quad m_5 = \frac{s_1}{h_2} \frac{u_{ref}}{u_e^2} \frac{\partial u_e}{\partial z} + s_1 K_{12} \frac{u_{ref}}{u_e}$$

$$m_6 = \frac{s_1}{h_1 h_2 \sin\theta} \frac{1}{\sqrt{u_e s_1}} \frac{\partial}{\partial z} \left(\sqrt{u_e s_1}\, h_1 \frac{u_{ref}}{u_e} \sin\theta\right) \tag{28}$$

$$m_7 = \frac{s_1}{h_2} \frac{u_{ref}}{u_e}, \quad m_8 = s_1 K_2 \left(\frac{u_{ref}}{u_e}\right)^2 \csc\theta$$

$$m_9 = s_1 K_1 \frac{u_e}{u_{ref}} \csc\theta, \quad m_{10} = \frac{s_1}{h_1}$$

$$m_{11} = m_2 + m_5 \frac{w_e}{u_{ref}} + m_8 \left(\frac{w_e}{u_{ref}}\right)^2$$

$$m_{12} = m_4 \frac{w_e}{u_{ref}} + m_3 \left(\frac{w_e}{u_{ref}}\right)^2 + m_9$$

$$+ \frac{m_{10}}{u_{ref}} \frac{\partial w_e}{\partial x} + \frac{m_7 w_e}{u_{ref}^2} \frac{\partial w_e}{\partial z}$$

To transform the longitudinal attachment-line flow equations and the boundary conditions, we use the transformed coordinates given by (21) and define the two-component vector potential by

$$u h_2 \sin\theta = \frac{\partial\psi}{\partial y}, \qquad w_z h_1 \sin\theta = \frac{\partial\phi}{\partial y}$$

$$v h_1 h_2 \sin\theta = -\left(\frac{\partial\psi}{\partial x} + \phi\right) \tag{29}$$

with ϕ and ψ still given by (23). With these variables, the longitudinal attachment-line equations in the transformed coordinates can be written as

$$(bf'')' + m_1 ff'' - m_2 (f')^2 + m_6 f''g + m_{11}$$

$$= \frac{s_1}{h_1}\left(f' \frac{\partial f'}{\partial x} - f'' \frac{\partial f}{\partial x}\right) \tag{30}$$

$$(bg'')' + m_1 g''f - m_4 f'g' - m_3 (g')^2 + m_6 gg'' - m_9 (f')^2$$

$$+ m_{12} = \frac{s_1}{h_1}\left(f' \frac{\partial g'}{\partial x} - g'' \frac{\partial f}{\partial x}\right) \tag{31}$$

The boundary conditions and the coefficients m_1 to m_{12} are the same as in (26) and in (28) except now

$$\eta = \eta_\infty: \qquad g' = \frac{w_{ze}}{u_{ref}}$$

$$m_3 = \frac{s_1}{h_2} \frac{u_{ref}}{u_e}, \qquad m_6 = m_3$$

$$m_9 = 0, \qquad m_{11} = m_2$$

$$m_{12} = m_3 \left(\frac{w_{ze}}{u_{ref}}\right)^2 + m_4 \frac{w_{ze}}{u_{ref}} + \frac{s}{h_1} \frac{1}{u_{ref}} \frac{\partial w_{ze}}{\partial x} \tag{32}$$

In terms of the transformed variables, the algebraic eddy-viscosity formulas as given by (17) to (20) become

$$(\varepsilon_m)_i = \frac{1}{\sqrt{R_x}} \eta^2 \left[1 - \exp\left(-\frac{y}{A}\right)\right]^2 \left[(f'')^2 + \left(\frac{u_{ref}}{u_e}\right)^2 (g'')^2 + 2 \frac{u_{ref}}{u_e} f''g'' \cos\theta\right]^{\frac{1}{2}} \tag{33}$$

$$(\varepsilon_m)_o = 0.0168 \sqrt{R_x} \int_0^{\eta_\infty} \left\{\left[1 + \left(\frac{w_e}{u_e}\right)^2 + 2\left(\frac{w_e}{u_e}\right)\cos\theta\right]^{\frac{1}{2}} - \left[(f')^2 + \left(\frac{u_{ref}}{u_e}\right)^2 (g')^2 + 2 \frac{u_{ref}}{u_e} f'g' \cos\theta\right]^{\frac{1}{2}}\right\} d\eta \tag{34}$$

Here $R_x = u_e s_1/\nu$ and

$$\frac{y}{A} = \frac{R_x^{1/4}}{26}\eta \left[(f_w'')^2 + \left(\frac{u_{ref}}{u_e}\right)^2 (g_w'')^2 + 2\,\frac{u_{ref}}{u_e} f_w'' g_w'' \cos\theta \right]^{1/4} \tag{35}$$

3. COORDINATE SYSTEM

Since, in general, a ship hull is a complicated nondevelopable surface, a Cartesian coordinate system is not suitable for boundary-layer calculations. Most existing merchant and naval vessels possess the following features: a flat bottom [$\bar{y} = f(\bar{x},\bar{z})$ is not a single-valued function]; a bottom which is not parallel to the water surface; and a bow which has a submerged bulb extending toward the origin. In addition, the problem is further complicated by the existence of a free surface, corresponding to the water level of a partly-submerged hull. The chosen coordinate system must be sufficiently general to allow these various features to be represented in the boundary-layer calculations.

The streamline coordinate system is superficially attractive but the determination of the streamlines, the orthogonal lines, and the associated geometrical parameters requires considerable effort. They are dependent on the Froude number, and also on the Reynolds number if the displacement effect is taken into account. Consequently, and in addition to being hard to compute, this coordinate system becomes uneconomical to use when the effect of the Froude number and the Reynolds number are to be systematically examined.

A desirable requirement of a coordinate system for the boundary-layer calculations is that it be calculated only once. Miloh and Patel (1972) proposed an orthogonal coordinate system which depends only on the body geometry and is calculated once and for all. This coordinate system has been applied by Chang and Patel (1975) to boundary-layer calculations on two simple ship hulls: ellipsoid and double elliptic ship. One of the coordinates is taken as lines of $x = \bar{x}$ = constant and the other as $z(\bar{x},\bar{z})$ = constant, which is orthogonal to x = constant lines everywhere on the ship hull, and is obtained from the solution of the differential equation

$$\frac{d\bar{z}}{d\bar{x}} = -\frac{f_{\bar{x}} f_{\bar{z}}}{1 + f_{\bar{z}}^2} \tag{36}$$

Here $\bar{y} = f(\bar{x},\bar{z})$ defines the ship hull, and $(\bar{x},\bar{y},\bar{z})$ denote the Cartesian coordinates. The major advantage of this coordinate system is its simplicity. Because one of the coordinates is subject to the condition (36), there is no guarantee that the boundaries of the ship hull are coincident with the coordinate lines. Furthermore, for a ship with flat bottom for which $\bar{y} = f(\bar{x},\bar{z})$ is not a single-valued function, one of the coordinates cannot be calculated from (36). The coordinate system is limited, therefore, to some special geometries only.

In this study we adopt a nonorthogonal coordinate system similar to that developed by Cebeci, Kaups, and Ramsey (1977) for arbitrary wings. It is based on body geometries only and, hence, it is calculated once and for all. In addition, the system can deal with the peculiar features of most merchant and naval vessels discussed previously. The details of this coordinate system are described briefly in the following paragraph.

Now consider the ship hull as given in the usual Cartesian coordinate system; that is, $\bar{x}$ along the ship axis, $\bar{y}$ and $\bar{z}$ in the cross-plane (see Figure 1). We select $x = \bar{x}$ = constant as one of the coordinates and the other coordinate, z, lies in the $\bar{y}\bar{z}$-plane. Because the coordinate system is nonorthogonal, we are free to select the values of z in the plane to satisfy the condition that the boundary lines of the ship hull are coincident with z = constant coordinate lines. There are several ways of finding the z-values. Here z is determined by mapping each $\bar{y}\bar{z}$ crossplane into a half or hull unit circle depending on whether the crossplane intercepts the free surface or is completely submerged. The polar angle, normalized by π or 2π on the unit circle, is taken as z-values. The z-values then range from 0 to 1 on each crossplane. The advantage of the mapping method is that equi-interval, z = constant coordinate lines are automatically concentrated in the region of large curvature where the boundary-layer characteristics are expected to vary greatly. Hence the number of z = constant coordinate lines can be reduced without loss of accuracy.

There are several methods available for the mapping of an arbitrary body onto a unit circle. Here we use the numerical mapping method developed by Halsey (1977). It makes full use of Fast Fourier Transform techniques and has no restrictions on the shape of the body to be mapped. To map a smooth crossplane onto a unit circle, the procedure is fairly easy. If there are inner corner points, or trailing-edge and leading-edge corner points (see Figure 2) caused by the reflection of the crossplane, they must be removed before mapping is performed to improve numerical accuracy and to provide rapid convergence. The inner corner points are rounded off by using Fourier series expansion technique and the leading-edge and/or trailing-edge corner points are removed by using the Karman-Trefftz mapping. For details see Halsey (1977).

To use the mapping method to find the coordinate system, it is only necessary to define the ship hull as a family of points in the x = constant planes, to locate the intersection of the ship hull and the free surface, and to indicate whether corner points exist. The data in each plane is then mapped into a unit circle as $\bar{y}$ vs z and $\bar{z}$ vs z and interpolated for constant values of z. Another set of spline fits, in the planes z = constant for $\bar{y}$ vs x and $\bar{z}$ vs x, completes the definition of the coordinate

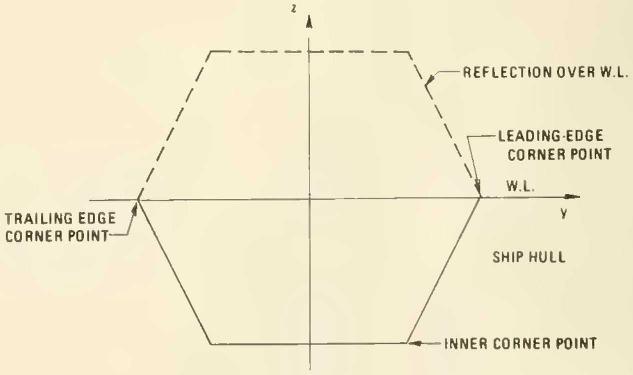

FIGURE 2. Notation of corner points used in the mapping procedure.

system. The lines formed by the intersection of the planes x = constant and z = constant with the hull constitute the nonorthogonal coordinate net on the surface, and the third boundary-layer coordinate is taken as the distance normal to the surface in accordance with first-order boundary-layer approximation.

Since the spline-fitting also yields derivatives, the metric coefficient and the geodesic curvatures of the coordinate lines can be calculated from the formulas given below.

The metric coefficients:

$$h_1^2 = 1 + \left(\frac{\partial \bar{z}}{\partial x}\right)_z^2 + \left(\frac{\partial \bar{y}}{\partial x}\right)_z^2 \qquad (37a)$$

$$h_2^2 = \left(\frac{\partial \bar{y}}{\partial z}\right)_x^2 + \left(\frac{\partial \bar{z}}{\partial x}\right)_x^2 \qquad (37b)$$

The angle between the coordinate lines:

$$\cos\theta = \frac{1}{h_1 h_2}\left[\left(\frac{\partial \bar{y}}{\partial z}\right)_x \left(\frac{\partial \bar{y}}{\partial x}\right)_z + \left(\frac{\partial \bar{z}}{\partial x}\right)_z \left(\frac{\partial \bar{z}}{\partial z}\right)_x\right] \qquad (38)$$

The geodesic curvature of the z = constant line:

$$K_1 = \frac{1}{h_1^4 h_2 \sin\theta}\left\{\left[\left(\frac{\partial \bar{y}}{\partial z}\right)_x \left(\frac{\partial \bar{z}}{\partial x}\right)_z - \left(\frac{\partial \bar{y}}{\partial x}\right)_z \left(\frac{\partial \bar{z}}{\partial z}\right)\right]_x \left[\left(\frac{\partial \bar{z}}{\partial x}\frac{\partial^2 \bar{y}}{\partial x^2} - \frac{\partial \bar{y}}{\partial x}\frac{\partial^2 \bar{z}}{\partial x^2}\right)_z\right] + \left[\left(\frac{\partial \bar{y}}{\partial z}\right)_x \left(\frac{\partial^2 \bar{y}}{\partial x^2}\right)_z + \left(\frac{\partial \bar{z}}{\partial z}\right)_x \left(\frac{\partial^2 \bar{z}}{\partial x^2}\right)_z\right]\right\} \qquad (39)$$

The geodesic curvature of the x = constant line:

$$K_2 = \frac{-1}{h_1 h_2^4 \sin\theta}\left[\left(\frac{\partial \bar{y}}{\partial z}\right)_x \left(\frac{\partial \bar{z}}{\partial x}\right)_z - \left(\frac{\partial \bar{y}}{\partial x}\right)_z \left(\frac{\partial \bar{z}}{\partial z}\right)_x\right] \left[\left(\frac{\partial \bar{z}}{\partial z}\frac{\partial^2 \bar{y}}{\partial z^2} - \frac{\partial \bar{y}}{\partial z}\frac{\partial^2 \bar{z}}{\partial z^2}\right)_x\right] \qquad (40)$$

The other parameters K_{12} and K_{21} are calculated from (6). It may be noted that K_1 and K_2 can also be obtained from (5). This provides a check on the expressions given by (39) and (40).

In the boundary-layer calculations, we need the invisid velocity components along the surface coordinates. Let $\vec{V}$ be the total velocity vector on the hull, $(\bar{u},\bar{v},\bar{w})$ the corresponding velocity components in the Cartesian coordinates, and (u_e,w_e) in the adopted surface coordinates. As can be seen from Figure 3,

$$u_e = \frac{\vec{V}\cdot\vec{t}_1 - \vec{V}\cdot\vec{t}_2\cos\theta}{\sin^2\theta} \qquad (41)$$

$$w_e = \frac{\vec{V}\cdot\vec{t}_2 - \vec{V}\cdot\vec{t}_1\cos\theta}{\sin^2\theta} \qquad (42)$$

Here $\vec{t}_1$ and $\vec{t}_2$ are the unit tangent vectors along x and z coordinates and are given by

$$\vec{t}_1 = \frac{1}{h_1}\left[\vec{i} + \left(\frac{\partial \bar{y}}{\partial x}\right)_z \vec{j} + \left(\frac{\partial \bar{z}}{\partial x}\right)_z \vec{k}\right] \qquad (43)$$

$$\vec{t}_2 = \frac{1}{h_2}\left[\left(\frac{\partial \bar{y}}{\partial z}\right)_x \vec{j} + \left(\frac{\partial \bar{z}}{\partial z}\right)_x \vec{k}\right] \qquad (44)$$

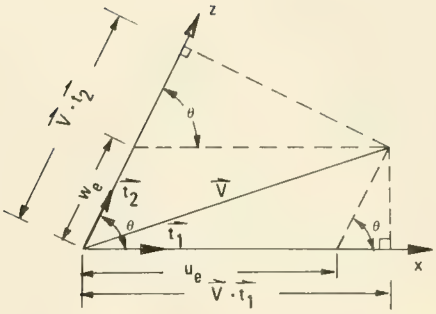

FIGURE 3. Resolution of the velocity components.

With the definition of $\vec{V}$ and with the use of (43) and (44), Eqs. (41) and (42) can be written as

$$u_e = \frac{1}{\sin^2\theta}\left\{\left[\bar{u} + \bar{v}\left(\frac{\partial \bar{y}}{\partial x}\right)_z + \bar{w}\left(\frac{\partial \bar{z}}{\partial x}\right)_z\right]\frac{1}{h_1} - \frac{\cos\theta}{h_2}\left[\bar{v}\left(\frac{\partial \bar{y}}{\partial z}\right)_x + \bar{w}\left(\frac{\partial \bar{z}}{\partial z}\right)_x\right]\right\} \qquad (45)$$

$$w_e = \frac{1}{\sin^2\theta}\left\{\frac{1}{h_2}\left[\bar{v}\left(\frac{\partial \bar{y}}{\partial z}\right)_x + \bar{w}\left(\frac{\partial \bar{z}}{\partial z}\right)_x\right] - \frac{\cos\theta}{h_1}\left[\bar{u} + \bar{v}\left(\frac{\partial \bar{y}}{\partial x}\right)_z + \bar{w}\left(\frac{\partial z}{\partial x}\right)_z\right]\right\} \qquad (46)$$

4. NUMERICAL METHOD

We use the Box method to solve the boundary-layer equations given in Section 2. This is a two-point finite-difference method developed by Keller and Cebeci. This method has been applied to two-dimensional flows as well as three-dimensional flows and has been found to be efficient and accurate. Descriptions of this method have been presented in a series of papers and reports and a detailed presentation is contained in a recent book by Cebeci and Bradshaw (1977).

In using this numerical method, or any other method, care must be taken in obtaining solutions of the equations when the transverse velocity component, w, contains regions of flow reversal. Such changes in w-profiles will lead to numerical instabilities resulting from integration opposed to the flow direction unless appropriate changes are made in the integration procedure. Here we use the procedure developed by Cebeci and Stewartson (1977). In this new and very powerful procedure, which follows the characteristics of the locally plane flow, the direction of w at each grid point across the boundary layer is checked and difference equations are written accordingly. At each point to be calculated, the backward characteristics which determine the domain of dependence, are computed from the local values of the velocity. Since the characteristics must be determined as part of the solution a Newton iteration process is used in the calculation procedure to correctly determine the exact shape of the domain of dependence.

To illustrate the basic numerical method, we shall, at first, consider the solution of the longitudinal attachment-line Eqs. (30) and (31) and then the solution of the full three-dimensional flow equations as given by (24) and (25). We shall not discuss the Cebeci-Stewartson procedure for computing three-dimensional flows with the transverse velocity, w, containing flow reversal since that procedure will be fully described in a forthcoming paper.

Difference Equations for the Longitudinal Attachment-Line Equations

According to the Box method, we first reduce the Eqs. (30), (31), (32), and (26) into a system of five first-order equations by introducing new dependent variables $u(x,z,\eta)$, $v(x,z,\eta)$, $w(x,z,\eta)$, $t(x,z,\eta)$, and $\theta(x,z,\eta)$. Equations (30) and (31) then can be written as

$$u' = v \tag{47a}$$

$$w' = t \tag{47b}$$

$$(bv)' + \theta v - m_2 u^2 + m_{11} = m_{10}\, u \frac{\partial u}{\partial x} \tag{47c}$$

$$(bt)' + \theta t - m_4 uw - m_3 w^2 - m_9 u^2 + m_{12} = m_{10}\, u \frac{\partial w}{\partial x} \tag{47d}$$

$$\theta' = m_1 u + m_6 w + m_{10} \frac{\partial u}{\partial x} \tag{47e}$$

The boundary conditions (26) and (32) become

$$\eta = 0: \qquad u = w = \theta = 0 \tag{48a}$$

$$\eta = \eta_\infty: \qquad u = 1, \qquad w = w_{ze}/u_{ref} \tag{48b}$$

We next consider the net rectangle shown in Figure 4 and denote the net points by

$$x_0 = 0 \qquad x_n = x_{n-1} + k_n \qquad n = 1, 2, \ldots, N$$

$$\eta_0 = 0 \qquad \eta_j = \eta_{j-1} + h_j \qquad j = 1, 2, \ldots, J$$

We approximate the quantities (u,v,g,t,θ) at points (x_n,η_j) of the net by functions denoted by $(u_j^n, v_j^n, w_j^n, t_j^n, \theta_j^n)$. We also employ the notation for points and quantities midway between net points and for any net function s_j^n.

$$x_{n-1/2} = \frac{1}{2}\left[x_n + x_{n-1}\right], \quad \eta_{j-1/2} = \frac{1}{2}\left(\eta_j + \eta_{j-1}\right)$$

$$s_j^{n-1/2} = \frac{1}{2}\left(s_j^n + s_j^{n-1}\right), \quad s_{j-1/2} = \frac{1}{2}\left(s_j^n + s_{j-1}^n\right) \tag{49}$$

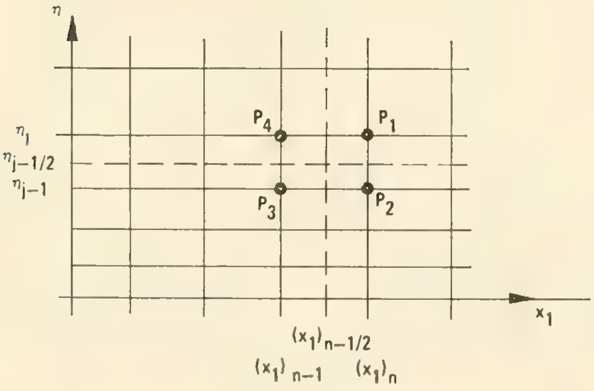

FIGURE 4. Net rectangle for the longitudinal attachment-line equations.

The difference equations which are to approximate (47) are formulated by considering one mesh rectangle as in Figure 4. We approximate (47a,b) using centered difference quotients and average them about the midpoint $(x_n, \eta_{j-1/2})$ of the segment P_1P_2.

$$h_j^{-1}(u_j^n - u_{j-1}^n) = v_{j-1/2}^n \tag{50a}$$

$$h_j^{-1}(w_j^n - w_{j-1}^n) = t_{j-1/2}^n \tag{50b}$$

Similarly, (47c,d,e) are approximated by centering them about the midpoint $x_{n-1/2}, \eta_{j-1/2}$ of the rectangle $P_1P_2P_3P_4$. This gives

$$h_j^{-1}\left[(bv)_j^n - (bv)_{j-1}^n\right] + (\theta v)_{j-1/2}^n - (m_2^n + \alpha_n)(u^2)_{j-1/2}^n = R_{j-1/2}^{n-1} - m_{11}^n \tag{50c}$$

$$\begin{aligned} &h_j^{-1}\left[(bt)_j^n - (bt)_{j-1}^n\right] + (\theta t)_{j-1/2}^n \\ &- (m_4^n + \alpha_n)(uw)_{j-1/2}^n - m_3^n (w^2)_{j-1/2}^n - m_9^n (u^2)_{j-1/2}^n \\ &+ \alpha_n\left[w_{j-1/2}^{n-1} u_{j-1/2}^n - u_{j-1/2}^{n-1} w_{j-1/2}^n\right] \\ &= S_{j-1/2}^{n-1} - m_{12}^n \end{aligned} \tag{50d}$$

$$h_j^{-1}\left(\theta_j^n - \theta_{j-1}^n\right) - \left(m_1^n + 2\alpha_n\right)u_{j-1/2}^n - m_6^n w_{j-1/2}^n = T_{j-1/2}^{n-1} \tag{50e}$$

Here

$$\begin{aligned} R_{j-1/2}^{n-1} = -\alpha_n (u^2)_{j-1/2}^{n-1} &- \left\{ h_j^{-1}\left[(bv)_j^{n-1} - (bv)_{j-1}^{n-1}\right] + (\theta v)_{j-1/2}^{n-1} \right. \\ &\left. - m_2^{n-1} (u^2)_{j-1/2}^{n-1} + m_{11}^{n-1} \right\} \end{aligned} \tag{51a}$$

$$\begin{aligned} S_{j-1/2}^{n-1} = -\alpha_n (uw)_{j-1/2}^{n-1} &- \left\{ h_j^{-1}\left[(bt)_j^{n-1} - (bt)_{j-1}^{n-1}\right] + (\theta t)_{j-1/2}^{n-1} \right. \\ &\left. - m_3^{n-1} (w^2)_{j-1/2}^{n-1} - m_9^{n-1} (u^2)_{j-1/2}^{n-1} \right\} \end{aligned} \tag{51b}$$

$$\begin{aligned} T_{j-1/2}^{n-1} = -2\alpha_n u_{j-1/2}^{n-1} &- \left\{ h_j^{-1}\left(\theta_j^{n-1} - \theta_{j-1}^{n-1}\right) - m_1^{n-1} u_{j-1/2}^{n-1} \right. \\ &\left. - m_6^{n-1} w_{j-1/2}^{n-1} \right\} \end{aligned} \tag{51c}$$

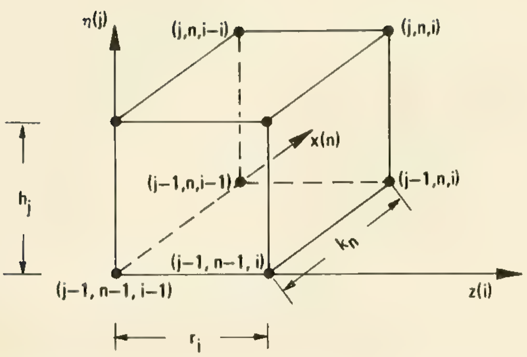

FIGURE 5. Net cube for the difference equations for three-dimensional flows, $w_j > 0$.

$$\alpha_n = \frac{m_{10}^{n-1/2}}{x_n - x_{n-1}} \tag{51d}$$

Difference Equations for the Full Three-Dimensional Equations

The difference equations for the full three-dimensional equations, as given by (24) and (25), are again expressed in terms of a first-order system. With the definitions given by (47a) and (47b), they are written as

$$(bv)' + \theta v - m_2 u^2 - m_5 uw - m_8 w^2 + m_{11}$$

$$= m_{10}\, u \frac{\partial u}{\partial x} + m_7 w \frac{\partial u}{\partial z} \tag{52a}$$

$$(bt)' + \theta t - m_4 uw - m_3 w^2 - m_9 u^2 + m_{12}$$

$$= m_{10}\, u \frac{\partial w}{\partial x} + m_7 w \frac{\partial w}{\partial z} \tag{52b}$$

$$\theta' = m_1 u + m_6 w + m_{10} \frac{\partial u}{\partial x} + m_7 \frac{\partial w}{\partial z} \tag{52c}$$

Their boundary conditions, (26) become:

$$\eta = 0: \qquad u = w = \theta = 0 \tag{53a}$$

$$\eta = \eta_\infty: \qquad u = 1, \qquad w = w_e/u_{ref} \tag{53b}$$

The difference equations for (47a) and (47b) are the same as those given by (50a) and (50b): they are written for the midpoint $[(x)_n, (z)_i, \eta_{j-1/2}]$ of the net cube shown in Figure 5; that is,

$$h_j^{-1}\left(u_j^{n,i} - u_{j-1}^{n,i}\right) = v_{j-1/2}^{n,i},$$

$$h_j^{-1}\left(w_j^{n,i} - w_{j-1}^{n,i}\right) = t_{j-1/2}^{n,i} \tag{54}$$

The difference equations which are to approximate (52a,b,c) are rather lengthy. To illustrate the difference equations for these three equations, we consider the following model equation

$$(bv)' + \theta v + m_{11} = m_{10}\, u \frac{\partial u}{\partial x} + m_7 w \frac{\partial u}{\partial z} \tag{55}$$

The difference equations for (55) are:

$$h_j^{-1}\left[(\overline{bv})_j - (\overline{bv})_{j-1}\right] + (\overline{\theta v})_{j-1/2} + (m_{11})_{j-1/2}^{n-1/2}$$

$$= (m_{10})_{i-1/2}^{n-1/2} \bar{u}_{j-1/2} \frac{\bar{u}_n - \bar{u}_{n-1}}{k_n}$$

$$+ (m_7)_{i-1/2}^{n-1/2} \bar{w}_{j-1/2} \frac{\bar{u}_i - \bar{u}_{i-1}}{r_i} \tag{56}$$

Here, for example,

$$\bar{v}_j = \frac{1}{4}\left(v_j^{n,i} + v_j^{n,i-1} + v_j^{n-1,i-1} + v_j^{n-1,i}\right)$$

$$\bar{u}_n = \frac{1}{4}\left(u_j^{n,i} + u_j^{n,i-1} + u_{j-1}^{n,i} + u_{j-1}^{n,i-1}\right)$$

$$\bar{u}_i = \frac{1}{4}\left(u_j^{n,i} + u_j^{n-1,i} + u_{j-1}^{n,i} + u_{j-1}^{n-1,i}\right) \tag{57}$$

and

$$(m_{11})_{i-1/2}^{n-1/2}$$

$$= \frac{1}{4}\left[(m_{11})_i^n + (m_{11})_{i-1}^n + (m_{11})_i^{n-1} + (m_{11})_{i-1}^{n-1}\right]$$

$$z_0 = 0 \qquad z_i = z_{i-1} + r_i \qquad i = 1, 2, \ldots, I \tag{58}$$

Solution of the Difference Equations

The difference equations (50) for the longitudinal attachment-line flow and the difference equations for (52) are nonlinear algebraic equations. We use Newton's method to linearize them and then solve the resulting linear system by the block-elimination method discussed by Keller (1974). A brief description of it will be given for the streamwise attachment-line equations.

Using Newton's method, the linearized difference equations for the system given by (50) are:

$$\delta u_j - \delta u_{j-1} - \frac{h_j}{2}(\delta v_j + \delta v_{j-1}) = (r_1)_j \tag{59a}$$

$$\delta w_j - \delta w_{j-1} - \frac{h_j}{2}(\delta t_j + \delta t_{j-1}) = (r_2)_j \tag{59b}$$

$$(\zeta_1)_j \delta v_j + (\zeta_2)\delta v_{j-1} + (\zeta_3)_j \delta\theta_j + (\zeta_4)_j \delta\theta_{j-1}$$

$$+ (\zeta_5)_j \delta u_j + (\zeta_6)_j \delta u_{j-1} = (r_3)_j \tag{59c}$$

$$(\beta_1)_j \delta t_j + (\beta_2)_j \delta t_{j-1} + (\beta_3)_j \delta\theta_j + (\beta_4)_j \delta\theta_{j-1}$$

$$+ (\beta_5)_j \delta w_j + (\beta_6)_j \delta w_{j-1} + (\beta_7)_j \delta u_j + (\beta_8)_j \delta u_{j-1}$$

$$= (r_4)_j \tag{59d}$$

$$(\sigma_1)_j \delta\theta_j + (\sigma_2)_j \delta\theta_{j-1} + (\sigma_3)_j \delta u_j + (\sigma_4)_j \delta u_{j-1}$$

$$+ (\sigma_5)_j \delta w_j + (\sigma_6)_j \delta w_{j-1} = (r_5)_j \tag{59e}$$

Here we have dropped the superscripts n, i and have defined $(r_k)_j$, $(\zeta_k)_j$, $(\beta_k)_j$, and $(\sigma_k)_j$ by

$$r_1 = u_{j-1} - u_j + h_j v_{j-1/2} \tag{60a}$$

$$r_2 = w_{j-1} - w_j + h_j t_{j-1/2} \tag{60b}$$

$$\begin{aligned}(r_3)_j = R^{n-1}_{j-1/2} - m_{11} &- \Big[(bv)'_{j-1/2} + (\theta v)_{j-1/2} \\ &- (m_2 + \alpha_n)(u^2)_{j-1/2} \Big]\end{aligned} \tag{60c}$$

$$\begin{aligned}(r_4)_j = S^{n-1}_{j-1/2} - m_{12} &- \Big[(bt)'_{j-1/2} + (\theta t)_{j-1/2} - (m_4 + \alpha_n)(uw)_{j-1/2} \\ &- m_3 (w^2)_{j-1/2} - m_9 (u^2)_{j-1/2} \\ &+ \alpha_n \Big(w^{n-1}_{j-1/2}\, u_{j-1/2} - u^{n-1}_{j-1/2}\, w_{j-1/2} \Big) \Big]\end{aligned} \tag{60d}$$

$$\begin{aligned}(r_5)_j = T^{n-1}_{j-1/2} &- \Big[\theta'_{j-1/2} - (m_1 + 2\alpha_n) u_{j-1/2} - m_6 w_{j-1/2} \Big]\end{aligned} \tag{60e}$$

$$(\zeta_1)_j = \frac{b_j}{h_j} + \frac{1}{2}\theta_j \tag{61a}$$

$$(\zeta_2)_j = -\frac{b_{j-1}}{h_j} + \frac{1}{2}\theta_{j-1} \tag{61b}$$

$$(\zeta_3)_j = \frac{1}{2} v_j \tag{61c}$$

$$(\zeta_4)_j = \frac{1}{2} v_{j-1} \tag{61d}$$

$$(\zeta_5)_j = -(m_2 + \alpha_n) u_j \tag{61e}$$

$$(\zeta_6)_j = -(m_2 + \alpha_n) u_{j-1} \tag{61f}$$

$$(\beta_1)_j = (\zeta_1)_j \tag{62a}$$

$$(\beta_2)_j = (\zeta_2)_j \tag{62b}$$

$$(\beta_3)_j = \frac{1}{2} t_j \tag{62c}$$

$$(\beta_4)_j = \frac{1}{2} t_{j-1} \tag{62d}$$

$$(\beta_5)_j = -\frac{1}{2}(m_4 + \alpha_n) u_j - m_3 w_j - \frac{1}{2}\alpha_n\, u^{n-1}_{j-1/2} \tag{62e}$$

$$\begin{aligned}(\beta_6)_j = &-\frac{1}{2}(m_4 + \alpha_n) u_{j-1} - m_3 w_{j-1} \\ &- \frac{1}{2}\alpha_n\, u^{n-1}_{j-1/2}\end{aligned} \tag{62f}$$

$$(\beta_7)_j = -\frac{1}{2}(m_4 + \alpha_n) w_j - m_9 u_j + \frac{1}{2}\alpha_n\, w^{n-1}_{j-1/2} \tag{62g}$$

$$\begin{aligned}(\beta_8)_j = &-\frac{1}{2}(m_4 + \alpha_n) w_{j-1} - m_9 u_{j-1} \\ &+ \frac{1}{2}\alpha_n\, w^{n-1}_{j-1/2}\end{aligned} \tag{62h}$$

$$(\sigma_1)_j = \frac{1}{h_j} \tag{63a}$$

$$(\sigma_2)_j = -\frac{1}{h_j} \tag{63b}$$

$$(\sigma_3)_j = -\frac{1}{2}(m_1 + 2\alpha_n) \tag{63c}$$

$$(\sigma_4)_j = -\frac{1}{2}(m_1 + 2\alpha_n) \tag{63d}$$

$$(\sigma_5)_j = -\frac{1}{2} m_6 \tag{63e}$$

$$(\sigma_6)_j = -\frac{1}{2} m_6 \tag{63f}$$

The boundary conditions become

$$\delta u_0 = \delta w_0 = \delta\theta_0 = 0, \qquad \delta u_J = \delta w_J = 0 \tag{64}$$

The solution of the linear system given by (59) and (64) is obtained by using the block elimination method. According to this method, the system is written as

$$\mathbb{A}\,\underset{\approx}{\delta} = \underset{\approx}{r} \tag{65}$$

Here

$$\mathbb{A} = \begin{bmatrix} A_0 & C_0 & & & & & \\ B_1 & A_1 & C_1 & & & & \\ & \ddots & \ddots & \ddots & & & \\ & & B_j & A_j & C_j & & \\ & & & \ddots & \ddots & \ddots & \\ & & & & B_{J-1} & A_{J-1} & C_{J-1} \\ & & & & & B_J & A_J \end{bmatrix}$$

$$\underset{\sim}{\delta} = \begin{bmatrix} \underset{\sim}{\delta}_0 \\ \underset{\sim}{\delta}_1 \\ \vdots \\ \underset{\sim}{\delta}_j \\ \vdots \\ \underset{\sim}{\delta}_J \end{bmatrix}, \quad \underset{\sim}{r} = \begin{bmatrix} \underset{\sim}{r}_1 \\ \underset{\sim}{r}_2 \\ \vdots \\ \underset{\sim}{r}_j \\ \vdots \\ \underset{\sim}{r}_5 \end{bmatrix}, \quad \underset{\sim}{r}_j = \begin{bmatrix} (r_1)_j \\ (r_2)_j \\ (r_3)_j \\ (r_4)_j \\ (r_5)_j \end{bmatrix}, \quad \underset{\sim}{\delta}_j = \begin{bmatrix} \delta u_j \\ \delta v_j \\ \delta w_j \\ \delta t_j \\ \delta \theta_j \end{bmatrix}$$

The A_j, B_j, C_j in $\mathbb{A}$ denote 5x5 matrices. The solution of (65) is obtained by the procedure described in Cebeci and Bradshaw (1977).

5. RESULTS

Turbulent Flow Calculations for a Curved Duct and Comparison with Experiment

The turbulence model described in Section 2 has been used with considerable success to compute a wide range of two-dimensional turbulent boundary layers [see for example Cebeci and Smith (1974)]. The model has also been used to compute three-dimensional flows and again is found to yield accurate results [see for example Cebeci (1974, 1975) and Cebeci, Kaups, and Moser (1976)]. To further test the model for three-dimensional flows, we have considered the experimental data taken in a 60° curved duct of rectangular cross section. Figure 6 shows a sketch of the flow geometry. The experimental data are due to Vermeulen (1971). Here z denotes the distance from the outer wall, measured along normals to the wall; x denotes the arc length along the outer wall; and y denotes distance normal to the plane x,z.

To test the computed results with the data, it is necessary to specify the initial profiles given by experiment. This can be done in a number of ways. In the study reported by Cebeci, Kaups, and Moser (1976) the profiles were generated by using Coles' velocity profile formula. That formula, which represents the experimental data rather well for two-dimensional flows, was not very satisfactory for three-dimensional flows. Here we abandon the use of Coles' formula in favor of Thompson's two-parameter velocity profiles as described and improved by Galbraith and Head (1975). According to this formula, the dimensionless u/u_e velocity profile is given by

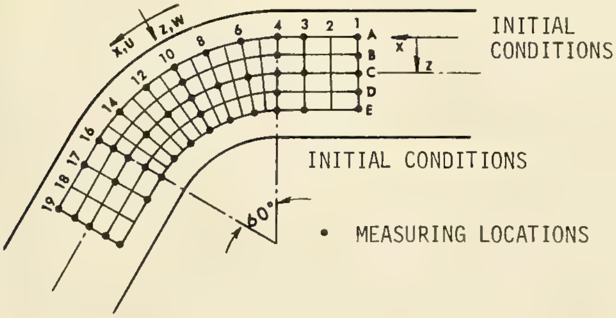

FIGURE 6. Coordinate system and notation for the curved duct.

$$\frac{u}{u_e} = \gamma_s \left(\frac{u}{u_e}\right)_{\text{inner}} + (1 - \gamma_s) \qquad (66)$$

Here γ_s is an intermittency factor defined by the following empirical formulas:

$$0 < \frac{y}{\delta_0} \leq 0.05 \qquad \gamma_s = 1$$

$$0.05 < \frac{y}{\delta_0} \leq 0.3 \qquad \gamma_s = 1 - 2.64214\left(\frac{y}{\delta_0} - 0.05\right)^2$$

$$0.3 < \frac{y}{\delta_0} \leq 0.7 \qquad \gamma_s = 4.4053\left(\frac{y}{\delta_0} - 0.5\right)^3 - 1.8502\left(\frac{y}{\delta_0} - 0.5\right) + 0.5$$

$$0.7 < \frac{y}{\delta_0} \leq 0.95 \qquad \gamma_s = 2.64214\left(\frac{y}{\delta_0} - 0.05\right)^2$$

$$\frac{y}{\delta_0} > 0.95 \qquad \gamma_s = 0.0$$

The dimensionless velocity profile for the inner layer, that is, $(u/u_e)_{\text{inner}}$, is given by

$$y^+ < 4 \qquad u^+ = y^+$$

$$4 < y^+ < 30 \qquad u^+ = c_1 + c_2 \ln y^+ + c_3(\ln y^+)^2 + c_4(\ln y^+)^3$$

$$y^+ > 30 \qquad u^+ = 5.50 \ln y^+ + 5.45$$

Here $c_1 = 4.187$, $c_2 = -5.745$, $c_3 = 5.110$, $c_4 = -0.767$, $y^+ = yu_\tau/\nu$, $u_\tau = (\tau_w/\rho)^{1/2}$, $u^+ = u/u_\tau$, and δ_o is a parameter which is a function of θ, c_f, and H.

To find the functional relationship between δ_o, c_f, θ, and H, we use the definitions of displacement thickness, δ^*, and momentum thickness, θ. Substituting (66) into the definition of δ^*, after some algebra, we get

$$\frac{\delta^*}{\delta_o}\left(1 - \frac{A_1}{R_{\delta^*}}\right) = 0.5 + \sqrt{\frac{c_f}{2}}\left[A_4 \ln \frac{\delta^*}{\delta_o} - A_3 - A_2 \ln\left(R_{\delta^*}\sqrt{\frac{c_f}{2}}\right)\right] \qquad (67)$$

where

$$A_1 = 50.679, \quad A_2 = 1.1942, \quad A_3 = 0.7943, \quad A_4 = 1.195.$$

An expression similar to that given by (67) can also be obtained if we substitute (66) into the definition of θ. However, the resulting expression is quite complicated. For this reason, the expression for θ is obtained numerically, and for a given value of θ and H, the corresponding values of c_f and δ_o are computed from that equation and from (67).

Equation (66) is recommended for two-dimensional flows. Here we assume that it also applies to the streamwise velocity profile by replacing u/u_e by u_s/u_{s_e} with c_f now representing the streamwise skin-friction coefficient.

In order to generate the crossflow velocity component (u_n/u_{s_e}), we use Mager's expression and define u_n/u_{s_e} by

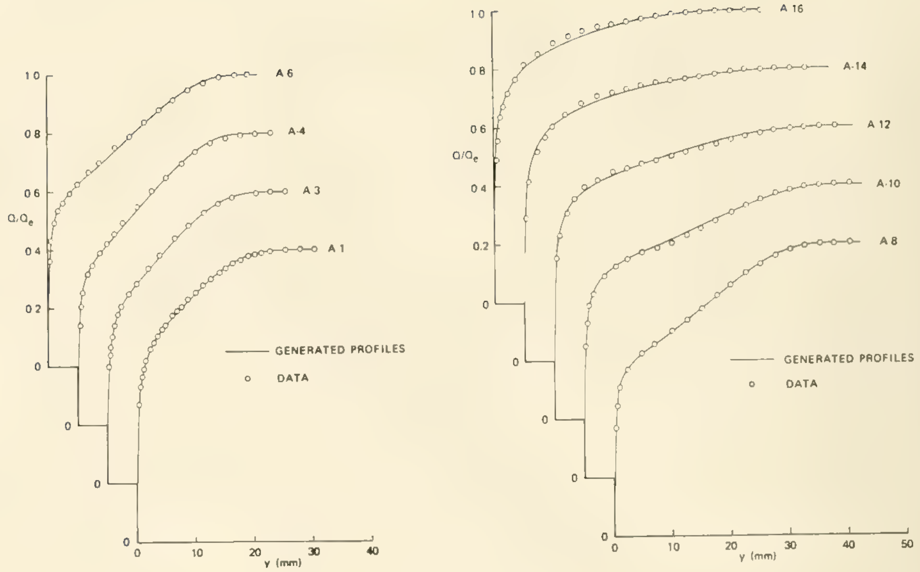

FIGURE 7. Comparison of generated initial total velocity profiles with Vermeulen's data.

$$\frac{u_n}{u_{s_e}} = \frac{u_s}{u_{s_e}} \left(1 - \frac{y}{\delta}\right)^2 \tan\beta_w \tag{68}$$

with the limiting crossflow angle β_w obtained from the experimental data.

Once the streamwise and crossflow velocity profiles are calculated by the above procedure, we compute the velocity profiles u/u_e and w/w_e in the orthogonal directions x and z by the following relationships

$$\frac{u}{u_e} = \frac{u_s}{u_{s_e}} - \frac{u_n}{u_{s_e}} \frac{w_e}{u_e} \tag{69a}$$

$$\frac{w}{w_e} = \frac{u_s}{u_{s_e}} + \frac{u_n}{u_{s_e}} \frac{u_e}{w_e} \tag{69b}$$

Figure 7 shows a comparison of generated and experimental total velocity profiles along the line A. As can be seen, the procedure discussed above for generating the initial velocity profiles from the experimental data is quite good. This is important for an accurate evaluation of a turbulent model, especially for three-dimensional flows. Here

$$\frac{Q}{Q_e} = \left(\frac{u^2 + w^2}{u_e^2 + w_e^2}\right)^{\frac{1}{2}} \tag{70}$$

The solution of the boundary-layer equations also requires the specification of the metric coefficients and the geodesic curvatures. They are calculated from the following expression:

$$h_1 = \begin{cases} 1 & \text{straight section} \\ 1 - z/R_o & \text{curved section} \end{cases}$$
$$h_2 = 1.0, \qquad K_2 = 0 \tag{71}$$
$$K_1 = \begin{cases} 0 & \text{straight section} \\ 1/(R_o - z) & \text{curved section} \end{cases}$$

A comparison of calculated and experimental values of streamwise momentum thickness, θ_{11}, shape factor, H_{11}, skin-friction coefficient, c_f, and limiting crossflow angle, β_w, is shown in Figures 8, 9, 10, and 11, respectively, along the lines B, C, D, E. Here the limiting crossflow angle is computed from

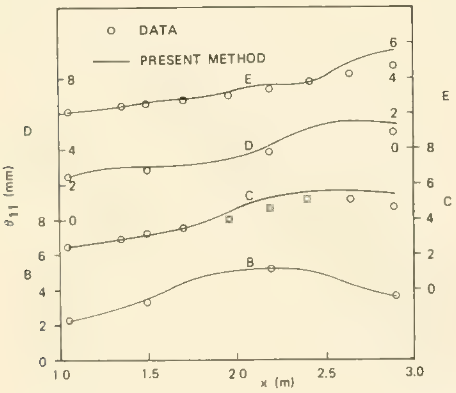

FIGURE 8. Comparison of computed momentum thickness with Vermeulen's data.

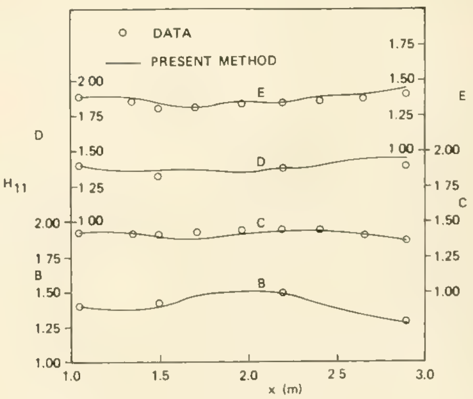

FIGURE 9. Comparison of computed shape factor with Vermeulen's data.

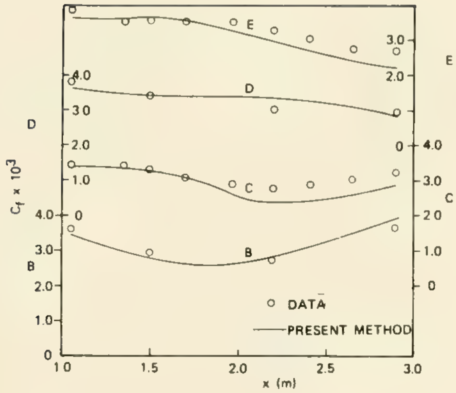

FIGURE 10. Comparison of computed skin friction coefficient with Vermeulen's data.

$$\tan\beta_w = \frac{w_e/u_e[(u_{ref}/u_e)g''_w - f''_w]}{(w_e/u_e)^2\ (u_{ref}/w_e)g''_w + f''_w} \tag{72}$$

Figures 12 and 13 show a comparison of calculated and experimental total velocity profiles and crossflow angle profiles along the lines C and E. Here the crossflow angle is computed from

$$\sin\beta_w = \frac{w_e/u_e[(u_{ref}/w_e)g' - f']}{Q/Q_e\ (Q_e/u_e)^2} \tag{73}$$

As in Figures 8 through 11, again the agreement between calculated results and experiment is very good. The computed results follow the trend in the experimental data well and indicate that the present turbulence model, as in two-dimensional flows, is quite satisfactory for three-dimensional flows.

Results for a Double Elliptic Ship Model

To test our method for ship hulls, we have considered two separate hulls. The first one, which is discussed in this section, is a double elliptic ship whose hull is given analytically. The second one, which is discussed in the next section, is ship model 5350 which has a rather complex shape. Its hull is represented section-by-section in tabular form and contains all the features of most merchant and naval vessels. It proves an excellent test case to study the computational difficulties associated with real ship hulls.

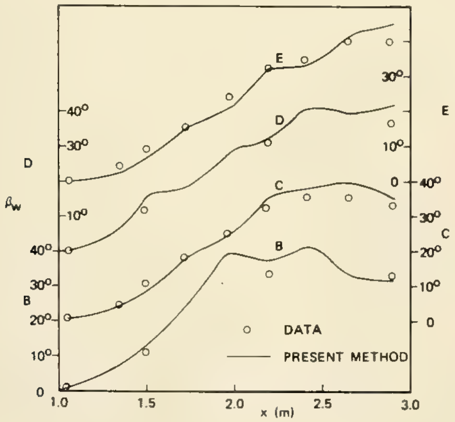

FIGURE 11. Comparison of computed limiting crossflow angle with Vermeulen's data.

The double elliptic ship model can be analytically represented by

$$\bar{y} = f(\bar{x},\bar{z}) = B\left[1-\left(\frac{\bar{x}}{L}\right)^2\right]^{\frac{1}{2}}\left[1-\left(\frac{\bar{z}}{H}\right)^2\right]^{\frac{1}{2}} \tag{74}$$

It has round edges except for the sharp corners at $\bar{x} = \pm L$ and $\bar{z} = \pm H$. The body of L:H:B = 1.0:0.125:0.1 together with the nonorthogonal coordinate nets on the hull is shown in Figure 14.

The potential-flow solutions were obtained from the Douglas-Neumann computer program for three-dimensional flows. To get the solutions, 120 control elements on the surface were used, 12 along the $\bar{x}$-direction and 10 along the $\bar{z}$-direction.

Before we describe our boundary-layer calculations, it is useful to discuss the pressure distribution for this body shown in Figure 15. As can be seen from the figure, the streamwise pressure gradient is initially favorable in the bow region and then adverse up to the midpoint of the body. This is followed by a region of favorable pressure gradient and then by a shape adverse pressure gradient very close to the stern. The crosswise pressure gradient varies in a more complex manner. Near the bow the pressure decreases down from the water surface to a minimum and then increases as the keel is reached. As the flow moves downstream, the location of the minimum pressure moves up and reaches the water surface at about x/L = -0.80. The minimum pressure remains at the water surface to about x/L = 0.80 and then moves toward the keel. As a result, near the bow and the stern, one may expect flow reversal of the crossflow across the boundary layer does not reverse direction from the keel to the water surface. This conclusion is drawn from considering the pressure gradients only. The real situation may be somewhat modified because, in addition, there are the upstream effects and the curvature effects on the flow characteristics.

The boundary-layer computation starts with turbulent flow from $\bar{x}/L = -0.90$. We have tried to start the computation from $\bar{x}/L = -0.97$ and $\bar{x}/L = -0.95$. However, flow separation was observed at $\bar{x}/L = -0.90$ near the keel due to the sharp curvature and adverse pressure gradient in the bow region and can be seen from Figure 15. In the previous calculations of Chang and Patel (1975) and Cebeci and Chang (1977), the flow separation near the bow was not found due to the orthogonal coordinate system they adopted in which the second net point from the keel is so far from the keel that the region of adverse pressure gradient is omitted.

In our boundary-layer calculations, we have used 40 points along the x-direction and 16 points along the z-direction. In the normal direction, we have taken approximately 40 points. The nonuniform grid structure described in Cebeci and Bradshaw (1977) is employed in the normal direction so that the grid points are concentrated near the wall where the velocity gradients are large.

Some of the computed results for $R_L = 10^7$ are shown in Figures 16 and 18. Figure 16 shows the spanwise distributions of the pressure coefficients, c_p, local skin-friction coefficient, c_f, the shape

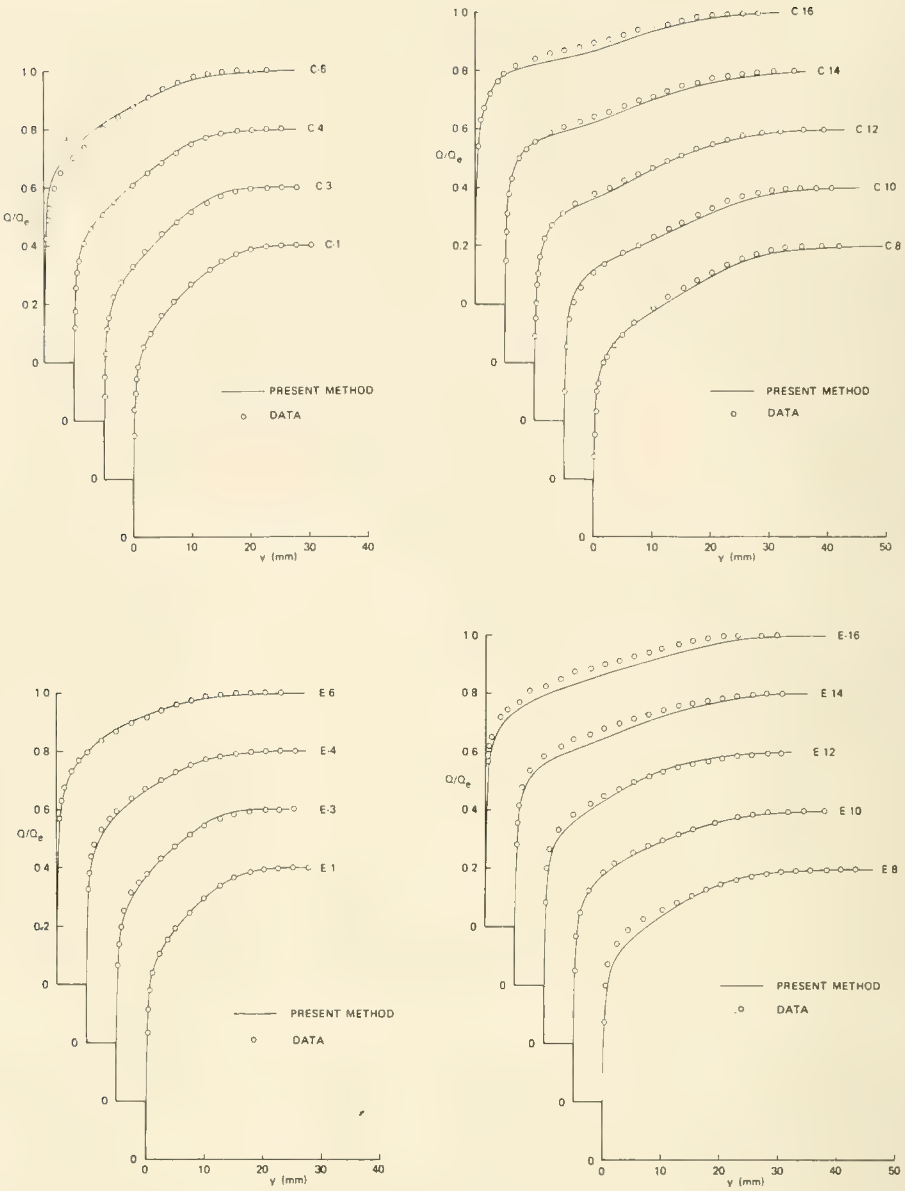

FIGURE 12. Comparison of computed total velocity profiles with Vermeulen's data.

factor, H_{11}, the Reynolds number based on the momentum thickness, R_θ, and the limiting crossflow angle for x/L = -0.85, 0.0, and 0.75. As can be seen from these figures, the boundary-layer parameters vary greatly near the keel where the curvatures and the pressure gradients are large and remain almost unchanged near the surface where the curvatures and the pressure gradients are small. Except at x/L = -0.85, the limiting crossflow angle is positive. This implies that the crossflow near the wall moves from the keel to the free surface as predicted from the pressure distribution. Figure 17 shows typical longitudinal and transverse velocity profiles at z = 0.6 for several values of (x/l), and Figure 18 shows typical transverse velocity profiles at (x/L) = -0.2 for several values of z. As can be seen from Figures 17(b) and 18, the transverse velocity component undergoes drastic changes in the longitudinal and transverse directions under the influence of pressure gradient and body geometry. As was discussed before, when the transverse velocity changes sign across the boundary layer and contains regions of reverse flow, numerical instabilities results from integration opposed to flow direction unless appropriate changes are made in the integration procedure. The new numerical procedure of Cebeci and Stewartson (1977) handles this situation very well and does not show any signs of breakdown resulting from flow reversal of transverse velocity component.

Results for Ship Model 5350

The ship model 5350, unlike the one discussed in the previous section, is a realistic tanker model. The geometry of the hull is so complicated that it is represented in tabular form section by section. The model possesses all the special features of existing merchant and naval vessels, that is, a bottom which is flat and not parallel to the still-water surface and an extended bow completely submerged under the water surface, and consequently

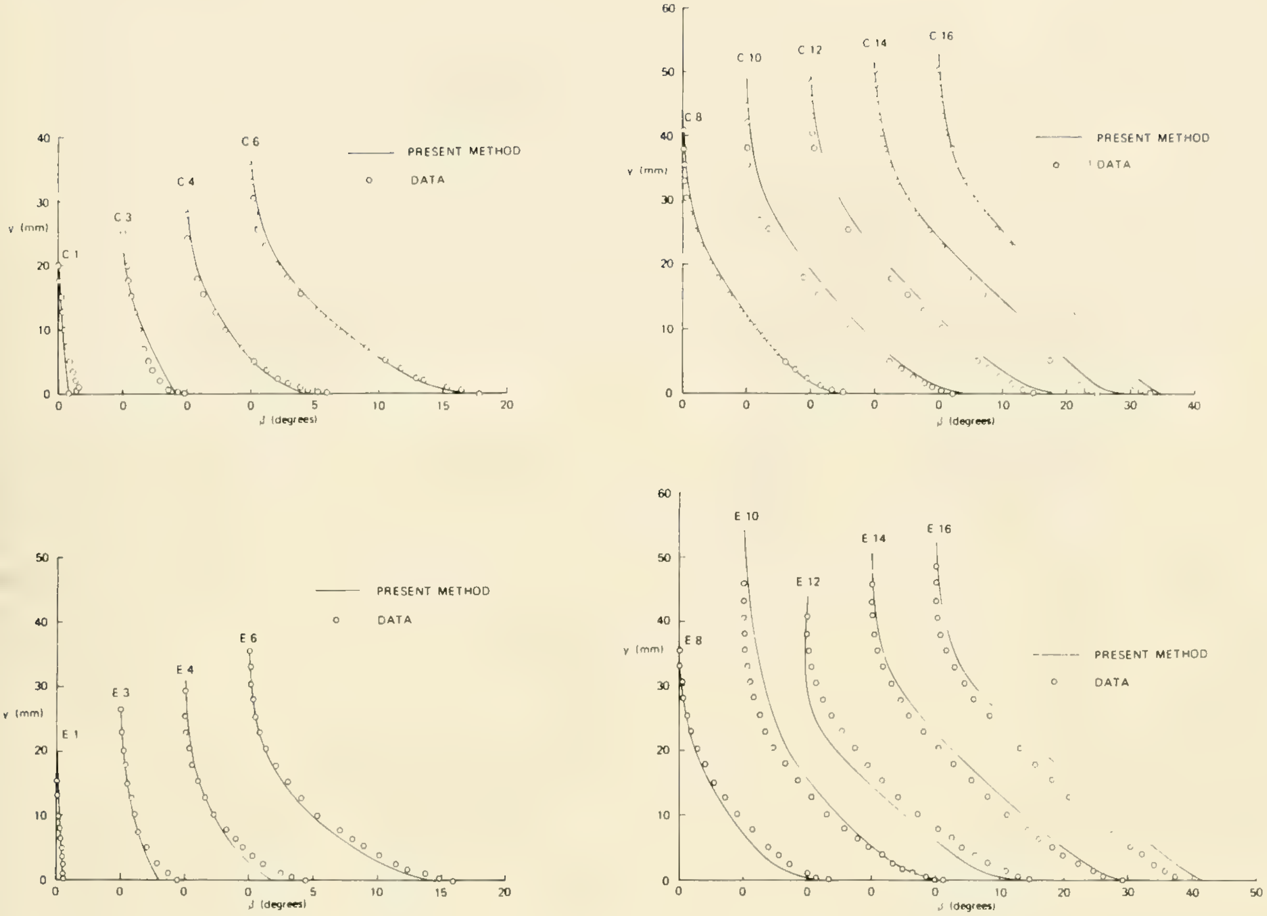

FIGURE 13. Comparison of computed crossflow angle with Vermeulen's data.

serves as an excellent case on which to apply our method.

Figure 19 shows a three-dimensional picture of this ship model together with our nonorthogonal coordinate system. We see from this figure that, as a by-product of the mapping method discussed earlier, the z = const. coordinate lines are concentrated in the bow and corner regions where the curvature is large. Figure 20 shows different cross-sections (indicated by solid lines) and interpolated values obtained by a cubic-spline method (indicated by circles) from which the geometric parameters are obtained.

The inviscid velocity distribution for the model is obtained by using the Douglas-Neumann method treating the model as a double ship model. Figure 21 shows the pressure distribution for the entire ship and Figure 22 shows a detailed pressure distribution for the bow region. We see from these figures that the longitudinal pressure gradient near the keel

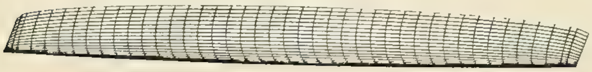

FIGURE 14. Three-dimensional picture of double elliptic ship model with the nonorthogonal coordinate system.

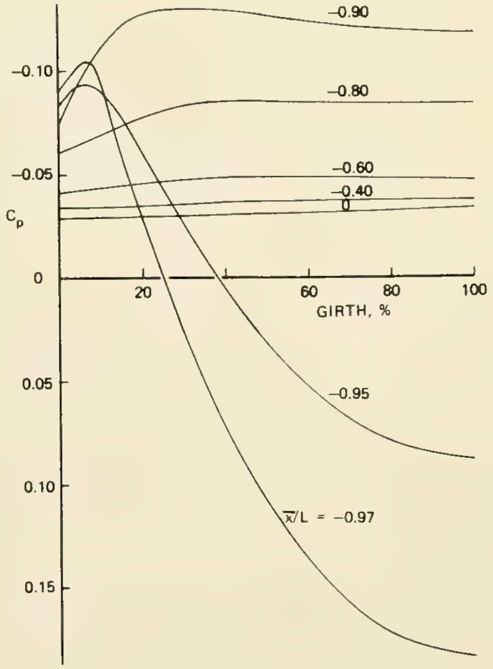

FIGURE 15. Pressure distribution for the double-elliptic ship.

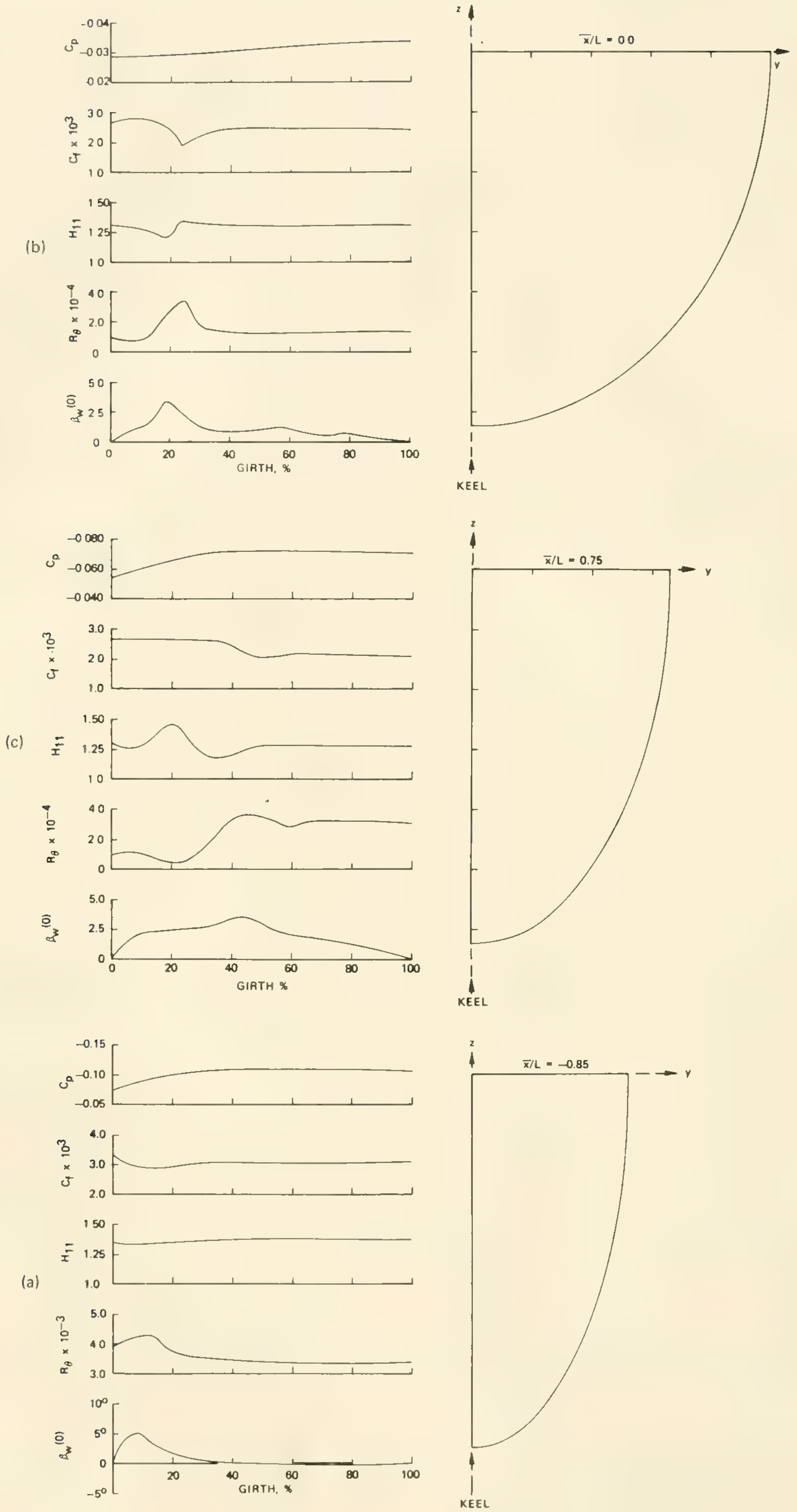

FIGURE 16. Computed Cp, c_f, H_{11}, R_θ, and β_w for the double-elliptic ship model for $R_L = 10^7$ at (a) x/L = -0.85, (b) x/L = 0.0, (c) x/L = 0.75.

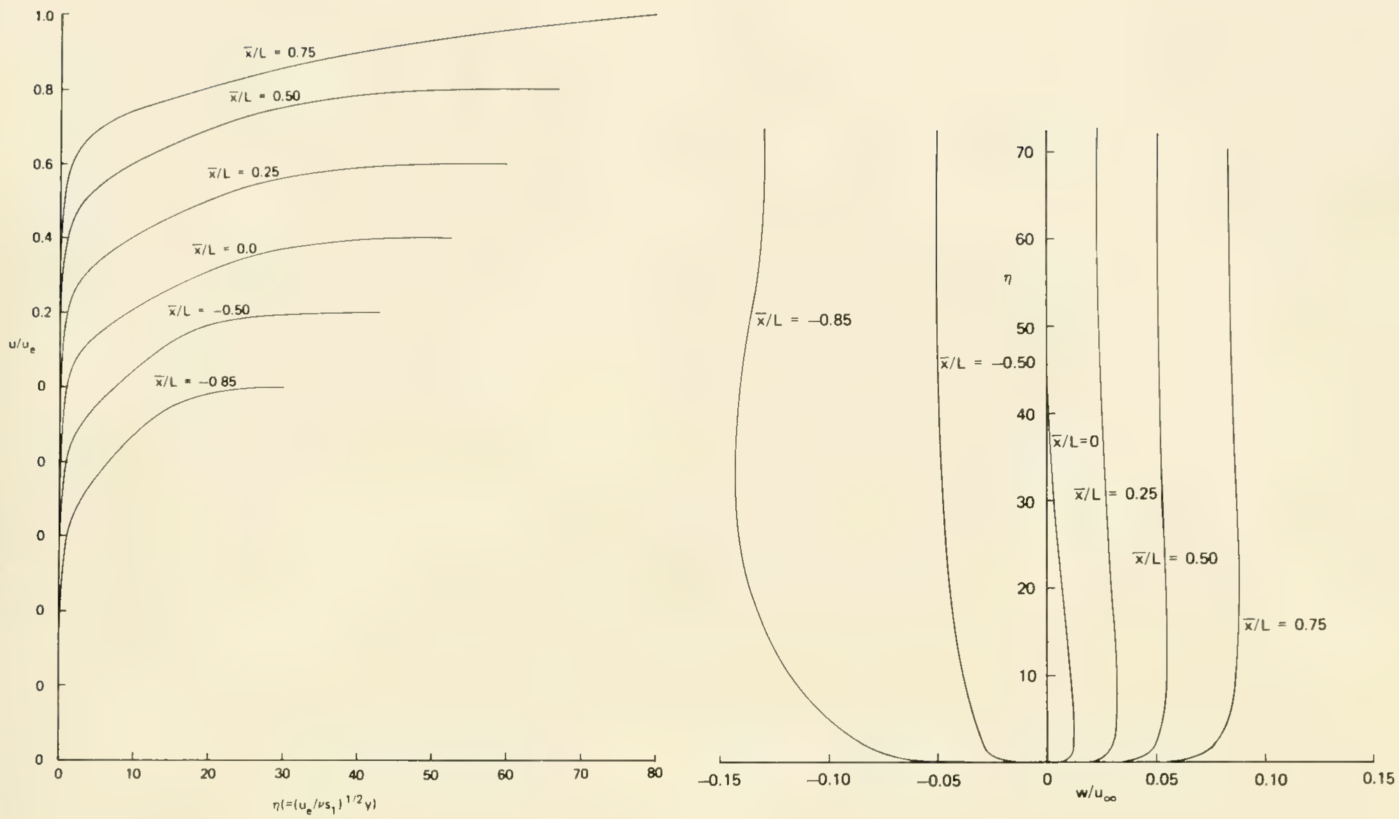

FIGURE 17. Computed longitudinal and transverse velocity profiles for the double-elliptic ship model for $R_L = 10^7$ at $z = 0.6$.

is favorable and then later becomes adverse. The pressure gradient in the transverse direction decreases rapidly from the keel to a minimum value and then increases continuously up to the free surface. Due to this rapid pressure variation in the bow region, preliminary boundary-layer calculations showed flow separation and required an approximate procedure to generate the solutions for $x < 22.5$ m. After that ($x > 22.5$), the three-dimensional boundary-layer calculations were performed for a given inviscid pressure distribution. The initial conditions at $x = 22.5$ m were generated by solving the boundary-layer equations in which the z-wise derivatives for a constant z were neglected.

Figures 23 to 25 show some of the computed results for $R_L = 3 \times 10^8$. Figure 23 shows the variation of c_p, c_f, R_θ, H_{11}, and β_w at the cross-planes of $x = 30$ m, 105 m, and 210 m. Typical streamwise velocity profiles at $x = 105$ m and $z = 0.2$ are shown in Figure 24 and typical crossflow velocity profiles at $x = 60$ m are shown in Figure 25. As can be seen from these figures, the crossflow velocity profiles show great variations and indicate clearly the flow reversal that takes place in the crossflow plane. This implies that differential methods based on two-dimensional and/or small crossflow approximations as well as methods based on integral methods are not adequate to boundary-layer calculations on ship hulls. Other interesting results that emerge from these calculations are the sudden jumps of the limiting crossflow angle from positive to negative, and the thickening of the boundary layer in the corner region of the crossplanes. The jumps of the crossflow angle indicates the convergence of the flow from

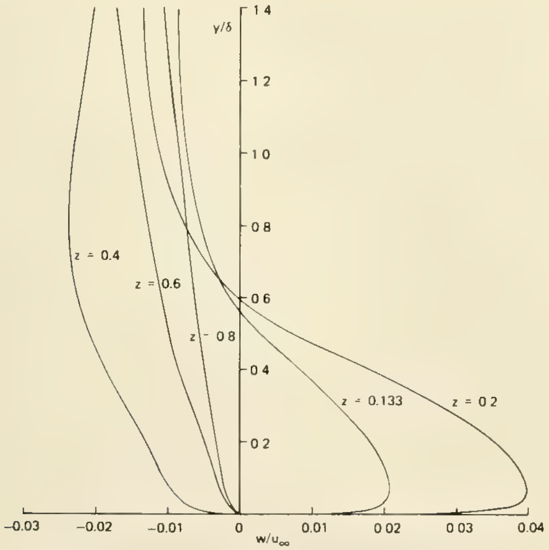

FIGURE 18. Computed transverse velocity profiles.

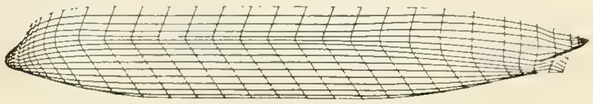

FIGURE 19. Three-dimensional view of ship model 5350 with the nonorthogonal coordinate system.

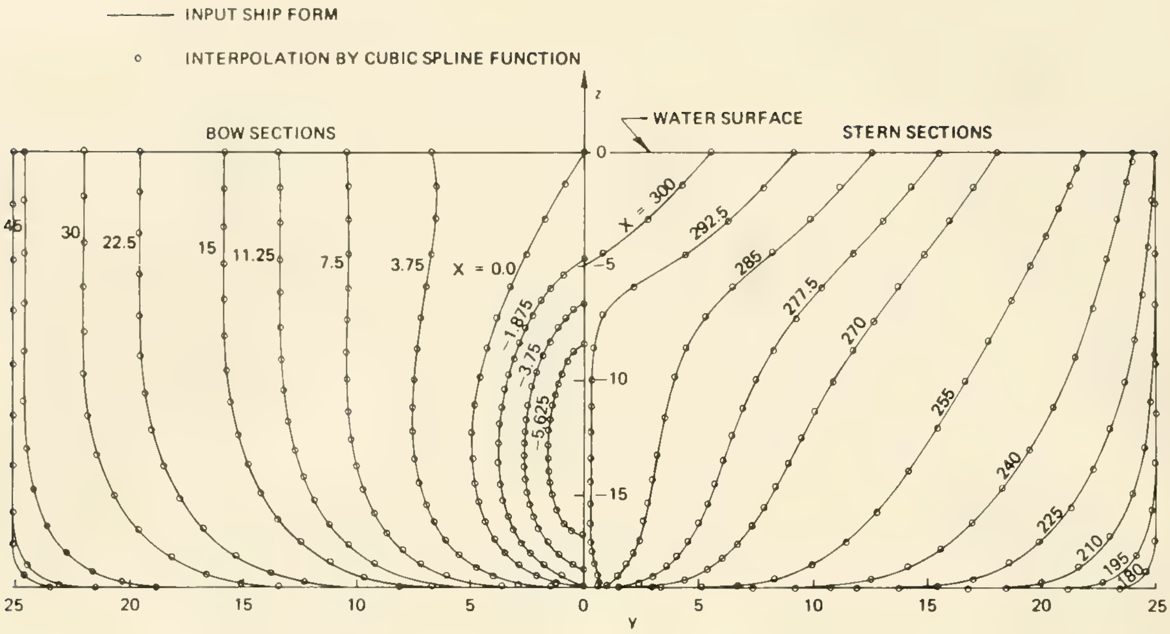

FIGURE 20. Body plan for ship model 5350.

both sides of the corner region and, hence, enhances the thickening of the boundary layer. This thickening of the boundary layer in the corner region of ship hulls has been verified experimentally by Hoffmann (1976).

6. CONCLUDING REMARKS AND FUTURE WORK

According to the studies presented in this paper, the three-dimensional boundary layers on ship hulls can be computed very efficiently and effectively. The turbulence model, as in two-dimensional flows, again yields satisfactory results for three-dimensional flows. This has been demonstrated by Soejima and Yamazaki (1978) who also have applied the present turbulence model to compute three-dimensional boundary layers on ship hulls. However, there are additional studies and problem areas that need to be considered and investigated before the present method can become a more effective tool to design ships. They are briefly discussed below.

Generation of Initial Conditions on Arbitrary Bow Configurations

In Section 5, we presented calculations for the ship model 5350 and mentioned that due to flow separation in the bow region, we had to start the boundary-layer calculations at some distance away from the bow. Additional studies are required to generate the initial conditions on the bow. These studies can lead to a better design of bow configurations and to better handling of bilge vortices, which contribute to the total drag of the ship. However, this is by no means an easy task. Consider, for example, the ship model 5350 discussed earlier. A sketch of the bulbous nose with a plausible inviscid streamline distribution is shown in Figure 26. We assume that the ship is symmetrical about the keel plane and there is a nodal attachment point on the bulbous nose at B. If the ship is floating, then the water line is determined by conditions of constant pressure and zero normal velocity. Hence the intersection A of the plane of symmetry with the water line and the

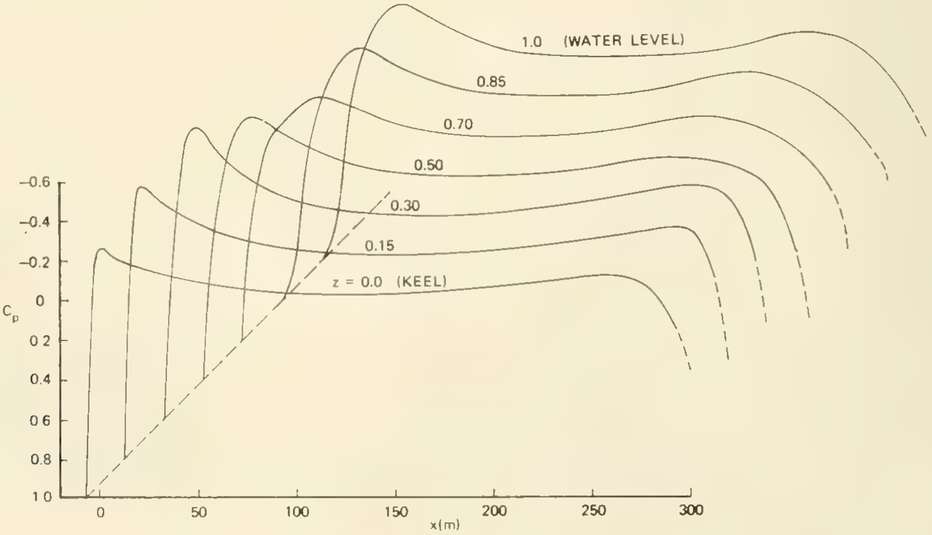

FIGURE 21. Pressure distribution for the entire ship model 5350.

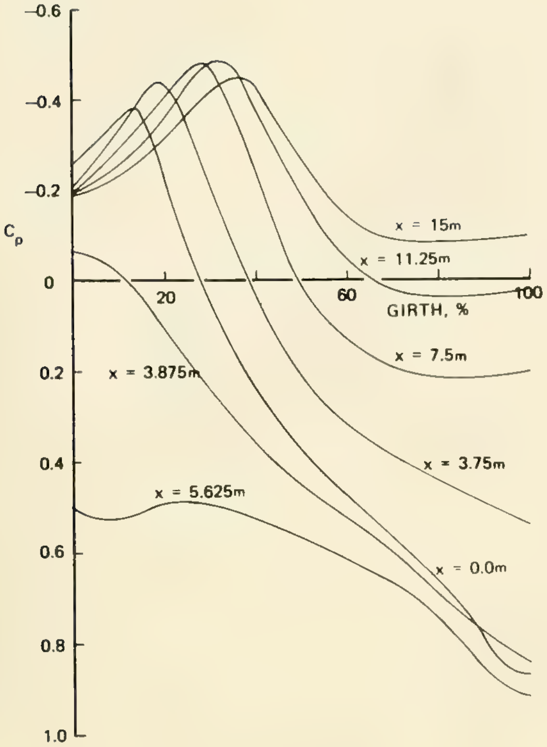

FIGURE 22. Pressure distribution for the bow region of ship model 5350.

bow is a saddle point with the streamlines of the inviscid flow converging on A along the line BA and diverging along an orthogonal direction. It is known that the boundary-layer equations can always be solved at B but that at A the situation is more complicated and furthermore it is still not entirely clear what their role is in relation to the general solution. It is likely, however, that provided no reversed flow occurs at A in the component of the solution along the direction BA, then separation can be avoided along this line by appropriate choice of design. Furthermore, if separation does occur, its effect may be limited. The recently developed Cebeci-Stewartson procedure (1977), however, can be applied to the present problem but there are some hurdles to be overcome.

Of particular difficulty is the choice of coordinate system on which to compute the solution and to join it with the already well-established method downstream of CD. We have seen that in the case of the prolate spheroid (see Cebeci, Khattab, and Stewartson (1978)) it is helpful to have a mesh which is effectively Cartesian near the nose and the methods which were used to produce it in the earlier study are applicable to any body which can be represented by a paraboloid of revolution in the neighborhood of the nose. Now here we have a paraboloid near B but not one of revolution, but we believe that the necessary generalization is possible. The mesh now has to match with that which has proved convenient downstream of CD. Again we believe that a smooth transition can be achieved by building into the mesh sides, right from CBA, an appropriate spacing such that the points of a uniform mesh on CD are also points of this mesh although not, of course, at a constant value of one of the coordinates. Our evidence for this is based on a successful scheme that we have already worked out for the prolate spheroid, Cebeci, Khattab, and Stewartson (1978).

Other aspects that need further study include the condition at the water-line section. It has been usual to assume that the normal velocity is zero at the undisturbed free surface. This is not quite correct and the error may have implications for the nature of the solution near A and especially the question of separation along BA. Even if separation does occur, it may be possible to handle the post-separation solution, since it probably extends only over a limited region of the ship, by means of an interaction theory, i.e., modifying the inviscid flow by means of a displacement surface.

Viscous-Inviscid Flow Interaction

The present boundary-layer calculations are done for a given pressure distribution obtained from an inviscid flow theroy. In regions where the boundary-layer thickness is small, the inviscid pressure distribution does not differ much from the actual one; as a result, the boundary-layer calculations are satisfactory and agree well with experiment, see, for example, the papers by Cebeci, Kaups, and Moser (1976) and by Soejima and Yamazaki (1978). When the boundary-layer thickness is large, which is the case near the stern region, the effect of viscous flows on the inviscid pressure distribution must be taken into account. One possible way this can be done is to compute the displacement surface for a given inviscid pressure distribution and iterate. Such a procedure is absolutely necessary to account for the thickening of the boundary layer as was observed by Soejima and Yamazaki (1978).

Prediction of Wake Behind Ship Hulls

The present boundary-layer calculations can be done up to some distance close to the stern; after that, flow separation occurs. Since one, and probably the biggest, reason why one is interested in boundary-layer calculations on ship hulls, is the calculation of drag of the hull, additional studies should be directed to perform the calculations in the separated region and in the wake behind the ship. Recent calculation methods developed and reported by Cebeci, Keller, and Williams (1978) for separated flows by using inverse boundary-layer theory and recent calculation methods developed and reported by Cebeci, Thiele and Stewartson (1978) for two-dimensional wake flows are appropriate for these purposes.

PRINCIPAL NOTATION

A	Van Driest damping parameter, see (18b)
A_1, A_2, A_3, A_4	constants
c_f	local skin-friction coefficient in streamwise direction
C_1, C_2, C_3, C_4	constants
f	transformed vector potential for ψ
g	transformed vector potential for ϕ
h_1, h_2	metric coefficients
h_j	net spacing in η-direction
H, H_{11}	boundary-layer shape factor along streamwise direction, δ^*/θ_{11}

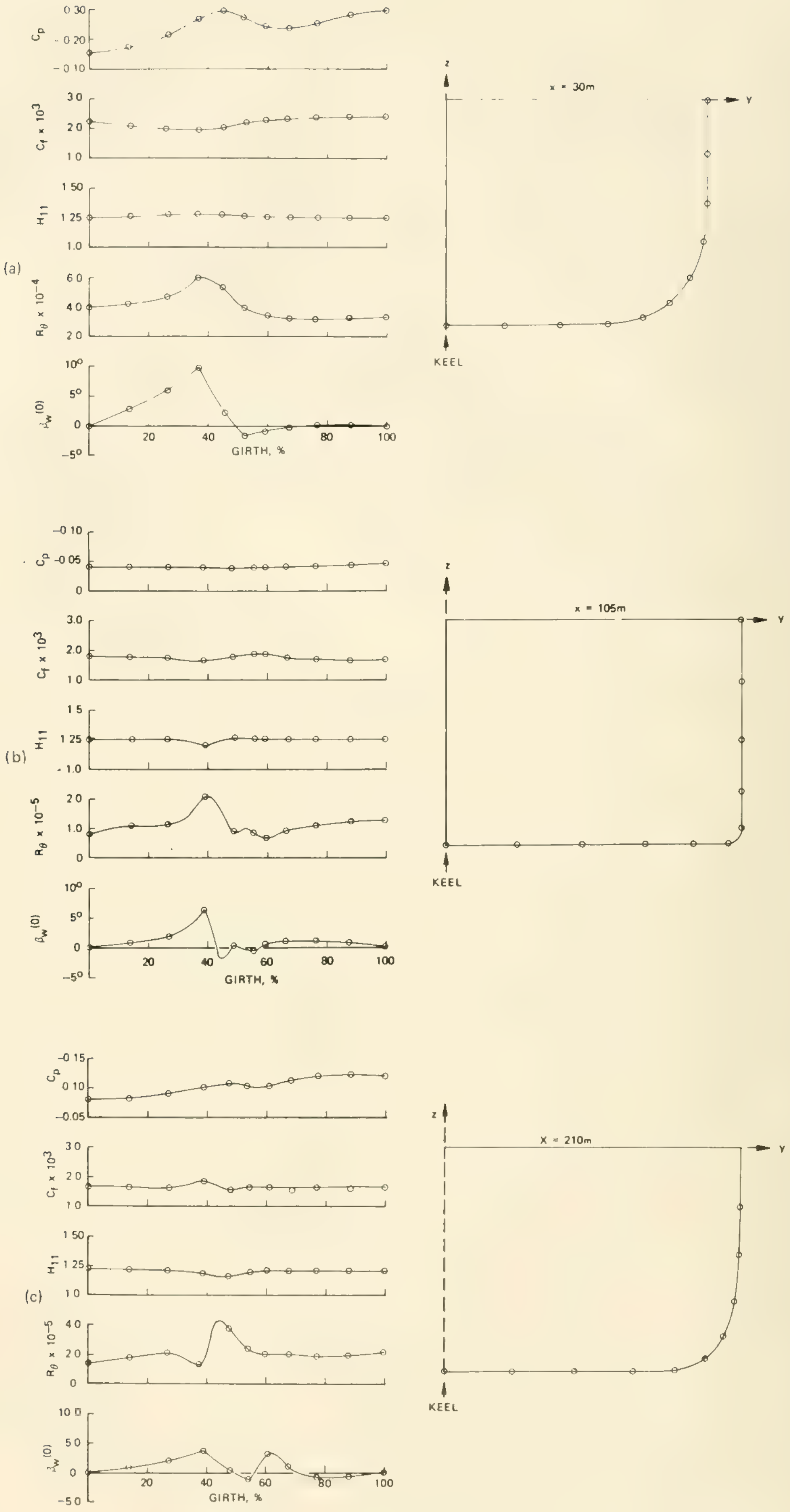

FIGURE 23. Computed c_p, c_f, H_{11}, R_θ, and β_w for ship model 5350 for $R_L = 3 \times 10^8$ at (a) x = 30m, (b) x = 105m, and (c) x = 210m.

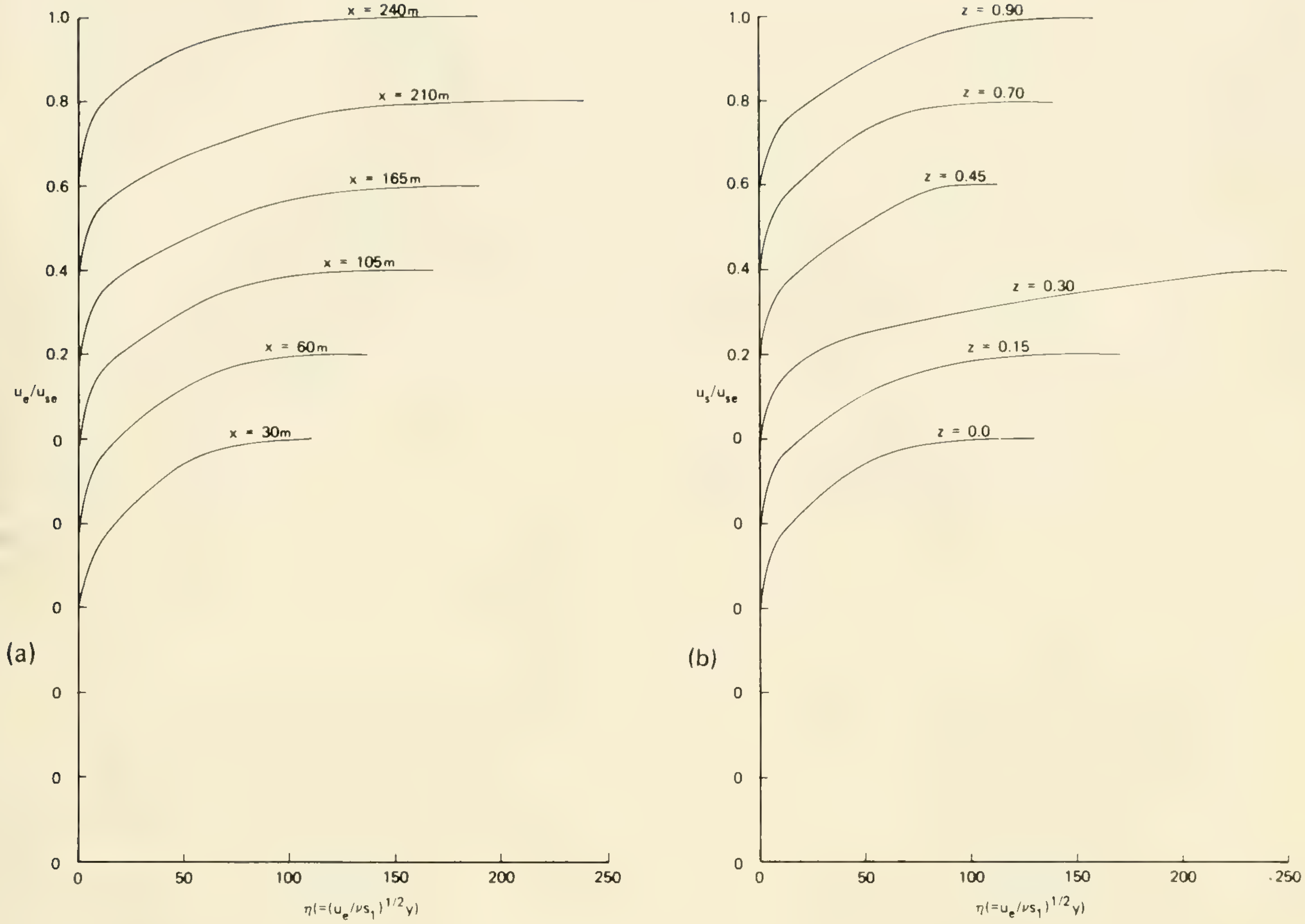

FIGURE 24. Computed streamwise velocity profiles for ship model 5350 for $R_L = 3 \times 10^8$ along (a) z = 0.2 and (b) x = 105m coordinate lines.

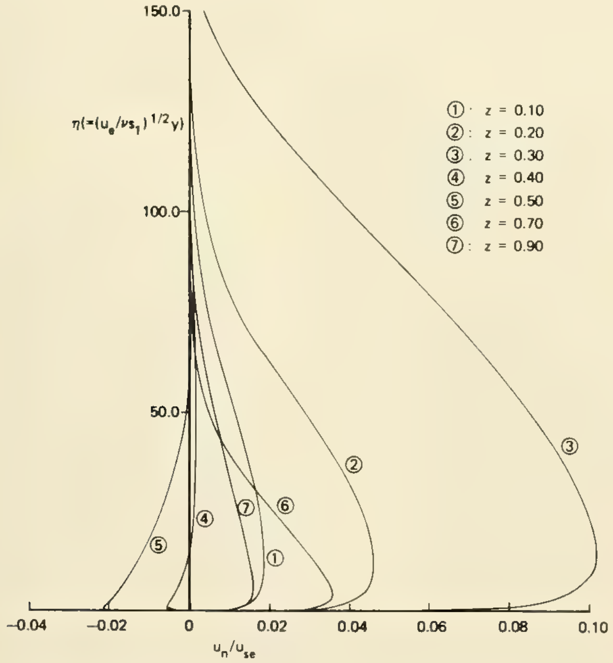

FIGURE 25. Computed crosswise velocity profiles for ship model 5350.

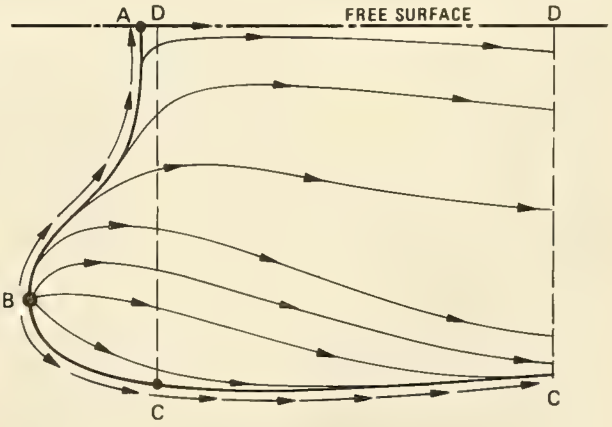

FIGURE 26. Pattern of streamlines near the bow of ship model 5350.

k_n	net spacing in x-direction
K_1, K_2	geodesic curvatures, see (5)
K_{12}, K_{21}	geometric parameters, see (6)
L	mixing length, see (18a), or reference length
$m_1, m_2, \ldots m_{12}$	coefficients, see (28) or (32)
p	static pressure
Q	total velocity in the boundary layer
R_x, R_L	Reynolds numbers, $u_e s_1/\nu$ and $u_\infty L/\nu$
R_{δ^*}	Reynolds number, $u_{s_e}\delta^*/\nu$
R_θ	Reynolds number, $u_{s_e}\theta_{11}/\nu$
s	arc length along coordinate line
$\vec{t}_1, \vec{t}_2$	unit tangent vectors along x and z directions
$u, v, w,$	velocity components in the x,y,z directions
$\bar{u}, \bar{v}, \bar{w}$	velocity components in the Cartesian coordinate
u_s, u_n	velocity components in boundary layer parallel and normal, respectively, to external streamline
u_τ	friction velocity, see (18c)
u_∞	freestream velocity
u_{ref}	reference velocity
x, y, z	nonorthogonal boundary-layer coordinates
$\bar{x}, \bar{y}, \bar{z}$	Cartesian coordinates
$-\rho\overline{u'v'}, -\rho\overline{v'w'}$	Reynolds stresses
β	crossflow angle
β_w	limiting crossflow angle
δ	boundary-layer thickness
δ^*	displacement thickness, $\int_0^\infty (1 - u_s/u_{s_e})dy$
ε_m	eddy viscosity
ε_m^+	dimensionless eddy viscosity, ε_m/ν
η	similarity variable for y, see (21)
θ_{11}	momentum thickness, $\int_0^\infty u_s/u_{s_e}(1 - u_s/u_{s_e})dy$
μ	dynamic viscosity
ν	kinematic viscosity
ρ	density
τ	shear stress
ϕ, ψ	two-component vector potentials, see (23)

Subscripts

e	boundary-layer edge
s	streamwise direction
t	total value
w	wall

primes denote differentiation with respect to η

ACKNOWLEDGMENT

This work was supported by the David Taylor Naval Ship Research and Development Center under contract N00014-76-C-0950.

REFERENCES

Chang, K. C., and V. C. Patel (1975). Calculation of three-dimensional boundary layers on ship forms. *Iowa Institute of Hydraulic Research, Rept. No. 176.*

Cebeci, T. (1974). Calculation of three-dimensional boundary layers, pt. 1, swept infinite cylinders and small crossflow. *AIAA J., 12,* 779.

Cebeci, T. (1975). Calculation of three-dimensional boundary layers, pt. 2, three-dimensional flows in Cartesian coordinates. *AIAA J., 13,* 1056.

Cebeci, T., and P. Bradshaw (1977). *Momentum Transfer in Boundary Layers*, McGraw-Hill/Hemisphere Co., Washington, D.C.

Cebeci, T., and K. C. Chang (1977). A general method for calculating three-dimensional laminar and turbulent boundary layers on ship hulls. 1. Coordinate system, numerical method and preliminary results. *Rept., Dept. of Mech. Engg., California State Univ. at Long Beach.*

Cebeci, T., and A. M. O. Smith (1974). *Analysis of Turbulent Boundary Layers*, Academic Press, New York.

Cebeci. T., and K. Stewartson (1977). A new numerical procedure for solving three-dimensional boundary layers with negative crossflow, to be published.

Cebeci, T., K. Kaups, and A. Moser (1976). Calculation of three-dimensional boundary layers, pt. 3, three-dimensional incompressible flows in curvilinear orthogonal coordinates. *AIAA J., 14,* 1090.

Cebeci, T., K. Kaups, and J. A. Ramsey (1977). A general method for calculating three-dimensional compressible laminar and turbulent boundary layers on arbitrary wings. *NASA CR-2777.*

Cebeci, T., A. A. Khattab, and K. Stewartson (1978). On nose separation, paper in preparation.

Cebeci, T., H. B. Keller, and P. G. Williams (1978). Separating boundary-layer flow calculations, paper submitted for publication.

Cebeci, T., F. Thiele, and K. Stewartson (1978). On near wake laminar and turbulent shear layers, to be published.

Gadd, G. E. (1970). The approximate calculation of turbulent boundary-layer development on ship hulls. *RINA paper W5.*

Galbraith, R. A. McD., and M. R. Head (1975). Eddy viscosity and mixing length from measured boundary-layer developments. *Aeronautical Quarterly, XXVI,* 133.

Halsey, N. D. (1977). Potential flow analysis of multiple bodies using conformal mapping. *M.S. thesis, Dept. of Mech. Engg., California State Univ. at Long Beach.*

Hoffmann, H. P. (1976). Untersuchung der 3-dimensionalen, turbulenten grenzschicht an einem schiffsdoppelmodell in windkanal. *Institut für Schiffbau der Universität, Hamburg, Bericht Nr. 343.*

Lin, J. D., and R. S. Hall (1966). A study of the flow past a ship-like body. *Univ. of Conn., Civil Engineering Dept., Report No. CE66-7.*

Miloh, T., V. C. Patel (1972). Orthogonal coordinate systems for three-dimensional boundary layers with particular reference to ship forms. *Iowa Institute of Hydraulic Research, Rept. No. 138.*

Rastogi, A. K., and W. Rodi (1978). Calculation of general three-dimensional turbulent boundary layers. *AIAA J., 16,* 151.

Soejima, S., and R. Yamazaki (1978). Calculation of three-dimensional boundary layers on ship hull forms. *Trans. West-Japan Soc. Naval Architechs, 55,* 43.

Vermeulen, A. J. (1971). Measurements of three-dimensional turbulent boundary layers. *Ph.D. thesis, Univ. of Cambridge.*

Study on the Structure of Ship Vortices Generated by Full Sterns

Hiraku Tanaka and Takayasu Ueda
Ship Research Institute
Tokyo, Japan

ABSTRACT

Many attempts have been made to measure the vorticity distribution of vessels tested at the Ship Research Institute. This led to the successful development of the rotor-type vortexmeter and a method for its calibration. In order to investigate the structure of the full ship stern vortices and gain an understanding of interaction of the vortices and propeller, the wake flow behind two geosim models was studied experimentally.

Using this vortexmeter, detailed diagrams of the vorticity distribution are presented for the discussion of the structure and scale effects on the stern vortices. The authors found the existence of a separating vortex sheet in the vorticity distribution and indicated that, by using the vorticity concentrated on the vortex sheet (Max. line), it was possible to simulate the original vorticity distribution. With these experimental results the relation between the vorticity distribution and the propeller performance on the geosim models was also analyzed.

1. INTRODUCTION

In recent years, the knowledge of the wake structure including stern vortices has made it essential for the ship builder to obtain a better understanding of the stern vibration with full stern forms. Nevertheless, the stern vortex characteristics such as its geometry and structure as well as the scale effect remained obscure. This situation may be partially due to the fact that the stern vortices do not cause serious problems in the resistance augmentation or in the self-propulsion factors.

To overcome this lack of detailed knowledge, systematic investigations have been made concerning the problems of full ship models with unstable propulsive performance. This research was begun in 1975 under the Research Panel SR 159 of the Shipbuilding Research Association of Japan (Chairman, Prof. H. Sasajima) which was mainly concerned with the following areas: sources of the unstable phenomenon, the unsymmetrical flows accompanying this phenomenon, and the procedure for testing model ships exhibiting this kind of phenomenon.

Throughout the Panel discussion there was great interest in the behavior of the stern vortices as the basic approach to understanding this phenomenon and this led to the request for quantitative data regarding the stern vortices. The major part of this paper was completed during the course of this Panel's activities in which one of the authors was placed in charge of developing a technique for measuring the fluctuating stern vortices. As a result of the discussions, a rotor-type vortexmeter for obtaining a detailed description of the structure of the stern vortices was adopted.

Needless to say, by obtaining an illustrative model of the stern vortices it will be possible to develop a mathematical model which will be extremely useful for understanding the flow around the full ship stern. Various vortex models have been suggested by Tagori (1966), Sasajima (1973), and Hoekstra (1977). The structure of the stern vortices can be roughly described by a stream line which, flowing upward around the bottom of the hull, separates at a separation line formed at the bilge. This flow rolls up at the boundary layer around the bilge forming a separated sheet with vorticity.

Sasajima has suggested a simplified model of conical separating sheets as shown in Figure 1-1. He assumed that the separating sheet could be described by a triangular plane with which he attempted to explain the basic character of the stern vortices. This vortex model shown in Figure 1-1 has a core enclosed with a separating line (S-S'), an attachment line (A-S') and the surface of the separating sheet. In this model it was assumed that the direction, velocity, and vorticity of the flow along this developed vortex sheet would

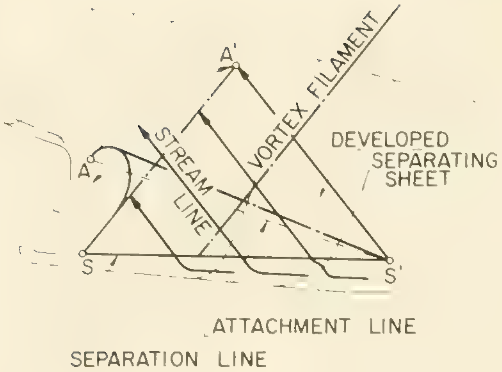

FIGURE 1-1. [Sasajima (1973)].

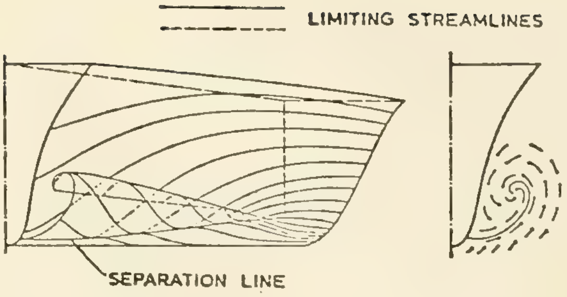

FIGURE 1-2. [Hoekstra (1977)].

Illustrative models of stern vortices

have the same values as they had at the point the flow passed on the separation line.

Hoekstra's vortex model also had a conical separating sheet with a cusp as shown in Figure 1-2. Although the stream along the separating sheet flows upward and rolls inside, it does not touch the hull surface to form an attachment line.

In addition to the study on the scale effect of the stern vortices by Huse (1977), the studies based on the theory of the three-dimensional boundary layer by Okuno and Himeno (1977) has made it possible to discuss the detailed structure of the stern vortices. However, these studies did not pay much attention to the vorticity distribution. The authors concluded through their study that the prominent features of the stern vortices could be revealed by studying diagrams of the vorticity distribution.

2. ROTOR-TYPE VORTEXMETER

Although numerous efforts have been made to investigate the stern vortices, the state of the art for measuring the vorticity distribution in aft section of a model ship remains less developed than the techniques for measuring the wake distribution. This is evident by the few papers in which the complete data of the vorticity distribution has been published. This is largely attributable to problems in developing vortexmeters for towing tank measurements.

In the authors' experience the problems in using five-hole Pitot tubes for measuring the vorticity have been in maintaining sufficient accuracy throughout the measurements. The analysis of vorticity distribution which includes finite difference methods results in insufficient precision. Besides, for one mesh point of a vorticity measurement, it is necessary to use the flow velocity data from four adjacent mesh points which makes it difficult to perform measurements close to the hull surface as well as to measure fluctuating vortex flows.

The study of stern vortices has been greatly stimulated by flow visualization developments and especially noteworthy contributions have been made by researchers using tuft grid observations. However, flow visualization for observing the vortex flow has a weak point illustrated in the following discussion.

Superimposing an arbitrary irrotational flow on a vortex flow, the resulting total flow should have the same vorticity as the original vortex. An example is shown in Figure 2 which is a velocity vector diagram of a circular vortex core superimposed on a parallel flow. Examining this figure, it can safely be said that few people would be able to estimate an exact geometry or locate the center of the vortex from only this vector diagram of the total flow (or from a photo or sketch of the tuft grid observation).

One of the authors [Tanaka (1971)] suggested adopting a rotor-type vortexmeter for towing tank measurements. He applied this technique to analyze the stern vortices generated by a submerged body running near the free surface. The application of the vortexmeter is reported in many aerodynamic investigations dating back to the 50's, and it was proposed for ship research by Gadd and Hogben [1962].

The vital problem in adopting the rotor-type vortexmeter for towing tank research lies in the accurate calibration of the rotor. This is mainly due to the fact that no one has succeeded in generating a stable vortex useful for the calibration in a steady flow field.

The rotor-type vortexmeter utilizes the principle that four-unpitched vanes mounted on a rotating shaft, shown in Figure 3, are not affected by any parallel and shear flow and only respond to a

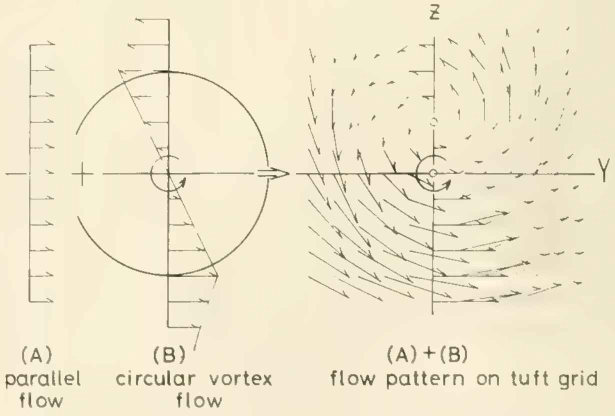

(A) parallel flow

(B) circular vortex flow

(A)+(B) flow pattern on tuft grid

FIGURE 2. Tuft grid pattern due to a circular vortex and a parallel flow.

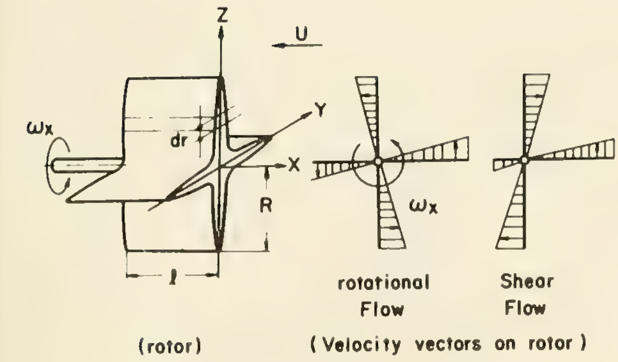

FIGURE 3. Principle of rotor-type vortexmeter.

rotational flow. When the rotating shaft of a vortexmeter is parallel with vorticity axis, the rotor turns with angular velocity of $W-S$, where S is the slip due to rotational friction of the rotor shaft and W is the vorticity in the fluid. At present, the slip S can be estimated using the following technique.

Using the simple consideration of the elementary wing, the torque Q due to a rotor element having small length dr in a radial direction can be determined from Eq. (1), where C_L, ℓ, and U are lifting derivative, cord length of vane, and advance speed respectively.

$$Q(r) = \tfrac{1}{2}\rho \ell U^2 C_{L\gamma} \frac{\omega r}{U}\, r dr \qquad (1)$$

where

$$C_{L\gamma} = \frac{\partial CL}{\partial \gamma} = \frac{\partial}{\partial \gamma} \frac{L.F.}{\tfrac{1}{2}\rho \ell R U^2} \quad ,$$

R. and *L.F.* are the rotor radius and lifting force respectively. In the flow with uniform vorticity distribution, the magnitude of the torque acting on the rotor becomes:

$$Q(\omega) = 2\int_{-R}^{R} Q(r)dr = (2/3)\rho \ell R^3 U C_{L\gamma}\omega \qquad (2)$$

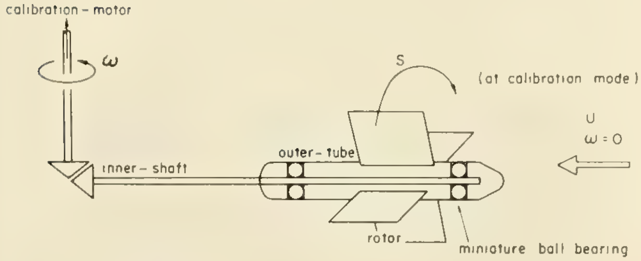

DIRECTIONS

modes	angular velocity			speed
	in fluid	rotor	shaft	
calibration	0	S	ω	U
vortex-measurement	ω	$\omega_0 = \omega - S$	0	U

FIGURE 4. Principle of rotor-type vortexmeter calibration.

Then, the slip of the rotor in a rotational flow can be determined by following equation, where q shows rotational friction of the shaft.

$$S = \frac{|q|}{(2/3)\rho \ell R^3 U C_{L\gamma}} \qquad (3)$$

For the calculation of S, the rotational friction of the ball bearings q should be determined experimentally. This problem will be briefly discussed later.

As previously stated, since the generation of a stable vortex for the calibration is presently not feasible, a mechanical calibration was attempted in which vorticities mechanically act on the rotor through the shaft of the rotor. This principle of the calibration is shown in Figure 4 where a newly designed rotor shaft is composed of duplicate inner-shaft and outer-tubes. The outer-tube is mounted on the outer rings of the ball bearings and the vanes are fitted on the outer-tube. The inner-shaft is connected to a calibration-motor.

To obtain the slip S, the vortexmeter is calibrated in an irrotational flow in which it travels along at a constant speed. The inner-shaft is driven by the calibration-motor at an angular velocity, ω, and the rotor turns at an angular velocity, S, in response to the condition of the ball bearing's frictional torque and the hydrodynamic characteristics of the rotor.

From the measured vorticity, ω_0, we can estimate the vorticity in fluid as $\omega = \omega_0 + S$. According to the authors' experience, if the frictional torque, q, is approximately 10^{-6} kg-m it is possible to consider $S = 0$ except in the case of fairly slow speed (cf. Figure 25). This means that the calibration of the vortexmeter seems unnecessary for ordinary test conditions.

Although ball bearings exhibiting frictional torque values less than $q = 0.7\ 10^{-6}$kg-m in air were chosen in manufacturing the vortexmeter, there was no direct measurement of the frictional torque of the miniature ball bearings in water. The frictional torque, q, also can be determined by measuring the torque on the outer-tube generated by inner-shaft turning in water. According to the results of these measurements, it can be said that there is hardly any difference between the frictional torque value of the bearings when they are used in water or air.

An example of a vortexmeter is shown in Figures 5 and 6. The diameter and length of the rotor are 30mm and 18mm respectively, section of the vane is lenticular shaped with a thickness ratio $t/\ell = 1/q$. A transducer for rotating the rotor is used in connection with a photo-transistor which makes 4 pulses-signals in one revolution. Assuming $C_{L\gamma} = 0.6\pi$, $q = 10^{-6}$kg-m and $U = 1.5$ m/s, it is possible to make a rough estimate of the vortexmeter's precision from the value of slip obtained by Eq. (3). From these values, the slip value, S, equals 10^{-2}r.p.s. which corresponds to 1% error relative to a normal vorticity of $\omega = 1$ r.p.s.

As will be mentioned later, the vortex cores of the stern vortex near the hull surface have a very steep gradient in vorticity distribution. Therefore, it is useful to consider the vorticity values measured by the rotor with a finite diameter at such boundaries. It is clear from the Eq.(1) that a mean value of a torque during a turn due to a wind element dr (see Figure 3) corresponds to a

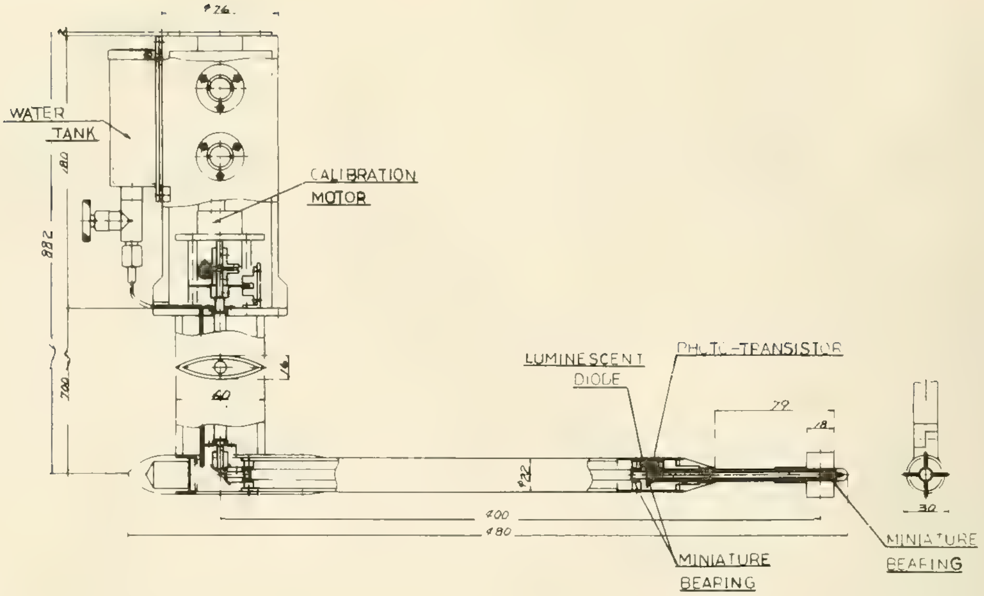

FIGURE 5. Rotor-type vortexmeter.

mean value of the vorticity in a path of a wing element.

$$\overline{Q(r)} = \tfrac{1}{2}\rho \ell U C_L \, r \, \overline{\omega(r)} dr \qquad (4)$$

$$\overline{Q(r)} = \frac{1}{2\pi}\int_0^{2\pi} Q(\theta,r)d\theta, \ \overline{\omega(r)} = \frac{1}{2\pi}\int_0^{2\pi} \omega(\theta,r)d\theta$$

On the other hand, concerning the vorticity gradient influence on the radial portion of the rotor, from the following equation it can be understood that the tip of the rotor has a higher sensitivity:

$$2\int_{-R}^{R} \overline{Q(r)}dr = \rho \ell U C_L f \int_{-R}^{R} r^2\overline{\omega(r)}dr \qquad (5)$$

In practice, using only large models, the error due to the finite diameter of the rotor can be eliminated. Such a problem is also present when determining the mesh interval in the vorticity measurement by a five-hole Pitot tube.

3. EXPERIMENTS AND RESULTS

The ship models used in the experiments exhibited an unstable propulsive performance in ballast condition. In recent studies, it has been recognized that the limiting stream line around the stern and the pressure distribution change along with the thrust fluctuation in the self-propulsion tests of the model ship. The influence of these phenomena on the ship design has been reported by Watanabe and Tanibayashi (1977) and Watanabe et al. (1972).

A special feature of this phenomenon was that it appeared only in the self-propulsion tests and was not observed on the towing tests. Thus, while this phenomenon easily appeared in the self-propulsion tests at Froude number 0.18 and 65% full displacement, at the same conditions there was no indication of this phenomenon during the tests concerned in this report. The body plan of the 4 and 7m geosim models are shown in Figure 7 and the principal dimensions are summarized in Table 1.

The intent of the experiments was twofold: first to determine the structure of the stern vortices using the rotor-type vortexmeter, and secondly, to investigate the performance of the propeller working in the presence of these stern vortices.

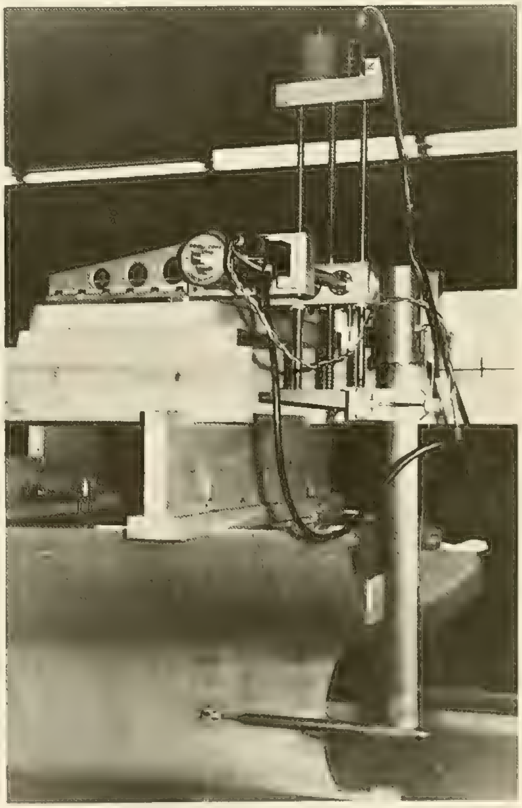

FIGURE 6. Rotor-type vortexmeter and stern of model.

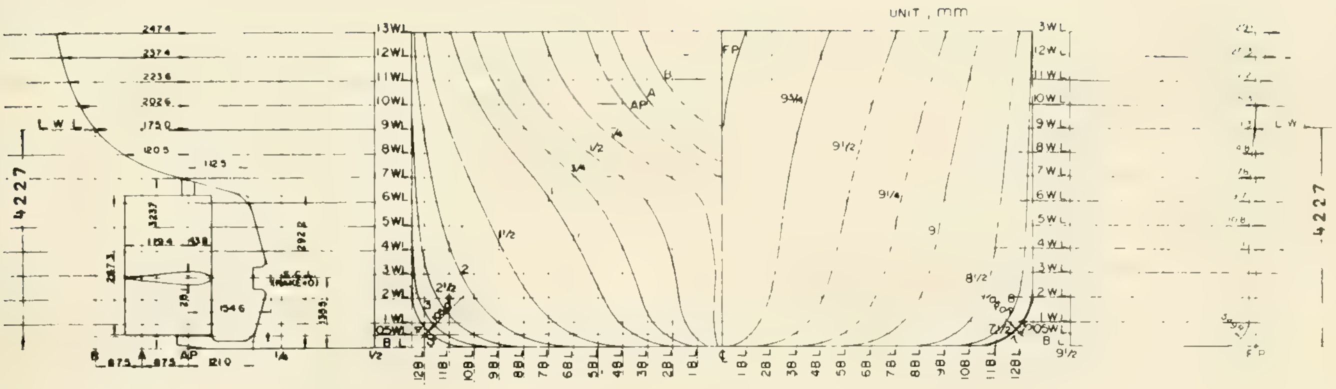
UNIT , mm
13WL
12WL
11WL
10WL
9WL
8WL
7WL
6WL
5WL
4WL
3WL
2WL
1WL
0.5WL
BL
3WL
12WL
11WL
10WL
9WL
8WL
7WL
6WL
5WL
4WL
3WL
2WL
1WL
0.5WL
BL
LWL
4227
4227
2474
2374
2236
2026
1750
1205
125
FP
AP
A
B
9 3/4
9 1/2
9 1/4
9
8 1/2
1/2
1/4
3/4
1 1/2
2
2 1/2
1
9 1/2
875
875
1210
12BL
11BL
10BL
9BL
8BL
7BL
6BL
5BL
4BL
3BL
2BL
1BL
1BL
2BL
3BL
4BL
5BL
6BL
7BL
8BL
9BL
10BL
11BL
12BL

FIGURE 7. Body plan of model.

Also as a reference, the vorticity distribution was measured by the five-hole Pitot tube for comparison with the rotor-type vortexmeter measurements

The positions where the vorticity distribution of the stern vortices was measured, are shown in Table 2 in which sq.st. 1/8 correspond with the section of the propeller disk. The effects of velocities of the model ship are studied at several mesh points.

In order to discuss the scale effect of the vorticity distribution, the results of measurements on both models are shown in Figures 8 and 9, and the induced velocity vectors on the Y-Z plane which are calculated with the vorticity distribution, are shown in Figures 10 and 11.

The interval of mesh drawn on both diagrams of vorticity distributions and velocity vectors, corresponds to a non-dimensional length of 0.5% Lpp. The values of equi-vorticity contours in diagrams of vorticity distribution are non-dimensional vortices defined as follows:

$$\xi_\chi = \frac{2\pi\omega_\chi \mathrm{Lpp}}{U} \tag{6}$$

where ω_x shows the vorticity in r.p.s. which corresponds to twice the number of rotor revolutions. Considering a diagram of vorticity distribution as a geographical contour map, the vortex core can be compared to a typical plateau. The fact can clearly be seen in the foreward detections, especially sq.st. 1/2 in Figure 12. In this connection, the vorticity distribution is sq.st. 1/4 and A are presented in Figures 13 and 14 respectively.

TABLE 1 Principal Particulars of Models

	Model Ship No.	M-7	M-4
Hull	Length (m): Lpp	7.000	4.000
	Breadth (m)	1.167	0.667
	Breadth Draft Ratio	2.760	
	Block Coefficient	0.802	
	Longitudinal Prismatic Coeff.	0.810	
Propellor	Pitch Ratio (const.)	0.7143	
	Boss Ratio	0.180	
	Expanded Area Ratio	0.665	
	Number of Blades	5	

TABLE 2 Measurement Positions of Vorticity Distribution

Model \ Sq. St.	1/2	1/4	1/8 *1	A *3
M-7	Port	Port	Port *2 Starboard	Port
M-4			Port *2 Starboard	

Notes

*1 Corresponds to propeller position
*2 Measured by vortexmeter and 5-hole Pitot tube
*3 Corresponds to Sq.St. -1/8

As a reference, the induced velocity vector diagram on sq.st. 1/4 is shown in Figure 15. Furthermore the vorticity distribution (for M.No.M-7) obtained by the five-hole Pitot tube (diameter 12mm, angle between center and side

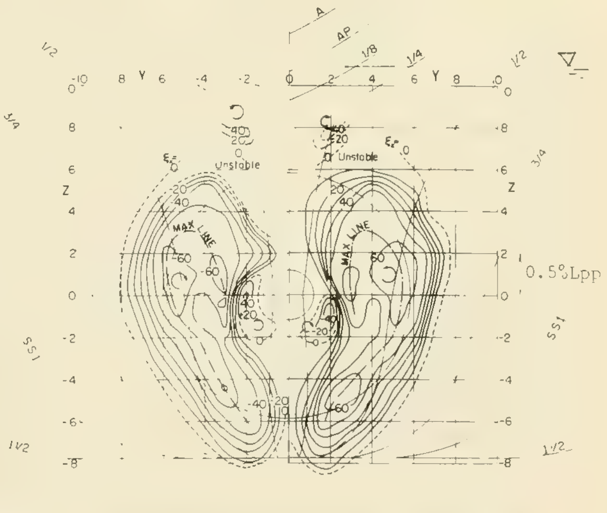

FIGURE 8. Vorticity distribution of M.No.M-7 at Sq.St. 1/8.

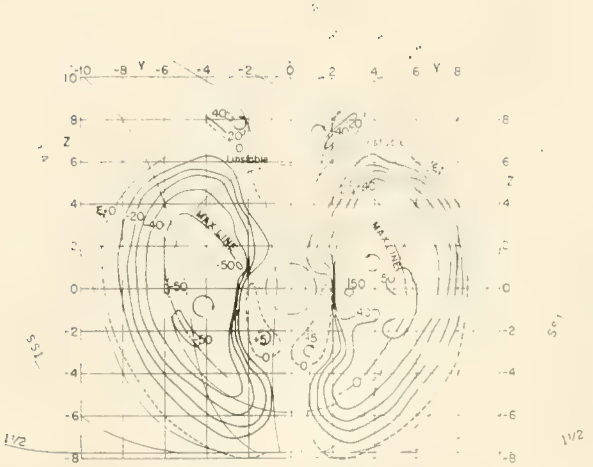

FIGURE 9. Vorticity distribution of M.No.M-4 at Sq.St. 1/8.

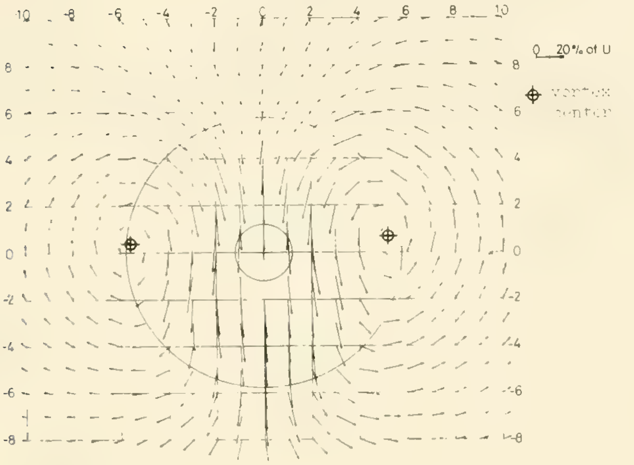

FIGURE 10. Velocity vectors on y-z plane due to stern vortices (M.No.M-7, Sq.St. 1/8).

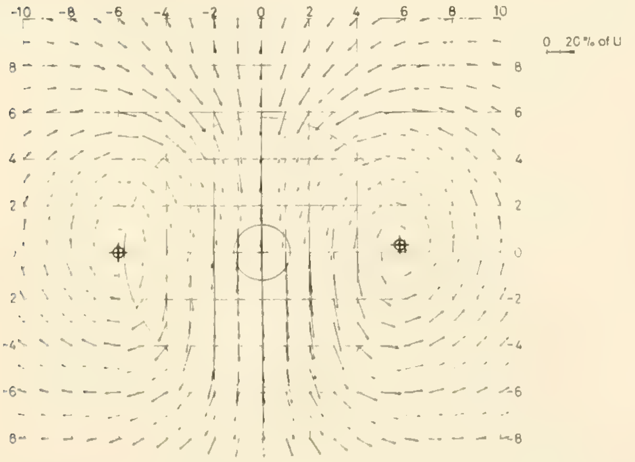

FIGURE 11. Velocity vectors on y-z plane due to stern vortices (M.No.M-4, Sq.St. 1/8).

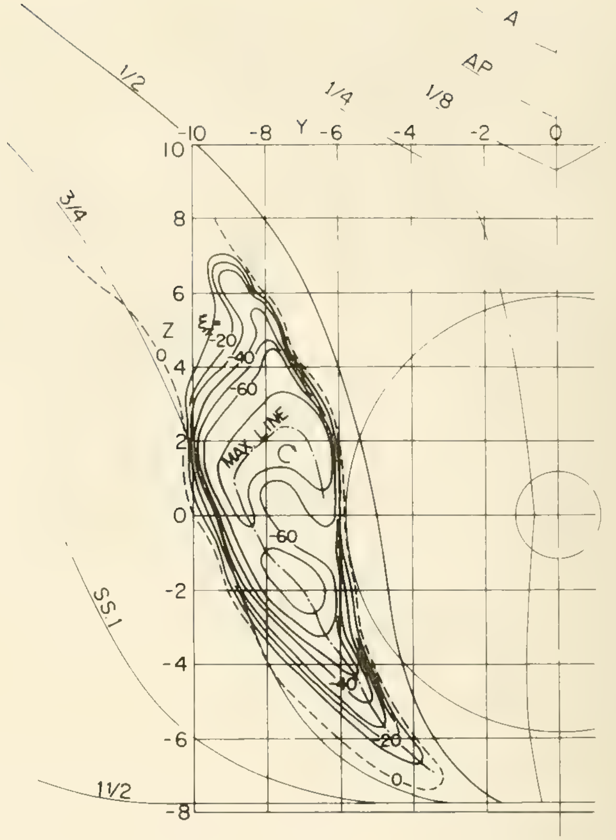

FIGURE 12. Vorticity distribution of M.No.M-7 at Sq.St. 1/2.

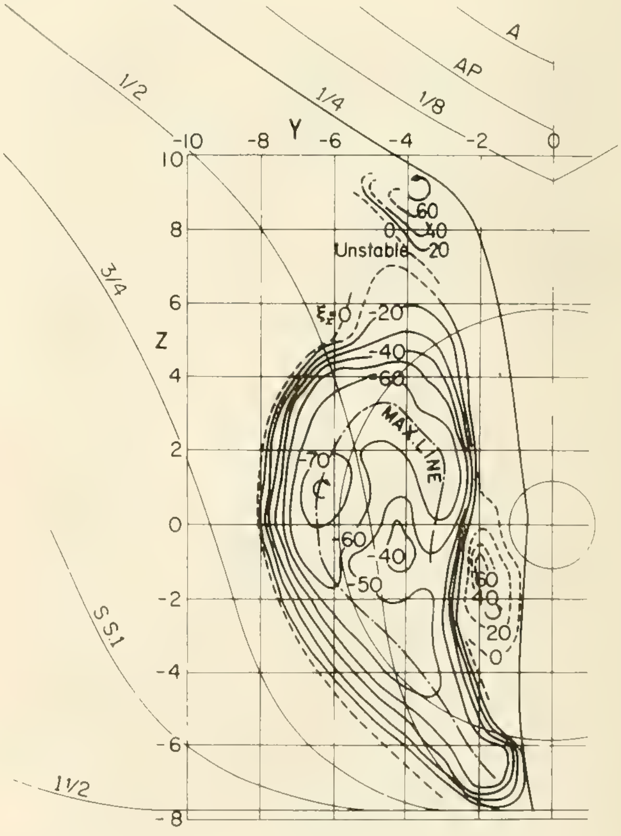

FIGURE 13. Vorticity distribution of M.No.M-7 at Sq.St. 1/4.

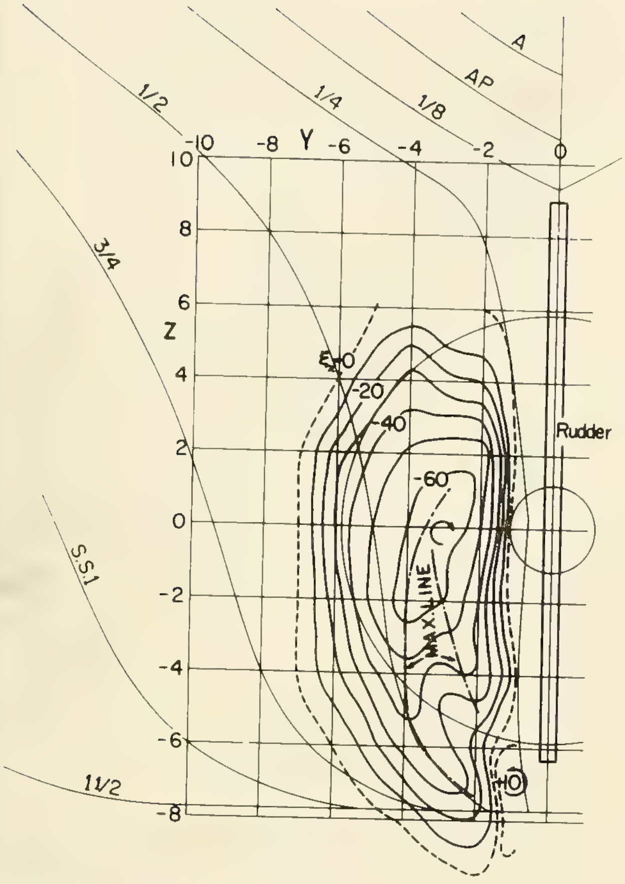

FIGURE 14. Vorticity distribution of M.No.M-7 at Sq.St. A.

holes 25°) is shown in Figure 16 and the wake distributions and the velocity vectors by the five-hole Pitot tube are shown in Figures 17, 18, 19, and 20 respectively.

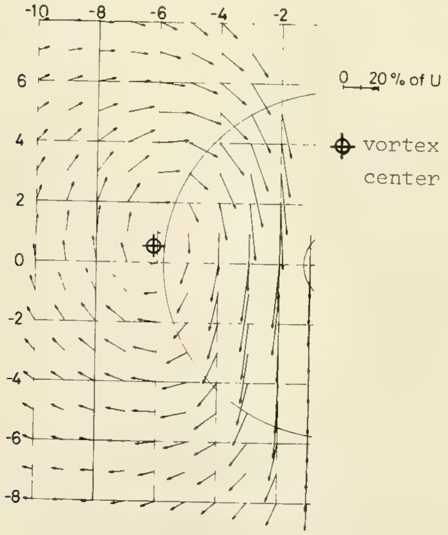

FIGURE 15. Velocity vectors on y-z plane due to stern vortices (M.No.M-7, Sq.St. 1/4).

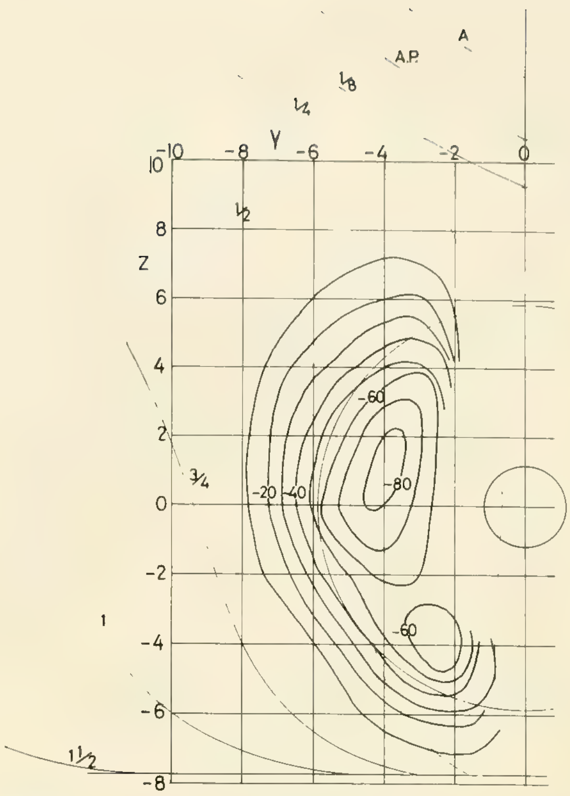

FIGURE 16. Vorticity distribution measured by 5-hole pitot tube (M.No.M-7, Sq. St. 1/8).

4. DISCUSSIONS AND APPLICATIONS OF THE RESULTS

Remarks on Vorticity Measurements

The rotor-type vortexmeter performed as expected. As seen from a comparison between Figures 8 and 16, the rotor-type vortexmeter is more sensitive and can be used to obtain a finer vorticity distribution contour than the five-hole Pitot tube. While both vorticity distribution diagrams appear to have a similar shaped vortex core, they have fairly different values. The distinguishing difference is mainly in the pattern of the distribution. Although the plateau-type distribution would be the expected form of the typical vortex cores in the vorticity distribution obtained by the vortexmeter, the plateau-type is broken in Figure 16. It can be said that the difference between these results indicate the usefulness of the vortexmeter's resolving ability.

Contrary to the general opinion that a geometry of the stern vortices is fluctuating, in the authors' measurements, the vorticity and geometry of the stern vortices were generally quite stable. However, there is an unstable vorticity-zone at the top of the main vortex core indicated in Figures 8, 9, and others. Through these experiences, it can be shown that the dynamic character of the vortexmeter is one of its prominent features.

While the present diameter of the vortexmeter's rotor was selected for maintaining its accuracy in measurement, it is possible that the rotor diameter is too large for the 4m geosim model (M.No.M-4). Furthermore, it appears that there were some

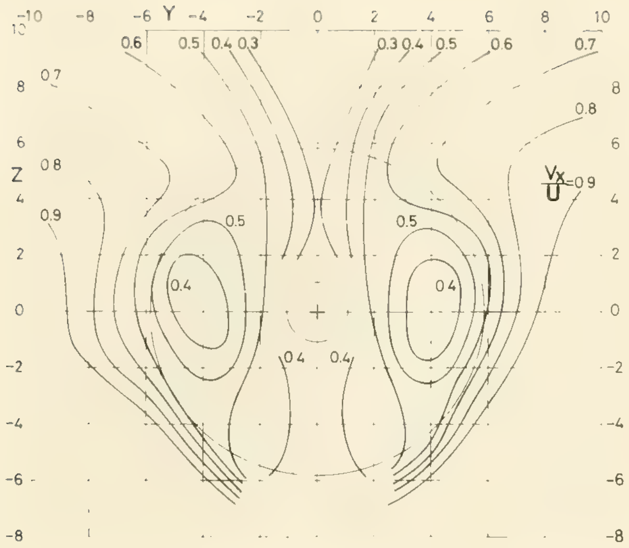

FIGURE 17. Wake distribution (M.No.M-7, Sq.St. 1/8).

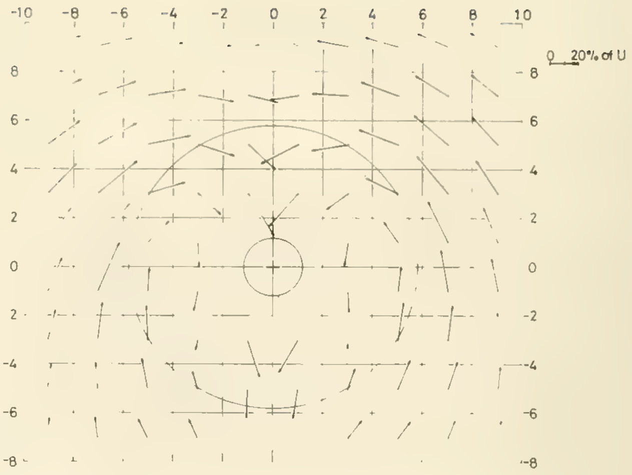

FIGURE 19. Velocity vectors on y-z plane (M.No.M-7, Sq.St. 1/8).

problems due to the presence of an oblique flow in those experiments. It is recommended in further work that the characteristics of the rotor in a strong oblique flow should be studied.

Structure of the Stern Vortices

As stated in the previous section, the equi-vorticity contours of the stern vortices can be compared with plateaus in geographical contours. Furthermore, in examining carefully the diagrams of the vorticity distribution, there is a line of concentrated vorticity on the "table of plateau," which is denoted by the "Max. line" in this paper and indicated in the contours. The Max. line can be clearly shown in a cross section of the diagrams of the contour as seen in Figures 21 and 22.

The Max. line can be considered as a kind of a ridge on this plateau; it is steep in the forward section and becomes gently sloping while shifting afterward. It is noticeable that the Max. line seems to show the existence of a separating vortex sheet. As is well known, stream lines flow from under the bottom of a hull up the boundary layer at the bilge and turn into part of the vortex sheet. Although the vortex sheet previously mentioned has only been used as a hydrodynamic description, the authors are able to show its existence in the flow behind the full stern as well as provide quantitative measurements.

The development of the vortex sheet depends mainly on the potential flow and the induced flow from the vorticity. Its development is strongly affected by each ship form, with effects of model ship velocity and the Reynolds number effect mainly limited to the diffusion of the vorticity. In a comparison between Figure 8 and Figure 9, the forms of the Max. line which correspond to a form

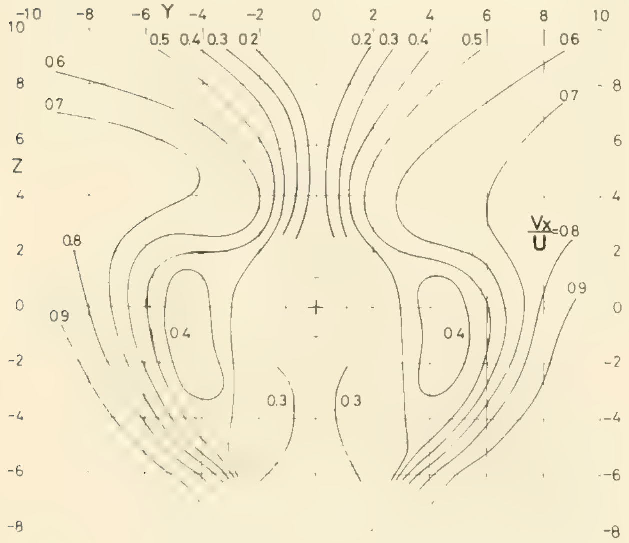

FIGURE 18. Wake distribution (M.No.M-4, Sq.St. 1/8).

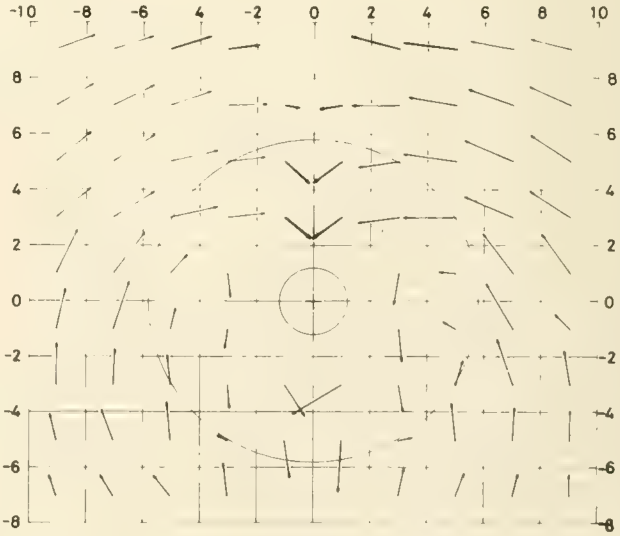

FIGURE 20. Velocity vectors on y-z plane (M.No.M-4, Sq.St. 1/8).

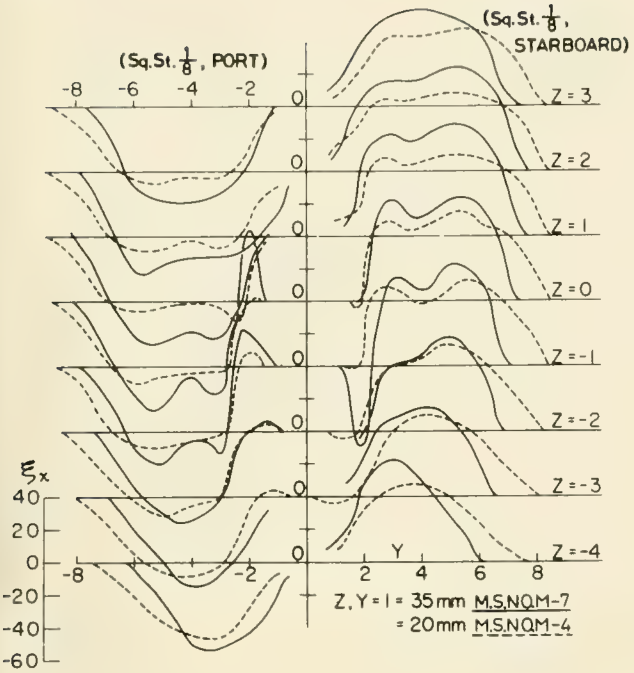

FIGURE 21. Cross section of vorticity distribution (M.No.M-7 and M-4, Sq.St. 1/8).

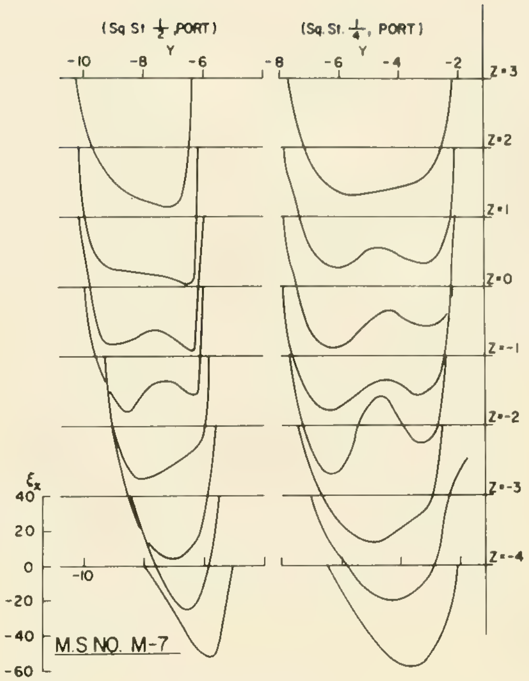

FIGURE 22. Cross section of vorticity distribution (M.No.M-7, at Sq.St. 1/2 and 1/4).

of the vortex sheet are fairly similar for both geosim models. On the other hand, the difference in breadth of each model's vortex core seems to be due to the effect of difference in Reynolds number.

Furthermore, the suitability of adopting the idea of the Max. line is shown by the following facts. Assuming that all the vorticity of the stern vortices are concentrated on the Max. line for computing the induced velocities, the resultant velocity vector diagrams are similar to the complete flow field velocity. For instance, Figure 23 is a diagram of velocity vectors, which have the same circulation value as Figure 8 but with the vorticity concentrated on the Max. line divided by ten, of circular vortices with mean strength on the original Max. line. It can be seen that both diagrams of the velocity vector, Figure 10 and Figure 23, are fairly similar. This will allow not only simplified treatment of the stern vortices but also should simplify future numerical analysis of the stern vortices.

In order to predict the wake of full stern ships, it is necessary to estimate the wake component due to the stern vortices in addition to the potential and frictional wake components used in Sasajima's wake prediction method. The concept of the Max. line in the vorticity distribution also may lead to the wake component due to the stern vortices.

In order to discuss the relation between the stern vortices and the wake distribution, an illustrative model of the stern vortices is presented in Figure 24. A stream line flowing under the bottom of a ship, separates around the bilge and forms a part of the separating vortex sheet. The vortex sheet crosses to the hull surface near the propeller bossing where the authors denote the secondary separation line. And at the secondary separation line, the vortex sheet makes the cross flow with the limiting stream line flowing aft passing through the tunnel of the vortex sheet. The crossed flow generates a reversed vortex at the secondary separation line as seen in the diagrams of the vorticity distribution.

The flow passing through the tunnel of the vortex sheet can be found at the section of the propeller disk (sq.st. 1/8) which appears as an eye in the wake distribution pattern in Figures 17 and 18. This fact may be proved by the Max. line which just covers the eye.

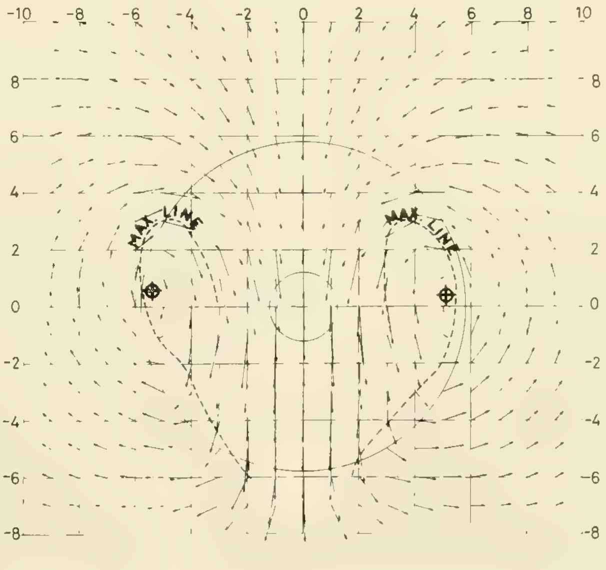

FIGURE 23. Velocity vectors due to concentrated vorticity on max. line (M.No.M-7, Sq.St. 1/8).

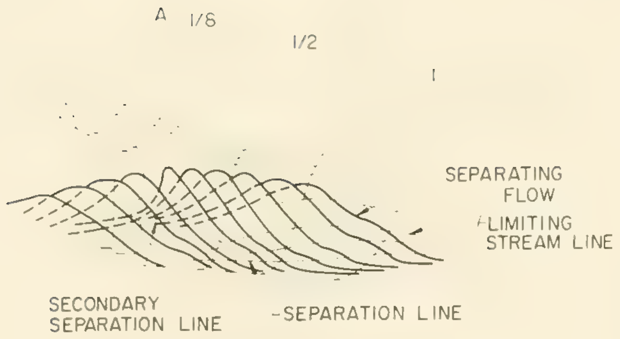

FIGURE 24. Illustrative model of stern vortices.

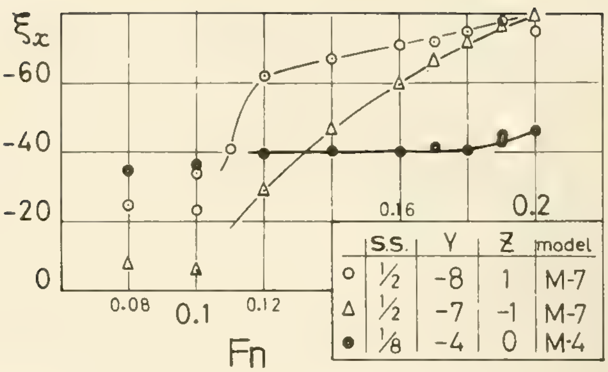

FIGURE 25. Relation between vorticity and velocity of model ship.

This tunnel vortex sheet is quite different from the conical vortex sheet used in the model proposed by Sasajima or Hoekstra. Considering the flow as passing through this tunnel makes it possible to discuss the relationships of the wake flow, limiting stream line, attachment line, and the stern vortices.

Regarding the wake patterns of vessel with a full stern, the authors suppose that if the Max. line can be considered independent of the Reynolds number, then the "eye" in the ship's wake pattern should be in approximately same location as shown in Figures 17 and 18. The above mentioned facts will lead to further studies for prediction of ship's wake, using the potential and frictional wake patterns estimated by Sasajima's method.

Actually, the authors cannot verify the relationship between the stern vortices and Reynolds number because the range of the scale ratio used in geosim models tested is too small for a discussion of the similarity of the stern vortices. However, it can be said that the alternation of the Max. line between both models seems relatively smaller than that of the wake pattern. Furthermore, the vortex center, which is defined as the vanishing point of the induced velocity vector due to the stern vortices, has shifted a distance corresponding to only 4% of the propeller diameter as seen in comparing Figures 10 and 11. While the model size has comparatively small effect on the shape of the Max. line, the model size causes differences in the diffusion of the vorticity. Thus, from the calculation of the circulation of the vortex cores presented in Figures 8 and 9, it was found that the circulation of M.No.M-4 was smaller than M.No.N-7. The magnitudes of these differences were 6% smaller on the portside and 8% smaller on the starboard side of M.No.M-7. However, even for the same model ship, the difference in the port and starboard side stern vortex circulation was on the order of 8%, so it is not possible to reach a definite conclusion about the significance of the differences in the geosim tests.

Since the authors limited study to vessel speeds corresponding to Froude number 0.18, the effects on the velocity due to the stern vortices still remains obscure. However, the authors can indicate some examples in which the vorticity has been measured at the several mesh points as seen in Figure 25. If the free surface effect could be neglected, the non-dimensional vorticity ξ_x should be constant. Although the cause of the different results explicitly shown in Figure 25 remains unknown, it may not be said that the rotor-shaft friction of the vortexmeter can be safely considered as negligible in a range of very slow speeds such as $F_n < 0.1$.

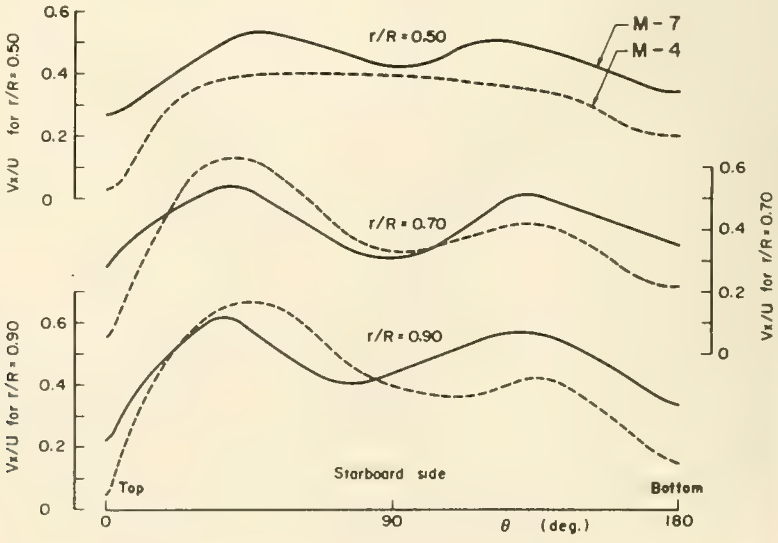

FIGURE 26. Circumferential distribution of wake flow on propeller disk, V_x/U.

Effect on Propeller Operation Due to Tangential Stern Vortex Flow

In the previous section, the authors have mainly discussed the structure of the stern vortices obtained from the towing experiments. As was reported by Hoekstra (1977) it can be considered that the structure and geometry of the stern vortices is strongly affected by the flow induced propeller thrust. However, the authors have studied the forces and moments on the working propeller as a preliminary problem, assuming the structure of the stern vortices is not changed by the influences of the propeller suction.

The forces and moments on the propeller are remarkably related to the pattern of the flow distribution at the propeller disk location. The flow distribution relevant to the present problem, is composed of the wake component, V_x/U, and the tangential components, V_T/U, which were obatained by the five-hole Pitot tube. The authors assumed that the tangential components could be further decomposed into the component obtained by the vortexmeter, V_{TV}/U, and other components. Although each component has already been shown in previous figures, for convenience the circumferential distributions of V_x/U, V_T/U, and V_{TV}/U at 90%, 70%, and 50% of the disk radius are shown respectively in Figures 26, 27, and 28. Furthermore, the authors have included the tangential velocity vector component, V_{TV}/U, in Figure 29.

In order to determine the propeller forces and moments induced by the stern vortices, the authors have performed the following calculations using the unsteady lifting surface theory developed by Koyama (1975). The authors thus calculated the thrust and torque of the propeller, along with the vertical and horizontal forces and moments imparted by the propeller shaft of the working propeller with and without stern vortex flow. The definitions concerning the forces and moments are shown in Figure 30.

The authors have assumed for the calculation that the tangential flow obtained from the subtractive procedure (V_T/U - V_{TV}/U) simulates one eliminating the effect of the stern vortices, and a common wake flow can be used for both calculations with and without the stern vortices.

Since the results of the calculation for M.No.M-4 are quite similar to the results of M.No.M-7, only the results of M.No.M-7 are shown in Figures 31 and 32. Figure 31 indicates a comparison of the torque and thrust on a blade of the propeller with and without the stern vortex flow. Total torque, thrust, and other forces and moments on the propeller (indicating propeller turning angle 0° to

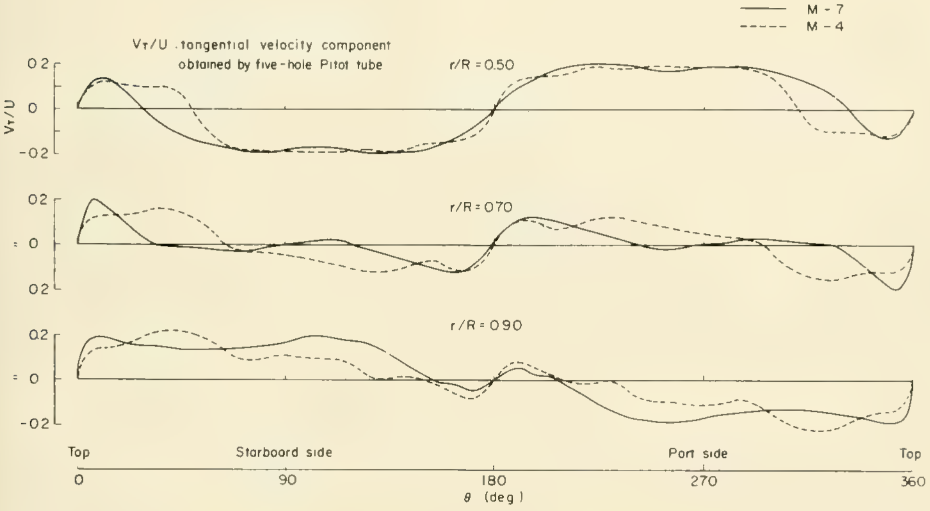

FIGURE 27. Circumferential distribution of tangential flow on propeller disk, V_T/U.

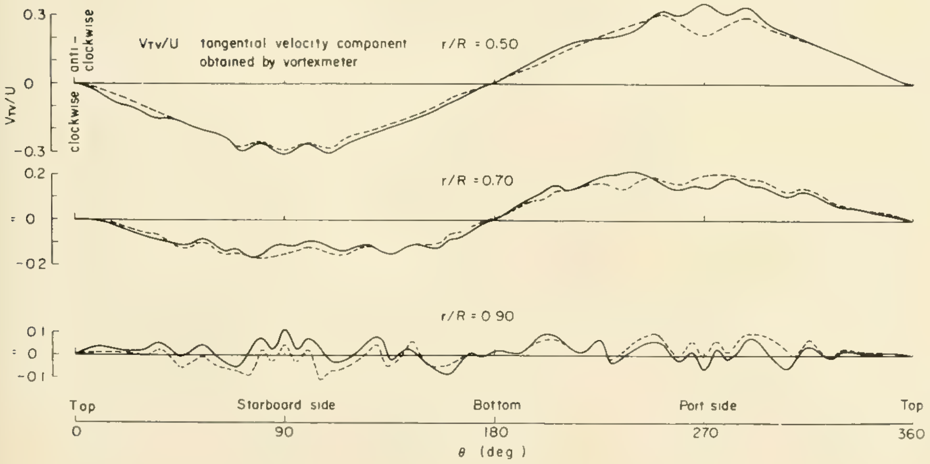

FIGURE 28. Circumferential distribution of tangential flow on propeller disk (induced flow), V_{TV}/U.

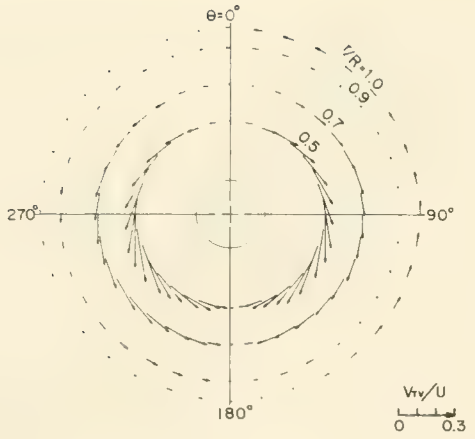

FIGURE 29. Tangential velocity vector due to induced flow on propeller disk (M-7).

72°) are shown in Figure 32. According to the results, main effects of the stern vortices flow appeared on the vertical force (F_V) and the horizontal bending moment (M_H) of the propeller, but the other components are almost negligible.

It can be concluded that the effect of the stern vortices is fairly limited to a few components of forces and moments generated by propeller. The results may be attributed to the tangential flow around the propeller caused by the stern vortices. It is mainly concentrated at the underside near the bossing, and does not severely appear on the propeller tip as shown in Figure 29.

5. CONCLUSION

The authors developed the rotor-type vortexmeter, giving careful attention to the calibration method of the vortexmeter, and, by using it in these tests, showed its high utility.

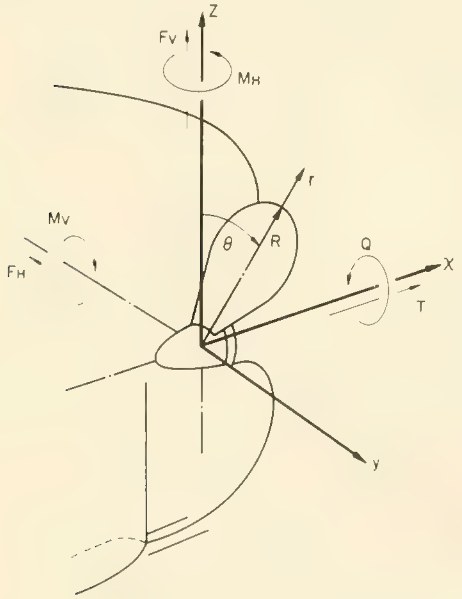

FIGURE 30. Definitions of forces and moments due to propeller.

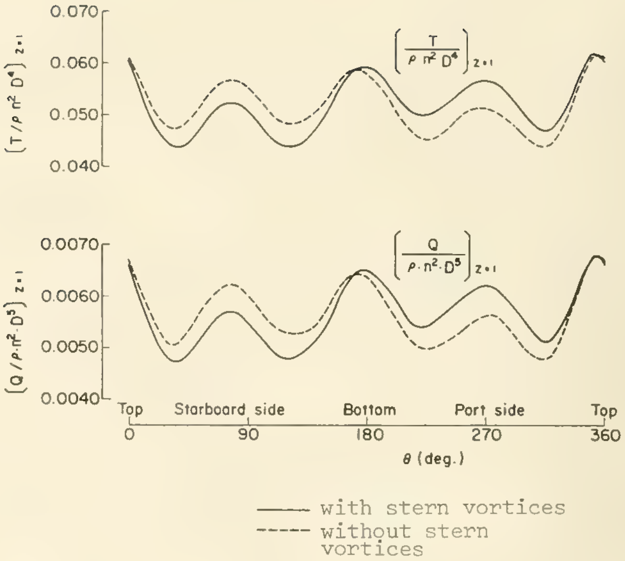

FIGURE 31. Variations of thrust and torque coefficients on one blade (M-7).

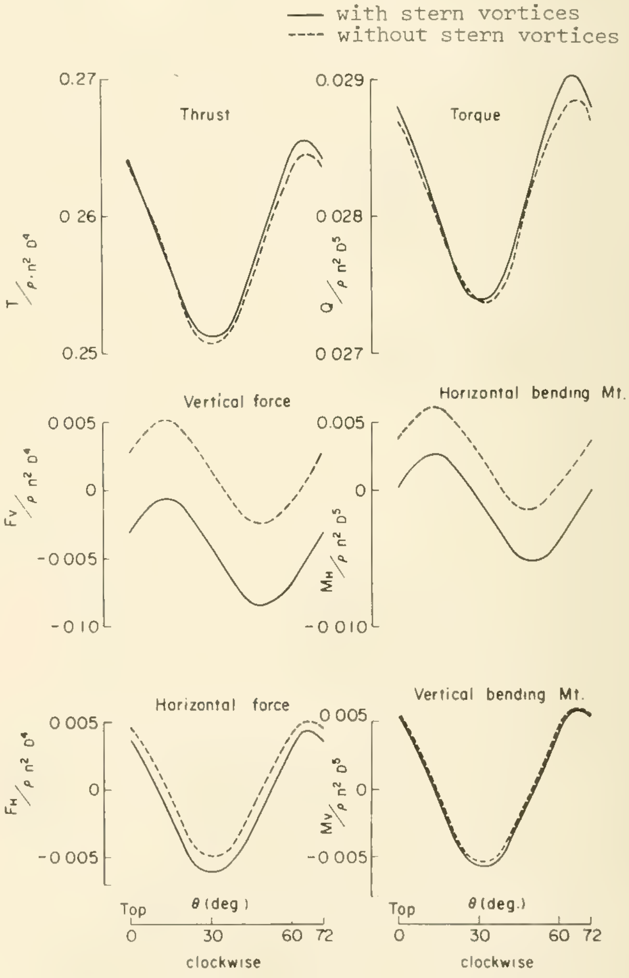

FIGURE 32. Variations of force and moment coefficients on propeller (M-7).

Measuring the vorticity distribution around the full stern of the geosim models, the authors determined the structure of the stern vortices and found the presence of a concentrated vorticity line in the vortex core which corresponds to the separating vortex sheet of the stern vortex.

As an application of the results, the effect on the propeller operation due to the induced flow of the stern vortices has been studied. The effect is fairly limited to a few components of forces and moments generated by the propeller. Consequently, it can be said that the effect of the stern vortices on the performance of the propeller and propeller excited vibratory shaft forces and moments is relatively small. However, in the case of this ship model, this effect appears to change the direction of the vertical force and the horizontal bending moment acting through the propeller shaft.

ACKNOWLEDGMENT

This research program has been carried out mainly under the foundation of the Research Panel SR 159 of Shipbuilding Research Association of Japan. The authors would like to express their appreciation to Profs. H. Sasajima and I. Tanaka, who led the Panel, for their valuable suggestions.

The materials described in the present paper have been kindly prepared by the members of the Ship Research Institute among whom the authors are especially grateful to Mr. K. Takahashi, Mr. T. Haraguchi, Mr. Z. Ishizaka, Mr. N. Sugai, and Miss H. Handa, for their helpful support.

REFERENCES

Gadd, G. E., and N. Hogben (1962). An appraisal of the ship resistance problem in the light of measurements of the wake pattern. *N.P.L. Ship Rep.* 36.

Hoekstra, M. (1977). An investigation into the effect of propeller hull interaction on the structures of the wake field. *Proceedings of Symposium on Hydrodynamics of Ship and Offshore Propulsion Systems.*

Huse, E. (1977). Bilge Vortex Scale Effect. *Proceedings of Symposium on Hydrodynamics of Ship and Offshore Propulsion Systems.*

Koyama, K. (1975). A Numerical Method for Propeller Lifting Surface in Non-Uniform Flow and Its Application. *Journal of the Society of Naval Architects of Japan, 137,* 78 (Japanese).

Okuno, T., and Yoji Himeno (1977). Distribution of Wall Shear Stress and Gross Flow in Three-Dimensional Turbulent Boundary Layer on Ship Hull. *Journal of the Kansai Society of Naval Architects of Japan, 165,* 83 (Japanese).

Sasajima, H. (1973). On scale effect of ship resistance, Text of Symposium on Viscous Resistance. *The Society of Naval Architects of Japan,* 213 (Japanese).

Tagori, T. (1966). Investigations on vortices generated at the bilge. *Proceedings of 11th I.T.T.C.,* 54.

Tanaka, H. (1975). A study of resistance of shallow-running flat submerged bodies. *Selected Papers from Journal of the Society of Naval Architects of Japan, 13,* 15.

Watanabe, K., K. Yokoo, T. Fujita, and H. Kitagawa (1972). Study on flow pattern around the stern of full ship form by use of the geosims. *Journal of the Society of Naval Architects of Japan, 131,* 9.

Watanabe, K., and H. Tanibayashi (1977). Unusual phenomenon of the stern of full ship models. *Proceedings of Symposium on Hydrodynamics of Ship and Offshore Propulsion Systems.*

Session IV

SHIP BOUNDARY LAYERS AND PROPELLER HULL INTERACTION

TAKAO INUI
Session Chairman
The University of Tokyo
Tokyo, Japan

Wake Scale Effects on a Twin-Screw Displacement Ship

Arthur M. Reed and William G. Day, Jr.
David W. Taylor Naval Ship Research and Development Center, Bethesda, Maryland

ABSTRACT

The results of a wake survey and boundary layer profile measurements on a full-scale twin-screw displacement ship are presented. The corresponding model-scale measurements are also presented. The full-scale wake measurements consist of the three velocity components which contribute to the nominal wake in the propeller plane, at four radii. The full-scale boundary layer profile was obtained at three longitudinal locations with and without the propeller operating. The model-scale nominal wake was determined in a towing tank using five-hole pitot tubes while the model-scale boundary layer measurements were made on a double model in a wind tunnel using hot wire anemometers.

In order to identify the scale effects between the model and ship, the deviation of the velocity in the propeller disk from a uniform axial flow has been separated into the velocity field due to shaft inclination in a uniform stream, the perturbation due to the hull and its boundary layer, and the viscous wake due to the appendages. The principal contribution to this perturbation from the axial flow is the effect of inclining the shaft in the uniform stream. The perturbation of the flow due to the potential flow about the hull is small, as are the effects of the displacement thickness of the boundary layer of the hull. The proposed scheme for predicting the viscous wakes of the shaft and struts meets with little success. Nevertheless, some conclusions are drawn as to how these wakes will vary between the ship and model.

1. INTRODUCTION

If unsteady propeller force and hull loading predictions are to be precise, the inflow to the propeller must be known accurately. At the present time the nominal wake of a model is measured and extrapolated to full scale assuming geometric similarity. The extrapolation fails to take into account any of the scale effects which may possibly exist between model and full scale. This paper presents preliminary results from a series of full-scale nominal wake and boundary layer velocity profile measurements on a high-speed transom-stern ship. In addition, the corresponding model-scale measurements are reported, along with a series of analytical predictions, which are intended to identify the principal contributions to the wake.

This is not the first investigation of this nature. However, it is the first project to successfully measure the three velocity components in the propeller disk of a high-speed twin-screw transom-stern hull form. The British have performed an extensive series of experiments on a frigate, [Canham (1975)], and the Japanese and Germans have performed flow measurements on several full-form ships. The Japanese and German experiments were conducted on single screw tanker forms and are reported in an extensive series of reports [see for instance: Namimatsu et al.(1973), Namimatsu and Muraoka (1973), Schuster et al.(1968), Takahashi et al.(1970), Taniguchi and Fujita (1970), and Yokoo (1974)].

While the British measurements were obtained on the ship type of interest, a high-speed transom-stern ship, only the longitudinal velocity component in the propeller plane was obtained. This resulted in the loss of the important tangential and radial velocity components. In the case of twin-screw transom-stern ships, these velocity components are generally very significant due to the inclination of the shaft to the direction of the free-stream.

The Japanese, on the other hand, were able to measure all three velocity components in the wake, but they had to make their measurements in a plane ahead of the propeller disk. Due to the full sterns of the tankers, the flow into the propeller is highly influenced by viscous effects, and as a consequence is highly affected by changes in

Reynolds number. Therefore, while treating a much more difficult problem, the results of the tanker experiments are not applicable to the scaling of the wakes of high-speed hull forms.

The full-scale velocity component ratios which are presented here were obtained at a speed of 15 knots; the corresponding Froude and Reynolds numbers were 0.36 and 4.10×10^8 respectively. The model wake survey was conducted in a towing tank at the full-scale Froude number. This resulted in a model speed of 5.22 knots, and a Reynolds number of 1.56×10^7. The full-scale boundary layer measurements were conducted at four speeds between 6.2 and 16.5 knots. These speeds correspond to Reynolds numbers between 1.7×10^8 and 4.5×10^8 respectively. The model-scale boundary layer measurements were obtained on a double model in a wind tunnel at a Reynolds number of 1.68×10^7.

Significant differences are observed between the model and full-scale velocity components, particularly in the magnitudes of the radial and tangential velocity components. These differences are in the regions away from the ship's hull and appendages; therefore, these differences do not seem to be due to Reynolds number effects. A more likely explanation is a lack of ship-model similarity, possibly due to unexplained differences in hull form or initial trim.

In order to obtain an understanding of the components which contribute most significantly to the deviation of the wake from uniform axial flow, an attempt has been made to predict the velocity components as seen by the propeller. To make this prediction, the velocity field (in shaft coordinates) was decomposed into its major components as follows:

Velocity = Uniform Stream
+ Perturbation due to Hull
+ Perturbation due to Hull Boundary Layer
+ Viscous Wake of Struts
+ Viscous Wake of Shafting

The results of this decomposition show that the inclination of the propeller shaft to the free stream is the most significant factor contributing to the deviation of the velocity from a purely axial uniform flow. In particular, approximately 70 percent of the measured radial and tangential flow is contributed by the inclination of the shaft to the uniform stream. The boundary layer of the hull is found to contribute insignificantly to the perturbation of the free stream. Although the viscous wake of the shafts and struts makes a significant contribution to the nonuniformity of the flow, the empirical technique proposed herein overpredicts the wake of the struts and underpredicts the wake of the shafting.

2. BACKGROUND

During the last ten to fifteen years there has been a marked increase in the installed horsepower per shaft on high-speed commercial and naval vessels. This increase in power has led to increased steady and unsteady forces on propellers, and increased loads on the hull surface. If adequate structural designs are to be developed for the propeller, its shafting, and the shaft supports; then the unsteady forces and moments on the propeller must be known accurately. Similarly, if the hull is to be habitable and to have minimal vibration, the structural design must adequately account for the propeller-induced surface forces. The propeller forces and surface loads can in turn only be accurate if they are determined using the full-scale flow into the propeller.

Several theories exist for predicting the unsteady forces and moments acting on a propeller in a nonuniform flow, and the hull-surface forces induced by a propeller. Tsakona et al. (1974) and Frydenlund and Kerwin (1977) report on two of the theories for the unsteady forces on a propeller; Vorus (1974) reports on a theory for predicting the hull-surface forces. In these theories, the flow into the propeller is used in conjunction with an unsteady lifting-surface theory to predict the unsteady forces on the propeller and hull as the propeller rotates through the nonuniform flow.

Typically, a propeller is wake adapted, that is, designed to the radial distribution of the circumferential mean velocity. The alternating forces are determined by considering the propeller in a nonuniform flow circumferentially. The variations of the forces and moments in the nonuniform stream from those in the uniform stream are then considered to be the unsteady forces and moments on the propeller.

The longitudinal component of the velocity in the propeller disk is the principal component of the velocity on a transom stern ship with inclined shafts. Typically the radial and tangential components vary sinusoidally around the propeller disk, and have peaks which are 20 to 25 percent of the longitudinal velocity component. However, in the process of determining the circumferential average of the radial and tangential velocity components, these components are reduced to 1 or 2 percent of the longitudinal velocity component. Because of this, the tangential velocity component contributes very little to the angle of attack on a propeller blade as computed for the propeller design. However, in unsteady force calculations, the longitudinal velocity component varies from its mean by 10 to 15 percent while the radial and tangential components vary by 1000 percent from their means. Thus the variation in the tangential velocity component contributes significantly to the changes in the angle of attack on a propeller blade as it rotates through the wake. These changes in angle of attack in turn result in the unsteady forces and moments on the propeller.

Experiments by Boswell [Boswell et al. 1976)], show that the maximum unsteady loads on the propeller occur in the area where the tangential flow velocities in the propeller disk are at their maximum. As will be seen later, it is the tangential velocity components that are in least agreement between model and full scale. It is this fact that makes the issue of wake scaling important to the accurate determination of the unsteady forces on a full-scale propeller.

3. TRIAL VESSEL AND INSTRUMENTATION

A number of criteria went into the selection of the ship on which the full-scale measurements would be made. The hull form and appendage arrangement of the ship had to correspond to that which is typical of high-speed twin-screw commercial and naval vessels. The ship had to be available for an extended period of time and a means of propelling the ship had to be available.

Of the ships which were in the U.S. Navy fleet, four classes seemed to meet the geometric criteria, and a means of propelling them could be identified. These were the Gearing Class (DD 710), Forrest Sherman Class (DD 931), Spruance Class (DD 963), and the Asheville Class (PG 84). However, of these classes, only the Asheville Class, which was being decommissioned, met the criterion of long term availability. As it tourned out, the David W. Taylor Naval Ship Research and Development Center (DTNSRDC) already had one of these ships under its control, the Research Vessel (R/V) ATHENA.

The ATHENA had the added advantage that an extensive series of model- and full-scale correlation experiments were already planned. Unsteady blade loads, stresses, and pressure distributions were going to be obtained full scale. The blade loading measurements were also going to be repeated at model scale. This blade loading data complement the full-scale wake data, and would result in some of the most complete correlation data of this type for any ship and model.

The R/V ATHENA is a twin-screw aluminum hull CODOG (COmbined Diesel Or Gas Turbine) propelled high-speed displacement ship. Formerly designated PG 94, the 46.9 meter LWL ship was decommissioned in 1975 and placed in service as a high-speed towing platform for DTNSRDC. The hull form and propulsion arrangements are similar to today's destroyers and frigates which are propelled by controllable-, reversible- pitch propellers using gas turbines as prime movers. The principal dimensions and form coefficients for R/V ATHENA are presented in Figure 1. Figure 1 also shows the body plan, and bow and stern profiles of the ship. Figure 2 shows a drawing of the propeller.

The ATHENA is equipped with two Cummins 750 V-12 diesels for low speed propulsion and a single General Electric LM 1500 gas turbine for high-speed propulsion. In the diesel mode, the ATHENA is capable of speeds of around 14 knots. Under gas turbine power, she can attain a speed of 40 knots. The ATHENA is appended with twin shafts, struts, and rudders typical of most high-speed transom stern ships. In addition, she also has two anti-roll fins located just aft of amidships.

Once the ATHENA was selected for the study of wake scaling, the question of how to propel the ship had to be resolved. The ATHENA is small enough that she could be towed by either one or two ships at speeds high enough to provide useful data, or she could be propelled on one shaft and measurements could be made on the other shaft. The two-ship tow would have been the most ideal means of propelling the ship during the experiments, because it would have allowed the ATHENA to be towed with no yaw angle, and outside the wake of another ship. However, the logistics of this option made it much less practical than propelling on one shaft.

A series of model experiments was instituted, aimed at determining whether or not single shaft propulsion could provide good course keeping ability with minimal yaw angles. Flow visualiza-

Coefficients

Scale Ratio	$\lambda = L_S/L_M$	8.25
Block Coefficient	C_B	0.48
Prismatic Coefficient	C_P	0.63
Length/Beam Ratio	L/B	7.04
Beam/Draft Ratio	B/T	3.89
Displacement/Length Ratio	Δ_L	7.15

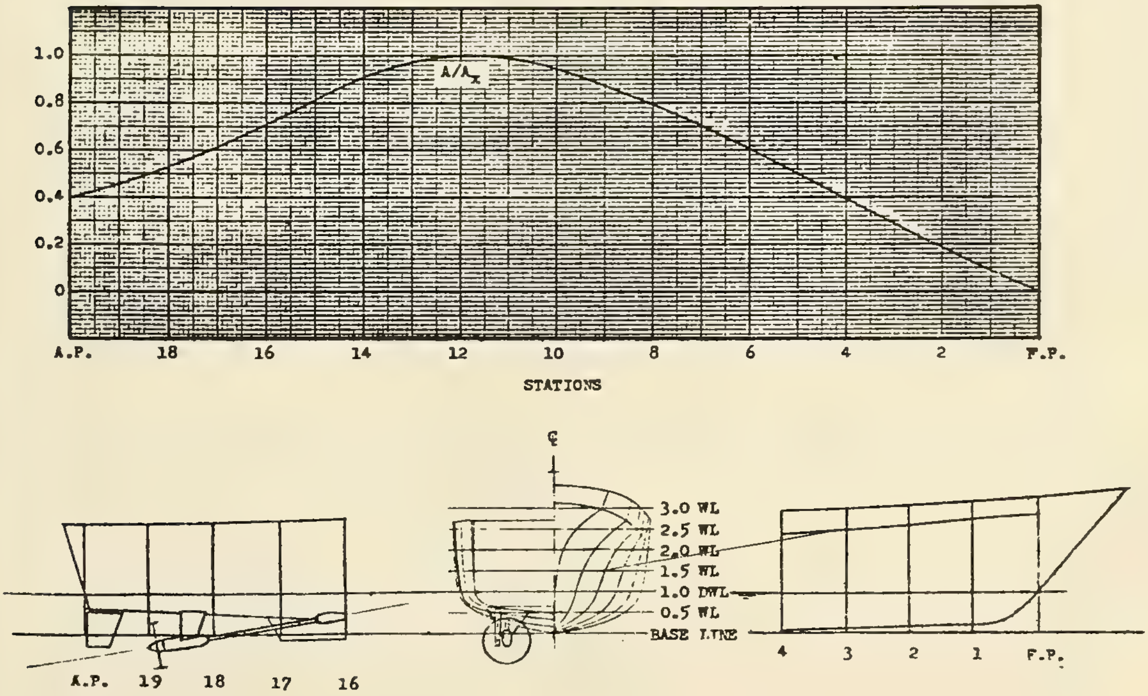

FIGURE 1.

	PROP. NO.	LINEAR RATIO	DIA. MODEL	DIA. SHIP	PITCH MODEL AT 70 PCT	PITCH SHIP AT 70 PCT.	PITCH RATIO AT 70 PCT.	NUMBER OF BLADES	EXP. AREA	E.A./D.A.	M.W.R.	PROJ. AREA	P.A./D.A.	B.T.F.	RAKE ANGLE AT TIP	ROTATION	SHIP RPM	SECTION LENGTH MODEL AT 70 PCT.
INCHES MM	4710	8.250	8.727 221.67	72.000 1828.80	9.697 246.30	[illegible]	[illegible]	4	46.358 29908.6	0.775	0.443	40.100 25871.1	0.670	0.048	0.000	R.H.	4950	4.698 119.33
INCHES MM	4711	8.250	8.727 221.67	72.000 1828.80	9.697 246.30	[illegible]	[illegible]	4	46.358 29908.6	0.775	0.443	40.100 25871.1	0.670	0.048	0.000	L.H.	4950	4.698 119.33

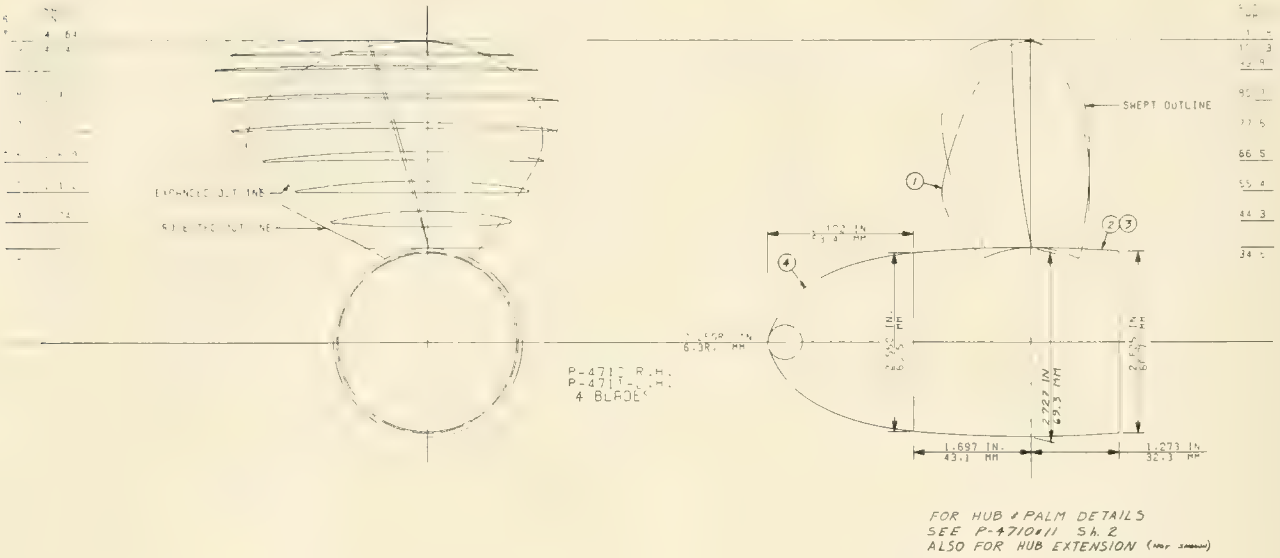

FIGURE 2. Controllable-pitch propeller geometry.

tion studies in the circulating water channel at DTNSRDC indicated that yaw angles of less than four degrees would provide satisfactory inflows to the propeller disk, and still exclude the wake of the roll fins. Subsequent self-propulsion model experiments using only one shaft, indicated that with the rudder set at one degree to port, the ship would have less than one degree of yaw and insignificant sway. Therefore, the decision was made to propel the ship on one shaft rather than to tow the ship.

The instrumentation which was installed on the ATHENA consisted of three types. Five- and thirteen-hole pitot tubes were used to determine the velocity field in the propeller plane on the starboard side, and ahead of the struts on both the port and starboard sides.* A set of eight boundary layer probes were used to measure the boundary layer profile at four symmetric locations on the port and starboard sides of the ship. Finally a piezoelectric pitot tube, a five-hole pitot tube with piezoelectric pressure transducers mounted on its face, was used to measure the time-varying flow ahead of the operating propeller.

The locations of the pitot tube rakes and boundary layer probes are shown in Figures 3 and 4. The location of the struts and the shape of the after stations are shown in Figure 5. As can be seen in these figures and in Figures 6 and 7, which show photographs of the actual pitot tube rakes mounted on the ship, two rakes of four pitot tubes each were mounted on opposite sides of the propeller hub. These rakes were attached to the crank disks for two of the propeller blades. The details of one rake with pitot tubes mounted are shown in Figure 8.

Figure 9 shows a close-up photograph of one of the full-scale boundary layers probes. These probes, which extended 0.46 meters from the hull, contained 13 pitot tubes. Ten of the pitot tubes were total head tubes, and three were Prandtl tubes.

4. CORRELATION MODELS AND INSTRUMENTATION

The model correlation experiments were performed using two fiberglass models designated DTNSRDC Models 5365 and 5366. These models, which were built to the lines of the ATHENA, had a scale ratio of 1 to 8.25; the principal dimensions of these models are listed with the ship dimensions on Figure 1. A full set of appendages including shafts, V-struts, rudders, roll stabilizer fins, and a centerline skeg were fitted to each model. Model 5365 was a ship model which was used for the correlation wake surveys performed in the towing tank to investigate the scale effects between the model and ship wake surveys. Model 5366 was a mirror image double model obtained by reflecting the lines of the ATHENA about the mean water line corresponding to a full-scale speed of fifteen knots. This model was used for the boundary layer correlation experiments which were made in a wind tunnel.

The model-scale wake survey was made on the ship model, Model 5365, using five-hole pitot tubes. The pitot tubes were mounted on a rake, the shaft of which was placed through the strut bossings and stern tube on the model. Figures 10, 11, and 12 show the model which was used for the wake surveys, and the details of the pitot tube rake mounted on the stern of the model. Two papers, one by Hadler and Cheng (1965) and the other by Hale and Norrie (1967), give a thorough description of

---

*For the details of the instrumentation design and operation see Troesch et al. (1978).

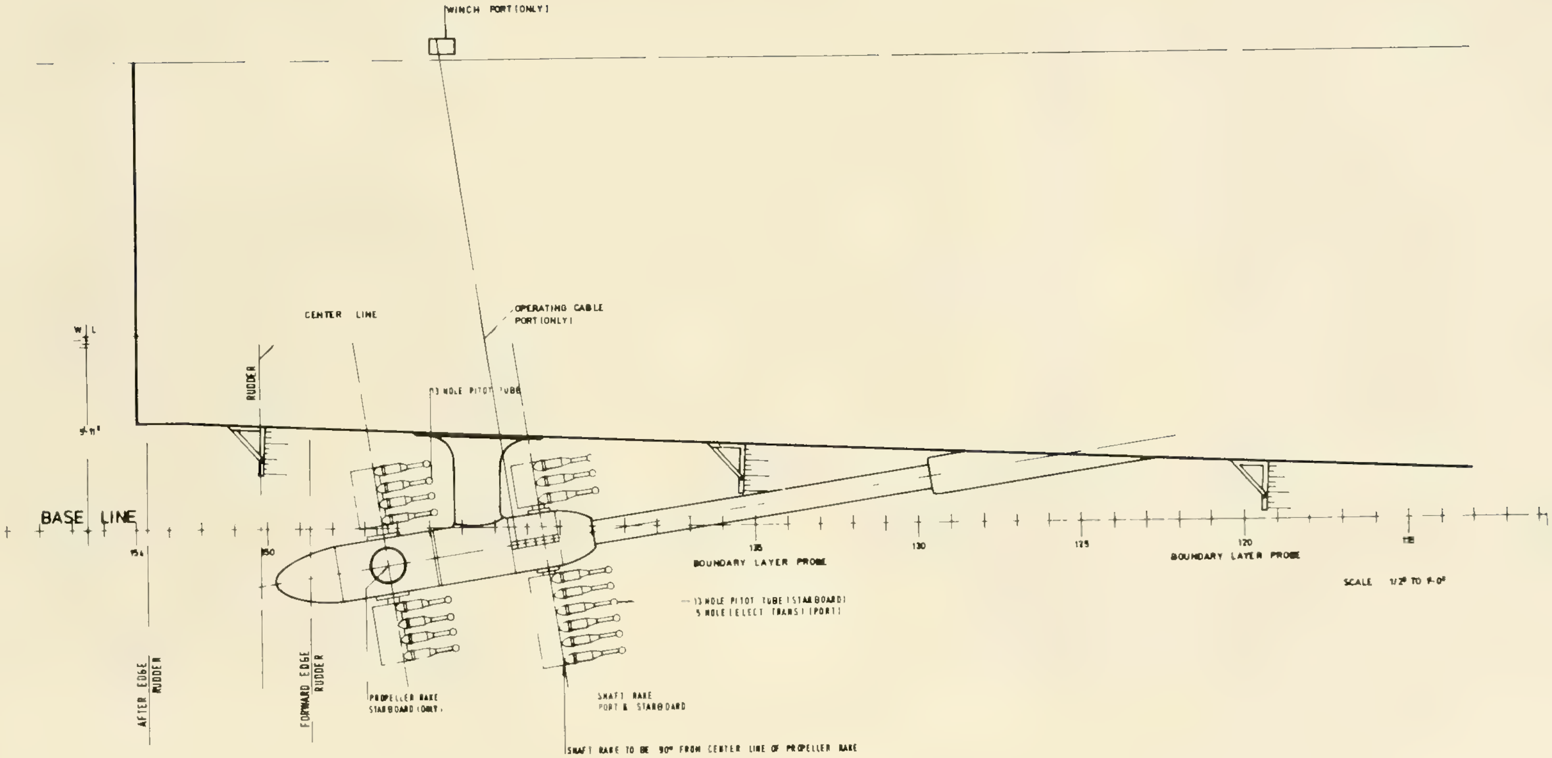
WINCH PORT (ONLY)
OPERATING CABLE
PORT (ONLY)
CENTER LINE
W L
5'-11"
RUDDER
13 HOLE PITOT TUBE
BASE LINE
154
150
135
130
125
120
115
BOUNDARY LAYER PROBE
BOUNDARY LAYER PROBE
SCALE 1/2" TO 1'-0"
13 HOLE PITOT TUBE (STARBOARD)
5 HOLE (ELECT TRANS) (PORT)
AFTER EDGE
RUDDER
FORWARD EDGE
RUDDER
PROPELLER RAKE
STARBOARD (ONLY)
SHAFT RAKE
PORT & STARBOARD
SHAFT RAKE TO BE 90° FROM CENTER LINE OF PROPELLER RAKE

NOTE: ALL PITOT TUBES 5 HOLES UNLESS NOTED.

FIGURE 3. Profile view of hull showing installation of wake rakes and boundary layer rakes.

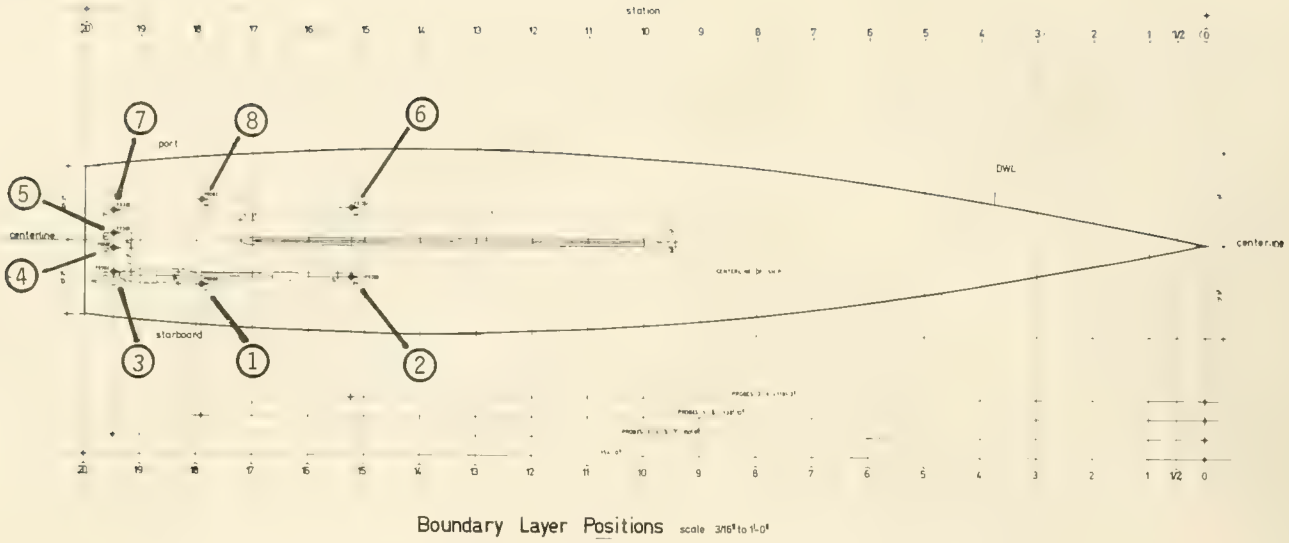
station
20
19
18
17
16
15
14
13
12
11
10
9
8
7
6
5
4
3
2
1
1/2
0
7
8
6
5
4
3
1
2
port
starboard
centerline
centerline
DWL
Boundary Layer Positions scale 3/16" to 1'-0"

FIGURE 4. Plan view of hull showing boundary layer rake locations.

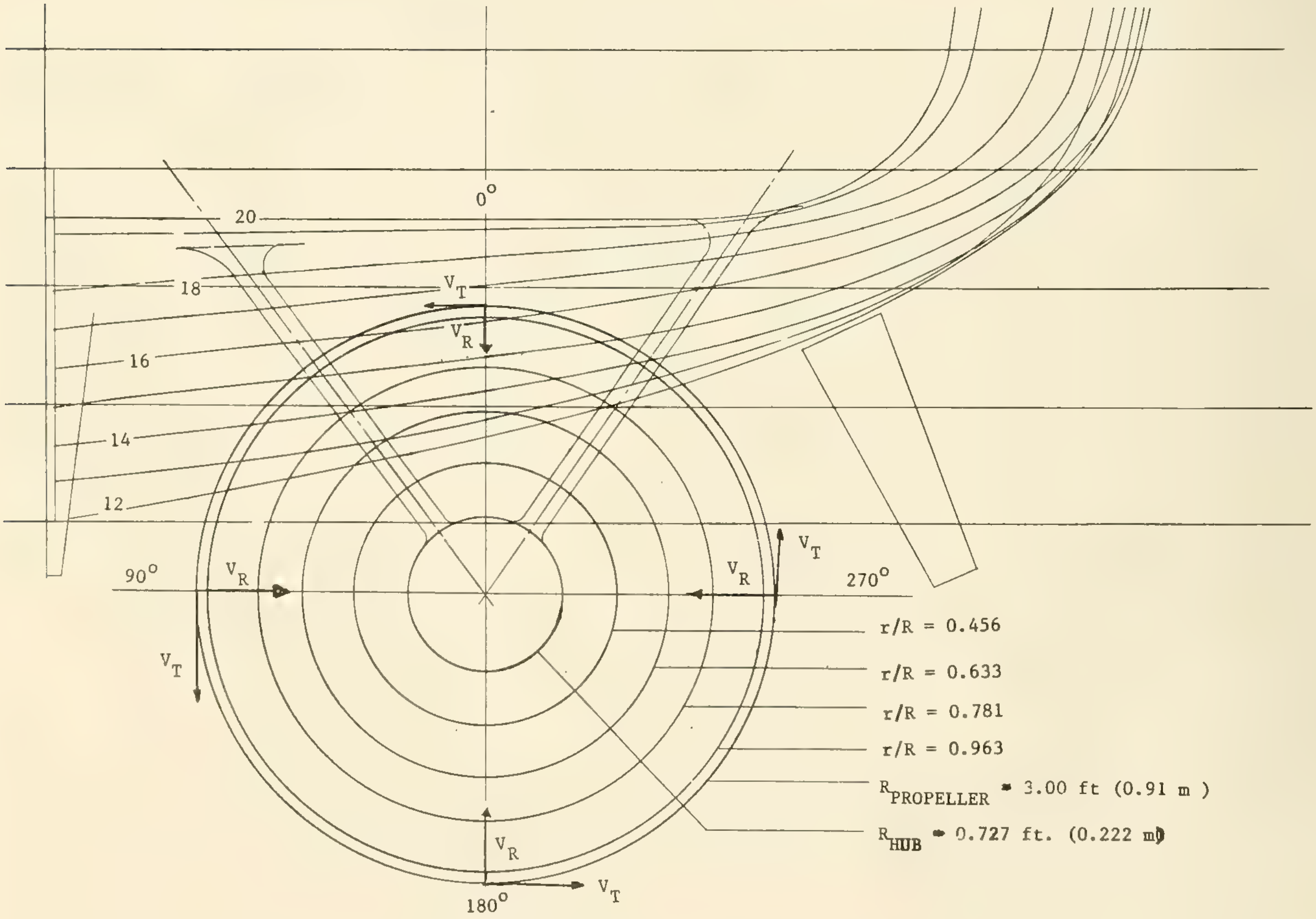
20
18
16
14
12
0°
90°
270°
180°
V_T
V_R
V_R
V_T
V_R
V_T
V_R
V_T
r/R = 0.456
r/R = 0.633
r/R = 0.781
r/R = 0.963
$R_{PROPELLER}$ = 3.00 ft (0.91 m)
R_{HUB} = 0.727 ft. (0.222 m)

FIGURE 5. Afterbody sections of ATHENA hull showing radii of wake measurements.

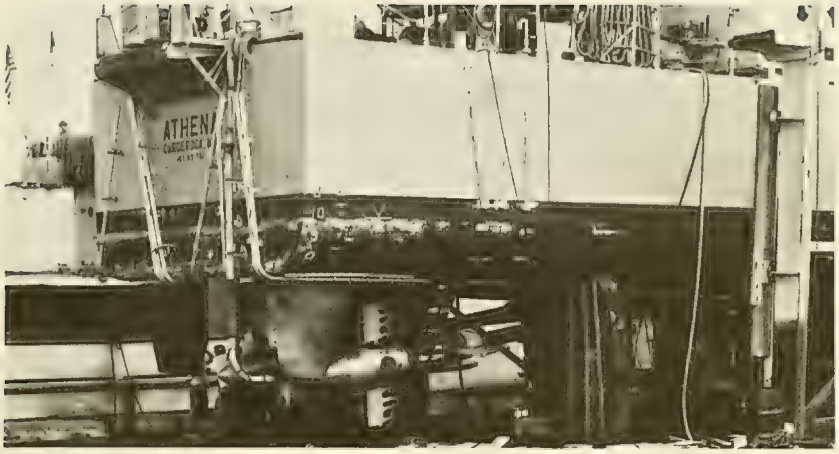

FIGURE 6. Starboard side view of R/V ATHENA in drydock.

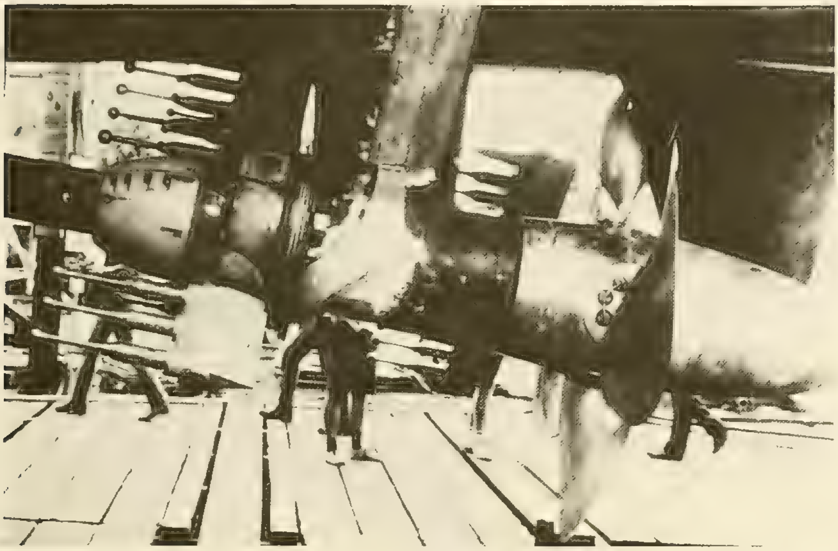

FIGURE 7. Port side wake rakes and propeller on R/V ATHENA.

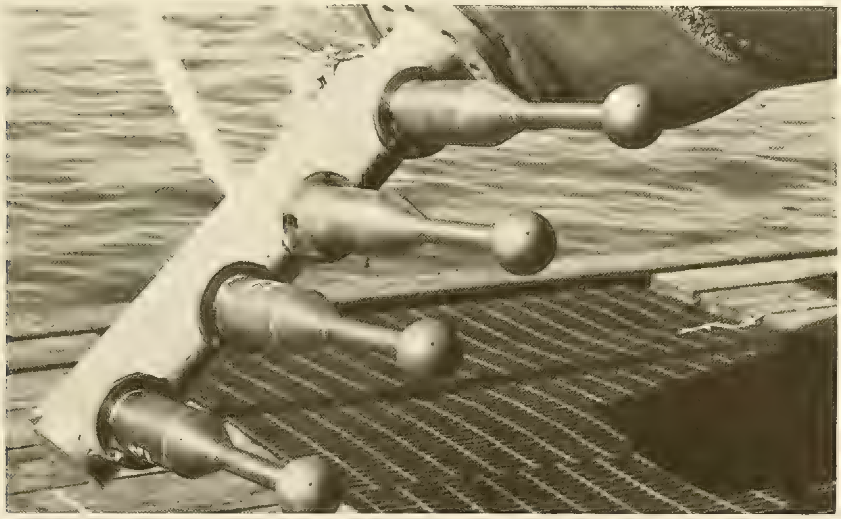

FIGURE 8. Close-up view of five-hole pitot tube rake on starboard shaft on R/V ATHENA.

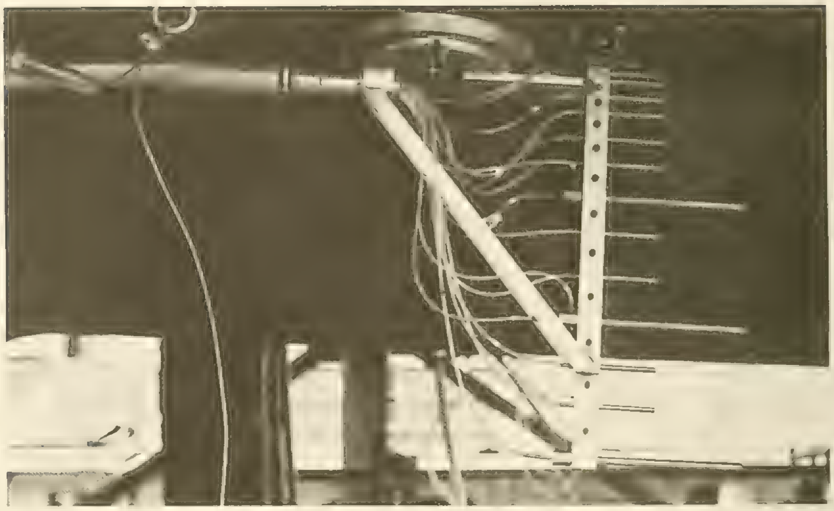

FIGURE 9. Close-up view of boundary layer rake on R/V ATHENA.

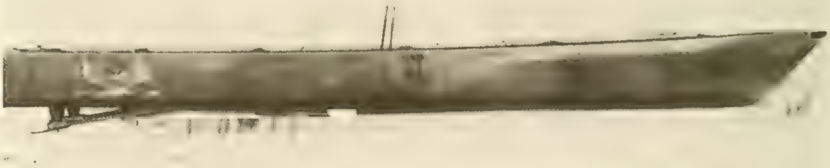

FIGURE 10. Fitting room photograph of DTNSRDC model 5365 representing R/V ATHENA.

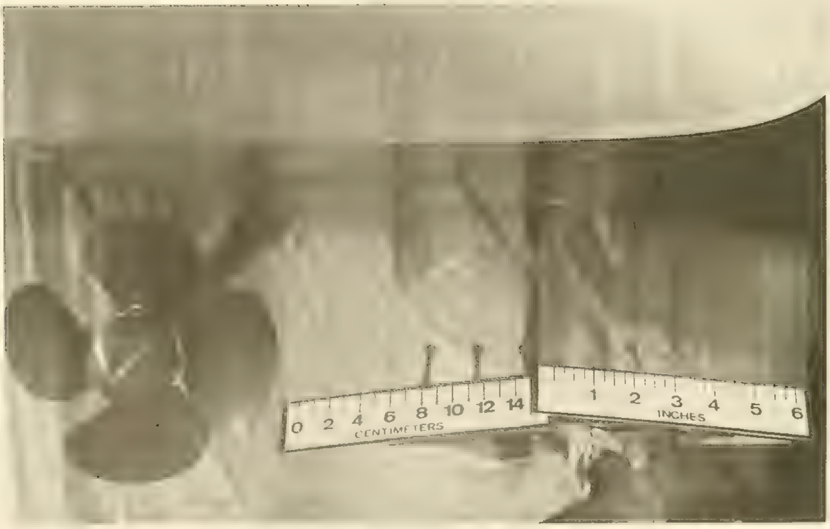
0 2 4 6 8 10 12 14
CENTIMETERS
1 2 3 4 5 6
INCHES

FIGURE 11. After end view of DTNSRDC model 5365 fitted with a rake of five-hole pitot tubes on the starboard shaft.

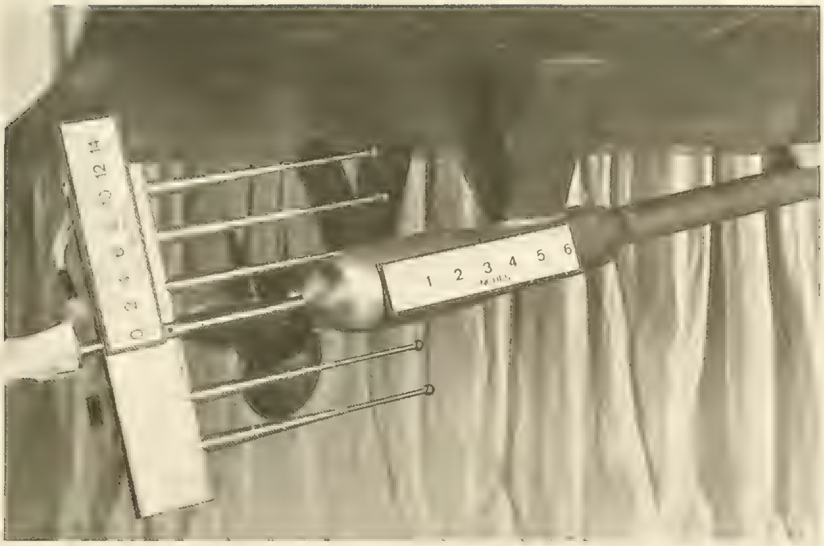

FIGURE 12. Afterbody profile view of DTNSRDC model 5365 fitted with a rake of five-hole pitot tubes on the starboard shaft.

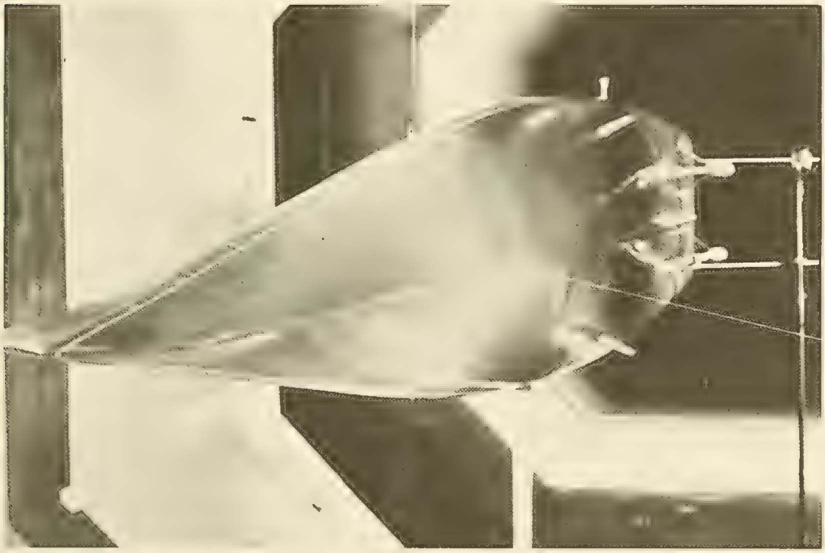

FIGURE 13. Double model installed in DTNSRDC wind tunnel.

the use and calibration of five-hole pitot tubes.

The boundary layer velocity profile measurements on the double model, Model 5366, in the wind tunnel were obtained using a hot wire anemometer. The model was mounted on its side and the anemometer was moved in the horizontal direction by a rack and pinion drive. The rack and pinion, with its stepping motor, allowed the position of the anemometer to be set to within a fraction of a millimeter.

Figure 13 shows the double model mounted in the wind tunnel. The vertical strut at the stern of the model is the support for the anemometry, and the bottom horizontal bar is an arm to steady the strut. The top horizontal bar is the traversing arm on which the hot wire anemometer is mounted. A close-up of the hot wire anemometer is shown in Figure 14; a centimeter scale is shown in the background of the photograph.

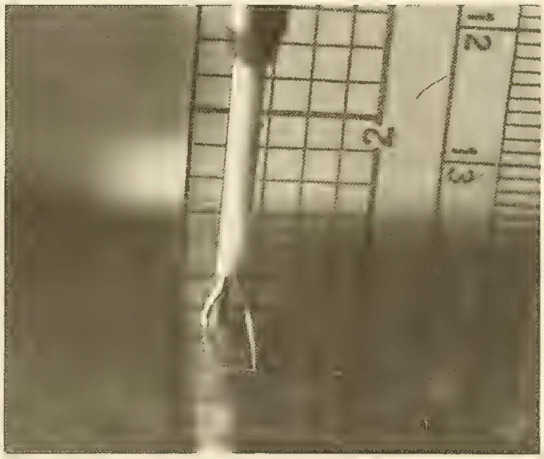

FIGURE 14. Hot-wire anemometer probe used for model wind-tunnel boundary layer profile measurements.

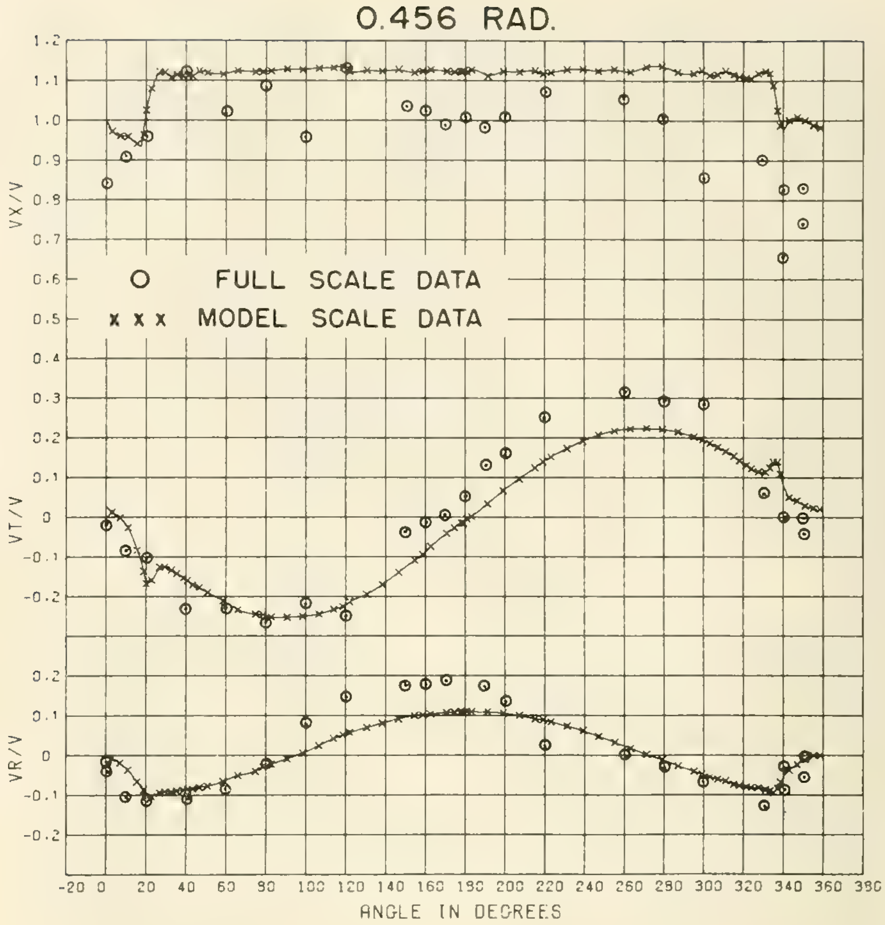

FIGURE 15. Velocity component ratios for R/V ATHENA and DTNSRDC model 5365 at 0.456 radius.

5. FULL-SCALE WAKE SURVEY AND BOUNDARY LAYER MEASUREMENTS

The full scale trials were run in the Atlantic Ocean off the Florida Coast near the mouth of the St. Johns River. The conditions for the trials were excellent as is shown in Table 1, which gives the trial agenda and sea conditions. The full-scale measurements were divided into four trials. Trial 1 consisted of a wake survey in the propeller disk, and ahead of the struts on the port and starboard sides.* The objective of the measurements ahead of the struts was to determine the differences in the wake both with and without the propeller operating. Trial 2 consisted of a repeat of the wake survey in the propeller disk. However, for this repeat trial, the two rakes ahead of the struts on the starboard shaft were removed to eliminate any possibility of interference in the measurements. Trial 3 consisted of boundary layer profile measurements on the port and starboard sides of the hull. Again, the purpose of these measurements on both sides of the ship was to determine the effects of propeller induction on the development of the boundary layer. Trial 4 consisted of measurements of the time varying pressures in a plane ahead of the operating propeller. The results of Trial 4 are discussed in Appendix A.

The pitot tubes on the rake in the propeller plane were located at non-dimensional radii (local radius divided by propeller radius) of 0.456, 0.633, 0.781, and 0.964. The angular position of the rake was adjusted by turning the entire shaft using the jacking gear. The shaft could be rotated through approximately 230°, and because of this an overlap of 50° could be obtained in the data around 180°.

The data from the wake survey at 15 knots are given, along with the corresponding model data, on Figures 15 through 18. This ship speed corresponded to a Froude number of 0.36 and a Reynolds number of 4.14×10^8. The data are presented as velocity component ratios, where the velocities are given in cylindrical coordinates centered about the propeller shaft. The longitudinal velocity component (VX) is positive for flow toward the stern. The tangential velocity component (VT) is taken to be positive in the counterclockwise direction when looking forward on the starboard shaft. The radial velocity component (VR) is taken as positive inward. The angles are defined positive in the counterclockwise direction, with zero directly upward. The conventions for the angles and the directions of the velocity components are shown on Figure 5. These conventions are those of Hadler and Cheng (1965), except that the data is presented on the starboard shaft rather than on the port shaft. Therefore, the angles increase in the opposite direction from Hadler and Cheng, as do the tangential velocity components.

---

*Note: The data from the wake surveys ahead of the struts and in the propeller disk at a lower speed are not reported in this paper, but will be reported in the future.

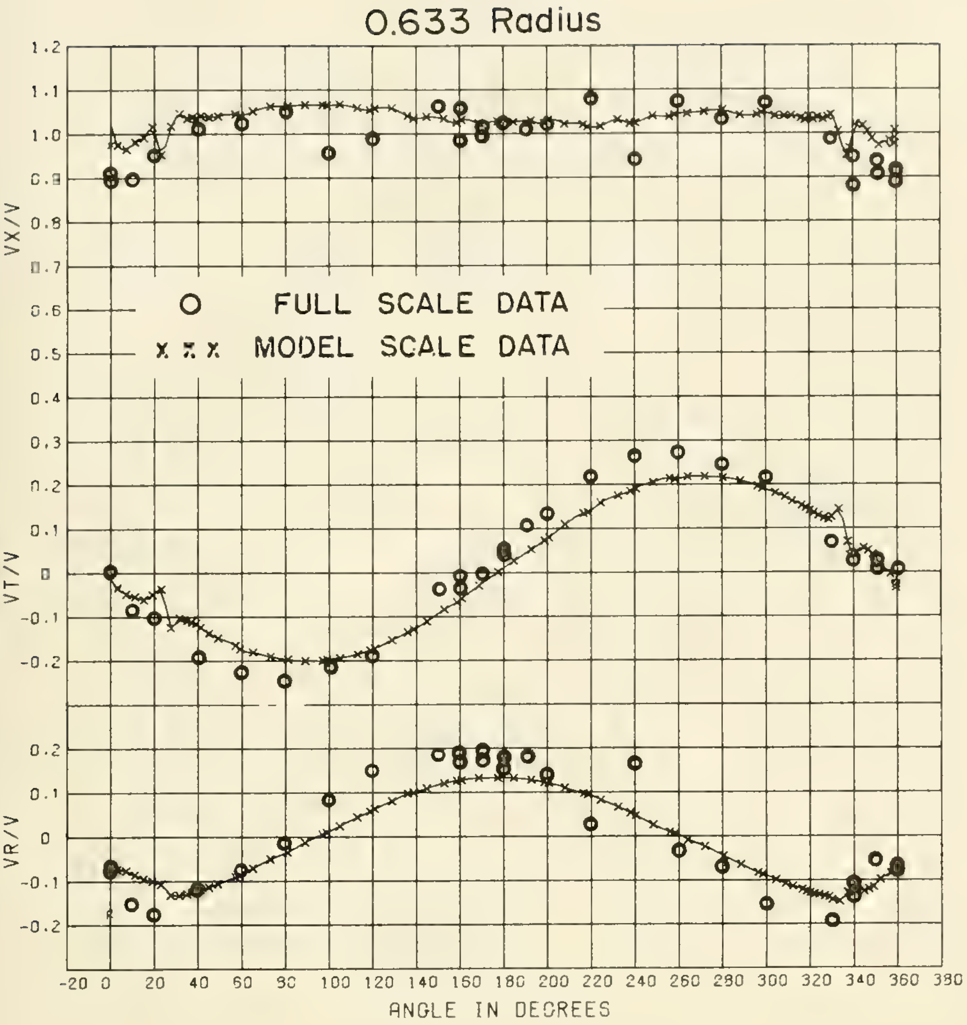

FIGURE 16. Velocity component ratios for R/V ATHENA and DTNSRDC model 5365 at 0.633 radius.

There are not sufficient data at any one radius or circumferential position to adequately define the limits of accuracy for the full-scale measurements. A comparison between two different pitot tubes at any one radius may be made in the region between 150 and 200° where the data overlap. At all radii the longitudinal velocity component ratios show the greatest scatter in the full-scale data. In particular at the innermost radius (r/R = 0.456), the scatter in the longitudinal velocity component ratios is greatest, approximately plus or minus ten percent. The scatter in the longitudinal velocity component ratios at other radii is significantly less than that, more nearly plus or minus five percent. The increased scatter in the longitudinal velocity component ratios is due to the computation procedure which uses the average of the longitudinal velocity components from both the radial and tangential velocity computations.

The full-scale wake survey provided a unique opportunity to study the development of a turbulent boundary layer on a ship, and also the effects of propeller action on the boundary layer. The full-scale boundary layer was measured at the eight locations which are shown on Figures 3 and 4, at four speeds. These speeds were 6.2, 9.1, 14.8, and 16.5 knots; these speeds correspond to Reynolds numbers of 1.74×10^8, 2.56×10^8, 4.14×10^8, and 4.63×10^8 respectively.

The data obtained at location 1, for all four speeds, are plotted on Figure 19. Except for the data at 6.2 knots, which show a great deal of scatter, the data are quite consistent with the fullness of the boundary layer increasing as the Reynolds number increases. The data obtained at 14.8 knots ($R_n = 4.14 \times 10^8$) for location 1, 2, and 3 are plotted in Figures 20, 21, and 22 along with the corresponding model data at the same Froude number. The data from Locations 1, 2, and 3 are plotted again in Figures 23, 24, and 25 along with the data for the corresponding locations on the port side with the propeller operating.

6. MODEL-SCALE WAKE SURVEY AND BOUNDARY LAYER MEASUREMENTS

For the model-scale wake survey, Model 5365 was ballasted while at rest to the drafts corresponding to those of the ship during the full-scale wake survey. The model was then towed at 5.22 knots (2.685 m/s), the Froude-scaled speed which corresponds to 15 knots full-scale. The velocity component ratios were measured with a rake of five-hole pitot tubes at radii corresponding exactly to the

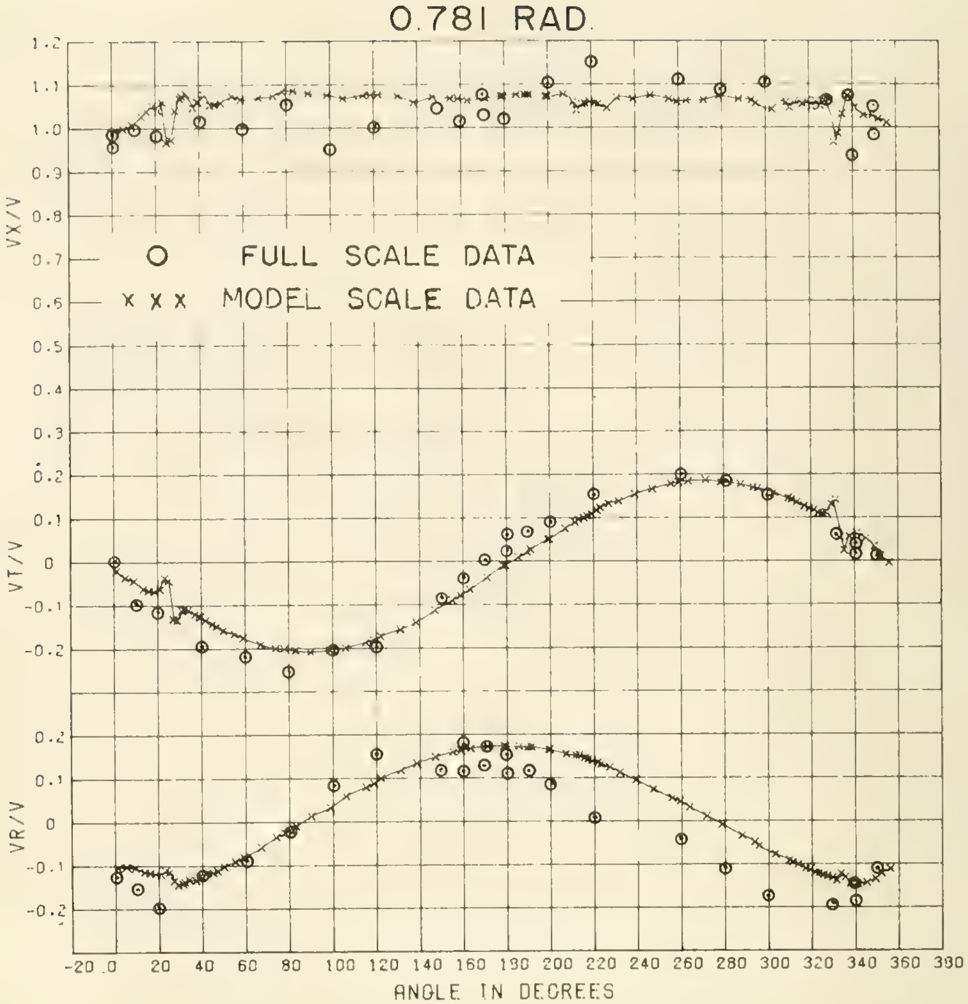

FIGURE 17. Velocity component ratios for R/V ATHENA and DTNSRDC model 5365 at 0.781 radius.

full-scale wake survey radii, slowing a direct one-to-one comparison of the data. The data from this wake survey are plotted on Figures 15 through 18.

It is customary to perform wake survey experiments in the towing tank by towing the model at a speed corresponding to the Froude-scaled speed of the ship. In order to investigate the effects of Reynolds number on the model-scale wake, a second wake survey was run at an increased speed. This second speed was the highest speed for which steady data would be obtained, 13.5 knots (6.9 m/s). For this second wake survey, the sinkage and trim of the model were kept the same as at the 5.2 knot condition. This was done in an attempt to separate the effects of sinkage and trim, which is dependent on Froude number, from other speed effects.

The data from the model-scale wake surveys at 5.2 knots ($F_n = 0.36$, $R_n = 1.56 \times 10^7$) and 13.5 knots ($F_n = 0.93$, $R_n = 4.04 \times 10^7$) are presented in Figure 26. The longitudinal and radial velocity component ratios at these two speeds show no difference. However, the tangential velocity component ratios obtained at 13.5 knots have peaks which are 4 to 6 percent lower than those obtained at 5.2 knots. This is contrary to what might be exepcted, in that the increased Reynolds number should produce a thinner boundary layer and therefore, a flow which more closely approaches the potential flow around the hull. This anomalous result is probably due to the increased Froude number and the corresponding change in the wave pattern around the model.

The model-scale boundary layer profile measurements were made in a wind tunnel using hot wire anemometers. The double model was manufactured so as to take into account the dynamic trim of the ship. Although this cannot take into account the effects of the free surface, it does account for the angle of the shafting to the free stream, which contributes significantly to the radial and tangential velocity components.

The model scale boundary layer profile was obtained at a Reynolds number of 1.68×10^7, which was intended to equal the Reynolds number of the model in the towing tank at a Froude number of 0.36. The Reynolds number in the wind tunnel in fact turned out to be about 8 percent higher than the Reynolds number in the towing tank. However, this was not considered to be critical to the correlation of the model and ship data.

The boundary layer profiles obtained in the wind tunnel, without the propeller operating, at Locations 1, 2, and 3 are given in Figures 20, 21, and 22; where they are plotted against the full scale data at the corresponding locations. The data obtained at the same locations with and without the propeller operating are plotted against the

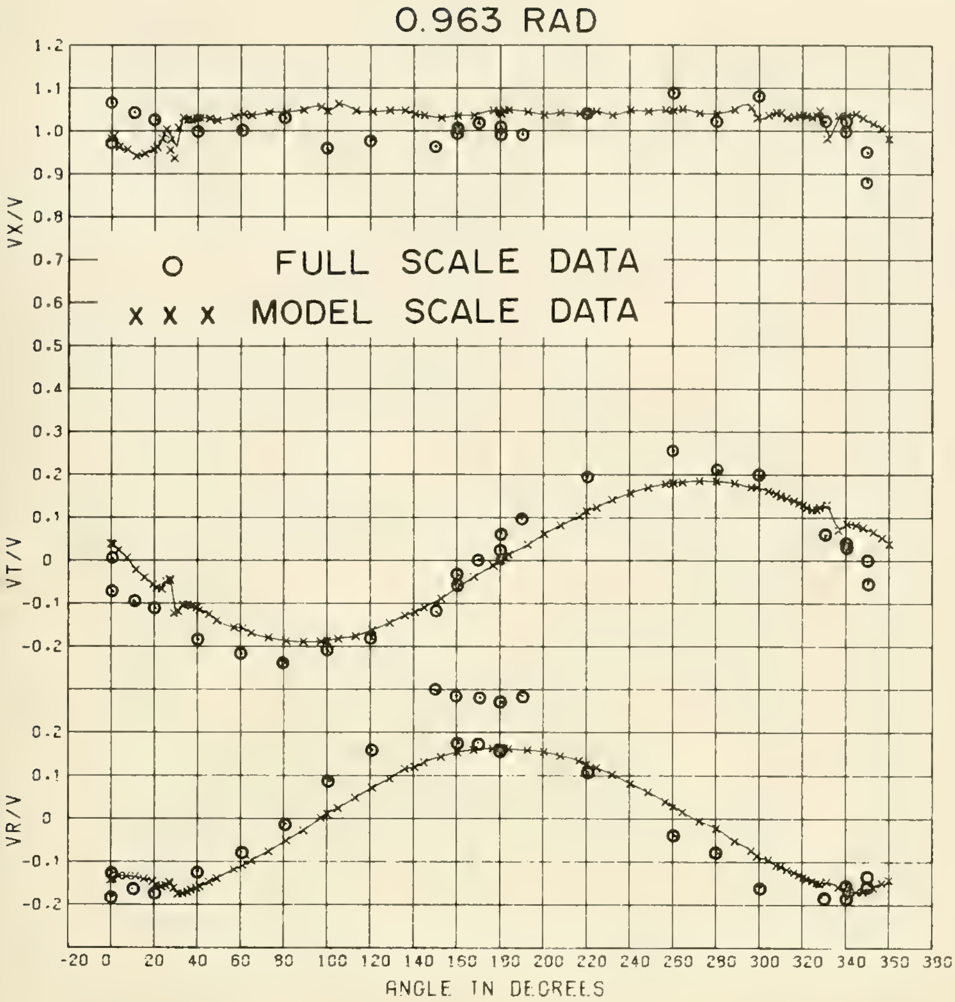

FIGURE 18. Velocity component ratios for R/V ATHENA and DTNSRDC model 5365 at 0.963 radius.

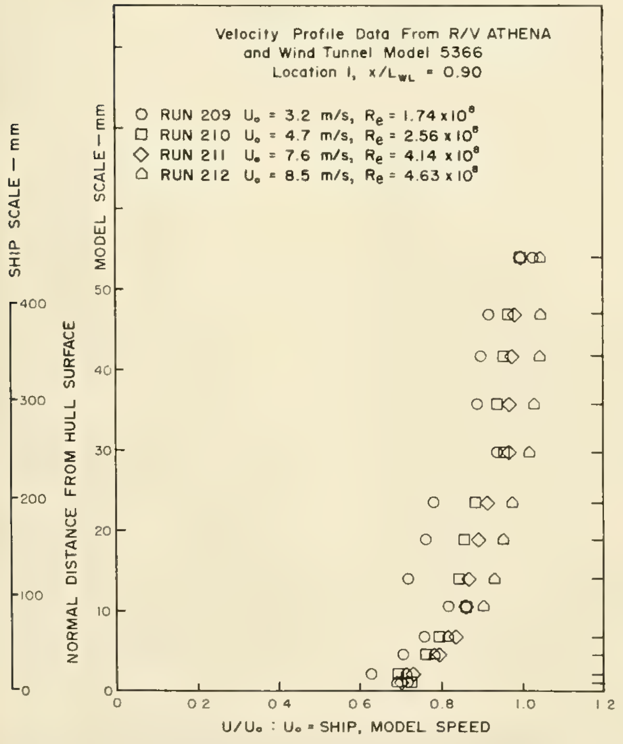

FIGURE 19. Velocity profile data from R/V ATHENA measured at four speeds at location 1.

corresponding data from the ship in Figures 23, 24, and 25. This is the extent of the model scale boundary layer data.

The accuracy of the model scale measurements with five-hole pitot tubes is known reasonably well. Model wake survey data have been repeated in past experiments, with the circumferential mean longitudinal velocity components repeating within 0.01 of the free stream velocity. The velocity component ratios for the model data are repeatable to within plus or minus one percent, except in areas where steep velocity gradients occur. In the areas where high velocity gradients exist, such as behind the shaft struts, the five-hole pitot tube has much lower accuracy. Experiments with hot wire anemometers have shown that they are at least as accurate as five-hole pitot tubes. In fact, in regions where there are steep velocity gradients, hot wire anemometers may be an order of magnitude more accurate than pitot tubes.

7. COMPARISON OF MODEL- AND FULL-SCALE DATA

A study of the velocity component ratios presented in Figures 15 through 18 shows that the degree of scatter of the full-scale data is higher than that of the model data. This is due to the higher variations in both pressure measurement and ship speed. In particular, the full-scale data for the longitudinal velocity component ratio at the innermost radius (r/R - 0.456) show the largest scatter,

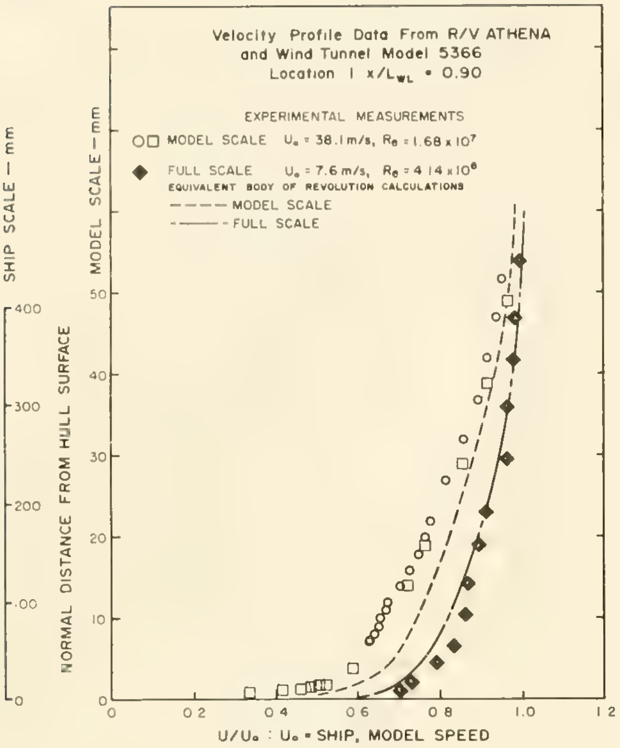

FIGURE 20. Measured and calculated boundary layer velocity profiles for R/V ATHENA and wind tunnel model 5366 at location 1.

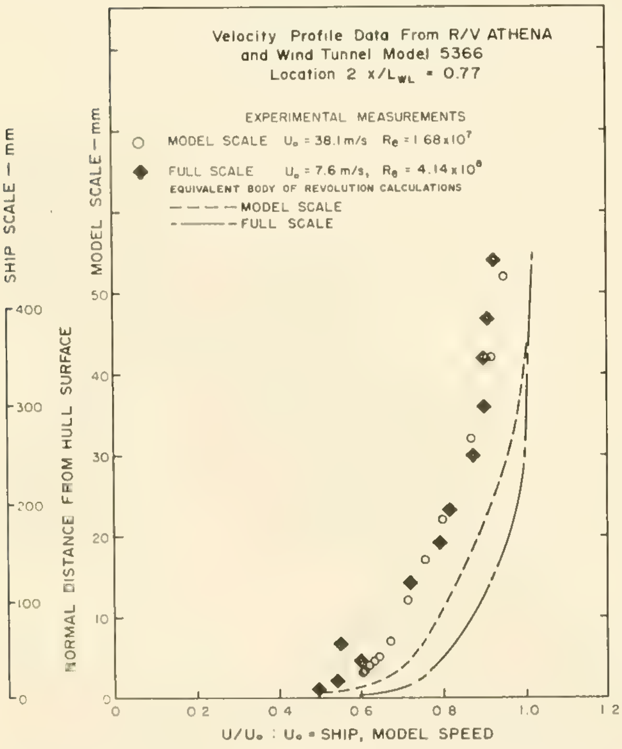

FIGURE 21. Measured and calculated boundary layer velocity profiles for R/V ATHENA and wind tunnel model 5366 at location 2.

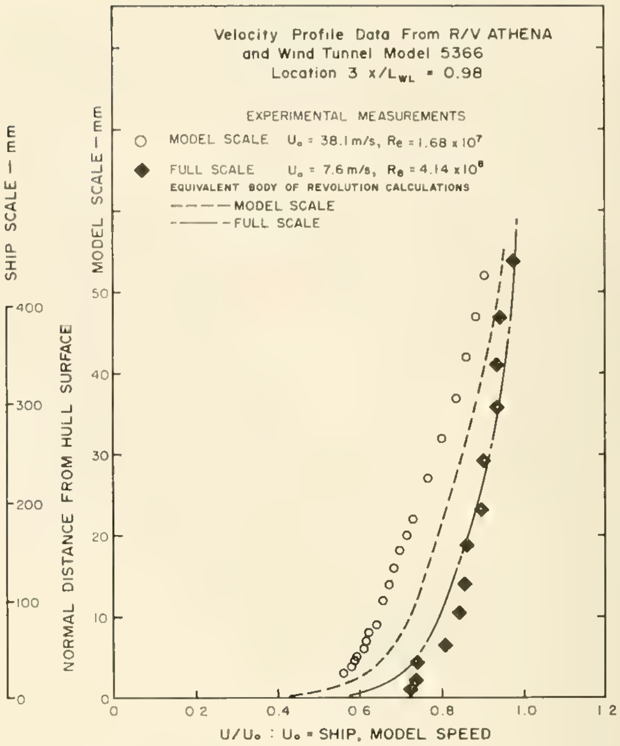

FIGURE 22. Measured and calculated boundary layer velocity profiles for R/V ATHENA and wind tunnel model 5366 at location 3.

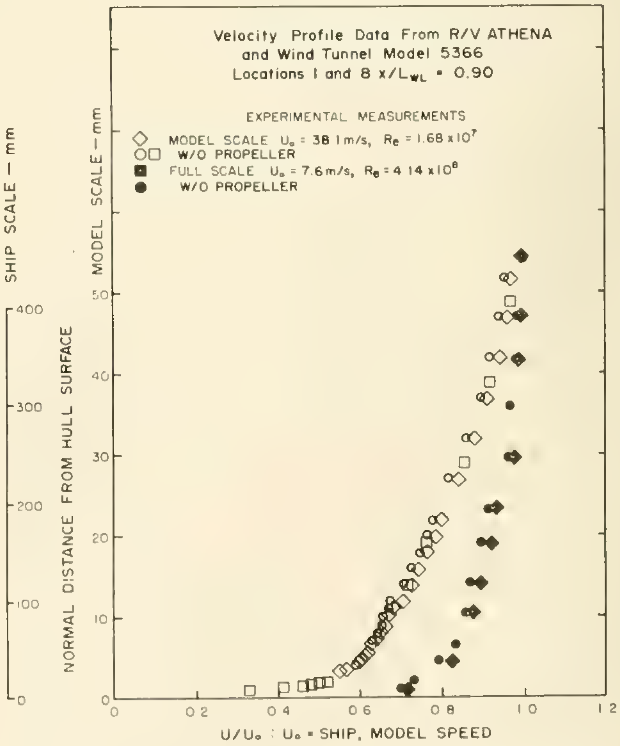

FIGURE 23. Measured boundary layer velocity profiles for R/V ATHENA and wind tunnel model 5366 with and without propeller at locations 1 and 8.

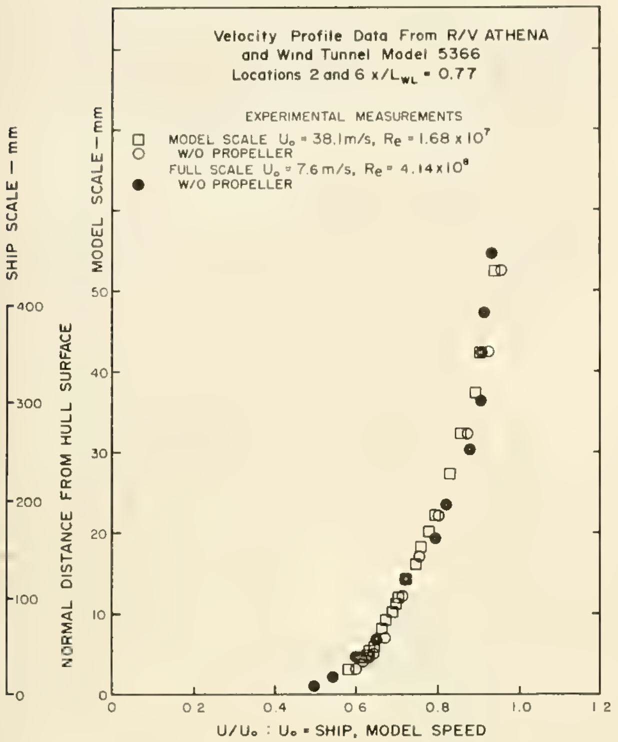

FIGURE 24. Measured boundary layer velocity profiles for R/V ATHENA and wind tunnel model 5366 with and without propeller at locations 2 and 6.

and the greatest deviation from the model-scale wake.

In part, this scatter is also due to the fact that the longitudinal velocity component ratios presented are an average of the longitudinal velocity component as measured in the tangential plane and in the radial plane. Therefore, any scatter error in either the tangential or radial plane measurements will influence the calculation of the longitudinal component. Another factor which probably contributed to increased scatter at the innermost radius is the close proximity of the pitot tube to the strut bossing.

The longitudinal velocity component ratio at the innermost radius is about 10 percent lower for the ship than for the model, while the peaks of the tangential and radial velocity component ratios are about 10 percent higher for the ship than for the model. Although there are undoubtedly scale effects on the shafting and strut bossing at this radius, another significant factor is that the bossing on the ship is proportionately much longer than on the model. This is due to the collar to which the pitot tube rakes ahead of the struts were attached.

At the outer radii the longitudinal velocity component ratios for the ship are 2-4 percent lower than those for the model. The peaks of the radial and tangential velocity component ratios at the outer radii are 8-10 percent higher for the ship than for the model. At the two innermost radii, the shift in the radial and tangential velocity component ratios indicate that there is a stronger upflow on the ship than the model, in the region under and outboard of the propeller hub. This effect is much weaker, and has shifted to the inside on the two outer radii. One possible cause of the shift at the outer radii is the fact that the full scale trial was performed with a propeller operating on the port shaft, while the model data were collected without the propeller present. However, the most likely source of the increased upward flow is a difference in attitude between the ship and model.

The models were run at a number of Reynolds numbers in the towing tank and wind tunnel and the longitudinal velocity component was measured at a single location near the hull for these various Reynolds numbers. The results of these measurements are plotted in Figure 27. These results indicate that for a Reynolds number greater than 10^7 there is very little effect of either Reynolds number or Froude number on the longitudinal velocity component. Therefore, in cases where it is desirable to obtain accurate longitudinal velocity component measurements, the model should be run at the correct Froude trim, at a Reynolds number greater than 10^7.

A comparison of the boundary layer profiles presented in Figures 20, 21, and 22 shows that, as might be expected, the model velocity profile is not as fully developed as the full-scale velocity profile at Locations 1 and 3. This is clearly a consequence of the one decade difference in Reynolds number between the model and ship. However, at Location 2, the model- and full-scale boundary layer velocity profiles almost coincide. This is clearly an anomalous situation, particularly because even at 0.46 meters from the hull full scale, the velocity has not reached the free-stream velocity, let alone the potential flow velocity which is even higher. The most likely explanation for the low full-scale velocity profile is a mal-

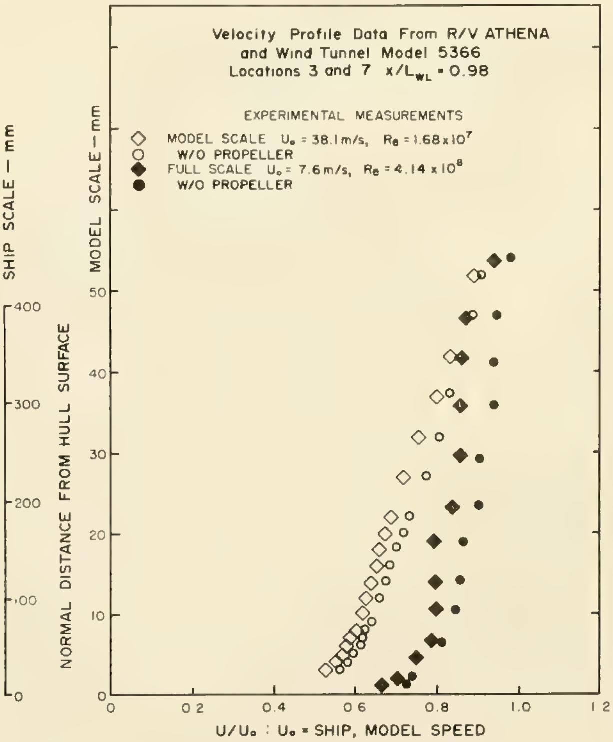

FIGURE 25. Measured boundary layer velocity profiles for R/V ATHENA and wind tunnel model 5366 with and without propeller locations 3 and 7.

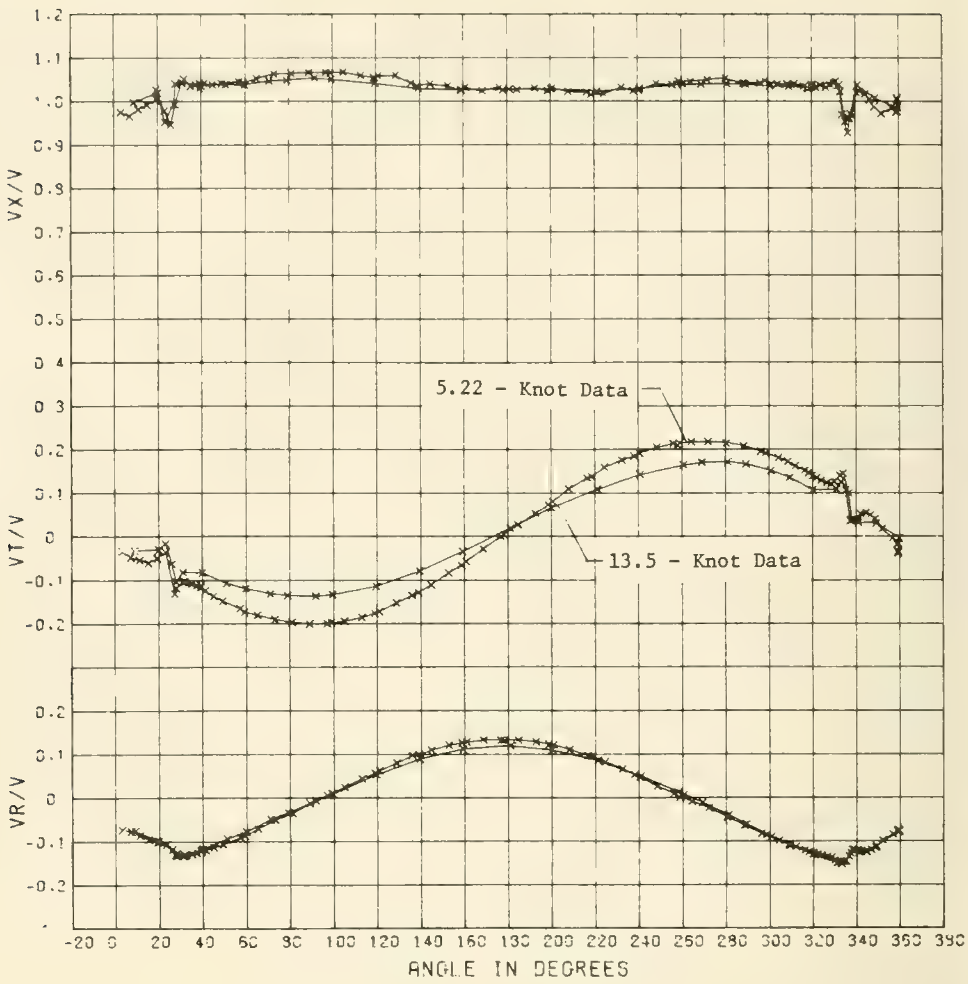

FIGURE 26. Velocity component ratios for DTNSRDC model 5365 at 0.633 radius for model speeds of 5.22 knots and 13.5 knots.

function in the instrumentation but a check of the data records indicated no obvious errors in the data.

The results of boundary layer profile measurement with the propeller operating, plotted in Figures 23, 24, and 25 indicate that the data at positions 1 and 8, just ahead of the propeller, show a slight increase in velocity profile due to the propeller suction. The increases are about the same at both model- and ship-scale. The data at positions 3 and 7, behind the propeller, show rather significant increases in the velocity profile for both scales. This is undoubtedly due to the wake of the propeller. From the model-scale data, at Locations 2 and 6, there is no noticeable difference in the data obtained with or without the propeller operating. This is consistent with the separation between the boundary layer probe and the propeller. There is no ship-scale data ahead of the operating propeller at location 6 due to the failure of that boundary layer probe.

In order to evaluate our ability to predict the boundary layer of the hull, a series of boundary layer calculations were instituted. For these calculations, the ship was approximated as a body of revolution, and the boundary layer was calculated using the standard DTNSRDC method for bodies of revolution [Wang and Huang (1976)]. Two methods for generating the bodies of revolution were tested. In one, the body was generated with radii equal to the square root of twice the sectional area of the ship; and in the other, the body was generated using circumferences equal to twice the girth of the ship. The boundary layer calculations using the body of revolution based on sectional area agreed best with the experimental data.

The results of the equivalent body of revolution calculations are plotted with the experimental data on Figures 20, 21, and 22. The calculations for the ship at Locations 1 and 3 agree reasonably well with the full-scale data. However, at the model-scale, the calculations do not agree nearly as well. This is probably due to the fact that at lower Reynolds numbers, the boundary layer is much more sensitive to errors in the flow velocity and pressure gradient than at higher speeds. As stated previously, the data at Location 2 is anomalous, as is shown by a comparison with the calculated boundary layer profile.

8. PREDICTION OF NOMINAL WAKE

Although the model- and full-scale wake of the R/V ATHENA both agree qualitatively, there are some substantial quantitative differences between the model- and full-scale velocity components. To develop an understanding of the origins of these differences, it was necessary to predict the wake of both the model- and full-scale ship analytically. Since the hull of the ATHENA showed no separation, it appeared that the presence of the hull could be

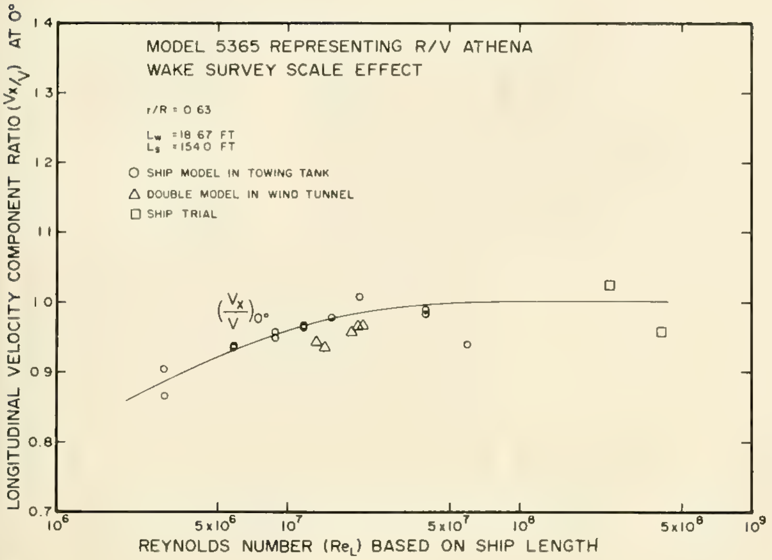

FIGURE 27. Longitudinal velocity component ratio at 0-degree position of 0.633 radius as a function of Reynolds number based on hull length.

dealt with primarily by potential flow techniques, combined with calculations of the boundary layer displacement thickness. It was also assumed that the viscous flow about the appendages could be dealt with empirically.

The velocity in the propeller disk, expressed in shaft coordinates, was decomposed as follows:

Velocity = Uniform Stream
+ Perturbation due to Hull
+ Perturbation due to Boundary Layer
+ Viscous Wake of Struts
+ Viscous Wake of Shafting.

The principal factor contributing to the radial and tangential components of the velocity in the propeller plane is the inclination of the shaft to the free stream. The shafting of the ATHENA makes an angle of 8.9° with the baseline. In addition, at 15 knots (F_n = 0.36), the ATHENA takes a bow-up trim of 0.3° as indicated by model experiments. Thus, the propeller shaft is inclined a total of 9.2° to the incident stream. The effect of resolving the incident stream into shaft coordinates is shown on Figure 28.

The effects of perturbing the incident stream by the presence of the hull were obtained by means of potential flow calculations. For the purposes of this study, the free surface was represented by the zero Froude number condition, and the calculations were made for a double model in an infinite fluid. The hull was reflected about the mean waterline at 15 knots, and flow about the resulting body was computed using the DTNSRDC potential flow program [Dawson and Dean (1972)]. The results of this computation are also shown on Figure 28. As can be seen, the effects due to the perturbation of the incident flow by the hull are small, on the order of two percent of the ship speed.

The effects of the displacement thickness of the boundary layer were considered next. The intention was to increase the thickness of the hull by the displacement thickness of the boundary layer, and to repeat the potential flow calculations. However, at its thickest point, the model scale boundary layer determined from the equivalent body of revolution calculations, would only have increased the thickness of the hull by 1 percent of the beam. The full-scale boundary layer would have increased the thickness even less. Since the complete hull potential flow had only a two percent effect, the revised potential flow was not computed for such a small change in effective hull shape. The error due to neglecting the displacement thickness of the boundary layer is probably much less than the error incurred by making the zero Froude number approximation for the potential flow calculations. Therefore, the velocity component ratios based on only the first potential flow calculations are presented in Figures 29 through 32.

The velocity defect caused by the struts was predicted using an empirical scheme based on data from aerodynamics. The velocity defect was computed using the following formula from page 584 of Goldstein (1965).

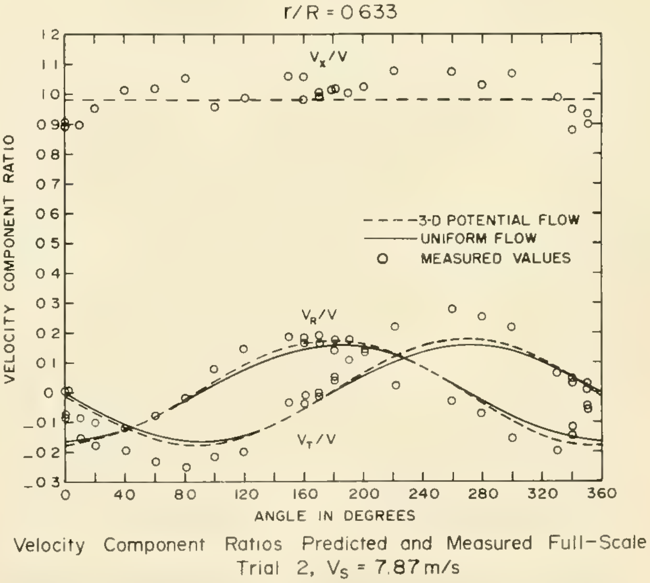

FIGURE 28. Effect of shaft inclination and hull potential flow on velocity component ratios for R/V ATHENA at 0.633 radius.

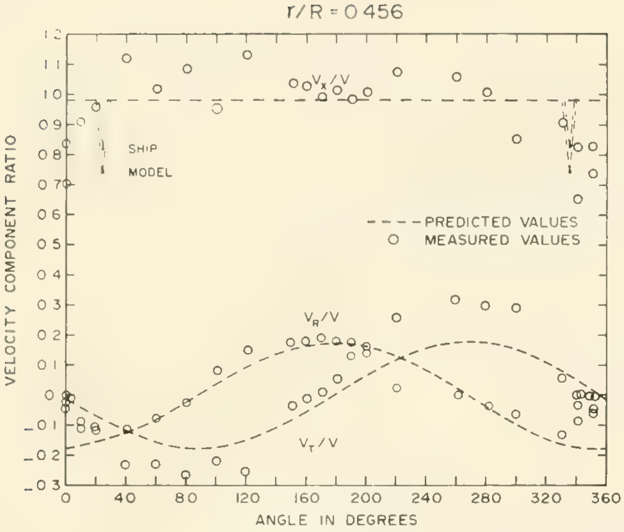

Velocity Component Ratios Predicted and Measured Full-Scale Trial 2, V_S = 7.87 m/s

FIGURE 29. Predicted and measured values of velocity component ratios for R/V ATHENA at 0.456 radius.

$$U_{max}/U_o = \eta_o{}^3/18a_1x^{\frac{1}{2}}$$

and

$$\eta_o{}^3/2a_1, = 10D/\eta_o\rho U_o$$

where U_{max} is the velocity defect, U_o the free-stream velocity, η_o is the nondimensional wake half width, x is the nondimensional distance from the strut, D is the strut drag, and ρ the fluid density. These formulas predict the longitudinal velocity defect in terms of the strut drag, wake thickness, and distance behind the strut.

The shaft struts on R/V ATHENA are Navy EPH sections with a chord-to-thickness ratio of 6.

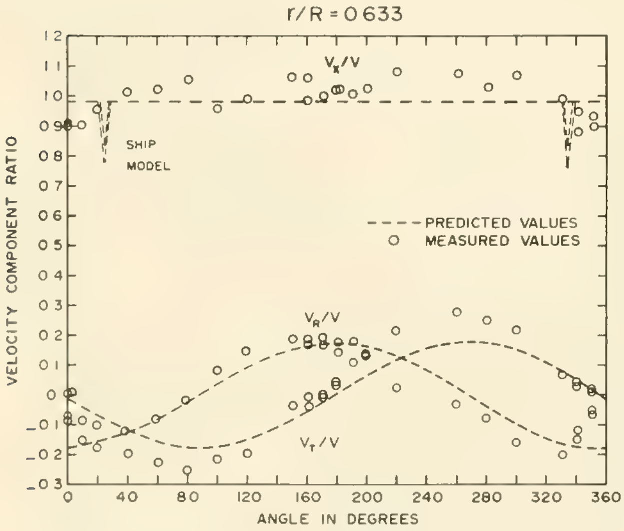

Velocity Component Ratios Predicted and Measured Full-Scale Trial 2, V_S = 7.87 m/s

FIGURE 30. Predicted and measured values of velocity component ratios for R/V ATHENA at 0.633 radius.

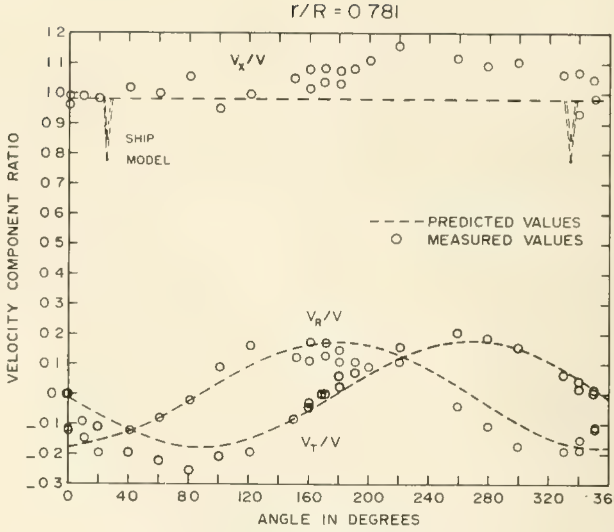

Velocity Component Ratios Predicted and Measured Full-Scale Trial 2, V_S = 7.87 m/s

FIGURE 31. Predicted and measured values of velocity component ratios for R/V ATHENA at 0.781 radius.

Assuming that the drag on the EPH section would not be too different from the drag on an elliptic section of the same thickness-chord ratio, many data for a number of elliptic sections were collected. These data are plotted on Figure 33 as a function of Reynolds number.

The nondimensional wake half-width was predicted using Equation (4) from Silverstein et al. (1938):

$$\eta_o = 0.68 \ C_D^{\frac{1}{2}} \ (X + 0.15)^{\frac{1}{2}}$$

In this equation η_o is again the nondimensional half width of the wake, X is the nondimensional distance from the strut, and C_D is the drag coefficient per unit length of the strut.

Using the strut Reynolds numbers based on chord length, of 1.46 × 10^5 for the ship, the correspond-

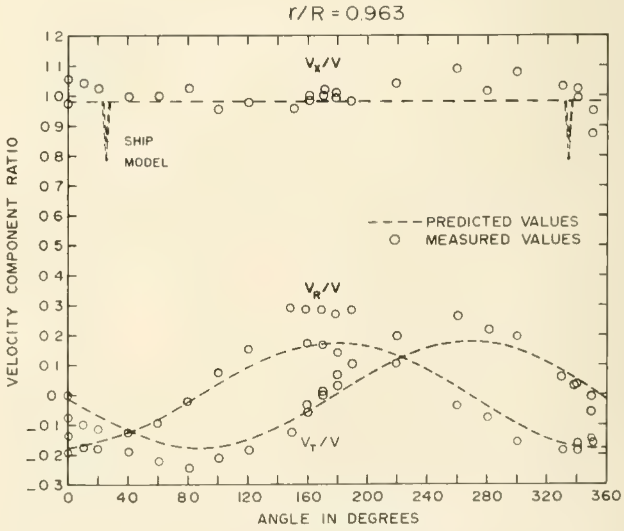

Velocity Component Ratios Predicted and Measured Full-Scale Trial 2, V_S = 7.87 m/s

FIGURE 32. Predicted and measured values of velocity component ratios for R/V ATHENA at 0.963 radius.

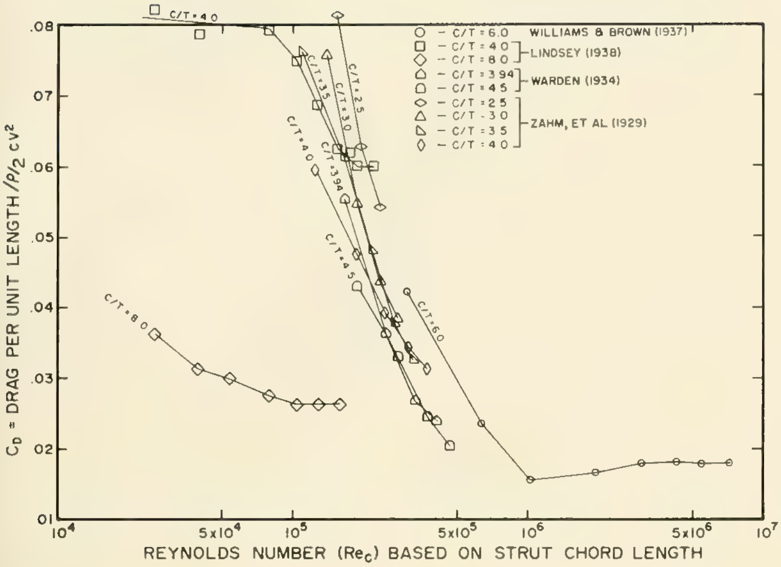

FIGURE 33. Drag coefficients of elliptical section struts as a function of Reynolds number based on chord length.

ing drag coefficients are found to be 0.050 and 0.018 for the model and ship, respectively. Subsitution of these drag coefficients into the above formulas from Silverstein, et al. (1938) and Goldstein (1965) yields the velocity defects which are shown on Figures 29 through 32.

These computed velocity defects due to strut wake are significantly greater than the velocity defects which were observed at either model or full scale. The cause of this over-prediction is probably the fact that the formulas from Goldstein are derived by assuming that the wake is being calculated far enough downstream that the cross flow terms in the momentum equation can be neglected. This is an assumption which is undoubtedly violated in the region near the struts, where the wake has been predicted.

Although the empirical method for predicting the wake of the shaft struts was not successful, it does at least provide some insight into how the wake should vary with Reynolds number. Both the width of the wake of the struts and the velocity defect in the wake of the struts are proportional to the square root of the drag coefficient of the section. Therefore, the velocity defect and the width of the wake should both decrease (like the square root of the ratio of the drag coefficients) as the Reynolds number increases. However, the full-scale wake survey data were not collected at angular increments spaced closely enough to confirm this scaling law.

The empirical method for predicting the wake behind an inclined shaft is not as well defined as the methods for predicting the wake behind the struts. Following the methodology of Chiu and Lienhard (1967), it was assumed that the separated flow behind a yawed cylinder is a function of the component of the velocity normal to the cylinder. Following the method of Roshko (1955) and (1958), an estimate of the velocity defect in the wake of the shaft was developed based on the pressure coefficient at the point of separation and the Strouhal number.

Data showing the base pressure* behind a circular cylinder have been collected, and are presented as a function of Reynolds number in Figure 34. Based on this data and the Reynolds number based on cross flow velocity, the pressure coefficients for the model ($R_n = 1.63 \times 10^4$) and ship ($R_n = 4.26 \times 10^5$) were found to be -1.1 and -0.2 respectively. These pressure coefficients resulted in a predicted velocity defect, perpendicular to the shaft axis, of 0.25 for the model and 0.10 for the ship. However, when resolved back into the direction of the flow, the shaft wake is less than two percent of model speed and one percent of ship speed. This is significantly less than than the velocity defect which is measured for either the model or the ship. In fact, if the velocity defect in the direction normal to the shaft were 100 percent of the forward speed, the velocity defect in the wake would only be seven percent, still less than the velocity defect measured experimentally.

These results are not surprising when one considers the discussion in Chiu and Lienhard (1969). In this discussion, data are presented which point out that the wake of an inclined shaft is in general not parallel to the shaft. This is due to the axial component of the flow along the cylinder which develops a boundary layer which separates. The Reynolds number for separation in the axial direction on the shaft is independent of the Reynolds number of the flow normal to the shaft. In addition, the data from Bursnall and Loftin (1952), show that as a circular cylinder is inclined further and further to the flow, the transverse Reynolds number at which separation takes place becomes lower and lower.

9. CONCLUSIONS

Significant differences have been found in the tangential and radial velocity component ratios between the ship and the model wake surveys. In particular, the full-scale tangential velocity component ratio has a peak amplitude approximately eight to ten percentage points higher than that at model scale. Similarly, the ship radial velocity component peak is higher by six to eight percentage points. These differences cannot be attributed to scale effects. The most likely cause seems to

---

*Note: The base pressure is not necessarily the pressure at the separation point because there is usually some pressure variation in the separated region.

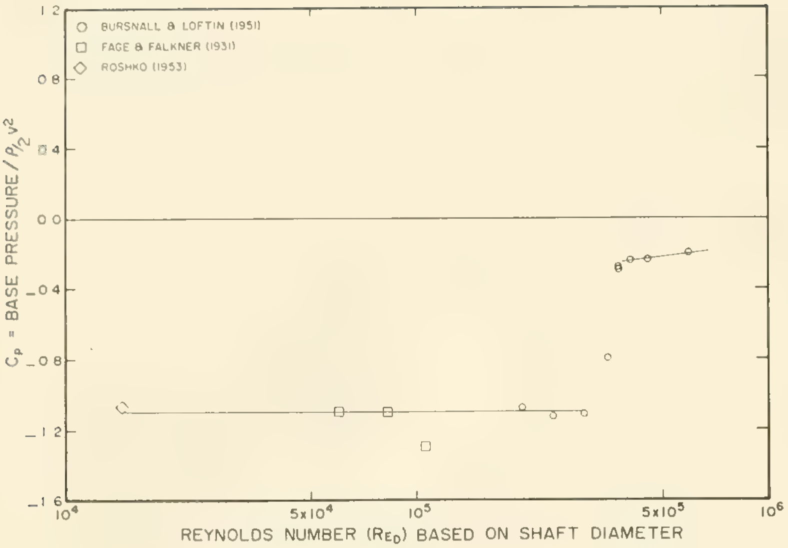

FIGURE 34. Base pressure coefficients of cylindrical shafts as a function of Reynolds number based on shaft diameter.

be a difference in trim between model- and full-scale. Because the model was ballasted to the draft of the ship, further work will be required to identify the source of these differences.

The longitudinal velocity component ratios for the full-scale trial show a much greater scatter than the tangential and radial components. For this reason it is unclear that any difference is shown by these data, when compared to model-scale data. The innermost radius (r/R = 0.456) does show that the high longitudinal velocity component normally measured at these inner radii is not found full scale. This may not be the result of scale effects on the shafting and strut bossing, but the fact that the full-scale bossing is longer than the model-scale bossing. This is a result which will have to be investigated by further model experiments.

The results from model experiments in both the wind tunnel and in the towing tank, and from the full-scale trial indicate that for a circumferential position near the hull, there was little difference in longitudinal velocity component ratio for speeds corresponding to Reynolds numbers greater than 10^7. Therefore, when measuring only the longitudinal velocity component ratios experimentally, the model should be run at the trim corresponding to that of the Froude-scaled speed and at a speed high enough to yield a Reynolds number of greater than 10^7.

The attempt at predicting the wake for this high-speed displacement ship showed that the most important contribution to the variation in tangential and radial velocity component ratios was the shaft angle to the flow. The calculation of the potential flow around the hull and the resulting velocity components showed that the effect of the perturbation due to the hull was small. The effects of the boundary layer of the hull on the wake were also shown to be small.

In summary it may be stated that the full-scale and model wakes differ by approximately ten percent of the ship speed. These differences cannot be adequately explained at this time. Further work on wake of appendages is recommended as one step in improving the understanding of these differences.

ACKNOWLEDGEMENTS

This work was performed under the controllable-pitch propeller research program sponsored by C. L. Miller of the Naval Sea Systems Command (NAVSEA 0331G) administered by the David W. Taylor Naval Ship Research and Development Center (DTNSRDC).

The authors wish to express their appreciation to personnel of the Ship Performance Department of DTNSRDC, the University of Michigan, and the crew of R/V ATHENA from MAR Inc. for their assistance in conducting the full-scale trial and model experiments which provided the data for this paper. CHI Associates, Inc. and Rosenblatt Inc. are also acknowledged for their assistance in the preparation of this paper.

BIBLIOGRAPHY

Boswell, R. J., J. J. Nelka, and S. B. Denny (1976). Experimental Determination of Mean and Unsteady Loads on a Model C. P. Propeller Blade for Various Simulated Modes of Ship Operation. *Eleventh ONR Symposium on Naval Hydrodynamics*, London, England, VIII 75-110.

Bursnall, W. J., and L. K. Loftin (1952). Experimental Investigation of the Pressure Distribution about a Yawed Circular Cylinder in the Critical Reynolds Number Range. *NACA Tech. Note 2463*

Canham, J. J. S. (1975). Resistance, Propulsion and Wake Tests with HMS Penelope. *Trans. Royal Inst. of Naval Arch., 117*, 61-94.

Chiu, W. S., and J. H. Lienhard (1967). On Real Fluid Flow Over Yawed Circular Cylinders. *Jour. Basic Engineering, Trans. ASME, Series D, 89*, 851-857.

___(1969) Discussion to: On Real Fluid Flow Over Yawed Circular Cylinders. *Jour. Basic Engineering, Trans. ASME, 91*, 132-134.

Dawson, C., and J. Dean (1972). The XYZ Potential Flow Program. *NSRDC Report 3892*.

Denny, S. B., H. A. Themak, and J. J. Nelka (1975). Hydrodynamic Design Considerations for the

Controllable-Pitch Propeller for the Guided Missile Frigate. *Naval Eng. Jour., 87,* 2; 72-81.

Fage, A., and V. M. Falkner (1931). Further Experiments on the Flow Around a Circular Cylinder. *British A.R.C. Reports and Memoranda No. 1369,* 186-208.

Frydenlund, O., and J. E. Kerwin (1977). The Development of Numerical Methods for the Computation of Unsteady Propeller Forces. *Norwegian Maritime Research,* 17-28.

Goldstein, S. (1965). *Modern Developments in Fluid Dynamics, Vol. II.* Dover Publications, Inc., New York, pp. 331-702.

Hale, M. R., and D. H. Norrie (1967). The Analysis and Calibration of the Five-Hole Spherical Pitot. *ASME Paper 67-WA/FE-24.*

Hadler, J. B., and H. M. Cheng (1965). Analysis of Experimental Wake Data in Way of Propeller Plane of Single- and Twin-Screw Ship Models. *Trans. Soc. Naval Arch. and Mar. Eng., 73,* 287-414.

Lindsey, W. F. (1938). Drag of Cylinders of Simple Shape. *NACA Report 619,* 169-176.

Namimatsu, M., and K. Muraoka (1973). The Wake Distribution of a Full Form Ship. *IHI Engineering Review, 7,* 3.

Namimatsu, M., K. Muraoka, S. Yamashita, and H. Kishimoto (1973). Wake Distribution of Ship and Model on Full Ship Form. *J. Soc. Naval Arch. Japan, 134* (Japanese), 65-73.

Novack, S. M., P. W. C. M. Van Oirschot, H. P. Young, and D. A. O'Neil (1977). Increased Profits for Gas Turbine Container Ships by Unique Applications of Combustion Technology and Hydrodynamics. *Trans. Soc. Naval Arch. and Mar. Eng., 85.*

Rains, D. A. (1975) DD 963 Power Plant. *Marine Technology, 12,* 1; 1-24.

Roshko, A. (1953). On the Development of Turbulent Wakes from Vortex Streets. *NACA Report 1191,* 801-824.

___(1954) On the Drag and Shedding Frequency of Two-Deminsional Bluff Bodies. *NACA Tech. Note 3169.*

___(1955) On the Wake and Drag of Bluff Bodies. *J. Aero. Sci., 22,* 124-132.

Schuster, S., H. Grothues-Spork, H. Thieme, and H. Schwanecke (1968). Meteor-Messfahrten 1967. *Jahrbuch der STG, 62,* 159-204.

Silverstein, A., S. Katzoff, and W. K. Bullivant (1938). Downwash and Wake Behind Plain and Flapped Airfoils. *NACA Report 651,* 179-206.

Takahashi, H., T. Ueda, M. Nakato, Y. Yamazaki, M. Ogura, K. Yokoo, H. Tanaka, and S. Omata (1971). Measurement of Velocity Distribution Ahead of the Propeller Disk of the Ship. *J. Soc. of Naval Arch. West. Japan, 129* (Japanese), 153-168.

Taniguchi, K., and T. Fujita (1970). Comparison of Velocity Distribution in the Boundary Layer Between Ship and Model. *J. Soc. Naval Arch. Japan,* 127.

Troesch, A., V. A. Phelps, and J. Hackett (1978). Full-Scale Wake and Boundary Layer Survey Instrumentation Feasibility Study. *Dept. Naval Arch. and Mar. Eng. Report, Univ. of Mich.*

Tsakonas, S., W. R. Jacobs, and M. R. Ali (1973). An Exact Linear Lifting-Surface Theory for Marine Propeller in a Nonuniform Flow Field. *J. Ship Res., 17,* 196-207.

Vorus, W. S. (1974). A Method for Analyzing the Propeller-Induced Vibratory Forces Acting on the Surface of a Ship Stern. *Trans Soc. Naval Arch. Mar. Eng., 82,* 186-210.

Wang, H. T., and T. T. Huang (1976). User's Manual for FORTRAN IV Computer Program for Calculating the Potential Flow/Boundary Layer Interaction on Axisymmetric Bodies. *DTNSRDC Ship Performance Dept. Report 737-01.*

Warden, R. (1934). Resistance of Certain Strut Forms. *British A.R.C. Reports and Memoranda 1599,* 217-247.

Wennberg, P. K. (1966). The Design of the Main Propulsion Machinery Plant Installed in the USCGC HAMILTON (WPG-715). *Trans. Soc. Naval Arch. and Mar. Eng., 74,* 29-69.

Williams, D. H., and A. F. Brown (1937). Experiments on an Elliptic Cylinder in the Compressed Air Tunnel. *British A.R.C. Reports and Memoranda 1817,* 103-112.

Yokoo, K. (1974). Measurement of Full-Scale Wake Characteristics and Their Prediction From Model Results--State of the Art. *Symposium on High Powered Propulsion of Large Ships,* Wageningen, pp. XI.1-28.

Zahm, A. F., R. H. Smith, and F. A. Louden (1929). Forces on Elliptic Cylinder in Uniform Air Stream. *NACA Report 289,* 217-232.

APPENDIX A - TIME-VARYING PRESSURE MEASUREMENTS AHEAD OF AN OPERATING PROPELLER

During Trial 4, the time-varying pressures at the head of a piezoelectric pitot tube were obtained as a function of shaft position. The pressures were measured for each six degrees of shaft rotation for the pitot tube at a fixed angle. Measurements were obtained at four angular positions of the pitot tube and at two ship speeds.

It should be noted that due to the fact that the pitot tube is approximately one diameter of the propeller forward of the propeller disk, the amplitude of the pressure oscillation is only 1 percent of the mean pressure signal. Due to the failure of two of the pressure transducers in the head of the pitot tube, it was impossible to obtain any data on the variation of the flow velocity with angular position.

During each of the runs with the piezoelectric pitot tube, data were collected for a period of time totalling between 5 and 10 minutes. All of the data points for each angular position of the shaft were then averaged to obtain a mean level for each signal. Figures A-1, A-2, and A-3 show these averaged pressure signals as a function of angular position. Runs 209 and 205 were both obtained at the same ship speed (15 knots) and shaft speed

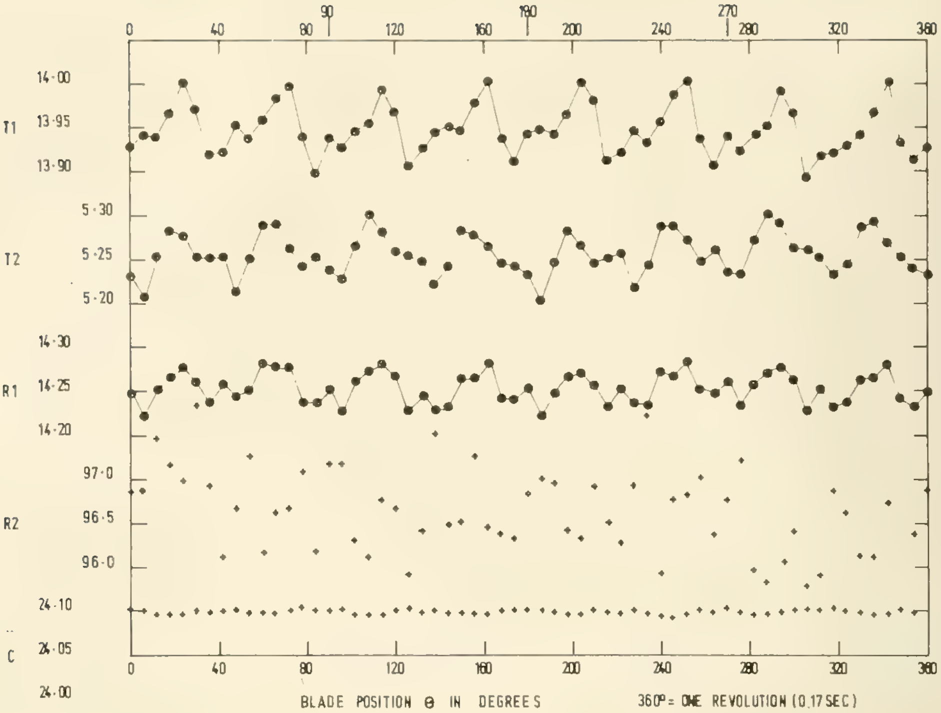

FIGURE A-1. Circumferential distribution of piezoelectric pressure transducer signals for 15-knot run 209.

(345 rpm), but with the pitot tube in different angular positions, 180° for Run 205 and 300° for Run 209. Run 208 was obtained at a speed of 8.9 knots and a propeller speed of 245 rpm, with the pitot tube at 300°.

As can clearly be seen from the data obtained during Run 209, the pressure signal from the three operating pressure transducers is periodic. There is an obvious periodicity at twice blade frequency (eighth harmonic in shaft frequency). A Fourier series analysis of the data from the two 15-knot runs showed that the second harmonic in blade frequency was the dominant harmonic in all three signals. For Run 209, the amplitude of the eighth harmonic was 3 percent and those of the other harmonics were generally less than 10 percent of the eighth harmonic. The only exception to this is the sixteenth harmonic which is again of increased magnitude. Although the magnitude of the harmonics from Run 205 were lower than those from Run 209 the saem results apply. There is not obvious periodicity in the data from Run 208. However, a harmonic analysis of this data shows that the twelfth harmonic is dominant, although not nearly to the same extent as in the cases of the high speed runs.

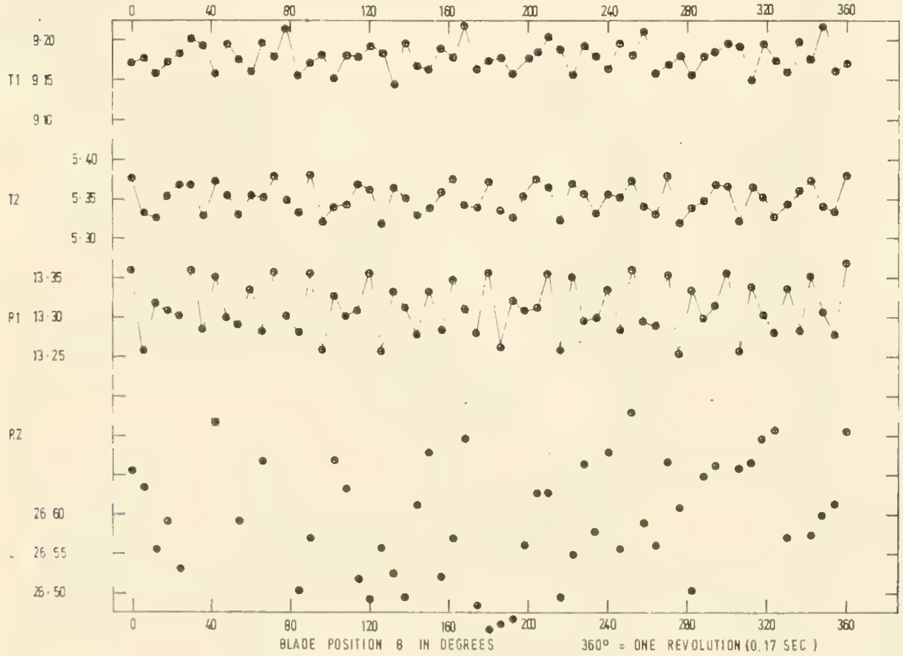

FIGURE A-2. Circumferential distribution of piezoelectric pressure transducer signals for 15-knot run 205.

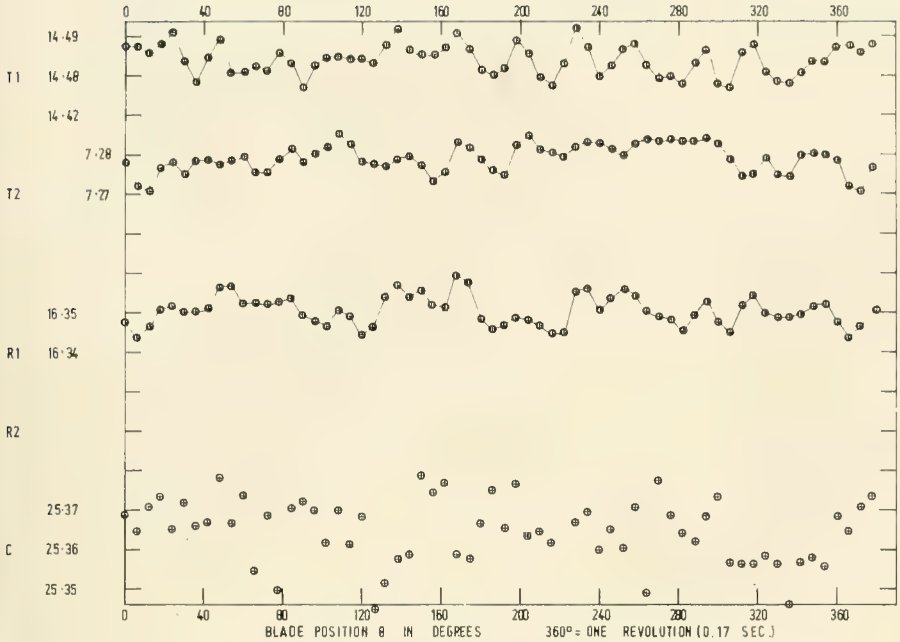

FIGURE A-3. Circumferential distribution of piezoelectric pressure transducer signals for 8.9-knot run 208.

Influence of Propeller Action on Flow Field Around a Hull

Shunichi Ishida
Ishikawajima-Harima Heavy Industries Co, Ltd.
Yokohama, Japan

ABSTRACT

Flow field in the vicinity of a hull is analyzed by using acceleration potential, and an approximate calculation method is derived. The present method can calculate the change of pressure on the hull caused by a propeller action. Numerical results by the present method are shown with experimental results.

Wake far from a ship is analyzed by using Oseen's approximation, and an optimum condition is given for wake energy recovery by a propeller. This condition is examined by the results of the self-propulsion tests and the wake survey measurements at distant positions behind a ship.

1. INTRODUCTION

When a hull is towed in still water, a flow field is induced around the hull. This flow field is very complicated, and becomes more complicated by propeller action. Many researchers have studied experimentally and theoretically the phenomena caused by the interaction of the hull and propeller, [Yamazaki et al. (1972)]. Unfortunately, however, the number of practical uses of the study results is less than those derived in other fields of naval hydrodynamics. One of the reasons is because the various suggested methods are themselves complicated owing to the complexity of the phenomena.

It has been popularly known that both the equations and the boundary conditions which describe flow field can be simplified, and analyzed easily if disturbance by an object in the flow is a small quantity of the first order. One of the typical examples is the method of acceleration potential in inviscid flow fields used for propeller theory [Tsakonas et al. (1973)]. Another example is Oseen's method in a viscous flow field used for the separation of hull resistance components [Baba (1969)].

In this paper, the above-mentioned concept is applied to analysis of flow fields induced by the interaction of the hull and propeller, and the author derives practical methods relating to the propeller-induced pressure change on the hull and wake energy recovery by the propeller. Section 2 explains coordinate systems used in this paper. In Section 3, the author applies the method of acceleration potential for analysis of inviscid flow fields in the vicinity of the hull, and derives a method which can be used to calculate the change of pressure induced by a propeller on a hull surface. In Section 4, the author applies Oseen's method for analysis of wake far from the hull, and derives a method to predict recovery of wake energy by the propeller. Then, this method is examined by the experimental results obtained from self-propulsion tests and the wake survey. Section 5 concludes this paper.

2. COORDINATE SYSTEMS

We assume that a ship with a single propeller is moving with a constant speed on the free surface of still water. At first, we define a coordinate system O-XYZ fixed in space and a coordinate system o-xyz fixed on the hull as indicated in Figure 1. The coordinate system O-XYZ is an orthogonal coordinate system, in which the XZ-plane coincides with the still water surface and the positive direction of Y-axis coincides with an upward vertical line. The coordinate system o-xyz is a moving coordinate system in which the origin o is moving on the X-axis in the negative direction with a constant velocity U, and this sytem satisfies the following relationship with O-XYZ:

$$X = x - Ut,\ Y = y,\ Z = z, \qquad (1)$$

where t represents time.

Next, we define two more coordinate systems

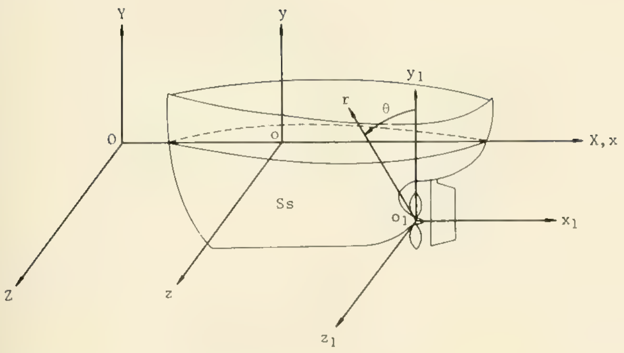

FIGURE 1. Coordinate systems.

o_1-$x_1y_1z_1$ and o_1-$x_1r\theta$ related with the propeller as indicated in Figure 1. In the coordinate system o_1-$x_1y_1z_1$, the origin o_1 coincides with the propeller center and we assume that the x_1-axis coincides with the propeller axis and is parallel to the x-axis. Further, the coordinate system o_1-$x_1y_1z_1$ has the following relationship with the coordinate system o-xyz:

$$x = x_p + x_1,\ y = -f + y_1,\ z = z_1, \tag{2}$$

where $(x_p, -f, o)$ are the coordinates of the propeller center on o-xyz. Moreover, the following relationship is satisfied between o_1-$x_1y_1z_1$ and o_1-$x_1r\theta$:

$$x_1 = x_1,\ y_1 = r\cos\theta,\ z_1 = r\sin\theta. \tag{3}$$

3. PRESSURE ON A HULL SURFACE AND ACCELERATION POTENTIAL

Pressure generated on the hull surface in the towed condition differs from that in the self-propulsion condition because of the influence of propeller action. The time-independent part of this change corresponds to the pressure component of the thrust deduction and the time-dependent part corresponds to the propeller-induced surface force. Now, with conventional methods devised to calculate these forces, numerical procedures tend to be extremely troublesome. Consequently, a great deal of calculation time is required, especially in calculating propeller induced velocity, and it is hard to apply to a practical hull of a complicated form. Hence, an easy method with which the calculations of propeller influences can be reduced is needed.

In this chapter, the method which can calculate change of pressure induced by a propeller on the hull surface is explained. This method can be obtained by using acceleration potential.

Fundamental Equation

In this section, we assume that the flow field around the hull is inviscid. This assumption may be considered reasonable in solving the problem of pressure on the hull surface when the boundary layer on the hull surface is thin.

At first, let us examine the flow field around the hull in the towed condition. Denoting the velocity potential of disturbance due to the hull by $\phi_s(x,y,z)$, the velocity potential for the overall flow field can be expressed by $U\cdot x+\phi_s$, and the following equation must be satisfied for ϕ_s:

$$\frac{\partial^2\phi_s}{\partial x^2} + \frac{\partial^2\phi_s}{\partial y^2} + \frac{\partial^2\phi_s}{\partial z^2} = 0\ . \tag{4}$$

Boundary conditions are given as follows. On the hull surface, S_s, the following equation must be satisfied:

$$\left(U + \frac{\partial\phi_s}{\partial x}\right)\cdot n_x + \frac{\partial\phi_s}{\partial y}\cdot n_y + \frac{\partial\phi_s}{\partial z}\cdot n_z \Big|_{\text{on } S_s} = 0\ , \tag{5}$$

where n_x, n_y, and n_z represent x-, y-, and z- components of the outward normal unit vector on S_s. On the free surface, we have two boundary conditions. One of them can be obtained from the Bernoulli's law and the condition of constant pressure there, as follows:

$$\frac{1}{2}\left[\left(\frac{\partial\phi_s}{\partial x}\right)^2 + \left(\frac{\partial\phi_s}{\partial y}\right)^2 + \left(\frac{\partial\phi_s}{\partial z}\right)^2\right] + U\frac{\partial\phi_s}{\partial x} + gy\ \Big|_{y=\zeta_s} = 0, \tag{6}$$

where $\zeta_s(x,z)$ represents the vertical displacement of the free surface, namely, wave height. Another boundary condition on the free surface is the kinematical condition as indicated below:

$$\left(U + \frac{\partial\phi_s}{\partial x}\right)\cdot\frac{\partial\zeta_s}{\partial x} - \frac{\partial\phi_s}{\partial y} + \frac{\partial\phi_s}{\partial z}\cdot\frac{\partial\zeta_s}{\partial z}\ \Big|_{y=\zeta_s} = 0. \tag{7}$$

At infinity, the following boundary conditions might be given:

$$\text{Derivatives of } \phi_s \to 0 \text{ when } \sqrt{x^2 + y^2 + z^2} \to \infty\ ,$$

$$\zeta_s \to 0 \text{ when } \sqrt{x^2 + z^2} \to \infty\ . \tag{8}$$

Next, let us examine the flow field around the hull in the self-propulsion condition. We assume, similarly to the towed condition, that the velocity potential of disturbance exists. Then, we can express the velocity potential of the overall flow field by $U\cdot x + \phi_s + \phi^*$. Here, the $\phi^*(x,y,z;t)$ represents the change of the velocity potential due to the propeller action when the moving condition is changed from the towed condition to the self-propulsion condition, and ϕ^* must satisfy the following equation:

$$\frac{\partial^2\phi^*}{\partial x^2} + \frac{\partial^2\phi^*}{\partial y^2} + \frac{\partial^2\phi^*}{\partial z^2} = 0\ . \tag{9}$$

We can also obtain the boundary conditions under the self-propulsion condition in the same manner as under the towed condition. In this case, however, time derivatives appear in some conditons by the influence of propeller rotation. On the hull surface, the following boundary condition is given:

$$\left(U + \frac{\partial\phi_s}{\partial x} + \frac{\partial\phi^*}{\partial x}\right)\cdot n_x + \left(\frac{\partial\phi_s}{\partial y} + \frac{\partial\phi^*}{\partial y}\right)\cdot n_y + \left(\frac{\partial\phi_s}{\partial z} + \frac{\partial\phi^*}{\partial z}\right)\cdot n_z\ \Big|\ \text{on } S_s = 0\ . \tag{10}$$

On the free surface, the condition of constant pressure and the kinematical condition can be given as follows:

$$\frac{1}{2}\left[\left(\frac{\partial\phi_s}{\partial x}+\frac{\partial\phi^*}{\partial x}\right)^2+\left(\frac{\partial\phi_s}{\partial y}+\frac{\partial\phi^*}{\partial y}\right)^2+\left(\frac{\partial\phi_s}{\partial z}+\frac{\partial\phi^*}{\partial z}\right)^2\right]$$

$$+\,U\left(\frac{\partial\phi_s}{\partial x}+\frac{\partial\phi^*}{\partial x}\right)+\frac{\partial\phi^*}{\partial t}+gy\,\Big|_{y=\zeta_{sp}}=0\,. \qquad (11)$$

$$\left(U+\frac{\partial\phi_s}{\partial x}+\frac{\partial\phi^*}{\partial x}\right)\cdot\frac{\partial\zeta_{sp}}{\partial x}-\left(\frac{\partial\phi_s}{\partial y}+\frac{\partial\phi^*}{\partial y}\right)$$

$$+\left(\frac{\partial\phi_s}{\partial z}+\frac{\partial\phi^*}{\partial z}\right)\cdot\frac{\partial\zeta_{sp}}{\partial z}+\frac{\partial\zeta_{sp}}{\partial t}\,\Bigg|_{y=\zeta_{sp}}=0\,. \qquad (12)$$

where ζ_{sp} represents the wave height in the self-propulsion condition. At infinity, the following boundary conditions might be given:

$$\text{Derivatives of } \phi_s+\phi^*\rightarrow 0 \text{ when } \sqrt{x^2+y^2+z^2}\rightarrow\infty,$$

$$\zeta_{sp}\rightarrow 0 \text{ when } \sqrt{x^2+z^2}\rightarrow\infty\,. \qquad (13)$$

Finally, using the equations derived under the towed condition and the self-propulsion condition described above, let us derive the equation and boundary conditions for ϕ^* which express the change of the flow field around the hull due to the propeller action. At first, ϕ^* must satisfy the Laplace equation (9). Next, let us obtain the boundary conditions for ϕ^*. On the hull surface, the following relationship is given from (5) and (10):

$$\frac{\partial\phi^*}{\partial x}\cdot n_x+\frac{\partial\phi^*}{\partial y}\cdot n_y+\frac{\partial\phi^*}{\partial z}\cdot n_z\,\Big|_{\text{on } S_s}=0\,. \qquad (14)$$

On the free surface, the following equation is given from (6) and (11) in correspondence with the condition of constant pressure:

$$\frac{1}{2}\left[\left(\frac{\partial\phi_s}{\partial x}+\frac{\partial\phi^*}{\partial x}\right)^2+\left(\frac{\partial\phi_s}{\partial y}+\frac{\partial\phi^*}{\partial y}\right)^2+\left(\frac{\partial\phi_s}{\partial z}+\frac{\partial\phi^*}{\partial z}\right)^2\right]$$

$$+\,U\left(\frac{\partial\phi_s}{\partial x}+\frac{\partial\phi^*}{\partial x}\right)+\frac{\partial\phi^*}{\partial t}+gy\,\Bigg|_{y=\zeta_{sp}}$$

$$=\frac{1}{2}\left[\left(\frac{\partial\phi_s}{\partial x}\right)^2+\left(\frac{\partial\phi_s}{\partial y}\right)^2+\left(\frac{\partial\phi_s}{\partial z}\right)^2\right]+U\frac{\partial\phi_s}{\partial x}+gy\,\Big|_{y=\zeta_{sp}}\,. \qquad (15)$$

And, using (7) and (12), the following equation is given in correspondence with the kinematical condition:

$$\left(U+\frac{\partial\phi_s}{\partial x}+\frac{\partial\phi^*}{\partial x}\right)\cdot\frac{\partial\phi_{sp}}{\partial x}-\left(\frac{\partial\phi_s}{\partial y}+\frac{\partial\phi^*}{\partial y}\right)$$

$$+\left(\frac{\partial\phi_s}{\partial z}+\frac{\partial\phi^*}{\partial z}\right)\cdot\frac{\partial\zeta_{sp}}{\partial z}+\frac{\partial\zeta_{sp}}{\partial t}\,\Bigg|_{y=\zeta_{sp}}$$

$$=\left(U+\frac{\partial\phi_s}{\partial x}\right)\cdot\frac{\partial\zeta_s}{\partial x}-\frac{\partial\phi_s}{\partial y}+\frac{\partial\phi_s}{\partial z}\cdot\frac{\partial\zeta_s}{\partial z}\,\Bigg|_{y=\zeta_s}\,. \qquad (16)$$

At infinity, the following boundary conditions might be given:

$$\text{Derivatives of } \phi^*\rightarrow 0 \text{ when } \sqrt{x^2+z^2}\rightarrow\infty\,,$$

$$\zeta^*\rightarrow 0 \text{ when } \sqrt{x^2+z^2}\rightarrow\infty\,, \qquad (17)$$

where ζ^* $(x,z;t)$ represents change of wave height due to the propeller action and the following relationship must be satisfied:

$$\zeta^*=\zeta sp-\zeta s. \qquad (18)$$

Acceleration Potential and Approximate Calculation Method

Acceleration Potential

The purpose of this section is to indicate that the equation and the boundary conditions for ϕ^* derived in the previous section can be expressed in the terms of acceleration potential on the assumption of thin hull.

At first, using the assumption of thin hull, we express the shape of the hull as follows:

$$z=\varepsilon\cdot f(x,y) \quad \text{in } S_s^*\,, \qquad (19)$$

where ε represents a small quantity of the first order and S_s^* represents a projected plane of the hull surface, S_S, in the xy-plane. And, it seems reasonable to develop all our quantities in powers of ε, as follows:

$$\phi_s=\varepsilon\phi_1+\varepsilon^2\phi_2+\ldots\quad, \qquad (20)$$

$$\phi^*=\varepsilon\phi_1^*+\varepsilon^2\phi_2^*+\ldots\quad, \qquad (21)$$

$$\zeta_s=\varepsilon\zeta_1+\varepsilon^2\zeta_2+\ldots\quad, \qquad (22)$$

$$\zeta_{sp}=\varepsilon\zeta_1'+\varepsilon^2\zeta_2'+\ldots\quad, \qquad (23)$$

Thus, ζ^* can also be developed as follows:

$$\zeta^*=\varepsilon\zeta_1^*+\varepsilon^2\zeta_2^*+\ldots\quad. \qquad (24)$$

Next, we proceed to obtain the equation and boundary conditions for ϕ_1^* which correspond to the first order of ε by substituting the development (20)~(24) into the equation and boundary conditions for ϕ^* in the previous section. The following equation in Ω_1^* can be obtained from (9) and (21):

$$\frac{\partial^2\phi_1^*}{\partial x^2}+\frac{\partial^2\phi_1^*}{\partial y^2}+\frac{\partial^2\phi_1^*}{\partial z^2}=0\,. \qquad (25)$$

Let us consider the boundary conditions for ϕ_1^*. First, using Eq. (19), we can estimate the magnitude of n_x, n_y, n_z in the Eq. (14) as follows:

$$n_x=0(\varepsilon)\,,\quad n_y=0(\varepsilon)\,,\quad n_z=0(1)\,, \qquad (26)$$

where 0 denotes the order symbol. In addition, we obtain from (19) and (21)

$$\frac{\partial\phi^*}{\partial x}\,\Big|_{z=\varepsilon f(x,y)}=\varepsilon\,\frac{\partial\phi_1^*}{\partial x}\,\Big|_{z=0}+0(\varepsilon^2)\,, \qquad (27)$$

$$\left.\frac{\partial\phi^*}{\partial y}\right|_{z=\varepsilon f(x,y)} = \varepsilon\left.\frac{\partial\phi_1^*}{\partial y}\right|_{z=0} + 0(\varepsilon^2)\,, \qquad (28)$$

$$\left.\frac{\partial\phi^*}{\partial x}\right|_{z=\varepsilon f(x,y)} = \varepsilon\left.\frac{\partial\phi_1^*}{\partial z}\right|_{z=0} + 0(\varepsilon^2)\,. \qquad (29)$$

Hence, by substituting (26)~(29) into (14), we can obtain

$$\left.\frac{\partial\phi_1^*}{\partial z}\right|_{z=0} = 0 \text{ in } S_s^*\,. \qquad (30)$$

Further, for the boundary conditions on the free surface, the following equation can be obtained by substituting (20)~(24) into (15):

$$\left. U\frac{\partial\phi_1^*}{\partial x} + \frac{\partial\phi_1^*}{\partial t} + g\zeta_1^*\right|_{y=0} = 0\,. \qquad (31)$$

And, in correspondence with the Eq. (16), the following equation is also obtained:

$$\left. U\frac{\partial\zeta_1^*}{\partial x} - \frac{\partial\phi_1^*}{\partial y} + \frac{\partial\zeta_1}{\partial t}\right|_{y=0} = 0\,. \qquad (32)$$

Hence, eliminating ζ_1^* from (31) and (32), we can obtain the boundary conditions on the free surface:

$$\left.\frac{\partial^2\phi_1^*}{\partial x^2} + \frac{2}{U}\frac{\partial^2\phi_1^*}{\partial x\partial t} + \frac{1}{U^2}\frac{\partial^2\phi_1^*}{\partial t^2} + \frac{g}{U^2}\frac{\partial\phi_1^*}{\partial y}\right|_{y=0} = 0\,. \qquad (33)$$

Moreover, at infinity, boundary conditions are given as follows by (17), (21) and (24):

$$\text{Derivatives of } \phi_1^* \to 0 \text{ when } \sqrt{x^2+y^2+z^2} \to \infty\,, \qquad (34)$$

$$\zeta_1^* \to 0 \text{ when } \sqrt{x^2+z^2} \to \infty\,. \qquad (35)$$

Now, let us denote the pressure of the flow field in the towed condition and that in the self-propulsion condition by $p_s(x,y,z)$ and $p_{sp}(x,y,z;t)$ respectively. By substituting (20) and (21) into Bernoulli's expression, we can obtain

$$\frac{p_s}{\rho_f} = -gy - \varepsilon U\frac{\partial\phi_1}{\partial x} + 0(\varepsilon^2)\,, \qquad (36)$$

$$\frac{p_{sp}}{\rho_f} = -gy - \varepsilon U\left(\frac{\partial\phi_1}{\partial x} + \frac{\partial\phi_1^*}{\partial x}\right) - \varepsilon\frac{\partial\phi_1^*}{\partial t} + 0(\varepsilon^2)\,, \qquad (37)$$

where ρ_f represents fluid density. Hence, the pressure change, $\psi(x,y,z;t)$, due to the interaction of the hull and propeller is given by the following equation:

$$\frac{\psi}{\rho_f} = \frac{1}{\rho_f}(p_{sp} - p_s) = -\varepsilon\left(U\frac{\partial\phi_1^*}{\partial x} + \frac{\partial\phi_1}{\partial t}\right). \qquad (38)$$

This equation shows that the magnitude of ψ is of the order of ε. Moreover, ψ/ρ_f can be considered as an acceleration potential as is obvious from the relationship with ϕ_1^*.

Finally, we proceed to convert Eqs. (25), (30), (33), (34), and (35) for ϕ_1^* to equations for ψ by using the relationship (38). Using (25) and (38), ψ must satisfy the following equation:

$$\frac{\partial^2\psi}{\partial x^2} + \frac{\partial^2\psi}{\partial y^2} + \frac{\partial^2\psi}{\partial z^2} = 0\,. \qquad (39)$$

On the hull surface, S_s, we can obtain from (26) the following equation:

$$\left.\frac{\partial\psi}{\partial n}\right|_{\text{on } S_s} = \left. n_x\frac{\partial\psi}{\partial x} + n_y\frac{\partial\psi}{\partial y} + n_z\frac{\partial\psi}{\partial z}\right|_{\text{on } S_s}$$

$$= -\left.\frac{\partial\psi}{\partial z}\right|_{z=0} + 0(\varepsilon^2) \text{ in } S_s^*\,. \qquad (40)$$

On the other hand, if (x,y) is a point on S_s^*, the following equation can be obtained from (30) and (38):

$$-\frac{1}{\rho_f}\left.\frac{\partial\psi}{\partial z}\right|_{z=0} = \varepsilon\lim_{z\to 0}\left(U\frac{\partial}{\partial x} + \frac{\partial}{\partial t}\right)\frac{\partial\phi_1^*}{\partial z}$$

$$= \varepsilon\left(U\frac{\partial}{\partial x} + \frac{\partial}{\partial t}\right)\cdot\left[\frac{\partial\phi_1^*}{\partial z}(z=0)\right] = 0\,. \qquad (41)$$

Thus, the hull surface condition for ϕ_1^* can be converted to that for ψ as follows:

$$\left.\frac{\partial\psi}{\partial n}\right|_{\text{on } S_s} = 0\,. \qquad (42)$$

Similarly, the free surface condition (33) for ϕ_1^* can be converted to that for ψ as follows:

$$\left.\frac{\partial^2\psi}{\partial x^2} + \frac{2}{U}\frac{\partial^2\psi}{\partial x\partial t} + \frac{1}{U^2}\frac{\partial^2\psi}{\partial t^2} + \frac{g\partial\psi}{U^2\partial y}\right|_{y=0} = 0\,. \qquad (43)$$

Moreover, for the boundary condition at infinity, the following equation is given from (34) and (35):

$$\psi \to 0 \text{ when } \sqrt{x^2+y^2+z^2} \to \infty\,. \qquad (44)$$

Integral Equation

We proceed to seek the solution of ψ which is the harmonic function in the region bounded above by the plane $y=0$ and elsewhere by the hull surface and satisfies boundary conditions (42), (43), and (44).

At first, we separate the solution into the two parts and write it as follows:

$$\psi(x,y,z;t) = V(x,y,z;t) + W(x,y,z;t)\,, \qquad (45)$$

where both V and W are the harmonic functions in the region as indicated above. Moreover, let W represent the pressure induced by a rotating propeller moving straight ahead with a constant speed in still water and a free surface. Now, we have many formulas for $W^*(x,y,z;t)$ which represents the pressure induced by an N-bladed propeller moving in infinite space. One of the formulas for W^* is given on the assumption of thin blades as follows [Jakobs et al. (1972)]:

$$W^* = \sum_{\nu=0}^{\infty} W_\nu{}^*(x,y,z)\, e^{j\nu\Omega t}$$

$$= \sum_{\nu=0}^{\infty} \frac{1}{4\pi} \int_{S_p} dS \sum_{q=1}^{N} \sum_{\lambda=0}^{\infty} L'_\lambda(\xi',\rho,\theta_0)\, e^{j\lambda(\Omega t-\bar{\theta}q)} \frac{\partial}{\partial n_p}\left(\frac{1}{R}\right), \tag{46}$$

$$\text{where } \bar{\theta}_q = \frac{2\pi}{N}(q-1), \tag{47}$$

with j = imaginary unit, Ω = angular speed of the propeller, S_p = lifting surface of propeller, $L_\lambda{}'$ = pressure jump across S_p, (ξ',ρ,θ_0) = point on S_p, n_p = normal unit vector at S_p, and R = distance between (ξ',ρ,θ_0) and (x,y,z). Hence, using W^* and the method of the mirror image, we can obtain a W which satisfies the boundary conditions (43) and (44). Then, we can write W as follows:

$$W = \sum_{\nu=0}^{\infty} W_\nu(x,y,z)\, e^{j\nu\Omega t}. \tag{48}$$

Next, let us consider V. Then, we assume that V and ψ can be developed in correspondence with the development (48) as indicated below:

$$\psi = \sum_{\nu=0}^{\infty} \psi_\nu(x,y,z)\, e^{j\nu\Omega t}, \tag{49}$$

$$V = \sum_{\nu=0}^{\infty} V_\nu(x,y,z)\, e^{j\nu\Omega t}. \tag{50}$$

Hence, using (42) and (44), we have

$$\left.\frac{\partial V_\nu{}^{(e)}}{\partial n}\right|_{\text{On } S_s} = -\left.\frac{\partial W_\nu}{\partial n}\right|_{\text{On } S_s}, \tag{51}$$

$$V_\nu{}^{(e)} \to 0 \text{ when } \sqrt{x^2+y^2+z^2} \to \infty, \tag{52}$$

where the suffix, (e), means the outside of the hull surface. In the same manner, from Eq. (43), we have

$$\left.\frac{\partial^2 V_\nu}{\partial x^2} + K_0\frac{\partial V_\nu}{\partial y} + K_1\frac{\partial V_\nu}{\partial x} + K_2 V_\nu \right|_{y=0} = 0, \tag{53}$$

where

$$K_0 = \frac{g}{U^2}, \quad K_1 = \frac{2j\nu\Omega}{U}, \quad K_2 = -\frac{\nu^2\Omega^2}{U^2}. \tag{54}$$

Now, we suppose that we know the functions $G_\nu(\xi,\eta,\zeta;x,y,z)$ $(\nu=0,1,2,\ldots..)$ such that the G_ν are harmonic functions for $\eta<0$ except at (x,y,z) where G_ν have a singularity of first order, and G_ν satisfy the boundary conditions:

$$\left.\frac{\partial^2 G_\nu}{\partial \xi^2} + K_0\frac{\partial G_\nu}{\partial \eta} + K_1\frac{\partial G_\nu}{\partial \xi} + K_2 G_\nu \right|_{\eta=0} = 0, \tag{55}$$

$$G_\nu \to 0 \text{ when } \sqrt{x^2+y^2+z^2} \to \infty. \tag{56}$$

Then, we can obtain the following equation by using (52), (53), (55), and (56) with the method of Green's function:

$$4\pi V_\nu{}^{(e)}(Q_e) = \int_{S_s} dS\left\{\left(\frac{\partial V_\nu{}^{(i)}}{\partial n} - \frac{\partial V_\nu{}^{(e)}}{\partial n}\right)_Q G\,(Q;Q_e) + \left(V_\nu{}^{(e)} - V_\nu{}^{(i)}\right)_Q \frac{\partial}{\partial n_Q} G_\nu\left(Q;Q_e\right)\right\}, \tag{57}$$

where Q_e denotes a point outside S_s, Q denotes a point on S_s, and the suffix, (i), means the inside of the hull surface. Then, we seek a solution of $V_\nu{}^{(i)}$ which satisfies the boundary conditon on S_s as follows:

$$\left.\frac{\partial V_\nu{}^{(i)}}{\partial n}\right|_{\text{on } S_s} = -\left.\frac{\partial W_\nu}{\partial n}\right|_{\text{on } S_s}. \tag{58}$$

Then, using (53) and (58), we can obtain an internal solution as follows:

$$V_\nu^{(i)} = -W_\nu. \tag{59}$$

Therefore, by substituting (51), (58), and (59) into (57), the external solution $V_\nu^{(e)}$ must satisfy

$$4\pi V_\nu^{(e)}(Q_e) = \int_{S_s} dS \left(V_\nu^{(e)} + W_\nu\right)_Q \frac{\partial}{\partial n_Q} G_\nu\left(Q;Q_e\right) \tag{60}$$

Finally, we have the following equation by adding $4\pi W_\nu(Q_e)$ to both sides of the Eq. (60):

$$4\pi\, \psi_\nu^{(e)}(Q_e) = 4\pi\, W_\nu(Q_e) + \int_{S_s} dS\, \psi_\nu^{(e)}(Q) \frac{\partial}{\partial n_Q} G_\nu(Q;Q_e). \tag{61}$$

In this equation, letting Q_o be the limit of Q_e on S_s, we can get

$$\psi_\nu^{(e)}(Q_o) - \frac{1}{2\pi}\int_{S_s} dS\, \psi_\nu^{(e)}(Q) \frac{\partial}{\partial n_Q} G_\nu(Q;Q_o)$$

$$= 2W_\nu(Q_o), \tag{62}$$

because the singularity of first order exists in the G_ν. This $\psi_\nu^{(e)}(Q_o)$ is exactly the change of pressure on the hull surface caused by the propeller which we intend to calculate. If W_ν and G_ν can be given a priori, Eq. (62) can be considered to be an integral equation for the unknown $\psi_\nu(e)(Q_o)$. Thus, the problem of calculating the change of pressure on a hull surface caused by a propeller changes to the problem of solving an integral equation.

Time-Independent Change of Pressure On the Hull

Now, we proceed to give W_0 and G_0 for a steady case $(\nu=0)$. $G_0(\xi,\eta,\zeta;x,y,z)$ can be written as follows based on a wave making theory:

$$G_0(\xi,\eta,\zeta;x,y,z) = \frac{1}{\sqrt{(\xi-x)^2 + (\eta-y)^2 + (\zeta-z)^2}} + \frac{1}{\sqrt{(\xi-x)^2 + (\eta+y)^2 + (\zeta-z)^2}}$$

$$+ \frac{2}{\pi} \int_{-\frac{\pi}{2}}^{\frac{\pi}{2}} d\theta \int_0^\infty dk \frac{k \exp (k \overline{\eta+y} + ikp')}{k - K_0 \sec^2\theta} , \qquad (63)$$

where $p' = (\xi-x) \cos \theta + (\zeta-z) \sin \theta$. (64)

We can get W_0 by using Eq. (46) as follows. The first step is to rewrite the integrated term in the right side of Eq. (46) by the transformation

$$\frac{\partial}{\partial n_p} (\frac{1}{R}) \rightarrow \frac{\partial}{\partial n_p} G_0 . \qquad (65)$$

Then, using the rewritten expression, we can obtain W_0 as follows:

$$W_0(x,y,z) = W^*_\nu(x,y,z) \left. e^{j\nu\Omega t}\right|_{\nu=0} . \qquad (66)$$

It should be understood from the above explanation that L_λ' must be given to calculate W_0. In order to obtain L_λ' precisely, we must consider the boundary conditions on the propeller surface which have been disregarded in the discussion up to this step. To do so, however, requires complicated calculations as seen in the conventional methods for the problems of the hull-propeller interaction. The complexity of the calculations have caused the conventional methods to be impractical as described in the Section 1. Hence, the author introduces the following approximation. The steady change of pressure on a hull surface which we are now examining corresponds to a pressure component of thrust deduction. We can consider that obtaining the thrust deduction is the same as obtaining pressure on the hull surface as a percentage of the mean propeller thrust, T_0. Hence, the relationship between unknown L_0' and known T_0 can be given as follows:

$$-\sum_{q=1}^{N} \int_{S_p} dS[L_0'(\xi' \rho,\theta_0)]_x = T_0 , \qquad (67)$$

where $[\qquad]_x$ denotes the component in x direction. Now, the L_λ' can be considered as the jump of the pressure change across the propeller surface due to the interaction of the hull and propeller, and consequently, Eq. (67) may be considered as the approximate boundary condition on the propeller surface for $\psi^{(e)}_\nu(Q_o)$. By giving an arbitrary function, L_λ', which satisfies the auxiliary Eq. (67) and calculating W_0 by (46), (65), and (66), we can solve the integral equation, (62). This is the approximate calculation method proposed in this paper.

Numerical Procedure

The purpose of this section is to describe the numerical procedure for the method explained in the previous section. Here, for convenience' sake, let us denote $\psi_0^{(e)}$ in (62) by ψ^*.

Numerical Calculation

The integral equation, (62) is an integral equation of Fredholm type of the 2nd kind. Generally, it is impossible to obtain analytic solutions of the integral equation for S_s in an arbitrary form. Thus, various approximation methods have been suggested. In this paper, a definite integral is approximated by a finite sum, the equation is converted to a linear equation, and this equation is solved numerically.

At first, the following approximations are used:

(i) A hull in an arbitrary form is replaced by a polyhedron. The form of each surface named "element" is a plane quadrilateral.

(ii) On each element, the unknown function $\psi^*(Q_o)$ is assumed to be constant.

Using this approximation, the continuous function $\psi^*(Q_o)$ is replaced by the discrete quantities, ψ^*_i ($i=1,2,\ldots\ldots, M$), for the total number, M, of the elements. A control point, Q_o, where W_0 (Q_o) must be calculated, is selected for each element. Thus, we have the following transformation:

$$\int_{S_s} dS\ \psi^*(Q)\frac{\partial}{\partial n_Q} G_0 (Q;Q_o) \doteq \sum_i^M \psi^*_i \int_{i^{th}\text{ element}} dS_Q' \frac{\partial G_0}{\partial n_Q'}(Q';Q_o), \qquad (68)$$

where dS_Q', n_Q', and Q' denote values on the elements. The definite integral in the right side of this equation is an influence function from point Q to point Q_o and we denote this function by $A_{Q_o,Q}$. On calculating $A_{Q_o,Q}$, the existence of a singular point, a so called doublet, becomes a problem. However, there are many numerical calculation methods for this case. In this paper, the Hess-Smith method is used [Hess and Smith (1967)]. Further, selection of a control point is also a problem. However, for this problem various methods have also been suggested in the analysis of potential flow field. In this paper, each element is selected to be similar to a rectangle, and the point of intersection of its diagonal lines is employed as the control point. Finally, the hull surface after St.$1^{1/2}$ is taken into consideration, and it is divided more narrowly near stern in the longitudinal direction and approximately equally in the depth direction.

Thus, each element, A_i, i'($i,i'= 1,2,\ldots.,M$), which corresponds to $A_{Q_o,Q}$ can be calculated and $W_0(Q_o)$, can be calculated for each control point. Then, the integral equation of unknown function, $\psi^*(Q_o)$, is converted to a linear equation of unknown, ψ_i^*.

Now, in the calculation of $W_0(Q_o)$, the author uses the approximation that the number of propeller blades is infinite. Then, in correspondence with (46), (47), (65), and (66), we can get the following relations:

$$W_0(Q_o) \doteq \frac{1}{8\pi^2} \int_{r_B}^{r_o} dr \int_0^{2\pi} d\,\theta\, N\, \Gamma\,(r,\theta) \frac{\partial}{\partial n_\infty} \tilde{G}_0\,, \tag{69}$$

$$\tilde{G}_0(r,\theta;x,y,z) = G_0(x_p,\ r\cos\theta - f,\ \sin\theta;\ x,y,z), \tag{70}$$

$$\frac{\partial}{\partial n_\infty} = -\frac{\partial}{\partial x} - \frac{h}{r^2}\frac{\partial}{\partial\theta}\,, \quad h = \frac{\bar{H}}{2\pi}\,, \tag{71}$$

where $\bar{H}$ represents a mean pitch of the propeller blade, and r_B and r_o represent respectively radius of the boss and radius of the propeller. Moreover, $\Gamma(r,\theta)$ represents the thrust per unit length in the radial direction of the propeller blade elements and can be developed as follows:

$$\Gamma(r,\theta) = \sum_{\lambda=0}^{\infty} \Gamma_\lambda(r) e^{-j\lambda\theta}\ . \tag{72}$$

We can also get the following equation in correspondence with the Eq. (67):

$$T_0 = \int_{r_B}^{r_o} dr\ N\Gamma_0(r)\,. \tag{73}$$

Further, for the calculation of W_0 in Eq. (69), it is approximated that Γ_0 is an elliptic distribution against r, and Γ_1, Γ_2 ....are disregarded.

Examples

The numerical calculations are performed in the case of two combinations of the hull and propeller shown in Table 1. Figure 2 shows the body plan of hulls. In order to examine the correctness of the approximation used in the calculation of W_0, the procedure as follows is performed. First, performance of the propeller in the nominal wake is calculated to obtain Γ_λ and L_λ'. Next, by using the five combinations of distribution forms of Γ_λ, L_λ' and the number of the propeller blades as follows:

TABLE 1 Particulars and Operating Condition

SHIP	L_{PP}	L_{pp}/B	B/T	C_B	D	Z	U	F_n	n_M
L	6.00	6.50	2.86	.572	.215	5	2.05	.267	9.55
T	7.00	6.00	2.63	.829	.210	5	1.27	.153	8.52

L_{pp} = Length between perpendiculars (meter), B = Breadth,
T = Draft at mid-section, C_B = Block coefficient,
D = Propeller diameter (meter), Z = Number of propeller blades,
U = Ship speed (meter/second), F_n = Froude number,
n_M = Propeller's number of revolution per second.

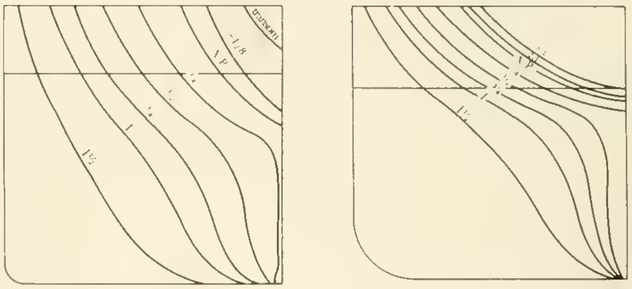

T ship L ship

FIGURE 2. Body plan.

(a) N; finite, using L_0', L_1', ... , L_7' in (66)
(b) N; infinite, using Γ_0, Γ_1, ... , Γ_7 in (69)
(c) N; finite, using L_0' only in (66)
(d) N; infinite, using Γ_0 only in (69)
(e) N; infinite, using Γ_0: elliptic in (69) ,

The W_0 are calculated. Then, by substituting these W_0 in (62), the pressure changes, ψ^*, are calculated and indicated in a non-dimensional form in Figure 3. As shown in Figure 3, the ψ^* barely differ due to the distribution form of Γ, L', and the number of propeller blades. Hence, the approximation of the elliptic distribution is reasonable.

Experiment

The experiment was performed at the towing tank of IHI by applying a standard hull surface pressure measurement [Namimatsu, (1976)]. For the ships indicated in Table 1, pressures on the hull surface are measured under both the towed and the self-propulsion condition. Differences of the measured pressure between the towed and the self-propulsion condition are used for the experimental values of the pressure change caused by the propeller.

Figure 4 shows the comparison of the experimental values to the calculated values, which are obtained by approximating Γ_0 as the elliptic distribution. In addition, Table 2 shows the pressure component, t_p, of the thrust deduction fraction, t, which is the sum of the pressure change. The comparison indicates better agreement for the L ship (a thinner ship).

Discussion

The calculation method in this paper is derived by expressing the equations and boundary conditions (which determine the change of the flow field due to the interaction of the hull and propeller) in the form of an acceleration potential. For this reason, this method nominally requires calculations of pressures induced by the hull and propeller, while the conventional methods, which express flow fields in the form of a velocity potential, require

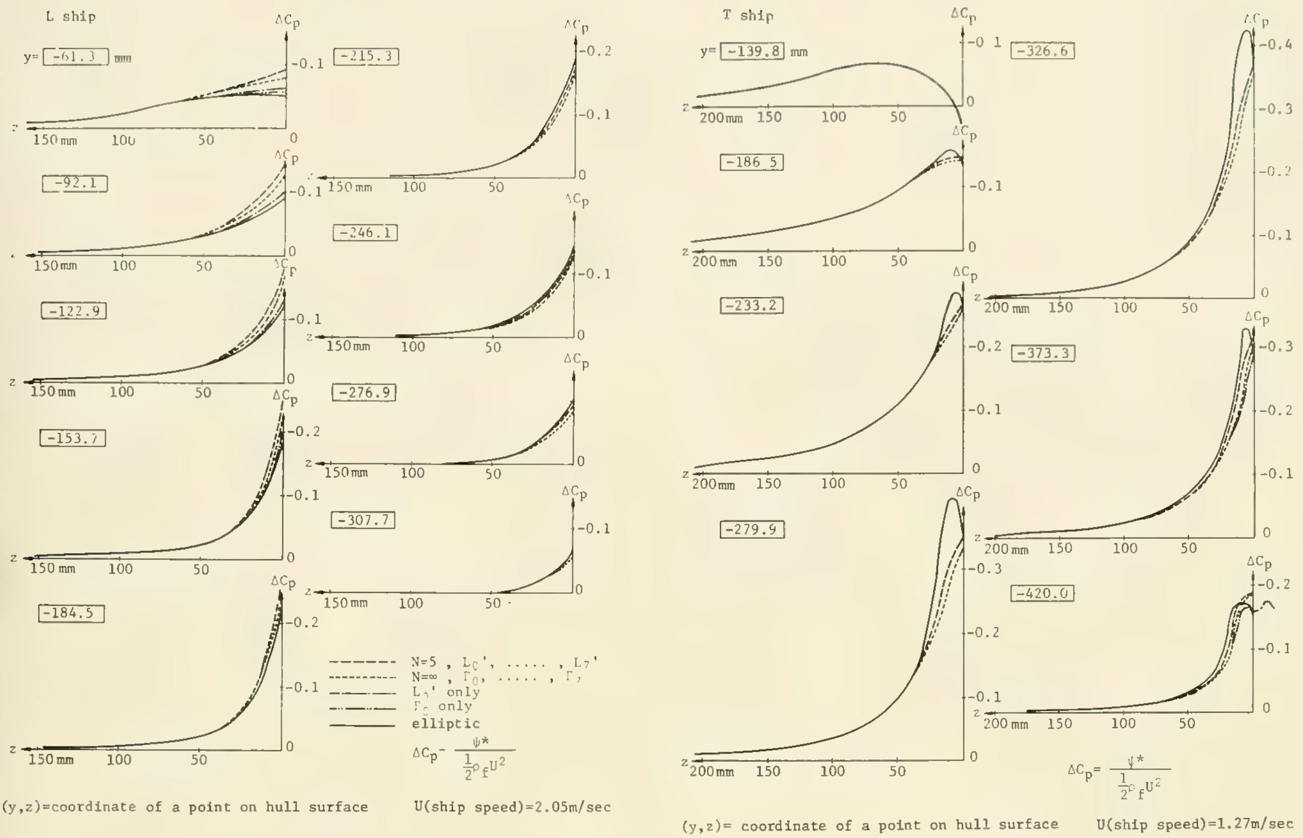

(y,z)=coordinate of a point on hull surface U(ship speed)=2.05m/sec

(y,z)= coordinate of a point on hull surface U(ship speed)=1.27m/sec

FIGURE 3. Numerical calculation of pressure change on a hull.

calculations of pressures and velocities induced by the hull and propeller. Generally, the calculations of induced pressure require less time in comparison with the calculations of induced velocity. Thus, when the present method is used, the time required for numerical calculations can be reduced to a practical value. This method can also be applied for the calculation of propeller-induced surface forces [Ishida, (1975)].

It is anticipated that the results derived by this method may be worse as the calculation point moves closer to the stern, because, in this method, the assumption of a thin hull is used, propeller boundary conditions are simplified, and the rudder is disregarded. When the actual experimental values are examined, it seems that the anticipation may be correct. However, it is more appropriate to consider that the majority of the error is due to the fact that the flow field around the hull is assumed to be inviscid.

4. WAKE ENERGY RECOVERY BY A PROPELLER

A towed hull pulls still water forward, but when the hull is self-propelled, the propeller accelerates this forward flow toward the back, and thus, the propeller recovers wake energy. Hence, it is important for the improvement of propulsion efficiency of a ship to know how the wake energy can be recovered effectively. The present, self-propulsion test method can give information for the wake energy recovery as a propulsion factor. This method is, however, insufficient to tell us how wake energy should be effectively recovered. This is due to the fact that the balance of force is a basic principle of analysis in the method, in which the balance of energy is not given sufficient consideration, and further, because almost no information on the flow field can be given. To cover the fault of the self-propulsion test method, a knowledge of the overall flow field is necessary and the distribution of energy in the flow must be found. In the vicinity of the propeller, however, the flow field is so complicated that experimental measurement and theoretical analysis are difficult. Hence, we might consider, as a practical approximation, an attempt to estimate wake energy recovery by a propeller through an analysis of the wake at a position far from the propeller.

In the next section, the phenomena of the interaction in a distant wake are analyzed by the use of Oseen's approximation to determine under what

TABLE 2 Thrust Deduction Fraction

SHIP	t	t_p	$t_p{}^*$
L	.166	.140	.109
T	.201	.160	.200

t_p is obtained from pressure measurement.
$t_p{}^*$ is calculated by present method.

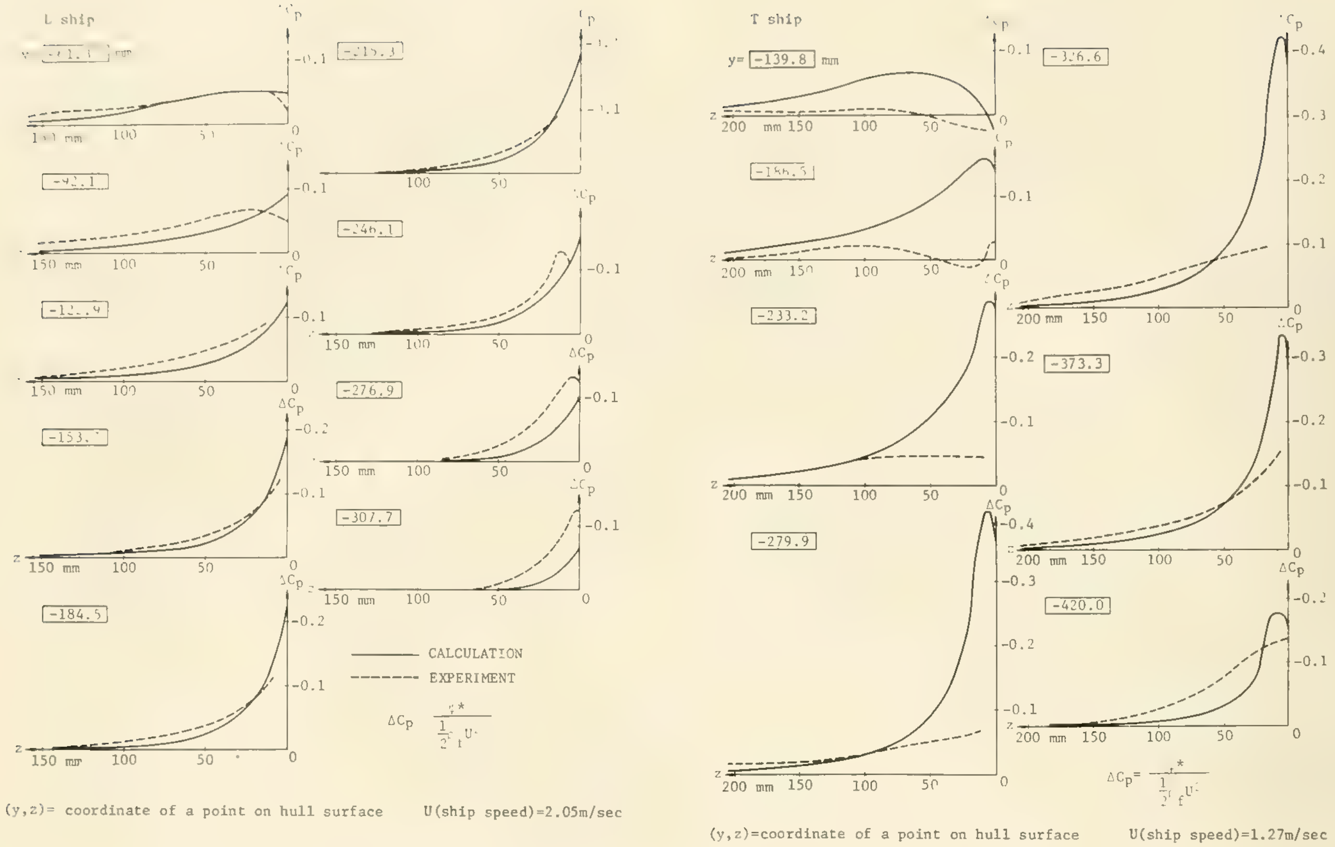

(y,z)= coordinate of a point on hull surface U(ship speed)=2.05m/sec

(y,z)=coordinate of a point on hull surface U(ship speed)=1.27m/sec

FIGURE 4. Comparison between calculated and experimental value.

conditions the wake energy is effectively recovered by the propeller.

Fundamental Equation

In this section, we assume that a ship is stationary in a uniform flow of speed U. We proceed to examine the balances of force and energy between the ship and the flow field.

Now, for the surfaces where force and energy are surveyed, we define six rectangular cross-sections in addition to the hull and propeller surfaces. These six rectangular cross-sections are indicated in Figure 5. Two vertical planes are in right angle to the direction of the uniform flow at the front and rear of the hull. The free surface and the bottom of the water are held between the two vertical planes, and two more vertical planes are parallel to the uniform flow at infinite distances to the right and left of the hull. Further for simplicity, we assume that the flow field is independent of time even if a propeller exists and a coefficient of diffusion, μ_e, due to viscosity or turbulent flow is constant. Moreover, notations used here have the same meaning as those in Section 3.

At first, let us examine the input and output of momentum at the individual surveyed surface in the towed condition. Then, as a result, the total resistance, R_t, can be given by the integration on the rectangular cross section, S_A, in the rear of the hull as follows:

$$R_t = \int_{S_A} dS[p_0 - p_s + 2\mu_e \frac{\partial u_s}{\partial x} - \rho_f u_s(U+u_s)] + \frac{1}{2}\rho_f g \int_{-b}^{b} dz\, \zeta_s^2 , \qquad (74)$$

where u, v, and w represent x-, y-, and z-components of disturbance velocity and b represents the half width of S_A at the free surface. Further, p_0 represents the pressure at $x = -\infty$. Moreover, when the energy balance is examined, kinetic energy lost when the uniform flow passes along the hull must be equal to the sum of the energy dissipated to the outside through the surveyed surfaces by heat and work. Thus, we can obtain the equation as follows:

$$\frac{\rho_f}{2}\int_{S_A} dS[U^2 - \overline{(U+u_s}^2 + v_s^2 + w_s^2)](U + u_s)$$

$$= \int_{V_f} dV\, \Phi_s(e) - \int_{S_A} dS \{(p_0-p)(U+u_s)$$

$$+ \mu_e \left[2\left(U + u_s\right) \frac{\partial u_s}{\partial x} + v_s \left(\frac{\partial v_s}{\partial x} + \frac{\partial u_s}{\partial y} \right) + w_s \left(\frac{\partial w_s}{\partial x} + \frac{\partial u_s}{\partial z} \right) \right] \Bigg\}, \tag{75}$$

where V_f denotes the flow field surrounded by the survey surfaces, and

$$\Phi_s(e) = \mu_e \left[2\left(\frac{\partial u_s}{\partial x}\right)^2 + 2\left(\frac{\partial v_s}{\partial y}\right)^2 + 2\left(\frac{\partial w_s}{\partial z}\right)^2 + \left(\frac{\partial w_s}{\partial y} + \frac{\partial v_s}{\partial z}\right)^2 + \left(\frac{\partial w_s}{\partial x} + \frac{\partial u_s}{\partial z}\right)^2 + \left(\frac{\partial u_s}{\partial y} + \frac{\partial v_s}{\partial x}\right)^2 \right. . \tag{76}$$

By using (74) and (75), the effective horsepower, EHP, can be expressed as follows:

$$\begin{aligned} \mathrm{EHP} = {} & \int_{V_f} dV\, \Phi_s(e) + \frac{\rho_f}{2} \int_{S_A} dS\,(u_s^2+v_s^2+w_s^2)(U+u_s) \\ & + \frac{U\rho_f g}{2} \int_{-b}^{b} dz\,\xi_s^2 + \int_{S_A} dS\, u_s(p_s-p_0) \\ & - \mu_e \int_{S_A} dS \left[2u_s \frac{\partial u_s}{\partial x} + v_s \left(\frac{\partial v_s}{\partial x} + \frac{\partial u_s}{\partial y} \right) + w_s \left(\frac{\partial w_s}{\partial x} + \frac{\partial u_s}{\partial z} \right) \right] . \end{aligned} \tag{77}$$

The first term on the right side expresses heat energy, the second term expresses the increase of kinetic energy, the third term expresses the increase of potential energy, and the fourth and fifth terms express work toward the outside of V_f. This equation, (77) gives the work, EHP, transmitted to the fluid through the hull when the hull is towed in still water.

Next, the self-propulsion condition can be considered in the same manner as the towed condition. The equation for the balance of forces is as follows:

$$\Delta R = \int_{S_A} dS \left[p_0 - p_{sp} + 2\mu_e \frac{\partial u_{sp}}{\partial x} - \rho_f u_{sp}(U+u_{sp}) \right] + \frac{1}{2}\rho_f g \int_{-b}^{b} dz\, \zeta_{sp}^2, \tag{78}$$

where the subscript sp denotes the self-propulsion condition and ΔR represents the skin friction correction which is used for the ordinary propulsion test at the towing tank. When the energy balance is considered, we can get the following equation:

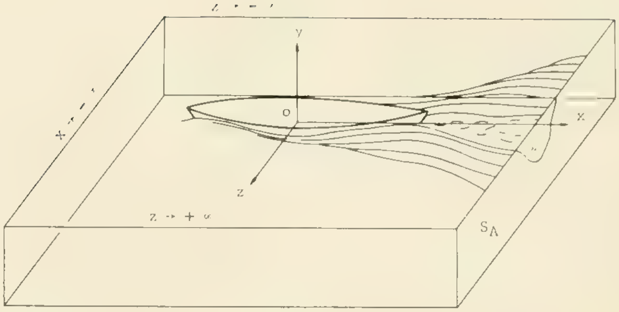

FIGURE 5. Survey surfaces.

$$\begin{aligned} \mathrm{DHP} = {} & \int_{V_f} dV\, \Phi_{sp}(e) \\ & - \frac{\rho_f}{2} \int_{S_A} dS \left[U^2 - \left(\overline{U+u_{sp}}^{\,2} + v_{sp}^2 + w_{sp}^2 \right) \right] (U+u_{sp}) \\ & - \int_{S_A} dS \Bigg\{ (p_0 - p_{sp})(U+u_{sp}) \\ & + \mu_e \left[2(U+u_{sp}) \frac{\partial u_{sp}}{\partial x} + v_{sp} \left(\frac{\partial v_{sp}}{\partial x} + \frac{\partial u_{sp}}{\partial y} \right) + w_{sp} \left(\frac{\partial w_{sp}}{\partial x} + \frac{\partial u_{sp}}{\partial z} \right) \right] \Bigg\} . \end{aligned} \tag{79}$$

where

$$\Phi_{sp}(e) = \mu_e \left[2\left(\frac{\partial u_{sp}}{\partial x}\right)^2 + 2\left(\frac{\partial v_{sp}}{\partial y}\right)^2 + 2\left(\frac{\partial w_{sp}}{\partial z}\right)^2 + \left(\frac{\partial u_{sp}}{\partial y} + \frac{\partial v_{sp}}{\partial x}\right)^2 + \left(\frac{\partial v_{sp}}{\partial z} + \frac{\partial w_{sp}}{\partial y}\right)^2 + \left(\frac{\partial w_{sp}}{\partial x} + \frac{\partial u_{sp}}{\partial z}\right)^2 \right] . \tag{80}$$

Then, using (78) and (79), we can get the following equation:

$$\begin{aligned} \mathrm{DHP} + U\Delta R = {} & \int_{V_f} dV\, \Phi_{sp}(e) \\ & + \frac{\rho_f}{2} \int_{S_A} dS\,(u_{sp}^2 + v_{sp}^2 + w_{sp}^2)(U + u_{sp}) \\ & + \frac{U\rho_f g}{2} \int_{-b}^{b} dz\, \zeta_{sp}^2 + \int_{S_A} dS\, u_{sp}(p_{sp} - p_0) \end{aligned}$$

$$- \mu_e \int_{S_A} dS \left[2u_{sp} \frac{\partial u_{sp}}{\partial x} + v_{sp} \left(\frac{\partial w_{sp}}{\partial x} + \frac{\partial u_{sp}}{\partial y} \right) + w_{sp} \left(\frac{\partial w_{sp}}{\partial x} + \frac{\partial u_{sp}}{\partial z} \right) \right] . \tag{81}$$

This equation reveals that the work transmitted to the fluid by the ship moving in still water with a constant speed, U (sum of the delivered horsepower and the work UΔR caused by skin friction correction), changes in the fluid and is dissipated as heat, kinetic energy, potential energy, and work through the surface S_A.

Oseen's Approximation and Problem of Variations

We assume that the hull is thin and S_A is placed sufficiently far behind the hull. Then, the integrations on S_A which appear in the right side of the Eqs. (74), (77), (78), and (81) can be approximated as indicated in the Appendix. Hence, the following equations can be obtained:

$$R_t = \rho_f g \int_\omega dS(H_0 - H_s) + \frac{\rho_f}{2} \int_{S_A} dS \left[\left(\frac{\partial \phi_s}{\partial y} \right)^2 + \left(\frac{\partial \phi_s}{\partial x} \right)^2 - \left(\frac{\partial \phi_s}{\partial x} \right) \right]^2 + \frac{\rho_f g}{2} \int_{-b}^{b} dz \zeta_s^2 , \tag{82}$$

$$\Delta R = \rho_f g \int_\omega dS(H_0 - H_{sp}) + \frac{\rho_f}{2} \int_{S_A} dS \left[\left(\frac{\partial \phi_{sp}}{\partial y} \right)^2 + \left(\frac{\partial \phi_{sp}}{\partial z} \right)^2 - \left(\frac{\partial \phi_{sp}}{\partial x} \right)^2 \right] + \frac{\rho_f g}{2} \int_{-b}^{b} dz\, \zeta_{sp}^2 , \tag{83}$$

where H_0, H_s, and H_{sp} represent the total head as follows:

$$H_0 = \frac{p_0}{\rho_f g} + y + \frac{U^2}{2g} , \tag{84}$$

$$H_s = \frac{p_s}{\rho_f g} + y + \frac{1}{2g} (\overline{U+u_s}^{\,2} + v_s^2 + w_s^2) , \tag{85}$$

$$H_{sp} = \frac{p_{sp}}{\rho_f g} + y + \frac{1}{2g} (\overline{U+u_{sp}}^{\,2} + v_{sp}^2 + w_{sp}^2) . \tag{86}$$

Further, ω represents the sectional area in which $H_0 - H$ is not equal to zero at S_A.
And,

$$\mathrm{EHP} = \int_{V_f} dV\, \Phi_s(e) + \frac{\rho_f g^2}{U} \int_\omega dS(H_0 - H_s)^2 + \frac{\rho_f U}{2} \int_{S_A} dS \left[\left(\frac{\partial \phi_s}{\partial y} \right)^2 + \left(\frac{\partial \phi_s}{\partial z} \right)^2 - \left(\frac{\partial \phi_s}{\partial x} \right)^2 \right] + \frac{\rho_f g U}{2} \int_{-b}^{b} dz\, \zeta_s^2 , \tag{87}$$

$$\mathrm{DHP} + U\Delta R = \int_{V_f} dV\, \Phi_{sp}(e) + \frac{\rho_f g^2}{U} \int_\omega dS(H_0 - H_{sp})^2 + \frac{\rho_f U}{2} \int_{S_A} dS \left[\left(\frac{\partial \phi_{sp}}{\partial y} \right)^2 + \left(\frac{\partial \phi_{sp}}{\partial z} \right)^2 - \left(\frac{\partial \phi_{sp}}{\partial x} \right)^2 \right] + \frac{\rho_f g U}{2} \int_{-b}^{b} dz\, \zeta_{sp}^2 \tag{88}$$

In the Eqs. (82) and (83) for the balance of force, the forces R_t and ΔR, given to the fluid from the outside are divided into the force related to the viscosity expressed by the first term and the force related to the wave making expressed by the second and third terms. In Eqs. (87) and (88) for the balance of energy, the energies EHP and DHP + UΔR given to the fluid from the outside are independently divided into the first and second terms which represent the energy related to viscosity and into the third term and the fourth term which represent the energy related to wave making.

Now, using (87) and (88) which show that the viscous energy and the potential energy are independent of each other, it is obvious that the condition for minimizing the viscous energy in (88) is a necessary condition for minimizing the DHP. We proceed, therefore, to obtain the minimum condition of the viscous energy which corresponds to the optimum condition for the energy recovery by the propeller. For this discussion, we assume that in the right side of Eq. (88), the first and second terms change independently or that the increase and decrease of the second term have, at least, a positive correlation with the increase and decrease of the first term. Based on this assumption, let us consider the conditions required in minimizing the following function:

$$E(H_0 - H_{sp}) \equiv \frac{\rho_f g^2}{U} \int_\omega dS\,(H_0 - H_{sp})^2 . \tag{89}$$

Using (83), the following equation is obtained:

$$\rho_f g \int_\omega dS(H_0 - H_{sp}) = \Delta R - R_w , \tag{90}$$

where R_w denotes a wave making resistance under a self-propulsion condition. This R_w might be approximately equal to a wave making resistance under the towed condition. Furthermore, ΔR can also be given by the total resistance under the towed condition. Hence, it can be considered that, under the self-propulsion condition, the following equation is given:

$$\rho_f g \int_\omega dS(H_0 - H_{sp}) \doteq C, \tag{91}$$

where C is constant and can be decided by the towed condition. Thus, the problem of minimization of E is converted to the problem of variations for minimization of E given by (89) under the constraint condition (91). It is obvious that the following solution exists for the problem of variations:

$$H_0 - H_{sp} = \text{constant}. \tag{92}$$

Furthermore, although it is omitted here, at least the conditions that the ship speed and displacement are constant are implicitly required in addition to this constraint condition.

Let us consider the meaning of Eq. (92). Since $H_0 - H_s$ and $H_0 - H_{sp}$ are proportional to the viscous wake in a position far from the hull as indicated in the Appendix, $(H_0 - H_s)^2$ and $(H_0 - H_{sp})^2$ are proportional to the kinetic energy of the viscous wake. Hence, the minimization of E corresponds to the minimization of the kinetic energy of the viscous wake. And, it can be considered that the condition (92) is the condition for minimizing the kinetic energy left in the wake by recovering the kinetic energy of the viscous wake with the propeller.

The optimum condition for this energy recovery is obtained under the assumption that the constant C of Eq. (91) is given as the constant decided by the towed condition. In other words, it is considered that condition (92) gives only the condition for the propeller to accelerate flow effectively under the assumption. If, however, the wave making resistance is zero under a purely self-propulsion condition, then ($\Delta R \equiv 0$) C can be expressed as $C \equiv 0$ regardless of the towed condition. Therefore, it can be considered that this fact indicates condition (92) applies not only to the optimization of the flow acceleration by the propeller but also to the optimization of the hull-propeller combination for effective recovery of the wake energy.

The author proceeds to examine the correctness of this condition in the following sections by using results of the self-propulsion tests and wake survey measurements.

Experiment

Total head at a wake far from the hull was measured at the towing tank of IHI. The measurements were performed for the ships and operating conditions indicated in the Table 1 under both the towed and the self-propulsion conditions. The measurement cross-sections which correspond to plane S_A were three vertical cross-sections of $0.3L_{pp}$, $0.5L_{pp}$, and $0.7L_{pp}$ behind A.P. Figure 6 shows the total head loss distribution of the towed condition in the non-dimensional forms and also shows $H_p{}^*$ which is the change of total head loss by the propeller action. Here, $H_p{}^*$ is obtained as follows:

$$H_p^* = (H_0 - H_{sp}) - (H_0 - H_s) . \tag{93}$$

We observe that in the towed condition the wake of the T ship spreads to the relatively lower region of the flow field. Further, we can see that the peak of the total head distribution in the towed condition agrees well with the peak of the change distribution for the T ship, but not for the L ship. In addition, Table 3 shows results of the

TABLE 3 Self-propulsion and Towed Test Data and Wake Survey

SHIP	F_n	t	w	η_H	R_t	R_w	Δ_R	F_s	f_{sp}
L	.267	.166	.271	1.14	5.57	.408	2.11	5.42	1.50
T	.153	.201	.495	1.58	3.92	.130	1.60	3.87	1.39

w = Effective wake, R_t = Total resistance from towing test (kg.),
R_w = Wave resistance from wave analysis at towed condition (kg.),
ΔR = Skin friction correction (kg.),
f_s = $\rho_f g \int dS(H_0 - H_s)$ at 0.7 L_{pp} behind ship in towed condition (kg.),
f_{sp} = $\rho_f g \int ds(H_0 - H_{sp})$ at 0.7 L_{pp} behind ship in self-propulsion condition (kg.).

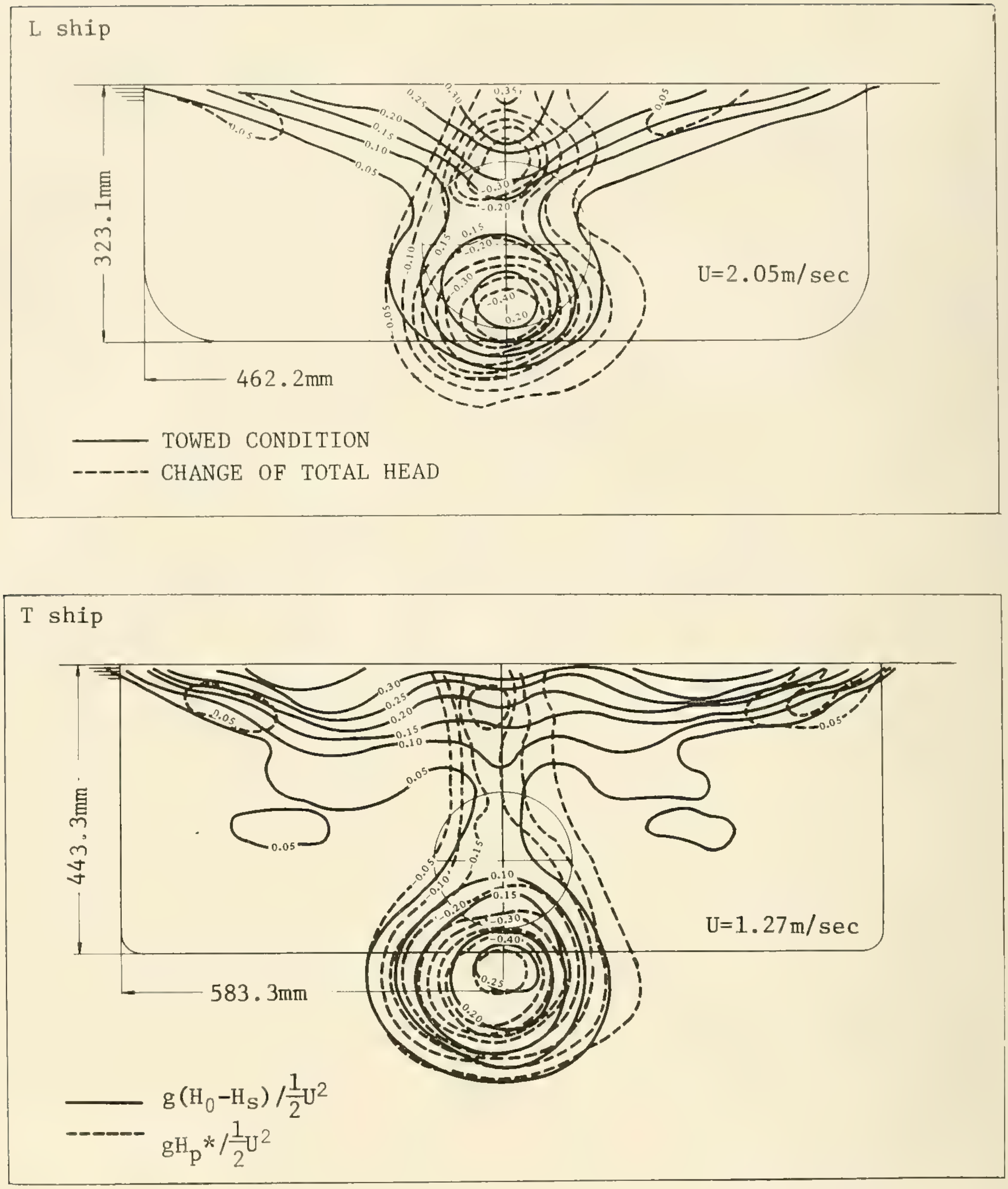

FIGURE 6. Total head distribution far from a ship.

MEASUREMENT SECTION
$0.3L_{pp}$ behind A.P.

self-propulstion test and the towing test, and viscous resistances obtained from the wake survey.

Discussion

By analyzing the wake at a distant position behind a ship, an estimate of the recovery of the wake energy by the propeller is made, and the optimum condition (92) is given. Table 3 shows that hull efficiency is better for the T ship than for the L ship. Results of the self-propulsion test, therefore, indicate that the energy recovery by the propeller is better for the T ship. On the other hand, results of wake survey measurement far from a ship indicate that for the T ship, the peak of the head change distribution agrees well with the peak of the head distribution in the towed condition. Hence, it can be considered that the propeller of the T ship makes the wake flatter in order to adapt the conditon (92).

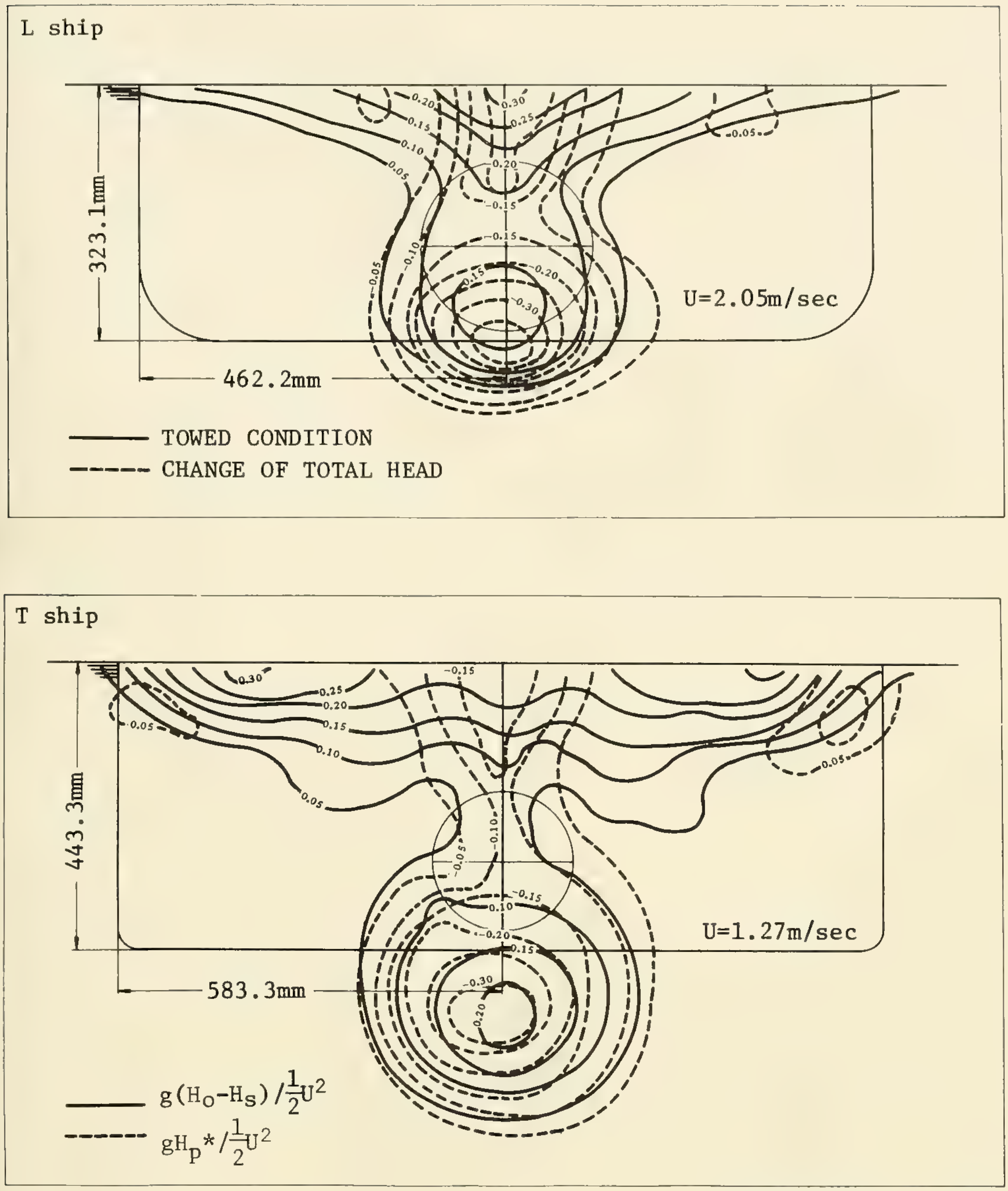

MEASUREMENT SECTION
$0.5L_{DD}$ behind A.P. FIGURE 6. (continued).

Thus, condition (92) is not contradictory to the results of the self-propulsion test.

5. CONCLUSION

From the theoretical and experimental studies for the interaction of the hull and propeller, the following conclusions are derived:

(i) Flow field in the vicinity of a hull is analyzed by using acceleration potential, and the approximate calculation method is derived. This method can be used to calculate the change of pressure on the hull and has a higher practical applicability than conventional methods.

(ii) For the analysis of the wake at a distant position behind a ship Oseen's approximation is used, and the optimum condition is given for the wake energy recovery by the propeller. This condition is examined by the results of the self-propulsion tests and the wake survey measurements.

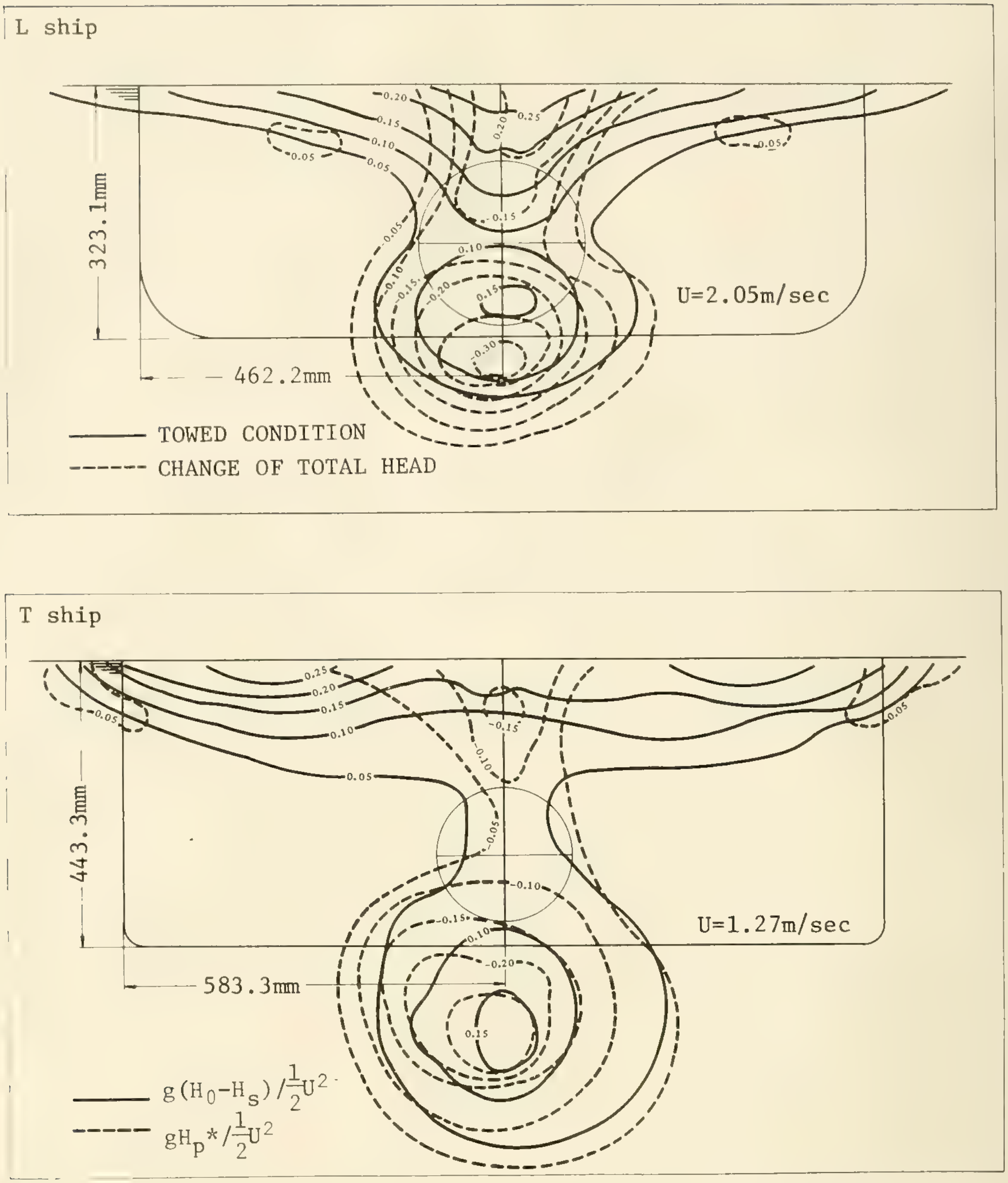

MEASUREMENT SECTION
$0.7L_{pp}$ behind A.P.

FIGURE 6. (continued).

ACKNOWLEDGMENT

Before closing this paper, the author would like to express his deep thanks to Prof. R. Yamazaki of Kyushu University who kindly examined the contents. The author also thanks Prof. T. Jinnaka and all members of IHI Yokohama Ship Model Basin who provided him with kind guidance and cooperation.

REFERENCES

Baba, E. (1969). Study on Separation of Ship Resistance Component. *J. of the Society of Naval Architect of Japan, 125,* 9.

Hess, J. L., and A. M. O. Smith (1967). Calculation of Potential Flow about Arbitrary Bodies. *Progress in Aeronautical Science, 8.*

Ishida, S. (1975). On an Approximate Calculus of the Propeller-induced Surface Force. *J. of the Society of Naval Architect of Japan, 138*, 111.

Jacobs, W. R., J. Mercier, and S. Tsakonas (1972). Theory and Measurements of the Propeller-Induced Vibratory Pressure Field. *J. of Ship Research, 16*, 2; 124.

Namimatsu, M. (1976). A Measuring Method of Hull Pressure Resistance and Its Application. *J. of the Society of Naval Architects of Japan, 139*, 13.

Tsakonas, S., W. R. Jacobs, and M. R. Ali (1973). An "Exact" Linear Lifting-Surface Theory for a Marine Propeller in a Nonuniform Flow Field. *J. of Ship Research, 17*, 4; 196.

Yamazaki, R., K. Nakatake, and K. Ueda (1972). On the Propulsion Theory of Ships on Still Water. *Memoirs of the Faculty of Engineering, Kyushu University, 31*, No. 4.

APPENDIX

Let us examine the definite integral in Eqs. (74) and (78) for the balance of force and the definite integral in Eqs. (77) and (81) for the balance of energy. At first, we denote these integrals by F_f and F_e as follows:

$$F_f \equiv \int_{S_A} dS \left[p_0 - p + 2\mu_e \frac{\partial u}{\partial x} - \rho_f u(U + u) \right] + \frac{1}{2}\rho_f g \int_{-b}^{b} dz\, \zeta^2 \quad , \tag{94}$$

$$F_e \equiv \frac{\rho_f}{2} \int_{S_A} dS \left\{ (u^2 + v^2 + w^2)(U+u) + u(p-p_0) \right. \tag{95}$$

$$\left. - \mu_e \left[2u\frac{\partial u}{\partial x} + v\left(\frac{\partial v}{\partial x} + \frac{\partial u}{\partial y}\right) + w\left(\frac{\partial w}{\partial x} + \frac{\partial u}{\partial z}\right) \right] \right\} + \frac{U\rho_f g}{2} \int_{-b}^{b} dz \zeta^2 .$$

If the terms to which μ_e is related are assumed to be small, F_f and F_e can be rewritten as follows:

$$F_f = \rho_f g \int_{\omega} d\omega (H_0 - H) + \frac{\rho_f}{2} \int_{S_A} dS (v^2 + w^2 - u^2) + \frac{\rho_f g}{2} \int_{-b}^{b} dz \quad \zeta^2 \quad , \tag{96}$$

$$F_e = -\rho_f g \int_{\omega} d\omega \cdot u(H_0 - H) + \frac{\rho_f U}{2} \int_{S_A} dS (v^2 + w^2 - u^2) + \frac{\rho_f g U}{2} \int_{-b}^{b} dz \quad \zeta^2 \quad , \tag{97}$$

where H represents total head as follows:

$$H = \frac{p}{\rho_f g} + y + \frac{1}{2g}\left[\overline{U+u}^2 + v^2 + w^2 \right] \quad . \tag{98}$$

Now, using Oseen's approximation, the following relationship can be written:

$$u = \frac{\partial \phi}{\partial x} + u' , \ v = \frac{\partial \phi}{\partial y} + v' , \ w = \frac{\partial \phi}{\partial z} + w' , \tag{99}$$

where ϕ represents velocity potential, and u', v', and w' represent velocity components of rotational motion which are zero at other than ω. Then, pressure, p, and wave height, ζ, can be expressed as follows:

$$p = -\rho_f g y - \rho_f U \frac{\partial \phi}{\partial x} , \tag{100}$$

$$\zeta = \zeta_p + \zeta' \quad , \tag{101}$$

where ζ_p is due to a potential motion and ζ' is due to a rotational motion.
Substituting (99), (100), and (101) into (96) and (97), we can get

$$F_f = \frac{\rho_f}{2} \int_{S_A} dS \left[\left(\frac{\partial \phi}{\partial y}\right)^2 + \left(\frac{\partial \phi}{\partial z}\right)^2 - \left(\frac{\partial \phi}{\partial x}\right)^2 \right] + \frac{\rho_f g}{2} \int_{-b}^{b} dz \quad \zeta_p{}^2 + \frac{\rho_f g}{2} \int_{-b'}^{b'} dz \ \zeta'^2$$

$$+ \rho_f g \int_{-b'}^{b'} dz \ \zeta_p \zeta' - \rho_f \int_{\omega} d\omega \left[2\frac{\partial \phi}{\partial x} u' + u'^2 + (\nabla\phi)^2 + Uu' \right] , \tag{102}$$

$$F_e = \frac{\rho_f U}{2} \int_{S_A} dS \left[\left(\frac{\partial\phi}{\partial y}\right)^2 + \left(\frac{\partial\phi}{\partial z}\right)^2 - \left(\frac{\partial\phi}{\partial x}\right)^2\right]$$

$$+ \frac{\rho_f gU}{2} \int_{-b}^{b} dz\ \zeta_p{}^2 + \frac{\rho_f gU}{2} \int_{-b'}^{b'} ds\ \zeta'^2$$

$$+ \rho_f gU \int_{-b'}^{b'} dz\ \zeta_p \zeta' + \int_{\omega} dS\ f'_e \ , \qquad (103)$$

where

$$f_e' = \frac{\rho_f U}{2}(u'^2 + v'^2 + w'^2) + \rho_f U \left(v'\frac{\partial\phi}{\partial y} + w'\frac{\partial\phi}{\partial z}\right)$$

$$+ \left(\frac{\rho_f}{2}\frac{\partial\phi}{\partial x} + \frac{\rho_f}{2} u'\right) \left[(\nabla\phi)^2 + (u'^2 + v'^2 + w'^2)\right.$$

$$\left. + \left(u'\frac{\partial\phi}{\partial x} + v'\frac{\partial\phi}{\partial y} + w'\frac{\partial\phi}{\partial y}\right)\right] , \qquad (104)$$

and b' represents the half width of ω at the free surface. If only the largest terms in ω are kept in the definite integral in Eqs. (102) and (103), the following approximate equations can be obtained:

$$F_f = \frac{\rho_f}{2} \int_{S_A} dS \left[\left(\frac{\partial\phi}{\partial y}\right)^2 + \left(\frac{\partial\phi}{\partial z}\right)^2 - \left(\frac{\partial\phi}{\partial x}\right)^2\right]$$

$$+ \frac{\rho_f g}{2} \int_{-b}^{b} dz\ \zeta_p^2 - \rho_f U \int_{\omega} d\omega\ u' \ , \qquad (105)$$

$$F_e = \frac{\rho_f U}{2} \int_{S_A} dS \left[\left(\frac{\partial\phi}{\partial y}\right)^2 + \left(\frac{\partial\phi}{\partial z}\right)^2 - \left(\frac{\partial\phi}{\partial x}\right)^2\right]$$

$$+ \frac{\rho_f gU}{2} \int_{-b}^{b} dz\ \zeta_p^2 + \rho_f U \int_{\omega} d\omega\ u'^2 . \qquad (106)$$

Since the following relationship is approximately satisfied in a wake far from the hull:

$$u' \doteq - \frac{g}{U} (H_0 - H), \qquad (107)$$

Eqs. (82), (83), (87), and (88) can be obtained from (74), (77), (78), and (81) by substituting this relation into (105) and (106).

Prediction Of the Velocity Field in Way of the Ship Propeller

Igor A. Titov, Alexander F. Poostoshniy, and
Oleg P. Orlov
Krylov Ship Research Institute
Leningrad, U.S.S.R.

ABSTRACT

The paper covers the problems involved in determining the velocity field in way of the ship propeller. The analysis is given for both the structure of the stern viscous flow and its change due to the ship propeller operation.

The method is offered for scaling the nominal field of axial velocities based on the use of both the semi-empirical theory of the boundary layer and theory of free turbulence, and the engineering method of estimating the action of the working propeller upon the velocity field.

As an illustration, the data of studying the influences of the scale effect and the working ship propeller upon the velocity distribution and total wake flow are presented in reference to a moderate displacement tanker.

1. INTRODUCTION

The need for a reliable definition of nonstationary loads acting on the propeller blades and shafting, and also of the intensity of hull vibration and cavitation phenomenon, has placed the wake flow problem among the most important problems of ship hydromechanics in the last few years. Though this problem first originated mainly in connection with the building of large full ships, it is of no less importance in the design of modern high speed container ships and some other classes of ships. In this sphere of hydromechanics shipbuilders are facing two main problems: a) prediction of the velocity field in way of the propeller for a ship of given lines as based on geosim model test results and b) finding solutions which provide a more favorable distribution of the wake flow. The rationalized formation of the afterbody wake is also one of the possible reserves of ship propulsion which do not yet appear to be fully realized.

At present, the problem of the afterbody wake and particularly its prediction attracts the attention of a growing number of specialists in research centers of the advanced shipbuilding nations including the USSR. In view of the extreme complexity of the afterbody flow pattern in the presence of the propeller-induced disturbances, the problem of the wake flow is still far from being solved. The laws regulating the development of wake flow and also the dependence of the velocity distributions at the propeller disk upon the shape of the afterbody lines are not quite clear. The test methods of defining the ship model wakes and model-to-ship correlation methods are as yet imperfect. Therefore the accuracy of the flow nonuniformity data obtained in way of the propeller and used as a basis for calculation of the abovementioned hydrodynamic characteristics does not satisfy the requirements of modern practice. Hence, a detailed investigation of this phenomenon is needed.

In our opinion the most important tasks are as follows: First, comprehensive physical studies of the afterbody velocity field. These would allow for better understanding and proper evaluation of the effects of different factors on the formation of wake flow in that region and help create a flow model exhibiting the main features of the phenomenon and capable of being investigated by analytical methods. At this stage the theoretical studies are essential primarily for a better understanding and more proper analysis of the test results, as well as for improving the general knowledge of both the flow laws and the scheme of breaking the wake into components. Second, the results of the experiment and the qualitative theoretical conclusions should be the basis for the development:

- methods for simulation of the nominal wake or methods for theoretical estimation of the scale effect at early stages of designing;
- methods for experimental definition of the effective wake and approximate methods for the evaluation of propeller effect using the nominal velocity field data. Since the velocity field in way of the

propeller is normally defined in the idealized conditions of the towing tank, it is absolutely necessary to evaluate and take account of the effect of operating conditions, i.e., the effect that increasing the roughness of the hull surface as well as the ship motions and drift have on the extent of flow nonuniformity at the afterbody. There are also some additional tasks, such as improvement of the method used for definition of the ducted propeller velocity field, estimation of a possible change in the wake flow over the propeller axial length, and thinking over the practicability of the methods of disturbing action upon the flow pattern with preset requirements. The methods of experimental definition of the flow velocities in the vicinity of the hull model are no less important. It is impossible to cover the results of all the above studies in a short report like this, so we shall restrict ourselves to the following traditional problems: the scale effect of the velocity field and the propeller effect on the flow formation at the stern.

2. SCALE EFFECT OF THE NOMINAL VELOCITY FIELD

The decrease of the mean wake in a model--ship correlation with sufficient accuracy can be attributed to variation in total frictional losses. The problem of simulating the local wake is far more complicated. The flow in way of the propeller is a combination of two three-dimensional flows: the boundary layer in the upper part of the afterbody with intensive secondary flows characteristic of this region and the initial part of the wake developing behind the hull which may contain discrete vortices resulting from the boundary layer separation in way of the bilge where the flow lines from under the bottom are extending to hull side surface (Figure 1 and 2). As shown by experiments, the contribution of each of these factors depends on afterbody fullness, stern frame form, buttock angles, and some other parameters.

The distributions of the relative axial velocities $U_x/Y_\delta(y/\delta;Rn)$ are different for the boundary layer, the wake, and the vortex effect region, and largely depend on the afterbody lines and the history of the flow. The solution of the scale effect problem by a purely experimental way is not practicable, so when the general laws of variation in the flow characteristics are established for model - ship correlation, the approximate methods of the semiempirical theory of turbulent boundary layer and of the free turbulence theory are of great importance; also important are comprehensive physical investigations of the afterbody flow which are necessary for the refinement of the flow model and formulation of the simplifying assumptions. Such investigations should cover the whole of the viscous wake region (Figure 1 and 2) and not be limited to the disk propeller area as is usually done in practice.

The phenomenon being too complicated, a general approach to simulating the flow seems to be unattainable at present. Therefore, it is expedient to discuss some particular models of the flow. Some of the flows may be considered as the most common types which can easily be investigated. These are:

a) the velocity field of a single-screw ship of moderate fullness with V-shaped or U-shaped frames where the contribution of bilge vortices is not significant;

b) the velocity field of high-speed, twin-screw container ships;

a more complex pattern and more complex scaling laws are characteristic for

c) the velocity field of full ships ($\delta > 0.8$) with U-shaped frames where the intensive bilge vortices are formed;

d) the velocity field of the very full ships with the boundary layer separation at the afterbody.

Model "a"

The calculation data obtained for a three-dimensional boundary layer lead to the conclusion that with moderate transverse flows the variation in characteristics of the main flow accounting to Rn does not differ markedly from those obtained for a two-dimensional boundary layer. Hence, for practical estimation of the axial velocity field in the upper part of the afterbody (Figure 1) we can use, without introducing large errors, the boundary layer correlation schemes developed to fit the two-dimensional flow on the basis of the logarithmic law and the velocity defect law. For simulating the wake flow use can be made, with some assumptions, of the known Prandtl asymptotic solution for a two-dimensional flow which was obtained on the assumption that the flow is barotropic and that the velocity defect, ΔU, is

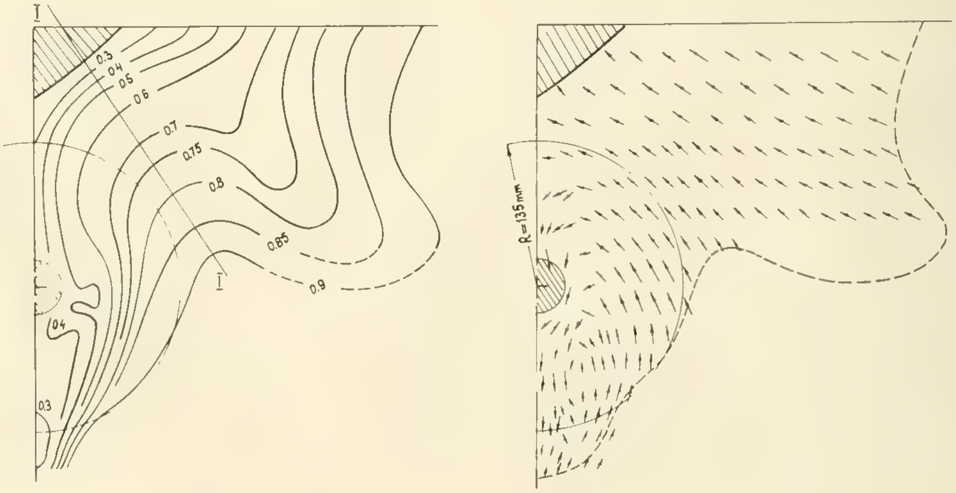

FIGURE 1. Nominal velocity field in the propeller plane for a model of tanker with moderate block coefficient, $C_B = 0.73$ (model 1).

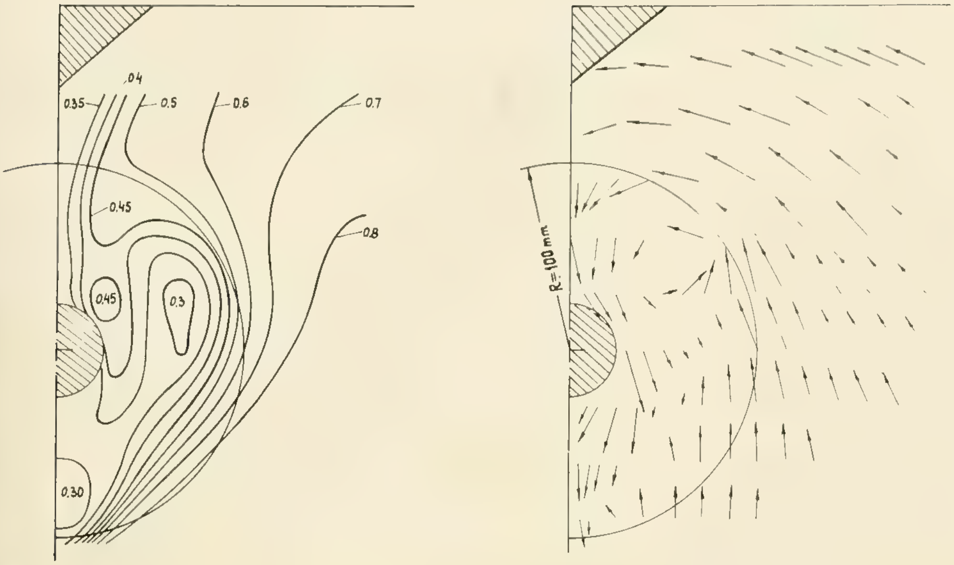

FIGURE 2. Nominal velocity field in the propeller plane of a "Krym"-type tanker model, $C_B = 0.83$ (model 2).

insignificant as compared to the velocity at the boundary of the wake flow:

$$\Delta\overline{U} = \frac{U_\delta - U_x}{U_\delta} \simeq K_1 \times (C_D/\Delta X)^{\frac{1}{2}} \times f(y/b) \qquad (1)$$

$$\overline{b} = \frac{b}{L} = K_2 \times (C_D\Delta X)^{\frac{1}{2}} \qquad (2)$$

where ΔX is the relative distance between the body trailing edge and the wake flow section under study. Naturally, these relations do not provide a reliable qualitative definition of the flow characteristics at the initial part of the three-dimensional wake which develops with the longitudinal pressure gradient. However, the above relations are considered to be quite suitable for simulating the wake field velocity because the deviations due to the effect of some factors ignored here can be mutually compensating. The practical method of correlation is based on the assumption of a negligible effect of the potential component and of a free streamline flow around the hull. The effect that the variation of the transverse velocity component has upon the axial flow with the increase in Rn is also considered insignificant. The initial experimental data for the model are defined in the Cartesian system as velocity or wake distributions against the transverse coordinate, $\overline{y} = y/L$, with the different constant values of $\overline{z}$. The coefficients, K_1, and K_2, in Eqs. (1) and (2) are assumed to be constant in the geosim horizontal sections of the wake.

Then

$$W_{FS} = W_{Fm}\sqrt{C_{FO}(Rn_S)/C_{FO}(Rn_m)}, \text{ for } y/b = \text{const} \qquad (3)$$

$$\overline{b}_S = b_S/L_S = b_m\sqrt{C_{FO}(Rn_s)/C_{FO}(Rn_m)} \qquad (4)$$

where

C_{FO} = frictional resistance coefficient in two-dimensional flow;
b = width of the wake;
$W_{FS,m}$ = frictional wake ship, model.

Such a scheme of simulation makes it possible to take into account the variation in both the wake thickness and the form of the nondimensional profile U_x/U_δ.

Model - ship correlation data for a tanker of

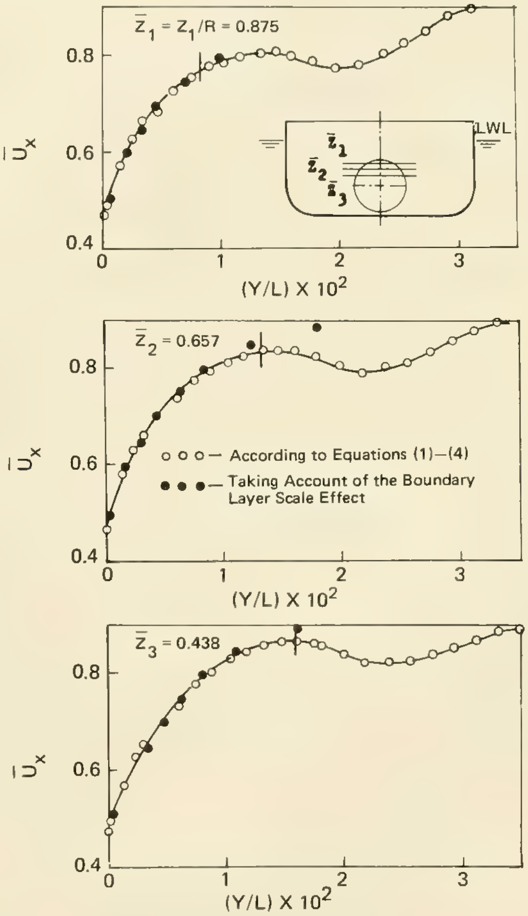

FIGURE 3. Velocity distribution in wake extrapolated to full scale.

medium displacement are shown in Figure 3 as an illustration. Isotaches (lines U = const) plotted in Figure 1 show that the upper part of the propeller disk is in the hull boundary layer region and here the flow contraction will take place almost normal to the constant velocity lines rather than to the longitudinal center plane. In this connection an attempt was made to evaluate the variation of the flow velocities in the upper part of the propeller disk using the approximate method reported at the 13th ITTC, which provides quite a good agreement with the full-scale test data, and those obtained by calculation of the three-dimensional boundary layer [Boltenko et al. (1972)]. The results of the refined model--ship correlation for this model within the propeller disk practically coincide. Velocity deviations of 3-4% V are observed only in the vicinity of the viscous wake boundary in its upper sections (outside the propeller disk), Figure 3. However, in some cases (e.g., with pronounced V-shaped afterbody frames) the hull boundary layer can play a more significant role in the formation of the wake flow, and in that case its effect should additionally be taken into consideration. Similar practical methods based on more general assumptions with respect to regularities in the variations of the axial velocities were given by the towing tanks of Europe and Japan [Sasajima and Tanaka (1966), Hoekstra (1977), Dyne (1974)]. For comparison Figure 4 shows the model--ship correlation results obtained by the Japanese method* for some specific profiles of the wake of the model under consideration. As is seen, this method leads to a greater contraction of the wake in model--ship correlation and does not take into account the variations of the velocity defect in the centerline plane. However, apart from some limited regions in the vicinity of θ = 0° and 180° the circumferential distribution of axial velocities $U_x(\zeta\theta)$ calculated by both methods differs slightly (Figure 5). For the above reasons substantial discrepancies in the vicinity of θ = 0° and θ = 180° can give rise to an appreciable change in the harmonic spectrum of the field especially in the amplitudes of the even harmonics.

At present it is difficult to find an acceptable practical method of simulating the transverse velocities, though the semiempirical theory indicates the possibility of a noticeable scale effect of the secondary flow velocities in the three-dimensional boundary layer of the ship.

Model "b"

The flow nonuniformity in way of the propeller of the twin-screw ship is mainly due to the hull boundary layer and the additional loss of velocity in the wake behind appendages

$$W = \frac{V - U}{V} = \frac{V - U_\delta}{V} + \frac{U_\delta - U_H}{U_\delta} \cdot \frac{U_\delta}{V} + \frac{U_H - V_x}{U_\delta} \cdot \frac{U_\delta}{V} = W_P + W_{FO} + \Delta W_F \quad (5)$$

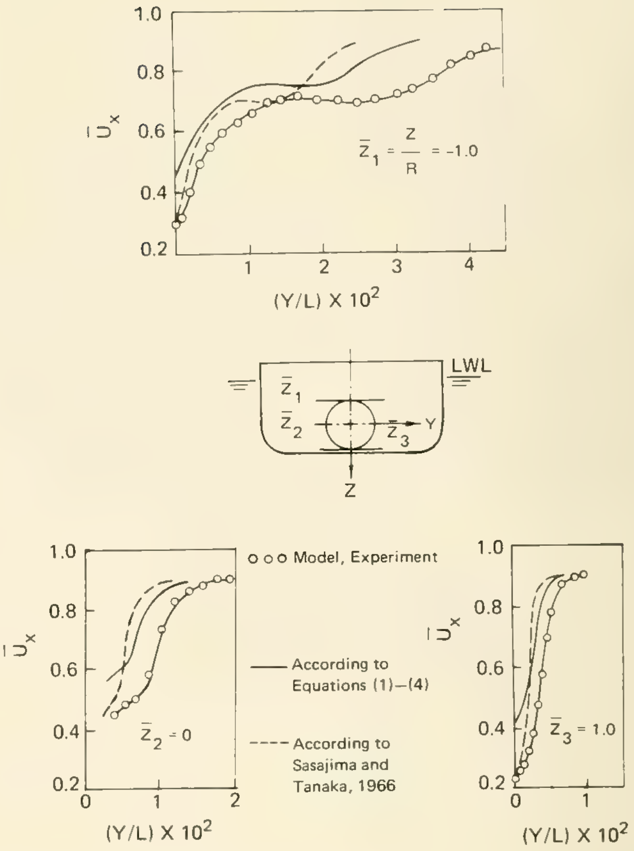

FIGURE 4. Full scale wake predicted by different methods.

where

W_P = potential component of the wake;

W_{FO} = viscous wake due to the effect of the hull boundary layer;

ΔW_F = additional losses of velocity in the wake behind the appendages;

U = horizontal local velocity

U_H = horizontal local velocity in the "bare" hull boundary layer.

The investigation of the wake scale effect for a twin-screw ship, with a probable interaction between the wake components, involves a number of complex hydrodynamic problems. They include that of the hull three-dimensional boundary layer, also the wake behind the propeller shaft fairing placed at an angle of attack to the flow inside the boundary layer, in which case not only is the mean velocity $V_H(y)$ changed but also the extent and the scale of the "outside" flow turbulence. Then there is also the wake--boundary layer interaction problem and, finally, oblique flow around the circular cylinder (shaft) placed in the turbulent boundary layer. Many of the above problems are concerned with some insufficiently known aspects of hydrodynamics of viscous fluid and, therefore, cannot be completely solved for the present. As with the previous case, approximation schemes can be used for practical estimations. By way of illustration let us consider the model--ship correlation data for a twin-screw ship equipped with propeller-shaft fairings.

---

*The method of Japanese researches was used as described by Dyen (1974).

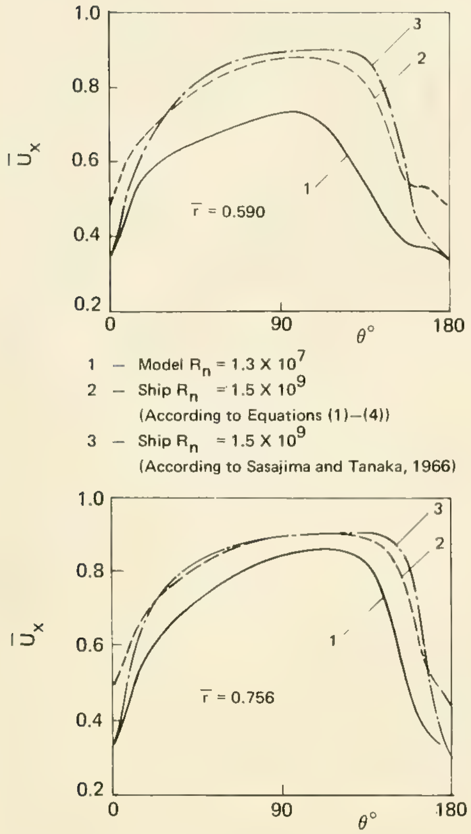

FIGURE 5. Full scale circumferential velocity distribution predicted by different methods.

The experiments show that, in the vicinity of the heavily-loaded blade sections which are at a distance from the hub, the interaction between the boundary layer and the wake behind the fairing can be considered insignificant; the effect of supporting vortices at the fairing junction is also negligible or not found at all because provision is usually made for a smooth transition of the fairing to the shaft body. This enables simulation of each component of the viscous wake $W_{FO}(Rn)$ and $\Delta W_F(Rn)$ to be investigated separately with the total scale effect to be determined by the method of superpositions. Here it is expedient to make measurements in the Cartesian system of coordinates as well. For the model--ship correlation of the wake behind the hull the method described by Boltenko et al. (1972) is used. When simulating a component of the wake ΔW_F caused by the flow around appendages, use can be made of the relationships of the free turbulence theory (1) and (2). According to data of the flow visualization, it can be considered with an accuracy sufficient for practical purposes that the streamlines on the fairing are arranged equidistant to the hull surface, and that in evaluating the scale effect the strip theory can be used. Then

$$\Delta W_{FS} = \Delta W_{Fm} \frac{\bar{U}_{HS}}{\bar{U}_{Hm}} \sqrt{C_{DS}/C_{Dm}} \quad \text{for } \bar{z} = \frac{z}{L} = \text{const}$$

$$\bar{y} = \frac{y}{b} = \text{const} \qquad (6)$$

$$\bar{b}_S = \bar{b}_m \sqrt{C_{DS}/C_{Dm}} \qquad (7)$$

where

C_D = coefficient of the fairing resistance at section at a given distance $\bar{z}$ from hull surface (Figure 6);
U_H = velocity in the hull boundary layer at a given distance $\bar{z}$ from its surface;
b = width of wake behind the fairing at the propeller.

From the model-ship correlation data shown in Figure 6 it is seen that the flow nonuniformity varies almost equally due to the scale effect of the hull boundary layer and the wake behind the shaft fairing. The mean circumferential axial wake is reduced approximately by one half.

Model "c"

The discrete vortices, which develop due to separation from the bilge, with their axes oriented in the direction of the main flow may have, in some cases, especially where the flow is around the U-shaped stern frames, a noticeable effect on the afterbody flow pattern. Generally there are two vortices arranged symmetrically in relation to the center plane; however, sometimes more complex vortical systems can be observed in the flow around full ships. The development of the bilge vortices leads not only to redistribution of the tangential velocities at the propeller, but to the additional nonuniformity of the axial wake as well due to

a) redistribution of the velocities of the main flow in the hull boundary layer and in the wake behind the hull under the action of the vortex-induced transverse velocities and

b) variation of the axial velocities in the vortex turbulent cores, the transverse dimensions

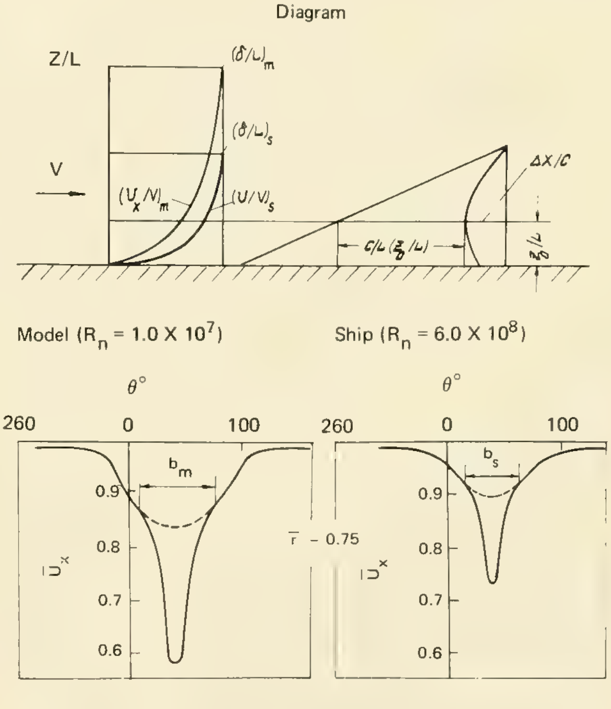

FIGURE 6. Scale effect estimates for nominal velocity distribution at propeller of a twin-screw ship with shafting fairings.

of which can be rather large as shown in Figure 2.

Thus the whole flow field containing bilge vortices can be divided into three parts:

1) the region of turbulent core,
2) the region of vortex effect on the hull boundary layer and
3) the region of nondisturbed flow in the boundary layer or in the wake (Figure 7).

The laws for changing the relative velocities in each of these regions are different in model-ship correlation.

Evaluating the scale effect of disturbances in the boundary layer is rather a complicated task partly due to the difficulty of distinguishing these disturbances in the nonuniform three-dimensional boundary layer of the hull. Therefore, at the initial stages of investigation the principal attention was paid to the specific features of such kind of flow in simplified conditions, i.e., under the assumption that artificial vortex systems were produced by means of profiles of small aspect ratio at the boundary layer of a flat surface [Poostoshniy (1975)]. For such simpler flows one can use the approximate methods of evaluating the scale effect of axial velocities in the region where influence of the vortex is observed. These methods will be based on a combination of experiment and theory or approximate semiempirical schemes, which is most important for having a general idea of the phenomenon.

Extra losses of axial velocities in the vortex cores are rather high for some ship models (reaching 20-30% of the mean wake value); these losses are also to be studied in detail.

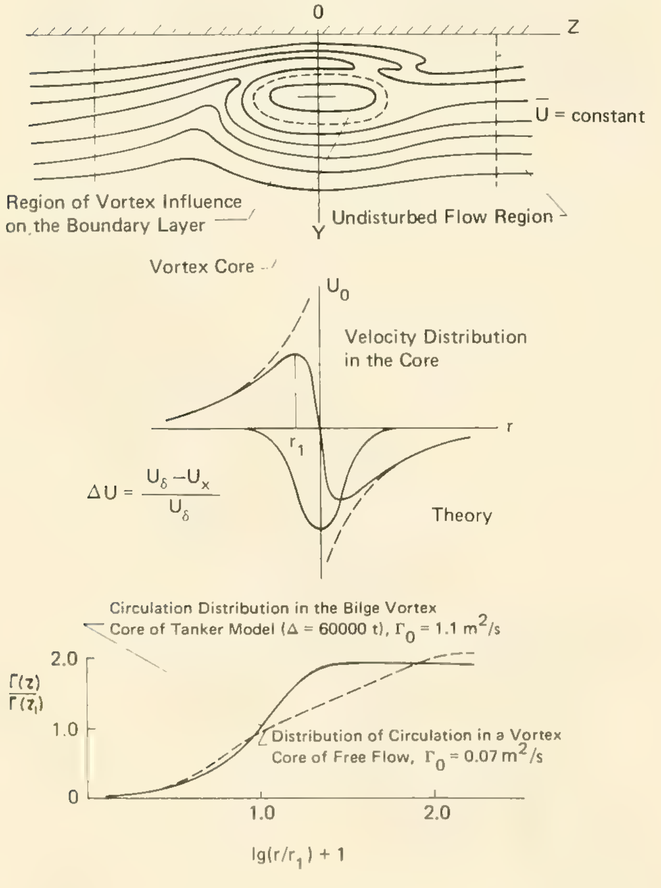
0
Z
$\bar{U}$ = constant
Region of Vortex Influence on the Boundary Layer
Undisturbed Flow Region
Y
Vortex Core
U_0
Velocity Distribution in the Core
r
r_1
$\Delta U = \frac{U_\delta - U_x}{U_\delta}$
Theory
Circulation Distribution in the Bilge Vortex Core of Tanker Model (Δ = 60000 t), $\Gamma_0 = 1.1\ m^2/s$
2.0
$\frac{\Gamma(z)}{\Gamma(z_1)}$
1.0
0
Distribution of Circulation in a Vortex Core of Free Flow, $\Gamma_0 = 0.07\ m^2/s$
1.0
2.0
$\lg(r/r_1) + 1$

FIGURE 7. Velocity field in the boundary layer with longitudinal discrete vortices.

As shown by the experiments (Figure 6) the circulation distribution law for the cores of bilge vortices is similar to that for the vortex cores in the free flow. So, in order to evaluate the scale effect of a relative defect of the axial velocity in the core, i.e., the core allowance, use can be made of the theoretical relationships derived for linear turbulent vortices.

Calculated results which are based upon rather a small amount of data on the variation in eddy viscosity coefficients with Rn obtained during model tank tests and fall-scale hydrodynamic experiments lead to the conclusion that a model-ship correlation involves relative decrease of the core size. However, far from decreasing, the wake allowance, unlike that for the boundary layer, may even be markedly growing. Some additional variation in the distribution of axial velocities in the core caused by an increase in Rn may also be due to an increase in the longitudinal pressure gradient at the stern owing to the reverse effect of the hull boundary layer on the external potential flow both on model and ship.

It is impossible at present to develop a flow model of this complexity, define the component velocities changing under different model-ship correlation laws and, finally, determine these laws; in other words it is impossible to develop a well-founded method for simulation of a three-dimensional wake flow with discrete vortices. The results of the above-mentioned preliminary studies are of qualitative character and need experimental verification. A series of comparative model and full-scale tests carried out mainly by Japanese researchers [Namimatsu and Muroaka (1973), Taniguchi and Fujita (1969)] confirm the existence of bilge vortices in full-scale conditions as well, though the data reported in the above papers are inadequate to judge the quantitative aspect of the phenomenon. We can only observe that the disturbances induced by the vortices in the flow around a ship are less noticeable, i.e., the flow is cleaned up. Therefore the attempt to use a more generalized model (model "a") seems to be justified also in this case, i.e., in the presence of developed bilge vortices, or at least an attempt to establish limits for the application of this flow model should be made. Comparative data obtained from model and full-scale tests are a decisive factor here.

Unfortunately no data of nominal wake distribution at the propeller are available. For an indirect evaluation of the scale effect of nominal wake we shall make use of the test data obtained in Japan for a 36000 t (displacement) tanker and its 1/37- and 1/20-scale models [Taniguchi and Fujita (1969)]. The measurements were taken in the boundary layer near the sternpost at a distance of 1.1D from the propeller disk. In laboratory conditions the velocity field was measured both during the towing tests and self-propelled tests. The tests performed with the model (λ = 1:20) allow the propeller effect at the measurement plane to be considered as negligible (~0.05 V) and practically constant within the region equivalent to the propeller disk area. The comparison between the velocity distribution in the wake transverse section for $\bar{z} = \bar{z}_p$ (where $\bar{z}_p$ = propeller axis level) and the circumferential distribution of the axial velocities (Figures 8 and 9) for this tanker and those for a "Krym"-type tanker shows that the simplified method of model-ship cor-

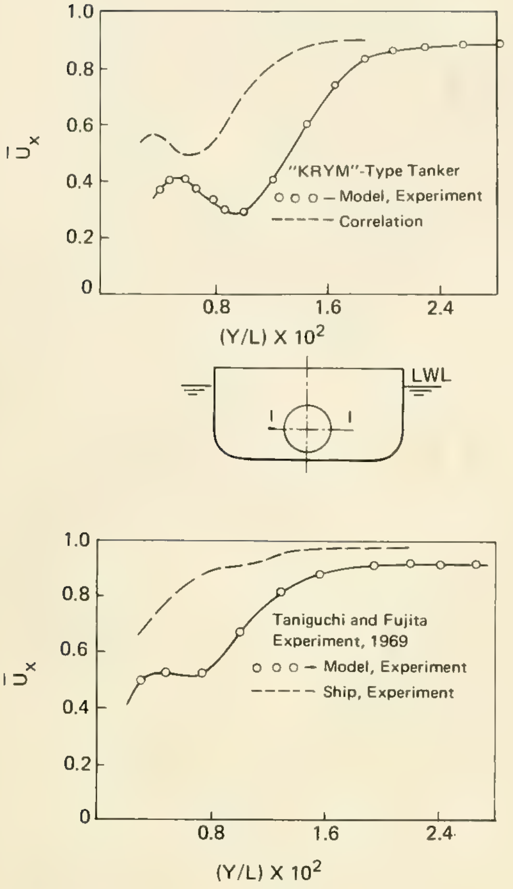

FIGURE 8. Comparison of velocity distributions for model and ship wake.

relation reveals the characteristic features of variation in the velocity field and its harmonic spectrum. However, these conclusions cannot be considered reliable enough; they need further verification.

Model "d"

Several years ago, simulation of the velocity field in the case of afterbody boundary layer separation attracted the special attention of researchers in connection with the development of very large tankers with high block coefficients and a tendency to decrease the length-to-breadth ratio. Although this problem has lost its vitality by now, studies in this field are being continued. The attempts in Japan and in the Soviet Union to theoretically and experimentally evaluate the scale effect of separation of three-dimensional and even two-dimensional boundary layers do not yet allow any definite conclusions to be made, even regarding the qualitative aspect of the phenomenon, or the development of the most approximate scheme of variation with Rn number, not only in the velocity distribution, but also in the mean value of the wake. Thus the problem of simulating the characteristics of flow at the stern with the boundary layer separation remains one of the unsolved problems in ship hydrodynamics.

3. PROPELLER EFFECT UPON THE WAKE DISTRIBUTION

Consideration of the wake scale effect when using the nominal velocity field as initial data will not always improve the agreement between the calculations and full-scale measurements of nonstationary loads acting on the shafting and, particularly, of the constant bending moment component defined by the analysis of the first harmonic. Systematic model basin test results indicate that signigicant variations of the velocity distribution at the stern may be due to the propeller performance. Several factors are to be taken into account when analysing the causes of this phenomenon. The most important among these are the propeller-induced acceleration of flow and, hence, the decrease of the layer thickness upstream, and the effect of propeller-induced radial velocity in the immediate vicinity of the propeller.

Thus it becomes necessary to investigate the ship-hull boundary layer and the wake taking into account the transverse pressure gradient. Semi-empirical theories do not permit this problem to be solved and are adequate only for the most approximate estimations of the flow history. Therefore, just as in studying some features of the nominal wake flow mentioned above, preliminary theoretical investigations of the velocity field under simplified conditions are of great importance here. Although these results are not directly applicable to the ship, they may be useful for a better understanding of the main relationships of the phenomena under study and for the devleopment of practical methods to obtain the effective wake. In this connection one cannot but mention the important contribution of American scientists to the investigation of the axisymmetrical problem, particularly, the latest works by Huang and Cox (1977).

To obtain approximate estimates of the effective

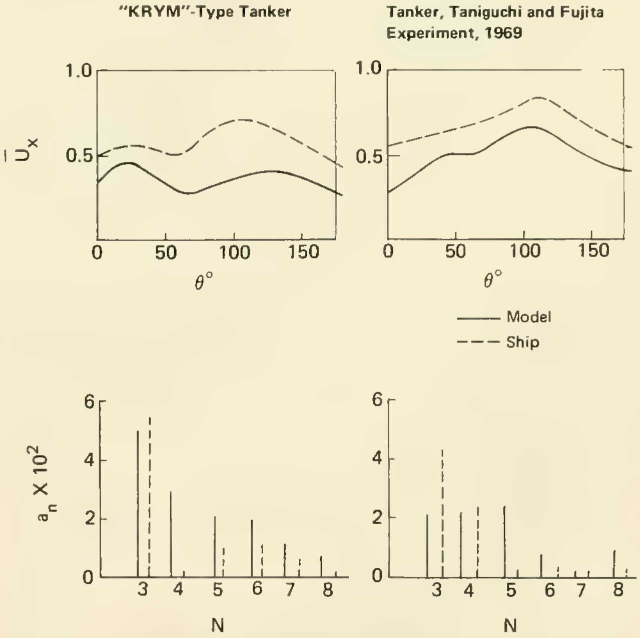

FIGURE 9. Circumferential velocity distribution and harmonic spectrum for model and ship.

wake, both in our practice and in the practice of other model tanks, use has been made in recent years of engineering procedures based on the results of nominal velocity field measurements and propeller theory relationships [Hoekstra (1977), Raestad (1972), Nagamatsu and Sasajima (1975)].

If we assume that the propeller effects are mainly due to the factors mentioned above, the propeller can be thought of as having a large diameter when evaluating the mean wake field.

This assumption will result in a decrease of the wake coefficient. The decrease of the frictional-resisted wake due to the propeller effect can be taken as inversely proportional to the square root of the diameter. Then,

$$W_{Fe} = W_{FN}/(1 + w_a/2V_A)^{1/4} \qquad (8)$$

where

$$w_a/V_A = \sqrt{1 + C_{Th}} - 1$$

$$C_{Th} = \frac{T}{(\rho V^2/2)F}$$

To define the potential component W_{pe} it is reasonable to apply the known propeller theory relationship

$$\begin{aligned} W_{pe} &= W_{pN} + (t_0/2) \times (w_z/V) \\ &= W_{pN} + \frac{t_0}{2}\,[\sqrt{1 + C_{Th}} - 1] \qquad (9) \end{aligned}$$

where

W_{pN} = experimentally defined potential component of the nominal wake field,

t_0 = thrust deduction at zero velocity of model.

Allowing for the smallness of the 2nd term in (9), the thrust deduction fraction undergoing only minor changes can be assumed for single-screw ships to be t_0 = 0.07-0.10 (the last figure relating to fuller hull shapes).

The final expression for the mean effective wake field (taking into account the scale effect) has the form,

$$\begin{aligned} W_e = {} & [W_{pN}(Rn_m) + t_0/2(\sqrt{1 + C_{Th}} - 1)] \\ & + \frac{W_{FN}}{\sqrt[4]{1/2(\sqrt{1 + C_{Th}} + 1)}} \times \frac{C_{FO}(Rn_s)}{C_{FO}(Rn_m)} \qquad (10) \end{aligned}$$

where

C_{FO} = frictional resistance coefficient in two-dimensional flow.

Relationship (10) displays good agreement with the model test data (see Table 1) and W_e values close to those obtained from the full-scale test analysis.

As can be seen from the Table, all known approximate methods yield practically the same results.

By making some additional assumptions, similar methods can also be applied for an approximate estimation of the circumferential distribution of the effective wake, and in the main they correctly reflect the variation trends of the flow at the stern while the propeller is in operation. However, they do not permit: taking into account and evaluating some qualitative changes in the hull boundary layer, which may take place due to propeller operation, such as variation in circulation of bilge vortices and their positions in relation to the ship hull; the possibility of preventing or reducing the separation about the stern zone with the propeller in operation; and, on the other hand, the possibility of the boundary layer separation in the vicinity of the stern above the propeller. Therefore, when performing a quantitative analysis of the effect the propeller has on the wake and the harmonic spectrum of the velocity field, these methods, in spite of their relative simplicity and convenience, should be applied rather carefully, as for most tentative estimates.

At the present stage of the wake problem investigation the development of experimental methods is of decisive importance.

Both for the improvement of the general knowledge of propeller effects on the flow pattern at the stern and for the solution of problems associated with ship form design, the accumulation of data on the effective velocity fields for ships of various types and the improvement of model test methods is of great importance, especially those taking account propeller induced velocities or eliminating the same from measurement data.

A practical method for estimating the effective velocity field, U_x, by way of flow velocity measurements at some distance ahead of the propeller in "open water" and behind the hull, was given in Titov and Otlesnov (1975). For measured data analysis the quasi-steady theory was accepted.

When the hydrodynamic flow angle, β_1, of a propeller blade section for the propeller operating in "open water" is equal to that behind the hull,

$$tg\beta_1 = (V_A + W_a')/\omega\tau = (U_{xe} + W_a'')/(\omega\tau - U_{\theta e}) \qquad (11)$$

where

W_a' and W_a'' = axial induced velocities ahead of the propeller in "open water" and behind the hull

$U_{\theta e}$ = circumferential component of the effective velocity field

The axial component of the effective velocity field ahead of the propeller is determined from the relation

TABLE 1. Comparison of the Mean Effective Wake Calculated by Approximate Methods With That Obtained from Self-Propelled Tests (Model No. 1)

Titov - Poostoshniy method	0.345
Nagamatsu - Sasajima method (1975)	0.340
Roestad method (1972)	0.355
Self-propulsion test data	0.350
Nominal wake	0.390

$$V_A/(V_A + W'_a) \approx U_{xe}/(U_{xe} + W''_a) \quad (12)$$

following from the equality of forces on the propeller blade section.

However, another approach to the problem of experimental determination of the effective wake is also possible based on the data analysis of measured flow velocities and total head pressure immediately ahead of the propeller and behind it. In this case, measurements are taken only with the propeller in operation behind the hull.

As is known, the circumferential induced velocity at propeller section, W_θ, in "open water" is proportional to the jump in the total head at the propeller disk

$$\rho\omega\tau W_\theta(\zeta\theta) = H_2(\tau\theta) - H_1(\tau\theta) \quad (13)$$

It can be shown that this relationship is also valid for the propeller behind the hull, if the variation of the circumferential induced velocity of the hull wake, U_θ, is negligible within the axial length of the propeller or between the sections where measurements are taken. In this case total head pressures at sections 1 and 2 (see Figure 10), ahead of the propeller and behind it are, respectively, equal to

$$H_1(\tau\theta) = P_1 + \frac{\rho}{2}\left[(U_{x1})^2 + U_{\theta 1}^2 + U_{\tau 1}^2\right]$$

$$H_2(\tau\theta) = P_2 + \frac{\rho}{2}\left[(U_{x2})^2 + (W_{\theta 1} + U_{\theta 2})^2 + (W_{\tau 2} + U_{\tau 2})^2\right] \quad (14)$$

where

$U_{x_1} = U_{xe_1} + W_{a_1}$ = axial flow velocity at section 1

$U_{x_2} = U_{xe_2} + W_{a_2}$ = axial flow velocity at section 2

W_{a_1}, W_θ and W_τ = propeller induced velocity components at respective sections

Theoretical investigation results of propeller induced velocities and test data make it possible to linearly approximate component variations of the induced velocity, $W_a(x)$, within the limits of the propeller axial length. It is believed that the axial component variation of the wake in this region is small and also obeys the linear law.

With the above assumptions, in order to determine the design effective velocity, U_{xe}, at section X_0 where the condition

$$W_a(X_0) + \frac{W_{a_\infty}}{2} \quad (15)$$

is observed, we obtain the following set of equations:

$$tg\beta_1 = \frac{U_{xe}(X_0) + W_{a_\infty}/2}{\omega\tau - w_\theta/2 + U_\theta} \quad (16)$$

$$\frac{W_{a_\infty}}{2} = \frac{W_\theta/2}{tg\beta_1} \quad (17)$$

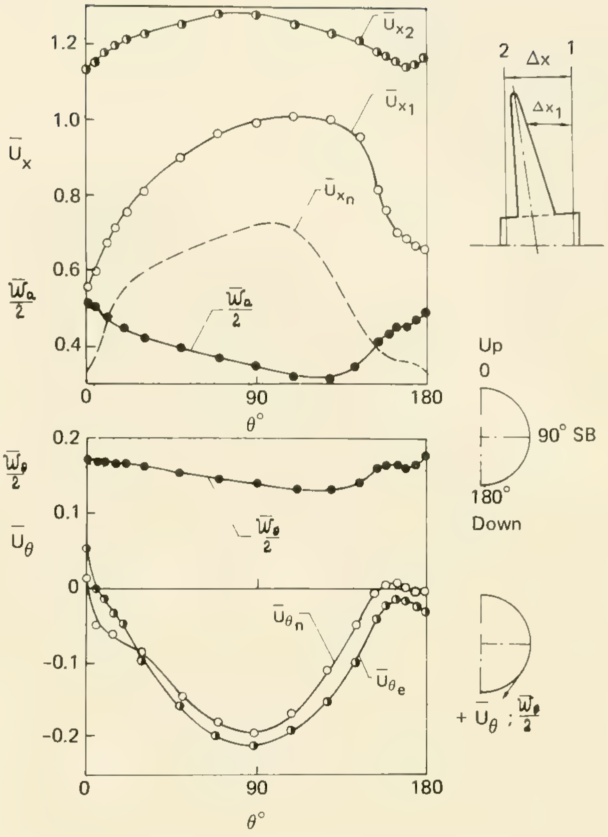

FIGURE 10. Circumferential distribution of velocity components in way of propeller ($\bar{r}$ = 0.590).

$$U_{x0}(X_0) = U_{xe}(X\ ) + \frac{w_{a_\infty}}{2} = U_{x_1} + \frac{U_{x_2} - U_{x_1}}{\Delta X} x\Delta X_1 \quad (18)$$

where

β_1 = hydrodynamic flow angle of a propeller blade section

ΔX = distance between sections 1 and 2

$\Delta X_1 = X_0 - X_1$ = distance between section 1 and the point of calculation

In propeller theory it is generally taken that the above condition is met at the propeller disk plane corresponding to the midspan section of the blade, and, in the case of blade rake, corresponding to the midsection of the blade at a relative radius, $\bar{\tau}$ = 0.7.

However the calculation results of variations in the anomalous induced velocity, $W_a(X)$, of the propeller with the finite axial length indicate that in fact the point must be found upstream of the propeller disc plane.

This conclusion is confirmed by the experimental investigation results of the propeller velocity field in open water. Taking account of these data it is more reasonable to assume the point of calculation, corresponding to condition (15), to be on the leading edge of the blade.

Application of this procedure can be illustrated on a medium size tanker model (Model 1).

Experimental studies of the velocity field for the operating propeller were performed during free-running model tests with the operational relative speed, Fn = $V/\sqrt{gL_{11}}$ = 0.22. Wake characteristics ahead of and behind the propeller were measured at equal distances from the propeller centre with a 6-point probe [devised at our model tank, Otlesnov (1969)], which enables simultaneous measurements of total head pressure, (H), static pressure, (P), and flow angles in the horizontal and vertical planes in the immediate vicinity of the propeller. When processing the measured data and analysing the nominal wake, use was made of calibration relationships which took into account the interference of flow angles in the vertical and horizontal planes with the readings of the probe. Figures 10 and 11 illustrate the initial data and the calculated induced velocities for the starboard-side of the propeller disk (right-hand rotation) in the region where sections experience maximum loading.

Comparison (Figure 12) of the nominal velocity field with the effective velocity field calculated from Eqs. (11)-(12) and (13)-(18) shows the pronounced effect the propeller has on the wake at the lower part of the propeller disk and the minor effect at the upper part of the same. This may be accounted for by a better possibility for momentum exchange between the external flow and the viscous wake under the action of radial induced velocities in a relatively thin wake at the lower part of the propeller disk, and a worse possibility at the upper part where the thickness of the viscous wake is much greater (see isotachs in Figure 1).

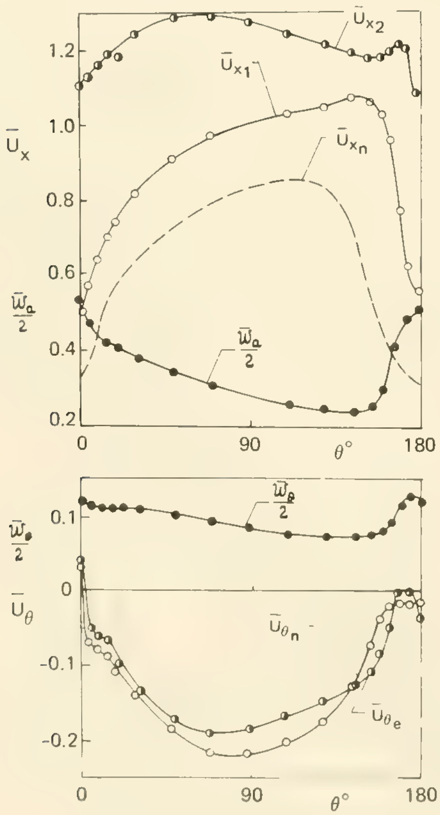

FIGURE 11. Circumferential distribution of velocity components in way of propeller ($\bar{r}$ = 0.756).

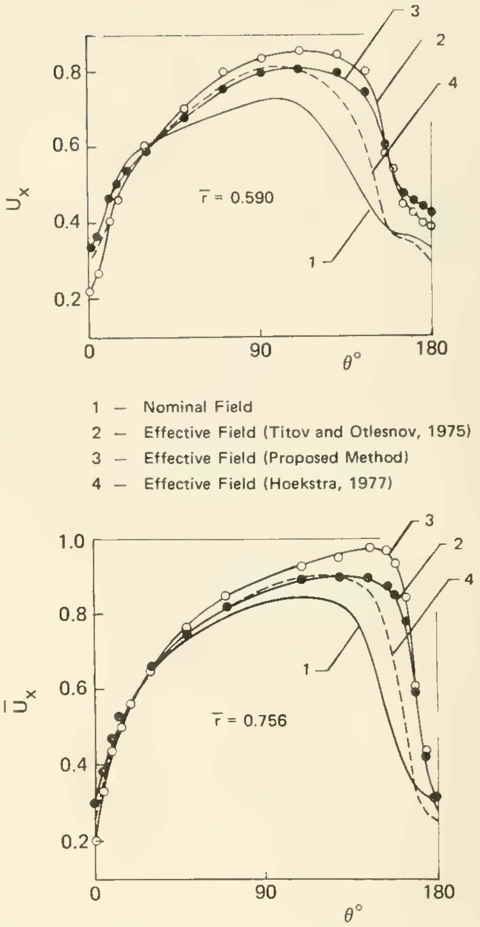

FIGURE 12. Influence of propeller operation on velocity distributions.

The above two methods for defining effective field axial velocities yield results which, as a whole, show satisfactory agreement. However there are some systematic discrepancies in the regions of θ ≈ 0° and θ ≈ 80-160°, and additional analysis is required to explain these.

Besides, the velocity distribution data obtained on the basis of measurements ahead of and behind the propeller in operation make it possible to find the thrust distribution (load coefficient of propeller, C_{Th},) over the propeller disk area

$$C_{Th}(\zeta\theta) = \left(\frac{W_a + U_{xe}}{U_{xe}}\right)^2 - 1 \qquad (19)$$

Figure 13 and the equivalent system of singularities

$$Q(\zeta\theta) = W_a/U_{xe} \qquad (20)$$

In its turn, the knowledge of this system of singularities allows one to calculate the induced velocities over the total wake region ahead of the propeller, and perform a more detailed analysis of the effect the nonuniformity of load distribution over the disk has on thrust deduction.

The following conclusions can be drawn from the comparison of Fourier transform coefficients for the circumferential distribution of axial velocities of the nominal field obtained for the model and ship

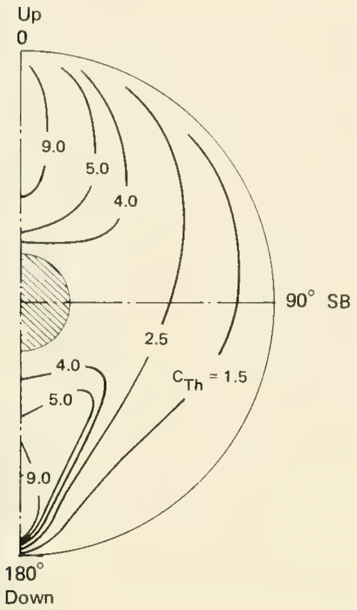

FIGURE 13. Load distribution over the propeller disk (based on effective velocity field measurements).

(model-ship correlation), as well as of the velocity field in model tests taking account of propeller effects. The amplitudes of harmonics determining the nonstationary hydrodynamic forces and moments (Figures 14 and 15) may vary several times under the influence of the above factors.

It should be mentioned that no definite regularity could be observed here. With some relative radii the amplitudes increase, with others they decrease.

As the variation in harmonic spectrum of the velocity field is of rather a complicated nature let us illustrate the effect the variation of axial velocities due to scale effect and propeller operation has on the constant component of the hydrodynamic bending moment in the vertical plane which is mainly defined by the first decomposition harmonic [Voitkunskiy (1973)];

$$M_{V0} = M_{Z0} - P_{y0} \cdot \frac{e}{2} \qquad (21)$$

where

$$M_{Z0} = JC_1/4\int_{\bar{\tau}_0}^{1} f\bar{\tau}[a_1+(1/f\bar{\tau})(J+2K_T/C_1)a_{1\theta}]d\bar{\tau} \qquad (22)$$

$$P_{y0} = -JC_2\int_{\bar{\tau}_0}^{1} f/\bar{\tau}[b_1+(1/f\bar{\tau})(J+2K_Q/C_2)b_{1\theta}]d\bar{\tau} \qquad (23)$$

$J = V_A/nD$

$\bar{\tau}_0$ = relative radius of propeller hub

K_T, K_Q = thrust and torque coefficients at design speed

a_1, b_1 = Fourier transform coefficients for the cosines and sines of the first harmonic of axial velocity on a given radius

$a_{1\theta}, b_{1\theta}$ = Fourier transform coefficients for the cosine and sine of the first harmonic of tangential velocity on a given radius

C_1, C_2 = coefficients

f = coefficient depending on radius

e = distance between the design propeller shaft section and the propeller disk

The distributions of transverse relative velocities $\bar{U}_\theta = U_\theta/V$ were taken as equal.

Table 2 shows the design estimates of relative values of the constant component, M_{V0}/K_Q, as based on various initial data.

As can be seen, the calculated results based on the nominal velocity field data may differ (even qualitatively) from those obtained with consideration for the scale effect or the effect of operating propeller. Although the local variations of the nominal field due to the scale effect or propeller operation are quantities of the same order (see Figures 5 and 12), the constant component values of the bending moment in the vertical plane determined from the effective field prove to be 4-5 times as large. Physically this may be due to the fact that, in contrast to the scale effect, the propeller effect on the viscous flow in the upper parts of the propeller disk differs from that in the lower part. In the upper part of the disk (θ = 0 - 90°) the effective field distribution of velocities in way of the heavier loaded blade sections differs only slightly from the nominal field distribution, while in its lower part (θ = 90-180°) the effective field velocities are much in excess of the nominal field velocities (by a factor of 1.5-2). This increases the asymmetry of circumferential distribution of the effective field axial

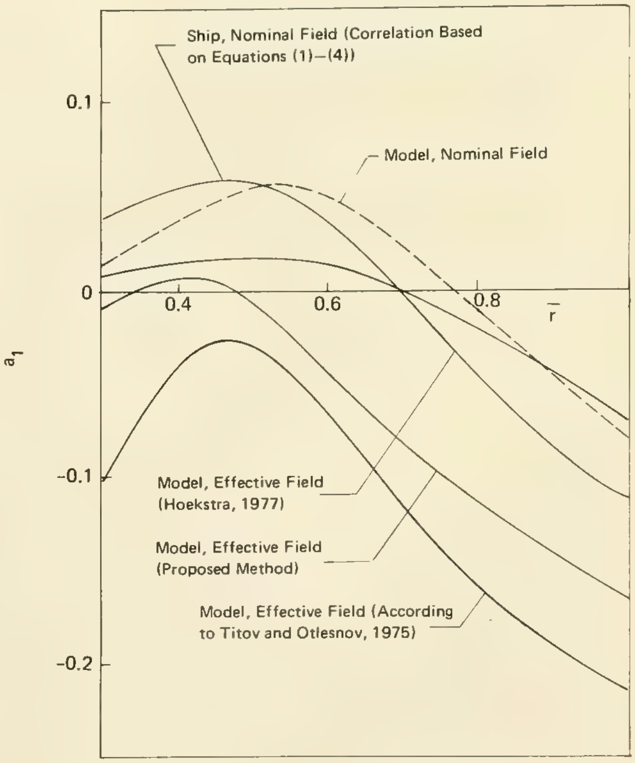

FIGURE 14. Influence of scale effect and propeller operation on harmonic spectrum.

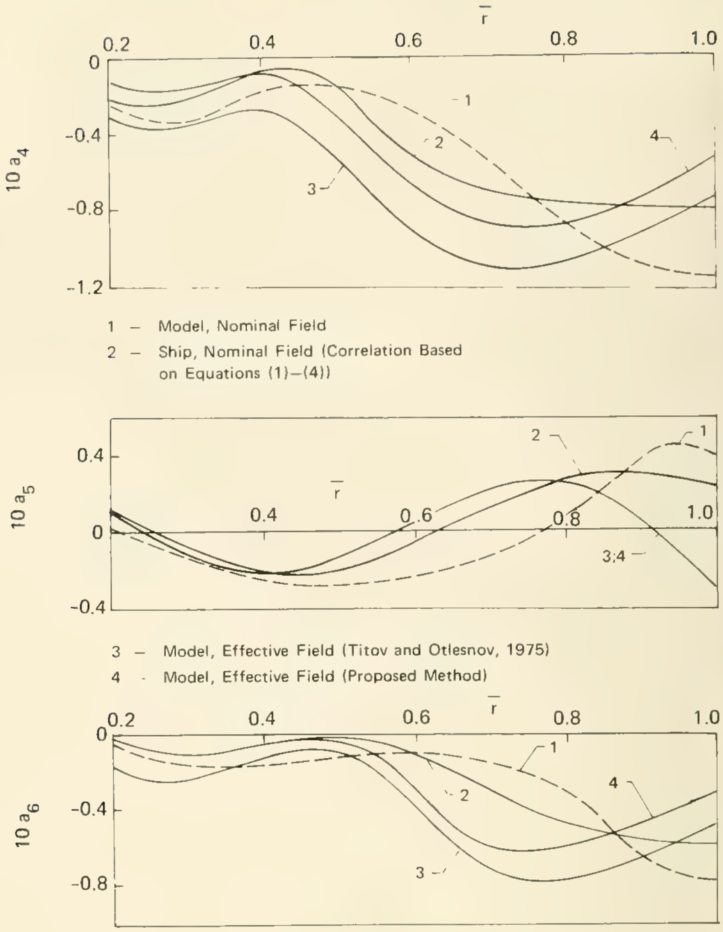

FIGURE 15. Influence of scale effect and propeller operation on harmonic spectrum.

velocities and results in an increase of the constant component of the moment in the vertical plane. The M_{V0}/K_Q values calculated from the effective velocity field approximate those observed for full-scale ships of this type under operational conditions. This fact confirms the importance of taking into account propeller operation when simulating the velocity field at the propeller. The propeller effect upon the velocity field is dependent on the load, ship hull form and afterbody shape, initial nominal field, and the relationship between propeller screw size and wake thickness, i.e., on the propeller immersion into the viscous wake.

The full-scale conditions of effective field formation are likely to differ from the model ones. Hence, the next step in studying the prediction of the flow velocity field in way of the propeller will be the development of procedures which enable simultaneous consideration of both the scale-effect and the effect of propeller operation on the wake at the stern.

TABLE 2. Variation in the Constant Component of Bending Moment Depending on the Velocity Distribution at the Propeller (Model 1)

Initial Data	Model. Experiment. Nominal Field	Model-ship Correlation Using Equations (1)-(4)	Model. Estimation of Propeller Effect According to Hoekstra (1977)	Model. Experiment Consideration of Propeller Effect by Using Equations (11)-(12)	Model. Experiment Consideration of Propeller Effect by Using Equations (13)-(18)
M_{V0}/K_Q	0.04	-0.07	-0.08	-0.35	-0.25

REFERENCES

Boltenko, V. P., O. P. Orlov, and A. F. Poostoshniy (1972). Determination of the boundary layer characteristics of ships from model test data, *13th ITTC, Material of Interest*, Berlin/Hamburg.

Dyne, G. (1974). A study of the scale effect on wake, propeller cavitation, and vibratory pressure at hull of two tanker models, *Transactions the Society of Naval Architects and Marine Engineers 82*, 162-185.

Hoekstra, M. (1977). An investigation into the effect of propeller hull interaction on the structures of the wake field, Symposium "*Hydrodynamics of Ship and Off-shore Propulsion Systems*," Oslo, March.

Huang, T. T., and B. D. Cox (1977). Interaction of afterbody boundary layer and propeller. *Proceedings of Symposium of Hydrodynamics of Ship and Offshore Propulsion Systems*, Oslo, March 20-25.

Nagamatsu, T., and T. Sasajima (1975). Effect of propeller suction on wake. *Symposium on Propulsive Performance of High Block Ships*, Tokyo, June.

Namimatsu, M., and K. Muraoka (1973). Wake distribution of full form ship. *IHI Engineering Review*, *7*, 3; 12pp.

Otlesnov, Yu. P. (1969). New means for measuring unsteady characteristics of ship wake in a towing tank. *Proc. 12th ITTC*, Rome.

Poostoshniy, A. F. (1975). Features of flow around the hull and full hull resistance structure, in *Problems of Ship Applied Hydromechanics*, I. A. Titov, ed., Izd. Sudostroeynie, 54-92 (in Russian).

Raestad, A. E. (1972). Estimation of a marine propeller's induced effects on the hull wake field-scale effects on hull wake field. *Report No. 72-3-M, Det Norske Veritas*.

Taniguchi, K., and T. Fujita (1969). Comparison of velocity distribution in the boundary layer of ship and model. *Proc. 12th ITTC*, Rome.

Titov, I. A., and Yu. P. Otlesnov (1975). Some aspects of propeller-hull interaction. *Swedish-Soviet Propeller Symposium*, Moscow.

Sasajima, H., and I. Tanaka (1966). On the estimation of wake of ships. *Proc. 11th ITTC, SNAJ*, Tokyo.

Voitkunsky, Ya. I., R. Ya. Pershits, and I. A. Titov (1973). A manual on ship theory. *Sudostroyenie*, Leningrad. (In Russian).

Recent Theoretical and Experimental Developments in the Prediction of Propeller Induced Vibration Forces on Nearby Boundaries

Bruce D. Cox and Edwin P. Rood
David W. Taylor Naval Ship Research and Development Center
Bethesda, Maryland

William S. Vorus
University of Michigan
Ann Arbor, Michigan

John P. Breslin
Stevens Institute of Technology
Hoboken, New Jersey

ABSTRACT

This paper concerns recent advances in the theory and numerical solution of propeller induced pressure forces acting on ship hull surfaces. The analysis is formulated in terms of the diffracted potential flow about general three-dimensional hull boundaries in the presence of a free surface. The influence of the propeller is derived from lifting-surface theory, explicitly accounting for finite blade number, blade thickness and skew, and radial and chordwise loading (steady and unsteady, but subcavitating). Two methods have been developed to calculate the periodic forces. In the direct approach, time-dependent source singularities are distributed over the body surface with the strengths determined for a prescribed propeller onset flow. The force is then found by applying the extended Lagally theorem. In the second approach, based on a special application of Green's theorem, the force is obtained by finding the velocity potential at the propeller generated by the boundary executing simple oscillatory motions.

A towing tank experiment is described in which blade frequency forces were measured on a body of revolution adjacent to a propeller operating in virtually uniform flow. The simplifications of body shape and propeller loading provided a physical model which could be treated in a reasonably exact fashion by the theory. The body consisted of two parts. A heavy afterbody, attached to the towing strut, acted as a seismic mass at all but very low frequencies. The forces were measured on a light, rigid forebody supported from the afterbody by a specially designed strain-gaged flexure assembly. Tests with two propellers differing only in blade thickness revealed the separate contributions of blade loading and thickness and the results obtained agree favorably with the analytical predictions.

1. INTRODUCTION

Propeller induced ship hull virbration continues to be a major source of uncertainty and, indeed, frustration to the naval architect. Today we witness a trend toward larger and faster ships with higher power being delivered to the propeller. These designs are inherently more susceptible to propeller related vibration problems, as has been learned from bitter and usually costly experience and this situation has focused renewed attention on the need for improved methods to predict propeller exciting forces - methods which are both reliable and practical for application during the design process.

Two distinct, but related types of propeller exciting forces (and moments) produce hull vibration. Unsteady blade loads developed by the propeller operating in the nonuniform ship wake and transmitted to the hull directly through the propeller shafting are termed *bearing forces*. Periodic pressure forces acting on the surface of the hull, arising from the propeller unsteady velocity and pressure fields, are called *surface forces*. Various approaches have been developed to predict these forces from model tests. For example, bearing forces are measured on a model propeller in a water tunnel using wake screens to simulate the flow at the ship stern. Surface pressures can be obtained from measurements of transducers distributed over the surface of the model hull afterbody. Alternatively, the entire hull afterbody can be cantilevered on a flexure assembly instrumented to measure the total surface force [separated stern technique, Stuntz et al. (1960)].

The foregoing experimental techniques, and others [most notably Lewis (1969)], have proven to be costly and difficult to carry out in practice. Moreover, a large number of experiments would be required to examine all the pertinent physical parameters, including hull form, propeller clearances, blade geometry and loading characteristics. Consequently, researchers are attempting to develop theories and numerical procedures for calculating propeller exciting forces. An analytical approach offers a means to economically evaluate competing propeller-hull design concepts as well as to diagnose at-sea vibration problems and identify corrective measures.

The present paper concerns recent advances in the theory for propeller induced surface forces. A general three-dimensional boundary intercepting the propeller disturbance field poses a formidable diffraction problem. As a first step, it is necessary to determine both the time-average and unsteady loading on the propeller. All of the components of loading, together with blade thickness, contribute to the propeller induced flow impinging on the hull and the resultant unsteady pressure. Fortunately, as a result of much past work in the analytical prediction of bearing forces, there now exist powerful theoretical methods for calculating unsteady propeller loading in a prescribed nonuniform flow. The analysis rests on a lifting-surface representation of the propeller, explicitly accounting for number of blades, radial and chordwise distribution of loading, thickness, and skew. While further refinements and improvements, such as the prediction of transient blade surface cavitation, are needed, the calculation of blade loading can now be done with sufficient accuracy to address the surface force analysis. Also, as these improvements in the propeller calculation become available, they can be incorporated into the surface force calculation without fundamental changes.

Previous analyses of the surface forces are formulated in terms of the diffracted potential flow about the solid boundary in the presence of a given propeller onset flow. To facilitate the analysis, it was necessary to introduce simplified representations of both the propeller and the boundary as outlined by Breslin (1962) and more recently, Vorus (1974). For example, analytical expressions for the vibratory force produced on a long flat strip and a circular cylinder adjacent a propeller in uniform flow were derived some years ago [Tsakonas et al. (1962) and Breslin (1962)]. These investigations provided useful insights regarding the importance of propeller tip clearance and number of blades. However, such approximate treatments neglect what are now known to be certain essential physics of the propeller-hull interaction. The net force on a long boundary may be deceptively small because of cancellation of large out-of-phase force components developed fore and aft of the propeller. On a hull which terminated in the immediate vicinity of the propeller, such cancellation will not occur. Also, the components of unsteady blade loading at or near blade frequency can produce much larger surface forces than those arising from the steady loading and thickness. Components of blade loading at higher frequencies, while relatively smaller in amplitude, generate field pressures which decay much more slowly, encompassing a large portion of the hull afterbody and resulting in a significant integrated force. For this same reason, an experimental determination of the total surface force by measurement of pressures at selected positions on the hull boundary can be disastrously misleading. In view of these circumstances, it is now generally accepted that a satisfactory theory must represent the hull boundary in a reasonably exact fashion, accommodate the presence of the free surface, and account for all constituents of propeller loading.

This paper sets forth a comprehensive theory for propeller-hull interaction and describes procedures for calculating the periodic forces acting on the hull surface. The paper is divided into five sections. In the first section, the problem for the diffracted potential flow about the hull is formulated, in which the propeller unsteady disturbance is assumed to be of small amplitude and high frequency. In keeping with the desire for first order results, the high frequency linearized free surface conditon applies. However, the zero normal velocity condition is satisfied exactly at the hull boundary. Formulae for the surface pressures and forces may then be expressed in terms of the propeller velocity potential and the unknown diffraction potential. The following section deals with the representation of the propeller. Dipole singularities with strenths related to the blade pressure loading and thickness are distributed over helicoidal surfaces approximating the geometry of the actual blade surfaces. Based on this model, expressions for the field point velocity potential arising from loading and thickness are developed. Examination of these formulae and their asymptotic behavior at large distances reveals important propagation characteristics associated with the unsteady blade loading components at and near blade frequency.

In the subsequent sections, two methods of solution are developed for determining the surface forces. The direct approach consists of distributing time-dependent source singularities over the hull surface with the source strenths determined for a prescribed propeller onset flow using a modified Douglas-Neumann calculation [Hess and Smith (1964)]. The force on the body is then found by applying the extended Lagally theorem to the hull singularities. In an alternative approach, based on a special application of Green's theorem, the force is obtained by finding the velocity potential at the propeller produced by the hull boundary executing simple oscillatory motion.

In the final section, a towing tank experiment is described in which blade frequency forces were measured on a body of revolution adjacent to a propeller operating in uniform flow. The simplifications of body shape and propeller loading provided a physical model which could be treated in a reasonably exact fashion by the theory. Despite these simplifications, certain classical problems were encountered in the design of the experiment including the measurement of a relatively small force, avoidance of system resonances in the frequency range of interest, and retrieval of the force signal from background noise. A two-part body design was developed, similar in concept to the separated stern technique mentioned earlier. A heavy afterbody attached to the towing strut, behaved as a seismic mass at all but very low frequencies. Forces were measured on a light rigid forebody, supported from the afterbody by a specially designed and dynamically calibrated straingaged flexure assembly.

Tests were performed with two propellers differing only in blade thickness in order to reveal the separate contributions of loading and thickness. The measured forces (amplitude and phase) were obtained for a range of speeds and advance coefficients and for two positions of the propeller relative to the test body. The results agree favorably with the theoretical predictions. It is recommended that this experimental technique be extended to study the effects of nonuniform flow and intermittent blade surface cavitation.

2. FORMULATION OF THE PROBLEM

Consider a ship moving at constant speed U through otherwise undisturbed water. We seek to determine the periodic forces and moments exerted on the ship hull surface arising from the unsteady propeller velocity and pressure fields. The fluid is considered to be incompressible and inviscid and within the domain bounded by the free surface, the hull boundary, and the propeller blades (and trailing vortex wakes), the flow is assumed to be irrotational. Under these circumstances, a fluid velocity potential exists which can be expressed in terms of steady and unsteady components as

$$\Phi(\vec{x},t) = Ux + \phi_S(\vec{x}) + \phi_P(\vec{x},t) + \phi_D(\vec{x},t)$$

Here, $\vec{x} = (x,y,z)$ is a cartesian coordinate system fixed to the ship with the x and y axes in the waterline plane, and z-axis directed upward. $\phi_S(\vec{x})$ is the steady disturbance flow about the bare hull in the presence of the free surface, $\phi_P(\vec{x},t)$ is the propeller potential, and $\phi_D(\vec{x},t)$ is the potential of the flow arising from the propeller-hull interaction, often termed the scattering or diffraction potential. It should be noted that the presence of the viscous, rotational wake of the ship is ignored in the diffraction problem, i.e., it is assumed that the unsteady pressure forces on the hull can be derived from potential flow considerations alone.

The propeller potential is periodic in time and, by virtue of the symmetry of identical, equally spaced blades, may be expressed as a Fourier series with harmonics in blade passage frequency as

$$\phi_P(\vec{x},t) = \sum_{n=0}^{\infty} \phi_{P_n}(\vec{x})e^{inN\omega t} \tag{1}$$

with ϕ_{Pn} being the complex amplitude of nth harmonic. (In this and all subsequent expressions involving $e^{inN\omega t}$ the real part is understood to be taken.) Similarly, the diffraction potential will be of the form

$$\phi_D(\vec{x},t) = \sum_{n=0}^{\infty} \phi_{D_n}(\vec{x})e^{inN\omega t} \tag{2}$$

We now consider the boundary value problem for the potential $\phi = \phi_P + \phi_D$, assuming the fluid disturbance velocities to be small compared to the ship speed, i.e., $|\nabla\phi|$ and $|\nabla\phi_S| \ll U$. Within the fluid domain, the potential must satisfy Laplace's equation

$$\nabla^2\phi_n(\vec{x}) = 0 \tag{3}$$

At large depth and distances upstream of the hull and propeller the disturbance must vanish

$$\begin{aligned} \nabla\phi_n &\to 0 \qquad x \to -\infty \\ &\to 0 \qquad z \to -\infty \end{aligned} \tag{4}$$

and at large downstream distances, $x \to +\infty$, ϕ_n satisfies a suitable radiation condition.

The boundary condition on the hull surface, denoted by S, requires that the fluid velocity must be tangent to the surface, or

$$\vec{n} \cdot \nabla\phi_n(\vec{x}) = 0 \qquad \vec{x} \text{ on } S \tag{5}$$

$\vec{n}$ being the outward unit normal vector to the surface (see Figure 1). Here we have assumed the hull to be rigid and stationary with respect to the translating coordinate system (i.e. hull motion and deformation due to propeller excitation is ignored).

The linearized free surface boundary condition may be written in the form

$$-(nN\omega)^2\phi_n + (2inN\omega U)\frac{\partial\phi_n}{\partial x} + U^2\frac{\partial^2\phi_n}{\partial x^2} + g\frac{\partial\phi_n}{\partial z} = 0$$

$$\text{on } z = 0 \tag{6}$$

In order to establish the relative magnitude of terms the equation is recast in nondimensional form using the ship speed U and propeller radius R_0 for reference length and time scales, obtaining

$$-\phi_n + 2i\varepsilon\frac{\partial\phi_n}{\partial x} + \varepsilon^2\frac{\partial^2\phi_n}{\partial x^2} + \frac{gR_o}{U^2}\varepsilon^2\frac{\partial\phi_n}{\partial z} = 0 \text{ on } z = 0$$

where $\varepsilon = J/\pi nN$, J being the propeller advance coefficient. It may now be observed that typical propeller applications, $\varepsilon \ll 1$ and the first term will dominate. Thus, as a first approximation the free surface boundary condition (6) reduces to

$$\phi_n(\vec{x}) = 0 \qquad \text{on } z = 0 \tag{7}$$

This completes the statement of the boundary value problem for the diffraction potential as summarized in Figure 1. It should be noted that by virtue of (7), the function $\phi_n(\vec{x})$ can be analytically continued into the upper half plane, $z > 0$, in a straightforward manner. As will be shown in subsequent sections a solution can be constructed in terms of

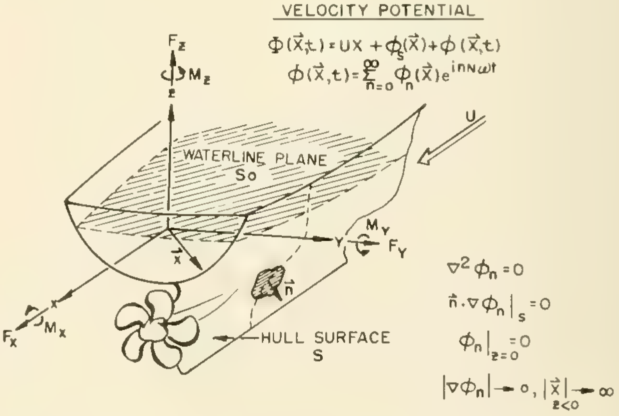
VELOCITY POTENTIAL
$\Phi(\vec{x},t) = UX + \phi_S(\vec{x}) + \phi(\vec{x},t)$
$\phi(\vec{x},t) = \sum_{n=0}^{\infty}\phi_n(\vec{x})e^{inN\omega t}$
F_z
M_z
z
U
WATERLINE PLANE
So
M_Y
Y
F_Y
$\vec{x}$
$\vec{n}$
x
F_x
M_x
HULL SURFACE
S
$\nabla^2\phi_n = 0$
$\vec{n}\cdot\nabla\phi_n|_S = 0$
$\phi_n|_{z=0} = 0$
$|\nabla\phi_n| \to 0, \ |\vec{x}|_{z<0} \to \infty$

FIGURE 1. Coordinate system and boundary value problem in propeller-hull interaction analysis.

appropriate "images" of the propeller and hull singularity systems.

Upon solving for the velocity potential, all other quantities of interest can be determined. The linearized, unsteady component of pressure is given by*

$$p(\vec{x},t) = -\rho\left(\frac{\partial\phi}{\partial t} + \vec{V}_s \cdot \nabla\phi\right), \quad \vec{V}_s(\vec{x}) = \vec{i}U + \nabla\phi_s(\vec{x}) \tag{8}$$

or from (1) and (2),

$$p(x,t) = -\rho \sum_{n=0}^{\infty} [inN\omega\phi_n + \vec{V}_s \cdot \nabla\phi_n]\, e^{inN\omega t}$$

$$= \sum_{n=0}^{\infty} p_n(\vec{x})\, e^{inN\omega t} \tag{9}$$

where the $p_n(\vec{x})$ are amplitudes of harmonics of the unsteady pressure. The periodic force, $\vec{F}(t)$, and moment, $\vec{M}(t)$ acting on the hull surface (see Figure 1) may be written as

$$\vec{F}(t) = -\iint_S p\, \vec{n}\, dS \tag{10}$$

and

$$\vec{M}(t) = -\iint_S p\, \vec{x} \times \vec{n}\, dS \tag{11}$$

Inserting the expression for p, one obtains the amplitudes of the force and moment harmonics, as

$$\vec{F}_n = \rho \iint_S (inN\omega\phi_n + \vec{V}_s \cdot \nabla\phi_n)\vec{n}\, dS \tag{12}$$

and

$$\vec{M}_n = \rho \iint_S (inN\omega\phi_n + \vec{V}_s \cdot \nabla\phi_n)\, \vec{x} \times \vec{n}\, dS \tag{13}$$

Until now, the propeller potential has been regarded as a known function. Before proceeding with the surface force analysis, it is appropriate to discuss the analytical representation of the propeller and the velocities and pressures induced at arbitrary field points.

3. REPRESENTATION OF THE PROPELLER

The primary source of propeller exciting forces is the spatially nonuniform wake of the hull in which the propeller operates. As viewed in a coordinate system rotating with the propeller, the flow approaching the propeller consists of time-average or circumferential mean component and an oscillatory component. The oscillatory component gives rise to unsteady loading on the blades in a manner analogous to a hydrofoil encountering a sinusoidal gust. This unsteady loading, summed over all the blades, yields periodic shaft forces at blade frequency and integer multiples. In contrast, the periodic pressure forces acting on the hull surface arise from the induced velocity and pressure fields from both the mean and unsteady components of loading, as well as the blade thickness, because of the varying aspect of the rotating blades relative to the fixed hull boundary.

Propeller theory for unsteady flow has developed as a logical extension of linearized lifting-surface theory for hydrofoils. It is assumed that the oscillatory components of the wake velocities are small compared to the mean, and can be resolved by Fourier analysis into "wake harmonics," the fundamental harmonic being the shaft rotation frequency. Each of these harmonics, within the linear approximation, will produce a component of unsteady blade loading with the same frequency. By virtue of the propeller's symmetry, upon summing over all the blades, only certain harmonics of the loading will contribute to the net force on the shaft. However, all the harmonics of loading contribute to the forces on an individual blade, and, as will be seen, to the radiated pressure field of the propeller.

The propeller lifting-surface theory developed by Tsakonas et al. (1973) is adopted in the present work. This analysis and associated computer programs have been successfully applied in recent propeller designs to minimize bearing forces, e.g., Valentine and Dashnaw (1975). In addition, the analysis has been extended to compute field point velocities and pressures, including the contributions from the image of the propeller arising from the presence of the free surface. As the details of the development of these formulae have been largely reported in the literature, we shall not burden this paper by recounting them, being content to outline the procedure.

Blade Loading Potential

The linearized equation of motion for unsteady flow, referred to a non-rotating cylindrical coordinate system (x,r,φ) centered at the propeller axis (Figure 2), may be written

$$p = -\rho'\left(\frac{\partial\phi_p}{\partial t} + U\frac{\partial\phi_p}{\partial x}\right) \tag{14}$$

which has the solution

$$\phi_p(x,r,\varphi,t) = -\frac{1}{\rho' U}\int_{-\infty}^{x} p\left(x',r,\varphi,t-\frac{x-x'}{U}\right)dx' \tag{15}$$

where p is the pressure induced by the loadings on the blades due to camber and incidence and ρ', for later convenience, denotes the fluid density. Here the angles of attack are produced by each axial and tangential spatial harmonic of the nominal hull

---

*To be strictly consistent with the high frequency approximation, the convective pressure term should be discarded. However, this term adds no serious burden to the ensuing analyses and by retaining it, numerical calculations can be used to demonstrate that the contribution from this term is, in fact, negligibly small.

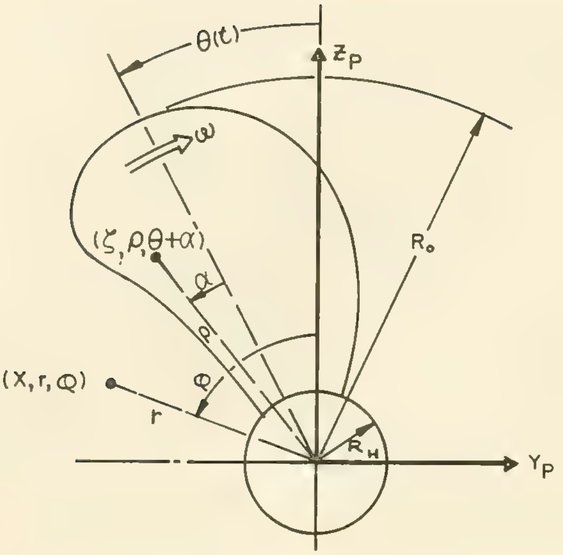

FIGURE 2. Propeller coordinate system-projected view looking upstream.

wake which is presumed to be known from wake survey measurements.

The pressure induced at a field point by a single blade is given by the following distribution of pressure dipoles

$$p(x,r\varphi,t) = \frac{1}{4\pi}\iint_{S_p}\sum_{\lambda=0}^{M}\Delta p\lambda(\xi,\rho)e^{-i\lambda\omega t}\frac{\partial}{\partial n_p}\frac{1}{R}\,dS \tag{16}$$

where Δp_λ is the complex amplitude of the pressure loading on the blade arising from the wake harmonic order λ and, as illustrated in Figure 3,

S_p is the surface of the blade, represented approximately by the helicoidal surface $\xi = U/\omega\ \alpha$

n_p is the distance directed normal to the surface S_p

$R = [(x-\xi)^2 + r^2 + \rho^2 - 2r\rho\cos(\theta + \alpha - \varphi)]$ is the distance from a point $(\xi,\rho,\theta + \alpha)$ in the surface S_p to the field point (x,r,φ)

$\theta = -\omega t$ is the angular position of the blade

We note that the representation of the blade is only approximate for a wake adapted propeller, being correct for a constant pitch propeller in uniform flow. Here we also assume that the pressure jumps on the blades, Δp_λ, have been previously calculated by the unsteady lifting-surface theory such as developed and programmed by Tsakonas et al. (1973).

To place the harmonic content of 1/R in evidence, the following identity can be used

$$\frac{1}{R} = \frac{1}{\pi}\sum_{m=-\infty}^{\infty}\int_{-\infty}^{\infty}A_{|m|}(r,\rho,|k|)e^{ik(x-\xi)}dk\ e^{im(\theta+\alpha-\varphi)} \tag{17}$$

where the amplitude $A_{|m|}$ is given by

$$\begin{aligned} &I_{|m|}(|k|\rho)K_{|m|}(|k|r) \qquad \rho < r < \infty \\ &I_{|m|}(|k|r)K_{|m|}(|k|\rho) \qquad 0 < r < \rho \end{aligned} \tag{18}$$

I_m and K_m being the modified Bessel functions of the second kind of order m.

To secure the pressure field for an N-bladed propeller, the blade position angle θ is replaced by $\theta + 2\pi n/N$ and the sum over n from n = 0 to N - 1 carried out. This sum yields a factor N and the constraints on the frequencies λ and m, given by $\lambda - m = \ell N$ with $\ell = 0,\pm1,\pm2,\pm3$...i.e., products of terms for which $\lambda - m \neq \ell N$ will sum to zero. The *total* induced pressure at any field is secured by summing over ℓ from $-\infty$ to $+\infty$.

Upon use of (15), (16) and (17) and looking after the shifted time variable, using $\theta = -\omega t$ which shifts to $-\omega t + \omega/U\ (x-x')$, one obtains the velocity potential in the form

$$\phi_p(x,r,\varphi,t) = -\frac{N}{\rho' U}\sum_{\ell=-\infty}^{\infty}e^{i\ell N\omega t}\sum_{\lambda=0}^{M}\iint_{S_p}\Delta p_\lambda\ (\xi,\rho)P_m(x,r,\varphi;\xi,\rho)\ dS \tag{19}$$

in which the propagation function, P_m, is given by

$$P_m = \frac{e^{-i\frac{\ell N\omega}{U}x}}{4\pi^2}\int_{-\infty}^{\infty}A_{|m|}\frac{\partial}{\partial n_p}\left\{e^{-ik\xi}\int_{-\infty}^{x}e^{i\left(k + \frac{\ell N\omega}{U}x'\right)}dx'\ e^{im(\alpha-\varphi)}\right\}dk \tag{20}$$

where for each ℓ, $m = \lambda - \ell N$, and M is a practical upper bound of the wake harmonic order number beyond which the amplitudes of the wake harmonics are so small as to render negligible values of Δp_λ for all $\lambda > M$. (A value of M = 8 is reasonable). Details of further reductions of the integrals involved in (19) and (20) may be found in Jacobs and Tsakonas (1975).

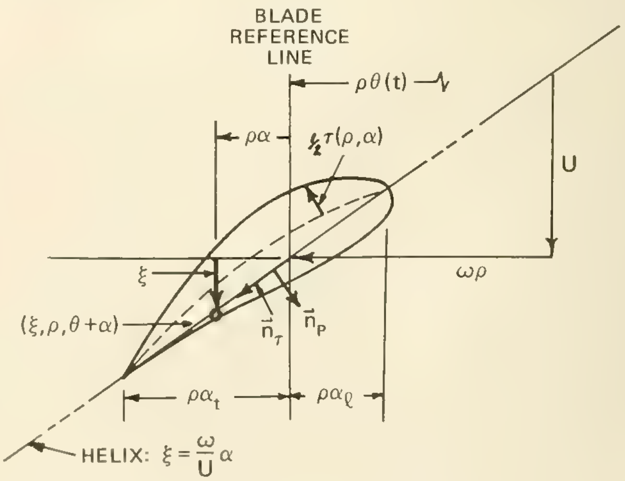

FIGURE 3. Propeller coordinate system-expanded view of blade section at radius ρ.

To account for the presence of the free surface which, at the frequencies of interest acts as a zero potential surface (see Eq. (7), we merely add to (19) the potential $\phi_{p_i} = -\phi_p(x, r_i, \varphi_i, t)$ in which

$$r_i = \sqrt{y_p{}^2 + (2d - z_p)^2} = r \text{ when } z_p = d \qquad (21)$$

$$\varphi_i = \tan^{-1}\left(\frac{-y_p}{2d - z_p}\right) = \varphi \text{ when } z_p = d \text{ and}$$

$$-\pi/2 \le \varphi_i \le \pi/r, \varphi_i(y=0) = 0 \qquad (22)$$

where d is the distance or depth of the propeller axis below the free surface; y_p, z_p are the transverse and vertical coordinates of any field point (Figure 2). Thus, the total potential arising from the loadings on an N-bladed propeller in the presence of the free surface (neglecting the feed-back on Δp_λ from the free surface) is

$$\phi_p + \phi_{p_i} = -\frac{N}{\rho' U} \sum_{\ell=-\infty}^{\infty} e^{i\ell N\omega t} \sum_{\lambda=0}^{M} \iint_{S_p} \Delta p_\lambda(\xi, \rho)[P_m(x, r, \varphi; \xi, \rho) - P_m(x, r_i, \varphi_i; \xi, \rho)]\, dS \qquad (23)$$

and the spatial derivatives of this function yield the velocities induced by the propeller and its negative image in the free surface. Clearly $\phi_p + \phi_{p_i} \equiv 0$ for all x and y_p for $z_p \equiv d$.

Blade Thickness Potential

The potential, ϕ_τ, induced by blade thickness may be constructed from a distribution of dipoles (with axes tangent to the helical arc along the blade at any radius) whose strenths are given by V_τ, V being the local relative resultant velocity and τ the local thickness provided by the expanded blade section drawing. Using the helical geometry as before, one can obtain

$$\phi_\tau(x, r, \varphi, t) = \frac{1}{4\pi} \int_{R_h}^{R_o} \int_{\alpha_\ell}^{\alpha_t} \sqrt{U^2 + (\omega\rho)^2}\, \tau(\rho, \alpha) \frac{\partial}{\partial\alpha} \frac{1}{R}\, d\alpha\, d\rho \qquad (24)$$

where $\alpha_\ell(\rho)$ and $\alpha_t(\rho)$ are the angular coordinates of the blade leading and trailing edges.

To allow for the free surface, $1/R$ is replaced by $1/R - 1/R_i$ with R_i being the distance from the reflection of the dummy point in the free surface to the field point on or below the water surface, making use of relations (21) and (22). Again, to place the harmonic content of $1/R$ and $1/R_i$ in evidence and to facilitate integrations over the blade surface, the Fourier expansion (17) can be applied.

Asymptotics of the Loading Potential

The fact that the disturbances induced by each of the pressure jumps Δp_λ are propagated by widely different functions of the space variables x, r, φ must be emphasized as these behaviors have a most significant impact on the pressure, velocities, and the resultant forces generated on the hull. These diverse characteristics can best be illustrated by examining the asymptotics of the potential for upstream locations which are large only with respect to the *x-wise extent* of the blade surface. The x-wise extent of the blades is given by the (chord) . sin ψ_p, ψ_p being the local pitch angle which, in the radial region of heaviest loading, is normally of the order of 25°. For merchant ships, the blade chord in this region is of the order of one-half the radius and, hence, the x-wise extent of the significant position of a propeller is only about 0.2 radius. Thus, for axial distances of the order of one diameter, the x-wise extent of the important region of the blade can certainly be neglected in an asymptotic analysis.

Using the expansion of R^{-1} given by

$$R^{-1} = \frac{1}{\pi\sqrt{\rho r}} \sum_{m=-\infty}^{\infty} Q_{m-1/2}(Z)\, e^{im(\theta+\alpha-\varphi)}$$

where Q is the associated Legendre function, and

$$Z = \frac{(x-\xi)^2 + r^2 + \rho^2}{2\rho r}$$

and retaining only the leading term in the expansion of Q for large Z, one can arrive at the following behaviors for the consituents of the loading potential, i.e., $\phi_p = \phi_T + \phi_Q$, ϕ_T being the part associated with thrust loading and ϕ_Q being that arising from the torque-producting loading in the forms:

$$\phi_T \to \frac{i}{4\pi^2\rho'\omega} \sum_{\substack{\ell=-\infty \\ (m \equiv \lambda - \ell N)}}^{\infty} \sum_{\lambda=0}^{M} \frac{C_{|m|} r^{|m|} e^{-i\ell N\theta}}{\ell} \int_{R_h}^{R_0} L_m{}^{(\lambda)}(\rho)\rho^{|m|} \left\{\frac{xe^{-im\varphi}}{(x^2+r^2+\rho^2)^{|m|+3/2}} - \frac{xe^{-im\varphi_i}}{[x^2+r^2+\rho^2+4d(d-z_p)]^{|m|+3/2}}\right\} d\rho \qquad (25)$$

$$\phi_Q \to \frac{U}{4\pi^2\rho'\omega^2} \sum_{\substack{\ell=-\infty \\ (m \equiv \lambda - \ell N)}}^{\infty} \sum_{\lambda=0}^{M} \frac{mC_{|m|} r^{|m|} e^{-i\ell N\theta}}{(1+2|m|)\ell}$$

continued on page 284

$$\int_{R_h}^{R_o} L_m^{(\lambda)}(\rho)\rho^{|m|-2} \left\{ \frac{e^{-im\varphi}}{(x^2+r^2+\rho^2)^{|m|+1/2}} - \frac{e^{-im\varphi_i}}{[x^2+r^2+\rho^2+4d(d-z_p)]^{|m|+1/2}} \right\} d\rho \qquad (26)$$

where

$$C_{|m|} = \frac{(2|m|+1)\Gamma(1/2)\Gamma(|m|+1/2)}{\Gamma(|m|+1)}$$, Γ being the Gamma function (27)

and

$$L_m^{(\lambda)} = \rho \int_{\alpha_\ell}^{\alpha_t} \Delta p_\lambda(\rho,\alpha)\, e^{im\alpha}\, d\alpha$$, the load density (28)

Here the effect of the free surface is included by the last terms in each integrand. To exclude the free surface, take the propeller depth of submergence $d = \infty$.

Limiting our attention to blade rate ($\ell = 1, -1$), we see that, although the mean pressure jumps Δp_0 ($\lambda = 0$) are much larger than those at all other wake harmonics, the propagation functions for $m = \lambda - \ell N = \pm N$ exhibit extremely rapid decay with increasing x. In addition, we observe that the radial loading for $m = \pm N$ obtained from Δp_0 is weighted by the oscillatory function $e^{iN\alpha}$ which has the effect of producing an $L_N(o)$ which is inversely proportional to N. In contrast, the contribution for $\lambda = N$, i.e., $m = 0$, is of the form

$$L_0^{(N)} = \int \Delta p_N \, d\alpha \quad ,$$

which has a "non-destructive" weighting function of unity. Another feature which reduces the mean loading contribution to the generation of forces on the hull (wherein integration over the athwartship variable y_p is involved) is the presence of the space angular function

$$e^{iN\varphi} = e^{-iN(\tan^{-1} y_p/z_p)}$$

yielding pressures and velocities at different y_p which are not in phase. In strong contrast in the propagation mode for the blade frequency loading Δp_N (for which $m = 0$), ϕ_T has no dependence on φ or φ_i, and all y_p locations receive velocities and pressures which are in phase with each other. On the other hand, the coefficient $C_{|m|}$ is large for $\lambda = 0$ (being 6.5 for a 5-bladed propeller), whereas $C_0 = \pi$, the multiplier for the contribution from the blade frequency Δp's.

These observations are succinctly summarized in Tables 1 and 2 for the case of a 5-bladed propeller, displaying the rate of decay with x, the variation of the influence coefficients $C_{|m|}$ and $mC_{|m|}/1+2|m|$, and the dependence on the angular space coordinates φ and φ_i, without and with the free surface effect for the dominant terms at blade frequency arising from the loading at wake harmonics $\lambda = 0$, $N - 1$, N and $N + 1$.

One may observe in Tables 1 and 2 that the effect of the free surface does not generally increase the rate of attenuation of the potentials with x except at or near all points in the vertical plane $y_p \equiv 0$ *with the exception of the* $\phi_T^{(N)}$ *and* $\phi_O^{(N)}$ *arising from blade frequency loading on the blades, i.e.,* $\lambda = N$ *and* $m = 0$, *which show a change from* x^{-2} *to* x^{-4} *and* x^{-1} *to* x^{-3} *everywhere, respectively.*

A dramatic contrast in the force-generating capabilities of the pressure field components arising from the mean (the largest) and the blade-frequency loadings on the blades can be found by integrating the pressures

$$-\rho' \frac{\partial\phi_T(o)}{\partial t} \quad \text{and} \quad -\rho' \frac{\partial\phi_T(N)}{\partial t}$$

over a rectangular region of half-breadth b arranged symmetrically z_0 units above the propeller and extending from −f radii forward to s radii downstream of the propeller plane. Upon defining the coefficient of the vertical force on the rectangle as $Z_T^{(\lambda)} = F_z^{(\lambda)}/\rho' n^2 D^4$, we can arrive at the following

TABLE 1. ASYMPTOTIC CHARACTERISTICS OF BLADE FREQUENCY COMPONENTS OF THE THRUST-ASSOCIATED POTENTIAL ϕ_T FOR A 5-BLADED PROPELLER FOR LARGE AXIAL DISTANCES

Wake Order λ	Propagation Order m	Influence Coef. $C_{\|m\|}$	Relative Loading* $\frac{L_m^{(\lambda)}**}{2\rho a_h}$	Dependence on x, φ and φ_i Without Free Surface	With Free Surface	With Free Surface ($y_p = 0$)
0	-5	8.48	26.7	$\frac{x\, e^{+i5\varphi}}{\|x\|^{13}}$	$\frac{x(e^{i5\varphi} - e^{i5\varphi_i})}{\|x\|^{13}}$	$\frac{26d(d-z_p)x}{\|x\|^{15}}$
N - 1 = 4	-1	4.71	4.8	$\frac{x\, e^{+i\varphi}}{\|x\|^5}$	$\frac{x(e^{i\varphi} - e^{i\varphi_i})}{\|x\|^5}$	$\frac{10d(d-z_p)x}{\|x\|^7}$
N = 5	0	3.14	1	$\frac{x}{\|x\|^3}$	$\frac{6xd(d-z_p)}{\|x\|^5}$	$\frac{6xd(d-z_p)}{\|x\|^5}$
N + 1 = 6	1	4.71	2.1	$\frac{x\, e^{-i\varphi}}{\|x\|^5}$	$\frac{x(e^{-i\varphi} - e^{-i\varphi_i})}{\|x\|^5}$	$\frac{10d(d-z_p)x}{\|x\|^7}$

TABLE 2. ASYMPTOTIC CHARACTERISTICS OF BLADE FREQUENCY COMPONENTS OF THE TORQUE-ASSOCIATED POTENTIAL ϕ_Q FOR A 5-BLADED PROPELLER AT LARGE AXIAL DISTANCES

Wake Order λ	Propagation Order m	Influence Coef. $\frac{mC_{\lvert m\rvert}}{1+2\lvert m\rvert}$	Relative Loading* $\frac{L_m^{(\lambda)}}{2\rho\theta_b}$	Dependence on x, φ and φ_i		
				Without Free Surface	With Free Surface	With Free Surface $(y_P = 0)$
0	-5	-3.86	26.7	$\frac{e^{i5\varphi}}{\lvert x\rvert^{11}}$	$\frac{e^{i5\varphi}-e^{i5\varphi_i}}{\lvert x\rvert^{11}}$	$\frac{22d(d-z_p)}{\lvert x\rvert^{13}}$
N - 1 = 4	-1	-1.57	4.8	$\frac{e^{i\varphi}}{\lvert x\rvert^{3}}$	$\frac{e^{i\varphi}-e^{i\varphi_i}}{\lvert x\rvert^{3}}$	$\frac{6d(d-z_p)}{\lvert x\rvert^{5}}$
N = 5	0	0	1	$\frac{1}{\lvert x\rvert}$	$\frac{2d(d-z_p)}{\lvert x\rvert^{3}}$	$\frac{2d(d-z_p)}{\lvert x\rvert^{3}}$
N + 1 = 6	1	1.57	2.1	$\frac{e^{-i\varphi}}{\lvert x\rvert^{3}}$	$\frac{e^{-i\varphi}-e^{-i\varphi_i}}{\lvert x\rvert^{3}}$	$\frac{6d(d-z_p)}{\lvert x\rvert^{5}}$

*These are relative values as obtained from calculations of a 5-bladed propeller using the wake of the SS Michigan.

** $\frac{L_m^{(\lambda)}}{2\rho\alpha_b} = \frac{1}{2\alpha_b}\int_{-\alpha_b}^{\alpha_b} \Delta p_\lambda(\rho,\alpha)\, e^{im\alpha}\, d\alpha \simeq \Delta p_\lambda(\rho)\, \frac{\sin m\alpha_b}{m\alpha_b}$ for Δp_λ independent of α

expressions for the moduli of the blade-frequency forces, viz.,

$$\lvert Z_T{}^{(o)}\rvert = \frac{C_N \sqrt{(z_o^2+b^2)^{N+1}}}{4\pi^2\rho' n^2 R_o^2} \sin [(N+1)\gamma_o] \int_{0,2}^{1.0} \rho^{N+1} \Delta p_o(\rho) \sin N\alpha_b \left\{ \left(\sqrt{s^2+z^2+\rho^2}\right)^{-(2N+1)} - \left(\sqrt{f^2+z^2+\rho^2}\right)^{-(2N+1)} \right\} d\rho \tag{29}$$

where

$$C_N = \frac{(1.3.5\ldots(2N-1))}{2^N (N+1)!} \text{ and } \gamma_o = \tan^{-1}\left(\frac{b}{z_o}\right)$$

for the contribution from the mean loading, (λ = 0), and

$$\lvert Z_T{}^{(N)}\rvert = \frac{N}{8\pi\rho' n^2 R_o^2} \int_{0.2}^{1.0} \rho \lvert \Delta p_N \rvert \ln \left(\frac{(b+\sqrt{s^2+z_o^2+\rho^2+b^2})}{(b+\sqrt{f^2+z_o^2+\rho^2+b^2})} \sqrt{\frac{f^2+z_o^2+\rho^2}{s^2+z_o^2+\rho^2}} \right) d\rho \tag{30}$$

for the contribution from the blade-frequency loading on the blades.

Evaluations of (29) and (30) were carried on a hand calculator for various integration lengths f forward of a propeller using assumed radial distributions of Δp_o and Δp_N and representative values from computer calculations for a 5-bladed 22.5 ft propeller in a single-screw ship (model) wake. The calculations were made for a flat-bottomed hull of half-breadth $b = 2\ R_o$ at $z_o = 1.5\ R_o$ (25 percent tip clearance) and a stern overhang $s = 1$. Results shown on Figure 4 show dramatically that the force arising from the blade-frequency (b-f) loading *is (asymptotically) 65 times larger than that from the mean blade loading* when the free-surface effects are omitted (note that $\Delta p_o = 40\ \Delta p_5$). Furthermore, the total force due to b-f blade loading rises very slowly to its asymptotic value as the integration length is increased and even the force from mean blade loading requires integration of the pressure to three radii forward of the propeller.

To allow approximately for the effect of the free surface, one can subtract terms of the same form as (29) and (30) with $z_o{}^2$ replaced by $z_o{}^2 + 4dh$ with d being the depth of submergence of the propeller axis and h the hull draft in way of the propeller. The reduction in force for d = 3.5 and h = 2 is significant for $Z_T{}^{(N)}$ but is found negligible for the smaller force. As expected, the asymptotic value $Z_T{}^{(N)}(f \to \infty)$ is more quickly achieved due to the presence of the free surface, but, nevertheless, requiring that one integrate to some 8 diameters to achieve the final value.

These results tell us that the current practice in European model basins (in which b-f pressures are measured on models in the vicinity of the propeller and these are integrated in an attempt to secure the b-f hull force) is highly suspect because the slowly decaying pressures from b-f blade loadings contribute large sectional force densities far from the propeller. This effect is exacerbated by the "growing" cross-sectional shape as one integrates forward which is not accounted for in the constant beam "ship" used in the foregoing analysis.

As an order of magnitude formula, one might use (30) for f = ∞ with the correction for the free surface included. This reduces to the complex amplitude

$$Z_T^{(N)} = \frac{N}{8\pi\rho' n^2 R_o^2} \int_{0.2}^{1.0} \rho \Delta p_n \; \ell n \left(\frac{(b+\sqrt{s^2+z_o^2+\rho^2+b^2})}{(b+\sqrt{s^2+z_o^2+\rho^2+b^2+4dh})} \sqrt{\frac{s^2+z_o^2+\rho^2+4dh}{s^2+z_o^2+\rho^2}} \right) d\rho \tag{31}$$

(which must not be used for hull drafts in way of the propeller, h, which are small, as clearly $Z_T^{(N)} \to 0$ as $h \to 0$). In practice, $\Delta p_N = a_N(\rho) \cos N\theta + b_N(\rho) \sin N\theta$, a_N, b_N being the chordwise average in-phase and quadrature blade pressures given by the unsteady lifting surface calculation.

With the foregoing considerations of the propeller in mind, we now return to the surface force problem for a general three-dimensional hull boundary and prescribed propeller onset flow. In the following section, a procedure is described for determining the diffraction potential and the surface pressures and forces in terms of singularities distributed over the surface of the hull.

4. A DIRECT APPROACH FOR DETERMINING SURFACE FORCES

A "frontal attack" on the problem of predicting the vibration forces generated on an arbitrary hull by the induced flow of the propeller, (and its free surface image) is to construct the potential of the hull in the presence of these onset flows. This procedure was first applied by Breslin and Eng (1965) to a realistic hull form. At that time, however, only the mean loading and the blade thickness were accounted for in the flow impinging on the hull and the computer time was observed to be excessive. In contrast to these earlier efforts, the propeller flow is now composed of all constituents of loading and the (high frequency) images arising from the presence of the free surface.

A solution for the potential, ϕ_n, which satisfies equations (3), (4), and (7), is constructed by distributing source singularities, $\sigma_n(\vec{x})e^{inN\omega t}$, over the surface of the hull, such that

$$\phi_n(\vec{x}) = -\frac{1}{4\pi} \iint_S \sigma_n(\vec{x'}) \left(\frac{1}{|\vec{x}-\vec{x'}|} - \frac{1}{|\vec{x}-\vec{x'_i}|} \right) dS(\vec{x'}) + \phi_{P_n} + \phi_{P_i} \tag{32}$$

where the region of integration is over the submerged portion of the hull and $\vec{x_i}$ is the distance from an

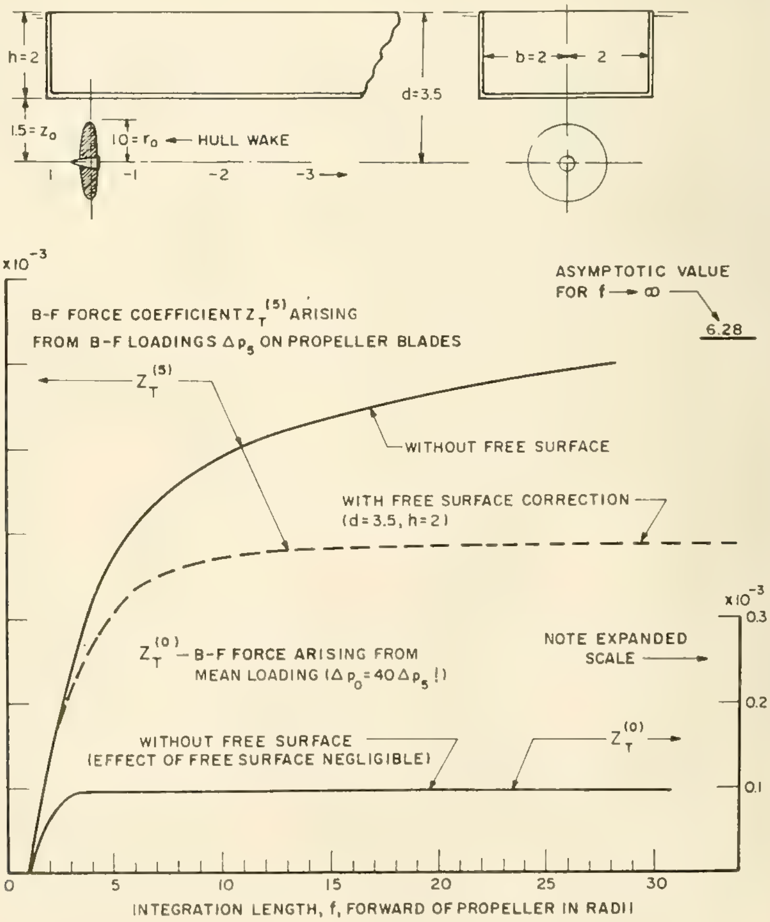

FIGURE 4. Approximate moduli of B-F forces on barge-like ship from pressures emanating from mean and B-F loadings on a 5 bladed propeller (in a single screw ship wake) as a function of integration length forward of propeller.

"image" hull point to the field point, i.e, if $\vec{x}' = (x',y',z')$, then $\vec{x}'_i = x',y',-z')$. The source strengths $\sigma_n(\vec{x})$ can be determined by applying the hull boundary condition (5) yielding an integral equation

$$\frac{\sigma_n(\vec{x})}{2} - \frac{1}{4\pi} \iint_S \sigma_n(\vec{x}')\vec{n} \cdot \nabla \left(\frac{1}{|\vec{x}-\vec{x}'|} - \frac{1}{|\vec{x}-\vec{x}'_i|} \right) dS$$

$$+ \vec{n}(\vec{x}) \cdot (\nabla\phi_{P_n} + \nabla\phi_{P_{i_n}}) = 0, \ \vec{x} \text{ on } S \qquad (33)$$

The integral term gives the contribution from all source elements other than at the point of interest on the hull. The contribution from the source at that point is given by the first term, $\sigma_n(x)/2$.

Equation (33) with $\vec{n} \cdot [\nabla\phi_{P_n} + \nabla\phi_{P_{i_n}}]$ as a known input is solved numerically by the generalized Douglas-Neumann program [Hess and Smith (1964)]. In practice, the hull surface is divided up into quadrilateral elements over which σ_n is considered constant and the integral equation is replaced by a set of simultaneous algebraic equations. Care must be exercised to insure that the sizes of the elements are small compared to the spatial "wave length" of the propeller-induced velocity field. This is particularly the case for field points just downstream of the propeller since the velocity components rapidly become proportional to sines and cosines of $N(\omega/U\, x-\gamma)$ so that the wave length of these signatures is $\lambda = 2\pi U/N\omega$, which, for $J \sim 1$ and $N = 5$, becomes $\lambda = 0.4R_0$. In order to obtain representations of an entire cycle, it is necessary to take element lengths of one-quarter of this length or about $0.10R_0$. Upstream, the induced flow is monotonic in x and the element sizes can be made much larger without loss of accuracy.

It is acknowledged that the above-described process does not, in principle, completely solve the problem since the feedback of the hull sources on the instantaneous flow experienced by the propeller is not included in the propeller loadings Δp_λ. To do this would require joining the integral equation for the propeller loadings (with input from the propeller generated hull sources) to Eq. (33) to form a pair of integral equations for Δp_λ and σ_n, which, when solved interatively to convergence, would yield the complete solution. For the present, we are content to ignore the hull feedback on the propeller.

Once the source densities on the hull surface are found, it is convenient to determine the force induced on the hull in terms of simple integral operations on these sources. Although the Lagally theorem and its extension by Cummins (1957) is known for submerged bodies, it is necessary to develop a form which is suitable for use for floating bodies beset by high frequency flows.

The force as given earlier by Eq. (12) may be considered as the sum of two terms $\vec{F}_n^{(1)}$ and $\vec{F}_n^{(2)}$ given by

$$\vec{F}_n^{(1)} = i\rho nN\omega \iint_S \phi_n \vec{n} dS \qquad (34)$$

and

$$\vec{F}_n^{(2)} = \rho \iint_S \vec{V}_s \cdot \nabla\phi_n \vec{n} dS \qquad (35)$$

Since $\phi_n = 0$ on $z = 0$, the region of integration in (34) may be extended to include the hull waterline plane S_0 (see Figure 1), thus forming a closed surface about the volume ∀ *inside* the submerged portion of the hull, and

$$\vec{F}_n^{(1)} = i\rho nN\omega \iint_{S+S_0} \phi_n^+ \vec{n} dS \qquad (36)$$

where the symbols $(\ )^+$ and $(\ )^-$ are used to denote a quantity evalutated on the outside and inside of the surface of integration respectively. Noting that for $\phi_n(\vec{x})$ given by (32), $\phi_n^+ = \phi_n^-$ (i.e. the potential is continuous across a surface distribution of source singularities), and using the vector identity $\vec{n} = \vec{n} \cdot \nabla\vec{x}$, one obtains

$$\vec{F}_n^{(1)} = i\rho nN\omega \iint_{S+S_0} \phi_n^- \vec{n} \cdot \nabla\vec{x} dS(\vec{x}) \qquad (37)$$

By means of Green's reciprocal theorem applied to the volume ∀, (37) becomes

$$\vec{F}_n^{(1)} = i\rho nN\omega \iint_{S+S_0} \vec{x}\vec{n} \cdot \nabla\phi_n^- \, dS(\vec{x}) \qquad (38)$$

since $\nabla \cdot \nabla(\vec{x}) \equiv 0$ and $\nabla^2\phi_n^- = 0$ in ∀. A fundamental property of a surface distribution of source singularities relates the jump in the normal derivative of the potential to the local source strength, viz.

$$\vec{n} \cdot \nabla\phi_n^+ = \vec{n} \cdot \nabla\phi_n^- + \sigma_n \qquad (39)$$

But since $\vec{n} \cdot \nabla\phi_n^+ = 0$ on S by virtue of the boundary condition (5), Eq. (38) may be written as

$$\vec{F}_n^{(1)} = -i\rho nN\omega \iint_S \vec{x}\, \sigma_n(\vec{x}) \, dS(\vec{x}) +$$

$$i\rho nN\omega \iint_{S_0} \vec{x} \frac{\partial\phi_n}{\partial z} dS(\vec{x}) \qquad (40)$$

The first term in (40) has the same structure as that derived by Cummins (1957) for submerged bodies generated by internal singularities. The second term arises from the capping of the volume by extending the free surface through the ship (proposed originally by Breslin in 1971). For the important case of the vertical force, F_{z_n}, we obtain

$$F_{z_n}^{(1)} = i\rho nN\omega \iint_S z\, \sigma_n(\vec{x}) \, dS(\vec{x}) \qquad (41)$$

A similar analysis can be applied to the convective term $\vec{F}_n^{(2)}$ (see appendix A) to obtain

$$\vec{F}_n(2) = -\rho \iint_S \sigma_S \nabla(\phi_{P_n} + \phi_{P_{i_n}})\, dS +$$

$$\rho \iint_{S_0} \nabla\phi_{\bar{S}} \frac{\partial\phi_n}{\partial z}\, dS \tag{42}$$

in which again the first term exhibits the same form as for a submerged body and the second term accounts for the intersection with the free surface. If it is assumed that $\partial\phi_S/\partial z = 0$ on $z = 0$ (rigid wall free surface condition for the steady flow about the hull, i.e., low Froude number approximation), then from (42)

$$F_{z_n}(2) = -\rho \int_S \sigma_S \frac{\partial}{\partial z}(\phi_{P_n} + \phi_{P_{i_n}})\, dS \tag{43}$$

and the total vertical force, $F_{z_n}(1) + F_{z_n}(2)$, becomes

$$F_{z_n} = -\rho \iint_S \left[inN\omega z\, \sigma_n + \sigma_S \frac{\partial}{\partial z}(\phi_{P_n} + \phi_{P_{i_n}}) \right] dS \tag{44}$$

As noted earlier, the first term under the integral will dominate because of the large multiplying factor $nN\omega$. This will be confirmed in the calculated example to be presented subsequently. First, however, we outline an alternative approach for determining the vibratory hull force which avoids the need to solve for the diffraction potential.

5. AN ALTERNATIVE METHOD FOR DETERMINING THE VIBRATORY HULL FORCES

Vorus (1971, 1974, 1976) has developed an alternative procedure for determining the vibratory hull surface forces which eliminates the need to solve for the hull diffraction potential in the presence of the propeller onset flow. The ith oscillatory force or moment, F_{in}, exerted by the pressure on the hull may be written from (12) and (13) as

$$F_{in} = \rho \iint_S (inN\omega\phi_n + \vec{V}_S \cdot \nabla\phi_n)\, \vec{n} \cdot \vec{\alpha}_1\, dS \tag{45}$$

where the $\vec{\alpha}_1$ are defined as

$$\begin{aligned} \vec{\alpha}_1 &= \vec{i} & \vec{\alpha}_4 &= y\,\vec{k} - z\,\vec{j} \\ \vec{\alpha}_2 &= \vec{j} & \vec{\alpha}_5 &= z\,\vec{i} - x\,\vec{k} \\ \vec{\alpha}_3 &= \vec{k} & \vec{\alpha}_6 &= x\,\vec{j} - y\,\vec{i} \end{aligned} \tag{46}$$

Vorus has shown that the solution for F_{in}, with no additional approximation, is given by the formula

$$F_{in} = \frac{N\omega}{\pi} \int_{-\pi/N\omega}^{\pi/N\omega} dt\, e^{-inN\omega t} \iint_{Sp_N} dS(\xi,\rho,\theta + \alpha)$$

$$\left[\rho' \sqrt{U^2 + (\omega\rho)^2}\, \tau n_\tau \cdot \nabla H_{in} + \frac{\nabla p}{U} \int_{\xi}^{\omega} d\xi'\, e^{\frac{inN\omega}{U}(\xi-\xi')}\, \vec{n}_P \cdot \nabla H_{in} \right] \tag{47}$$

All of the variables in (47) pertain to the propeller except H_{in}. H_{in} is the amplitude of the fluid velocity potential due to the bare hull travelling backwards with speed U across the water surface and oscillating with unit amplitude in the ith direction and at the frequency $nN\omega$. Since the details of the derivation of this formula may be found in the cited literature we will only outline major steps as follows.

The second term in (45) can be rewritten using the following vector identity

$$(\vec{V}_S \cdot \nabla\phi_n)(\vec{\alpha}_i \cdot \vec{n}) = (\nabla\phi_n \cdot \vec{\alpha}_i)(\vec{V}_S \cdot \vec{n}) +$$
$$\nabla x[\phi_n(\vec{\alpha}_i \times \vec{V}_S)] \cdot \vec{n} - \phi_n \nabla x\, (\vec{\alpha}_i \times \vec{V}_S) \cdot \vec{n} \tag{48}$$

Only the last term contributes to (45), because $\vec{V}_S \cdot \vec{n} = 0$ (steady flow hull boundary condition) and, by Stokes' theorem

$$\iint_S \nabla x\, [(\phi_n(\vec{\alpha}_i \times \vec{V}_s)] \cdot \vec{n}\, dS = \oint \phi_n(\vec{\alpha} \times \vec{V}_S)\, d\vec{\ell} = 0 \tag{49}$$

where the line integral is taken along the hull waterline on which $\phi_n = 0$. Consequently, Eq. (45) becomes

$$F_{in} = \rho \iint_S \phi_n\, [inN\omega\vec{\alpha}_i - \nabla x(\vec{\alpha}_i \times \vec{V}_S)] \cdot \vec{n}\, dS \tag{50}$$

and, upon introducing the function H_{in} which satisfies

$$\nabla^2 H_{in} = 0 \qquad \text{in fluid domain} \tag{51}$$

$$H_{in} = 0 \qquad z = 0,\ \text{outside } S \tag{52}$$

$$\vec{n} \cdot \nabla H_{in} = \vec{n} \cdot [inN\omega\, \vec{\alpha}_i - \nabla x(\vec{\alpha}_i \times \vec{V}_S)] \text{ on } S \tag{53}$$

$$\nabla H_{in} \to 0 \quad \text{as } |\vec{x}| \to \infty,\ z < 0 \tag{54}$$

equation (50) is given by

$$F_{in} = \rho \iint_S \phi_n\, \vec{n} \cdot \nabla H_{in}\, dS \tag{55}$$

This form can be identified as one of the terms in Green's theorem applied to the functions ϕ_n and H_{in} in the fluid domain bounded by the hull surface S, the free surface $z = 0$, and the surfaces of the propeller blades Sp_N, and slipstream, Sp_N, which yields

$$F_{in} = -\frac{N}{\pi\omega} \int_{-\pi/N\omega}^{\pi/N\omega} dt\, e^{-inN\omega t} \left[\iint_{Sp_N} H_{in} \right.$$

$$\left(\frac{\partial \phi_p^+}{\partial n_p} - \frac{\partial \phi_p^-}{\partial n_p} \right) dS + \iint\limits_{Sp_N + Sw_N} (\phi_p^+ - \phi_p^-) \vec{n}_p \cdot \nabla H_{in} \, dS \Bigg] \tag{56}$$

where $\phi_p^+ - \phi_p^-$ is the jump in the propeller potential across the blade and slipstream surfaces. The two terms in (56) can be identified as the contributions from blade loading and thickness, and with further manipulation can be brought into the form of (47).

Equation (47) indicates that the velocity corresponding to the potential H_{in} is evaluated over the propeller blades and slipstream. The propeller representation by distributions of dipoles directed normal and tangential to the blade pitch surface is the same as previously discussed. In the formula, the velocity induced by the bare hull, ∇H_{in}, is resolved into components in the directions of the dipoles, multiplied by the dipole strengths, and the products integrated over the blade and slipstream surfaces. The first integral in (47), in time, extracts the nth Fourier harmonic. Both the blade position and the dipole strengths are functions of time.

In the case of vertical force analyses, an approximation to the improper integral in (47) has been found to yield acceptable results. Let I be defined as

$$I = \int_{\xi}^{\infty} e^{\frac{inN\omega}{U}(\xi - \xi')} \vec{n}_p \cdot \nabla H_{in} \, d\xi' \tag{57}$$

If the oscillating exponential varies more rapidly than ∇H_{in}, then the argument of the exponential can be considered as "large" and I can be expanded in an asymptotic series. ∇H_{in} should vary relatively slowly aft in the propeller slipstream for vertical oscillation of the bare hull and an asymptotic evaluation should therefore be valid. (Such a treatment may not apply to an athwartship analysis, for example, where a rudder is involved in the bare hull oscillation.) To proceed with the asymptotic representation, (57) is integrated by parts yielding

$$I = -\frac{U}{inN\omega} e^{\frac{inN\omega}{U}(\xi - \xi')} \vec{n}_p \cdot \nabla H_{in} \Big|_{\xi}^{\infty}$$

$$+ \frac{U}{inN\omega} \int_{\xi}^{\infty} e^{\frac{inN\omega}{U}(\xi - \xi')} \frac{\partial}{\partial \xi'} \vec{n}_P \cdot \nabla H_{in} \, d\xi'$$

For the conditions stated, the integral term is higher order. Hence, to one term,

$$I \sim \frac{U}{inN\omega} \vec{n}_P \cdot \nabla H_{in}(\xi) \tag{58}$$

and (47) reduces to

$$F_{in} = \frac{N\omega}{\pi} \int_{-\pi/N\omega}^{\pi/N\omega} dt \, e^{-inN\omega t} \iint\limits_{Sp_N} dS \, [\rho' V \tau \vec{n}_\tau$$

$$+ \frac{\Delta p}{inN\omega} \vec{n}_P] \cdot \nabla H_{in} \tag{59}$$

in which the induced flow is evaluated exclusively on the surface of all N propeller blades Sp_N.

6. COMPARISON OF THEORY AND EXPERIMENT FOR A BODY OF REVOLUTION

An experiment was conducted to measure the periodic forces on a body of revolution adjacent to a propeller loading provided a configuration which could be treated in a reasonably exact fashion by potential flow theory. As such, the experiment was intended as a fundamental check on the theory and computer-aided numerical procedures. However, it is believed that the experimental technique can be extended in the future to study more general hull geometries and the effects of unsteady propeller loading and transient cavitation.

In the following sections, the experimental apparatus and procedures are described and the force measurements are compared with the analytical predictions.

Test Body and Propellers

The experiments were performed in the DTNSRDC Deep-Water Basin [(22 feet (6.7 m) deep, 51 feet (15.5 m) wide, and 2600 feet (792 m) long)]. Both the body and propeller were supported and towed from Carriage II which has a drive system capable of maintaining speed to within 0.01 knot.

Forces were measured on the forward half of an ellipsoid of revolution with a length/diameter ratio of 5.65. This "half body" was mounted by a specially designed strain-gaged flexure assembly to the forward end of a massive streamlined afterbody, attached to the towing carriage by a single strut. The propeller was driven by the DTNSRDC 35-horse-power dynamometer, separately supported from the towing carriage and positioned so that both the propeller shaft and body axes were aligned parallel to the direction of flow as illustrated in Figure 5.

The half body consisted of a 0.25 inch (0.64 cm) thick fiberglass shell measuring 36.0 inches (0.91 m) in length and 12.75 inches (0.324 m) in maximum diameter. The shell was filled with polyester foam in order to minimize the mass and obtain a high natural frequency, sufficiently above the propeller blade rate frequency range to reduce nonlinear resonance effects. The aluminum, free-flooded afterbody, together with its support strut had a low natural frequency to prevent mechanical vibrations from the propeller dynamometer gears and shafts passing through to the body force dynamometer. The towing strut was attached to a large frame, mounted on the propeller dynamometer structure. Slotted pads supporting the frame permitted transverse and longitudinal adjustment of the body location and orientation. Vibration isolating mounts were placed in the framework to further inhibit "pass through" vibrations.

Vibratory forces were measured for two propellers. DTNSRDC propeller 4118 is a 3-bladed, 12-inch (0.305 m) diameter aluminum propeller designed for uniform flow. Propeller 4119 is identical to 4118, except

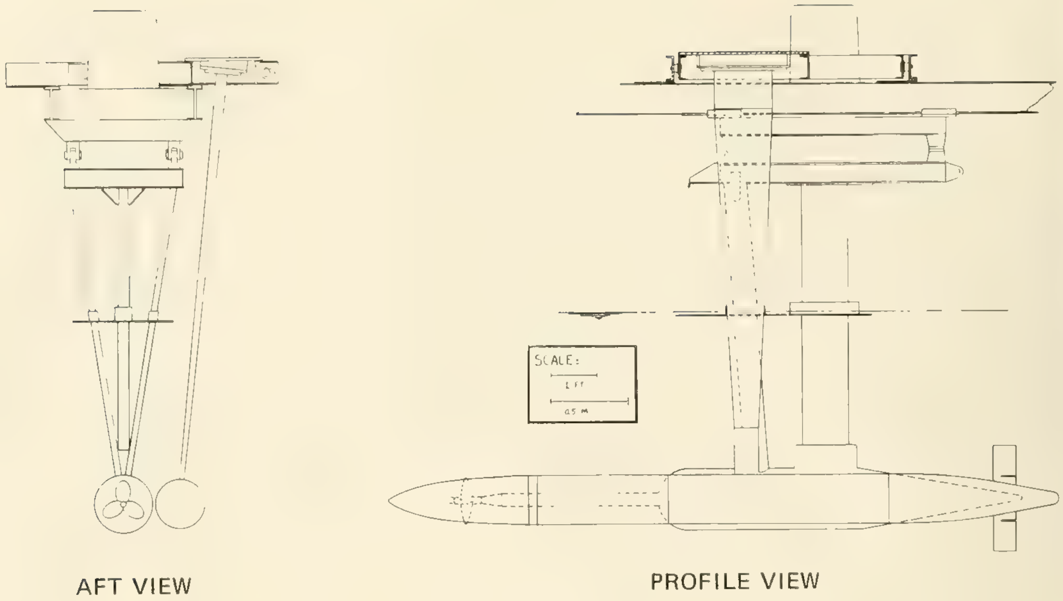

FIGURE 5. Experimental arrangement.

that it has twice the blade thickness (and a slight difference in pitch to correct for the added thickness). The principal design characteristics of the propellers are listed in Table 3. The propellers were designed by lifting-surface methods and both open water performance [Denny (1968)] and field point pressure measurements [Denny (1967)] have been reported. It should be noted that the theoretical predictions of field point pressures agree very well with the experimental measurements (at design advance coefficient) and the same propeller theory is applied in the present surface force calculations.

The Force Dynamometer

A dynamometer was developed to measure the horizontal component of the unsteady forces produced on the half body by the propeller. The half body is cantilevered from the afterbody on five (5) flexures. Forces are determined by measuring the strain in one flexure, while the other four flexures absorb the vertical force and moments as illustrated schematically in Figure 6. The measurement flexure transmits vertical forces and moments with miminal stress while resisting a large part of the horizontal force (calculated to be over 90 percent).

Two competing requirements governed the flexure design - the need to resolve small forces and the desire to maintain the natural frequency of the flexure-half body system far above the propeller excitation frequency. Also the flexure was expected to experience large (static) forces arising from flow misalignment and hydrostatic loading.

From the relationships for stress and stiffness of a simple cantilevered beam, it is known that for a given force, the flexure should have a low stiffness in order to produce maximum strain. This in turn would require a small body mass to keep the natural frequency high. However, if the body is too small, the resulting propeller force signal becomes difficult to retrieve in the presence of background noise. Although sophisticated techniques were employed to reduce electrical noise and boost signal power, it was not possible to completely eliminate mechanical noise generated by the rumbling carriage. With these compromises in mind, the flexure was designed for a frequency ratio of 0.5, producing minimally acceptable stress levels of 1000 psi (6.9 μPa) for the one pound (0.454 kg) force in this experiment.

TABLE 3. PROPELLER GEOMETRY

	4118	4119
DIAMETER, INCHES	12.0	12.0
NO OF BLADES	3	3
PITCH RATIO ($0.7 R_0$)	1.077	1.084
EXPANDED AREA RATIO	0.606	0.606
BLADE THICKNESS FRACTION	0.040	0.080
NACA MEANLINE	a = 0.80	a = 0.80

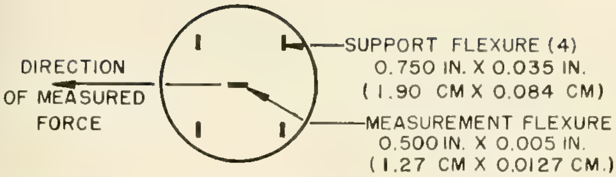

FIGURE 6. Schematic diagram of flexure arrangement.

For simplicity and economy, the flexure consisted of conventional steel shim stock clamped between the half body and the afterbody by sets of wedges. The flexures were pinned and epoxied to the wedges prior to insertion into the dynamometer plate. Before assembly, eight strain gages were mounted and waterproofed, with one gage placed at each corner of the two large faces of the flexure. The gages were electrically compensated for tension (or compression) and torsion. In order to check vertical alignment to the flow, two of the support flexures were also strain-gaged.

Calculations indicated that the measured strain in the flexure due to dynamic forces would be 135 percent of the strain due to a static force with the same amplitude, assuming small damping. Also, the phase angle of the strain relative to the applied force would be affected by the large ratio of excitation frequency to the natural frequency. Consequently, the experiment incorporated an internally mounted electromagnetic voice coil to calibrate the measurement flexure as a function of force amplitude, frequency, and forward speed. Initially, with a series of known static forces applied to the body, a current was applied to the coil to return the body to its unloaded position, as indicated by the strain output from the measurement flexure. These static calibrations revealed that the coil current varied linearly with applied force and that the flexure strain was virtually independent (less than 2 percent variation) of the axial location of the applied force.

Dynamic calibrations of the dynamometer were performed using a frequency generator and amplifier with the known sinusoidal current directly input to the coil. (It is assumed that in the low frequency range of interest, 0 to 60 Hz, the applied force is independent of frequency). The response amplitude (relative to the applied current or force) was found to vary linearly with the applied force. By averaging the data, the transfer function for each frequency and forward speed was determined as shown in Figure 7. These results revealed anomalous behaviour for frequencies of 20 Hz and 50-60 Hz, which were later identified as resonant frequencies associated with the towing structure.

Instrumentation and Data Acquisition

During each data run the following physical quantities were measured (see Figure 8): the force on the half body, the surface pressure at two locations on the body, the distance between the body and the propeller (tip clearance), propeller blade angular position and rotation speed, the forward speed of the towing carriage, and the horizontal accelerations of the afterbody.

Pressures were measured by metal diaphragm solid-state gages (KULITE XTMS-1-190) flush mounted to the half body surface. The propeller tip clearance which varied slightly with forward speed, was determined by measuring the distance between the 35-horsepower dynamometer body and the test afterbody at two axial positions using linear variable differential transformers (Schaevitz 1000 HCD). These low friction devices recorded relative movement without transmitting mechanical vibration.

The propeller blade angular position and rotation speed were measured by a Baldwin Shaft Position Encoder mounted on the 35-horsepower dynamometer tachometer shaft, generating one interrupt per degree of revolution and another interrupt once per revolution. During the experiments each data channel was sampled for each six degree increment of propeller rotation, thus providing 20 samples per cycle for blade frequency quantities. (The time lag between successively sampled channels and the delay between the encoder interrupt and capture of the sample, together amounting to several degrees of rotation, were later accounted for in the data reduction). Analog data output from the measurement tranducer was digitized and stored on magnetic tape. Data for each angular position of the propeller were summed and averaged over several hundred revolutions in an attempt to reinforce the signal of interest while self-cancelling random noise.

In order to determine the blade-frequency components of the unsteady force (and pressure) on the half body, a Fourier analysis was applied to the averaged data to yield the coefficients of the series

$$F(\theta) = \frac{a_o}{2} + \sum_{m=1}^{9} a_m \cos m\theta + b_m \sin m\theta, -\pi \leq \theta \leq \pi$$

$$= \frac{a_o}{2} + \sum_{m=1}^{9} c_m \cos(m\theta - \gamma_m) \qquad (60)$$

in which θ(t) is the blade position angle (Figure 8). For the three-bladed propellers, the nondimen-

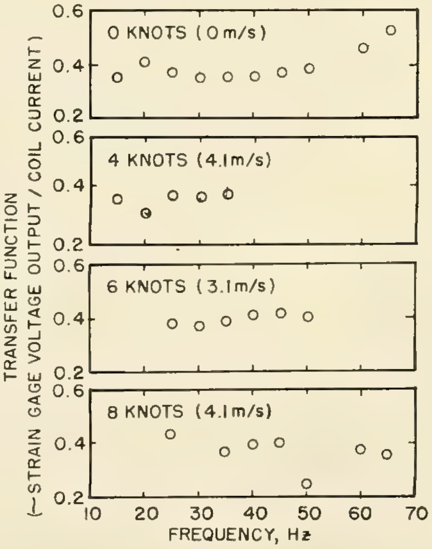

FIGURE 7. Force dynamometer amplitude response as a function of frequency for several forward speeds.

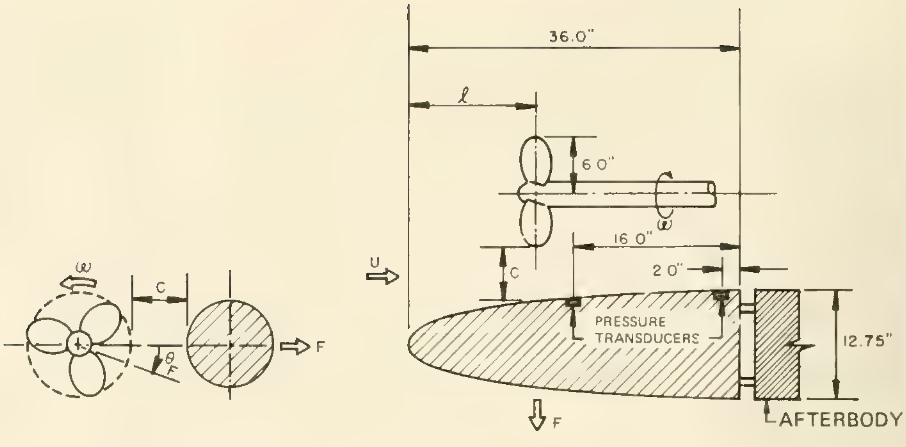

AFT VIEW IN PROPELLER PLANE

PLAN VIEW

FIGURE 8. Schematic diagram of experiment.

sional amplitude and phase of the blade frequency force F_3, are given by

$$C_F \equiv \frac{|F_3|}{\rho n^2 D^4} = \sqrt{a_3^2 + b_3^2} \tag{61}$$

$$\theta_F = \frac{1}{3} \tan^{-1} (b_3/a_3) \tag{62}$$

where the phase angle, θ_F, is the position of the reference blade when the force is a positive maximum or, from Figure 8, θ_F is the angle by which the force leads the blade position.

Experimental Results

Force measurements with propeller 4118 located 16.0 in. (6.3 cm) aft of the nose of the body and with a nominal tip clearance of 3.0 in. (1.18 cm) are given in Figure 9. The force generally increases in amplitude and lags further with higher propeller loading. The data points at design J (0.83) for speeds of 4 and 8 knots show good agreement. In Figure 10, the blade frequency pressure induced on the body in the plane of the propeller [x = 16.0 in. (6.3 cm)] shows a monotonic increase in amplitude with increased propeller loading and repeats well for different speeds.

Force measurements with propellers 4118 and 4119 positioned 10.0 in (3.94 cm) aft of the nose of the body [4.5 inc. (1.77 cm) tip clearance] are shown in Figure 11. Over the range of propeller advance coefficient, the force amplitude tends to increase with increased propeller loading and the effect of thickness is demonstrated.

The data exhibit some scatter for reasons not yet fully understood and further calibration experiments and data runs are needed. The variation in the data for different speeds (and hence different propeller excitation frequencies) is particularly disturbing. It may be noted that a post-test examination of the raw (unaveraged) data for the flexure, displacement, and afterbody accelerometers revealed three specific sources of difficulty. First, low amplitude data, particularly for speeds of 6 knots and a blade frequency of 35 Hz, was difficult to process. An example of this type of run and comparison with a good data run is shown in Figure 12. Generally, the low amplitude data resulted in force coefficients much below the values obtained from the higher amplitude data. Second, for certain runs the data were overscale on the individual records, but not in the averaged plot. These overscales, if abundant, produced anomolies. Third, structural resonances of 18-20 Hz and 55-60 Hz grossly distort data for blade frequencies with these values. To the extent possible, data contaminated by these problems were discarded and are not in the results presented.

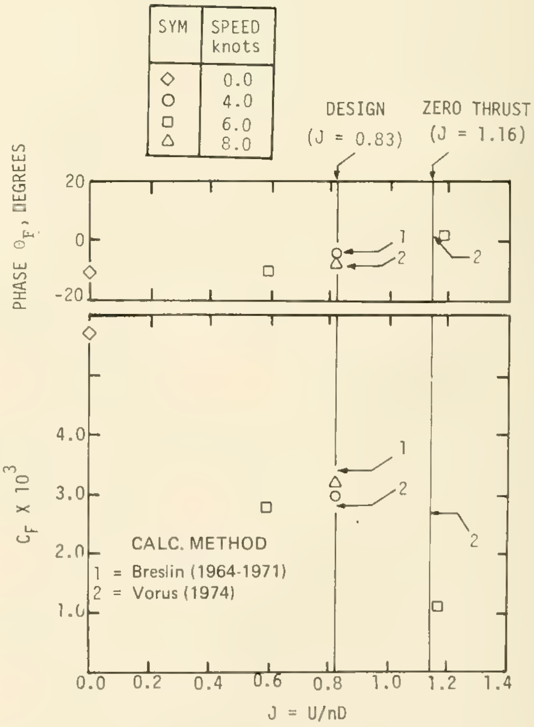

FIGURE 9. Calculated and measured blade frequency force for propeller located at ℓ = 16.0 in. with tip clearance C = 3.0 in.

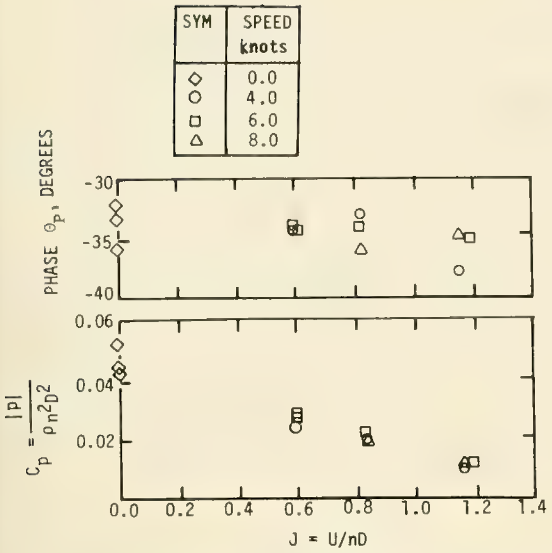

FIGURE 10. Blade frequency induced pressure on body with propeller 4118 located at ℓ = 16 in. and a tip clearance C = 3.0 in.

Application of the Theory

Direct Approach - Extended Lagally Theorem (Breslin and Eng, 1965)

The test body surface was divided into 154 elements as shown in Figure 13 with finer subdivisions made in way of the nearest approach of the propeller blades. Panels 93 through 100 were used to close the body. The geometry of these elements, together with the normal velocity induced by the propeller due to loading and blade thickness formed the input to the generalized Hess-Smith program which inverts Eq. (33) to yield the source densities on each of the panels.

A typical velocity variation, as given in Figure 14, shows that, downstream of the propeller, the loading contribution is oscillatory, requiring great care as the body sections are becoming larger. This test case presents a somewhat difficult application of this technique for this reason. In the ship case, there is only a small portion of the hull downstream of the propeller, and the sections are generally becoming smaller. As a result of this non-ship arrangement, difficulty was encountered in securing an accurate answer, requiring several adjustments of the size and location of the source panels.

A calculation for a single set of conditions, specified by the geometry of DTNSRDC Propeller 4118 set at a tip clearance of 3.0 inches (1.18 cm) at an axial distance of 16.0 inches (6.3 cm) downstream of the nose of the body gives a blade-frequency force coefficient $C_F = 3.4 \times 10^{-3}$ and a phase angle $\theta_F = -2.0°$. These results are quite close to the measured values shown in Figure 9. It should be remarked that the evaluation included the Lagally force corresponding to the integral of the convective pressures, i.e., the action of the transverse propeller velocity component on the sources which generate the body in the uniform axial flow. This contribution, as expected, is indeed small yielding only 1.0 percent of the force arising from the time rate of change of the potential. This surely justifies the order of magnitude argument given earlier.

Alternative Approach - Oscillatory Body Potential (Vorus, 1974)

In order to apply Eq. (47) to the experimental configuration, it is convenient to consider the velocity potential H_{in} of the body travelling backwards and executing simple *vertical* oscillations, so that $\vec{\alpha}_i = \vec{\alpha}_3 = \vec{k}$ in Eq. (53). The free surface condition $H_{in} = 0$ on $z = 0$, Eq. (54), can be satisfied by reflecting the body surface into the upper half space and satisfying the body boundary condition additionally on the image surface, S_i. In Appendix B it is shown that the *vertical force induced by the propeller on a ship in the free surface is equal to the force on the "double hull" deeply submerged.* If we make the further assumption that the force due to the convective pressure can be omitted, the problem for H_{in} now reduces to

$$\nabla^2 H_{in} = 0 \quad \text{in } \overset{*}{\forall} \tag{63}$$

$$\vec{n} \cdot \nabla H_{in} = inN\omega(\vec{n}\cdot\vec{k}) \quad \text{on } S + S_i \tag{64}$$

$$\nabla H_{in} \to 0, \ |\vec{x}| \to \infty \tag{65}$$

where $\overset{*}{\forall}$ is the whole space outside the "double-hull" surface, $S + S_i$.

This method is particularly convenient in the present application because the velocity potential of an oscillating spheroid is well known, e.g. Lamb (1932). With slightly modified notation

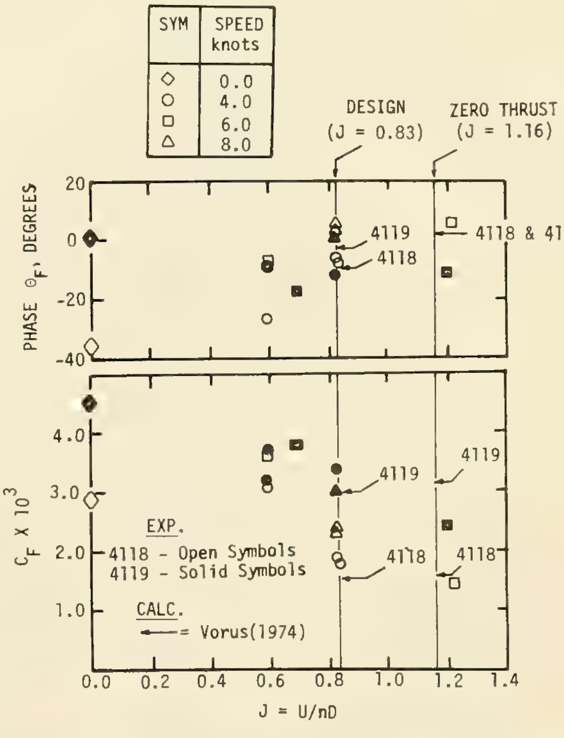

FIGURE 11. Calculated and measured blade frequency force for propellers 4118 and 4119 located at ℓ = 10.0 in. with tip clearance C = 4.5 in.

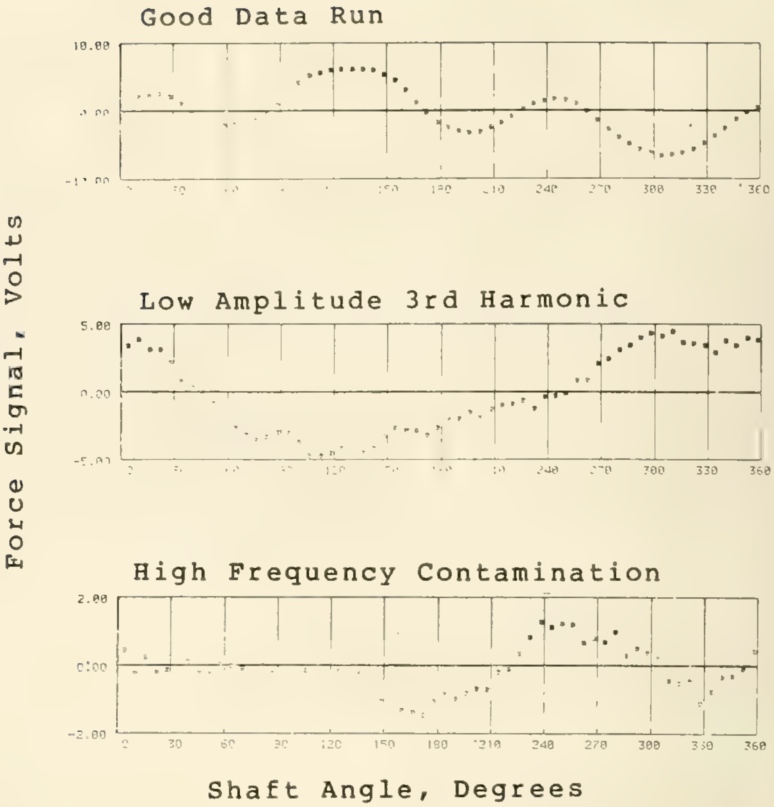

FIGURE 12. Examples of force measurement flexure signal output - data averaged over several hundred propeller revolutions.

$$H_{in}(\zeta,\mu,\varphi) = -inN\omega c_1 c_2 \zeta \sqrt{1-\mu^2}\left(\frac{1}{2}\,\ell n\,\frac{\gamma+1}{\gamma-1} - \frac{\gamma}{\zeta^2}\right)\cos\varphi \qquad (66)$$

Here $\gamma = \sqrt{1+\zeta^2}$ and (ζ,μ,φ) are the spheroidal coordinates defined by

$$x = c_1\,\mu\,\sqrt{\zeta^2+1},\quad r = c_1\,\zeta\,\sqrt{1-\mu^2},\quad \varphi=\varphi$$

with

$$0 \le \zeta \le \infty,\ -1 \le \mu \le 1,\ \varphi 0 \le \varphi < 2\pi$$

and (x,r,φ) is a cylindrical coordinate system with the origin at the center of the spheroid and the major axis extending from $x = L/2$ to $+ L/2$. The constants, c_1 and c_2 in (66) are readily determined in terms of the spheroid's maximum diameter/length ratio, δ, as

$$\frac{c_1}{L} = \sqrt{\frac{1-\delta^2}{2}},\quad c_1 = \text{focal length} \qquad (67)$$

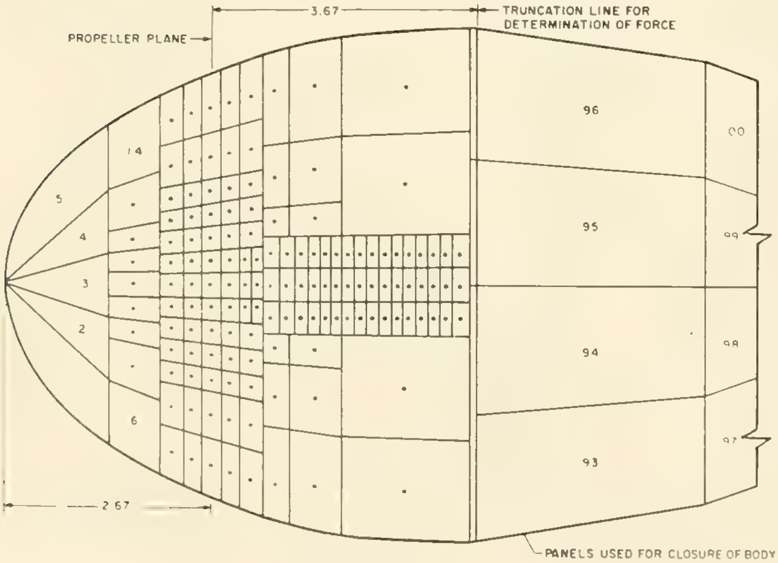
3.67
TRUNCATION LINE FOR DETERMINATION OF FORCE
PROPELLER PLANE
14
5
4
3
2
6
96
95
94
93
00
99
98
97
2.67
PANELS USED FOR CLOSURE OF BODY

FIGURE 13. Schematic of expanded surface of DTNSRDC ellipsoidal test body divided into 154 source panels (dimensions in multiples of propeller radius).

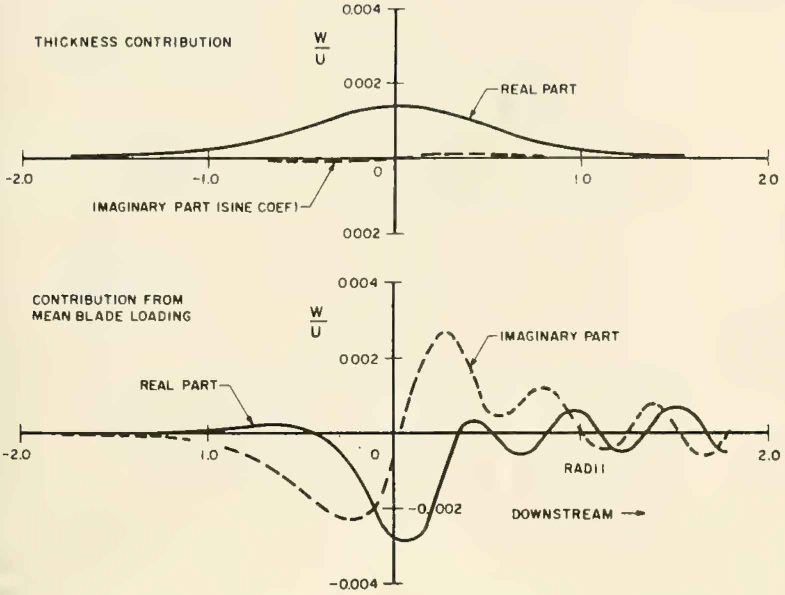

FIGURE 14. Variation of blade frequency vertical velocities induced by 3-bladed DTNSRDC propeller 4118 at $r = 1.5R_o$ and $\phi = 0$.

$$\frac{1}{c_2} = \frac{1}{2}\,\ell n \left(\frac{2[1+\sqrt{1-\delta^2}]}{\delta} - 1\right) + \frac{(1-2\delta^2)\sqrt{1-\delta^2}}{\delta^2} \tag{68}$$

and by a suitable coordinate transformation from (μ,ζ) to (x,r), the velocity ∇H_{in} can be calculated at an arbitrary point on the propeller blades.

In general the propeller dipole strength representing blade loading is a function of blade position $\theta(t)$, i.e., $\Delta p = \Delta p(\rho,\alpha+\theta(t))$. However, in the present experiments the inflow to the propeller is uniform so that the loading is steady and $\Delta p = \Delta p(\rho,\alpha)$. The blades of propellers 4118 and 4119 employ NACA a = 0.8 meanline sections. For this section, and assuming a radially elliptical distribution of bound circulation, the pressure jump across the blade is given by

$$\Delta p(\rho,\alpha) \simeq \frac{8T\sqrt{1-\left(\frac{2\rho - R_H - R_o}{R_o - R_H}\right)^2}}{0.9(\alpha_1 - \alpha_\ell)\,\pi(R_o^2 - R_H^2)N} \cdot F(\alpha) \tag{69}$$

in which

$$F(\alpha) = \begin{cases} 1 & \alpha_\ell \le \alpha \le 0.8\,\alpha_t + 0.2\,\alpha_\ell \\ 5\left(\dfrac{\alpha_t - \alpha}{\alpha_t - \alpha_\ell}\right) & 0.8\,\alpha_t + 0.2\,\alpha_\ell \le \alpha \le \alpha_t \end{cases} \tag{70}$$

and T is the steady propeller thrust.

The calculated values of the forces produced on the spheroid for conditions corresponding to those in the experiment are summarized in Table 4 showing the separate contributions arising from blade loading and thickness as well as the total forces. The latter are also displayed in Figures 9 and 11 and agree quite well with the measurements.

Additional parametric calculations were performed to study the effect of propeller location on the force produced on an ellipsoid arising from propeller mean loading and thickness. In Figure 15 the attenuation in force (amplitude) with increasing tip clearance is illustrated. (The phase was found to be essentially independent of tip clearance). Calculations are presented in Figure 16 for a series of axial positions of the propeller with the tip clearance held fixed. As the propeller is moved aft from the nose of the body, the force increases

TABLE 4. FORCE CALCULATIONS USING METHOD OF VORUS (1974)

PROPELLER	LOCATION	CONTRIBUTION	$C_F \times 10^3$	θ_F, DEG.
4118	ℓ = 16.0 IN. C = 3.0 IN.	MEAN LOADING THICKNESS TOTAL	1.50 2.77 2.90	-31.80 1.90 - 8.20
4118	ℓ = 10.0 IN. C = 4.5 IN.	MEAN LOADING THICKNESS TOTAL	0.88 1.58 1.52	-34.70 2.1 - 8.9
4119	ℓ = 10.0 IN C = 4.5 IN.	MEAN LOADING THICKNESS TOTAL	0.88 3.16 2.97	-34.70 2.1 - 3.3

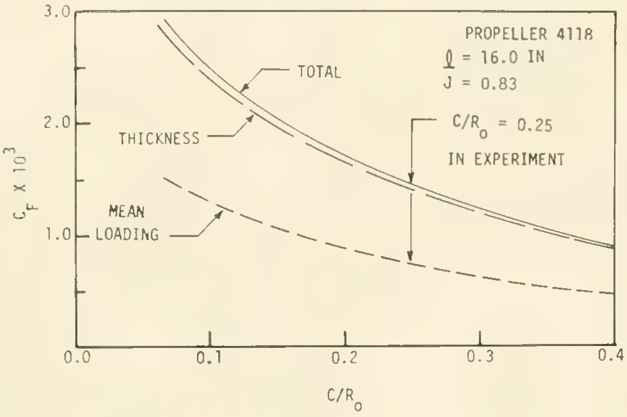

FIGURE 15. Modulus of blade-frequency force on ellipsoid as a function of propeller tip clearance [calculated using method of Vorus (1974)].

rapidly, largely due to the thickness contribution.

CONCLUDING REMARKS

The analytical methods given in this paper can be applied to a wide range of problems in which it is desired to determine the unsteady pressures and forces generated by a propeller on a nearby boundary. The formulation is quite general, being applicable to arbitrary hull (and appendage) geometries, and propeller locations, geometry, and loading characteristics. The assumption of high frequency propeller excitation, which greatly simplifies the treatment of the free surface, is not at all restrictive in most cases of practical engineering interest. A severe limitation, to be sure, is the restriction to subcavitating propellers. However, researchers are actively pursuing this subject and as procedures for predicting transient blade cavity geometry and the attendant pressure field become available, this important feature can be incorporated into the analytical representation of the propeller and the analysis of induced forces.

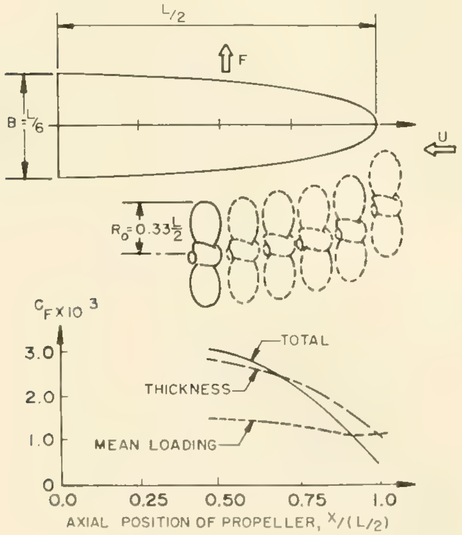

FIGURE 16. Modulus of lateral blade-frequency force produced on an ellipsoid of revolution (L/B = 6.0) as a function of propeller axial position (constant tip clearance, $C/R_0 = 0.25$)-calculated for DTNSRDC propeller 4118 using method of Vorus (1974).

As with any theoretical development of this kind, the usefulness and limitations can only be fully ascertained by comparison with a sufficient number of experimental measurements. The comparisons presented in this paper for the simple case of a body of revolution adjacent to a propeller in uniform flow represent an encouraging first check. This experimental technique can be extended to examine, in a systematic manner, the effects of nonuniform flow (unsteady blade loading and cavitation) and more general body shapes. For example, wire screens selected to produce certain wake harmonics can be towed upstream of the propeller. At the same time, the need is evident to undertake calculations for comparison with results of the many experiments reported during the past several decades.

ACKNOWLEDGMENTS

This work was jointly supported by the American Bureau of Shipping (ABS) and the Maritime Administration (MarAd). The continued interest and encouragement by Mr. S. Stiansen and Dr. H. H. Chen (ABS) and Mr. R. Falls (MarAd) is greatly acknowledged. Prior support of the Office of Naval Research, Fluid Dynamics Division, enabled the development of the velocity field program. The authors are also indebted to Mr. D. Valentine and Dr. S. Tsakonas of the Division Laboratory for their painstaking effort in developing the programs and to Messrs. H. Saulant and M. Jeffers (DTNSRDC) for invaluable assistance in the design and conduct of the experiments.

REFERENCES

Breslin, J. P. (1962). Review and Extension of Theory for Near-Field Propeller-Induced Vibratory Effects, *Proceedings Fourth Symposium on Naval Hydrodynamics*, ACR-92, Office of Naval Research, Washington, D. C.

Breslin, J. P., and K. Eng (1965). A Method for Computing Propeller-Induced Vibratory Forces on Ships, *Proceedings First Conference on Ship Vibration*, Stevens Institute of Technology, Hoboken, New Jersey; available as DTMB Report 2002.

Cummins, W. E. (1957). The Force and Moment on a Body in a Time-Varying Potential Flow, *J. Ship Research, 1*, 1: 7.

Denny, S. B. (1967). Comparisons of Experimentally Determined and Theoretically Predicted Pressures in the Vicinity of a Marine Propeller, *NSRDC Report 2349*.

Denny, S. B. (1968). Cavitation and Open-Water Performance Tests of a Series of Propellers Designed by Lifting-Surface Methods, *NSRDC Report 2878*.

Hess, J. L., and A. M. O. Smith (1964). Calculation of Nonlifting Potential Flow about Arbitrary Three-Dimensional Bodies, *J. Ship Research*, 8, 2: 22.

Jacobs, W. R., and S. Tsakonas (1975). Propeller-Induced Velocity Field due to Thickness and Loading Effects, *J. Ship Research, 19,* 1; 44.

Lamb, H. (1932). *Hydrodynamics,* Dover Publications, 6th Edition.

Lewis, F. M. (1969). Propeller Vibration Forces in Single Screw-Ships, *Transactions Society of Naval Architects and Marine Engineers, 77,* 318.

Lin, W. C. (1974). The Force and Moment on a Twin-Hull Ship in a Steady Potential Flow, *Proceedings Tenth Symposium on Naval Hydrodynamics, ACR-204,* Office of Naval Research, Washington, D. C.

Stuntz, G. R., P. C. Pien, W. B. Hinterthan, and N. L. Ficken (1960). Series 60 - The Effect of Variation in Afterbody Shape upon Resistance, Power, Wake Distribution, and Propeller Excited Vibratory Forces, *Transactions Society of Naval Architects and Marine Engineers, 68,* 292.

Tsakonas, S., J. P. Breslin, and W. R. Jacobs (1962). The Vibratory Force and Moment Produced by a Marine Propeller on a Long Rigid Strip. *J. Ship Research, 5,* 4; 21.

Tsakonas, S., W. R. Jacobs, and M. R. Ali (1973). An "Exact" Linear Lifting-Surface Theory for a Marine Propeller in a Nonuniform Flow Field, *J. Ship Research, 17,* 4; 196.

Valentine, D. T., and F. J. Dashnaw (1975). Highly Skewed Propeller for SAN CLEMENTE Ore/Bulk/Oil Carrier Design Considerations, Model and Full-Scale Evaluation, *Proceedings First Ship Technology and Research Symposium,* Society of Naval Architects and Marine Engineers, Washington, D. C.

Vorus, W. S. (1971). An Integrated Approach to the Determination of Propeller-Generated Vibratory Forces Acting on a Ship Hull, *Department of Naval Architecture and Marine Engineering, University of Michigan, Report 072.*

Vorus, W. S. (1974). A Method for Analyzing the Propeller-Induced Vibratory Forces Acting on the Surface of a Ship Stern. *Transactions Society of Naval Architects and Marine Engineers, 82,* 186.

Vorus, W. S. (1976). Calculation of Propeller-Induced Forces, Force Distributions and Pressures; Free-Surface Effects, *J. Ship Research, 28,* 2; 107.

APPENDIX A

THE LAGALLY FORCE ON A FLOATING BODY REPRESENTED BY A SURFACE DISTRIBUTION OF SOURCE SINGULARITIES

The force $\vec{F}_n^{(2)}$ arising from the convective term of the linearized unsteady pressure, Eq. (35), is given by

$$\vec{F}_n{}^{(2)} = \rho \iint_S \vec{V}_s^+ \cdot \nabla\phi_n^+ \vec{n}\, dS \qquad \text{(A-1)}$$

where, as before, the symbols $(\ )^-$ and $(\ )^+$ denote quantities inside and outside the hull surface, S. We assume that the solutions for $\vec{V}_s$ and ϕ_n are known in terms of distributions of source singularities and images over the surface S as

$$\phi_s(\vec{x}) = -\frac{1}{4\pi}\iint_S \sigma_s(\vec{x}')\left[\frac{1}{|\vec{x}-\vec{x}'|} + \frac{1}{|\vec{x}-\vec{x}'_i|} + G(x,x')\right] dS$$

$$\vec{V}_s = \vec{i}U + \nabla\phi_s \qquad \text{(A-2)}$$

$$\phi_n(\vec{x}) = -\frac{1}{4\pi}\iint_S \sigma_n(\vec{x}')\left[\frac{1}{|\vec{x}-\vec{x}'|} - \frac{1}{|\vec{x}-\vec{x}'_i|}\right] dS + \phi_{P_n}$$

$$+ \phi_{P_{i_n}} \qquad \text{(A-3)}$$

in which $\sigma_s(\vec{x})$ and $\sigma_n(\vec{x})$ are the source singularity strengths, $\vec{x}'_i$ is the image point of $\vec{x}$, and $G(\vec{x},\vec{x}')$ is the "wave potential" of a source located at $\vec{x}'$ and is regular in the half plane $z < 0$. The derivatives of these functions on each side of the surface S are related to the source strengths in the form

$$\vec{V}_s{}^+ = \vec{V}_s{}^- + \vec{n}\sigma_s \qquad \text{(A-4)}$$

$$\nabla\phi_n^+ = \nabla\phi_n^- + \vec{n}\sigma_n \qquad \vec{x} \text{ on S} \qquad \text{(A-5)}$$

from which it follows that

$$\vec{V}_s^+ \cdot \nabla\phi_n^+ = \vec{V}_s^- \cdot \nabla\phi_n^- - \sigma_s\,\sigma_n \qquad \text{(A-6)}$$

since $\vec{V}_s^+ \cdot \vec{n} = \nabla\phi_n^+ \cdot \vec{n} = 0$.

We now apply Green's theorem to the functions $\vec{V}_s^-$ and $\nabla\phi_n^-$ in the closed volume $\forall$ surrounded by the surface S and S_o, where S_o is the hull waterline plane, obtaining

$$\iint_{S+S_o} \vec{V}_s^- \cdot \nabla\phi_n^- \vec{n}\, dS = \iiint_{\forall} \nabla(\vec{V}_s^- \cdot \nabla\phi_n^-)\, d\forall$$

$$= \iiint_{\forall} [\vec{V}_s^- \cdot \nabla(\nabla\phi_n^-) + \nabla\phi_n^- \cdot \nabla\vec{V}_s^-]\, d\forall \qquad \text{(A-7)}$$

since $\nabla \times \vec{V}_s^- = \nabla \times \nabla\phi_n^- = 0$ in $\forall$. Using Gauss' theorem and the fact that $\nabla \cdot \vec{V}_{s^-} = \nabla \cdot \nabla\phi_{n^-} = 0$ in $\forall$, (A-7) may be written as

$$\iint_{S+S_o} V_s^- \cdot \nabla\phi_n^-\, n\, dS =$$

$$\iint_{S+S_o} [\vec{V}_s^- (\nabla\phi_n^- \cdot n) + \nabla\phi_n^- (V_s^- \cdot n)]\, dS \qquad \text{(A-8)}$$

and hence

$$\iint_S V_s^- \cdot \nabla\phi_n^- \vec{n}\, dS = \iint_S [\vec{V}_s^- (\nabla\phi_n^- \cdot \vec{n}) + \nabla\phi_n^- (\vec{V}_s^- \cdot \vec{n})]\, dS + \iint_{S_0} [\vec{V}_s^- (\nabla\phi_n^- \cdot \vec{n}) + \nabla\phi_n^- (\vec{V}_s^- \cdot \vec{n}) - \vec{V}_s^- \cdot \nabla\phi_n^- \vec{n}]\, dS \qquad (A\text{-}9)$$

The last two terms in the integral over S_0 combine to yield

$$\vec{n}(\vec{V}_s \cdot \nabla\phi_n^-) - \nabla\phi_n^- (\vec{V}_s^- \cdot \vec{n}) = \phi_n^- n \cdot \nabla\vec{V}_s^- - (\vec{n} \times \nabla) \times \phi_n^- \vec{V}_s^- \qquad (A\text{-}10)$$

The first term on the righthand side of (A-10) vanishes since $\phi_n \equiv 0$ on S_0. The second term also vanishes, since by Stokes' theorem

$$\iint_S (\vec{n} \times \nabla) \times \phi_n^- \vec{V}_s^- = \oint_{c_0} d\vec{x} \times \phi_n^- \vec{V}_s^- = 0 \qquad (A\text{-}11)$$

where the contour c_0 is taken as the hull waterline. Consequently, using (A-6), (A-9), and (A-10), the expression for the force becomes

$$\vec{F}_n^{(2)} = \rho \iint_S [\vec{V}_s^- (\nabla\phi_n^- \cdot \vec{n}) + \nabla\phi_n^- (\vec{V}_s^- \cdot \vec{n}) - \sigma_s \sigma_n \vec{n}]\, dS + \rho \iint_{S_0} \vec{V}_s^- (\nabla\phi_n^- \cdot \vec{n})\, dS \qquad (A\text{-}12)$$

The contribution from the free stream, $\vec{i}U$(in $\vec{V}_s$), vanishes since

$$\iint_{S+S_0} \vec{i}U (\nabla\phi_n^- \cdot \vec{n})\, dS = \vec{i}U \iiint_{\forall} \nabla^2\phi_n^-\, d\forall = 0$$

Also noting that $\nabla\phi_n^- \cdot \vec{n} = -\sigma_n$ and $\vec{V}_s^- \cdot \vec{n} = -\sigma_s$, (A-11) reduces to

$$\vec{F}_n^{(2)} = -\rho \iint_S [\sigma_n \nabla\phi_s^- + \sigma_s \nabla\phi_n^- + \sigma_s \sigma_n \vec{n}]\, dS + \rho \iint_{S_0} \nabla\phi_s^- \nabla\phi_n^- \cdot \vec{n}\, dS \qquad (A\text{-}13)$$

or, upon defining

$$\nabla\hat{\phi}_s \equiv \frac{\nabla\phi_s^+ + \nabla\phi_s^-}{2}$$

$$\nabla\hat{\phi}_n \equiv \frac{\nabla\phi_n^+ + \nabla\phi_n^-}{2} \qquad (A\text{-}14)$$

(A-13) becomes

$$\vec{F}_n^{(2)} = -\rho \iint_S (\sigma_n \nabla\hat{\phi}_s + \sigma_s \nabla\hat{\phi}_n)\, dS + \rho \iint_{S_0} \nabla\phi_s^- \frac{\partial\phi_n^-}{\partial z}\, dS \qquad (A\text{-}15)$$

The first term has the same structure as the *steady flow* Lagally force derived by Lin (1974) for a linearized source sheet representation of a slender strut piercing the free surface. The second term arises from the intersection of the hull with the free surface in unsteady flow.

In the low Froude number approximation, $\partial\phi_s/\partial z = 0$ on $z = 0$ (rigid wall representation of the free surface), and $G(x,x') \to 0$. In this case (A-2) and (A-3) yield

$$\nabla\hat{\phi}_s = +\frac{1}{4\pi} \iint_S \sigma_s(\vec{x}') \left(\frac{\vec{x}-\vec{x}'}{|\vec{x}-\vec{x}'|^3} + \frac{\vec{x}-\vec{x}'_i}{|\vec{x}-\vec{x}'_i|^3} \right) dS$$

and

$$\nabla\hat{\phi}_n = +\frac{1}{4\pi} \iint_S \sigma_n(\vec{x}') \left(\frac{\vec{x}-\vec{x}'}{|\vec{x}-\vec{x}'|^3} - \frac{\vec{x}-\vec{x}'_i}{|\vec{x}-\vec{x}'_i|^3} \right) dS + \nabla\phi_{P_n} + \nabla\phi_{P_{i_n}} \qquad (A\text{-}16)$$

for $\vec{x}$ on S, and where the integrals are to be interpreted in the principal value sense. Inserting these expressions into (A-15) and performing the integrations, the equation for the force reduces to

$$\vec{F}_n^{(2)} = -\rho \iint_S \sigma_s (\nabla\phi_{P_n} + \nabla\phi_{P_{i_n}})\, dS + \rho \iint_{S_0} \nabla\phi_s^- \frac{\partial\phi_n^-}{\partial z}\, dS \qquad (A\text{-}17)$$

which is the result given as Eq. (42) in the text. The reduction in the first term reflects the fact that there is no net force arising from the mutual interaction of the body sources.

APPENDIX B
REDUCTION OF THE ANALYSIS OF PROPELLER INDUCED VERTICAL SURFACE FORCE TO AN INFINITE FLUID PROBLEM

The linearized unsteady pressure at a point, $\vec{x}$, on the ship hull surface is given by (8) as

$$p(\vec{x},t) = -\rho \left[\frac{\partial\phi}{\partial t}(\vec{x},t) + \overline{V}_s(\vec{x}) \cdot \nabla\phi(\vec{x},t) \right] \qquad (B\text{-}1)$$

and the vertical force acting in the hull, from (10), is

$$F_z(t) = - \iint_S p(\vec{x},t)\, \vec{n} \cdot \vec{k}\, dS \qquad \text{(B-2)}$$

In the high frequency approximation, $\phi = 0$ on the free surface, $z = 0$, and this condition can be satisfied by constructing an image of the hull surface and a negative image of the propeller in the upper half space and allowing the fluid domain to extend to infinity in all directions. The negative image propeller is identical to the propeller proper, but rotates in the opposite direction and the signs of the dipole singularities representating the effects of loading and thickness are reversed from those of their images in the lower half space.

The image hull surface, S_i, is identical geometrically to S, but the signs of the singularities on S_i required to diffract the unsteady flow from the "two propellers" will be reversed from these on S due to the symmetry. The magnitudes of the singularities at image points will be equal.

The steady flow about the bare hull, $\vec{V}_S$, in the low Froude number approximation will satisfy the rigid wall free surface condition $\vec{V}_S \cdot \vec{k} = 0$. In this case, the steadily moving hull can be reflected into the upper half plane with a *positive* image singularity system, i.e., the singularities on the image surface, S_i will be of the same sign as the singularities on S to diffract the velocity $\vec{i}U$.

Because of the assumed linearity, the unsteady potential may therefore be considered as the sum of contributions from the propeller and hull and their respective images.

$$\phi = \phi_P + \phi_H + \phi_{Pi} + \phi_{Hi} \qquad \text{(B-3)}$$

where

$$\begin{aligned} \phi_H(\vec{x},t) &= - \phi_{Hi}(\vec{x}_i,t) \\ \phi_P(\vec{x},t) &= - \phi_{Pi}(\vec{x}_i,t) \\ \vec{x}_i &= (x,y,-z) \end{aligned} \qquad \text{(B-4)}$$

for all (x,y,z) outside the surface $S + S_i$. If we define $\phi_{PH} = \phi_P + \phi_H$ then it follows that

$$\phi(\vec{x},t) = \phi_{PH}(\vec{x},t) - \phi_{PH}(\vec{x}_i,t) \quad \text{all } \vec{x} \qquad \text{(B-5)}$$

Therefore, *the complete unsteady potential in the fluid beneath the zero potential free surface can be obtained entirely from consideration of the propeller and the double-hull in an infinite fluid.*

The unsteady pressure at a point on the hull surface S is now given by

$$p(x,t) = - p \left[\frac{\partial \phi_{PH}}{\partial t}(\vec{x},t) + \vec{V}_S(\vec{x}) \cdot \nabla\phi_{PH}(\vec{x},t) - \frac{\partial \phi_{HP}}{\partial t}(\vec{x}_i,t) - \vec{V}_S(\vec{x}) \cdot \nabla\phi_{PH}(\vec{x}_i,t) \right]$$

Now if $\vec{V}_S = (U + u_S, v_S, w_S)$, the symmetry of $\vec{V}_S$ is such that u_S and v_S are even in z, while w_S is odd in z. It follows that

$$\vec{V}_S(\vec{x}) \cdot \nabla\phi_{PH}(\vec{x}_i,t) = \vec{V}_S(\vec{x}_i) \cdot \nabla\phi_{PH}(\vec{x}_i,t)$$

and hence

$$p(x,t) = P_{PH}(\vec{x},t) - P_{PH}(\vec{x}_i,t) \qquad \text{(B-6)}$$

in which

$$P_{PH} = - \rho \left(\frac{\partial \phi_{PH}}{\partial t} + \vec{V}_S \cdot \nabla\phi_{PH} \right)$$

Thus, *the unsteady pressure at points on the hull can be obtained from calculations, or measurements, of pressures at image points on the double-hull, with the double-hull and propeller deeply submerged.*

Turning now to the formula (B-2) for the vertical force, we obtain

$$F_z(t) = - \iint_S p_{PH}(\vec{x},t)\vec{n} \cdot \vec{k}\, dS + \iint_S p_{HP}(\vec{x}_i,t)\vec{n} \cdot \vec{k}\, dS \qquad \text{(B-7)}$$

But since $\vec{n}(\vec{x}) \cdot \vec{k} = -n(x_i) \cdot k$, (B-7) may be written as

$$F_z(t) = - \iint_S p_{HP}(\vec{x},t)\vec{n}(\vec{x}) \cdot \vec{k}\, dS - \iint_S p_{HP}(\vec{x}_i,t)\vec{n}(\vec{x}_i) \cdot \vec{k}\, dS \qquad \text{(B-8)}$$

or, since the image hull S_i is geometrically identical to the hull proper,

$$F_z(t) = - \iint_{S+S_i} p_{HP}(\vec{x},t)\, \vec{n} \cdot k\, dS$$

and consequently *the unsteady vertical force on the hull can be obtained from force calculations, or force measurements, using the double model and propeller deeply submerged.*

A Determination of the Free Air Content and Velocity in Front of the "Sydney-Express" Propeller in Connection with Pressure Fluctuation Measurements

A. P. Keller
Technical University Munich
and
E. A. Weitendorf
University of Hamburg,
Federal Republic of Germany

ABSTRACT

The Special Research Pool within the Institut für Schiffbau and the Hamburg Shipmodel Basin (HSVA) in collaboration with the Technical University Munich and Det norske Veritas executed extensive full-scale measurements on the Single-Screw Container Ship "Sydney-Express." The main task of the project was the determination of the free air content of the seawater in front of the propeller during the voyage from Australia to Europe.

Simultaneously the velocity was measured at the control point within the Laser-beam, where the free air content was measured by the scattered light technique. Additional investigations were a determination of the water-quality, high speed films and sterophotography of the cavitation at the blade, and pressure fluctuation measurements above the propeller.

1. INTRODUCTION

For several years the dynamic behaviour of small gas bubbles or nuclei in hydrodynamic pressure fields has been recognized as an important influence on cavitation inception and its extent. Besides other scale effects in the field of model propeller testing, the importance of this influence of nuclei, which also effects propeller excited pressure fluctuation measurements, was often underestimated and neglected. Thus, for instance, the results by van Oossanen and van der Kooy (1973) have shown that for equal non-dimensional flow conditions but different absolute revolutions (i.e. n = 20 and n = 30 Hz) the non-dimensional propeller excited pressure amplitudes were different. After the development by Keller (1973) of a practicable laser-scattered-light (LSL) method for measuring the undissolved air content, systematic cavitation and pressure fluctuation measurements were carried out in the medium cavitation tunnel of the Hamburg Ship Model Basin (HSVA) with the model propeller of the "Sydney Express" [Keller and Weitendorf (1975)]. The results were similar to those by van Oossanen and van der Kooy. Due to the additional application of the (LSL) technique, the differences of the nondimensional pressure amplitudes for different revolutions could be clearly explained by the influence of the free air content or nuclei on the cavitation. A further finding was that the non-dimensional pressure amplitudes and the cavitation for a revolution of n = 15 Hz were increasing with growing free air content, whereas the cavitation and those amplitudes for n = 30 Hz remained more or less constant. The different behaviour for n = 15 Hz and n = 30 Hz were explained by Isay and Lederer (1976, 1977). Using the theory of bubble dynamics they found that the reactions of the bubbles on the respective pressure gradient of the propeller blades at n = 15 or n = 30 Hz were different. Further, these investigations led to criteria of cavitation similarity of such a kind that the number of nuclei per unit volume of the model flow had to be increased compared with the number of nuclei of the full scale flow. By geosim tests with hydrofoils or propellers it should be determined to what extent these additional criteria for cavitation similarity are applicable.

Keeping in mind these physical connections, the full scale trials on the container ship "Sydney Express" were planned. These investigations were the first attempt to measure the nuclei distribution in seawater around a ship by means of the LSL technique. The nuclei distribution could serve as a basic value for the geosim tests and perhaps as a comparative standard value of the water quality for model cavitation investigations. Furthermore, the experiences, made during the almost adventurous measurements on the "Sydney Express" with the LSL technique in front of a full scale propeller, could be of common interest because the introduction of optical laser methods is a promising tool in the research fields of boundary layers and propeller flows.

The additional investigations on the "Sydney Express" help in full-scale model correlation only slightly; the main purpose of these measurements was the securing and better interpretation of the scattered light results. The following additional measurements were performed:

1. Propeller-excited pressure fluctuation measurements with six pressure pick-ups above the propeller.
2. Cavitation observations for determination of the thickness and extent of the cavity by means of stereo photography.
3. Investigations of water-quality by means of a simple scattered light method (Aminco-colorimeter) for detecting suspended particles and total air content by means of a Van-Slyke-apparatus. For both measurements water samples were taken.
4. Velocity measurements in the control volume of the scattered light measurement in order to estimate the bubble concentration.

The "Sydney Express", as one of the fastest German single screw merchant ships, was chosen for the investigations because its propeller has an interesting cavitation extent.

2. SHIP DATA AND PREPARATION OF THE MEASUREMENTS

The single screw, turbine-driven ship "Sydney Express" has been built by Messrs. Blohm and Voss AG, Hamburg (No. 872) and belongs to the so-called second generation of container ships.

The main data of the ship are given in Table 1:

TABLE 1 - "Sydney Express" - Data

Ship Data			
Length b.p.	L_{pp}	=	210.00 m
Breadth, moulded	B_m	=	30.50 m
Design Draft	D	=	11.00 m
Block coefficient	C_B	=	0.616
Displacement (Design)	∇	=	43,457 m^3
Container	about		1,600
Max. Power	P_D		23,870 kw
Service Speed	V_S	=	22.0 kn

Propeller Data			
Diameter	D_P	=	7.00 m
Pitch (mean)	P_m	=	6.550 m
Blade-Area-Ratio	A_e/A_o	=	0.78
Number of Blades	z	=	5

The necessary conversions of the ship construction for the installation of the measuring devices in the after peak of the ship were carried out at the Hapag-Lloyd ship yard at Bremerhaven during the latter part of September 1977. Figure 1 shows allusively to what an extent the narrow steel construction had to be cut free. The installation of three windows for the reception of the scattered laser light proved to be the most complicated of all installations. For reasons of the ship's safety and also to enable proper cleaning these windows were pushed through 350 mm sluice valves together with their tubular guide pipes. The windows, of which only that opening was marked in Figure 1 which had been used for measurements, were arranged between frames 12 and 13. Also, the fitting of the three 350 mm sluice valves required skillful improvisation on the spot. The installations of the sluice valves for the pressure pick-ups, dimensioned in Figure 1, and of the cavitation observation windows were carried out without any difficulties.

In addition, all electric lines were laid out from the measuring pick-ups to the measuring container during this period. The necessary amplifiers, digital magnetic tape recorders, and computer (HP 2100 A) with its peripheral equipment were located in this measuring container. The measuring container was located in hole 6 directly on the tank deck of the after peak, in the last bay. For the determination of the performance data of the ship, strain gauges were attached to the shaft. In addition, the shipborne electro-magnetic log (system Plath) for determination of the ship's speed was connected to the computer via an isolation amplifier. Thus, the ship's speed and power could also be recorded at each pressure fluctuation- and LSL-measurement. A recalibration of the log was made on the outward voyage in the North Sea by means of a speed measurement carried out by the Hamburg Ship Model Basin using their method with a resistance log.

3. PROPELLER EXCITED PRESSURE FLUCTUATIONS AND CAVITATION OBSERVATIONS

The measurements of the propeller excited pressure fluctuations were started on the outward voyage when leaving the English Channel and continued until the arrival at Marseille (Tests No. 1-11). Further details on these measurements as well as for the pressure fluctuation measurements carried out in the Mediterranean (Tests No. 13-16) are given in Tables 2a and 2 b.

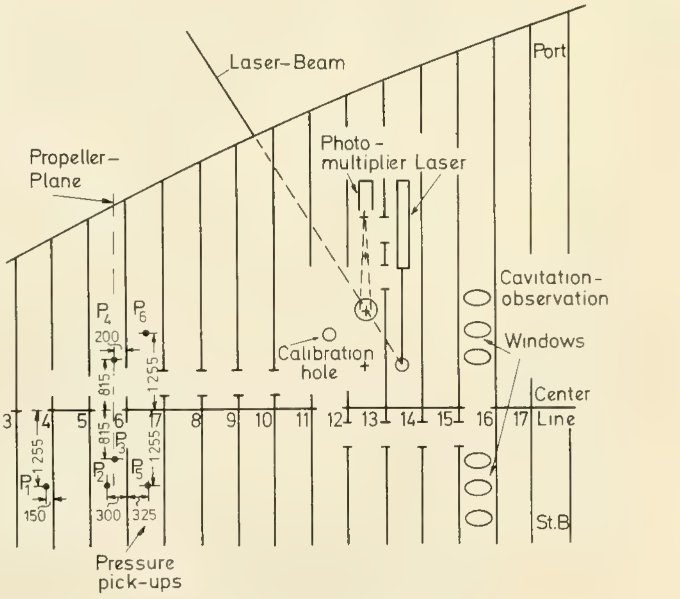

FIGURE 1. Locations of test setups.

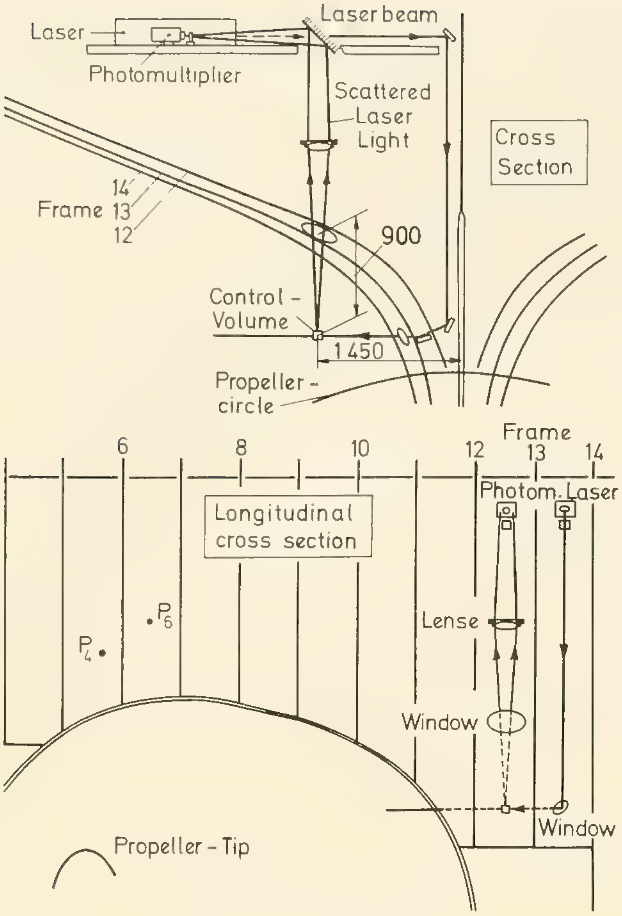

FIGURE 2. Arrangement of test setups.

The results of the pressure fluctuation measurements for the Tests No. 1-4, 11 and 13-16 are given in Figure 3 showing the dimensionless pressure amplitudes of the blade frequency for the pressure pick-ups P1, P3, P4, and P6. They have been harmonically analysed on the HP-computer in the measuring container. As usual with right-hand propellers the pressure pick-up on the starboard side (here: P3) clearly shows higher values than that on the port side (P4). Figure 4 shows the amplitudes measured by these two pressure pick-ups up to the 15th harmonic. The harmonic analysis has been carried out for a "representative" revolution, resulting from the average of 60 propeller revolutions.

Figure 5 shows the pressure fluctuations measurements versus propeller rpm for the pick-ups P3 and P4 for two drafts applied during the voyage in the Indian Ocean. At this point in time the propeller was already damaged. Further data of these measurement runs can be found in the Tables 3a to 3h. Examples of the results of harmonic analyses up to the 15th harmonic order for the pressure pick-ups P3 and P4 are shown in Figure 6. In Figure 7 a comparison is given of the pressure amplitudes of these harmonic orders for the pick-up P4 (port) in shallow and deep water. In shallow water the pressure amplitudes are only slightly higher (5.8%) than that in deep water. With the pick-up P3 (starboard) the difference was even smaller (1.0% increase).

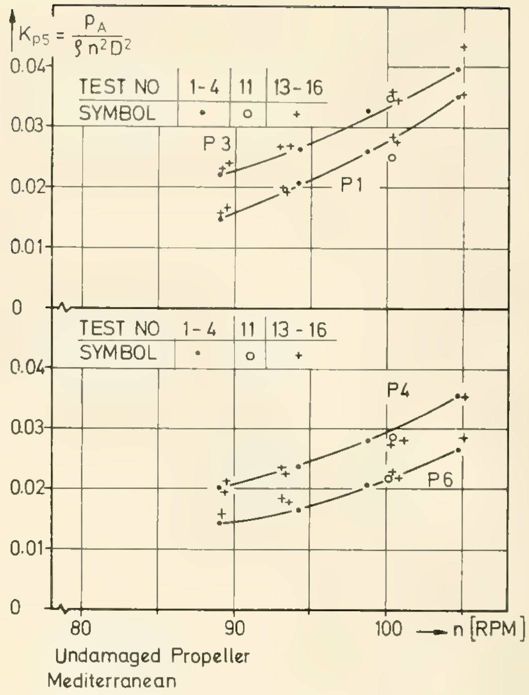

FIGURE 3. Pressure fluctuations.

The lower pressure amplitudes of the blade frequency in the Indian Ocean (Figures 5 and 6) compared with that in the Mediterranean (Figures 3 and 4) are to be attributed to a significantly stronger, but mainly stationary cavitation of the damaged blade (No. 3). A comparison between Figures 4 and 6 shows that due to the damage the pressure amplitudes of the "not-blade-number" frequencies have been strongly increased in opposition to the blade frequency. It should be noted that the ship superstructure vibrated strongly after the propeller had been damaged. This damage resulted from a ground-

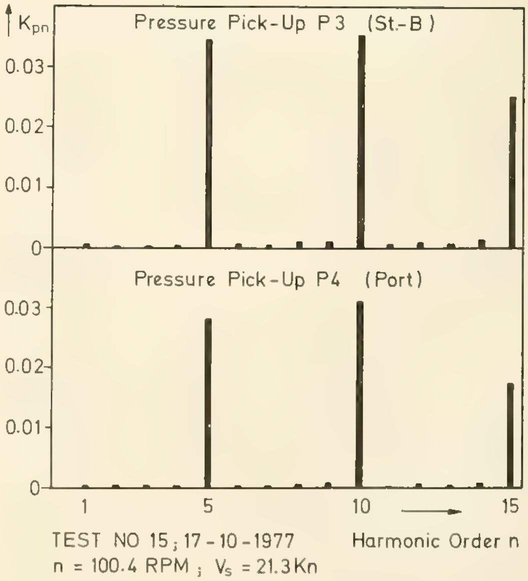

FIGURE 4. Harmonic components of pressure fluctuations.

Table 2a

Test No.	1	2	3	4	11
Date	← 9.10.1977 →				12.10.77
Speed V_S [kn]	17.2	18.6	19.8	21.4	20.7
Revolution n [RPM]	89.1	94.3	98.8	104.7	100.4
Power P_D [MW]	11.4	13.0	14.6	16.8	14.9
Draft aft [m]	8.94	8.94	8.94	8.94	8.33
Draft forward [m]	6.35	6.35	6.35	6.35	6.96
Course	209°	231°	231°	230°	37°
Sea region	← English Channel →				Medit.
Wind [Beauf]	4	4	4	4	0
Wind direction	180°	180°	180°	180°	0
Water Depth [m]	36	35	41	51	1040

Table 2b

Measurements in the Mediterranean

Test No.	13	14	15	16
Date	← 17.10.1977 →			
Speed V_S [kn]	18.6	19.5	21.3	22.3
Revolution n [RPM]	89.5	93.2	100.6	105.1
Power P_D [MW]	10.4	12.2	15.7	17.1
Draft aft [m]	9.73	9.73	9.73	9.73
Draft forward [m]	9.63	9.63	9.63	9.63
Course	115°	114°	114°	114°
Sea region	← 36°45'N; 18°49'E (Mediterr.)			
Wind [Beauf]	← 3 ÷ 4 →			
Wind direction	← 90° →			
Water Depth [m]	← 3500 →			

Table 3a

Measurements in the Indian Ocean

Test No.	47	59	60	61	62	65
Date	30.11.77	← 1.12.77 →				2.12.77
Speed V_S [kn]	21.2	21.4	21.3	21.3	21.3	21.3
Revolution n [RPM]	101.1	101.6	101.2	101.8	101.0	101.3
Power P_D [MW]	21.7	—	—	—	—	—
Draft aft [m]	9.30	← 9.30 →				9.30
Draft forward [m]	7.62	← 7.62 →				7.62
Course	294°	← 294° →				294°
Sea region or position	16°13'S; 87°28'E	← 12°46'S; 79°46'E →				9°09'S; 71°47'E
Wind [Beauf]	6	← 3 →				2 - 3
Wind direction	100°	← 70° →				230°
Water Depth [m]	3300	← 4900 →				2000

Table 3b

Measurements in the Indian Ocean

Test No.	70	71	72
Date	← 4.12.77 →		
Speed V_S [kn]	21.8	22.1	21.8
Revolution n [RPM]	101.7	101.9	101.3
Power P_D [MW]	—	—	—
Draft aft [m]	← 9.37 →		
Draft forward [m]	← 8.08 →		
Course	← 314° →		
Sea region or position	← 2°58'N; 59°44'E →		
Wind [Beauf]	← 1 ÷ 2 →		
Wind direction	← 235° →		
Water Depth [m]	← 3250 →		

Table 3c

Measurements in the Indian Ocean

Test No.	73	74	75	76	77	78
Date	← 4.12.77 →					
Speed V_S [kn]	21.1	20.9	—	—	17.1	16.9
Revolution n [RPM]	97.2	96.8	95.4	92.6	82.9	82.5
Power P_D [MW]	—	—	—	—	—	11.6
Draft aft [m]	← 9.37 →					
Draft forward [m]	← 8.08 →					
Course	← 314° →					
Sea region or pos.	← 2°58'N; 59°44'E →					
Wind [Beauf]	← 1 ÷ 2 →					
Wind direction	← 235° →					
Water Depth [m]	← 3250 →					

Table 3d Measurements in the Indian Ocean

Test No.	79	80	81	82	83
Date	4.12.77				
Speed V_s [kn]	11.9	11.9	11.9	11.7	12.0
Revolution n [RPM]	59.2	60.1	61.3	60.9	61.3
Power P_D [MW]	7.1	7.3	—	—	—
Draft aft [m]	9.37	9.37	9.75	9.75	9.75
Draft forward [m]	8.08	8.08	7.82	7.82	7.82
Course	314°				
Sea region or pos.	2°58'N;59°44'E;		3°15'N;59°27'E		
Wind [Beauf]	1 ÷ 2				
Wind direction	225°				
Water Depth [m]	3250	3250	3250	3250	3250

Table 3e Measurements in the Indian Ocean

Test No.	84	85	86	87	88	89
Date	4.12.77			5.12.77		
Speed V_s [kn]	17.5	17.5	17.5	19.7	20.4	20.4
Revolution n [RPM]	85.3	85.1	85.2	95.4	96.5	96.3
Power P_D [MW]	—	—	—	13.9	—	—
Draft aft [m]	9.75					
Draft forward [m]	7.82					
Course	314°					
Sea region or pos.	3°15'N; 59°27'E					
Wind [Beauf]	1 ÷ 2					
Wind direction	230°					
Water Depth [m]	3250					

Table 3f Measurements in the Indian Ocean

Test No.	90	91	92
Date	5.12.77		
Speed V_s [kn]	21.6		
Revolution n [RPM]	100.8	101.3	101.3
Power P_D [MW]	—	–	—
Draft aft [m]	9.75		
Draft forward [m]	7.82		
Course	314°		
Sea region or position	3°15'N; 59°27'E		
Wind [Beauf]	0 ÷ 1		
Wind direction	230°		
Water Depth [m]	3250		

Table 3g Measurements in the Indian Ocean

Test No.	93	94	95	96	97
Date	5.12.77				
Speed V_s [kn]	21.3	21.4	21.2	21.2	21.4
Revolution n [RPM]	101.0	101.0	101.0	101.2	101.2
Power P_D [MW]	—	—	—	—	22.2
Draft aft [m]	8.63				
Draft forward [m]	8.23				
Course	317°				
Sea region of pos.	8°28'N; 54°40'E				
Wind [Beauf]	4				
Wind direction	45°				
Water Depth [m]	3600				

Table 3h Measurements in the Gulf of Aden

Test No.	99	100	101	103	104	105
Date	6.12.77			7.12.77		
Speed V_s [kn]	22.4	22.2	22.3	22.3	22.3	22.5
Revolution n [RPM]	103.1	102.3	102.8	101.8	101.9	101.7
Power P_D [MW]	16.9	—	—	17.0	—	—
Draft aft [m]	8.63					
Draft forward [m]	8.23					
Course	273°			273°		
Sea region or pos.	12°21'N; 47°03'E			Bab-el-Mandab		
Wind [Beauf]	0					
Wind direction	—					
Water Depth [m]	2300			37	38	40

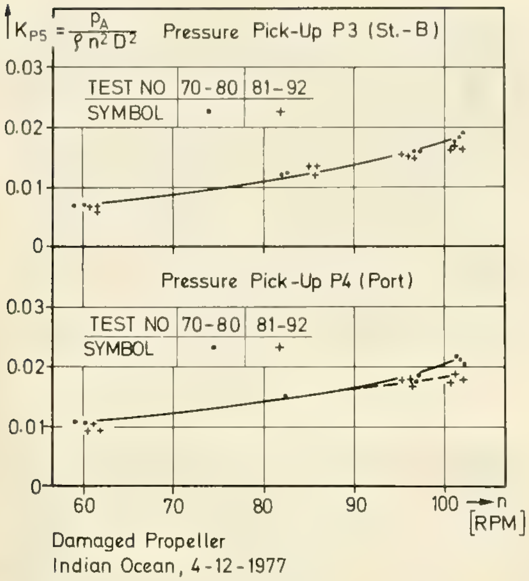

FIGURE 5. Pressure fluctuations during laser-scattered-light (LSL)-measurement.

ing due to a thunderstorm at the entrance of the Suez Channel. The cavitation of the damaged blade was so strong that it existed during the total propeller revolution. This could be seen through the cavitation observation windows. Unfortunately, no photographies were made because the measuring crew of Det Norske Veritas carrying out the cavitation observations left the ship in Port Said.

In the Mediterranean, however, a large number (about 800) of black-white photographs of the undamaged propeller were made with the equipment of Det Norske Veritas with stroboscopic lighting. Since pictures were always taken with two Hasselblad cameras it might be possible to carry out stereometric measurements of the cavitation layers in dependence of the blade positions. As an example for the cavitation extension of n = 105 rpm a collection of photographs is shown in Figure 8. These pictures were made with a camera with a fisheye-objective. The photographed condition belongs to Test No. 16.

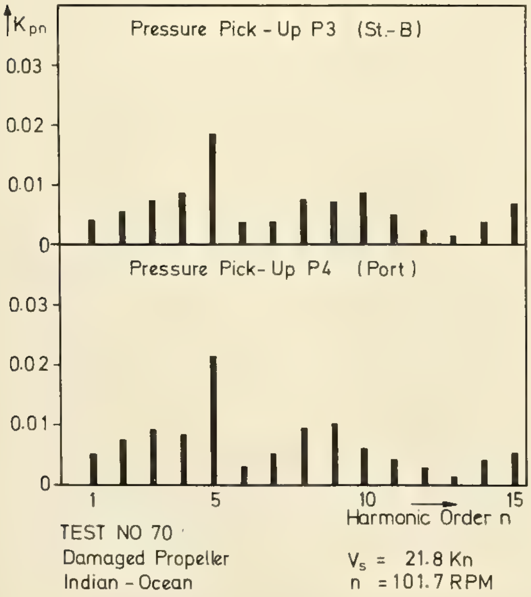

FIGURE 6. Harmonic components of pressure fluctuations during LSL-measurement.

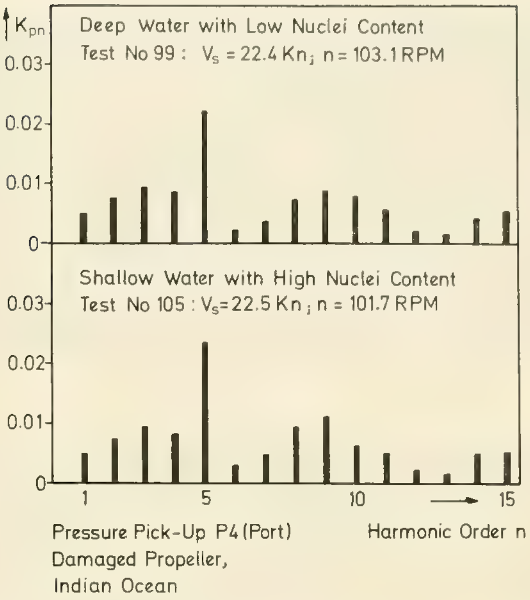

FIGURE 7. Harmonic components of pressure fluctuations.

4. INVESTIGATION OF THE WATER QUALITY

Measurements of Suspended Particles

In addition to nuclei measurements, which will be described later, the content of suspended particles was investigated as often as possible. This was necessary for two reasons: the LSL-method does not allow direct differentiation between solid and gaseous particles. Thus it became necessary to estimate the proportion of dirt or organic particles (probably contained in the water) in the measured nuclei sprectra. For these investigations a scattered-light instrument (nephelometer) was used; the J4-7439 fluoro-colorimeter of the American Instrument Company (Aminco). The Aminco-scattered-light instrument works on almost the same physical principle as the LSL instrument. Water samples of $1\ cm^3$, investigated in the Aminco-colorimeter under a scattered light angle of 90° were exposed to a green light (514 nm) as in the laser control volume. The geographical positions where the Aminco scattered light measurements were carried out (as well as all the other measurements described in this report) are shown in Figure 9.

The results of the Aminco scattered light investigations, given in Figure 10, were obtained in the following way:

Water samples were taken from the condenser inflow of the ship's turbine during the voyage. One part of this water was poured through a filter with a pore size of 0.4 μm. Another part was used for unfiltered samples, which previously were roughly degassed by stirring and shaking. Subsequently, the unfiltered and filtered samples were investigated

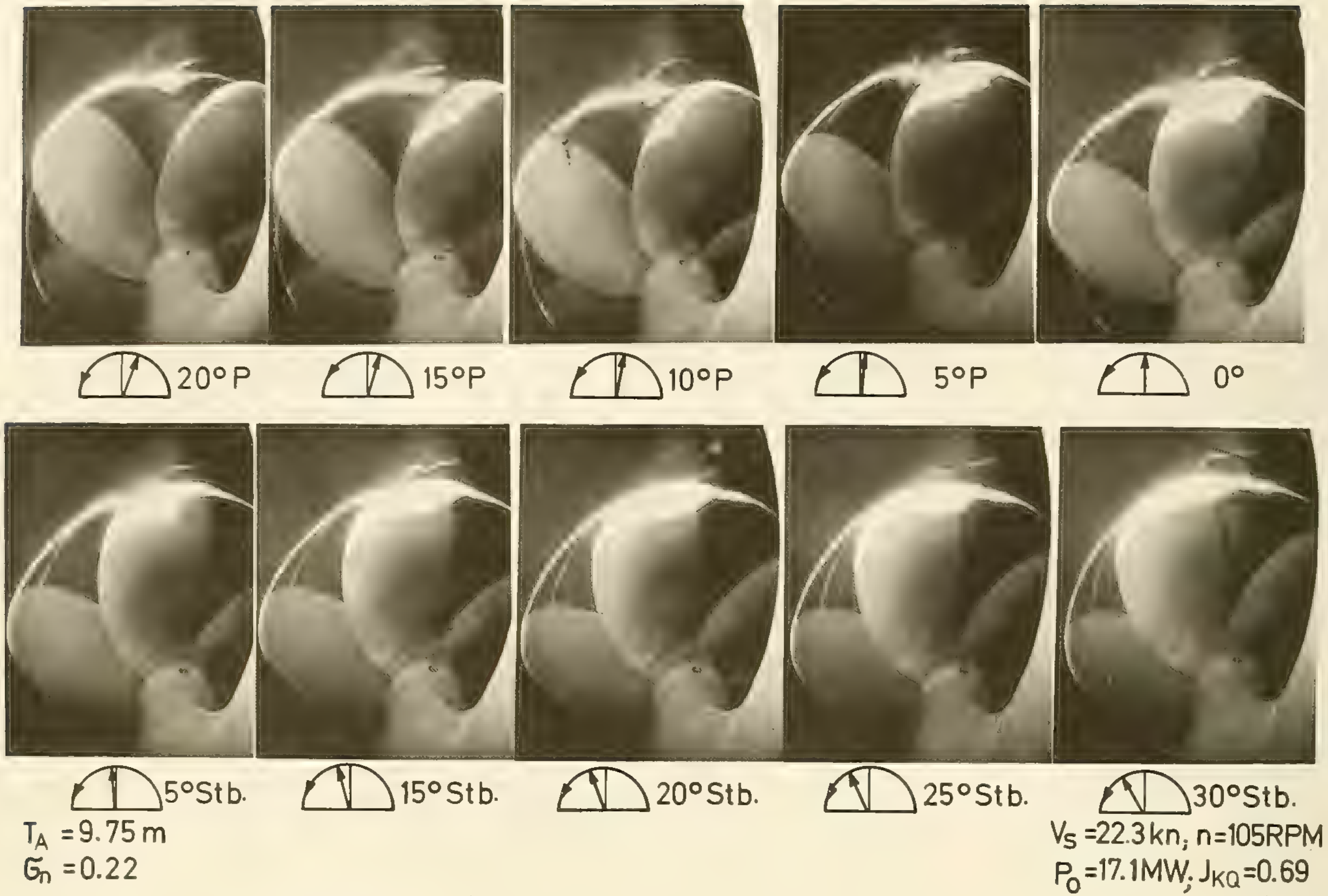
20°P
15°P
10°P
5°P
0°
5°Stb.
15°Stb.
20°Stb.
25°Stb.
30°Stb.
T_A =9.75 m
σ_n =0.22
V_S =22.3 kn; n=105RPM
P_0=17.1MW; J_{KQ}=0.69

FIGURE 8. Cavitation "Sydney-Expess."

in the Aminco-colorimeter. The deflection of the meter for the filtered sample was adjusted on the indicating scale to "0", which served as reference value. Measured values of unfiltered samples are shown in Figure 10; Relative Intensity is an arbitrary unit.

The first measurements, at the end of October, were made with a one-hole-aperture in the beam path, the following ones with a four-hole-aperture due to a thereby increased intensity.

In order to obtain a general idea of the sensitivity of the Aminco scattered light method, standard solutions were produced using the plastic spheres also used for the calibration of the LSL-instrument. It is apparent from this that five parts per cm^3 with a diameter of D = 25.7 μm could still be measured.

Many results from investigations of sea water did not show any difference between filtered and unfiltered samples. The content of suspended particles was thus very small in the Indian Ocean; it was below the response level of the Aminco-device. The samples taken on the 7th December 1977 contained, however, suspended particles. They descended from the shallow water region of the Bab-el-Mandab at the entrance to the Red Sea.

The lack of knowledge about the back scattering qualities of the particles appears to be a problem when applying this scattered light method with the Aminco-colorimeter. A more expanded and intensive investigations of suspended particles, for instance, with coulter counter, could not be carried out within the frame of this research work.

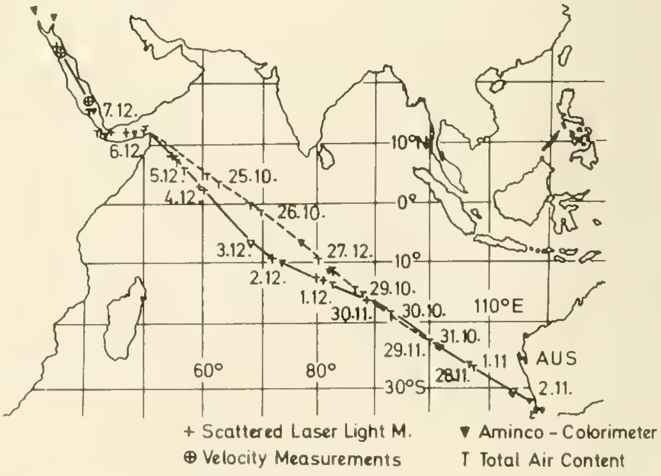
7.12.
6.12.
5.12.
25.10.
4.12.
26.10.
10°N
0°
3.12.
27.12.
10°
2.12.
29.10.
1.12.
30.11.
30.10.
110°E
31.10.
29.11.
1.11
AUS
60°
80°
28.11.
30°S
2.11.
+ Scattered Laser Light M.
⊕ Velocity Measurements
▼ Aminco - Colorimeter
T Total Air Content

FIGURE 9. Positions of measurements.

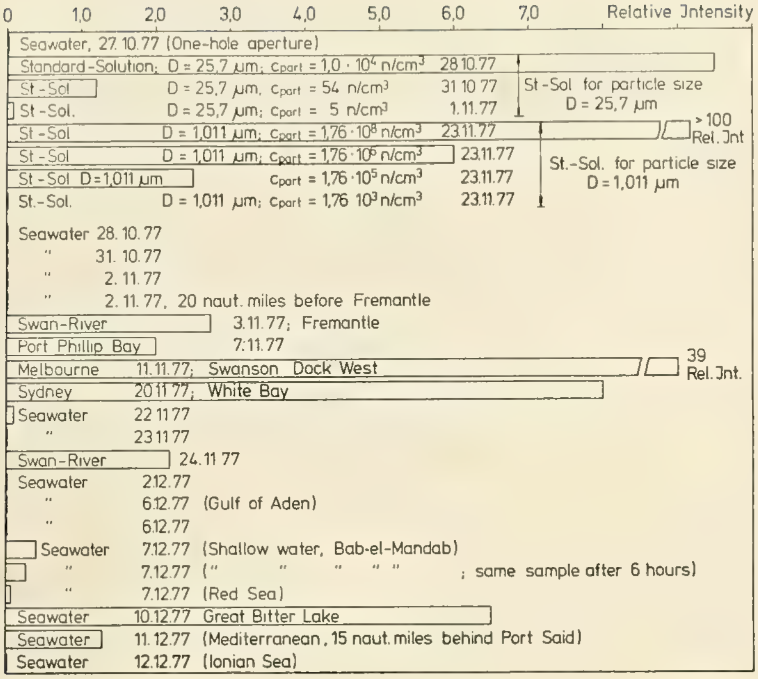

FIGURE 10. Measured suspended particles.

Measurements of Total Air Content

Although the water should always just be saturated at the surface, the gas concentration c_o of the sea water was also continuously determined from water samples with a Van-Slyke-apparatus. The results are given in Figure 11, in dependence of the temperature.

For the calculation of the gas content ratio, $\varepsilon = c_o/c_s$, the gas saturation capacity, c_s, is necessary for the specific salt content and temperature. Since the corresponding data were not known some water samples were left overnight in a basin with a large surface and the gas concentration c_s was determined on the following day, which in this case should indeed correspond to the saturation concentration c_s. The two values obtained for the saturation concentration c_s are also plotted in Figure 11 (with the symbol ⌖). They are within the range of tolerance of the measured total gas content, c_O, for the voyage leading southward. Subsequently the measured total gas content present values which correspond to the gas content ratio, $\varepsilon = 1$, i.e., to saturated water. Due to the dissolved salt the total gas content values, c_O, for sea water should lie below the values for fresh water. This is, in fact, the case with the exception of some values of the voyage leading northward. It must be left to other investigations to find out whether the wind, seaway, and temperature "history" of the sea surface has an influence on the total gas content.

5. MEASUREMENTS OF THE NUCLEI SPECTRA AND LOCAL VELOCITY

Device for Nuclei Measurement

The LSL method was applied to the measurement of the nuclei spectra in front of the "Sydney Express" propeller. This method was also applied to the model tests, described by Keller and Weitendorf (1975). Detailed information about the measurement principle has been supplied, for instance, by Keller (1970, 1973). Thus, it is not necessary to go into the details.

Compared with previous measurements carried out in the laboratory the measuring distances were essentially larger at these full scale investigations. Thus, some new components for the measuring device were required. The distance between the measuring volume and the receiving lens amounted up to 2 m so that the laser power and the diameter of the receiving lens had to be markedly increased, in order to obtain usuable measuring signals.

The arrangement of the measuring unit on board is shown in Figures 1 and 2. The path of the laser beam is bent three times and enters the water almost horizontally; the path of the beam of the receiving system is bent once and proceeds in the water vertically. With this arrangement the flow direction

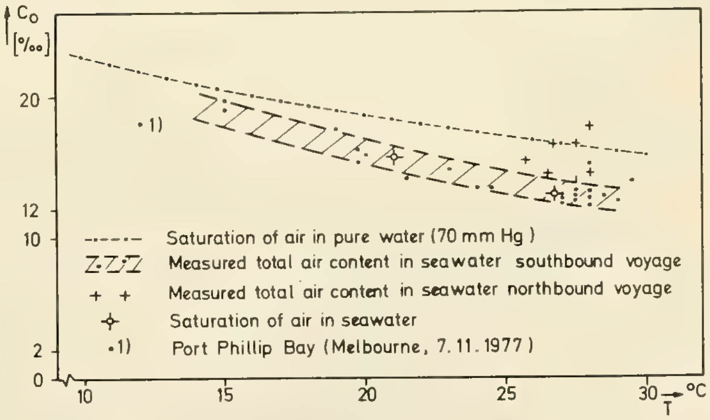

FIGURE 11. Measured total air-content.

and the direction of the laser beam as well as the optical axis of the scattered light receiving system are standing vertically, one upon another. This is optimal for the measuring technique used.

The homogenization of the laser beam, i.e. the conversion of the Gaussian intensity distribution over the beam cross section into a rectangular distribution, was made with a special filter. The homogenous intensity distribution as well as the shape of the laser beam (square or rectangular) were maintained quite well by the very long focal length of the laser system (about 6 m).

The control volume, optically defined, was positioned in such a way that the stream line through the control volume came into the range of the propeller tip. The position of the control volume in front of the propeller was determined by the position of the reception window of the scattered light between frames 12 and 13, i.e., 4.2 m in front of the propeller plane. The additional geometrical fixing of the control volume in the vertical direction resulted from the laser window (located between frames 13 and 14) with its horizontal beam outlet into the water. Subsequently the positions for the control volume was fixed as follows: 90 cm of the ship's hull vertically downward and 145 cm from midship on the port side between frames 12 and 13 (see Figure 2).

The Calibration Device

The relationship between the photomultiplier impulse amplitude and the size of nuclei was determined by a calibration with latex spheres. For this purpose a special device was put through an opening in the ship's hull when the ship stopped in calm water. With this device it was possible to maneuver a fine nozzle near to the control volume and to inject the latex spheres into the control volume. The apparatus was operated by means of small hydraulic elements from the inside of the ship (Figure 12).

For the calibration latex spheres of 45 and 25 µm were used. The corresponding photomultiplier impulse amplitudes fit excellently to the theoretical curve of the scattered light intensity. The measuring range was set to 8-117 µm for the nuclei diameter.

In addition to the scattered light intensity, the dimensions of the control volume were important data for the determination of nuclei spectra and nuclei concentration. Since a direct measurement or calculation of the cross section of the laser beam in the control volume was not possible in this case, a new method had to be applied to determine the laser beam dimensions. By means of the above mentioned hydraulic device a small rotating wheel with thin platinum wires was adjusted in such a way that the wires cut the laser beam vertically at the location of the control volume. Thus the light in the direction of the photomultiplier was scattered. The dimensions could then be determined from the width of the photomultiplier impulses, the distance between the axis of the small wheel, and the light point on the small platinum wires (determined by crossed platinum wires) and the revolution number of the small wheel. The diameter (25 µm) of the platinum wire had also to be considered. The exact knowledge of the control volume dimensions was also important for the measurements of the local velocity, as described below.

The dimension of the control volume in the longitudinal direction of the laser beam was adjusted as usual through the measuring slit in front of the photomultiplier, after the enlargement factor of the reception optic was determined. This again was done by means of the hydraulic device with which an object, whose dimensions were known, was placed in the control volume; its picture was measured in the plane of the measuring slit.

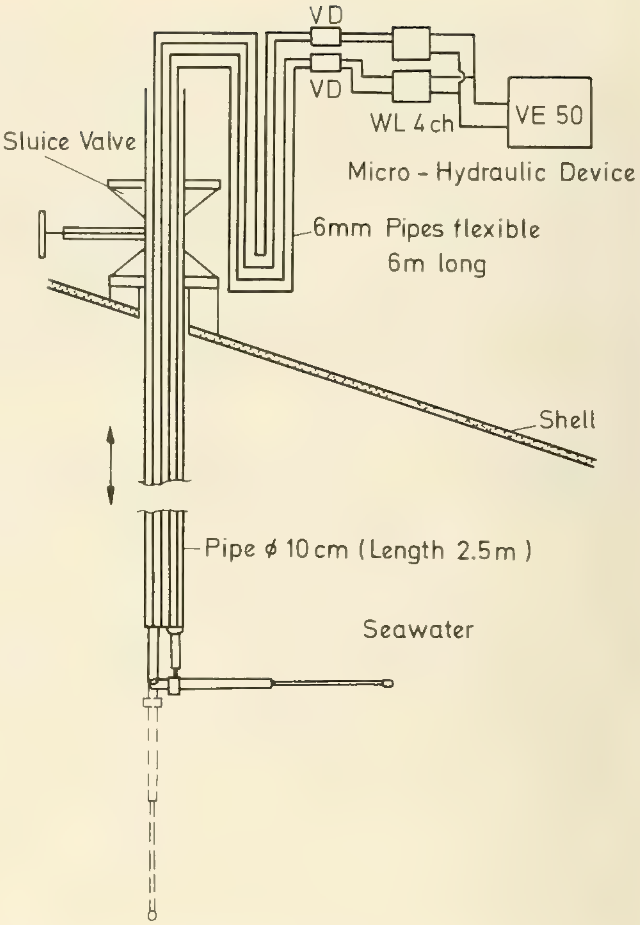

FIGURE 12. Calibration device and arrangement.

For the nuclei measurement the dimensions of the control volume were then fixed as follows: 0.86 mm × 0.86 mm × 1.33 mm = 0.98 mm^3. The cross section of the control volume rectangular to the flow direction amounted to 0.86 mm × 1.33 mm = 1.14mm^2. This detail was required for the determination of the nuclei concentration.

Measurement of Local Velocity

When the cross section of the control volume and the number of the nuclei measured per unit time, were known, it was necessary in addition to know the local flow velocity at the control volume in order to determine the nuclei concentration. Since the conversion of model test results from wake field measurements to full scale appeared to be too inaccurate for the determination of the local velocity and because the measurement of the velocity with a Prandtl tube, for instance, was not possible, a new method was applied to measure the velocity and flow direction. If the dimensions of the control volume in the flow direction are known, the velocity can be determined from the measured impulse width. In order to estimate the local flow direction at the control volume, an aperture is put into the beam path of the laser (Figure 13), which gives the laser ray a rectangular shape. This aperture is turned until the photomultiplier impulses have reached a maximum. Then it is possible to determine from the position of the aperture the position of the plane, formed by the flow direction and the laser beam. If now the measuring slit is turned until the half width of the distribution of the impulse width has reached a minimum, it is possible to read - from the position of the measuring slit - the plane which is formed by the flow direction and the optical axis of the reception system. The flow direction in the volume results from the intersection of the two determined planes; the impulse width gives the flow velocity, and the impulse width spectra provides information on the degree of the turbulence flow.

In this way flow characteristics can be determined, undisturbedly and locally, with one measurement; otherwise they could only be determined with a three-component measurement. Furthermore, the control volume simultaneously reaches the optimum inclination for the measurement of the nuclei size. Thus one signal provides data about the distribution of nuclei size and about the flow field.

Large particles or bubbles require a longer period to completely cross the control volume than smaller particles at the same speed. This means that besides the larger impulse amplitude there is also a larger impulse width. These facts have to be considered in the measurement of the velocity. Therefore, a single-channel discriminator is inserted into the impulse processing electronics. The discriminator choses for the measurement only impulses of the amplitude or a strongly limited range of amplitudes. Thus it is possible to draw a clear conclusion from the measured impulse width on the speed of the particles in the control volume.

The new technique to measure the velocity is illustrated in the Appendix. A rectangular beam cross section whose breadth is the vertical to the flow direction, has proved to be the optimum for the measurement of velocity and the determination of the flow direction.

General Remarks

Originally it was planned to shift the height of the measuring point on the optical axis of the reception system by different laser beam directions. In addition, this axis should be shifted laterally through two additional observation windows between the frames 12 and 13. This would make it possible to measure at several points in the plane between the frames 12 and 13. Unfortunately, this could not be realized due to lack of time, because the installation of the measuring equipment at the beginning of the voyage had taken too much time.

It is not intended to describe all the difficulties which occurred at the installation of the equipment. The problem of vibration, however, must be mentioned.

To protect the laser, vibration damping should be guaranteed as far as possible. It was, however, observed during the outward voyage that the pneumatic vibration isolation, which had a resonant frequency of $f_o = 1.8$ up to 3.0 Hz, could not be used, - even if the exciting blade frequency of the propeller was within the range of 8 and 9 Hz. Excitations occurred, of course, also at a propeller speed of $f = 1.8$ Hz and due to seaway frequencies. When it was obvious that different damper devices also did not help, the support, on which the laser and the photomultiplier were fixed, had to be stiffly connected with the steel construction of the after peak. This labor and the laser adjustments required more than half the time of the voyage to Australia during difficult climatic conditions. The laser adjustment was carried out mainly when the ship was stopped. The calibration of the nuclei impulses and the determination of the control volume, in which the nuclei were measured, were also carried out during these periods. These were kindly granted by the captain and his officers and had to be regarded as a special concession since the "Sydney Express" was on a fixed schedule. In this connection it must also be mentioned that the calibrations and later the measurements, made on the return voyage, could only be carried out after dark. For this reason, extra maneuvering watches had to be set in the engine control room, usually while the ship had a "16-hours-unattended-machinery-space".

The above mentioned stiff support solved the

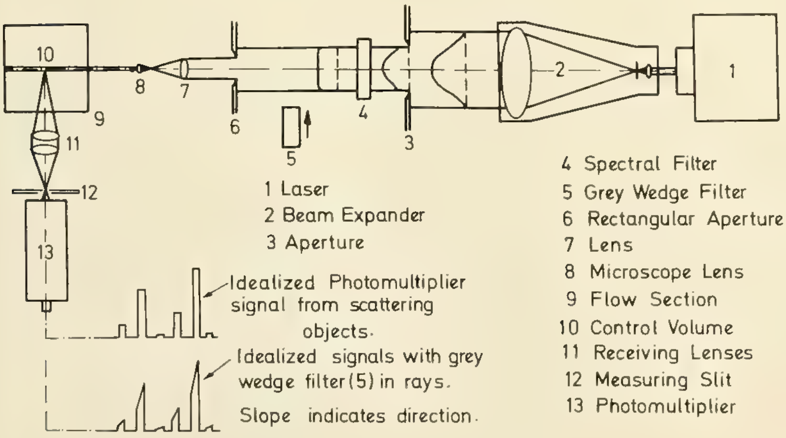

FIGURE 13. Principle of LSL-measurements.

vibration problem almost completely. It provided, however, the risk that the laser might fail. Fortunately, this did not happen. The laser, a Coherent-Radiation (4 Watt) product, achieved the same performance (900 mW), to which it was adjusted at the beginning, up to the end of the voyage without any failure. The small vibration still observed at the measuring point had no significant effect.

6. RESULTS OF MEASUREMENTS

Local Velocity

It was mentioned already that the number of measurements originally planned could not be carried out due to lack of time. Thus, for instance, the size and the direction of the local velocity could only be determined at one measuring point. This measurement took much time since there was no special electronic device available. It was the first measurement of this kind and it was included in the program at a late date, which made it impossible to establish a special measurement before the departure. The measurement was, therefore, partly performed with the electronic device which was also used for the scattered light measurements, and with some special interfaces.

The velocity and one plane of the flow direction at the place of the control volume could be determined for one velocity. At the ship's speed of 22 kn the velocity at the measuring point amounted to 7.22 m/s and the direction was found at an angle of 5° downward. The corresponding result from the model test for the geometrically corresponding position of the "Sydney Express" amounted to 7.47 m/s. This model test, however, was carried out for the propeller plane of the towed model, without a running propeller. - In full sale, on the other hand, the plane formed by the flow direction and by the optical axis of the reception device could not be determined due to lack of time.

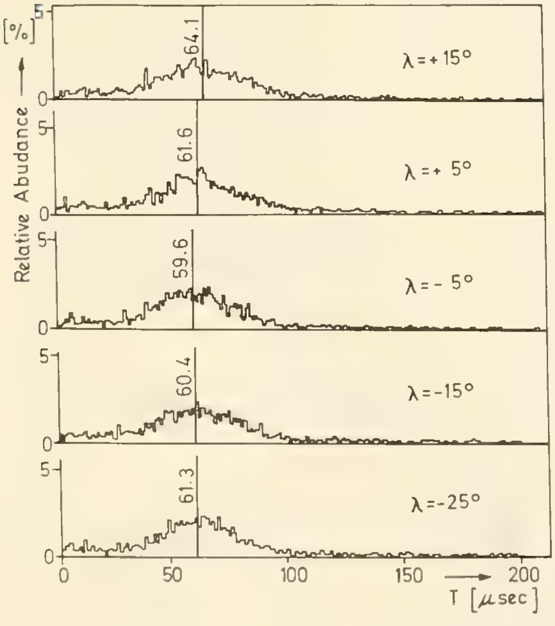

FIGURE 14. Pulse width distribution and mean pulse width dependent on the inclination of the flow.

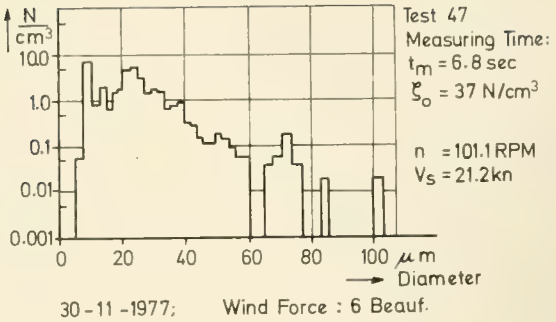

FIGURE 15. Nuclei distribution.

The ratio, local velocity to ship's speed, 7.22 m/s to 11.32 m/s, and which corresponds to the local wake in the control volume for the ship at 22 kn, was applied for all nuclei concentration measurements. The nuclei concentration was then calculated from the recorded ship's velocity, the measuring period, and the measuring cross section.

Figure 14 shows examples of the velocity measurement and also the change of the impulse width distribution for the rotation of the rectangular laser aperture. The value λ = 0° corresponds to the horizontal plane. At 5° downward (λ = -5°) the mean impulse width, evaluated on the HP-computer, reaches its minimum at 59.6 μsec. The large half-width of the distribution curve results from the turbulent flow. With a laminar flow the distribution curve would be smaller. (See Figures A 2.2 and A 2.3).

On the basis of these measurements a quantitative statement about the turbulent degree of the flow cannot yet be made. On the one hand we have no experience with this measuring technique, on the other hand the ratio, length to width of the laser beam cross-section, was too small at this measurement (2:1). At high turbulent flow the corners of the beam cross-section were dispersed by a relatively high amount of nuclei which resulted in shorter photomultiplier impulses than with nuclei running through the middle of the beam. A higher ratio, length to width, would be more favourable.

The first practical experiences with this measuring technique are so promising that its further development is being promoted. The advantages which this measuring procedure offers in connection with the determination of the size of nuclei are quite remarkable.

Nuclei Spectra

About one third of the spectra obtained between 30 November and 7 December 1977 are demonstrated in Figures 15 through 24. The spectra contain the respective sum of nuclei per cm^3 for the respective range of diameters. In the diagrams one range of diameter is marked by a horizontal line. The single ranges of diameters do not have the same width. The dissimilarity of these spectra, which obviously results from different conditions, will later be described in detail.

First, it has to be noticed that for all spectra in the range of a bubble diameter from 20 to 40 μm (micron) there is either a relative maximum or an absolute maximum of nuclei. The relative maximum

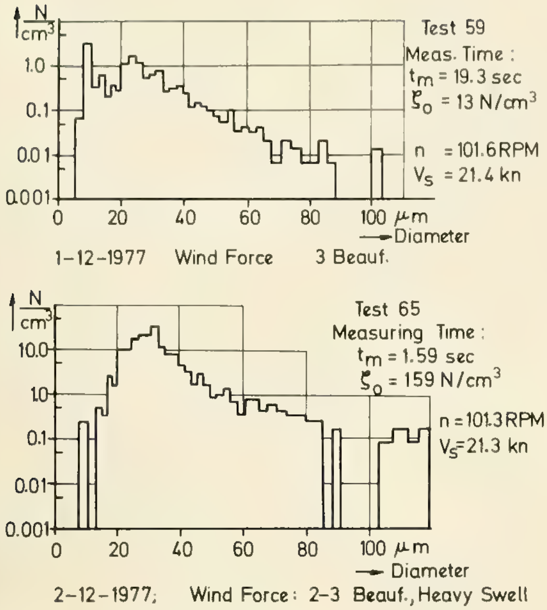

FIGURE 16. Nuclei distributions in seaways.

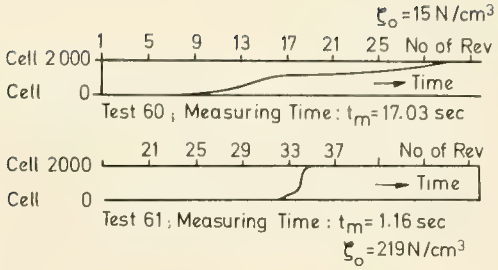

FIGURE 18. Nuclei distributions in a seaway.

was detected in Test 47 - Figure 15, Tests 60 and 62 - Figure 17 and Tests 90 to 92 - Figure 20. The absolute maximum was detected in Test 61 - Figure 17 and Test 65 - Figure 16. The strong fluctuation of the number of nuclei per cm^3 (nuclei concentration ζ_0) can be read from the diagrams. Figures 15 to 17 as well as 18 and 19 show spectra which have been measured in different seaways. During the performance of Tests 47 to 62 (Figures 15 to 17) there was a seaway and swell from astern. The strong pitching motions of the "Sydney Express" resulted in a strong fluctuation of the nuclei concentration, i.e. from ζ_0 = 21 N/cm^3 to ζ_0 = 219 N/cm^3 in the Tests 62 and 61 - Figure 17. Depending on the quality of the water, either swarms of bubbles or clear water, which hits the control volume of the laser beam, 2000 nuclei were counted more or less quickly. The process of counting the 2000 bubbles is demonstrated in Figure 25 for two cases. There the analog-output voltage of the memory is plotted against time and propeller revolutions respectively. The output voltage of 1 Volt is reached by the memory when its 2000 cells are filled. In Test 61, 2000 bubbles were counted within 1.16 s and in Test 60 within 17.03 s at an almost linear processing of the output voltage. Figures 18 and 19 show also a series of nuclei spectra measured, one immediately after the other, at a seaway of Beaufort 4. At this series the direction of the seaway was, however, athwartships up to "slightly from fore". The seaway motions of the "Sydney Express" (length 210 m) were very small in this case. Subsequently the number ζ_0 of nuclei per cm^3 was higher than the smallest number

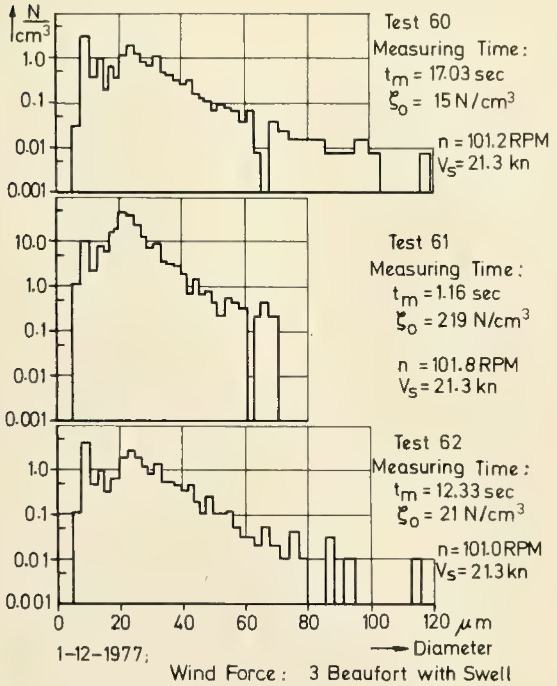

FIGURE 17. Nuclei distributions in a seaway.

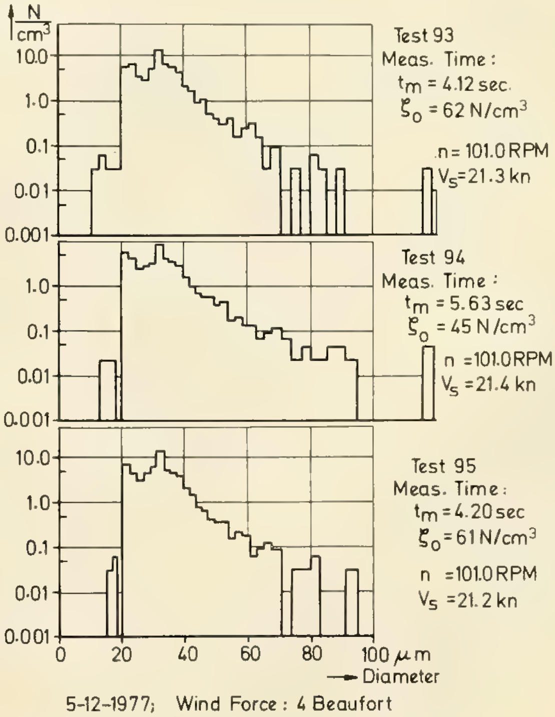

FIGURE 19. Nuclei distributions in a seaway.

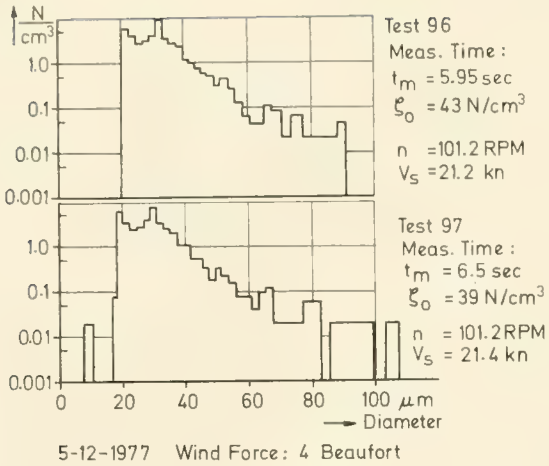

FIGURE 20. Nuclei distribution for calm water.

with the pitching ship but still within the narrow range of $\zeta_0 = 39$ up to $\zeta_0 = 62$ N/cm³. Considering the Tests 47 to 65 (Figures 15 to 17) and the Tests 93 to 97 (Figures 18 and 19) it can be said that in a seaway the nuclei concentration ζ_0 is higher than in smooth water, and further, that the influence of shipmotions on the concentration ζ_0 superimpose on the influence of the seaway.

The measurement series carried out with the Tests 90 and 92 (Figure 20) under ideal weather conditions, show on one hand the good repetitive accuracy of the results for a constant speed in good weather. In this case the number of nuclei per cm³ amounts to ζ_0 = 18, 19, and 18 N/cm³ at constant measuring periods of 13.6, 13.2, and 13.9 for 2000 nuclei. This, however, shows - on the other hand - a clearly lower concentration, ζ_0, than with the Tests 61 and 65 in a seaway (Figures 17 and 16).

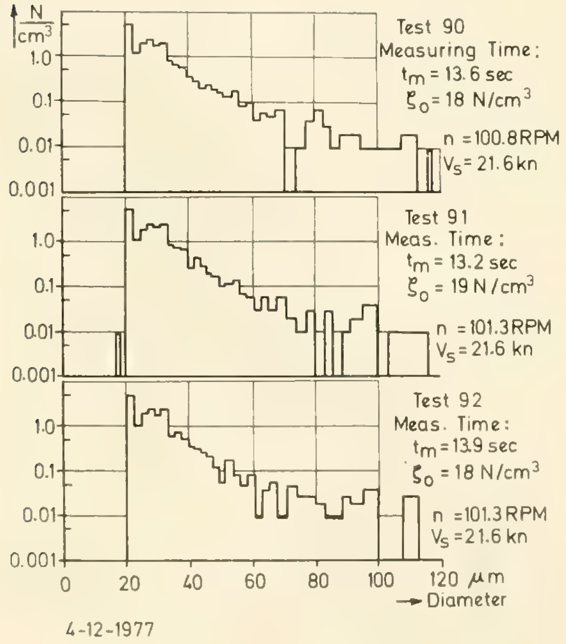

FIGURE 21. Nuclei distributions for different ship speeds.

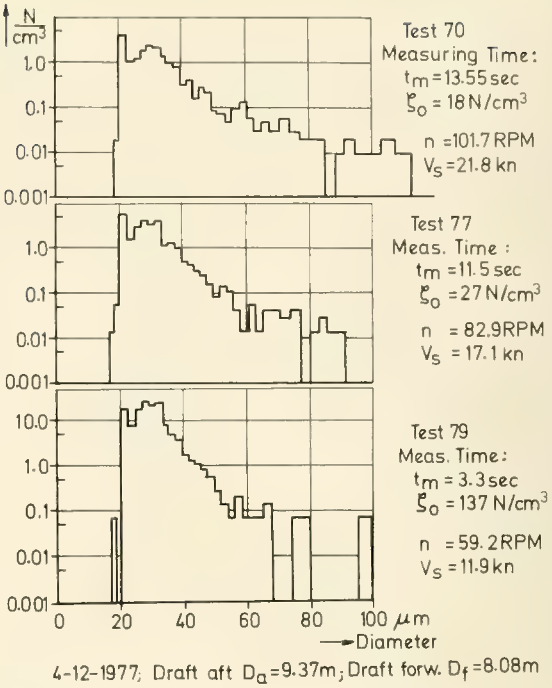

FIGURE 22. Nuclei distributions for different ship speeds.

A further difference, previously mentioned, has to be noticed when comparing measurements in a seaway and in calm weather. Whilst with typical spectra in a seaway (Tests 61 and 65) the absolute maximum is between the nuclei sizes 30 and 40 µm, it can be detected for calm weather in the smallest measured nuclei range. This phenomenon will be described later (in Section 7). The measuring series of different speeds for two drafts are

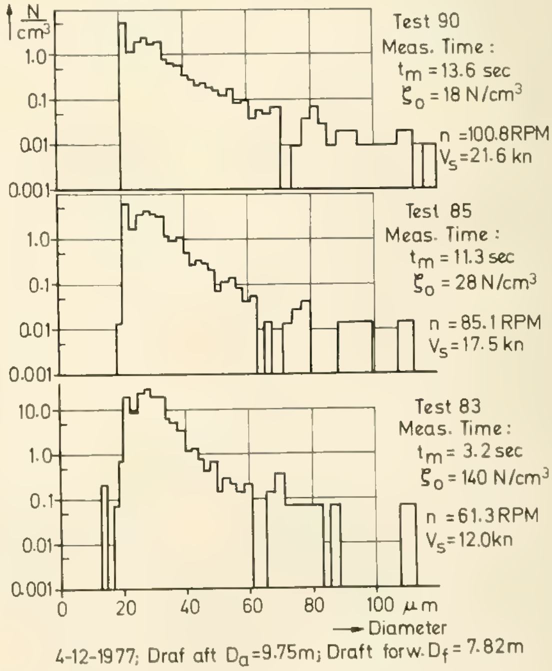

FIGURE 23. Nuclei distributions on deep water.

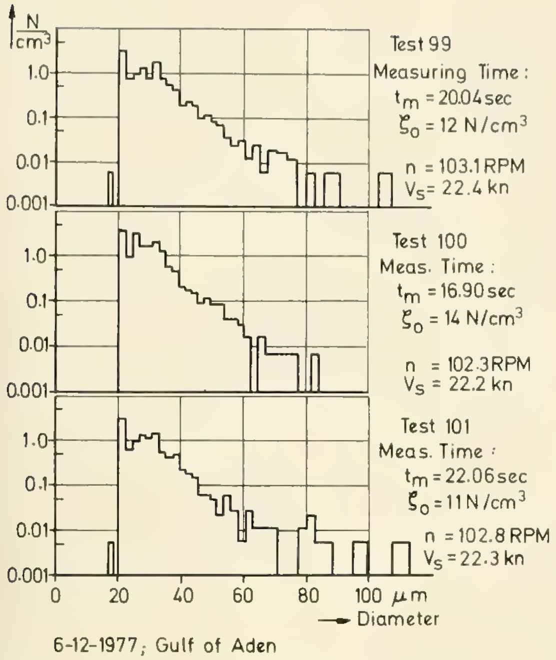

FIGURE 24. Nuclei and particle distributions on shallow water.

shown in Figures 21 and 22. In the second case the "Sydney Express" was ballasted with 5,160 tons of water. In both series it should be noted that with decreasing speed the number ζ_0 of nuclei per cm^3 increases. At the lowest speed of ca. V_S= 12 kn the bubble range of a diameter between 20 and 40 µm contains the absolute maximum number of bubbles. The differences between the two cases are, however, small. The differences between the drafts were obviously not sufficient to provide stronger differences between the nuclei spectra.

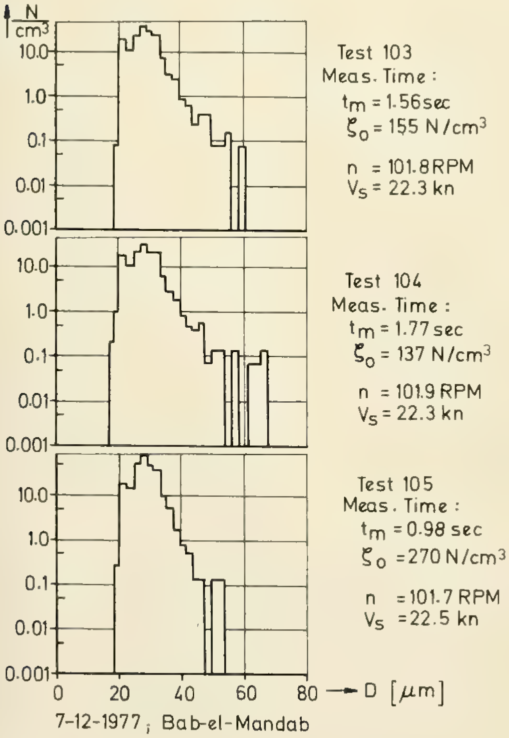

FIGURE 25. Analog output of memory.

The two measurement series shown in Figures 23 and 24 were made under ideal weather conditions, the one 7 hours later than the other. The spectra from Figure 23 were obtained in deep water in the Gulf of Aden; the spectra shown in Figure 24 were obtained from shallow water at the entrance of the Red Sea at Bab-el-Mandab. With these two series it was intended to clarify the point that the propeller excited vibrations which occur on shallow water result (apart from the shallow water effect) to a higher extent from a stronger instationary cavitation, which arises on occount of an increased nuclei concentration in shallow water. It must be said that this question could not be answered. On the other hand a comparison of these two measurement series shows that the number of nuclei per cm^3 (nuclei concentration ζ_0) increases from a ζ_0 of 11 to 14 N/cm^3 in deep water to a ζ_0 of 155 to 270 N/cm^3 in shallow water. This will be described in the following Section. The absolute maximum of ζ_0 is here again in the range between the nuclei diameter of 20 to 40 µm. In this connection it should be noted that hardly any nuclei with a diameter of above 60 µm were detected.

7. DISCUSSION OF THE RESULTS OF NUCLEI SPECTRA AND COMPARISON WITH OTHER INVESTIGATIONS

Simultaneously with the nuclei measurements in shallow water - Figure 24 - water samples have been taken. The results of the tests carried out with these water samples with the Aminco scattered light device appear in Figure 10. These samples from the shallow water region at Bab-el-Mandab showed a Relative Intensity of 0.4 for the difference between unfiltered and filtered water. Even after six hours the unfiltered sample still showed a Relative Intensity of 0.28. From this it can be concluded that the suspended particles, existing at this coastal strip, settled in the samples within six hours. From this Aminco scattered light measurement it can further be concluded that the high nuclei concentration shown by the LSL measurement - of the shallow water measurement series, Figure 24 - results mainly from suspended particles. There were probably also solid particles concerned (it is likely to be sand at the coast of Arabia) which show no inclusion of gas. This is assumed because the cavitation did not increase in the shallow water. The corresponding propeller excited pressure fluctuations in deep and in shallow water show practically no difference, Figure 7.

In Figure 26 the results of the laser-scattered-light technique and the Aminco scattered light measurement for investigations in shallow water (Test 105) are shown together. Figures 27 and 28 (in the diagrams marked with "Sydney Express") show further results of the Aminco-scattered-light measurements and the LSL measurements. In the Aminco scattered light investigations the differences between unfiltered and filtered water were equal to zero [Δ(Rel.-Int.) = 0] in these cases. This means that the concentrations of the suspended particles were imperceptibly small; they were in any case below the response level of the device.

In each top diagram of Figures 27 and 28, results of the investigations of suspended particles from

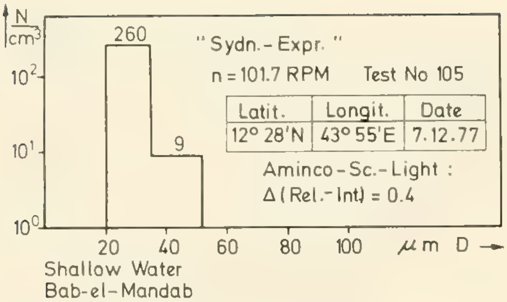

FIGURE 26. LSL-technique compared with Aminco-Sc.-Light measurement.

comparable locations are shown which were carried out on the occasion of the Indian Ocean expedition of the "Meteor". For the investigations, which have been made by Krey et al. (1971), the so-called inverted microscope and the Zeiss particle-counter were used. These results lie always one magnitude above the "Sydney Express" measurements for the operating revolution (n = 101 rpm). In case of the low revolution number of n = 60 rpm the nuclei concentration measured at the "Sydney Express" expedition (ζ_0 = 15 N/cm^3) reaches the values from the "Meteor" expedition in the range 20 - 35 µm and exceeds in the range 35 - 92 µm. Since, furthermore, the water sample tests carried out with the Aminco scattered light device do not show any difference between filtered and unfiltered water (medium diagram - Figure 27) it is justified to state that with the LSL measurement mainly bubbles were recorded. The investigation of Keller et al. (1974) of the optical qualities of the latex spheres, applied for the calibration, supports this fact. According to his investigation the latex spheres show scattering characteristics similar to the bubbles. Therefore, it can be said that the sensitivity of the LSL measurements is - to a certain extent - adjusted to the scattering behavior of bubbles via the calibration. With the LSL technique mainly bubbles are measured whose number is always smaller than that of all solid and gaseous nuclei. It is known, for instance, that silica algae are almost transparent. It is, therefore, understandable that there must exist differences between the LSL method on the one hand and the microscope method (with coloration perhaps) and the conductivity measurement with Coulter Counter on the other hand. The assumption that, with the LSL method, mainly bubbles are measured is supported by the good conformity of the LSL method with the holographic method of an ITTC-comparison measuring, Peterson et al. (1975). In this investigation a holographic method, the laser scattering light method, and a microscope method have been compared with each other. The first two methods agreed well with each other in the range of the bubble sizes 20-40 µm, whilst the microscope method also showed a nuclei concentration higher by one order of magnitude. The higher concentration of nuclei according to the microscope method apparently results from mistakes arising from the focusing of the nuclei. Similar difficulties might also occur with the inverted microscope applied at the "Meteor" expedition. This argument, however, does not say that the highest nuclei concentration of the "Sydney Express"-investigation, frequently occurring in the smallest ranges of size, results from bubbles only. (See, for instance, Test 70 - Figure 27 and Test 99 - Figure 28 or all diagrams of Figure 20). In the class of the smallest size nuclei solid particles which always exist in the sea water have certainly also been measured.

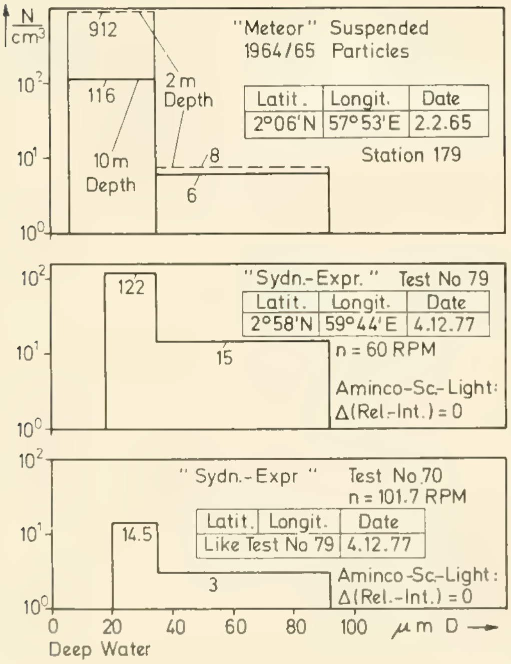

FIGURE 27. LSL-technique compared with other investigations.

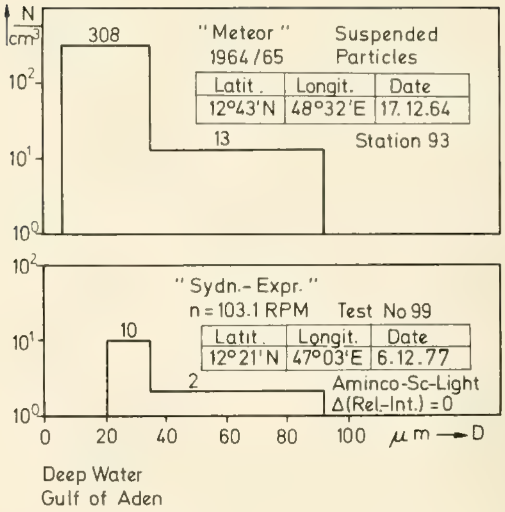

FIGURE 28. LSL-technique compared with other investigations.

Oceanographic studies with the Coulter Counter, for instance, carried out in the Gulf of California by Zeitzschel (1970) show a strong increase in the number of particles with a diameter of 14 to 4 µm. In addition, Zeitzschel cites the size distribution of particulate carbon in the Indian Ocean by means of fractional filtration investigated by Mullin

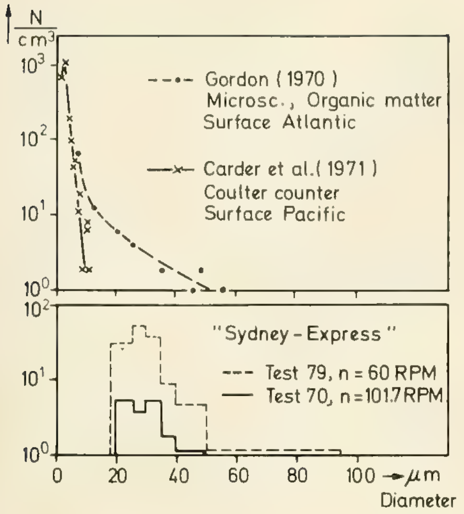

FIGURE 29. LSL-technique compared with other investigations.

(1965). In Mullin's report the following average percentage in the different size categories for near surface samples (15 m) are given: 500 - 350 µm: 3%; 350 - 125 µm: 5%; 125 - 95 µm: 4%; 95 - 60 µm: 6%; 60 - 33 µm: 6%; 33 - 10 µm: 18%; and 10 - 1 µm: 58%. The content of organic carbon can amount to 4.5 - 34% of the particulate matter in the different regions of the oceans [see Zeitzschel (1970)]. Zeitzschel continues: "It can be concluded from the results obtained at the Gulf of California and the above mentioned references that small particles, mainly in the range from 1 to 10 µm in diameter, predominate in offshore surface waters of the oceans." Investigations by Gordon (1970) and Carder et al. (1971), which are compared with our results in Figure 29, revealed the same results. It is obvious that the "Sydney Express" results - ending at a diameter of 10 to 20 µm for reasons of intensity - would probably show strongly increasing particle numbers below this range. This can be seen from the results of Gordon (1970) and Carder et al. (1971) which have been published by Jerlov and Nielsen (1974).

The fact that a large number of small particles in sea water show every arbitrary geometrical shape (according to Zeitzschel) also reminds one of the shapes of particles from the water of a cavitation tunnel, shown by Peterson et al. (1975) - Figure 6.

These sea water particles of different shapes (diameter 1 to 10 µm), which according to Figure 29 are always available in a high concentration can easily nucleate cavitation, as we know from many investigations [(e.g., Peterson (1972) and Keller (1973)].

The problem of the difference between real shapes of the nuclei, detected by the laser beam in the sea water and the diameters evaluated for the measuring results can only be mentioned here. In this connection one should remember that the calibrations on the "Sydney Express" were performed with latex spheres, whereas the real shape of the nuclei in the seawater is unknown. This problem also arises with the Aminco-method and with the Coulter Counter measurements, the latter working, however, according to the conductivity principle.

A further uncertainty is probably included in the comparison of results obtained from oceanographic studies carried out with water samples from the open sea and those obtained from laser scattered light measurements carried out in the flow and in the boundary layer of the ship. The low-pressure area of the boundary layer with its vortices of different size most likely have a great influence on the conversion of pore nuclei into bubbles when they are moved from the calm free sea through the boundary layer of the ship and thereby increase. Due to the long running-time along the ship's hull diffusion will also have an effect.

These physical processes accompanying the growing of the bubbles in the low-pressure areas of the boundary layers and the effect of diffusion could be the explanation for the fact that the lower speeds (12 kn, Tests 79 and 83) show a larger bubble concentration ζ_0 (due to the long running-time along the ship's hull) than the higher speeds (21.6 - 21.8 kn, Tests 70 and 90) with a shorter running-time. (See measuring series with different speeds - Figures 21 and 22). Thus - at a ship's speed of about 60 rpm - a characteristic size of bubbles has been formed. The measurements in a seaway (Tests 61 and 65 - Figures 17 and 16) show similar characteristic sizes of bubbles between 20 and 30 µm. In a seaway the turbulence is larger due to wave and ship motions. According to Sevik and Park (1973) the turbulence can lead to characteristic bubble sizes in connection with the pressure history.

All considerations concerning bubble sizes must finally lead to those bubbles participating in the cavitation process. According to the calculations by Isay and Lederer (1977), small bubbles, which can also arise from pore nuclei, will grow faster than big ones (Figure 30). The result of such

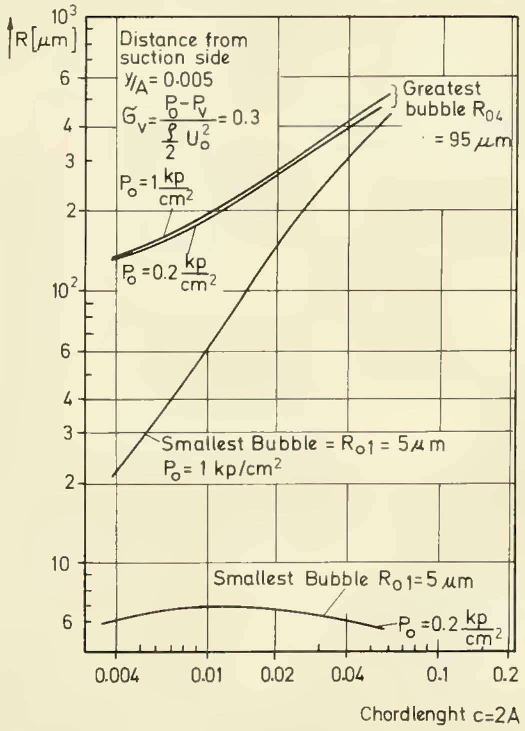

FIGURE 30. Calculated growth of a single bubble in a hydrofoil flow [Isay and Lederer (1977)].

calculations is valid for a hydrofoil of length c = 10 cm, wherein the pressure distribution was calculated by means of the profile theory for incompressible flow with the completion of shock pressures caused by the compressibility of the water. With these calculations one question remains unsolved: Up to which negative values can the local pressures on the profile really decrease in natural water? On the full scale propeller of the "Sydney Express" the local pressure gradients are probably steep and reach negative pressures, causing bubbles with a diameter of 10 μm, or less, to cavitate. Regarding the measurements, bubbles with diameters of about 10 μm to 20 μm were still recorded in the results from Test 47 (Figure 15) up to Test 65 (Figure 16). For unknown reasons, however, from Test No. 65 on nuclei with a diameter of less than 20 μm frequently could not be measured. On the other hand one has to consider that, the smaller the nuclei concentration ζ_0 becomes, the smaller the bubbles enlarged by cavitation.

It is apparent from these remarks that it would have been desirable to record bubbles or nuclei with a diameter below 5 μm. But this was impossible even with a 4 Watt laser which delivers 900 mW on the green line. Therefore, it has to be admitted that not all bubbles, which possibly are participating in the cavitation process, could be detected. The question arises whether this will be possible without any doubt in the future and if it is necessary or not. Also the following aspects would have to be considered: the required laser intensity is limited; the exact local pressure distribution on the propeller blades is difficult to determine and on the other hand the tensile stress that can actually be supported by the sea-water is quantitatively unknown.

Before closing this paragraph a personal impression in connection with the bubble sizes should be mentioned which is supported by the collection of photographs in Figure 8 and by numerous additional pictures and propeller observations on the "Sydney Express": The propeller will always find in the flow a sufficient number of small nuclei leading to cavitation. Therefore, the fullscale cavitation will always be more stable than the model cavitation with its smaller negative pressures and its different nuclei distribution.

The white foam on the cavitation pictures of the full-scale propeller clearly indicates a large number of nuclei, which have led to cavitation and grown together.

8. SUMMARY

The comprehensive laser scattered light measurements on the "Sydney Express" showed the following:

1. The nuclei spectra measured in a seaway in the Indian Ocean are quite different: In the range of the nuclei diameter of 20 - 40 μm either a relative or an an absolute maximum of nuclei was measured. (Figure 16). The motions of the ship, especially the pitching motion, are in this connection as decisive as the wave motions on the sea surface (Figures 18 and 19). The nuclei of this range (diameter: 20 to 40 μm), consist of bubbles, since the scattered light method, carried out at the same time with the Aminco-colorimeter did not show any difference between unfiltered and filtered water.
2. In good weather conditions the absolute maximum of the bubbles with a diameter between 20 and 40 μm (Figure 20) disappears. The nuclei of smallest diameter show the largest nuclei concentration. It probably consists of bubbles and suspended particles, as the comparison with microscope- and Coulter Counter measurements has shown.
3. Measurements made at different speeds (Figures 21 and 22) have again resulted in an absolute maximum at a diameter of 20 to 40 μm for the smallest ship speed at 12 kn. These nuclei certainly consist of bubbles, since the Aminco measurement in this case also did not show any differences.
4. Measurements in shallow water show an absolute maximum at a diameter between 20 and 40 μm. The majority of these nuclei consists of suspended particles, as the Aminco scattered light measurement have shown. These suspended particles probably do not contribute to cavitation, since the comparison of propeller excited pressure fluctuation measurements between deep and shallow water shows practically no difference (Figure 7).
5. The ship's vibrations caused by the propeller do pose a big problem for measurements of this type. The insensibility of the laser against vibrational stresses, however, after it was stiffly connected with the ship, was suprisingly good. Even the high loading caused by the temperature did not create any bad effects in the laser.
6. Future laser measurements should possibly anticipate diameter ranges below 5 μm. A more precise determination of suspended particles requires a greater effort than the present method.
7. Further results of this trial will be published later.

ACKNOWLEDGMENT

The comprehensive measurements on the "Sydney Express" represented a project of the Sonderforschungsbereich 98 "Schiffstechnik und Schiffbau" (Special Research Pool 98 "Marine Technology and Naval Architecture") to which Det Norske Veritas (propeller observation) contributed. The project was sponsored by the Deutsche Forschungsgemeinschaft.

The authors wish to express their gratitude to Hapag-Lloyd who made the "Sydney Express" available for this investigation. Many thanks are expressed to Captain W. Scharrnbeck, the Chief Engineer H. Zwingmann, and the whole crew of the "Sydney Express", who, by their excellent co-operation, made possible the measurements and good results.

The authors are grateful to: Ing.(grad) L. Hoffman (Hamburg Ship Model Basin - electronics, programming and evaluation); U. Steidlinger and W. Folkers, (Institute for Shipbuilding, Hamburg), and F. Meier (Technical University Munich) - all three provided for the mechanical construction and repair on board; Mrs. U. Schmidt (Institute for Shipbuilding, Hamburg - for drawing the diagrams); Miss A. van Blericq (Hamburg Ship Model Basin - for the translation of the German original into English); and Mrs. I. Jurschek (Institute for Shipbuilding - for typing the manuscript). Dr. R. Doerffer (Institute for Hydrobiology of the Hamburg University, SFB 94) recommended the Aminco scattered light device and made suggestions concerning oceanography.

REFERENCES

Carder, K. L., G. F. Beardsley, and H. Pak (1971). *J. Geophys. Res. 76* 5070-5077.

Gordon, D. C., Jr. (1970). *Deep-Sea-Res. 17,* 175-185.

Isay, W.-H., and L. Lederer (1977). Kavitation an Flügelprofilen. (Cavitation on Hydrofoils). *Schiffstechnik 24,* 161.

Jerlov, N. G., and E. S. Nielsen (1974). *Optical Aspects of Oceanography.* Academic Press, London and New York.

Keller, A. P. (1970). Ein Streulicht-Zählverfahren, angewandt zur Bestimmung des Kavitationskeimspektrums. (A Scattered-Light Counting Method used for the Determination of the Cavitation Nuclei Spectrum) *Optics 32,* 165.

Keller, A. P. (1973). Experimentelle und theoretische Untersuchungen zum Problem der modellmäßigen Behandlung von Strömungskavitation. (Experimental and Theoretical Investigations on the Problem of Cavitation in a Flow with Models). *Versuchsanstalt für Wasserbau der Technischen Universität München. Rep. 26/1973.*

Keller, A. P., E. Yilmaz, and F. G. Hammit (1974). Comparative Investigations of the Scattered-Light Counting Method for the Registration of Cavitation Nuclei and the Coulter Counter. *University of Michigan, Rep. UMICH 01357-36-T.*

Keller, A. P., and E.-A. Weitendorf (1975). Der Einfluß des ungelösten Gasgehaltes auf die Kavitationserscheinungen an einem Propeller und auf die von ihm erregten Druckschwankungen. (Influence of Undissolved Air Content on Cavitation Phenomena at the Propeller Blades and on Induced Hull Pressure Amplitudes). *Institut für Schiffbau, Universität Hamburg. Rep. 321A.*

Krey, J., R. Boje, M. Gillbricht, and J. Lenz (1971). Planktologischchemische Daten der "Meteor"-Expedition in den Indischen Ozean 1964/65. (Planktological-Chemical Data of the "Meteor"-Expedition to the Indian Ocean 1964/65). *"Meteor" Forschungsergebnisse,* edited by Deutsche Forschungsgemeinschaft, Reihe D-No. 9; Borntraeger-Verlag, Berlin-Stuttgart.

Lederer, L. (1976). Profilströmungen unter Berücksichtigung der Dynamik von Kavitationsblasen. (Hydrofoil Flow with Regard to Bubble Dynamics). *Institut für Schiffbau, Universität Hamburg. Rep. 341.*

Mullin, M. M. (1965). Size Fraction of Particulate Organic Carbon in the Surface Waters of the Western Indian Ocean. Limnol. *Oceanogr. 10,* 453.

Oossanen, P. van, and J. van der Kooy (1973). Vibratory hull forces induced by cavitating propellers. *Transactions RINA 115,* 111.

Peterson, F. B. (1972). Hydrodynamic Cavitation and some Considerations of the Influence of Free Gas Content. *9th Symposium on Naval Hydrodynamics, 2* 1131, Paris.

Peterson, F. B., F. Danel, A. P. Keller, and Y. Lecoffre (1975). Comparative Measurements of Bubble and Particulate Spectra by three Optical Methods. *14th ITTC, Ottawa. 2,* 27.

Sevik, M., and S. H. Park (1973). The Splitting of Drops and Bubbles by Turbulent Fluid Flow. *Transaction ASME, Journ. of Fluids Engineering, 95,* Series 1, No. 1; 53.

Zeitzschel, B. (1970). The Quantity, Composition and Distribution of Suspended Particulate Matter in the Gulf of California. *Marine Biology, 7,* 4; 305.

APPENDIX

DESCRIPTION OF THE NOVEL TYPE OF VELOCITY MEASUREMENT

When particles or bubbles pass through a light beam, they scatter a finite amount of light which is dependent principally on the object shape, size, index of refraction, and optical characteristics of the beam. For this technique a small, homogeneously illuminated control volume (see No. 10 in Figure 13) is optically defined by the cross-sectional dimensions of the laser beam and the optics of the system detecting the scattered light (see No. 11 and 12 in Figure 13).

The amplitude of the electrical output pulses from the photomultiplier (see No. 13 in Figure 13) is proportional to the "nucleus" size, and thus is the parameter used for "nucleus" spectrum determination.

The pulse width corresponds to the time in which the scatterer remains in the scattering volume, and therefore, by knowing the dimensions of the control volume, the velocity of the "nuclei", i.e., the flow velocity, can be evaluated.

The sketch in Figure A 2.1 shows the shapes of the optically bounded measuring volume for different positions of the rectangular laser aperture and the measuring slit in front of the photomultiplier. The time the "nuclei" need to cross the control volume is a function of the dimensions of the volume in the flow direction, and of the flow velocity. Therefore, the resulting photomultiplier pulse width is a measure of the flow velocity if the dimensions of the control volume are known. To get an accurate relation between pulse width and flow velocity, only nuclei of one known size, defined by their pulse height, should be selected.

Example I in Figure A 2.2 displays an arbitrary position of the control volume relative to the flow direction. In that case, even for laminar flow one gets a certain fluctuation for the pulse widths, because the dimensions of the volume in the flow direction are not equal.

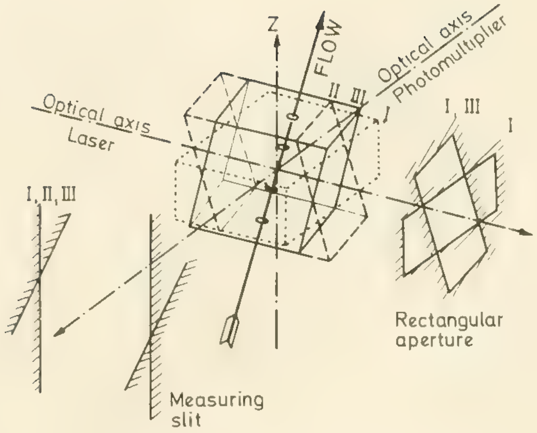

FIGURE A2.1. Principle of velocity measurement.

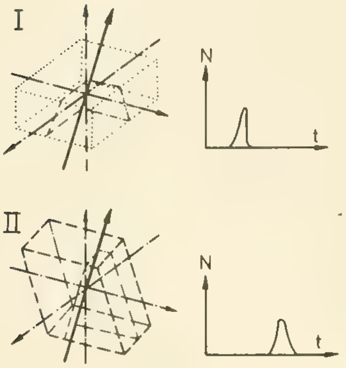

FIGURE A2.2. Sketch of inclined control volume and received photomultiplier signals.

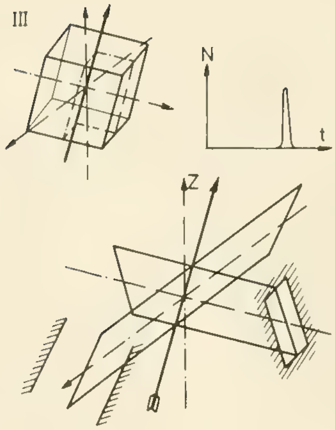

FIGURE A2.3. Sketch of inclined control volume and flow direction.

In example II Figure A 2.2 the main axis of the rectangular aperture is positioned parallel to the projection of the flow direction versus the plane vertical to the optical axis of the laser, and consequently the peak of the pulse width distribution is at a maximum value of t.

In example III in Figure A 2.3 the direction of the measuring slit is also parallel to the projection of the flow direction versus the plane vertical to the optical axis of the photomultiplier, so that all dimensions of the measuring volume in the direction of the flow are the same, and the pulse width distribution therefore shows its most narrow shape. The peak of the distribution indicates the velocity in the main direction, whilst the shape of the curve is a measure of the turbulence level.

The direction of flow can now be determined by the position of the rectangular aperture and the measuring slit. They each define a plane containing the corresponding optical axis, whereby the line of intersection represents the direction of the main flow in this region.

Discussion

ORVAR BJORHEDEN and TORE DALVAG

We congratulate the authors of this very interesting paper. For hull designers as well as propeller manufactures the problem of predicting the propeller induced vibration forces is a most essential task indeed. In this context we wish to inform you briefly about some recent developments at the KMW* Marine Laboratory related to the model testing technique applied in our cavitation tunnels.

The first item concerns the method of hull wake simulation. For some time the well-known dummy technique, involving ship afterbody models and transverse net screens, has been used in our tunnels for the purpose of simulating model wake pattern. This is a rather time consuming process since the net screens have to be adjusted step by step until the correlation with the wake pattern obtained in the towing tank appears satisfactory. Moreover, the method has some technical drawbacks as regards the stability of the wake as well as the interaction between propeller and hull and the influence of the propeller on the wake pattern. In connection with hydro-acoustic tests, cavitation occurring on the nets may worsen the background noise level.

In order to eliminate the above drawbacks a new technique involving longer afterbody hull dummies has been introduced. The method aims at simulating the full-scale ship wake pattern based upon the concept of equivalent relative boundary layer thickness, i.e., the frictional boundary layer thickness in relation to some characteristic length, e.g., the propeller diameter should be the same in the model and in full-scale. For ordinary cavitation testing purposes utilizing propeller model diameters around 250 mm and tunnels speeds of 4 to 8 m/sec this criterion results in hull dummy lengths of 2.5 to 3.5 m for most types of vessels. In principal, the model stern contour as well as the aftermost water-lines are made to scale, whilst the maximum breadth of the dummy is chosen on the basis of 2-dimensional potential flow calculations comparing the ship water-lines in unrestricted water to the dummy lines within the boundaries of the cavitation tunnel test section and aiming at similarity in the potential wake distribution.

Figure 1 shows a picture of a 3 m hull dummy used for the testing of a 150 m, single screw, container ship. In Figures 2 and 3 the model wake distribution as obtained in the towing tank and then corrected for scale effect according to the so-called Sasajima method is given. In Figure 4, finally, a comparison between the corrected model wake and the wake distribution obtained in the cavitation tunnel is shown for a few radii close to the propeller blade tip. As can be seen from the diagrams, the agreement is quite good, particularly as regards the wake peak in the 12 o'clock propeller blade position.

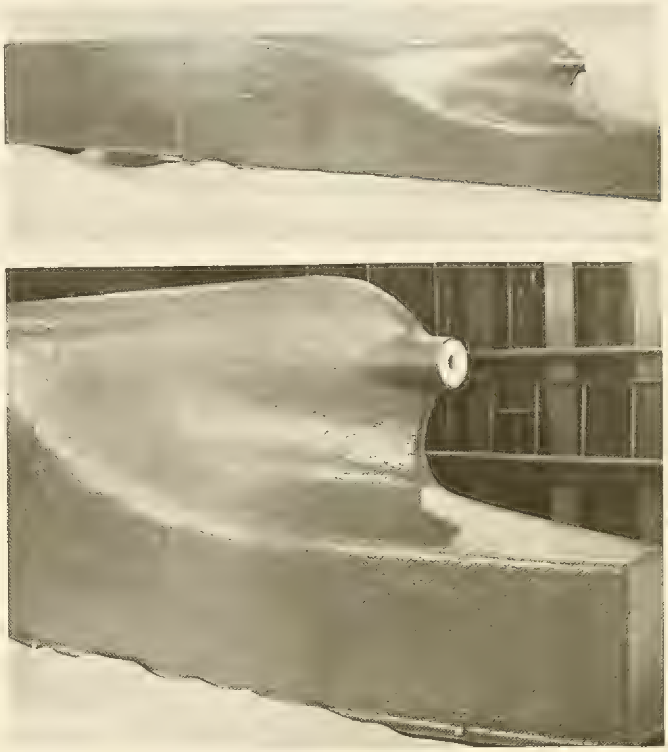

Figure 1. Hull dummy for wake simulation in cavitation tunnel.

Apart from the advantage of a quicker and more direct simulation of the full-scale wake, the method with long afterbody dummies results in a far more stable wake distribution which in turn implies more consistent recordings of fluctuating propeller forces, propeller induced pressure pulses against the hull, etc. Probably, the interaction between propeller and hull is also more realistic with this method of wake simulation as compared to the method utilizing transverse nets.

The second item refers to the instrumentation employed for recording of propeller forces and the propeller induced pressure pulses on a ship's hull. In both KMW tunnels a data collecting and evaluation system consisting of an on-line connected desk computer together with a printer and a plotter has been used for several years. For the measurement of propeller induced pressure pulses with the aid of pressure pickups fitted into the hull, a pulse sampling technique giving time averaged values from a number of propeller revolutions at each blade position has been the practice. With this method the pressure signals are given in analogue form and recordings can be obtained from only one pickup at a time. Recently, a new data collecting unit was put into service enabling simultaneous recording on 6 channels and storing test results from every

---

*Karlstads Mekaniska Werkstad

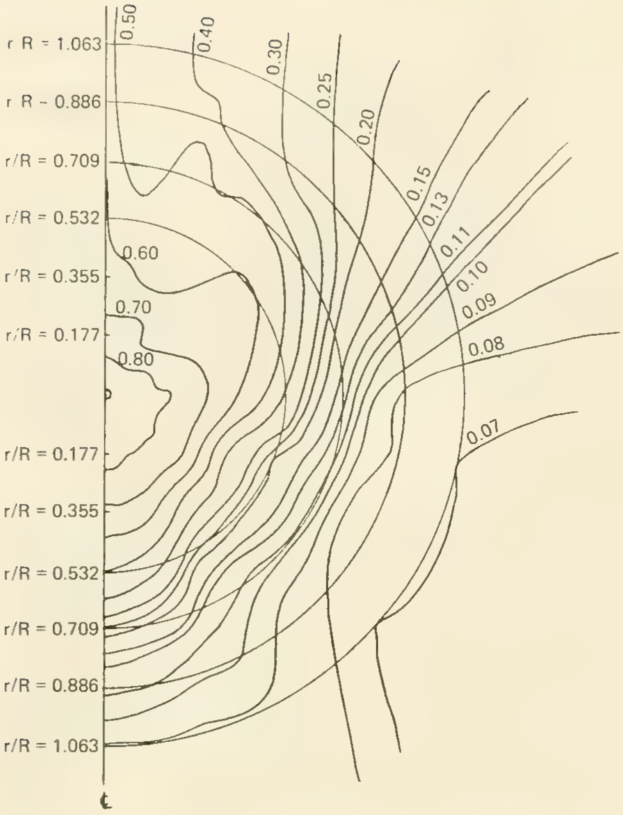

Figure 2. Model wake distribution as obtained in towing tank.

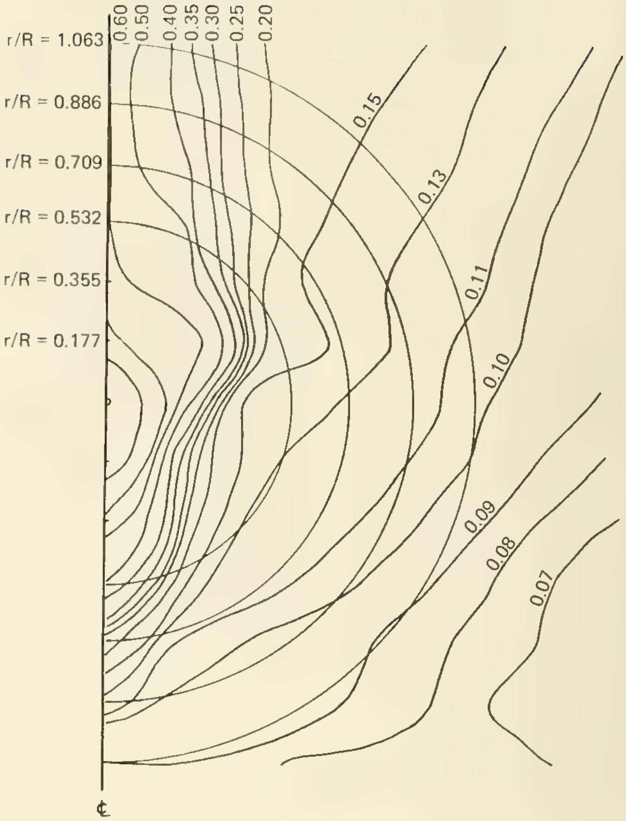

Figure 3. Wake distribution corrected for scale effect according to the Sasajima method.

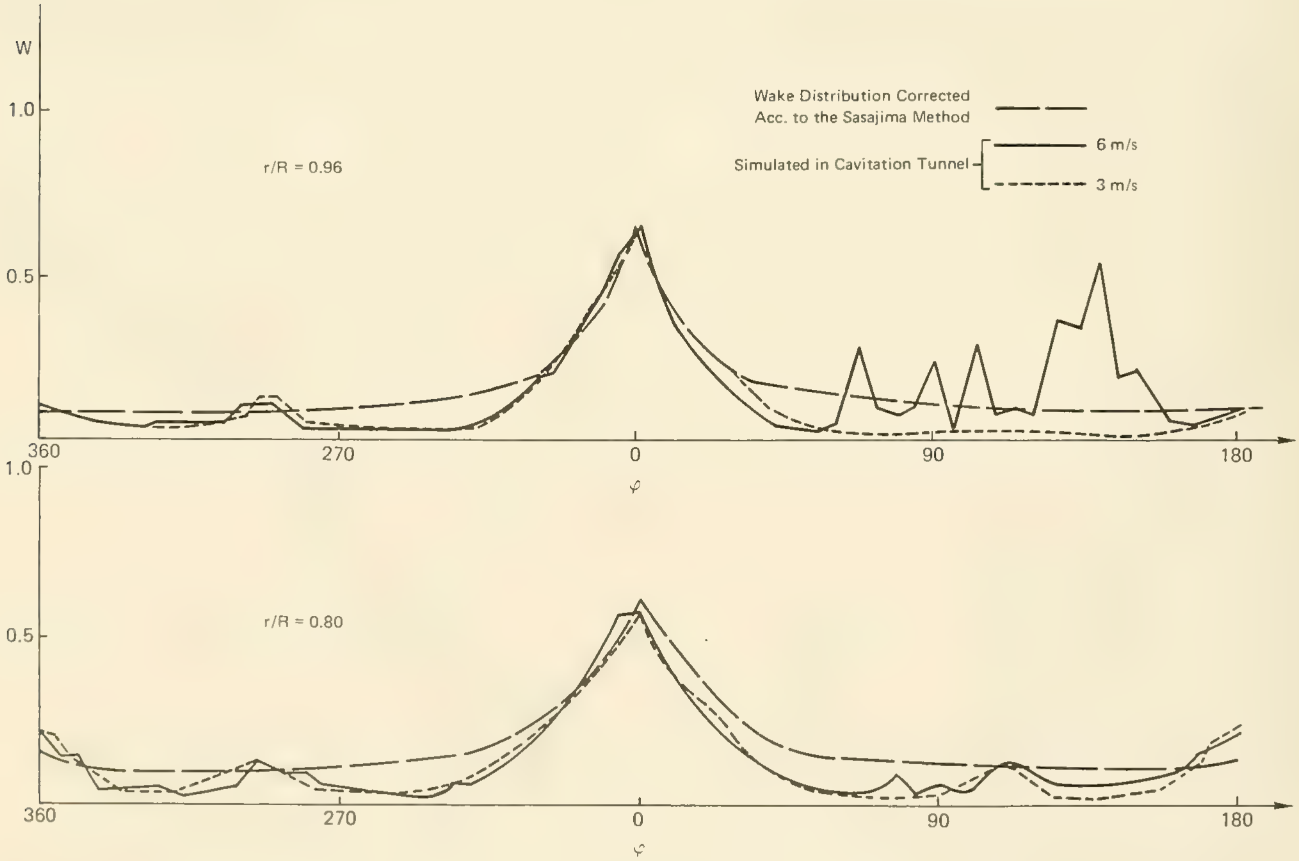

[illegible] mparison between corrected model wake and wake simulated in cavitation tunnel.

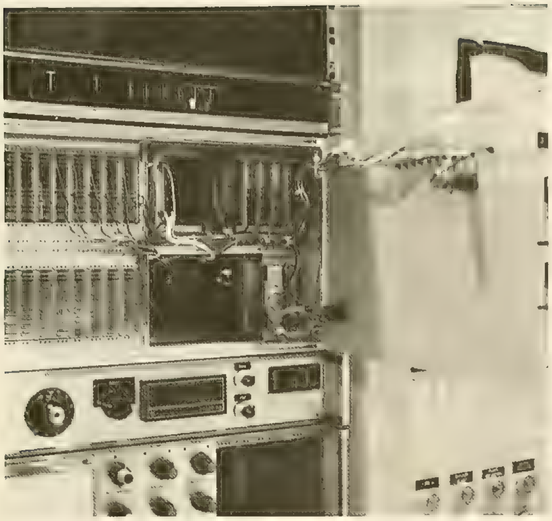

Figure 5. Data collecting memory.

Figure 5. Desk calculator with printer and plotter.

second degree of a propeller revolution in digital form in a RAM semi-conductor memory controlled by the desk calculator. With this instrument, instantaneous or time averaged test results can be stored and are readily available for printing, plotting, transformation to full scale, and harmonic analysis as well as integration of resulting hull surface forces and similar calculations with the aid of the desk calculator.

ERLING HUSE

The authors in their presentation draw attention to the problem of calculating cavity geometry and thus the excitation force due to cavitation. At the Norwegian Ship Model Tank in Trondheim we are at present developing a procedure to overcome this difficulty. In the cavitation tunnel we measure the propeller-induced pressure at only 4 positions on the hull model above the propeller. The measurements are made for non-cavitating as well as cavitating propellers. From the results of these measurements we calculate an equivalent singularity distribution to represent the propeller. This is next combined with a theory similar to that of Dr. Vorus to obtain the excitation force on the hull referring to any given vibratory mode of the hull.

As a second comment on the paper I notice in Figure 4 integration areas extending up to 30 propeller diameters upstream. This is, in my opinion, not very realistic because one is then passing one or more nodal points of practically occurring modes of vibration.

O. RUTGERSSON

First I would like to congratulate the authors on this interesting paper. The possibility of calculating hull forces and moments and their distributions directly on the body without the roundabout way over freestream pressures and solid boundary factors is especially elegant. Being somewhat involved in calculations and measurements of pressure fluctuations (with and without cavitation) at SSPA* I would like to ask if the authors intend to use this new method also to calculate solid boundary factors for different afterbody shapes and propeller configurations?

Unfortunately the authors' investigation is limited to non-cavitating propellers. This is a severe limitation as the contribution from the transient cavitation often is of a much higher magnitude than the contributions from blade loading and thickness. When discussing this subject the authors declare that methods "for predicting transient blade cavity geometry and the attendant pressure field" are not available. I would like to ask why the methods developed by Huse (1972), Johnsson and Søndvedt (1972), and van Oossanen (1974) have not been considered? These methods have been used in Europe for several years and the agreement with experiments is usually good.

---

*Statens Skeppsprovningsanstalt, Goteborg, Sweden

I agree that it is important that the integration of hull forces and moments is carried out over a not too small part of the hull surface. This is even more important when the forces from a cavitating propeller are considered, as those pressures have a slower decay than those induced by a non-cavitating propeller [Lindgren and Johnsson (1977)].

Assuming that the hull forces should be used for an estimation of the vibration level for a certain ship project, I think that the problem is far more complicated than just a matter of integration area. First, the described method is a near field theory where the influence of the propagation velocity of the pressure wave has been neglected. When calculating forces far from the propeller this could cause some difficulties. Secondly, the ship hull is not a rigid body. The vibration response will therefore be dependent not only on the hull forces but also on their location relative to the nodes of the vibration mode. Forces located close to the nodes will contribute very little and those located on different sides of a node will more or less cancel each other. Calculations with the Finite Element Method have shown that hull forces aft of the aftermost node are particularly efficient in exciting high vibration levels. This could be the explanation for rather good results often being achieved in vibration calculations in spite of the fact that the excitation forces have been obtained by integration over a rather small area.

The correct treatment of the problem will, of course, include vibration calculations, with a very detailed Finite Element model with the complete excitation forces and moments. Since this is very complicated and expensive it is seldom done. Instead, different approximate procedures have been developed by different institutions. Referring to the integration problems the authors claim that "the current practice in European model basins is highly suspect." I very much doubt that this is current practice. At SSPA for example, we use the pressure fluctuations in a reference point above the propeller as a basis for estimation of the risk of vibration. On the basis of full-scale measurements we have established an approximate relation between excitation at this point and the vibrations at another reference point [(Lindgren and Johnsson (1977)].

REFERENCES

Huse, E.,(1972). Pressure Fluctuation on the Hull Induced by Cavitating Propellers. *Norwegian Ship Model Experiment Tank Publ. No. III.*

Johnsson, C. A., and T. Søndvedt, (1972). Propeller Excitation and Response of 230,000 TDW Tankers. *SSPA Publ. No. 70.*

Oossanen, P. van, (1974). Calculation of Performance and Cavitation Characteristics of Propellers Including Effects of Non-Uniform Flow and Viscosity. *NSMB Publ. No. 457.*

Lindgren, H., and C. A. Johnsson, (1977). On the Influence of Cavitation on Propeller Excited Vibratory Forces and Some Means of Reducing its Effect. *PRADS-International Symp. Tokyo.*

Authors' Reply

BRUCE D. COX, WILLIAM S. VORUS, JOHN P. BRESLIN,
and EDWIN P. ROOD

Our thanks to the discussers for their interest and encouraging remarks. On Mr. Rutgersson's question of calculating solid boundary factors, we do believe it would be useful to perform computations for a series of hull afterbody forms and propellers. The results would illustrate sensitivity to the various physical parameters and could provide guidance during the early stages of a ship design. However, for realistic predictions of propeller exciting forces, the complete calculation should be carried out using the actual wake, hull geometry, and propeller design under consideration.

As noted in the paper and by Mr. Rutgersson, only the non-cavitating propeller case is considered which is a severe limitation in many pratical applications. The principal purpose of the paper was to present analytical methods and simple formilae for predicting hull surface forces for a given representation of the propeller and show comparisons with experiments. Future improvements in the propeller theory, in particular, the allowance for transient cavitation, can be incorporated quite readily into the surface force analysis. It can be shown [Breslin (1977)] that the time rate of change of the cavity volume plays a crucial role in generating the propeller pressure field. We are familiar with a number of proposed methods for predicting blade cavity geometry including those cited by Mr. Rutgersson. These approaches for the most part are empirical. An alternative procedure, described in Mr. Huse's discussion, consists of finding an "equivalent" singularity distribution so as to produce agreement between calculated and measured values of pressure at selected locations near the propeller. The problem of analytically predicting the proper singularity distribution to represent the cavity volume dynamics is now the subject of active research.

We agree with Mr. Rutgersson that compressibility effects should be examined when considering the far field pressures generated by a propeller. A 5-bladed propeller operating at 100 rpm produces a blade rate frequency disturbance with a acoustic wavelength on the order of 600 feet. The relative phase of the distrubances generated far ahead of the propeller may be important in the integrated pressure force amplitude and phase.

The theory presented in this paper assumes a rigid hull boundary, intended to provide a first estimate of propeller exciting forces acting on the hull girder. Certainly for detailed stress and vibration analyses, the interplay between fluid loading and hull structural deformation would have to be accounted for. In principle, the present theory can be extended to satisfy the boundary condition on a deformable body. The complete analysis would then involve coupled equations describing the fluid loading and structural response, and could be solved by finite methods.

REFERENCE

Breslin, J. P., (1977). A Theory for the Vibratory Forces on a Flat Plate Arising from Intermittant Propeller Blade Cavitation. *Symposium on Hydrodynamics of Ship and Offshore Propulsion Systems, Oslo, Norway*

Session V

CAVITATION

ERLING HUSE
Session Chairman
The Ship Research Institute of Norway
Trondheim, Norway

Pressure Fields and Cavitation in Turbulent Shear Flows

Roger E. A. Arndt
University of Minnesota
Minneapolis, Minnesota

William K. George
State University of New York at Buffalo
Buffalo, New York

ABSTRACT

Cavitation in turbulent shear flows is the result of a complex interaction between an unsteady pressure field and a distribution of free stream nuclei. Experimental evidence indicates that cavitation is incited by negative peaks in pressure that are as high as ten times the rms level. This paper reviews the current state of knowledge of turbulent pressure fields and presents new theory on spectra in a Lagrangian frame of reference. Cavitation data are analyzed in terms of the available theory on the unsteady pressure field. It is postulated that one heretofore unconsidered factor in cavitation scaling is the highly intermittent pressure fluctuations which contribute to the high frequency end of the pressure spectrum. Because of limitations on the response time of cavitation nuclei, these pressure fluctuations play no role in the inception process in laboratory experiments. However, in large scale prototype flows, cavitation nuclei are relatively more responsive to a wider range of the pressure spectrum and this can lead to substantially higher values of the critical cavitation index. Unfortunately, this issue is clouded by the fact that higher cavitation indices can be found in prototype flows because of gas content effects. Some cavitation noise data are also examined within the context of available theory. The spectrum of cavitation noise in free shear flows has some similarity to the noise data found by Blake et al. (1977) with the exception that there appears to be a greater uncertainty in the scaling of the rate of cavitation events which leads to a substantial spread in the available data.

1. INTRODUCTION

The physical processes involved in cavitation inception have been studied for many years. Much of this research has been directed toward an understanding of the dynamics of bubble growth and the determination of the sources of cavitation nuclei and their size and number in a given flow situation. This research has led to a general understanding of some of the environmental factors involved in scaling experimental results from model to prototype. More recently, considerable attention has been paid to the details of the boundary layer flow over streamlined bodies and the role of viscous effects in the cavitation process. This research has shown that viscous effects such as laminar separation and transition to turbulence can have a major impact on the inception process and that there can be considerable variation between model and prototype in the critical conditions for cavitation.

In the absence of viscous effects, the scaling problem reduces to an understanding of the size distribution of nuclei and the temporal response of these nuclei to pressure variations as viewed in a Lagrangian frame of reference. This was first treated in detail by Plesset (1949). As already mentioned, consideration of viscous effects shows that the cavitation inception process can be considerably altered by either laminar separation or transition to turbulent flow. Obviously these phenomena are interrelated and are strongly Reynolds number dependent. The recognition of the importance of these factors has had considerable impact on the direction of cavitation research in recent years. Several papers in this symposium deal directly with this aspect of the cavitation scaling problem.

It is reasonably well understood that intense pressure fluctuations, either at the trailing edge of a laminar separation bubble or in the transition region, can have a major effect on the inception process on streamlined bodies. However, these phenomena will be excluded from this review. The focus of this paper will be on the relationship between the temporal pressure field and cavitation inception in free turbulent shear flows and fully developed boundary layer flows. Scant attention has been given to this problem, even though the topic is of practical significance. Turbulent shear flows are very common in practice and what cavitation data are available for these flows indicate that there can be significant scale effects. For example, Lienhard and Goss (1971) present a collection of cavitation data for submerged jets. It is observed that the critical value of the cavitation index increases with an increase in jet diameter, with no upper bound on the cavitation index being defined by the available data. The cavitation index is observed to vary from 0.15 to 3.0 over a size range of 0.1 cm to 13 cm. Arndt (1978) reviews the available data for cavitation in the wake of a sharp edged disk. These data increase monotonically with Reynolds number and again no upper limit on the critical cavitation index can be determined from the available data. At present, it can be said that laboratory experiments do not provide a reasonable estimate of the conditions that can be encountered under prototype conditions. From a practical point of view the situation is much more critical than the scaling problems associated with streamlined bodies since at present there is no definable upper limit on the cavitation index for these free shear flows.

There are a myriad of factors that enter into the inception process in turbulent shear flows. As a minimum, we need information on the turbulent pressure field, such as spectra and probability density. We require an understanding of the diffusion of nuclei within the flow, and we need to know how these nuclei respond to temporal fluctuations in pressure. In taking into account the bubble dynamics inherent in the problem, consideration must also be given to gas in solution which can have an influence on both bubble growth and collapse.

The theory of bubble dynamics is well founded and reasonable estimates of critical pressure can be determined under flow conditions that are well defined. Needless to say, the flow conditions in a turbulent shear flow cannot be defined in sufficient detail. However, the problem of flow noise has led to a more comprehensive understanding of turbulence; in particular, recent aeroacoustic research has provided a wealth of data on turbulent pressure fluctuations. These data are a by-product of the need for understanding turbulence as a source of sound. At this point in time, it seems only logical to review the inception problem in terms of both classical bubble dynamics and the more recent results of the field of aeroacoustics.

2. THEORETICAL CONSIDERATIONS FOR CAVITATION

Cavitation Index

The most fundamental parameter for cavitating flows is the cavitation index

$$\sigma = \frac{p_o - p_v}{\frac{1}{2}\rho U_o^2}$$

wherein p_o is a reference pressure, p_v the vapor pressure, U_o a reference velocity, and ρ the density of the liquid. The flow state of primary interest in this paper is characterized by a limited amount of cavitation in an otherwise single phase flow. There is a specific value of σ associated with this flow condition, which for convenience will be defined as the critical index:

$$\sigma_c = \frac{p_{oc} - p_v}{\frac{1}{2}\rho U_o^2}$$

If it is necessary to have completely cavitation free conditions, one design objective for various hydronautical vehicles is the minimization of σ_c.

Cavity flows are assumed identical in model and prototype for geometrically similar bodies when σ is constant, irrespective of variations in physical size, velocity, temperature, type of fluid etc. In practice σ_c is found to vary over wide limits. Simply stated, these so-called scale effects are due to deviations in two basic assumptions inherent in the cavitation scaling law; namely that the pressure scales with velocity squared and the critical pressure for inception is the vapor pressure, p_v. As will be shown, the two factors can be interrelated, since in principle the critical pressure is a function of the time scale of the pressure field.

In order to provide a foundation for the ensuing discussion, consider a steady uniform flow over a streamlined body devoid of any viscous effects. The following identity can be written:

$$\sigma = \frac{p - p_v}{\frac{1}{2}\rho U_o^2} - C_p$$

wherein C_p is a pressure coefficent defined in the usual manner. Generally speaking, C_p is defined by the pressure on the surface of a given body. It is generally assumed that cavitation first occurs when the minimum pressure, p_m, is equal to the vapor pressure, p_v. This results in the well-known scaling law

$$\sigma_c = - C_{p_m}$$

Consider next the case where the pressure in the cavitation zone is less than the minimum pressure measured on the surface of the body, then

$$\sigma = \frac{p_{ml} - p_v}{\frac{1}{2}\rho U_o^2} - C_p + \frac{p - p_{ml}}{\frac{1}{2}\rho U_o^2}$$

Here we have to distinguish between the pressure at the surface of the body p, and the pressure sensed by cavitating nuclei, p_{ml}. Assuming cavitation occurs when $p_{ml} = p_v$ we have

$$\sigma_c = - C_p + \frac{p - p_{ml}}{\frac{1}{2}\rho U_o^2} \qquad (1)$$

Equation (1) is one version of the superposition equation that is commonly referred to in the literature.

Bubble Dynamics

It is generally accepted that the process of cavitation inception is a consequence of the rapid or explosive growth of small bubbles or nuclei which become unstable due to a change in ambient pressure. These nuclei can be either imbedded in the flow or find their origins in small cracks and crevices at the surfaces bounding a given flow. The details of how these nuclei can exist have been considered by many investigators. A summary of this work is offered by Holl (1969, 1970).

Theoretically, liquids are capable of sustaining large values of tension. However, the nuclei in the flow act as sites for cavitation inception and prevent the existence of significant tensions. The mechanics of the inception process are adequately described by the Rayleigh-Plesset equation, which considers the dynamic equilibrium of a spherical bubble containing vapor and non-condensable gas and subject to an external pressure $p_{ml}(t)$:

$$R\ddot{R} + \frac{3}{2}\dot{R}^2 = \frac{1}{\rho}\left[p_v + p_g - p_{ml}(t) - \frac{2S}{R} - 4\,\mu\,\frac{\dot{R}}{R}\right] \qquad (2)$$

wherein R is the bubble radius and dots denote differentiation with respect to time. It should be emphasized here that even for the case of steady flow over a streamlined body, $p_{ml}(t)$ is a function of time since we are concerned with the pressure history sensed by a moving bubble. If the problem is simplified to consider the static equilibrium of a bubble, we find that there is a critical value of $p_v - p_{ml}$ below which static equilibrium is not possible. This is found to be

$$(p_v - p_{ml})_c = 4S/3R^* \qquad (3)$$

wherein R* is defined as the critical bubble radius. Substitution of Eq. (3) into Eq. (2) with dynamical terms identically zero will indicate that R* is a function of the partial pressure of noncondensable gas within the bubble. If $p_{ml}(t)$ varies rapidly in comparison to the response time of the nuclei, then even greater values of tension are possible. Thus in general we can write

$$\frac{p_v - p_{ml}}{4S/3R^*} = \phi\left[t_c\,\sqrt{\frac{S}{\rho R_*^{\,3}}}\right]$$

where

$$\phi(o) = \infty, \quad \phi(\infty) = 1$$

The function ϕ depends on the flow field. The argument of ϕ contains a characteristic time scale of the pressure field (t_c) and a characteristic response time of the nuclei, $(\rho R_*^{\,3}/S)^{1/2}$. In the case of a streamlined body in the absence of viscous effects, t_c would be proportional to the quotient of body diameter and velocity. In the case of cavitation induced by turbulence, the characteristic time scale could be any of the turbulence time scales. For example,

$$L_{11}/\sqrt{\overline{u_1'^2}}$$

is often appropriate. The factor $(\rho R_*^{\,3}/S)^{1/2}$ is derived from the asymptotic solution to Eq. (2) for the case of negligible gas diffusion. Under these conditions

$$p_g \sim \frac{1}{R^3}$$

and the growth rate stabilizes at a value given by

$$\dot{R} = \sqrt{\frac{2}{3}\,\frac{p_v - p_{ml}}{\rho}} \qquad (4)$$

Assuming a characteristic bubble response time given by $R^*/\dot{R}$, with $p_v - p_{ml} = 4S/3R^*$, we obtain

$$T_B \equiv \frac{R^*}{R} = 0.87\sqrt{\frac{\rho R_*^{\,3}}{S}} \qquad (5)$$

A typical variation of ϕ based on the theoretical computations of Keller (1974) is given in Arndt (1974).

The Influence of Dissolved and Free Gas

The discussion in the previous section is based on the assumption of a healthy supply of free nuclei which is generally the case in recirculating water tunnels and in the field. Generally speaking, a reduction in σ_c due to bubble dynamic effects usually only occurs on model scale. To some extent the level of dissolved gas and the number and size of free nuclei are interrelated. Some recent experimental results are documented in Arndt and Keller (1976). The level of dissolved gas can play an important direct role when the time of exposure to reduced pressure is relatively long. Under these circumstances Holl (1960) has shown that gaseous cavitation can occur at values of σ much greater than those for vaporous cavitation. Using an equilibrium theory, Holl (1960) deduced an upper limit on σ_c given by

$$\sigma_c = -\,C_{pm} + \frac{\alpha\beta}{\frac{1}{2}\,\rho\,U_o^{\,2}} \qquad (6)$$

wherein α is the concentration of dissolved gas and β is Henry's constant.

In summary, an overview of the effects of bubble dynamics and free and dissolved gas indicates that short exposure times such as are the case in a model implies that cavitation will occur at pressures lower than vapor pressure and σ_c is less than expected. Long exposure time, such as can occur in vortical motion of all types, including large scale turbulence, implies the possibility of gaseous cavitation with σ_c being greater than expected.

3. PRESSURE FLUCTUATIONS IN TURBULENT SHEAR FLOWS

Background

Considerable progress has been made over the last five years in the understanding turbulent pressure fluctuations in free shear flows in an Eulerian frame of reference. Of particular importance is the development of pressure sensing techniques which under certain circumstances can lead to reliable measurements of pressure fluctuations.

The first theoretical arguments on the pressure fluctuations associated with turbulent flow appear to be due to Obukov and Heisenberg [Batchelor (1953)]. Heisenberg argued that Kolmogorov scaling should be possible for small scale pressure fluctuations. Batchelor (1951) was able to calculate the mean square intensity of the pressure fluctuations as well as the mean square fluctuating pressure gradient in a homogeneous, isotropic turbulent flow. This work was extended by Kraichnan (1956) to the physically impossible but conceptually useful case of a shear flow having a constant mean velocity gradient and homogeneous and isotropic turbulence.

Apparently there were no attempts made to extend this theoretical work until the 1970's when George (1974a), Beuther, George, and Arndt (1977a, b, c) and George and Beuther (1977) applied the concepts developed by Batchelor and Kraichnan to the calculation of the turbulent pressure spectrum in honogeneous, isotropic turbulent flows with and without shear. When compared with experimental evidence gathered in turbulent mixing layers, the theory is found to be remarkably accurate. The predicted spectrum (with no adjustable constants) agrees with pressure measurements in turbulent jet mixing layers from several sources, including those of Fuchs (1972a), Jones and his co-workers (1977), and the authors themselves. As shown in Figure 1, the experimental data and the theory are remarkably consistent, especially in light of the fact that several different experimental techniques and different flow facilities are involved.

The current state of knowledge of turbulent pressure fluctuations can be summarized as follows:

1) Pressure fluctuations in a shear flow can arise from three sources. The first two involve interaction of the turbulence with the mean shear. These are second order and third order interactions, of which only the second order interactions are important at small scales. The last involves only interactions of the turbulence with itself.

2) Kolmogorov similarity arguments can be applied to each of the spectra arising from these terms. These arguments are valid for the small scale fluctuations.

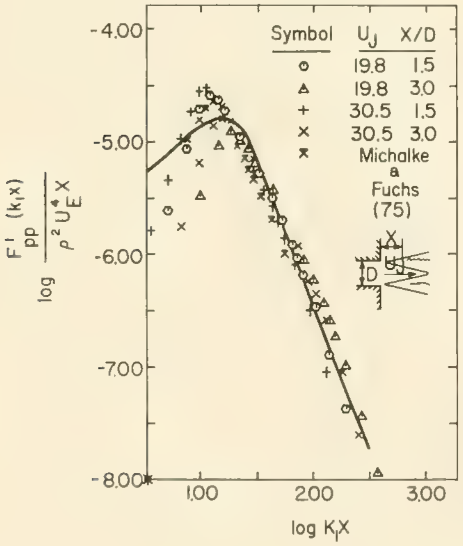

FIGURE 1. Experimental confirmation of the theoretical pressure spectrum for a turbulent jet.

3) If the turbulent Reynolds number is high enough, there exists an inertial subrange in each of the three spectra in which

$$\pi_{MS1}\ (k) = \alpha_{s1}\rho^2\ \varepsilon^{2/3}\ Kk^{-11/3}$$

$$\pi_{MS2}\ (k) = \alpha_{s2}\rho^2\ \varepsilon\ Kk^{-9/3}$$

$$\pi_T(k) = \alpha_T\rho^2\ \varepsilon^{4/3}\ k^{-7/3}$$

wherein $\alpha_{s1} \cong 2$, $\alpha_{s2} \cong 0$, $\alpha_T \cong 1.3$, ε is the rate of dissipation of turbulent energy per unit volume, *K* is the mean shear, and k is the disturbance wave number.

4) There is considerable evidence that coherent structures play an important role in determination of at least the large scale pressure fluctuations [Fuchs and Michalke (1975), Fuchs (1972a, b), Chan (1974a, b), and Chan (1976)].

Relation to Cavitation

Since the above spectral results are expressed in Eulerian frames, they cannot be directly applied to the problem of cavitation inception which is a Lagrangian problem. Nonetheless, Kolomogorov scaling has been successful in an Eulerian frame of reference and therefore we can, with some confidence, infer that similar scaling will be valid for Lagrangian time spectra (i.e. the frequency spectra that would be seen by a moving material point). The results of such an exercise are as follows:

1) The Lagrangian turbulent spectrum can be separated into interaction of the turbulence with the mean shear and the interaction of the turbulence with itself.

2) The high frequency (analogous to small scale) will be well described by Kolmogorov scaling such that

$$\frac{1}{\rho^2}\ \Lambda pps\ (\omega) = K^2\ \nu^{5/2}\ \varepsilon^{-\frac{1}{2}}\ f_s\ \left(\frac{\omega}{\omega_d}\right)$$

$$\frac{1}{\rho^2}\ \Lambda ppT\ (\omega) = \nu^{3/2}\ \varepsilon^{\frac{1}{2}}\ f_T\ \left(\frac{\omega}{\omega_d}\right)$$

where

$$\omega_d = \left(\frac{\varepsilon}{\nu}\right)^{\frac{1}{2}}$$

3) In the inertial subrange these reduce to

$$\frac{1}{\rho^2}\ \Lambda pps\ (\omega) = K^2\ \nu^{5/2}\ \varepsilon^{-\frac{1}{2}}\ \left(\frac{\omega}{\omega_d}\right)^{-5}$$

$$\frac{1}{\rho^2}\ \Lambda ppT\ (\omega) = \nu^{3/2}\ \varepsilon^{\frac{1}{2}}\ \left(\frac{\omega}{\omega_d}\right)^{-3}$$

In summary it appears plausible to assume that the basic picture of pressure fluctuations arising from mean-shear turbulence interactions will be unchanged in a Lagrangian frame of reference, although the actual spectra are different. The postulated relations for Lagrangian spectra should be directly applicable to any Lagrangian phenomenon; in particular the relations should be applicable to the inception of nuclei in a fluctuating pressure field.

In relating the information on the pressure field to the problem at hand, it is evident that two criteria must be satisfied for turbulence induced inception:

1) The pressure must dip to the vapor pressure or lower.

2) The pressure minimum must persist for a time that is long in comparison to the characteristic time scale of the bubble, say T_B (taken to be the time scale for growth at inception).

Both factors lead to scale effects. Consider first the second factor. The preceding arguments for the pressure field in a Lagrangian frame of reference lead to the hypothetical spectrum shown in Figure 2. For convenience we have normalized the spectrum with respect to the mean square pressure and the Lagrangian time scale $\mathcal{T}$. (c.f. Tennekes and Lumley, Chapter 8). Requirement (2) for bubble growth is plotted at the frequency $\omega = 1/T_B$. It is clear that as long as $\omega << 1/T_B$, any pressure flucuation persists for a time longer than the time scale of the bubble. Thus at frequencies less than $\omega = 1/T_B$ cavitation inception can occur with minimal local tension. Moreover, by integrating the spectrum from $\omega = 0$ to $\omega = 1/T_B$, we can determine that fraction of the mean square pressure which can contribute to bubble growth without appreciable tension (assuming a normal distribution of nuclei).

Consider now the effect of maintaining T_B constant while varying the Reynolds number. Taking $\mathcal{T} \sim \ell/u'$ and noting that there are essentially no pressure fluctuations of interest above the Kolmogorov frequency, $\omega = (\varepsilon/\nu)^{\frac{1}{2}}$ we find that after $1/T_B$, exceeds $(\varepsilon/\nu)^{\frac{1}{2}}$, the entire spectrum can potentially contribute to bubble growth. This will occur when the Reynolds number is roughly $u\ell/\nu \sim (\ell/uT_B)^2$. By noting the spectral dependence on frequency and performing a running integral, a plot such as shown in Figure 3 can be generated. This graph illustrates how rapidly the asymptotic state is reached. This occurs when $\mathcal{T}/T_B^{-1} > \mathcal{T}(\varepsilon/\nu)^{\frac{1}{2}} \geq (u'\ell/\nu)^{\frac{1}{2}}$ or when $\ell/u'T_B > (u'\ell/\nu)^{\frac{1}{2}}$ as previously stated.

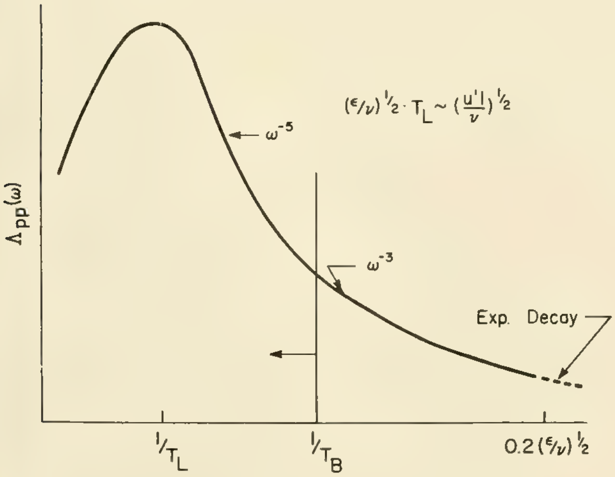

FIGURE 2. Hypothetical pressure spectrum in a Lagrangian frame of reference.

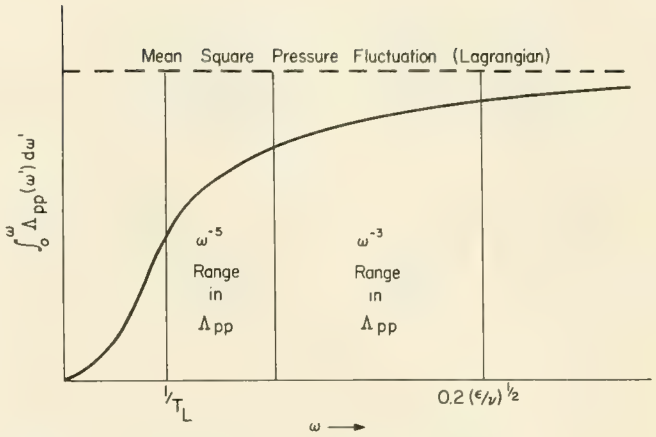

FIGURE 3. Integration of Lagrangian pressure spectrum.

As an example,* cavitation is observed to occur in submerged jets at an axial position, x, that is roughly one diameter from the nozzle. Assuming the dissipation rate to be approximately $0.05U_J^3/x$, where U_J is the jet velocity, results in a criterion that the jet diameter must exceed the following before scale effects are absent: $d > 0.05U_J^3T_B^2/\nu$. Using typical values of $U_J = 10$ m/s and $T_B = 10^{-3}$ sec., we conclude that the asymptote is reached for $d \sim 50$ meters. Thus size effects could be important in many model experiments.

Effect of Intermittency at Small Scale

In 1947, Batchelor and Townsend concluded from observations of the velocity derivatives in turbulent flow that the fine structure of the turbulence (small scales, high frequency) was spatially localized and highly intermittant in high Reynolds number flows. Subsequent work [c.f. Kuo and Corrsin (1971)] has confirmed that there is a decrease in the relative volume occupied by the fine structure as the Reynolds number is increased. Thus the spatial intermittancy increases with Reynolds number. The effect of this phenomenon on filtered hot wire signals is shown in Figure 4. These data are derived from Kuo and Corrsin (1971). It is obvious from these data that the signal is increasingly intermittant as the filter frequency is moved to higher and higher values.

Since the dissipation of turbulent energy takes place at the smallest scales of motion, it is clear from these observations that the rate of dissipation of turbulent energy must vary widely with space and time. It was this consideration that led

*Strictly speaking, these results are only applicable when the Lagrangian turbulent field is stationary. In most flows of interest this is seldom the case. However, the smallest scales of motion can often be considered to be in quasi-equilibrium.

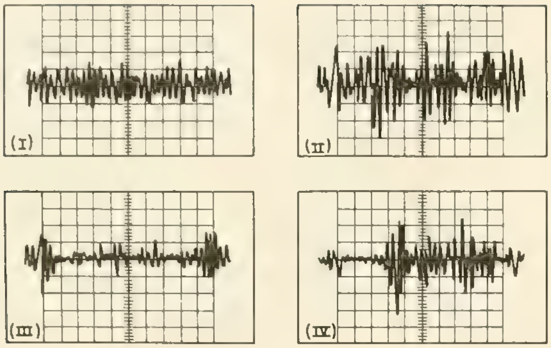

FIGURE 4. Filtered hot-wire signals in grid-generated turbulence [adapted from Kuo and Corrsin (1971)]. (i) f_m = 200 Hz, f/f_m = 0.52, 20 ms/division (horizontal scale); (ii) 1 kHz, 0.52, 4; (iii) 6, 0.52, 1; (iv) high-pass signal, f_c = kHz, 1 ms/division.

Kolmogorov (1962) to reformulate his original similarity hypothesis in terms of the average rate of dissipation of turbulent energy $\langle\varepsilon\rangle$, and to assume that the logarithm of ε was governed by a normal distribution. Later work by Gurvich and Yaglom (1967) showed that any non-negative quantity governed by fine scale components has a$_2$log normal distribution with a variance given by $\Sigma = A + B \ln R_\ell$ where A is a constant depending on the structure of the flow, B is a universal constant and R_ℓ is the turbulence Reynolds number.

These results have implications for the cavitation problem at hand. Beuther, George, and Arndt (1977a, b) have shown that Kolmogorov similarity scaling is applicable to the high wave number turbulent pressure spectrum. As a consequence of this and the observed intermittancy and spatial localization of small scale velocity fluctuations, it is reasonable to expect the same trend in the small scale pressure fluctuations. This could result in an important cavitation scale effect.

To make this point clear, a set of hypothetical band passed pressure signals at high and low Reynolds number are presented in Figure 5. For the sake of argument, assume that the filter is set around a range of frequencies which will result in bubble growth ($\omega T_B \leq 1$). Since the spectra of these two signals will be identified in terms of Kolmogorov variables and since the low Reynolds number signal is less intermittant, there is a greater probability that the high Reynolds number signal will contain more intense deviations from the mean. In particular, with all other factors held equal it is more likely that the local pressure will fall below the critical pressure when the Reynolds number is high, even though the spectra are identical. This is shown in Figure 5. If the log normal arguments were applicable, then it can be expected that this will depend on the Reynolds number.

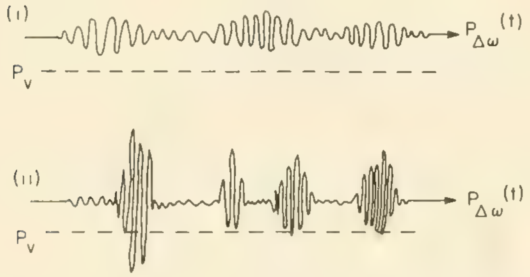

FIGURE 5. Hypothetical band-passed pressure signals: (i) low turbulent Reynolds numbers, (ii) high turbulent Reynolds number.

The effect of intermittancy coupled with effects cited earlier could be of considerable importance to the problem of predicting cavitation inception in the prototype from small scale experiments in the laboratory. The Reynolds number in model and prototype can vary by many orders of magnitude. For example, experimental observations of boundary layer cavitation by Arndt and Ippen (1968) were carried out at Reynolds numbers, $u'\delta/\nu$, of the order 5000. On large ships, Reynolds numbers of 10^6 and greater are not uncommon.

Coherency of the Pressure Field

An important factor related to cavitation inception in jets is the existence of coherent structure in the flow. Cavitation in highly turbulent jets is observed to occur in ring like bursts, smoke rings if you will. These bursts appear to have a Strouhal frequency fd/U_J of approximately 0.5. This point is underscored by some recent work of Fuchs (1974). Fuchs made 2 and 3 probe pressure correlations as shown in Figure 6. His results are summarized in Table 1. Signals filtered at a Strouhal number of 0.45 were highly coherent. For comparison, velocity correlations are shown in parentheses indicating that the velocity field is much less coherent than the pressure field.

The Turbulent Boundary Layer

Because of the relative ease of measurement, there exists a considerable body of experimental data

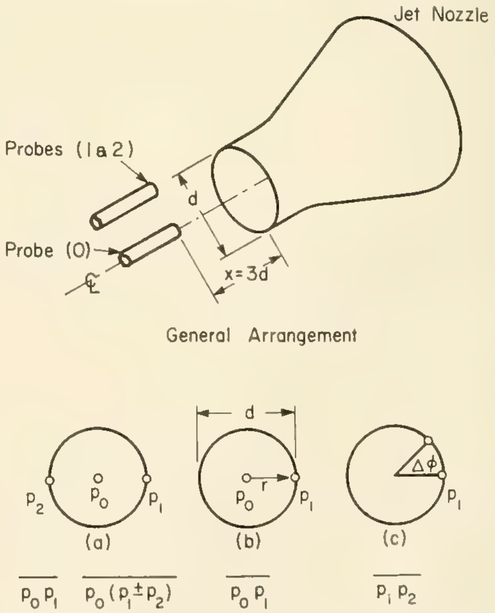

FIGURE 6. Measurement of pressure coherency in a turbulent jet [adapted from Fuchs (1974)].

for wall pressure due to turbulent boundary layer flow. However, in many ways less is known about the turbulent pressure field for boundary layers than for free turbulent shear flows. Not only is the theoretical problem made more difficult (impossible to the present) by the presence of the wall, the experimental problem is considerably complicated by the dynamical significance of the small scales near the wall.

Thus, in spite of over two decades of concentrated attention we cannot say with confidence even what the rms wall pressure level is, although recent evidence points to a value of [Willmarth (1975)]:

$$p' = c\,\rho\,u_*^2$$

$$c = 2 \text{ to } 3$$

The basic problem is that the most interesting part of a turbulent boundary layer appears to the region near the wall where intense dynamical activity apparently gives rise to the overall boundary layer activity. While the details of the process are debatable, most investigators concur on the importance of the wall region on overall boundary layer development. Unfortunately, under most experimental conditions, the scales of primary activity are smaller than standard wall pressure probes can resolve [Willmarth (1975)]. Thus we have virtually no information concerning the contribution of the small scales to the pressure field, although we suspect that the small scales are significant or even dominant.

Pressure Spectra in Boundary Layers

Our knowledge of the pressure spectra may be summarized as follows:

1) Pressure fluctuations arising from motions in the main part of the boundary layer ($y/\delta > 0.1$) scale with the outer parameters u_* and δ.

2) Pressure fluctuations arising from the inner part of the boundary layer scale with the inner parameters:
   a) hydraulically smooth, u_*, ν
   b) hydraulically rough, u_*, h; where h is roughness height

3) Pressure fluctuations arising from the inertial sublayer (logarithmic layer) scale only with u_* and y, the distance from the wall.

4) The wall pressure spectrum is a composite of all these factors and has a distinct region corresponding to each factor.

A composite picture of the wall pressure spectrum is shown in Figures 7a and 7b. The $1/k$ range is evident in both the inner and outer scalings and arises from the inertial sublayer contribution [Bradshaw (1967)].

The pressure spectrum within the near wall region should closely resemble the wall spectrum (although this has never been confirmed). The spectrum in the main part of the boundary layer, should, however, resemble that obtained for a free shear flow at high Reynolds numbers. Again there is no information available to either prove or disprove this conjecture.

The Lagrangian model developed in the preceding section depends in part on the assumption that a material point is in a stationary random field. As long as the Eulerian field is homogeneous, there is no problem. This is approximately true in many shear flows, but is never true in a turbulent boundary layer. Thus our Lagrangian spectral picture must be abandoned entirely (or used with great restraint).

However, a number of features of the Lagrangian model can be applied to this problem. In particular, the "spectral peaks" in the outer flow can be identified with the Lagrangian integral scale, $\mathcal{J} \sim \ell/u'$. The highest frequencies in the flow will

Table 1. Normalized correlation functions with pressure probes arranged as shown in Figure 6 (corresponding velocity correlations in brackets).

	Signals Unfiltered	Signals Filtered at St = 0.45
$\dfrac{\overline{p_0 p_1}}{\sqrt{\overline{p_0^2}}\ \sqrt{\overline{p_1^2}}}$	+0.35 (+0.03)	0.66 (0.13)
$\dfrac{\overline{p_0\ (p_1+p_2)}}{\sqrt{\overline{p_0^2}}\ \sqrt{\overline{(p_1+p_2)^2}}}$	+0.57 (+0.07)	0.83 (0.19)
$\dfrac{\overline{p_0\ (p_1-p_2)}}{\sqrt{\overline{p_0^2}}\ \sqrt{\overline{(p_1-p_2)^2}}}$	-0.07 (+0.04)	0.06 (0.02)

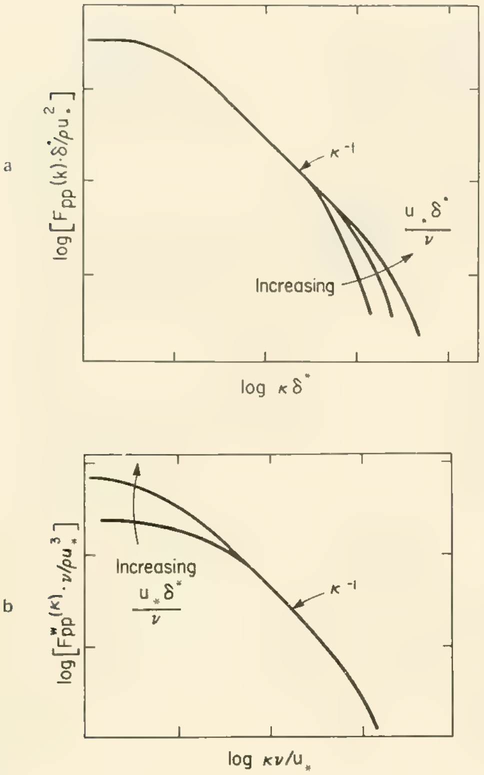

FIGURE 7. Wall pressure spectra: (a) outer scaling, (b) inner scaling.

be u_*^2/ν or $u*/h$, depending on whether the wall is hydraulically smooth or rough, and there will be increasing intermittency with increasing Reynolds number. The latter effect is most interesting and is quite evident in the many observations of dye streaks in the wall layer [cf Kim, Kline, and Reynolds (1971)].

Effect of the Pressure Field on Cavitation

Whether or not the pressure fluctuations play a role in the cavitation inception process, depends on the previously cited criteria:

1) The minimum pressure must fall below a critical level.
2) The minimum pressure must persist below the critical level for a finite length of time.

The first criterion depends greatly on the yet unresolved question of intermittency and its effect on the probability density of the pressure fluctuations. At this point in time we can say that the critical cavitation index will increase with Reynolds number because larger excursions from the mean pressure are more likely. Without justification, it is hypothesized that the effect on the pressure variance will be approximated by a log-normal dependence on the Reynolds number. Detailed study of the wall pressure such as that proposed by George (1975) should aid considerably in resolving this question.

The question of time scale is more easily confronted. Since most of the energy in the pressure spectrum scales with u_* and δ it is clear that the criteria for bubble growth without appreciable tension reduces to

$$u_* T_B/\delta \leq 1$$

In words, we again require a pressure fluctuation to persist for a time which is long in comparison to the response time of a typical nucleus.

Since ν/u_*^2 is the shortest time scale in a smooth wall boundary layer, all of the pressure spectrum is sampled by the nuclei when

$$u_*^2 T_B/\nu < 1$$

This criterion is especially important in view of the highly intermittant process near the wall.

For rough walls, the last criterion can be expressed in terms of the roughness height h by

$$u_* T_B/h < 1$$

Since in fully rough flow $u_* h/\nu > 1$, it is clear that the small scale criterion is more easily satisfied with rough wall experiments.

In summary, the information we have on pressure fields in turbulent boundary layers and its relationship to cavitation inception can be summarized as follows:

Significant scale effects can be expected when $u' T_B/\delta > 1$. As the ratio of T_B to the smallest time scale in the flow decreases, the scale effect would be expected to level off i.e. when $u_*^2 T_B/\nu$ or $u_* T_B/h < 1$. Further increase in the cavitation number with Reynolds number will be due to the Reynolds number dependent effects on the probability density of the pressure fluctuations as a result of increased intermittancy of the small scale structure. The latter effect should produce a more gradual dependence of the cavitation index on Reynolds number than the former effect.

The picture, as displayed above, is plausible and perhaps even appealing, but it must be viewed simply as conjecture until definitive experimental information is made available. An important hint of the relevance of these results can be found in the work of Arndt and Ippen (1967) where it was found that the region of maximum cavitation in a rough boundary layer shifted inward with a decrease in $u_* T_B/h$. However, the change in this parameter varied only by a factor of 15 in their experiments. This will be discussed in more detail in subsequent sections.

4. CAVITATION INCEPTION DATA

A rather limited amount of experimental data have been collected under controlled conditions. The types of flows considered to date include the wake behind a sharp edged disk, submerged jets from nozzles and orifices, and smooth and rough boundary layers. There is a dearth of information relating the observed cavitation inception with the turbulence parameters. Some of the earlier efforts in this direction are summarized in a paper by Arndt and Daily (1969) and by Arndt (1974b). A collation of available data is presented in Figure 8. Here the data are presented in the form of Eq. (1):

$$\sigma_c + C_p = f\,(C_f)$$

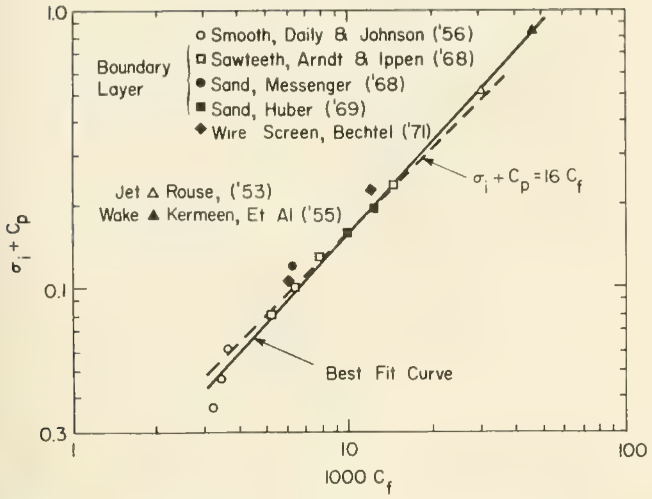

FIGURE 8. Collation of cavitation inception data.

wherein

$$C_f = \left| \begin{array}{ll} 2\tau_0/\rho U^2 & \text{Boundary Layer Flow} \\ & \\ \dfrac{\overline{u_1 u_2}}{U_o} & \text{Free Shear Flows} \end{array} \right.$$

In this expression C_f is computed either from the measured wall shear in the case of boundary layer flows or from turbulence measurements made in the air at comparable Reynolds numbers for the case of a free jet and a wake. The measured value of C_p is only significant for the case of the disk wake and the pressure data was determined from the experimental work of Carmodi (1964). The available data seem to be well approximated by the relation

$$\sigma_c + C_p = 16\ C_f$$

which was originally proposed for boundary layer flow by Arndt and Ippen (1968). These data would seem to imply that a relatively simple scaling law already exists and would further imply that the previous discussion in this paper on turbulence effects is superfluous. This is not the case. Arndt and Ippen (1968) made observations of the bubble growth in turbulent boundary layers. Some of their results are depicted in Figures 9 and 10. Figure 9 shows sample bubble growth data. The growth rate is observed to stabilize at a constant value during most of the growth phase. Using Eq. (4), the levels of local tension are found to be quite small, of the order 20 to 100 millibar. These data correspond to observations in a rough boundary layer. Of particular interest is the fact that, in all cases, the life time for bubble growth is a fraction of the Lagrangian time scale, $\mathcal{J} = \delta/u'$. In fact growth times were observed to be of the order h/u_*. Unfortunately there is not enough experimental evidence available to completely illuminate this point. As shown in Figure 10, cavitation occurs roughly in the center of the boundary layer with a tendency for the zone of maximum cavitation to shift inward as $u_* T_B/h_s$ decreases from about 1.5 to approximately 0.1*. In the cited boundary layer experiments, C_p is negligible. Thus $\sigma_c = 16\ C_f$. Noting that p' is approximately 2.5 ρu_*^2 at the wall, we estimate that cavitation is incited by negative peaks in pressure of order 6 p'. This compares favorably with Rouse's (1953) data for jet cavitation which indicate that negative peaks of order 10 p' are responsible for cavitation.

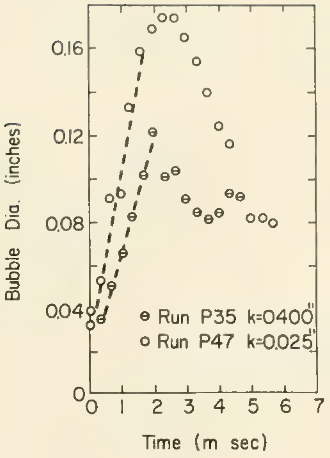

FIGURE 9. Sample bubble growth data [after Arndt and Ippen (1968)].

A strong dependence on Reynolds number can be observed even in free shear flows. Figure 11 contains cavitation data for a sharp edged disk. These data were obtained in both water tunnels and a new depressurized tow tank facility located at the Netherlands Ship Model Basin. The water tunnel data are for cavitation desinence, whereas the tow tank data are for cavitation inception determined acoustically. The cross hatched data were determined in a water tunnel at high velocities by Keermeen and Parkin (1957). All the other data were obtained at relatively low velocities (2 - 10 m/sec). There is considerable scatter in these data and this is traceable to gas content effects

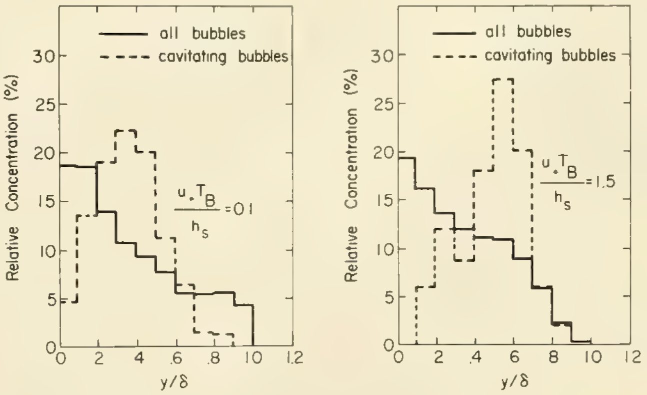

FIGURE 10. Observation of cavitation in turbulent boundary layers [after Arndt and Ippen (1968)].

---

*T_B was estimated from Eq. (5) using observed values of R_* reported in Arndt and Ippen (1967). For convenience, the results are normalized to equivalent sand grain roughness, h_s.

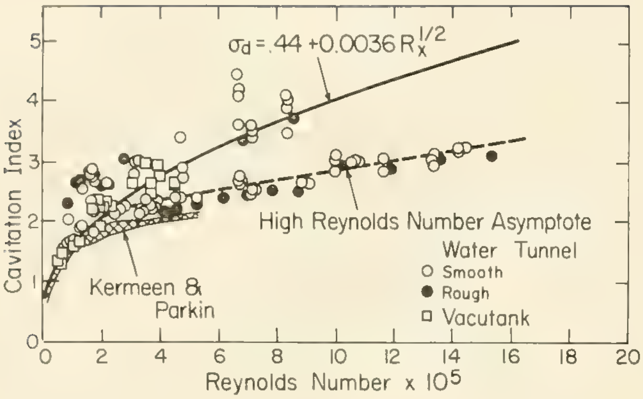

FIGURE 11. Cavitation inception data for a sharp-edged disk.

which are dominate at low velocities as will be discussed later. At low Reynolds number the data appear to be satisfied by the empirical relationship discussed by Arndt (1976):

$$\sigma_c = 0.44 + 0.0036\ (Ud/\nu)^{\frac{1}{2}} \tag{7}$$

It was found that the tow tank data agree with this relationship at relatively high Reynolds numbers. Equation (7) was developed from a model which assumes laminar boundary layer flow on the face of the disk. It would be expected that this condition would be satisfied at higher Reynolds numbers in a tow tank than in a highly turbulent water tunnel. At high Reynolds number (and also high velocity where gas content effects are negligible), there is a continuous upward trend in the data with increasing Reynolds number. This underscores the need for further work as suggested in the introduction to this paper.

A systematic investigation of gas content effects in free shear flow was recently reported by Baker et al. (1976). Cavitation inception in confined jets, generated either by an orifice plate or a nozzle, was determined as a function of total gas content in the liquid. The results are shown in Figure 12. When the liquid was undersaturated at test section pressure, the critical cavitation index was independent of gas content and roughly equal to that observed by Rouse (1953) for an unconfined jet. When the flow is supersaturated, the cavitation index is found to vary linearly with gas content as predicted by the equilibrium theory, Eq. (6). This effect occurs even though the Lagrangian time scale is much shorter than typical times for bubble growth by gaseous diffusion. For example, in the cited cavitation data, a typical residence time for a nucleus within a large eddy is roughly 1/15 of a second. At a gas content of 7ppm and a jet velocity of approximately 10 m/s, inception occurs at a mean pressure equivalent to a relative saturation level of 1.25. Epstein and Plesset (1950) show that for growth by gaseous diffusion alone, 567 seconds is required for a 10^{-3} cm nucleus to increase its size by a factor of 10. One additional point should be kept in mind here. The local pressure within an eddy is much less than the mean pressure and highly supersaturated conditions can occur locally. Arndt and Keller (1976) also reported extreme gas content effects in their experiments with disks when the flow was supersaturated. The magnitude of the effect also depends on the number of nuclei in the flow. Gas content effects were noted only in their water tunnel experiments (where there is a healthy supply of nuclei). No gas content effects on inception were noted in the tow tank (where the flow is highly supersaturated but there is a dearth of nuclei). Thus the picture becomes more cloudy as the influence of dissolved, noncondensable gas is taken into consideration.

5. SOME REMARKS ON CAVITATION NOISE

A complete discussion on cavitation noise would be beyond the scope of this paper. Recognizing the unique features of cavitation inception in turbulent shear flows, it appears appropriate to review what is known about cavitation noise under the same circumstances.

The general features of cavitation noise were reviewed by Fitzpatrick and Strasberg (1956), Baiter (1974), and Ross (1976). The spectrum of cavitation noise can in its simplest form be defined as the linear superposition of N cavitation events per unit time. Thus we can write

$$S(f) = N\ G(f) \tag{8}$$

The function G(f) is the spectrum of a single cavitation event. If p_b is the instantaneous acoustic pressure due to the growth and collapse of a single bubble, then by definition

$$\int_0^\infty G(f)\,df = \int_{-\infty}^\infty p_b^{\,2}\ dt$$

Fitzpatrick and Strasberg (1956) have shown that a characteristic bubble spectrum can be written in the form

$$G(f\tau_0) = \frac{r^2 G(f)}{\rho R_m^{\ 4}\ p_o}$$

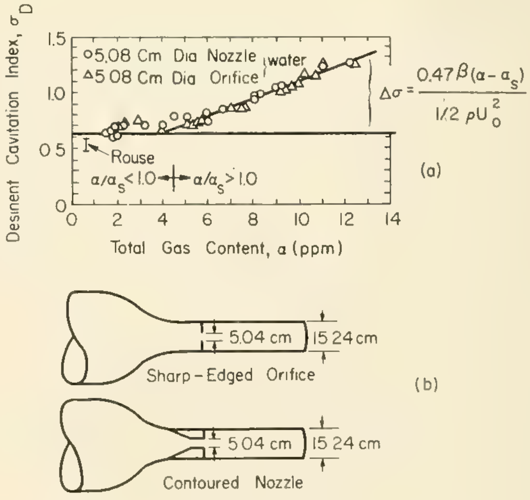

FIGURE 12. Cavitation inception in confined jets.

wherein τ_o is a characteristic bubble collapse time, R_m is the maximum bubble radius, and R is the distance to the observer. In addition, it appears reasonable to assume that N is related to the number of nuclei per unit volume, n, the velocity, the size of a given flow field, and the relative level of cavitation. Therefore we write

$$N/nU_o d^2 = f(\sigma/\sigma_c)$$

Thus a normalized version of Eq. (8) would be

$$\frac{S(f)\,\left(\frac{r}{d}\right)^2}{\rho U_o p_o n R_m^4} = f(\sigma/\sigma_c)\; G(f\tau_o) \qquad (9)$$

It is difficult to obtain appropriate scaling factors for R_m and τ_o in a turbulent shear flow. The problem is discussed briefly by Arndt and Keller (1976). Lacking more detailed information, the following assumptions can be used

$$R_m \sim d$$

$$\tau_o \sim d/U\sigma^{1/2}$$

If we interpret S(f) as the mean square acoustic pressure in a frequency band Δf, Eq. (9) can be written in the form

$$\frac{\left(\overline{p_a^2}/\rho^2 U_o^4\right)}{(\Delta f d/U_o)} \cdot \frac{(r/d)^2}{\sigma n d^3} = f\;(\sigma/\sigma_c)\; G(fd/U\sigma^{1/2}) \qquad (10)$$

Blake et al. (1977) circumvented the requirement of measuring n. They reasoned that

$$\int_0^\infty G(f)df = \int_{-\infty}^{\infty} p_b^2\; dt = \gamma\tau_o\; \overline{p_b^2}$$

wherein $\overline{p_b^2}$ is the time mean square of p_b and $\gamma\tau_o$ is the total lifetime of the bubble (including growth, initial collapse times and rebounding times). Further, they simply reasoned that

$$\overline{p_a^2} = N\; \overline{p_b^2}$$

or that

$$S(\tau_o f) = N\tau_o\; \gamma G(f\tau_o)$$

This results in the normalized spectrum

$$S(\tau_o f) = \frac{\overline{p_a^2}(f,\Delta f)}{\Delta f N}\; \frac{\gamma\tau_o r^2}{R_m^4 \rho p_o} \qquad (11)$$

Making the same assumptions as before, we would expect that

$$\frac{\overline{p_a^2}}{(\Delta f d/U_o)} \cdot \frac{(r/d)^2}{\sigma^{3/2}} = N\; G'(fd/U\sigma^{1/2}) \qquad (12)$$

Blake et al. were able to determine $S(\tau_0 f)$ for the case of noise due to cavitation on a hydrofoil using measured values of R_m. They assumed N equal to unity and found that Eq. (11) resulted in excellent collapse of the data.

Arndt (1978) used Eq. (12) to normalize cavitation data previously reported by Arndt and Keller (1976). These data correspond to noise from cavitation in the wake of a disk and were collected under a variety of conditions in both a water tunnel and in a depressurized towing tank. Both the level of dissolved gas and the number of free nuclei were monitored. As shown in Figure 13, the normalization is not very successful. It would appear that Eq. (10) would be more effective in taking all of the variables into account. However, n could only be measured in unison with acoustic observations in the water tunnel. Because of the nature of the laser scattering measurements used to determine n in the depressurized towing tank, these measurements had to be made separately from the acoustic measurements. The assumed form for $S(f\tau_o)$ in Eqs. (10) and (11) varies by a factor $nd^3/\sigma^{1/2}$. As an example, n in the depressurized towing tank appeared to be relatively constant and equal to about $15/cm^3$. Therefore the factor $nd^3/\sigma^{1/2}$ was found to have a maximum variation of 23 dB. This does not account for the scatter shown and one can only assume that there are other complicating factors. It should be emphasized that these data were collected under carefully controlled conditions. This underscores the fact that the current state of knowledge in this area is poor.

6. CONCLUSIONS

Cavitation inception in turbulent shear flows is the result of a complex interaction between an unsteady pressure field and a distribution of free stream nuclei. There is a dearth of data relating cavitation inception and the turbulent pressure field. What little information that is available indicates that negative peaks in pressure having a magnitude as high as ten times the root mean square

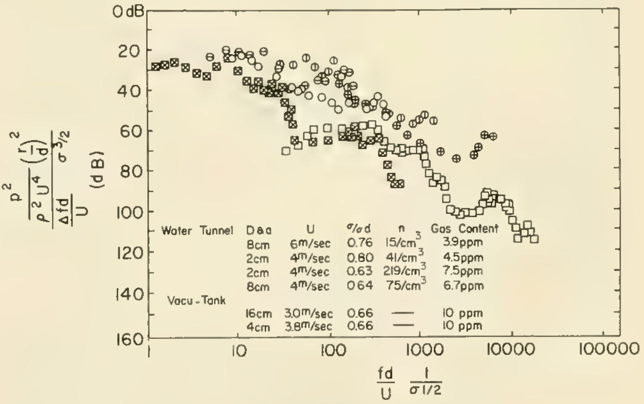

FIGURE 13. Normalized cavitation noise spectra.

pressure can excite cavitation inception. This fact alone indicates that consideration should be given to the details of the turbulent pressure field. The available evidence indicates that two basic factors related to the pressure field enter into the scale effects. First, as the scale of the flow increases, cavitation nuclei are relatively more responsive to a wider range of pressure fluctuations. Secondly, the available evidence indicates that large deviations from the mean pressure are more probable with increasing Reynolds number. This would explain some of the observed increases in cavitation index with physical scale. In view of the almost total lack of information on the statistics of turbulent pressure field (aside from some correlation and spectral data) and the potential importance of this knowledge to understanding cavitation, it is strongly recommended that careful experiments be initiated to remedy the situation. Such experiments have been proposed by George (1974b, 1975).

Direct application of the pressure field information to cavitation is unfortunately clouded by gas content effects which also increase the cavitation index with increasing exposure time. The fact that a reasonably precise scaling law for cavitation noise has not yet been found (perhaps a consequence of the lack of knowledge about the pressure field) further complicates interpretation of experiments and theory. Therefore it is also strongly recommended that the problem of the response of cavitation nuclei to turbulence receive particular attention. Such experiments have been proposed by Arndt (1978).

ACKNOWLEDGMENTS

R. E. A. Arndt gratefully acknowledges the support of the Air Force Office of Scientific Research and the Seed Research Fund of the St. Anthony Falls Hydraulic Laboratory. W. K. George gratefully acknowledges the support of the National Science Foundation under grants from the Engineering (Fluid Dynamics) and Atmospheric Sciences (Meterology) Programs and the Air Force Office of Scientific Research. Both authors are grateful to Mrs. Sandra Peterson who typed the manuscript.

REFERENCES

Arndt, R. E. A. (1974a). Cavitation inception and how it scales: a review of the problem with a summary of recent research. *Proc. Symposium on High Powered Propulsion of Ships*, Wageningen, The Netherlands, December (available from the Netherlands Ship Model Basin).

Arndt, R. E. A. (1974b). Pressure fields and cavitation. *Trans. 7th IAHR Symposium*, Vienna, September.

Arndt, R. E. A. (1976). Semi-empirical analysis of cavitation in the wake of a sharp edged disk. *J. of Fluids Engr.*, September.

Arndt, R. E. A. (1977). Cavitation and erosion: an overview. *Proc. Corrosion/77*, Natl. Assoc. of Corrosion Engineers, San Francisco, Calif.

Arndt, R. E. A. (1978). Investigation of the effects of dissolved gas and free nuclei on cavitation and noise in the wake of a sharp edged disk. *Proc. Joint IAHR/ASME/ASCE Symposium on Fluid Machinery*, Ft. Collings, Colorado.

Arndt, R. E. A., and J. W. Daily (1969). Cavitation in turbulent boundary layers. *Proc. of Symposium on Cavitation State of Knowledge*, ASME, 64-86.

Arndt, R. E. A., and A. T. Ippen (1967). Cavitation near surfaces of distributed roughness. *MIT Hydrodynamics Laboratory Report No. 104*.

Arndt, R. E. A., and A. T. Ippen (1968). Rough surface effects on cavitation inception, *J. of Basic Engr., Trans. ASME, Series D*, 249-261.

Arndt, R. E. A., and A. Keller (1976). Free gas content effects on cavitation inception and noise in a free shear flow. *Proc. IAHR Symposium on Two Phase Flow and Cavitation in Power Generation Systems*.

Baker, C. B., J. W. Holl, and R. E. A. Arndt (1976). The influence of gas content and polyethelene oxide additive upon confined jet cavitation in water. *ASME Polyphase Forum*, March.

Baiter, J. J. (1974). Aspects of cavitation noise. *Proc. Symposium on High Powered Propulsion of Ships*, Wageningen, The Netherlands, Dec.

Batchelor, G. K. (1951). Pressure fluctuations in isotropic turbulence. *Proc. Camb. Phil. Soc.*, *47*, 2; 359-374.

Batchelor, G. K. (1953). *The Theory of Homogeneous Turbulence*, Cambridge University Press.

Batchelor, G. K., and A. A. Townsend (1949). The nature of turbulence at large wavenumbers. *Proc. Royal Soc. (London)*, *A199*, 1057; 238-255.

Beuther, P., W. K. George, and R. E. A. Arndt (1977a). Modelling of pressure spectra in a turbulent shear flow. *93rd Meeting Acoustical Soc. of Amer.*, State College, June.

Beuther, P., W. K. George, and R. E. A. Arndt (1977b). Pressure spectra in a turbulent shear flow. *Bulletin Amer. Phys. Soc.*, *22*, 12, December.

Beuther, P., W. K. George, and R. E. A. Arndt (1977c). Pressure spectra in homogeneous isotropic turbulent flow. *Bulletin Amer. Phys. Soc.*, *22*, 12, December.

Blake, W. K., M. J. Wolpert, and F. E. Geib (1977). Cavitation noise and inception as influenced by boundary layer development on a hydrofoil. *J. Fluid Mech.*, *80*, Part 4, 617-640.

Bradshaw, P., (1967). Inactive motion and pressure fluctuations in turbulent boundary layers. *J. Fluid Mech.*, *30*, 241.

Chan, Y. Y. (1974a). Pressure sources for a wave model of jet noise. *AIAA J.*, *12*, 2.

Chan, Y. Y. (1974b). Spatial waves in turbulent jets. *Physics of Fluids*, *17*, 1.

Chan, Y. Y. (1976). Noise generated wavelike eddies in a turbulent jet. *ICAS* paper, No. 76-42.

Epstein, P. S., and M. S. Plesset (1950). On the stability of gas bubbles in liquid gas solutions. *J. Chem. Phys.*, *18*, 11, November, 1505-1509.

Fitzpatrick, H. M., and M. Strasberg (1956). Hydrodynamic sources of sound. *Proc. 1st Symposium on Naval Hydrodynamics*, Natl. Acad. of Sciences, Natl. Res. Council, Publication 515, September.

Fuchs, H. V. (1972a). Measurements of pressure fluctuations within subsonic turbulent jets. *J. Sound and Vib.*, *22*, 3.

Fuchs, H. V. (1972b). Space correlations of the fluctuating pressure in subsonic turbulent jets, *J. Sound and Vib.*, *23*, 1; 77-99.

Fuchs, H. V. (1974). Analysis of circumferentially coherent pressure fluctuations relevant to jet noise. *Colloquium on Coherent Structure in Turbulence*, Southampton.

Fuchs, H. V., and A. Michalke (1975). On turbulence and noise of an axisymmetric shear flow. *J. Fluid Mech., 70,* 1.

George, W. K. (1974a). The equilibrium range of turbulent pressure spectra, *Bull. of the Amer. Phys. Soc., 19,* 1158.

George, W. K. (1974b). Proposal to General Hydrodynamics Research.

George, W. K. (1975). Proposal to ONR, Fluid Dynamics Branch and presentation at David H. Taylor Naval Ship Research and Development Center, February.

Gurvich, A. A., and A. M. Yaglem (1967). Breakdown of eddies and probability distribution for small scale turbulence, *Phys Fluids, 10,* Supplement, S59-S65.

Heisinberg, W. (1948). Zur statistichen theorie den turbulenz. *F. Phisik, 124,* 7-12; 359-374.

Holl, J. W. (1960). An effect of air content on the occurrence of cavitation. *J. Basic Engr., Trans. ASME, Series D, 82,* 941-946.

Holl, J. W. (1969). Limited cavitation. *Proc. of the Symposium on Cavitation State of Knowledge,* ASME, June, 26-63.

Holl, J. W. (1970). Nuclei and cavitation. *Tran. ASME, J. of Basic Engr.,* December, 681-688.

Jones, B. G., R. J. Adrian, C. K. Nithianandan, and H. P. Planchen, Jr. (1977). Spectra of turbulent static pressure fluctuations in jet mixing layers, *AIAA Paper No. 77-1370.*

Keller, A. P. (1974). Investigations concerning scale effects of the inception of cavitation. *Proc. Conf. on Cavitation, Inst. of M. E.,* Heriot-Watt University, September.

Kermeen, R. W., and B. R. Parkin (1957). Incipient cavitation and wake flow behind sharp-edged disks. *Report 85-4,* Hydrodynamics Laboratory, California Institute of Tech., August.

Kim, H. T., S. J. Kline, and W. C. Reynolds (1971). The production of turbulence near a smooth wall in a turbulent boundary layer. *J. of Fluid Mech., 50,* 133.

Kolmogorov, A. N. (1962). A refinement of previous hypotheses concerning the local structure of turbulence in a viscous incompressible fluid at high Reynolds number. *J. Fluid Mech., 13,* 1; 82-85.

Kraichnan, R. H. (1956). Pressure fluctuations in turbulent flow over a flat plate. *J. Acoust. Soc. Amer., 28,* 3.

Lienhard, J. H., and C. D. Goss (1971). Influence of size and configuration on cavitation in submerged orifice flows. *ASME Paper No. 71-FE-39.*

Monin, A. S. and A. M. Yaglem (1975). *Statistical Fluid Mechanics: Mechanics of Turbulence,* Vol. II, MIT Press, Cambridge.

Obukov, A. M. (1949). Pressure fluctuations in a turbulent flow. *Dokl. Acad. Nauk., SSSR, 66,* 1; 17-20.

Plesset, M. S. (1949). The dynamics of cavitation bubbles. *J. of Applied Mech.,* September, 277-282.

Ross, D. (1976). *Mechanics of Underwater Noise,* Pergamon Press.

Rouse, H. (1953). Cavitation in the mixing zone of a submerged jet. *La Houille Blanche,* February.

Tennekes, H., and J. L. Lumley (1972). *A First Course in Turbulence.* MIT Press.

Willmarth, W. W. (1975). Pressure fluctuations beneath turbulent boundary layers. *Annual Review of Fluid Mech., 7,* Palo Alto, Calif.

Secondary Flow Generated Vortex Cavitation

Michael L. Billet
The Pennsylvania State University
State College, Pennsylvania

ABSTRACT

Secondary flow theories are employed to calculate the secondary vorticity near the inner wall of a rotor for several flow conditions. This calculated vorticity is used in a simple vortex model to calculate the minimum pressure coefficient of the resulting vortex behind the rotor. The influence of inflow velocity distributions on the generation of secondary vorticity is discussed. Comparisons are given between the calculated pressure coefficients and the measured cavitation indices of the vortex.

1. INTRODUCTION

Secondary flows generate additional streamwise vorticity when a boundary layer flow is turned by a rotor. The apparent effect of this additional vorticity is evidenced by the high cavitation numbers of the vortex formed downstream of the rotor plane. One example of the cavitation associated with a vortex can be found in the draft tube of a Francis turbine operating in the part load range. The cavitation depends directly on the square of the streamwise vorticity associated with the vortex. In most cases, the critical cavitation numbers typical of this vortex are often higher than those associated with any other type of rotor cavitation.

Previous experimental results have shown that a cavitation inception prediction of this vortex is a very difficult problem. All rotors operating with a wall boundary layer have a vortex along the inner wall. The appearance of this cavitating vortex varies from rotor to rotor. The critical cavitation number can vary as much as an order of magnitude. Small variations in the wall boundary layer can cause a significant change in the critical cavitation number.

Some confusion in cavitation inception data associated with this vortex is due to a confusion of types of cavitation, i.e., vaporous versus nonvaporous cavitation. Vortex flows tend to be good collectors of gas bubbles which can cause nonvaporous cavitation. This often leads to confusing nonvaporous for vaporous cavitation giving high cavitation numbers. In general, results indicate for vaporous limited cavitation that

$$\sigma_\ell \lesssim -C_{P_{min}}. \qquad (1)$$

Thus, the minimum pressure coefficient is of particular importance in a study of vortex cavitation inception.

It is appropriate then to find a simple description of the vortex in order to calculate its minimum pressure coefficient. Unfortunately, the vortex is composed of a finite number of vortex filaments and a difficulty arises in specifying this number. This is particularly difficult when the vortex exists in the low pressure region near the inner wall of the complicated flow behind a rotor. In this region, there are vortex filaments in the primary flow in addition to the secondary vortex filaments which can influence this vortex. The combined effect of these filaments is to induce a swirl velocity distribution, V_θ, which can be easily measured.

Some preliminary tests show that in many cases small changes in the incoming velocity profile near the inner wall cause large differences in the critical cavitation number of the vortex. Measurements of the primary flow field show only a change in downstream velocity profile near the inner wall. This is especially true if the rotor was designed to be unloaded near the inner wall. For these cases, changes in the critical cavitation number can be directly related to changes in the secondary vorticity near the rotor inner wall.

The secondary vorticity can roll-up into a vortex like flow in the blade passage or it can simply combine with other vortex filaments aft of the rotor to form a larger vortex flow. In either case, there will be a circulation and a characteristic dimension of the passage vorticity which will determine the critical cavitation number of the resulting vortex.

In this paper, a brief summary is given of the method for calculating the secondary vorticity in the blade passage with comparisons to flow field measurements. Initially, the primary flow field through the rotor had to be determined in order to calculate the passage secondary vorticity. This was accomplished by using a streamline curvature method. Flow field results are given in detail for one basic flow configuration so named Basic Flow No. 1. Comparisons between the calculated minimum pressure coefficients and measured critical cavitation indices are given for several basic flow configurations or inflow velocity distributions.

2. CALCULATION OF FLOW FIELD

Primary Flow Field

A schematic of the calculation procedure for the flow through a rotor is given in Figure 1. This outlines the iterative procedure for the calculations and indicates the point at which refinements to the deviation angle are necessary and where secondary flow calculations are employed.

It is important to realize that in this discussion the flow field is being solved for a given rotor configuration. For this case, the boundary conditions are (1) the geometric or metal angles of the blades, (2) the rpm of the rotor, (3) the velocity profile far upstream of the rotor plane, and (4) the bounding streamlines of the flow.

After solving for the bounding streamlines, the iterative calculation procedure is started by establishing the velocity profile far upstream of the rotor. The initial conditions (Step 1) to the solution for this boundary condition are (1) bounding streamtube and (2) velocity profile in rotor plane without rotor. With this information, the initial streamlines without rotor can be calculated using the streamline curvature equations (Step 2). The result of this calculation is the boundary condition of an initial velocity or energy profile at a station far upstream of the rotor plane.

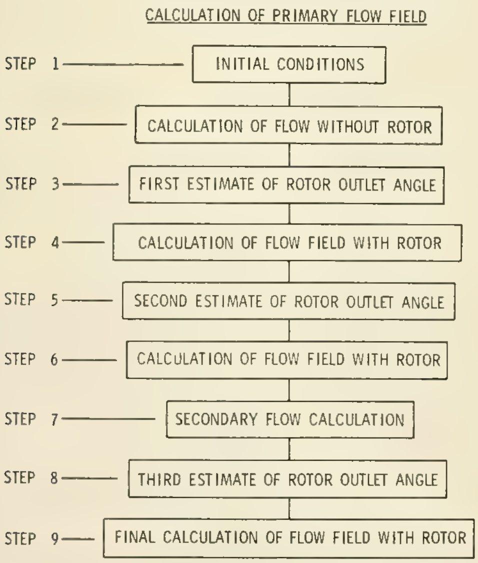
CALCULATION OF PRIMARY FLOW FIELD
STEP 1
INITIAL CONDITIONS
STEP 2
CALCULATION OF FLOW WITHOUT ROTOR
STEP 3
FIRST ESTIMATE OF ROTOR OUTLET ANGLE
STEP 4
CALCULATION OF FLOW FIELD WITH ROTOR
STEP 5
SECOND ESTIMATE OF ROTOR OUTLET ANGLE
STEP 6
CALCULATION OF FLOW FIELD WITH ROTOR
STEP 7
SECONDARY FLOW CALCULATION
STEP 8
THIRD ESTIMATE OF ROTOR OUTLET ANGLE
STEP 9
FINAL CALCULATION OF FLOW FIELD WITH ROTOR

FIGURE 1. Schematic of calculation procedure for primary flow field.

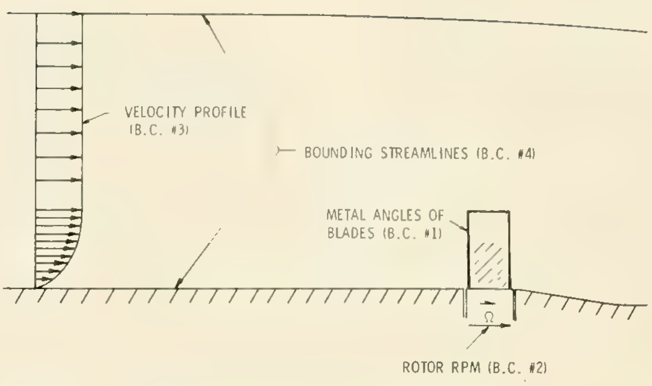
VELOCITY PROFILE (B.C. #3)
BOUNDING STREAMLINES (B.C. #4)
METAL ANGLES OF BLADES (B.C. #1)
Ω
ROTOR RPM (B.C. #2)

FIGURE 2. Schematic of boundary conditions.

Knowing the blade metal angles, the first estimate of the flow outlet angles (Step 3) can be calculated. These flow outlet angles depend on the blade metal angles and on a deviation angle. The deviation angle correlation developed by Howell as discussed in Horlock (1973) is initially applied. This relationship considers only thin blade sections and assumes that each blade section operates near design incidence. As shown in Figure 2, all of the boundary conditions are now known and the flow field can be solved with the rotor included (Step 4) by using the streamline curvature equations [McBride (1977)].

Once a converged solution is obtained for the flow field using Howell's deviation angles (Step 4), the axial velocity distribution is known whereby the inlet angles can be estimated in addition to the acceleration through the rotor. Now a second estimate of the rotor outlet angles (Step 5) can be made. For this deviation angle, the effects of acceleration, $\Delta\delta'$, blade camber, δ_0, and blade thickness, $\Delta\delta^*$, are calculated separately. For the calculation of the deviation term due to axial acceleration through the rotor, an equation developed by Lakshminarayana (1974) is applied. For the calculation of deviation terms due to camber and thickness effects, the data obtained by the National Aeronautics and Space Administration [Lieblein (1965)] are used. The result is an improved outlet flow angle profile which can be used to again calculate the flow field (Step 6).

The converged solution of the flow field (Step 6) is then used to solve the secondary vorticity equations (Step 7) and to determine a deviation term, $\Delta\delta_s$, which is due to nonsymmetric flow effects. The details of the secondary flow calculations will be discussed later in this paper. An improved outlet flow angle profile (Step 8) is obtained by adding this secondary flow term to the deviation terms thus far calculated to obtain

$$\beta_2^* = \beta_2 - \Delta\delta' + \Delta\delta^* + \delta_0 + \Delta\delta_s \quad , \qquad (2)$$

where β_2^* is the outlet flow angle and β_2 is the blade metal outlet angle. This outlet flow angle distribution is then used as a boundary condition in the calculation of the flow field (Step 9).

Finally, all of the deviation angle calculations are checked based on the flow field calculated in Step 9. If the angles did not change significantly then the result obtained in Step 9 is used as the final flow field.

In all, twenty-eight streamlines were calculated

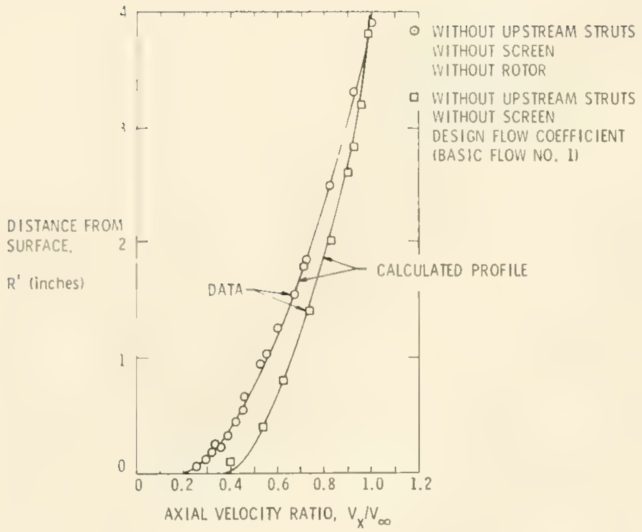

FIGURE 3. Comparison between velocity profile with/without rotor.

through the rotor with the first streamline being at the inner wall and the last streamline going through the rotor tip. The streamlines were spaced more closely near the inner wall because the secondary flow calculations are most important near the wall. Also, the streamline curvature equations are inviscid so that there is a finite velocity at the inner wall streamline.

A sample of the calculations for the flow field is given in Figures 3,4, and 5 for the flow configuration called Basic Flow No. 1. For Basic Flow No. 1, the boundary layer entering the rotor is axisymmetric with no upstream distribution such as screens or struts forward of the rotor which is operating at its design flow coefficient. In Figure 3, the calculated axial velocity profile in the plane of the rotor without the rotor and the calculated axial velocity profile in front of the rotor with the rotor operating on design is shown. In addition, experimental data measured in the 48-inch water tunnel by a LDA system are given for a comparison. In Figure 4, the calculated outlet velocity profiles are shown with comparison to measured data. Finally, Figure 5 shows the calculated and measured tangential velocity, component, V_θ, downstream of the rotor plane where cavitation occurs under certain flow conditions. In general, the flow field calculations show very good agreement with the experimental data.

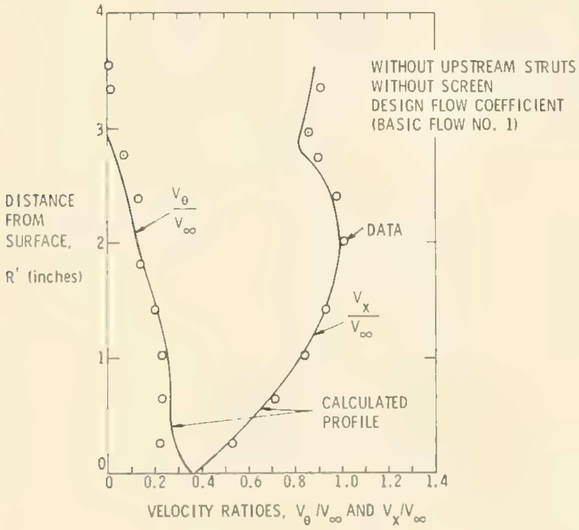

FIGURE 4. Rotor outlet velocity profiles for basic flow no. 1.

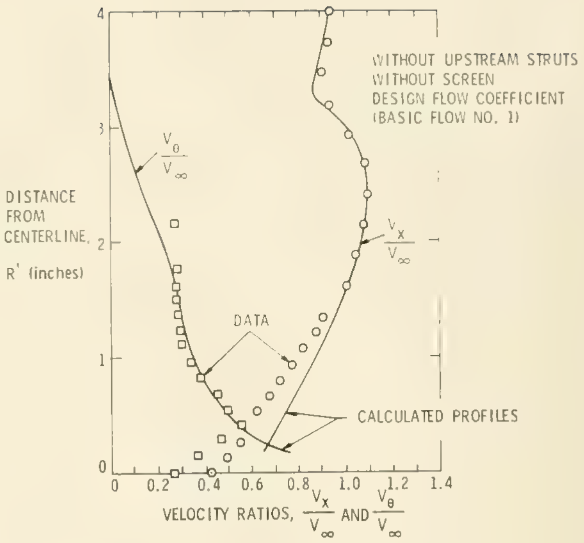

FIGURE 5. Tangential and axial velocity profiles at cap.

Secondary Flow Field

The major equations used in the streamline curvature method for calculation of the flow field were derived from the principles of conservation of mass, momentum, and energy. The fluid was assumed to be incompressible, inviscid, and steady. In addition, the flow field was assumed to be axisymmetric.

The resultant equations allow for streamline curvature and for vorticity in the flow. However, it is important to realize that the solution to the flow field does not contain all of the vorticity. In particular, only the circumferential vorticity is totally included. The other components of vorticity contain derivatives with respect to the circumferential direction which are assumed to be zero. As discussed by Hawthorne and Novak (1969), the neglected vorticity terms can be related to the secondary flows that occur in the blade passage along the inner wall.

Using the generalized vorticity equations, Lakshminarayana and Horlock (1973) derived a set of incompressible vorticity equations valid for a rotor operating with an incoming velocity gradient. Their expressions for the absolute vorticities, ω_s', ω_n', defined along relative streamlines, s', n', were modified for the boundary conditions imposed by this problem and were integrated. The resulting equations are

$$\omega_{n_2}' = \omega_{n_1}' \cdot \frac{W_1 \; a_{b_1}'}{W_2 \; a_{b_2}'} \qquad (3)$$

and

$$\omega_{s_2}' = W_2 \int_1^2 \frac{2\omega_n'}{WR'}\, ds' + W_2 \int_1^2 \frac{2\Omega_b'\omega_n'}{W^2}\, ds' - W_2 \int_1^2 \frac{2\Omega_n'\omega_b'}{W^2}\, ds' + \omega_{s_1}' \left\{\frac{W_2}{W_1}\right\} \qquad (4)$$

where the primes refer to a rotating frame of reference and the subscripts, 1, 2, refer to computing stations along a streamline within the rotor. As shown in Figure 6, s', n', b' represent the natural coordinates for the relative flow, W is the relative velocity, ω_s' and ω_n' are absolute vorticity resolved along the relative streamline, s', and the principal normal direction, n', Ω is the rotor rotation vector, and R' is the radius of curvature of the relative streamline.

The means by which the streamwise component of vorticity is produced in this relative flow are similar to those discussed by many investigators for a stationary system. However, it is important to note that additional secondary vorticity is generated when $\vec{\Omega} \times \vec{W}$ has a component in the relative streamwise direction. Rotation has no effect when the absolute vorticity vector lies in the s'-n' plane and the rotation, $\vec{\Omega}$, has no component in the binormal direction, $\vec{b}'$.

These equations were employed to calculate the secondary vorticity along a relative streamline through the rotor. All of the quantities in the equations were calculated by an iterative procedure using the primary flow calculations. The initial normal component of absolute vorticity, ω_{n1}, for a streamline was calculated from the incoming axial velocity profile to the rotor. In all, the vorticity along twenty-eight streamlines was calculated.

As an example, Figure 7 shows the importance of each term in Eq. 4 in the rotor exit plane for Basic Flow No. 1. The sum of these terms is given in Figure 8. The secondary passage vorticity is the difference between the exit vorticity, ω_{s_2}', and the inlet vorticity, ω_{s_1}', along a streamline.

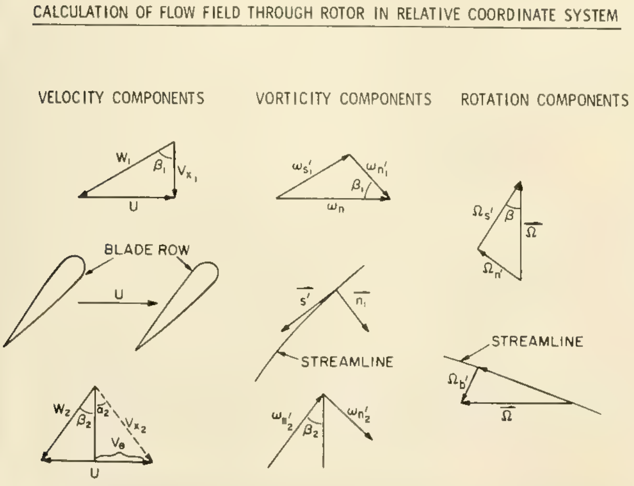

FIGURE 6. Description of relative coordinate system.

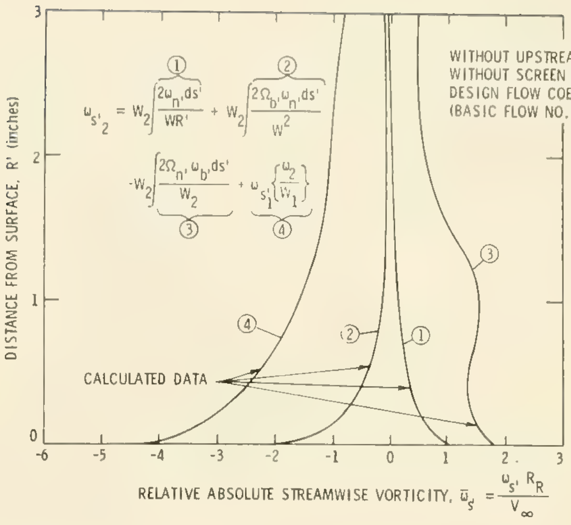

FIGURE 7. Streamwise passage vorticity for basic flow no. 1.

The effect of this additional vorticity, $\omega_{s_2}' - \omega_{s_1}'$, is to induce secondary velocities which are assumed to occur at the exit plane of the rotor. It is important to note that the normal component of vorticity, ω_{n_2}', is accounted for in the axisymmetric flow analysis. Thus, only streamwise secondary vorticity calculated as a function of radius influences the flow field.

The effect of the streamwise component of vorticity within the blade passage is similar to that obtained in the flow through a curved duct [Hawthorne, (1961), Eichenberger, (1953)]; however, there is the difficulty of devising a reasonable approximate method of satisfying the Kutta-Joukowski condition at the exit of the rotor. The method used in this investigation assumes that the flow is contained in a duct defined by the blades and streamlines of the primary flow leaving the exit of each blade. In this exit plane, a flow solution devised by Hawthorne and Novak (1969) was applied. The secondary stream-

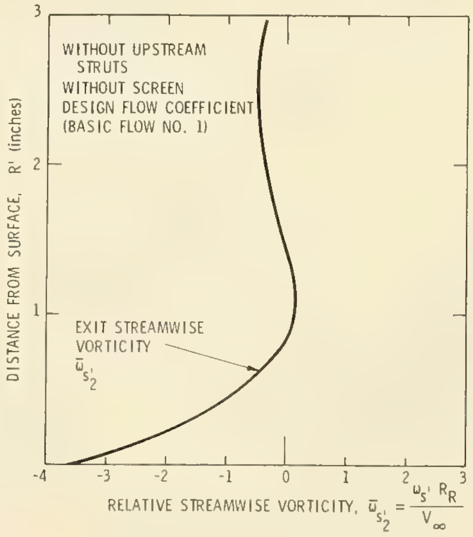

FIGURE 8. Relative passage streamwise vorticity at rotor exit plane for basic flow no. 1.

wise vorticity was divided into tangential and axial components whereby the former, $(\omega_{s_2}'-\omega_{s_1}')\sin\beta_2$, causes a radial gradient of axial velocity and the latter leads to an equation for a stream function describing the radial and tangential velocities in the exit plane, r,θ.

The form of the secondary stream function equation is

$$\nabla^2\Psi(r,\theta) = \frac{\partial\Psi^2}{\partial r} + \frac{1}{r}\frac{\partial\Psi}{\partial r} + \frac{1}{r^2}\frac{\partial^2\Psi}{\partial\theta^2} = \frac{v_x}{r^2}\frac{d}{dr}(r\tan\beta_2^*)$$

$$- (\omega_{s_2}'-\omega_{s_1}')\sec\beta_2^* \quad = F(r). \qquad (5)$$

where v_x is the secondary axial velocity and is obtained from the solution of the tangential component of streamwise vorticity. The solution to Eq. (5) was found by applying standard differential techniques. The solution and the necessary boundary conditions will not be discussed in this brief paper.

The deviation angle due to the secondary flow can be calculated using

$$\Delta\delta_s = -\frac{N\cos^2\beta_2^*}{2\pi V_x}\int_0^{2\pi/N}\frac{\partial\Psi}{\partial r}\,dr \qquad (6)$$

where N is the number of blades and Ψ is obtained from the solution of Eq. (5). The axial velocity, V_x, and outlet angle, β_2^*, are determined in the calculation of the primary flow field.

The results of the secondary flow calculations for various basic flows indicate that the effects are significant only near the inner wall where the incoming vorticity is the largest. The deviation angles calculated for Basic Flow No. 1 are shown in Table 1.

TABLE 1. Deviation Angles for Basic Flow No. 1

Normalized Distance from Surface R/R_R	Deviation Angles $\Delta\delta_s$
0.00	-5.4°
0.04	-2.9°
0.14	-1.0°
0.24	$<0.2^\circ$
0.34	
0.44	
0.54	
0.64	

3. CAVITATION EXPERIMENTS

The cavitation experiments were conducted in the 48-inch diameter water tunnel located in the Garfield Thomas Water Tunnel Building of the Applied Research Laboratory at The Pennsylvania State University. In all cases, desinent cavitation was employed as the experimental measure of the critical cavitation number. The cavitation in the vortex system occurred on the rotor cap. Also, the occurrence of the cavitation was very sporadic.

The air content of 3.1 ppm was chosen for all of the cavitation experiments because gas effects are reduced and the relative saturation level was always much less than unity. Desinent cavitation number data were obtained for different incoming velocity profiles to the rotor. The incoming velocity profile was varied by changes in the configuration of the upstream surface in addition to varying the rotor flow coefficient. Results were obtained with/without upstream struts, with/without a screen on the upstream surface, and on/off design rotor flow coefficients. In all, there were sixteen different flow configurations or Basic Flow Nos. tested.

Figures 9-11 display the effects on the desinent cavitation number over a range of velocities due to variations in the inflow velocity distribution. In general, the cavitation number increased for increasing free stream velocity for all flow configurations shown. As shown in Figure 9, the addition of upstream struts which consisted of four struts placed at the 0°, 90°, 180°, 270° points on the upstream surface caused the cavitation number to

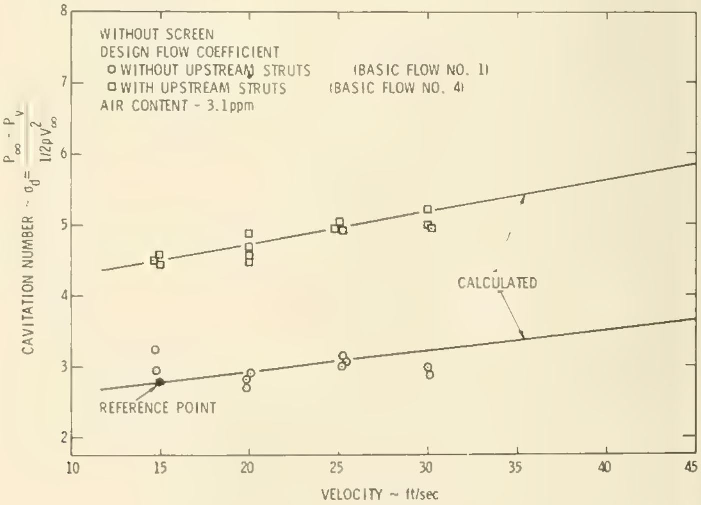

FIGURE 9. Correlation with cavitation data for basic flow nos. 1 and 4.

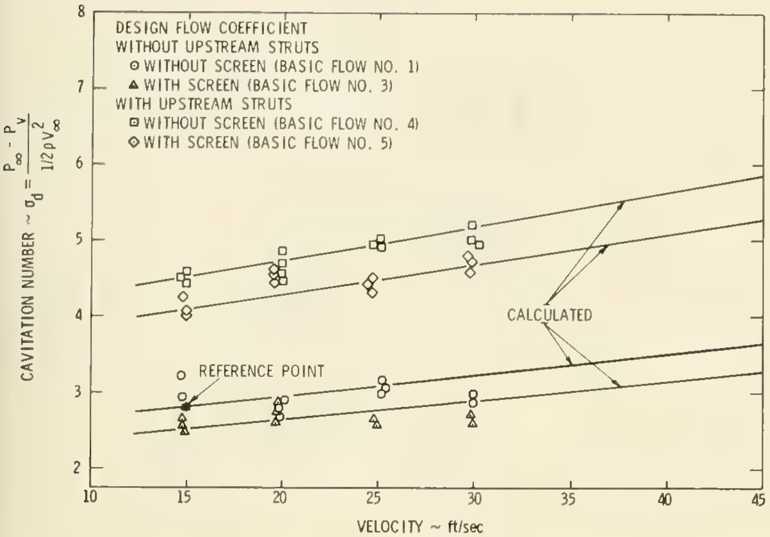

FIGURE 10. Correlation with cavitation data for basic flow nos. 1, 3, 4, and 5.

increase. In contrast to this result, the addition of upstream screens causes the cavitation number to decrease as shown in Figure 10. Data in Figure 11 show that a decrease in the flow coefficient by 10% causes a dramatic increase in the cavitation number, whereas a 10% increase in the flow coefficient causes the opposite trend which is not shown in the figures. Additional cavitation results are given in Billet (1976).

4. CORRELATION OF SECONDARY FLOWS WITH THE CRITICAL CAVITATION NUMBER

Because of the complicated flow field where the vortex exists, an absolute calculation of Cp_{min} of the cavitating region would be very difficult. The minimum pressure associated with the cavitation occurs within the vortex which is located along the inner wall. This minimum pressure is not only determined by the vorticity associated with the vortex but also by the location of the vortex in the primary flow field.

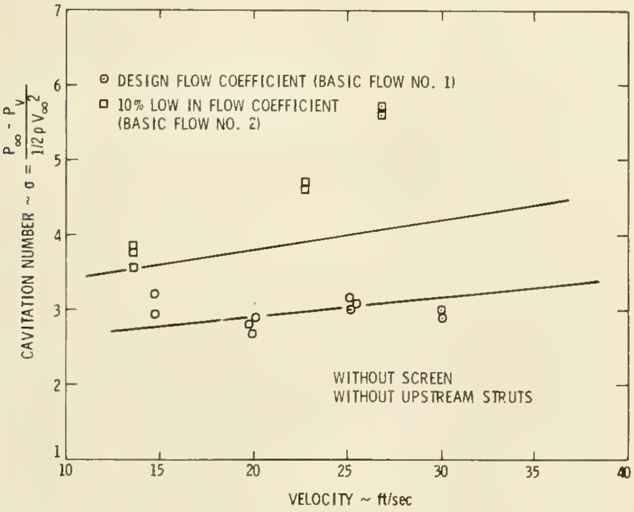

FIGURE 11. Correlation with cavitation data for basic flow nos. 1 and 2.

Considering only the vortex, there are many factors which can influence the minimum pressure coefficient. If one models a vortex by a simple rotational core combined with an irrotational outer flow, the Cp_{min} is found to be

$$Cp_{min} = -2\left\{\frac{\Gamma}{2\pi r_c V_\infty}\right\}^2 \tag{7}$$

where Γ is the circulation and r_c is the radius of the core. Thus, the factors which influence Cp_{min} are those which influence the circulation or core size.

Assuming that secondary flows control the vortex, Eq. (7) can be used to predict changes in critical cavitation number due to changes in the secondary vorticity produced along the inner wall. Therefore, Eq. (7) can be arranged into the form

$$\frac{Cp_{min_A}}{Cp_{min_B}} = \frac{\left[\frac{\Gamma}{r_c V_\infty}\right]_A^2}{\left[\frac{\Gamma}{r_c V_\infty}\right]_B^2} \tag{8}$$

where Γ is now the integrated component of streamwise passage vorticity and r_c is approximated by the characteristic dimension of the resulting passage vorticity. The letters A and B refer to different flow states.

The passage streamwise vorticity was calculated along several mean streamlines in the blade passage by the method outlined in this paper for four basic flow configurations which are described in the left hand column of Table 2. For all flow configurations considered, the results show a large amount of streamwise vorticity at the rotor exit plane near the inner wall. An example of the exit streamwise passage vorticity is shown in Figure 8 for Basic Flow No. 1.

As can be seen in Figure 8, the vorticity near

TABLE 2 - Vortex Circulation and Core Size Calculated Flow Vorticity Data

Basic Flows	Circulation Γ (in^2/sec)	Characteristic Dimension R_c (inch)	Nondimensional Ratio ($\Gamma/r_c V_\infty$)	Planar Momentum Thickness θ (inch)
Basic Flow No. 1				
without upstream struts without screen design flow coefficient	- 11.64	0.81	-0.080	0.85
Basic Flow No. 2				
without upstream struts without screen 0.9 design flow coefficient	- 8.23	0.57	-0.091	0.71
Basic Flow No. 3				
without upstream struts with screen design flow coefficient	- 10.99	0.20	-0.076	0.94
Basic Flow No. 4				
with upstream struts without screen design flow coefficient	- 8.29	0.45	-0.102	1.01

the inner wall has a characteristic dimension associated with it. A measure of the circulation associated with this vorticity can be found by integrating the vorticity from the inner wall to the radius where the vorticity changes sign. In addition, the characteristic dimension of the passage streamwise vorticity must be related to the difference between the radius where the vorticity changes sign and the inner wall radius. The results for several basic flow configurations are shown in Table 2. Also, the nondimensional ratio, $\Gamma/r_c V_\infty$, which is a measure of the minimum pressure coefficient of the vortex is given in addition to the planar momentum thickness of the mean boundary layer profile entering the rotor for each flow configuration.

In order to make absolute comparisons between calculated minimum pressure coefficients and cavitation data, a reference point is necessary and the effect of Reynolds number must be calculated. A reference point for Basic Flow No. 1 of $\sigma = 2.8$ at a velocity of 15 ft/sec was chosen. The influence of Reynolds number was determined by solving for the relative streamwise vorticity at two different free stream velocities. For these calculations, a boundary layer profile at the reference Reynolds number was used in one calculation and the boundary layer profile at three times the reference number was used in the other calculation.

Now using Eq. (8) with Basic Flow No. 1 as the reference point, comparisons between cavitation data and Cp_{min} calculated using the passage streamwise vorticity can be made. Some of the results are shown in Figures 9, 10, and 11. As can be noted, the changes in Cp_{min} or σ for the vortex as calculated, using secondary flow theory, correlate well with the cavitation results. Only the correlation with the rotor operating off-design (Basic Flow No. 2) is poor at the higher velocities. It is felt that this is due to primary flow problems.

5. SUMMARY

A secondary flow analysis has been developed which can be employed to assess the effect of inflow velocity distribution on the strength and core size of a vortex. This analysis has been successfully applied to a rotor where the secondary flows dominate the flow field near the inner wall.

NOMENCLATURE

a_b' - streamline spacing in bi-normal direction
R_R - radius of rotor
W - relative velocity
β_2 - relative outlet metal angle
β_2^* - relative outlet air angle
$\Delta\delta'$ - deviation angle due to axial velocity acceleration
$\Delta\delta_s$ - deviation angle due to secondary flows
σ_o - deviation angle due to blade camber
σ - cavitation number $\equiv (P_\infty - P_v)/(1/2\rho V_\infty^2)$
σ_ℓ - limited cavitation number
σ_d - desinent cavitation number
ω_s' - component of absolute vorticity vector in relative streamwise direction
ω_n' - component of absolute vorticity vector in relative normal direction
ω_b' - component of absolute vorticity vector in relative bi-normal direction
Ω_n' - component of rotation vector in relative normal direction
Ω_b' - component of rotation vector in relative bi-normal direction

ACKNOWLEDGMENT

This research was carried out under the Naval Sea Systems Command General Hydromechanics Research

Program, subproject SR 023 01 01, administered by the David W. Taylor Naval Ship Research and Development Center, Contract N0001773-C-1418.

REFERENCES

Billet, M. L. (1976). Cavitation results for a secondary flow generated trailing vortex. *Applied Research Laboratory TM 76-234.*

Eichenberger, H. (1953). *J. Math. and Phys. 32;* 34.

Hawthorne, W. R. (1961). *Proc. Seminar Aero. Sci.,* Bangalore, India, 305.

Hawthorne, W. R., and R. A. Novak (1969). The aerodynamics of turbo-machinery. *Ann. Rev. Fluid Mechanics 1;* 341.

Horlock, J. H. (1973). *Axial Flow Compressors,* R. E. Krieger Company, New York, 55-60.

Lakshminarayana, B. (1974). Discussion of Wilson, Mani, and Acosta - A note on the influence of axial velocity ratios on cascade performance. *NASA SP-304,* 127.

Lakshminarayana, B., and J. H. Horlock (1973). Generalized expressions for secondary vorticity using intrinsic coordinates. *J. Fluid Mech. 59;* 97.

Lieblein, S. (1965). Experimental flow in two-dimensional cascades. *NASA SP-36,* 209.

McBride, M. W. (1977). A streamline curvature method of analyzing axisymmetrical axial, mixed, and radial flow turbomachinery. *Applied Research Laboratory TM 77-219.*

On the Linearized Theory of Hub Cavity with Swirl

G. H. Schmidt
Technical University of Delft
and
J. A. Sparenberg
University of Groningen
The Netherlands

ABSTRACT

In general, there is a cavity astern of the hub of a ship screw. This cavity is rather stable and is roughly in the shape of a long circular cylinder. There is circulation about it, which occurs in the case of a real screw propeller, when the circulation around the blades at their roots is nonzero. Because the divergence of the vorticity field is zero, this circulation at the roots "flows" downstream in the form of circulation about the hub. At the end of the hub the flow contracts and the swirl velocity increases. The pressure becomes lower and a cavity forms where the pressure decreases to the vapor pressure.

We introduce the following simplifications: First, we neglect the influence of the finite number of blades and consider a half infinite axially symmetric hub immersed in an inviscid and incompressible fluid. The incoming flow consists of a homogeneous part, parallel to the axis of the hub in the direction of the endpoint, and of a swirl which represents the circulation around the hub. In the upstream direction the hub tends to a circular cylinder while its radius tends to zero towards the end point. Second, our theory will be linear: The difference between the radius of the hub and the radius of the cavity is assumed to be small and quantities which are quadratic in this difference will, in general, be neglected.

Using these simplifications we determine the shape of the cavity for given values of, for instance, the swirl, the incoming velocity, the ambient pressure, and the vapor pressure. The surface tension is also included in the general formulation of the problem. The more detailed considerations, as well as the numerical calculations, will be confined to zero surface tension.

One of the unknowns of the problem is the position of the point of separation. This position can be determined by demanding that the pressure exceeds the vapor pressure everywhere on the wetted surface of the hub and by demanding that the flow cannot penetrate the surface of the hub.

The shape of the cavity is roughly a circular cylinder. There are waves on the surface of this cylinder which are, within the limitations of our theory, steady with respect to the hub, and their crests and throughs are perpendicular to the axis of the hub. We will give numerical results for the wavelengths and amplitudes of the waves as functions of, for instance, the incoming velocity and of the shape of the hub.

1. INTRODUCTION

A long cavity generally begins somewhere at the end of the hub of a ship screw. This cavity, which has circulation around it, does not close or widen, it has a rather stable mean value to its radius. The circulation or swirl occurs in the case of a real screw propeller when the circulation around the blades at their roots is not zero. Because the divergence of the vorticity field is zero, this circulation at the roots "flows" downstream in the form of circulation about the hub and then about the cavity.

In order to gain some insight in this phenomenon we introduce some simplifications. We neglect the influence of the finite number of blades and consider a half infinite axially symmetric hub immersed in an inviscid and incompressible fluid. The incoming flow consists of a homogeneous part parallel to the axis of the hub in the direction of the endpoint and of a swirl which represents the circulation around the hub. In the upstream direction the hub tends to a circular cylinder while its radius tends to zero towards the end point. Hence, near the endpoint the flow contracts and the swirl velocity increases proportional to the inverse of the radius. This means that the pressure becomes lower and a cavity starts where the pressure decreases to the vapor pressure of the fluid. Another approximation is that our theory will be linear. In order for this theory to be valid it is necessary that there be no abrupt changes in radius of the hub and cavity. In real fluids the viscosity can have an important influence on the point of separation [Wu (1972)], however, this effect is too complicated to be treated by our method. We will not take into account the dependence of the local vapor pressure on the curvature of the interface between vapor and liquid. Surface tension is included in the general formulation of the problem. The more detailed considerations, as well as the numerical calculations, will be confined to zero surface tension.

One of the unknowns of the problem is the value of the axial coordinate of the point of separation. This value can be determined by demanding that there is no place at the wetted area where the pressure is lower than the prescribed pressure in the cavity and by demanding that the flow cannot penetrate the surface of the hub.

The problem is very similar to the shrink fit problem, in the theory of elasticity, of an unbounded elastic medium with a circular two-sided infinite hole [Sparenberg (1958)]. This hole is occupied by a half infinite axially symmetric rigid body and the problem is to calculate the contact pressure between the body and surrounding medium when for instance shear stresses are supposed to be zero. Also, in this case, the edge of the region of contact has to be determined.

The way in which we solve our problem is analogous to the way in which the aforementioned elastic problem can be solved. First we determine a Green function. This is, in our case, the deformation of the two-sided infinite cavity with swirl when a rotationally symmetric pressure of a Dirac δ function type is applied at the circular cylindrical wall. By using this Green function as a kernel we can write down a Wiener-Hopf integral equation for the unknown contact pressure causing the fluid flow along the hub. This integral equation is solved numerically by the finite element method.

2. EQUATIONS OF MOTION AND BOUNDARY CONDITIONS

First we consider a two-sided infinite circular undisturbed cavity of radius r_c, with swirl in an inviscid and incompressible fluid of density ~ρ.

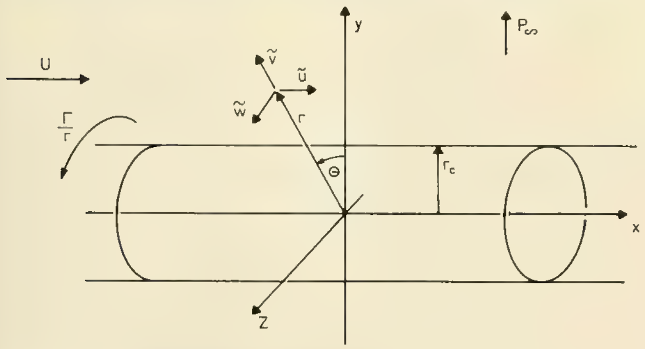

FIGURE 1. Undisturbed cavity flow.

The undisturbed velocity field and pressure field are

$$\tilde{u} = U,\ \tilde{v} = 0,\ \tilde{w} = \frac{\Gamma}{r},\ \tilde{p} = p_o(r),\ r \geq r_c, \tag{1}$$

where $\tilde{u}$, $\tilde{v}$, and $\tilde{w}$ are the velocity components in the x, r, and θ direction, $\tilde{p}$ is the pressure, and Γ is 2π times the circulation around the axis. From Bernoulli's equation it follows that

$$p_o(r) = p_\infty - \rho\Gamma^2/2r^2 \tag{2}$$

p_∞ is the ambient pressure in the fluid and $p_o(r) \to p_\infty$ for $r \to \infty$. On the wall of the cavity for $r \to r_c$ we have

$$p_o(r_c) = p_\infty - \rho\Gamma^2/2r_c^{\,2} = p_c - \rho\sigma/r_c \tag{3}$$

where p_c is the pressure inside the cavity and ρσ is the surface tension of the fluid. In the following we assume

$$p_\infty - p_c > 0 \tag{4}$$

hence, the ambient pressure at infinity is larger than the pressure in the cavity. From (3) it follows

$$r_c = \frac{-\rho\sigma + \sqrt{\rho^2\sigma^2 + 2\,\rho\Gamma^2\,(p_\infty - p_c)}.}{2\,(p_\infty - p_c)} \tag{5}$$

We had to choose the positive root under the assumption (4). For $(p_\infty - p_c) < 0$ we would have chosen the negative root, however, this would yield an unstable situation. In the case of zero surface tension (5) simplifies to

$$r_c = \Gamma\sqrt{\rho/2(p_\infty - p_c)} \tag{6}$$

The equations of motion for a time dependent fluid flow are

$$\frac{\partial\tilde{u}}{\partial t} + \tilde{u}\,\frac{\partial\tilde{u}}{\partial x} + \tilde{v}\,\frac{\partial\tilde{u}}{\partial r} = -\frac{1}{\rho}\frac{\partial\tilde{p}}{\partial x}\ , \tag{7}$$

$$\frac{\partial\tilde{v}}{\partial t} + \tilde{u}\,\frac{\partial\tilde{v}}{\partial x} + \tilde{v}\,\frac{\partial\tilde{v}}{\partial r} - \frac{\tilde{w}^2}{r} = -\frac{1}{\rho}\frac{\partial\tilde{p}}{\partial r}\ , \tag{8}$$

$$\frac{\partial\tilde{w}}{\partial t} + \tilde{u}\,\frac{\partial\tilde{w}}{\partial x} + \tilde{v}\,\frac{\partial\tilde{w}}{\partial r} + \frac{\tilde{v}\tilde{w}}{r} = 0\ . \tag{9}$$

Also, we have to satisfy

$$\operatorname{div}(\tilde{u},\ \tilde{v},\ \tilde{w}) = \frac{\partial\tilde{u}}{\partial x} + \frac{\partial\tilde{v}}{\partial r} + \frac{\tilde{v}}{r} = 0. \tag{10}$$

For a disturbed motion which satisfies (7)...(10) it remains true that (1)

$$\tilde{w} = \frac{\Gamma}{r}\ , \tag{11}$$

otherwise a circular contour floating with the fluid would change its circulation which is impossible when external force fields inside the fluid are absent. This follows also from (9) which is satisfied by (11). Hence substituting (11) into (7), ...(10) we are left with the following three equations for the three unknown functions $\tilde{u}$, $\tilde{v}$, and $\tilde{p}$,

$$\frac{\partial \tilde{u}}{\partial t} + \tilde{u}\frac{\partial \tilde{u}}{\partial x} + \tilde{v}\frac{\partial \tilde{u}}{\partial r} = -\frac{1}{\rho}\frac{\partial \tilde{p}}{\partial x} , \qquad (12)$$

$$\frac{\partial \tilde{v}}{\partial t} + \tilde{u}\frac{\partial \tilde{v}}{\partial x} + \tilde{v}\frac{\partial \tilde{v}}{\partial r} = -\frac{1}{\rho}\frac{\partial \tilde{p}}{r} + \frac{\Gamma^2}{r^3} \qquad (13)$$

$$\frac{\partial \tilde{u}}{\partial x} + \frac{\partial \tilde{v}}{\partial r} + \frac{\tilde{v}}{r} = 0 \quad . \qquad (14)$$

We now linearize these equations with respect to the undisturbed swirl flow,

$$\tilde{u} = U + u,\ \tilde{v} = v,\ \tilde{p} = p_o + p, \qquad (15)$$

where the perturbation quantities u(x,r,t), v(x,r,t), and p(x,r,t,) are supposed to be of $O(\varepsilon)$. Substituting (15) into (12)...(14), neglecting terms of $O(\varepsilon^2)$ and using (2) we find

$$\frac{\partial u}{\partial t} + U\frac{\partial v}{\partial x} = -\frac{1}{\rho}\frac{\partial p}{\partial x} , \qquad (16)$$

$$\frac{\partial v}{\partial t} + U\frac{\partial v}{\partial x} = -\frac{1}{\rho}\frac{\partial p}{\partial r} , \qquad (17)$$

$$\frac{\partial u}{\partial x} + \frac{\partial v}{\partial r} + \frac{v}{r} = 0 \qquad (18)$$

Because the (u, v) velocity field is without rotation we can write

$$(u,\ v) = (\frac{\partial \phi}{\partial x} , \frac{\partial \phi}{\partial r}) \qquad (19)$$

where $\phi = \phi(x, r, t)$ is a scaler potential function satisfied by (18)

$$\frac{\partial^2 \phi}{\partial x^2} + \frac{\partial^2 \phi}{\partial r^2} + \frac{1}{r}\frac{\partial \phi}{\partial r} = 0 \ . \qquad (20)$$

We now suppose the disturbed cavity wall to be at

$$r = r_c + \delta r_c , \qquad (21)$$

where $\delta r_c(x, t)$ is $O(\varepsilon)$. On this axial symmetric boundary we demand the difference between the pressures inside the cavity and in the fluid to be in equilibrium with the effect of the surface tension and with some still unspecified external normal loading $\rho U^2 f(x, t)$ of the cavity wall,

$$\tilde{p} = p_c - \sigma\rho \ (\frac{1}{R_1} + \frac{1}{R_2}) + \rho U^2 f(x,t) ,\ r = r_c + \delta r_c , \ (22).$$

where R_1 and R_2 are the principle radii of curvature of the boundary, reckoned positive when the centers of curvature are at the side of the cavity.

Within the accuracy of our linearized theory we can put

$$R_1 = r_c + \delta r_c , \qquad R_2 = -\left(\frac{\partial^2}{\partial x^2}\ \delta r_c\right)^{-1} \qquad (23)$$

Substituting (23) into (22) and using (2) and (15) we find

$$p_\infty - (\rho\Gamma^2/_2 r^2) + p = p_c - \sigma\rho \ (\frac{1}{r} - \frac{\partial^2}{\partial x^2}\ \delta r_c) + \rho U^2 f ,$$

$$r = r_c + \delta r_c . \qquad (24)$$

Expanding the functions of r in (24) with respect to δr_c, neglecting second order quantities, and using (3) the boundary condition (24) changes into

$$p(x,\ r_c,\ t) = (-\frac{\rho\Gamma^2}{r_c^{\ 3}} + \frac{\sigma\rho}{r_c^{\ 2}})\delta r_c + \sigma\rho \frac{\partial^2}{\partial x^2}\ \partial r_c + \rho U^2 f. \qquad (25)$$

From (16) we find, because $p \to 0$ and $\phi \to 0$ for $x \to -\infty$,

$$p = -\rho U \frac{\partial \phi}{\partial x} - \frac{\partial \phi}{\partial t} , \qquad (26)$$

which is Bernoulli's law for the unstationary linearized flow. Herewith the dynamical boundary condition (25) becomes

$$U\frac{\partial \phi}{\partial x} + \frac{\partial \phi}{\partial t} = (\frac{\Gamma^2}{r_c^3} - \frac{\sigma}{r_c^2})\ \delta r_c - \sigma\frac{\partial^2}{\partial x^2}\ \delta r_c - U^2 f. \qquad (27)$$

The kinematical condition at the boundary of the cavity is

$$\frac{\partial}{\partial t}\ \delta r_c + U\frac{\partial}{\partial x}\ \delta r_c = \frac{\partial \phi}{\partial r} . \qquad (28)$$

Hence, we must solve (20) under the conditions (27) and (28) while $\phi \to 0$ for $r \to \infty$ and for $x \to -\infty$.

3. THE GREEN FUNCTION

We suppose the dimensionless loading of the boundary (22) to have the form

$$f(x,t) = f(x)\ e^{\tilde{\varepsilon}t} , \qquad (29)$$

where $\tilde{\varepsilon}$ is a "small" positive parameter which has no connection with the linearization parameter ε. Because our problem is linear we assume

$$\phi(x,r,t) = \phi(x,r)\ e^{\tilde{\varepsilon}t} ,\ \delta r_c(x,t) = \delta r_c(x) e^{\tilde{\varepsilon}t} \ . \qquad (30)$$

Then equation (20) and the boundary conditions (27) and (28) change into

$$(\frac{\partial^2}{\partial_x^{\ 2}} + \frac{\partial^2}{\partial_r^{\ 2}} + \frac{1}{r}\frac{\partial}{\partial r})\ \phi(x,r) = 0, \qquad (31)$$

$$\left(\varepsilon + U\frac{\partial}{\partial x}\right)\ \phi(x,r_c) - \left(\frac{\Gamma^2}{r_c^{\ 3}} - \frac{\sigma}{r_c^2}\right)\delta r_c(x) +$$

$$\sigma\frac{\partial^2}{r_c^{\ 2}}\ \delta r_c(x) = U^2 f(x), \qquad (32)$$

$$\varepsilon\delta r_c(x) + U\frac{\partial}{\partial x}\,\delta r_c(x) - \frac{\partial}{\partial r}\,\phi(x,r_c) = 0\ . \qquad (33)$$

We introduce the Fourier transform $\bar{g}(\mu)$ of a function $g(x)$ by

$$\bar{g}(\mu) = \frac{1}{\sqrt{2\pi}}\int_{-\infty}^{+\infty} g(x)e^{i\mu x}dx,\ g(x) = \frac{1}{\sqrt{2\pi}}\int_{-\infty}^{+\infty} g(\lambda)e^{-i\mu x}d\mu. \qquad (34)$$

Transformation of (31) yields

$$\left(\frac{\partial^2}{\partial r^2} + \frac{1}{r}\frac{\partial}{\partial r} - \mu^2\right)\phi\,(\mu,r) = 0\ . \qquad (35)$$

Hence, for real μ

$$\phi\,(\mu r) = A_1(\mu)\,K_0(|\mu|r) + A_2(\mu)I_0(|\mu|r), \qquad (36)$$

where K_0 and I_0 are modified Bessel functions. Because $\phi \to 0$ for $r \to \infty$ we have

$$A_2\ (\mu) \equiv 0. \qquad (37)$$

Substitution of (36) with (37) into (32) and (33) yields

$$(\tilde{\varepsilon}-i\mu U)\ K_0\ (|\mu|r_c)\ A_1(\mu) - \left(\frac{\Gamma^2}{r_c^3} - \frac{\sigma}{r_c^2} + \mu^2\sigma\right)\overline{\delta r_c}\ (\mu)$$

$$= -U^2\bar{f}(\mu), \qquad (38)$$

$$|\mu|\ K_1(|\mu|r_c)\ A_1(\mu) + (\tilde{\varepsilon}-i\mu U)\ \overline{\delta r_c}\ (\mu) = 0. \qquad (39)$$

Solving (38) and (39) for $\overline{\delta r_c}\ (\mu)$ and applying the inverse Fourier transformation we obtain

$$\delta r_c(x) =$$

$$\frac{U^2}{\sqrt{2\pi}}\int_{-\infty}^{+\infty}\frac{\bar{f}(\mu)\,|\mu|K_1(|\mu|r_c)e^{-i\mu x}du}{[(\tilde{\varepsilon}-i\mu U)^2K_0(|\mu|r_c)+(\frac{\Gamma^2}{r_c^3} - \frac{\sigma}{r^2}+\mu^2\sigma)\,|\mu|K_1(|\mu|r_c)]} \qquad (40)$$

We now choose

$$f(x) = \delta(x)\quad , \qquad (41)$$

where $\delta(x)$ is the delta function of Dirac, hence $\bar{f}(\mu) = 1/\sqrt{2\pi}$. Next we split the range of integration into two parts namely $-\infty < \mu < 0$ and $0 < \mu < \infty$ and neglect terms of $0(\tilde{\varepsilon}^2)$ in the denominator, then we find

$$k(x) \overset{\text{def}}{=} \delta r_c(x)\big|_{f(x)=\delta(x)} =$$

$$-\frac{1}{2\pi}\int_0^\infty \frac{K_1(\xi)e^{\frac{i\xi x}{rc}}\,d\xi}{(\xi-\frac{2i\tilde{\varepsilon}r_c}{U})K_0(\xi)-(\alpha+\beta\xi^2)K_1(\xi)}$$

$$-\frac{1}{2n}\int_0^\infty \frac{K_1(\xi)\ell\varepsilon^{\frac{-i\xi x}{rc}}\,d\xi}{(\xi+\frac{2i\tilde{\varepsilon}r_c}{U})K_0(\xi) - (\alpha+\beta\xi^2)K_1(\xi)}\ , \qquad (42)$$

where α and β are dimensionless quantities given by

$$\alpha = \frac{1}{U^2}\left(\frac{\Gamma^2}{r_c^{\ 2}} - \frac{\sigma}{r_c}\right)\quad ,\beta = \frac{\sigma}{r_cU^2}\quad . \qquad (43)$$

It can be easily proved that under the assumption (4),

$$\alpha/\beta = \sqrt{1 + \left[2\Gamma^2(p_\infty - p_c)/\rho\sigma^2\right]}\ \ \geq 1. \qquad (44)$$

In order to find the Green function for the stationary case we have to take the limit $\tilde{\varepsilon} \to 0$ in (42).

We now make some remarks for the case $\sigma \neq 0$ and hence $\beta \neq 0$.

First, the integrals in (42) are absolutely convergent for $0 \leq x < \infty$. This means that when surface tension is present Green's function $k(x)$ is finite even at the point of application of the singular loading (41). This could be expected because the surface tension can be represented by a membrane placed at the boundary of the cavity and a membrane has the possibility to locally sustend such a loading by a jump in its first derivative while its deformation is still a continuous function of x.

Second, we consider the denominators in (42) for $\tilde{\varepsilon} = 0$ and look for positive real roots of

$$\left(\frac{\alpha}{\xi} + \beta\ \xi\right) = \frac{K_0(\xi)}{K_1(\xi)}\quad . \qquad (45)$$

The left hand side of (45) is curved upwards for $\xi > 0$, while the right hand side is curved downwards. The proof of the latter statement is rather complicated and will not be given here. However, taking this for granted, it means that there are none or two real positive roots, which is analogous to the case of ordinary gravity waves with surface tension. One of the roots corresponds to a wave primarily due to the swirl, the other one to capillarity. [Whitham (1973), p.446]

4. THE CASE OF ZERO SURFACE TENSION

Green's function (42) in the stationary case for zero surface tension, when we take a different positive value for $\tilde{\varepsilon}$ which of course is irrelevant, is

$$k(x) = \lim_{\tilde{\varepsilon}\to 0}\left[-\frac{1}{2\pi}\int_0^\infty\frac{K_1(\xi)\ e^{i\frac{\xi x}{r_c}}\,d\xi}{[(\xi-i\ \tilde{\varepsilon})K_0(\xi)-\ \alpha\ K_1(\xi)]}\right.$$

$$\left.-\frac{1}{2\pi}\int_0^\infty\frac{K_1(\xi)\ e^{-i\frac{\xi x}{r_c}}\,d\xi}{[(\xi+i\ \tilde{\varepsilon})K_0(\xi)\ -\ \alpha\ K_1(\xi)]}\right] \overset{\text{def}}{=} I_1 + I_2 \qquad (46)$$

First we investigate the number of poles of the integrands for $\tilde{\varepsilon} = 0$, hence, the number of positive real roots of

$$\alpha = \xi \frac{K_o(\xi)}{K_1(\xi)} \quad , \ \xi > 0. \tag{47}$$

where now (43) $\alpha = \Gamma^2/U^2 r_c^{\ 2} = 2(p_\infty - p_c)/\rho U^2$.

From the well known expansions of $K_0(\xi)$ and $K_1(\xi)$ it follows that the right hand side of (47) is zero for $\xi = 0$ and tends to infinity for $\xi \to \infty$. We prove that this function increases monotonically with ξ, hence, we have to consider

$$\frac{d}{d\xi}\, \xi \frac{K_o(\xi)}{K_1(\xi)} = 2 \frac{K_o(\xi)}{K_1(\xi)} - \xi + \xi \frac{K_o^{\ 2}(\xi)}{K_1^{\ 2}(\xi)} \quad . \tag{48}$$

Instead of proving that the right hand side of (48) is positive we will show that

$$2\, K_o(\xi)\, K_1(\xi) - \xi\, K_1^{\,2}(\xi) + \xi\, K_o^{\ 2}(\xi) > 0 \quad . \tag{49}$$

This is easily shown to be true for $\xi \to \infty$. Hence, when the derivative of (49) is negative the function itself has to be positive. This derivative,

$$-2\, K_o(\xi)\ [K_1(\xi) + \xi\, K_o(\xi)]/\xi - K_1^{\,2}(\xi) + K_o^{\ 2}(\xi), \tag{50}$$

is negative, since $K_1(\xi)$ for $0 < \xi < \infty$. This means that the right hand side of (47) increases monotonically, hence, there is one and only one root $\xi = \xi_o$ of (47) in $0 < \xi < \infty$.

We will estimate the value of ξ_o. Therefore we show that

$$(\xi+1)\ K_o(\xi) - \xi\, K_1(\xi) > 0. \tag{51}$$

From well-known expansions for K_o and K_1, this inequality holds for $\xi \to \infty$. The derivative of the left hand side of (51) being

$$(\xi+1)\ [K_0(\xi) - K_1(\xi)] \ , \tag{52}$$

is clearly negative, and hence (51) holds in $0 < \xi < \infty$. From $K_1(\xi) > K_0(\xi)$ and (51) it follows that the root ξ_o of (47) satisfies

$$\alpha < \xi_o < \tfrac{1}{2}\alpha + (\tfrac{1}{4}\alpha^2 + \alpha)^{\frac{1}{2}} \ . \tag{53}$$

Second we have to determine at which side of the real axis this root is situated when $\tilde{\varepsilon}$ is small but not zero. Consider the denominator of the first integral of (46), hence a root of

$$(\xi - i\,\tilde{\varepsilon})\ K_o(\xi) - \alpha\, K_1(\xi) = 0. \tag{54}$$

The zero in the neighborhood of the real axis of (54) is assumed as

$$\xi = \xi_o + \delta\ \xi, \tag{55}$$

where ξ_o satisfies (47) or (54) with $\tilde{\varepsilon} = 0$. Substituting (55) into (54), expanding the modified Bessel functions, and using the definition of ξ_o we find

$$\delta\ \xi = \frac{i\ \tilde{\varepsilon}\ K_o(\xi_o)K_1(\xi_o)}{\{2K_1(\xi_o)K_o(\xi_o) - \xi_o K_1^{\,2}(\xi_o) + \xi_o K_o^{\ 2}(\xi_o)\}} \ . \tag{56}$$

Hence by (49) we find that

$$\mathrm{Im}(\xi_o + \delta\ \xi) > 0, \tag{57}$$

or the pole of the integrand of the first integral in (46) is slightly above the real axis for $\tilde{\varepsilon}$ small and $\tilde{\varepsilon} > 0$. In the same way the pole of the integrand of the second integral in (46) is slightly below the real axis.

Now we want to give a different representation of (46). We distinguish between two cases $x > 0$ and $x < 0$. In the case of $x > 0$ we rotate the direction of integration of I_1 and I_2 as follows.

$$I_1 \to (0, +i\infty) \quad , \ I_2 \to (0, -i\infty) \ , \tag{58}$$

and in the case of $x < 0$

$$I_1 \to (0, -i\infty) \ , \ I_2 \to (0, +i\infty) \ . \tag{59}$$

From the foregoing it follows, that for $x > 0$, a pole has to be added to I_1 as well as to I_2. The question arises: are there still other poles in the complex half plane $\mathrm{Re}\ \xi > 0$ which are passed by rotating the lines of integration? We now shall give a proof that this does not happen. This proof was kindly given to us by our colleague Prof. Dr. B. L. J. Braaksma.

Consider the function

$$F(\xi) \overset{\text{def}}{=\!=} \xi\, K_o(\xi) - \alpha\, K_1(\xi) = -\ [\xi K_1{}'(\xi) + (\alpha+1)K_1(\xi)], \tag{60}$$

which is real for real values of ξ. Suppose s_1 with $\mathrm{Re}\ s_1 \geq 0$ and $\mathrm{Im}\ s_1 \neq 0$ is a zero of $F(\xi)$, then also $s_2 = \bar{s}_1$ (complex conjugated value) is such a zero. The functions $K_1(s_j\xi)$, $j = 1,2$, satisfy

$$[\xi^2 \frac{d^2}{d\xi^2} + \xi \frac{d}{d\xi} - (s_j^2\, \xi^2 + 1)]\ K_1(s_j\xi) = 0 \ , \ j = 1,2. \tag{61}$$

Multiplying (61) by $K_1(s_k\xi)$ with $k = 2$ for $j = 1$ and $k = 1$ for $j = 2$, we find by subtracting the results

$$(s_1^2 - s_2^2)\xi K_1(s_1\xi)K_1(s_2\xi) = \frac{d}{d\xi}\ \xi[K_1(s_2\xi)\ \frac{d}{d\xi}\ K_1(s_1\xi) - K_1(s_1\xi)\frac{d}{d\xi}K_1(s_2\xi)] \tag{62}$$

Hence

$$(s_1^2 - s_2^2) \int_1^\infty \xi\ K_1(s_1\xi)K_1(s_2\xi)d\xi = \xi[(K_1(s_2\xi)\frac{d}{d\xi}K_1(s_1\xi)_\infty - K_1(s_1\xi)\frac{d}{d\xi}K_1(s_2\xi)]\Big|_1 \tag{63}$$

It is easily seen that the right hand side vanishes for $\xi \to \infty$ and because s_1 and s_2 are zeros of $F(\xi)$ (57) this right hand side also vanishes for $\xi \to 1$. Because the integral is positive we have found that the assumption $\mathrm{Im}\, s_1 = -\mathrm{Im}\, s_2 \neq 0$ yields a contradiction. It follows that no other residues have to be added to the resulting integrals after the rotations as denoted in (58) and (59) besides the two we mentioned for $x > 0$.

Using some formulae from Watson (1922) we find

$$K_0(\pm i\xi) = \frac{\pi i}{2}[\mp J_0(\xi) + iY_0(\xi)] \quad , \xi > 0, \tag{64}$$

$$K_1(\pm i\xi) = -\frac{\pi}{2}[J_1(\xi) \pm iY_1(\xi)] \quad , \xi > 0, \tag{65}$$

Adding poles to the integrals in the case $x > 0$ we can transform the Green function (46) into

$$k(x) = h(x) + \begin{cases} A \sin bx, & x > 0 \\ 0, & x < 0 \end{cases} , \tag{66}$$

where

$$h(x) = -\frac{2}{\pi^2}\int_0^\infty \frac{e^{-\frac{\xi|x|}{r_c}}\, d\xi}{[\xi J_0(\xi)+\alpha J_1(\xi)]^2+[\xi Y_1(\xi)+\alpha Y_1(\xi)]^2}, \tag{67}$$

and

$$A = 2\xi_0/(2\alpha+\alpha^2-\xi_0^2) \quad , \quad b = \xi_0/r_c \tag{68}$$

The function $h(x)$ is symmetric, $h(x) = h(-x)$. For $x \to 0$ it has a logarithmic singularity because for $x = 0$ the integrand as a function of ξ, behaves as $\pi/2\xi$, hence

$$h(x) \simeq \frac{1}{\pi}\ln x \quad , \quad x \to 0. \tag{69}$$

For $x \to \infty$ the behavior of $h(x)$ depends on the behavior of the integrand in (67). For $\xi \to 0$, this turns out to be as

$$(4\alpha^2/\pi^2\xi^2)+O(\xi^3\ln\xi) \quad . \tag{70}$$

Then it follows from Doetsch (1943) p. 233 that

$$h(x) \approx -\pi r_c/\alpha^2|x|^3 \qquad |x| \to \infty \; . \tag{71}$$

Now suppose that for $x < 0$ the shape of the cavity is prescribed.

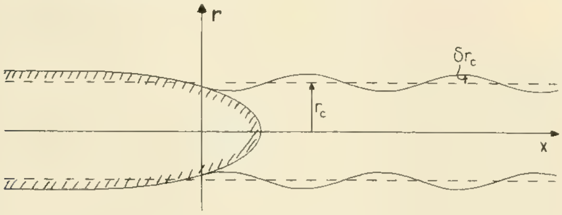

FIGURE 2. Flow with swirl along hub.

$$r = r_c + \delta r_c(x) \quad , \quad -\infty < x < 0 \tag{72}$$

and that the unknown pressure between hub and fluid is $p_c + \rho U^2 f(x)$.

Then we have to solve the following integral equation

$$\int_{-\infty}^{0} k(x-x')\, f(x')dx' = \delta r_c(x) \quad , \quad x < 0, \tag{73}$$

which is of the Wiener-Hopf type.

5. THE EXPLICIT SOLUTION OF $\alpha K_1(\xi) - \xi K_0(\xi) = 0$

In order to find an explicit solution of Eq. (47) we first have to make some preliminary considerations. Assume the following loading of the otherwise undisturbed cavity boundary

$$f(x) = \varepsilon_1 \delta(x), \tag{74}$$

where ε_1 is a small parameter. By (66) we find for the deformation of the cavity

$$\delta r_c(x) = \varepsilon_1 h(x) + \begin{cases} \varepsilon_1 A \sin bx, & x > 0, \\ 0, & x < 0. \end{cases} \tag{75}$$

Next we consider

$$f(x) = -\varepsilon_1 \quad , \quad x < 0 \; ; \; f(x) = 0, \; x > 0. \tag{76}$$

The loading given in (74) is the derivative with respect to x of the loading given in (76). Hence the derivative of the deformation $\delta^* r_c(x)$ caused by (76) has to be equal to (75), we take

$$\delta^* r_c(x) = -\varepsilon_1 \int_x^\infty h(\xi)d\xi + \begin{cases} -\varepsilon_1 \frac{A}{b}\cos bx, & x > 0, \\ -\varepsilon_1 \frac{A}{b}, & x < 0, \end{cases} \tag{77}$$

where we have chosen the constant of integration in such a way that for $x \to +\infty$ we have a harmonic wave with mean value zero.

Finally consider

$$f(x) = 0 \quad , \; x < 0 \quad ; \quad f(x) = \varepsilon_1 \quad , \; x > 0. \tag{78}$$

The loading given in (74) is also, in this case, the derivative with respect to x of the loading given in (78). Hence the same argument applies as before. However, now the constant of integration has to be chosen so that the disturbance tends to zero for $x \to -\infty$, we find

$$\delta^{**} r_c(x) = \varepsilon_1 \int_{-\infty}^{x} h(\xi)d\xi + \begin{cases} \varepsilon_1 \frac{A}{b}(1-\cos bx), & x > 0, \\ 0, & x < 0. \end{cases} \tag{79}$$

Subtraction of the disturbances (77) and (79) yields

$$\delta^* r_c(x) - \delta^{**} r_c(x) = -\varepsilon_1 \int_{-\infty}^{+\infty} h(\xi) d\xi - \varepsilon_1 \frac{A}{b} ,$$

$$-\infty < x < \infty , \qquad (80)$$

which is constant as could be expected because belongs to a constant loading of magnitude $-\varepsilon_1 \rho U^2$ of the whole cavity.

This displacement however can be calculated in another way by using (6) where we have to replace p_c by

$$p_c + \rho U^2 f = p_c - \varepsilon_1 \rho U^2 . \qquad (81)$$

Expanding (6) with respect to ε_1, we find

$$r_c + \delta^* r_c - \delta^{**} r_c = \sqrt{\frac{\rho}{2}} \frac{\Gamma}{(p_\infty - p_c + \varepsilon_1 \rho U^2)^{\frac{1}{2}}}$$

$$\approx \sqrt{\frac{\rho}{2}} \frac{\Gamma}{(p_\infty - p_c)^{\frac{1}{2}}} (1 - \frac{\varepsilon_1 \rho U^2}{2 (p_\infty - p_c)}) . \qquad (82)$$

Combining (80) and (82) yields

$$\rho U^2 r_c / 2 (p_\infty - p_c) = \int_{-\infty}^{+\infty} h(x) dx + A/b \qquad (83)$$

Substituting $h(\xi)$, A, and b from (67) and (68) into (83) and carrying out the integration with respect to x we find after some reductions

$$\alpha^{-1} - 2 (2\alpha + \alpha^2 - \xi_0^2)^{-1} = L \qquad (84)$$

where

$$L = - \frac{4}{\pi^2} \int_0^\infty \frac{d\xi}{\xi \{ [\xi J_o(\xi) + \alpha J_1(\xi)]^2 + [\xi Y_o(\xi) + \alpha Y_1(\xi)]^2 \}} \qquad (85)$$

Solution of (84) with respect to ξ_o yields

$$\xi_o(\alpha) = \alpha . \{ 1 + \frac{2L}{(\alpha L - 1} \}^{\frac{1}{2}} \qquad (86)$$

by which we have found the unique solution of (47) for ξ real and $\xi > 0$. This derivation rests on some mechanical considerations such as uniqueness of the solutions in relation to radiation conditions. The result however, which is interesting from the point of view of zeros of transcedental equations connected with Bessel functions, has been verified by others in a more straight forward way and found to be correct.

By (86) it follows that an axial symmetric wave moving along the cavity with velocity U has a wavelength $\lambda(U)$ given by

$$\lambda(U) = 2\pi/b = [\pi\Gamma/\xi_o(\alpha)] \, [2\rho/(p_\infty - p_c)]$$

$$\alpha = 2 (p_\infty - p_c)/\rho U^2 \qquad (87)$$

Equation (87) describes the dispersion of these waves when surface tension is neglected.

6. NUMERICAL SOLUTION OF THE INTEGRAL EQUATION

In the left hand side of (73) the function $k(x)$ is given by (66-68) and the dimensionless quantity $f(x')$ is unknown. For $x < 0$ the right hand side is determined by the geometry of the hub. Let this geometry be described by

$$r = r_h(x) = r_c + \delta r_h(x) , \qquad (88)$$

where $r_h(x)$ is a given function. Then the right hand side is known up to an unknown shift, s, of the hub along the x-axis, since the position of the point of separation is a priori unknown. Hence for $x < 0$ we can write (73) as

$$\int_{-\infty}^{0} k(x - x') \, f(x') \, dx' = \delta r_h (x + s), \; x < 0 \qquad (89)$$

where the function $f(x')$ and s are unknown. First we will describe how $f(x')$ is computed numerically from (89) for arbitrary values of s. Then s will be determined by a condition to be satisfied by f at $x = 0$.

We make some remarks concerning the behavior of $f(x')$ for $x' \uparrow 0$ and for $x' \to -\infty$. As will be shown in the Appendix, the behavior of $f(x')$ near the origin is, for arbitrary values of s,

$$f(x') \approx 2\pi^{-1/2} B \, |x'|^{1/2} , \qquad x' \uparrow 0 \qquad (90)$$

where B is some constant which will be discussed later.

The hub has a constant radius far upstream, hence $\delta r_h(x)$ tends to a finite value for $x \to -\infty$. Since the kernel $k(x)$ vanishes for $x \to -\infty$, the perturbation due to the end part of the hub vanishes far upstream. Hence, the pressure distribution there is the same as that of a two-sided infinitely long hub with constant radius. This case was also considered in the preceding section. We find $f(-\infty)$ from (82), with $-\varepsilon_1 = f(-\infty)$, and (6) and (87);

$$f(-\infty) = \alpha \; \delta r_h(-\infty)/r_c . \qquad (91)$$

In order to transform (89) into a discrete function we choose n + 1 points on the negative x-axis:

$$-\infty < x_n < x_{n-1} < \ldots < x_1 < x_o = 0, \qquad (92)$$

and construct n coordinate functions, $f(x)$, ..., $f_n(x)$, defined on $-\infty \le x \le 0$ as follows: For $m = 2, \ldots, n-1$ the function $f_m(x)$ vanishes outside the interval (x_{m+1}, x_{m-1}), and inside this interval its value is

$$f_m(x) = (x - x_{m+1}) / (x_m - x_{m+1}), \; x_{m+1} \le x \le x_m , \qquad (93a)$$

$$f_m(x) = (x - x_{m-1}) / (x_m - x_{m-1}) . \; x_{m-} \le x \le x_{m-1} . \qquad (93b)$$

The function $f_1(x)$ vanishes for $x \le x_2$, and:

$$f_1(x| = |x|^{1/2} / |x_1|^{1/2} \quad , \quad x_1 \leq x \leq 0, \tag{94a}$$

$$f_1(x) = (x - x_2) / (x_1 - x_2). \; x_2 \leq x \leq x_1 \, . \tag{94b}$$

Finally $f_n(x)$ vanishes for $x_{n-1} \leq x \leq 0$ and:

$$f_n(x) = (x - x_{n-1}) / (x_n - x_{n-1}), \; x_n \leq x \leq x_{n-1} \tag{95a}$$

$$f_n(x) = 1 \quad , \qquad x \leq x_n \tag{95b}$$

These functions are plotted in Figure 3. We approximate the function f(x') in (89) by a linear combination of the coordinate functions:

$$f(x') = \sum_{m=1}^{n} C_m f_m(x') \quad , \tag{96}$$

where the C_m are unknown coefficients. In order to approximate f(x') well near the origin, we have chosen f_1 in a special way and, besides, the points x_m are more densily distributed near the origin. Since f(x') is almost constant for large negative values of x', we have chosen f_n to be constant in $(-\infty, x_n)$.

Next we have to determine the coefficients $C_1, \ldots, C_n$. We substitute (96) into (89) and then the C_m must be chosen so that the difference between the right hand side and the left hand side of (89) is as small as possible, in the sense of some norm. The computed values of the C_m appeared to depend strongly on which norm was chosen for this difference; many of these norms give unreliable results. We obtained reliable values of the C_m as follows:

Equation (89) with $x = x_\ell$, $\ell=0,1,\ldots, n-2$ yields

$$\sum_{m=1}^{n} M_{\ell m} C_m = \delta r_h (x_\ell + s), \quad \ell = 0, \ldots, n-2 \tag{97}$$

where:

$$M_{\ell m} = \int_{-\infty}^{0} k(x_\ell - x') \, f_m(x') \, dx' \, . \tag{98}$$

At the points x_{n-1} and x_n we minimize the difference between the right hand side and the left hand side of (89). The expression

$$\sum_{\ell=n-1}^{n} \Big[\sum_{m=1}^{n} M_{\ell m} C_m - \delta r_h (x_\ell + s)\Big]^2 \tag{99}$$

is a quadrative, non-negative function of the C_m. Now the $C_1, \ldots, C_n$ are determined so that they minimize (99) with the constraints (97).

We have checked these numerically computed values of the C_m as follows. First, the computed approximation has the square root character (90) even in the interval $(x_3, 0)$. Second, the value of C_n equals the right hand side of (91) within an error of 0.5%. Third, if we replace the kernel k(x) in (89) by a kernel $\tilde{k}(x)$, which has the same behavior (69) at the origin, and which for $x \to \infty$ is also given by a term A sin bx as in (66), then (89) can be solved effectively by the Wiener-Hopf method. If we apply our numerical method to (89) with the kernel $\tilde{k}$, then the numerically computed function, f, equals the analytically computed solution within an error of 1%.

We have tried to compute the $C_1, \ldots, C_n$ in different ways; for instance:

i) By collocating the points $x_o, \ldots, x_n$ with the exception of one point x_i, so that the number of equations equals the number of unknowns. This method had to be rejected because the computed approximation for f(x) appeared to have oscillations near x_i.

ii) By minimizing the sum of squares of the differences between the right hand and the left hand side of (88) at the points $x_o, \ldots, x_n$. We have also rejected this method, because oscillation occurred in f(x) near the origin.

We make some remarks concerning the computation of the matrix elements. $M_{\ell m}$ in (98). For m = 1, ..., n - 1 the integrand is non-zero only in a bounded region. The kernel k(x) is written as the sum of a logarithm and a function which is bounded at x - 0. The integral over the logarithm is evaluated analytically; the remaining term is integrated numerically. For m = n the integrand is non-zero in an unbounded region. For $x \leq x_n$ we have $f_n(x) = 1$ and we must evaluate

$$\int_{-\infty}^{x_n} k(x_1 - x') \, dx' \, . \tag{100}$$

Note, that the integrand does not tend to zero for $x' \to -\infty$, as follows from (66). However, the expression (100) represents the deformation of the cavity due to a loading which equals a step-function. This deformation has been computed in (76,77).

We now come to the determination of the shift, s. The pressure in x < 0 at $r = r_c$ must exceed the vapor pressure. Hence, by (22) with $\sigma = 0$, we must have $f \geq 0$, and by (90), $B \geq 0$. As will be shown in the Appendix, the shape of the cavity for small values of x is given

$$\delta r_c(x) = \delta r_h(0) + \delta r_h{}'(0)x - 4B(x^3/\pi)^{1/2}/3, \; x \downarrow 0 \tag{101}$$

This implies that the radius of curvature tends to zero for $x \downarrow o$. Since the fluid may not penetrate

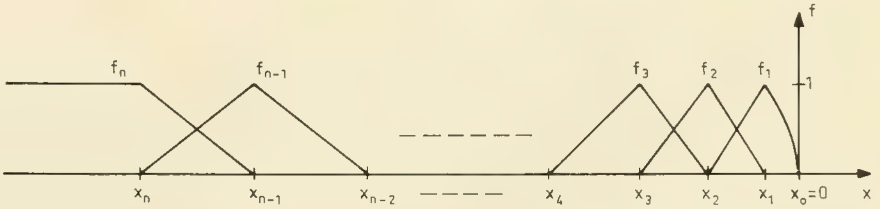

FIGURE 3. The coordinate functions $f_1, \ldots f_n$.

the hub, we must have $B \leq 0$ for a hub with a smooth surface. We found above that $B \geq 0$ and hence B must vanish. For our numerical approximation this implies that the coefficient, C_1, must vanish. Now the value of the shift, s, is determined by iteration so that C_1 vanishes.

When f(x) has been computed we can compute the shape of the cavity in $x > 0$ with a numerical integration of (73) for $x > 0$. Using (40) with $\sigma = 0$, we can derive an expression for $\delta r_c(x)$ for $x \to \infty$. The derivation is similar to the derivation of (66) and, therefore we give the result only:

$$\delta r_c(x) \approx \frac{2\xi_o}{\alpha^2+2\alpha-\xi_o^2}\{A_1 \sin(\xi_o x/r_c) + A_2 \cos(\xi_o x/r_c)\}, \tag{102}$$

where:

$$A_1 = \lim_{\varepsilon \downarrow 0} \int_{-\infty}^{0} e^{\varepsilon x} \cos(\xi_o x/r_c)\, f(x)\, dx, \tag{103a}$$

$$A_2 = \lim_{\varepsilon \downarrow 0} \int_{-\infty}^{0} e^{\varepsilon x} \sin(\xi_2 x/r_c)\, f(x)\, dx. \tag{103b}$$

7. NUMERICAL RESULTS

In this section we give computermade plots of the shape of the cavity $\delta r_c(x)$ for a number of shapes of the hub $\delta r_h(x)$ and for a number of values of the dimensionless parameter α. We consider the case of zero surface tension, hence α is given by (87) or by (43) with $\sigma = 0$:

$$\alpha = \frac{2(p_\infty - p_c)}{\rho U^2} = \frac{\Gamma^2}{U^2\, r_c^{\,2}} \tag{104}$$

It follows from (88) that $\delta r_h(x)$ depends on r_c for a fixed hub. The value of r_c is given by (6):

$$r_c = \left(\frac{\rho}{2}\right)^{\frac{1}{2}}\Gamma(p_\infty - p_c)^{-\frac{1}{2}} \tag{105}$$

However we can vary α without changing $\delta r_h(x)$ by varying U and keeping ρ, Γ and $p_\infty - p_c$ constant.

In the Figure 4 the function $\delta r_h(x)$ is plotted; it consists of a straight horizontal line and part of a parabola. The x-axis is chosen so that $x = 0$ at the point of separation. No scale-unit is given in the vertical direction, since $\delta r_h(x)$ and $\delta r_c(x)$ are the linearized perturbations of the undisturbed

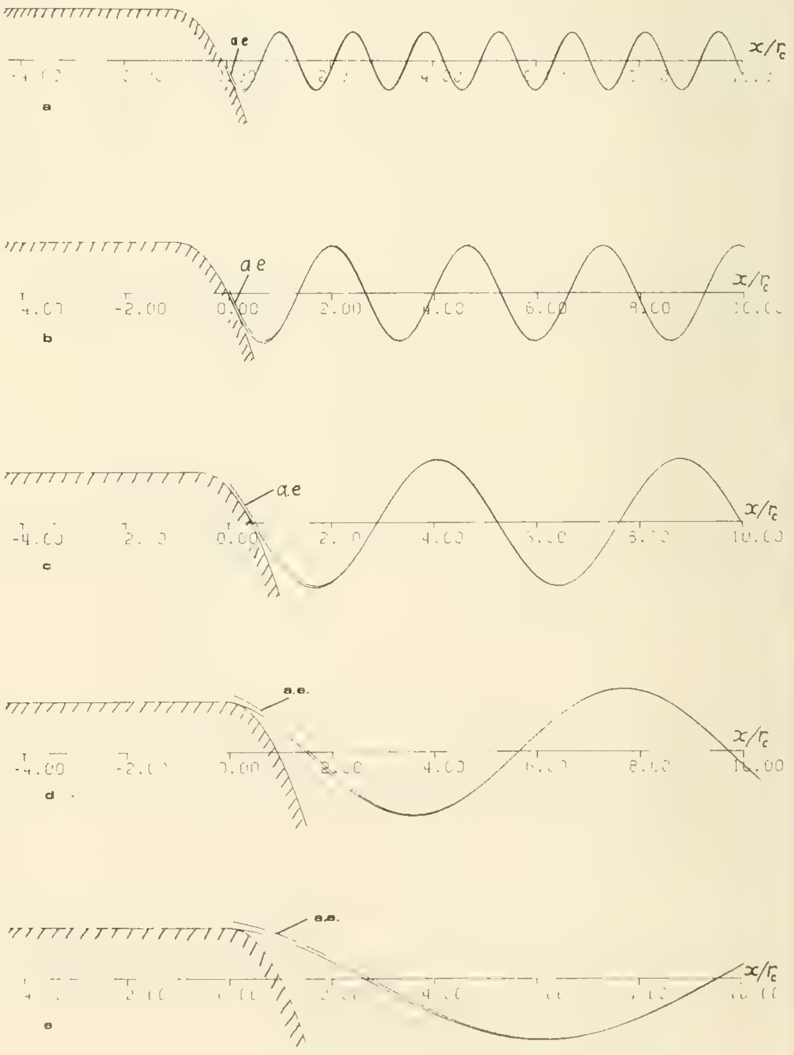

FIGURE 4. The functions $\delta r_h\ [(x+s)/r_c]$ (hatched curve), $\delta r_c(x/r_c)$ and the asymptotic expression (102) (a.e.). The values of α are a)4, b)2, c)1, d)0.5, e)0.25. The point of separation is at x=0. δr_h is given by $\delta r_h(x/r_c) = 1$ for $x < 0$ and $= 1-(x/r_c)^2$ for $x > 0$. The values of s/r_c are a)1.092, b)1.017, c)0.558, d)0.070, e)0.014.

cavity (1); see Figure 2. The dimensionless quantity x/r_c is on the horizontal axis. In $x > 0$ the numerically computed function $\delta r_c(x)$ is plotted and also the asymptotic expression (102) is given. It appears that the asymptotic expression is a good approximation for $\delta r_c(x)$ also for rather small values of x/r_c.

The Figures 4(a) through (e) correspond to decreasing values of α. This is equivalent to increasing values of the speed U with constant ρ, Γ, and $p_\infty - p_c$. The length of the waves on the cavity is an increasing function of α, as was stated in Section 4. Further we observe from these figures the following:

i) An increase of the speed U induces an increase of the amplitude of the waves on the cavity.

ii) When U is relatively large, the point of separation is near the point where $\delta r_h(x)$ attains the value $\delta r_h(-\infty)$. When U is small, the point of separation is near the point where $\delta r_h(x) = 0$.

The latter phenomenon is easily understood, since we can imagine two reasons for which the fluid may separate from the hub: First, the radius of curvature of the hub may be so small that the fluid particles are unable to keep contact with the hub. This effect dominates in the case of a relatively high speed U. Second, the value of $\delta r_h(x)$ may become negative. Then the centrifugal force makes the fluid particles leave the hub. This effect is important in the case of a low speed.

In Figure 5 we have plotted the same functions for a different shape of the hub. Here $\delta r_h(x)$ consists of a straight line, a part of a parabola, and another straight line. It appears that qualitatively the same effects occur.

In Figure 6 we have only one value of the parameter, α, ($\alpha = 1$), but we have plotted a family of functions $\delta r_h(x)$. The plot of $\delta r_c(x)$ is omitted, and we have indicated the point of separation with a dot. The amplitudes of the waves in $\delta r_c(x)$ at $x = \infty$ are denoted in a table underneath Figure 6. These numbers are the amplitudes divided by $\delta r_h(-\infty)$.

From this figure we observe the following:

iii) If $\delta r_h(x)$ decreases abruptly as a function of x, then the amplitude of the waves on the cavity is relatively large.

iv) The sign of $\delta r_h(x)$ at the point of separation can be positive or negative, depending on the function $\delta r_h(x)$. If $\delta r_h(x)$ decreases more and more slowly as a function of x, then the value of $\delta r_h(x)$ at the point of separation approaches zero from below.

We will compare the effects on the cavity by changing α, or U with constant ρ and $p_\infty - p_c$, and of the function $\delta r_h(x)$. In order to give a rough description of the dependence on $\delta r_h(x)$, we use the

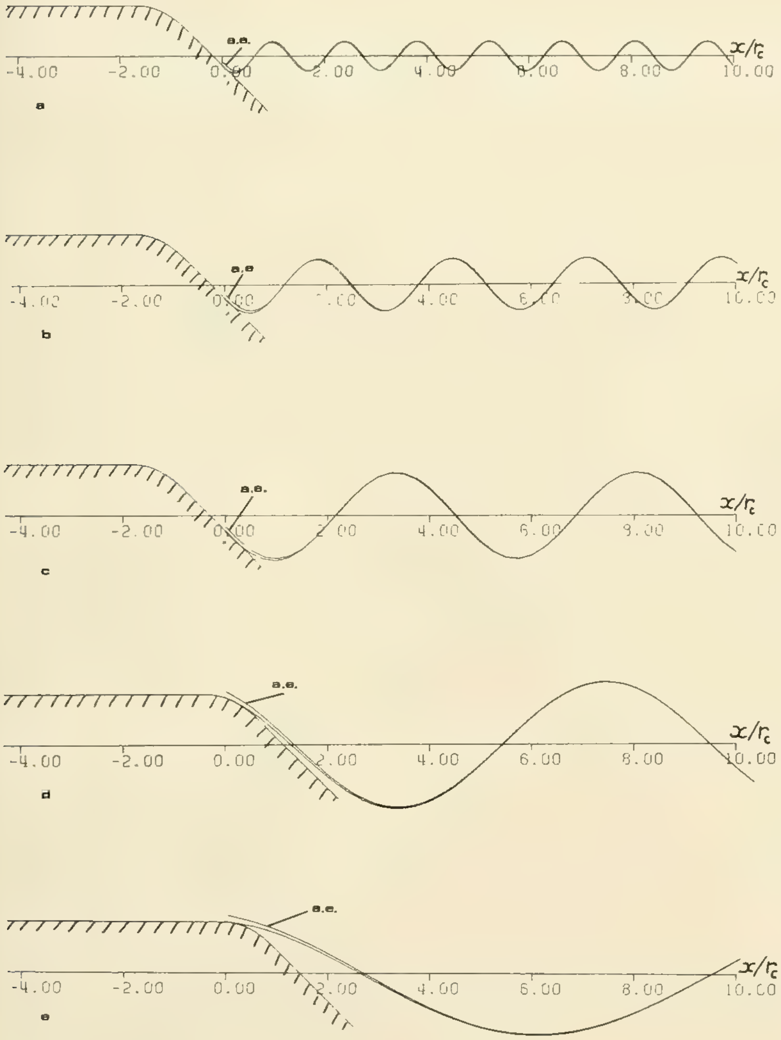

FIGURE 5. The functions $\delta r_h[(x+s)/r_c]$ (hatched curve), $\delta r_c(x/r_c)$ and the asymptotic expression (102) (a.e.). The values of α are a)4, b)2, c)1, d)0.5, e)0.25. The point of separation is at x=0. δr_h is given by $\delta r_h(x/r_c)=1$ for $x < 0$, $= 1-(x/r_c)^2/2$ for $0 < x < r_c$, and $=1.5-x/r$ for $x > r_c$. The values of s/r_c are a)1.683, b)1.759, c)1.805, d)0.361, e)0.052.

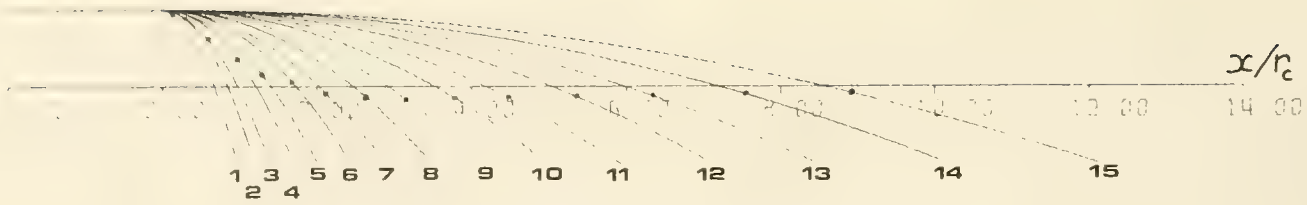

	λ	A
1	2.0	1.27
2	1.4	1.27
3	0.98	1.24
4	0.686	1.17
5	0.480	1.06
6	0.336	0.942
7	0.235	0.822
8	0.165	0.709
9	0.115	0.607
10	0.0807	0.516
11	0.0565	0.437
12	0.0395	0.370
13	0.0277	0.311
14	0.0194	0.262
15	0.0136	0.220

FIGURE 6. A family of functions $\delta r_h(x/r_c)$ with $\alpha = 1$. They are given by $\delta r_h(x/r_c)=1$ for $x < 0$ and $=1-\lambda(x/r_c)^2$ for $x > 0$. The value of λ is given in the table. The point of separation is denoted by a dot. The amplitude of the waves at $x = \infty$ divided by $r_h(-\infty)$, denoted by A, is also given in the table.

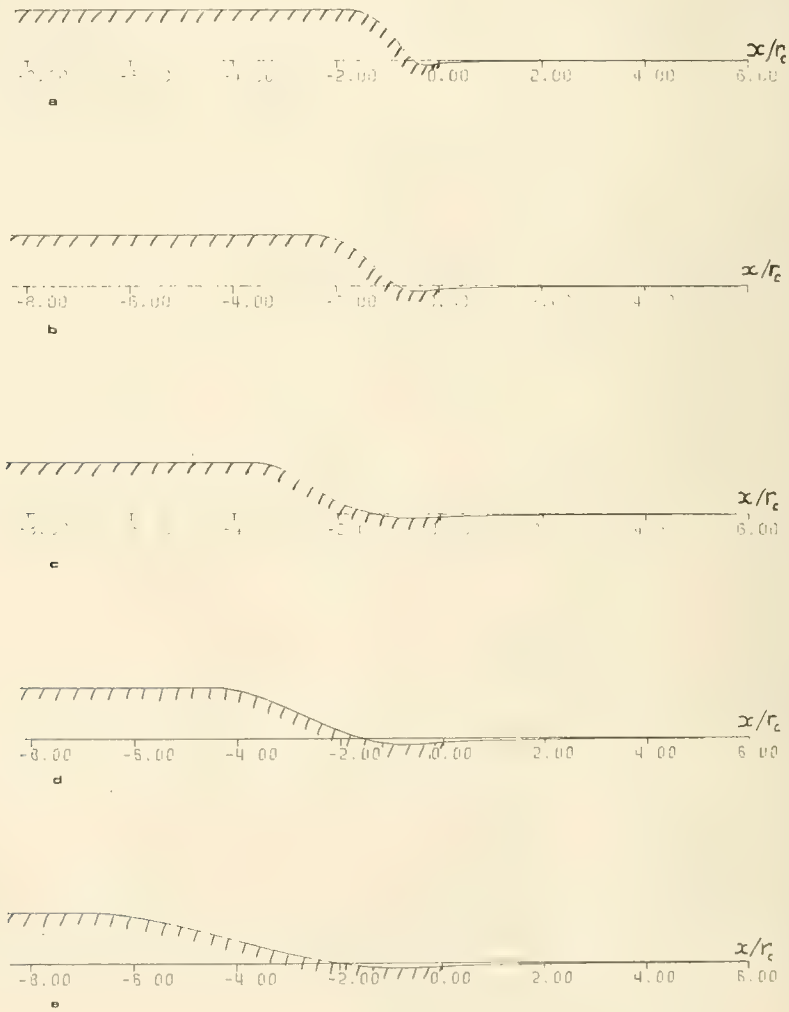

FIGURE 7. The functions $\delta r_h(x/r_c)$ (hatched curve) and $\delta r_c(x/r_c)$ for vanishing waves at $x = \infty$. The values of α are a) 4, b) 2, c) 1, d) 0.5, e) 0.25. The point of separation is at $x = 0$.

curvature κ of the hub, which must be interpreted as some mean value of the curvature of $\delta r_h(x)$ in the wetted region not too far upstream.

First we consider the amplitude of the waves on the cavity. This amplitude is an increasing function of both U and κ, as follows from i) and iii). Next we consider the point of separation. An increase of U or κ tends to shift this point from the point where $\delta r_h(x) = 0$ to the point where $\delta r_h(x) = \delta r_h(-\infty)$ as follows from ii) and iv). Hence in these respects, an increase of U has roughly the same effect as an increase of κ. However, the length of the waves on the cavity is, as follows from the previous theory (87), independent of κ but is a decreasing function of U.

Finally we consider a shape of the hub which induces, for some value of α, no waves on the cavity at $x = \infty$. The existence of nontrivial shapes can be shown as follows. Let $\delta r_{h1}(x)$ and $\delta r_{h2}(x)$ be two shapes of the hub and let $\delta r_{c1}(x)$ and $\delta r_{c2}(x)$ be the corresponding shapes of the cavity for some value of α. In each case the point of separation is at $x = 0$. We choose $\lambda > 0$ so that the amplitude of $\lambda \delta r_{c1}(x)$ at $x = \infty$ equals the amplitude of $\delta r_{c2}(x)$. (Notice that their wavelength is already the same.) Next we choose a shift, $s \geq 0$, so that

$$\lim_{x \to \infty} \lambda \delta r_{c1}(x+s) + \delta r_{c2}(x) = 0. \qquad (106)$$

Now we construct a shape, $\delta r_h(x)$, which induces no waves at infinity, as follows:

$$\delta r_h(x) = \lambda \delta r_{h1}(x+s) + \delta r_{h2}(x), \quad x < -s \qquad (107)$$

$$\delta r_h(x) = \lambda \delta r_{c1}(x+s) + \delta r_{h2}(x). \quad -s < x < 0$$

The dimensionless load f was introduced in (22). By virtue of the linearity of our equations we obtain the load corresponding to the shape (107) by shifting the load due to δr_{h1} over a distance s, multiplying it by λ and summing the load due to δr_{h2}. This load is nonnegative in $x \leq 0$ and vanishes in $x > 0$. The condition for the point of separation described in the preceding section is satisfied at $x = 0$. The shape of the cavity is obtained by a similar construction as for the load f. The value of $\delta r_c(x)$ tends to zero for $x \to \infty$ by virtue of (106).

Using this method we have constructed five functions $\delta r_h(x)$ which induce no waves at $x = \infty$ for five different values of α respectively. The functions δr_{h1} and δr_{h2} are the functions plotted in Figures 4 and 5 respectively. The results are plotted in Figure 7. The point of separation is at $x = 0$. The value of $\delta r_h(x)$ in $x > 0$ is unessential.

APPENDIX

SOME RESULTS DERIVED BY USING WIENER-HOPF-TECHNIQUE

In equation (73) we let the path of integration be from $-\infty$ to ∞ and we assume the load $f(x)$ to vanish for $x > 0$. Then applying Fourier transform (34) to both sides of this equation, we obtain:

$$\overline{\delta r_c}(\xi) = \bar{k}(\xi)\, \bar{f}(\xi), \qquad (A,1)$$

where:

$$\bar{k}(\xi) = K_1(|\xi|)\, [(\alpha K_1(|\xi|) - |\xi|\, K_0|\xi|)]^{-1}. \qquad (A,2)$$

Here we have chosen the unit of length to be equal to r_c, so that $r_c = 1$. We have to solve (A,1) with $f(x) = 0$ for $x > 0$ and with $\delta r_c(x)$ being prescribed for $x < 0$.

In order to apply Wiener-Hopf-Technique, we need a multiplicative decomposition of $\bar{k}(\xi)$. We define:

$$H(\xi) = -\bar{k}(\xi)\, (\xi^2 - \xi^2_o)\, (\xi^2 + 1)^{-1/2}, \qquad (A,3)$$

where ξ_o is the root of (47). This function is continuous and positive in $-\infty < \xi < \infty$. By virtue of well-known asymptotic expressions for the Bessel functions, K_o and K_1, we have:

$$H(\xi) = 1 + O\,(1/\xi). \quad \xi \to \pm \infty \quad . \qquad (A,4)$$

Hence, we can decompose $H(\xi)$ in the usual way, see for instance Noble (1958); we find:

$$H(\xi) = H^-(\xi) \,/\, H^+(\xi) \quad , \qquad (A,5)$$

where:

$$H^{\pm}(\xi) = \exp\left\{\frac{i}{2\pi} \int_{C^{\mp}} \ln\ [H(\zeta)]\, \frac{d\zeta}{\zeta-\xi}\right\} \qquad (A,6)$$

This represents two equations; the upper or the lower of the ± signs must be read. The contour of C^+ (resp. C^-) is the real axis, indented into the upper (resp. lower) half of the complex ζ-plane at $\zeta = \xi$. The function $H^+(\xi)$ [resp. $H^-(\xi)$] is analytic in the upper (resp. lower) halfplane. Using (A,2-3) and (A,5) we can write (A,1) as

$$\overline{\delta r_c}(\xi)\, (\xi^2 - \xi^2_o)\, (\xi+i)^{-1/2}\, H^+(\xi) =$$

$$-(\xi-i)^{1/2}\, H^-(\xi)\, \bar{f}(\xi). \qquad (A,7)$$

The function $(\xi+i)^{\frac{1}{2}}$ has a cut from $-i$ to $-i\infty$ and $(\xi-i)^{1/2}$ has a cut from i to $i\infty$. They are both chosen so that they are positive for $\xi \to \infty$.

The function $\delta r_c(x)$ is prescribed for $x \leq 0$. First we assume:

$$\delta r_c(x) = e^{\lambda x} \qquad x < 0 \qquad (A,8)$$

for some positive λ; later we discuss the general case. Fourier transformation gives:

$$\overline{\delta r_c}(\xi) = -i\ (2\pi)^{-1/2}\ (\xi - i\lambda)^{-1} + \delta r_c^{\,+}(\xi), \qquad (A,9)$$

where

$$\delta r_c^{\,+}(\xi) = (2\pi)^{-1/2} \int_0^{\infty} e^{i\xi x}\ \delta r_c(x)\, dx \qquad (A,10)$$

is unknown. We substitute (A,9) into (A,7) and separate functions which are analytic in the upper half plane and respectively in the lower one. Therefore we write:

$$i(2\pi)^{-1/2}(\xi-i\lambda)^{-1}\ (\xi+i)^{-1/2}\ H^{+}(\xi) = h^{+}(\xi) + h^{-}(\xi)\ , \qquad (A,11)$$

where:

$$h^{-}(\xi) = \frac{-i}{(2\pi)^{1/2}}\ \frac{H^{+}(i\lambda)}{(i\lambda+i)^{1/2}}\ \frac{1}{\xi-i\lambda} \qquad (A,12)$$

is analytic in the lower half of the complex ξ-plane, and:

$$h^{+}(\xi) = \frac{i}{(2\pi)^{1/2}}\ \left[\frac{H^{+}(i\lambda)}{(i\lambda+i)^{1/2}} - \frac{H^{+}(\xi)}{(\xi+i)^{1/2}}\right] \frac{1}{\xi-i\lambda} \qquad (A,13)$$

is analytic in the upper half plane. Using (A,9) and (A, 11) we can write (A,7) as:

$$[\delta r_c^{\ +}(\xi)\ (\xi+i)^{-1/2}\ H^{+}(\xi)] + h^{+}(\xi)]\ \ (\xi^2 - \xi_o^2) =$$

$$-h^{-}(\xi)\ (\xi^2 - \xi_o^2) - (\xi - i)^{1/2}\ H^{-}(\xi)\ \bar{f}(\xi)\ . \qquad (A,14)$$

The function $\delta r_c^{\ +}(\xi)$ is analytic in the upper half plane by virtue of (A,10). Hence the left hand side of (A,14) is analytic in the upper half plane. Since f(x) vanishes for x > 0, $f(\xi)$ is analytic in the lower half plane and hence the right hand side of (A,14) is also analytic there. Hence, both sides of (A,14) represent an entire function. The $H^{\pm}(\xi)$ tend to 1 and the $h^{\pm}(\xi)$ are $O(1/\xi)$ for $\xi \to \infty$. We assume $\delta r_c(\xi)\ \xi^{1/2}$ and $f(\xi)\ \xi^{1/2}$ to be bounded for $\xi \to \infty$. Then the entire function must be a first order polynomial $C_o + C_1\ \xi$, where the values of the constants C_o and C_1 will be given later. We can now solve for the unknowns δr_c and f:

$$\delta r_c^{\ +}(\xi) = \frac{(\xi+i)^{1/2}}{H^{+}(\xi)}\ \ \left[\frac{C_o+C_1\xi}{\xi^2-\xi_o^2} - h^{+}(\xi)\right], \qquad (A,15)$$

$$\bar{f}(\xi) = -\frac{(\xi-i)^{-1/2}}{H^{-}(\xi)}\ \ [C_o + C_1\ \xi + h^{-}(\xi)\ (\xi^2 - \xi_o^2)] \quad (A,16$$

The value of C_1 is chosen so that $\bar{f}(\xi)$ is $O(\xi^{-1/2})$ for $\xi \to \infty$. Hence, by (A,12):

$$C_1 = i\ (2\pi)^{-1/2}\ (i\lambda+i)^{-1/2}\ H^{+}(i\lambda)\ . \qquad (A,17)$$

We choose C_o so that $\bar{f}(\xi)$ is an order smaller, i.e., $O(\xi^{-3/2})$, for $\xi \to \infty$; hence:

$$C_o = -\ (2\pi)^{-1/2}\ \ (i\lambda+i)^{-1/2}\ H^{+}(i\lambda)\ . \qquad (A,18)$$

The meaning of this choice for f(x) will be discussed later.

We obtain f(x) with the inverse Fourier transform:

$$f(x) = \frac{-1}{(2\pi)^{1/2}} \int_{-\infty}^{\infty} e^{-i\xi x}\ \frac{(\xi-i)^{1/2}}{H^{-}(\xi)}$$

$$[C_o + C_1\xi + h^{-}(\xi)\ (\xi^2 - \xi_o^2)]d\xi\ . \qquad (A,19)$$

Since the integrand is analytic in the lower half of the ξ-plane, the right hand side of (A,19) vanishes for x > 0, as follows from the calculus of residues. In order to obtain an expression for f(x) for x ↑ 0 we investigate the integrand in (A,19) for $\xi \to +\infty$. The function f(x) is continuous at x = 0, since the integrand is $O(\xi^{-3/2})$. Hence $f(0^-) = 0$. For real values of ξ we have, by (A,6):

$$H^{\pm}(\xi) = (H(\xi))^{\mp 1/2}\ \exp\left\{\frac{i}{2\pi} \oint_{-\infty}^{\infty}\ \ell n\ [H(\zeta)]\ \frac{d\zeta}{\zeta-\xi}\right\}, (A,20)$$

where the integral is a Cauchy principal-value. Hence for real ξ we have

$$[H^{-}(\xi)]^{-1} = 1 + \tilde{H}(\xi), \qquad (A,21)$$

where $H(\xi)$ is a continuous function, which is $O(1/\xi)$ for $\xi \to +\infty$ by (A,4). Therefore, if the factor $H^{-}(\xi)$ in the denominator in the integrand in (A,19) is omitted, the value of the integral changes by a term which is O(x) for x ↑ 0. The other factors in the integrand in (A,19) are an exponential and a rational function of ξ. Using the calculus of residues and Tauberian theorems we can obtain an asymptotic expression for the value of this integral for x ↑ 0. We do not go into details and give the result only:

$$f(x) \approx 2\pi^{-1/2}\ \ B\ \ |x|^{1/2}\ , \quad x \uparrow 0 \qquad (A,22)$$

where:

$$B = (\lambda^2 + \varepsilon_o^2)\ (\lambda + 1)^{-1/2}\ H^{+}(i\lambda)\ . \qquad (a,23)$$

In a similar way we investigate $\delta r_c(x)$ for x ↓ 0. Substitution of (A,17) and A,18) into (A,15) and then into (A,9) gives:

$$\overline{\delta r_c}\ (\xi) =$$

$$\frac{i}{(2\pi)^{1/2}}\ \frac{H^{+}(i\lambda)}{(i\lambda+i)^{1/2}}\ \frac{(\xi+1)^{1/2}}{H^{+}(\xi)}\ \frac{\lambda^2\xi_o^2}{(\xi^2-\xi_o^2)(\xi-i\lambda)} \qquad (A,24)$$

This expression is $O(\xi^{-5/2})$ for $\xi \to \infty$ and hence $\delta r_c(x)$ and its first derivative are continuous at x = 0. An expression for x ↓ 0 is obtained in the same way as for f(x):

$$\delta r_c(x) \approx \delta r_c(0) + \delta r_o'(0)\ \ x - \frac{4}{3\pi^{1/2}}\ B\ x^{3/2}\ \ x \downarrow 0. \qquad (A,25)$$

At this point we return to our choice (A,18) for C_o. If (A,18) does not hold, then it can be shown that:

$$f(x) \approx B^{*} \quad |x|^{-1/2} \quad , \qquad x \uparrow 0, \tag{A,26}$$

$$\delta r_c(x) \approx \delta r_c(0) - B^{**} x^{1/2} \quad , \quad x \downarrow 0, \tag{A,27}$$

where the constants B* and B** have the same sign. The condition f$\geq$ 0 implies B* $\geq$ 0 and the condition that the fluid does not penetrate the hub implies, in the case of a smooth hub, that B** $\leq$ 0. Hence they must vanish both, which is achieved only by giving C_0 the value (A,18).

Finally we consider a hub of arbitrary shape. By virtue of the Laplace transform we can write:

$$\delta r_c(x) = \frac{1}{2\pi i} \int_{c-i\infty}^{c+i\infty} g(\lambda) e^{\lambda x} \, d\lambda \quad , \quad x < 0 \quad , \tag{A,28}$$

where c is a positive number, and:

$$g(\lambda\ ) = \int_{-\infty}^{0} e^{-\lambda x} \quad \delta r_c(x) \, dx \quad . \tag{A,29}$$

First we assume that $\delta r_c(x)$ is such that the integral in (A,29) is absolutely convergent for $\lambda = c$, but our results will appear to hold for a more general case. By virtue of the linearity of our questions, the expressions (A,22) and (A,25) hold with B given by:

$$B = \frac{1}{2\pi i} \int_{c-i\infty}^{c+i\infty} g\ (\lambda) \ (\lambda^2 + \xi_0^2) \ (\lambda+1)^{-1/2} \ H^{+}(i\lambda) \, d\lambda. \tag{A,30}$$

Substitution of (A,29) into (A,30), interchanging the order of integration, and applying partial integration with respect to x twice, gives:

$$B = \int_{\infty}^{0} L(x) \quad \{\xi_0^2 \delta r_c(x) + \delta r_c''(x)\} \, dx \ , \tag{A,31}$$

where

$$L(x) = \frac{1}{2\pi i} \int_{c-i\infty}^{c+i\infty} e^{-\lambda x} \frac{H^{+}(i\lambda)}{(\lambda+1)^{1/2}} \, d\lambda \ , \ x < 0. \tag{A,32}$$

In this expression for L(x) we substitute $i\lambda = \mu$, take the limit $c \downarrow 0$ and use some symmetry-properties of $H^{+}(\mu)$. Then we find:

$$L(x) = \frac{1}{\pi} \int_{0}^{\infty} \text{Re} \left[e^{i\mu x} \ \frac{H^{+}(\mu)}{(1-i\mu)^{1/2}} \right] d\mu, \ x < 0, \tag{A,33}$$

Since the integrand in this expression is $O(\mu^{-1/2})$ we can derive for L(x):

$$L(x) \approx \pi^{-1/2} \quad |x|^{-1/2} \quad , \qquad x \uparrow 0 \ . \tag{A,34}$$

As stated in Section 6, the position of the point of separation is determined by the condition B = 0. By (A,31) this condition becomes:

$$\int_{-\infty}^{0} L(x) \left[\xi_0^2 \quad \delta r_c(x) + \delta r_c \quad (x)\right] dx = 0. \tag{A,35}$$

We can give an interpretation to the two terms in this integrand. There are two reasons for which the fluid may separate from the hub. First the value of δr_c may become negative, so that the centrifugal force makes the fluid particles leave the hub. This corresponds to the first term in the integrand. Second, the radius of curvature of the hub may be so small that the fluid particles are unable to keep contact with the hub. This corresponds to the second term in the integrand.

REFERENCES

Doetsch, G. (1943). *Laplace Transformation.* Dover Publications.

Noble, B. (1958). *Methods Based on the Wiener-Hopf Technique.* Pergamon Press

Sparenberg, J. A. (1958). On a shrinkfit problem. *Applied Scientific Research,* Section A, Vol. 7.

Watson, G. N. (1922). *Theory of Bessel functions.* Cambridge University Press.

Whitham, G. B. (1973). *Linear and Non Linear waves.* J. Wiley and Sons.

Wu, Th. Y. (1972). Cavity and Wake flows. *Annual Review of Fluid Mechanics, 4.*

Unsteady Cavitation on an Oscillating Hydrofoil

Young T. Shen and Frank B. Peterson
David W. Taylor Naval Ship Research and Development Center, Bethesda, Maryland

ABSTRACT

Bent trailing edges and erosion are often observed on marine propellers and are attributed mainly to unsteady cavitation caused by the nonuniformity of the flow field behind a ship's hull. In order to improve the physical understanding of the cavitation inception and the formation of cloud cavitation on marine propellers, a large two dimensional hydrofoil was tested in the DTNSRDC 36-inch water tunnel under pitching motion. Fully wetted, time dependent, experimental pressure distributions were compared with Giesing's unsteady wing theory. The influence of reduced frequency and pressure distribution on inception was determined. A simplified mathematical model to predict unsteady cavitation inception, was formulated. Good correlation between theoretical prediction and experimental measurements on cavitation inception was observed. The reduced frequency, maximum cavity length, foil surface pressure variation, and time sequential photographs were correlated with the formation of cloud cavitation. A physical model based on the instability of a free shear layer defining a near-wake region provides a reasonable explanation of the observed results.

1. INTRODUCTION

Hydrofoil craft are typically designed to operate both in calm water and waves; and marine propellers normally operate in the nonuniform flow field behind a ship. Unfortunately, due to the complexity of the experiments, only a few experiments have been specifically concerned with unsteady leading edge sheet cavitation on hydrofoils and propellers, Morgan and Peterson (1977). It is the intent of this paper to report the results of experiments concerned with leading edge sheet cavitation on an oscillating two dimensional hydrofoil. Following a brief review of the most pertinent experimental data available in the literature, an analytical method for the prediction of inception will be developed and compared with the experimental data. Once the cavity is present on the foil, cavity instabilities develop due to the foil oscillation and also due to the inherent instability of the cavitation process. This general process of instability in the leading edge sheet cavity is the subject of this paper.

It has been observed by innumerable investigators that a leading edge sheet cavity can, under certain circumstances, be quasi steady with relatively few collapsing vapor bubbles to produce erosion. However, if a propeller blade enters a wake field, the inception angle of attack at the leading edge may not agree with the uniform flow inception angle. In addition, the developed cavity may exhibit instabilities not produced in uniform flow fields. One form of cavity instability is manifest by the shedding of a significant portion of the sheet cavity. This shed portion appears to be composed of microscopic bubbles and is commonly referred to as "cloud" cavitation, van Manen (1962). Cloud cavitation is now considered to be one of the main causes of erosion and bent trailing edges, Tanibayashi (1973).

Model experiments have been performed by many organizations in an attempt to simulate full-scale wake fields in which propellers operate. One of the first detailed experiments concerned with unsteady cavitation was reported by Ito (1962). These experiments were with pitching three dimensional hydrofoils and propellers in a wake field. A principle result directly applicable to the work to be reported here was that the reduced frequency had an important influence on the cavitation. He also concluded that the "critical" reduced frequency at which a leading edge sheet cavity broke up into cloud cavitation was 0.3 to 0.4. His latter conclusion will be considered in more detail in the context of the results to be reported here.

A recent discussion of this subject was given by Tanibayashi (1962). He concluded that the occurrence of cloud cavitation in nonuniform flow cannot be predicted on the basis of uniform flow experiments. In earlier work by Tanibayashi and Chiba (1968), it was concluded from experiments with an oscillating two dimensional foil that an unsteady flow was required for the formation of cloud cavitation. However, unlike the earlier results of Ito, no distinct critical reduced frequency was found. Since these latter results were for nominally hemispherical travelling bubbles, instead of a leading edge sheet, it remains to be established whether the type of cavitation in the growth phase is of importance to cloud cavitation formation.

Chiba and Hoshino (1976) carried out extensive measurements of induced pressures on a flat plate above a propeller. On the basis of comparing results with and without a wake field and with and without cavitation, they determined that strong pressure impulses were detected on the flat plate and these correlated with the presence of cloud cavitation.

Strong pressure fluctuations of very short duration have also been detected by Meijer (1959) on the surface of a cavitating two dimensional foil. He attributed these pressure fluctuations to a stagnation point at the rear of the sheet cavity passing over a pressure gage. Chiba (1975) has attempted to correlate cavity collapse on a two dimensional oscillating foil with the response from a pressure gage mounted in the foil. He concluded that, as expected, when the shed vapor collapses large pressure impulses occur. The essential points for both of these experiments are that foil mounted pressure gages can be used in the presence of cavitation and when correlated in time with photographs can assist in the interpretation of the physical processes involved. This technique was also used in interpreting the results to be reported here.

Two other oscillating foil experiments have also been reported, Miyata (1972), Miyata et al. (1972), and Radhi (1975), that demonstrate the importance of the reduced frequency on the whole cavity inception, growth, and collapse process. Both have shown that for the particular conditions of their experiments, inception could be delayed. The greatest suppression occurred for reduced frequencies in the range of 0.4 to 0.5. Both of these experiments will be discussed later in more detail within the context of the results to be reported in this paper.

All of the experiments reviewed above describe various aspects of cavitation instabilities that are associated with the cavitation performance of oscillating foils and propellers in a wake. This cavitation performance appears to be uniquely related to the unsteady flow field that exists over the cavitating surface. In the sections that follow analytical and experimental results will be presented in an effort to provide a better understanding of how these various results are related and of the associated physical processes involved.

2. EXPERIMENTAL APPARATUS AND TEST PROCEDURE

Foil and Instrumentation

The foil was machined from 17-4 PH stainless steel to a rectangular wing of Joukowski section with the trailing edge modified to eliminate the cusp. To simulate the viscous effects at the leading edge as close to a prototype as possible, the model was designed with a chord length of 24.1 cm and a span of 77.5 cm. The maximum thickness to chord ratio is 10.5 percent. The foil surface was hand finished within 0.38 μm RMS surface smoothness.

Pressure transducers were installed at a distance of 7.96, 24.1, and 60.3 mm from the leading edge. These locations correspond to 3.3, 10, and 25 percent of chord length from the leading edge. Kulite semiconductor pressure gages of the diaphram type were mounted within a Helmholtz chamber connected to the foil surface by a pinhole. With this arrangement one could measure the unsteady surface pressures due to foil oscillation and high frequency pressure fluctuations inside the boundary layer over a pressure range of ±207 KPa (±30 PSI) and a calibrated frequency range of 0 to 2 kHz. In order to increase the spatial resolution in measuring the local pressure fluctuations inside the boundary layer, the diameter of the pinholes installed on the foil surface were kept at 0.31 mm (0.012 inches), (see Figure 1). This arrangement also reduces the danger of cavitation damage to the pressure transducers. Extreme care was taken to fill the Helmholtz-type chamber through the pinhole under vacuum with deaerated water to minimize the possible occurrence of an air bubble trapped inside the chamber. If a gas bubble was present within the gage chamber, the resonant frequency of the chamber would be reduced below its 3880 Hz value. For example, with the above procedures for filling the gage chamber at a pressure of 3.4 KPa, a bubble of 0.6 mm diameter at atmospheric pressure is produced. This bubble will lower the chamber's resonant frequency to 1100 Hz. The danger of becoming a Helmholtz resonator was not observed in our dynamic calibration tests up to 2000 Hz. The calibration procedure used here was developed by the National Bureau of Standards, Hilten (1972), modified to the extent that water rather than silicone oil was the fluid medium. Since it was very important to determine the relative phase difference between the foil angle and the pressure gage signals, all amplication and recording equipment was selected to minimize the introduction of unwanted phase shifts.

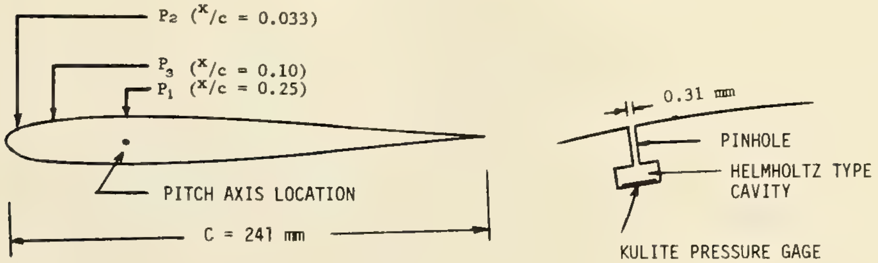

FIGURE 1. A sketch of the foil and three pressure gage locations.

Photographic Instrumentation

All photographs used to document the inception and cavity instability processes were taken with two 35 mm cameras. Illumination was provided by strobe lights having a light duration of 10 microseconds. With the camera shutter open, the first frame of a sequence was taken when a foil position indicator triggered the strobe lights. Each succeeding exposure was taken 10 and 1/25 foil oscillations after the preceeding exposure. An electrical pulse from a light detector was recorded on a channel of the same magnetic tape that was used to record the foil position, pressure gage responses, and a time code. Oscillograph records then allowed a direct correlation between these events. Both top and spanwise photographs were taken simultaneously by exposing the film with one set of flash lamps. In order to focus the camera lens in the same region as the location of the pressure gages when viewing in the spanwise direction, the camera was elevated at an angle of 4° and directed slightly downstream by an angle of 10°.

High-speed 16 mm movies were taken at a rate of 9,300 frames per second to assist in the interpretation of the 35 mm pulse camera sequential photographs. Adequate exposure for these photographs was achieved by using high intensity tungsten filament flash bulbs of 25 millisecond duration.

Test Section

The closed jet, test section of the 36-inch water tunnel was modified by the insertion of sidewall liners to provide two flat sides as shown in Figure 2. On each end of the foil a disc was attached. This disc rotated in a sidewall recess. Thus the foil could be rotated without gap cavitation occurring between the end of the foil and the sidewall of the tunnel. One sidewall assembly was fitted with clear plastic windows to permit side view photography.

The foil was oscillated by a mechanism whose conceptual design is shown in Figure 3. With this type of design the foil mean angle (α_0) can be adjusted statically and the amplitude of foil oscillation (α_1) can be continuously adjusted between $0^\circ \leq \alpha_1 \leq 4^\circ$ while in operation. The oscillation frequency is continuously variable between $4 \text{ Hz} \leq f \leq 25 \text{ Hz}$. Air bags, shown in Figure 3, were installed to reduce the fluctuating torque requirements on the motor drive system.

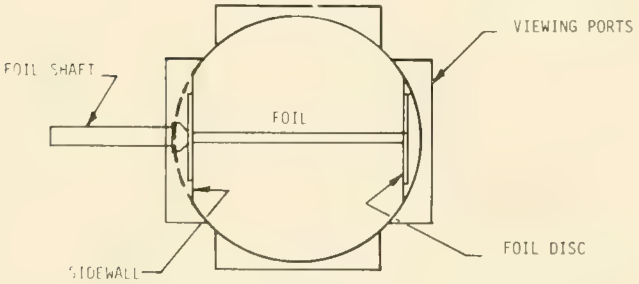

FIGURE 2. Schematic of closed jet test section.

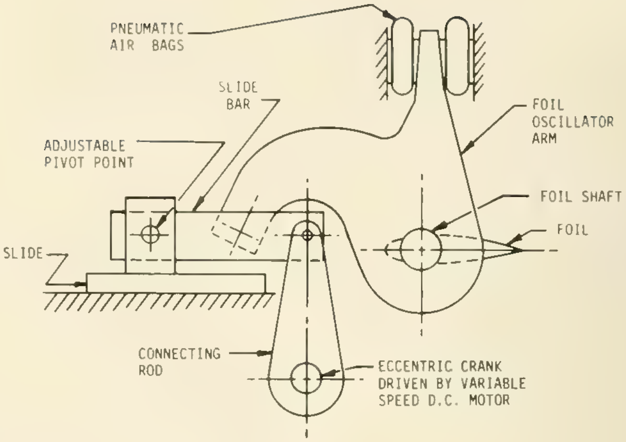

FIGURE 3. Conceptual design of foil oscillation mechanism.

Water Tunnel Resonant Frequencies

The study of cavity dynamics in a water tunnel gives rise to a fundamental question, namely, the effect of tunnel compliance on transient cavity flows. If the tunnel was perfectly rigid and if there were no free surfaces other than that of the cavity itself, then an infinite pressure difference in an incompressible medium would be required to create a changing cavity volume. To make sure that this kind of tunnel effect would not be present in our model tests, a hydraulically operated piston having a frequency range of 0 to 45 Hz was initially oscillated in a test section opening to simulate the maximum expected change of cavity volume. A sharp peak of fundamental tunnel resonance was observed at 4.7 Hz. Consequently, all of the foil oscillation experiments reported here were carried out at frequencies either above or below this resonant frequency.

Data Reduction

Due to the installation of two sidewall liners in the test section, the tunnel velocity was corrected according to the area-ratio rule. The tape recorded time histories of foil angle and pressures were digitized using a Raytheon 704 minicomputer and reduced using algorithms implemented on the DTNSRDC CDC-6000 series digital computers. The time histories were recorded on one inch magnetic tape at 15 inches per second (38 cm/s) using IRIG standard intermediate band, frequency modulation techniques. During digitization, these data were filtered using eight-pole Butterworth low pass filters that have a -3 db signal attenuation frequency at 40 Hz. They were then sampled at 125 hertz. The run lengths used in the data reduction were nominally 40 seconds. For the oscillating foil data the computer output consists of values of mean and standard deviations, sine wave amplitudes and frequencies, and transfer function magnitudes and phases. Mean and standard deviation values were obtained from the stationary foil data. For the transfer functions, the system input was foil angle, where the pressures were responses to this input. For the dynamic runs, foil angle was sinusoidal;

nominally one percent of this channel's signal energy consisted of harmonics or noise.

The methods used in data reduction are now described. The mean value, μ, and the standard deviation, σ_x, were calculated in the usual manner. The sine wave amplitudes and frequencies, and the transfer functions were obtained using operations on measured autospectra and cross spectra. These spectra were obtained using overlapped fast Fourier transform (FFT) processing of windowed data segments, Nuttall (1971), where the following reduction parameters were used: FFT size of 1024, 50 percent overlap ratio, and full cosine data window. The true autospectrum of a sine wave is an impulse, $0.5A^2\delta(f - f_o)$; the measured autospectrum is this true spectrum convolved with the spectral window. The spectral window associated with the cosine has the form:

$$\left(\frac{\sin \pi f}{f\pi(1-f^2)}\right)^2$$

The wave frequency is, in general, not sampled at a rate which is an integral multiple of the sampled frequency. Thus, the measured spectrum consists of this spectral window sampled at evenly spaced frequencies where the location of the samples relative to the sine wave frequency or spectral window maximum is unknown. The sine wave frequency and amplitude are found by fitting the spectral window shape to the three largest samples that are closest to where the sine wave is expected. The transfer functions are given by the cross spectra between the input and output data channels divided by the autospectra of the input channel. The transfer functions were evaluated at the frequency of oscillation of the foil. Quadratic interpolation between spectral samples was used to obtain the cross and autospectrum values. Once evaluated, the complex transfer functions were converted to magnitudes and phases. The transfer function magnitude is then the output sine wave amplitude, and the transfer function phase is the phase angle of this output sine wave. Except for data runs when cavitation was present, the cross spectra coherency was always greater than 0.98; this high coherency implies low noise and high linearity at the foil oscillation frequency.

3. UNSTEADY HYDRODYNAMICS IN FULLY WETTED FLOW

Basic knowledge in the general field of unsteady aerodynamics has been compiled, condensed, and presented by several authors [for example see Abramson (1967)]. Available experimental hydrodynamics information for oscillating wings and foils is very limited, especially at high values of Reynolds number. Most of the available experimental data concern lift, drag, and moment coefficients from flutter and craft control investigations. For cavitation inception studies, accurate determination of the pressure distribution, especially around the leading edge, is of major importance. In the present investigation, three pressure gage transducers were installed on the foil to measure the unsteady surface pressures. Experimental data were then correlated with an available unsteady flow theory with the intent of providing adequate information to analyze unsteady cavitation inception.

The foil was pitched about an axis at ¼ chord length from the leading edge. The instantaneous foil angle α is given by

$$\alpha = \alpha_o + \alpha_1 \sin \omega t \tag{1}$$

where α_o, α_1, and ω are the mean foil angle, pitch amplitude, and circular frequency of pitch oscillation. Let $C_p(t)$, C_{ps}, and $C_{pu}(t)$ denote the total pressure coefficient, the magnitude of the steady pressure coefficient at the foil mean angle, and the magnitude of the dynamic pressure coefficient, respectively. At a given location on the foil, it is assumed that:

$$C_p(t) = \frac{P(t) - P_\infty}{\frac{1}{2}\rho V_\infty^2} = \frac{P_s + P_u(t) - P_\infty}{\frac{1}{2}\rho V_\infty^2} = C_{ps} + C_{pu}(t) \tag{2}$$

where

$$C_{ps} = \frac{P_s - P_\infty}{\frac{1}{2}\rho V_\infty^2} \tag{3}$$

and

$$C_{pu}(t) = \frac{P_u(t)}{\frac{1}{2}\rho V_\infty^2} \tag{4}$$

where $P(t)$, P_s, $P_u(t)$, and ρ are the local total pressure on the foil, static pressure on the foil, dynamic pressure on the foil, and the fluid density, respectively; P_∞ and V_∞ denote the freestream pressure and freestream velocity. We have:

$$-C_{pu}(t) = -\left|\Delta C_{pu}\right| \sin(\omega t + \phi) \tag{5}$$

where $|\Delta C_{pu}|$ and ϕ are the amplitude of dynamic pressure response and phase angle, respectively. A positive value of ϕ means that the pressure response leads the foil angle.

Let the Reynolds number, Rn, and the reduced frequency, K, be defined by

$$R_n = \frac{V_\infty C}{\nu} \tag{6}$$

and

$$K = \frac{\omega C}{2 V_\infty} \tag{7}$$

where C, ν, and ω are the chord length, kinematic viscosity of the fluid, and the circular frequency of the oscillating foil, respectively. Fully wetted experiments covered the range of Reynolds number $Rn = 1.2$ to 3.7×10^6 and reduced frequency $K = 0.23$ to 2.30. The test results are given in Tables 1a to 1c. The phase angles and the amplitude of dynamic pressure response per radian of pitch oscillation are given in Figures 4 and 5 at values of $\alpha_1 = 0.5$, 1.0, and 2.0°.

An unsteady potential flow theory for small-amplitude motion recently developed, Giesing (1968), is used here to correlate the experimental results. The unsteady part of the pressure coefficient is

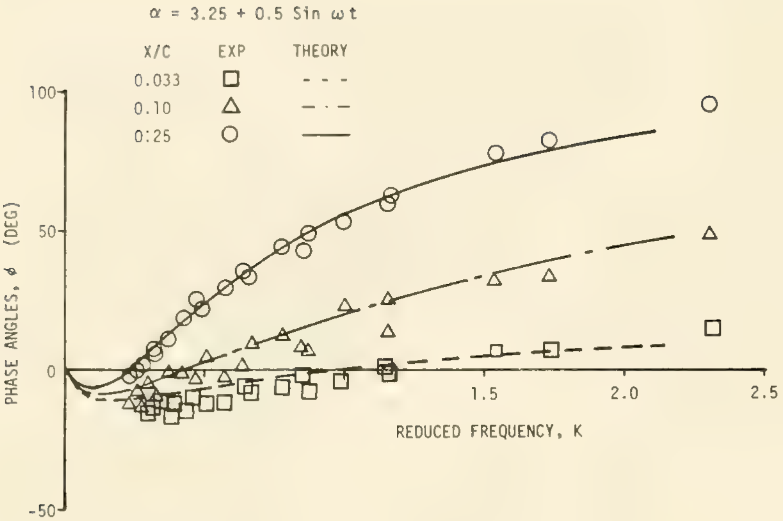

FIGURE 4a. Phase angles of dynamic pressure response at pitch amplitude α_1 = 0.5 deg.

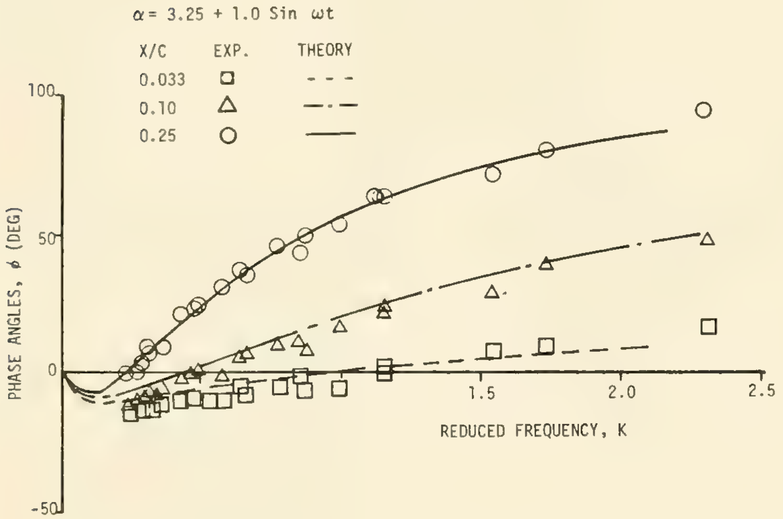

FIGURE 4b. Phase angles of dynamic pressure response at pitch amplitude α_1 = 1.0 deg.

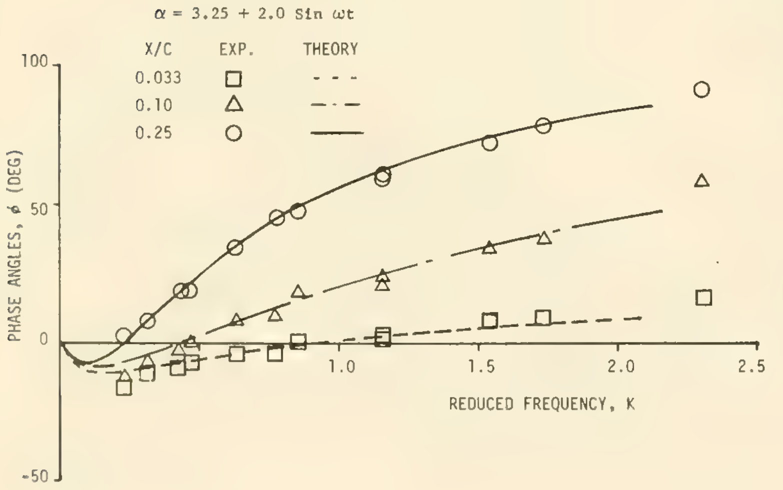

FIGURE 4c. Phase angles of dynamic pressure response at α_1 = 2.0 deg.

obtained as the difference between the total pressure coefficient minus the steady part. The steady solution is based on an exact nonlinear theory. The theoretical values obtained from Giesing's program are plotted on Figures 4 and 5 along with the experimental data.

The phase angles obtained from experiments and calculations will be discussed first. As seen in Figures 4a to 4c, the agreement between experimental measurements and theoretical calculations of pressure and phase angles is quite good for all three pressure locations. The agreement is good between experimental measurements and theoretical predictions of magnitudes of dynamic pressure for the cases of X/C = 0.25 and 0.10, as seen in Figures 5a to 5c. At low values of K the measured pressure coefficients are seen to be slightly lower than the values calculated for the case of X/C = 0.033. The exact cause of this small discrepancy between measurements and theoretical calculations has not been determined.

The cause of small discrepancies between the theory and experiments requires further investigation. Nevertheless, the overall good agreement observed between our experimental measurements and Giesing's method is extremely encouraging. It is noted that Giesing's method is based on unsteady potential flow theory. The combined theoretical and experimental results by McCroskey (1975, 1977) indicate that unsteady viscous effects on oscillating airfoils are much less important than the unsteady potential flow effects, if the boundary layer does not interact significantly with the main flow. The present study appears to agree with his conclusion for the case of a fully wetted foil. On the basis of this relatively good agreement between Giesing's method and the experimental data, this method will be used in the next section to predict cavitation inception as a function of the reduced frequency, K.

4. UNSTEADY EFFECTS ON CAVITATION INCEPTION

The major objective of this section is to examine what effect unsteadiness has on cavitation inception. The question of the occurrence of cavitation is of particular importance when comparing model test results for marine propellers or hydrofoils with the full-scale prototype data. We would like to know whether a noncavitating model is also free from cavitation in the prototype. When calculating the flow about propeller blades or hydrofoils, it is important to know whether the cavitation bubbles form on the blades, and if so, under what circumstances. The cavitation number σ, defined by

$$\sigma = \frac{P_\infty - P_V}{\frac{1}{2} \rho V_\infty^2} \qquad (8)$$

has proved useful as a coefficient for describing the cavitation process. Here, ρ and P_v denote the density and vapor pressure of the fluid and P_∞ and V_∞ denote the freestream static pressure and the freestream velocity, respectively.

In addition to the incoming flow properties such as freestream turbulence and nuclei content, the surface finish and boundary layer characteristics on the body surface are also of paramount importance to the cavitation inception process Acosta and Parkin (1975). To limit the scope of the test program, air content of the water was not varied. The air content was measured with 70% saturation in reference to atmospheric pressure at a water temperature of 22.2° C and tunnel pressure of 103.6 kPa.

The foil was pitched sinusoidally around an axis at the quarter chord location aft of the foil leading edge. The cavitation tests were carried out by lowering the ambient pressure from the previous fully wetted tests. The determination of cavitation inception was based on visual observations. For every test condition, 30 pictures were taken to record the cavitation process on the foil. A picture was taken every ten oscillations plus 1/25 of the time period of the foil oscillation. Thus, a series of high quality short duration photos were taken that together simulate one and 1/5 cycles of the foil oscillation. A pulse signal was simultaneously recorded on magnetic tape when a picture was taken. In this way, each cavity pattern observed on the foil could be related directly to the instantaneous angle of attack of the foil.

Analytical Prediction

A simplified mathematical model will be formulated first to explore the possible effect of unsteadiness on cavitation inception. A significant delay in dynamic stall was observed experimentally and discussed in a recent review paper by McCroskey (1975), who showed that the pressure gradient dC_p/dx around the leading edge was of paramount importance in dynamic stall. The studies by Carta (1971) indicate that the mechanism involved in the delay of dynamic stall is the large reduction of unfavorable pressure gradient dC_p/dx during any unsteady motion.

The mechanism involved in cavitation inception is different from the mechanism of aerodynamic stall. It is generally assumed that cavitation occurs on a body when the local pressure, including the unsteady pressure fluctuations within the boundary layer, falls to or below the vapor pressure of the surrounding fluid, Huang and Peterson (1976). Aside from the effect of nuclei content of the water, it is the value of the local pressure coefficient that governs the occurrence of cavitation. Prior to the occurrence of cavitation on an oscillating foil, the foil is in a fully wetted condition. Thus, the knowledge of pressure distribution on the foil in the fully wetted condition can be expected to provide useful information for unsteady cavitation inception prediction.

As previously mentioned, the combined theoretical and experimental results reviewed and summarized by McCroskey (1977) indicate that unsteady viscous effects on oscillating airfoils are much less important than unsteady potential flow effects, if the boundary layer does not interact significantly with the main flow. In the present study, as discussed in the previous section, the three pressure coefficients measured at three points around the leading edge are predicted reasonably well by Giesing's method both in amplitude and phase within the range of reduced frequencies examined. This unsteady potential flow theory will now be used to investigate cavitation inception.

In the tests, the foil was oscillated about a mean angle of 3.25°. The mean values of dynamic foil loadings determined from measurements are

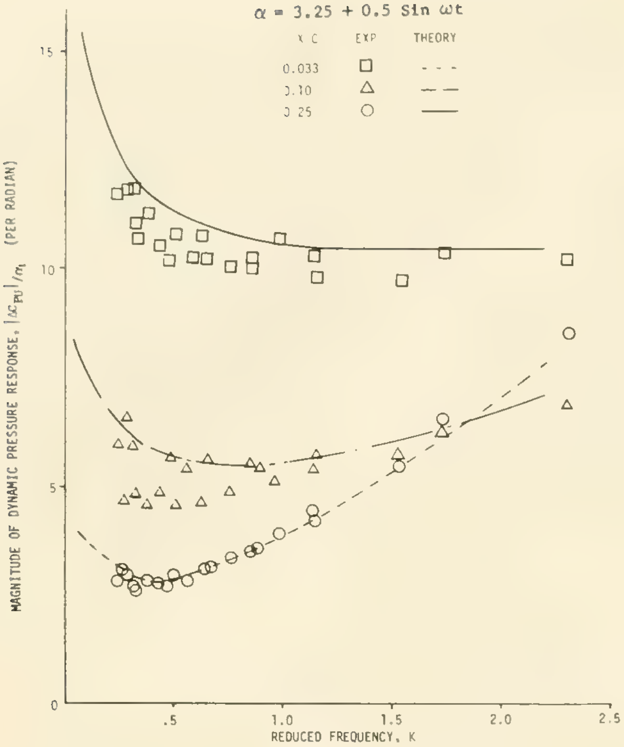

FIGURE 5a. Magnitude of dynamic pressure response at α_1 = 0.5 deg.

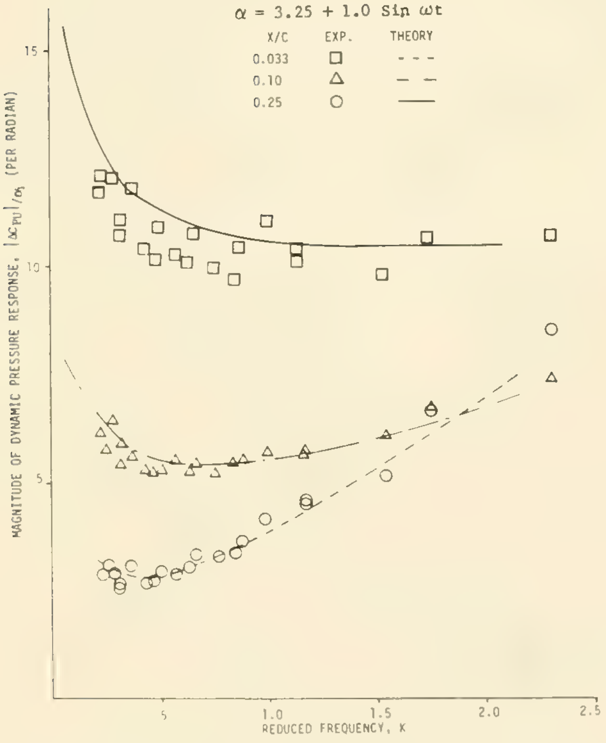

FIGURE 5b. Magnitude of dynamic pressure response at α_1 = 1.0 deg.

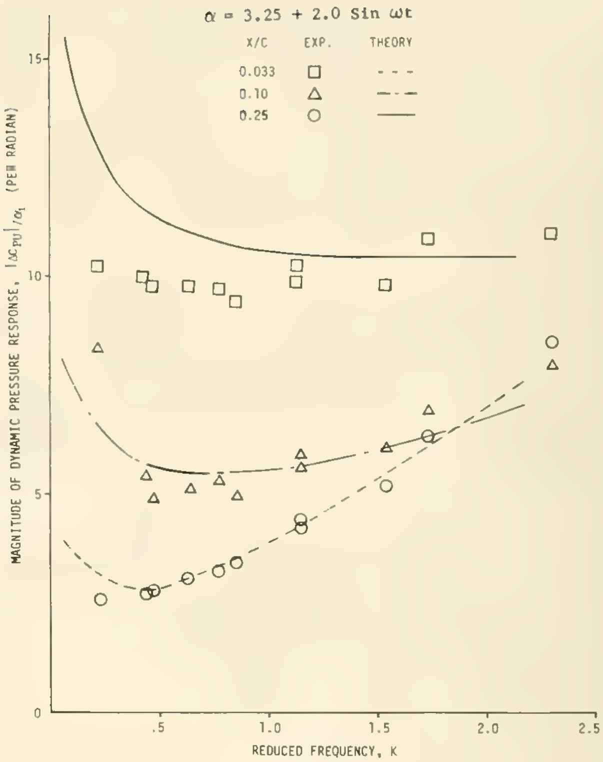

FIGURE 5c. Magnitude of dynamic pressure response at α_1 = 2.0 deg.

plotted in Figure 6. Aside from some scatter in the data, they are seen to be independent of frequency (or reduced frequency). The steady pressure distribution calculated theoretically at 3.25° is given in Figure 7. A suction peak appears at around 1.8 percent of the chord length aft of the leading edge. Reasonably good agreement between the theoretical prediction and the three experimental measurements should be noted. Experimental data confirm the basic assumption made in Eq. (2) that the total pressure coefficient $C_p(t)$ is the sum of the dynamic pressure coefficient $C_{pu}(t)$ plus the static pressure coefficient C_{ps} at the mean foil angle, i.e.

$$C_p(t) = C_{ps} + C_{pu}(t)$$

We will now proceed to examine the possible relationship between the dynamic pressure coefficient $C_{pu}(t)$ and the static pressure coefficient C_{ps}. Let the instantaneous foil angle be expressed as in Eq. (1). The dynamic pressure response is then given by

$$-C_{pu}(t) = -\left|\Delta C_{pu}\right| \cdot \sin(\omega t + \phi) \qquad (5)$$

Here $|\Delta C_{pu}|$ and ϕ are the amplitude and phase angles. They are functions of reduced frequency K and location X/C. They can be obtained either from experimental measurements or theoretical calculations. In the following study, Giesing's program will be used to compute these variables. In our oscillating tests, the mean foil angle was always maintained at α = 3.25°. The type of cavitation observed in our

TABLE 1a - MEASURED DYNAMIC PRESSURE RESPONSE AT PITCH AMPLITUDE α_1 = 0.5 DEG.

					x/c = 0.25		x/c = 0.10		x/c = 0.033	
Run Number	V	f	K	R_n	ϕ	$\lvert\Delta C_{pu}\rvert/\alpha_1$	ϕ	$\lvert\Delta C_{pu}\rvert/\alpha_1$	ϕ	$\lvert\Delta C_{pu}\rvert/\alpha_1$
	m/s	HZ		$x10^{-6}$	Deg	Per Radian	Deg	Per Radian	Deg	Per Radian
7002	4.88	5.5	.846	1.2	43.4	3.48	7.1	5.58	-3.1	9.92
7006	4.88	10.0	1.539	1.2	77.7	5.40	31.2	5.60	7.0	9.62
7010	4.88	15.0	2.305	1.2	95.7	8.51	48.3	6.77	15.5	10.10
7014	6.71	5.5	.635	1.7	35.8	3.07	1.2	5.69	-6.4	10.15
7019	6.71	10.0	1.154	1.7	58.4	4.13	13.6	5.72	.1	9.72
7024	6.71	15.0	1.730	1.7	81.6	6.59	32.5	6.21	7.6	10.32
7029	9.75	5.5	.423	2.4	18.3	2.69	-2.0	4.74	-11.5	10.43
7034	9.75	10.0	.769	2.4	44.9	3.34	12.6	4.79	-7.1	9.93
7039	9.75	15.0	1.153	2.4	62.2	4.45	24.8	5.32	-2.3	10.21
8002	13.11	5.5	.317	3.3	5.7	2.61	-11.3	5.89	-15.1	10.90
8006	13.11	10.0	.576	3.3	29.5	2.76	-3.2	5.33	-12.4	10.10
8010	13.11	15.0	.865	3.3	48.5	3.50	6.4	5.36	-8.2	10.19
8029	6.71	4.0	.462	1.7	24.9	2.65	-4.3	5.60	-9.2	10.09
8041	9.75	4.0	.308	2.4	7.1	2.58	-7.6	4.78	-13.3	10.64
8045	13.11	4.0	.231	3.3	-2.5	2.77	-13.3	5.86	-15.8	11.68
8057	14.94	5.5	.282	3.7	.7	2.88	-15.1	6.62	-16.6	11.80
1121	11.58	4.0	.264	2.8	-.9	3.05	-9.9	4.54	-15.0	11.85
1122	11.58	5.5	.363	2.8	10.5	2.86	-1.0	4.44	-13.3	11.12
1123	11.58	7.5	.495	2.8	20.3	2.91	4.3	4.44	-11.6	10.77
1124	11.58	10.0	.660	2.8	32.1	3.03	10.0	4.53	-9.5	10.72
1125	11.58	15.0	.990	2.8	52.3	3.93	24.0	5.00	-5.4	10.69

TABLE 1b - MEASURED DYNAMIC PRESSURE RESPONSE AT PITCH AMPLITUDE α_1 = 1.0 DEG.

					x/c = 0.25		x/c = 0.10		x/c = 0.033	
Run Number	V	f	K	R_n	ϕ	$\lvert\Delta C_{pu}\rvert/\alpha_1$	ϕ	$\lvert\Delta C_{pu}\rvert/\alpha_1$	ϕ	$\lvert\Delta C_{pu}\rvert/\alpha_1$
	m/s	HZ		$x10^{-6}$	Deg	Per Radian	Deg	Per Radian	Deg	Per Radian
7003	4.88	5.5	.846	1.2	42.4	3.39	10.5	5.46	-1.5	9.66
7007	4.88	10.0	1.539	1.2	71.1	5.13	28.5	6.09	7.4	9.77
7011	4.88	15.0	2.305	1.2	93.6	8.51	47.0	7.40	16.0	10.73
7015	6.71	5.5	.635	1.7	37.4	3.04	5.8	5.28	-5.3	10.03
7020	6.71	10.0	1.154	1.7	62.8	4.57	23.6	5.67	2.0	10.05
7025	6.71	15.0	1.730	1.7	79.5	6.71	38.8	6.75	8.6	10.70
7030	9.75	5.5	.423	2.4	20.7	2.67	-2.6	5.26	-10.4	10.36
7035	9.75	10.0	.769	2.4	44.9	3.28	9.5	5.19	-5.3	9.91
7040	9.75	15.0	1.153	2.4	62.6	4.64	20.9	5.76	-.6	10.41
8003	13.11	5.5	.317	3.3	7.6	2.64	-9.5	5.91	-13.6	11.03
8007	13.11	10.0	.576	3.3	30.9	2.81	-1.9	5.45	-10.2	10.22
8011	13.11	15.0	.865	3.3	49.0	3.63	6.8	5.65	-6.9	10.40
8030	6.71	4.0	.462	1.7	23.5	2.69	-1.1	5.13	-8.6	10.07
8042	9.75	4.0	.308	2.4	8.2	2.59	-7.9	5.34	-12.4	10.72
8046	13.11	4.0	.231	3.3	-.8	2.78	-11.8	6.13	-14.2	11.76
8058	14.94	5.5	.282	3.7	3.5	2.90	-11.8	6.46	-14.8	11.96
1017	11.58	4.0	.264	2.8	-.3	3.08	-11.3	5.76	-13.9	12.09
1018	11.58	5.5	.362	2.8	9.4	3.03	-6.3	5.58	-12.7	11.83
1019	11.58	7.5	.493	2.8	21.7	2.97	.6	5.22	-10.5	10.99
1020	11.58	10.0	.660	2.8	34.2	3.33	6.1	5.40	-9.0	10.83
1021	11.58	15.0	.988	2.8	52.2	4.15	15.5	5.69	-4.9	11.10

TABLE 1c - MEASURED DYNAMIC PRESSURE RESPONSE AT PITCH AMPLITUDE
α_1 = 1.5 DEG

					x/c = 0.25		x/c = 0.10		x/c = 0.033	
Run Number	V	f	K	R_n	ϕ	$\lvert\Delta C_{pu}\rvert/\alpha_1$	ϕ	$\lvert\Delta C_{pu}\rvert/\alpha_1$	ϕ	$\lvert\Delta C_{pu}\rvert/\alpha_1$
	m/s	HZ		$x10^{-6}$	Deg	Per Radian	Deg	Per Radian	Deg	Per Radian
7031	9.75	5.5	.423	2.4	21.0	2.65	-3.2	5.50	-10.0	10.26
7036	9.75	10.0	.769	2.4	46.5	3.22	8.3	5.30	-5.1	9.76
7041	9.75	15.0	1.153	2.4	62.3	4.62	19.0	5.98	-.2	10.40
8004	13.11	5.5	.317	3.3	9.0	2.57	-8.6	5.72	-13.0	10.79
8008	13.11	10.0	.576	3.3	31.5	2.78	-1.0	5.39	-9.7	10.19
8012	13.11	15.0	.865	3.3	50.2	3.63	8.4	5.62	-5.7	10.35
α_1 = 2.0 DEG										
7004	4.88	5.5	.846	1.2	46.7	3.36	16.9	4.93	-.7	9.34
7008	4.88	10.0	1.539	1.2	71.3	5.14	33.7	6.01	7.2	9.76
7012	4.88	15.0	2.305	1.2	90.7	8.47	49.0	7.96	16.0	10.98
7016	6.71	5.5	.635	1.7	33.0	3.01	7.4	5.06	-4.9	9.75
7021	6.71	10.0	1.154	1.7	58.5	4.16	23.2	5.59	2.0	9.83
7026	6.71	15.0	1.730	1.7	77.8	6.30	36.4	6.91	8.7	10.87
7032	9.75	5.5	.423	2.4	19.4	2.63	-2.8	5.38	-9.7	9.99
7037	9.75	10.0	.769	2.4	44.7	3.18	8.3	5.30	-5.0	9.68
7042	9.75	15.0	1.153	2.4	60.9	4.42	19.2	5.92	0.0	10.26
8031	6.71	4.0	.462	1.7	18.8	2.70	-.1	4.86	-8.3	9.67
8047	13.11	4.0	.231	3.3	2.0	2.50	-13.0	8.35	-16.5	10.16
α_1 = 2.5 DEG										
7017	6.71	515	.635	1.7	32.8	2.89	6.9	4.91	-4.8	9.34
7022	6.71	10.0	1.154	1.7	57.7	4.01	21.6	5.54	1.6	9.71
7027	6.71	15.0	1.730	1.7	77.9	6.00	36.4	6.59	8.8	10.33

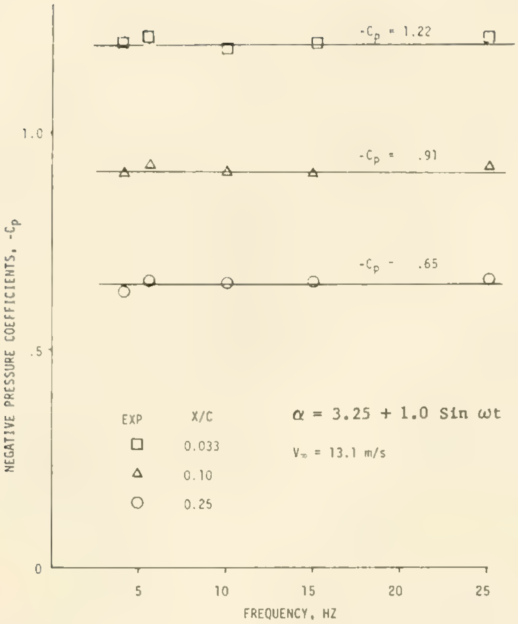

FIGURE 6. Mean pressure coefficients deduced from oscillating tests.

test program always initiated near the foil leading edge.

Let $(dC_p/d\alpha)_s$ denote the static pressure gradient with respect to foil angle at a given location on the foil. Similarly, let $(dC_p/d\alpha)_u$ denote the dynamic pressure gradient with respect to foil angle at the same location on the foil with the reduced frequency, K, as the parameter. To simplify the writing, they will be referred to as the "static" and "dynamic" angular pressure gradients respectively. Let $\xi(k)$ be the ratio of dynamic angular pressure gradient versus static angular pressure gradient at a given location on the foil, namely

$$\xi(K) = (dC_p/d\alpha)_u / (dC_p/d\alpha)_s \qquad (9)$$

This ratio $\xi(K)$ and the phase angle ϕ for several locations and reduced frequencies have been calculated and are given in Table 2. The static angular pressure gradient $(dC_p/d\alpha)_s$ at a given location is approximated for mean foil angles of 3.3 to 4.3° since leading edge cavitation inception typically occurred within this range. As seen in Table 2, for a given reduced frequency, the amount of reduction in dynamic pressure ratio (ξ) remains almost a constant value in the range of $0.004 < X/C < 0.06$ which covers the foil region over which leading-edge cavitation occurs. Consequently, if the foil is oscillated around the mean foil angle α_o, the shape of the pressure distribution in the neighborhood of the suction peak and the peak location are essentially the same for both zero

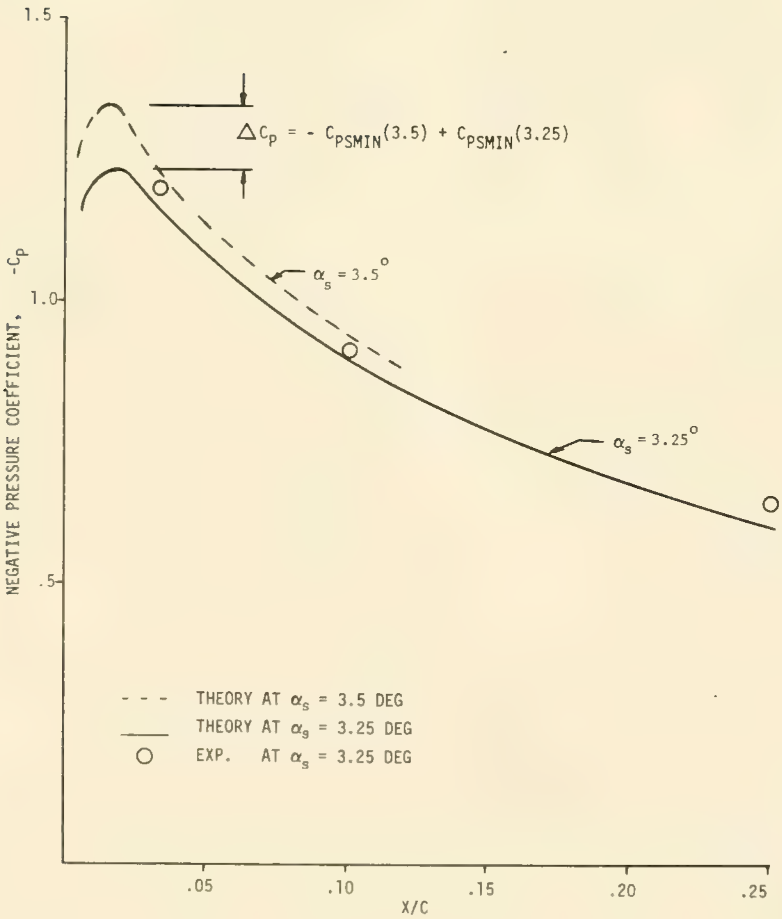

FIGURE 7. Static pressure distributions at foil angles of 3.5 and 3.25 deg.

TABLE 2 - THEORETICALLY CALCULATED DYNAMIC PRESSURE
RESPONSE AT VARIOUS (x/c) LOCATIONS

	REDUCED FREQUENCY, K							
	0.05	0.1	0.3	0.5	0.75	1.0	1.5	2.0
At x/c = 0.0046, $(\frac{dc_p}{d\alpha})_s$ = 33.52								
ϕ	-7.47	-10.53	-11.25	-9.53	-7.91	-6.97	-6.26	-5.96
$\lvert\Delta C_{pu}\rvert/\alpha_1$	30.18	28.10	22.41	21.87	20.97	20.57	20.27	20.19
ξ	.90	.84	.67	.65	.63	.61	.61	.60
At x/c = 0.0073, $(\frac{dc_p}{d\alpha})_s$ = 30.25								
ϕ	-7.46	-10.51	-11.11	-9.25	-7.45	-6.32	-5.26	-4.61
$\lvert\Delta C_{pu}\rvert/\alpha_1$	28.03	26.09	21.72	20.28	19.44	19.06	18.77	18.68
ξ	.93	.86	.72	.67	.65	.63	.62	.62
At x/c = 0.0117, $(\frac{dc_p}{d\alpha})_s$ = 26.59								
ϕ	-7.44	-10.46	-10.88	-8.78	-6.66	-5.22	-3.56	-2.31
$\lvert\Delta C_{pu}\rvert/\alpha_1$	24.28	22.59	18.78	17.51	16.77	16.44	16.19	16.10
ξ	.91	.85	.70	.66	.63	.62	.61	.61
At x/c = 0.018, $(\frac{dc_p}{d\alpha})_s$ = 23.0								
ϕ	-7.41	-10.38	-10.53	-8.08	-5.48	-3.58	-1.02	+1.13
$\lvert\Delta C_{pu}\rvert/\alpha_1$	20.72	19.27	15.99	14.89	14.25	13.96	13.75	13.67
ξ	.91	.83	.70	.65	.62	.61	.60	.60
At x/c = 0.026, $(\frac{dc_p}{d\alpha})_s$ = 19.65								
ϕ	-7.37	-10.28	-10.08	-7.19	-4.01	-1.52	+2.15	+5.40
$\lvert\Delta C_{pu}\rvert/\alpha_1$	17.72	16.47	13.63	12.67	12.12	11.88	11.71	11.68
ξ	.90	.84	.69	.65	.62	.61	.60	.60
At x/c = 0.035, $(\frac{dc_p}{d\alpha})_s$ = 16.79								
ϕ	-7.31	-10.16	-9.53	-6.10	-2.22	+.96	+5.96	+10.51
$\lvert\Delta C_{pu}\rvert/\alpha_1$	15.28	14.19	11.72	10.87	10.40	10.20	10.09	10.11
ξ	.91	.85	.70	.65	.62	.61	.60	.60
At x/c = 0.058, $(\frac{dc_p}{d\alpha})_s$ = 12.78								
ϕ	-7.18	-9.84	-8.10	-3.33	+2.33	+7.23	+15.41	+22.84
$\lvert\Delta C_{pu}\rvert/\alpha_1$	11.68	10.84	8.89	8.23	7.88	7.78	7.83	8.05
ξ	.92	.85	.69	.65	.62	.61	.61	.63

and nonzero reduced frequencies. This is an important conclusion which will be utilized later in the analytical prediction of cavitation inception.

We will now proceed to develop a criterion to define the unsteady leading edge cavitation inception. Let α_{is} denote the cavitation inception angle measured in a stationary test for given values of σ and Rn. As an example, at a cavitation number of $\sigma = 1.15$ and $Rn = 3 \times 10^6$, cavitation inception occurred experimentally at $\alpha_{is} = 3.5°$. The corresponding pressure distribution calculated using potential flow theory is given in Figure 7 with a suction peak appearing at around 1.6 percent chord aft of the leading edge. Let C_{psmin} (α_{is}) denote the minimum value of the static pressure coefficient C_{ps}, at the foil angle $\alpha = \alpha_{is}$. It has been generally assumed that cavitation inception occurs when $-C_{psmin}$ $(\alpha_{is}) = \sigma$. Obviously, this simple relationship is not realized in the present test results (See Figure 7). This kind of discrepancy in applying the above scaling law for cavitation inception is a classic problem and has been extensively discussed in the literature [for example see Morgan and Peterson (1977) and Acosta and Parkin (1975)].

One of the possible reasons for this discrepancy is that a finite amount of time is required for nuclei to grow. Thus, cavitation inception will depend not only on the magnitude of the suction pressure peak, but it will also depend on the shape of the pressure distribution in the neighborhood of the suction peak and the peak location. Since, as shown previously, these two features of the pressure distribution are essentially the same for zero and nonzero reduced frequencies of interest here, it will be assumed that the amount of time required for nuclei to grow is approximately the same for both a stationary and oscillating foil. Consequently, it is assumed that cavitation inception occurs on the foil at nonzero reduced frequencies when the magnitude of $-C_{psmin}$ (α_{is}) is encountered during the foil oscillation, for given values of σ and Rn.

An analytical method will now be developed to predict leading edge cavitation inception on a oscillating foil based on inception measurements made on a stationary foil. Let ΔC_p be given by

$$\Delta C_p = \left| C_{Psmin}(\alpha_{is}) - C_{psmin}(\alpha_o) \right| \tag{10}$$

where C_{psmin} (α_o) denotes the minimum value of the static pressure coefficient at $\alpha = \alpha_o$ and C_{psmin} (α_{is}) is the minimum static pressure coefficient at the cavitation inception angle α_{is}. According to our assumption, unsteady cavitation occurs when the difference in the static loading ΔC_p between α_{is} and α_o is produced by the dynamic loading at some instant of time t_i. Thus, unsteady cavitation occurs if

$$\left| C_{pu}(t_i) \right| = \Delta C_p \tag{11}$$

where $|C_{pu}(t_i)|$ is the magnitude of the dynamic pressure response at time $t = t_i$. If the value of $\alpha_{is} - \alpha_o$ is small it follows from Eqs. (5) and (11) that

$$\alpha_1 \, (dC_p/d\alpha)_u \sin(\omega t_i + \phi) \approx (\alpha_{is} - \alpha_o)(dC_p/d\alpha)_s \tag{12}$$

where t_i corresponds to that instant of time at which Eq. (11) is satisfied. Small-amplitude motion has been assumed. The static angular pressure gradient is to be evaluated at the location of the suction peak corresponding to the steady condition $\alpha = \alpha_o$. The unsteady inception angle α_{iu} for a given reduced frequency K is obtained from Eqs. (1) and (12).

$$\alpha_{iu} = \alpha_o + (\alpha_{is} - \alpha_o)\frac{\cos\phi}{\xi} - \alpha_1 \sin\phi\sqrt{1 - \left(\frac{\alpha_{is} - \alpha_o}{\alpha_1 \xi}\right)^2}, \quad (\alpha_1 \neq 0) \tag{13}$$

As a consequence of Eq. (12), no singularity is expected inside the square root. Due to the unsteady effect the inception angle α_{iu} is generally different from α_{is}. Let $\Delta\alpha$ be

$$\Delta\alpha = \alpha_{iu} - \alpha_{is} \tag{14}$$

which can be used to measure the magnitude of the unsteady effect. From Eq. (13), it follows that

$$\Delta\alpha = (\alpha_{is} - \alpha_o)\left(\frac{\cos\phi}{\xi} - 1\right) - \alpha_1 \sin\phi \sqrt{1 - \left(\frac{\alpha_{is} - \alpha_o}{\alpha_1 \xi}\right)^2} \tag{15}$$

$$(\alpha_1 \neq 0)$$

For the case where the phase angle ϕ is small at the location of inception, we have

$$\Delta\alpha = (\alpha_{is} - \alpha_o)\left(\frac{1}{\xi} - 1\right) - \alpha_1\phi \sqrt{1 - \left(\frac{\alpha_{is} - \alpha_o}{\alpha_1 \xi}\right)^2} \tag{16}$$

Although a small phase angle, ϕ, approximation is not required, it is useful to make this approximation for the sake of discussing the implications of Eq. (15). The first term on the right-hand side represents the effect of the ratio of dynamic to static angular pressure gradients $\xi(K)$ on unsteady cavitation inception. The second term represents the effect of phase angle, amplitude of oscillation, and the ratio of pressure gradients on cavitation inception. For example, as seen in Figure 4 the phase angles of dynamic pressure response at the leading edge lag behind the foil angle (negative ϕ) for values of K less than 1.0 at X/C = 0.033. Due to this phase lag, the occurrence of unsteady cavitation inception is further delayed. Contributing

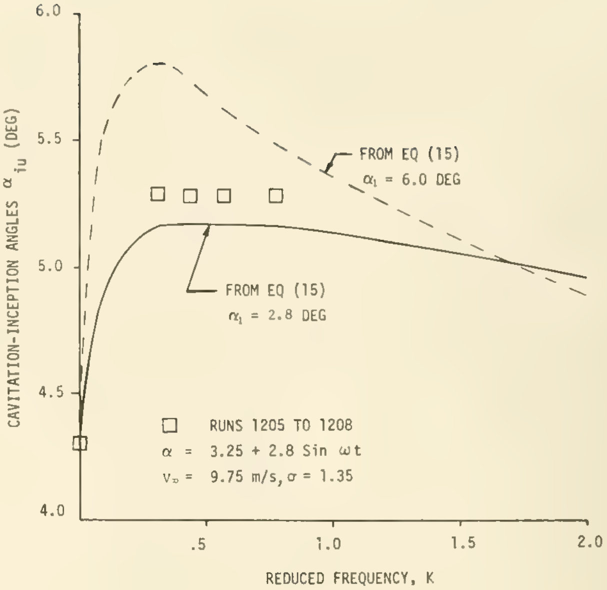

FIGURE 8. Measured cavitation-inception angles for test runs 1205 to 1208, α_1 = 2.8 deg.

TABLE 3 - EXPERIMENTAL RESULTS ON UNSTEADY CAVITATION-INCEPTION ANGLES, α_{iu}

Run No.	V m/s	f HZ	R_n x10^{-6}	K	σ	α_1 Deg	α_{is} Deg	α_{iu} Deg
1205	9.75	4.0	2.4	.307	1.35	2.8	4.3	5.28
1206	9.75	5.5	2.4	.423	1.35	2.8	4.3	5.28
1207	9.75	7.5	2.4	.577	1.35	2.8	4.3	5.28
1208	9.75	10.0	2.4	.768	1.35	2.8	4.3	5.28
1301	11.49	4.0	2.8	.264	1.13	.95	3.5	3.94
1302	11.49	5.5	2.8	.362	1.13	.95	3.5	3.94
1303	11.49	7.5	2.8	.494	1.13	.95	3.5	3.94
1304	11.49	10.0	2.8	.659	1.13	.95	3.5	3.94
1305	11.49	15.0	2.8	.988	1.13	.95	3.5	3.94
1306	11.49	25.0	2.8	1.646	1.13	.95	3.5	3.71 ~ 3.94
1307	14.78	4.0	3.7	.205	1.12	1.00	3.5	3.71 ~ 3.94
1308	14.78	5.5	3.7	.282	1.12	1.00	3.5	3.71
1309	14.78	7.5	3.7	.384	1.12	1.00	3.5	3.94
1310	14.78	10.0	3.7	.512	1.12	1.00	3.5	3.94
1401	11.49	4.0	2.8	.264	1.13	1.55	3.5	3.90 ~ 4.20
1402	11.49	5.5	2.8	.362	1.13	1.55	3.5	3.90 ~ 4.20
1403	11.49	7.5	2.8	.494	1.13	1.55	3.5	4.20
1404	11.49	10.0	2.8	.659	1.13	1.55	3.5	4.20
1405	11.49	15.0	2.8	.987	1.13	1.55	3.5	4.20
1406	11.49	25.0	2.8	1.646	1.13	1.55	3.5	3.60 ~ 3.90
1407	14.78	4.0	3.7	.205	1.14	1.55	3.5	3.90
1408	14.78	5.5	3.7	.282	1.14	1.55	3.5	4.20
1409	14.78	7.5	3.7	.384	1.14	1.55	3.5	4.20
1410	14.78	10.0	3.7	.513	1.14	1.55	3.5	3.90
1501	16.42	4.0	4.1	.185	1.15	.95	3.5	3.71
1502	16.42	5.5	4.1	.255	1.15	.95	3.5	3.71
1503	16.42	7.5	4.1	.347	1.15	.95	3.5	3.71
1504	16.42	10.0	4.1	.462	1.15	.95	3.5	3.94
1505	16.42	15.0	4.1	.694	1.15	.95	3.5	3.71
1506	16.42	25.0	4.1	1.157	1.15	.95	3.5	3.71 ~ 3.94

TABLE 4 - THEORETICAL CALCULATION OF $\Delta\alpha$ AND α_{iu} FOR TEST SERIES 1205 TO 1208 AT x/c = 0.018

K	ϕ DEG	ξ	$\Delta\alpha$ DEG	α_{iu} DEG
0.05	-7.41	.91	.42	4.72
0.1	-10.38	.83	.64	4.94
0.3	-10.53	.70	.86	5.16
0.5	-8.08	.65	.87	5.17
0.75	-5.48	.62	.85	5.15
1.0	-3.58	.61	.83	5.13
1.5	-1.02	.60	.74	5.04
2.0	+1.13	.60	.66	4.96

NOTE:

α_{is} = 4.30 DEG.

α_o = 3.25 DEG.

α_1 = 2.80 DEG.

to the inception delay is the oscillation amplitude α_1. It is noted that the effect of oscillation amplitude on inception angle is strongly coupled with the phase angle. Thus, there will be no effect of α_1 on inception if there is no phase shift. This is a consequence of the small oscillation amplitude assumption. As the reduced frequency K approaches zero, $\xi \to 1$ and $\phi \to 0$, and the steady-state inception angle ($\Delta\alpha \to 0$) is recovered.

Experimental Results

The range of Reynolds numbers covered in the cavitation tests was 2.4 to 4.1 × 10^6. Because it is shown in Acosta and Parkin (1975) and Huang and Peterson (1976) that the existence of laminar separation may trigger premature cavitation in model tests, the boundary layer characteristics on the foil under stationary conditions were calculated. Within the Reynolds number range of the test program, the occurrence of laminar separation around the leading edge was not predicted. Flow visualization with dye injection supported this conclusion. The unsteady effect of foil oscillations on the boundary layer characteristics was not included in the calculation.

In order to simulate prototype viscous effects as closely as possible, the model was tested at high tunnel speeds (11.5 to 16.4 m/s). For a given body shape the laminar boundary layer thickness based on chord length decreases approximately as $(Rn)^{-\frac{1}{2}}$. The effect of surface roughness on flow characteristics becomes more important at higher Reynolds number. This roughness effect was found in the present model tests with cavitation appearing prematurely in a few "weak" spots even though the surface was highly polished. This caused some difficulty in determining accurate values of cavitation inception angle. The relative importance of this uncertainty was minimized by applying the same cavitation inception criteria to both the steady and unsteady test results.

Six series of oscillating foil tests were carried out. The test conditions and the test results are given in Table 3. Only 30 pictures were taken to cover one and 1/5 cycles of oscillating motion, and thus the angle at which inception occurred can only be related to two successive pictures. Therefore, in some cases, the inception angle is given in terms of a small range of angles instead of a single value.

The test results from runs 1205 to 1208 are shown in Figure 8. In these cases, the foil was oscillated around a mean angle α_0 = 3.25° with a

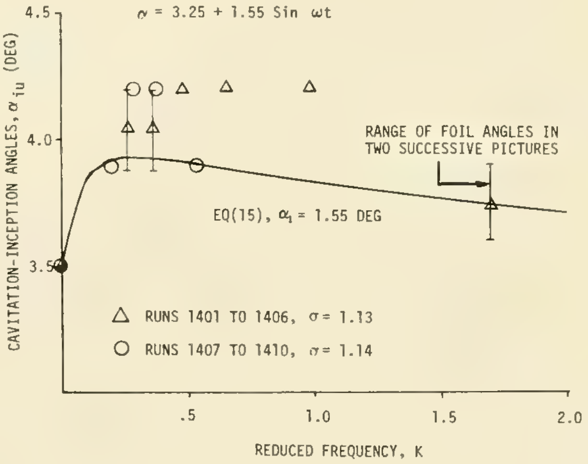

FIGURE 9. Measured cavitation-inception angles for runs 1401 to 1410.

TABLE 5 - THEORETICAL CALCULATION OF $\Delta\alpha$ AND α_{iu} FOR TEST SERIES 1401 TO 1410 AT x/c = 0.018

K	ϕ DEG.	ξ	$\Delta\alpha$ DEG.	α_{iu} DEG.
0.05	-7.41	.91	.23	3.73
0.1	-10.38	.83	.34	3.84
0.3	-10.53	.70	.42	3.92
0.5	-8.08	.65	.40	3.90
0.75	-5.48	.62	.36	3.86
1.0	-3.58	.61	.33	3.83
1.5	-1.02	.60	.26	3.76
2.0	+1.13	.60	.20	3.70

NOTE:

α_{is} = 3.5 DEG.

α_o = 3.25 DEG.

α_1 = 1.55 DEG.

TABLE 6 - THEORETICAL CALCULATION OF $\Delta\alpha$ AND α_{iu} FOR TEST SERIES 1301 TO 1306
1501 TO 1506 AT x/c = 0.018

K	ϕ DEG	ξ	$\Delta\alpha$ DEG	α_{iu} DEG	NOTE:
0.05	-7.41	.91	.14	3.64	α_{is} = 3.5 DEG
0.1	-10.38	.83	.21	3.71	
0.3	-10.53	.70	.26	3.76	α_0 = 3.25 DEG
0.5	-8.08	.65	.25	3.75	
0.75	-5.48	.62	.23	3.73	α_1 = .95 DEG
1.0	-3.58	.61	.22	3.72	
1.5	-1.02	.60	.18	3.68	
2.0	+1.13	.60	.15	3.65	

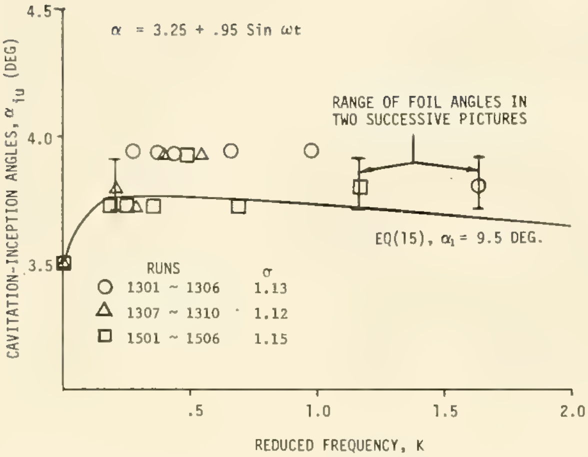

FIGURE 10. Measured cavitation-inception angles for runs 1301 to 1310 and 1501 to 1506.

pitch amplitude of α_0 = 2.8° and cavitation number σ = 1.35. The measured cavitation inception angle at the stationary condition was α_{is} = 4.3°. Within the range of reduced frequency $0.3 \leq K \leq 0.77$, the measured unsteady cavitation inception angles were α_{iu} = 5.28°. That is, a significant delay of cavitation inception was observed at nonzero reduced frequencies. The unsteady inception angles computed from Eq. (15) will now be examined. A previous discussion indicates that the suction pressure peak with the foil in oscillation is located at essentially the same X/C position as the suction peak corresponding to the steady condition $\alpha = \alpha_0$. As seen in Figure 7, the steady suction peak occurs at a location near X/C = 0.018. The predicted results based on Eq. (15) for the unsteady cavitation inception are given in Table 4 and plotted in Figure 8 along with the experimental data. The phase angle ϕ, and the ratio of dynamic to static angular pressure gradients, ξ, used in the prediction were calculated with Geising's computer program. Reasonably good agreement between theoretical calculations and experimental measurements is observed.

The test results from runs 1401 to 1406 and runs 1407 to 1410 are given in Table 3 and plotted in Figure 9. In these cases, the foil was oscillated around α_0 = 3.25° with a pitch amplitude of α_1 = 1.55° and cavitation number of σ = 1.14. The measured cavitation inception angle at the stationary condition is α_{is} = 3.5°. The measured unsteady inception angles vary from α_{iu} = 3.9 to 4.2° between K = 0.2 to 1.0 and α_{iu} = 3.6 to 3.9° at K = 1.65. The theoretical results obtained from Eq. (15) are given in Table 5 and plotted in Figure 9. Once again, a significant delay in cavitation inception is observed experimentally and predicted theoretically at nonzero reduced frequencies. The agreement is fair. Part of the discrepancy between theory and experiment may be due to the lack of accurate resolution in measuring foil angles, since only 30 pictures were taken to simulate 1 and 1/5 cycles of foil oscillation. The phase angle ϕ is seen to change the sign from negative to positive values at K above 1.5. Consequently, at high values of reduced frequencies the amount of reduction in cavitation inception delay is reduced. This trend is observed experimentally and predicted theoretically.

The test results from runs 1301 to 1306, 1307

TABLE 7 - THEORETICAL CALCULATION OF $\Delta\alpha$ AND α_{iu}
AT x/c = 0.018

K	ϕ DEG	ξ	$\Delta\alpha$ DEG	α_{iu} DEG	NOTE:
0.05	-7.41	.91	.85	5.15	α_{is} = 4.3 DEG
0.1	-10.38	.83	1.25	5.55	
0.3	-10.53	.70	1.49	5.79	α_0 = 3.25 DEG
0.5	-8.08	.65	1.36	5.66	
0.75	-5.48	.62	1.19	5.49	α_1 = 6.0 DEG
1.0	-3.58	.61	1.06	5.36	
1.5	-1.02	.60	.80	5.10	
2.0	+1.13	.60	.59	4.89	

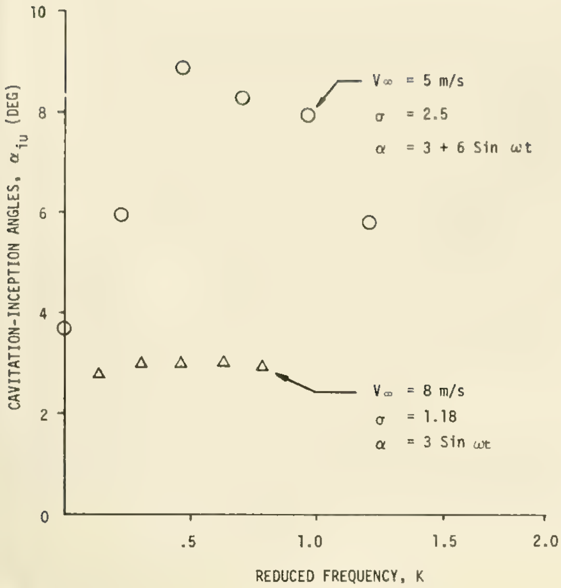

FIGURE 11. Measured cavitation-inception angles by Miyata (1972).

to 1310 and 1501 to 1506 are given in Table 3 and plotted in Figure 10. The foil was oscillated around $\alpha_0 = 3.25°$ with a pitch amplitude of $\alpha_1 = 0.95°$ and cavitation number $\sigma = 1.12$ to 1.15. The measured cavitation inception angle at the stationary condition is $\alpha_{is} = 3.5°$. The measured maximum steady inception angles are $\alpha_{iu} = 3.70$ to 3.93°. Once again, a significant delay in cavitation inception at nonzero reduced frequencies is measured. The theoretical calculations based on Eq. (15) are given in Table 6 and plotted in Figure 10. The agreement is reasonably good.

In order to provide an insight into the effect of α_1 on cavitation delay, a theoretical example is computed in Table 7 and plotted in Figure 8. The foil is assumed to pitch around $\alpha_0 = 3.25°$ with an amplitude of $\alpha_1 = 6.0°$. The stationary cavitation inception angle is assumed to be $\alpha_{is} = 4.3°$. It is seen in Figure 8 that a significant delay in cavitation inception can be expected if the pitch amplitude is increased. This trend is also observed experimentally by comparing Figures 9 and 10.

A two-dimensional foil undergoing pitch oscillations around an axis located at mid-chord was tested by Miyata et al. (1972). Two of the typical test results are produced in Figure 11 for comparison. For the data shown the foil was oscillated with a pitch amplitude of $\alpha_1 = 6.0°$. As expected (See Figure 8) a significant increase in the angle of cavitation inception is noticed for $0 < K < 1.2$. For the second set of data shown in Figure 11, the foil was oscillated with a pitch amplitude of $\alpha_1 = 3.0°$. A similarity between Figure 8 and Figure 11 is noticed. Although the foil shapes and the locations of pitch axes are different between Miyata's experiments and ours, the effect of unsteadiness on cavitation inception is similar for two model tests. A similar trend is also noticed in Radhi's experiments (1975).

In the review papers by Acosta and Parkin (1975) and Huang and Peterson (1976), one is clearly reminded that even under steady conditions the cavitation inception process is extremely complex.

The theoretical prediction of cavitation inception angle under steady conditions is still very difficult. However, if the steady-state inception angle α_{is} is known from model tests, the effect of unsteadiness on cavitation inception may be estimated reasonably well by Eq. (15). Further investigations are needed to explore discrepancies between theory and experiment and the applicability of Eq. (15) to different foil shapes and for pitch axis different from the ones examined here.

5. LEADING EDGE SHEET CAVITY INSTABILITY

Wu (1972) has provided a very useful review of the physics of cavity and wake flows which may help to explain the observations of the present experiment. The essence of his description, applicable to the partial cavity condition, is that the free shear layer enveloping the cavity is unstable. The cavity occupies a portion of what can be referred to as the wake bubble or near wake, physically delineated in steady flow by a dividing streamline that is characterized by a constant or nearly constant pressure. For the condition where the cavity within the near wake is unsteady, the region is, strictly speaking, not defined by a streamline but by a material line which is difficult to observe experimentally. Because of this difficulty, we will initially assume that a quasisteady approximation is valid. When the cavity is just beyond the inception condition, its surface should be smooth as would be expected with a laminar shear layer. As the cavity grows in length the free shear layer would tend to become unstable. Transition from a laminar to turbulent shear layer initially takes place at the downstream end of the near-wake. A further extension of the cavity length causes transition to gradually move upstream along the free shear layer and the far-wake becomes irregular. This is comparable to the bursting of a short laminar separation bubble in a single phase fluid. With a continued increase in cavity length, transition can begin at the leading edge of the cavity.

In applying here the general features of the near-wake outlined by Wu (1972) no assumption is made as to whether the cavity occupies all of the near-wake region since the detailed physics of the region downstream of the cavity trailing edge are uncertain. One possibility is that the roll-up of the shear layer into vortices is completed at the near-wake closure where the vortices break away. If this occurs, it is reasonable to expect a periodicity in this shedding process.

The variation in foil pressure at the P_1 location (see Figure 1) can give a useful insight into what is happening both downstream of the cavity and within the cavity when the foil is oscillaing with a pitch amplitude (α_1) of 1.55°. Figure 12 shows an oscillograph record of the pressure variation P_1 for a cavity that reaches its maximum length downstream of the gage location. (A) is the region where the foil surface is fully wetted and the pressure appears to follow the variation expected as the angle of attack, α, is varied. At point (B), the cavity begins to cover the gage and in this example the pressure drops from the fully wetted pressure of 31.7 kPa to the cavity pressure in 0.003 seconds. The cavity pressure remains constant, except for several pressure spikes (C) of

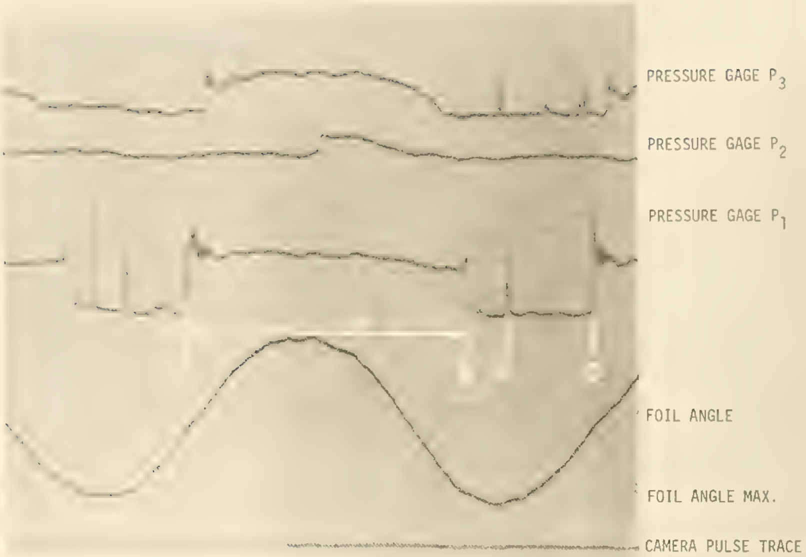

FIGURE 12. Sample oscillograph record for the variation in foil surface pressure with foil angle at $K = 0.26$, $V_\infty = 11.5$ m/s, $P_\infty = 76.2$ kPa, $\alpha = 3.25^\circ + 1.55 \sin \omega t$.

millisecond duration, until the trailing edge of the cavity recedes past the P_1 gage (point D).

The absolute magnitude of the cavity pressure could not be accurately determined from these experiments since the in situ pressure gages were not calibrated for the condition of a gas/liquid interface at the entrance to Helmholtz-type chamber over each gage. As shown in Figure 12, point B, the growing cavity does not appear to produce large foil surface pressure fluctuations at its downstream edge. However, when the cavity recedes, (ie., point D) then the foil surface pressure fluctuations can be comparable to the magnitude of the dynamic pressure.

Based on photographic records it appears that when the cavity is expanding, its trailing edge is disturbed as one would expect if the shear layer were unstable at that location. Beginning at the cavity trailing edge and then moving forward, the cavity surface becomes highly disturbed, irregular, and bubbles are introduced into the shear layer, just as one would expect when transition in the shear layer moves forward. The cavity pressure, as measured by the gages P_1, P_2 and P_3, remains constant throughout this change in the surface of the cavity.

During the early stages of sheet cavity growth, when only the cavity trailing edge appears disturbed, small regions of bubbles are shed from the sheet cavity trailing edge. This shedding process becomes more accentuated as the sheet cavity length increases and more of its surface becomes disturbed. High speed movies taken at 9,300 frames per second clearly show the highly turbulent characteristics originating at the trailing edge of the sheet cavity and progressively moving upstream.

The sequence of vapor shedding from the cavity trailing edge, as determined by high speed movies taken at 9,300 frames per second, is as in the sketches of Figure 13. The photographs of Figure 14 demonstrate a phase in the vapor bubble shedding process from the sheet cavity as sketched in 13c with two regions of shed vapor downstream. It should be noted that since the foil surface is very smooth, a reflection of the shed vapor is seen in the side views. Therefore a dashed line has been added to Figure 14 to indicate the separation of the vapor and its reflected image. This shedding process is periodic and for the example shown in Figure 14 the shedding frequency at a given spanwise location is nominally 700 hertz. The view shown in Figure 14 covers nominally the center third of the foil span. Visual observations with strobescopic lighting indicate that the leading edge sheet cavitation, for nonzero values of K, typically consists of a series of 3 dimensional cavities across the span.

In Figure 15 the top view shows a depression in the cavity surface (a) just above P_1 and a rise in cavity height (b) just downstream of the depression. At this instant a pressure "spike" is detected by P_1 (see for example C in Figure 13). This condition precedes the shedding of a small region of vapor bubbles upstream of the sheet cavity trailing edge and significantly deforms the cavity trailing edge shape. It is the forerunner of the condition that will be referred to in this paper as "cloud" cavitation. It is interesting to note that after correlation of over 600 photographs of the leading edge sheet cavitation with the pressure gage signal, the pressure "spike" always occurs when a depression in the cavity surface exists over the pressure gage. The converse, however, was not observed, ie., the "spike" can occur when no depression was discernable in the photographs. These "spikes" can occur without any significant gross change in the observed character of the sheet cavity surface in the general

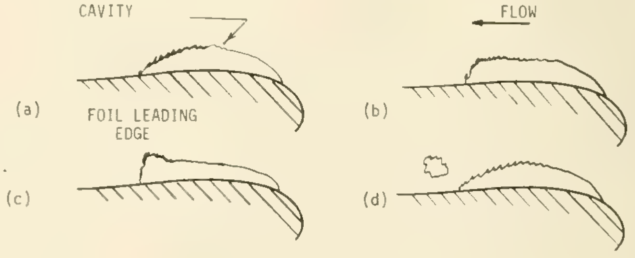

FIGURE 13. Sequence of vapor shedding from the cavity trailing edge.

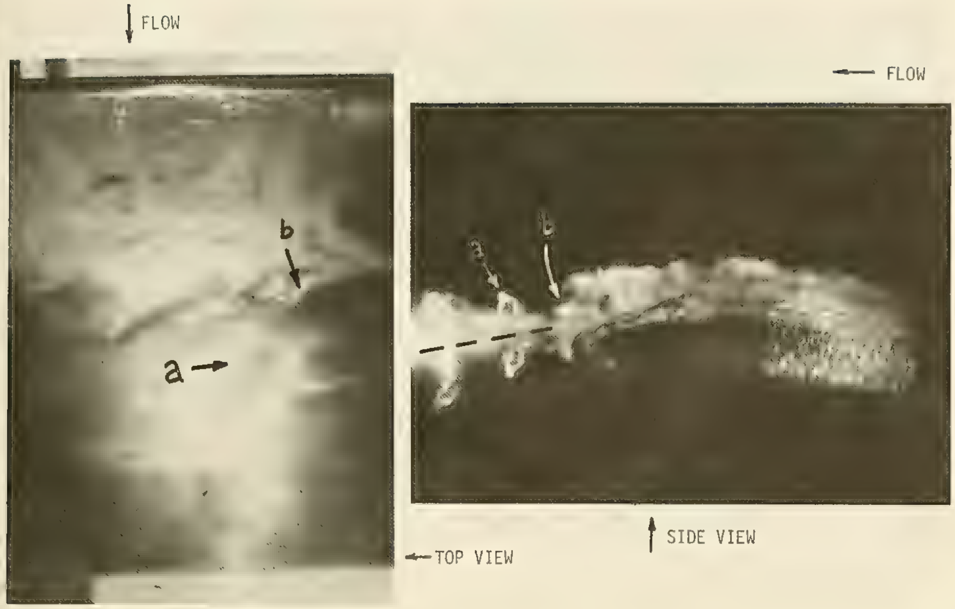

FIGURE 14. Progressive shedding of vapor from sheet cavity trailing edge, $K = 0.26$, $V_\infty = 11.5$ m/s, $P_\infty = 76.2$ kPa, $\alpha = 3.25^0 + 1.55^0 \sin \omega t$.

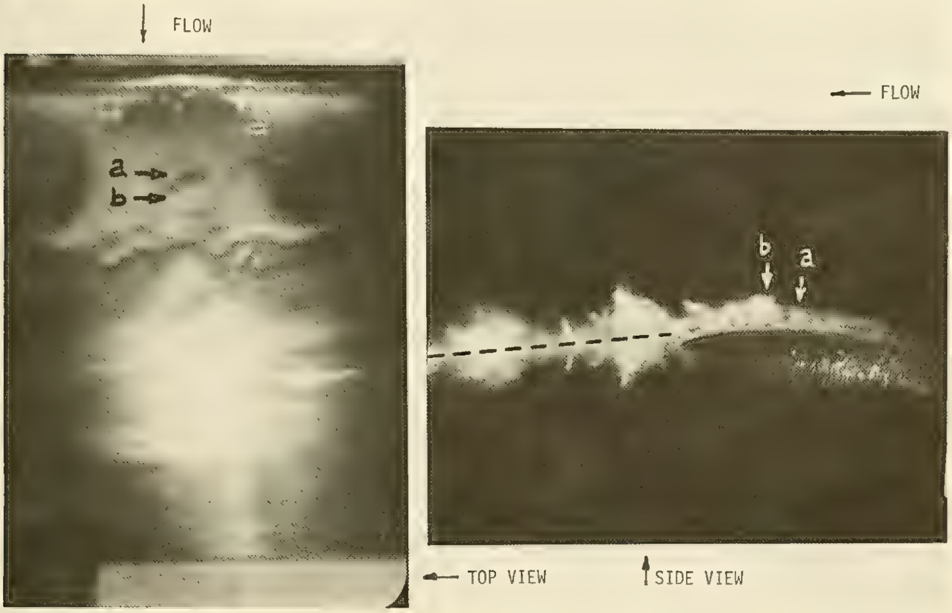

FIGURE 15. Cavity surface depression producing pressure "SPIKE" P_1 gage location, $K = 0.36$, $V_\infty = 11.5$ m/s, $P_\infty = 76.2$ kPa, $\alpha = 3.25^0 + 1.55^0 \sin \omega t$.

vicinity of a pressure gage. Since numerous pressure "spikes" can occur during the life of the sheet cavity it appears improbable that they are due to the interaction of a postulated reentrant jet with the sheet cavity surfaces [Knapp et al. (1970)]. These "spikes" frequently have amplitudes which are comparable to the dynamic pressure and certainly exceed the estimated static pressure in the free shear layer over the pressure gage location. Quite possibly, these pressure "spikes" are due to the free shear layer itself since they only occur when the cavity surface indicates a turbulent shear layer is present. When the reduced frequency is high, for example at $K = 1.65$, the fully wetted pressure variation leads the foil angle by 68° and then no pressure "spikes" are produced at the pressure gage location as can be seen in Figure 16. At these high reduced frequencies the periodic shedding from the sheet cavity trailing edge downstream of the pressure gage is still observed.

The last aspect of the leading edge sheet cavity instability to be described in this paper is that which will be called cloud cavitation. The three principle features of cloud cavitation for $K \geq 0$ are as follows:

(1) A large surface area of the sheet cavity becomes highly distorted and undergoes a significant increase of overall cavity height in the distorted region, (Figure 17).
(2) Once this distorted region begins to separate from the main part of the sheet cavity, the upstream portion of the sheet cavity develops a smooth surface and a reduced thickness (Figures 18 and 19).
(3) The trailing edge of the smooth surfaced

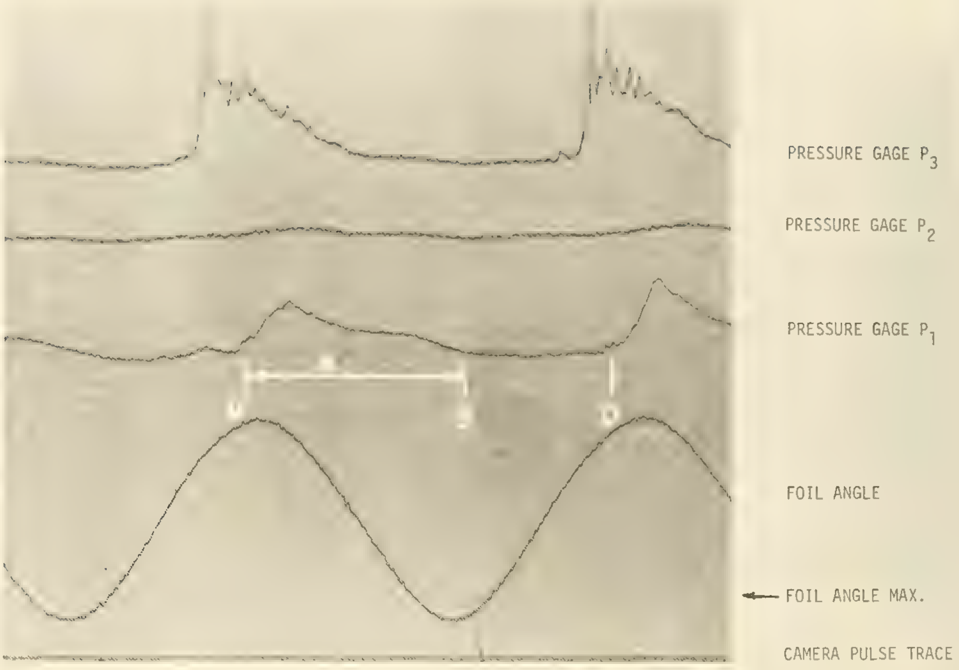

FIGURE 16. Sample oscillograph record for the variation in foil surface pressure with foil angle at K = 1.65, $V_\infty = 11.5$ m/s, $P_\infty = 76.2$ kPa, $\alpha = 3.25^\circ + 1.55^\circ \sin \omega t$.

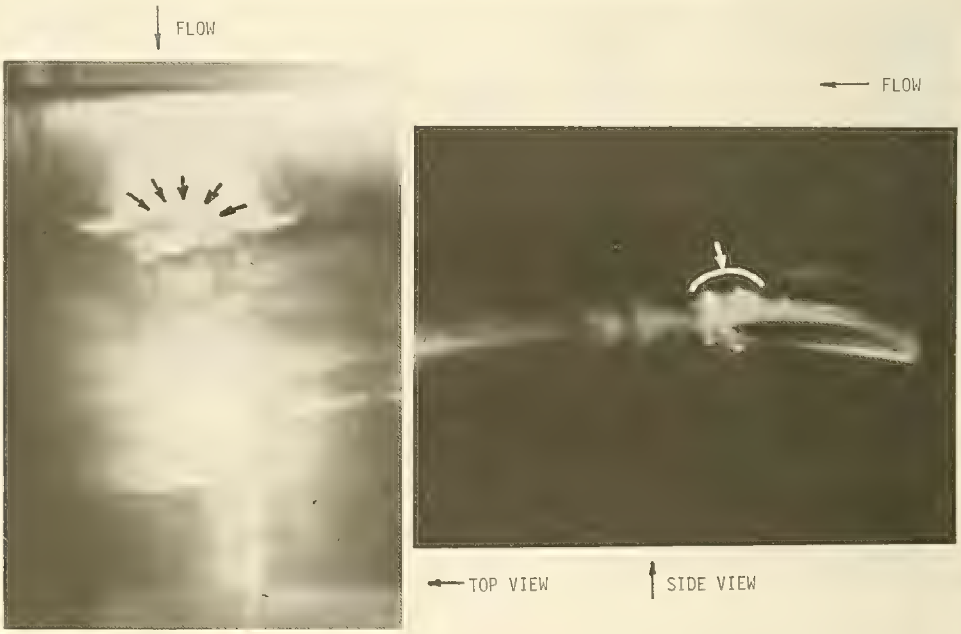

FIGURE 17. Initial stage in the process of cloud cavitation formation, K = 0.51, $V_\infty = 14.8$ m/s, $P_\infty = 124.1$ kPa, $\alpha = 3.25 + 0.95^\circ \sin \omega t$.

region then moves downstream, becomes unstable at its trailing edge, and quickly develops the characteristic appearance of the leading edge sheet cavity elsewhere along the span (see feature a in Figure 20); or, the trailing edge of the smooth portion of the sheet cavity moves upstream to the foil leading edge and the cavity disappears (Figure 21). In Figure 21 a dye trace injected at the foil leading edge can be seen.

When the foil is stationary (K=0) cloud cavitation shedding can be very periodic as can be seen in Figure 22 which shows the oscillograph trace of the pressure gage response. The frequency of shedding for the condition illustrated in Figure 22 is 42 Hz based on the response of the pressure gage P_1. Figure 23 shows a photograph of the type of cavitation that produced the time pressure history of Figure 22. In Figure 23, (a) is a cloud just in the process of being shed, (b) is a cloud previously shed at a nearby spanwise location, and (c) is a cloud shed earlier at the same location as (a). The cavities did not shed in the manner of the two-dimensional separation which typically occurs in sharp leading edge foils [Song (1969), Besch (1969), Wade and Acosta (1965)]. Instead, cavity shedding was highly three-dimensional and more or less independent of the sheet cavity instability occurring several cavity lengths away along the foil span. However, it appears that for the trailing edge shedding and the cloud cavitation (at least

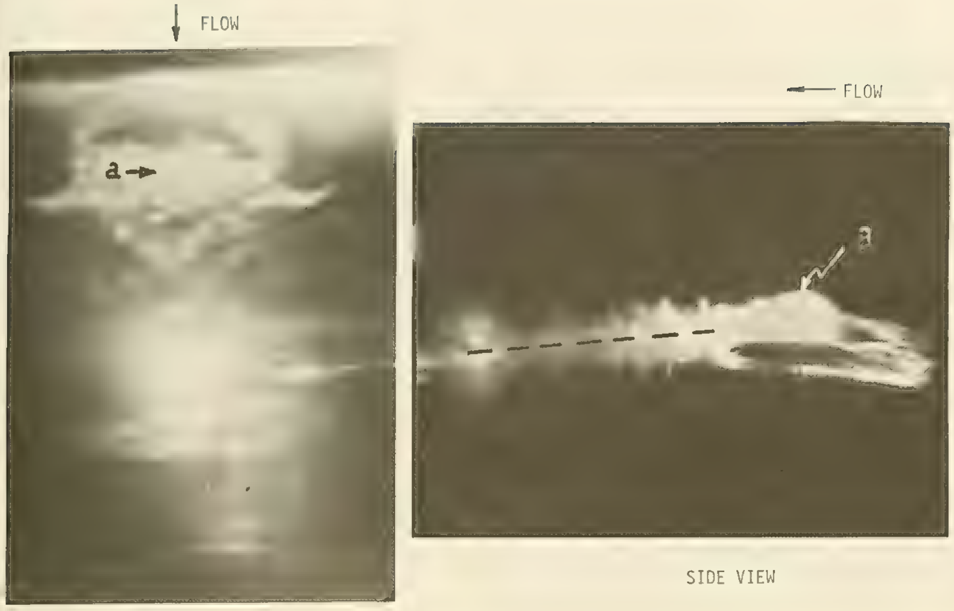

SIDE VIEW

TOP VIEW

FIGURE 18. Cloud cavity separation from leading edge sheet cavity (example 1), $K = 0.99$, $V_\infty = 11.5$ m/s, $P_\infty = 76.2$ kPa, $\alpha = 3.25 + 1.55 \sin \omega t$.

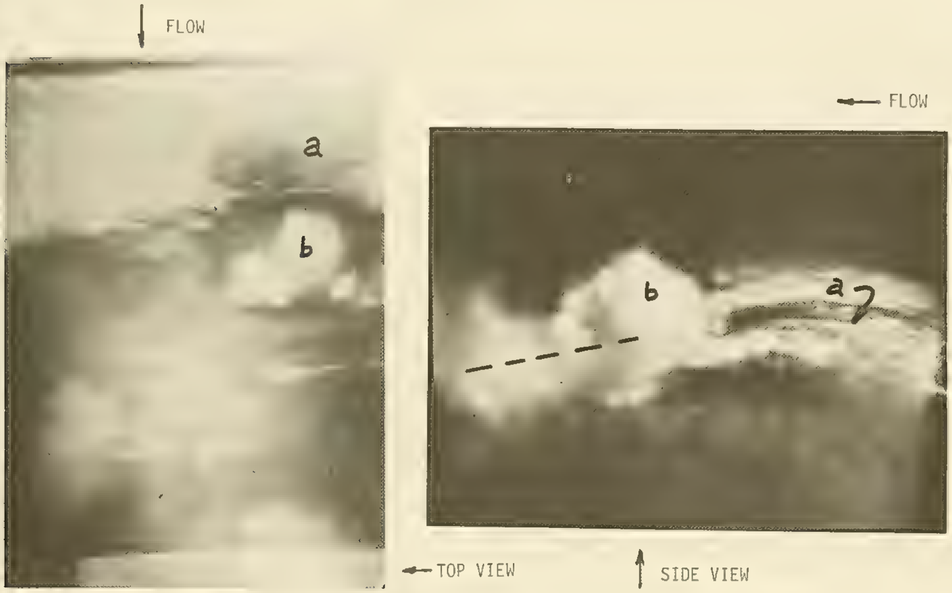

TOP VIEW

SIDE VIEW

FIGURE 19. Cloud cavity separation from leading edge sheet cavity (example 2), $K = 0$, $V_\infty = 14.8$ m/s, $P_\infty = 124.1$ kPa, $\alpha = 3.25^\circ$.

for $K = 0$) shedding occurrence alternated between several spanwise locations. This is clearly seen in Figure 23.

Several other aspects of the cavity shedding process were apparent. The shed vapor had an initial gross rotation with the same direction as occurs in the free shear layer. This was evident from the high speed movies viewing the cavitation along the span (ie., a side view), and can also be inferred from the pulse camera photographs taken from the same view. The gross volume of the shed vapor had relatively little dispersion prior to its collapse but frequently developed within it regions of apparent bubble coalesence prior to collapse, as can be seen in Figures 14 and 24.

On the basis of the previously described definition of cloud cavitation, its occurrence was determined from available photographs. The presence of cloud cavitation as a function of the ratio of maximum sheet cavity length, ℓ_m, to chord length, C, and reduced frequency K is shown in Figure 25. The data used to define the condition for the occurrence of cloud cavitation were all taken at nominally the same value of σ. Figure 25 shows that for a given ($\ell_{m/c}$) value, cloud cavitation can occur at nonzero K values whereas none would be apparent for $K = 0$. For example, if test conditions were adjusted such that $\ell_{m/c} = 0.36$, at $0.3 < K < 0.4$, then one could conclude as did Ito (1976) that there was a "critical" reduced frequency associated with the onset of cloud cavitation.

Figure 25 also shows two curves representative of the influence of the value of α_1 on cloud cavitation. It is readily apparent from the data in Figure 25 that the conditions for cloud cavitation cannot be simulated by quasi-steady experiments. As shown in Figure 25, cavity length is strongly dependent on K. If the angle of a stationary foil

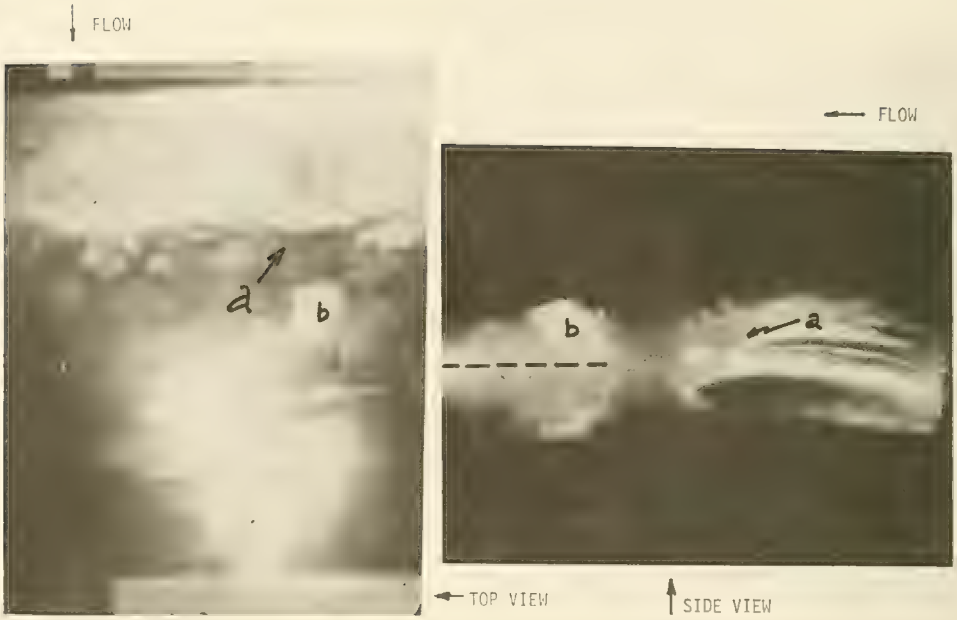

FIGURE 20. Final stage in cloud shedding process, $K = 0.21$, $V_\infty = 14.8$ m/s, $P_\infty = 124.1$ kPa, $\alpha = 3.25 + 0.95 \sin \omega t$.

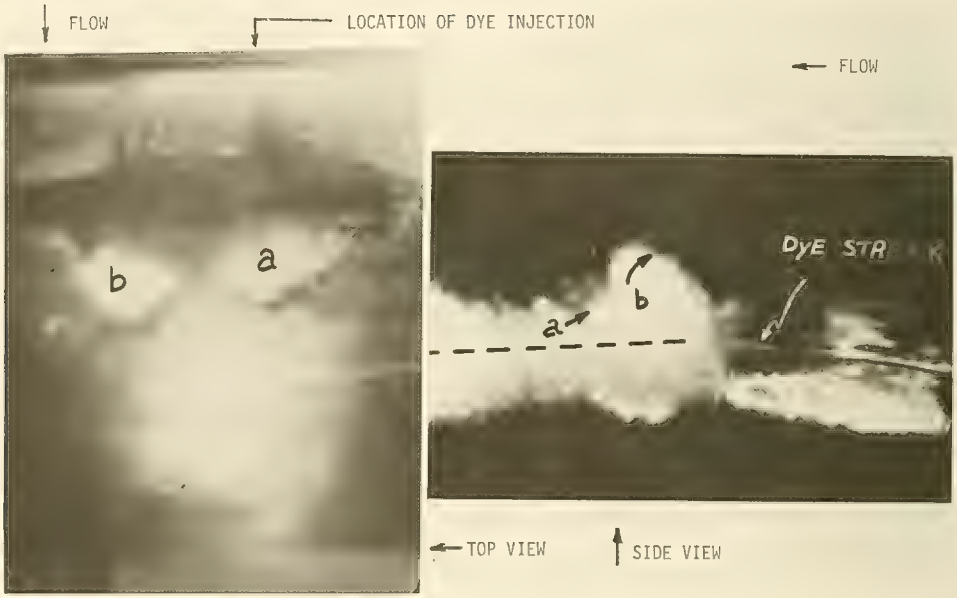

FIGURE 21. Desinent condition for leading edge sheet cavity; $K = 0.49$, $V_\infty = 11.5$ m/s, $P_\infty = 76.2$ kPa, $\alpha = 3.25 + 1.55 \sin \omega t$.

was set to the maximum angle the oscillating foil attained (4.2° for $\alpha_1 = 0.95$ in Figure 25), the maximum cavity length could be as much as a factor of two larger than for finite values of K (eg., $K = 1.2$).

The data plotted in Figure 26 show that within the accuracy of the experiments, a variation in velocity from 11.5 to 16.4 m/s produced no significant change in the results shown in Figure 25 other than that expected for the small variation in σ that occurred between tests. It appears that the parameters of K, σ, and α_1, are sufficient to correlate all of the present data with the presence of cloud cavitation.

6. CONCLUSIONS

In order to improve the physical understanding of the cavitation inception process and the formation of cloud cavitation on marine propellers, a large two-dimensional hydrofoil was tested in the DTNSRDC 36-inch Water Tunnel under pitching motion. The foil was instrumented with pressure transducers to measure the unsteady surface pressure due to foil oscillation, and photos were taken to correlate cavitation inception and cavity patterns.

Prior to the occurrence of cavitation on an oscillating foil, the foil is in a fully wetted condition. Knowledge of the pressure distribution on a fully wetted foil can be expected to provide useful information for prediction of unsteady cavitation. Fully wetted, time dependent, experimental pressure distributions were compared with results from Giesing's method for calculating unsteady potential flow. Good correlation between the prediction and the experimental measurements was obtained for both dynamic pressure amplitudes and phase angles within the range of reduced frequencies investigated ($K = 0.23$ to 2.30). This good corre-

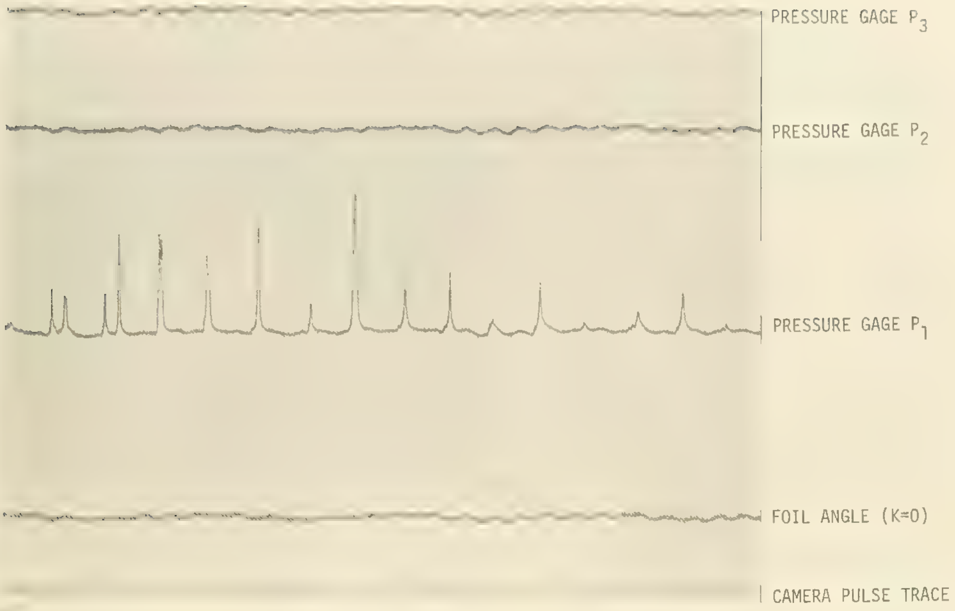

FIGURE 22. Surface pressure fluctuations for K = 0, V_∞ 11.5 m/s, P_∞ = 76.2 kPa, α = 3.25°.

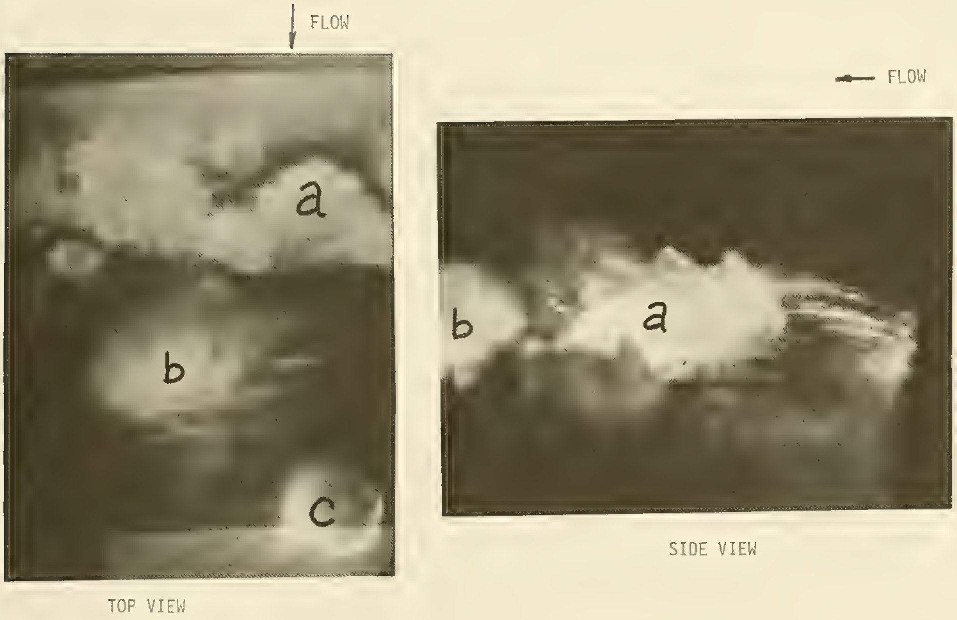

FIGURE 23. Alternate spanwise cloud cavitation shedding for K = 0, V_∞ = 11.5 m/s, P_∞ = 76.2 kPa, α = 3.25.

lation supports McCroskey's conclusion that unsteady viscous effects on fully wetted oscillating airfoils are less important than unsteady potential flow effects, if the boundary layer does not interact significantly with the main flow.

Six series of oscillating foil experiments were carried out in this test program to study the leading edge sheet cavity growth and collapse. A simplified mathematical model was developed to explain experimental results for leading edge sheet cavitation inception. The mathematical model utilizes Giesing's method for calculating the unsteady potential flow. A significant delay in unsteady cavitation inception was both predicted and measured. A further delay in cavitation inception was also observed and predicted with increasing pitch amplitude. It is shown that unsteady cavitation inception is a function of:

(1) the ratio of dynamic to static angular pressure gradients

$$(dC_p/d\alpha)_u \;/\; (dC_p/d\alpha)_s$$

and,

(2) the phase shift between the foil angle and the dynamic pressure response.

Due to the phase lag in pressure response a significant delay in unsteady cavitation inception is predicted theoretically and observed experimentally. Additionally, the angle at which cavitation inception occurs increases with increasing pitch amplitude. This effect results from a change in the phase angle.

It is well known that even in a steady condition the cavitation inception process is extremely complex. The theoretical prediction is still very difficult.

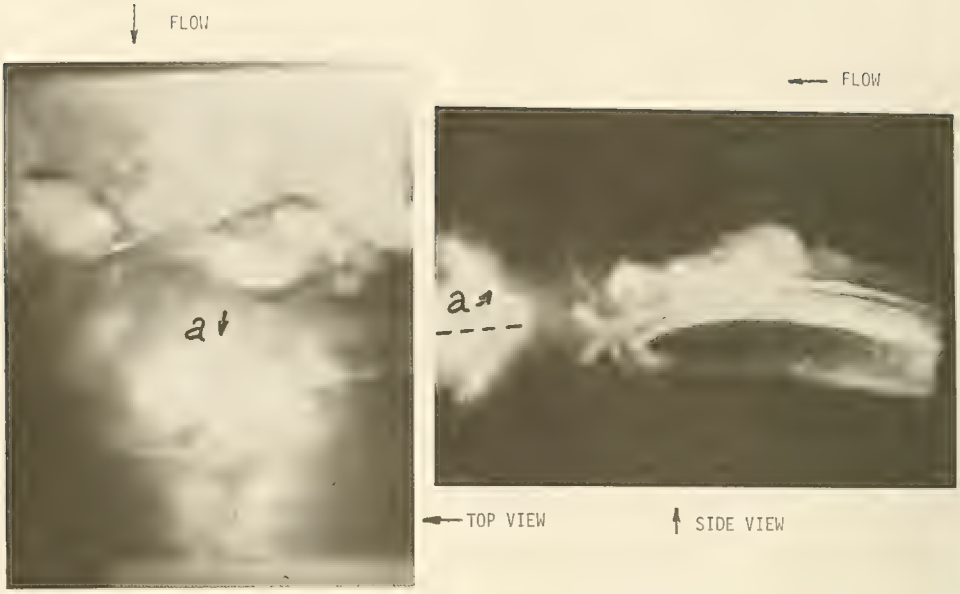
FLOW
FLOW
a
a
TOP VIEW
SIDE VIEW

FIGURE 24. Apparent coalescence of vapor bubbles within cloud cavity; K = 0.28, V_∞ = 14.8 m/s, P_∞ = 124.1 kPa, α = 3.25° + 1.55° sin ωt.

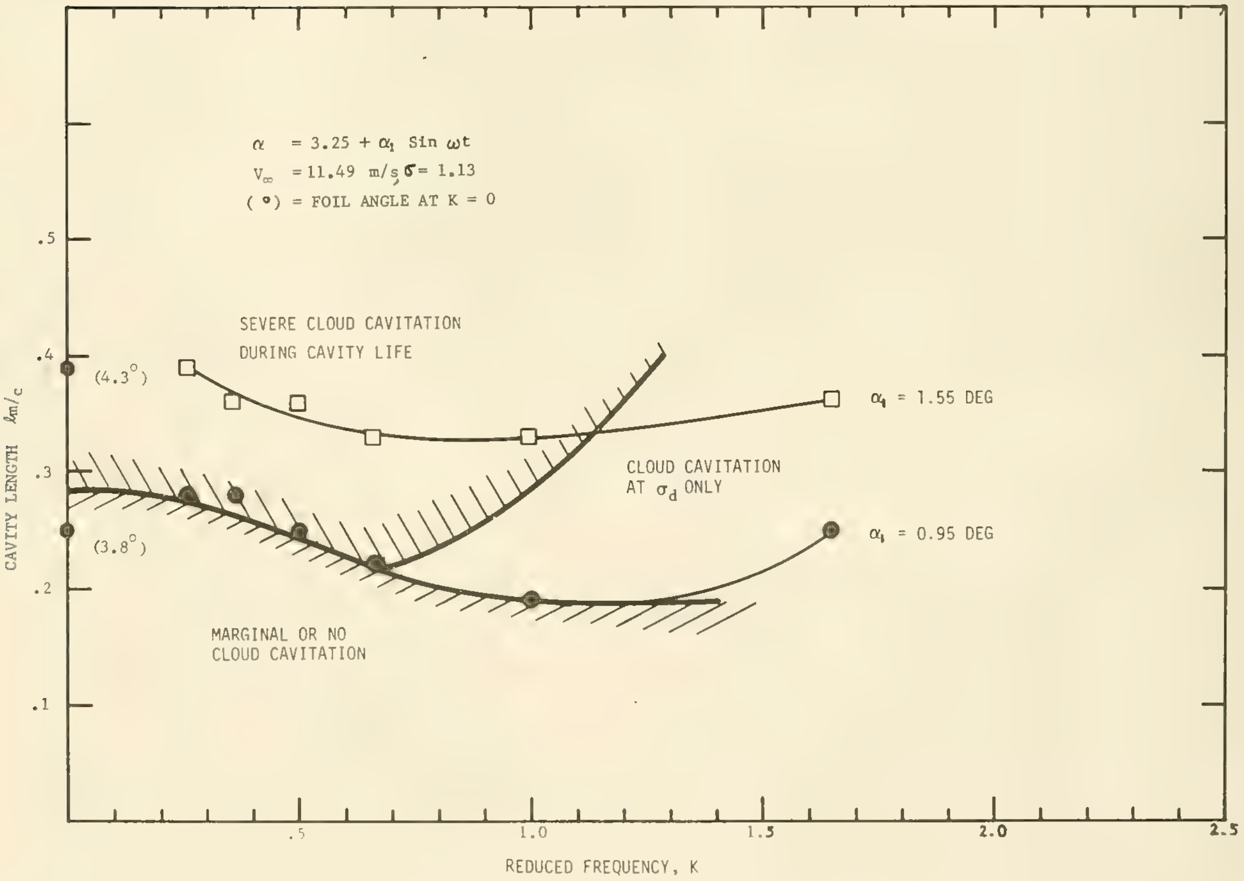

FIGURE 25. Variation in cloud cavitation with reduced frequency K and pitch amplitude α_1.

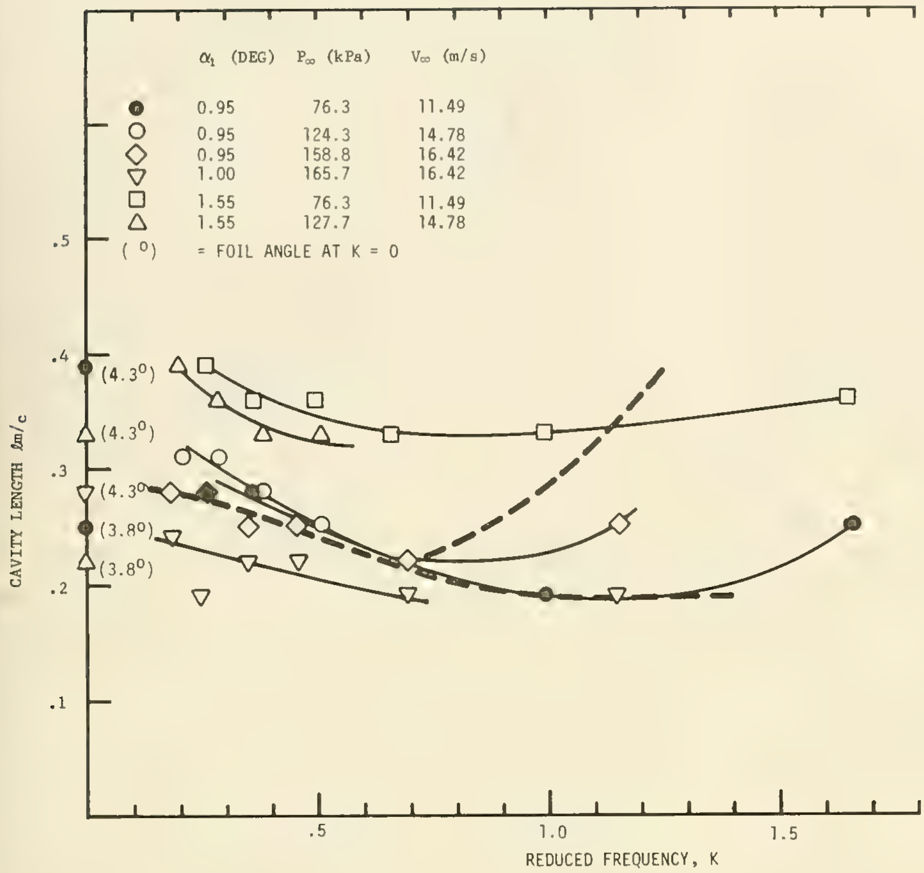

FIGURE 26. Influence of V_∞, P_∞, α_1, and K on cavity length ($\ell m/c$).

Nevertheless, if the inception angle α_{is} is known from the steady model tests, the unsteady effect on cavitation inception, to the first order, may be estimated by the present method. Since the present tests were carried out with only one foil shape and only one pitch axis location, further experiments are required, and in particular, the range of variables should be extended.

Based on photographic observations of the leading edge sheet cavitation instabilities, it appears that the free shear layer and near-wake stability concepts reviewed by Wu (1972) give a reasonable qualitative description of the physical process. The inherent instability of the free shear layer and associated vortex shedding appear to provide a reasonable model for the breakup of a sheet cavity. However, the detailed hydrodynamics associated with the near-wake closure region can still only be postulated. The commonly held concept of a reentrant jet, Wu (1972), may provide a reasonable description applicable to the closure of the near-wake region during the actual shedding of vapor. For sheet cavitation extending over only a portion of the foil chord this reentrant jet may not actually penetrate the cavity itself but penetrate only a locally separated region just downstream of the sheet cavity trailing edge. In any event, the presence of a reentrant jet is not required to explain the inherent instability and breakup of the sheet cavity.

For the conditions of the experiments reported here, where the gross flow is nominally two dimensional, the cavity instability is not coherent to a significant extent along the foil span. In other words, the cavity instability is highly three-dimensional and appears to be principally dependent on conditions in the immediate upstream free shear layer flow. The most extreme form of cavity instability is manifest as a large shed cloud of vapor and thus referred to in the literature as "cloud" cavitation.

Within the context of the experimental results reported here, the principle parameters controlling the formation of cloud cavitation are reduced frequency, K, cavitation number, σ and foil oscillation amplitude, α_1. The maximum cavity length, $(\ell_{m/c})$, is a function of these three parameters. However, it has been shown that predictions of $\ell_{m/c}$ at finite reduced frequencies cannot be based on the cavitation observations at zero reduced frequency. With σ constant, the results show that it is possible to have no cloud cavitation at finite reduced frequencies - even though it was present on a stationary foil set to the maximum unsteady angle. However, if the steady foil is set to the mean angle of oscillation, α_o, and no cloud cavitation is present, then it is easily shown that at finite reduced frequencies cloud cavitation will be present. Thus, Ito's conclusion that there exists a "critical" reduced frequency for the onset of cloud cavitation appears to be the result of the specific chosen values of the parameters, K, σ, and α_1.

The implication of the above results is that the prediction of the occurrence of cloud cavitation for hydrofoils in waves and propellers in wakes cannot be based solely on the performance in calm water or uniform flow.

ACKNOWLEDGMENTS

Grateful appreciation is expressed to Mr. G. Kuiper for his skill in the pressure gage dynamic calibration, assistance in the test set-up and his helpful discussions. Grateful appreciation is also due to Mr. R. Pierce for his excellent work in performing the data reduction. Finally, the reviews and constructive comments by Mr. J. McCarthy and Dr. W. Morgan are greatly appreciated.

The work described in this paper was sponsored by Naval Sea Systems Command and the General Hydrodynamic Research Program at DTNSRDC.

REFERENCES

Morgan, W. B., and F. B. Peterson (1977). Cavitation Inception, A Review-Progress Since 17th ATTC. *Proceedings 18th ATTC,* Annapolis, MD.

van Manen, J. D. (1962). Bent Trailing Edges of Propeller Blades of High Powered Single Screw Ships. *Proceedings of IAHR Symposium,* Sendai, Japan

Tanibayashi, H. (1973). Practical Approach to Unsteady Problems of Propellers. *International Shipbuilding Progress, 20,* No. 226.

Ito, T. (1962). An Experimental Investigation into the Unsteady Cavitation of Marine Propellers. *Proceedings of IAHR - Symposium on Cavitation and Hydraulic Machinery,* Sendai, Japan.

Tanibayashi, H., and N. Chiba (1968). Unsteady Cavitation of Oscillating Hydrofoil. *Mitsubishi Heavy Industries Technical Report* (in Japanese), 5, No. 2.

Chiba, N., and T. Hoshino (1976). Effect of Unsteady Cavity on Propeller Induced Hydrodynamic Pressure, *Journal of the Society of Naval Architects of Japan, 139.*

Meijer, M. C. (1959). Some Experiments on Partly Cavitating Hydrofoils. *International Shipbuilding Progress, 6,* No. 60.

Chiba, N. (1975). Behavior of Cavity Collapse as a Cause of Cavitation Damage of Propeller Blades. *Cavity Flows, ASME Symposium Proceedings, 1975,* 11-18.

Miyata, H. (1972). *Pressure Characteristics and Cavitation.* M. S. Thesis, Department of Naval Architecture, Tokyo University.

Miyata, H. et al. (1972). Pressure Characteristics and Cavitation on an Oscillating Hydrofoil. *Journal of the Society of Naval Architects of Japan, 132.* 10; 107-115.

Radhi, M. H. (1975). *Theoretische und Experimentelle Untersuchung uber den Kavitationseinsatz an Schwingenden Tragflugelprofilen.* PhD Thesis, Technischen Universitat Berlin, D83.

Hilten, J. S., et al. (1972). A Simple Sinusoidal Hydraulic Pressure Calibration. *National Bureau of Standards, Technical Note 720.*

Nuttall, A. H. (1971). Spectral Estimation by Means of Overlapped Fast Fourier Transform Proceeding of Windowed Data. *NUSC Report 4169.*

Abramson, H. N. (1967). Hydroelasticity with Special Reference to Hydrofoil Craft. *NSRDC Report 2557.*

Giesing, J. P. (1968). Two-Dimensional Potential Flow Theory for Multiple Bodies in Small - Amplitude Motion. *Douglas Aircraft Company, Report No. DAC-67028.*

McCroskey, W. J. (1977). Some Current Research in Unsteady Fluid Dynamics - the 1976 Freeman Scholar Lecture. *Trans. ASME Journal of Fluid Engineers, 99,* Series 1, No. 1, 8-38.

McCroskey, W. J. (1975). Recent Review in Dynamic Stall. *Proceedings, Unsteady Aerodynamics Symposium,* The University of Arizona, 1-34.

Acosta, A. J., and B. R. Parkin (1975). Cavitation-Inception - A Selective Review. *Journal of Ship Research, 19,* 4; 193-205.

Carta, F. O. (1971). Effect of Unsteady Pressure Gradient Reduction on Dynamic Stall Delay. *Journal of Aircraft, 8,* 10; 839-841.

Huang, T., and F. B. Peterson (1976). Influence of Viscous Effects on Model/Full Scale Cavitation Scaling. *Journal of Ship Research 20,* 215-223.

Wu, T. Y. (1972). Cavity and Wake Flows. *Annual Review of Fluid Mechanics, 4.*

Knapp, T. R., et al. (1970). *Cavitation.* McGraw-Hill Book Company.

Song, C. S. (1969). Vibration of Cavitating Hydrofoils. *St. Anthony Falls Hydraulic Laboratory, University of Minnesota, Project Report No. 111.*

Besch, P. K. (1969). Flutter and Cavity-Induced Oscillation of a Two-Degree-of-Freedom Hydrofoil in Two-Dimensional Cavitating Flow. *NSRDC Report 3000.*

Wade, R. B., and Acosta, A. J. (1965). Experimental Observations on the Flow Past a Plano-Convex Hydrofoil, *J. Eng. for Power, ASME, No. 65-FE3,* 1-10.

Cavitation on Hydrofoils in Turbulent Shear Flow

H. Murai, A. Ihara, and Y. Tsurumi
Tohoku University, Sendai, Japan

ABSTRACT

Conditions and positions of inception, locations of zones, and aspects and behaviors of bubbles and cavities of cavitations occurring on two hydrofoils with the profiles of Clark Y 11.7 and 08 in shear flows and a uniform flow have been observed and measured, and correlated with measured pressure distributions on the hydrofoils and turbulence levels and size distributions of cavitation nuclei in free streams.

At attack angles small for the profile, traveling cavitations begin near positions of minimum pressure and at cavitation numbers about the same as absolute values of minimum pressure coefficients, irrespective of flow shears in free streams provided local values are used. Discrepancies between conditions and positions of inceptions and pressure coefficients and their distributions, and sizes of traveling bubbles depend on qualities of free streams.

On the hydrofoil with the Clark Y 11.7 profile, a traveling bubble in a zone of rising pressure, deforms, creating a projection in shear flow, or two projections in uniform flow, leaves only the projection and then collapses. On the hydrofoil with 08 profile, a traveling bubble collapses after the deformation caused by the instability of the bubble surface. On both hydrofils, bubbles collapsing symmetrically and asymmetrically, looking like micro jets forming, can be found.

At attack angles large for the profile, fixed cavitations occur. Conditions and positions of inception are similar to those of traveling cavitations. In the boundary layers on both side walls, fixed cavitations occur at relatively large cavitation numbers, possibly equal to the absolute values of local minimum pressure coefficients, and even develop beyond the boundary layers. Cavitation zones on the low-speed side are larger than those on the other side, and those occurring in the boundary layers of uniform free streams are of an intermediate size.

At attack angles intermediate for the profile, fixed and traveling cavitations occur at the same time and tend to become fixed only on the Clark Y 11.7 profile. On the 08 profile, fixed cavitations at the leading edge and traveling cavitations at about the mid-chord appear at the same time in shear flows, but only fixed cavitations occur and develop at the leading edge in uniform flows.

1. INTRODUCTION

Many researches on the cavitation characteristics of hydrofoil profiles have been published, and the appearance, the degree, and the effects on the hydrodynamic behavior of hydrofoil of the incipient and developed cavitations occurring on hydrofoils have been discussed by Numachi (1939, 1954), Daily (1944, 1949), and Kermeen (1956a, 1956b). Recently, the effects of the behavior of boundary layers and the turbulence in the free stream on the inception and development of cavitations on hydrofoils were reported by Casey (1974), Numachi (1975), and Blake et al. (1977). Although they have been concerned with cavitation occurring on hydrofoils in a free stream of uniform velocity, actual blades of hydraulic machines, including ships' propellers, work mostly in nonuniform flow, and the effect of nonuniformity might have to be examined as well.

Investigations on cavitation occurring in shear layers have been made by Daily and Johnson (1956) in a zone of wall shear turbulence, by Kermeen and Parkin (1957) in a wake behind a circular plate and by Rouse et al. (1950) and Rouse (1953) in submerged jets. But research concerning the cavitation occurring on hydrofoils laid in a free stream with a shear is not available as far as the authors are aware.

The present report is intended to clarify the influence of the spanwise shear, uniform in the core and the accompaning boundary layers on both sides of the free stream and its turbulence on the

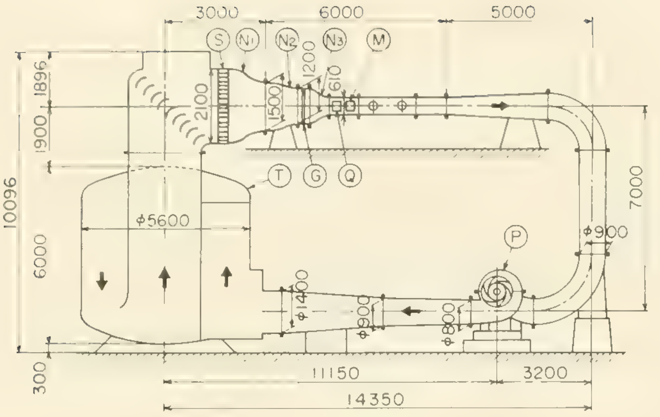

FIGURE 1. High speed water tunnel.

inception and development of cavitation and the aspect and behavior of cavitation cavities occurring on two hydrofoil profiles with different cavitation characteristics.

2. EXPERIMENTAL APPARATUS AND METHODS

High Speed Water Tunnel

The water tunnel used for the experiment is shown schematically in Figure 1. The tunnel contains 180m^3 of water. The water is circulated by the centrifugal pump, P, whose revolution is controllable. Bubbles generated in the measuring section, the duct, and the pump mainly disappear in the reservior T. In the reservoir the water first flows upward to the free surface at the top of the reservoir, and then down very slowly through an area of 20m^2 to the bottom. Two spaces, one at the entrance corner of T and the other at the top of the tunnel, separate bubbles from the water and continuously remove the separated air. The water sucked up from the bottom of T turns to the horizontal direction through corner vanes, and enters the measuring section through the honey comb, S, made of synthetic-resin pipes of 26mm diameter, 6mm thick, and 450mm long. Then it flows through two nozzles, N1 and N2, which contract the cross section from 2100×1400mm^2 to 1500×1000mm^2 and to 1200×200mm^2, the room for installing the shear grid, and the nozzle for contracting the cross section from 1200×200mm^2 to 610×200mm^2. The contraction ratio is 24:1 in all. The water flowing out of the measuring section flows through the diffuser and back to the circulating pump P.

The tunnel pressure is controlled by introducing compressed air to the top of the reservoir or by lowering the free surface led from the top of the tunnel, the maximum and minimum pressures being 48×10^5 Pa and -0.8×10^5 Pa. The flow velocity at the measuring section is controlled from the measuring station by controlling the speed of the circulating pump P.

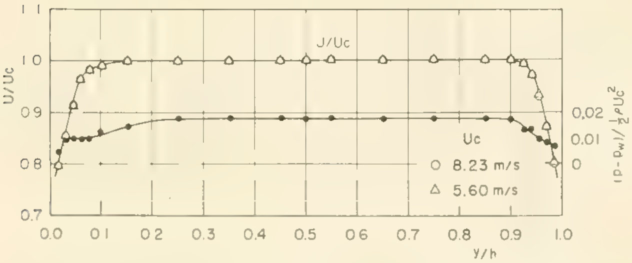

FIGURE 2. Velocity distribution at no grid condition.

Measuring Section

The measuring section has a cross section 200mm wide and 610mm high and its total length is 3000mm. The first upstream 1000mm has two plexiglass windows in each side, and upper and lower wall. In this experiment, the hydrofoil is installed through two downstream-side windows in both side walls. Figure 2 shows the spanwise distributions of the velocity and the static pressure at the position of the mid-chord of the hydrofoil in the case of no grid. The velocity profile is almost uniform except in the 10% the boundary layers on both side walls. The static pressure, expressed as the difference from that at the side wall, is constant within the accuracy of this experiment.

Hydrofoils

Two hydrofoils have been prepared for the experiment, each of which has 100mm chord and 700mm span. Two profiles have been selected; one is Clark Y 11.7 and the other 08, dimensions of which are shown in Table 1. The former is selected for the purpose of examining the influence of the behavior of the boundary layer on the hydrofoil surfaces on the inception and development of cavitation and the aspects of cavitation bubbles or cavities, because it has a round nose and a surface pressure distribution rising toward the trailing edge. The latter is selected as a typical profile among ones designed by Numachi (1952) for high-speed flows, and has a sharp leading edge and comparatively good cavitation characteristics for its simple shape.

The hydrofoil of the Clark Y 11.7 profile has 14 and 13 piezometer holes of 0.4mm diameter on the suction and pressure surfaces respectively, and one of the 08 profile has 13 and 13 piezometer holes,

Table 1 Profile Forms of Hydrofoils

Clark Y 11.7			08		
X	Y		X	Y	
	Upper	Lower		Upper	Lower
0.0	3.50	3.50	0.0	0.16	0.16
1.25	5.45	1.93	1.25	0.35	0.0
2.5	6.50	1.47	2.5	0.73	0.0
5.0	7.90	0.93	5.0	1.47	0.0
7.5	8.85	0.63	10.0	2.79	0.0
10.0	9.60	0.42	15.0	3.95	0.0
15.0	10.68	0.15	20.0	5.02	0.0
20.0	11.36	0.03	30.0	6.62	0.0
30.0	11.70	0.0	50.0	8.00	0.0
40.0	11.40	0.0	70.0	6.62	0.0
50.0	10.52	0.0	80.0	5.02	0.0
60.0	9.15	0.0	90.0	2.79	0.0
70.0	7.35	0.0	95.0	1.47	0.0
80.0	5.22	0.0	97.5	0.73	0.0
90.0	2.80	0.0	98.75	0.35	0.0
100.0	0.12	0.0	100.0	0.16	0.16

Table 2 Positions of Piezometer Holes

Clark Y 11.7	Upper X %		Lower X %	O_8	Upper X %		Lower X %
1	0			1	3.0	14	3.0
2	3.0	15	3.0	2	6.0	15	6.0
3	6.0	16	6.1	3	10.0	16	10.0
4	10.1	17	10.1	4	15.0	17	15.0
5	15.1	18	14.8	5	20.0	18	20.0
6	20.1	19	20.1	6	30.0	19	30.0
7	30.0	20	30.1	7	40.0	20	40.0
8	40.5	21	39.9	8	50.0	21	50.0
9	50.1	22	50.0	9	60.0	22	60.0
10	60.2	23	60.0	10	70.0	23	70.0
11	70.4	24	69.8	11	80.0	24	80.0
12	80.3	25	79.8	12	85.0	25	85.0
13	85.0	26	84.8	13	90.0	26	90.0
14	90.2	27	89.6				

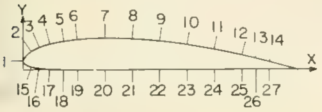

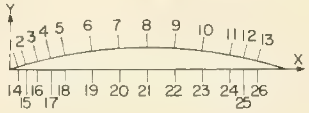

as are shown in Table 2. The holes are inclined to the direction of the free streams as to have no influence on the pressures measurements of each other. Pressures are measured by using a mercury-water manometer.

For measurements of pressure distributions, the hydrofoil is shifted spanwise so as to allow the piezometer holes to cover the whole 200mm span. For observations of cavitations, the part of hydrofoil having no piezometer hole is used.

Shear Grids

In order to examine the influence of shear flow, the free stream at the measuring section has been made to have the simplest shear, that is, uniform shear. The grids for creating uniform shear flow are composed of straight rods arranged perpendicular to the free stream and the hydrofoil span with non-uniform spacings calculated by using the theory of Owen and Zienkiewicz (1957). The spaces near both side walls were modified according to Liverey and Turner, (1964) and Adachi and Kato (1973) and are shown in Table 3. In order to make two different free streams having the same shear but different turbulence, two grids were made, composed of rods with different diameters, 20mm for No. 1 and 15mm for No. 2.

TABLE 3 Rod Spacings of Shear Grids

Grid No. 1				
Rod Number	1	2	3	4
distance from low-speed side wall (mm)	20.1	59.9	103.4	153.3

Grid No. 2					
Rod Number	1	2	3	4	5
distance from low-speed side wall (mm)	16	47.4	81.5	118.4	161.2

The shear grid is installed at a position 1500mm upstream from the mid-chord of hydrofoil, where the cross section of the duct is about twice as great as that of the measuring section so as to keep the grid free from cavitation.

Measurement of Velocity and Static Pressure at the Measuring Section

Spanwise distributions of the velocity and the static pressure are measured at the position of the mid-chord of the hydrofoil in the absence of the hydrofoil, by using a Prandtl-type Pitot tube of 3mm diameter. They corresponded to the difference of static pressures at the inlet and exit of the second nozzle, N_2, and the static pressures at the exit of the nozzle and the position 530mm upstream and 170mm below the position of the mid-chord of hydrofoil.

It has been pointed out by Lighthill (1957) that total pressures measured by using a Pitot-tube in a shear flow exhibit larger values than real ones due to displacement effects of a Pitot-tube. The displacement thickness of the boundary layer on the Pitot-tube used in this experiment, having a ratio of outer to inner diameters of 0.6, is calculated as about 0.54mm by use of the empirical equation presented by Yound and Mass (1936) and Macmillan (1956). The error in this experiment caused by the displacement thickness is the order of 0.08mm/s for a shear factor of 0.15 in the core of the shear flow so that it can be neglected, except in the boundary layers. There the shear factor, on which the error is proportional, is considerably large, especially near both side walls.

The static pressure at the measuring section is limited due to the following two reasons: at the upper limit, by the strength of the differential piezometer used for detecting the velocity at the measuring section; and at the lower limit by the need to prevent the shear grid from cavitating. The prescribed velocities at the measuring section are determined so as to keep the static pressure at the measuring section within the above-written limits for obtaining the inception and development of cavitation corresponding to the angles of attack of the hydrofoils, as shown in Table 4.

Measurement of Turbulence

Spanwise distributions of the components of turbulent velocity in the directions parallel to the free stream and perpendicular to the free stream and the hydrofoil span are measured at the position of the mid-chord of hydrofoil (in the absence of it) by using the Laser-Doppler velocimeter, DISA 55L Mark II. Each component of turbulent velocity is

TABLE 4 Velocity and Pressure at the Test Section on Cavitation Experiments

α(rad)	Velocity (m/s)	Pressure (10^5 Pa)
0.0	11.0	-0.64 ~ -0.45
0.052	10.0	-0.65 ~ -0.35
0.105	9.0	-0.60 ~ -0.11
0.157	8.0	-0.33 ~ +0.40

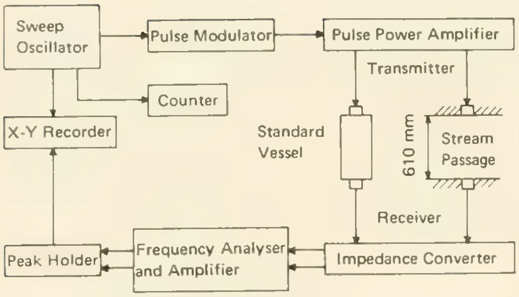

FIGURE 3. Schematic diagram for nuclei measurements.

detected as an absolute value of the root mean square.

Observations and Measurements of Cavitation

Cavitation inceptions are seen by the naked eye under 50Hz, stroboscopic 3μs flash illumination. An incipient cavitation number is defined by using the static pressure at which the inception is detected while reducing the static pressure at a low rate and the local free stream velocity. However, in the boundary layers the velocities at outside edges are taken while the free stream velocity is kept at the prescribed value. Desinences are too intermittent and indefinite to be detected definitely in the course of raising the static pressure.

For the measurements of positions of inception and the observations of appearances of cavitation bubbles or cavities, photographs of 3 μs exposure and high-speed motion pictures of 3000 frames per second and 2 μs exposure for each frame were taken. For the high-speed photography, the high-speed camera, FASTAX, was used synchronized with the high-speed stroboscope made by E. G. and E Co. Ltd. For the measurements of average locations and shapes of cavitation regions, photographs of 1/60 s exposure were used.

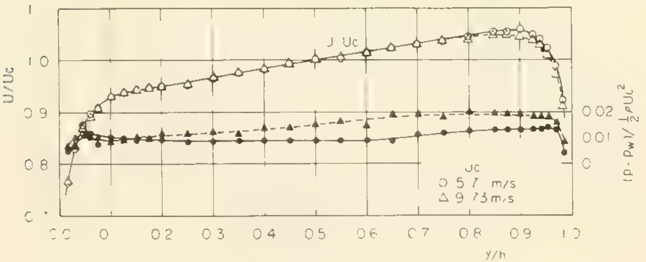

(a) Grid No.1

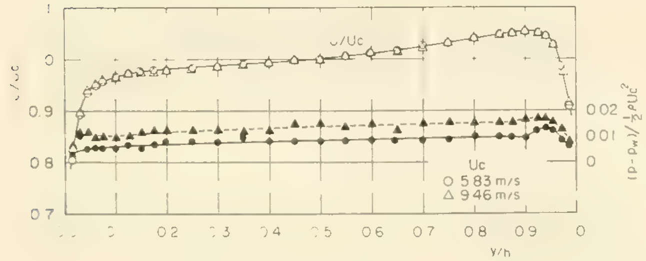

(b) Grid No.2

FIGURE 4. Velocity and static pressure distribution for shear grids.

Relative Measurement of Cavitation Nuclei

Size distributions of gas nuclei are measured by using the sound-attenuation method of Schiebe 1969. The measuring system is shown in Figure 3. The frequency range of swept pulses was 20kHz~1000 kHz. Both probes for emission and reception were 25mm diameters, made of a crystal, and exposed directly to water. The measurements were relative ones for comparison between the three cases of no grid and grids No. 1 and No. 2 because the system has not yet been calibrated for bubbles with prescribed definite diameters.

Measurements were carried out at four positions in the spanwise direction at the mid-chord of hydrofoil perpendicular to the free stream and the hydrofoil span.

3. RESULTS OF EXPERIMENT AND DISCUSSIONS

Shear Flow at Measuring Section

The velocity profiles normalized by each velocity at the mid-span and the distributions of the static pressure expressed as the difference from one at the side wall and normalized by each dynamic pressure at the mid-span for the grids No. 1 and No. 2 are shown in Figure 4. The flow shear for grid No. 1 is uniform in the free stream core and the non-dimensional shear factor is 0.15. That for grid No. 2 is about the same as for grid No. 1 at half the core of the free stream on the high-speed side but smaller at the other half. The non-dimensional shear factor is 0.06. Both have boundary layers of 10% thickness span on both sides. The static pressure is higher in the free stream core than on the side walls by about 1% or a little more of the dynamic pressure at mid-span. Scatters of plots are within the accuracy of this experiment.

Spanwise Distribution of Turbulence

Root mean squares of two components of turbulent velocity, one stream-wise and the other perpendicular to it and the hydrofoil span, are measured in every free stream, and shown in Figure 5 normalized by Uc. The velocity at the mid-span was kept at 9.86 m/s. When both are expressed as the turbulence levels based on the local velocity of free stream, U, for the cases of the two shear grids, both u'/U and w'/U vary so little in the spanwise direction that they can be regarded as constant

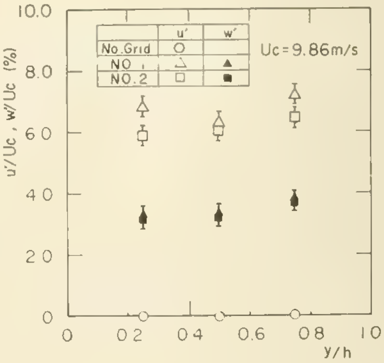

FIGURE 5. Spanwise distribution of turbulence.

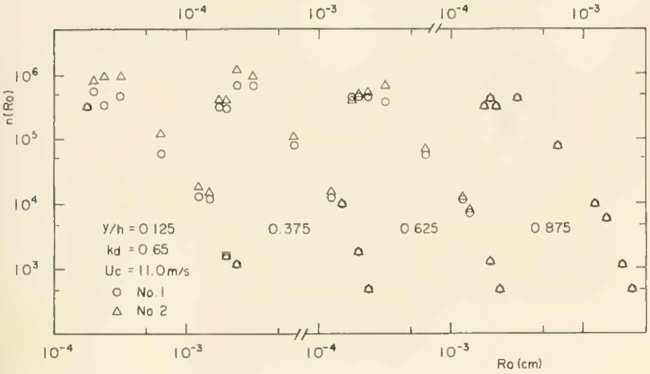

FIGURE 6. Spanwise variation of size distribution of cavitation nuclei.

within the accuracy of this measurement. u'/U was 6.8 and 6.2% in the case of grids No. 1 and No. 2, respectively, and w'/U was 3.6% in the case of both two shear grids. It has been reported by Harris et al. (1977) that in a shear flow generated by a shear grid, w' and the other lateral component of turbulent velocity, say v', are almost the same. If it is also assumed that v' = w' in this experiment, the resultant turbulence levels were 8.5 and 8.0% in the case of the grids No. 1 and No. 2, respectively, in the core of the free stream. In the case of no grid both u'/U and w'/U were 0.1%, and the turbulence can be regarded as isotropic at a level of 0.17%, in the core of free stream.

Spanwise Variation of Size Distribution of Cavitation Nuclei

Attenuations of sound pressures were measured at four positions in the spanwise direction (12.5, 37.5, 62.5, and 87.5% span) from the low-speed side at the position of mid-chord in the absence of the hydrofoil, and at the cavitation numbers of 2.75 and 0.65. Because the levels of attenuated sound pressures were not calibrated for micro bubbles of known sizes, sound pressure levels in the shear flows at each measuring position were compared with one in the uniform flow in which any spanwise variation was not noticed. Frequencies and differences of sound pressure levels were related to equivalent radii, and to differences of the numbers of cavitation nuclei from those in the uniform flow by using the formulae presented by Richardson (1947) and Gavrilov (1964).

At a cavitation number of 2.75, any noticeable difference of size distributions between the shear flows and the uniform flow was not found. At a cavitation number of 0.65, however, remarkable differences were noticed as can be seen in Figure 6. Numbers of nuclei with radii smaller than 24μm in both shear flows are considerably larger than those in uniform flow, and the larger the numbers of nuclei the smaller the nuclei radii are. Size distributions in the two shear flows were not so different from each other in the high-speed sides of free streams, but in the low-speed sides, the shear flow made by the grid No. 2 is richer in nuclei, especially in the range of small radii, than the other.

Cavitation Inception

Spanwise variations of local incipient cavitation numbers are plotted in Figure 7 for the Clark Y 11.7 profile, and in Figure 8 for the O_8 profile. Also, spanwise variations of positions of minimum pressure for the case of no grid, grid No. 1, and grid No. 2, are shown.

Clark Y 11.7 Profile

In the case of no grid incipient cavitation numbers, kdi, are a little smaller than absolute values of minimum pressure coefficients, |Cpmin|'s over the whole span at the attack angles, α, of 0 and 0.052 rad, and in the core of free stream at α's of 0.105 and 0.157 rad. Differences between kdi's and |Cpmin|'s increase as α increases until

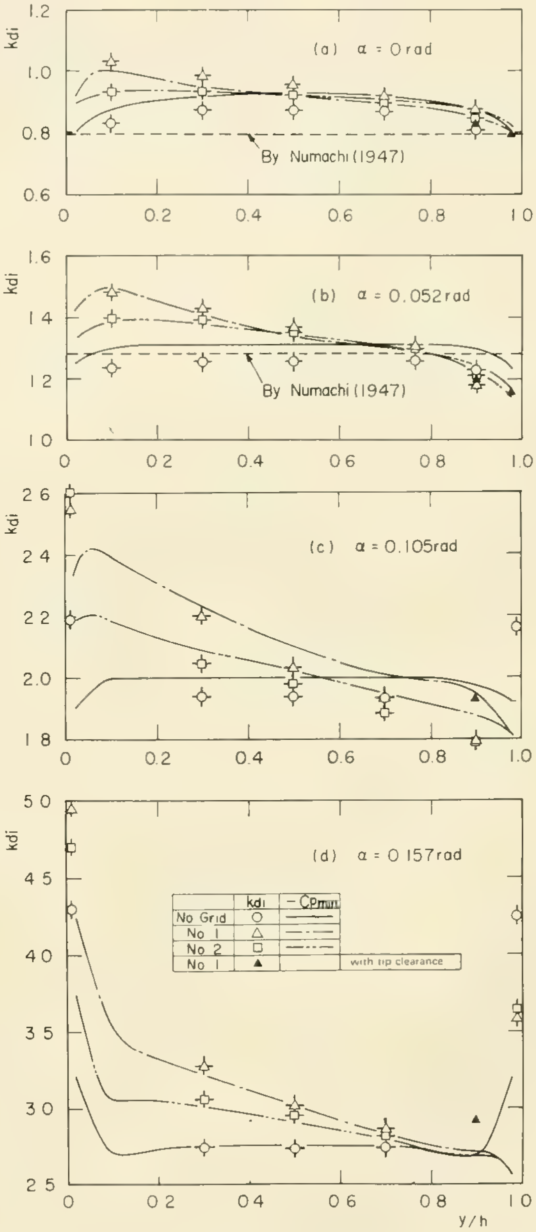

FIGURE 7. Spanwise variation of incipient cavitation numbers for the Clark Y 11.7 profile.

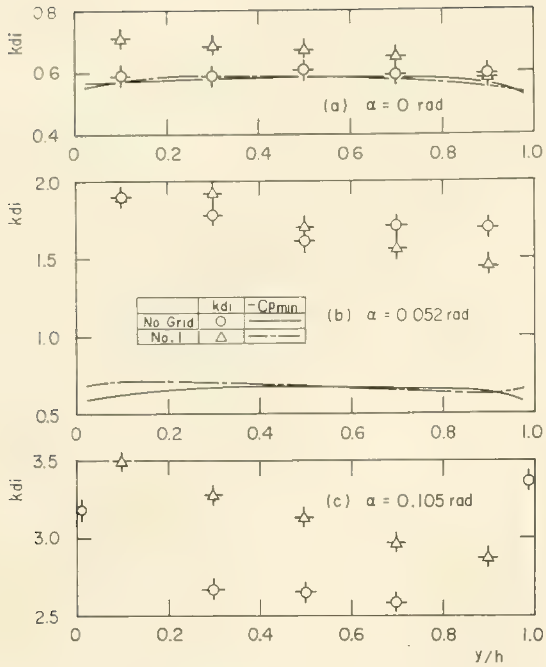

FIGURE 8. Spanwise variation of incipient cavitation numbers for the O_8 profile.

it reaches 0.105 rad, but become smaller at α = 0.157 rad.

At α's not smaller than 0.105 rad, fixed cavitations occur in the boundary layers at positions very close to both side walls at kd's much greater than local |Cpmin|'s. At the same time a zone of cavitation widens spanwise beyond each boundary layer with the inception so that detection of inception becomes difficult in the region neighboring both boundary layers on the side walls. This is the reason the lack of points between y/h = 0.025 ~ 0.3 and 0.7 ~ 0.975. Frequency distributions of cavitation occurrences analyzed by using high speed motion pictures for 1 second illustrate those facts, as can be seen in Figure 9.

In free streams with shears made by the grids No. 1 and No. 2, kdi's almost equal or are a little larger than local |Cpmin|'s. They vary spanwise under the influences of the flow shears in the core and the boundary layers on both side walls, and the accompanied secondary flows, except at α = 0.105 rad, which indicates that these free streams are rich in cavitation nuclei. At α = 0.105 rad, kdi is a little smaller than |Cpmin|, which can be assumed to be due to cavitations changing from traveling to fixed, as mentioned in the next section.

Differences between kdi's and |Cpmin|'s in the boundary layers are larger than those in the case of no grid on the low-speed side, but are the contrary on the high-speed side, due to the secondary flows induced by the flow shears in the cores. The above-mentioned effect is most remarkable at α = 0.105 rad: kdi's in the boundary layer on the low-speed side in cases of the shear grids are larger than those not only in the case of no grid but also |Cpmin|'s in the boundary layer, though only by a little. The mechanism causing the effect has been examined by measuring spanwise variations of static pressures on three points near the leading edge in the boundary layer on the low speed side at the attack angle of 0.105 rad in the case of the grid No. 2. It was confirmed that the detected incipient cavitation number, 2.53, in the boundary layer lies near the largest absolute value of the pressure coefficient based on the local velocities in the zone between 3 and 5 mm from the side wall. However, measured velocities in the zone are not very reliable. Symbols ▲ in Figure 7 show kdi's when the hydrofoil has a tip clearance of about 0.1mm on the high-speed side in the case of grid No. 1. It was found that effects of a boundary layer are weakened by tip clearances, especially at large angles of attack, although another cavitation occurs at the tip clearance.

08 Profile

At 0 angle of attack, traveling cavitations occurred and kdi almost coincide with |Cpmin| in the case of no grid, but were larger than the latter in the case of grid No. 1. The difference decreases spanwise toward the high-speed side, in correspondence with the size distribution of cavitation nuclei. At angles of attack larger than 0 rad, however, fixed cavitations occurred and kdi's were much larger than measured |Cpmin|'s because of the lack of a piezometer hole at the position of the largest |Cpmin|, which is closer to the leading edge than the closest hole at 3% chord. At α = 0.052 rad, in the case of the grid No. 1, another cavitation of the traveling type appears around the position of the measured second |Cpmin| and the kd almost coincided with the measured |Cpmin|. kdi's in the case of grid No. 1 were smaller than those in the other case on the high-speed side. The discrepancey can be surmised as due to the discrepancy between structures of laminar separation bubbles just behind the leading edge in the two cases because of the difference between turbulence levels. At α = 0.105 rad, kdi in the case of the grid No. 1 was larger than in the case of no grid in the core of free stream, but was the opposite in the boundary layer on the high-speed side wall. In the case of no grid, cavitations with long and wide zones occurred in the boundary layers on both sides close to the side walls and the leading edge as with the Clark Y 11.7 profile.

Location of Incipient and Developed Cavitations

Spanwise variations of positions of cavitation inception and front and rear edges of (time) average zones of developed cavitation are shown in Figures 10 and 11 for the profiles Clark Y 11.7 and 08 respectively. Also are shown spanwise variations

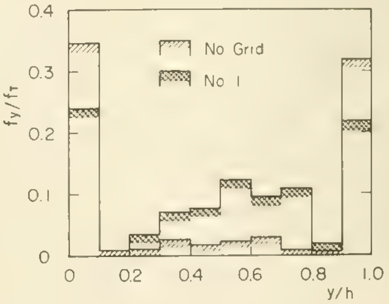

FIGURE 9. Frequency distribution of cavitation occurrence.

of positions of minimum pressure, in each case indicated in the figures. The bottom and the second (at α = 0, 0.052 rad) groups show the positions of inception or front edges of cavitation zones and refer to the scales written on the right-hand side, and the other groups show rear edges of cavitation zones and refer to the scales written on the left-hand side. Open symbols correspond to traveling cavitations and closed and semi-closed

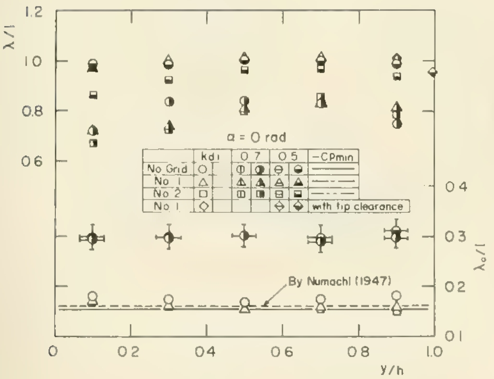

(a)
Clark Y 11.7
α = 0 rad

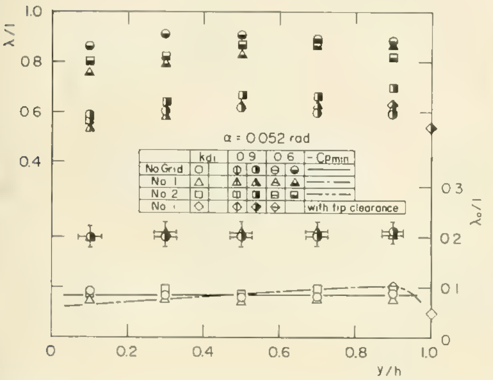

(b)
Clark Y 11.7
α = 0.052 rad

FIGURE 10 (a)(b). Spanwise variations of position of inception and front and rear edges of cavitation zones for the Clark Y 11.7 profile.

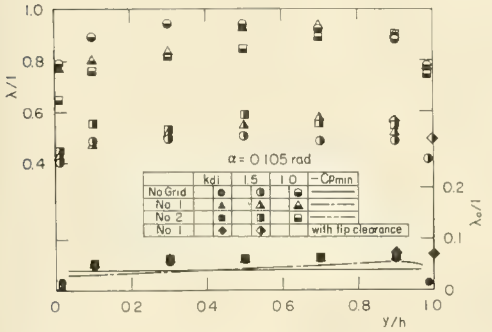

(c)
Clark Y 11.7
α = 0.105 rad

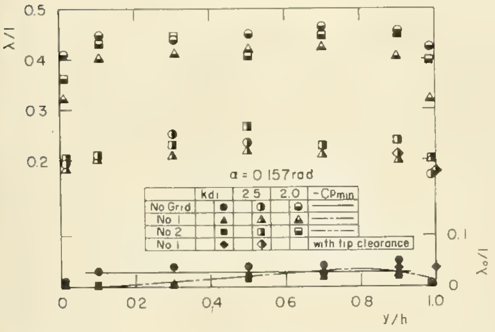

(d)
Clark Y 11.7
α = 0.157 rad

FIGURE 10 (c)(d). Spanwise variations of position of inception and front and rear edges of cavitation zones for the Clark Y 11.7 profile.

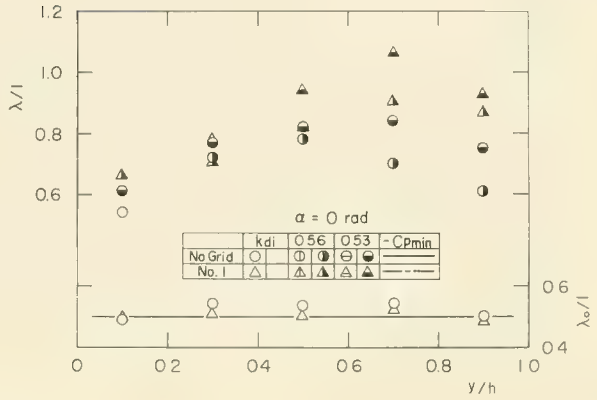

(a)
O_8
α = 0 rad

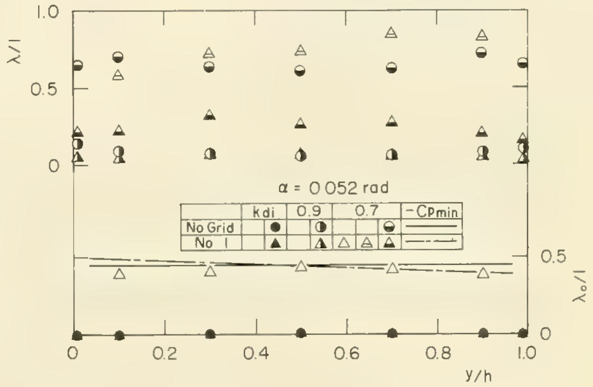

(b)
O_8
α = 0.052 rad

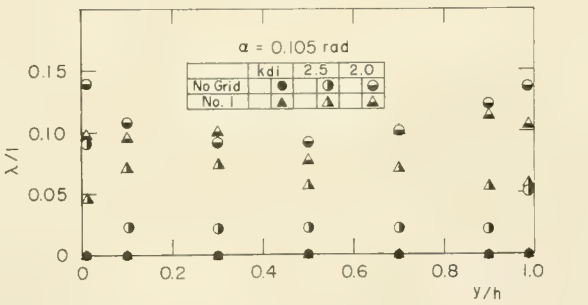

(c)
O_8
α = 0.105 rad

FIGURE 11. Spanwise variation of the position of inception and the front and rear edges of cavitation zones for the O_8 profile.

symbols to fixed. kd's indicated in the figure are based on the velocity at the mid-span.

Clark Y 11.7 Profile

In the case of no grid, traveling cavitations occurred a little downstream from positions of minimum pressure at $\alpha = 0$ and 0.052 rad. Front edges of average zones of cavitation move forward beyond positions of minimum pressure as kd is reduced, uniformly in the core of the free stream. At $\alpha = 0.105$ rad, in the core of the free stream, cavitations, mainly traveling mixed with fixed, occurred just downstream from positions of minimum pressure. However, with a small decrease of kd from the incipient, the type of cavitation changes to fixed and the front edges of cavitation zones move backward from positions of inception and forward with a further decrease of kd. In the boundary layers on both side walls, fixed cavitations occurred very close to the leading edge of the profile and to the side walls, and front edges of cavitation zones move little as kd is reduced. At $\alpha = 0.157$ rad, fixed cavitations occurred just downstream from positions of minimum pressure and front edges of cavitation zones moved forward just a little and never exceeded positions of minimum pressure, in the core of free stream. In the boundary layers on both side walls, fixed cavitations occurred just downstream from the leading edge of the profile and almost attached to the side walls, and front edges of cavitation zones moved little as kd was reduced.

At all attack angles, lines of rear edges of cavitation zones have shapes similar to the velocity profile at kd's a little smaller than the incipient. But rear edges move backward with a further decrease of kd to be almost uniform in the spanwise direction.

In cases of grids No. 1 and No. 2, positions of inception are closer to positions of minimum pressure than in the case of no grid, in correspondence with size distributions of cavitation nuclei: Front edges of cavitation zones move forward beyond positions of minimum pressure in the cores of free streams at $\alpha = 0$, 0.052, and 0.105 rad. At $\alpha = 0$, 0.052, and 0.105 rad, incipient cavitations are of the traveling type, but at $\alpha = 0.105$ rad, in the cores of the free stream, cavitations sometimes change their type from traveling to fixed as kd is reduced, and in those cases front edges of zones of fixed cavitations move backward from the inception position. In the boundary layer on the low-speed side wall a fixed cavitation occurred very close to the leading edge of the profile and to the side wall, but no inception of cavitation of any type can be detected in the boundary layer on the other side wall, in the range of kd in this experiment. At $\alpha = 0.157$ rad, fixed cavitations occurred at positions of minimum pressure, including the boundary layers on both side walls, and front edges of cavitation zones move little.

At kd's a little smaller than the incipient, lengths of cavitations are larger on the high-speed side than on the other side at $\alpha = 0$ and 0.052 rad. At $\alpha = 0.105$ and 0.157 rad, however, they are larger near the wall on the low-speed side than on zones more distant from the wall. Rear edges of cavitation zones have a tendency to be uniform in the spanwise direction at all attack angles as cavitations develop.

Much difference between the two grids in the locations and movements of cavitation zones cannot be found.

08 Profile

At 0 angle of attack, positions of cavitation inception and movements of front and rear edges of cavitation zones with a decrease of kd, compared with positions of minimum pressure, are quite similar to those of the Clark Y 11.7 profile in the cases of no grid and grid No. 1. However, at α's larger than 0, fixed cavitations always occurred at the leading edge over the whole span, irrespective of the existence of the shear grid. Front edges of cavitation zones never moved from the leading edge as kd's were reduced. Lengths of cavitation zones do not grow much, owing to the steep negative-pressure zones just behind the leading edge, until kd's are reduced to about the second $|\mathrm{Cpmin}|$'s. But in the case of no grid, once kd's increase, they develop suddenly beyond positions of minimum pressure and tend to be uniform in the spanwise direction as can be seen in Figure 13(b) at $\alpha = 0.052$ and kd = 0.7. In the case of grid No. 1, however, lengths of the fixed cavitation do not grow enough to reach positions of minimum pressure. Instead cavitations of the traveling type appear around positions of the second minimum pressure, as can be seen in Figure 13(b) at $\alpha = 0.052$ and kd = 0.7 and as shown in Figure 11(b) by the symbols Δ. The length of the cavitation zone is about the same as that in the case of no grid in the free stream core but smaller than that in the boundary layers on both sides, at the beginning of development. At $\alpha = 0.105$ rad, the length of the cavitation zone is much larger than that in the case of no grid at the beginning of development, but becomes about the same as the others with a further decrease of kd.

Aspect and Behavior of Cavitation Bubbles and Cavities

Figures 12 and 13 show several examples among the 3μs-exposure photographs and an example of high-speed motion pictures of cavitations taken at the inception and each stage of development occurring on the Clark Y 11.7 and 08 profiles, respectively. Cavitation numbers indicated in the figure on the left hand side are based on the velocity at the mid-span.

Clark Y 11.7 Profile

At $\alpha = 0$ and 0.052 rad, incipient cavitations are of the traveling type in all cases, and in general, the bubble radius and number of bubbles in the case of no grid were the largest and the smallest, respectively, of the three cases, followed by the case of grid No. 1, which agrees with the size distributions of cavitation nuclei given previously. Each bubble is circular when observed perpendicular to the hydrofoil surface, but as the cavitation number is reduced, two, in the case of no grid, or one, in both cases of two shear grids, horn-like projections are projected behind each bubble from the downstream or both sides. The groups of plots lying second from the bottom in Figures 10(a)(b) show positions of the upstream tips of the projec-

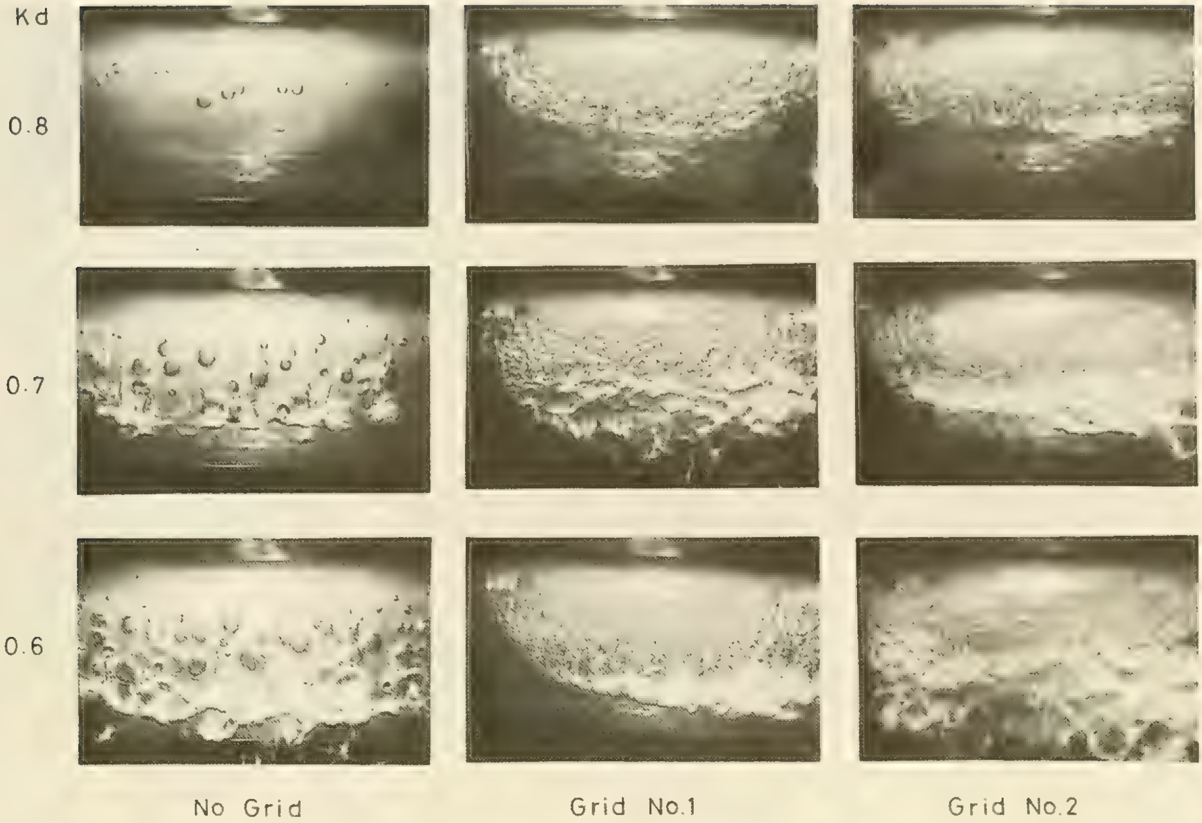
Kd
0.8
0.7
0.6
No Grid
Grid No.1
Grid No.2

(a) $\alpha = 0$ rad

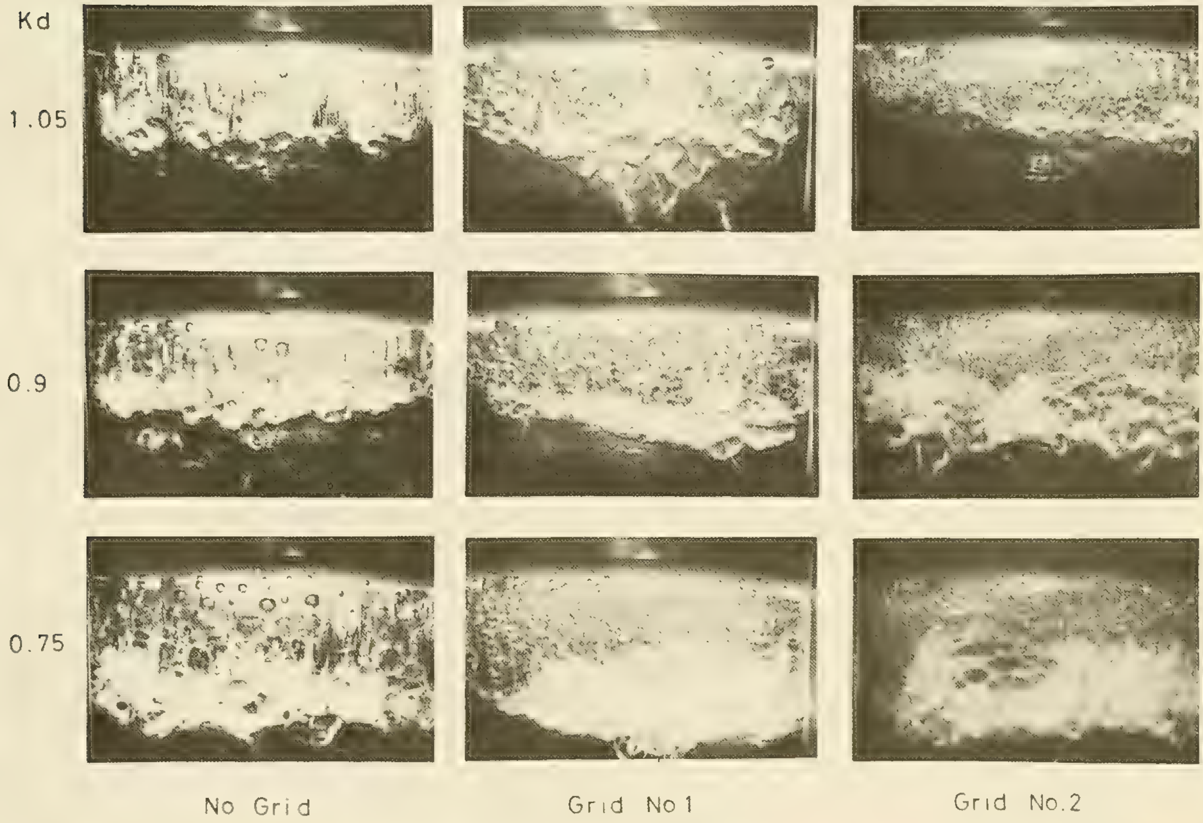
Kd
1.05
0.9
0.75
No Grid
Grid No 1
Grid No.2

(b) $\alpha = 0.052$ rad

FIGURE 12 (a)(b). Cavitation on the hydrofoil of the Clark Y 11.7 profile.

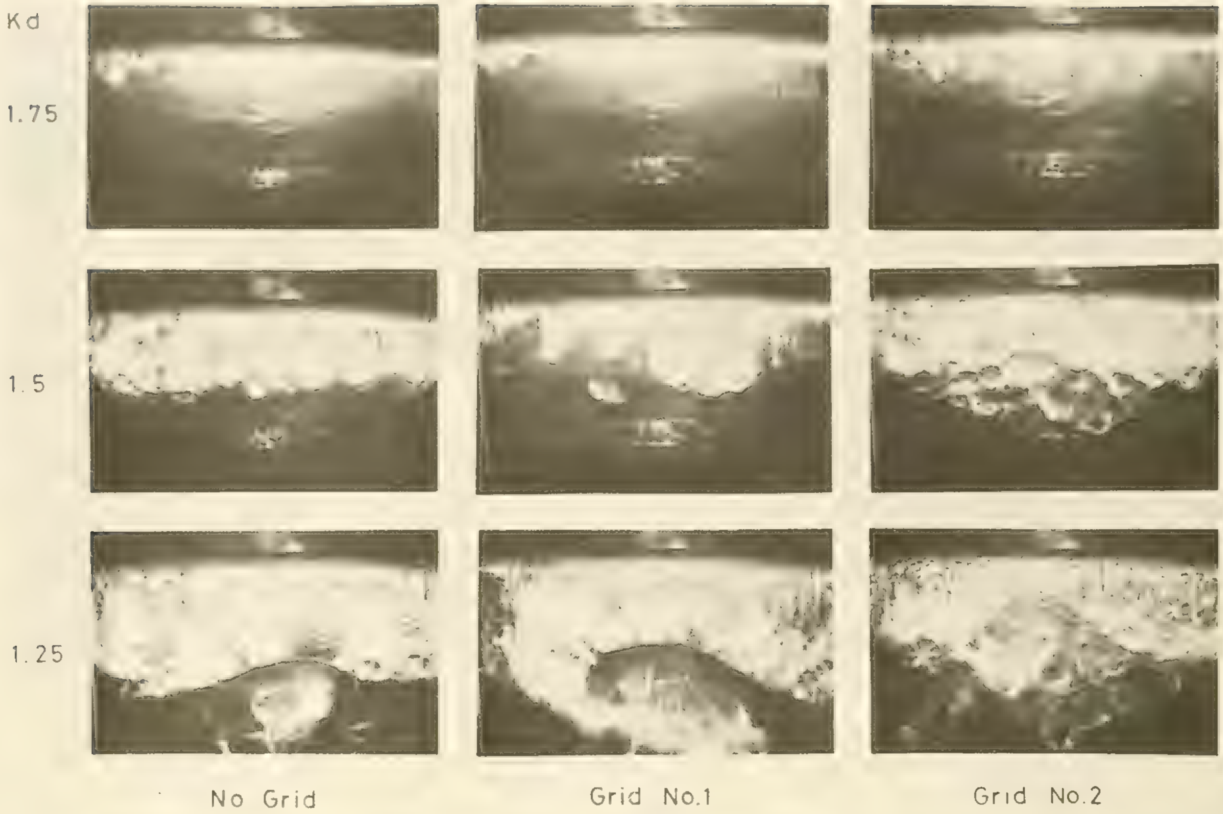
Kd
1.75
1.5
1.25
No Grid
Grid No.1
Grid No.2

(c) $\alpha = 0.105$ rad

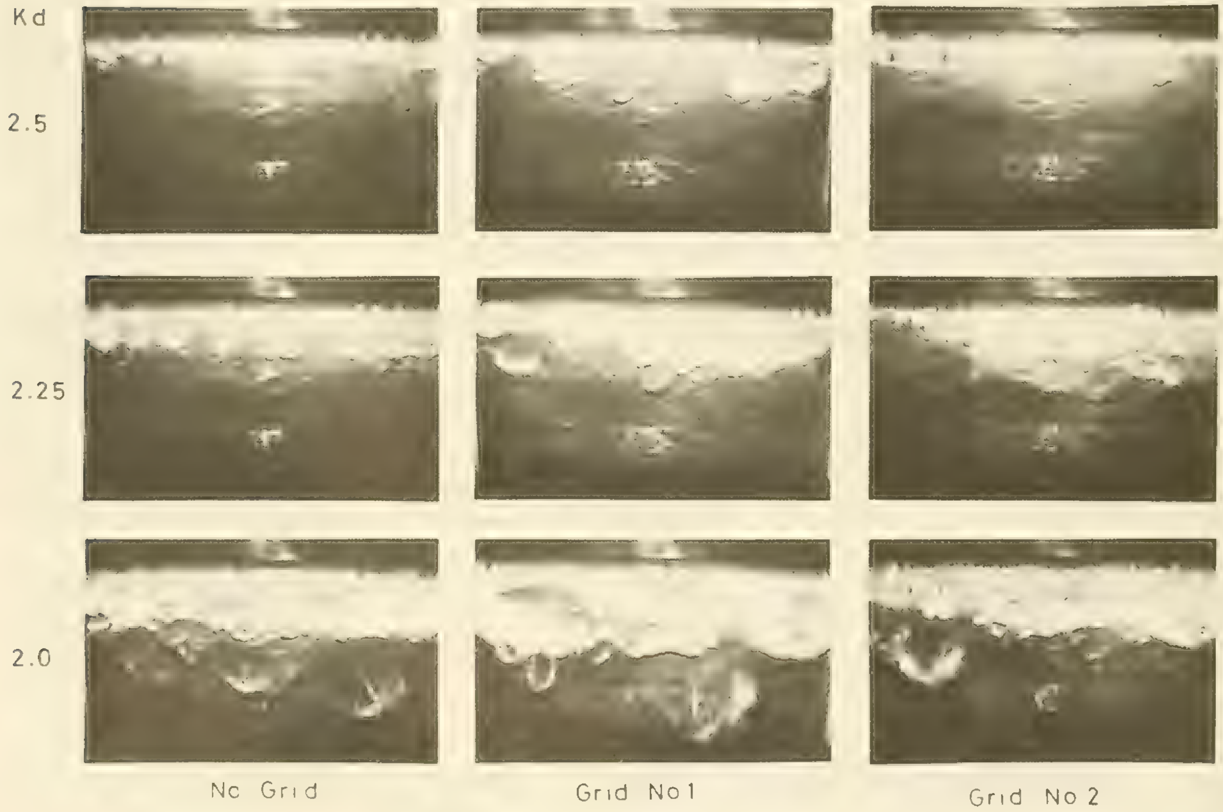
Kd
2.5
2.25
2.0
No Grid
Grid No 1
Grid No 2

(d) $\alpha = 0.157$ rad

FIGURE 12 (c)(d). Cavitation on the hydrofoil of the Clark Y 11.7 profile.

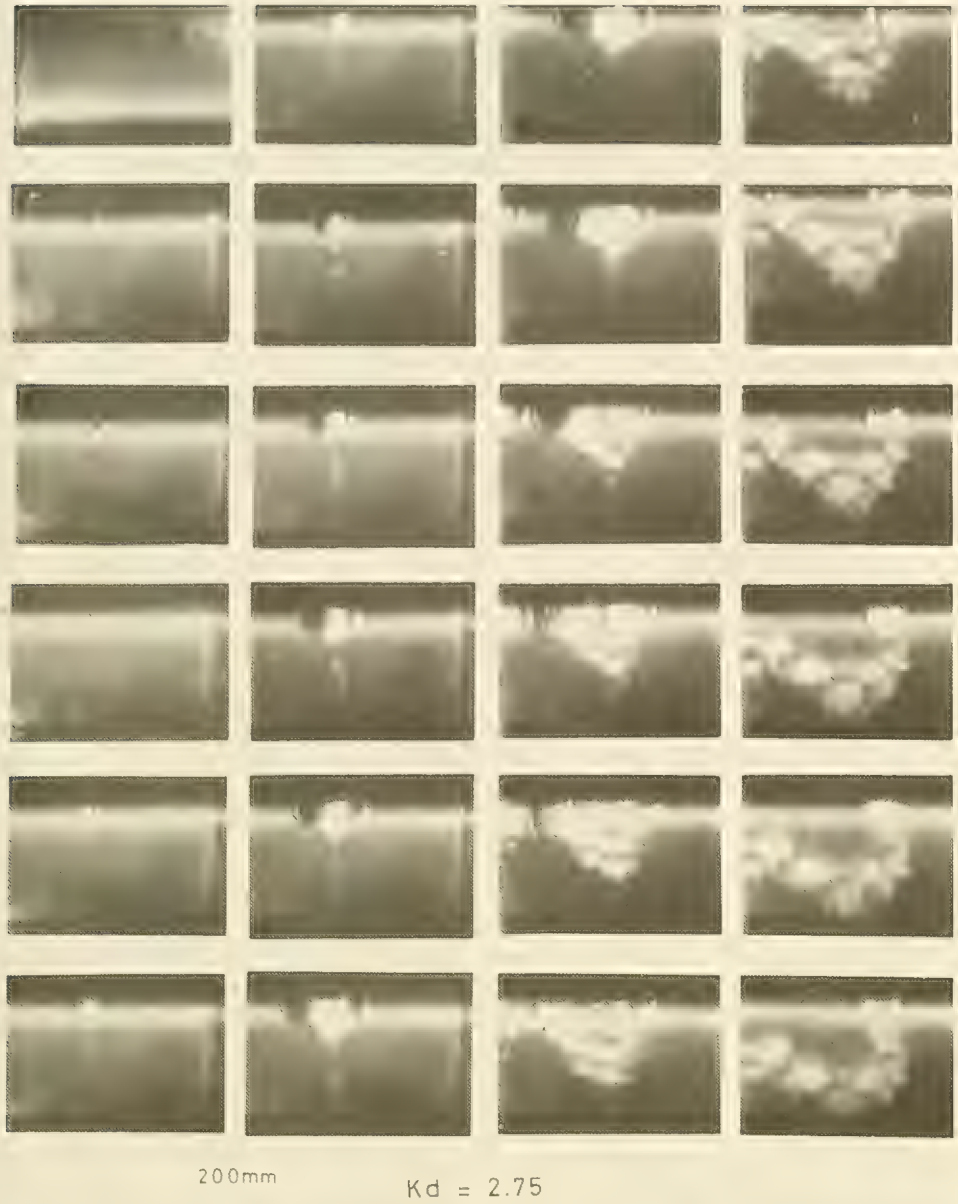

FIGURE 12 (e). Behavior of fixed cavitation on the hydrofoil of the Clark Y 11.7 profile, α = 0.157 rad, flow up to down, 12 ms between frames, 2μs exposure.

tions, which seem to be little affected by either kd or the shear of the free stream. The projections, in the case of no grid, are supposed to be generated in cores of trailing vortices and adhere to the hydrofoil surface, because velocities of the bubbles exceed those of surrounding water in regions downstream from positions of minimum pressure. It can be seen in high speed motion pictures shown in Figure 12(f) that the main body of bubbles, having generated projections, decay, leave behind them projections of two string-like bubbles, and then collapse. In cases of the two shear grids, bubbles are inclined upward toward the high-speed side due to the secondary flow caused by the flow shears. Trailing vortices on the low-speed side reach the hydrofoil surface easier than those on the high-speed side. Bubbles which generate projections become fewer as kd is reduced in the case of the shear grids. Several bubbles can be found which seem to collapse and generate micro jets.

At α = 0.105 rad, cavitations of both types, traveling and fixed, appear, though the former are fewer than the latter. Front edges of fixed cavitation zones are round compared with tips of the above-mentioned projections. At α = 0.157 rad, only fixed cavitations occur. A cycle of formation of the break off of a fixed cavity is shown in high speed motion pictures in Figure 12(e). At first, a clear bubble is generated, like those observed in our laboratory on the surface of an axisymmetrical body with a hemispherical nose. The bubble develops in both streamwise and spanwise directions. The middle part of the spanwise breadth of the bubble becomes bubbly, then wavy, and after the development of the middle part breaks off in pieces of microbubble clouds which are transported downstream although a few remaining small parts grow and disappear.

08 Profile

At 0 angle of attack tiny bubbles of traveling cavitation can be found at a kd a little smaller than kdi, in both cases of no grid and the grid No. 1. Little difference between sizes of the bubbles can be noticed, although bubbles can hardly be found on the low-speed side in the case of the grid No. 1. As cavitation numbers are reduced, however, the bubbles grow larger and are fewer in the case of no grid, due to the difference in size of cavitation nuclei as stated above. Bubbles deforming to generate projections like those on the Clark Y 11.7 profile can barely be found. Instead, cavities collapsing to clusters of small bubbles appear. The discrepancy of the collapse aspect between the two hydrofoils can be considered to be caused by the difference of pressure distributions. Cavitations of the above type become more than traveling bubbles with the decrease of kd, in the case of the grid No. 1.

At $\alpha = 0.052$ rad, only fixed cavitations occurred at the leading edge in cases of both no grid and grid No. 1. The fixed cavitations grown without changing the front edges of cavitation zones from the leading edge and develop their lengths slowly until the kd's are reduced to about the second $|Cpmin|$'s, being about equal to each other and existing at the mid-chord in both cases. Nonuniformity of lengths can be found in the case of grid No. 1. When kd's reach the second $|Cpmin|$'s, however, a remarkable difference in the aspects of cavitations between the two cases occurs in spite of only a small difference in the measured pressure distribution. In the case of no grid, fixed cavitation develops beyond the position of minimum pressure, whereas in the case of grid No. 1, the rear edge of the zone of fixed cavitation does not reach the position of minimum pressure. Instead, another cavitation of the traveling type appears around the position of minimum pressure, and bubbles of the traveling cavitation are found more on the high-speed side. The mechanism of this difference can be surmised as follows: a free shear layer on an interface between cavity and water may be laminar near the point of inception in either case, but the distance necessary for its transition in the case of no grid is larger than in the case of grid No. 1 because of the difference of the turbulence level in the free stream between the two cases, and the distance necessary for a cavity surface to reattach the hydrofoil surface might be the same. The fact that the cavity surfaces in Figure 13(b) at kd = 0.7 are clear in the case of no grid but wavy in the other case may show this. Furthermore, the effect of rolling up the cavity surface caused by the secondary flow may be expected in shear flow.

At $\alpha = 0.105$ rad, only fixed cavitations can be

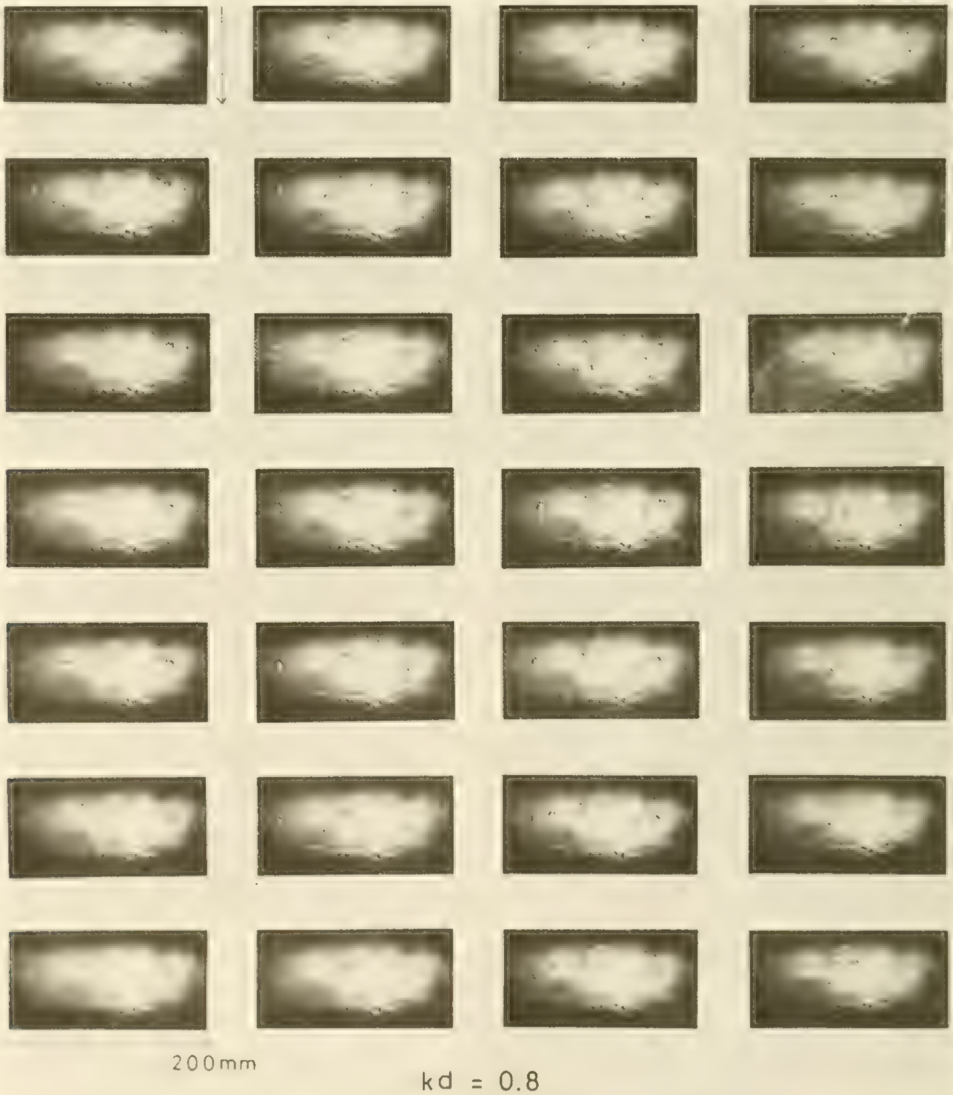

FIGURE 12 (f). Behavior of traveling cavitation on the hydrofoil of the Clark Y 11.7 profile, $\alpha = 0$ rad, flow up to down, 0.3 ms between frames, 2μs exposure.

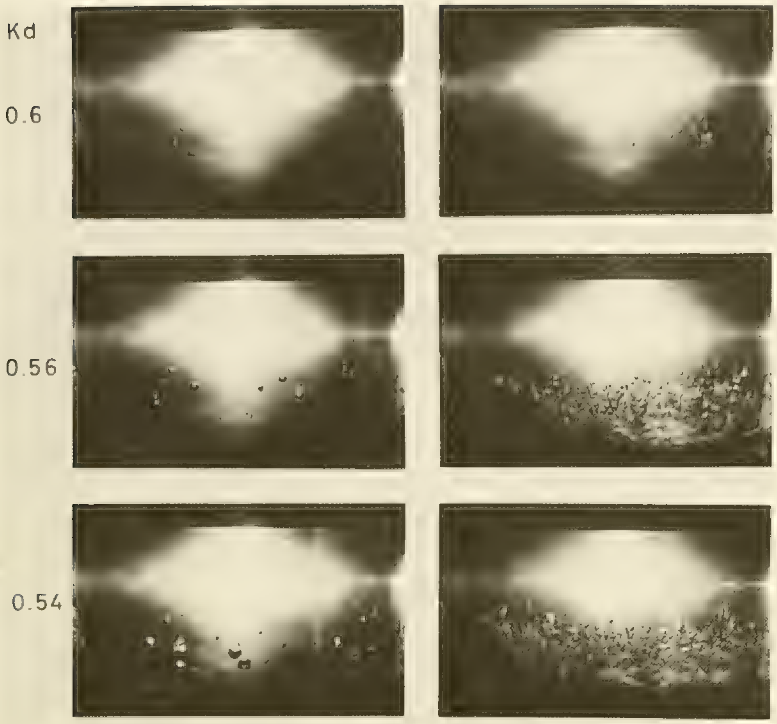

(a) α = 0 rad

FIGURE 13 (a). Cavitation on the hydrofoil of the O_8 profile.

found in both cases. Even in the case of the grid No. 1, much uniformity of cavitation zones can be found, although some tail wisps of cavitation can be found in the case of no grid, e. g., ones gathered in cores of streamwise vortices.

4. CONCLUDING REMARKS

Conditions and positions of inception, locations of zones, and the aspect and behavior of bubbles and cavities of cavitations occurring on two hydrofoils with the profiles of Clark Y 11.7 and 08 in shear flows made by shear grids and a uniform flow have been observed and measured. They have been correlated with measured pressure distributions on the hydrofoils and the qualities of free streams, i.e. turbulence levels and size distributions of cavitation nuclei in free streams. The main conclusions deduced from the results may be summarized as follows.

At attack angles small for the profile, when pressure distributions have gradual chordwise changes, traveling cavitations incept near positions of minimum pressure and at cavitation numbers about equal to absolute values of minimum pressure coefficients, irrespective of flow shears in free streams, provided local values influenced by flow shears are used. Discrepancies between conditions and positions of inceptions, and pressure coefficients and their distributions depend on the free stream qualities. The sizes of traveling bubbles depends on the size distribution of cavitation nuclei.

On the hydrofoil with the Clark Y 11.7 profile, having a relatively large positive pressure gradient, a traveling bubble in a zone of rising pressure deforms, creating a projection in shear flow, or two projections in uniform flow, leaves only the projection and then collapses. On the hydrofoil with the 08 profile having gradual pressure gradient, a traveling bubble collapses after the deformation caused by the instability of bubble surface. On both hydrofoils, bubbles collapsing symmetrically and asymmetrically, looking like micro jets forming can be found.

At attack angles larger for the profile, when the pressure distribution declines steeply followed by a relatively large positive pressure gradient, fixed cavitations occur. Conditions and positions of inception are similar to those of traveling cavitations, although discrepancies of them from pressure coefficients and their distributions are less than those of traveling cavitations. In the boundary layers on both side walls, fixed cavitations occur at relatively large cavitation numbers, possibly equal to absolute values of local minimum pressure coefficients. They develop in both streamwise and spanwise directions even far enough beyond the boundary layers to affect cavitation inceptions in zones neighboring the boundary layers. Cavitation zones on the low-speed side are larger than those on the high-speed side. Fixed cavitations of this kind occur in the boundary layers on both sides of uniform free streams also.

At attack angles intermediate for the profile, fixed and traveling cavitations occur at the same time and tend to become fixed only on the Clark Y 11.7 profile. On the 08 profile, fixed cavitations at the leading edge and traveling cavitations at about the mid-chord appear at the same time in shear flows, but only fixed cavitations occur and develop at the leading edge in uniform flows. Discrepancies of conditions and positions of inception from pressure coefficients and their distributions are the largest of the three cases mentioned on the Clark Y 11.7 profile, but about the same as above mentioned two cases, on the 08 profile.

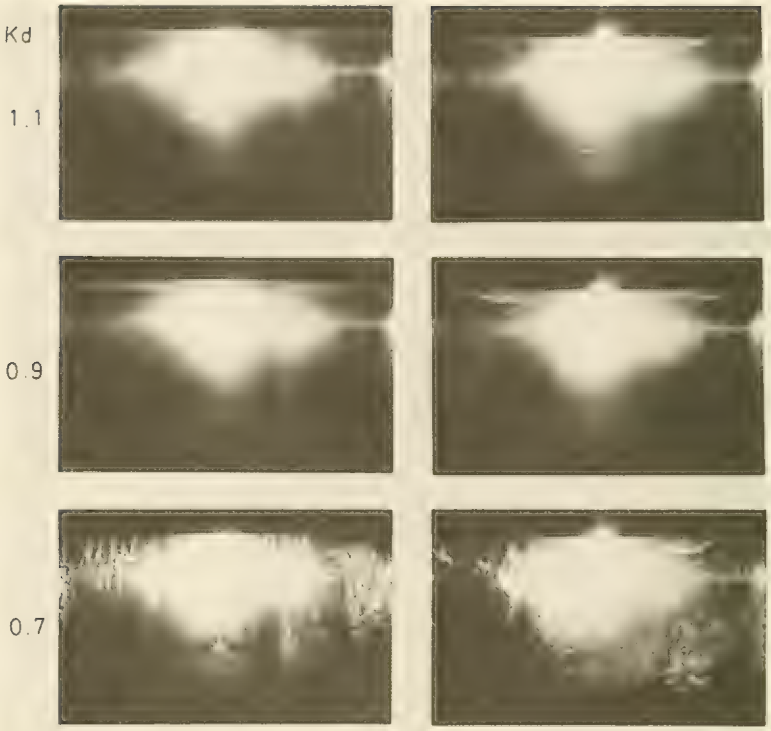

(b) $\alpha = 0.052$ rad

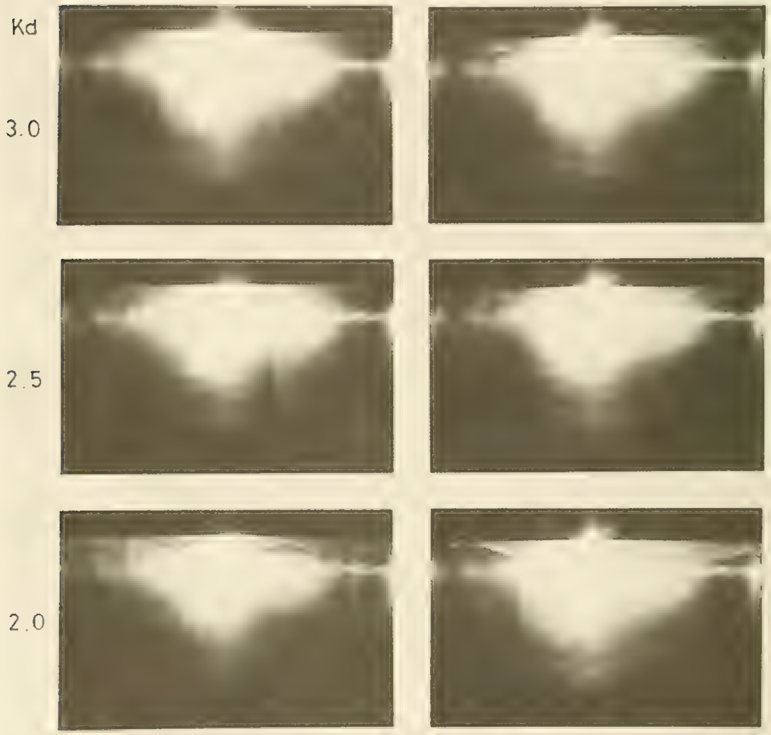

FIGURE 13 (b) (c). Cavitation on the hydrofoil of the O_8 profile.

(c) $\alpha = 0.105$ rad

ACKNOWLEDGMENT

The authors wish to express their thanks to Mr. S. Onuma, the technician of Institute of High Speed Mechanics for his assistance in the experiment.

NOMENCLATURE

Cp:	pressure coefficient
|Cpmin| :	absolute value of minimum pressure coefficient
f_T:	number of total occurrences of cavitation
f_y:	number of local occurrences of cavitation at position y
h:	width of measuring section
kd:	cavitation number
kdi:	incipient cavitation number
l:	chord length of hydrofoil
$n(R_0)$:	number of bubbles at radius R_0
p:	static pressure at hydrofoil surface or in free stream
p_w:	static pressure at side wall of measuring section
R_0:	bubble radius
U:	local free stream velocity
Uc:	velocity at mid span of hydrofoil installed in measuring section
u', v', w':	RMS values of turbulence velocity components parallel to free stream, parallel to hydrofoil span and perpendicular to u' and v', respectively
X, Y; x, y :	co-ordinate system fixed in hydrofoil; the X(x) axis is parallel and the Y(y) axis is perpendicular to the chord of the hydrofoil
α :	attack angle in radian
ρ :	water density
λ :	chordwise distance from leading edge of hydrofoil to rear edge of cavitation zone
λ_0 :	chordwise distance from leading edge of hydrofoil to inception point or front edge of cavitation zone

REFERENCES

Adachi, T., and E. Kato (1973). An experimental study on the turbulent linear shear flow. *J. Japan Soc. Aeronautical & Space Sci. 21*, 573.

Blake, W. K., M. J. Wolpert, and F. E. Gieb (1977). Cavitation noise and inception as influenced by boundary-layer development on a hydrofoil. *J. Fluid Mech. 80*, 617.

Casey, M. Y. (1974). The inception of attached cavitation from laminar separation bubbles on hydrofoils, *Proc. Confe. Cavitation* held at Edinburgh, 1.

Daily, J. W. (1944). Force and cavitation characteristics of the NACA 4412 Hydrofoil, *Calif. Inst. of Tech. Hydrody. Lab. ND 19*.

Daily, J. W. (1949). Cavitation characteristics and infinite-aspect ratio characteristics of a hydrofoil Section. *Trans. ASME 71*, 269.

Daily, J. W., and Johnson (1956). Turbulence and boundary-layer effects on cavitation inception from gas nuclei. *Trans. ASME, 78*, 1695.

Gavrilov, L. C. (1964). On the size distribution of gas bubbles in water. *Soviet Phy.-Acoust. 15*, 1.

Harris, V. G., J. A. H. Graham, and S. Corrsin (1977). Further experiments in nearly homogeneous turbulent shear flow. *J. Fluid Mech. 81*, 657.

Kermeen, P. W. (1956). Water tunnel tests of NACA 4412 and Walchner profile 7 hydrofoils in non-cavitating and cavitating flow. *Calif. Inst. of Tech. Hydrodyn. Lab. 47-5*.

Kermeen, P. W. (1956). Water tunnel tests of NACA 66-012 hydrofoil in non-cavitating and cavitating flows. *Calif. Inst. of Tech. Hydrodyn. Lab. 47-7*.

Kermeen, R. W., and B. R. Parkin (1957). Incipient cavitation and wake flow behind sharp-edged disks. *Calif. Inst. Tech. Engr. Div. 85-4*.

Lighthill, M. G. (1957). Contribution to the theory of the Pitot-tube displacement effect. *J. Fluid Mech. 2*, 493.

Liversy, J. L., and J. T. Turner (1964). The generation of symmetrical duct velocity profiles of high uniform shear. *J. Fluid Mech. 20*, 201.

Macmillan, F. A. (1956). Experiments on pitot tubes in shear flow. *Aero. Res. Counc.*, London *18235*.

Numachi, F., and T. Kurokawa (1939). Über den Einfluss des Luftgehaltes auf die Kavitationsentstehung am Tragflügel. *Tech. Rep. Tohoku Imp. Univ. 13*, 236. *Werft-Reederei-Hafen, Bd.XX*.

Numachi, F. (1954). Summary Report on the research of cavitation phenomena obtained hitherto by our Institute. *Rep. Inst. High Speed Mech.* Tohoku Univ. *4*, 159.

Numachi, F. (1975). Effect of turbulence in free stream on cavitation incipience of hydrofoil. *J. Fluid Engr. Trans. ASME 97*, 180.

Numachi, F., M. Nakamura, and I. Chida (1952). Cavitation tests on hydrofoil profiles of simple form for blade elements. *Memoirs Inst. High Speed Mech.* Tohoku Univ. *6*, 113.

Owen, P. R., and H. K. Zienkiewiez (1957). The production of uniform shear flow in a wind tunnel. *J. Fluid Mech. 2*, 521.

Rechardson, J. M. (1947). *J. Acoust. Soc. Amer. 19*, 666.

Rouse, H. and A. H. Abdul-Fetouh (1950). Characteristics of irrotational flow through axially symmetric orifices. *J. Applied Mech., Trans. ASME 17*, 421.

Rouse, H. (1953). Cavitation in the mixing zone of a submerged jet. *La Houille Blanche, Janu-Feb*, 9.

Schiebe, F. R. (1969). The influence of gas nuclei size distribution on transient cavitation near inception. *Univ. Minnesota Proj. Rep. 107*.

Young, A. D., and J. N. Maas (1936). Behavior of Pitot tube in a transverse total-pressure gradient. *Aero. Res. Counc.*, London, *Rep. and Mem. 1770*.

Scale Effects on Propeller Cavitation Inception

G. Kuiper
Netherlands Ship Model Basin
Wageningen, The Netherlands

ABSTRACT

The boundary layer of four propeller models in uniform flow is investigated and related with cavitation inception. Laminar separation is found to be an important phenomenon on model propellers. The radius where laminar separation starts is found to be a limit for the radial extent of cavitation. No inception takes place in regions of laminar flow. The effect of nuclei in the flow is investigated using electrolysis. Nuclei seem to be important for cavitation inception when laminar separation occurs, but they do not initiate sheet cavitation, when the boundary layer flow is laminar. When the boundary layer on the blades is tripped to turbulence by roughness at the leading edge it is shown that this changes the cavitation by restoring cavitation inception at the vapour pressure. The effect of electrolysis on cavitation becomes very small when the propeller blades are roughened. Calculations of the pressure distribution and the laminar boundary layer were made and related with test results.

1. INTRODUCTION

When cavitation patters, observed on full scale ship propellers, are compared with observations on model scale, differences are often found [e.g., Bindel (1969), Okamoto et al. (1975)]. These differences are caused by two main factors: incorrect scaling of the incoming flow of the propeller, including propeller-hull interaction, and incorrect scaling of cavitation.

Considerable efforts have been made to improve the simulation of the incoming flow by testing the cavitating propeller model behind the ship model in a large cavitation tunnel or in a depressurized towing tank, or by correcting the measured model wake to simulate the full scale wake in a cavitation tunnel [Sasajima and Tanaka (1966), Hoekstra (1975)]. In this paper the problem of proper scaling of cavitation will be investigated.

Scaling rules for cavitating propellers can be formulated using dimensional analysis when the relevant parameters are known. This results in the following well-known dimensionless quantities:

the advance ratio $$J = \frac{V_A}{nD} \qquad (1)$$

the cavitation index $$\sigma_N = \frac{p_o - p_v + \rho g h}{\frac{1}{2}\rho n^2 D^2} \qquad (2)$$

the Froude number $$Fr = \frac{n^2 D}{g} \qquad (3)$$

the Reynolds number $$Re_N = \frac{nD^2}{\nu} \qquad (4)$$

where V_A = advance velocity of the propeller

n = number of propeller revolutions

D = propeller diameter

p_o = pressure at some reference level

p_v = vapour pressure

ρ = density of water

g = acceleration due to gravity

h = vertical distance from reference level

ν = kinematic viscosity

When these dimensionless parameters are kept the same for model and prototype, the cavitation behaviour of a propeller is independent of size, provided that no additional parameters play a role in the cavitation process.

The choice of the cavitation index as a parameter implies the assumption that inception occurs when the local pressure is equal to the vapour pressure. When the inception pressure deviates from the vapour pressure these deviations are called "scale effects on cavitation inception".

Two scaling problems do arise now. First it is impossible to maintain the Froude number and the Reynolds number at the same time. The Reynolds number is abandoned and is lowered on model scale by a factor of $\lambda^{3/2}$, where λ is the scale ratio. Even if the Froude number is not maintained it is practically impossible to obtain the full scale Reynolds number on model scale. The second scaling problem is that nuclei play a role in cavitation inception. Both problems manifest themselves as scale effects.

Pure water can withstand very high tensions and nuclei are necessary to generate inception of cavitation. Nuclei are mostly considered to be gas pockets in the fluid, possibly trapped in small crevices of hydrophobic particles. For a review see Holl (1970). In a cavitation tunnel, however, the flow will also contain free air bubbles which come out of solution at the pump, at sharp corners, or at the cavitating propeller in the test section. Resorbers are used to bring the free gas back into solution, or the tunnel can be prepressurized. When no large nuclei are present, however, scale effects on cavitation become larger [Hill and Wislicenus (1961)]. Inception of cavitation becomes related to the pressure at which the largest gas bubbles become unstable and start to expand, and this pressure is lower than the vapour pressure when the nuclei are small [Daily and Johnson (1956)]. In a towing tank there are very few nuclei since they will rise to the surface or to go into solution. Therefore Noordzij (1976) created additional nuclei in the NSMB Depressurized Towing Tank by electrolysis and showed the "stabilizing" influence of nuclei on propeller cavitation behind a ship model. A similar effect was reached by Albrecht and Bjorheden (1975) who injected additional nuclei into the water of their free surface cavitation tunnel after the low pressure in the test section had deaerated the water so much that nuclei were no longer formed in the tunnel.

It is very difficult to control the nuclei content of the incoming flow [Schiebe (1969)]. When the nuclei are large enough, the inception pressure will be close to the vapour pressure. However, when the nuclei are too large they can lead to "gaseous cavitation" [Holl (1970)] with inception above the vapour pressure, or they can be removed from the region of lowest pressures by the pressure gradient in the flow, as was theoretically shown by Johnson and Hsieh (1966).

Variation of the Reynolds number leads to viscous effects on cavitation inception. Arakeri and Acosta (1973) and Casey (1974) showed the effect of the boundary layer on cavitation inception. Laminar separation was shown to be especially important. Arakeri and Acosta (1973) visualized the boundary layer by a schlieren technique and they tentatively related the cavitation index at inception and the pressure coefficient at laminar separation or at transition. Increased pressure fluctuations in the reattachment region of a laminar separation bubble and in the transition region were measured by Arakeri (1975) and by Huang and Hannan (1975). Van der Meulen (1976) also observed the inception process on headforms by means of holography. He showed that suppression of laminar separation by polymers also could suppress cavitation inception. The relation between the inception pressure and the pressure at laminar separation or transition was not always confirmed. In a recent case study [Kuiper (1978)], it was shown that viscous effects were responsible for a delay in cavitation inception on a propeller model. Additional nuclei had no effect in this case, but it was not yet clear if nuclei did interact with the boundary layer to create cavitation inception.

In this study, scale effects on cavitation on three propellers with different characteristics were investigated. When a propeller operates in a wake, scaling problems of the incoming flow and of cavitation cannot be separated. Therefore the propellers were tested in uniform axial flow. The tests were carried out mainly in the Depressurized Towing Tank. A description of this facility is given by Kuiper (1974). The advantages of this tank for the research on scale effects on cavitation inception are the, supposedly, very low and constant turbulence level and nuclei content, the uniform inflow of the propeller, and the absence of wall effects. Both advance speed and propeller revolutions can be controlled very accurately. The range of Reynolds numbers which can be tested is lower than in a cavitation tunnel (maximum carriage speed is 4 m/sec.) but is not smaller.

The aim of the present study is to gain insight into the occurrence of scale effects on cavitating propellers and to develop means to improve the correlation with full scale observations. Paint tests were carried out to visualize the boundary layer flow on the propeller blades. Methods to calculate the pressure distribution on the blades are discussed and the calculated pressure distributions are used for the interpretation of the results of the paint tests and the cavitation observations. The nuclei content is varied by using electrolysis, and roughness at the leading edge of the propeller blades is applied to make the boundary layer on the blades turbulent, thus simulating a higher Reynolds number. The relation between the boundary layer on the blades and cavitation inception is shown and the effect of leading edge roughness and electrolysis is investigated.

2. TEST PROGRAM

Propellers and Test Conditions

Four propellers were investigated in uniform flow. Propeller A is the propeller which was investigated behind a model in a case study by Kuiper (1978). This propeller showed viscous scale effects on cavitation inception but was insensitive for electrolysis (Figure 1). Behind the model, this propeller operated in a nozzle. In this study it was tested without a nozzle.

Propeller B is the propeller which was tested by Noordzij (1976) behind a model. This propeller was very strongly influenced by electrolysis. Without electrolysis the sheet cavitation varied per revolution, (Figure 2). With electrolysis the

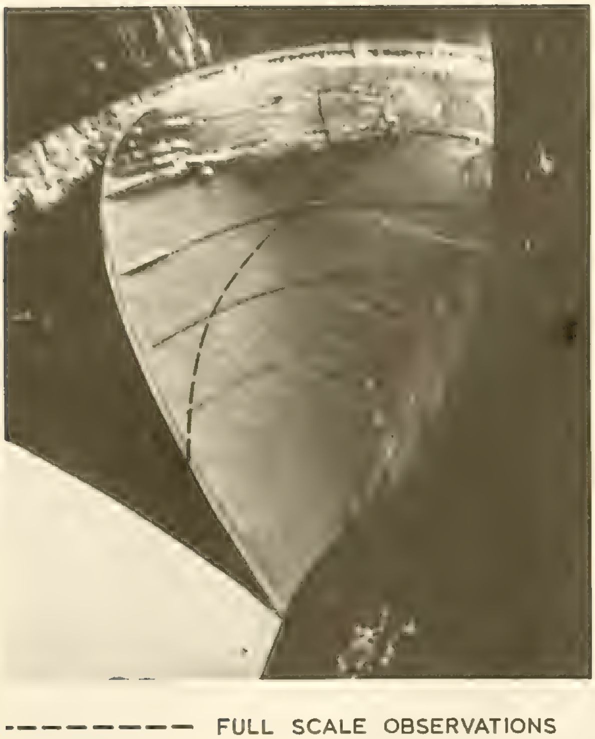

FIGURE 1. Viscous effects on cavitation inception on propeller A behing the model.

cavitation pattern was present and identical at every revolution. This "stabilizing" effect of nuclei is important because it affects the induced pressure fluctuations on the hull.

Propeller C had a very distinct collapse of the cavity when the blades left the wake peak, as can be seen in Figure 3. This irregular collapse of the cavity was thought to be caused by viscous effects and it can also strongly influence the pressure fluctuations on the hull.

Propeller D was not tested in cavitating conditions. It was used only for boundary layer visualization. This propeller is an example of a smaller propeller model used behind models with a maximum length of 7 meters. This propeller was made of a copper-nickel-aluminium alloy (CUNIAL). Propellers A, B and C were of aluminium.

The most important geometrical characteristics of the four propellers are given in Figure 4. The complete description, necessary for the calculations, is given in the Appendix. Most tests were done in the NSMB Depressurized Towing Tank. To obtain uniform inflow the propellers were mounted on a right-angle drive unit, which was kept afloat by a catamaran-type vessel, as shown in Figure 5. Only a few comparative tests were done in a cavitation tunnel.

The following parameters were varied:

-The propeller loading. Two advance ratio's were used, namely 70% and 40% of the pitch ratio at r/R=0.7. (Slip ratio's of 30% and 60% respectively). The slip ratio of 30% corresponds to a loading which is about normal behind the ship, the slip ratio of 60% corresponds to an overloaded condition, as occurs when the blades are in a wake peak. Propeller A was also investigated at an intermediate loading with a slip of 40% .

-The nuclei content. At 1 meter in front of the propeller an electrolysis grid was mounted, as shown in Figure 5. The wires had a diameter of 0.2 mm and a current of 0.2A was used to generate nuclei. The propeller shaft was at 0.4 meter below the water level and the lowest wire at 0.5 meter. Therefore the effect of electrolysis could only be observed in the upper half of the propeller disk.

-The propeller boundary layer. Two ways of affecting the boundary layer were used. First, sandroughness at the leading edge was used to trip the boundary layer to turbulence. Second, the

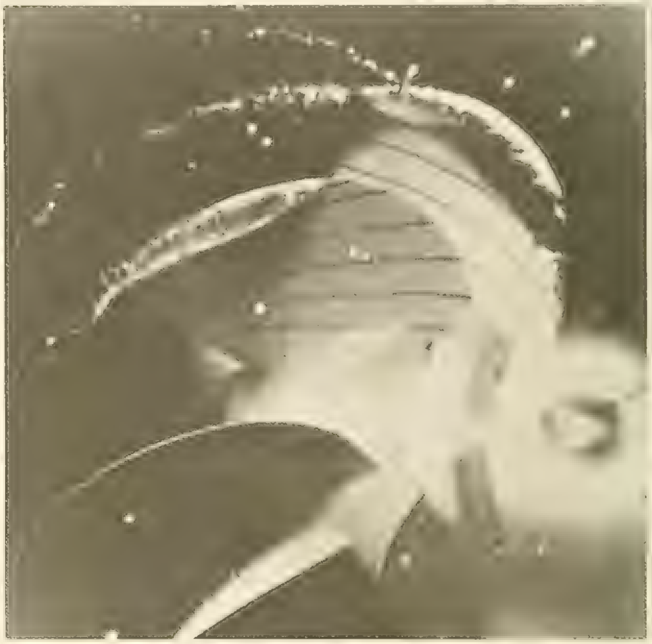

WITHOUT ELECTROLYSIS

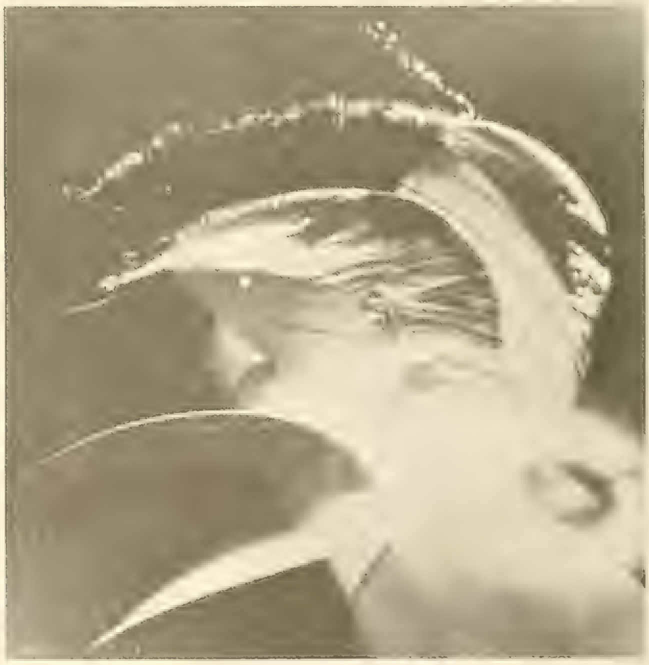

WITH ELECTROLYSIS

FIGURE 2. Effect of electrolysis on propeller B behind the model.

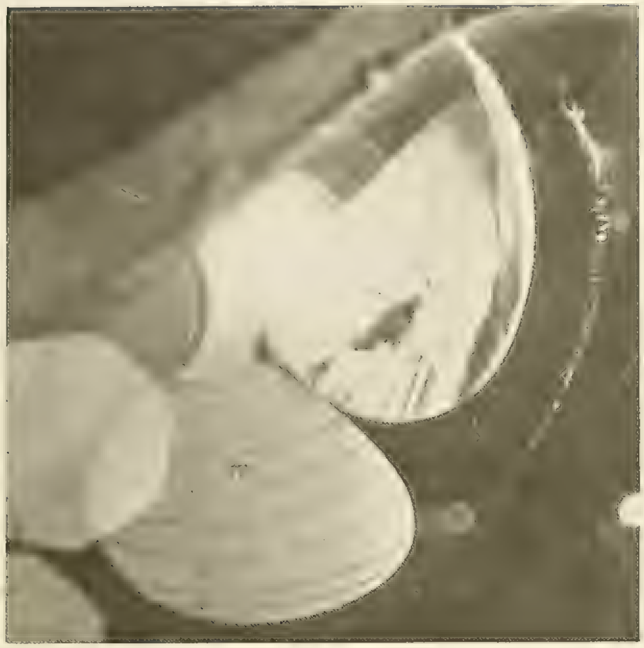

FIGURE 3. Irregular collapse of cavitation on propeller C behind the model.

propeller Reynolds number was varied with a factor of about three.

-The cavitation index. Three values of the cavitation index were used: σ_{NT}=1.5, 2.0, and 2.5. The reference level of the cavitation index was always taken at the propeller tip in the top position. In this paper most cavitation observations will be shown at σ_{NT}=1.5. At higher revolutions a lower cavitation index was possible: σ_{NT}=0.5 in the towing tank and σ_{NT}=1.0 in the cavitation tunnel.

Paint Observations

To visualize the character of the boundary layer at the propeller blades a surface oil flow technique was used [Maltby, ed. (1962)]. This technique was adapted for use in water on propellers by Meyne (1972) and Sasajima (1975). It is particularly useful on rotating bodies because the difference in friction coefficient between laminar and turbulent boundary layer flow, in combination with the centrifugal force acting on the paint, creates a clear difference in the direction of the paint-streaks in laminar and turbulent regions.

The paint, used in our paint tests, consisted of lead-oxide, diluted with linseed oil and coloured with red "Dayglo" pigment. This mixture produced a finely detailed pattern of streaks on the metal surface of the propeller. When the propeller blades were painted yellow with a thin layer of zinc-chromate primer, as is done with the cavitation observations to improve contrast and to avoid reflections, no streaks were formed. Consequently the flow visualization tests were done with the propellers not painted.

The viscosity of the paint was controlled by the amount of linseed oil and was chosen such that the formation of the pattern took about one full run in the towing tank. At least 500 revolutions were always available to form the pattern. To reach the desired condition took about 100 revolutions, most of them very close to the final condition. Paint tests were also done in the cavitation tunnel. The pictures obtained there were more profuse, especially at high tunnel velocities, because of the relatively long time it took to reach a stable condition. For runs longer than

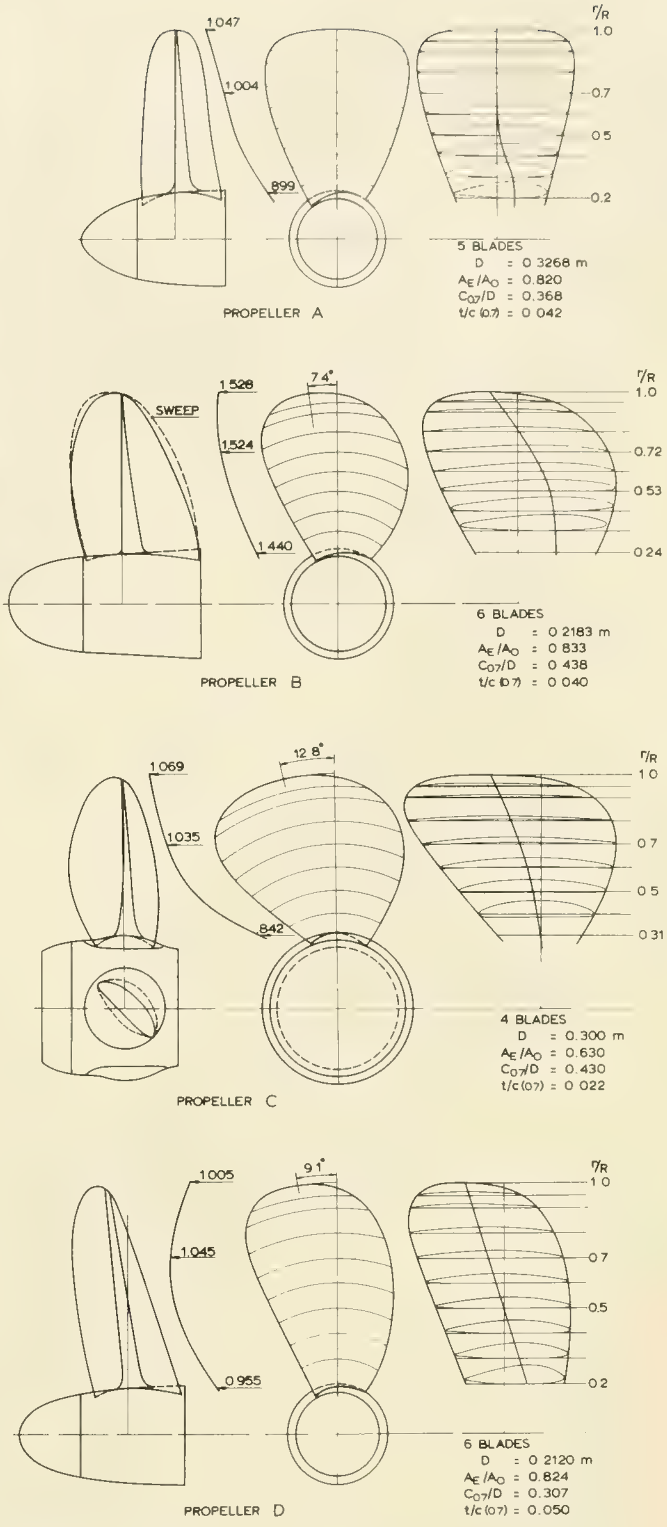
1.047
1.004
899
r/R
1.0
0.7
0.5
0.2
5 BLADES
D = 0.3268 m
A_E/A_O = 0.820
C_{07}/D = 0.368
t/c (0.7) = 0.042
PROPELLER A
1.528
7.4°
SWEEP
1.524
1.440
r/R
1.0
0.72
0.53
0.24
6 BLADES
D = 0.2183 m
A_E/A_O = 0.833
C_{07}/D = 0.438
t/c (0.7) = 0.040
PROPELLER B
1.069
12.8°
1.035
842
r/R
1.0
0.7
0.5
0.31
4 BLADES
D = 0.300 m
A_E/A_O = 0.630
C_{07}/D = 0.430
t/c (07) = 0.022
PROPELLER C
1.005
9.1°
1.045
0.955
r/R
1.0
0.7
0.5
0.2
6 BLADES
D = 0.2120 m
A_E/A_O = 0.824
C_{07}/D = 0.307
t/c (07) = 0.050
PROPELLER D

FIGURE 4. Geometry of propellers.

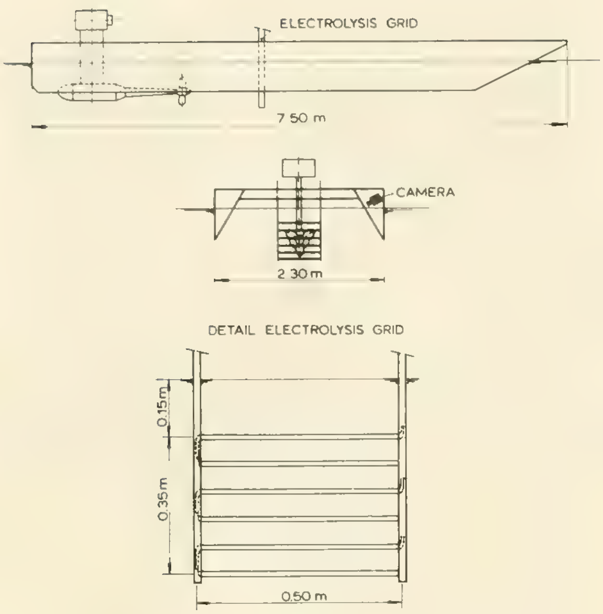

FIGURE 5. Test equipment for open-water tests.

a few minutes the viscosity of the lead-oxide is too low and the blades are cleaned by the flow.

The paint is put on the propeller blades at the leading edge to about 10% of the chord. The layer must be rather thick to provide enough paint to cover the whole blade. Some pictures were taken with UV light using the fluoriscent properties of the pigment. The bulk of the pictures of the paint tests was taken in colour photography with natural light. This gave good colour prints, but unfortunately the contrast in monochrome paper turned out to be rather poor.

Roughness at the Leading Edge

To trip the boundary layer to turbulence the leading edge of the propeller blades was covered with carborundum. The leading edge of the propeller blade is wetted with watery thin varnish to about 0.5 mm from the leading edge. This is done by touching the leading edge with a pad wetted with varnish. The softness of the pad determines the length of the wetted area from the leading edge. Then carborundum is put on the wetted area by spreading the grains on a felt cloth and by wiping the wetted leading edge with that cloth. Two grains sizes were used: 30 µm (31-37) and 60 µm (53-62). Microscopic inspection afterwards is necessary. An example is given in Figure 6.

3. CALCULATION OF PRESSURE DISTRIBUTION

The analysis of boundary layer phenomena and of cavitation on propeller blades becomes very speculative when the pressure distribution is not known. No firm experimental verification of calculations of the pressure distribution is available yet, only the total thrust and torque give some evidence of the value of calculations. The calculations are always potential flow calculations and the effect of viscosity on the propeller sections cannot yet be derived with suitable accuracy. Since the propeller thrust is least sensitive to viscous effects this quantity gives the most reliable verification of calculations. When the propeller geometry and the nominal inflow are known two approaches are available to obtain the distribution of propeller loading, viz. the lifting line theory and the lifting surface theory. Hereafter, both approaches will be considered with models going back to the work of Lerbs (1952) for the former and Sparenberg (1960) for the latter theory.

Lifting Line Calculations

The lifting line theory concentrates the loading of a propeller section at one point. Using the induction factor method [Wrench (1957)], a relation between the hydrodynamic pitch angle, β_i, and the circulation, Γ, at each section is found.

$$\beta_i(i) = F[\Gamma(r)] \tag{5}$$

When a given propeller is analysed β_i and Γ are unknown. To find them a second relation is necessary, which is derived from two-dimensional profile characteristics. The lift coefficient

$$C_L = \left(\frac{dC_L}{d\alpha}\right)(\alpha+\alpha_o) \tag{6}$$

where α_o is the zero lift angle of the propeller section. Since the angle of attack α is taken from

$$\alpha = (\beta_p - \beta_i). \tag{7}$$

where β_p is the known geometrical pitch angle, a second relation is formulated between C_L (or Γ) and β_i, in which $dC_L/d\alpha$, is assumed to be known.

When the two-dimensional value for $dC_L/d\alpha$, based on the geometry of the propeller section, is used the results are rather drastically wrong. This is caused mainly by the finite length of the propeller section, which creates a distribution of induced velocities affecting camber and angle of attack.

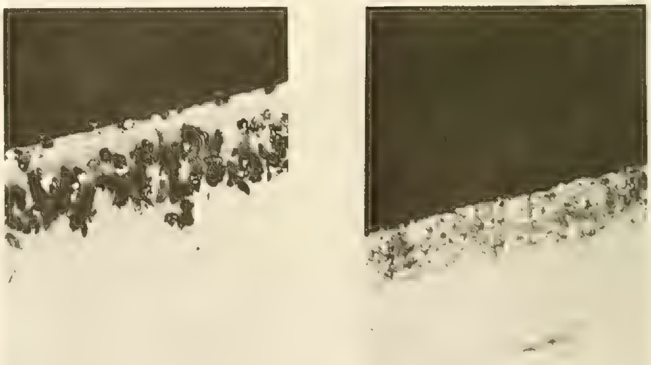

60 µm
CARBORUNDUM

30 µm
CARBORUNDUM

FIGURE 6. Microscopic picture of leading edge roughness.

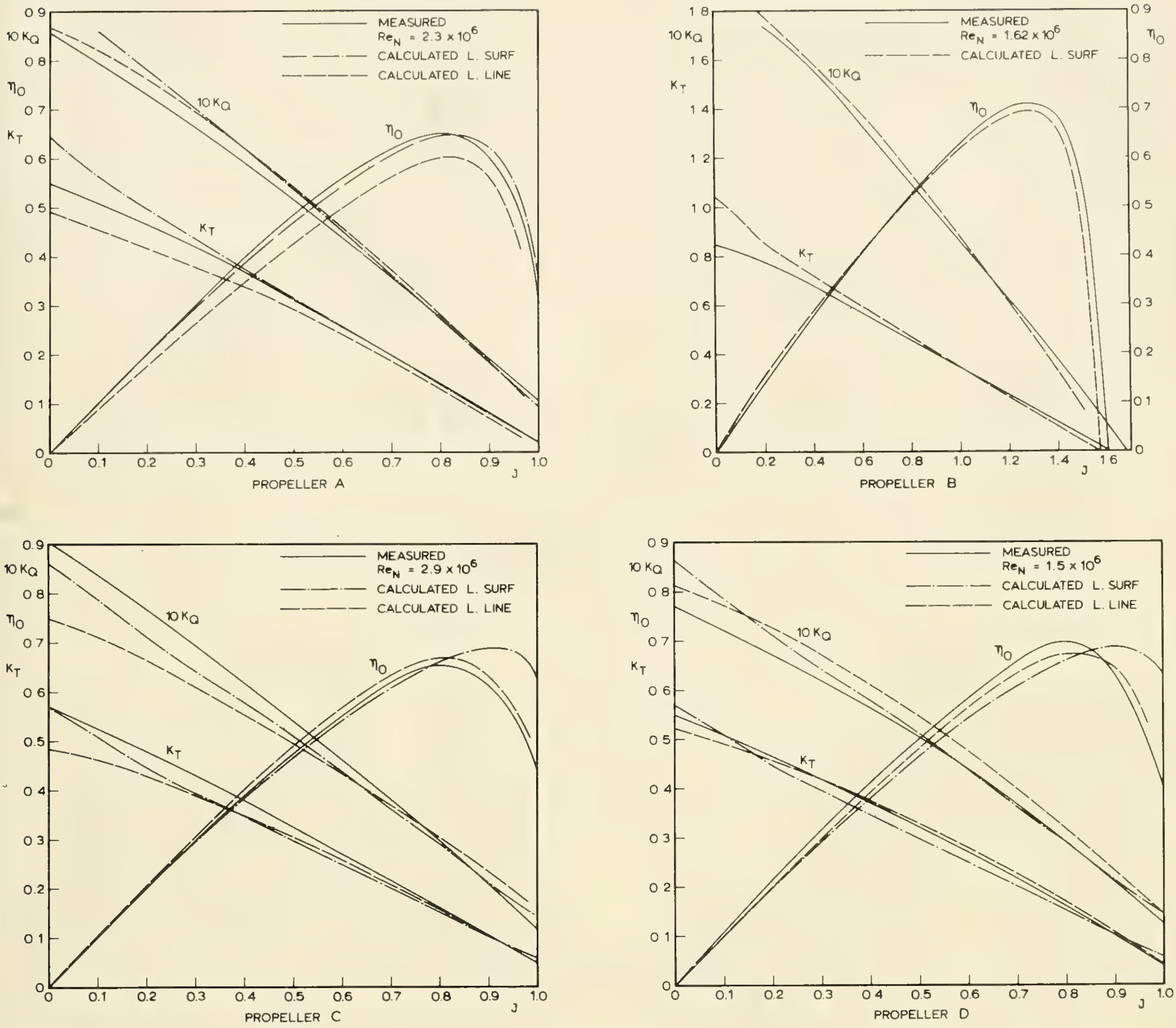

FIGURE 7. Propeller open-water characteristics.

So Eq. 6 has to be corrected to obtain a three-dimensional lift curve. At one point of the lift curve, at the ideal angle of attack, results of systematic lifting surface calculations are available [Morgan et al. (1968)] and they can be expressed as correction factors on camber, K_C, and the angle of attack, K_α. Van Oossanen (1974) used these correction factors to define the three-dimensional lift curve over the whole range of angles of attack instead of at the ideal angle of attack only. He wrote

$$\left(\frac{dC_L}{d\alpha}\right)_{3d} = \frac{dC_L}{d\alpha} \cdot \frac{1}{K_C} \qquad (8)$$

and

$$\alpha_{o_{3d}} = (K -1)\alpha_i - \alpha_o \qquad (9)$$

where α_i is the ideal angle of attack of the propeller section. Substitution of these three-dimensional values in Eq. 6 makes it possible to solve the set of Eqs. 5-7, resulting in a radial distribution of β_i, α_o, and C_L.

In Figure 7 the calculated open-water characteristics using this approach are compared with experiments. The agreement between measurements and calculations is acceptable. Propeller B could not be calculated since the regression formula's for K_C and K_α in the program were restricted to a maximum pitch ratio of 1.4.

Viscosity is taken into account by assuming a viscous lift slope

$$\left(\frac{dC_L}{d\alpha}\right)/2\pi = 0.947-0.76\left(\frac{t}{c}\right)^3$$

where t= max. thickness of propeller section
c= chord length of propeller section

The drag is calculated using the characteristics of the equivalent profiles of the NSMB B-series propellers.

Lifting Surface Calculations

The lifting surface theory calculates the induced velocities over the propeller blades, in chordwise and radial direction, thus including the effects of finite aspect ratio of the blades. The drawback is that the theory is linearized, which restricts the validity to lightly loaded propellers.

Van Gent (1977) has shown in his thesis how heavily loaded propellers can be treated with a linearized theory since the vorticity in the wake induces an additional axial velocity component in the propeller plane, keeping the angles of attack of the propeller sections small.

The boundary conditions on the propeller blades are fulfilled at a number of chordwise and spanwise points. In our calculations four chordwise and ten radial points per blade were chosen. The pitch of the vortex sheet in the wake was taken rather arbitrarily as the pitch at 0.7D.

A very approximate description of the viscous effects is used. The drag force of the propeller sections is split into two parts: a drag force as a result of losses in the suction peak at the leading edge and a drag force due to friction. The latter is calculated using a friction coefficient of 0.0080, irrespective of the Reynolds number. The first drag force is taken as half the theoretical suction force. The same correction is also applied to the sectional lift, which is obtained from chordwise integration of the lift distribution. In the calculation of the induced velocities the geometrical pitch angle is reduced by 3/4 degree to simulate viscous effects on the zero lift angle.

The open-water diagrams as calculated with the lifting surface theory as described by Van Gent (1977) are shown in Figure 7 together with experimental results and lifting line calculations. The general agreement with measurements is as good as the lifting line calculations. This makes clear that the linearized lifting surface theory can indeed produce reliable open-water characteristics up to high propeller loadings. At very low advance ratio's the calculations deviate from the measurements but this might well be caused by an erroneous estimate of the viscous effects.

Calculation of the Pressure Distribution

Lifting line as well as lifting surface calculations give the radial distribution of the lift coefficient, of the angle of attack, and of the induced camber (or camber distribution) which can be translated into a zero lift angle. In Figure 8 these results are compared for propeller A at 40% slip. The lifting line calculation gives a higher loading at the tip and a lower loading at inner radii, compared with the lifting surface calculation. This is characteristic for all four propellers in all conditions. The total thrust does not differ very much. Large differences, however, are found for the angle of attack and for the zero lift angle.

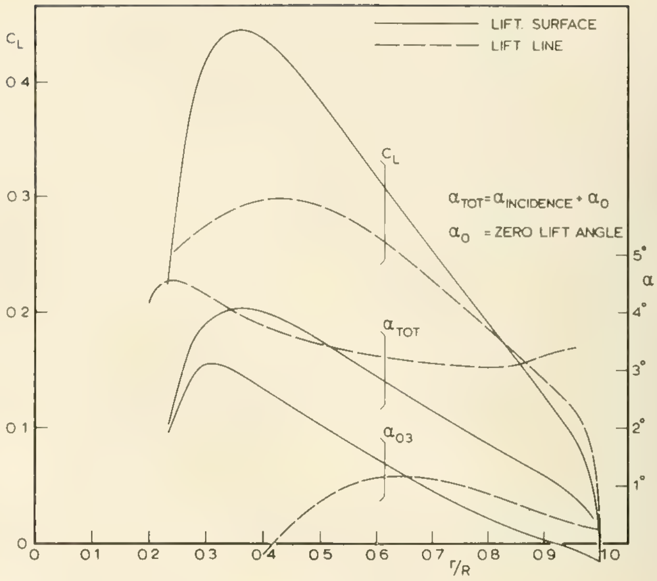

FIGURE 8. Radial distribution of lift coefficient and angle of attack on propeller A at 40% slip.

Since these values will be used in the calculation of the pressure distribution this discrepancy needs further attention.

The source of the discrepancy is the choice of Eqs. 8 and 9, used in the lifting line calculation. The reduction of the slope of the lift curve with the lifting surface correction factor for the camber, K_C (Eq. 8), is an empirical one, first suggested by Lerbs (1951) when he analyzed the lift slopes of his "equivalent profiles". The physical meaning of this correction is not clear, but it still can lead to correct results for thrust and torque, since the lift slope for the equivalent profiles was derived using a lifting line theory and experimental values of thrust and torque. Therefore, this correction for the lift slope, used in combination with the same lifting line theory, should give results for thrust and torque not too far from the experimental results. The definition of the three dimensional zero lift angle (Eq. 9) is another empirical relation, bringing the calculated open water characteristics in line with experiments. However, this does not necessarily mean that the three dimensional angle of incidence and zero lift angle have a physical meaning and can be used for the calculation of the pressure distribution. Therefore, the results of the lifting surface calculations are used in the following to calculate the pressure distribution.

To calculate the pressure distribution on the blades, the effect of propeller thickness has to be calculated and the leading edge singularity of the lift distribution has to be dealt with. Tsakonas et al. (1976) calculated the pressure distribution on the propeller blades using a singularity distribution for the thickness, in combination with a linearized lifting surface theory. These calculations, however, remain linearized, producing an infinite velocity at the leading edge, which was removed by the Lighthill correction for thin airfoils [Lighthill (1951)]. In our study, three-dimensional effects on the pressure distribution are neglected. Interaction effects between thickness

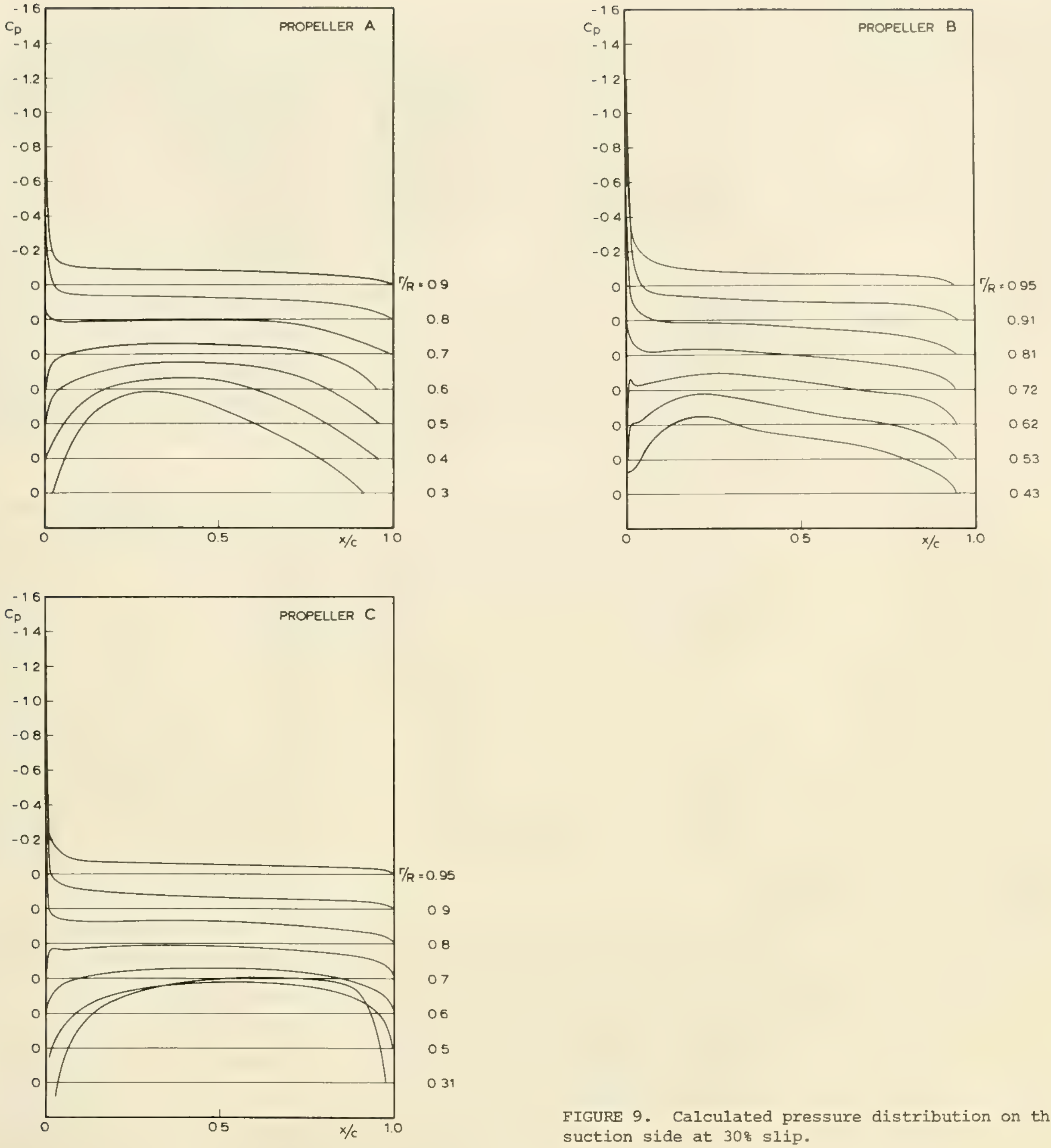

FIGURE 9. Calculated pressure distribution on the suction side at 30% slip.

and loading, which occur due to the non-planar surface of the propeller blades are taken into account by a correction factor [Morgan et al. (1968)]. This makes it possible to apply conformal mapping to calculate the pressure distribution. An approximation of the original theory of Theodorsen (1932), known as Goldstein's third approximation [Goldstein (1948)] was used. The determination of the "effective geometry" was done using a camber line, derived from the calculated induced velocities of the lifting surface calculation. This can be done because the problem is linearized. The calculated induced camberline and the geometrical thickness distribution were combined in the NACA-manner to obtain the geometry of the effective profile. The pressure distribution on the propeller section was then calculated using the induced angle of attack from the lifting surface calculation. The lift coefficient, which is found from the lifting surface calculation, is maintained using the method of Pinkerton (1934). This is necessary because the potential flow lift coefficient of the effective profile is slightly lower at inner radii, where the sections become thicker. The differences are of the order of 0.02. In Figures 9 and 10 the calculated pressure distributions at the suction side are given for propellers A, B, and C.

4. RESULTS OF PAINT TESTS

In Figure 11 the paint patterns are shown for propellers A, B, and C at 30% slip and at Reynolds numbers typical for testing behind 12 meter models.

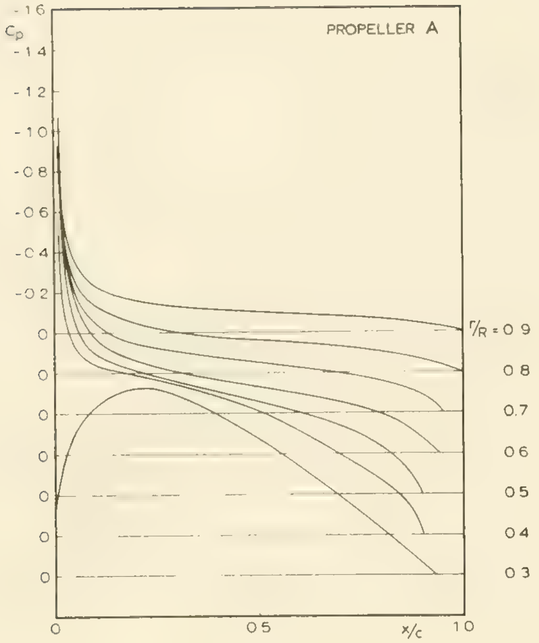

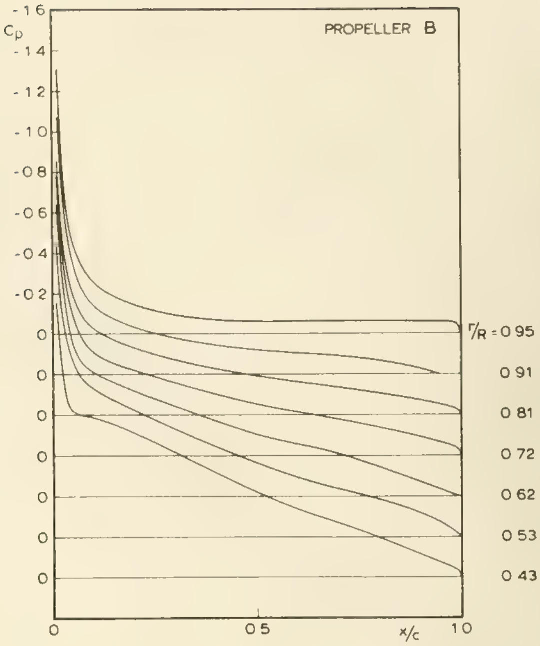

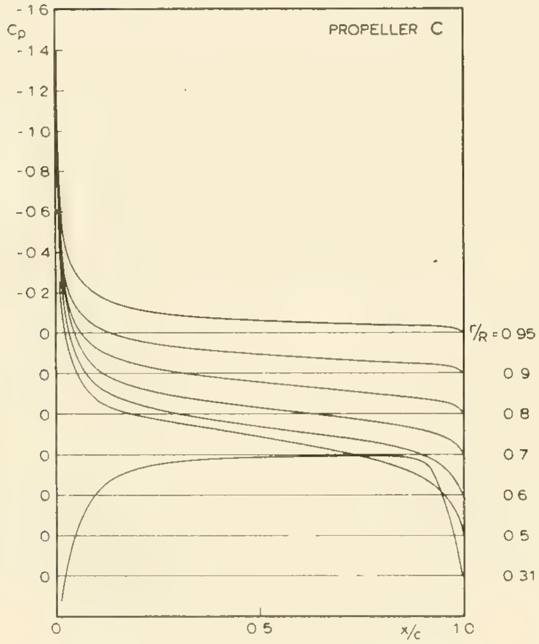

FIGURE 10. Calculated pressure distribution on the suction side at 60% slip.

These pictures were taken with UV-illumination. At the leading edge the paint is removed, due to high local velocities. The streaks are formed gradually, either in a nearly tangential direction (the turbulent region) or pointed outwards (the laminar region). The transition from laminar to turbulent boundary layer flow is shown by a change in direction of the streaks.

Laminar boundary layer flow occurs in all cases near the leading edge. Transition in chordwise direction to turbulent boundary layer flow occurs gradually, but a transition region can be distinguished and at the trailing edge the boundary layer is turbulent. When the paint streaks are nearly in the radial direction the flow is separated. At inner radii the boundary layer if often close to separation. Laminar separation was clearly present on propeller D, as is shown in Figure 12. At 60% slip the radius where laminar separation is replaced by natural transition can be seen by the sharp corner in the paint streaks.

At the suction side near the tip a turbulent region exists immediately from the leading edge (Figure 11). An increase in propeller loading showed a radial increase of the turbulent region at outer radii, as illustrated in Figure 12. The change in radial direction of the laminar region near the leading edge to the turbulent region at outer radii on the suction side is abrupt and nearly discontinuous, as sketched in detail in Figure 13. The laminar region is cut off and the region of natural transition at inner radii does not reach the leading edge. We will designate the radius where this discontinuity occurs, the critical

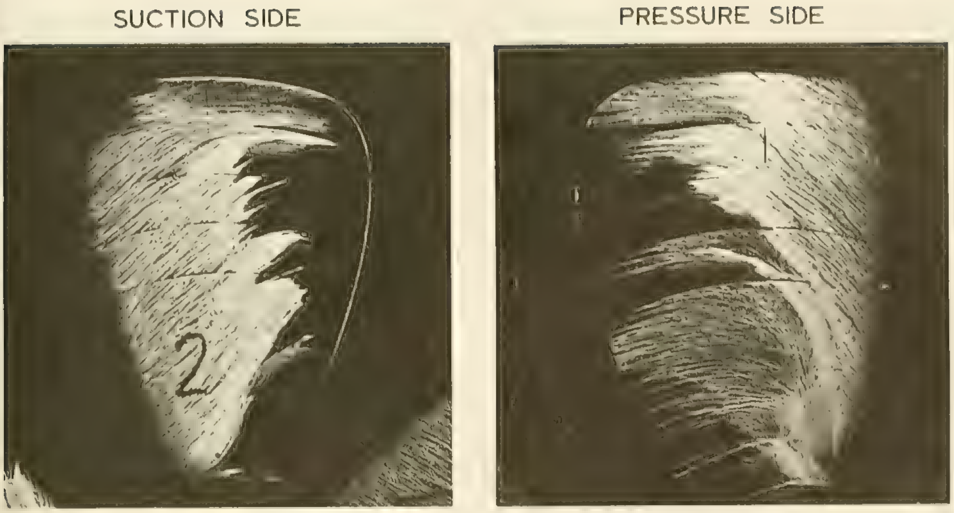

PROPELLER A , $Re_N = 0.73 \times 10^6$

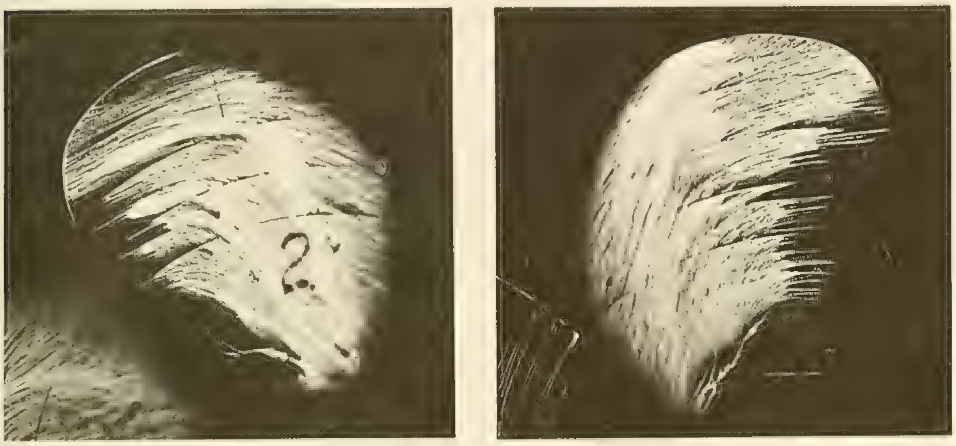

PROPELLER B , $Re_N = 0.51 \times 10^6$

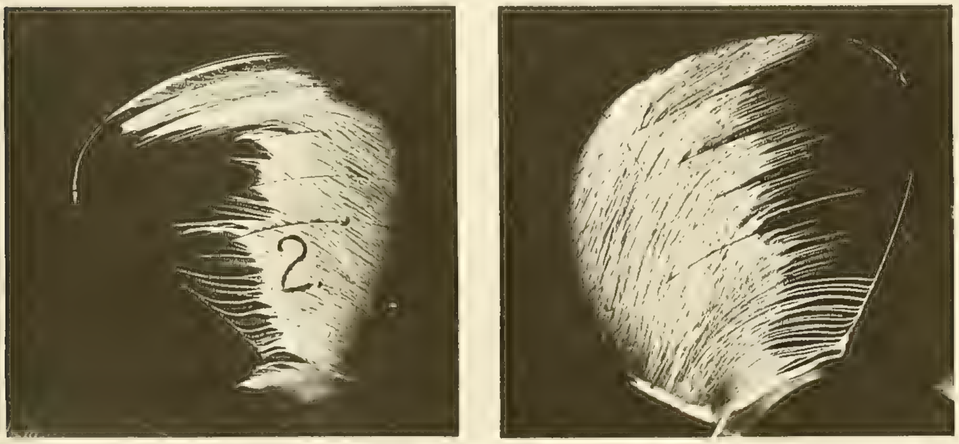

PROPELLER C , $Re_N = 0.66 \times 10^6$

FIGURE 11. Paint patterns at 30% slip.

radius of the propeller. Such a critical radius can also be observed from the paint pattern of Sasajima (1975) and of Meyne (1972). This critical radius turned out to be very important for cavitation inception and could be discerned in all cases. No photographs are shown because of the bad contrast of the monochrome prints. (Figure 16).

On propeller B at 60% slip a separation bubble at the leading edge was observed, connected with a stagnation region near the tip on the suction side, which indicated the position of the tip vortex. In the direction of the hub the laminar separation bubble extended exactly until the critical radius. This lead us to the hypothesis that laminar separation near the leading edge was the cause of the discontinuous character of the paint streaks at the critical radius. To verify the hypothesis of laminar separation at the critical radius, boundary layer

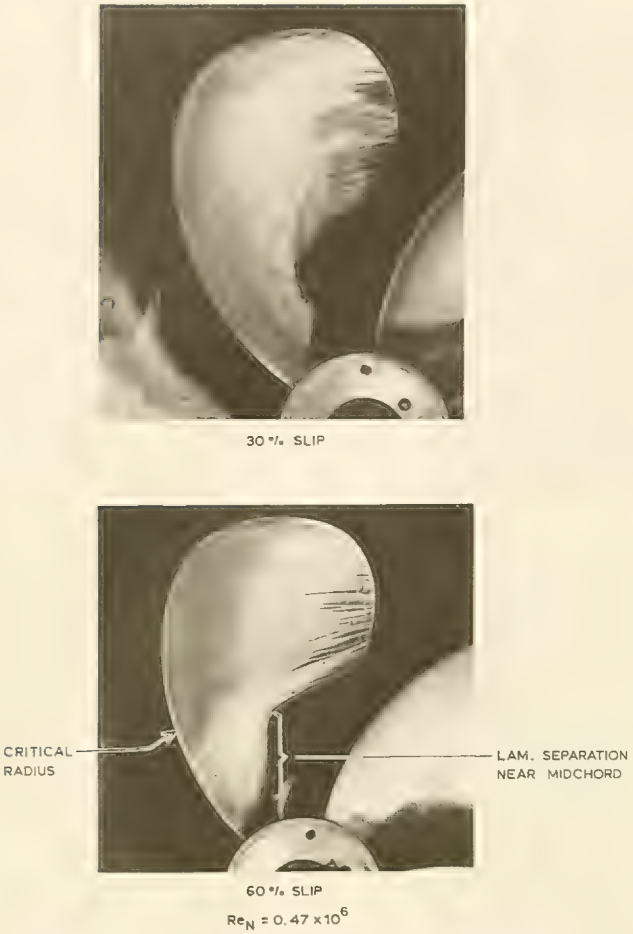

FIGURE 12. Variation of the critical radius with propeller loading on propeller D (suction side).

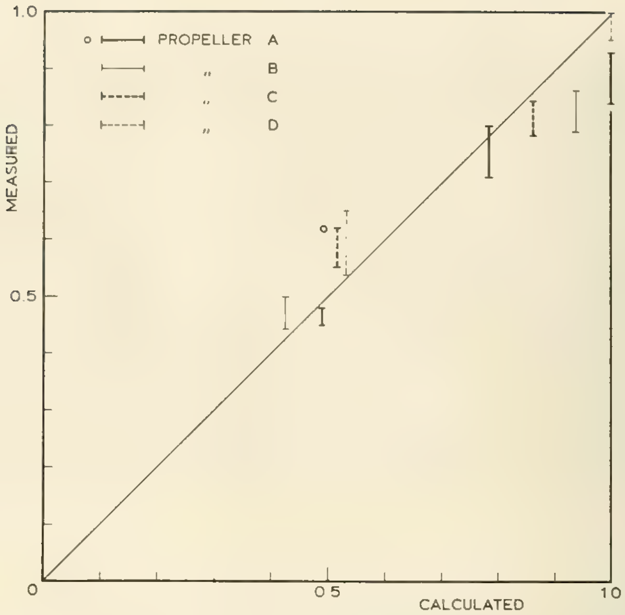

FIGURE 14. Correlation of calculated radius of laminar separation and measured critical radius.

calculations were made, using the pressure distributions as calculated in Section 3. The laminar boundary layer was calculated with Thwaites' method [Thwaites (1949)]. Laminar separation was predicted using Curle and Skan's (1957) criterion. This calculation method does not take into account the delaying effect of rotation on laminar separation, but since laminar separation occurs very close to the leading edge the effect of rotation on the development of the boundary layer will still be small. The correlation between the calculated and the observed critical radius is given in Figure 14, and this correlation is quite good. The critical radius at all conditions and the variation of the critical radius between the propeller blades can also be found from Figure 14. As can be seen, the variation of the critical radius per blade in one condition can be considerable, showing the sensitivity of laminar separation to the manufacturing accuracy. The critical radius per blade, however, reproduced remarkably.

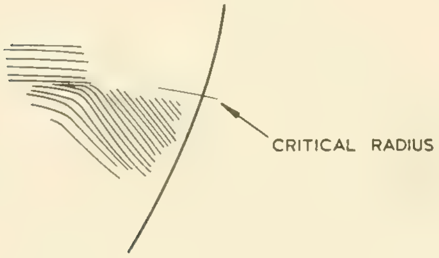

FIGURE 13. Discontinuity of paint streaks at the critical radius.

The position of laminar separation is independent of the Reynolds number. So another check on the hypothesis of laminar separation at the critical radius is the independence of the critical radius from the Reynolds number. Propellers A and C were therefore tested with about twice the original number of revolutions. Propeller A was also investigated in a cavitation tunnel: the highest Reynolds number in the towing tank was repeated and another condition with about three times the original Reynolds number was tested. The paint tests in the cavitation tunnel were less accurate since turbulent spots occurred, which caused a wedge shaped tangential streak through the laminar pattern. This was strongest at the higher Reynolds numbers.

Figure 15 gives the critical radius as a function of Reynolds number for the blades available for comparison. There is a slight trend for the critical radius to decrease with increasing Reynolds number, but this is only very slight. The critical radius is strongly dependent on the propeller loading and a slight increase of the propeller loading with increasing Reynolds number might cause the decrease of the critical radius. For comparison the observations of Sasajima are also drawn in Figure 15. He observes a larger shift of the critical radius with Reynolds number, but his results from the tank show no variation with Reynolds number. The variations found in the cavitation tunnel might well be caused by variations in propeller loading or by wall effects. The conclusion seems justified that the critical radius is independent of the Reynolds number, at least until natural transition occurs close to the minimum pressure point. In that case a critical radius no longer exists.

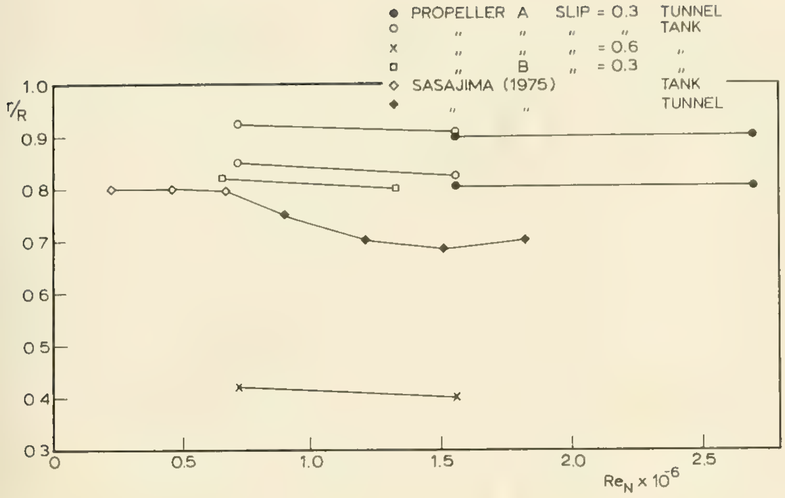

FIGURE 15. Effect of Reynolds number on the critical radius.

It is important to note that in Figure 12 at 60% slip the radius where laminar separation occurs near midchord is not the critical radius, although in this case the difference between both is small. With increasing Reynolds number, however, the region of laminar separation near midchord will decrease, while the critical radius will remain unchanged. The distance between the sharp corner in the paint streaks of Figure 12b and the critical radius will therefore increase with increasing Reynolds number.

An increase of Reynolds number causes a shift in the chordwise position of the transition region at radii inside the critical radius, as is illustrated in Figure 16. This was also observed on the pressure side. In Figure 17 the chordwise position of the transition region is given at r/R=0.7 as a function of the sectional Reynolds number, which is related to the entrance velocity and the chordlength of the propeller section at that radius. The transition region is averaged in Figure 17. This makes clear that a complete turbulent boundary layer at a radius of 0.7R requires sectional Reynolds numbers of about 5×10^6. At the suction side, turbulent flow at this radius also occurs when the loading is increased, i.e. the critical radius is smaller than 0.7.

Empirical criteria for transition of the boundary layer to turbulence have been given as a relation between the Reynolds numbers based on the length from the stagnation point, Re_x, and based on the momentum thickness, Re_θ. [Michel (1951), Smith (1956)]. Van Oossanen used the Smith line

$$Re_{\theta_{trans}} = 1.174\ Re_x^{\ 0.46} \qquad (10)$$

as a criterion. When the relation between Re_θ and Re_x over the chord was calculated, both on the suction side and on the pressure side, this relation was so closely parallel to the criterion of Eq. 10 that no reliable intersection was possible. When there is a strong negative pressure peak at the leading edge the relation between Re_θ and Re_x is such that Eq. 10 always predicts transition very close to the leading edge. When the pressure distribution was nearly shockfree, the prediction was erroneous.

To calculate the transition region, calculation

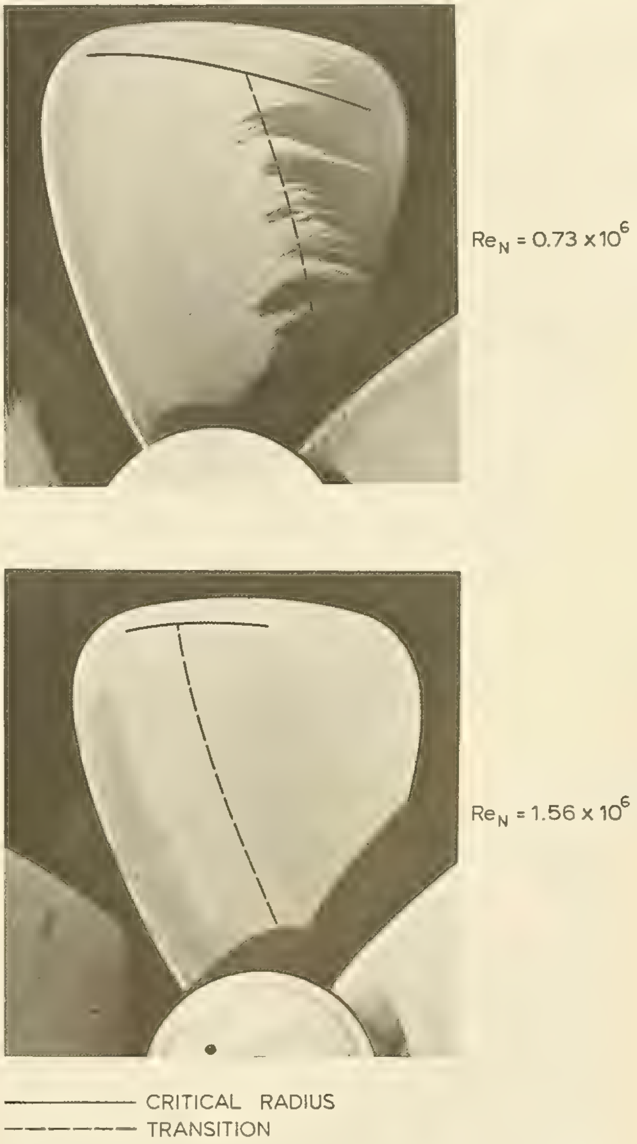

FIGURE 16. Effect of Reynolds number on the transition region. Propeller A at 30% slip.

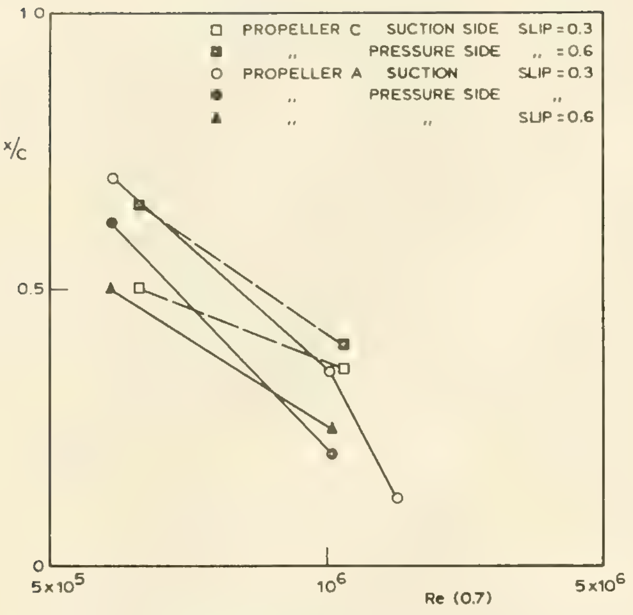

FIGURE 17. Chordwise position of natural transition inside the critical radius.

of the stability of the laminar boundary layer might give better results [Smith and Camberoni (1956)]. Since transition occurs far from the leading edge, the effect of rotation can be important. When the calculation scheme of Arakeri (1973) is used it is possible to take the effect of rotation into account using Meyne's (1972) results. This was beyond the scope of this paper.

5. CAVITATION OBSERVATIONS

The cavitation on propellers A, B, and C is sketched in Figure 18 for both slip ratio's. The cavitation index at the blade tip in top position, σ_{NT} (Eq. 2) was always 1.5. The Reynolds numbers Re_N, were about 5×10^5. At 30% slip the condition is not far from inception and a cavitating tip vortex is present in nearly all cases. However, in some cases at low Reynolds numbers, propellers A and C were observed without any cavitation. This was not due to intermittent cavitation during one test, but occurred when tests were repeated with time-intervals of some weeks. During one test the observations were quite consistent, indicating that the variations are caused by factors which are still not under enough control, e.g., air content, nuclei content, turbulence.

Correlation with Paint Test

Of interest is the correlation of the radial extent of the cavity with the observed critical radius, found from the paint test. In Figure 18 the observed position of the critical radius is indicated, as well as the calculated ideal inception radius, which is the radius where the minimum pressure on the blades equals the vapor pressure. Also indicated is the cavitation, observed when the leading edge was roughened, as will be discussed in the next section.

On propeller A and on propeller B at 30% slip the radial extent of the cavitation is clearly restricted by the observed critical radius. Sometimes there is a small difference between the critical radius and the inception radius, which is probably caused by a change in the pressure distribution by the cavitation.

The calculated ideal inception radii at 60% slip should be considered with caustion. They are close to the hub and the influence of the hub is not taken into account in the calculations. For example on propeller B at 60% slip the inception radius is larger than calculated. In that case the critical radius is smaller than the inception radius and does not cause any viscous effects on cavitation. The distance between the ideal inception radius and the critical radius on propeller C is small, so the scale effects due to the critical radius will be small too.

We can conclude that no cavitation occurred in regions of laminar flow near the leading edge. The radial extent of cavitation can be seriously restricted by the critical radius. Since the critical radius is connected with laminar separation this means that variation of the Reynolds number does not remove this restriction until very high Reynolds numbers. From Figure 17 the sectional Reynolds number at r/R=0.7 has to exceed 5×10^6, whereas a value of 3×10^5 is mostly considered enough to avoid Reynolds effects on thrust and torque.

Variation of Reynolds Number

Propellers A and C were tested at a higher Reynolds number in the towing tank, while propeller A was

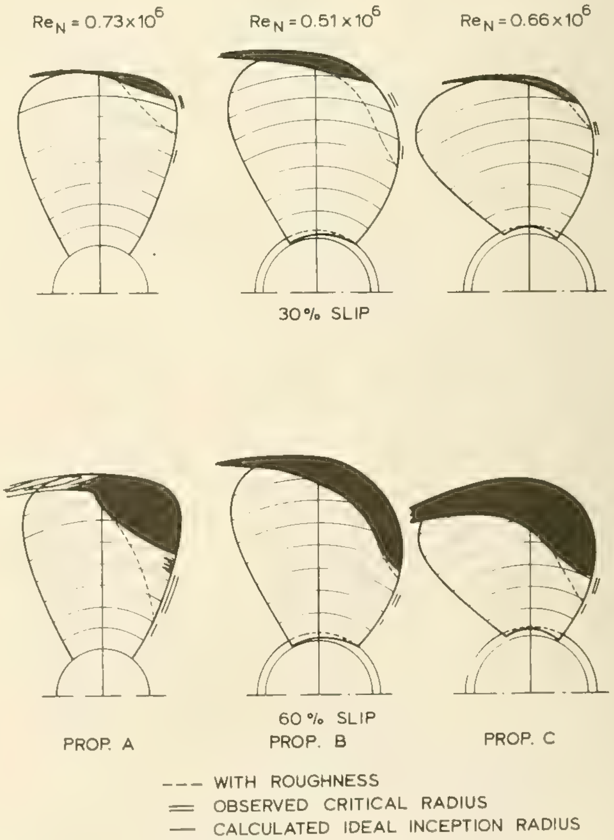

FIGURE 18. Cavitation observations at $\sigma_{NT} = 1.5$.

also tested in the cavitation tunnel at two Reynolds numbers. No differences in cavitation pattern due to variation of the Reynolds number were observed in the towing tank. Notably the radial extent of the cavity was unchanged, which confirmed that the critical radius restricted cavitation inception independent of the Reynolds number. The results of propeller A at 30% slip are shown in Figure 19. In this figure the observations of the tests in the cavitation tunnel are also shown. These show some differences requiring further attention. The cavity in the cavitation tunnel at $Re_N=1.56\times10^6$ is somewhat larger than in the towing tank, but the difference is not significant and is probably caused by a slight difference in propeller loading. (The tunnel condition was taken at a K_T-value derived from the open water measurements. The flow velocity was not measured). Remarkable are the spots of cavitation at $Re_N=1.56\times10^6$ which increased in number when time increased!

At $Re_N=2.72\times10^6$ there is a sheet outside r/R=0.9, the same as at $Re_N=1.56\times10^6$. The spots however, have increased in number and they coalesce at some distance from the leading edge, forming a cavity until about r/R=0.8 with isolated spots until r/R=0.7, which is the ideal inception radius. The increase of the number of spots with time was not observed in this situation, but the time to reach a stable condition was much longer than at lower Reynolds numbers.

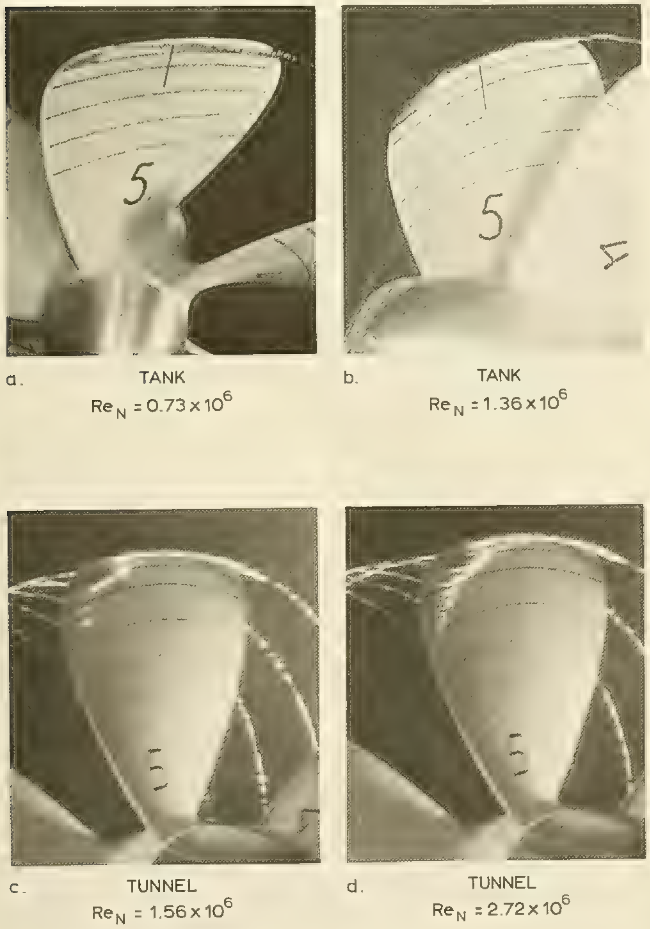

a. TANK $Re_N = 0.73\times10^6$ b. TANK $Re_N = 1.36\times10^6$

c. TUNNEL $Re_N = 1.56\times10^6$ d. TUNNEL $Re_N = 2.72\times10^6$

FIGURE 19. Effect of Reynolds number on propeller A at 30% slip with $\sigma_{NT} = 1.5$.

The occurrence of cavitating spots in the laminar region agrees with the observation of turbulent streaks in the paint tests in the cavitation tunnel at higher Reynolds numbers. Therefore, it is conjectured that, in the tunnel, tiny particles were deposited on the leading edge of the propeller, thus creating turbulent streaks. The number of these streaks may increase with time, and these turbulent streaks cause spots of cavitation.

Another possible effect is that the propeller is not hydrodynamically smooth. With increasing Reynolds number the boundary layer becomes thinner and more sensitive to local roughness. In this case the streaks would always be in the same position. Not enough observations were made to verify this, but the strongly reduced occurrence of turbulent spots in the towing tank points to the flow as the origin of the disturbances. The occurrence of these streaks was also apparent in the tank when the pressure was drastically lowered, as is shown in Figure 20. It is of course very important to recognize these cavitating spots since they indicate a region of laminar boundary layer flow and a possible restriction of the radial extent and the volume of the cavity.

The effect of Reynolds number on cavitation in the region from the critical radius to the tip is small. In nearly all cases cavitation took place in this region at low Reynolds numbers. In some cases no cavitation was present in this region at a low Reynolds number, as shown in Figure 21. A paint test is included to show the critical radius. At a higher Reynolds number, cavitation was present until the critical radius. The ideal inception radius in this case is at r/R=0.7. A similar effect was sometimes seen at propeller C and can be explained by the fact that the reattachment region, where inception is assumed to occur, shifts to lower pressure regions with increasing Reynolds number. Calculations of such an effect are given by Huang and Peterson (1977). It is not certain, however, that the Reynolds number is the only variable since application of electrolysis also caused inception at low Reynolds numbers. Apparently the nuclei distribution becomes more critical with lower Reynolds numbers.

Observations with $\sigma_{NT} = 0.5$

Laminar boundary layer flow was seen to prevent sheet cavitation at the leading edge. To see if there is some threshold for inception the cavitation index was drastically lowered to $\sigma_{TN}=0.5$. This was only possible at high Reynolds numbers. In Figure 22 propeller A is shown at 30% slip, a condition comparable with Figure 19b, but at a low cavitation index. It is clear that even in this extreme condition no cavitation occurred in the laminar flow region.

A comparison of the local cavitation index with the pressure coefficients as given in Figure 9 shows that, e.g., at r/R=0.8, the minimum pressure coefficient is 0.54 while the cavitation index at that radius is 0.08 to 0.012, depending on the position of the blade. The cavitation index at this radius is lower than the pressure coefficient over most of the propeller section. When turbulent spots appeared inside the critical radius these spots were supercavitating, as is also shown in Figure 20.

Bubble cavitation can be expected near midchord

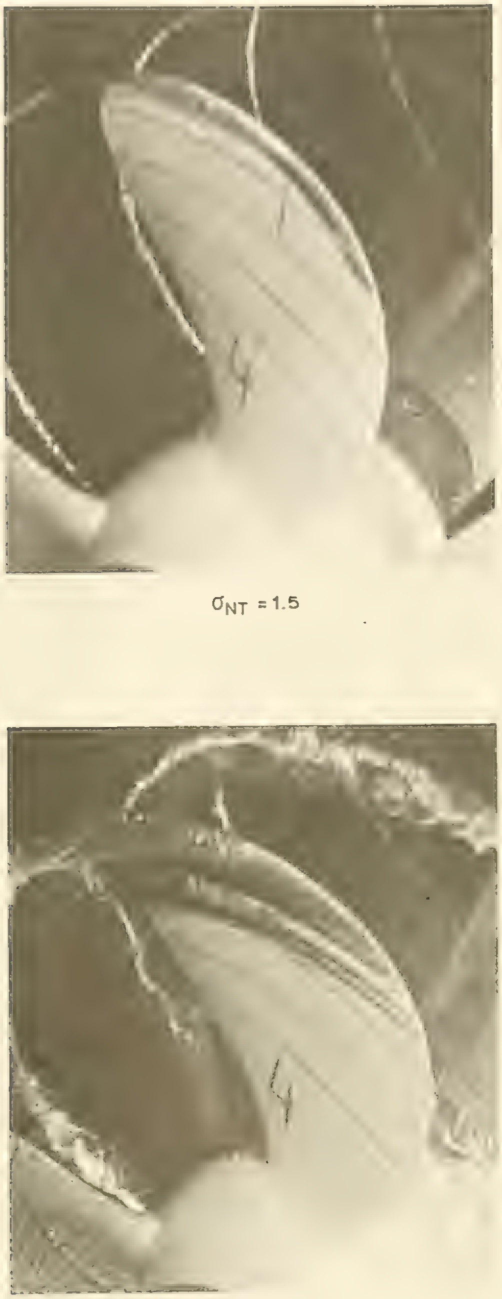

$\sigma_{NT} = 1.5$

$\sigma_{NT} = 0.5$

$Re_N = 1.29 \times 10^6$

FIGURE 20. Turbulent streaks inside the critical radius at higher Reynolds numbers. Propeller C at 30% slip.

at inner radii, where the minimum pressure exists near midchord. At propeller A at r/R=0.6 the cavitation index is between 0.13 and 0.20, at σ_{NT}=0.5, while the minimum pressure coefficient is 0.26. As can be seen in Figure 22 no bubble cavitation occurred. The cavitating spot at midchord is a dent in the propeller surface and illustrates the low local pressure. Similar observations were made with propeller C at σ_{NT}=0.5. No threshold for sheet cavitation could be established and no bubble cavitation occurred near midchord at inner radii. Both phenomena are suspected to be caused by a lack of nuclei. So electrolysis was applied, as will be discussed in the next section.

6. VARIATION OF NUCLEI CONTENT BY ELECTROLYSIS

Some measurements in the NSMB Depressurized Towing Tank with the scattered light method indicated that the nuclei content of this tank was nearly independent of the pressure. The density of small nuclei (17 μm) was 1.2×10^7 m^{-3} and that of the largest available nuclei (45 μm) was 1.2×10^5 m^{-3}. [This corresponds with nuclei number densities, as defined by Gates (1977) of 9×10^{11} and 2.4×10^{10} respectively]. A description of the measuring technique which was used is given by Keller (1974). A comparison with similar measurements in the NSMB large cavitation tunnel [Arndt and Keller (1976)] shows that the nuclei content is lower than that in the cavitation tunnel at the lowest air content by a factor of about 5. The nuclei content in the cavitation tunnel was very much dependent on the total air content of the water, showing variations of a factor of 10 between high (12.5 ppm) and low (6.3 ppm) air content. This dependency was absent

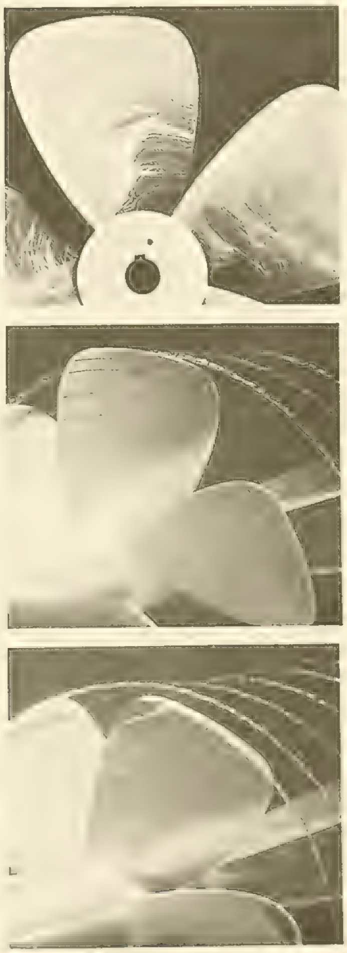

PAINT OBSERVATION

$Re_N = 0.73 \times 10^6$

CAVITATION OBSERVATION

$Re_N = 0.73 \times 10^6$

$\sigma_{NT} = 1.71$

CAVITATION OBSERVATION

$Re_N = 1.56 \times 10^6$

$\sigma_{NT} = 2.09$

FIGURE 21. Effect of Reynolds number on cavitation inception outside the critical radius. Propeller A at 40% slip.

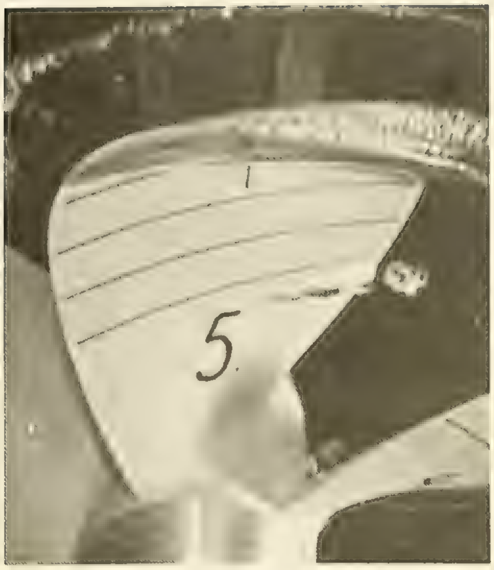

$Re_N = 1.56 \times 10^6$

$\sigma_{NT} = 0.5$

FIGURE 22. Cavitation at very low cavitation index. Propeller A at 30% slip.

in the Depressurized Towing Tank. So when cavitation observations in the tank are compared with observations in the tunnel, we can assume that the nuclei content in the tunnel is always larger than that in the tank by at least a factor of 10. Perhaps most important, however, is that in the tank nuclei greater than 60 μm are absent.

The nuclei content in the tank has been varied using electrolysis, as described in Section 2. The nuclei size distribution from the wires of 0.2 mm diameter has not been measured. Exploratory photographic observations showed that the bubbles coming from the wires are in the range of 50 to 100 μm under comparable conditions.

The influence of the wires on the propeller boundary layer was checked by a paint test on propeller A at 30% slip. The paint patterns with and without wires were identical. So we assume that the turbulence, coming from the wires, did not affect the propeller boundary layer. This assumption should be treated with some caution, because Gates (1977) showed widely different effects of flow turbulence on two headforms, both with laminar separation.

Gates also showed that large amounts of nuclei can influence the boundary layer. Notably the laminar separation bubble on his hemispherical headform was removed. To see if this was also the case in our tests a paint test was carried out with propeller A at 30% slip. The cavitation index was just above inception, so cavitation was avoided. To correct for the higher pressure in this condition the current through the electrolysis wires was increased to produce the same volume of gas per second as in the cavitating condition. No effect on the paint pattern could be observed. Especially the critical radius remained unchanged. So we assume that the nuclei had no disturbing effect on the boundary layer. As to the effect of electrolysis on the cavitation pattern, three regions on the suction side of the propeller blades can be distinguished:

a. At radii larger than the critical radius, where, at least near the critical radius, laminar separation takes place.
b. At radii smaller than the critical radius having a negative pressure peak at the leading edge.
c. At radii smaller than the critical radius having a pressure distribution which is nearly shockfree.

At radii larger than the critical radius no effect of electrolysis on sheet cavitation could be seen in those cases where it was present. In the few cases where no cavitation was present in this region application of electrolysis restored inception. An example of absence of cavitation, apparently due to a lack of nuclei, is shown in Figure 23, where blade 3 of propeller C at 60% slip showed considerable cavitation , while blade 4 was free of sheet cavitation during the whole run (9 photographs in 3 different blade positions).

Absence of cavitation in regions of laminar separation, however, is an exception in the steady case. A possible explanation is that the water is never completely without nuclei and sooner or later a nucleus will expand in the separated region and cause inception. After inception cavitation seems to be more or less self-sustaining. This agrees with the observation of Gates (1977) that inception on a hemispherical body appeared to be insensitive to freestream nuclei content as long as laminar separation took place. The situation is different, however, in the unsteady case, when a blade passes a wake peak. Only a very restricted time is available for inception at every propeller revolution and a high frequency of encounters with nuclei is necessary to obtain inception at every revolution. This can explain why the "stabilizing" effect of electrolysis is more pronounced behind a ship model than in the open-water tests of the current test program.

At higher Reynolds numbers absence of cavitation in regions of laminar separation was not observed. Apart from viscous effects this can also be caused by an increase in encounter frequency of nuclei, since an increase in Reynolds number of the same propeller models always implied an increase in propeller revolutions.

At radii smaller than the critical radius electrolysis surprisingly had no effect at all. No cavitation was initiated in the minimum pressure peak, although the pressure was far below the vapor pressure. Even the cavitation pattern at very low cavitation index, as shown in Figure 22, was unchanged. It is not clear yet why the nuclei do not expand. Possibly nuclei do not reach the minimum pressure region due to a screening effect as described by Johnson and Hsieh (1966). In a situation as shown in Figure 23, however, nuclei promoted cavitation inception and were not pushed away. This is only possible when the critical size of nuclei in a laminar flow region is different from the critical size in the reattachment region of a laminar separation bubble.

The third region which has to be considered is the region where the pressure distribution is nearly shockfree and has its minimum pressure near midchord. When the pressure is low in these regions bubble cavitation can be expected. A situation

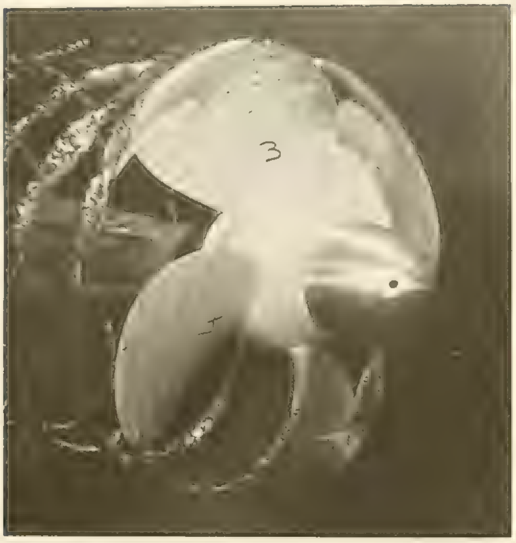

$Re_N = 0.66 \times 10^6$

$\sigma_{NT} = 1.5$

FIGURE 23. Inconsistency of cavitation inception outside the critical radius at low nuclei content. Propeller C at 60% slip.

like this is shown in Figure 22, but none or only a few transient bubbles were seen.

Electrolysis sometimes restores bubble cavitation in this region, but in many cases it does not. This inconsistency could even be found on the same propeller in virtually the same condition when tested repeatedly with long time intervals. In one case an abundant amount of large bubbles was visible without causing bubble cavitation, while an amount of invisibly small nuclei did cause bubble cavitation in the same condition. In Figure 19d it was seen that in the cavitation tunnel cavitating spots at the leading edge were formed at high Reynolds numbers. When the cavitation index was lowered, bubble cavitation occurred in the wake of these spots, while at radii in between of the spots no bubble cavitation was observed. When the cavitation index was lowered to about $\sigma_{NT}=0.5$ the spots were connected with intense bubble cavitation, as shown in Figure 24. It can be seen that the bubble cavitation is related to the spots at the leading edge. Apparently the stream nuclei, which were abundant in the tunnel at this low cavitation index, did not create bubble cavitation, while nuclei, generated by a cavitating spot created intense bubble cavitation. The possible relation between pressure distribution, boundary layer, and nuclei distribution must be studied to analyse these phenomena.

7. VARIATION OF THE BOUNDARY LAYER BY ROUGHNESS AT THE LEADING EDGE

In all tests, at least one of the propeller blades was roughened at the leading edge, as described in Section 2. With paint tests, it was verified that the laminar regions were changed into turbulent ones. Although the grain size of 30 µm and 60 µm is larger in comparison with the boundary layer thickness, there was a lower limit in the region which had to be covered with carborundum to cause turbulent flow. For thin sections an evenly distributed layer of carborundum of say 0.5% of the chord was necessary to trip the boundary layer. There was little difference between the effect of 30 µm and 60 µm carborundum. At thick sections to be effective roughness was necessary until about the minimum pressure point. At the pressure side the boundary layer remained increasingly laminar when the loading increased. At 70% slip the the pressure side of the roughened blades was completely laminar near the leading edge.

Attention, given until now to the propeller boundary layer, was focussed on the effect on torque and thrust. Calculation methods to account for Reynolds effects on open-water characteristics are based on the assumption of turbulent boundary layer flow on the propeller model [Lerbs (1951)] or on an empirical value in between fully turbulent and fully laminar, as compiled by Lindgren (1972). From the paint tests however, we saw that the turbulent region at the suction side strongly depends on the propeller loading. The difference between the dimensionless thrust and torque coefficients, therefore, will not only depend on the Reynolds number, but also on the propeller loading.

In order to eliminate the dependency of thrust and torque coefficients on the Reynolds number, turbulence stimulators have been used. Sasajima (1975) used studs, Yasaki and Tsuda (1972) and Tsuda et al. (1977) used trip wires at some distance from the leading edge. Apart from changing the boundary layer, these devices also have considerable resistance of their own. Effects both on thrust and torque are difficult to separate. The influence of roughness at the leading edge on thrust and

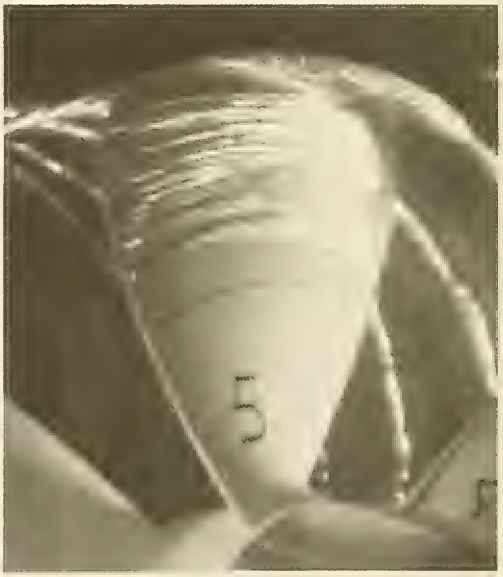

$Re_N = 2.72 \times 10^6$

$\sigma_{NT} = 0.5$

FIGURE 24. Bubble cavitation in the wake of spots at the leading edge. Propeller A at 30% slip in the cavitation tunnel.

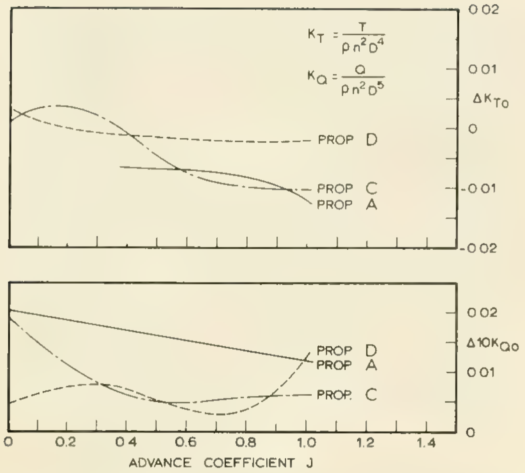

FIGURE 25. Effect of leading-edge roughness on torque and thrust coefficients.

torque coefficients is given in Figure 25. These measurements were carried out with a special dynamometer inside the propeller hub to assure that the differences were not insignificant due to inaccuracy of the measurements. The accuracy in Figure 25 is still only about ± 0.005.

Using Lindgren (1972), the value of ΔK_Q between fully turbulent and fully laminar boundary layer flow on the propeller is 0.0035. The actual influence of the roughness at the leading edge is smaller, so that we can conclude that the resistance due to the carborundum was very small. An analysis of the effect of roughness at the leading edge on the performance of the propeller is beyond the scope of this paper.

The effect of leading edge roughness on cavitation is sketched in Figure 18. The radial extent of the cavitation is increased in those cases where the critical radius was a limit for cavitation. The risk of scale effects on cavitation inception due to laminar boundary layer flow is largest at low propeller loadings, when the risk of laminar separation is smallest. But it still can be considerable at high loadings, as is shown in Figure 26, where propeller A is shown with and without roughness at 60% slip.

Application of roughness at the leading edge is expected to cause two problems. First the geometry of the leading edge may be altered, having a profound influence on the minimum pressure peak. Secondly, the local inception index may be changed due to roughness. The effect on the shape of the leading edge can only be minimized by using small grain sizes. However, to obtain a turbulent boundary layer the current 30 μm grainsize was about the minimum and no differences in cavitation behavior were observed between blades roughened with 30 μm and 60 μm roughness. The effect of surface irregularities on cavitation inception can be large, as was shown by Holl (1965). Moreover, Holl points out that "the most disastrous place to locate surface roughness is at the point of minimum pressure of a parent body". This is exactly what cannot be avoided at the rather sharp leading edge of thin propeller sections. The situation very close to the leading edge, however, is different from the situation of an isolated roughness at a surface, as studied, e.g., by Holl (1965) and Benson (1966). Application of their results is also difficult, because the ratio between grainsize and boundary layer thickness without roughness, which is required for the calculations, varies rapidly in this region. The boundary layer thickness on the smooth blades near the end of the roughness was about 30 μm in all conditions, when no separation took place. At the position of laminar separation the boundary layer thickness was only a few μm. Thus, the ratio of grainsize to boundary layer thickness easily varies by a factor of ten. Application of inception calculations on distributed roughness [e.g., Arndt and Ippen (1968)] seems more appropriate, but this is difficult, because a friction coefficient is required for the calculations, as well as an "equivalent sandroughness". Both are strongly interrelated [Bohn (1972)] and especially near the leading edge these quantities are difficult to estimate.

The roughness elements do form a massive disturbance of the boundary layer and an increase in the

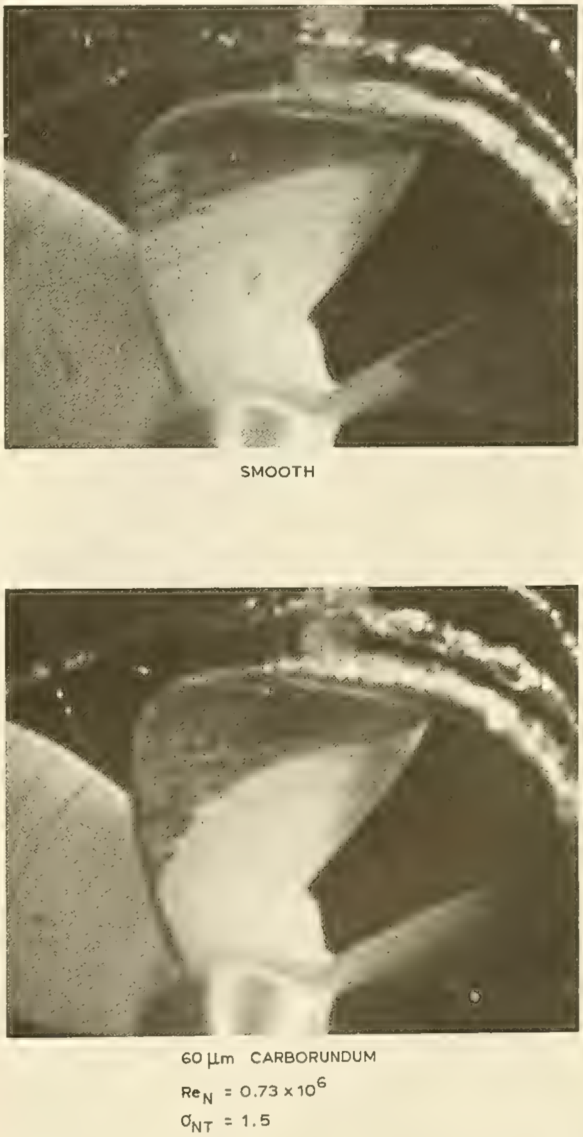

FIGURE 26. Effect of leading edge roughness on cavitation. Propeller A at 60% slip.

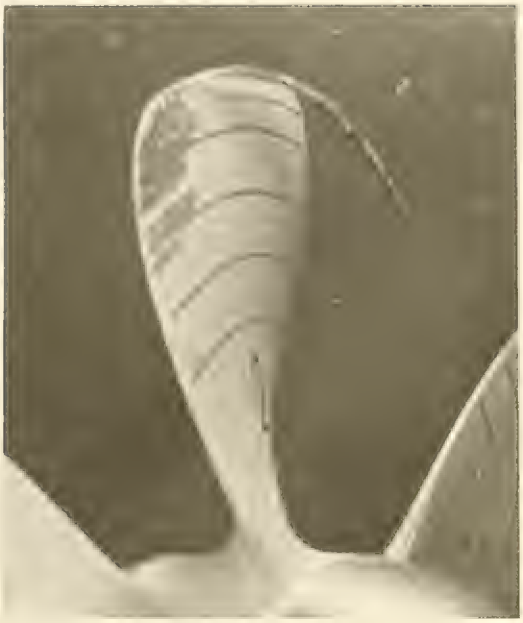

$Re_N = 0.73 \times 10^6$

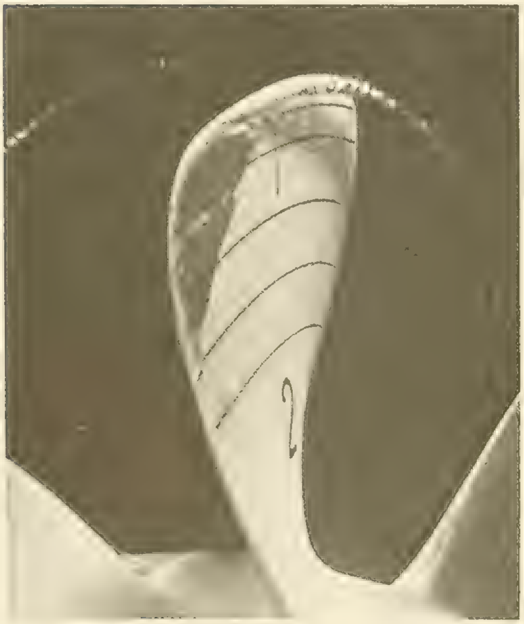

$Re_N = 1.36 \times 10^6$

60 μm CARBORUNDUM

$\sigma_{NT} = 1.5$

FIGURE 27. Effect of Reynolds number on spot cavitation at roughness elements. Propeller A at 30% slip.

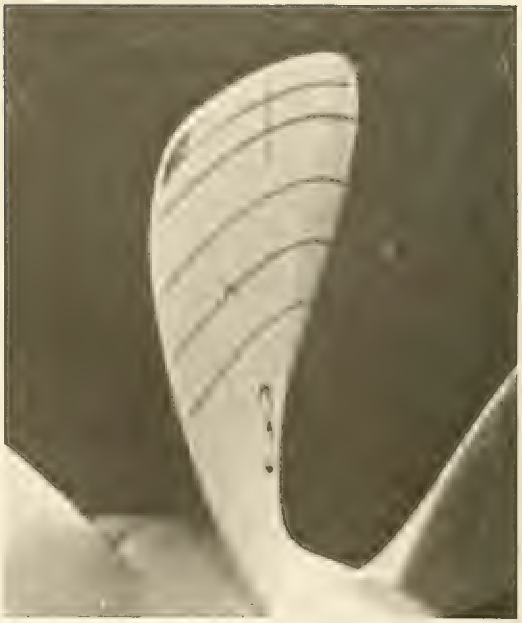

SMOOTH

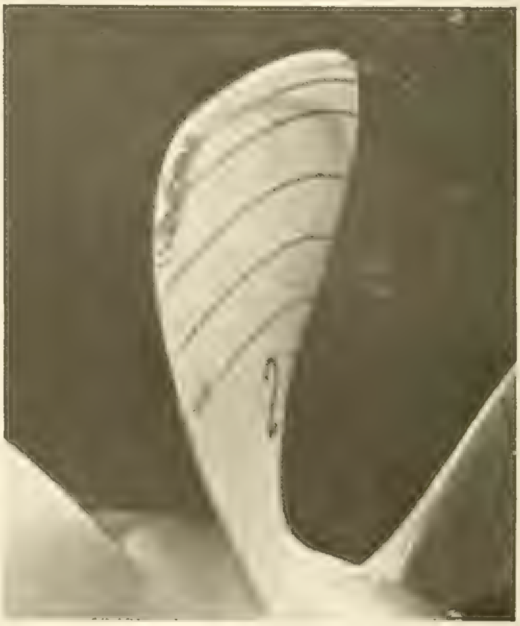

60 μm CARBORUNDUM

$Re_N = 0.73 \times 10^6$

$\sigma_{NT} = 2.5$

FIGURE 28. Effect of roughness near inception. Propeller A at 30% slip.

cavitation inception pressure to a value greater than the vapor pressure is possible, which would create additional scale effects on cavitation inception. To estimate the importance of a possible increase in cavitation inception index, the ideal inception radius is also given in Figure 18. This is the radius where cavitation should start when the calculations of the pressure distribution were correct and when no scale effects would occur. As can be seen, no cavitation occurs inside the ideal inception radius, indicating that the pressure at inception with roughness is not far from the vapor pressure. Assuming that full scale inception takes place near the minimum pressure point at the vapor pressure [$\sigma_i = -C_p$ (minimum)], application of sand-roughness can effectively simulate this situation at much lower Reynolds numbers. Further experiments are necessary to find out the precise effect of leading edge roughness on the flow and on the boundary layer. Holographic methods, as applied by van der Meulen (1976) in studying the effects of polymers can be attractive for these experiments.

When the effect of roughness at the leading edge is studied three regions on the model propeller can again be distinguished. At radii larger than the critical radius, where inception on the smooth blades takes place due to laminar separation, the cavitation behavior is unaffected by roughness. Cavitation was always present on the roughened blades. It is unknown if the sensitivity to nuclei in the unsteady case increases, as is suspected on the smooth blade. Experiences with several other propellers behind a model indicate that this is not the case and that nuclei have very little effect when roughness is applied.

In the laminar region, at radii smaller than the critical radius, roughness at the leading edge has its major effect, as described above. In some cases, however, problems appeared in the form of streaky cavitation as shown in Figure 27a. When the pressure on the blade sections was constant, as was the case for propeller A at r/R=0.7 and for propeller C at r/R=0.8, both at 30% slip (Figure 9), and when the Reynolds number was low, cavitating streaks were formed behind the roughness elements. In Figure 27b the same blade in the same condition at a higher Reynolds number is shown. Here a smooth cavity is seen. The roughness elements apparently suffer from laminar separation at low Reynolds number and cavitation occurs in the separated regions behind the roughness. The length of the spots is strongly dependent on the cavitation index, as is shown in Figure 28b, where the same situation as in Figure 27a is shown at a somewhat higher cavitation index. The spots disappeared and the propeller is near inception. Figure 28 also shows that inception of the sheet at the leading edge is not far from the vapor pressure, because the ideal inception radius in this case was 0.78. When roughness was applied, electrolysis had no further effect at radii smaller than the critical radius.

In the region with shockfree pressure distribution, bubble cavitation was seen to be promoted in some cases by roughness at the leading edge. The influence of roughness, however, was inconsistent again in this region, as it was with electrolysis. When there was cavitation at the leading edge due to the roughness, again bubble cavitation appeared at midchord, as is illustrated in Figure 29, where nuclei generated by cavitation at the leading edge created bubble cavitation at midchord. The cavitation index at 0.7R in Figure 29 is 0.18 and the minimum pressure coefficient from Figure 9 is 0.20, so the situation with roughness seems to be the situation without scale effects on cavitation inception. Nuclei in the flow, however, did not create bubble cavitation.

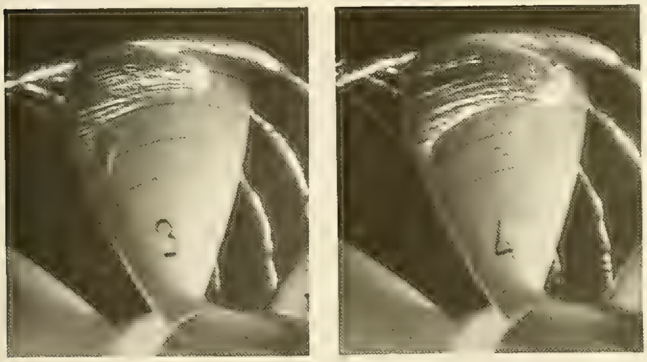
SMOOTH 60 µm CARBORUNDUM

$Re_N = 2.72 \times 10^6$

$\sigma_{NT} = 1.0$

FIGURE 29. Effect of leading edge roughness on bubble cavitation. Propeller A at 30% slip in the cavitation tunnel.

8. CONCLUSIONS

The results of the present test program can be summarized as follows:

1. On the suction side of a model propeller a critical radius can exist outside of which the boundary layer is turbulent from the leading edge. This critical radius is due to laminar separation, as was seen from some observations, from calculations (Figure 14), and from the Reynolds independency of the critical radius. (Figure 15).
2. To obtain natural transition near the leading edge on a propeller model, high Reynolds numbers ($Re_N > 2.5 \times 10^6$) are required.
3. The critical radius is a limit for the radial extent of sheet cavitation from the leading edge. An increase of nuclei by electrolysis is ineffective in the laminar region (Figure 22).
4. Outside the critical radius, cavitation is not inhibited (the inception pressure was not accurately determined), but a lack of nuclei at low Reynolds number seems to decrease the frequency of inception (Figure 23). In the unsteady case the nuclei content of the water is probably important in this region.
5. Roughness at the leading edge can effectively remove the critical radius, thus simulating a higher Reynolds number. Inception of cavitation at the roughness elements occurs close to the vapor pressure, which is assumed to be also the case on the prototype.
6. When the pressure distribution is very flat and the Reynolds number is low, the roughness elements can induce spots of cavitation. The length of these spots is strongly dependent on the cavitation index and is different from the cavity length at high Reynolds numbers. This is probably due to laminar separation at the roughness elements (Figure 27).
7. The inception of bubble cavitation near midchord at inner radii is not consistent. There seems to be an interaction between the pressure distribution, the nuclei distribution, and even the boundary layer. When cavitation at the leading edge is present, bubble cavitation occurs near midchord when the pressure is below or near the vapor pressure in that region.
8. Lifting line and lifting surface calculations can adequately predict the open-water characteristics of a propeller. For the calculation of the pressure distribution, however, lifting surface calculations are necessary. The correlation between calculations and the results of paint tests and cavitation observations is good.

From the previous investigations in uniform flow some tentative explanations can be given of the scale effects on cavitation as shown in Figures 1-3. The explanations can only be tentative since the unsteady pressure distribution on the propellers in the wake is not known. Propeller A in Figure 1 apparently had a critical radius at r/R=0.9 in this blade position, which was removed by roughness at the leading edge. Also, behind the model in some situations no cavitation at all occurred in the wake peak, which is expected to be due to a lack of nuclei (as seen in Figure 21).

The lack of nuclei is more apparent at propeller B. The critical radius is expected to be near the hub, but the low encounter frequency with nuclei of sufficient size makes cavitation inception more or less random. The irregular collapse of the cavity on propeller C is apparently due to a strong change in the pressure distribution, due to a sharp wake peak. The critical radius at the position of Figure 3 is near r/R=0.9 but the cavity at inner radii is still collapsing. This phenomenon could also be seen on high speed films, where the sheet cavity was seen to detach from the leading edge and collapse while moving with the flow. Some cavitating spots can be seen at r/R=0.8 on propeller C.

ACKNOWLEDGMENT

Part of this program was supported by the Dutch Ministry of Economic Affairs under the ICOSTE-program.

REFERENCES

Acosta, A. J., and B. R. Parkin (1975). Cavitation inception - a selective review. *J. of Ship Research, 19,* 193.

Albrecht, K., and O. Bjorheden (1975). Cavitation testing of propellers in a free surface tunnel utilizing micro air bubble control. *J. of Fluids Eng.,* 523.

Arakeri, V. H. (1973). Viscous effects in inception and development of cavitation on axi-symmetric bodies. *Thesis, Calif. Inst. of Techn. Report No. Eng. 183-1.*

Arakeri, V. H., and A. J. Acosta (1973). Viscous effects in the inception of cavitation on axi-symmetric bodies. *J. of Fluids Eng.,* 519.

Arakeri, V. H. (1975). A note on the transition observations on an axi-symmetric body and some related fluctuating wall pressure measurements. *Trans. A.S.M.E., 82.*

Arndt, R. E. A., and A. T. Ippen (1968). Rough surface effects on cavitation inception. *A.S.M.E., J. of Basic Eng.,* 249.

Arndt, R. E. A., and A. P. Keller (1976). Free gas content effects on cavitation inception and noise in a free shear flow. *Proc. of IAHR-Symposium,* Paris, France, 3.

Benson, B. W. (1966). Cavitation inception on three dimensional roughness elements. *David Taylor Model Basin, Rep. 2104.*

Bindel, S. G. (1969). Comparison between model and ship cavitation. *12th ITTC, Cavitation Committee, App. III,* 365.

Bohn, J. C. (1972). The influence of surface irregularities on cavitation: a collation and analysis of new and existing data with application to design problems. *Thesis. Penn State Univ., Ordnance Res. Lab., Tech. Mem., File No. 72-223.*

Casey, M. V. (1974). The inception of attached cavitation from laminar separation bubbles on hydrofoils. *Inst. of Mech. Eng., Conference on cavitation.* Edinburgh, Scotland.

Curle, S. C., and S. W. Skan (1957). Approximate methods for predicting separation properties of laminar boundary layers. *Aeron, Quart, 8,* 257.

Daily, J. W., and V. E. Johnson Jr. (1956). Turbulence and boundary layer effect on cavitation inception from gas nuclei. *Trans. A.S.M.E., 78, 1965.*

Gates, E. M. (1977). The influence of freestream turbulence, freestream nuclei populations and a drag-reducing polymer on cavitation inception on two axi-symmetric bodies. *Calif. Inst. of Techn. Report No. Eng. 183-2.*

Gent, W. van (1977). On the use of lifting surface theory for moderately and heavily loaded ship propellers. Thesis, *Netherlands Ship Model Basin, Publ. No. 536.*

Goldstein, S. (1948). Low-drag and suction airfoils. *J. of the Aeron Sciences, 15.*

Hoekstra, M. (1975). Prediction of full scale wake characteristics based on model wake survey. *Inst. Shipbuilding Progress, 22.*

Holl, J. W., and G. F. Wislicenus (1961). Scale effects on cavitation. *A.S.M.E. J. of Basic Eng., 83,* 385.

Holl, J. W. (1965). The estimation of the effect of surface irregularities on the inception of cavitation. *A.S.M.E. Symp. on Cavitation in Fluid Machinery, G. M. Wood et al. (eds),* 3.

Holl, J. W. (1970). Nuclei and cavitation. *Trans. A.S.M.E., J. of Basic Eng.,* 681.

Huang, T. T., and D. E. Hannan (1975). Pressure fluctuations in the regions of flow transition. *David Taylor Model Basin, Report No. 4728.*

Huang, T. T., and F. B. Peterson (1976). Viscous effects on model/full scale cavitation scaling. *J. of Ship Res., 20,* 25.

Johnson, V. E., and T. Hsieh (1966). The influence of trajectories of gas nuclei on cavitation inception. *Proc. 6th Symp. on Naval Hydrodynamics,* Wash. D. C., 7.

Keller, A. P. (1974). Investigations concerning scale effects of the inception of cavitation. *Proc. Conference on Cavitation, Inst. of Mech. Eng.,* Edinburgh, Scotland.

Kuiper, G. (1974). Cavitation testing of marine propellers in the NSMB Depressurized Towing Tank. *Proc. Conference on Cavitation, Inst. of Mech. Eng.,* Edinburgh, Scotland.

Kuiper, G. (1978). Cavitation scale effects, A case study. *Int. Shipbuilding Progress, 25.*

Lerbs, H. W. (1951). On the effects of scale and roughness on free running propellers. *J. of the Am. Soc. of Naval Arch., 63,* 58.

Lerbs, H. W. (1952). Moderately loaded propellers with a finite number of blades and an arbitrary distribution of circulation. *Trans. SNAME, 60.*

Lighthill, M. J. (1951). A new approach to thin aerofoil theory. *Aeron. Quart, 3.*

Lindgren, H. (1972). Ship model correlation method based on theoretical considerations. *Proc. 13th ITTC, Report of Performance Committee, App. 2,* 181.

Maltby, R. L., ed. (1962). Flow visualization in wind tunnels using indicators. *AGARDograph 70.*

Meulen, J. H. J. van der, (1976). A holographic study of cavitation on axi-symmetric bodies and the influence of polymer additives. *Thesis, Netherlands Ship Model Basin, Publ. No. 509.*

Meyne, K. (1972). Untersuchung der Propellergrenzschichtströmung und der Einfluss der Reibung auf die Propellerkenngrössen. *Jahrbuch der Schiffbautechnischen Gesellschaft 66,* 317.

Michel, R. (1951). Etude de la transition sur les profils d'ailestablissement d'un point de transition et calcul de la trainee de profil incompressible. *ONERA report 1/1578A.*

Morgan, Wm. B., V. Silovic, and S. B. Denny (1968). Propeller lifting surface corrections. *Trans. SNAME, 76.*

Noordzij, L. (1976). Some experiments on cavitation inception with propellers in the NSMB Depressurized Towing Tank. *Intern. Shipbuilding Progress, 23.*

Okamoto, H., K. Okada, Y. Saito, and T. Takahei (1975). Cavitation study of ducted propellers on large ships. *Trans. SNAME, 83.*

Oossanen, P. van (1974). Calculation of performance and cavitation characteristics of propellers including effects of non-uniform flow and viscosity. *Thesis, Neth. Ship Model Basin, Publ. No. 457.*

Pinkerton, R. M. (1934). Calculated and measured pressure distributions over the midspan section of the NACA 4412 airfoil. *NACA Rep. No. 569.*

Sasajima, H., and I. Tanaka (1966). On the estimation of wake of ships. *Proc. 11th ITTC,* Tokyo.

Sasajima, T. (1975). A study on the propeller surface flow in open and behind conditions. *Proc. 14th ITTC, 3,* 711.

Schiebe, F. R. (1969). The influence of gas nuclei size distribution on transient cavitation near inception. *Univ. of Minnesota, St. Anth. Falls Hydr. Lab., Proj. Report No. 107.*

Smith, A. M. O., and Nathalie Gamberoni (1956). Transition, pressure gradient and stability theory. *Douglas Aircraft Co. Rep. 26388.*

Smith, A. M. O. (1957). Transition, pressure gradient and stability theory. *IX Congres International de Mechanique Appliquée, IV.* Bruxelles, Belgium.

Sparenberg, J. A. (1962). Application of lifting surface theory to ship screws. *Royal Netherlands Acad. of Sciences. Series B, 5.*

Theodorsen, Th. (1932). Theory of wing sections of arbitrary shape. *NACA Report No. 411.*

Thwaites, B. (1949). Approximate calculation of the laminar boundary layer. *Aeron Quart, 1,* 245.

Tsakonas, S., W. R. Jacobs, and M. R. Ali (1976). Propeller blade pressure distribution due to loading and thickness effects. *Stevens Inst. of Techn., Report* S.T.T.-D.C.*-76-1869.*

Tsuda, T., S. Konishi, and S. Watanabe (1977). On the application of the low pitch and high revolution propeller to the self propulsion test. *ITTC Performance Committee.*

Wrench, J. W. (1957). The calculation of propeller induction factors. *David Taylor Model Basin, Rep. No. 1116.*

APPENDIX

The geometry of the four propellers, used in this study and shown in Figure 4, is given in this appendix. The output is from a propeller data base and is not dimensionless but in mm on model scale. Propellers A and C were stored in the data base on a different model scale than actually used in the tests, but this has no further impact. Calculations were made directly from this data-base.

At each radius, R, the pitch, P, is given, together with the distance to the generator line of the trailing edge, TE, the leading edge, LE, and the position of maximum thickness, TM. The positive direction is from the generator line to the leading edge.

The geometry of the propeller section is given by the thickness and the distance of the face of the propeller section above the pitch line. The ordinates of the section geometry are given as percentages of the distance between point of maximum thickness and leading edge (positive) or trailing edge (negative). The origin therefore always is at the point of maximum thickness of the profile.

The profile thickness at leading and trailing edge is finite in this appendix. The radii at the leading edge were determined by generating a spline through the profile contour or by interpolating in the transformed plane after conformal mapping. Both interpolating techniques gave nearly the same results and were very close to the actual propeller geometries.

PROPELLER A. (AT A DIAMETER OF 0.1785 m.)

DIAMETER = 178.46 mm.

(N.B. THE PROPELLER DIAMETER OF THE MODEL USED IN THE TEST PROGRAM WAS 326.8 mm.).

R	P	T E	L.E	MT
17,85	159,08	-18,28	22,34	8,15
22,31	162,43	-20,03	23,48	7,82
26,77	165,42	-21,75	24,65	6,98
35,69	170,55	-25,02	26,86	3,72
44,62	174,58	-28,09	28,98	1,11
53,54	177,23	-30,77	31,22	,12
62,46	179,26	-32,86	32,86	,00
71,38	181,51	-34,03	34,03	,00
75,85	182,77	-34,06	34,06	0,00
80,31	184,12	-33,54	33,54	0,00
84,77	185,45	-31,38	31,38	0,00
89,23	186,80	-21,54	21,54	0,00

PROFILE THICKNESS IN mm.

2 R/D	-100	-95	-90	-80	-70	-60	-50	-40	-20	0	20	40	50	60	70	80	85	90	95	100
,200	,65	1,19	1,72	2,79	3,76	4,62	5,35	5,97	6,87	7,23	7,09	6,64	6,26	5,76	5,12	4,32	3,84	3,27	2,54	1,80
,250	,64	1,14	1,65	2,66	3,56	4,36	5,05	5,62	6,44	6,75	6,62	6,20	5,85	5,39	4,79	4,03	3,58	3,04	2,34	1,63
,300	,61	1,08	1,56	2,51	3,35	4,10	4,74	5,27	5,98	6,28	6,17	5,77	5,45	5,02	4,46	3,74	3,31	2,81	2,13	1,45
,400	,53	,94	1,36	2,19	2,93	3,56	4,10	4,55	5,16	5,35	5,27	4,94	4,66	4,30	3,82	3,20	2,82	2,38	1,78	1,18
,500	,44	,79	1,14	1,85	2,46	3,01	3,46	3,82	4,30	4,46	4,40	4,12	3,89	3,58	3,19	2,66	2,34	1,96	1,44	,93
,600	,39	,67	,95	1,53	2,01	2,45	2,81	3,10	3,46	3,60	3,55	3,33	3,13	2,89	2,58	2,15	1,89	1,57	1,15	,73
,700	,22	,46	,69	1,16	1,54	1,89	2,21	2,39	2,67	2,77	2,73	2,56	2,41	2,22	1,98	1,65	1,45	1,20	,87	,56
,800	,27	,41	,55	,83	1,09	1,32	1,52	1,68	1,87	1,94	1,91	1,79	1,69	1,56	1,38	1,16	1,02	,84	,62	,41
,850	,26	,36	,47	,68	,88	1,06	1,21	1,33	1,49	1,54	1,52	1,42	1,34	1,23	1,11	,92	,81	,67	,50	,34
,900	,24	,32	,39	,55	,69	,83	,94	1,04	1,14	1,20	1,18	1,10	1,04	,96	,85	,72	,63	,52	,40	,28
,950	,22	,28	,33	,44	,53	,63	,71	,80	,89	,92	,91	,85	,80	,74	,66	,55	,49	,41	,33	,24
1,000	,21	,25	,29	,36	,44	,50	,56	,61	,68	,71	,70	,66	,62	,57	,51	,43	,39	,34	,24	,22

COORDINATES OF FACE OF PROPELLER SECTION.

2 R/D	-100	-95	-90	-80	-70	-60	-50	-40	-20	0	20	40	50	60	70	80	85	90	95	100
,200	2,03	1,53	1,34	,98	,68	,45	,28	,17	,05	,00	,02	,13	,22	,36	,56	,83	1,00	1,22	1,53	2,73
,250	1,74	1,27	1,11	,80	,55	,35	,22	,12	,03	,00	,01	,09	,16	,26	,42	,64	,79	,98	1,25	2,34
,300	1,52	1,08	,95	,69	,47	,31	,19	,10	,02	0,00	,00	,05	,10	,18	,30	,49	,62	,78	1,02	2,00
,400	1,17	,82	,72	,54	,38	,26	,16	,09	,01	-,00	-,01	-,01	,01	,04	,11	,23	,31	,43	,62	1,39
,500	,89	,61	,54	,42	,31	,22	,14	,09	,02	0,00	-,02	-,04	-,04	-,03	-,01	,06	,11	,19	,33	,93
,600	,61	,38	,34	,27	,20	,14	,09	,06	,01	-,00	-,02	-,06	-,07	-,08	-,08	-,05	-,02	,03	,13	,59
,700	,31	,18	,17	,14	,10	,06	,04	,02	,01	0,00	-,02	-,06	-,08	-,10	-,11	-,11	-,09	-,06	,01	,34
,800	,18	,04	,04	,03	,03	,02	,01	0,00	0,00	-,00	-,02	-,05	-,08	-,10	-,12	-,13	-,13	-,11	-,07	,16
,850	,13	-,02	-,01	0,00	0,00	0,00	-,00	-,00	0,00	0,00	-,02	-,05	-,07	-,09	-,11	-,12	-,12	-,11	-,09	,10
,900	,08	-,03	-,02	-,01	-,01	-,00	-,00	-,00	0,00	0,00	-,01	-,04	-,06	-,07	-,09	-,10	-,10	-,09	-,08	,07
,950	,09	-,01	-,01	,03	,01	,01	,01	0,00	0,00	-,00	-,01	-,02	-,03	-,04	-,05	-,06	-,05	-,05	-,04	,09
1,000	,15	,04	,04	,04	,03	,03	,02	,01	,00	-,00	-,00	-,01	-,01	-,01	-,01	0,00	,01	,02	,03	,14

TABLE A1

PROPELLER B.

DIAMETER = 218.3 mm.

R	P	T E.	L.E	MT
37.07	319.33	-29.52	45.98	19.12
47.37	323.93	-34.82	49.62	18.68
57.67	327.70	-39.80	51.33	16.58
67.97	330.60	-44.28	50.88	12.82
78.27	332.67	-47.82	47.93	7.55
88.57	333.83	-49.55	41.68	.98
98.87	334.17	-47.45	30.05	-6.57
104.02	334.00	-42.77	20.03	-10.48

PROFILE THICKNESS IN mm.

2 R/D	-100	-95	-90	-80	-70	-60	-50	-40	-20	0	20	40	50	60	70	80	85	90	95	100
.340	.03	2.03	3.40	4.48	5.69	6.67	7.45	8.04	8.75	8.95	8.87	8.50	7.62	6.89	6.15	5.08	4.25	3.36	2.32	.03
.434	.03	1.77	2.59	3.83	4.81	5.66	6.31	6.81	7.40	7.57	7.48	7.14	6.54	5.90	5.21	4.26	3.61	2.87	2.00	.03
.528	.03	1.53	2.21	3.21	4.03	4.70	5.23	5.64	6.12	6.25	6.17	5.87	5.46	4.94	4.32	3.52	3.01	2.42	1.70	.03
.623	.03	1.30	1.84	2.63	3.27	3.80	4.21	4.53	4.90	5.00	4.94	4.68	4.38	3.98	3.47	2.83	2.44	1.99	1.42	.03
.717	.13	1.07	1.46	2.06	2.55	2.93	3.24	3.51	3.76	3.83	3.77	3.56	3.35	3.06	2.67	2.18	1.90	1.57	1.16	.03
.811	.03	.82	1.12	1.51	1.85	2.12	2.33	2.48	2.66	2.72	2.68	2.52	2.38	2.18	1.91	1.57	1.38	1.15	.86	.03
.906	.03	.55	.73	.97	1.17	1.33	1.45	1.54	1.64	1.68	1.65	1.55	1.46	1.34	1.19	.99	.88	.74	.56	.03
.953	.03	.41	.54	.70	.83	.94	1.03	1.09	1.16	1.18	1.16	1.11	1.05	.95	.84	.71	.63	.54	.41	.03

COORDINATES OF FACE OF PROPELLER SECTION.

2 R/D	-100	-95	-90	-80	-70	-60	-50	-40	-20	0	20	40	50	60	70	80	85	90	95	100
.340	2.98	2.08	1.70	1.17	.78	.48	.27	.13	.01	-.01	.02	.18	.33	.56	.97	1.49	1.78	2.14	2.62	3.67
.434	1.81	1.08	.82	.50	.28	.13	.05	.01	.01	.01	.00	.06	.14	.28	.54	.90	1.10	1.36	1.70	2.57
.528	1.03	.45	.29	.13	.05	.01	.00	.02	.09	.09	.03	-.00	.02	.09	.22	.42	.55	.72	.96	1.66
.623	.59	.13	.04	.01	.01	.03	.08	.13	.22	.22	.13	.03	.00	.01	.05	.13	.19	.29	.43	.99
.717	.39	.04	-.00	.03	.08	.15	.21	.26	.35	.36	.27	.13	.07	.03	.01	.01	.02	.06	.12	.56
.811	.28	.02	.00	.07	.14	.20	.28	.34	.44	.45	.37	.24	.18	.11	.06	.02	.00	.00	.03	.33
.906	.19	.01	.01	.06	.12	.17	.23	.28	.36	.38	.34	.25	.20	.14	.09	.04	.02	.01	.01	.28
.953	.14	.01	.00	.04	.08	.12	.16	.19	.25	.27	.24	.16	.14	.11	.07	.03	.02	.00	.01	.15

TABLE A 2.

PROPELLER C. (AT A DIAMETER OF 0.24 m.).

DIAMETER = 240.00 mm.

(N.B. THE PROPELLER DIAMETER OF THE MODEL USED IN THE TEST PROGRAM WAS 300.0 mm.).

R	P	T E	L.E	MT
37,50	202,20	-22,90	22,90	,00
60,00	235,60	-43,70	34,70	-4,50
72,00	243,48	-54,05	38,65	-7,70
84,00	248,35	-63,40	40,00	-11,70
96,00	251,55	-70,20	37,70	-16,25
102,00	253,00	-72,05	34,35	-18,85
108,00	254,30	-71,60	28,60	-21,50
114,00	255,45	-66,90	18,30	-24,30
117,00	256,00	-62,30	7,40	-27,45

PROFILE THICKNESS IN mm.

2 R/D	-100	-95	-90	-80	-70	-60	-50	-40	-20	0	20	40	50	60	70	80	85	90	95	100
,313	1,19	3,67	5,08	6,95	8,18	9,09	9,80	10,35	11,04	11,27	11,05	10,35	9,80	9,07	8,13	6,87	6,06	5,06	3,68	,48
,530	,61	2,00	2,78	3,82	4,54	5,06	5,47	5,78	6,17	6,30	6,17	5,78	5,47	5,06	4,52	3,81	3,36	2,79	2,01	,62
,600	,43	1,43	2,00	2,74	3,23	3,61	3,92	4,16	4,44	4,53	4,44	4,16	3,93	3,63	3,25	2,74	2,41	2,00	1,44	,44
,700	,30	,98	1,37	1,88	2,23	2,50	2,70	2,86	3,05	3,12	3,05	2,86	2,70	2,50	2,23	1,88	1,65	1,37	,99	,30
,800	,19	,63	,88	1,21	1,44	1,61	1,74	1,84	1,96	2,01	1,96	1,84	1,74	1,61	1,43	1,21	1,06	,88	,63	,19
,850	,15	,49	,69	,94	1,12	1,25	1,36	1,43	1,53	1,57	1,53	1,44	1,36	1,25	1,12	,94	,83	,69	,49	,15
,900	,11	,38	,53	,73	,86	,97	1,04	1,10	1,18	1,21	1,18	1,10	1,04	,96	,86	,73	,64	,53	,38	,11
,950	,09	,29	,41	,56	,67	,75	,81	,86	,92	,93	,92	,86	,81	,75	,67	,56	,50	,41	,29	,09
,975	,08	,26	,36	,50	,59	,66	,72	,76	,81	,83	,81	,76	,72	,66	,59	,50	,44	,36	,26	,08

COORDINATES OF FACE OF PROPELLER SECTION.

2 R/D	-100	-95	-90	-80	-70	-60	-50	-40	-20	0	20	40	50	60	70	80	85	90	95	100
,313	,25	-1,34	-1,81	-2,26	-2,43	-2,53	-2,63	-2,73	-2,87	-2,93	-2,92	-2,80	-2,70	-2,55	-2,33	-2,03	-1,82	-1,50	-,94	,41
,500	,03	-,75	-,90	-,92	-,79	-,63	-,54	-,49	-,45	-,46	-,50	-,56	-,60	-,64	-,67	-,68	-,67	-,63	-,54	,09
,600	,01	-,50	-,55	-,43	-,19	,03	,15	,22	,31	,32	,27	,16	,08	-,00	-,10	-,20	-,25	-,29	-,30	,05
,700	,00	-,30	-,29	-,12	,14	,36	,51	,61	,71	,73	,68	,55	,46	,35	,23	,09	,01	-,06	-,13	,03
,800	-,00	-,17	-,14	,03	,24	,43	,56	,65	,74	,76	,71	,60	,52	,43	,32	,19	,11	,04	-,04	,02
,850	-,00	-,13	-,09	,05	,24	,40	,50	,58	,66	,67	,63	,54	,47	,39	,29	,18	,12	,05	-,02	,02
,900	-,00	-,09	-,06	,06	,21	,34	,43	,49	,56	,57	,54	,46	,41	,34	,26	,16	,11	,05	-,00	,01
,950	-,00	-,07	-,05	,05	,16	,27	,34	,39	,44	,45	,42	,36	,32	,27	,20	,13	,09	,04	-,00	,01
,975	-,00	-,07	-,05	,04	,14	,23	,29	,33	,37	,38	,36	,31	,27	,22	,17	,11	,07	,03	-,00	,01

TABLE A3

PROPELLER D.

DIAMETER = 212.0 mm.

R	P	T E	L.E	MT
21,20	203,52	-16,76	26,56	10,20
26,50	207,12	-19,08	27,56	8,52
31,80	210,32	-21,20	28,40	6,80
42,40	215,60	-25,68	29,52	3,40
53,00	219,24	-30,12	29,60	,00
63,60	221,32	-34,40	28,80	-3,40
74,20	221,44	-38,40	26,48	-6,80
84,80	220,00	-41,68	22,40	-10,20
90,10	218,80	-42,08	19,24	-11,92
95,40	217,12	-41,24	15,12	-13,60
100,70	215,20	-38,44	8,40	-15,32
103,35	214,20	-34,88	2,80	-16,16

PROFILE THICKNESS IN mm.

2 R/D	-100	-95	-90	-80	-70	-60	-50	-40	-20	0	20	40	50	60	70	80	85	90	95	100
,200	,72	1,35	1,96	3,10	4,13	5,35	5,84	6,49	7,45	7,84	7,68	7,16	6,73	6,15	5,42	4,50	3,95	3,30	2,45	,96
,250	,68	1,29	1,87	2,94	3,90	4,75	5,48	6,09	6,95	7,28	7,14	6,66	6,27	5,75	5,07	4,21	3,70	3,10	2,30	,88
,300	,64	1,22	1,76	2,76	3,65	4,43	5,10	5,66	6,44	6,72	6,60	6,16	5,81	5,33	4,71	3,92	3,44	2,88	2,13	,80
,400	,56	1,06	1,53	2,39	3,15	3,81	4,38	4,85	5,47	5,68	5,59	5,23	4,94	4,55	4,03	3,36	2,96	2,48	1,83	,68
,500	,52	,94	1,33	2,06	2,71	3,28	3,75	4,13	4,63	4,80	4,73	4,43	4,18	3,85	3,42	2,86	2,51	2,10	1,54	,56
,600	,48	,82	1,14	1,74	2,28	2,76	3,15	3,46	3,87	4,00	3,94	3,70	3,48	3,21	2,86	2,39	2,10	1,75	1,28	,48
,700	,44	,69	,95	1,43	1,87	2,26	2,59	2,84	3,17	3,23	3,23	3,03	2,85	2,63	2,33	1,95	1,70	1,40	1,02	,40
,800	,41	,58	,76	1,12	1,46	1,76	2,02	2,22	2,47	2,56	2,52	2,35	2,22	2,03	1,80	1,49	1,30	1,05	,76	,32
,850	,38	,52	,67	,97	1,26	1,51	1,73	1,90	2,13	2,20	2,17	2,02	1,90	1,74	1,53	1,26	1,09	,88	,63	,28
,900	,36	,47	,59	,83	1,05	1,26	1,44	1,59	1,78	1,84	1,81	1,68	1,58	1,44	1,26	1,03	,88	,70	,50	,24
,950	,34	,42	,51	,69	,85	1,01	1,15	1,27	1,43	1,48	1,45	1,35	1,26	1,14	1,00	,80	,67	,53	,38	,20
,975	,33	,39	,47	,62	,76	,89	1,01	1,11	1,25	1,30	1,28	1,18	1,10	1,00	,87	,69	,58	,47	,34	,20

COORDINATES OF FACE OF PROPELLER SECTION.

2 R/D	-100	-95	-90	-80	-70	-60	-50	-40	-20	0	20	40	50	60	70	80	85	90	95	100
,200	1,78	1,21	1,01	,67	,41	,22	,10	,04	,01	,00	,02	,11	,20	,33	,53	,81	,99	1,23	1,57	2,72
,250	1,65	1,11	,94	,64	,41	,23	,12	,05	,01	,00	,01	,08	,15	,25	,42	,65	,81	1,02	1,32	2,38
,300	1,50	1,00	,85	,59	,39	,24	,13	,06	,01	-,00	-,00	,05	,09	,17	,30	,50	,64	,81	1,08	2,04
,400	1,21	,82	,71	,52	,36	,24	,15	,08	,02	-,00	-,01	-,01	,01	,05	,12	,25	,34	,46	,66	1,45
,500	,96	,63	,56	,43	,32	,22	,15	,09	,02	-,00	-,02	-,04	-,04	-,03	,01	,08	,14	,23	,38	1,02
,600	,69	,41	,37	,29	,22	,15	,10	,06	,01	-,00	-,02	-,06	-,07	-,08	-,07	-,04	,00	,06	,18	,69
,700	,44	,21	,20	,16	,12	,08	,05	,03	,01	-,00	-,02	-,06	-,08	-,10	-,11	-,10	-,08	-,03	,05	,44
,800	,24	,06	,06	,06	,04	,03	,01	,00	,00	-,00	-,02	-,06	-,09	-,11	-,13	-,13	-,12	-,09	-,03	,24
,850	,18	,01	,02	,02	,02	,01	,01	,00	,00	-,00	-,02	-,06	-,08	-,10	-,12	-,12	-,11	-,08	-,04	,18
,900	,15	-,01	,00	,01	,02	,01	,01	,00	,00	-,00	-,02	-,04	-,06	-,08	-,09	-,09	-,07	-,05	-,02	,15
,950	,19	,03	,04	,04	,04	,03	,03	,02	,00	-,00	-,01	-,02	-,03	-,03	-,03	-,01	,01	,03	,05	,19
,975	,26	,10	,10	,09	,08	,06	,05	,03	,01	-,00	-,00	-,00	-,00	,01	,03	,05	,07	,10	,13	,26

TABLE A 4.

Discussion

SHIN TAMIYA, HIROHARU KATO, and YOSHIAKI KODAMA

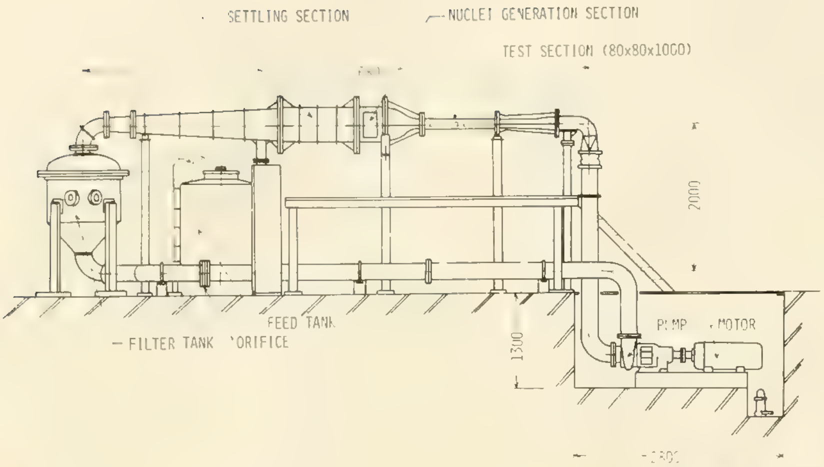

FIGURE 1. General arrangement.

The discussers appreciate the excellent research work on cavitation inception done at NSMB*. At the University of Tokyo the discussers also performed similar experiments using both hemispherical and ITTC headforms tested in our newly built cavitation tunnel. This tunnel has a filtering tank containing 60 cartridge type filters, which continuously remove air nuclei and solid particles larger than ca. 1 μm from water (Figure 1).

Figures 2 through 7 show the effect of electrolysis on cavitation inception. The photograph in Figure 3 was taken a few seconds after that in Figure 2. The flow conditions are exactly the same for Figures 2 and 3; the only difference is the presence of hydrogen bubble nuclei. The photographs in Figures 4 and 5, as well as 6 and 7, were also taken under the same conditions.

In the discussers' experiments the cavitation caused by electrolysis nuclei generates only bubble type cavitation. Even when sheet cavitation exists, the cavitation bubbles caused by the electrolysis nuclei seem to break up the sheet cavity.

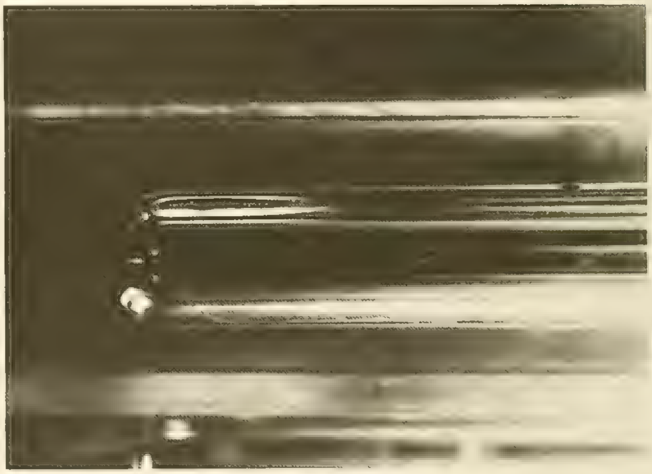

FIGURE 2. Without hydrogen bubbles V = 6.8 m/s, $\sigma = 0.81$.

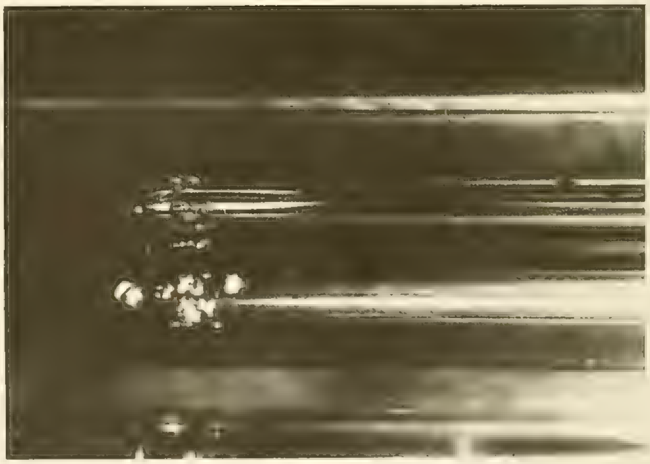

FIGURE 3. With hydrogen bubbles V = 6.8 m/s, $\sigma = 0.81$.

---

*Netherlands Ship Model Basin
#Statens Skeppsprovningsanstalt

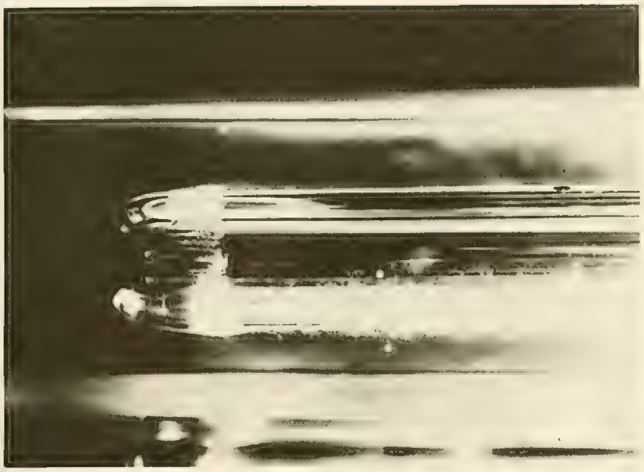

FIGURE 4. Without hydrogen bubbles V = 6.8 m/s, $\sigma = 0.71$.

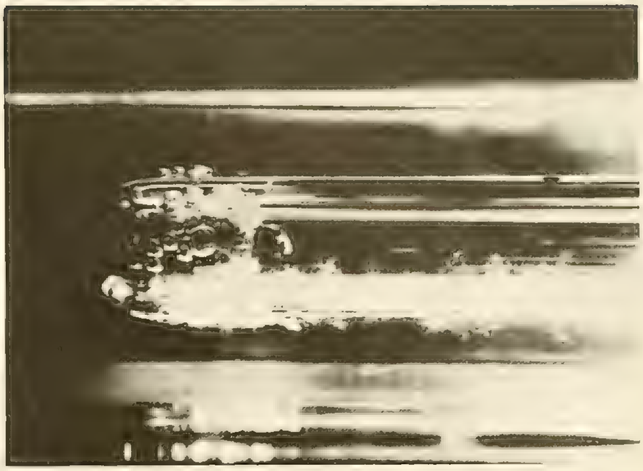

FIGURE 5. With hydrogen bubbles V = 6.8 m/s, $\sigma = 0.71$.

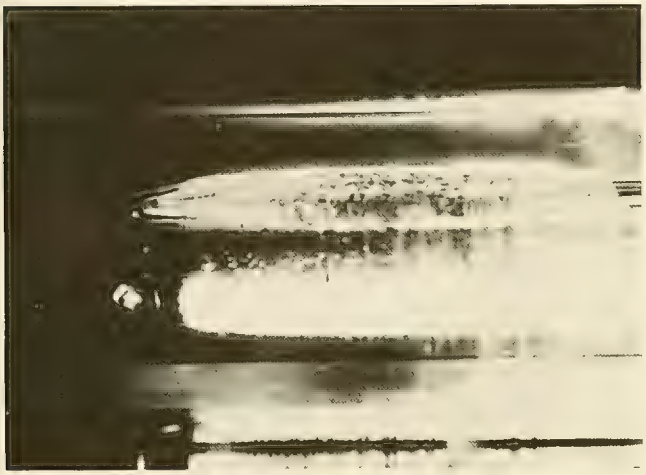

FIGURE 6. Without hydrogen bubbles V = 6.8 m/s, $\sigma = 0.60$.

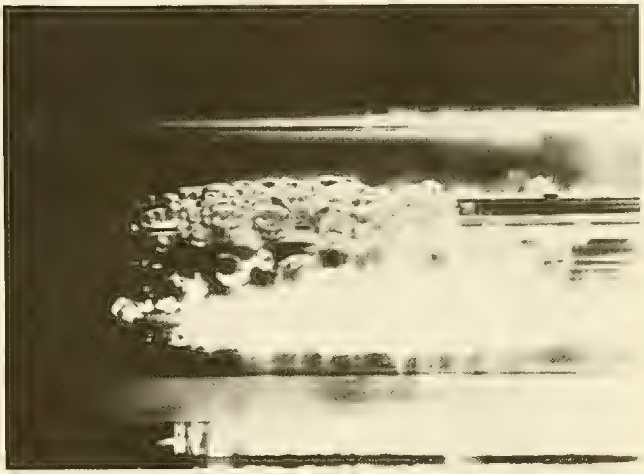

FIGURE 7. With hydrogen bubbles V = 6.8 m/s, $\sigma = 0.60$.

O. RUTGERSSON

I would like to congratulate the author of this interesting paper. As a complement to the data presented I think that some results obtained at SSPA# when testing high-speed propellers could be of some interest. A propeller of the supercavitating type was tested with three different gases in the water. Also, two different conditions of the blade surface were used, smooth polished and painted with a thin spray paint giving the surface some roughness.

In Figure 1 the propeller characteristics from these tests for homogenous flow at the cavitation number, $\sigma = 0.6$, are shown. In the partially cavitating region ($J > 1.0$) there is a very pronounced influence due to gas content for the polished propeller. For the painted propeller no such influence was found. Cavitation pictures at the advance ratio, $J = 1.1$, give the explanation for these differences. Figure 2 shows the cavitation at the lowest gas content ($\alpha/\alpha_S = 0.2$) for the polished propeller. The cavitation pattern is divided into two parts. The first part is a sheet starting at the leading edge. The second part is an unstable sheet of bubble cavitation at the aft part of the blade. Tests at higher gas contents (Figure 3, $\alpha/\alpha_S = 0.4$) show that the aft part cavitation now has a larger extension. The painted propeller (Figure 4) shows a rather different pattern for the aft part cavitation (the leading edge sheet is almost uninfluenced by gas content and roughness). The aft part cavitation now consists of a thin sheet of very small bubbles. The sheet also has a relatively larger extension on the painted propeller than on the polished propeller. Obviously it is the changes in this aftpart cavitation that cause the changes in propeller characteristics.

Full scale tests have also been conducted with this propeller design. In Figure 5 the full scale cavitation pattern corresponding to the model tests is shown. This cavitation pattern is very similar to that of the painted model propeller.

In the author's Figure 29 bubble cavitation is shown very similar to that in tests with the painted propeller at SSPA. The author concludes that this cavitation is inconsistent. Based on our experience with full scale cavitation, however, I think that the pattern shown could very well represent a full-scale case.

The influence of nuclei content and blade roughness on the cavitation pattern is found to be rather similar in the tests at NSMB and SSPA. The main difference is the necessary amount of roughness. This difference is possibly due to the difference in Reynolds number, about 10 times as high in the tests at SSPA as in those carried out at NSMB.

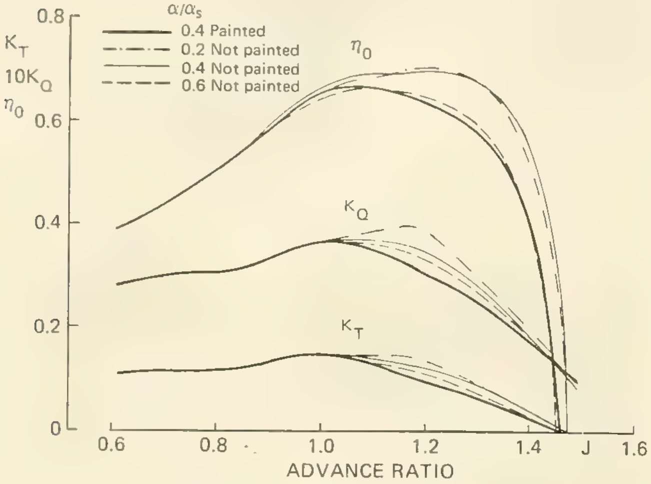

FIGURE 1. Propeller characteristics at $\delta = 0.6$.

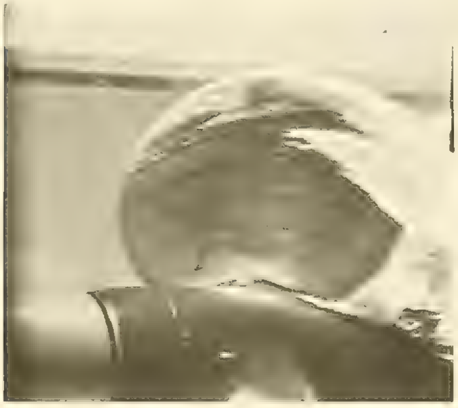

FIGURE 2. $J = 1.1$ $\alpha/\alpha_s = 0.2$ polished blade.

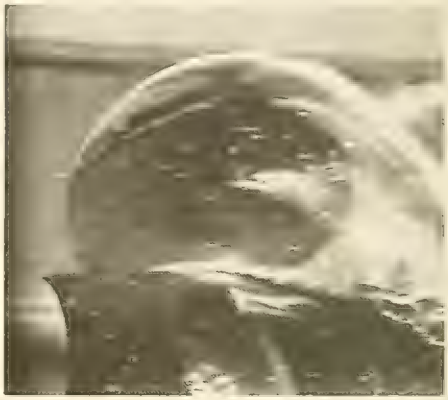

FIGURE 3. $J = 1.1$ $\alpha/\alpha_s = 0.4$ polished blade.

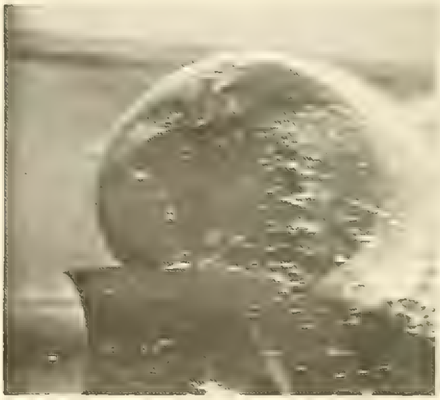

FIGURE 4. $J = 1.1$ $\alpha/\alpha_s = 0.4$ painted blade.

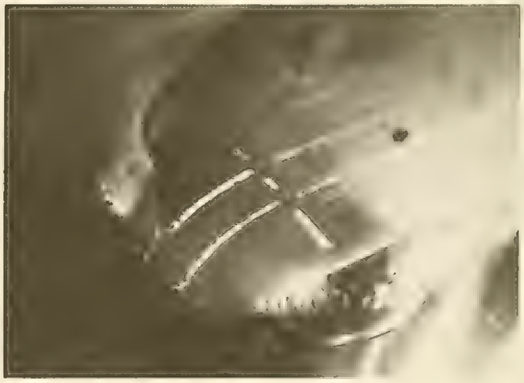

FIGURE 5. $J = 1.1$ $\delta = 0.65$ full scale.

Author's Reply

G. KUIPER

Both the hemisphere and the ITTC body are known to exhibit laminar separation in the range of Reynolds numbers (estimated at about 2 × 10^5) used in the experiments of Tamiya et al. as was already shown by Arakeri and Acosta (1973). They now point to an apparent discrepancy between the results as described in my paper and their observations: on the propellers nuclei were found to generate sheet cavitation in the very few cases where it was not yet present, and the nuclei never changed the appearance of the cavity.

First of all, the cavitation patterns, both with and without electrolysis, on the headforms of the discussers show a remarkable resemblance to various patterns shown on the ITTC bodies at other facilities [Lindgren and Johnsson (1966) and also reproduced by Gates and Acosta in their paper on this program] illustrating that the nuclei content was at least one of the factors causing the variation in type of cavitation observed at different facilities.

From the observations of the discussers it can be concluded that the nuclei, generated by electrolysis, removed the laminar separation bubble in the same manner as shown very clearly by Gates and Acosta in their symposium paper. This phenomenon was found when there were many large free stream bubbles in the flow, as can also be observed in the pictures of the discussers. In our case, however, we verified with a paint test that electrolysis did not remove the laminar separation bubble by verifying that the critical radius was unchanged.

The observations of the discussers show that an overdose of nuclei can change the situation considerably. Gates and Acosta assume that the free stream bubbles do trip the boundary layer. Another possibility, however, is that the dynamic behavior of the bubbles near the minimum pressure region changes the pressure distribution on the body, specifically by decreasing the low pressure peak. This would also remove laminar separation, leaving the boundary layer laminar over a longer distance. In fact the nuclei do not only affect cavitation inception but they change the free stream conditions, making a correct comparison of the inception phenomena impossible.

Rutgersson, in his discussion, gives an illustration of a possible effect of nuclei and roughness on bubble cavitation. With the pictures alone, only some assumptions can be made as to what happened on this propeller, but I will make an attempt to give an explanation.

Although the Reynolds number was rather high it looks like the boundary layer within r/R = 0.8 is laminar over a large portion of the chord, while the minimum pressure region is near midchord (Figure 2). An increase of the nuclei content leads to occasional cavitating spots, starting at the low pressure region (Figure 3). On the painted blade, however, the boundary layer seems to be turbulent and bubble cavitation starts there, near the minimum pressure region (Figure 4).

If my tentative description is correct there is a difference between the discussers' case and Figure 29 (and also Figure 24) from my paper, since there the boundary layer in the region of low pressure was turbulent, and still no bubble cavitation occurred. Only when cavitation, generated by roughness, at the leading edge took place, a separate region of bubble cavitation also appeared.

Whatever may be the case, it must be kept in mind that these descriptions of phenomena do not explain them, because it is not clear to me why there should be any interaction between the boundary layer and the free stream nuclei and which parameters would control this. I think more systematic research is necessary to be able to simulate bubble cavitation on model propellers in a reproducible way.

I agree with the suggestion of the author that the increased amount of bubble cavitation, as shown many times by roughened propeller models, may well be representative for full-scale cases. Bubble cavitation seems to be inhibited on scale models very easily. When bubble cavitation does occur on scale models the situation is so bad that invariably erosion problems do occur on full-scale. Ironically a better simulation of bubble cavitation may not make the interpretation easier.

In general both discussions have made it clear again that it is impossible to make general statements about the effect of nuclei or roughness. To make any interpretation and to avoid confusion the test conditions must be given as complete as possible. Finally, I thank the discussers for their discussions and for their kind attention to my paper.

Session VI

CAVITATION

BLAINE R. PARKIN
Session Chairman
Pennsylvania State University
State College, Pennsylvania

A Holographic Study of the Influence of Boundary Layer and Surface Characteristics on Incipient and Developed Cavitation on Axisymmetric Bodies

J. H. J. van der Meulen
Netherlands Ship Model Basin
Wageningen, The Netherlands

ABSTRACT

This paper describes an experimental investigation of boundary layer flow and cavitation phenomena on three axisymmetric bodies. The bodies possess different boundary layer or surface characteristics. The importance of these features for incipient and developed cavitation are studied by using in-line holography. A good correlation is found between observations and calculations of laminar flow separation and subsequent transition to turbulence of the separated shear layer. The influence of polymer additives on laminar flow separation is studied in detail. The results of this study explain the effect of cavitation suppression by polymer additives on certain bodies.

1. INTRODUCTION

Axisymmetric bodies have often been used to study the inception of cavitation. These studies were usually made by systematically varying the parameters related to the liquid flow (velocity, turbulence, air content, pressure history) or to the body (size, surface roughness, wettability). Although a considerable knowledge of cavitation was obtained in this way, a complete understanding of many cavitation phenomena was still lacking. A breakthrough was achieved by Acosta (1974) who emphasized the need for a thorough understanding of the basic fluid mechanics of the liquid flow surrounding the bodies in which cavitation takes place. This statement was based on an earlier study by Arakeri and Acosta (1973) in which the boundary layer flow was visualized by the employment of the schlieren method. Cavitation inception could be correlated with the occurrence of laminar flow separation. Unawareness of this important flow phenomenon had obscured the results of comparative cavitation studies with axisymmetric bodies, made in the past.

In general, it can be stated that cavitation inception on a body is affected by nuclei, viscous, and surface effects. The present study deals with the two latter effects. The use of holography, a three-dimensional imaging technique, enabled a new approach. The employment of this method for the observation of cavitation inception phenomena has been reported before by Van der Meulen and Oosterveld (1974). In the present study an extended version of the method has been used by which boundary layer flow phenomena also could be observed. Viscous effects were studied by comparing two axisymmetric bodies, a hemispherical nose having laminar flow separation and a blunt nose not having it. Surface effects were studied by comparing two hemispherical noses, one made of stainless steel, the other made of Teflon.

The phenomenon of turbulent-flow friction reduction by polymer additives of high molecular weight has been known for about thirty years. In recent years an increased interest has been shown on the effect of polymer additives on cavitation. In the present work the influence of polymer additives on the flow about the test bodies is studied and related with the influence on cavitation.

2. EXPERIMENTAL METHODS AND PROCEDURE

Description of Test Facility

The facility used is the high speed recirculating water tunnel of the Netherlands Ship Model Basin. Originally, the maximum speed in the 40 mm circular test section was 65 m/s and the maximum allowable tunnel pressure 35 kg/cm^2. A detailed description of this tunnel and its air content regulation system is given by Van der Meulen (1971, 1972). For the present study a new test section was made. It has a 50 mm square cross section with rounded corners (radius 10 mm), to limit the influence of the walls. The models, having a diameter of 10 mm, occupy 3.25 percent of the cross-sectional area of the test

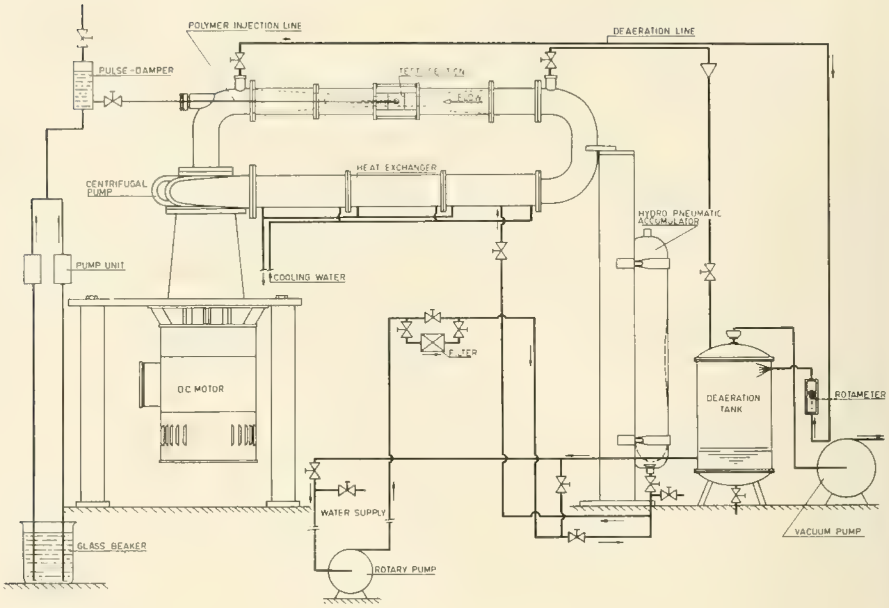
POLYMER INJECTION LINE
DEAERATION LINE
PULSE-DAMPER
TEST SECTION
FLOW
HEAT EXCHANGER
CENTRIFUGAL PUMP
HYDRO PNEUMATIC ACCUMULATOR
PUMP UNIT
COOLING WATER
FILTER
DC MOTOR
DEAERATION TANK
ROTAMETER
WATER SUPPLY
VACUUM PUMP
GLASS BEAKER
ROTARY PUMP

FIGURE 1. Schematic diagram of high speed cavitation tunnel with polymer injection system.

section. Injection of polymer solutions from the nose of the models was made by a Hughes Centurion-100 pump unit. The unit consists of a drive mechanism fitted with two pump heads. A pulse-damper was used to minimize flow variations. Further details are given by Van der Meulen (1974b). A schematic diagram of the tunnel with the polymer injection system is shown in Figure 1.

To measure the influence of polymer additives on the friction factor and the surface tension of the solutions, a turbulent-flow rheometer and a surface-tensionmeter have been used. Details on these measuring devices are given by Van der Meulen (1974a, 1976b).

Test Models

According to Arakeri and Acosta (1973), most axisymmetric models used in cavitation inception studies, such as the hemispherical nose and the ITTC standard headform, exhibit laminar boundary layer separation. It means that the laminar boundary layer is unable to overcome the adverse pressure gradient and the flow separates from the wall. Schiebe (1972) introduced a standard series of axisymmetric models which, theoretically, should not exhibit boundary layer separation. To distinguish between these two classes of axisymmetric models, a hemispherical nose and a blunt nose, selected from Schiebe's standard series, were used in the present investigations. Both models were made of stainless steel (SST). In addition, a third model (hemispherical nose) was used, made of Teflon. The contour of the blunt nose is derived from the combination of a normal source disk and a uniform flow. Schiebe (1972) calculated the dimensionless coordinates and pressure coefficients for a series of models in the range, $C_{P_{min}} = 0.33$ (point source) - 1.0. From this series a blunt nose with a minimum pressure coefficient of 0.75 was selected.

The diameter, D, of the cylindrical part of the hemispherical nose is 10.00 mm. Theoretically, the diameter of the blunt nose increases smoothly to an asymptotic value, D, with increasing axial distance, x. This value was set at 10.00 mm. However, for the manufacture of the blunt nose a minor deviation from the theoretical contour had to be permitted. Thus, the actual contour coincides

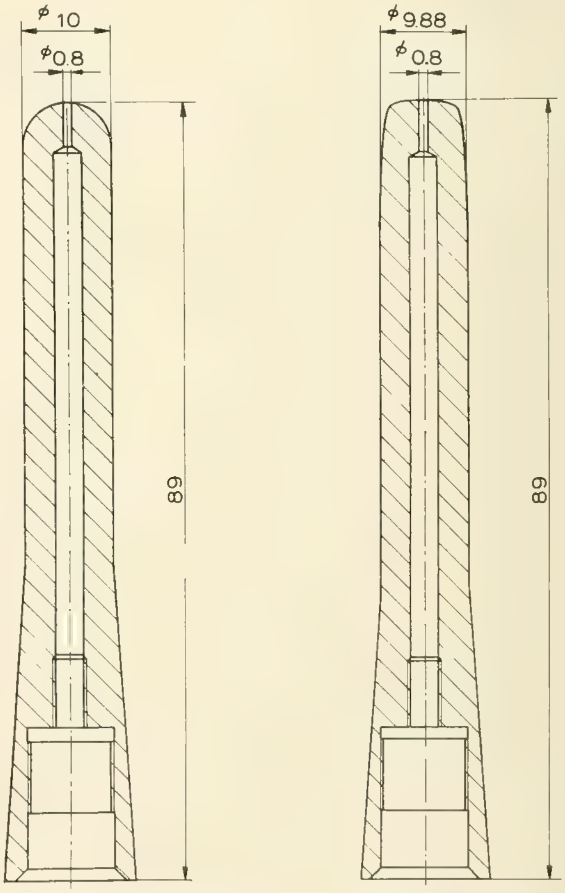
ϕ 10
ϕ0.8
89
ϕ9.88
ϕ0.8
89

HEMISPHERICAL NOSE BLUNT NOSE

FIGURE 2. Cross sections of stainless steel models (dimensions in mm).

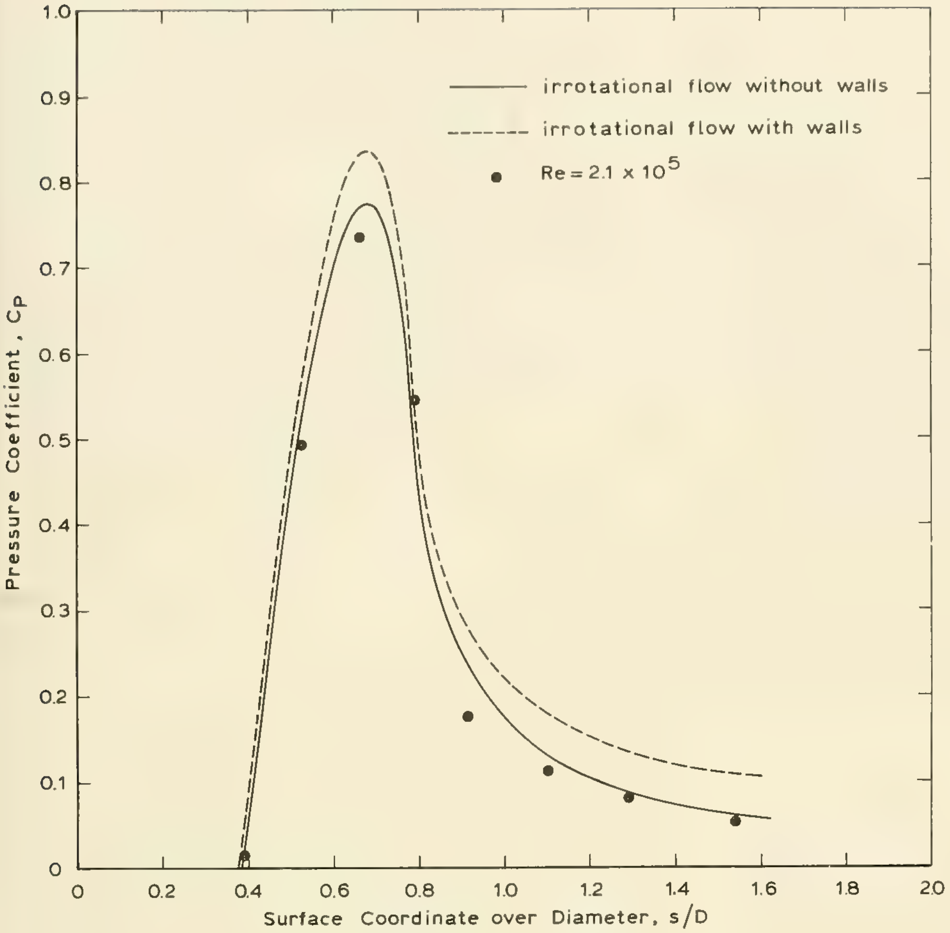

FIGURE 3. Computed pressure coefficient as a function of surface coordinate over diameter for hemispherical nose. Data points obtained from measurements by Rouse and McNown (1948) at Re = 2.1 x 10^5 are included.

with the theoretical contour over a distance, x/D = 0-1.6, and next changes smoothly into a circular cylinder with a diameter of 9.88 mm. The cross sections of the SST models are shown in Figure 2. For the Teflon hemispherical nose the dimensions are the same as for the SST hemispherical nose. However, the Teflon model was not made of solid Teflon but consisted of a Teflon nose slipped on a SST core. Extreme care has to be exercised in manufacturing models for cavitation studies. An accurate similarity of the model contour is essential, but a smooth surface is even more critical. The drastic effects of surface roughness, in particular isolated irregularities, on cavitation inception have been demonstrated by Holl (1960) and Arndt and Ippen (1968). The present models were made by Instrumentum TNO in Delft. The models were inspected by an optical comparator (magnification 50x). For the SST hemispherical nose the maximum deviation from the true contour was within 5 µm, for the Teflon hemispherical nose within 10 µm. For the blunt nose, the maximum deviation for $x/D < 0.3$ was within a few microns and for $x/D > 0.3$ within 10 µm. The mean surface roughness height for the SST models was 0.05 µm; for the Teflon model this value was considerably higher.

Computations of the pressure coefficient for the hemispherical nose and the blunt nose were made at the National Aerospace Laboratory NLR, The Netherlands. The velocity potential for irrotational flow along the model contour was computed with the variational finite element method according to Labrujère and Van der Vooren (1974). This method is suitable for axisymmetric flows. The relation between the pressure coefficient, C_P, and the velocity potential, ϕ, is given by

$$\left(\frac{\partial \phi}{\partial s}\right)^2 = V_0^2 \ (1+C_P) \qquad (1)$$

where s is the streamwise distance along the model contour and V_0 the free stream velocity. The pressure coefficient was computed in the absence of tunnel walls and with tunnel walls. In the latter case, it was necessary to substitute the square cross section with rounded corners by a circular one (diameter 55.44 mm), having the same cross-sectional area. For the hemispherical nose, the results are plotted in Figure 3. Also given are data points obtained from measurements by Rouse and McNown (1948) at a Reynolds number of 2.1 × 10^5. The computed C_P-values are claimed to be accurate within 0.1 percent. The C_P-value for irrotational flow in the absence of tunnel walls is 0.7746 at s/D = 0.6825 (γ = 78.2°). With tunnel walls the C_{Pmin}-value at the same location is 0.8367. For the blunt nose, the results are plotted in Figure 4. The computed C_P-values are accurate within 1 percent. The C_P-value for irrotational flow in the absence of tunnel walls is 0.750, which is consistent with the accurate computations by Schiebe (1972). With tunnel walls the C_{Pmin}-value is 0.802. Tabulated values of C_P are presented by Van der Meulen (1976b) and Labrujère (1976).

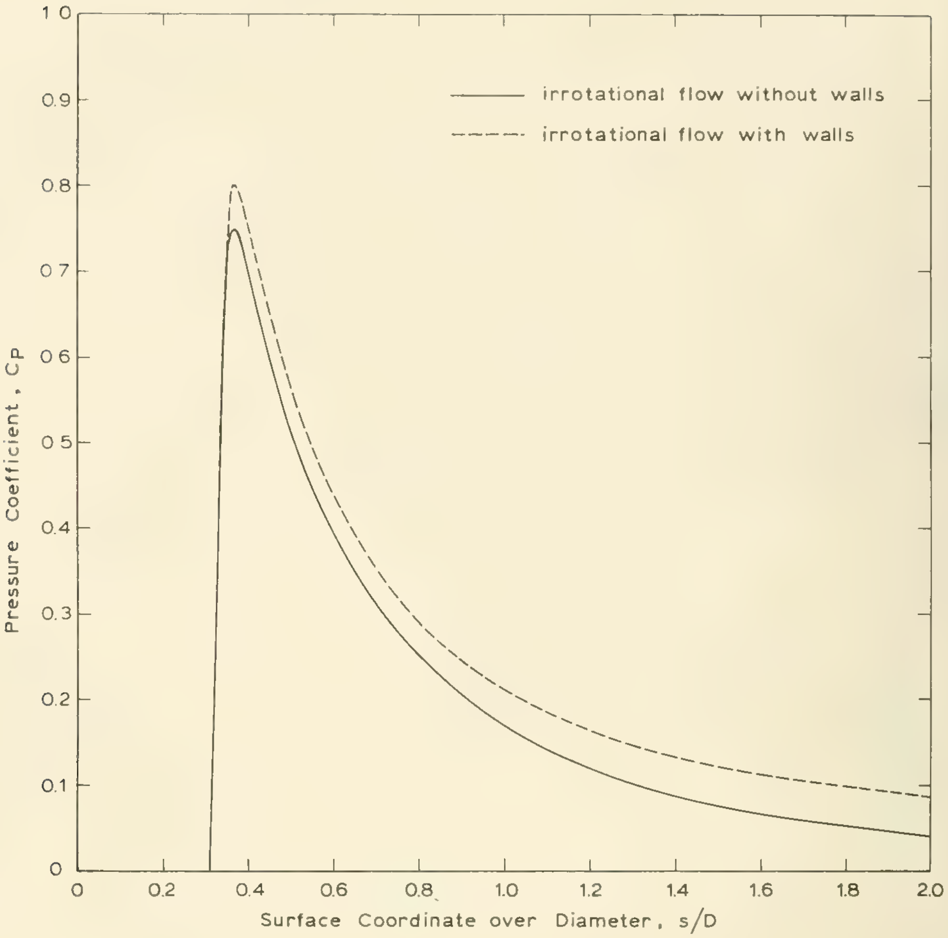

FIGURE 4. Computed pressure coefficient as a function of surface coordinate over diameter for blunt nose.

Holographic Method

In the present work, in-line holography has been used to study cavitation and flow phenomena about the test models. The method consists of making photographic records containing detailed information on the cavitation and flow patterns. Holography has become one of the most important areas of modern optics since the invention of the laser as a new light source. Holography is usually described as a method for storing wavefronts on a record from which the wavefronts may later be reconstructed. The record, formed in photosensitive material, is called a hologram. In forming holograms two sets of light waves are involved: the reference waves and the subject waves. In the present case of in-line holography only one set of waves is used basically. The undeflected light waves from this set of waves act as reference waves, the light waves deflected by the subject act as subject waves.

A schematic diagram of the applied optical system is shown in Figure 5. The light source is the Korad K-1QH pulsed ruby laser of the Institute of Applied Physics TNO-TH. To improve the resolution of the system, the red light from the ruby laser is converted to ultraviolet light, with a wavelength of 0.347 μm, in a KDP-crystal. The pulse duration is 25 nanoseconds and the maximum energy 4 mJ in the TEM_{00} mode. A telescopic system (L_2 and L_3) is used to obtain a laser beam with a diameter of 30 mm. A mirror reflects the beam into the test section of the tunnel. In the walls of the plexiglass test section, two optical glass windows are inserted. The location of the body in the test section is such that the nose is illuminated by the laser beam over a length of about 20 mm, and the body contour is imaged on the hologram. A shutter is placed on the first window. The camera containing the holographic plate is located close to the second window. Agfa-Gevaert Scientia Plates 8E56 and 8E75 with a resolution up to 3000 lines/mm were used as recording material. The ruby laser could also be used as a multiple switched laser. Two or three pulses with

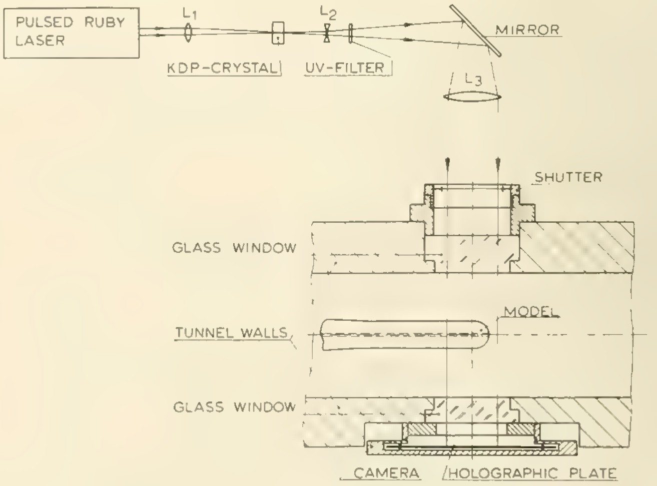

FIGURE 5. Schematic diagram of optical system for making holograms of cavitation or flow phenomena in test section of tunnel.

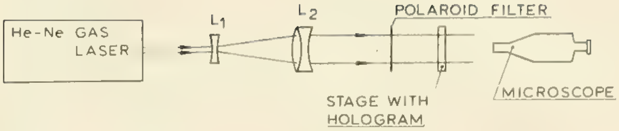

FIGURE 6. Schematic diagram of reconstruction set-up.

pulse separations of 50 or 100 μsec could be generated. This enabled multiple imaging of moving cavities on one hologram.

Reconstruction of the holograms was made with a continuous-wave He-Ne gas laser ($\lambda = 0.633$ μm). A schematic diagram of the reconstruction set-up is shown in Figure 6. The diameter of the laser beam is enlarged by the lenses, L_1 and L_2. The intensity of the light can be adjusted by a polaroid filter. The hologram is placed on a stage, fitted with guides so that the hologram can be moved in two orthogonal directions. The movement of the stage is measured on vernier scales. The reconstructed image is studied with a microscope with a magnification between 40x and 200x.

Flow Visualization Technique

A new technique had to be developed to visualize the boundary layer flow about the axisymmetric models. A description of the several methods investigated is given by Van der Meulen (1976b). The ultimate method consisted of injecting a sodium chloride solution into the boundary layer from a hole located at the stagnation point of the model. The diameter of the hole is 0.08 mm. The sodium chloride solution has a slightly different index of refraction from the surrounding fluid. The light emitted from the pulse laser will be deflected and the deflections are recorded in the hologram. Optimum conditions for flow visualization are given by Van der Meulen and Raterink (1977). In the present study, the ratio of the injection velocity, V_i, to the velocity in the test section, V_o, was usually between 0.1 and 0.2. The sodium chloride concentration was 2 percent. At first, the fluid was injected with a hypodermic syringe, but later on, a plunger with a constant motion was used.

Procedure

The tests performed in the high speed tunnel comprised flow visualization tests, cavitation tests and cavitation inception measurements. Essentially, the flow visualization and cavitation tests consisted of making holograms at prescribed conditions. Prior to each series of tests the model was cleaned and the tunnel refilled. To adjust the air content, the water was passed through the deaeration circuit for a period of 1½ h at a constant pressure in the deaeration tank. All tests were made at a constant air content, α, of about 5 cm^3/ℓ (1 cm^3 of air per liter of water at STP corresponds to 1.325 ppm by weight). For each test the temperature of the tunnel water was measured to obtain the dynamic viscosity and the vapor pressure. The average value of the water temperature was 20°C. The flow visualization tests covered a velocity range of 2 to 30 m/s. For the cavitation tests, the velocity ranged from 10 to 20 m/s. The effect of polymer additives on cavitation and cavitation inception was investigated by injecting a 500 ppm Polyox WSR-301 solution from the nose of the models. Polymer injection was provided by the Hughes Centurion-100 pump unit. The holograms were made at the instant of maximum injection rate. The injection rate was such that the average value of V_i/V_o was 0.17. For the cavitation inception measurements, the velocity ranged from 10 to 24 m/s. Inception (or desinence) was observed visually.

3. BOUNDARY LAYER STUDIES

Newtonian Flow

The holograms exhibited a distinct occurrence of laminar boundary layer separation on the hemispherical nose. The location of separation could be obtained quite accurately from the holograms. At this location the interference pattern usually showed a V-shape. This is shown in the photograph presented in Figure 7. This photograph also shows the laminar separation bubble itself and the subsequent transition to turbulence and reattachment of the separated shear layer. In the transition region, the flow is still visualized by the sodium chloride, but further downstream, where the turbulence becomes more developed, mixing of the sodium chloride prevents any further observations. The determination of the length and the maximum height of the laminar separation bubble from the holograms was somewhat complicated by the fact that the height of the bubble may show a maximum, as illustrated by case A in Figure 8, or that the outer flow line shows an inflexion point, as illustrated by case B in Figure 8. The location of separation for the

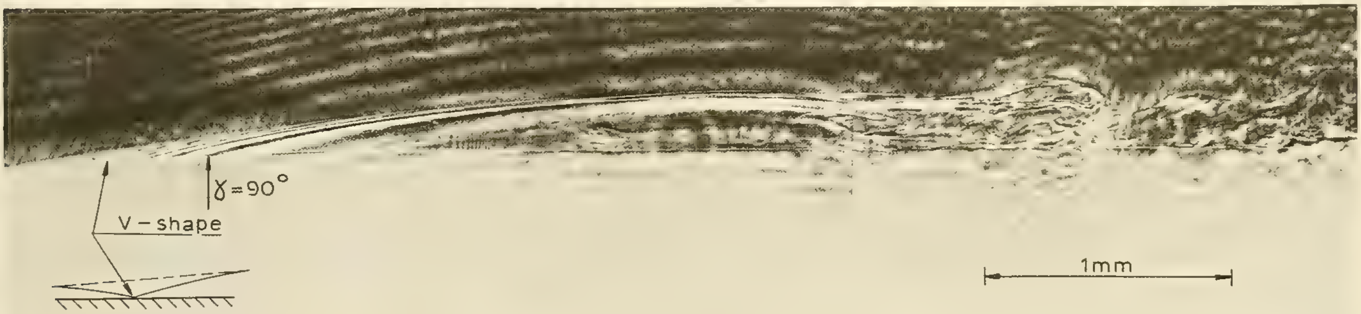

FIGURE 7. Photograph showing laminar separation bubble and subsequent transition to turbulence on SST hemispherical nose. The flow is from left to right. At the position of separation the interference pattern shows a "V". V_o = 4 m/s.

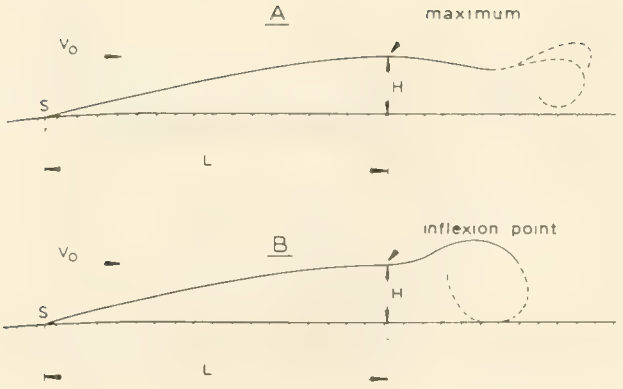

FIGURE 8. Observed shapes of laminar separation bubble on hemispherical nose (schematically) and definitions of length and maximum height of bubble.

hemispherical nose is given in Figure 9. In this figure the angular location of separation, γ_S, is plotted against the Reynolds number. Results on the length, L, the height, H, and the length to height ratio, L/H, of the separation bubble are presented in Figures 10, 11 and 12. Each data point refers to one hologram (values for the upper and lower side of the model are averaged). Most data points refer to the SST hemispherical nose, a few refer to the Teflon hemispherical nose.

The present observations are in agreement with those obtained earlier by Arakeri (1973) and Arakeri and Acosta (1973). From Figure 9 it follows that the boundary layer separation angle is independent on the Reynolds number, which is consistent with theory (Schlichting, 1965). For the SST hemispherical nose the average value of γ_S is 85.43°. This value is claimed to be quite accurate. To compare this experimental value with the theoretically predicted one, laminar boundary layer calculations were made using the method derived by Thwaites (1949). With this method the parameter m is calculated, where m is defined as

$$m = -\frac{\theta^2}{\nu}\ \frac{dU}{ds} \qquad (2)$$

and where θ is the momentum thickness, U the velocity at the edge of the boundary layer, ν the kinematic viscosity, and s the distance along the surface.

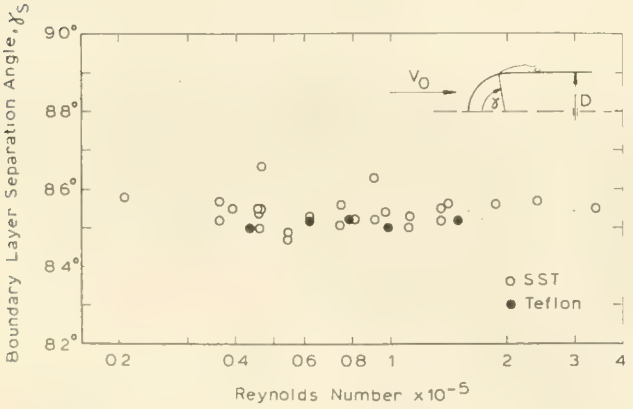

FIGURE 9. Boundary layer separation angle, γ_S, as a function of Reynolds number for hemispherical nose.

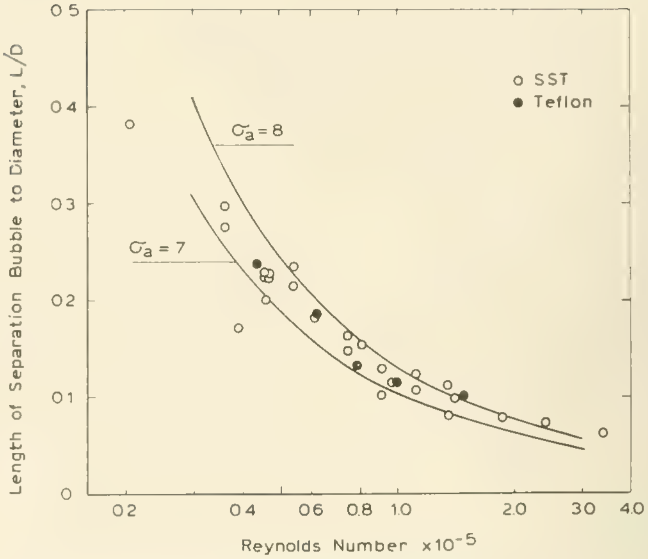

FIGURE 10. Length of separation bubble to diameter, L/D, as a function of Reynolds number for hemispherical nose. The solid lines refer to theoretical predictions.

Laminar boundary layer separation is said to occur for m = 0.09. The computations of γ_S were made with the accurate pressure distributions obtained earlier (Figure 3). For the actual case (with tunnel walls) γ_S was found to be 85.57°, and thus, in excellent agreement with the experimental value. The theoretical value of γ_S is hardly affected by the presence of the tunnel walls, since in the absence of tunnel walls we found γ_S = 85.53°. Arakeri (1973) found experimental and theoretical values of 87°. However, his computations were based on the experimental pressure distribution data by Rouse and McNown (1948), as shown in Figure 3.

The length and the height of the separation bubbles decrease gradually with increasing Reynolds number. The variations in length and height for a given Reynolds number are partly due to the different

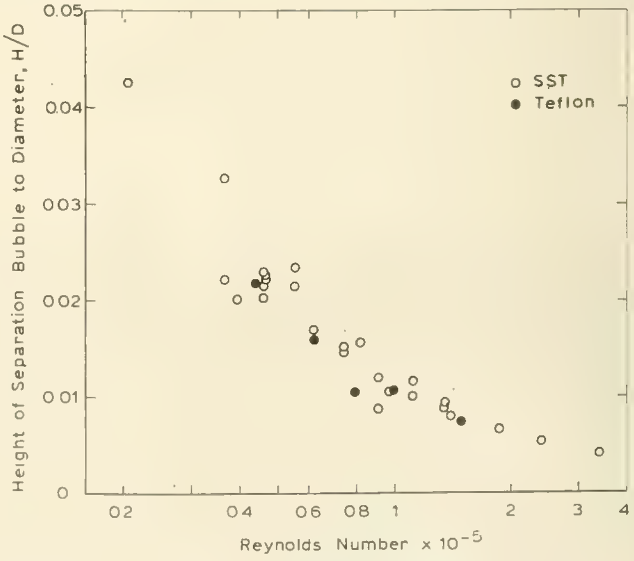

FIGURE 11. Height of separation bubble to diameter, H/D, as a function of Reynolds number for hemispherical nose.

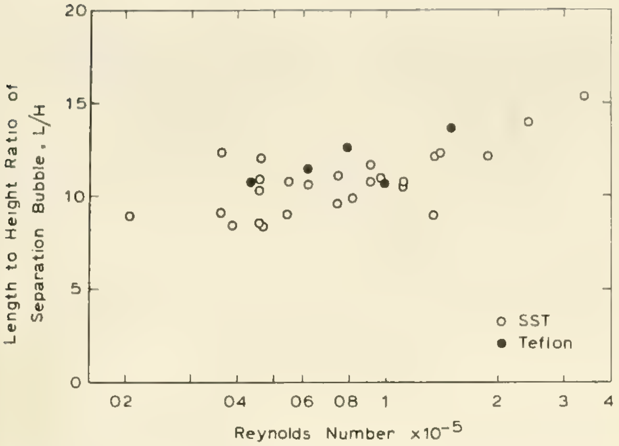

FIGURE 12. Length to height ratio of separation bubble, L/H, as a function of Reynolds number for hemispherical nose.

appearances of the separation bubbles near transition, as illustrated in Figure 8. The length to height ratio of the separation bubbles (Figure 12) is not very dependent on the Reynolds number. For the SST hemispherical nose an average value of 10.8 is found.

To compare experimental values of L with theoretical ones, it is necessary to calculate the location of transition on the separated shear layer. Recently, Van Ingen (1975) presented a calculation method for the laminar part of separation bubbles in which also the location of transition is predicted. The method is based on a solution of the Navier-Stokes equations, valid near the separation point. A relation is found for the separation streamline leaving the wall at an angle, δ. By using constant values of B, σ_a, and m_{sep}, to be obtained experimentally, a formula is derived to calculate the length of the separation bubble. It is assumed that the separation streamline is straight and that the angle δ is given by

$$\tan \delta = \frac{B}{Re_{\theta_{sep}}}, \tag{3}$$

where $Re_{\theta sep}$ is the Reynolds number based on the momentum thickness at separation, given by

$$Re_{\theta_{sep}} = \left(\frac{U\theta}{\nu} \right)_{sep} . \tag{4}$$

TABLE 1. Separation Streamline Angle δ For SST Hemispherical Nose, Derived from Holograms.

Re × 10^{-5}	$Re_{\theta sep}$	δ	B
0.21	56	14.6°	14.6
0.36	74	9.0°	11.8
0.62	97	7.0°	11.9
0.97	121	5.2°	11.1
1.35	144	4.4°	11.1
1.41	146	4.2°	10.8
1.87	169	4.3°	12.7
2.40	191	3.9°	13.0
3.40	228	2.8°	11.1

The amplification factor, σ_a, is defined as

$$\sigma_a = \ell n \frac{a}{a_{neutral}} , \tag{5}$$

where $a/a_{neutral}$ is the ratio of the amplitude of a disturbance to its amplitude at neutral stability. m_{sep} is the value of m at separation ($m_{sep} = 0.09$). According to Dobbinga et al. (1972), B is usually between 15 and 20, but lower values are also found. To obtain B for the present case, the separation streamline angle, δ, was derived from a series of holograms. The results are presented in Table 1. The average value of B is 12.0.

With Van Ingen's method, the location of transition has been calculated for $\sigma_a = 7$ and $\sigma_a = 8$, using $m_{sep} = 0.09$ and $B = 12$. The results are plotted in Figure 10. It is found that most experimental data points lie between the two theoretical curves. The best fit would be obtained for $\sigma_a = 7.5$. It should be noted that the present experimental data refer to the beginning of transition. In a recent paper, Van Ingen (1976) attempted to correlate the amplification factor with the turbulence level, Tu. For $\sigma_a = 7.5$, predicting the beginning of transition, we find Tu = 0.15%. Although the turbulence level in the high speed tunnel has not been measured, it is possible to obtain an approximate value (without considering noise aspects). Arakeri (1975a) measured the location of transition on a 1.5 caliber ogive in the axisymmetric test section of the CIT high speed water tunnel. The turbulence level in this tunnel was 0.2%. Recently, Arakeri (1977) performed similar measurements in the NSMB high speed water tunnel. The agreement between the transition data indicates that the turbulence level in both tunnels was approximately the same. Hence, the turbulence level in the NSMB tunnel may have been close to 0.2%, which is consistent with the value derived earlier. The above considerations on the turbulence level are, however, not confirmed by the measurements of Gates (1977), who found that the turbulence level had no effect whatsoever on the location of transition on a hemispherical nose.

As shown in Figures 9 through 12, the appearance of the laminar separation bubble on the Teflon hemispherical nose is the same as for the SST hemispherical nose. From Figure 10 it is found that the higher surface roughness of the Teflon body has no effect on transition. Apparently, the amplification of disturbances mainly occurs downstream of separation.

The blunt nose exhibited a laminar boundary layer with normal transition to turbulence. Laminar flow separation did not occur. A photograph showing transition is presented in Figure 13. A plot of the transition data is given in Figure 14. Since the outflow of the sodium chloride solution from the nose of the model was in some cases quite unstable, the determination of the precise location of transition provided some difficulties, but an upper or lower bound could still be indicated. In Figure 14 these data points are marked with an arrow. When the arrow is pointing upward the data point is considered to be the lower bound; when the arrow is pointing downward the data point is considered to be the upper bound. Silberman et al. (1973) made laminar boundary layer calculations for a series of blunt noses having $C_{p_{min}}$ values ranging

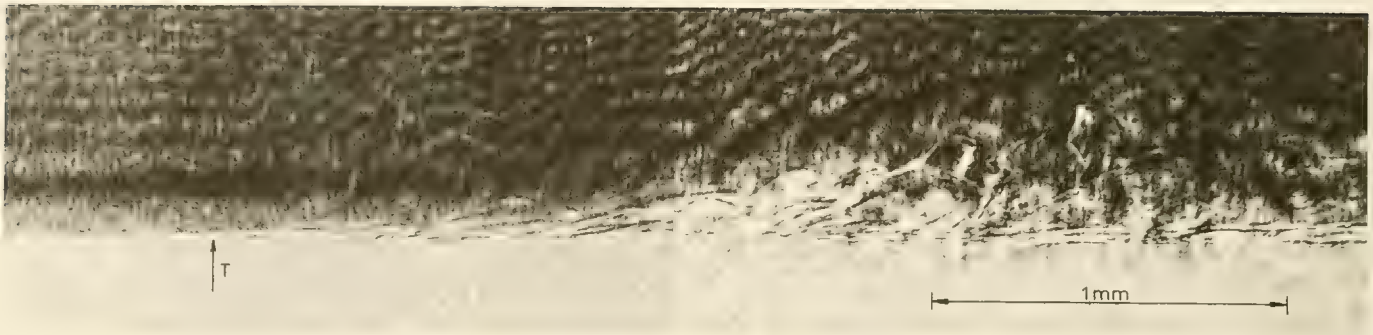

FIGURE 13. Photograph showing transition (T) from laminar to turbulent boundary layer on blunt nose ($s_T/D = 1.68$). The flow is from left to right, $V_o = 8$ m/s.

from 0.333 to 1.0. The calculations showed that none of the blunt noses were subjected to laminar separation. The present observations are in agreement with these theoretical predictions.

Non-Newtonian Flow

The influence of polymer additives on the boundary layer flow about the models was investigated by injecting a 500 ppm (parts per million by weight) Polyox WSR-301 solution from the nose of the models. To visualize the flow, the injection fluid contained 2 percent sodium chloride. For the SST hemispherical nose, the holograms showed that laminar flow separation was no longer present. An example is given by the photograph presented in Figure 15. At or shortly downstream from the location where Newtonian flow separation occurred, transition from laminar to turbulent boundary layer flow is observed. From the holograms made in the velocity range 4 to 20 m/s, it could be derived that transition to turbulence occurred close to the location of Newtonian flow separation. It was difficult, however, to indicate the precise location of transition.

Another important observation was that the sodium chloride was not completely mixed in the turbulent region, but was still able to show the existence of waves and streaks further downstream, till the end of the hologram. An example of this phenomenon has been given by Van der Meulen (1976b). For the Teflon hemispherical nose it was found that the influence of polymer additives on laminar flow separation was the same as for the SST hemispherical nose. Although the observations made with the blunt nose were somewhat obscured by the irregular outflow from the nose of the model, the main conclusion to be derived from the holograms is that the polymer causes early transition to turbulence. The approximate locations of transition are plotted in Figure 14.

The polymer concentration used during the above observations is rather high when compared to the most effective concentration for turbulent-flow friction reduction. From Figure 16, where the friction factor, f, for flow through a circular tube is given as a function of the Reynolds number, it can be derived that a Polyox WSR-301 concentration of about 20 ppm gives a maximum friction reduction. Additional holograms for the SST hemispherical nose

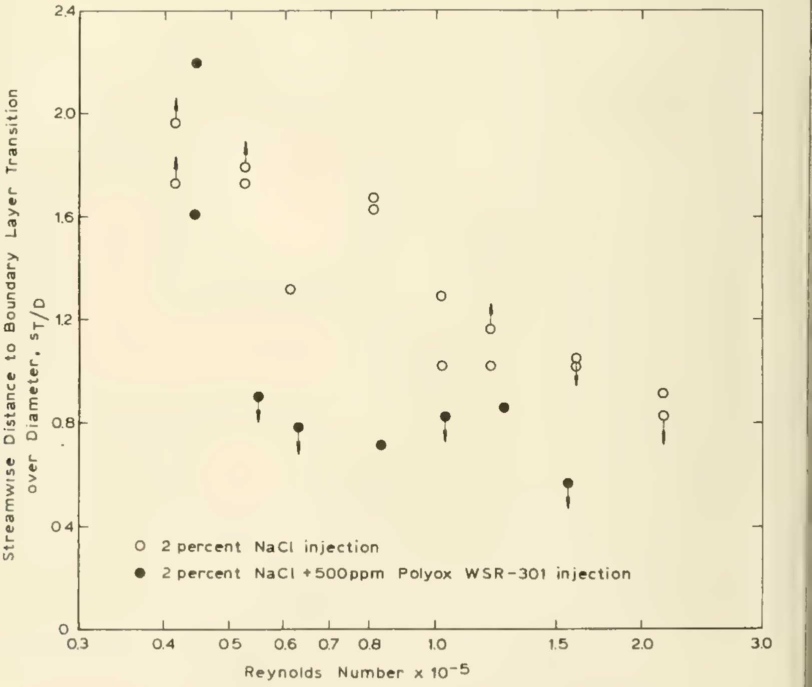

FIGURE 14. Streamwise distance to boundary layer transition over diameter, s_T/D, as a function of Reynolds number for blunt nose.

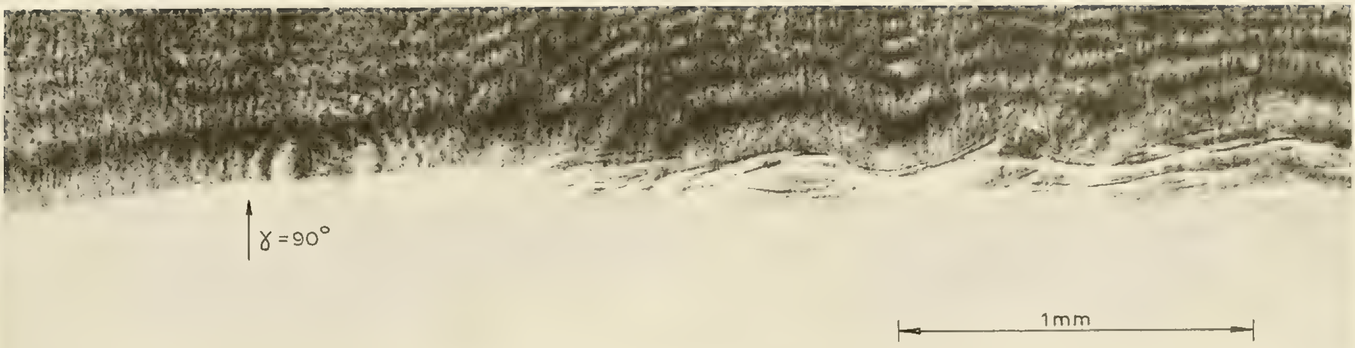

FIGURE 15. Photograph showing boundary layer flow about SST hemispherical nose when a solution of 500 ppm Polyox WSR-301 is injected. The flow is from left to right. V_o = 4 m/s.

were made at polymer concentrations of 100, 50, and 20 ppm. The injection rate was such that $V_i/V_o = 0.2$. The phenomena observed at these lower concentrations were the same as those found at 500 ppm. Recently, Gates (1977) studied the influence of polymer additives on laminar flow separation at low injection rates, and was able to find intermediate stages of separation suppression.

The study on the influence of polymer additives on laminar flow separation has been limited so far to the case where the polymer is present only in a thin layer adjacent to the body (the "inner part" of the boundary layer). To study the influence of polymer additives present in the "outer part" of the boundary layer, additional tests with the SST hemispherical nose were made in which the tunnel was filled with a 50 ppm Polyox WSR-301 solution. To prevent polymer degradation, the water speed in the test section was set at a low value of 4 m/s. Three different solutions were injected: a solution of 2 percent NaCl, a solution of 2 percent NaCl + 50 ppm Polyox and a solution of 2 percent NaCl + 500 ppm Polyox. The injection velocity V_i was 0.8 m/s ($V_i/V_o = 0.2$). Photographs showing the boundary layer flow are presented in Figure 17. For comparison a photograph is included showing the influence of polymer injection when the tunnel is filled with water (Figure 17a). When a 2 percent NaCl solution is injected (Figure 17b), the boundary layer first shows a tendency to become unstable but further downstream the instabilities are suppressed and the boundary layer is laminar again. When a 2 percent NaCl + 50 ppm Polyox solution is injected (Figure 17c), the boundary layer first shows a slight tendency to become unstable, but further downstream the boundary layer is laminar. When a 2 percent NaCl + 500 ppm Polyox solution is injected (Figure 17d), the boundary layer remains completely laminar, till the end of the hologram. The conclusions to be derived from these observations are that the presence of the polymer in the "inner part" of the boundary layer leads to destabilization, whereas the presence of the polymer in the "outer part" of the boundary layer leads to stabilization, and the latter effect is predominant. In all cases considered (Figure 17), laminar flow separation is suppressed.

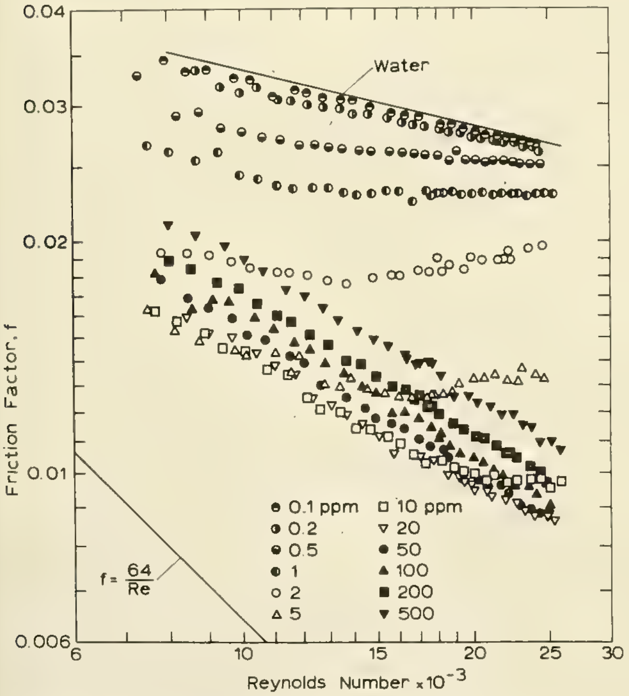

FIGURE 16. Friction factor of Polyox WSR-301 solutions in water as a function of Reynolds number, according to Van der Meulen (1974a).

An explanation of the various phenomena observed can, as yet, not be given. Apparently, some of the phenomena are in agreement with those reported elsewhere, others may not have been observed before. This is mainly due to the fact that numerous studies have been made on drag reduction in turbulent flow, but only a few were made on the influence of polymer additives on laminar flow. In studying laminar flow around circular cylinders, James and Acosta (1970) found that the streamline patterns with dilute polymer solutions were significantly different from those with Newtonian fluids because of viscoelastic effects. These effects may also play a dominant role in eliminating flow separation in those cases that the boundary layer remains laminar. In those cases where the boundary layer becomes turbulent due to the presence of the polymer in the "inner part" of the boundary layer, it is still questionable whether flow separation is eliminated by early turbulence by viscoelastic effects, or by a combination of these. The occurrence of early turbulence as found in the present study and reported before [Van der Meulen (1976a, 1976b), Gates (1977)] is consistent with the findings of others. According to Lumley (1973), polymer solutions producing drag

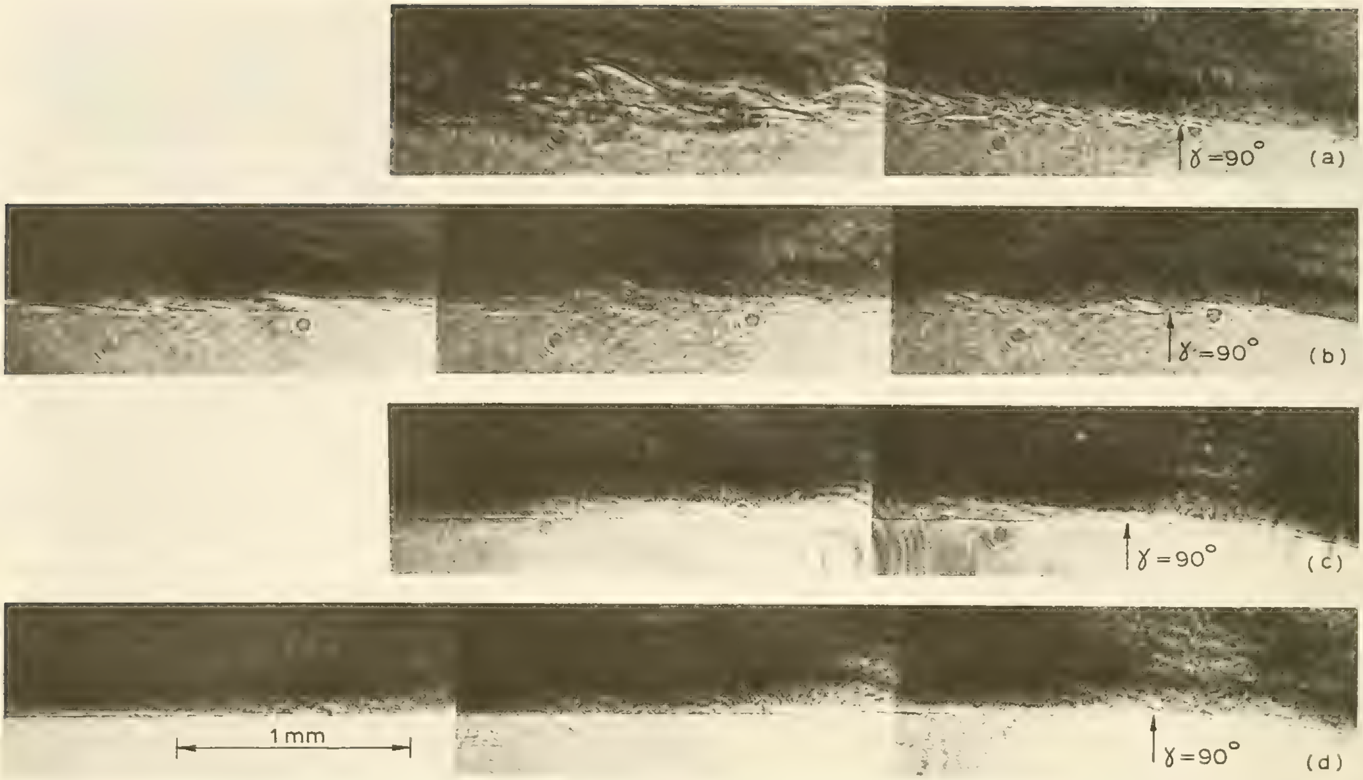

FIGURE 17. Photographs showing boundary layer flow about SST hemispherical nose. The flow is from right to left. V_o = 4 m/s. (a) Injection of 50 ppm Polyox in water. (b) Injection of water in 50 ppm Polyox. (c) Injection of 50 ppm Polyox in 50 ppm Polyox. (d) Injection of 500 ppm Polyox in 50 ppm Polyox.

reduction display a positive Weissenberg effect for which destabilization is predicted analytically. Destabilization is also predicted by the numerical analysis of Kümmerer (1976) on the stability of boundary layers in an idealized viscoelastic fluid. Experiments by Forame et al. (1972) and Paterson and Abernathy (1972) also suggest destabilization. On the other hand, Castro and Squire (1967) and White and McEligot (1970) found that polymer solutions in water cause a delay in transition to turbulence. According to Lumley (1973), drag-reducing polymers tend to increase the thickness of the viscous sublayer. Experimental evidence for this phenomenon has been provided by Rudd (1972), who measured velocity profiles in a polymer solution by using a laser dopplermeter. By examining the expansion behavior of isolated polymer molecules in a flow field, Lumley (1973) postulated a mechanism which predicted a decreased intensity of small-scale turbulence in the buffer layer and which also predicted that, in the maximum drag reduction regime, the turbulence should consist primarily of larger eddies. The present observations of waves and streaks along the surfaces of the models seem in agreement with the above predictions. They also agree with the observations made by Hoyt et al. (1974) on the structure of jets of polymer solution discharged in air.

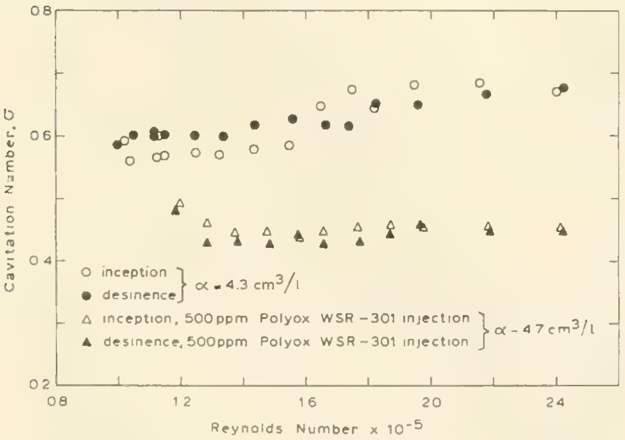

FIGURE 18. Cavitation inception and desinence number as a function of Reynolds number for SST hemispherical nose with and without polymer injection.

4. CAVITATION STUDIES

Inception

Cavitation inception data for the SST hemispherical nose are plotted in Figure 18. Inception was measured by gradually lowering the pressure until the first appearance of cavitation was observed. Desinence was measured by starting from developed cavitation and gradually raising the pressure until cavitation just disappeared. The type of cavitation mostly observed at inception was sheet cavitation. Also plotted in Figure 18 are cavitation inception data when a 500 ppm Polyox WSR-301 solution was injected from the nose of the model. The type of cavitation observed in this case was travelling bubble cavitation. Cavitation inception data for the Teflon hemispherical nose are plotted in Figure

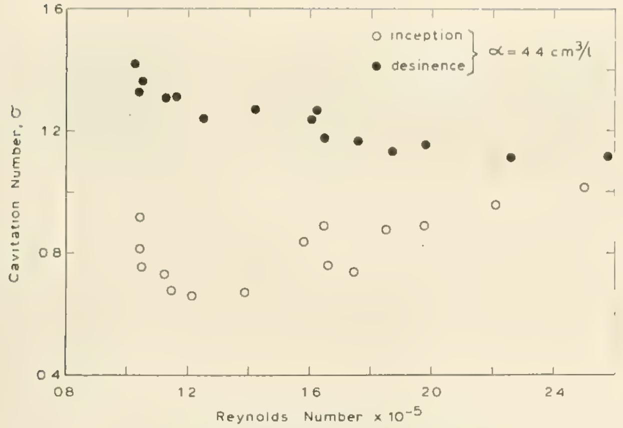

FIGURE 19. Cavitation inception and desinence number as a function of Reynolds number for Teflon hemispherical nose.

19. The type of cavitation observed at inception was spot cavitation. The spots were usually located between the pressure minimum ($\gamma = 78°$) and the transition of hemisphere and cylinder ($\gamma = 90°$). The most striking differences between the inception data for both models are: (a) the inception data for the Teflon model are much higher than for the SST model and (b) the Teflon model exhibits a strong cavitation hysteresis [Holl and Treaster (1966)] whereas the SST model exhibits no hysteresis. Such observations have been reported before by Reed (1969), Gupta (1969), and Van der Meulen (1971). Since the viscous flow behavior of the Teflon model is the same as for the SST model (see Section 3), the above differences can only be explained by surface effects. Teflon is a porous material and has a high contact angle. Both properties are essential features of the Harvey nucleus [Harvey et al. (1944)]. Hence, the Teflon surface acts as a host for surface nuclei, from which (gaseous) cavitation is initiated. The mechanism most probably involved with inception on the SST hemispherical nose has been described by Arakeri (1973). Inception takes place in the transition and reattachment region of the separation bubbles, where high pressure fluctuations occur [Arakeri (1975a)]. The nuclei may either originate from the surface (Arakeri) or from the stream where they become trapped in the strong vortices occurring in the reattachment region.

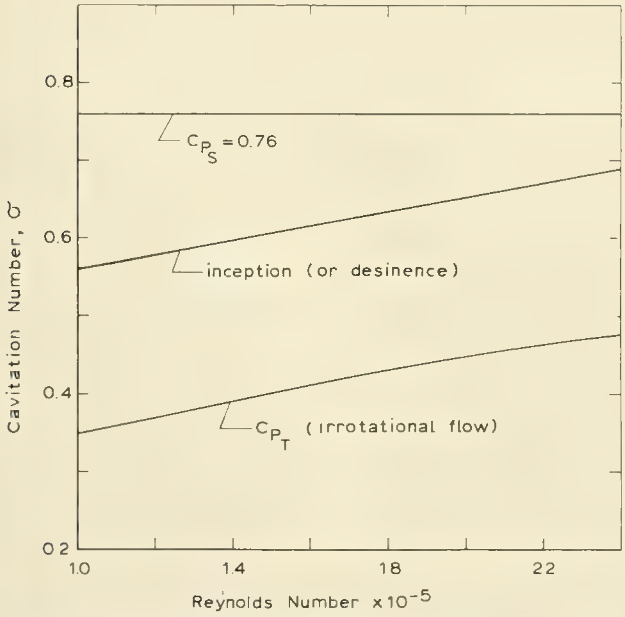

FIGURE 20. Comparison of cavitation inception (or desinence) number with pressure coefficient at separation, C_{P_S}, and at transition, C_{P_T}, for SST hemispherical nose.

When σ_i (or σ_d) for the SST hemispherical nose is to be compared with the pressure coefficient, several problems arise. The most obvious pressure to compare σ_i with would be the pressure coefficient at transition, C_{P_T}, since the onset of cavitation takes place at the location of transition. According to Arakeri (1973), however, the important pressure coefficient to compare σ_i with would be the pressure coefficient at separation, C_{P_S}. This opinion is probably based on the assumption that the pressure within the separation bubble is constant (and thus $C_{P_S} = C_{P_T}$) but, according to Van Ingen (1975), this is a good approximation only at low values of Re. A mean curve of the present inception (and desinence) data is plotted in Figure 20. Also plotted are $C_{P_S} = 0.76$ and C_{P_T} for irrotational flow, derived from Figures 3 and 10 (with $\sigma_a = 7.5$). The real (or viscous) values of C_{P_T} are unknown and should be obtained from pressure measurements. It can be estimated that the real values of C_{P_T} are considerably larger than those for irrotational flow, but still smaller than C_{P_S}. Thus it would seem that σ_i (or σ_d) can be correlated with the real value of C_{P_T}. In that case, it can be argued that the peak pressure fluctuations, measured by Arakeri (1975a), are creating the negative pressures necessary to overcome the stabilizing pressure in stream nuclei, caused by the surface tension.

Cavitation inception data for the blunt nose are plotted in Figure 21. Also plotted are inception data with polymer injection. At inception, a region of travelling bubbles was observed. The approximate location of this region was x/D = 0.2 - 1.0. In Section 4, a further analysis will be given of the type of cavitation occurring. The inception data show that the σ_i-and σ_d-values are almost identical and nearly constant ($\bar{\sigma}_{i,d} = 0.46$, in the absence of polymers). When σ_i is to be compared with a suitable pressure coefficient, the

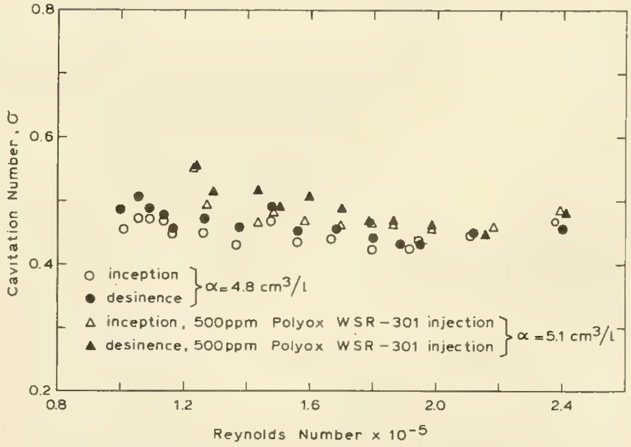

FIGURE 21. Cavitation inception and desinence number as a function of Reynolds number for blunt nose with and without polymer injection.

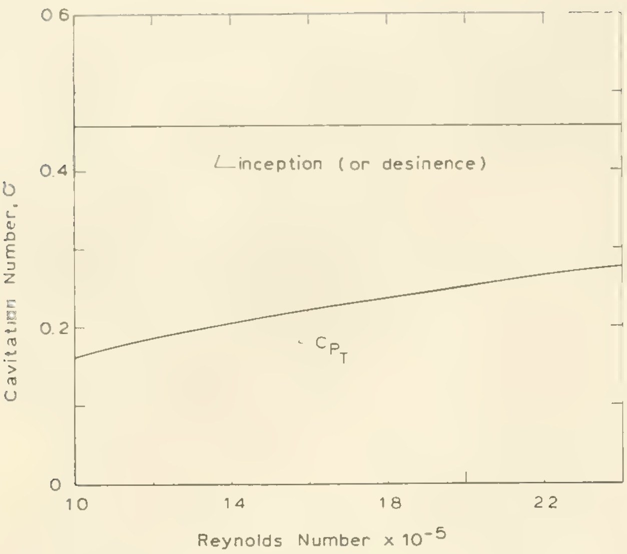

FIGURE 22. Comparison of cavitation inception (or desinence) number with pressure coefficient at transition, C_p, for blunt nose.

best choice would seem the pressure coefficient at the location of cavitation inception. However, this location can not precisely be indicated. For bodies with attached boundary layers, Arakeri (1973) suggested correlating σ_i with the pressure coefficient at transition, C_{P_T}. For a 1.5 caliber ogive a close correlation was found between measured values of σ_d and computed values of C_{P_T}. The same comparison can be made for the blunt nose. In Figure 22, $\bar{\sigma}_{i,d}$ and C_{P_T}, derived from Figures 4 and 14, are plotted against the Reynolds number. In this case it may be assumed that the real (or viscous) values of C_{P_T} are the same as those for irrotational flow. It is evident from Figure 22 that σ_i (or σ_d) cannot be correlated with C_{P_T}. The location where $C_{P_T} = 0.46$ (= $\bar{\sigma}_{i,d}$) is well in the laminar region of the boundary layer for the Reynolds numbers considered.

The influence of polymer additives on cavitation inception is a rather new phenomenon. Darner (1970) investigated the addition of polymers to water on acoustically induced cavitation inception. Ellis et al. (1970) reported on the effect of polymer solutions on flow-generated cavitation inception. The effect of the polymer was to suppress cavitation inception. An explanation for the effect could, as yet, not be given. Ting and Ellis (1974) studied the growth of individual gas bubbles in dilute polymer solutions but concluded that the polymers hardly affected bubble growth. From Figure 23 it is found that the surface tension is slightly reduced by small additions of Polyox WSR-301, but according to Hoyt (1973) this effect should cause earlier cavitation instead of cavitation suppression. From Figure 18, a considerable effect on σ_i and σ_d is found when a 500 ppm Polyox solutuion is injected from the nose of the SST hemispherical model. For Re above 1.2 × 10^5, the reduction amounts to 30 percent. For the mean value of σ_i and σ_d we have $\bar{\sigma}_{i,d} = 0.445$. The σ_i- and σ_d-values are independent of Re. From Figure 21 it is found that σ_i and σ_d are hardly affected by the injection of a 500 ppm Polyox solution from the nose of the blunt model. For Re above 1.2 × 10^5, the mean value of σ_i and σ_d in the absence of polymers is $\bar{\sigma}_{i,d} = 0.45$. Hence, inception on the SST hemispherical nose with polymer injection takes place at the same cavitation number as inception on the blunt nose in the absence of polymers.

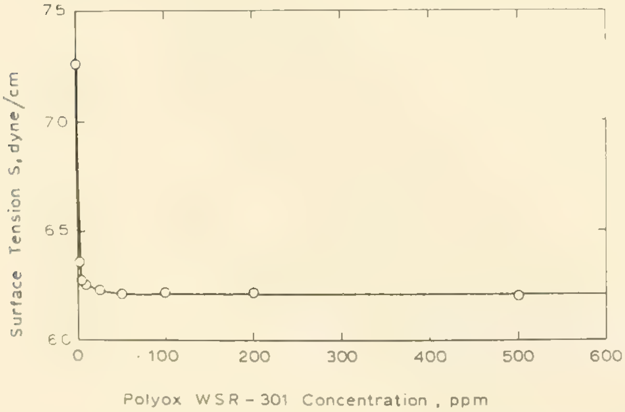

FIGURE 23. Surface tension as a function of Polyox WSR^{T}301 concentration in water, as measured in surface tensionmeter.

As found in Section 3, the influence of the polymer is to suppress the laminar boundary layer separation on the hemispherical nose. Hence, the strong pressure fluctuations, occurring at the position of transition and reattachment of the separated shear layer [Arakeri (1975a)] and being the principal mechanism for cavitation inception, are eliminated and cavitation will start at a much lower cavitation number. The flow visualization studies described in Section 3 do not only explain the suppression of cavitation inception by polymer injection, but also by having a polymer ocean [Ellis et al. (1970)]. Earlier studies by Van der Meulen (1973, 1974b) showed that polymer injection had hardly any effect on cavitation inception on a Teflon hemispherical nose. The reason for this finding is clear now, since cavitation inception on a Teflon hemispherical nose is related to surface effects and not to viscous effects.

Appearance on Hemispherical Models

The appearance of cavitation on the SST hemispherical nose is closely related to the occurrence of laminar boundary layer separation. Arakeri (1973) showed that cavitation bubbles are first observed at the location of transition and reattachment of the separated shear layer. This type of cavitation is usually called bubble cavitation. An example is shown in Figure 24a. The larger bubbles at the location of transition are preceded by smaller ones which, according to Arakeri (1973), are travelling upstream with the reverse flow in the separated region. With a reduction in σ, the larger bubbles create a single cavity as shown in Figure 24b. With a further reduction in σ, the cavity is filling the separated region, and a smooth attached cavity is observed (Figure 24c). This type of cavitation is usually called sheet cavitation. When σ is further reduced, the length and the height of the cavity extend, but the first part of the cavity remains smooth (Figure 24d, e). By analyzing double exposure holograms made of developed cavitation, it could be established that the first smooth part of the cavity is stable.

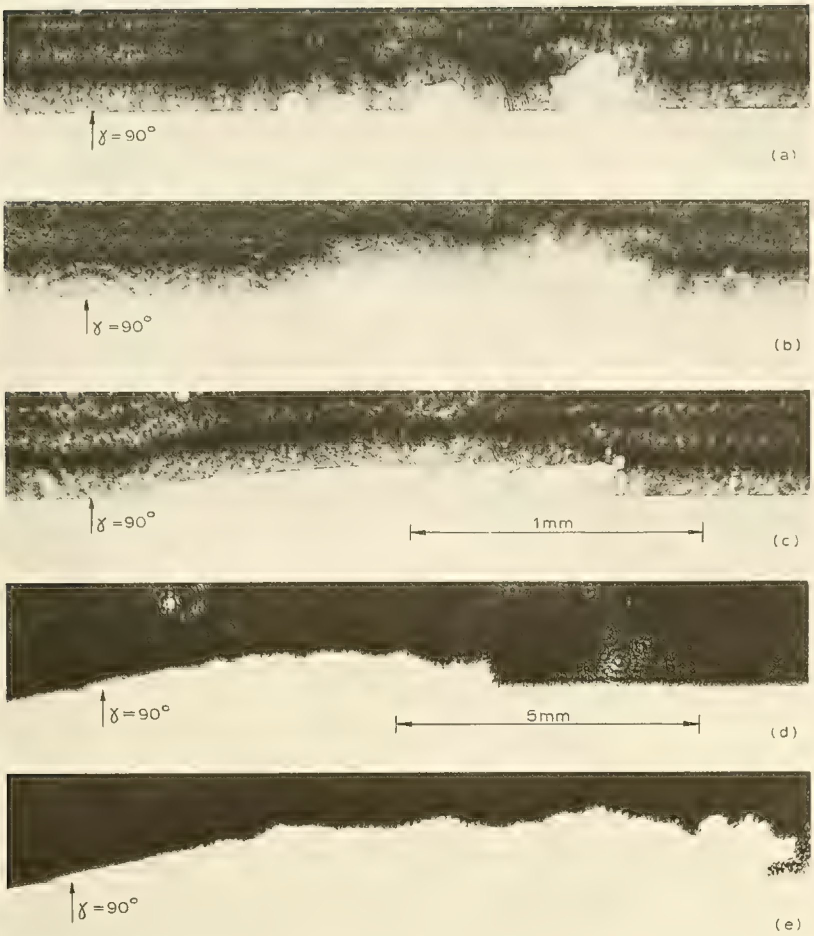

FIGURE 24. Photographs showing progressive development of cavitation on SST hemispherical nose. The flow is from left to right. $V_o = 13.2$ m/s. (a) $\sigma = 0.60$; (b) $\sigma = 0.59$; (c) $\sigma = 0.56$; (d) $\sigma = 0.47$; (e) $\sigma = 0.39$.

The appearance of cavitation on the Teflon hemispherical nose is closely related to the presence of weak spots on the surface. Discrete cavities originate from points located on the hemisphere. The cavities develop cone-shaped in the downstream direction. The first part of the cavity surface is smooth; the cavity leaves the wall at a very small angle. Some of these features can be observed on the photographs presented in Figure 25. The cavitation separation angle γ_{CS} for both hemispherical models is plotted in Figure 26. For the Teflon model it is found that the cavities start upstream of the minimum pressure point ($\gamma_{CS} < \gamma_{P_{min}}$), when σ is sufficiently low. For the SST model it is found that the cavities always start downstream of the minimum pressure point ($\gamma_{CS} < \gamma_{P_{min}}$). γ_{CS} is both a function of σ and Re. For a given Re, γ_{CS} decreases with decreasing σ and for a given σ, γ_{CS} decreases with increasing Re. These tendencies for the SST model are in agreement with the observations by Arakeri (1975b).

The shape of the cavity nose on the SST model has been analyzed further. A schematic drawing of the geometry of the cavity nose is presented in Figure 27. From a detailed study of the holograms it could be established that the cavity nose was circularly shaped. It was found that the nose angle β varied between 70° and 120°, but was independent of σ or Re. An average value of 90° was obtained from 28 cavity noses. Since the cavity nose is immersed in the separation bubble and the flow comes to a standstill near the cavity nose, it is to be expected that the nose angle equals the contact angle for the present liquid-gas-solid system. This is confirmed by the fact that, according to Adamson (1966), the contact angle for a water-air-steel system is 70°-90°. The nose radius r was independent of σ but, as shown in Figure 28, the radius decreases with increasing Re. The length of the sheet cavity (the smooth part preceding the developed cavity) is more or less independent of σ but decreases with increasing Re. In Table 2, mean values of L_{SC}/D are compared with corresponding values of L/D, obtained from Figure 10 (with $\sigma_a = 7.5$). From this table it can be concluded that transition to turbulence on the cavity surface is closely related to transition to turbulence on the fully wetted separated shear layer. The shape of the developed cavity is determined by the total length to maximum height ratio of the cavity, L_C/H_C, (in most cases the cavity reached its maximum height close to the trailing edge of the cavity). Values of this ratio are given in Figure 29. The mean value of L_C/H_C is 10.2. Since the mean value of the length to height ratio of the separation bubble is 10.8, it may be concluded that the shape of the developed cavity appearing on the SST hemispherical nose is strongly governed by the shape of the separation bubble.

With polymer injection, the cavities on the SST hemispherical nose are either attached or may show the appearance of travelling bubbles, resembling the type of cavitation observed on the blunt nose. Details are given by Van der Meulen (1976b).

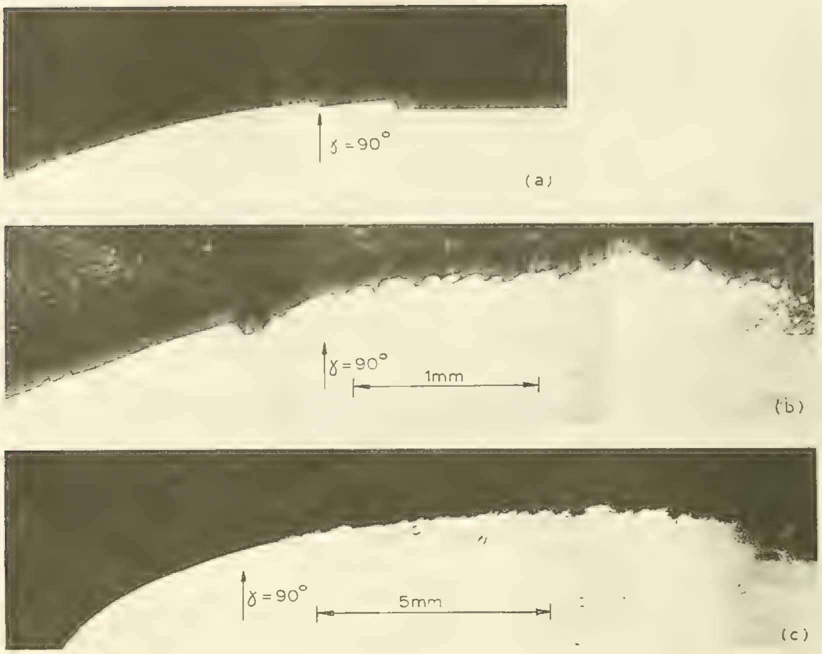

FIGURE 25. Photographs showing progressive development of cavitation on Teflon hemispherical nose. The flow is from left to right. V_0 = 13.2 m/s. (a) σ = 0.96; (b) σ = 0.63; (c) σ = 0.40.

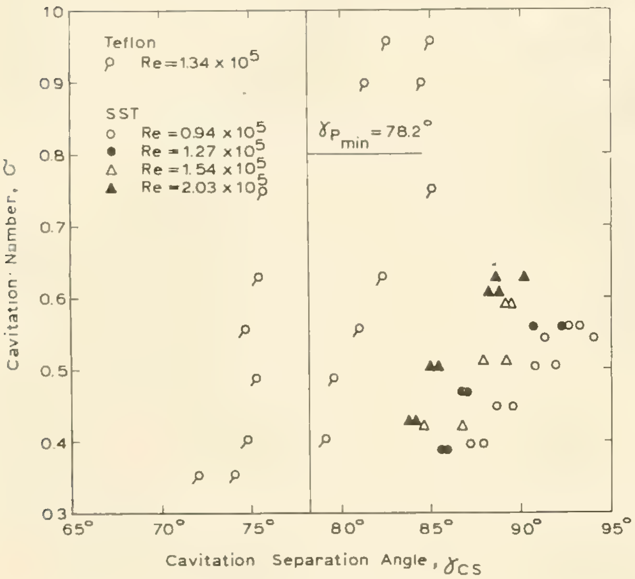

FIGURE 26. Cavitation separation angle, γ_{CS}, as a function of cavitation number and Reynolds number for hemispherical nose.

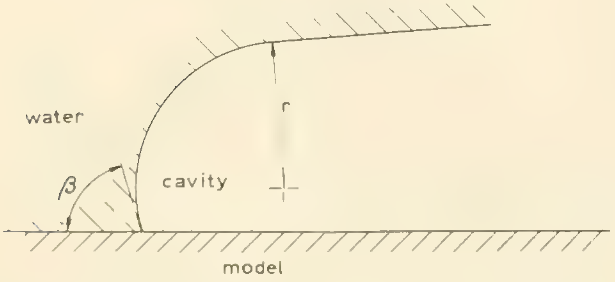

FIGURE 27. Schematic diagram of cavity nose on SST hemispherical model.

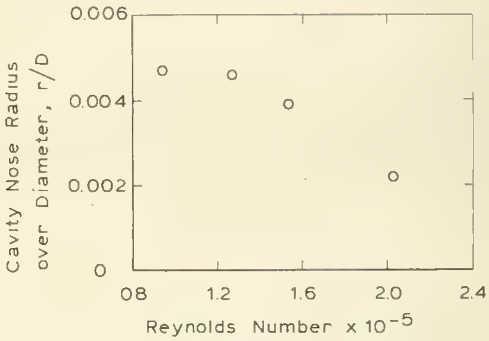

FIGURE 28. Cavity nose radius over diameter, r/D, as a function of Reynolds number for SST hemispherical model.

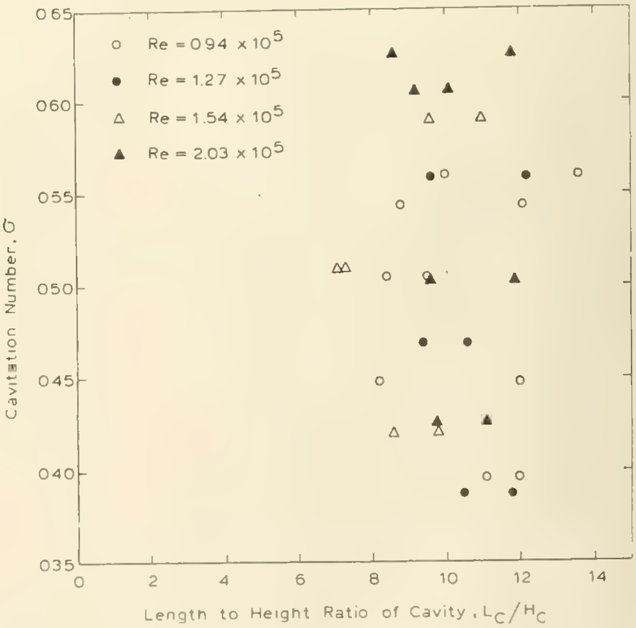

FIGURE 29. Total length to maximum height ratio of cavity, L_C/H_C, as a function of cavitation number and Reynolds number for SST hemispherical nose.

TABLE 2. Length of Sheet Cavity Over Diameter, L_{SC}/D, and length of Separation Bubble Over Diameter, L/D, for SST Hemispherical Nose.

Re × 10^{-5}	L_{SC}/D	L/D
0.94	0.156	0.124
1.27	0.124	0.096
1.54	0.070	0.084
2.03	0.074	0.068

Appearance on Blunt Model

The type of cavitation occurring on the blunt nose is typically travelling bubble cavitation. An example is shown in Figure 30a (σ = 0.33). When σ is reduced, a single transient cavity may develop, as shown in Figure 30b (σ = 0.28). The transient character of the cavities occurring on the blunt nose is clearly observed in the photographs taken from multiple exposure holograms. Figure 31 shows a photograph taken from a hologram, where three pulses were generated by the ruby laser with pulse separations of 50 μsec and 100 μsec respectively. The flow is from right to left. The picture shows the growth of a cavity near the nose of the model. The cavity is attached to the model and its shape is a spherical segment. The cavity grows (its radius increases) and, at the same time, travels along the surface with a velocity slightly below that of the surrounding fluid. When the cavity reaches a certain height, its shape becomes more like an attached bubble, as shown in Figure 32. In this figure, the flow is from left to right. The attached bubble hardly grows, travels along the surface, and finally collapses.

The streamwise distance to cavitation separation on the blunt nose obtained from a series of holograms taken at various values of σ and Re, is plotted in Figure 33. Also plotted are data points where no cavitation was observed in the hologram on either one or both sides of the model. It is found that the streamwise distance to cavitation separation decreases with increasing Re (apart from the scatter, typical for travelling bubble cavitation). For Re = 2.08 × 10^5, cavitation separation is located at a short distance from the pressure minimum [$(s/D)_{P_{min}}$ = 0.37].

The observations of the cavity growth as represented in Figure 31, enables a comparison with theory. Plesset (1949) analyzed experimental observations by Knapp and Hollander (1948) and compared the growth and collapse of bubbles on a 1.5 caliber ogive with the equation of motion for a bubble. The agreement was quite satisfactory. Recently, Persson (1975) introduced some refinements in the comparison. The present analysis is based on the so-called Rayleigh-Plesset equation according to Hsieh (1965). For a vapor bubble, the motion of the bubble wall is given by the equation

$$\rho\left(R\ddot{R} + \frac{3}{2}\dot{R}^2\right) = P_v - P - \frac{2S}{R} - \frac{4\mu\dot{R}}{R} \qquad (6)$$

where ρ is the liquid density, R the instantaneous bubble radius, P_v the vapor pressure, P the instantaneous ambient pressure, S the surface tension, and μ the dynamic viscosity. The dots indicate differentiation with respect to time t. The multiple exposure hologram (Figure 31) provided data on $R_0(t_0)$, R_1 $(t_0+50\mu s)$, and R_2 $(t_0+150\mu s)$, whereas P(t) could be derived from Figures 31 and 4. Equation (6) was solved numerically to obtain a theoretical value of R_2. The results of the computations are given in Table 3. To compare the significance of the right-hand side terms of Eq. (6), numerical values of these terms are presented in Table 4. The main conclusion to be derived from Table 3 is that the experimentally observed growth of the cavity on the blunt nose is fairly well represented by the Rayleigh-Plesset equation of motion. This is mainly due to the fact that the blunt nose does not exhibit laminar flow separation and viscous effects seem to be small.

The appearance of developed cavitation on the blunt nose with polymer injection was essentially the same as that without polymers. Details are given by Van der Meulen (1976b).

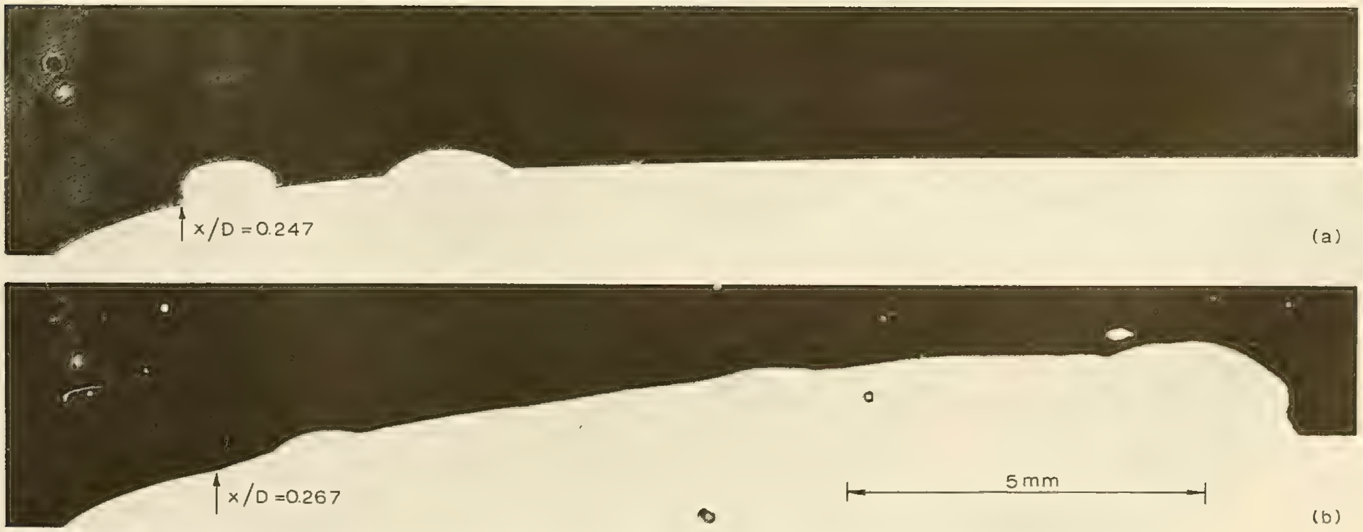

FIGURE 30. Photographs showing cavitation on blunt nose. The flow is from left to right. V_o = 12.8 m/s. (a) σ = 0.33; (b) σ = 0.28.

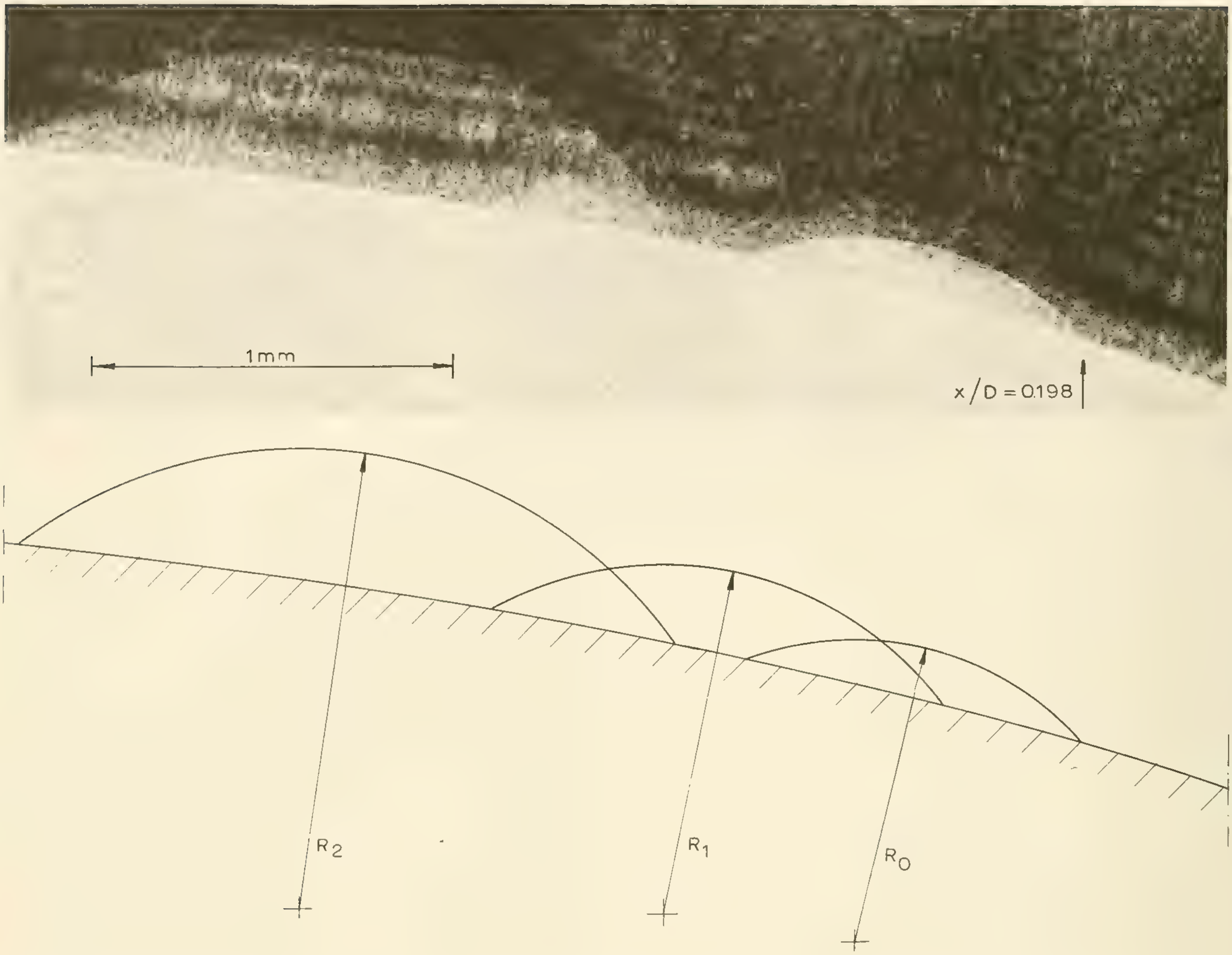

FIGURE 31. Photograph of multiple exposure hologram showing three stages of cavity growth near nose of blunt model. The pulse separations are $\Delta t_1 = 50$ μsec and $\Delta t_2 = 100$ μsec. The flow is from right to left. $V_o = 10$ m/s; $\sigma = 0.31$. The radii of the growing cavity are indicated on the lower figure.

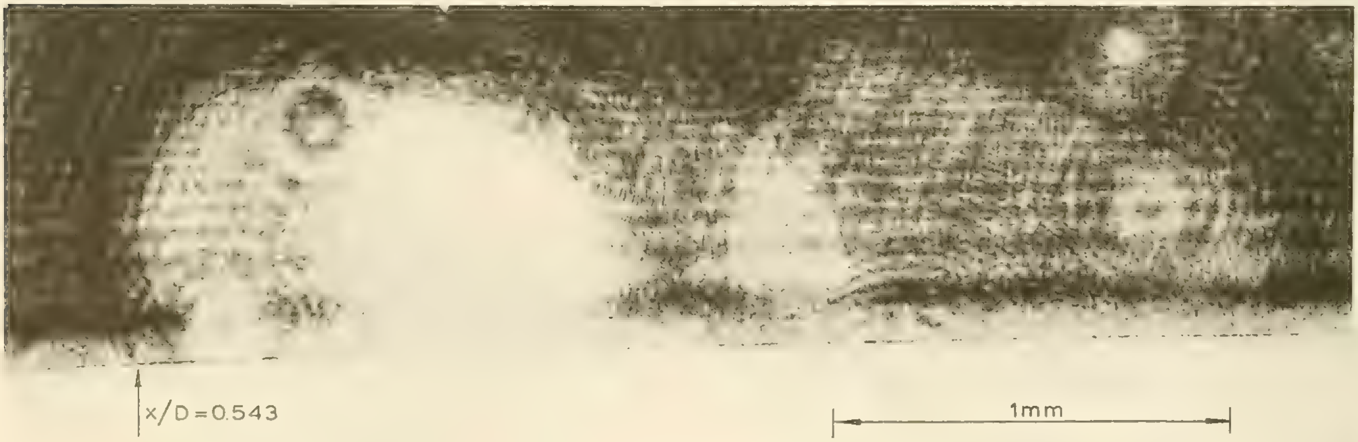

FIGURE 32. Photograph of multiple exposure hologram showing three stages of travelling bubble along blunt nose. The time separations are: $\Delta t_1 = 50$ μsec and $\Delta t_2 = 100$ μsec. The flow is from left to right. $V_o = 10$ m/s; $\sigma = 0.31$.

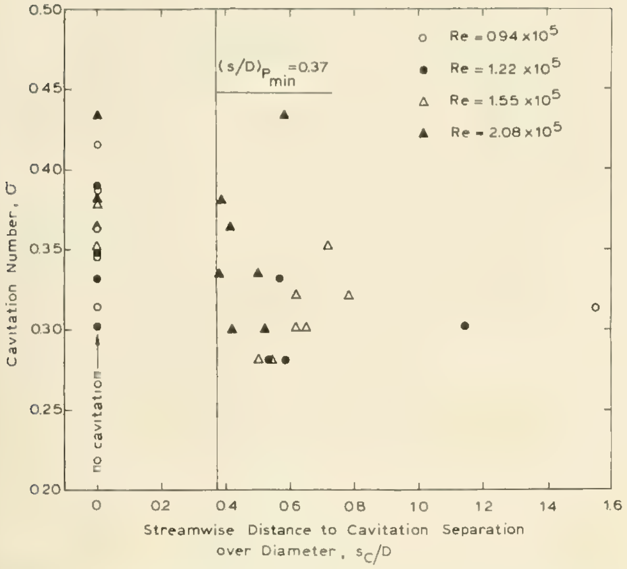

FIGURE 33. Streamwise distance to cavitation separation over diameter, s_C/D, as a function of cavitation number and Reynolds number for blunt nose. Also plotted are some data points where no cavitation was observed on one or both sides of the model.

5. CONCLUSIONS

The application of in-line holography and injection of a 2 percent sodium chloride solution from the nose of the axisymmetric bodies are useful methods to visualize the boundary layer and to obtain detailed information on boundary layer phenomena and cavitation patterns.

Laminar boundary layer separation and transition to turbulence of the separated shear layer on the hemispherical nose can be predicted quite accurately by existing approximate calculation methods.

Cavitation on axisymmetric bodies may be strongly influenced by boundary layer effects. For the SST hemispherical nose, inception and appearance of cavitation are both related to the location and appearance of the separation bubble. For the blunt nose, however, cavitation is apparently more related to nuclei effects than to viscous effects. The type of cavitation occuring in this case is travelling bubble cavitation. The growth of a cavity on the blunt nose is adequately described by the Rayleigh-Plesset equation of motion for a cavitation bubble.

TABLE 3. Theoretical (R) and Experimental (R_{exp}) Values of Bubble Radius for Cavity Growth on Blunt Nose (Figure 31).

t	$\ddot{R}$ m/sec^2	$\dot{R}$ m/sec	R mm	R_{exp} mm
t_o	-5710	2.93	0.84	0.84
t_o + 50 μs	-5290	2.66	0.98	0.98
t_o + 150 μs	-4540	2.17	1.23	1.28

TABLE 4. Influence of Vapor Pressure, P_V, Liquid Pressure, P, Surface Tension Pressure, 2 S/R, and Viscosity Pressure, $4\mu\,\dot{R}/R$, on Cavity Growth on Blunt Nose (Figure 31).

t	P_V N/m^2	P N/m^2	2 S/R N/m^2	$4\mu\,\dot{R}/R$ N/m^2
t_o	1940	-6320	170	15
t_o + 50 μs	1940	-3590	150	12
t_o + 150 μs	1940	+ 330	120	8

Surface effects on the Teflon hemispherical nose play a dominant role in both inception and appearance of cavitation.

The presence of polymers in the "inner part" of the boundary layer on the SST hemispherical nose leads to destabilization, whereas the presence of the polymer in the "outer part" of the boundary layer leads to stabilization, and the latter effect is predominant. For all cases considered, laminar boundary layer separation is suppressed.

Since the influence of polymer additives is to suppress laminar boundary layer separation on the hemispherical nose, the strong pressure fluctuations, occurring at the position of transition and reattachment of the separated shear layer and being the principal mechanism for cavitation inception, are eliminated and cavitation will start at much lower pressures. As a consequence, the cavitation characteristics of the SST hemispherical nose with polymer injection are approximately the same as those of the blunt nose without polymer injection.

NOTATION

B	Constant in Equation (3)
C_P	Pressure coefficient
$C_{P_{min}}$	Minimum pressure coefficient
C_{P_S}	Pressure coefficient at separation
C_{P_T}	Pressure coefficient at transition
D	Model diameter
H	Height of separation bubble
H_C	Height of cavity
L	Length of separation bubble
L_C	Length of cavity
L_{SC}	Length of sheet cavity
P	Static pressure
P_o	Free stream static pressure
P_{min}	Minimum static pressure
P_V	Vapor pressure
R	Bubble radius
Re	Reynolds number, V_oD/ν
$Re_{\theta sep}$	Equation (4)
S	Surface tension
Tu	Turbulence level
U	Velocity at edge of boundary layer
V_o	Free stream velocity
V_i	Injection velocity
a	Amplitude of disturbance
$a_{neutral}$	Amplitude of disturbance at neutral stability
f	Friction factor
m	Equation (2)
r	Nose radius of cavity

s	Surface coordinate
s_C	Streamwise distance to cavitation separation
s_T	Streamwise distance to boundary layer transition
x	Axial coordinate
α	Air content
β	Nose angle of cavity
γ	Angular coordinate
γ_S	Boundary layer separation angle
γ_{CS}	Cavitation separation angle
δ	Angle at which separation streamline leaves wall
θ	Momentum thickness
μ	Dynamic viscosity
ν	Kinematic viscosity
ρ	Liquid density
σ	Cavitation number, $(P_o-P_v)/\frac{1}{2}\rho V_o^2$
σ_i	Incipient cavitation number
σ_d	Desinent cavitation number
σ_a	Amplification factor
ϕ	Velocity potential

REFERENCES

Acosta, A. J. (1974). Cavitation and fluid machinery. *Cavitation Conf.*, Edinburgh, Scotland.

Adamson, A. W. (1966). *Physical chemistry of surfaces.* Interscience Publishers, New York.

Arakeri, V. H. (1973). Viscous effects in inception and development of cavitation on axisymmetric bodies. *Cal. Inst. Tech. Rep. E-183-1.*

Arakeri, V. H. (1975a). A note on the transition observations on an axisymmetric body and some related fluctuating wall pressure measurements. *J. Fluids Engng., Trans. A.S.M.E. 97*, 82.

Arakeri, V. H. (1975b). Viscous effects on the position of cavitation separation from smooth bodies. *J. Fluid Mech. 68*, 779.

Arakeri, V. H. (1977). Experimental investigation of laminar boundary layer stability with surface heating and cooling. *N.S.M.B. Rep. 01054-2-CT.*

Arakeri, V. H., and A. J. Acosta (1973). Viscous effects in the inception of cavitation on axisymmetric bodies. *J. Fluids Engng., Trans. A.S.M.E. 95*, 519.

Arndt, R. E. A., and A. T. Ippen (1968). Rough surface effects on cavitation inception. *J. Basic Engng., Trans. A.S.M.E. 90*, 249.

Castro, W., and W. Squire (1967). The effect of polymer additives on transition in pipe flow. *Appl. Scientific Res. 18*, 81.

Darner, C. L. (1970). Sonic cavitation in water. *N. L. R. Rep. 7131.*

Dobbinga, E., J. L. van Ingen, and J. W. Kooi (1972). Some research on two-dimensional laminar separation bubbles. *AGARD CP-102*, Lisbon.

Ellis, A. T., J. G. Waugh, and R. Y. Ting (1970). Cavitation suppression and stress effects in high-speed flows of water with dilute macromolecule additives. *J. Basic Engng., Trans. A.S.M.E. 92*, 405.

Forame, P. C., R. J. Hansen, and R. C. Little (1972). Observations of early turbulence in the pipe flow of drag reducing polymer solutions. *A.I.Ch.E. Journal 18*, 213.

Gates, E. M. (1977). The influence of freestream turbulence freestream nuclei populations and a drag-reducing polymer on cavitations inception on two axisymmetric bodies. *Cal. Inst. Tech. Rep. E-183-2.*

Gupta, S. K. (1969). The influence of porosity and contact angle on incipient and desinent cavitation. *M.S. thesis, Pennsylvania State University.*

Harvey, E. N., D. K. Barnes, W. D. McElroy, A. H. Whiteley, D. C. Pease, and K. W. Cooper (1944). Bubble formation in animals. *J. Cellular and Comparative Physiology 24*, 1.

Holl, J. W. (1960). The inception of cavitation on isolated surface irregularities. *J. Basic Engng., Trans. A.S.M.E. 82*, 169.

Holl, J. W., and A. L. Treaster (1966). Cavitation hysteresis. *J. Basic Engng., Trans. A.S.M.E. 88*, 199.

Hoyt, J. W. (1973). Jet cavitation in polymer solutions. *A.S.M.E. Cavitation and Polyphase Flow Forum*, 44.

Hoyt, J. W., J. J. Taylor, and C. D. Runge (1974). The structure of jets of water and polymer solution in air. *J. Fluid Mech. 63*, 635.

Hsieh, D. Y. (1965). Some analytical aspects of bubble dynamics. *J. Basic Engng., Trans. A.S.M.E. 87*, 991.

James, D. F., and A. J. Acosta (1970). The laminar flow of dilute polymer solutions around circular cylinders. *J. Fluid Mech. 42*, 269.

Knapp, R. T., and A. Hollander (1948). Laboratory investigations of the mechanism of cavitation. *Trans. A.S.M.E. 70*, 419.

Kümmerer, H. (1976). Numerische Untersuchungen zur Stabilität laminarer Grenzschichten in viskoelastischen Flüssigkeiten. *Rheol. Acta 15*, 579.

Labrujère, Th.E. (1976). Berekening van de wandinvloed voor twee lichamen in een watertunnel. *National Aerospace Laboratory Rep. NLR TR 76017 L.*

Labrujère, Th.E., and J. van der Vooren (1974). Finite element calculation of axisymmetric subcritical compressible flow. *National Aerospace Laboratory Rep. TR 74162 U.*

Lumley, J. L. (1973). Drag reduction in turbulent flow by polymer additives. *Macromolecular Reviews 7*, 263.

Paterson, R. W., and F. H. Abernathy (1972). Transition to turbulence in pipe flow for water and dilute solutions of polyethylene oxide. *J. Fluid Mech. 51*, 177.

Persson, B. O. (1975). Reconsideration of a problem in cavitation bubble dynamics. *J. Appl. Mech., Trans. A.S.M.E. 42*, 736.

Plesset, M. S. (1949). The dynamics of cavitation bubbles. *J. Appl. Mech., Trans. A.S.M.E. 16*, 277.

Reed, R. L. (1969). The influence of surface characteristics and pressure history on the inception of cavitation. *M. S. thesis, Pennsylvania State University.*

Rouse, H., and J. S. McNown (1948). Cavitation and pressure distribution; head forms at zero angle of yaw. *State University of Iowa, Eng. Bull. 32.*

Rudd, M. J. (1972). Velocity measurements made with a laser dopplermeter on the turbulent pipe flow of a dilute polymer solution. *J. Fluid Mech. 51*, 673.

Schiebe, F. R. (1972). Measurement of the cavitation susceptibility of water using standard bodies. *St. Anthony Falls Hydraulic Lab. Rep. 118.*

Schlichting, H. (1965). *Grenzschicht-Theorie*, Verlag G. Braun, Karlsruhe.

Silberman, E., F. R. Schiebe, and E. Mrosla (1973).

The use of standard bodies to measure the cavitation strength of water. *St. Anthony Falls Hydraulic Lab. Rep. 141*.

Thwaites, B. (1949). Approximate calculation of the laminar boundary layer. *Aero. Quart. 1*, 245.

Ting, R. Y., and A. T. Ellis (1974). Bubble growth in dilute polymer solutions. *Phys. of Fluids 17*, 1461.

Van der Meulen, J. H. J. (1971). Cavitation on hemispherical nosed teflon bodies. *IUTAM Symposium*, Leningrad.

Van der Meulen, J. H. J. (1972). Incipient and desinent cavitation on hemispherical nosed bodies. *Int. Shipb. Progress 19*, 21.

Van der Meulen, J. H. J. (1973). Cavitation suppression by polymer injection. *A.S.M.E. Cavitation and Polyphase Flow Forum*, 48.

Van der Meulen, J. H. J. (1974a). Friction reduction and degradation in turbulent flow of dilute polymer solutions. *Appl. Scientific Res. 29*, 161.

Van der Meulen, J. H. J. (1974b). The influence of polymer injection on cavitation. *Cavitation Conf.*, Edinburgh, Scotland.

Van der Meulen, J. H. J. (1976a) Holographic study of polymer effect on cavitation. *A.S.M.E. Cavitation and Polyphase Flow Forum*, 4.

Van der Meulen, J. H. J. (1976b). A holographic study of cavitation on axisymmetric bodies and the influence of polymer additives. *Ph.D. thesis*, Enschede.

Van der Meulen, J. H. J., and N. B. Oosterveld (1974). A holographic study of cavitation inception on a hemispherical nosed body. *Symp. High Powered Propulsion of Large Ships*, Wageningen.

Van der Meulen, J. H. J., and H. J. Raterink (1977). Flow visualization of boundary layers in water by in-line holography. *Int. Symp. on Flow Visualization*, Tokyo.

Van Ingen, J. L. (1975). On the calculation of laminar separation bubbles in two-dimensional incompressible flow. *AGARD, CP-168*, Göttingen.

Van Ingen, J. L. (1976). Transition, pressure gradient, suction, separation and stability theory. *Workshop Rand Corporation*, Santa Monica.

White, W. D., and D. M. McEligot (1970). Transition of mixtures of polymers in a dilute aqueous solution. *J. Basic Engng., Trans. A.S.M.E. 92*, 411.

Mechanism and Scaling of Cavitation Erosion

Hiroharu Kato
University of Tokyo

Toshio Maeda
Mitsubishi Heavy Industries Ltd.

Atsushi Magaino
University of Tokyo

Tokyo, Japan

ABSTRACT

Recently cavitation erosion has been primarily treated experimentally. However a need exists for both a theoretical cavitation erosion model and more quantitative erosion test methods. As a contribution to the state of the art, the authors have summarized their research at the University of Tokyo using the soft surface erosion test method (the aluminum erosion test).

Two test series were completed, the first using the NACA 16021 foil section and the second using the NACA 0015 foil section. Two-dimensional erosion tests were systematically made at various velocities and cavitation numbers to obtain a correspondence between the erosion and the hydrodynamic characteristics of the cavitation pattern. It was found that the estimation of the cavity length and its fluctuation are important factors in the prediction of the cavitation erosion.

The results of these tests are used to illustrate the effectiveness of Mean Depth of Deformation Rate, MDDR, as a Cavitation Erosion Index. These test results also served as a background for extending the cavitation erosion scaling theory, previously proposed by Kato, to include differences in the cavitation number.

After determining two empirical constants, the resulting predicted MDDR Cavitation Index was shown to be in good agreement with both Thiruvengadam's (1971) and the authors' test results.

In addition to this basic research, two additional studies are summarized. The first is a comparative test of the aluminum erosion test and the paint test and the second is a study in the influence of air injection in reducing the cavitation erosion intensity. The test results obtained from the paint and aluminum tests were found to be in good agreement and for routine cavitation erosion checks, the paint test should be adequate. It was found that small, air injection rates reduced the cavitation erosion intensity dramatically and large injection rates did not result in substantial reduction of the cavitation erosion intensity.

1. INTRODUCTION

Erosion is one of the largest problems caused by cavitation. Cavitation tests of model propellers have been made for the purpose of predicting cavitation erosion, especially for low-speed merchant ships. However, the prediction was mainly based on the observer's "feeling" of the cavitation pattern on the propeller blade. Recently a new testing method, i.e., paint test, was developed at several laboratories [Sasajima (1972) and Lindgren and Bjärne (1974)]. In this test the erosion intensity is judged by the area of paint peeled off.

At the University of Tokyo in the authors' laboratory, erosion tests of soft aluminum test pieces have been made for several years [Sato et al. (1974) and Sato (1976)]. The main purpose for developing the soft aluminum method are:

(1) Development of a quantitative prediction method for cavitation erosion.
(2) Obtain a deeper insight into the mechanism of cavitation erosion by the observation of eroded metal surface.
(3) Establishment of cavitation erosion scaling laws.

The test piece is usually made of pure aluminum, which is easy to obtain, has stable quality, good machinability, and is relatively cheap. Its mechanical properties can be roughly established by hardness and tensile tests. The erosion resistance of pure aluminum is very low and its surface is roughed by cavitation attack within one half hour of test exposure which is similar to the testing time of the paint test. The increase in roughness is a first indication of erosion [e.g., Young and Johnston (1969)]. It can be measured by a roughness tester and the quantitative erosion intensity can be obtained with sufficient accuracy.

Micro-appearances of the eroded surface such as the pit shape, can also be qualified by examination of roughness records and microscopic pictures of the surface.

The erosion intensity has been evaluated by mean depth of penetration (MDP) [e.g., Hammitt (1969)], or energy absorbed by the material eroded [e.g., Thiruvengadam (1966)]. In addition one of the authors recently proposed a new concept of erosion intensity, mean depth of deformation (MDD) which functions as a bridge between surface roughness, SR, and MDP [Kato (1975)]. Thus MDD corresponds to SR at the initial stage and MDP at the final stage of erosion.

This paper discusses the experimental results of two-dimensional aluminum foil sections (pure and aluminum alloy), various considerations of the erosion mechanism in connection with the hydrodynamic characteristics of the foil section along with the modeling and scaling of erosion, and summarizes experiments using an air injection system which the authors found very effective in cavitation erosion preventation. Nomenclature is shown at the end of this paper.

2. FOIL SECTION EROSION TEST

High Speed Cavitation Tunnel at University of Tokyo

Erosion tests of two-dimensional foil sections were made using a high speed cavitation tunnel at University of Tokyo. The test sections of this tunnel can be changed according to the experiment. For the present test two test sections were used. One was the rectangular high speed section with cross section dimensions of 100mm × 10mm. Test Series I was carried out using this section in 1976. Since the side wall effect was so large that the two-dimensionality of the flow was almost lost near the trailing edge of the foil section, it was concluded that the 10mm width was too narrow. Therefore the test section was modified to a 80mm × 15mm cross section prior to starting Test Series II in 1977. The maximum velocity of the section was about 50m/s.

The second test section was the rectangular low-speed section used only in Test Series II (1977). It has cross section dimensions of 120mm × 25mm and a maximum velocity of 35m/s.

Foil Section

Two foil sections (NACA 16021 and NACA 0015) were tested. The NACA 16021 foil section used in Test Series I (1976), was the same foil section used in Kohl's experiment [Kohl (1968)]. Kohl made his tests at an attack angle of $\alpha = 0°$. Since this foil section has no camber, when it is set at $\alpha = 0°$, the inception point of cavity appears around 60% chord. Thus, testing at $\alpha = 0°$ was not suitable for cavitation erosion tests, so the authors chose a test condition of $\alpha = 4°$. Since its chord and span are 40mm and 10mm respectively, the aspect ratio $\Lambda = 0.25$, was so small that the spanwise pattern of the cavity was not uniform. The cavity closed at midspan appearing as a kind of streak cavitation. Another disadvantage of using the NACA 16021 section is its chordwise pressure distribution which is the "roof-top" type. The cavity length drastically changes with only slight changes in the cavitation number. While this characteristic is desirable in practical applications, it was found to be undesirable in the present study since erosion would occur only in a narrow range of cavitation numbers which makes the experiment difficult.

Therefore prior to starting Test Series II in 1977, two major improvements were made. From wind tunnel tests the minimum aspect ratio necessary to maintain two-dimensional flow was found to be about $\Lambda = 0.4$ and an aspect ratio, $\Lambda = 0.5$, was chosen for Test Series II. The smaller foil was designed with a 30mm chord and a 15mm span and the larger foil section was designed with a 50mm chord and a 25mm span.

The second improvement was to change the foil section, from the NACA 16021 to the older NACA 0015, which has a chordwise pressure distribution of the "triangular" type. The experimental chordwise pressure distribution of this foil is compared in Figure 1 with the calculated pressure values. It can be seen that the agreement between the experiment and calculation is satisfactory.

Test Condition

In Test Series I (NACA 16021) the following items were tested:

(1) Relationships between the mean depth of deformation (MDD), mean depth of penetration (MDP), and surface roughness (SR).
(2) Effect of cavitation number, velocity, and the water's air content on the erosion intensity.
(3) Comparison between the results obtained by the soft aluminum erosion test and paint test.
(4) Influence of air injection on erosion prevention.

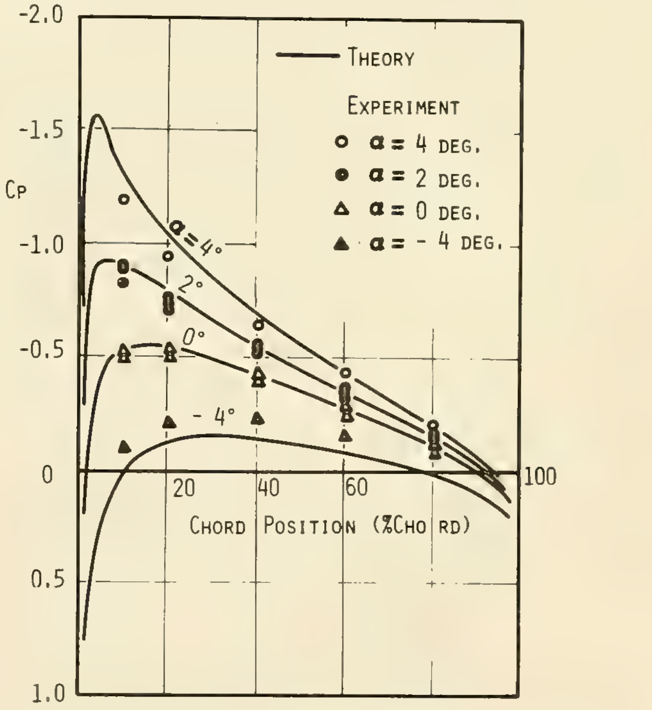

FIGURE 1. Comparison of suction side Cp for NACA 0015 foil section.

In Test Series I, the size and material of the foil section were not changed. The material was pure aluminum, JIS H2102-2 (AL > 99.5%).

In Test Series II (NACA 0015) the following items were tested.

(1) Effect of cavitation number, velocity, and chord length, and the hydrodynamic characteristics of the cavity flow, on the erosion intensity.

(2) Effect of material properties on the erosion intensity.

(3) Comparison of the soft aluminum and paint test results.

The test conditions are summarized in Table 1. The attack angle was $\alpha = 4°$ throughout Test Series I and II. In Test Series I, the air content was $\alpha/\alpha_s = 0.5$, while in Test Series II it was initially 0.2 and increased gradually during the experiment to a value of 0.4 by the end of the experiment.

In Test Series I-D, before the test began, air bubbles were injected into the cavitation tunnel to control air bubble content of the water. Then, the erosion test was completed to study the effect of air content on erosion.

Experiments with air injection from the foil surface were also carried out to study the positive utilization of erosion prevention effect of air bubbles.

At the start of the tests, the water temperature was about 25°C which increased during the high speed tests, reaching a maximum temperature of 50°C.

In addition to the erosion tests, measurements of the hydrodynamic characteristics such as cavity length, pressure distribution etc., were completed using a similar foil section made of stainless steel.

Material and Heat Treatment

In Test Series I the foil section material was pure aluminum (JIS H2102, 99.5%), while in Test Series II pure aluminum and two kinds of aluminum alloy, JIS H4163-2 (AA 5056) and JIS H4163-5 (AA 6063) were used. These materials were selected for their low erosion resistance, good corrosion resistance, and good machinability. The foil sections tested were machined by a NC-milling machine and the surface was smoothed by a buffing machine. The foils' surface roughness was found to be less than 1 μm in the virgin state.

Since the foil surface was work-hardened, a thin layer of the foil surface had a large degree of

Table 1 Experimental Conditions

	Series I NACA 16021 Foil Section				
	A	B	C	D	E
Purpose	Cav. No. & Flow Vel.		Duration	Air Cont.	Air Inject.
Foil Size	Chord 40mm, Span 10mm				
Material JIS*	Pure Aluminum H2102-2				
Attack Angle	4 deg.				
Flow Velocity	41.7 m/s	32.6 m/s	41.0 m/s	41.7 m/s	41.9 m/s
Cavitation Number	0.27 ∿0.51	0.27 ∿0.47	0.45	0.443	0.438
Exposure Time	60 min		9 hr	60 min	
Air Content	8∿10 ppm (α/α_s** = 0.4∿0.5)			8∿62 ppm	Air Inject.

	Series II NACA 0015 Foil Section				
	A	B	C	D	E
Purpose	Size, Vel., Cav. No. and Material				
Foil Size	Chord 50mm Span 25mm	Chord 30 mm, Span 15 mm			
Material JIS (AA)*	Pure Aluminum H2102-2			Aluminum Alloy H4163-5 (6063)	 H4163-2 (5056)
Attack Angle	4 deg.				
Flow Velocity	35.0 m/s		45.0 m/s		
Cavitation Number	0.716 ∿0.958	0.555 ∿1.119	0.810 ∿0.965	0.722 ∿0.916	0.722 ∿0.916
Exposure Time	30 min				
Air Content	4∿8 ppm (α/α_s** = 0.2∿0.4)				

* JIS : Japanese Industrial Standards

AA : The Aluminum Association

** α_s : Saturated Air Content at 25°, 1 ata.

Table 2 Chemical Composition and Mechanical Properties

		Pure Aluminum	Aluminum Alloy	
		JIS H2102-2	JIS H4163-5 (AA 6063)	JIS H4163-2 (AA 5056)
Chemical Composition	Cu (%)	0.01	0.00	∿0.10
	Si (%)	0.10	0.41	∿0.30
	Fe (%)	0.29	0.18	∿0.40
	Mn (%)	0.00	0.00	0.05∿0.20
	Mg (%)	0.01	0.05	4.5 ∿5.6
	Zn (%)	0.00	0.01	∿0.10
	Cr (%)	0.00	0.00	0.05∿0.20
	Ti (%)	0.00	0.01	0.00
	Al (%)	> 99.5	Rest	Rest
Mechanical Properties	Yield Stress (kg/mm^2)	1.70	9.00	11.30
	Tensile Strength (kg/mm^2)	7.60	17.80	28.35
	Vickers Hardness (kg/mm^2)	28.33	65.31	72.73
	Young's Modulus (kg/mm^2)	6430	6650	6870

hardness, requiring heat treatment to remove this work hardened layer. Following the Japanese Industrial Standards, pure aluminum and aluminum alloy H4163-2 were annealed for 1 hour at 400°C and foils made of aluminum alloy H4163-5, were annealed for 1 hour at 205°C.

The surface hardness before and after annealing are shown in Figure 2. This test was made using a micro Vickers hardness tester. The tensile test results are shown in Figure 3 and summarized with the composition of the materials in Table 2.

Surface Roughness (SR), Mean Depth of Penetration (MDP), and Mean Depth of Deformation (MDD)

For this study a NACA 16021 foil section was tested for 9 hours to find the relation among SR, MDP, and MDD. The result is shown in Figure 4. When a ductile material such as aluminum is exposed to cavitation, small pits detected by an increase in SR are formed at the first stage of erosion. At this stage there is no weight loss. This initial period is called the incubation period where after an initial increase, the SR value asymptotically approaches a larger value.

It is well known that MDP remains zero during the incubation period. The time rate of MDP/(MDPR) increases to the maximum (acceleration period) then decreases gradually (deceleration period). As a measure of erosion intensity the value of MDD, pro-

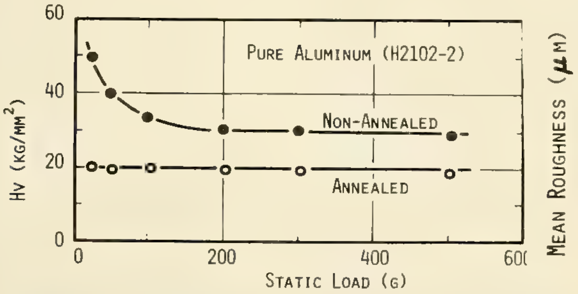

FIGURE 2. Result of Vickers hardness test [pure aluminum (H2102-2)].

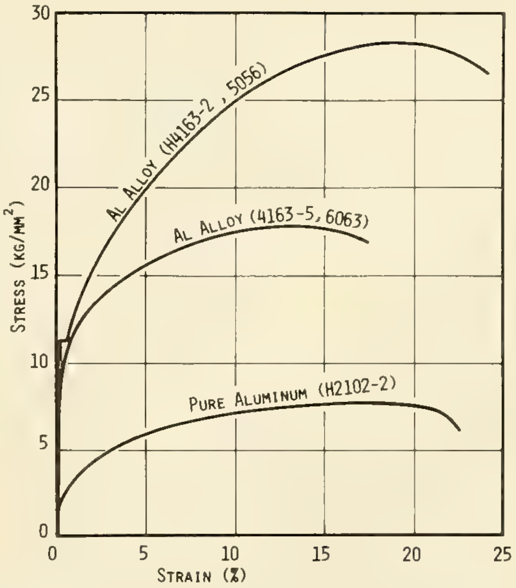

FIGURE 3. Comparison of tensile test result.

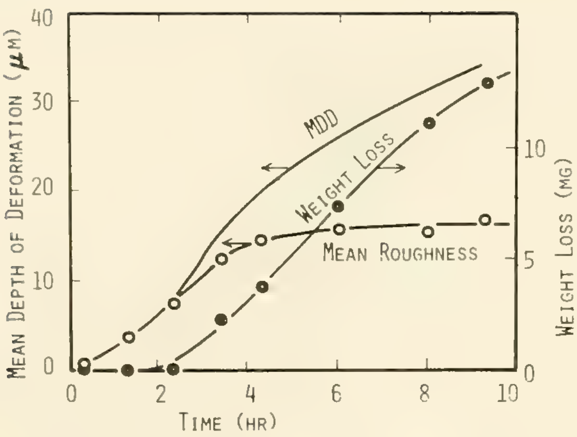

FIGURE 4. Extended duration cavitation test [NACA 16021, Pure Al (H2102-2), C = 40 mm, α = 4 deg.].

posed by one of the authors, seems to be more suitable than MDP. The advantages of using MDD are that it increases almost linearly over a wide range of exposure time as well as the fact that MDD corresponds to SR in the incubation period and to MDP after long exposure.

In the present tests, SR was measured to shorten the testing time. Usually the test was completed within 1 hour so the SR value coincides with MDD. The degree of erosion after a long exposure can be estimated using the measured SR.

3. HYDRODYNAMIC CHARACTERISTICS OF CAVITATION ON NACA 0015 FOIL SECTION

Cavity Length

Because erosion occurs at the collapsing point of the cavities namely the end of the cavity, it is important to know the cavity length for predicting cavitation erosion. Therefore, prior to the erosion tests, the cavity length and pressure distribution along the back surface of the NACA 0015 foil were measured. At the test condition 50 photographs were taken to measure the cavity length.

The results are shown in Figure 5. As seen in the figure, above $\sigma > 0.8$ the distribution of cavity length is characterized by a peak, but below $\sigma < 0.8$ the fluctuation becomes so large that there is no characteristic peak. For the supercavitation condition ($\sigma = 0.45$) the fluctuation is reduced and a characteristic peak can again be observed. The mean value of cavity length and its standard deviation are shown Figures 6 and 7. The cavity length increases linearly with smaller cavitation number, and the standard deviation begins to increase rapidly about $\sigma = 0.85$ as clearly seen in the figure.

It is well known that the cavity length of a partially cavitated foil can not be determined theoretically by linear cavity models. The cavity length predicted by a closed type cavity model is usually longer than the observed length. If we adopt a open type cavity model., the situation becomes reversed and the predicted cavity length becomes shorter than the observed length. Consequently a half-closed type model is usually adopted, but this model requires the opening of the cavity end to be determined experimentally.

In this study the cavity length was calculated using the half-closed type model by Nishiyama and Ito (1977). This method is based on linear theory using singularities (source and vortex) distributed on the cavitated foil. The calculated results are shown in Figure 7 where the opening δe was systematically changed. The contour of $\delta e = 0$ coincides with the closed cavity model. The circles in this figure represent the "mean" value of the observed cavity length. Using this mean value, the opening δe can be calculated showing that δe increases with smaller values of σ (see Figure 8).

Pressure Distribution and Cavity Shape

The theoretical pressure distribution and cavity shape for the back side of NACA 0015 foil section are shown in Figure 9 along with the corresponding experimental result. Here the Nishiyama-Ito's half-closed model was used with the δe values taken

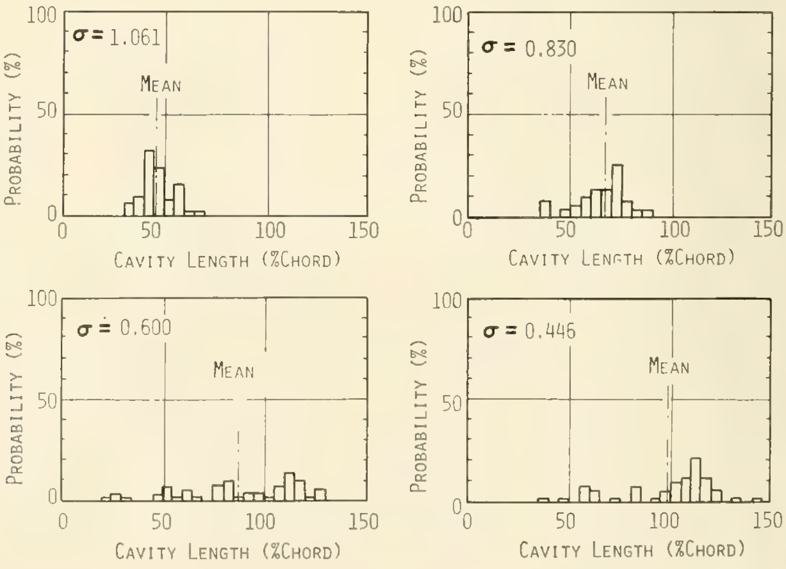

FIGURE 5. Fluctuation of cavity length (NACA 0015, α = 4 deg., V = 35.9 m/s).

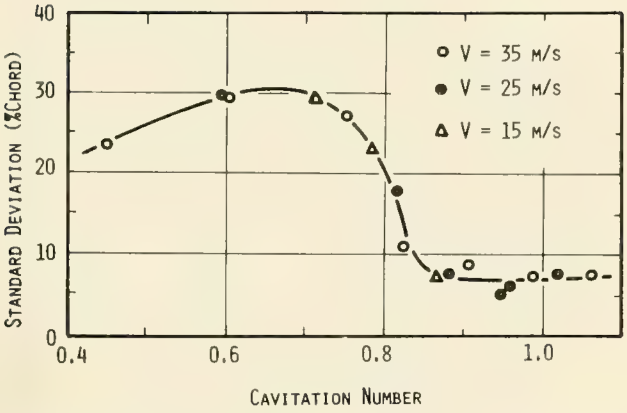

FIGURE 6. Standard deviation of measured cavity length (NACA 0015, $\alpha = 4$ deg.).

from Figure 8. The pressure distribution diverges to a positive infinite value at the end of cavity because of singularity at this point. This singularity makes the agreement between theoretical and experimental results very poor.

The cavity shape is also compared in Figure 9. The observed leading edge of the cavity is about 10% chord position. Whereas, in the theory the leading edge of the cavity begins at the leading edge of the foil. This appears to be one of the reasons why the calculated cavity thickness is much thicker than the experimental thickness even though the cavities have similar profiles.

4. EROSION TEST

Cavity Length and Position of Erosion

The roughness increment on the foil was measured for various exposure times. Spanwise roughness measurements were made over the entire chord at intervals corresponding to 5% the chord length. Two examples of the roughness distribution are shown in Figure 10. Arrow marks in this figure indicate the position of cavity end and the standard deviation of its fluctuation.

The figure clearly shows that the peak of erosion appears slightly downstream of the cavity end, and the erosion distribution agrees well with the cavity fluctuation. Namely, there is an obvious peak in the region of $\sigma > 0.8$, but in the region of $\sigma < 0.8$ the surface roughness distribution spreads over a wider range. This result indicates that the estimation of cavity length and its degree of fluctuation are important factors in the prediction of erosion intensity.

Effect of Hydrodynamic Factors on Erosion

Cavitation Number

The mean increment of surface roughness, SR, and its time rate of change can be determined from the roughness distribtuion shown in Figure 10. It corresponds to the mean depth of deformation rate (MDDR) because the test was finished within the incubation period. While Thiruvengadam has proposed adopting the rate of energy absorbed by the eroded material, which can be calculated by multiplying MDP by the energy absorbing capacity of the material per unit volume, the present research uses MDDR as a measure of erosion intensity in order to find which property is responsible for cavitation erosion.

It is known that the erosion intensity, MDDR, has a peak at the certain cavitation number. The change of measured MDDR to cavitation number is shown in Figure 11, where plots (a) and (b) refer to the NACA 0015 foil tests while plot (c) refers to the NACA 16021 foil tests. The test result of Kohl and Thiruvengadam are also presented in plot (d) [Kohl (1968) and Thiruvengadam (1971)]. As mentioned earlier, while the same foil section (NACA 16021) was tested in Test Series I, a different attack angle was used.

There are several differences in the results obtained in the NACA 0015 foil tests and the NACA

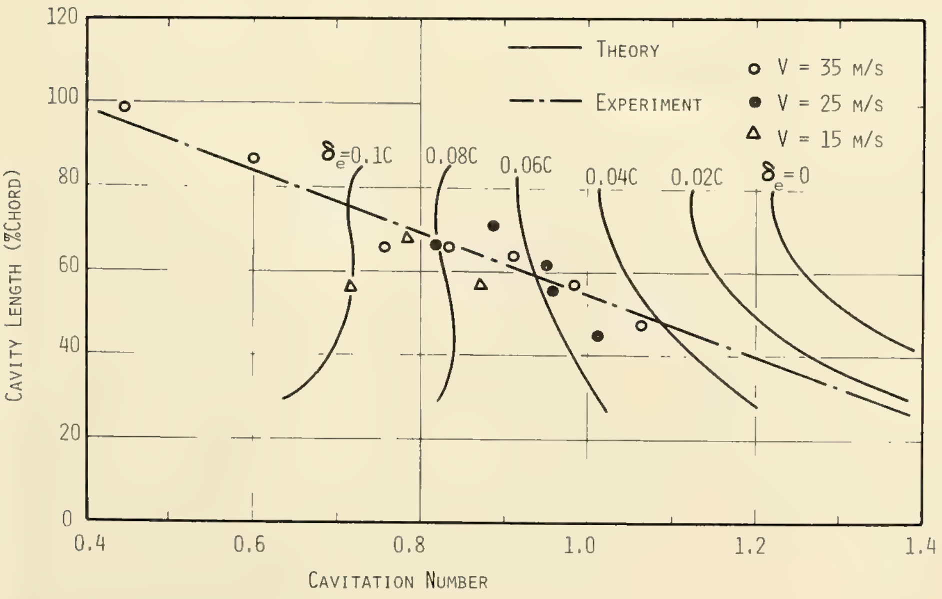

FIGURE 7. Comparison of calculated and observed mean cavity length (NACA 0015, $\alpha = 4$ deg.).

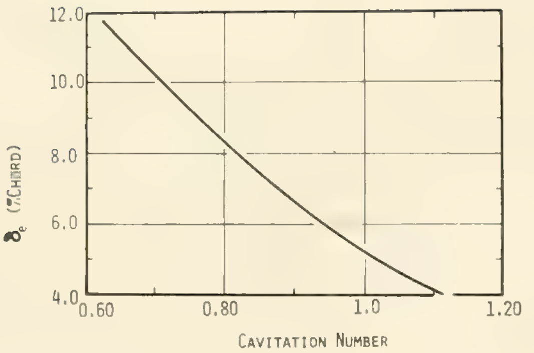

FIGURE 8. Derived relationship between δe and cavitation number for NACA 0015 foil, α = 4 deg.

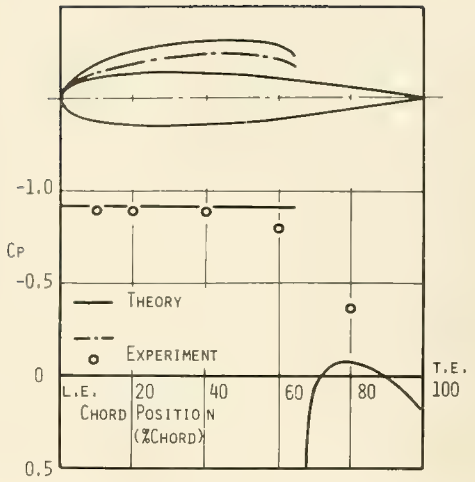

FIGURE 9. Comparison of NACA 0015 foil calculated cavity shape and Cp distribution with experiments at α = 4 deg.

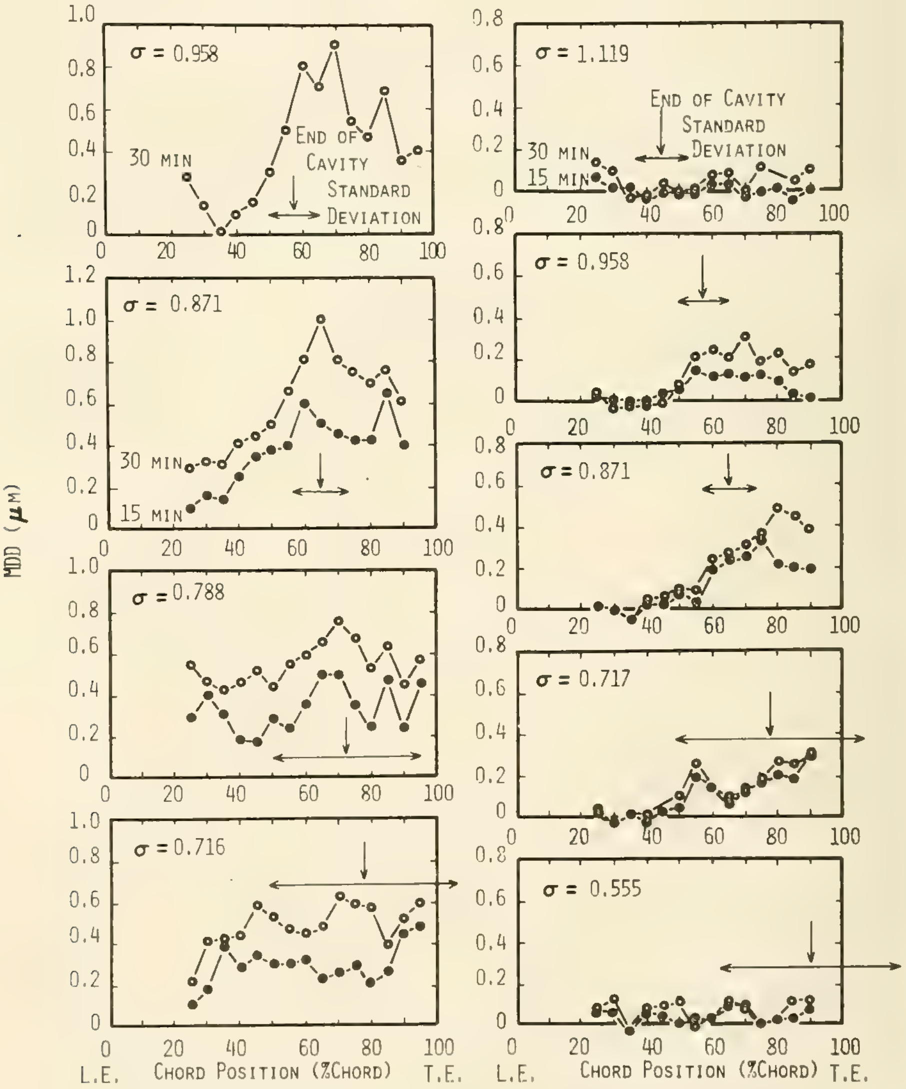

(a) C = 50 MM

(b) C = 30 MM

FIGURE 10. Illustration of MDD (Mean Depth of Deformation) data from NACA 0015 foil test [pure aluminum (H2102-2), α = 4 deg., V = 35 m/s].

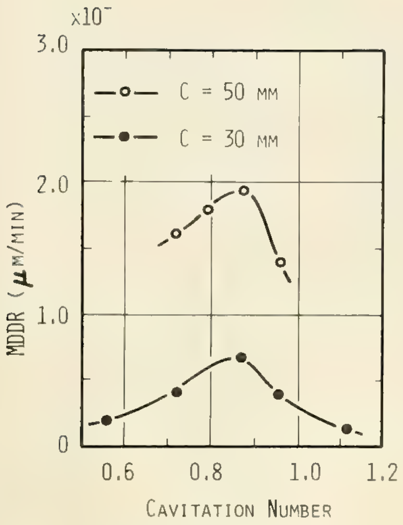

(a) NACA 0015, H2102-2, α = 4 deg., V = 35 m/s

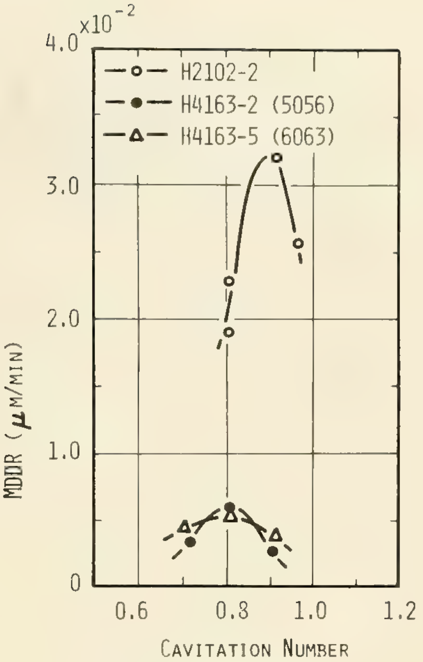

(b) NACA 0015, C = 30 mm α = 4 deg., V = 45 m/s

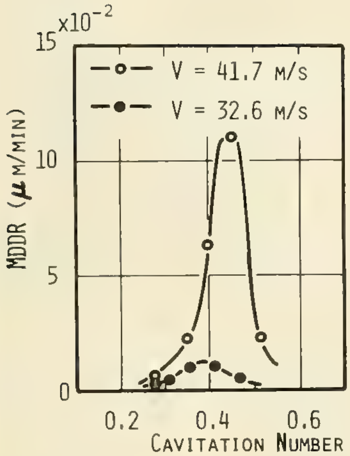

(c) NACA 16021, H2102-2, C = 40 mm, α = 4 deg.

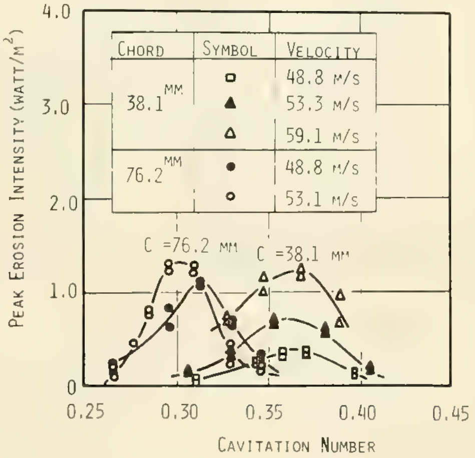

(d) NACA 16021, 1100F-A1 (Thiruvengadam, 1971)

FIGURE 11. Summary of MDDR erosion index and test results.

16021 foil tests. First, the width of the peak of NACA 16021 is narrower than the NACA 0015 peak. This is caused by the difference of pressure distribution between the two foil sections. The NACA 16021's distribution is flat, resulting in a larger change of cavity length with small changes in cavitation number. In contrast, the NACA 0015 section has a triangular pressure distribution so the difference between the inception cavitation number and supercavitation number is large. Since erosion occurs only when the cavity bubbles collapse on the foil surface, it seems quite reasonable that NACA 0015 has a much wider peak than the NACA 16021. Here the authors would like to point out that due to side wall effects the measured pressure distribution of the NACA 16021 foil and the peak value of $\sigma = 0.4$ can not be obtained directly by a two-dimensional calculation.

Another difference between these two results is the value of the maximum MDDR. It is much larger for the NACA 16021 foil when compared with the NACA 0015 foil results, even though the chord length and test velocity are not that much different. The main reason lies in the difference of cavity pattern. With the NACA 16021 section, the cavity inception is concentrated at the mid-span position and the cavity was a streak type. Correspondingly, the erosion pattern was a streak type, where a narrow and deep eroded groove was formed along the middle of foil. A picture of this groove taken by a scanning electron microscope is reproduced in Figure 12. Streak cavitation can induce severe erosion in comparison to sheet cavitation erosion which occurred in the NACA 0015 foil tests. The difference in the cavity patterns seems to cause this large difference in MDDR.

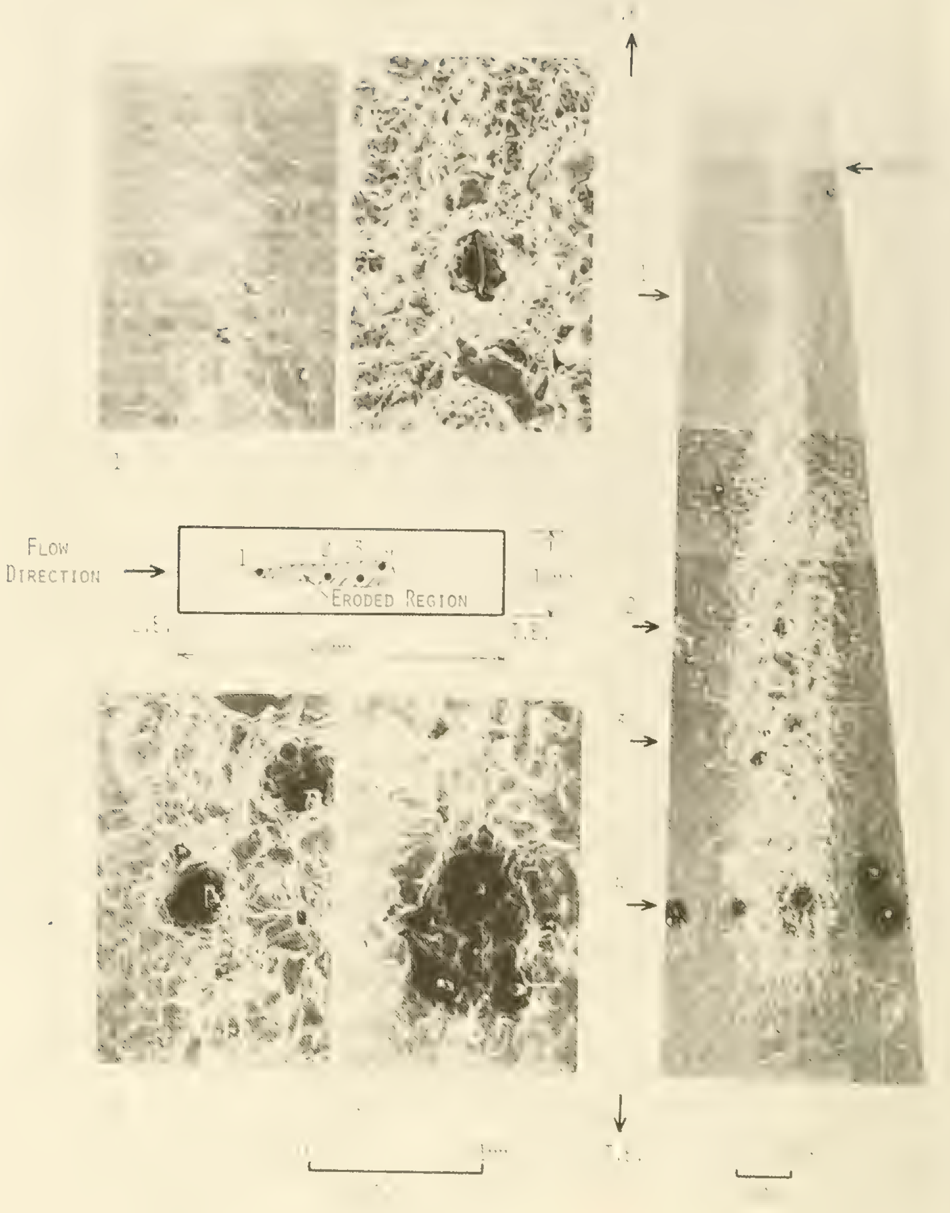

FIGURE 12. Scanning electron microscope photographs of eroded surface (NACA 16021, H2102-2, C = 40 mm, α = 4 deg., V = 41.7 m/s, σ = 0.450).

Referring to Figure 11 (b) in the 3 test series where only the material of the foil was changed, the position of maximum MDDR changes. This seems irrational because the flow condition is not changed by the material. The reason of this shift is the occurrence of the foil's bent trailing edge. On a full scale propeller, cavitation erosion is sometimes accompanied by a bent trailing edge. The same thing happened in the present test. The foil section made of pure aluminum is much weaker than those made from an aluminum alloy, and it was bent more at the trailing edge causing the shift of peak MDDR to the larger cavitation number.

An example of a bent trailing edge is shown by the profile view in Figure 13. The amount of bend is large at the corner of the trailing edge, which exaggerates considerably the shape shown in this figure. The bent trailing edge was observed on every NACA 0015 foil sections when the erosion occurred. On the contrary, it hardly appeared on NACA 16021 foil section because of its thicker trailing edge.

Velocity

It is well known that the erosion intensity is affected very much by the mean velocity since Knapp's suggestion of 6th power law [Knapp et al. (1970)]. The effect of velocity on the peak value of MDDR is shown in Figure 14. Usually the exponent obtained experimentally, has a large spread falling somewhat between 3 and 9. In the present tests with the NACA 16021 foil the exponent, n, was 9 and for the NACA 0015 foil tests the exponent, n, was 6.

Chord Length

The chord length of a foil also has a large effect on the erosion intensity. This is very

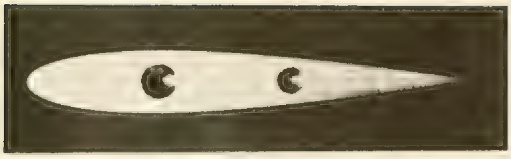

(a) BEFORE EXPERIMENT

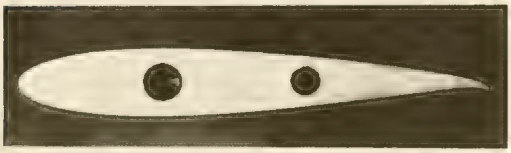

(b) AFTER EXPERIMENT

FIGURE 13. Impression of bent trailing edge.

important for marine propellers where the scale ratio between a full scale propeller and its model is large. Sometimes this ratio exceeds 30. As mentioned above, while the effect of the velocity difference is very large, we can still make a model test with the same tip speed as full scale by increasing the revolution of the model propeller. However it is very difficult to reduce the scale ratio of chord length.

Experimental verifications on this problem are also very poor. Thiruvengadam (1971) made his erosion tests using two chord lengths, 1.5 and 3 in. His result shows that the erosion intensity increases proportional to the chord length. The result obtained in the present test is shown in Figure 15. In the present tests the erosion intensity increases proportional to the square of chord length. The effects of hydrodynamic factors such as cavitation number, velocity, and chord length can be explained universally by a model of erosion mechanism. The details of this model will be given in Section 5.

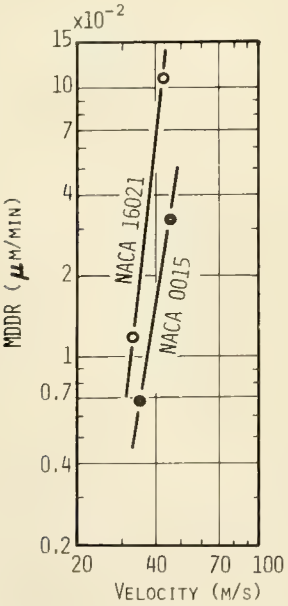

FIGURE 14. MDDR vs. velocity (NACA 0015 : H2102-2, C = 30 mm, α = 4 deg.) (NACA 16021 : H2102-2, C = 40 mm, α = 4 deg.).

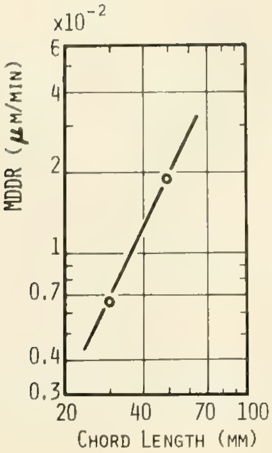

FIGURE 15. MDDR vs. chord length (NACA 0015, H2102-2, α = 4 deg., V = 35 m/s).

Air Content

The effect of air content was examined using the NACA 16021 foil section results. The air content was controlled as follows. As a pretreatment, the water was degassed to about 8ppm in a vacuum chamber and introduced into the cavitation tunnel. Then a certain amount of air was injected into the tunnel through an injection port before the test. In this case the ratio of gaseous air to total air content is much greater than found in ordinary water where the amount of air is an order of parts per million of total air content [Ahmed and Hammitt (1969)]. With increase of air content the value of MDDR decreases as seen in Figure 16. This tendency agrees with the test results of SSPA [Lindgren and Bjärne (1974)] and those of Stinebring et al. [Stinebring et al. (1977)]. The reason is attributed to the damping effect of air in a collapsing cavity bubble, attenuation effect of tiny air bubbles to shock wave, or a combination of both.

Material Properties

The effects of material properties on erosion are usually tested by accelerating devices such as vibrators, rotating discs, water jets etc. Summarizing these results, Heymann has made the chart shown in Figure 17 where the hardness of the material was taken as a factor governing the erosion [Heymann (1969)]. As seen in the figure the slope differs according to the material group, namely the slope of the steel group is steeper than that of aluminum and copper and brass group. This implies that the erosion resistance cannot be fully represented by hardness alone. Thus other material properties such as strain energy absorbed to material (engineering strain energy) [Thiruvengadam (1966)], ultimate resilience [Hobbs (1966)], or their com-

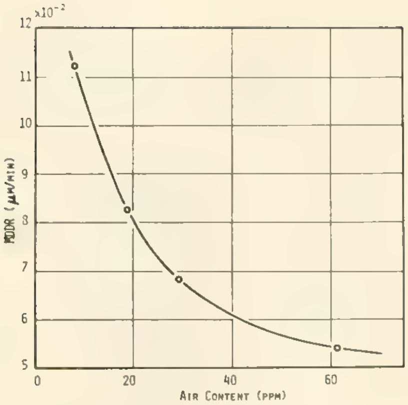

FIGURE 16. Effect of air content on MDDR (NACA 16021, H2102-2, C = 40 mm, α = 4 deg., V = 41.7 m/s, σ = 0.443).

bination [e.g. Hammitt et al. (1969)], have also been proposed by several researchers.

The present test results are also compared with those material properties, i.e., hardness, engineering strain energy, and ultimate resilience. Hardness seems to give the best representation as seen in Figure 18. This will be discussed in Section 5 dealing with modeling the erosion mechanism.

5. THEORETICAL CONSIDERATIONS

Review of Erosion Scaling Theory

Thiruvengadam has made several theoretical considerations on scaling of erosion. In 1971, he introduced a scaling formula [Thiruvengadam (1971)]. He assumed a statistical distribution of air nuclei and derived the efficiency of erosion, θ, as,

$$\theta = \frac{\sigma}{\delta}(\Delta\sigma)^{\frac{1}{2}}\exp\frac{-2.67}{W(\Delta\sigma)}, \qquad (1)$$

where δ, σ, Δσ, and W are nondimensional nuclei size, cavitation number, degree of cavitation, and Weber number respectively. Equation (1) is very attractive because it has no empirical constants. However the calculated values are quite different from the experimental values. While θ should be the order of 10^4 by the calculation, the θ obtained from model tests typically has an order of 10^{-10}. This discrepancy comes from the assumption that the total energy of the cavity bubbles generates the erosion. The theory shows that when the cavitation number is reduced, the efficiency, θ, increases from the point of cavitation inception to a maximum and then decreases to zero when cavitation number reaches zero. This tendency agrees qualitatively with experiments. It is expected, since the actual cavity becomes a supercavity at a certain cavitation number causing the erosion intensity to decrease greatly and in a practical sense reach zero.

One of the authors has proposed a model of erosion mechanism in which the discharged energy of the collapsing bubble is assumed to be distributed statistically as:

$$f(\varepsilon) = \frac{K_2}{V^3L^3}\ \varepsilon\ \exp\left(-\frac{K_1}{V^2L}\varepsilon\right) \qquad (2)$$

where f is the distribution function of energy density, ε, reached on the material surface. Then a scaling law for cavitation erosion was derived using an empirical formula for the erosion resistance of materials. A comparison with only the peak erosion intensity taken from Thiruvengadam's tests showed good agreement [Kato (1975)].

Consideration on Effect of Cavitation Number

As mentioned before, MDDR has a peak value of a certain cavitation number. This is due to a combination of the following two reasons. There is an increase in the collapsing cavity volume as the cavitation number decreases which causes increased erosion. On the other hand, the decrease of cavitation number causes an increase in the cavity length so the eroded area shifts towards the trailing edge of a foil. Also when the cavity length exceeds the chord length, the cavity does not collapse on the foil surface, causing no cavitation erosion. Usually the cavity length fluctuates and the erosion intensity will change continuously with the cavitation number. Although there seems to be a considerable decrease in the collapsing pressure of cavity decreasing cavitation number, the control factor of erosion intensity is the change of cavity length as mentioned above.

The decrease of erosion intensity at the right hand side of the MDDR peak in Figure 19 is caused by the lack of cavity and by too long a cavity on left hand side. By increasing the cavitation number, the cavity becomes intermittent, and if the cavity is stabilized by roughing the leading edge, the MDDR peak shifts to a higher cavitation number where the peak value is increased. This was verified in the authors' experiments as shown in Figure 20.

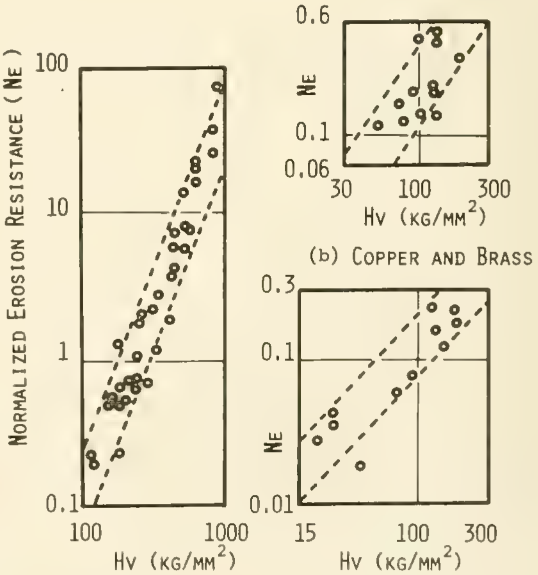

(a) STEEL

(b) COPPER AND BRASS

(c) ALUMINUM ALLOY

FIGURE 17. Vickers hardness vs. erosion resistance [Heymann (1969)].

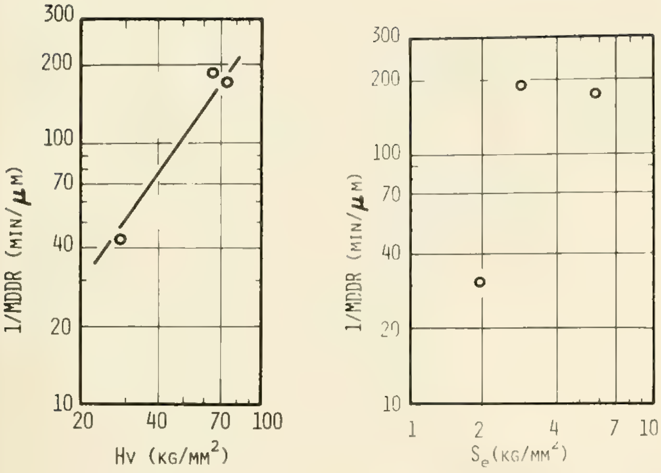

(a) Vickers Hardness (b) Engineering Strain Energy

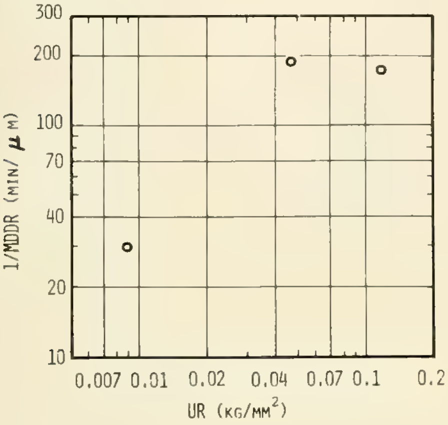

(c) Ultimate Resilience

FIGURE 18. MDDR vs. various mechanical properties of material (NACA 0015, C = 30 mm, α = 4 deg., V = 45 m/s).

Modelling of Cavitation Erosion and Scaling Factors

As mentioned above, one of the authors developed a model of the cavitation erosion mechanism. However it is limited to only constant cavitation numbers and the effects of material properties were derived empirically from accelerated tests. In the present paper, this model is developed further to treat differences in the cavitation number. The effect of the material's mechanical properties is also studied and a simple model is introduced.

The total energy of collapsing bubbles per unit is given as:

$$E_t = \eta(p-pv)Q \quad , \tag{3}$$

where η : probability of bubble collapses on a foil surface,
$p-p_v$: pressure difference at the collapse point,
Q : volumetric flow rate of cavitation bubbles.

Equation (3) can be modified:

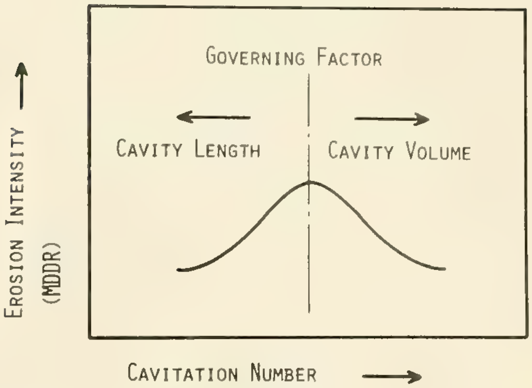

FIGURE 19. Illustration of MDDR peak characteristic (test data given in Figure 11).

$$E_t \propto \eta(p_\infty-p_V)\delta BV$$
$$\propto \eta\sigma\rho V^3 \left(\frac{\delta e}{L}\right) L^2 \quad , \tag{4}$$

where δ : displacement thickness of cavitation bubbles,
B : foil span,
δe : cavity thickness at the cavity end,
V : velocity,
L : reference length.

Assuming that a cavity bubble grows according to Knapp's similarity law, the volume, ∇, is:

$$\nabla \propto R^3 \propto \left(T\sqrt{\frac{\Delta p}{\rho}}\right)^3 \tag{5}$$

where $T \propto \frac{\lambda}{V}$, where λ is the cavity length. The pressure difference, Δp, is assumed as

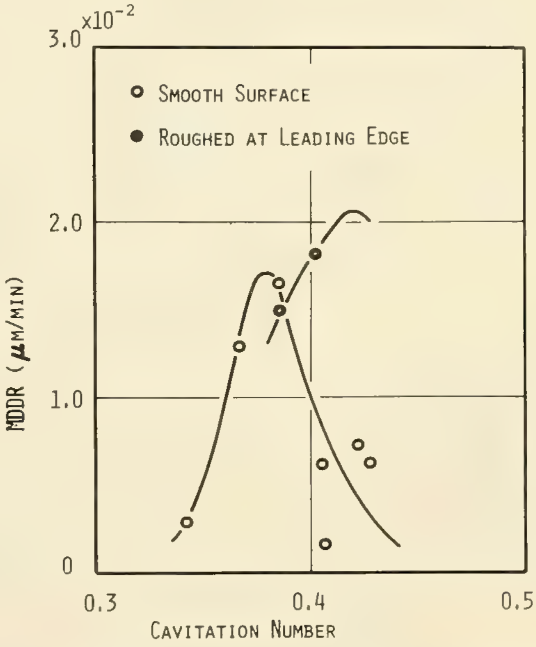

FIGURE 20. Impression of effect of roughened leading edge [NACA 16021, tested by Ozaki and Kiuchi (1975)].

$$\Delta p \propto p_v - p_{min}$$

$$\propto -(\sigma + Cp_{min})\rho V^2 . \qquad (6)$$

Combining Eqs. (5) and (6), the following equation is derived.

$$\nabla \propto \lambda^3 [-(\sigma + Cp_{min})]^{\frac{3}{2}} \qquad (7)$$

The number of cavity bubbles per unit time is then given as,

$$N \propto \frac{Q}{\nabla} \propto \frac{\bar{\delta}e\ V}{\bar{\lambda}^3 L\ [-(\sigma + Cp_{min})]^{\frac{3}{2}}} \qquad (8)$$

where $\bar{\lambda}$ as the nondimensional cavity length, $\bar{\lambda} \equiv \lambda/L$, $\bar{\delta}e$ is the nondimensional cavity thickness at the end, and $\bar{\delta}e \equiv \delta e/L$.

Here, we make the same assumption as in the previous paper [Kato (1975)] on the statistical energy distribution of cavity bubbles. The distribution is given as,

$$n = cE \exp(-aE) \quad , \qquad (9)$$

where n is the number of bubbles per unit time whose energy is between E and E + dE. Total number, N, and total energy of bubbles, E_t, are given as follows:

$$N = \int_0^\infty n dE = \frac{c}{a^2} \qquad (10)$$

$$E_t = \int_0^\infty E n dE = \frac{2c}{a^3} \quad ,$$

Constants a and c can be decided by combining Eqs. (4), (8), and (10).

$$a = \frac{K_1'}{\eta\rho V^2 L^3 \bar{\lambda}^3 [-(\sigma + Cp_{min})]^{\frac{3}{2}}}$$

$$c = \frac{K_2' \bar{\delta}e}{\eta^2\rho^2 V^3 L^7 \bar{\lambda}^9 \sigma^2 [-(\sigma + Cp_{min})]^{\frac{9}{2}}} \qquad (11)$$

where K_1' and K_2' are constants independent of the chord length, velocity and cavitation number. From Eq. (9), the distribution function of energy density, f, is derived as a function of energy density, ε. The detailed discussion of this point is given in the previous paper [Kato (1975)].

Substituting Eqs. (9) and (11) into the relation

$$f(\varepsilon) \propto L^2 n\ (\varepsilon L^2) \quad , \qquad (12)$$

the final expression for f is

$$f = C\ \varepsilon \exp(-A\varepsilon) \quad , \qquad (13)$$

where

$$A = \frac{K_1}{\eta\rho V^2 L^3 \bar{\lambda}^3 \sigma\ [-(\sigma + Cp_{min})]^{\frac{3}{2}}}$$

$$C = \frac{K_2\ \bar{\delta}e}{\eta^2\rho^2 V^3 L^3 \bar{\lambda}^9 \sigma^2\ [-(\sigma + Cp_{min})]^{\frac{9}{2}}} .$$

In the present case the chord length is taken as a suitable reference length, L.

Equation (13) is similar to Eq. (2), but it is extended to include differences in the cavitation numbers.

The next problem is the modelling of deformation of a material surface caused by the attack of collapsing bubbles. For the present tests, hardness seems the best property to express the erosion resistance of a material. However it was found to be insufficient as seen in Figures 17 and 18.

The methods of hardness testing can be divided into two types. One is the measurement of a dent size caused by the static load of a sphere or a pyramid on the material surface. The other method is the measurement of absorbed energy from dropping a certain test body on the surface. The Vickers hardness test made in the present study belongs to the first type.

When a pyramidal dent whose depth is d, is formed by a static load F (Figure 21), the energy used to the deformation is

$$E \propto Fd \quad . \qquad (14)$$

The hardness has the following relation by its definition.

$$H_v \propto \frac{F}{l^2} \propto \frac{F}{d^2} \quad . \qquad (15)$$

The increase of surface roughness (SR) by the single dent is given as

$$SR = \frac{\nabla}{S} \propto \frac{d^3}{S} \quad , \qquad (16)$$

where ∇ and S are the volume of the dent and reference area, respectively.

Combining equations (14) ~ (16),

$$SR \propto \frac{1}{H_v}\frac{E}{S} \propto \frac{e_p}{H_v} \qquad (17)$$

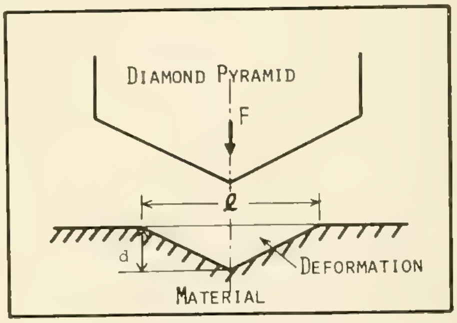

FIGURE 21. Model of Vickers hardness test method.

where e_p is the energy density absorbed by the material's plastic deformation. If e is small enough, the deformation is within the elastic limit and no permanent dent will be formed. When e exceeds a certain limit, e_c, the plastic deformation of surface occurs and a pernament dent is formed.

Then the following relation is derived:

$$\begin{aligned} e_p &= 0 && \text{for } e < e_c \\ e_p &= e - e_c && \text{for } e > e_c \quad , \end{aligned} \tag{18}$$

The above mentioned argument is valid for the actual case of erosion where many cavity bubbles collapse in a certain period if e is substituted to, ε, in these equations.

Then,

$$\begin{aligned} \varepsilon_p &= 0 && \text{for } \varepsilon < \varepsilon_c \\ \varepsilon_p &= \varepsilon - \varepsilon_c && \text{for } \varepsilon > \varepsilon_c \quad , \end{aligned} \tag{19}$$

and

$$\text{MDDR} \propto \frac{1}{H_v} \int_{\varepsilon_c}^{\infty} \varepsilon_p f(\varepsilon) d\varepsilon$$

$$= \frac{1}{H_v} \int_{\varepsilon_c}^{\infty} (\varepsilon - \varepsilon_c)\, C_\varepsilon \exp(-A\varepsilon) d\varepsilon \tag{20}$$

Integrating Eq. (20),

$$\text{MDDR} = \frac{K_2}{K_1{}^3} \frac{\rho V^3}{H_v} G(\sigma) \left(2 + \frac{K_1 \varepsilon_c}{\rho V^2 L F(\sigma)} \right)$$

$$\exp \left[- \frac{K_1 \varepsilon_c}{\rho V^2 L F(\sigma)} \right] \tag{21}$$

where

$$F(\sigma) \equiv \eta \bar{\lambda}^3 \sigma \left[-(\sigma + Cp_{min}) \right]^{\frac{3}{2}}$$

$$G(\sigma) \equiv \eta \sigma \bar{\delta} e \quad .$$

Here F and G are functions of cavitation number, where G is proportional to the total energy of the cavity reaching to the surface, and F is related to the individual energy of each cavity bubble.

The probability of the bubble collapse on the foil surface, η, is calculated using the estimated mean position of collapse and its fluctuation. In the case of the NACA 0015 foil section, the position was estimated as 1.3 λ from Figure 10 and the fluctuation is assumed to be the same as the cavity's fluctuations. The thickness at the end of cavity is taken from Figure 8. The value of F and G for NACA 0015 section were calculated at $\alpha = 4°$. The results are shown in Figure 22.

While the critical value of energy density, ε_c, should be expressed by the mechanical properties of material such as yield strength, Young's modulus etc., at the present stage, for lack of data we assume the following relation,

$$\varepsilon_c \propto \sigma_y{}^n \quad , \quad \sigma_y \ : \ \text{Yield strength} \tag{22}$$

and determine the power, n, from the erosion experiments.

Comparison with Test Result

The results of this theoretical model are compared with the erosion test of NACA 0015 section in Figure 23 where the two constants, K_1 and K_2, in Eq. (21) were determined using two different test points. In this figure those points are shown by dashed marks. The value of the power, n, was taken as n = 1/4 from the experimental results. The agreement between this theory and the test results is satisfactory.

The theory was also compared with Thiruvengadam's test result [Thiruvengadam (1971)]. In this case, no data about the cavity was measured, so only the peak value of erosion intensity was used in this comparison with the present theory. The agreement is almost perfect as seen in Figure 24 where one set of data was used to determine two constants. Photos in Figure 23 (b) also show the paint test results discussed in the next section.

Paint Test and Soft Aluminum Erosion Test

Recently the paint test has been routinely used at several research laboratories to predict erosion intensity, in contrast to the present research using the soft aluminum erosion test to predict erosion. Both of these two test methods have merits and demerits. The soft aluminum erosion test is somewhat troublesome and the surface of the material

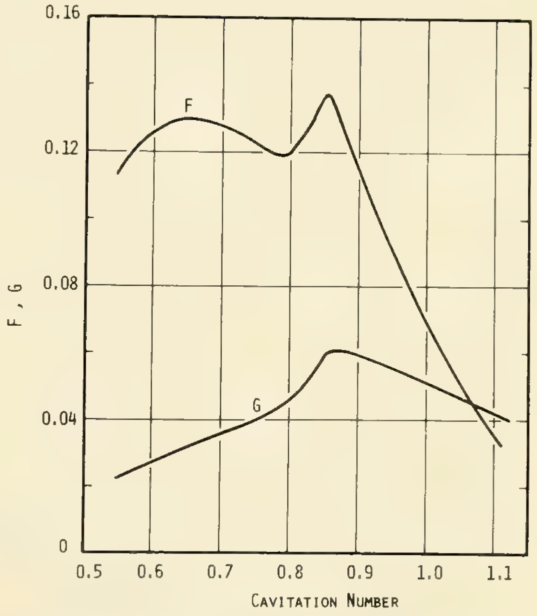

FIGURE 22. Derived F and G values for NACA 0015 foil section at α = 4 deg.

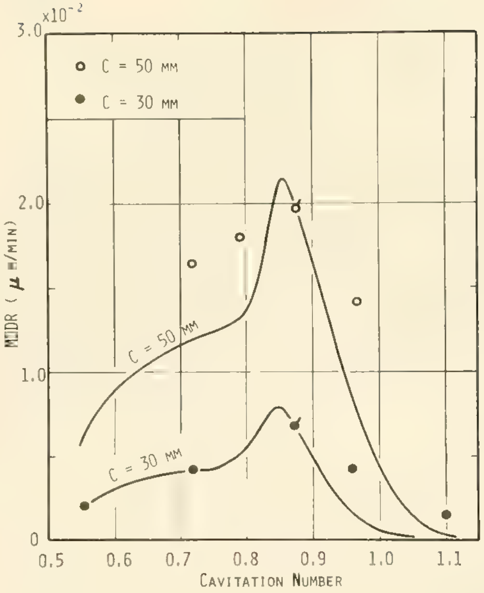

(a) Pure Aluminum (H2102-2), V = 35 m/s

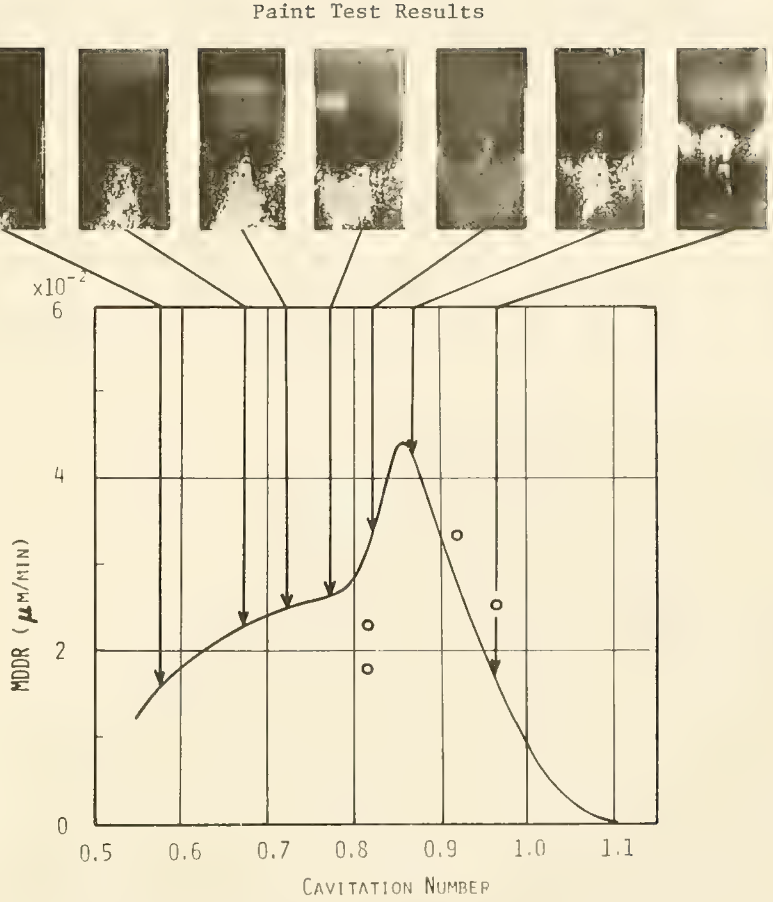

(b) Pure Aluminum (H2102-2), C = 30 mm, V = 45 m/s

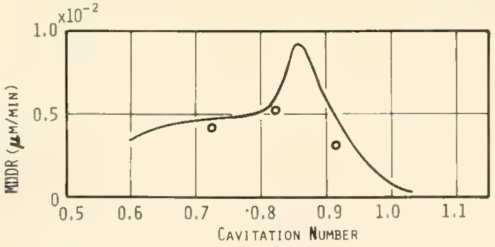

(c) Aluminum Alloy (H4163-5, 6063), C = 30 mm, α = 4 deg., V = 45 m/s

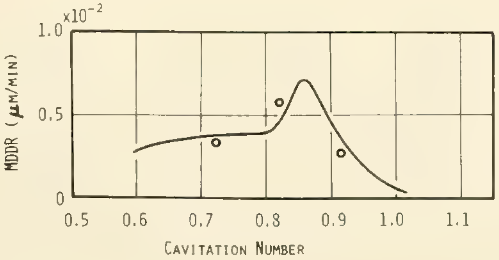

(d) Aluminum Alloy (H4163-2, 5056), C = 30 mm, α = 4 deg., V = 45 m/s

FIGURE 23. Comparison of predicted MDDR erosion index with experimental results (NACA 0015, α = 4 deg.).

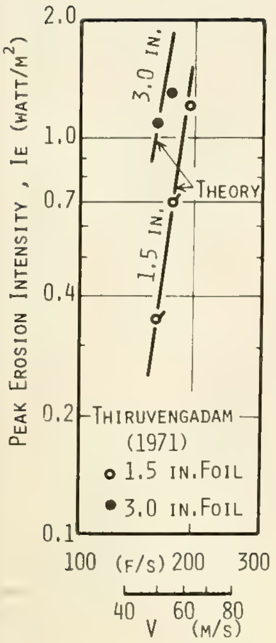

FIGURE 24. Comparison with Thiruvengadam's data (NACA 16021).

is destroyed, as a matter of course, after a long exposure to cavitation. But as mentioned in Section 1, it has the merits of yielding quantitative and reliable erosion data, a similar appearance of the full scale eroded surface, etc.

The paint test has just the opposite merits. It is a cheap and handy method. And although the conditions under which the paint is removed changes with very small changes in the paint composition, test procedure, etc., it appears that by developing standards, the paint test can be used to represent relative differences between similar models.

From this discussion of the paint test merits and demerits, the paint test appears suitable for daily routine tests of usual propellers. The soft aluminum test is suitable for making standard comparative tests at different research laboratories as well as for different types of propellers and for situations where critical erosion predicitions are required.

It is valuable to make a comparison of these test methods using the same foil section. After testing several kinds of paint, a marking paint "AOTAC" was found to be the best. Figure 23 (b) shows appearances of the painted surface after 5 min. test. They can be compared with the theory and the soft aluminum erosion test results shown in the same figure. The cavitation number of maximum erosion intensity is slightly different between the paint test and theory. But the general tendency agrees well and the paint test seems very useful especially for a comparative testing.

The position of maximum erosion intensity estimated from the paint test also agrees well with the chordwise distribution of MDD shown in Figure 10.

6. AIR INJECTION SYSTEM

Tiny air bubbles in the free stream reduce the erosion intensity by the action of their damping effect as mentioned in Section 4. To achieve a positive damping effect an air injection system with air bubbles injected from holes on the foil surface is sometimes adopted. This system has been used very effectively to prevent erosion on the inner surface of a full-scale ducted propeller [e.g., Okamoto et al. (1975) and Narita et al. (1977)]. However the mechanism of prevention is not yet fully explained, and the best injection position and/or the necessary amount of air injection have not been clarified.

The authors made the air inject test using NACA 16021 foil sections with three air injection holes of 0.5mm dia. drilled at 10% or 37.5% chord position (Figure 25). The tests were made at $\alpha = 4°$, $V = 41.9$m/s, and $\sigma = 0.438$. The previous test showed that the peak MDDR value falls somewhere between 40 ~ 45% chord. The injection position of 10% chord represents the injection near the leading edge of the section, and that of 37.5% chord represents the injection which insures effective coverage of the eroded area. Air was then injected at 2, 5, and 10 cc(normal)/min. The quantity of air was so small that separate air bubbles were found even at the 10 cc/min, and consequently the air jet column typical at high flow rate was not observed. As seen in Figure 26, the injection from 10% chord gives better performance and even as small a rate of the injection as 2 cc/min results in drastic decrease in the erosion intensity. With injection the MDDR value reduced to 1/5 of non-injection level. Increasing air volume, the value of MDDR decreases but the effect seems to become saturated with a larger rate of air injection.

7. CONCLUSIONS

(1) The purpose of the present research was to find the mechanism of cavitation erosion and its scaling laws with special reference to the relationship between the appearance of cavitation and the erosion intensity.

(2) Detailed observations of the cavity pattern were made on a two-dimensional foil section (NACA 0015). Then erosion tests, using the same foil section of pure aluminum and aluminum alloy, were made to measure the increase of surface roughness. The erosion intensity was also compared with the observed cavity pattern and other hydrodynamic

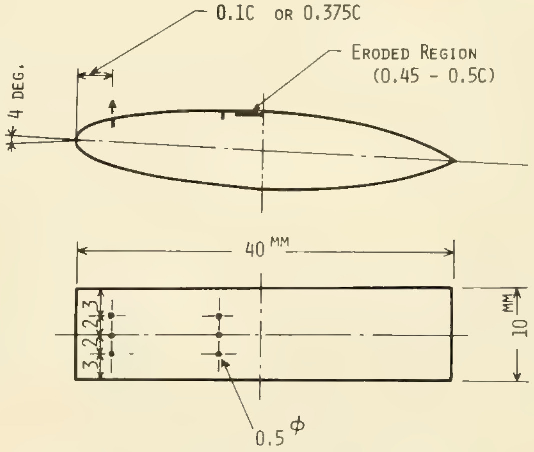

FIGURE 25. Location of air injection.

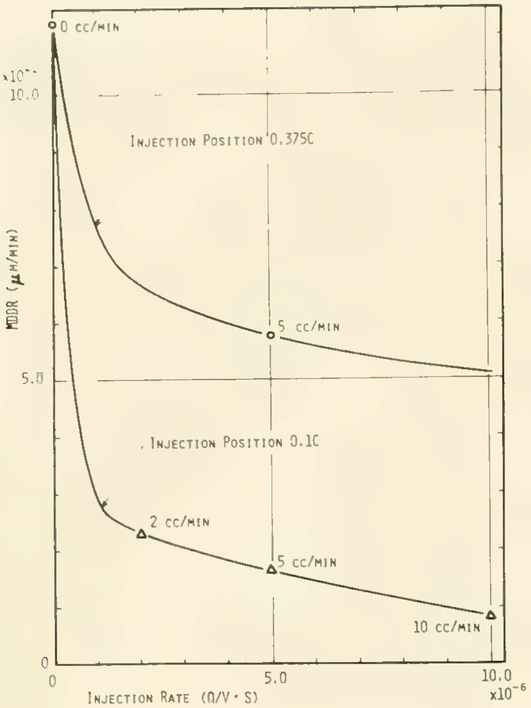

FIGURE 26. Effect of air injection on MDDR erosion index [NACA 16021, pure Al (H2102-2), $C = 40$ mm, $\alpha = 4$ deg., $V = 41.9$ m/s, $\sigma = 0.438$].

factors such as cavitation number, water velocity, etc.

(3) Modelling of cavitation erosion has been made assuming a statistical distribution of cavitation bubble. Using the model, a theory of erosion scaling was established which contains two constants given by the experiment. The erosion scaling of cavitation number, velocity, chord length, and material can be made by the theory. The theory has been shown to give good agreement with the authors' and Thiruvengadam's tests.

(4) Another two-dimensional foil section (NACA 16021) was also tested, but in this case the side wall effect was so large that the results were not compared with the theoretical calculations.

(5) The paint test also was made with the same foil section (NACA0015). The results of paint test agreed with that of the aluminum erosion test although it gives qualitative data.

(6) The effect of air content and air injection method was also investigated experimentally. The air injection was found to be very effective in preventing erosion.

ACKNOWLEDGMENTS

The authors would like to express their acknowledgments to Prof. S. Tamiya and members of the High Speed Dynamics Laboratory, University of Tokyo, for their many valuable discussions and help during the research work. They also wish to thank Mr. T. Komura, Mr. R. Latorre, and Miss N. Kaneda for their sincere help during the preparation of the paper.

This research work was financially supported by the Grant in Aid for Developmental Scientific Research (2), Ministry of Education, Japan (Research No. 185087) and the authors are grateful for the support.

NOMENCLATURE

A, a : constants
B : span
C : constant, chord length
c : constant
C_p : pressure coefficient
d : depth
E : energy
E_t : total energy of bubbles
e : energy density
F : force
f : energy density distribution function
H_v : Vickers hardness
K_1, K_1' : constants
K_2, K_2' : constants
L : reference length (chord length)
l : length
MDD : mean depth of deformation
MDDR : mean depth of deformation rate
MDP : mean depth of penetration
MDDR : mean depth of penetration rate
N : total number of cavity bubbles
n : distribution function of bubble number
p : pressure
Q : volumetric flow rate
R : bubble radius
S : area
SR : surface roughness
T : time
V : velocity
α : attack angle, air content
δ : thickness
δ_e : cavity thickness at the end
ε : energy density rate
η : probability
Λ : aspect ratio
λ : cavity length
ρ : density
σ : cavitation number
σ_y : yield stress
∇ : volume

SUBSCRIPTS

c : critical
min : minimum
p : plastic deformation
s : saturate
v : vapor
∞ : infinity
— : nondimensional value

REFERENCES

Ahmed, O., and F. G. Hammitt (1969). Determination of particle population spectra from water tunnel using Coulter counter. *Univ. of Michigan, Cav. and Multiphase Flow Lab. Rep. 01357-4-I, 08466-7-I.*

Hammitt, F. G., Y. C. Huang, C. L. Kling, T. M. Mitchell, Jr., and L. P. Solomon (1969). A statistically verified model for correlating volume loss due to cavitation or liquid impingement. *ASTM, STP 474,* 288.

Heymann, F. J. (1969). Toward quantitative prediction of liquid impact erosion. *ASTM, STP 474,* 212.

Hobbs, J. M. (1966). Experience with a 20-kc cavitation erosion test. *ASTM, STP 408,* 159.

Kato, H. (1975). A consideration on scaling laws of cavitation erosion. *Int. Ship. Prog., 22,* 253;305.

Knapp, R. T., J. W. Daily, and F. G. Hammitt (1970). *Cavitation.* McGraw-hill Book Co., New York.

Kohl, R. E. (1968). Experimental studies to establish scaling laws for modelling cavitation damage. *Hydronautics Tech. Rep.* 233-12.

Lindgren, H., and E. Bjärne (1974). Studies of propeller cavitation erosion. *Conf. on Cavitation,* 241.

Narita, H., Y. Kunitake, K. Holden, and B. Mugaas (1977). Investigation on the ducted propeller cavitation and the duct erosion prevention by the air injection system. *Symp. Hydrodynamics of Ship and Offshore Propulsion Systems,* Paper 11/3.

Nishiyama, T., and J. Ito (1977). Calculation of partially cavitating flow by singularity method (1st Report: Two-dimensional isolated hydrofoil). *Trans. JSME, 43,* 370; 2165, (in Japanese).

Okamoto, H., K. Okada, Y. Saito, and T. Takahei (1975). Cavitation study of ducted propeller on large ships. *Trans. SNAME, 83.*

Ozaki, H., and D. Kiuchi (1976). Cavitation erosion of two-dimensional foil sections. *Graduation thesis, Dept. Naval Arch., Univ. of Tokyo,* (in Japanese).

Sasajima, T. (1972). On cavitation erosion test method by using a painted model propeller. *Mitsubishi Tech. Rep.,* 9, (in Japanese).

Sato, R. (1976). Study on cavitation erosion. *3rd Lips Prop. Symp.,* 19.

Sato, R., S. Tamiya, and H. Kato (1974). Study on cavitation erosion. *Selected Papers from J. Soc. Naval Arch. Japan, 12,* 21.

Stinebring, D. R., R. E. A. Arndt, and J. W. Holl (1977). Scaling of cavitation damage. *J. Hydronautics, 11,* 3; 67.

Thiruvengadam, A. (1966). The concept of erosion strength. *ASTM, STP 408,* 22.

Thiruvengadam, A. (1971). Scaling laws for cavitation erosion. *Proc. IUTAM Symp. Lenigrad,* 405.

Young, S. G., and J. R. Johnston (1969). Accelerated cavitation damage of steels and superalloys in sodium and mercury. *ASTM, STP 408,* 186.

Experimental Investigations of Cavitation Noise

Göran Bark and Willem B. van Berlekom
The Swedish State Shipbuilding Experimental Tank,
Göteborg, Sweden

ABSTRACT

The requirement of low or acceptable noise levels onboard ships as well as low levels of radiated noise for special purpose ships can cause large problems for the naval architect. Low noise levels onboard ships are required in living quarters and also in some working spaces. The radiated noise field is of concern for instance for fishing vessels and ships with acoustical dynamic positioning systems.

One important source of noise in ships is cavitation and especially cavitating propellers. The cavitation noise can have a quite varying character. It may for example sound like a hiss or like sharp hammer blows. For the naval architect it is important to be able to predict and, if possible, to reduce undesired cavitation noise.

In this paper some of the research and development work on cavitation noise at the Swedish State Shipbuilding Experimental Tank (SSPA) will be described. This work at SSPA is mainly experimental and two projects will be described here in detail. One concerns the relation between cavity dynamics and cavitation noise. This work was carried out using an oscillating hydrofoil in the No. 1 SSPA cavitation tunnel. The other project concerns the relation between types of cavitation and cavitation noise. Different types of cavitation were generated in the tunnel using axisymmetric head forms and hydrofoils.

A great deal of effort has been made at SSPA to develop adequate methods for measuring cavitation noise in cavitation tunnels. A short review of the measuring techniques now in use is given in an introductory chapter. Besides the two projects mentioned above several other projects are, or have been, carried out at SSPA.

1. REVIEW OF MEASUREMENT TECHNIQUES AT SSPA

Measurements of cavitation noise started at SSPA as early as 1958. The first tests concerned cavitating axisymmetric head forms and were carried out in the SSPA cavitation tunnel No. 1. The measuring equipment was a waterfilled box attached to one of the plexiglass windows of the tunnel. A hydrophone was lowered into this box and could thus pick up the noise emanating from the source (propeller etc).

The transmission path from the noise source is through water, plexiglass, and water to the hydrophone. The transmission loss due to the presence of the plexiglass window is low. The drawbacks to this arrangement are reflected acoustic waves and vibrations in the box. The problem with the reflected waves may partly be overcome by carefully calibrating, or rather comparing, results from the hydrophone in a free field and in the box using the same known noise source. Vibration problems (from the vibrating tunnel plating) may be cured by using a pair of rubber bellows between the box and the window (see Figure 1).

The signal from the noise source is, however, still distorted as can be seen in Figure 2. This figure shows the noise from a cavitating propeller, as measured by the hydrophone in the box and a hydrophone near the propeller. The differences in the curves are striking and show that the general shape is seriously altered by the box. It is in fact almost impossible to analyse the signal in time-domain using the hydrophone in the box. Comparing results from 1/3 octave band analysis also shows differences, especially as regards the frequency dependence. These differences are, however, not as striking as those for signals in time-domain.

The arrangements for noise measurements at SSPA are at present:

1. Flush mounted pressure tranducers on the hull (Figure 3)
2. Flush mounted pressure transducers on the tunnel wall
3. Hydrophones in the flow field near the propeller (Figure 3)
4. Hydrophone in the water-filled box outside the tunnel

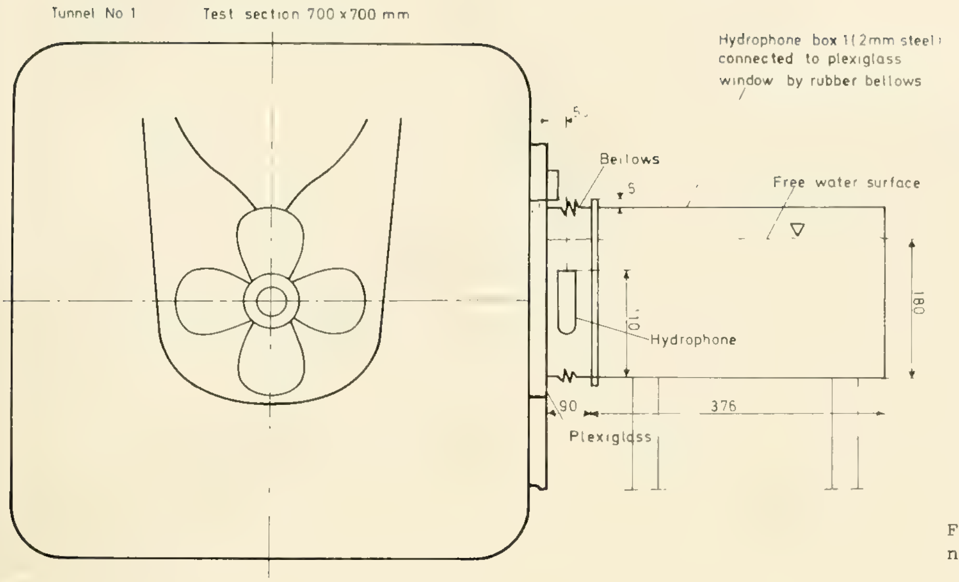
Tunnel No 1
Test section 700 x 700 mm
Hydrophone box 1 (2mm steel) connected to plexiglass window by rubber bellows
5
Bellows
5
Free water surface
110
Hydrophone
180
90
376
Plexiglass

FIGURE 1. First arrangement for noise measurement. (Tunnel No. 1)

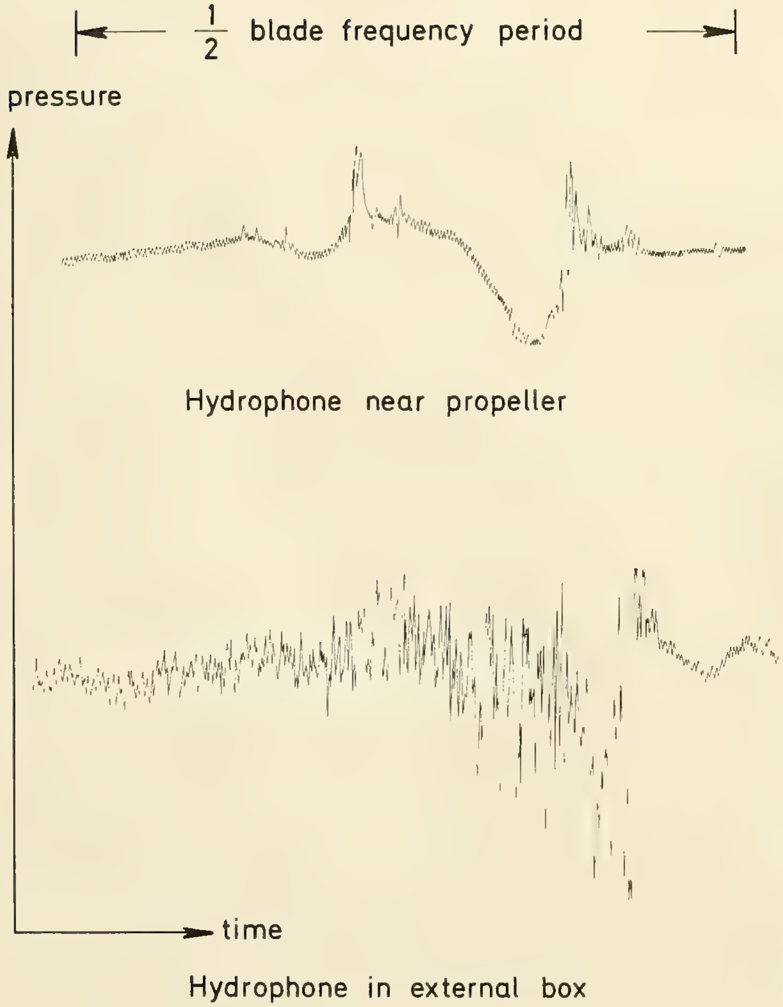

FIGURE 2. Pressure signals at different hydrophone positions.

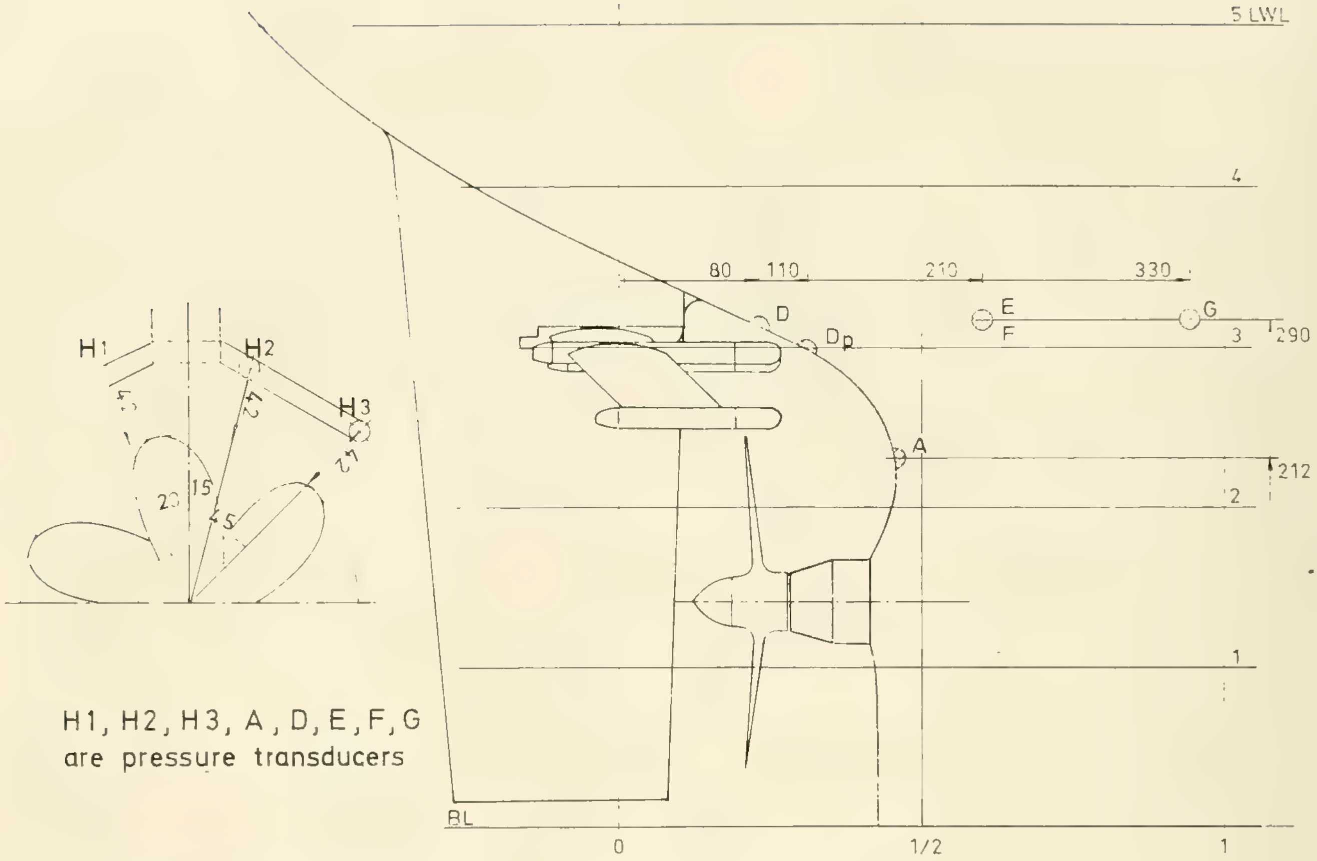

FIGURE 3. Arrangements for noise measurements on complete ship model. (Tunnel No. 2)

Arrangement 1 is intended to be the standard measurement procedure at SSPA and results are easily compared with full scale measurements using the same equipment. This arrangement gives essentially the near field noise from the propeller.

If it is of interest to know the radiated noise into the farfield, arrangement 2 can be used. Arrangement 4 also gives the farfield noise, but has its problems, as discussed above. Arrangement 2 has less problems with reflected acoustic waves and vibrations than arrangement 4. The main reason why arrangement 4 is still used is to compare results directly with older measurements. Arrangement 3 (Figure 3) has been especially developed for exploring the influence of variation in cavitation and the effect on the near field noise. Other arrangements of hydrophones have also been used for special purposes.

Since the main concern in the noise measurements is cavitation noise, the effect of flow noise due to the turbulent boundary is of minor importance. Usually the increase in noise level due to cavitation is quite substantial, as can be seen in Figure 4, which shows a typical example for a propeller in non-cavitating and cavitating condition.

2. EXPERIMENTS WITH AN OSCILLATING HYDROFOIL

Background to Experiments with Oscillating Hydrofoil

A typical example of the pressure signal from a cavitating propeller model is shown in Figure 5. The pressure was measured by a hydrophone near the

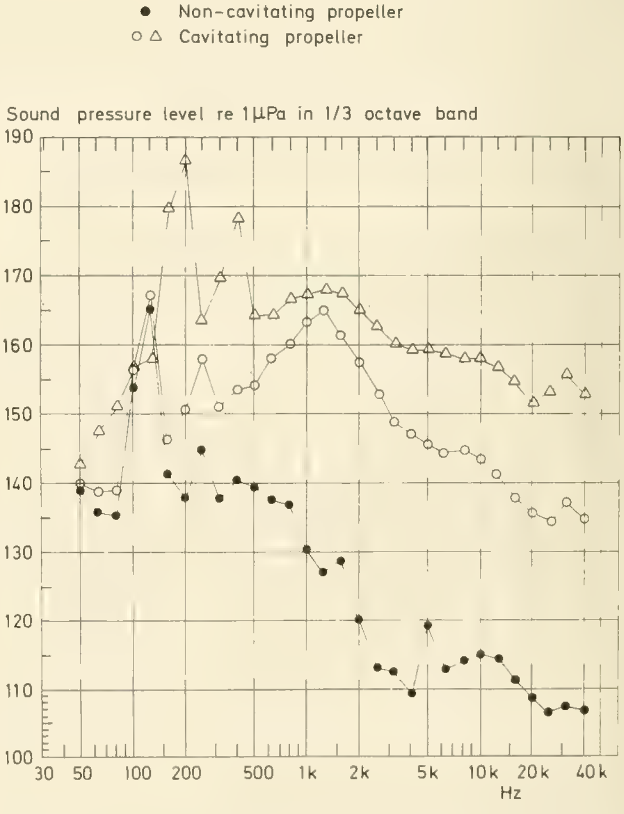

FIGURE 4. Noise measurements on propeller-model. (Tunnel No. 2)

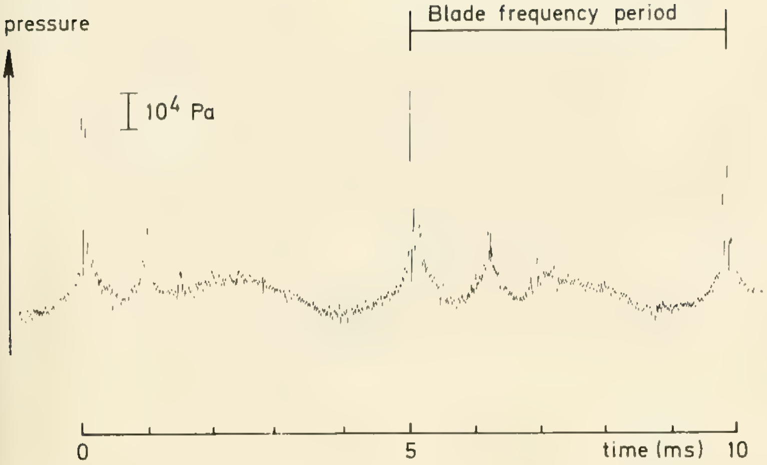

FIGURE 5. Pressure signal from a cavitating propeller model.

propeller. The signal corresponds to a spectrum of the the type shown in Figure 4 and typically is a rather slow variation of pressure interrupted by sharp and fairly infrequent pulses. The pulses are presumed to be generated during the final cavity collapse and they provide the main contribution to pressure levels at high frequencies. The pulses are often higher than the low frequency variations, but because of their low repetition frequency and wide frequency content the spectrum levels at high frequencies are lower than at low frequencies.

To understand the scaling of cavitation noise and how different types of cavitation noise are generated, and perhaps can be reduced, it is important to study the mechanism generating different types of noise. A suitable way to obtain such knowledge is to carry out high speed filming and synchronous measurement of the cavitation noise. The first idea was to carry out such measurements with a propeller model. Because of high tip speed, small dimensions, and the complicated geometry of a propeller it was decided to take the first step by performing such experiments with oscillating hydrofoils. By suitable oscillation of a hydrofoil it is possible to generate cavitation with approximately the same dynamic behavior as obtained from a propeller operating in a wake. The experiments with oscillating hydrofoils were supposed to shed some light on the following questions that originated from the search for methods of prediction and reduction of propeller cavitation noise:

1. Which are the characteristic properties of the pressure pulses from some special types of cavitation?
2. Are strong pulses generated by an orderly collapse of the whole cavity (e.g., a sheet cavity) or do they originate from large or small parts that separate from the main cavity? What is the geometry before and during collapse of cavities generating strong pulses?
3. How is the pressure pulse related to the size of the cavity? Is there, for example, any relation between the maximum extension of a sheet cavity and the final pressure pulse?
4. Is rebound of cavities important for generation of sharp pulses?
5. What part of the cavitation period is of main importance for the generation of different types of noise (slow pressure variations, sharp pulses, etc.)?
6. Which are the characteristic properties of the flow field, oscillation frequency, etc., causing cavitation with violent collapse?
7. To what extent is collapse time determined by the oscillation frequency of the hydrofoil?
8. To what extent does the cavity behavior seem predictable by theoretical methods? How realistic is it to think that a sufficiently good scaling from model to full scale is obtained for the most important cavitation events?

Experimental Set Up

Cavitation Tunnel

The tests were carried out in SSPA cavitation tunnel No. 1 (the samller one) equipped with test section No. 1 (500 × 500 mm).

Oscillation Apparatus

The hydrofoil was located horizontally in the test section and attached to an oscillation apparatus fixed to the test section wall (Figure 6). The hydrofoil was supported only at one end and forced to oscillate (rotate) around an axis fixed spanwise through the midchord point, i.e., the geometric angle of attack oscillated around an adjustable mean value, α_0, (Figure 7). The axis was driven by a connecting rod and an adjustable crankpin. By setting the crankpin the oscillation angle, $\tilde{\alpha}$, could be varied from 0 to 6°. With the hydrofoil used in these tests the oscillation frequency, f_{osc}, was varied from 0 to 15 Hz. The limits of water speed, α_0, $\tilde{\alpha}$, and f_{osc} were set by the strength of the hydrofoil and the background noise generated by the apparatus. One part of the background noise from such an apparatus is knocking in shaft bearings. To minimize this knocking, adjustable bearings were used. The motor, which was not dimensioned for this experiment, could deliver 16 kW at a maximum speed of 50 r/s.

The dynamic angle of attack, experienced by the leading edge of the hydrofoil, is composed of the geometric angle and of an angle caused by the motion of the leading edge. The angle is also affected by induced velocity. In the following only the geometric angle is considered (Figure 7).

The system with connecting rod and crankpin results in an approximately sinusoidal oscillation of the geometric angle of attack. This manner of

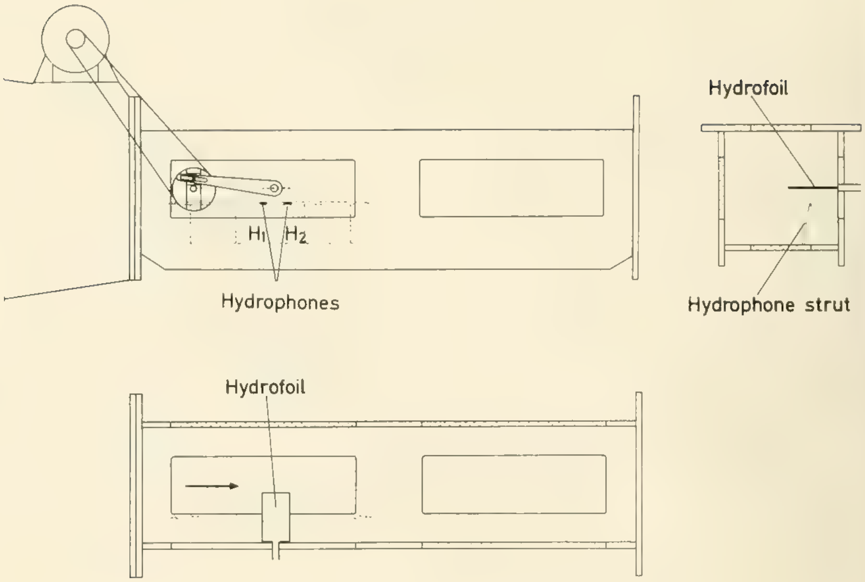

FIGURE 6. Experimental set up.

oscillation does not cause a time variation of the angle of attack that is completely similar to that of a propeller blade in a wake. The reason for using this sytem was that, due to its strength, high oscillation frequencies with large hydrofoils could be obtained. If similarity with propellers is most important it is probably better to use oscillation systems of the types constructed by Ito (1962) and Tanibayashi and Chiba (1977).

Hydrofoil

In these introductory experiments an existing hydrofoil, earlier used for studies in two-dimensional flow, was used. The profile has NACA 16 thickness-distribution and is typical of a relatively thick propeller blade at about 0.7 of propeller radius. The hydrofoil data are

Mean line a = 0.8
Camber ratio = f_y/c = 0.0144
Thickness ratio = s/c = 0.0681
Chord length = c = 120 mm
Span = 200 mm
Profile shown in Figure 7.

Noise Measuring Equipment

Two hydrophones (Brüel and Kjaer Type 8103 with frequency response 0.1 Hz - 140 kHz ±2 dB) were placed in notches in a tube supported by two hydrofoils in such a way that photographing of cavitation was permitted (Figure 6). The frequency response of the hydrophones mounted in this manner was checked by white noise. No significant change in the frequency response was detected.

The hydrophone signals were recorded on FM-channels on a Honeywell 5600-C tape-recorder (0-40 kHz at 60 ips tape speed). Recordings were also made on direct channels (300 Hz - 300 kHz at 60 ips). It was then possible to write out the complete signal (0-40 kHz) by use of tape speed reduction and UV-recorder.

Simultaneous with the hydrophone signals, a signal showing the events of maximum angle of attack was also recorded.

High-Speed Film Equipment

The requirements set up for the filming were that the film had to be synchronous with the noise recordings and permit measurements of cavity size as a function of time. The intention was not to measure the detailed behavior of small or very fast events. The minimum duration of the filming was set to about one second.

These requirements were met by a Stalex VS 1C camera capable of 3,000 frames/s. This is a 16 mm rotating prism camera taking rolls of 30 m film. Lenses with focus lengths of 9.8 and 50 mm were used. For synchronization the camera could release a flash at a preset time. The flash trigging signal was recorded on tape together with hydrophone signals and the flash was placed within the frame. Only one flash was released during each filming. The camera was also equipped with a crystal-controlled time-marker, making one light marking every millisecond on the edge of the film. This, together with the synchronization flash, made it possible to identify and follow cavitation behavior on the film together with the corresponding pressure

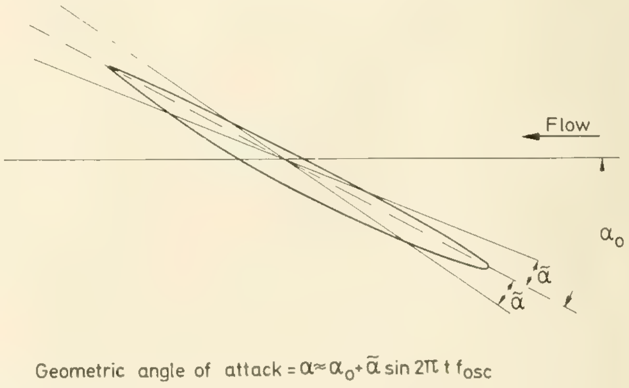
Flow
α_0
$\tilde{\alpha}$
$\tilde{\alpha}$
Geometric angle of attack = $\alpha \approx \alpha_0 + \tilde{\alpha} \sin 2\pi t f_{osc}$

FIGURE 7. Oscillating hydrofoil.

behavior recorded on tape. An example of the recorded signals is shown in Figure 8.

As light sources, two 1,000 Watt spotlights were used. To get a proper background without reflections the hydrofoil was painted with a red matte paint.

A test was performed with black and white film (Kodak 2479 RAR Film). The result was not very good, the contrast between hydrofoil and cavitation being too small. Color film (Kodak Vide News Film) was then used, with very good results.

Evaluation of Films and Pressure Signals

The pressure pulse generated by a cavity is related to the volume acceleration of the cavity and thus it is desirable to measure the cavity volume as a function of time. With complex cavities this is not very simple. An estimate of the cavity volume could be obtained if both cavity extent (area) and thickness were filmed synchronously. This is possible by the use of optical systems reflecting the two pictures into the same frame [Lehman (1966)]. No such attempts were made. Most photographs were taken in order to measure the cavity area on the suction side of the hydrofoil. To obtain information about the cavity thickness some photographs were, however, taken from the free end of the hydrofoil. A method of estimating the relative thickness, synchronous with the cavity area, was to measure the length of a cavity shadow generated by the directed light. The method, which was calibrated by use of spherical bubbles, was rather rough, but some general information of thickness behavior was obtained.

The photographs were studied by use of an analysis projector permitting single-frame projection on a focusing screen, where the area of the cavities could be measured by summing up elements in a pattern. For identification of cavitation events on the films and noise recordings the synchronization flash was the primary starting point. To increase the accuracy of identification of events far from the flash easily identifiable events, such as single bubble collapses, were used as reference points.

Experiments

The experiments with an oscillating hydrofoil presented in this paper are the first of this kind carried out at SSPA and they are to be regarded as introductory in several respects.

Only one hydrofoil was used. The following flow parameters were held constant during the tests:

Relative gas content (at atmospheric pressure) of the tunnel water was 25%

Water velocity in test section = U = 5.0 m/s

Cavitation number at the center of test section

$$= \sigma = \frac{p_0 - p_v}{\frac{1}{2}\rho U^2} = 0.76$$

where

p_0 = surrounding pressure = 11.850 Pa
p_v = vapor pressure of water (20°C) = 2.338 Pa
ρ = density of water = 998 kg/m^3

The following oscillation parameters were varied in the experiments (see Figure 7):

α_0 = mean angle of attack of the hydrofoil
$\tilde{\alpha}$ = oscillation angle
f_{osc} = oscillation frequency

In the figures the reduced frequency k_c is used:

$$k_c = \frac{\omega c}{2U} = \frac{\pi f_{osc} c}{U}$$

where

$\omega = 2\pi f_{osc}$
c = chord length of the hydrofoil
U = water velocity

After some introductory tests the following conditions of hydrofoil oscillation were selected from high-speed filming:

α_0 (o)	$\tilde{\alpha}$ (o)	f_{osc} (Hz)	k_c
3	3	3	0.23
"	"	7	0.53
"	"	10	0.75
"	"	15	1.13
3	4	1	0.08
"	"	2	0.15
"	"	3	0.23
"	"	4	0.30
"	"	7	0.53
"	"	10	0.75
"	"	14	1.06
4	3	3	0.23
"	"	7	0.53
"	"	10	0.75
"	"	15	1.13
4	5	3	0.23
"	"	7	0.53
"	"	10	0.75

Results

Primary results are presented as pressure signals from cavitating and non-cavitating hydrofoils, measurements of cavity area, and sketches of the cavitation pattern at various oscillation parameters.

Presentation of Results

In Figures 9 - 14 a survey of pressure signals and cavitation patterns at various oscillation conditions is shown. All pressure signals shown in these and other figures are from the hydrophone (H1) near the leading edge of the hydrofoil. For each condition some oscillation periods are shown. The length, $T_{osc} = 1/f_{osc}$, of an oscillation period is identified by the markings of maximum angle of attack, α_{max}. The figures show primarily cavitating conditions (cavitation number = 0.76) but in some cases signals from the corresponding non-cavitating condition is sketched (without the fine structure, which is apparatus noise). The pressure scale is given as a number of Pascal (Pa) per scale unit (su) defined at the top of the figures. The time scale is 6.15 ms/scale unit in all signal examples in Figures 9-13. For one of the oscillation periods the number of the oscillation period (relative to the synchronization flash) is shown in a circle, and for this period some additional data is given to the right. In the cavitation sketches are shown the maximum area extent, the maximum chordwise cavity length, ℓ_{max}, and the cavitation extent at

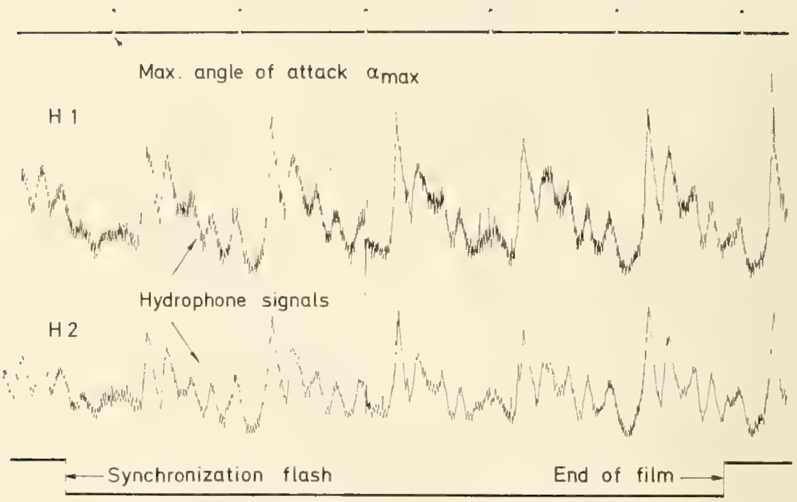

FIGURE 8. Measurements with oscillating hydrofoil. Recorded signals.

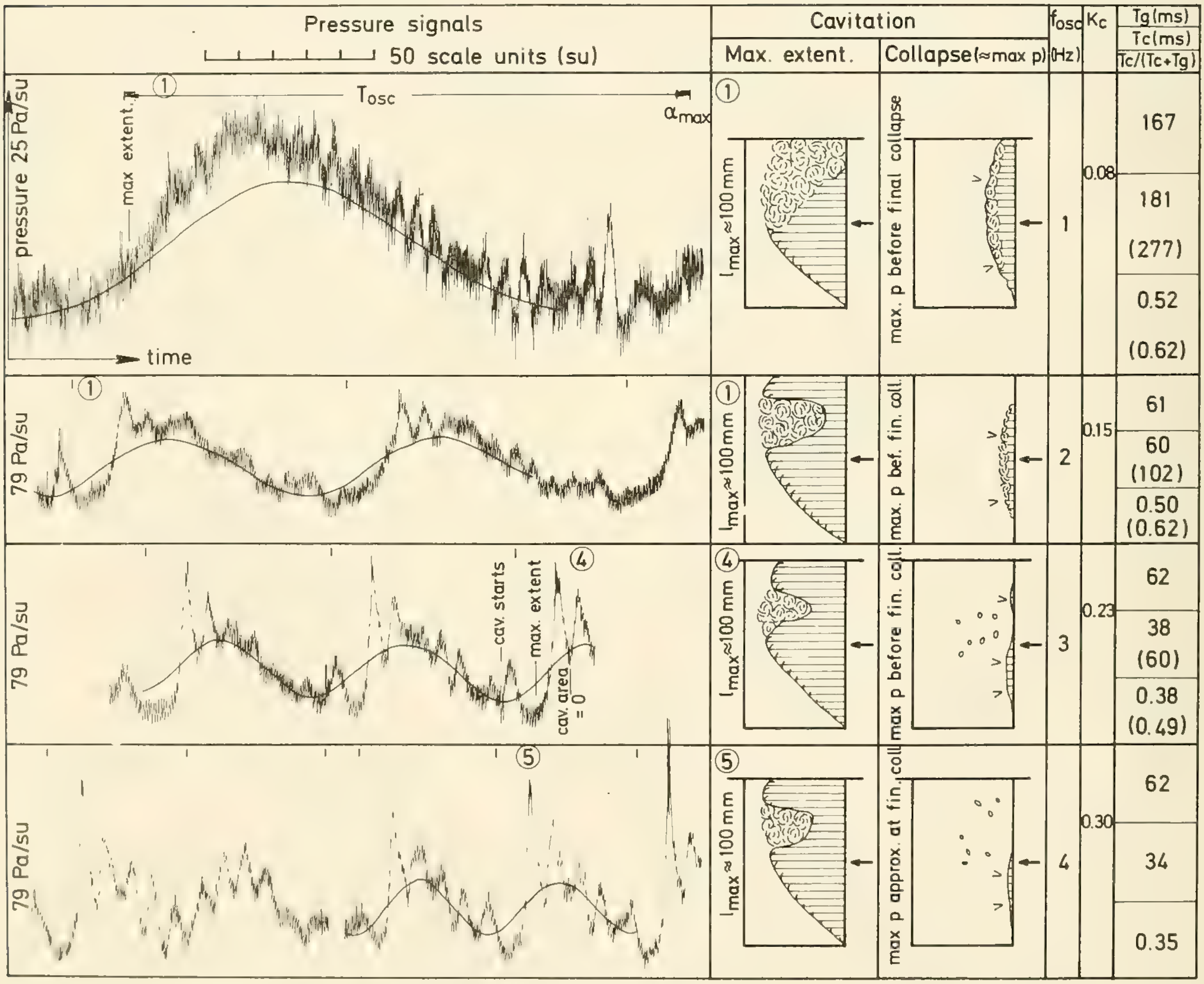

FIGURE 9. Oscillating hydrofoil. Pressure signals and cavitation. $\alpha_n = 3^\circ$ $\tilde{\alpha} = 4^\circ$.

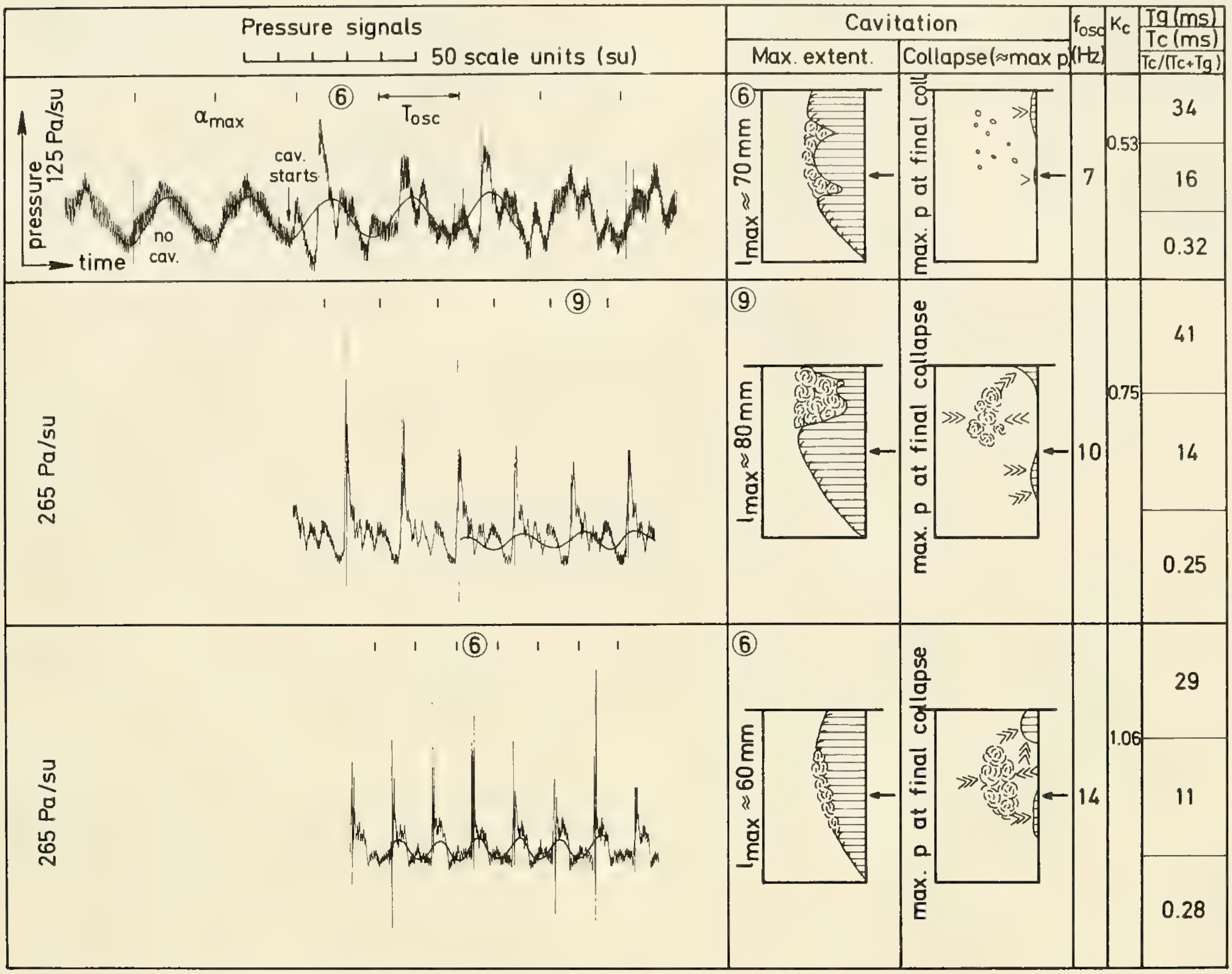

FIGURE 10. Oscillating hydrofoil. Pressure signals and cavitation. $\alpha_o = 3^o$ $\tilde{\alpha} = 4^o$.

(approximately) that moment when maximum pressure is generated. For rapidly collapsing cavities the cavitation patterns shown existed 1/3-2/3 milliseconds before the sharp pressure pulse. A note is also made as to whether or not the maximum pressure increase coincided with the final collapse (i.e., the complete disappearance of the cavity). The collapse velocity during the last stage is indicated by arrows:

> = slow motion of the cavity boundary in the direction of the arrow
>> = fast motion of the cavity boundary in the direction of the arrow
>>> = very fast motion of the cavity boundary in the direction of the arrow

At collapses with more or less spherical symmetry, arrows are placed opposite each other.

To the right is shown the cavity growth time, T_g, and the collapse time, T_c, for the complete cavity, measured by use of the time markings on the high-speed film. The collapse time is measured from the time of maximum area extent to that time when the cavity generated the maximum positive pressure. For rapidly collapsing cavities this event coincides with complete disappearance of the cavity. This was not the case for slowly collapsing cavities; for these cavities the collapse times for complete disappearance are also given (in parenthesis).

General

The general character of noise and cavitation behavior when the frequency of oscillation is varied is shown in Figures 9-14. The pressure signals from the cavitating hydrofoil are to be compared with signals from the non-cavitating hydrofoil (Figure 15) and with the curve in Figure 16, showing the schematic behavior of the pressure generated by a growing and collapsing cavity.

In comparisons of generated pressure from non-cavitating and cavitating hydrofoils the most striking difference is often the high and sharp pulses generated at the cavity collapse. The generation of such pulses is obtained especially when f_{osc} exceeds a certain value. Also the pressure increase corresponding to cavity growth and the pressure dip generated near maximum cavity extent are detectable.

The generated pressure pulses were classified into three main types:

- Slow pressure increase at cavity collapse (normally obtained at f_{osc} = 1-3 Hz)
- Fast pressure increase (f_{osc} = 4-7 Hz)
- Very fast pressure increase, i.e., sharp pulses (f_{osc} = 7-15 Hz)

Generation of High Frequency Noise

Sharp pulses (i.e., high frequency noise) were generated in three main ways:

A. By violent collapse of the main cavity (or a large part of it).

B. By collapse of small spherical bubbles occurring independently of the main cavity. The bubbles generated rather strong pulses.

C. By collapse of rather small irregular cavities separating continuously from the main cavity.

Of greatest interest is the generation process A, which was obtained at high f_{osc}. The high and sharp pulses were generated in three somewhat different ways:

A1. Separation of a rather large part of the main cavity at an early stage of the collapse. Thick cavity formations often separated in this way, especially if the cavity was long (large ℓ_{max}) and broken up by disturbances. At the end the collapse was often very violent and often followed by a violent rebound. Also the rebounded cavities (complex in form) cometimes collapsed violently. An example of this behaviour is shown in Figure 13 for f_{osc} = 7 Hz (oscillation period 5).

A2. Sharp pulses were also generated when a sheet collapsed towards the leading edge. The upstream cavity boundary was attached to the leading edge during the whole collapse. This process was normal at the conditions shown in Figures 11 and 12 and especially in cases where the main cavity was rather small. In these cases the whole collapse was orderly and without extensive separations of cavity parts from the main sheet. After the collapse was completed a rebound of small cavities occurred about 10 mm downstream from the leading edge and not at the center of collapse as in the case of more symmetrical collapses. Also in cases where large cavities separated from the main cavity the remaining, rather smooth sheet often collapsed in this way (Figure 10, 10 and 14 Hz, Figure 13, 7 and 10 Hz).

A3. In cases where the smooth sheet attached to the leading edge was long and narrow it was also cut off from the leading edge. For the downstream part, the collapse then became more symmetric and violent and with a violent rebound (Figure 11, 10 Hz and Figure 13, 7 Hz). This process often occurred near the end of collapse.

Spherical bubbles were very effective as genera-

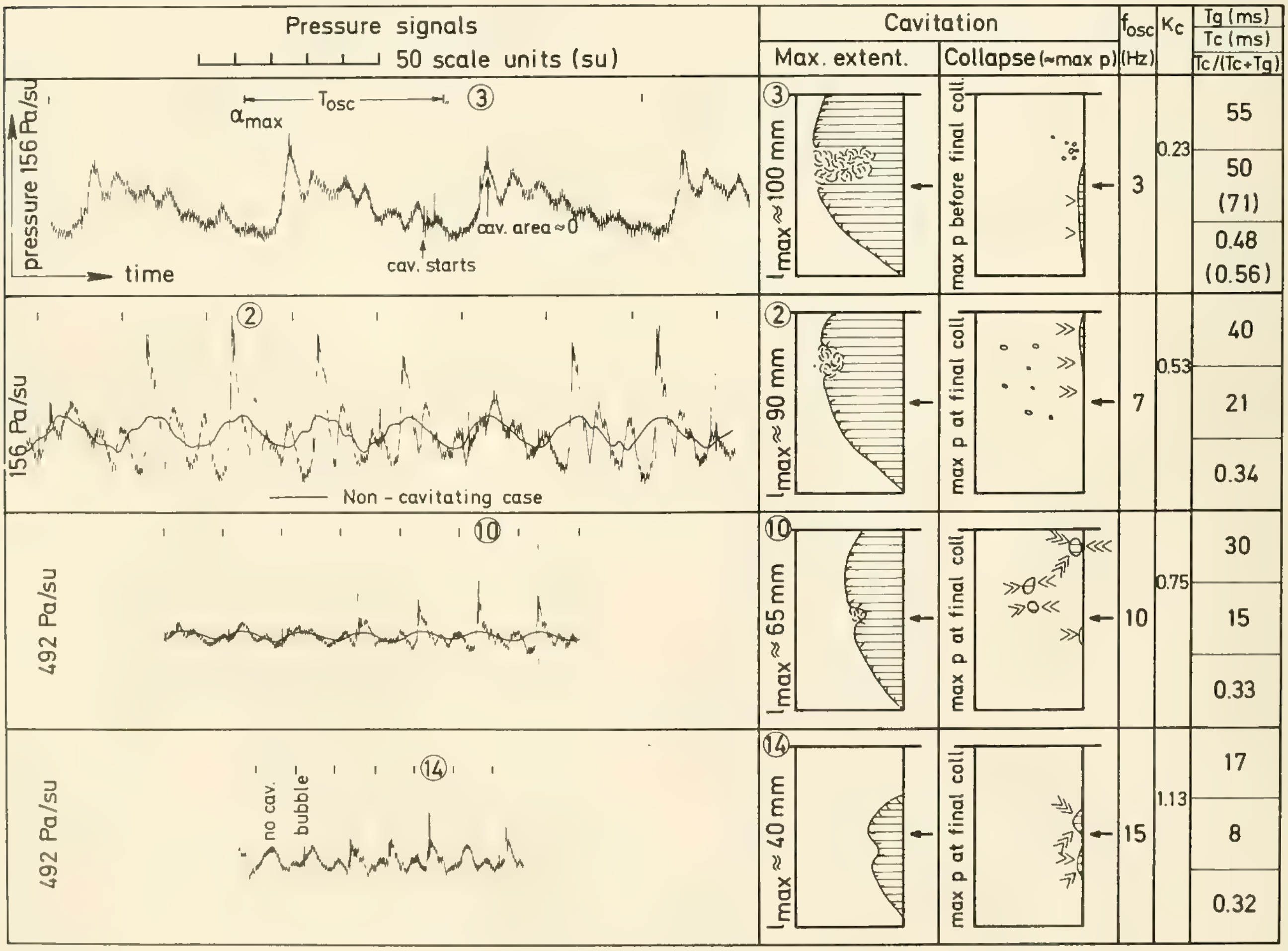

FIGURE 11. Oscillating hydrofoil. Pressure signals and cavitation. $\alpha_o = 3^\circ$ $\tilde{\alpha} = 3^\circ$.

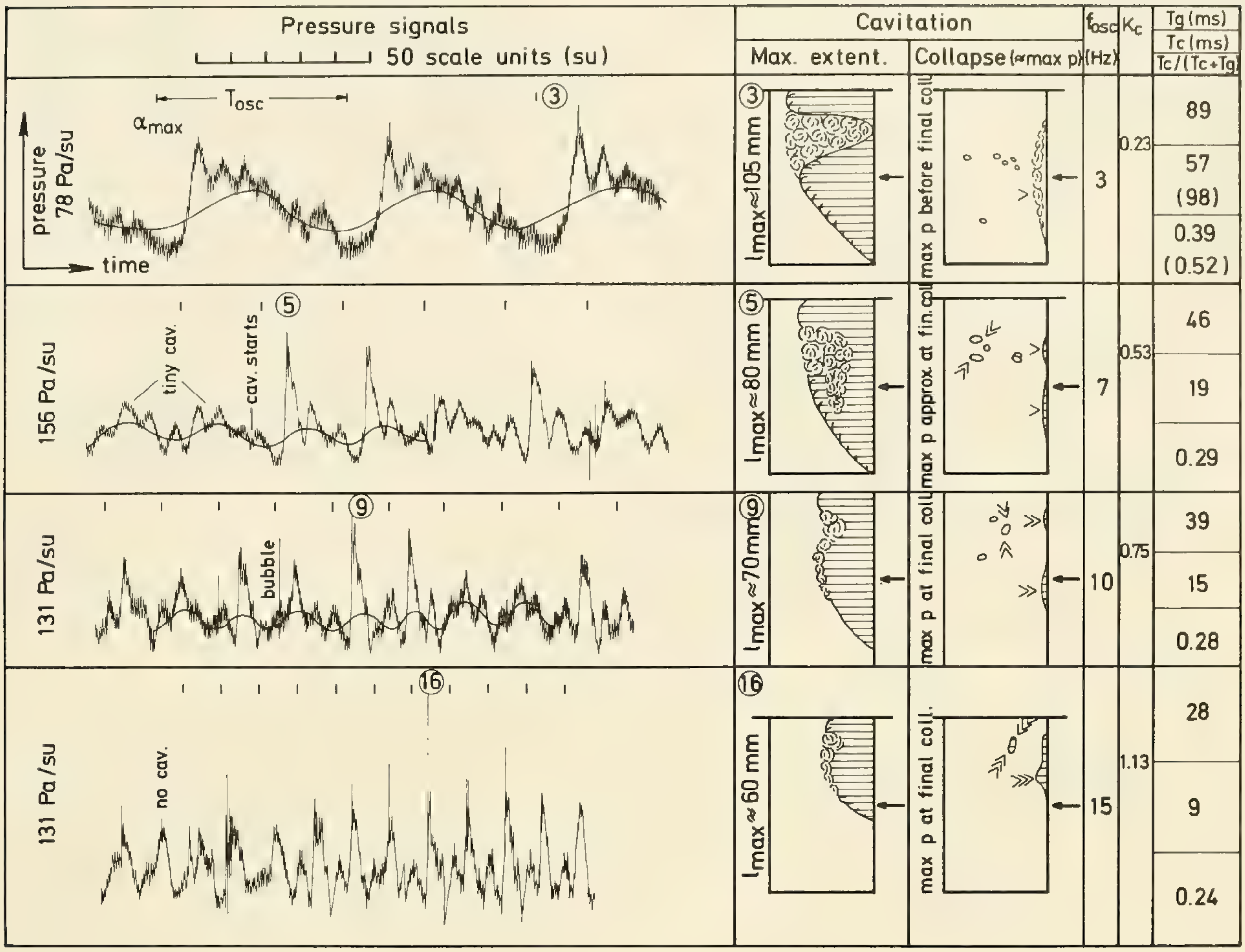

FIGURE 12. Oscillating hydrofoil. Pressure signals and cavitation. $\alpha_o = 4^\circ$ $\tilde{\alpha} = 3^\circ$.

tors of high frequency noise. This is discussed later in the text together with cavity area measurements.

The generation of high frequency noise by small irregular cavities, continuously separating from the main cavity is the only generation process when $f_{osc} = 0$. Also at low f_{osc} (about 1-2 Hz) this process generated pulses. The separation of small cavities from the main cavity decreased with increasing f_{osc}.

When the high frequency noise was obtained it was always generated during the last part of collapse of the *generating* cavity (i.e., a bubble could collapse and generate high frequency noise during the growth of the main cavity). This is not surprising, but it should be mentioned that at studies of propeller cavitation it has been noticed that the growth of cavities in some cases also generates rather fast pressure variations which indicates that high volume acceleration can also occur during growth.

Generation of Low Frequency Noise

The generation of low frequency noise (vibration generating pressure disturbances at multiples of propeller blade frequency) can be identified by inspection of signals from non-cavitating conditions, cavitating conditions, and the schematic pressure behavior shown in Figure 16. This is especially easy in cases where cavitation start is marked (Figure 9, 3 Hz, Figure 10, 7 Hz, Figure 11, 3 Hz, Figure 12, 7 Hz, Figure 13, 3 Hz) or where a non-cavitating period is followed by a cavitating one. In several cases it can be seen that a rather slow pressure increase is generated during the growth.

When the volume acceleration is directed inwards, during a period around the maximum cavity volume, negative pressure is generated (for example Figure 9, 3 Hz). This pressure variation is rather slow and is an essential part of the low frequency disturbance. Because of inertia effects in the motion of cavity walls this part of the motion will probably never contribute to really high frequencies.

In most of the figures it can be seen that contribution to the low frequency pressure is also obtained from the collapse. Especially at low f_{osc} the collapse seems important. The pressure increase during collapse is due to the outward-directed volume acceleration existing during the final part of collapse. This acceleration depends on the cavity geometry and the velocity of the cavity walls and it is in principle possible to obtain a collapse with constant volume velocity (no pressure generation), as well as a collapse with decreasing volume velocity, in which case a pressure increase is generated. It is supposed that both types of collapse can occur

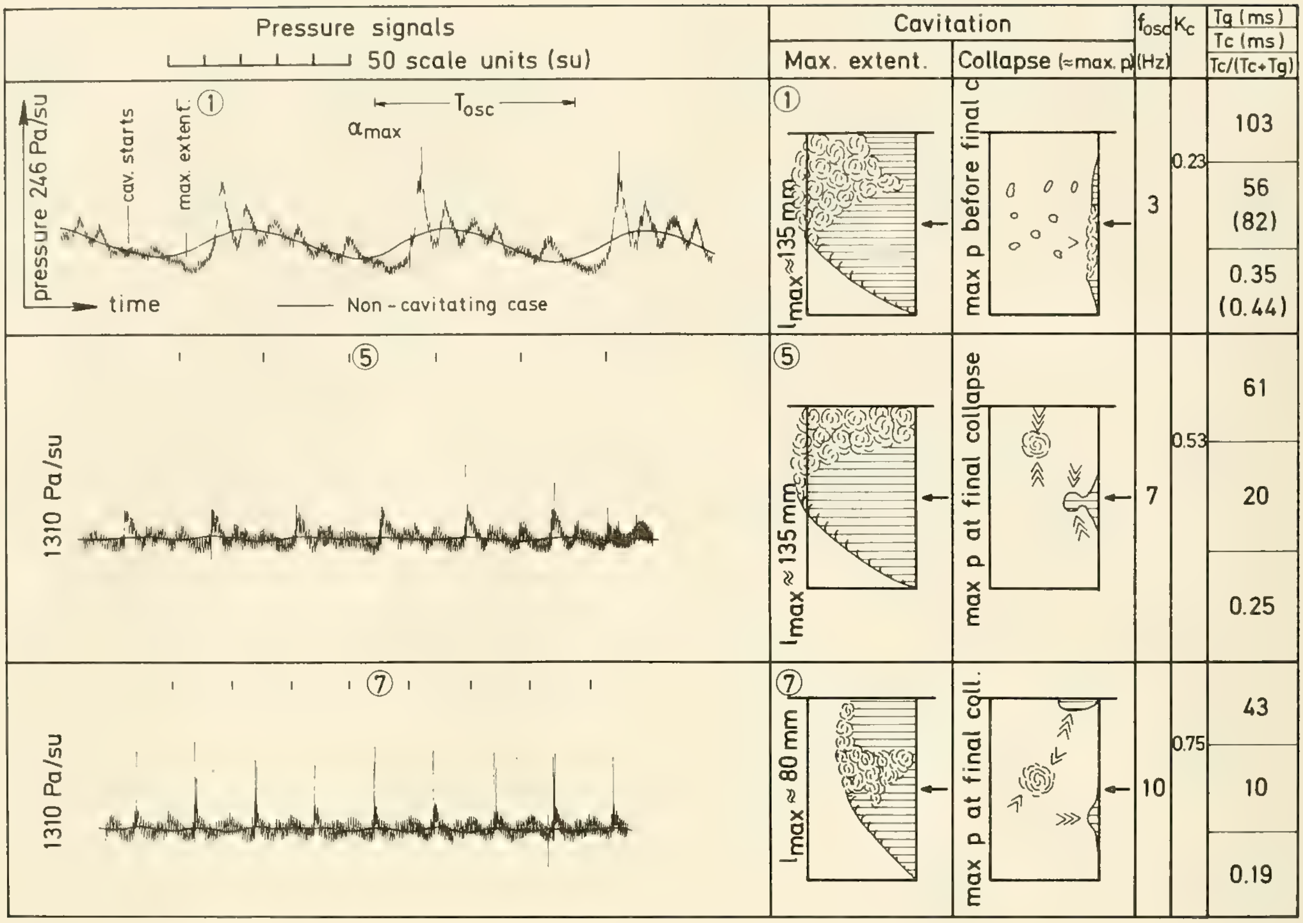

FIGURE 13. Oscillating hydrofoil. Pressure signals and cavitation. $\alpha_0 = 4^\circ$ $\tilde{\alpha} = 5^\circ$.

on propellers, depending on cavity geometry and time variation of the surrounding pressure.

The contribution from collapse obviously exists (see Figure 9, 1 and 2 Hz) but the quantitative results especially at f_{osc} = 3-7 Hz must be used with much prudence, because of the resonant character of the signal in these conditions. This is discussed in the Appendix.

Area Measurements of Some Cavities

For the condition $\alpha_0 = \tilde{\alpha} = 3^\circ$ and f_{osc} = 15 Hz some results from measurements of cavity area are shown in Figures 17-23. The main cavity includes the sheet and some small bubbles at the downstream edge, which follow the behavior of the sheet. Although the cavities in this condition were rather simple, with no large separations from the sheet, quite complex events often occurred during the last 1/2 millisecond of the collapse.

Some comments on the figures will be made:

1. From the shape of the area curves it can be seen that the growth of cavities was rather similar in all cases, while there are differences in the collapses. Compare, for example, Figures 17 and 20.
2. It is seen that 1-2 milliseconds before final collapse a slow or moderately fast pressure increase was obtained. During this time collapse is fast, but measurable. This pressure fluctuation corresponds to low or medium-high frequencies from a propeller (5-20 × blade frequency). The pressure fluctuation seems related to the dynamics of the main cavity, which at this stage was quite orderly.
3. During the last part of collapse very sharp pulses with durations less than 0.1 millisecond were generated. At this scale of time, measurements and detailed observations of cavity behavior were not possible. Some observations indicated, however, that the sharp pulses sometimes were generated by a rather well-ordered collapse. Figure 17 shows an example of this behavior. The cavity was in this case attached to the leading edge during the whole collapse.
4. More complex cases are shown in Figures 18, 21, 22, and 23. Several pulses were generated during a short time and it is impossible to separate the generating events (collapses and rebounds of several small cavities). Typical of these oscillation periods is that when the downstream cavity wall moves towards the leading edge, the cavity separates into two parts, both attached to the leading edge. This separation was caused by a growing disturbance on the cavity surface. The disturbance grew from the downstream edge towards the leading edge. (See also Figure 11). During the collapse some bubbles also separated from the downstream cavity edge and the disturbed area. These three cavity

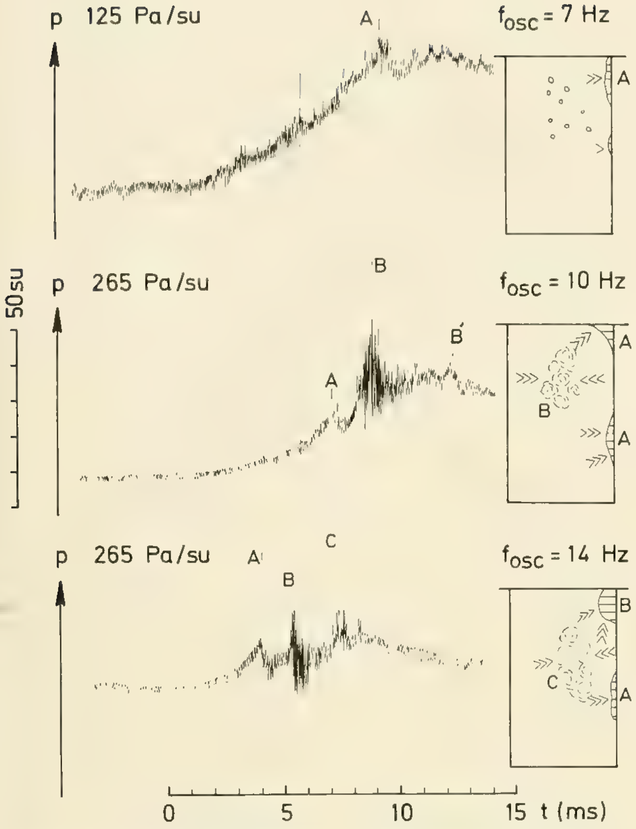

FIGURE 14. Pressure signals during collapse. Expanded signals from Figure 10.

groups seldom collapsed exactly simultaneously or with the same violence. For example, in the cases shown in Figures 18 and 21 a part of the cavities was cut off from the leading edge during the last millisecond of the collapse. This resulted in violent collapse of the cut-off parts.

From these examples it is understood that in a single oscillation period the character of the pressure signal is very sensitive to such things as simultaneousness and violence of separate cavitation events. Over many periods, normally used in measurements, the quantities are smoothed out to a mean value, which often is less sensitive to small disturbances.

5. In some cases small bubbles and irregular parts separated from the main cavity and collapsed rather fast. In the case shown in Figure 22 a group of small bubbles behind the main cavity (cavity B) collapsed violently, simultaneously with the main cavity, and it is impossible to determine which of the cavities generated the main pulse. Examples of cavities that seemed rather fast, but only generated small pulses are shown in Figure 18 (B) and 19 (C).
6. The most extensive rebounds resulted from cavities that were cut off from the leading edge and then collapsed fairly symmetrically. The cut-off normally occurred during the last one or two milliseconds and it often resulted in two cavities, one of which remained attached to the leading edge. The

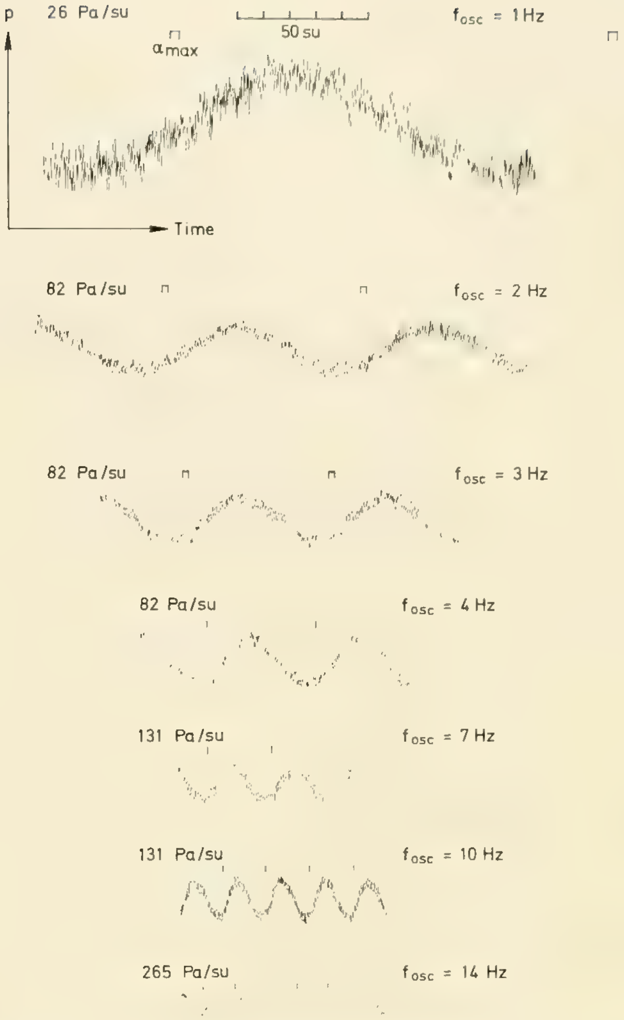

FIGURE 15. Pressure signals from non-cavitating hydrofoil. $\alpha_o = 3^o$ $\tilde{\alpha} = 4^o$.

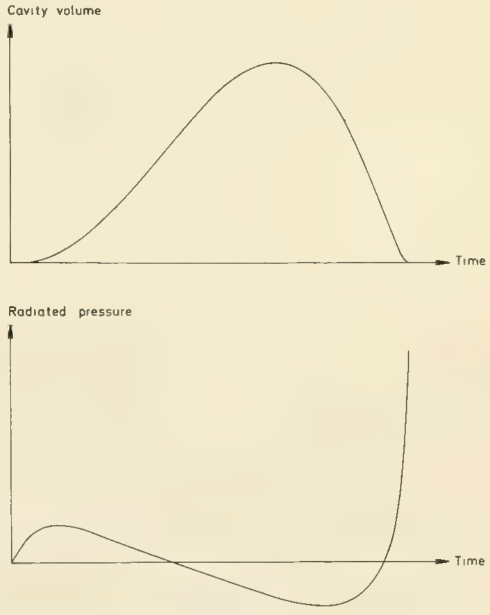

FIGURE 16. Schematic behavior of cavity volume and radiated pressure.

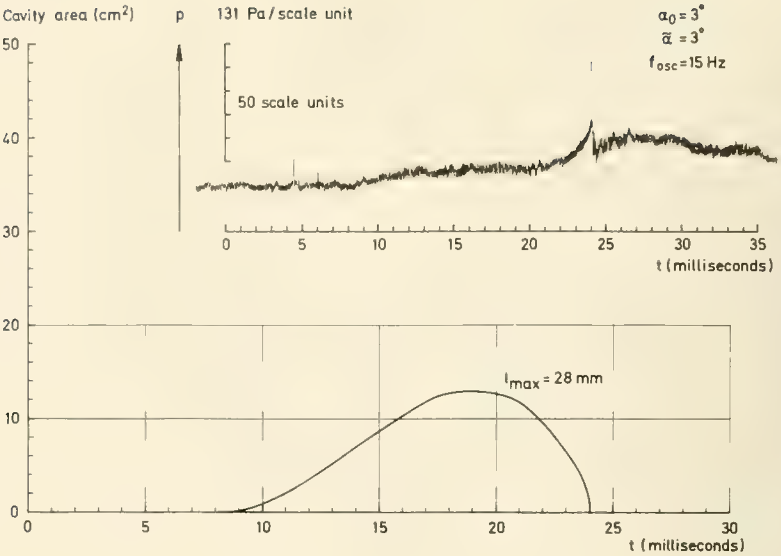

FIGURE 17. Cavity area and generated pressure. Oscillation period -1.

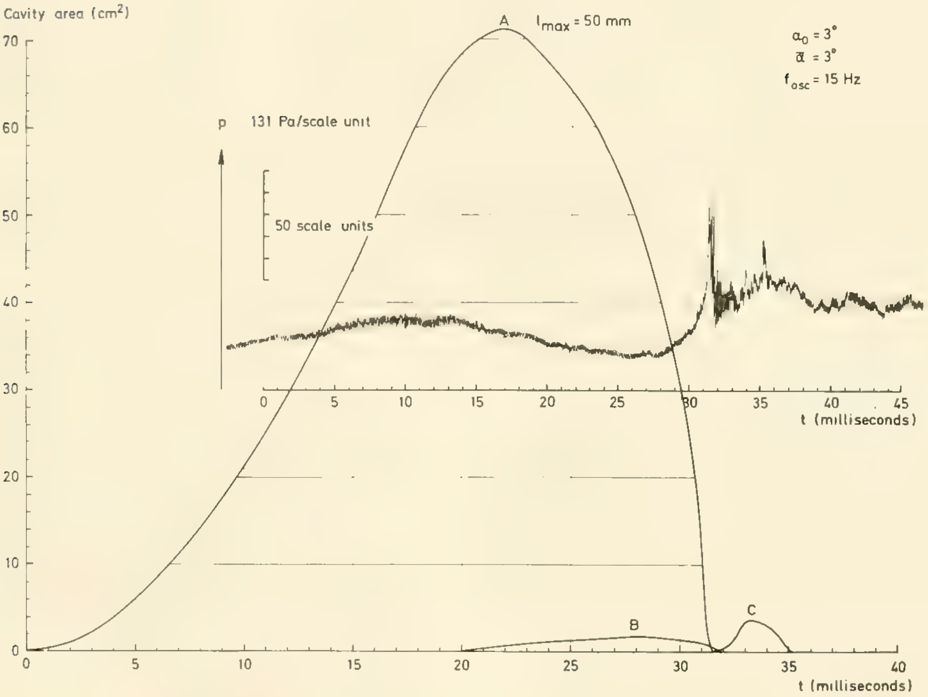

FIGURE 18. Cavity area and generated pressure. Oscillation period 4.

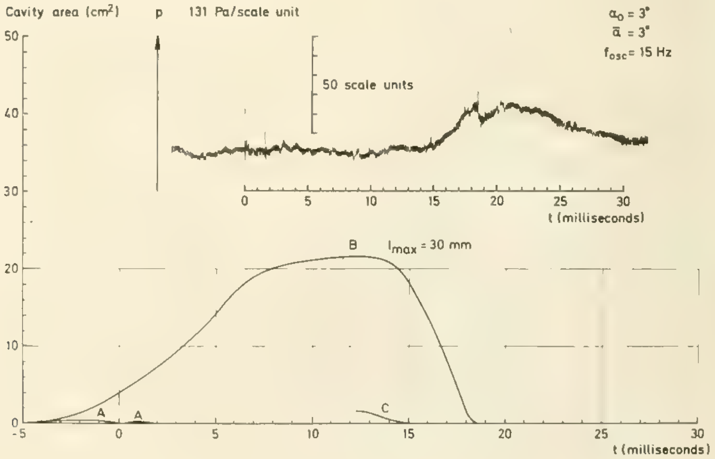

FIGURE 19. Cavity area and generated pressure. Oscillation period 6.

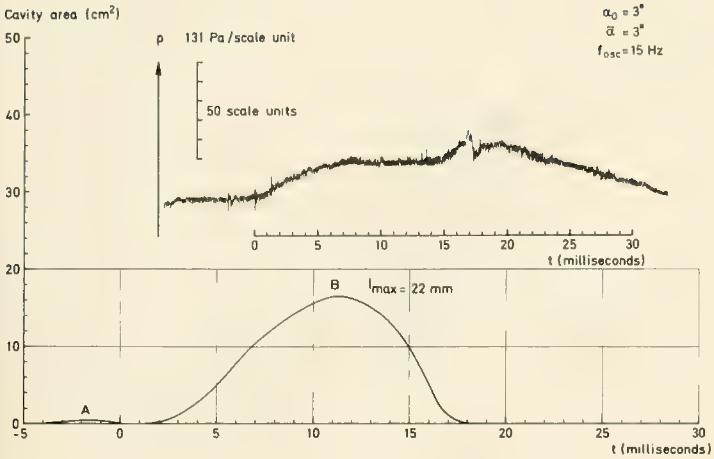

FIGURE 20. Cavity area and generated pressure. Oscillation period 7.

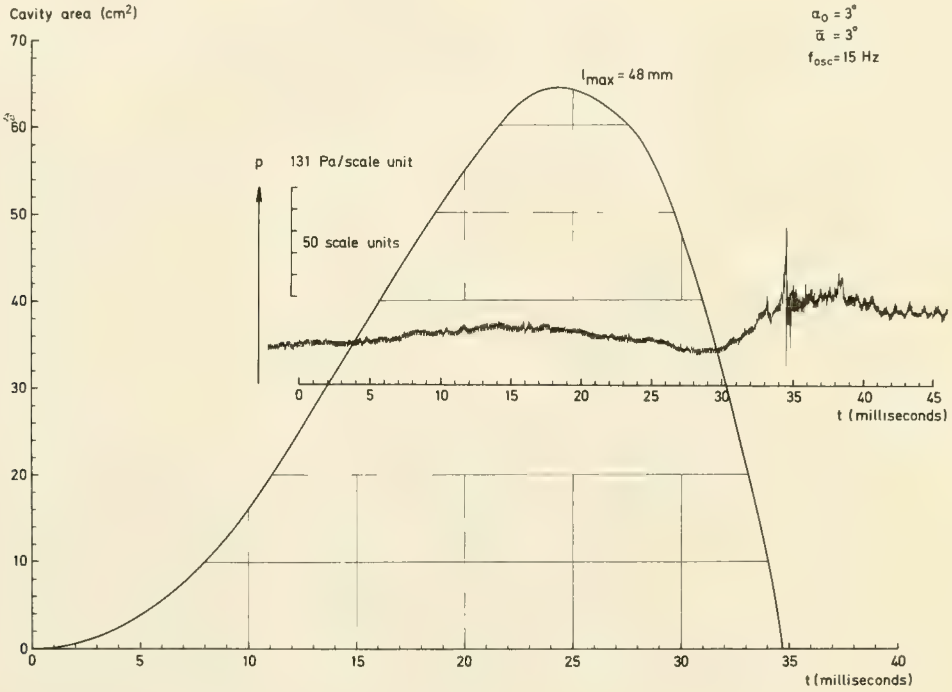

FIGURE 21. Cavity area and generated pressure. Oscillation period 12.

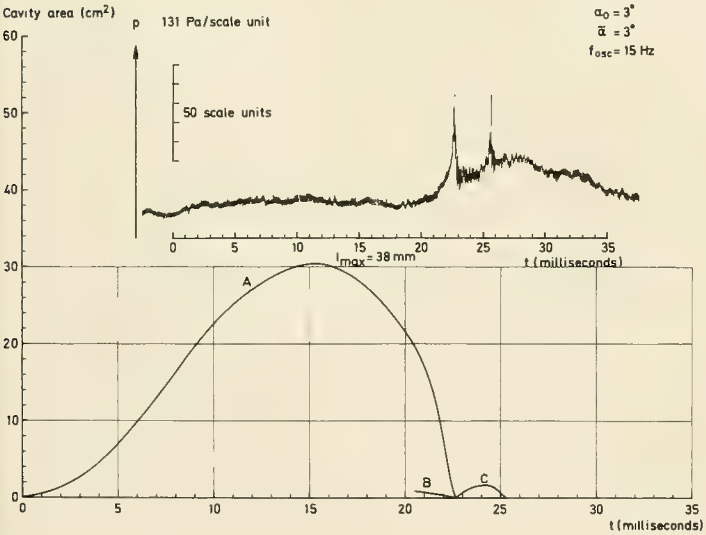

FIGURE 22. Cavity area and generated pressure. Oscillation period 13.

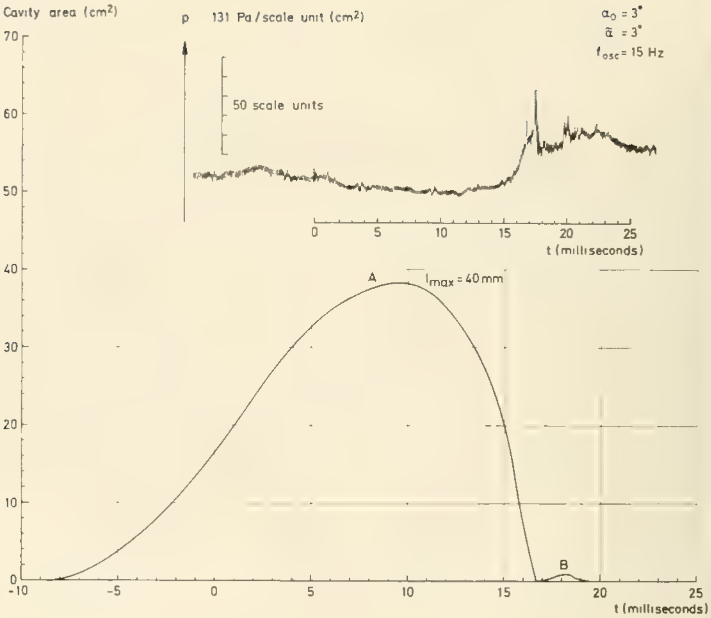

FIGURE 23. Cavity area and generated pressure. Oscillation period 14.

rebounded cavity (often a group of small cavities) collapsed after three to four milliseconds. Compared with the main cavity the area of the rebounded cavity was small (Figure 18 cavity C, Figure 22 cavity C and Figure 23 cavity B). The rebounded cavity often generated pulses of nearly the same height as the main cavity.

7. The equipment was not designed to measure small and fast collapsing cavities such as small bubbles, but an example of a diameter measurement of a bubble is shown in Figure 24. The area ($\pi d^2/4$) of the same cavity is plotted in Figure 19 (cavity A), where the sharp collapse pulses are also visible. Other examples of bubble collapses are shown in Figure 17 (time = $t \simeq 5$ ms), 18 ($t \simeq 10$), 20 ($t \simeq 0$, cavity A), and 23 ($t \simeq 0$). Bubble collapses are also shown in Figures 9-13.

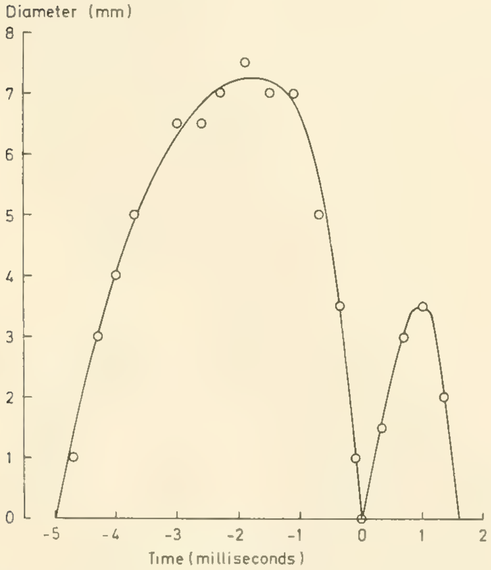

FIGURE 24. Diameter of a spherical cavity. (Cavity A in Figure 19.)

The bubbles studied appeared just before or during the growth of the main cavity and the pressure pulses were then easy to identify. The bubbles normally rebounded once or twice. From the size of the bubbles and the generated pressure it is obvious that the bubbles are very effective as sources of high frequency noise. During the first life cycle, the bubble surface was smooth, but in the rebound cycles it became rough as reported by other authors.

Dimensionless Presentation of Some Results

The pressure generation at collapse is related to the violence of the collapse and it is then natural to study the collapse time, T_c, for cavities generating different types of pressure pulses. Tc, given in Figures 9-13, is measured for the complete cavity, but in several cases it is only a separted part of the cavity that generates the main pressure pulse. Because of this simplification T_c is probably not significant for the generated pressure in all cases. The intention was, however, to study the relevance of parameters for the complete cavity.

In Figure 25 $T_c/(T_c + T_g)$, (T_g = growth time), is plotted for the cavities shown in Figures 9-13. As seen the steepness of the curves tends to stabilize at a lower value for f_{osc} resulting in sharp pulses. The growth and collapse are, however, not generally related to each other and Figure 25 may thus give a distorted picture of T_c-behaviour. In an effort to remove this drawback T_c/T_c' also was plotted, where T_c' is a hypothetical collapse time given by the formula for spherical cavities (Rayleigh 1917):

$$T_c' = 0.915\, \ell_{max} \left(\frac{\rho}{p_0 - p_v}\right)^{\frac{1}{2}}$$

$$= \frac{0.915\, \ell_{max}}{U} \left(\frac{2}{\sigma}\right)^{\frac{1}{2}}$$

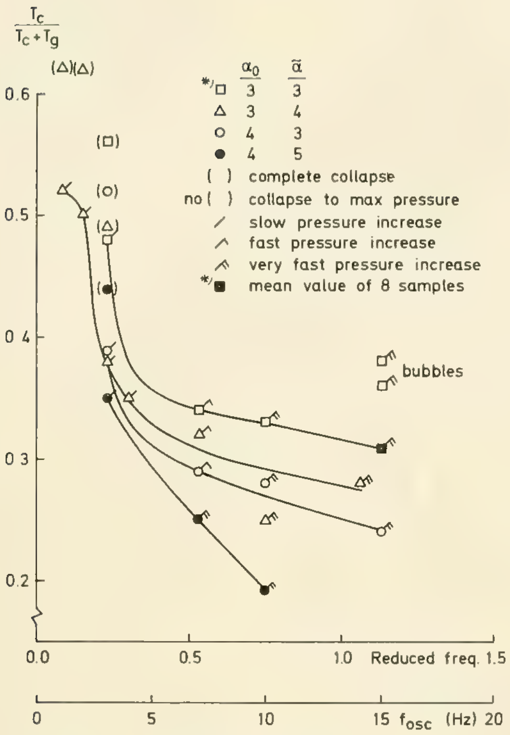

FIGURE 25. Normalized collapse time.

where

P_0 = surrounding pressure
p_v = vapor pressure
U = undisturbed velocity
ρ = density of water
σ = cavitation number

Of course this formula at best gives a time proportional to the collapse time of the sheet with maximum length, ℓ_{max}. As is shown in Figure 26 the tendency is simlar to that in Figure 25. The conclusion is that at high f_{osc} the collapse is mainly regulated by a surrounding pressure considerably higher than the pressure inside the cavity, which results in $T_c/T_c' \simeq$ constant and a violent collapse of the type predicted by classical theory [Rayleigh (1917)]. At low f_{osc} it can be supposed that during collapse the pressures outside and inside the cavity are approximately equal. Then a violent collapse will not occur and T_c/T_c' becomes considerably larger than for a "free" collapse.

If the cavity is considered as a monopole source the generated pressure, p, in the far field is

$$p = \frac{\rho}{4\pi r}\,\frac{d^2V(t - \frac{r}{c})}{dt^2} \qquad (1)$$

where

V = cavity volume
r = distance between cavity and hydrophone
c = velocity of sound
t = time

Applying this and classical theory of cavity collapse it can be shown [Ross (1976)] that the generated maximum pressure, p_{max}, at certain conditions is given by

$$p_{max} = \text{const}\,\frac{R_{max}\,\Delta P}{r}$$

where

R_{max} = the maximum radius of a spherical cavity
ΔP = $P_0 - p_v$
P_0 = surrounding pressure
p_v = vapour pressure

According to this

$$p^+ r/\ell_{max}\Delta P \qquad (2)$$

would be an appropriate coefficient to study for different cavities in our case. The parameters are:

p^+ = maximum pressure increase at collapse
ℓ_{max} = maximum chord-wise extension of the sheet cavity (for bubbles ℓ_{max} = diameter)

The distance r is measured individually for every collapse.

$$\Delta P = \frac{1}{2}\,\rho\,U^2\,\sigma \simeq 9{,}500\ \text{Pa}$$

Inherent in the coefficient above is an assumption about the collapse dynamics and, as the dynamics are dependent on cavity type, there is no universal value for the coefficient (2). For our purpose the coefficient may be seen as a measure of the pressure generation efficiency of different types of cavities. For spherical cavities this coefficient was used by Harrison (1952) and Blake et al. (1977).

Another treatment which leads to a dimensionless pressure coefficient is to suppose that a constant part of the potential energy available for collapse is radiated as noise [Levkovskii (1968)]. The dimensionless parameter derived from this assumption is

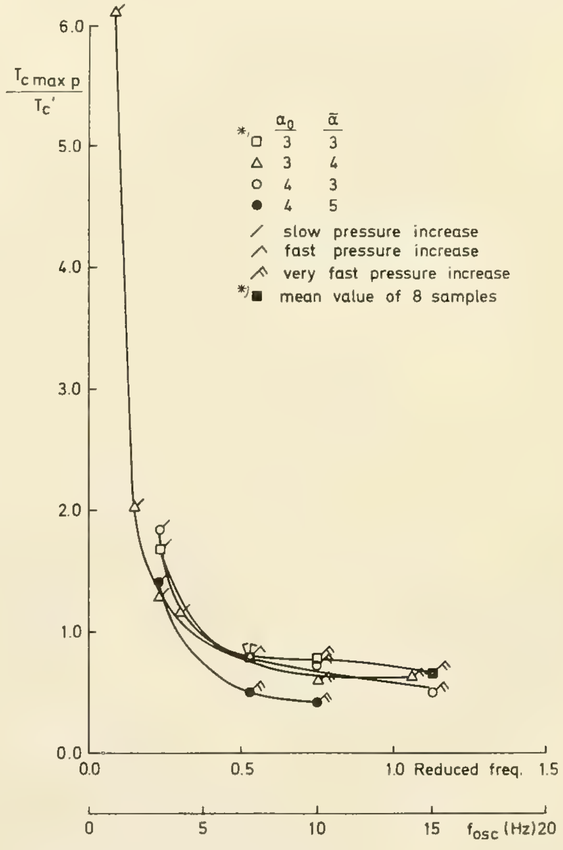

FIGURE 26. Normalized collapse time.

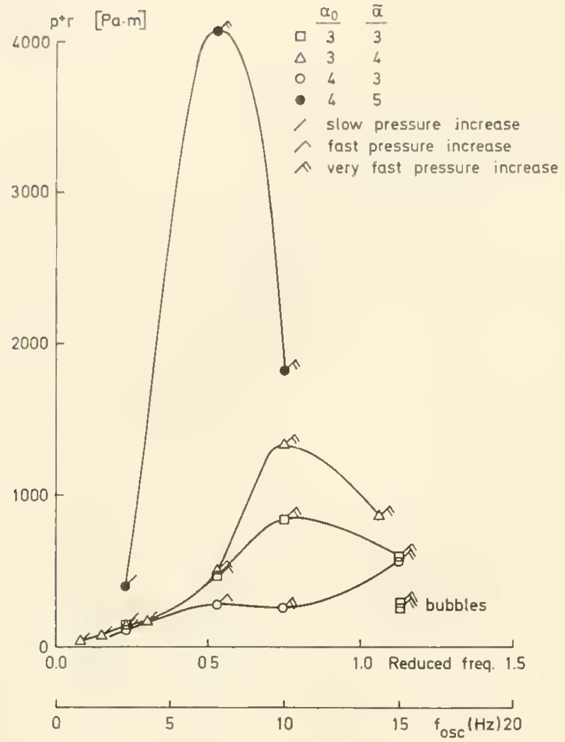

FIGURE 27. Pressure p^+ at collapse. Different conditions.

$$\frac{p^+ r\sqrt{\Delta t}}{R_{max}^{3/2}\sqrt{\rho\, c\Delta P}}$$

ρ = density of water
c = velocity of sound
Other symbols as above

Here it is necessary to know a time Δt proportional to the duration of the pressure pulse.

With the use of Δt some information about the real collapse dynamics is introduced and therefore coefficient (3) may be somewhat more universal than (2). Note, however, that for the original use of (3) similarity in cavitation was assumed.

Of interest for future work is to what extent the final pressure behavior can be described by measured cavity data. In this case it is more natural to think of methods to estimate d^2V/dt^2 in (1). It is then necessary to know V(t) or to assume a relation between d^2V/dt^2 and measured parameters, such as collapse time and cavity size. In this paper only the cavity area A(t) is presented. As a first approximation it will be assumed that V(t) is proportional to $A^{3/2}$ or ℓ^3_{max}. From the measurements of A(t) attempts were made to estimate d^2V/dt^2 by difference ratios in the conventional manners. This failed, due to uncertainty in A(t) during the final collapse. Then as a very rough assumption

$$\frac{d^2V}{dt^2} \approx \text{const}\,\frac{V_{max}}{T_c^{\,2}} \qquad (4)$$

was tested.

This is true only at very special circumstances. The assumption was, however, used and from (1) and (4) the following dimensionless pressure coefficient is obtained

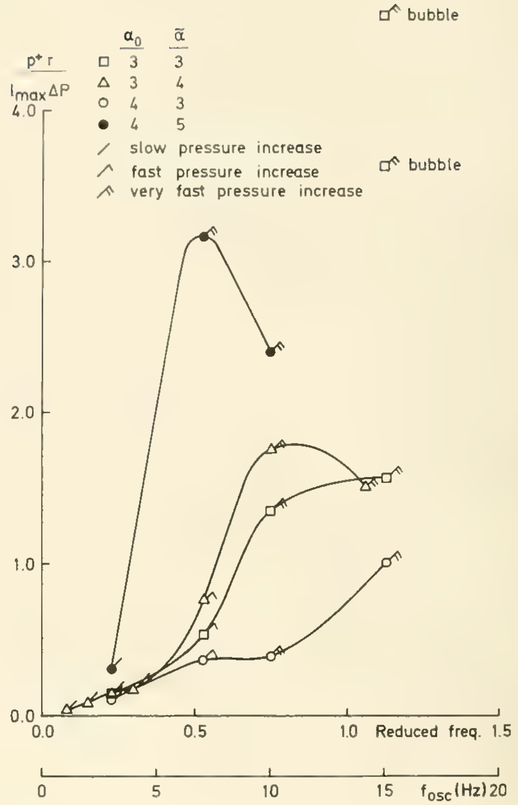

FIGURE 28. Pressure p^+ at collapse. Different conditions.

$$p^+r\ T_{c\ max}^2\ p/\ell^3_{max}\rho \qquad (5)$$

From the films it was observed that the cavity thickness seemed proportional to the length rather than to the square root of the cavity area and the following coefficient was obtained in cases where the area was measured.

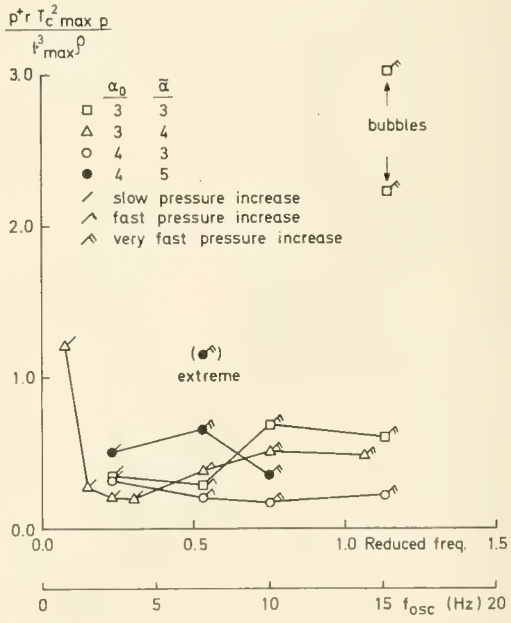

FIGURE 29. Pressure p^+ at collapse. Different conditions.

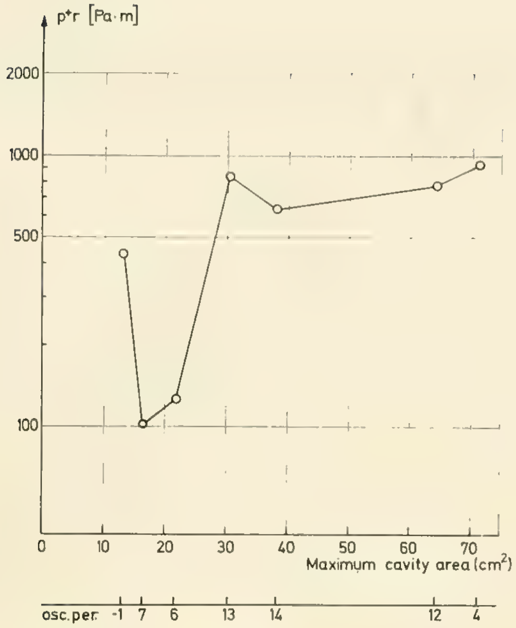

FIGURE 30. Pressure p^+ from different oscillation periods f_{osc} = 15 Hz, $\alpha_o = \tilde{\alpha} = 3^o$.

$$p^+r\,T^2_{c\,max}\,p/A_{max}\ell_{max}\rho \qquad (6)$$

In Figures 27, 28, and 29 results are shown for the different conditions shown in Figures 9-13. p^+r is shown in Figure 27 only to provide a reference for the other parameters.

Figure 28 shows that the generation efficiency increased strongly at a certain f_{osc} (or reduced frequency). The increase normally coincided with generation of very sharp pressure pulses and at these f_{osc} the relative collapse time had also reached the low value region (Figure 26). There is considerable scatter in generation efficiency. It must, however, be remembered that the plot is based on single cavitation events probably not always typical, the results must only be seen as a first hint of tendencies. The coefficient (3) gave results rather similar to those from (2) but with somewhat smaller dispersion. In Figure 29 it can be seen that with coefficient (5) the dispersion of the points was considerably decreased.

In Figures 30-32 results from Figures 17-23 are plotted. Only the dimensionless coefficients (2) and (6) are shown and it is seen that both attain approximately the same values for similar pulses, but neither of them brings the values of oscillation periods 6 and 7 into agreement with the others. The other coefficients give similar results. Also if the coefficients are based on values of area, time, etc. closer to the final collapse, the scatter is not decreased drastically. The conclusion of this is that, in the prediction of noise by theory or model tests, good similarity in certain cavitation events is important, and that these important events are not generally described by such simple parameters as T_c and V_{max}.

Because it was not possible to estimate d^2V/dt^2 directly from measured values of V(t) functions of the type:

$$V(t) = \text{const}[1 - \cos\phi(t)] \quad [\phi(t) \text{ is a polynomial with six variable parameters}]$$

were closely matched to nearly the whole collapse. The pressures then calculated by use of these functions agreed fairly well with measured values in many cases. These simple computations also demonstrated how sensitive the generated pressure often was to the final behavior of V(t) and it was easy to realize that parameters of the types discussed above can only be "universal" if they are applied to fairly similar cavitation events.

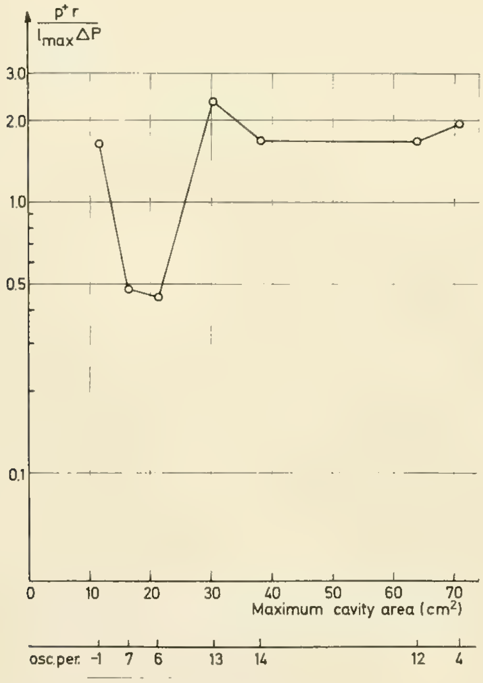

FIGURE 31. Pressure p^+ from different oscillation periods f_{osc} = 15 Hz, $\alpha_o = \tilde{\alpha} = 3^o$.

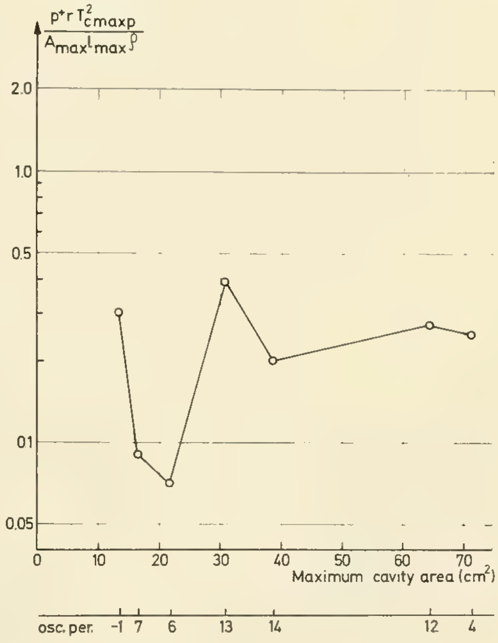

FIGURE 32. Pressure p^+ from different oscillation periods f_{osc} = 15 Hz, $\alpha_o = \tilde{\alpha} = 3^o$.

3. SUMMARY AND CONCLUSIONS FROM EXPERIMENTS WITH AN OSCILLATING HYDROFOIL

1. The generation of sharp pulses was dependent of the oscillation frequency. At low frequencies no high and sharp pulses were generated and above a certain frequency very high pulses were generated.
2. The sharpest and highest pulses were generated by cavities which separated from the main cavity and underwent a rather symmetrical and orderly collapse. Detailed studies showed, however, that a series of pulses was often generated, indicating that the collapse was not always simple at the very end.
3. Very high pulses could also be generated by cavities that were attached to the leading edge during the whole collapse.
4. The highest pressure generation efficiency was observed for spherical bubbles, which despite their smallness generated rather strong pulses.
5. The sharp pulses were generated during the very last part of the collapse.
6. Rebound of cavities was an important process for generation of sharp pulses. The most violent rebounds were obtained for separated cavities.
7. Low frequency noise was generated during the growth, near the time of maximum cavity extent and during the rather late stage of collapse. Because of a disturbing resonance the importance of collapse was, however, difficult to determine.

The basis of existing scaling laws for cavitation noise is mainly [see for example Levkovskii (1968) and Baiter (1974)]:

1. Ideas from theory and experiment concerning the dynamics and radiation properties of a single cavity.
2. Ideas concerning statistical properties of the pulse-generating events.

The dynamics and radiation depend on cavity geometry, cavity size, and the surrounding pressure. Scaling laws based on simple theory deal with model scale and magnitude of surrounding pressure, while similarity has to be assumed in cavitation behavior.

It has to be accepted that complete similarity in cavitation behavior will not occur, but if it is known which events in the cavitation process are crucial for generation of important pulses this will provide an indication of to what extent similarity is necessary for proper application of scaling laws.

Of course these introductory experiments cannot supply the final and complete answer, but the results indicate that one of the most important factors is that the separation of a cavity into parts is correctly scaled, the reason being that these separations are often the starting points for violent collapses. Especially when large parts are separated, this often begins at an early stage of the collapse, or is even initiated by disturbances during the growth of the main cavity.

Parameters that determine tendencies to separation of cavities have only been studied to a limited extent, but it is clear that the combination of a long (chord-wise) cavity and high reduced frequency causes extensive separation of large parts from the main sheet. From the plots of collapse times and pressure generation efficiency, $p^+r/\Delta P\ell_{max}$, as functions of reduced frequency it can be concluded that within special regions it is important that the time variations of the surrounding pressure be properly scaled. Such a scaling may be critical for the onset of separation of large cavity parts from the main cavity.

4. NOISE FROM DIFFERENT CAVITATION SOURCES

Introduction

In order to gain more information concerning the noise emitted from a cavitating source, tests with four axisymmetric head forms and two hydrofoils have been carried out in SSPA cavitation tunnel No. 1. The aim of these tests was to obtain well-defined and unambiguous types of cavitation, as bubble, sheet, and vortex cavitation. Comparisons of the noise levels from these different types of cavitation were made, as well as some investigations of the effect of free-stream velocity and gas content. The results reported here will only concern effects of the type of cavitation.

Test Set-Up

The tests were carried out in SSPA cavitation tunnel No. 1 test section, 0.5 m × 0.5 m. The noise was measured using arrangement 4 (hydrophone in water-filled box), see also Figure 1. In some of the later tests a flush-mounted hydrophone in the tunnel wall (arrangement 2) was used as well as a hydrophone in the flow field. Signals from the hydrophone(s) were registered by a tape recorder, but also directly analysed by a 1/3 octave band analyser and a narrow-band analyser. Main results given here are from the 1/3 octave band analysis.

Tests were carried out for a water speed 9 m/s, but with some additional tests at 7.5 m/s and 11 m/s. The gas content of the water at the tests was 10% and 40%, with some additional tests at higher gas content.

Test Set-Up

The first series of tests was carried out with axisymmetric head forms. The reason for this choice was that cavitation patterns for these bodies were well-known and well-defined from rather extensive tests [Johnsson (1972)]. The head forms used are given below, see also Figure 33.

Head form SSPA identification	Shape of nose contour	Cavitation number for cav inception	Type of cavitation
U1A	hemispherical	0.67	sheet
N39	flat+elliptic 3:1	0.4	bubble
N3	flat+elliptic 6:1	0.42	sheet
N10	flat+elliptic 4:1	0.43	sheet

The head forms were attached to a cylinder and a faired afterbody, which were suspended from the tunnel roof via a thin wing. The main difficulty at the tests was the low cavitation numbers needed. At cavitation numbers below 0.4 fairly extensive cavitation occurred at the wing-tunnel roof junction and at other imperfections along the tunnel walls. This cavitation caused rather excessive background

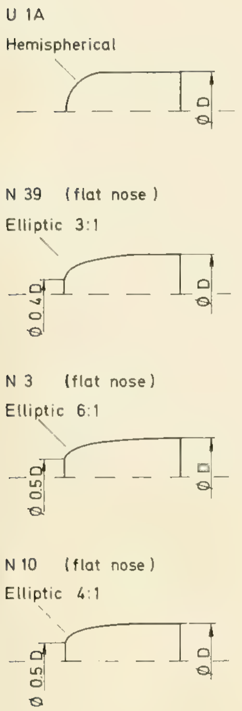

FIGURE 33. Axisymmetric head forms.

noise and made noise measurements almost impossible at low cavitation numbers. There is also some question whether such background noise from undesired cavitation was obtained at higher cavitation numbers than $\sigma = 0.4$, when cavitation numbers are increased. With regard to these findings the results given here are limited to cavitation numbers $\sigma \geq 0.6$ and only for decreasing pressure.

In Figure No. 34 1/3 octave band noise spectra for cavitation numbers $\sigma = 1$ and $\sigma = 0.6$ are given. At $\sigma = 1.0$ no visual cavitation was obtained and the noise levels are almost the same as for the empty tunnel (at the same velocity and cavitation number). At $\sigma = 0.6$ the cavitation is well developed for the hemispherical nose, for the other head forms no cavitation can be visually observed. There are, however, rather large differences in noise spectra for the three "non-cavitating" head forms. Thus head forms N3 and N10 have noise levels 10 to 20 dB above N39, for which the noise level is equal to non-cavitating or empty tunnel conditions. These differences cannot be attributed to unwanted cavitation on the wing or tunnel walls. In that case the noise levels for head form N39 should also have increased. The conclusion is thus that head forms N3 and N10 have audible but not visible cavitation.

From the tests with axisymmetric head forms it can be concluded that the cavitation numbers will be low, which implies that effects of unwanted cavitation will increase background noise levels and violate results for the cavitating head forms.

Tests with Hydrofoils

In order to obtain cavitation at higher cavitation numbers tests with two wings have been carried out. Using wings, vortex cavitation can also be obtained. The problem is here rather to obtain other types of cavitation without getting vortex cavitation.

One of the wings tested has cambered sections and elliptical planform, and the other has symmetric sections and trapezoidal planform, see Figure 35.

Wing (SSPA identification)	Angle of attack, α	Cavitation number for cav inception	Type of cavitation
Elliptic, cambered (16-12.12)	-2°	≈2	sheet
	+2°	2.5	vortex
	172°	3	vortex
Trapezoidal, symm rounded tip (K7 Vbl*)	0	0.5	bubble
	5°	≈1.5	vortex
Trapezoidal symm with end plate (K7 Vp3*)	5°	≈1.2	sheet

(*The wing K7 was tested with rounded tip, Vbl, and a small end plate, Vp3, see also Figure 35).

For the comparison of noise emitted from different types of cavitation it is important that these comparisons be made at the same cavitation number. One inherent difficulty is that pure bubble cavitation seems to be possible to obtain only at rather low cavitation numbers compared with the other cavitation types.

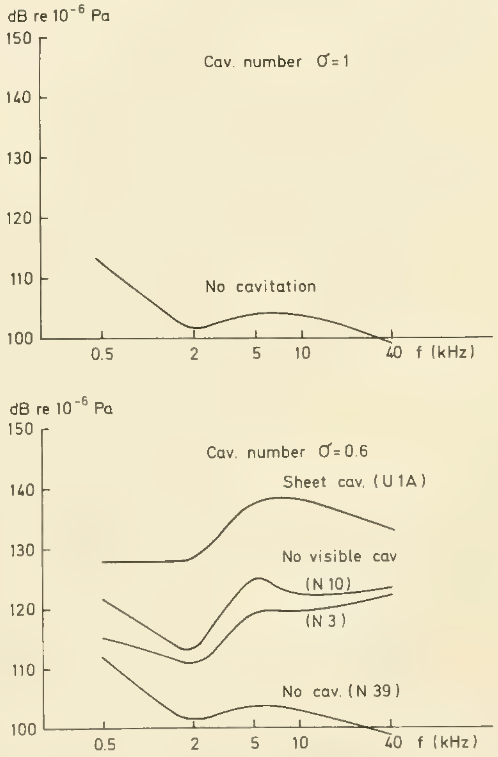

FIGURE 34. Axisymmetric head forms, cavitation noise (1/3 octave band). (Free stream velocity 9 m/s, gas content 10%.)

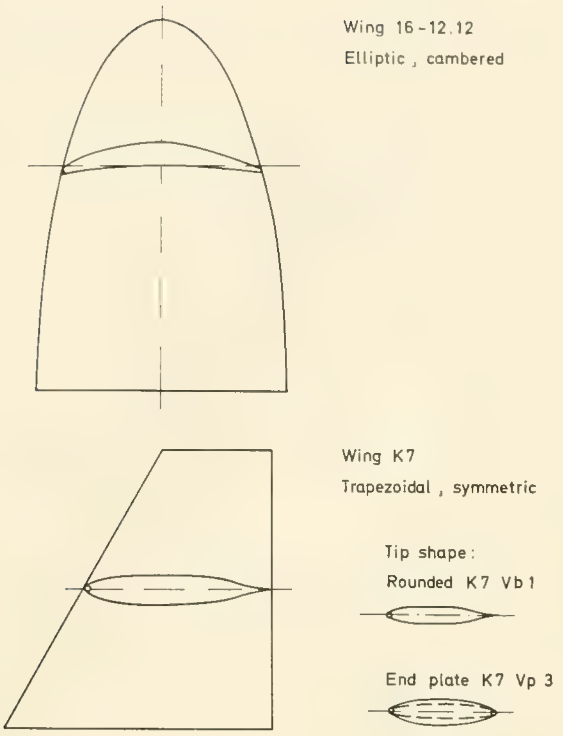

FIGURE 35. Wings.

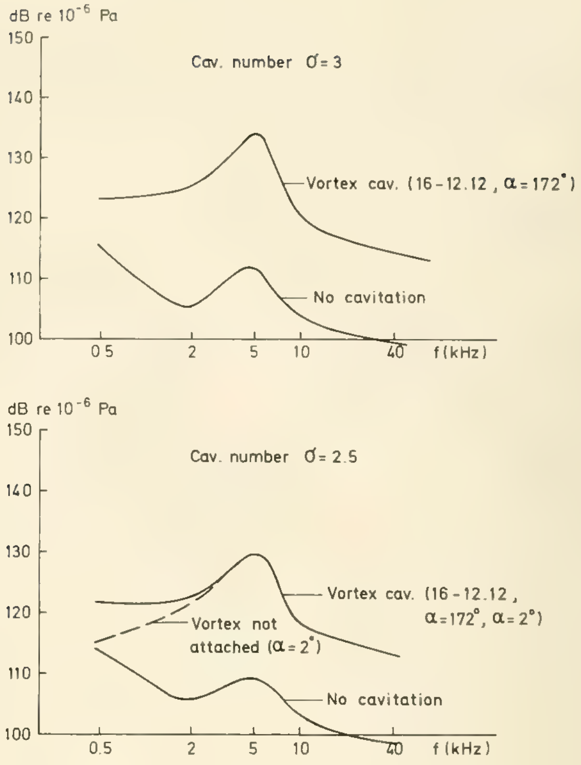

FIGURE 36. Wings, cavitation noise (1/3 octave band). (Free stream velocity 9 m/s, gas content 10%.)

Results from the tests are given here for five cavitation numbers, $\sigma = 3$, 2.5, 2, 1.5, and 1. The free stream velocity was 9 m/s and the gas content ratio was 10%. Results are given as faired curves for the noise levels from 1/3 octave band analysis.

For cavitation number $\sigma = 3$ (Figure 36) only the cambered wing 16-12.12 at $\alpha = 172°$ cavitates with vortex cavitation. Noise levels for the wings with no cavitation are of the same order as for the empty tunnel. The vortex cavitation at $\alpha = 172°$ gives an increase in noise levels of 15 to 20 dB compared with non-cavitating conditions.

At $\sigma = 2.5$ the wing 16-12.12 has vortex cavitation at $\alpha = 2°$ and $\alpha = 172°$, Figure 36. It is of interest to note that the vortex cavitation at $\alpha = 2°$ is not attached to the wing tip but starts behind the wing. This vortex can only be obtained when the pressure in the tunnel is increased (increasing cavitation number). The increase in noise level due to vortex cavitation here is also 15 to 20 dB.

For the cavitation number $\sigma = 2$ the wing 16-12.12 has vortex cavitation at $\alpha = 172°$, intermittent vortex cavitation at $\alpha = 2°$ and sheet cavitation at $\alpha = -2°$. The vortex cavitation gives an increase in noise level of the order of 15 dB. The sheet cavitation at $\alpha = -2°$ increases the noise levels at higher frequencies ($f > 5$ kHz), 10 to 15 dB above the level for vortex cavitation, see Figure 37.

At $\sigma = 1.5$ it can be noted that in some cases no pure types of cavitation can be obtained. Thus, wing 16-12.12 gives sheet cavitation at $\alpha = -2°$, vortex cavitation at $\alpha = 2°$ and vortex and bubble cavitation at $\alpha = 172°$. Results in Figure 37 show the largest increase of noise levels for sheet cavitation. Note also the differences between

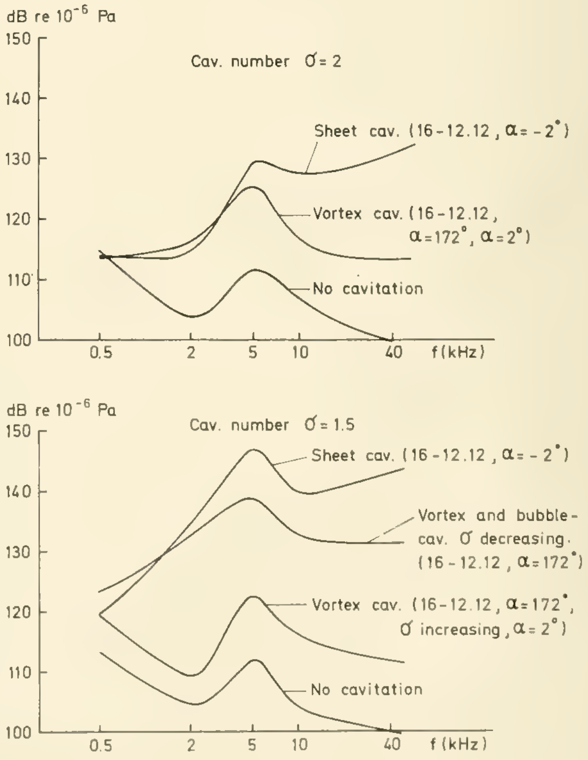

FIGURE 37. Wings, cavitation noise (1/3 octave band). (Free stream velocity 9 m/s, gas content 10%.)

decreasing and increasing cavitation number for $\alpha = 172°$. For decreasing σ small cavitation bubbles are obtained, which increase the noise level about 15 dB compared with increasing σ.

From the results at cavitation number $\sigma = 1.0$ (see Figure 38) it is obvious that bubble cavitation gives the largest increase in noise levels from 25 dB at low frequency (500 Hz) to 55 dB at high frequency (40 kHz). Sheet cavitation gives less increase but depends on the intensity of the cavitation. Thus for wing 16-12.12, $\alpha = -2°$, the sheet cavitation is extensive and gives an increase from 20 dB at low frequencies to 50 dB at high frequencies compared with non-cavitating condition. For wing K7 Vp3 the sheet cavitation is concentrated at the leading edge and an increase in noise level is only obtained for higher frequencies (> 2 kHz) and the increase at 40 kHz is of the order of 25 dB. The differences in noise level for wing K7 Vb1 for increasing and decreasing cavitation numbers can be attributed to differences in cavitation patterns. No pure vortex cavitation could be obtained at cavitation number $\sigma = 1.0$.

Conclusions from Tests with Head Forms and Hydrofoils

Tests with head forms are less suited as rather low cavitation numbers are needed. This may cause problems with high background levels due to undesired cavitation on tunnel walls etc. Tests with hydrofoils can be used to obtain effects on noise levels from different types of cavitation. There may, however, be some problems in obtaining pure cavitation types.

Vortex cavitation gives an increase in noise level of about 20 dB. It should be noted that differences in vortex cavitation can be obtained for increasing and decreasing pressure, which also show as differences in noise level. Also a vortex not attached to the wing causes increases in noise level. The increase in noise level due to vortex cavitation seems to be less for lower cavitation numbers.

Sheet cavitation gives substantially higher levels than vortex cavitation. The extent of the sheet has some influence on the noise level. For a fairly large sheet increases in noise level of 20 dB at 500 Hz to 50 dB at 40 kHz are obtained. For a small, leading edge sheet the increases in noise level are obtained for higher frequencies (f > 2 kHz) and for 40 kHz the increase is 25 dB.

Bubble cavitation gives the largest increases in noise level. Levels are for this case 5 to 10 dB above the levels for sheet cavitation.

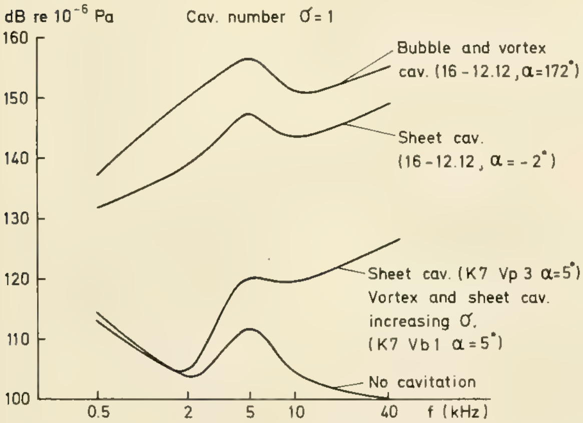

FIGURE 38. Wings, cavitation noise (1/3 octave band). (Free stream velocity 9 m/s, gas content 10%.)

ACKNOWLEDGMENT

This work is part of the research program at the Swedish State Shipbuilding Experimental Tank and the authors are indebted to Dr. Hans Edstrand and Mr. H. Lindgren for making this study possible. Part of the work reported here has been carried out with financial support from The Defence Material Administration of Sweden.

The authors would also like to express their sincere thanks to those members of the staff at SSPA who have taken part in the investigations and the analysis of the material.

REFERENCES

Baiter, J.-H. (1974). Aspects of Cavitation Noise. *Symposium on High Powered Propulsion of Large Ships*, Part 2, December 1974, Wageningen, The Netherlands. Publication No. 490, Netherlands Ship Model Basin, Wageningen, The Netherlands, pp. XXV 1-39.

Blake, W. K., M. J. Wolpert, and F. E. Geib (1977). Cavitation Noise and Inception as Influenced by Boundary-Layer Development on a Hydrofoil. *J. Fluid Mech. 80,* 4, pp. 617-640.

Harrison, M. (1952). An Experimental Study of Single Bubble Cavitation Noise. *J. Acoust. Soc. Am. 24,* 5; 776-782.

Itō, T. (1962). An Experimental Investigation into the Unsteady Cavitation of Marine Propellers. Proceedings of IAHR-Symposium, Sendai, Japan, 1962, *Cavitation and Hydraulic Machinery* edited by Numachi, F., Institute of High Speed Mechanics, Tōhoku University, Sendai, Japan, 439-459.

Johnsson, C.-A. (1972). Cavitation Inception Tests on Head Forms and Hydrofoils. *Thirteenth International Towing Tank Conference. Proceedings Volume 1* edited by Schuster. S., and M. Schmiechen. Versuchsanstalt für Wasserbau und Schiffbau, Berlin, Germany, 723-744.

Lehman, A. F. (1966). Determination of Cavity Volumes Forming on a Rotating Blade. *Eleventh International Towing Tank Conference, Tokyo 1966, Proceedings* edited by Kinoshita, M., Yokoo, K. The Society of Naval Architects of Japan, Tokyo, Japan, 250-253.

Levkovskii, Y. L. (1968). Modelling of Cavitation Noise. *Sov. Phys.-Acoust. 13,* 3; 337-339.

Rayleigh, Lord, (1917). On the Pressure Developed in a Liquid During the Collapse of a Spherical Cavity. Phil. Mag. *34,* 94-98.

Ross, D. (1976). *Mechanics of Underwater Noise.* Pergamon Press Inc., New York, USA, p. 218.

Tanibayashi, H., and N. Chiba (1977). Unsteady Cavitation of Oscillating Hydrofoil. *Mitsubishi Technical Bulletin 117.* Mitsubishi Heavy Industries, Ltd. Tokyo, Japan.

APPENDIX

LOW OSCILLATION FREQUENCIES MAINLY GENERATING RATHER SLOW PRESSURE PULSES

The following observations were typical for f_{osc} = 1-3 Hz and $\alpha_0 = 3°$, $\tilde{\alpha} = 4°$ (Figure 9) but most of the results are also valid for other angle conditions:

1. The maximum pressure increase is generated before the sheet cavity has disappeared completely. At the moment of maximum pressure increase the collapse slowed significantly and the rest of the collapse was very slow. Due to hysteresis the total collapse time was sometimes longer than the growth time, T_g. Typical for the collapse from maximum extent to maximum pressure was $T_c/(T_c + T_g) > 0.4$. The sheet cavities were attached to the leading edge during the whole collapse and only small parts were separated from the downstream cavity edge.
2. Already during growth a large part of the cavity is disturbed and consists of one part with a smooth surface and one with thick irregular cavity formations. From this total connected cavity, small parts were separated both during growth and collapse. Only a few of these parts collapsed violently, which is also confirmed by the pressure signals which do not contain many sharp pulses during growth and first part of collapse.

   At very low f_{osc} (1-2 Hz) these continuously occurring collapses of small cavities were, however, the only source of high-frequency noise. At these conditions also most sharp pulses were obtained in the hydrophone (H2) near the trailing edge.
3. At f_{osc} = 3 and 4 Hz the pressure increase often ends with a sharp pulse. The pulse was, however, not caused by an orderly and violent collapse of the main cavity, but instead by small cavities that separated from the main cavity and then collapsed separately. It was also observed that these rather violent collapses of small cavities mainly occurred during the time when the pressure was high owing to main cavity collapse.

   On a more expanded time scale it can also be seen that the sharp pulse is superimposed on a slower pressure increase. If not very clear, this tendency is still detectable in the 7 Hz-condition in Figure 14. This figure shows the pulse (oscillation period 6) in the 7 Hz-condition shown in Figure 10, but with the time axis expanded 40 times.
4. The cavitation sketches in Figures 9-13 show that for $f_{osc} \leq 4$ Hz the cavitation extent was approximately independent of f_{osc}, but that at higher f_{osc} the cavity did not develop to the full size. One reason for this may be that the time variation of the dynamic angle of attack is altered with f_{osc}.
5. Characteristic of low f_{osc} is also the fact that collapsing cavities show little tendency to rebound. Rebound is only obtained in small bubbles.

HIGH OSCILLATION FREQUENCIES MAINLY GENERATING SHARP PRESSURE PULSES

Below some observations are reported regarding the conditions $\alpha_0 = 3°$, $\tilde{\alpha} = 4°$ and f_{osc} = 10 and 14 Hz (Figure 10). Many of the results are also valid for other similar conditions. Typical observations are:

1. The sharp pulses are often much higher than slow pressure variations.
2. The duration of the final part of the sharp pulses seems (as long as can be determined in the recording) independent of f_{osc} (Figure 14). For the earlier parts of the cavitation period the dependency on f_{osc} is more complex due to different cavity sizes etc.
3. For this condition ($\alpha_0 = 3°$, $\tilde{\alpha} = 4°$) the complete change of cavity dynamics and pressure generation occurred between f_{osc} = 7 and 10 Hz (Figure 14). At 7 Hz the cavity mainly collapsed towards the leading edge. At 10 Hz a large part consisting of thick formations separated and performed a violent collapse at the middle of the hydrofoil (B in Figure 14). This collapse occurred about 1.4 milliseconds later than the collapse of those two parts (A) of the sheet that were attached to the leading edge during the whole collapse. Also these two parts collapsed rather violently, but a small pulse was generated. The thick separated cavity (B) consisted of several parts that did not collapse exactly simultaneously and, thus, a series of collapse and rebound pulses was generated. A significant rebound was only obtained from the separated cavity. The group of rebounded cavities collapsed rather slowly, resulting in a small pulse about 3.5 milliseconds after the collapse of the separated cavity (B'). In some oscillation periods the separated cavities and those attached to the leading edge collapsed almost simultaneously and it also happened that high pulses were generated at the collapse of rebounded cavities.
4. The cavitation behaviour at f_{osc} = 14 Hz is approximately similar to that at 10 Hz (Figures 10 and 14). The thick formation (C) separated and collapsed at a later stage. The first pulse (Figure 14) was generated by the outer cavity (A) attached to the leading edge. About 1.4 milliseconds later the other cavity (B) attached to the leading edge collapsed. This cavity was complex and generated a series of pulses. First about 3.5 milliseconds after the first pulse the thick formation (C) collapsed, generating a sharp pulse. No violent collapses were experienced by rebounded cavities in this case. The overall impression from these two conditions with f_{osc} = 10 and 14 Hz is that normally the separated thick cavities generated the highest pulses, but that in some cases pulses of almost equal height were generated by cavities attached to the leading edge.

Another behavior of the signal from the cavitating hydrofoil is a low frequency variation (about 23 Hz) that seems rather independent of f_{osc}. Sequences containing cavitating as well as non-cavitating periods indicate that the fluctuations were generated by cavitation (Figure 10, 7 Hz, Figure 11 and 12). Inspection of the films shows, however, that no cavitation is visible on the hydrofoil or about 0.5 chord-lengths downstream it (Figure 9, 11, 3 Hz). Here the most probable cause is that the cavitation started resonance vibrations in some structure. These vibrations probably cause disturbing errors in the pressure signal at some f_{osc}, mainly in the region 3-7 Hz, and quantitative results from such conditions must be used with care.

Cavitation Noise Modelling at Ship Hydrodynamic Laboratories

Gavriel A. Matveyev
and
Alexei S. Gorshkoff
Krylov Ship Research Institute
Leningrad, USSR

ABSTRACT

Theoretical and experimental correlation of visual and accoustical effects of cavitation are considered. The Froude similarity is treated critically because of the pressure effects on the coefficient of cavity energy transformation into cavitation noise as well as because of the increase of noise absorption or cavitation resistance of water. Though in large cavitation tunnels which have no free surface the nonstationary boundary conditions can be reproduced less perfectly, their capability of simulation at full-scale pressure is regarded as the leading factor. It is suggested that extrapolation formulae should take into account the effect of the rate of pressure increase (or pressure gradient) in the cavity collapse area. This corresponds to an increase in the square of acoustic pressure on the model, compared to the prototype, inversely proportional to the linear scale of modelling.

1. COMPARISON OF VISUAL AND ACOUSTIC EFFECTS OF CAVITATION

The occurrence of strong visual and noise effects of cavitation are usually considered to be coincident. When this coincidence is actually the case, it provides certain conveniences. The measurement of noisiness makes it possible to detect cavitation on structural elements not easily accessible for inspection. Visual observation of cavitation on models is used for the prediction of noisiness of various prototypes. However, the experiments involving visual and acoustical recording of cavitation indicate that there may be a considerable discrepancy between these two manifestations of cavitation. It is interesting to discover the nature and the cause of the discrepancy by means of a mathematical model of an elementary cavitation process which is described by the well-known differential equation of a single spherical cavity growth

$$R\ddot{R} + \frac{3}{2}\dot{R}^2 + \frac{2\gamma}{\rho R} - \frac{1}{\rho}\left[\left(p_o - p_d\right) + \frac{2\gamma}{R_o}\right]\left(\frac{R_o}{R}\right)^3 + 4\nu\frac{\dot{R}}{R}$$
$$= -\frac{1}{\rho}\left[\left(p_o - p_d\right) - p\right] \qquad (1)$$

Here R and R_o are the cavity radius and its initial value, respectively; p and p_o are the variable component and the initial value of ambient pressure; p_d, ρ, γ, and ν are vapor pressure, density, and the surface tension and kinematic tension coefficient, respectively.

Computations were made by equation (1) for the negative pressure pulse

$$p(\tau) = p_m \tau e^{1-\tau}; \quad \tau = \frac{t}{T} \qquad (2)$$

which is characterized by the time scale, T, and the amplitude, p_m. Such a pulse represents the region of negative pressure having the length, L, on the profile with the maximum negative pressure coefficient, C_{pm}, in the flow with velocity, U:

$$p_m = C_{pm} \cdot \frac{\rho U^2}{2}; \qquad T = \frac{L}{V}$$

Linearization of Eq. (1) with respect to $\delta = z - z_o$ for the small-amplitude oscillation frequency gives

$$f = \frac{1}{R_o}\sqrt{\frac{3(p_o - p_d)}{\rho} - \frac{2\gamma}{\rho R_o} - \left(\frac{2\nu}{R_o}\right)^2} \qquad (3)$$

According to (3), oscillatory properties of the cavity disappear at $p_o = 1$ ata when $R_o < 10^{-6}$ m. Bearing in mind that the natural period is limited by the pulse duration, T, computations were made for

$p_o = 10^4$ kg/m^2; $R_o = 10^{-6}+10^{-3}$ m; $L = 10^{-3}+10^{-1}$m;

$V = 10+20$ m/s; $C_{pm} = 1.5$.

The following value is taken as a measure of the accoustical effect of an elementary cavitation process to an accuracy of the potential energy transformation coefficient for the maximally expanded cavity:

$$G_{\alpha} = 10\ \ell og \frac{R_m^3 - R_o^3}{R_n^3} \qquad (4)$$

Here, R_n is the threshold value of the cavity radius which, for the sake of convenience and without limiting the generality of conclusions, is taken as 10^{-6} m. For large R_m/R_o values this measure differs only slightly from a simpler measure used in Figure 1

$$G'_{\alpha} = 30\ell g \frac{R_m}{R_o} \qquad (5)$$

The threshold of the visual observation of cavitation is taken as $R_{\beta} = 10^{-3}$ m, which coincides with the upper limit to the size of the cavitation nuclei under study. For the chosen measure of acoustic effect this threshold corresponds to 90 dB. Since the resolution of vision is limited by angular dimension, the measure of the visual effect where the distance to the object of observation remains constant is the first order, linear dimension of the cavity. Hence, when the origins coincide

$$G_B = \frac{1}{3} G_{\alpha}$$

and the processes below the level of G_{α} = 90 dB are out of visual observation.

Thus, leaving out of account the actual signal-noise ratios, the acoustical recording makes it possible to penetrate much deeper (by 2-3 orders) into the "microcavitation" region.

Worthy of notice is the qualitative similarity of the curves shown in Figure 1 to the experimental curves of cavitation noise increase against velocity which are given below, as well as by Sturman's data (1974). It is evident that at an early cavitation stage the predicted levels drop by 20 dB with the velocity decreasing 10-fold. This stage is usually regarded as free of cavitation.

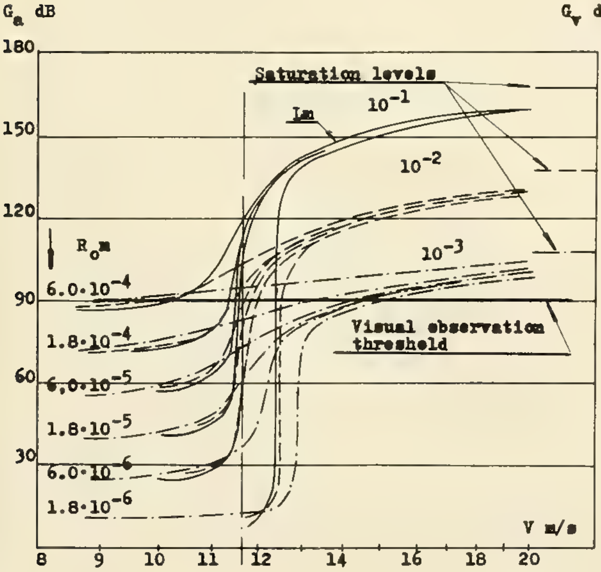

FIGURE 1. Calculated comparison of visual and acoustical effects of elementary cavitation process in a limited region of negative pressure.

With the increase of velocity there comes a stage which is sometimes referred to as "true" cavitation and in which the most intensive growth of cavities and cavitation noise is observed. This stage corresponds to a decrease and loss of static equilibrium of the cavity.

At the third stage the intensive cavity growth ceases and asymptotic saturation of the acoustic effect occurs due to the fact that the size of the cavity is nearing that of the zone of negative pressure. The asymptotic values of saturation shown in Figure 1 correspond to the rough estimation

$$G_{\alpha s} = 15 + 15\ \ell g C_{pm} + 30 \ell g \frac{L}{R_n} \qquad (6)$$

As to the relationship between visual and noise manifestations of cavitation, Figure 1 allows one to assert that:

- at sufficiently high levels of ambient noise the acoustic detection of cavitation may coincide with the visual detection or takes place even later;
- potentially, at a fairly low level of the ambient noise, the acoustic manifestation of cavitation must be detected much earlier than the visual one.

In particular, the acoustic effect of cavitation can be rather strong (e.g., an increase of noisiness by several dozens of decibels) in the case of "microscopic" cavitation invisible to the eye.

The indicated values are largely conditional as the threshold of visual detection may differ under different conditions. Nevertheless they are close to those obtained under laboratory conditions.

It is of interest that Figure 1 reveals such a contradictory phenomenon as vagueness in respect to cavitation inception. At high levels the curves for various nuclei coincide, so for a more correct determination of cavitation inception one should try to reduce rather than to increase the accuracy of recording methods. The increase of accuracy, as is shown in Figure 1, brings about increasing ambiguity of cavitation inception and expansion of the vagueness region to cover an increasing range of velocities. However, as the accuracy decreases, more and more small zones of cavitation inception are left out of control.

The above analysis simplifies the actual processes and can be at variance with them mainly due to the fact that the coefficient of cavity potential energy transformation into acoustic energy is not constant being a complex function of many parameters [Beniaminovich et al. (1975)]. Specifically it may have a much greater value for small cavities as compared to larger cavities.

2. EXPERIMENTAL STUDY ON MODELS

There is an urgent need for an effective and well-founded classification of a great variety of forms and types of cavitation which substantially differ in the mechanism of nonstationarity giving rise to noise and having other practical consequences of cavitation.

The following brief list of the forms and types of cavitation represents a more or less established practice with respect to marine propellers [Goncharov et al. (1977)].

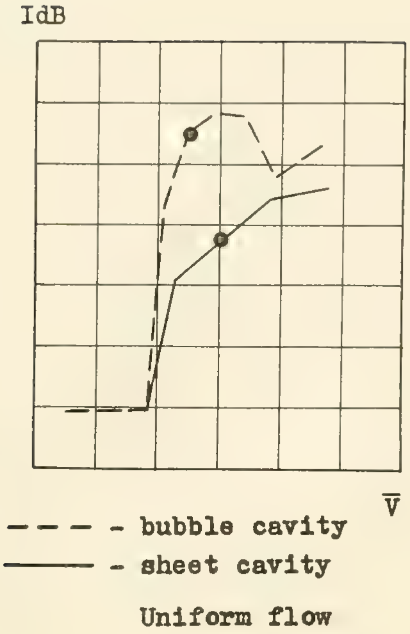

FIGURE 2. Development of noise and visual manifestation of cavitation at constant pressure vs. velocity, in reference to the conditions of cavitation noise detection.

According to the location of cavitation zones:

- vortex cavitation (in the cores of tip and axial vortices),
- leading edge cavitation (on the suction side and pressure side at the leading edge),
- blade-profile cavitation (in the region of large blade thicknesses).

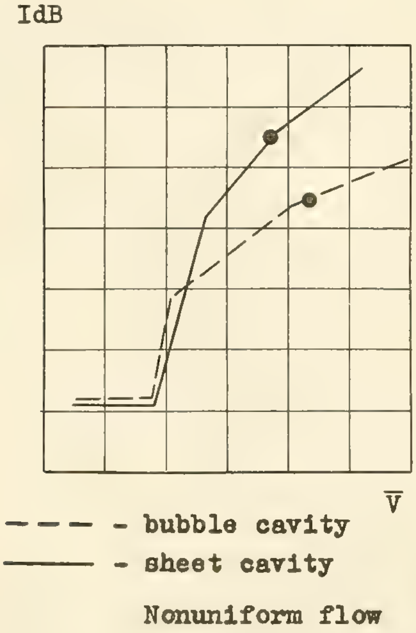

FIGURE 3. Development of noise and visual manifestation of cavitation at constant pressure vs. velocity, in reference to the conditions of cavitation noise detection.

- root cavitation (at the blade roots).

According to cavity pattern:

- bubble cavitation (with cavities moving with the flow through negative or increased pressure zones),
- sheet cavitation (with cavities which on the average are motionless in relation to the propeller).

By steadiness (uniformity) of the incoming flow:

- steady cavitation (noise and other effects result from the inner unsteadiness of the cavity which is steady on the average),
- unsteady cavitation (noise and other effects result from the cavity pulsations at an almost regular frequency, the phenomenon of cavitation buffeting),
- cavitation in an unsteady flow (noise and other effects here again result from the pulsations as well as from the probable disappearance of cavities with the frequency of flow condition change).

It seems extremely difficult to provide a comparative description of noisiness for about three dozen cavitation types characterized only by the above-mentioned features. Some guidance is given by the experimental data presented in Figures 2 to 5.

In steady-state conditions the bubble cavitation types are the most noisy (Figure 2). Among cavitation zones of different locations, vortex cavitation types are the least noisy (Figure 3), whereas pressure-side, leading-edge cavitation types are the most noisy (Figure 4).

In an unsteady (non-uniform) flow the relation between the noisiness of sheet cavitation and that of the bubble type is different (Figure 5).

The higher noisiness of the pressure-side leading-edge cavitation is accounted for by the rapid increase of pressure behind the suction zone (high gradient), which is typical of these conditions. In case of the bubble structure of a cavity this rapid pressure increase is accompanied by the increase of acceleration during the collapse. In case of the sheet structure it is accompanied by the

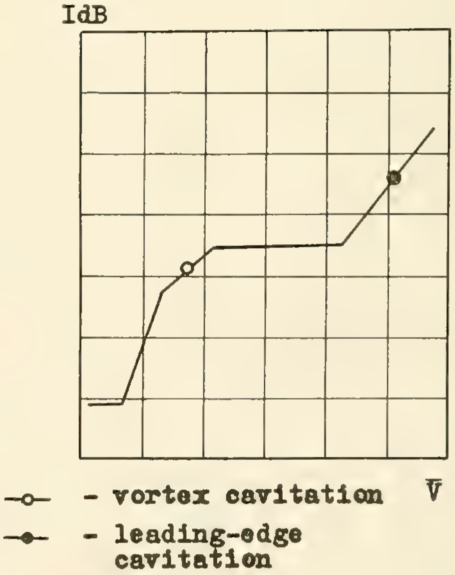

FIGURE 4. Development of noise and visual manifestation of vortex and leading-edge cavitation appearing in succession in a uniform flow at constant pressure.

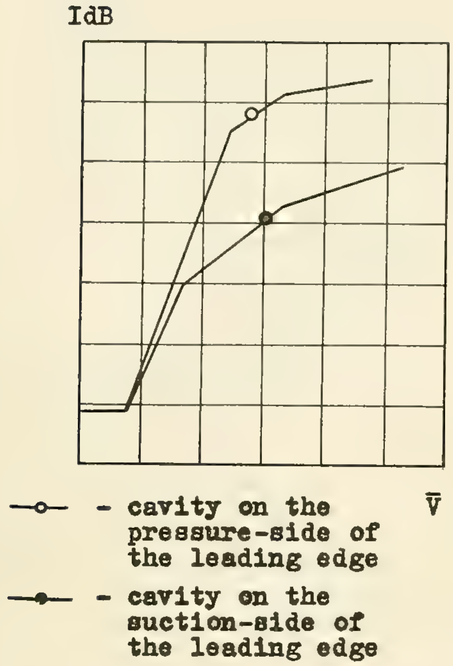

FIGURE 5. Development of noise and visual manifestation of cavitation on both pressure- and suction-side in a uniform flow at constant pressure.

unsteadiness of even small size cavities due to closure behind the maximum suction zone.

The change in the relative noise intensity of sheet and bubble cavities depends upon the fact that in the case of the bubble cavity structure the unsteadiness varies but slightly, whereas the volume of sheet cavities begins to severly pulsate. Passing over to the unsteady flow, we may even observe the reduction of bubble cavitation noise. This occurs when one portion of the propeller gets free from the cavity whereas, on the other portion thereof, the intensive development of cavitation is not accompanied by an increase of noise due to a saturation effect.

Individual points on the graphs shown in Figures 2 to 5 indicate moments of the first visual detection of cavitation. As is seen, in a large cavitation tunnel where the measurements were made, the above conclusion that the noise comes ahead of the visual detection of cavitation is to a variable degree valid for any type of cavitation.

3. MODEL-PROTOTYPE CORRELATION AND COMPARISON OF MODEL-TEST RESULTS WITH FULL-SCALE DATA

It is usually assumed [Levkovsky (1968) and Sturman (1974)] that the fraction of the cavity potential energy converted into cavitation noise (coefficient of transformation) is the same for the model and the full scale ship. Experience confirms the validity of the conflicting conclusions [Beniaminovich et al. (1975)] that are indirectly confirmed in some works. The coefficient of cavity energy transformation into noise proves to be strongly dependent on the absolute pressure, p_o. It is this fact, that was used by Beniaminovich et al. (1975) for explaining the reduction of the transformation coefficient by several orders with a decrease of pressure, p_o, from 1 to 0.4 ata. It is also emphasized that at sufficiently low p_o the collapse of cavities is not necessarily accompanied by shock wave generation.

Vacuum noise measurements, when performed in ship hydrodynamics laboratories engaged in cavitation research, show inadmissible noise absorption in the facility water unless measures are taken to insure additional removal of gaseous nuclei of cavitation from the water. By intensified water degassing the absorption may be reduced to an acceptable level, but the resulting growth of cavitation resistance of water leads to a drastic change of conditions for inception and development of cavitation [Gorshkoff and Lodkin (1966)]. In view of the complicated character of absolute pressure effects on the coefficient of cavity energy transformation into noice it appears to be good practice to perform cavitation noise measurements at a full-scale value of pressure.

That the Froude similarity will not be fulfilled under these conditions, can be accepted provided that adequate means are available for the description and reproduction of the conditions of flow non-uniformity behind the hull. This approach, used in a large cavitation tunnel in combination with correlation methods recommended by Levkovsky (1968), Sturman (1974), has shown that overestimated cavitation noise levels are predicted in this case. This was found to arise from the fact that the coefficient of cavity energy transformation into noise is approximately proportional to the rate of pressure growth leading to the cavity collapse. In modelling by the Froude method this pressure growth rate decreases as $\sqrt{L}$.

In case of large-scale modelling the comparison of model-test and full-scale data may not have revealed this discrepancy among other more pronounced ones. One can use pressure gradient instead of the rate of pressure variation with time. Then, for Froude similarity, the noise level model-to-full-scale extrapolator coincides with that used by Sturman (1974). Not so with modelling at full-scale absolute pressure. Here the proportionality of the transformation coefficient both to the velocity of pressure variation with time and to the pressure gradient involve the same extrapolator. Giving up the construction of dimensionless parameters of which, with a great number of constants involved, there is ample freedom of choice, the extrapolator suggested by Sturman (1974)

$$<p^2> \approx \frac{R_o^3 p_o N_o}{\tau^2} \tag{7}$$

can be substituted by the following:

$$<p^2> \approx \frac{R_o^3 p_o^3 U_o N_o}{\tau^2 L} \tag{8}$$

Here $<p^2>$ is the square of the acoustic pressure,
τ is the distance to the point of noise measurement,
N_o is the number of cavities collapsing in unit time.

If we assume in the regular way that the similarity of cavity patterns is observed and the noise is measured at similar points of the flow, then

$$R_o \approx L \quad , \quad N_o \approx \frac{U}{L} ,$$

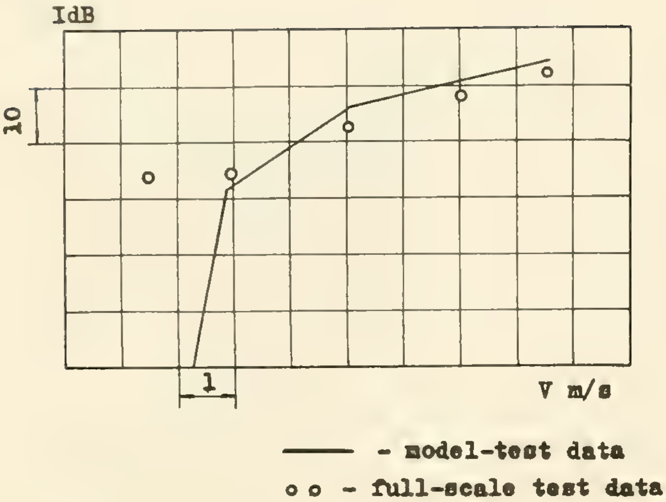

FIGURE 6. Comparison of noise levels extrapolated from model with measured full-scale data in a wide band of frequencies.

and $\tau \approx L$. The table below shows extrapolators for scaling the square of the acoustic pressure during cavitation from model to full-size with reference to the assumptions of constant and variable coefficients of cavity energy transformation into noise, η, and to fit the cases of constant Froude number and constant absolute pressure.

That the frequencies vary inversely in proportion to linear dimensions in modelling at a constant pressure may turn out to be a significant advantage, so the acoustic wave lengths change in proportion to linear dimensions of the model and wave interference patterns remain unchanged. In modelling by the Froude method wave lengths on the model are known to be $\sqrt{L}$ times larger than the model linear dimensions.

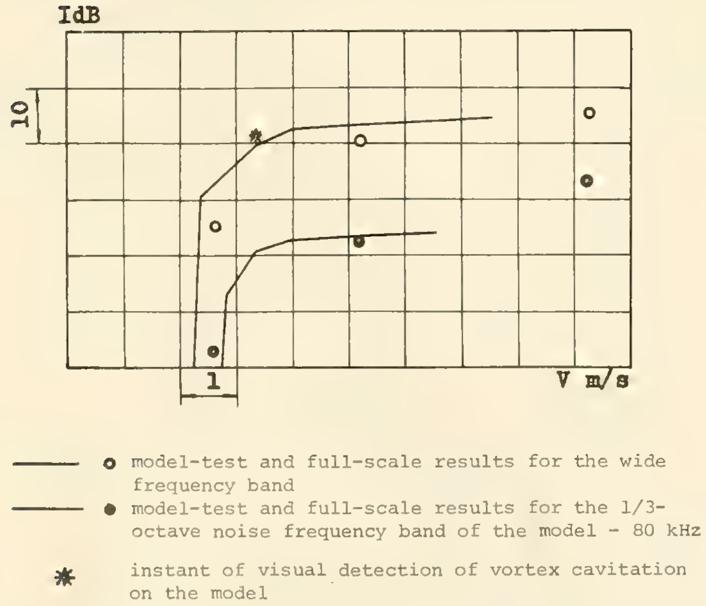

FIGURE 7. Comparison of noise levels extrapolated from model with measured full-scale data.

TABLE 1. Cavitation Noise Levels Scaling Extrapolator

	η = const	$\eta \approx \frac{P_o}{L}$	$\eta \approx \frac{P_o}{T}$
F_τ = const	$L^{3/2}$	$L^{3/2}$	L^2
P_o = const	1	1/L	1/L

Figure 6 shows the comparison between the model-test data (solid line) scaled the comparison between the model-test scale data (dotted line) for the noise level in a wide band of frequencies. Figure 7 gives a similar comparison with another prototype. Curves of cavitation noise increase are also compared in a 1/3-octact band for the model at the frequency of 80 kHz. In Figure 7 the moment of visual detection of cavitation is marked on the general level curve with an asterisk. Full-scale data are given here for individual rates of speed.

The scaling extrapolator (8) needs to be verified under full-scale conditions and is likely to be refined. However, the need for stability of the coefficient of cavity energy transformation into cavitation noise appears to be an indisputable argument for cavitation noisiness scaling with the full-scale pressure retained.

CONCLUSION

The two major conclusions can be formulated as follows:

- Scaling for cavitation noise measurements with the full-scale pressure retained gives a high value coefficient of cavity energy transformation into noise and substantial advantages in respect to:
  a) obtaining high levels of cavitation noise;
  b) similarity of sound waves to the model.
- Large-scale modelling with the full-scale pressure retained confirmed the possibility brought out by the analysis of an elementary cavitation process of acoustic detection of cavitation long before the cavity reaches the size that can be detected visually.

REFERENCES

Beniaminovich, M. B., K. A. Kondratovich, and I. V. Krutetsky (1975). On experimental determination of acoustic radiation energy during cavitation bubble collapse. (in Russian). *Symposium on Physics of Acoustics-Hydrodynamics Phenomena, Reports, Izd. "Nauka"*, Moscow.

Goncharov, O. N., A. S. Gorshkoff, and V. J. Vaniukhin (1977). Cavitation and its noise radiation in steady and unsteady flows. *9th All-Union*

Symposium on Physics of Acoustics-Hydrodynamics Phenomena, (in Russian), Reports, Vol. 2, Izd. Academy of Sciences of the USSR, Moscow.

Gorshkoff, A. S., and A. S. Lodkin (1966). The inception of cavitation under symmetrical streamlining round a body of revolution with blunt nose. *11th ITTC,* Tokyo.

Levkovsky, Yu. L. (1968). Scaling of cavitation noise, (in Russian). *Akustichesky zhurnal, 13,* 3. Moscow.

Sturman, A. M. (1974). Fundamental aspects of the effect of propeller cavitation on the radiated noise. *Proceedings of Symposium on High-Powered Propulsion of Large Ships*, Wageningen.

Fluid Jets and Fluid Sheets: A Direct Formulation

P. M. Naghdi
University of California
Berkeley, California

ABSTRACT

The object of this paper is to present an account of recent developments in the direct formulation of the theories of fluid jets and fluid sheets based on one and two-dimensional continuum *models* originating in the works of Duhem and E. and F. Cosserat. Following some preliminaries and descriptions of (three-dimensional) *jet-like* and *sheet-like* bodies, the rest of the paper is arranged in two parts, namely Part A (for fluid jets) and Part B (for fluid sheets), and can be read independently of each other. In each part, after providing the main ingredients of the direct model and a statement of the conservation laws, appropriate nonlinear differential equations are derived which include the effects of gravity and surface tension. Application of these theories to various one and two-dimensional fluid flow problems, including water waves, are discussed.

1. INTRODUCTION

Jets and sheets are a class of three-dimensional bodies whose boundary surfaces have special characteristic features. To this extent they are, respectively, similar to another class, namely that of rods and shells (or plates), although the nature of the specified surface (or boundary) conditions in the two classes may be different. Moreover, the kinematics of jets and rods are identical, as are the kinematics of sheets and shells. Indeed, it is only through their constitutive equations that a distinction appears between rods and jets on the one hand, and shells and sheets on the other. It is natural to inquire as to the possible utility of methods of approach in the construction of theories in the class of rods and shells for that of jets and sheets and vice versa. The main purpose of this paper is to call attention to the possible utility of a *direct approach* for jets and sheets, an approach which has met with considerable success in the case of rods and shells. The direct approach for fluid jets is based on a one-dimensional *model*, called a *Cosserat* (or a *directed*) *curve* which is defined in Section 3; and the direct approach for fluid sheets is based on a two-dimensional *model*, called a *Cosserat* (or a *directed*) *surface* which is defined in Section 5. It should be emphasized that a Cosserat curve and a Cosserat surface are not, respectively, just a one-dimensional curve and a two-dimensional surface; but are, in fact, endowed with some structure in the form of additional primitive kinematical vector fields.

The concept of 'directed' or 'oriented' media originated in the work of Duhem (1893) and a first systematic development of theories of oriented media in one, two, and three dimensions was carried out by E. and F. Cosserat (1909). In their work, the Cosserats represented the orientation of each point of their continuum by a set of mutually perpendicular rigid vectors. The purely kinematical aspects of oriented bodies characterized by ordinary displacement and the independent deformation of N deformable vectors in N-dimensional space has been discusssed by Ericksen and Truesdell (1958), who also introduced the terminology of *directors*.

A complete general theory of a Cosserat surface with a single deformable director given by Green et al. (1965) was developed within the framework of thermomechanics; and their derivation (Green et al. 1965) is carried out mainly from an appropriate energy equation, together with invariance requirements under superposed rigid body motions. A related development utilizing three directors at each point of the surface, in the context of a purely mechanical theory and with the use of a virtual work principle, is given by Cohen and DeSilva (1966). A further development of the basic theory of a Cosserat surface along with certain general considerations regarding the construction of nonlinear constitutive equations for elastic shells is given by Naghdi

(1972), which also contains additional historical remarks relevant to oriented continua and to the theory of thin elastic shells. A parallel development in the theory of a Cosserat curve with two deformable directors begins with a paper of Green and Laws (1966) whose derivation is carried out mainly from an appropriate energy equation, together with invariance requirements under superposed rigid body motions. A related theory of a directed curve with three deformable directors at each point of the curve, in the context of a purely mechanical theory and with the use of a virtual work principle, is given by Cohen (1966). A further development of the basic theory of a Cosserat curve along with certain general developments regarding the construction of nonlinear constitutive equations for elastic rods is given by Green et al. (1974a,b).

In general, two entirely different approaches may be adopted for the construction of one-dimensional and two-dimensional theories of mechanics pertaining to certain motions and (three-dimensional) media responses which are effectively confined, respectively, to one-dimensional and two-dimensional regions. For example, the theory of slender rods and that of fluid jets are both one-dimensional theories; and, similarly, the theory of thin shells and that of fluid sheets are both two-dimensional theories in the context of the particular classes of three-dimensional bodies mentioned earlier.

Of the two approaches just mentioned, one starts with the three-dimensional equations of the classical continuum mechanics and by applying approximation procedures strives to obtain one-dimensional (in the case of jets and rods) and two-dimensional (in the case of sheets and shells) field equations and constitutive equations for the medium under consideration. In the other approach, the particular medium response mentioned above is *modelled* as a one-dimensional and a two-dimensional *directed* continuum, namely a Cosserat curve and a Cosserat surface introduced earlier; and one then proceeds to the development of the field equations and the appropriate constitutive equations. If *full* information is desired regarding the motion and deformation of the continuum under study in the context of the classical three-dimensional theory, then there would be no need to develop a particular one-dimensional and a two-dimensional theory. In fact, the aim of one-dimensional and two-dimensional theories of the type mentioned above is to provide only practical information in some sense: for example, in the case of fluid sheets information concerning quantities which can be regarded as representing the medium response confined to a surface or its neighborhood as a consequence of the (three-dimensional) motion of the body, or the determination of certain weighted averages of quantities resulting from the (three-dimensional) motion of the body. A parallel remark may be made, of course, in the case of fluid jets. The desire for obtaining limited or partial information if the basic motivation for the construction of such one-dimensional and two-dimensional theories as those for slender rods and thin shells and for fluid flow problems of jets and sheets.

The nature of difficulties associated with the development of both the shell theory and the theory of water waves on the one hand, and that of rods and jets on the other, from the full three-dimensional equations is well known and has been elaborated upon on various occasions.* In view of these, it is reasonable to attempt to formulate one-dimensional and two-dimensional theories of the types described above by replacing the continuum characterizing the (three-dimensional) medium in question with an alternative model which would reflect the main features of the response of the three-dimensional medium and which would then permit the formulation of appropriate one-dimensional and two-dimensional theories by a *direct* approach and without the appeal to special assumptions or approximations generally employed in the derivation from the three-dimensional equations.

Of course, the introduction of an alternative model and formulation of one-dimensional and two-dimensional theories by the direct approach do not mean that one ignores the nature of the field equations in the three-dimensional theory. In fact, some of the developments of the field equations by direct procedures are materially aided or influenced by available information which can be obtained from the three-dimensional theory. For example, the integrated equations of motion from the three-dimensional equations provide guidelines for a statement of one and two-dimensional conservation laws in conjunction with the one and two-dimensional models, and also provide some insight into the nature of inertia terms and the kinetic energy in the direct formulation of the one-dimensional and two-dimensional theories.†

Inasmuch as most of the difficulties associated with the derivation of the one-dimensional and two-dimensional theories from the three-dimensional equations occur in the construction of the constitutive equations, it is in fact here that the direct approach offers a great deal of appeal. This construction, as well as the entire development by the direct approach, is exact in the sense that they rest on (one-dimensional and two-dimensional) postulates valid for nonlinear behavior of materials but clearly they cannot be expected to represent all the features that could only be predicted by the relevant full three-dimensional equations. Theories constructed via a direct approach necessarily satisfy the requirements of invariance under superposed rigid body motions that arise from physical considertions and, of course, they are also consistent and fully invariant in the mathematical sense. Moreover, the development by the direct approach is conceptually simple and does not have the difficulties involving approximations usually made in the development of the theory of thin shells and the theory of water waves (or the theories of slender rods and jets) from their corresponding three-dimensional equations.

Following some general background information and definitions of jet-like and sheet-like bodies in Section 2, the remainder of the paper is arranged in two parts which can be read independently of each other: one part (Part A) is concerned with the theory of fluid jets and the other (Part B) is devoted to the theory of fluid sheets and its application to water waves. In our discussion of the direct formulation of these two topics, considerably

---

[*] The nature of these difficulties with particular reference to shells is discussed by Naghdi (1972, Secs. 1,4,19,20,21). Some of the difficulties associated with both nonlinear and linear theories of water waves are noted by Naghdi (1974) and are also discussed in the first and final sections of the paper of Green et al. (1974c).

[†] See the remarks following Eqs. (26) and (50).

more space is devoted to fluid sheets and water waves. This is partly due to the fact that, in the context of the direct formulation, the theory of fluid sheets has to date received more attention than that of fluid jets. Thus, in Part A (Sections 3-4), we summarize the basic theory of a Cosserat curve and briefly discuss a restricted form of the theory for straight jets which are not necessarily circular. The resulting system of nonlinear ordinary differential equations includes the effects of surface tension and gravity and has been derived for both inviscid and viscous jets. We do not record these here; but we call attention in Section 4 to a number of existing solutions, which serve as evidence of the relevance and applicability of the direct formulation of the theory of fluid jets.

In Part B (Sections 5-8), after briefly describing the basic theory of a Cosserat surface in Section 5, we present in outline a derivation of a *restricted* theory in Section 6, and then obtain a system of nonlinear partial differential equations for the propagation of fairly long waves in a homogeneous stream of variable depth (Section 7). This system of differential equations, which includes the effects of surface tension and gravity, is derived for incompressible inviscid fluids. Some extensions of these results to nonhomogeneous and viscous fluids are available but these are not discussed here. In the final section of the paper we make a comparison between the differential equations derived in Section 7 and the systems of equations for water waves that are often used in the literature; and, on the basis of compelling physical considerations, argue as to why the system of equations of the direct formulation should in general be preferred to others. In Section 8, we also call attention to a number of existing solutions, which serve as further evidence of the relevance and applicability of the direct formulation of the theory of fluid sheets.

In the course of our development, sometimes the same symbol is utilized in Parts A and B to denote different quantities; but this should not give rise to confusion, as the two parts can be read independently of each other. Throughout the paper, Latin indices (subscripts or superscripts) take the values 1, 2, 3, Greek indices take the values 1, 2 only, and the usual convention for summation over a repeated index is employed.

2. GENERAL BACKGROUND

In this section, we provide appropriate definitions for *jet-like* and *sheet-like* bodies. To this end, consider a finite three-dimensional body, β, in a Euclidean 3-space, and let convected coordinates, θ^i $(i = 1, 2, 3)$, be assigned to each particle (or material point) of β. Further, let[‡] $\underset{\sim}{r}^*$ be the position vector, from a fixed origin, of a typical particle of β in the present configuration at time, t. Then, a motion of the (three-dimensional) body is defined by a vector-valued function, $\hat{\underset{\sim}{r}}^*$, which assigns position, $\underset{\sim}{r}^*$, to each particle of β at each instant of time, i.e.,[§]

$$\underset{\sim}{r}^* = \hat{\underset{\sim}{r}}^*(\theta^1,\theta^2,\theta^3,t) \quad . \tag{1}$$

We assume that the vector function, $\hat{\underset{\sim}{r}}^*$,--a 1-parameter family of configurations with t as the real parameter--is sufficiently smooth in the sense that it is differentiable with respect to θ^i and t as many times as required. In some developments, it may be more convenient to set $\theta^3 = \xi$ and adopt the notation

$$\theta^i = (\theta^\alpha,\xi) \quad , \quad \theta^3 = \xi \quad . \tag{2}$$

We recall the formulas

$$\underset{\sim}{g}_i = \frac{\partial \hat{\underset{\sim}{r}}^*}{\partial\theta^i} \ , \ g_{ij} = \underset{\sim}{g}_i \cdot \underset{\sim}{g}_j \ , \ g = \det(g_{ij}) \ ,$$

$$\underset{\sim}{g}^i \cdot \underset{\sim}{g}_j = \delta^i_j \ , \ \underset{\sim}{g}^i = g^{ij}\underset{\sim}{g}_j \ , \ \underset{\sim}{g}^i \cdot \underset{\sim}{g}^j = g^{ij} \ , \tag{3}$$

$$dv = g^{\frac{1}{2}} d\theta^1 d\theta^2 d\theta^3 \tag{4}$$

and further assume that[||]

$$g^{\frac{1}{2}} = [\underset{\sim}{g}_1 \underset{\sim}{g}_2 \underset{\sim}{g}_3] > 0 \quad . \tag{5}$$

In (4), $\underset{\sim}{g}_i$ and $\underset{\sim}{g}^i$ are the covariant and the contravariant base vectors at time, t, respectively, g_{ij} is the metric tensor, g^{ij} is its conjugate, δ^i_j is the Kronecker symbol in 3-space and dv the volume element in the present configuration.

The velocity vector, $\underset{\sim}{v}^*$, of a particle of the three-dimensional body in the present configuration is defined by

$$\underset{\sim}{v}^* = \dot{\underset{\sim}{r}}^* \quad , \tag{6}$$

where a superposed dot denotes material time differentiation with respect to t holding θ^i fixed. The stress vector $\underset{\sim}{t}$ across a surface in the present configuration with outward unit normal $\underset{\sim}{\nu}^*$ is given by

$$\underset{\sim}{t} = \nu^*_i \frac{\underset{\sim}{T}^i}{g^{\frac{1}{2}}} = \nu^*_i \tau^{ik} \underset{\sim}{g}_k \quad , \tag{7}$$

where

[‡] The use of an asterisk attached to various symbols is for later convenience. The corresponding symbols without the asterisks are reserved for different definitions or designations to be introduced later.

[§] Recall that when the particles of a continuum are referred to a convected coordinate system, the numerical values of the coordinates associated with each particle remain the same for all time. Although the use of a convected coordinate system is by no means essential, it is particularly suited to studies of special bodies (such as sheets, jets, shells, and rods) and often results in simplification of intermediate steps in the development of the subject.

[||] The choice of positive sign in (5) is for definiteness. Alternatively, for physically possible motions we only need to assume that $g^{\frac{1}{2}} \neq 0$ with the understanding that in any given motion $[\underset{\sim}{g}_1\underset{\sim}{g}_2\underset{\sim}{g}_3]$ is either > 0 or < 0. The condition (5) also requires that θ^i be a right-handed coordinate system.

$$\underset{\sim}{T}^i = g^{\frac{1}{2}}\tau^{ij}\underset{\sim}{g}_j = g^{\frac{1}{2}}\tau^{i}_{\cdot j}\underset{\sim}{g}^j \quad , \quad \underset{\sim}{v}^* = \overset{*}{v}_{i}\underset{\sim}{g}^i = v^{*i}\underset{\sim}{g}_i \ , \qquad (8)$$

and where τ^{ik} are the contravariant components of the symmetric stress tensor. In terms of quantities defined in (5)-(8), the local field equations which follow from the integral forms of the three-dimensional conservation laws for mass, linear momentum and moment of momentum, respectively, are

$$\dot{\overline{\rho^* g^{\frac{1}{2}}}} = 0 \quad ,$$

$$\underset{\sim}{T}^i_{,i} + \rho^*\underset{\sim}{f}^* g^{\frac{1}{2}} = \rho^* g^{\frac{1}{2}}\underset{\sim}{v}^* \quad , \quad \underset{\sim}{g}_i \times \underset{\sim}{T}^i = \underset{\sim}{0} \qquad (9)$$

where ρ^* is the three-dimensional mass density, $\underset{\sim}{f}^*$ is the body force field per unit mass, and a comma denotes partial differentiation with respect to θ^i.

A material line (not necessarily a straight line) in β can be defined by the equations, $\theta^\alpha = \theta^\alpha(\xi)$; the equation resulting from (1) with $\theta^\alpha = \theta^\alpha(\xi)$ represents the parametric form of this material line in the current configuration and defines a 1-parameter family of curves in space, each of which we assume to be smooth and nonintersecting. We refer to the space curve, $\theta^\alpha = 0$, in the current configuration by c. Any point of this curve is specified by the position vector, $\underset{\sim}{r}$, relative to the same fixed origin to which $\underset{\sim}{r}^*$ is referred, where

$$\underset{\sim}{r} = \hat{\underset{\sim}{r}}(\xi,t) = \hat{\underset{\sim}{r}}^*(0,0,\xi,t) \quad . \qquad (10)$$

Let a_3 denote the tangent vector along the ξ-curve. By (10) and $(3)_1$,

$$\underset{\sim}{a}_3 = \underset{\sim}{a}_3(\xi,t) = \frac{\partial\hat{\underset{\sim}{r}}}{\partial\xi} = \underset{\sim}{g}_3(0,0,\xi,t) \qquad (11)$$

and the unit principal normal, $\underset{\sim}{a}_1$, and the unit binormal vector, $\underset{\sim}{a}_2$, to c may be introduced as

$$\underset{\sim}{a}_1 = \underset{\sim}{a}_1(\xi,t) = \frac{\partial\underset{\sim}{a}_3/\partial\xi}{|\partial\underset{\sim}{a}_3/\partial\xi|} \quad ,$$

$$\underset{\sim}{a}_2 = \underset{\sim}{a}_2(\xi,t) = \frac{\underset{\sim}{a}_3}{|\underset{\sim}{a}_3|} \times \underset{\sim}{a}_1 \quad , \qquad (12)$$

$$|\underset{\sim}{a}_3| = (a_{33})^{\frac{1}{2}} \quad ,$$

$$a_{33} = \underset{\sim}{a}_3 \cdot \underset{\sim}{a}_3 \quad ,$$

$$[\underset{\sim}{a}_1\underset{\sim}{a}_2\underset{\sim}{a}_3] > 0 \quad , \qquad (12)$$

where the notation $|\underset{\sim}{a}_3|$ stands for the magnitude of $\underset{\sim}{a}_3$. The system of base vectors, $\underset{\sim}{a}_1$, are oriented along the Serret-Frenet triad and satisfy the differential equations

$$\frac{\partial\underset{\sim}{a}_1}{\partial\xi} = \tau(a_{33})^{\frac{1}{2}}\underset{\sim}{a}_2 - \kappa\underset{\sim}{a}_3 \quad ,$$

$$\frac{\partial\underset{\sim}{a}_2}{\partial\xi} = -\,\tau(a_{33})^{\frac{1}{2}}\underset{\sim}{a}_1 \quad ,$$

$$\frac{\partial\underset{\sim}{a}_3}{\partial\xi} = \underset{\sim}{a}_{33}\kappa\underset{\sim}{a}_1 + \frac{1}{2a_{33}}\frac{\partial a_{33}}{\partial\xi}\underset{\sim}{a}_3 \quad , \qquad (13)$$

where κ and τ denote, respectively, the curvature and the torsion of c. In the special case that c is a plane curve, we may choose a_1 as the unit normal to the curve and then $\underset{\sim}{a}_2$ will be perpendicular to the plane of a_1 and $\underset{\sim}{a}_3$. If c is a straight curve, then there is no unique Serret-Frenet triad and $\underset{\sim}{a}_i$ may be chosen as any orthogonal triad with a_1, a_2 as unit vectors. Equations (13) are not identical to the formulas of Frenet because the parameter, ξ, is not necessarily the arc length of c. It may be noted here that the convected coordinate, ξ, may be chosen to coincide with the arc length in any one configuration of the material curve, e.g., in the present configuration. However, in a general motion (involving different configurations) the arc length between any pair of particles changes while the convected coordinates of each particle must remain the same. Therefore, arc length would not qualify as a convected coordinate.

A material surface in β can be defined by the equation, $\xi = \xi(\theta^\alpha)$; the equation resulting from (1) with $\xi = \xi(\theta^\alpha)$ represents the parametric form of this material surface in the current configuration and defines a 1-parameter family of surfaces in space, each of which we assume to be smooth and nonintersecting. We refer to the surface, $\xi = 0$. in the current configuration by s. Any point of the surface, s, is specified by the position vector, $\underset{\sim}{r}$, relative to the same fixed origin to which $\underset{\sim}{r}^*$ is referred, where

$$\underset{\sim}{r} = \hat{\underset{\sim}{r}}(\theta^\alpha,t) = \hat{\underset{\sim}{r}}^*(\theta^\alpha,0,t) \quad . \qquad (14)$$

Let a_α denote the base vectors along the θ^α-curves on the surface, s. By (14) and $(3)_1$,

$$\underset{\sim}{a}_\alpha = \underset{\sim}{a}_\alpha(\theta^\gamma,t) = \frac{\partial\hat{\underset{\sim}{r}}}{\partial\theta^\alpha} = \underset{\sim}{g}_\alpha(\theta^\gamma,0,t) \quad , \qquad (15)$$

and the unit normal, $\underset{\sim}{a}_3 = \underset{\sim}{a}_3(\theta^\gamma,t)$, to s may be defined by[**]

$$\underset{\sim}{a}_\alpha \cdot \underset{\sim}{a}_3 = 0 \quad , \quad \underset{\sim}{a}_3 \cdot \underset{\sim}{a}_3 = 1 \quad ,$$

$$\underset{\sim}{a}_3 = \underset{\sim}{a}^3 \quad [\underset{\sim}{a}_1\underset{\sim}{a}_2\underset{\sim}{a}_3] > 0 \quad . \qquad (16)$$

In the next four paragraphs we provide appropriate definitions for jet-like and sheet-like bodies in fairly precise terms.

Definition of a Jet-like Body. A Representation for the Motion of a Slender Jet.

Consider a space curve c defined by the parametric equations, $\theta^\alpha = 0$, over a finite interval, $\xi_1 \leqq \xi \leqq \xi_2$. Let $\underset{\sim}{r}$ be the position vector of any point of c and let $\underset{\sim}{a}_1, \underset{\sim}{a}_2$ and a_3 denote its unit principal normal, unit binormal, and the tangent vector, respectively. At each point of c, imagine material filaments lying in the normal plane, i.e., the plane perpendicular to $\underset{\sim}{a}_3$, and forming the normal cross-section[††], α_n. The surface swept out by the closed boundary curve, $\partial\alpha_n$, of α_n is called the lateral surface. Such a three-dimensional body is called jet-like if the dimensions in the plane of the normal cross-section are *small* compared to some characteristic dimension, L(c), of c (see Figure 1), e.g., its local radius of curvature $1/\kappa$, or the length of c in the case of a straight curve. A jet-like body is said to be *slender* if the largest dimension of α_n is much smaller than L(c). If α_n is independent of ξ, the body is said to be of uniform cross-section, otherwise of variable cross-section. Since a material curve in the three-dimensional body, β, can be defined by the equations, $\theta^\alpha = \theta^\alpha(\xi)$, it follows that the equation resulting from (1) with $\theta^\alpha = \theta^\alpha(\xi)$ represents the parametric form of the material curve in the present configuration and defines a curve, c, in space at time, t, which we assume to be sufficiently smooth and nonintersecting. Every point of this curve has a position vector specified by (10). Let the (three-dimensional) jet-like body in some neighborhood of c be bounded by material surfaces, $\xi = \xi_1$, $\xi = \xi_2$, (indicated in Figure 1) and a material surface of the form

---

[**] The use of the same symbols for base vectors of a surface in (15)-(16) and for the triad of a space curve in (11)-(12) should not give rise to confusion. The main developments for jets and sheets are dealt with separately in the rest of the paper; this permits the use of the same symbol for different quantities in the case of jets and sheets without confusion.

$$F(\theta^1,\theta^2,\xi) = 0 \quad , \qquad (17)$$

which is chosen such that ξ = constant are curved sections of the body bounded by closed curves on this surface with c lying on or within (17). In the development of a general theory, it is preferable to leave unspecified the choice of the relation of the curve, c, to one on the boundary surface (17). In special cases or in specific applications, however, it is necessary to fix the relation of c to the surface (17).

Suppose now that $\hat{\underset{\sim}{r}}^*$ in (1) is a continuous function of θ^i,t and has continuous space derivatives of order 1 and continuous time derivatives of order 2 in the bounded region lying inside the surface (17) and between $\xi = \xi_1$, $\xi = \xi_2$. Hence, to any required degree of approximation $\hat{\underset{\sim}{r}}^*$ may be represented as a polynomial in θ^1, θ^2 with coefficients which are continuously differentiable functions of ξ, t. Instead of considering a general representation of this kind, we restrict attention here to the approximation.

$$\hat{\underset{\sim}{r}}^* = \underset{\sim}{r} + \theta^\alpha \underset{\sim}{d}_\alpha \quad , \qquad (18)$$

where $\underset{\sim}{r}$ is defined by (10) and $\underset{\sim}{d}_\alpha = \underset{\sim}{d}_\alpha(\xi,t)$.

Definition of a Sheet-like Body. A Representation for the Motion of a Thin Sheet.

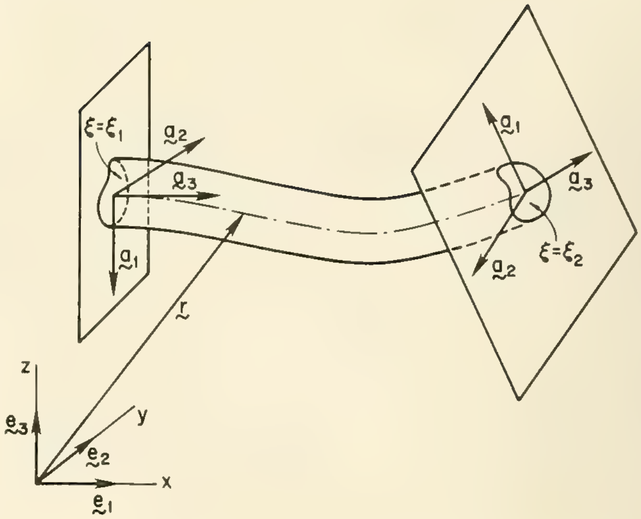

FIGURE 1. A jet-like body in the present configuration showing the line of centroids with position vector r and the end normal cross-sections $\xi = \xi_1$, $\xi = \xi_2$. Also shown are the unit principal normal a_1, the unit binormal a_2 and the tangent vector a_3 to the curve with position vector r.

Consider a two-dimensional surface, s, defined by the parametric equation, $\xi = 0$, over a finite coordinate patch, $\alpha' \leqq \theta^1 \leqq \alpha''$, $\beta' \leqq \theta^2 \leqq \beta''$. Let $\underset{\sim}{r}$ and $\underset{\sim}{a}_3$ denote, respectively, the position vector and the unit normal to s. At each point of s, imagine material filaments projecting normally above and below the surface, s. The surface formed by the material filaments constructed at the points of the closed boundary curve of s is called the *lateral surface*. Such a three-dimensional body is called a sheet if the dimension of the body along the normals, called the height and denoted by h, is *small*. A sheet is said to be *thin* if its thickness is much smaller than a certain characteristic length, L(s), of the surface, s, for example, the local minimum radius of curvature of the surface, or the smallest dimension of s in the case of a plane sheet. If h is constant, the sheet is said to be of uniform thickness, otherwise of variable thickness. Since a material surface in the three-dimensional body can be defined by the equation, $\xi = \xi(\theta^\alpha)$, it follows that the equations resulting from (1) and (2) with $\xi = \xi(\theta^\alpha)$ represent the parametric forms of the material surface in the present and the reference configurations, respectively. In particular, the equation, $\xi = 0$, defines a surface in space at time,

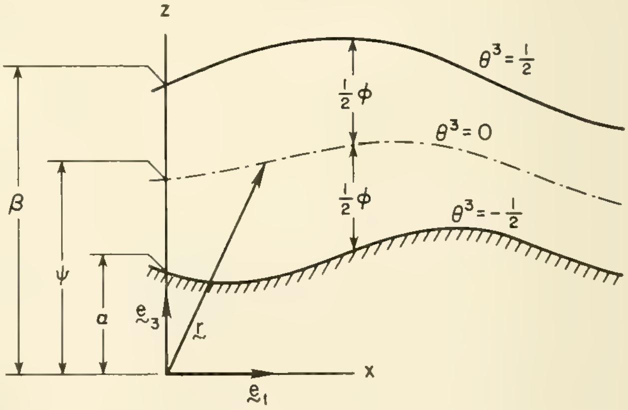

FIGURE 2. Sketch of the cross-section (y = const.) of a sheet of vertical thickness ϕ showing a wave motion propagating over a bottom of variable depth. Also shown is the surface $\theta^3 = 0$ (with position vector r and height Ψ) chosen such that the center mass of the (three-dimensional) fluid region lies on this surface. The top and bottom surfaces of height β and α are specified by $\theta^3 = 1/2$ and $\theta^3 = -1/2$, respectively.

[††] The *normal cross-section* of a jet is a portion of the normal plane to the curve, c, i.e., the intersection of the body and the normal plane.

t, which we assume to be smooth and nonintersecting. Every point of this surface has a position vector, $\mathbf{r}$, specified by (14). Let the boundary of the three-dimensional continuum be specified by the material surfaces

$$\xi = \xi_1(\theta^1,\theta^2) \quad , \quad \xi = \xi_2(\theta^1,\theta^2) \quad , \quad \xi_1 < \xi_2 \quad , \tag{19}$$

with the surface, $\xi = 0$, lying either on one of the two surfaces $(19)_{1,2}$ or between them (see, for example, Figure 2), and a material surface

$$f(\theta^1,\theta^2) = 0 \quad , \tag{20}$$

which is chosen such that ξ = const. forms closed smooth curves on the surface (20). As pointed out previously [Naghdi (1975)], in the development of a general theory, it is preferable to leave unspecified the choice of the relation of the surface, s, $(\xi = 0)$ to the major surfaces, s^+ and s^-. In special cases of the general theory or in specific applications, however, it is necessary to fix the relation of s to the surfaces $(19)_{1,2}$.

Suppose now that $\hat{\mathbf{r}}^*$ in (1) is a continuous function of θ^i,t, and has continuous space derivatives of order 1 and continuous time derivatives of order 2 in the bounded region, $\xi_1 \leq \xi \leq \xi_2$. Hence, to any required degree of approximation, $\hat{\mathbf{r}}^*$ may be represented as a polynomial in ξ with coefficients which are continuously differentiable functions of θ^α,t. However, instead of considering a general representation of this kind, we restrict attention here to the approximation

$$\hat{\mathbf{r}}^* = \mathbf{r} + \xi\mathbf{d} \quad , \tag{21}$$

where $\mathbf{r}$ is defined by (14) and $\mathbf{d} = \mathbf{d}(\theta^\alpha,t)$.

PART A

In Part A (Sections 3-4), we summarize the basic theory of a Cosserat (or a directed) curve and then briefly discuss a restricted form of the theory appropriate for straight fluid jets. Although we are concerned here mainly with the purely mechanical theory involving appropriate forms of the conservation laws for mass, linear momentum, and moment of momentum, we also include the conservation of energy. The latter is useful in some applications and supplies motivation for some requirements in the development of certain solutions.

3. THE BASIC THEORY OF A COSSERAT CURVE

Having defined a (three-dimensional) jet-like body in Section 2, we now formally introduce a direct *model* for such a body. Thus, a Cosserat (or a directed) curve, R, comprises a material curve, $\mathcal{L}$, (embedded in a Euclidean 3-space) and two deformable directors attached to every point of the curve, $\mathcal{L}$. The directors which are not necessarily along the unit principal normals and the unit binormals of the curve have, in particular, the property that they remain unaltered under superposed rigid body motions. Let the particles of $\mathcal{L}$ be identified by means of the convected coordinate, ξ, and let the curve occupied by $\mathcal{L}$ in the present configuration of R at time, t, be referred to as ℓ. Let $\mathbf{r}$ and $\mathbf{d}_\alpha$ $(\alpha = 1,2)$ denote the position vector of a typical point of ℓ and the directors at the same point, respectively, and also designate the tangent vector to the curve, ℓ, by $\mathbf{a}_3$. Then, a motion of the Cosserat curve is defined by vector-valued functions which assign a position, $\mathbf{r}$, and a pair of directors, $\mathbf{d}_\alpha$, to each particle of R at each instant of time, i.e.[§§]

$$\mathbf{r} = \hat{\mathbf{r}}(\xi,t) \quad , \quad \mathbf{d}_\alpha = \hat{\mathbf{d}}_\alpha(\xi,t) \quad , \quad [\mathbf{d}_1\mathbf{d}_2\mathbf{a}_3] > 0 \tag{22}$$

and the condition $(22)_3$ ensures that the directors, $\mathbf{d}_\alpha$, are nowhere tangent to ℓ and that $\mathbf{d}_1,\mathbf{d}_2$ never change their relative orientation with respect to each other and $\mathbf{a}_3$. The velocity and the director velocities are defined by

$$\mathbf{v} = \dot{\mathbf{r}} \quad , \quad \mathbf{w}_\alpha = \dot{\mathbf{d}}_\alpha \tag{23}$$

and from $(23)_1$ and (11) we have

$$\dot{\mathbf{a}}_3 = \frac{\partial\mathbf{v}}{\partial\xi} \quad , \tag{24}$$

where a superposed dot denotes material time differentiation with respect to t holding ξ fixed.

Consider an arbitrary part of the material curve, $\mathcal{L}$, in the present configuration, bounded by $\xi = \xi_1$ and $\xi = \xi_2$ $(\xi_1 < \xi_2)$, and let

$$ds = (a_{33})^{\frac{1}{2}}d\xi \quad , \quad a_{33} = \mathbf{a}_3 \cdot \mathbf{a}_3 \tag{25}$$

be the element of the arc length along the curve, ℓ. It is convenient at this point to define the following additional quantities: The mass density, $\rho = \rho(\xi,t)$, of the space curve, ℓ; the contact force, $\mathbf{n} = \mathbf{n}(\xi,t)$, and the contact director couples $\mathbf{p}^\alpha = \mathbf{p}^\alpha(\xi,t)$, each a three-dimensional vector field in the present configuration; the assigned force, $\mathbf{f} = \mathbf{f}(\xi,t)$, and the assigned director couples, $\boldsymbol{\ell}^\alpha = \boldsymbol{\ell}^\alpha(\xi,t)$, each a three-dimensional vector field and each per unit mass of the curve, ℓ; the intrinsic (curve) director couples, $\boldsymbol{\pi}^\alpha = \boldsymbol{\pi}^\alpha(\xi,t)$, per unit length of ℓ which make no contribution to the supply of momentum; the inertia coefficients, $y^\alpha = y^\alpha(\xi)$ and $y^{\alpha\beta} = y^{\alpha\beta}(\xi)$, with $y^{\alpha\beta}$ being components of a symmetric tensor, which are indenpendent of time; the specific internal energy, $\varepsilon = \varepsilon(\xi,t)$; the specific heat supply, $r = r(\xi,t)$, per unit time; and the heat flux, $h = h(\xi,t)$, along ℓ, in the direction of increasing ξ, per unit time. The assigned field, $\mathbf{f}$, represents the combined effect of (i) the stress vector on the lateral surface (17) of the jet-like body denoted by $\mathbf{f}_c$, and (ii) an integrated contribution arising from the three-dimensional body force denoted by $\mathbf{f}_b$, e.g., that due to gravity. A parallel statement holds for the assigned fields, $\boldsymbol{\ell}^\alpha$. Similarly, the assigned heat supply, r, represents the combined effect of (i) heat supply entering the lateral surface (17) of the jet-like body from the surrounding environment, denoted by r_c, and (ii) an integrated contribution arising from the three-dimensional heat supply denoted by r_b. Thus, we may write

---

[§§] For convenience, we adopt the notation for $\mathbf{r}$ in (10) and (18) also for the surface $(22)_1$. This permits an easy identification of the two curves, if desired. The choice of positive sign in $(22)_3$ is for definiteness. Alternatively, it will suffice to assume that $[\mathbf{d}_1\mathbf{d}_2\mathbf{a}_3] \neq 0$ with the understanding that in any given motion the scalar triple product $[\mathbf{d}_1\mathbf{d}_2\mathbf{a}_3]$ is either > 0 or < 0.

$$\utilde{f} = \utilde{f}_b + \utilde{f}_c \quad , \quad \utilde{\ell}^{\alpha} = \utilde{\ell}^{\alpha}_b + \utilde{\ell}^{\alpha}_c \quad , \quad r = r_b + r_c \quad . \tag{26}$$

The various quantities in (26) are free to be specified in a manner which depends on the particular application in mind and, in the context of the theory of a Cosserat curve, the intertia coefficients, y^{α}, $y^{\alpha\beta}$, and the mass density, ρ, require constitutive equations. Indeed, $\utilde{f}_c$, $\utilde{\ell}^{\alpha}_c$ and r_c, as well as $\utilde{f}_b$, $\utilde{\ell}^{\alpha}_b$ and r_b, can be identified with the corresponding expressions in a derivation from the three-dimensional equations [see, for example, Green et al. (1974a)]. Likewise, the inertia coefficients, y^{α}, $y^{\alpha\beta}$, and the mass density, ρ, may be identified with easily accessible results from the three-dimensional theory.

With the above definitions of the various field quantities and with reference to the present configuration, the conservation laws for a Cosserat curve are:

$$\frac{d}{dt}\int_{\xi_1}^{\xi_2} \rho \, ds = 0 \quad ,$$

$$\frac{d}{dt}\int_{\xi_1}^{\xi_2} \rho(\utilde{v} + y^{\alpha}\utilde{w}_{\alpha})ds = \int_{\xi_1}^{\xi_2} \rho\utilde{f}ds + [\utilde{n}]_{\xi_1}^{\xi_2} \quad ,$$

$$\frac{d}{dt}\int_{\xi_1}^{\xi_2} \rho(y^{\alpha}\utilde{v} + y^{\alpha\beta}\utilde{w}_{\beta})ds$$

$$= \int_{\xi_1}^{\xi_2} (\rho\ell^{\alpha} - (a_{33})^{-\frac{1}{2}}\utilde{\pi}^{\alpha})ds + [\utilde{p}a]_{\xi_1}^{\xi_2} \quad ,$$

$$\frac{d}{dt}\int_{\xi_1}^{\xi_2} \rho[\utilde{r} \times \utilde{v} + y^{\alpha}(\utilde{r} \times \utilde{w}_{\alpha} + \utilde{d}_{\alpha} \times \utilde{v})$$

$$+ \utilde{d}_{\alpha} \times y^{\alpha\beta}w_{\beta}]ds$$

$$= \int_{\xi_1}^{\xi_2} \rho(\utilde{r} \times \utilde{f} + \utilde{d}_{\alpha} \times \utilde{\ell}^{\alpha})ds$$

$$+ [\utilde{r} \times \utilde{n} + \utilde{d}_{\alpha} \times \utilde{p}^{\alpha}]_{\xi_1}^{\xi_2} \quad ,$$

$$\frac{d}{dt}\int_{\xi_1}^{\xi_2} \rho[\varepsilon + \tfrac{1}{2}(\utilde{v} \cdot \utilde{v} + 2y^{\alpha}\utilde{v} \cdot \utilde{w}_{\alpha} + y^{\alpha\beta}\utilde{w}_{\alpha} \cdot \utilde{w}_{\beta})ds$$

$$= \int_{\xi_1}^{\xi_2} \rho(r + \utilde{f} \cdot \utilde{v} + \utilde{\ell}a \cdot \utilde{w}_{\alpha})ds$$

$$+ [\utilde{n} \cdot \utilde{v} + \utilde{p}^{\alpha} \cdot \utilde{w}_{\alpha} - h]_{\xi_1}^{\xi_2} \quad , \tag{27}$$

where we have used the notation

$$[f(\xi,t)]_{\xi_1}^{\xi_2} = f(\xi_2,t) = f(\xi_1,t) \quad . \tag{28}$$

The first of (27) is a statement of the conservation of mass, the second is the conservation of linear momentum, the third that of the director momentum, the fourth is the conservation of moment of momentum, and the fifth represents the conservation of energy.

Under suitable continuity assumptions, the first four equations in (27) are equivalent to

$$\lambda = \lambda(\xi) = \rho(a_{33})^{\frac{1}{2}} \quad \text{or} \quad \dot{\rho}a_{33} + \rho\utilde{a}_3 \cdot \frac{\partial\utilde{v}}{\partial\xi} = 0 \ , \tag{29}$$

$$\frac{\partial\utilde{n}}{\partial\xi} + \lambda\utilde{f} = \lambda(\dot{\utilde{v}} + y^{\alpha}\utilde{w}_{\alpha}) \quad , \tag{30}$$

$$\frac{\partial p^{\alpha}}{\partial\xi} + \lambda\utilde{\ell}^{\alpha} = \utilde{\pi}^{\alpha} + \lambda(y^{\alpha}\dot{\utilde{v}} + y^{\alpha\beta}\utilde{w}_{\beta}) \quad , \tag{31}$$

$$\utilde{a}_3 \times \utilde{n} + \frac{\partial\utilde{m}}{\partial\xi} + \lambda\utilde{g} = 0 \quad , \tag{32}$$

$$\lambda r - \frac{\partial h}{\partial\xi} - \lambda\dot{\varepsilon} + P = 0 \quad , \tag{33}$$

where

$$\utilde{m} = \utilde{d}_{\alpha} \times \utilde{p}^{\alpha} \quad , \quad \utilde{g} = \utilde{d}_{\alpha} \times \utilde{q}^{\alpha} \quad ,$$

$$\utilde{q}^{\alpha} = \utilde{\ell}^{\alpha} - y^{\alpha}\dot{\utilde{v}} = y^{\alpha\beta}\utilde{w}_{\beta} \quad , \tag{34}$$

and

$$\lambda P = \utilde{n} \cdot \frac{\partial\utilde{v}}{\partial\xi} + \utilde{\pi}^{\alpha} \cdot \utilde{w}_{\alpha} + \utilde{p}^{\alpha} \cdot \frac{\partial\utilde{w}_{\alpha}}{\partial\xi} \tag{35}$$

is the mechanical power. With the help of (34), the local form of the moment of momentum equation (31) can be reduced to

$$\utilde{a}_3 \times \utilde{n} + \utilde{d}_{\alpha} \times \utilde{\pi}^{\alpha} + \frac{\partial\utilde{d}_{\alpha}}{\partial\xi} \times \utilde{p}^{\alpha} = 0 \quad . \tag{36}$$

It may be noted that the local field equations in the mechanical theory of a Cosserat curve have the same forms as those that can be derived from the three-dimensional equations; the latter can be derived by suitable integration of $(9)_{1,2,3}$ with respect to θ^1 and θ^2 and in terms of certain definitions for integrated mass density and resultants of stress [for details, see Green et al. (1974a)]. Moreover, given the approximation (18), there is a 1-1 correspondence between the one-dimensional field equations that follow from the conservation laws of a Cosserat curve and those that can be derived from the three-dimensional equations provided we identify the director d_{α} in (18) with $(22)_2$ and adopt the definitions of the resultants mentioned above. A similar 1-1 correspondence can be shown to hold between (33) and an integrated energy equation derived from the three-dimensional energy equation.

The above results include the local form of conservation of energy derived from $(27)_5$. For the purely mechanical theory in which the law of conservation of energy is excluded, the appropriate conservation laws are the first four of (27). In the context of the purely mechanical theory, it is worth recalling that the rate of work by all contact and assigned forces acting on the curve, ℓ, and its end points minus the rate of increase of the kinetic energy can be reduced to:

$$\int_{\xi_1}^{\xi_2}\rho(\mathbf{f}\cdot\mathbf{v}+\boldsymbol{\ell}^{\alpha}\cdot\mathbf{w}_{\alpha})ds+[\mathbf{n}\cdot\mathbf{v}+\mathbf{p}^{\alpha}\cdot\mathbf{w}_{\alpha}]_{\xi_1}^{\xi_2}$$

$$-\frac{d}{dt}\int_{\xi_1}^{\xi_2}\tfrac{1}{2}\rho(\mathbf{v}\cdot\mathbf{v}+2y^{\alpha}\mathbf{v}\cdot\mathbf{w}_{\alpha}+y^{\alpha\beta}\mathbf{w}_{\alpha}\cdot\mathbf{w}_{\beta})ds$$

$$=\int_{\xi_1}^{\xi_2}\rho P ds \quad , \tag{37}$$

where P is defined by (35).

Before closing this section, we note that the restriction imposed on the motion of the medium by the condition of incompressibility reduces to |||| [see Green (1976)]

$$\frac{d}{dt}[\mathbf{d}_1\mathbf{d}_2\mathbf{a}_3]=0 \tag{38}$$

and can alternatively be expressed in the form

$$\varepsilon^{\alpha\beta}\mathbf{d}_{\beta}\times\mathbf{a}_3\cdot\mathbf{w}_{\alpha}+\mathbf{d}_1\times\mathbf{d}_2\cdot\frac{\partial\mathbf{v}}{\partial\xi}=0 \quad , \tag{39}$$

where $\varepsilon^{\alpha\beta}$ is the permutation symbol in 2-spaces. To complete the theory of a Cosserat curve under the constraint condition (39), we assume that each of the functions, $\mathbf{n},\boldsymbol{\pi}^{\alpha}$, and $\mathbf{p}^{\alpha}$, is determined to within an additive constraint response so that

$$\mathbf{n}=\bar{\mathbf{n}}+\hat{\mathbf{n}} \quad , \quad \boldsymbol{\pi}^{\alpha}=\bar{\boldsymbol{\pi}}^{\alpha}+\hat{\boldsymbol{\pi}}^{\alpha} \quad , \quad \mathbf{p}^{\alpha}=\bar{\mathbf{p}}^{\alpha}+\hat{\mathbf{p}}^{\alpha} \quad , \tag{40}$$

where $\hat{\mathbf{n}}$, $\hat{\boldsymbol{\pi}}^{\alpha}$, and $\hat{\mathbf{p}}^{\alpha}$ are determined by constitutive equations and the functions $\bar{\mathbf{n}}(\xi,t)$, $\bar{\boldsymbol{\pi}}^{\alpha}(\xi,t)$, and $\bar{\mathbf{p}}^{\alpha}(\xi,t)$ are the response due to the constraint; the latter quantities are arbitrary functions of ξ,t and do no work. For an incompressible inviscid fluid jet, which models the properties of the three-dimensional inviscid fluid at constant temperature, we introduce the constitutive assumption that $\mathbf{n},\boldsymbol{\pi}^{\alpha}$, $\mathbf{p}^{\alpha}$ do not depend explicitly on the kinematic quantities, $\partial\mathbf{v}/\partial\xi,\mathbf{w}_{\alpha},\partial\mathbf{w}_{\alpha}/\partial\xi$, and are furthermore workless, i.e.,

$$\mathbf{n}\cdot\frac{\partial\mathbf{v}}{\partial\xi}+\boldsymbol{\pi}^{\alpha}\cdot\mathbf{w}_{\alpha}+\mathbf{p}^{\alpha}\cdot\frac{\partial\mathbf{w}_{\alpha}}{\partial\xi}=0 \quad , \tag{41}$$

provided $\mathbf{w}_{\alpha}$, $\partial\mathbf{v}/\partial\xi$ satisfy the constraint condition (39). It can then be shown that [Green and Laws (1968) and Green (1976)]

$$\mathbf{n}=-p_o'\mathbf{d}_1\times\mathbf{d}_2 \quad , \quad \boldsymbol{\pi}^{\alpha}=-p_o'\varepsilon^{\alpha\beta}\mathbf{d}_{\beta}\times\mathbf{a}_3 \quad ,$$

$$\mathbf{p}^{\alpha}=\mathbf{0} \quad , \tag{42}$$

where p_o' is an arbitrary scalar function of ξ,t. For an incompressible viscous jet, the constraint response, $\mathbf{n},\boldsymbol{\pi}^{\alpha},\mathbf{p}^{\alpha}$, are determined similarly with the use of the constraint condition (39), but constitutive equations are required for $\hat{\mathbf{n}},\hat{\boldsymbol{\pi}}^{\alpha},\hat{\mathbf{p}}^{\alpha}$ in (40). We do not record here the results for a viscous jet and refer the reader to Green (1976) and Caulk and Naghdi (1978b).

4. STRAIGHT FLUID JETS. ADDITIONAL REMARKS

We now specialize the results of the previous section to straight jets of elliptical cross-section. In order to display some details of the kinematics of a straight jet, including the rotation of the directors in a plane normal to the jet axis, it is convenient to introduce a fixed system of rectangular Cartesian coordinates (x,y,z) with the z-axis parallel to the jet. Further, let the unit base vectors of the rectangular Cartesian axes be denoted by $(\mathbf{i},\mathbf{j},\mathbf{k})$ and introduce, for later convenience, the additional base vectors

$$\mathbf{e}_1=\mathbf{i}\cos\theta+\mathbf{j}\sin\theta \quad ,$$

$$\mathbf{e}_2=-\mathbf{i}\sin\theta+\mathbf{j}\cos\theta \quad , \quad \mathbf{e}_3=\mathbf{k} \quad , \tag{43}$$

where θ is a smooth function of z and t. We assume that the directors are so restricted that they describe an elliptical cross-section of smoothly varying orientation along the length of the jet and that at each z = const., the base vectors, $\mathbf{e}_1$ and $\mathbf{e}_2$, lie along the major and minor axes of the ellipse, respectively. Then, the angle, θ, called the *sectional orientation*, specifies the orientation of the cross-section as a function of position. With this background, henceforth we restrict motions of the directed curve, R, such that in the present configuration at time, t,

$$\mathbf{r}=z(\xi,t)\mathbf{e}_3 \quad , \quad \mathbf{d}_1=\phi_1\mathbf{e}_1 \quad , \quad \mathbf{d}_2=\phi_2\mathbf{e}_2 \tag{44}$$

where ϕ_1 and ϕ_2 measure the semiaxes of the elliptical cross-section. In the case of a circular jet, $\phi_1=\phi_2$.

The complete theory also requires the specification of explicit values for $\lambda,y^{\alpha},y^{\alpha\beta},\mathbf{f}$ and $\boldsymbol{\ell}^{\alpha}$. In particular, the values for $\lambda,y^{\alpha},y^{\alpha\beta}$ may be obtained by an appeal to certain results from the three-dimensional description of the jet. Thus, recalling (18) and the remark made following (17), here we choose the curve, $\theta^{\alpha}=0$, as the line of centroids of the jet-like body and identify this curve with the curve, ℓ, in the theory of a Cosserat curve. This leads to the identification

$$\lambda=\rho(a_{33})^{\frac{1}{2}}=\int_{\alpha}\rho^{*}g^{\frac{1}{2}}d\theta^{1}d\theta^{2} \quad ,$$

$$\lambda y^{\alpha}=\int_{\alpha}\rho^{*}g^{\frac{1}{2}}\theta^{\alpha}d\theta^{1}d\theta^{2}=0 \quad ,$$

$$\lambda y^{\alpha\beta}=\int_{\alpha}\rho^{*}g^{\frac{1}{2}}\theta^{\alpha}\theta^{\beta}d\theta^{1}d\theta^{2} \quad , \tag{45}$$

where ρ^{*} is the three-dimensional mass density in (9) and the determinant g defined by $(3)_3$ is calculated from the approximation (18). Again, with

---

|||| In general, there are three conditions of incompressibility in the theory of incompressible directed fluid jets; for a discussion of these, see Caulk and Naghdi (1978a, Appendix). In restricted forms of the theory discussed in the next section, two of the three conditions are satisfied identically. The specification (38) is motivated from an examination of the incompressibility condition in the three-dimensional theory when the position vector is approximated by (18).

the use of (18) and the equations of motion $(9)_{2,3}$, the expressions for $\mathbf{f}$ and ℓ^α can be identified in terms of the integrated body force, $\mathbf{f}^*$, over the cross-sectional area, α, and specified pressure and surface tension over the boundary, $\partial\alpha$ of α [for details, see, for example, Caulk and Naghdi (1978a)]. We observe that since $y^\alpha = 0$ by $(45)_2$, the equations of motion (30) and (31) assume a slightly simpler form. We do not record here the details of the system of ordinary differential equations which can be obtained from (29)-(33) for both inviscid and linear viscous fluids. They are readily available in the papers cited: see Green and Laws (1968), Green (1975, 1976, 1977), and Caulk and Naghdi (1978a, b).

In the rest of this section, we briefly call attention to some available evidence of the relevance and applicability of the direct formulation of the fluid jets. Available solutions obtained to date are limited to those for straight jets and among these most of them deal with jets of circular cross-section. Some general aspects of compressible inviscid jets, including a discussion of ideal gas jets in the context of a thermodynamical theory, have been studied by Green (1975). Applications to incompressible circular jets for both inviscid and viscous fluids are contained in the papers of Green and Laws (1968) and of Green (1976). Green (1977) has also studied a steady motion of an incompressible inviscid fluid jet which does not twist along its axis. A more detailed analysis of the motion of a straight elliptical jet of an incompressible inviscid fluid in which the jet is allowed to twist along its axis is contained in a recent paper by Caulk and Naghdi (1978a). This study, which includes the effects of gravity and surface tension, utilizes the nonlinear differential equations of Section 3 with $\mathbf{r}$ and $\mathbf{d}_\alpha$ at time, t, specified in the form (44). A number of theorems are proved in the paper of Caulk and Naghdi (1978a) which pertain to the motion of a twisted elliptical jet and some special solutions are obtained which illustrate the influence of twist. Further, a system of linear equations, derived for small motions superposed on uniform flow of an incompressible circular jet, is employed by Caulk and Naghdi (1978b) to study the instability of some simple jet motions in the presence of surface tension, i.e., the so-called capillary instability that leads to disintegration of the jet. In particular, they [Caulk and Naghdi (1978b)] consider the breakup of both inviscid and viscous jets: in the case of an inviscid jet excellent agreement is obtained with the three-dimensional results of Rayleigh (1879a,b); and for a viscous jet, through a comparison with available three-dimensional numerical results [Chandrasekhar (1961)], the solution obtained is shown to be an improvement over an existing approximate solution of the problem by Weber (1931). A related study by Bogy (1978), concerning the instability of an incompressible viscous liquid jet of circular section, partly overlaps with the work of Caulk and Naghdi (1978b) on the temporal instability of a viscous jet, and considers the spatial instability of a semi-infinite jet formulated as a boundary-value problem.

PART B

In Part B (Sections 5-8), after briefly describing the basic theory of a Cosserat (or a directed) surface, we summarize a special case of the theory which is particularly suited for applications to problems of fluid sheets and to the propagation of fairly long water waves. For the sake of simplicity, we confine attention here to homogeneous fluids; but note that, as in Green and Naghdi (1977), the derivation can be modified to allow for variation of mass density with depth. Although we are concerned mainly with the purely mechanical theory involving appropriate forms of the conservation laws for mass, linear momentum, and moment of momentum, we also include the conservation of energy. The latter easily supplies motivation for some requirements in the development of certain solutions.

5. THE BASIC THEORY OF A COSSERAT SURFACE

Having introduced the notion of a (three-dimensional) sheet-like body in Section 2, we now formally define a direct *model* for such a body. Thus, a Cosserat (or directed) surface, $\mathcal{C}$, comprises a material surface, S, (embedded in a Euclidean 3-space) and a single deformable vector, called a director, attached to every point of the surface, S. The directors which are not necessarily along the unit normals to the surface have, in particular, the property that they remain unaltered under superposed rigid body motions. Let the particles of the material surface of $\mathcal{C}$ be identified by means of a system of convected coordinates, θ^α $(\alpha = 1,2)$, and let the surface occupied by S in the present configuration of $\mathcal{C}$ at time, t, be referred to as $\mathcal{S}$. Let $\mathbf{r}$ and $\mathbf{d}$ denote the position vector of a typical point of $\mathcal{S}$ and the director at the same point, respectively, and also designate the base vectors along the θ^α-curves on $\mathcal{S}$ by $\mathbf{a}_\alpha$. Then, a motion of the Cosserat surface is defined by vector-valued functions which assign position, $\mathbf{r}$, and director, $\mathbf{d}$, to each particle of $\mathcal{C}$ at each instant of time, i.e.,[*]

$$\mathbf{r} = \hat{\mathbf{r}}(\theta^\alpha,t) \quad , \quad \mathbf{d} = \hat{\mathbf{d}}(\theta^\alpha,t) \quad , \quad [\mathbf{a}_1\mathbf{a}_2\mathbf{d}] > 0 \tag{46}$$

and the condition $(46)_3$ ensures that the director, $\mathbf{d}$, is nowhere tangent to $\mathcal{S}$. The base vectors, $\mathbf{a}_\alpha$, and their reciprocals, $\mathbf{a}^\alpha$, the unit normal, $\mathbf{a}_3$, and the components of the metric tensors, $a_{\alpha\beta}$ and $a^{\alpha\beta}$, at each point of $\mathcal{S}$ are defined by

$$\mathbf{a}_\alpha, = \frac{\partial \mathbf{r}}{\partial \theta^\alpha} \quad , \quad \mathbf{a}^\alpha \cdot \mathbf{a}_\beta = \delta^\alpha_\beta \quad , \quad a_{\alpha\beta} = \mathbf{a}_\alpha \cdot \mathbf{a}_\beta \quad ,$$

$$a^{\alpha\beta} = \mathbf{a}^\alpha \cdot \mathbf{a}^\beta \quad , \quad a^{\frac{1}{2}}\mathbf{a}_3 = \mathbf{a}_1 \times \mathbf{a}_2 \quad ,$$

$$a = \det a_{\alpha\beta} \quad , \quad a^{\frac{1}{2}} = [\mathbf{a}_1\mathbf{a}_2\mathbf{a}_3] > 0 \quad , \tag{47}$$

where δ^α_β is the Kronecker delta in 2-space. The velocity and the director velocity vectors are defined by

$$\mathbf{v} = \dot{\mathbf{r}} \quad , \quad \mathbf{w} = \dot{\mathbf{d}} \quad , \tag{48}$$

---

[*] For convenience, we adopt the notation for $\mathbf{r}$ in (14) and (21) also for the surface $(46)_1$. This permits an easy identification of the two surfaces, if desired. The choice of positive sign in $(46)_3$ is for definiteness. Alternatively, it will suffice to assume that $[\mathbf{a}_1\mathbf{a}_2\mathbf{d}] \neq 0$ with the understanding that in any given motion the scalar triple product $[\mathbf{a}_1\mathbf{a}_2\mathbf{d}]$ is either > 0 or < 0.

where a superposed dot denotes differentiation with respect to t holding θ^α fixed.

Let $\mathcal{P}$, bounded by a closed curve, $\partial\mathcal{P}$, be a part of $\mathscr{S}$ occupied by an arbitrary material region of S in the present configuration at time, t, and let

$$\underset{\sim}{\nu} = \nu^\alpha \underset{\sim}{a}_\alpha = \nu_\alpha \underset{\sim}{a}^\alpha \qquad (49)$$

be the outward unit normal to $\partial\mathcal{P}$. It is convenient at this point to define certain additional quantities as follows: The mass density, $\rho = \rho(\theta^\gamma,t)$, of the surface, $\mathscr{S}$, in the present configuration; the contact force, $\underset{\sim}{N} = \underset{\sim}{N}(\theta^\gamma,t;\underset{\sim}{\nu})$, and the contact director force[†], $\underset{\sim}{M} = \underset{\sim}{M}(\theta^\gamma,t;\underset{\sim}{\nu})$, each per unit length of a curve in the present configuration; the assigned force, $\underset{\sim}{f} = \underset{\sim}{f}(\theta^\gamma,t)$, and the assigned director force, $\underset{\sim}{\ell} = \underset{\sim}{\ell}(\theta^\gamma,t)$, each per unit mass of the surface, $\mathscr{S}$; the intrinsic director force, $\underset{\sim}{m}$, per unit area of $\mathscr{S}$; the inertia coefficients, $\bar{k} = \bar{k}(\theta^\gamma)$ and $k = k(\theta^\gamma)$, which are independent of time; the specific internal energy, $\varepsilon = \varepsilon(\theta^\gamma,t)$; the heat flux, $h = h(\theta^\gamma,t;\underset{\sim}{\nu})$ per unit time and per unit length of a curve, $\partial\mathcal{P}$; the specific heat supply, $r = r(\theta^\gamma,t)$, per unit time; and the element of area, $d\sigma$, and the line element, ds, of the surface, $\mathscr{S}$. The assigned field, $\underset{\sim}{f}$, may be regarded as representing the combined effect of (i) the stress vector on the major surfaces of the sheet-like body denoted by $\underset{\sim}{f}_c$, e.g., that due to the ambient pressure of the surrounding medium, and (ii) an integrated contribution arising from the three-dimensional body force denoted by $\underset{\sim}{f}_b$, e.g., that due to gravity. A parallel statement holds for the assigned field, $\underset{\sim}{\ell}$. Similarly, the assigned heat supply, r, may be regarded as representing the combined effect of (i) heat supply entering the major surfaces of the sheet-like body from the surrounding environment, denoted by r_c, and (ii) a contribution arising from the three-dimensional heat supply, denoted by r_b. Thus, we may write

$$\underset{\sim}{f} = \underset{\sim}{f}_b + \underset{\sim}{f}_c \quad , \quad \underset{\sim}{\ell} = \underset{\sim}{\ell}_b + \underset{\sim}{\ell}_c \quad , \quad r = r_b + r_c \quad . (50)$$

The various quantities in (50) are free to be specified in a manner which depends on the particular application in mind and, in the context of the theory of a Cosserat surface, the inertia coefficients, $\bar{k}$, k and the mass density, ρ, require constitutive equations. Indeed, $\underset{\sim}{f}_c,\underset{\sim}{\ell}_c$ and r_c, as well as $\underset{\sim}{f}_b,\underset{\sim}{\ell}_b$ and r_b, can be identified with corresponding expressions in a derivation from the three-dimensional equations [for details, see Naghdi (1972,1974)]. Likewise, ρ and the coefficients, $\bar{k}$,k, may be identified with easily accessible results from the three-dimensional theory.

In terms of the above definitions, the conservation laws for a Cosserat surface can be stated in fairly general forms. We do not record these here since they are available elsewhere [Naghdi (1972), p. 482) or Naghdi (1974)]. Instead, we turn our attention to the relatively simple theory of the next section.

It may be noted that the local field equations in the mechanical theory of a Cosserat surface have the same forms as those that can be derived from the three-dimensional field equations $(9)_{1,2,3}$ by suitable integration between the limits, ξ_1 and ξ_2, and in terms of certain definitions for integrated mass density and resultants of stress [for details, see Naghdi (1972, Sections 11-12) or Naghdi (1974)]. Moreover, given the approximation (21), there is a 1-1 correspondence between the two-dimensional field equations that follow from the conservation laws of a Cosserat surface and those that can be derived from $(9)_{1,2,3}$ provided we identify the director, $\underset{\sim}{d}$, in (21) with $(46)_2$ and adopt the definitions of the resultants mentioned above. As similar 1-1 correspondence can be shown to hold between the two-dimensional energy equation in the theory of a Cosserat surface and an integrated energy equation derived from the three-dimensional energy equation.

6. A RESTRICTED THEORY OF A COSSERAT SURFACE

Special cases of the general theory can be obtained by the introduction of suitable constraints, thereby resulting in *constrained theories*. Alternatively, corresponding special cases can be developed in which the kinematic and the kinetic variables are suitably restricted a priori and then *restricted theories* are constructed by direct approach. Such special cases of the general theory have been discussed previously by Naghdi (1972, Sections 10 and 15) and by Green and Naghdi (1974) and are of particular interest in the context of elastic shell theory. We provide here an outline of a restricted theory developed by Green and Naghdi (1977) mainly for application to problems of fluid sheets. The resulting equations can also be obtained as a constrained case of those given for directed fluid sheets [Green and Naghdi (1976)], but it is more convenient to restrict the kinematic and the kinetic variables at the outset and construct a corresponding restricted theory from an appropriate set of conservation laws in integral form.

Let the director, $\underset{\sim}{d}$, while deforming along its length, always remain parallel to a fixed direction specified by a constant unit vector, $\underset{\sim}{b}$. It should be kept in mind that $\underset{\sim}{b}$ is fixed relative to the body and not relative to the space. Thus, recalling $(46)_2$ and $(48)_2$, we write

$$\underset{\sim}{d} = \phi(\theta^\alpha,t)\underset{\sim}{b} \quad , \quad \underset{\sim}{w} = w(\theta^\alpha,t)\underset{\sim}{b} \quad , \quad w = \dot{\phi} \quad . \quad (51)$$

Further, in view of the assumed form of $(51)_1$ for the director, it is convenient to decompose $\underset{\sim}{M}$,$\underset{\sim}{m}$ and $\underset{\sim}{\ell}$ into their components along and perpendicular to the unit vector, $\underset{\sim}{b}$, i.e.,

$$\begin{aligned} \underset{\sim}{M} &= M(\theta^\gamma,t;\underset{\sim}{\nu})\underset{\sim}{b} + \underset{\sim}{b} \times \underset{\sim}{S}(\theta^\gamma,t;\underset{\sim}{\nu}) \quad , \quad \underset{\sim}{S}\cdot\underset{\sim}{b} = 0 \quad , \\ \underset{\sim}{m} &= m(\theta^\gamma,t)\underset{\sim}{b} + \underset{\sim}{b} \times \underset{\sim}{s}(\theta^\gamma,t) \quad , \quad \underset{\sim}{s}\cdot\underset{\sim}{b} = 0 \quad , \\ \underset{\sim}{\ell} &= \ell(\theta^\gamma,t)\underset{\sim}{b} + \underset{\sim}{b} \times \underset{\sim}{c}(\theta^\gamma,t) \quad , \quad \underset{\sim}{c}\cdot\underset{\sim}{b} = 0 \quad , \quad (52) \end{aligned}$$

where M,m and ℓ are scalar functions and $\underset{\sim}{S}$,$\underset{\sim}{s}$,$\underset{\sim}{c}$ are vector functions of their arguments. According to the decomposition $(52)_1$ the vector, $\underset{\sim}{M}$, is resolved into two parts. One part is along $\underset{\sim}{b}$ and the other part is the perpendicular projection of $\underset{\sim}{M}$ onto the plane defined by $\underset{\sim}{S}\cdot\underset{\sim}{b} = 0$ which is perpendicular to

---

[†] The terminology of director couple is also used for $\underset{\sim}{M}$ depending on the physical dimension assumed for the director, $\underset{\sim}{d}$. Here we choose $\underset{\sim}{d}$ to have the physical dimension of length so that $\underset{\sim}{M}$ has the same physical dimension as $\underset{\sim}{N}$. For further discussion see Naghdi (1972, Ch. C) and Green and Naghdi (1976).

b. Parallel statements hold for vectors, $\mathbf{m}$ and $\boldsymbol{\ell}$, in $(52)_{2,3}$.

Also, it is convenient to decompose the assigned fields, $\mathbf{f}$ and ℓ, into two parts, one of which represents the three-dimensional body force acting on the continuum which is assumed to be derivable from a potential function, $\Omega(\mathbf{r},\phi)$, and the other which represents the effect of applied surface loads on the major surfaces of the fluid sheet. Thus, we write

$$\mathbf{f} = -\frac{\partial\Omega}{\partial\mathbf{r}} + \mathbf{f}_c \quad , \quad \ell = (-\frac{\partial\Omega}{\partial\phi} + \ell_c) \quad . \qquad (53)$$

With the foregoing definitions of the various field quantities and with reference to the present configuration, the conservation laws for a restricted theory of a Cosserat surface [different from the restricted and constrained theories discussed previously by Naghdi (1972) and by Green and Naghdi (1974)] are:

$$\frac{d}{dt}\int_P \rho d\sigma = 0 \quad ,$$

$$\frac{d}{dt}\int_P \rho(\mathbf{v} + \bar{k}w\mathbf{b})d\sigma = \int_P \rho\mathbf{f}d\sigma + \int_{\partial P} \mathbf{N}\, ds \quad ,$$

$$\frac{d}{dt}\int_P \rho(\bar{k}\mathbf{v} + kw\mathbf{b})wd\sigma = \mathbf{b}[\int_P (\rho\ell - m)d\sigma + \int_{\partial P} Mds]$$
$$+ \mathbf{b} \times [\int_P (\rho\mathbf{c} - \mathbf{s})d\sigma$$
$$+ \int_{\partial P} \mathbf{S}ds] \quad ,$$

$$\frac{d}{dt}\int_P \rho[\mathbf{r} \times \mathbf{v} + \bar{k}(\mathbf{r} \times w\mathbf{b} + \mathbf{d} \times \dot{\mathbf{v}})]d\sigma$$
$$= \int_P \rho[\mathbf{r} \times \mathbf{f} + \mathbf{d} \times (\mathbf{b} \times \mathbf{c})]d\sigma$$
$$+ \int_{\partial P}[\mathbf{r} \times \mathbf{N} + \mathbf{d} \times (\mathbf{b} \times \mathbf{S})]ds \quad ,$$

$$\frac{d}{dt}\int_P \rho[\varepsilon + \Omega + \tfrac{1}{2}(\mathbf{v} \cdot \mathbf{v} + 2\bar{k}\mathbf{v} \cdot w\mathbf{b} + kw^2)]d\sigma$$
$$= \int_P \rho(r + \mathbf{f}_c \cdot \mathbf{v} + \ell_c w)d\sigma$$
$$+ \int_{\partial P}(\mathbf{N} \cdot \mathbf{v} + Mw - h)ds \quad . \qquad (54)$$

In the above equations $(54)_1$ is a statement of conservation of mass, $(54)_2$ the conservation of linear momentum, $(54)_3$ that of the conservation of the director momentum, $(54)_4$ the conservation of moment of momentum and $(54)_5$ represents the conservation of energy. It should be noted that the quantities, M and ℓ make no contributions to the moment of momentum equation, and the quantities, $\mathbf{c}$ and $\mathbf{S}$, make no contribution to the equation for conservation of energy in the present restricted theory.

Under suitable continuity assumptions, the curve force, $\mathbf{N}$, the director force, $\mathbf{M}$, and the heat flux, h, can be expressed as

$$\mathbf{N} = \mathbf{N}^\alpha\nu_\alpha \quad ,$$

$$M = M^\alpha\nu_\alpha \quad , \quad \mathbf{S} = \mathbf{S}^\alpha\nu_\alpha \quad , \quad \mathbf{S}^\alpha \cdot \mathbf{b} = 0 \quad ,$$

$$h = q^\alpha\nu_\alpha \quad , \quad q^\alpha = \mathbf{q} \cdot \mathbf{a}^\alpha \quad , \qquad (55)$$

where $\mathbf{q}$ is the heat flux vector and the fields, $\mathbf{N}^\alpha$, $\mathbf{S}^\alpha, M^\alpha, q^\alpha$, are functions of θ^γ,t. The five conservation equations in (54) then yield the local equations‡

$$\rho a^{\frac{1}{2}} = \gamma(\theta^\gamma) \quad , \qquad (56)$$

$$(a^{\frac{1}{2}}\mathbf{N}^\alpha)_{,\alpha} + \gamma\mathbf{f} = \gamma(\dot{\mathbf{v}} + \bar{k}\dot{w}\mathbf{b}) \quad . \qquad (57)$$

$$(a^{\frac{1}{2}}M^\alpha)_{,\alpha} + \gamma\ell = ma^{\frac{1}{2}} + \gamma(\bar{k}\dot{\mathbf{v}} \cdot \mathbf{b} + k\dot{w}) \quad ,$$

$$(a^{\frac{1}{2}}\mathbf{S}^\alpha)_{,\alpha} + \gamma\mathbf{c} = a^{\frac{1}{2}}\mathbf{s} - \mathbf{b} \times \gamma\bar{k}\dot{\mathbf{v}} \quad , \qquad (58)$$

$$\mathbf{a}_\alpha \times \mathbf{N}^\alpha + \mathbf{d} \times (\mathbf{b} \times \mathbf{s}) + \mathbf{d}_{,\alpha} \times (\mathbf{b} \times \mathbf{S}^\alpha) = \mathbf{0} \quad , (59)$$

$$\rho r - \text{div}_s\, \mathbf{q} - \rho\dot{\varepsilon} + \mathbf{N}^\alpha \cdot \mathbf{v}_{,\alpha} + mw + M^\alpha w_{,\alpha} = 0 \quad , (60)$$

where "div_s" is the surface divergence operator defined by $\text{div}_s\, \mathbf{q} = \mathbf{q}_{,\alpha} \cdot \mathbf{a}^\alpha$ and a comma denotes partial differentiation with respect to the surface coordinates, θ^γ. It should be noted that the vector fields, $\mathbf{S}^\alpha$ and $\mathbf{s}$, are workless and do not contribute to the reduced energy equation (60).

The above results include (60), which is derived from $(54)_5$. For the purely mechanical theory in which the law of conservation of energy is excluded, the appropriate conservation laws are the first four of (54). In the context of the purely mechanical theory, it is worth recalling that the rate of work by all contact and assigned forces acting on P and on its boundary, ∂P, minus the rate of increase of the kinetic energy in P can be reduced to [see Naghdi (1972,1974)]:

$$\int_P \rho(\mathbf{f} \cdot \mathbf{v} + \ell \cdot w)d\sigma + \int_{\partial P}(\mathbf{N} \cdot \mathbf{v} + M \cdot w)ds$$
$$- \frac{d}{dt}\int_P \tfrac{1}{2}(\mathbf{v} \cdot \mathbf{v} + 2\bar{k}\mathbf{v} \cdot \mathbf{w} + kw^2)d\sigma = \int_P Pd\sigma \quad , (61)$$

where

$$P = \mathbf{N}^\alpha \cdot \mathbf{v}_{,\alpha} + mw + M^\alpha w_{,\alpha}$$

is the mechanical power.

Before closing this section, we also note that the restriction imposed on the motion of the medium by the condition of incompressibility, in the context of the restricted theory under discussion, reduces to§

---

‡In line with a remark made at the end of the previous section, we note that equations (56)-(60) can also be derived by suitable integration across the thickness of the sheet, respectively, from the three-dimensional equations $(9)_{1,2,3}$ and the three-dimensional energy equation.

§In general, there are two conditions of incompressibility in the theory of incompressible directed fluid sheets; for a discussion of these, see Naghdi (1974, Section 3). In our present discussion, since $\mathbf{d}$ is assumed to have the form $(51)_1$, the second condition is satisfied identically and the corresponding pressure (arising from the constraint response) is a part of the response functions for $\mathbf{S}^\alpha$ and $\mathbf{s}$. The specification (62) is motivated from an examination of the incompressibility condition in the three-dimensional theory when the position vector is approximated by (21).

$$\frac{d}{dt}\,[\mathbf{a}_1\mathbf{a}_2\mathbf{d}] = 0 \qquad (62)$$

and can alternatively be expressed in the form

$$[(\mathbf{d}\cdot\mathbf{a}_3)\mathbf{a}^\alpha - (\mathbf{d}\cdot\mathbf{a}^\alpha)\mathbf{a}_3]\cdot\mathbf{v}_{,\alpha} + \mathbf{a}_3\cdot\mathbf{w} = 0 \quad .(63)$$

For an incompressible inviscid fluid sheet, which models the properties of the three-dimensional inviscid fluid at constant temperature, we introduce the constitutive assumption that $\mathbf{N}^\alpha, m, \mathbf{M}^\alpha$ do not depend explicitly on the kinematical quantities, $\mathbf{v}_{,\alpha}$, $\mathbf{w}, \mathbf{w}_{,\alpha}$, and are furthermore workless, i.e.,

$$\mathbf{N}^\alpha\cdot\mathbf{v}_{,\alpha} + mw + \mathbf{M}^\alpha\mathbf{w}_{,\alpha} = 0 \quad , \qquad (64)$$

provided $\mathbf{v}_{,\alpha}$ and $\mathbf{w}$ satisfy the constraint condition (63). With the use of (51), it can then be shown that [see Green and Naghdi (1976, 1977)]

$$\mathbf{N}^\alpha = -\,p_o'\{(\mathbf{d}\cdot\mathbf{a}_3)\mathbf{a}^\alpha = (\mathbf{d}\cdot\mathbf{a}^\alpha)\mathbf{a}_3\}$$

$$= -\,p_o'\,\varepsilon^{\alpha\beta}\phi\mathbf{a}_\beta\times\mathbf{b} \quad ,$$

$$m = -\,p_o'\mathbf{a}_3\cdot\mathbf{b} \quad , \quad M^\alpha = 0 \quad , \qquad (65)$$

where p_o' is an arbitrary scalar function of θ^γ, t and $\varepsilon^{\alpha\beta}$ is the alternating tensor in 2-space. With the help of the energy equation (60) and the fact that the mechanical power vanishes identically for an incompressible inviscid fluid at constant temperature, it can be shown that [see the appendix of Green and Naghdi (1976)]

$$q^\alpha = 0 \quad , \quad \dot{\varepsilon} = 0 \quad , \quad r = 0 \quad .$$

7. WATER WAVES OF VARIABLE DEPTH

Within the scope of the restricted theory of the previous section, we include here an outline of a derivation of a system of nonlinear differential equations governing the two-dimensional motion of incompressible fluids for propagation of fairly long waves in a stream of water of variable initial depth. Our developments include the effects of gravity and surface tension but we assume that the mass density of the fluid does not vary with depth. However, a more general derivation for a nonhomogeneous inviscid fluid in which the mass density is allowed to vary with depth is given by Green and Naghdi (1977). Let $\mathbf{e}_1, \mathbf{e}_2, \mathbf{e}_3$ be a set of right-handed constant orthonormal base vectors associated with rectangular Cartesian axes and choose the unit vector, $\mathbf{b}$, to coincide with $\mathbf{e}_3$. Then, the position vector, $\mathbf{r}$, in $(46)_1$ and the director, $\mathbf{d}$, in $(51)_1$ can be represented as

$$\mathbf{r} = x\mathbf{e}_1 + y\mathbf{e}_2 + \psi\mathbf{e}_3 \quad , \quad \mathbf{d} = \phi\mathbf{e}_3 \quad , \qquad (66)$$

where x, y, ψ, ϕ are functions of θ^1, θ^2, t. The velocity, $\mathbf{v}$, and the director velocity now take the forms

$$\mathbf{v} = u\mathbf{e}_1 + v\mathbf{e}_2 + \lambda\mathbf{e}_3 \quad , \quad \mathbf{w} = w\mathbf{e}_3 \quad , \qquad (67)$$

where

$$u = \dot{x} \quad , \quad v = \dot{y} \quad , \quad \lambda = \dot{\psi} \quad , \quad w = \dot{\phi} \qquad (68)$$

and we note that the velocity components, u, v, λ, w, may be regarded as functions of either θ^1, θ^2, t or of x, y, t. From (67) follow the expressions

$$\dot{\mathbf{v}} = \dot{u}\mathbf{e}_1 + \dot{v}\mathbf{e}_2 + \dot{\lambda}\mathbf{e}_3 \quad , \quad \dot{\mathbf{w}} = \dot{w}\mathbf{e}_3 \qquad (69)$$

and

$$\dot{u} = u_t + uu_x + vu_y \quad , \quad \dot{v} = v_t + uv_x \;\; vv_y \quad ,$$

$$\dot{\lambda} = \lambda_t + u\lambda_x + v\lambda_y \quad , \quad \dot{w} - w_t + uw_x + vw_y \quad ,(70)$$

where the subscripts, x, y, t, designate partial differentiation with respect to x, y, t, when u, v, λ, w are regarded as functions of x, y, t. With the use of (67) and (70), the incompressibility condition (64) assumes the simpler form

$$\phi(u_x + v_y) + w = 0 \quad . \qquad (71)$$

In order to complete our development, we need to specify values for the assigned force, $\mathbf{f}$, and the assigned director force, $\boldsymbol{\ell}$, and to identify the coefficients, $\gamma, \bar{k}$ and k, which, in general, require constitutive equations. For this purpose we consider the corresponding fluid sheet in the three-dimensional theory in which an incompressible homogeneous fluid under gravity[‖], $-g^*\mathbf{e}_3$, flows over a bed specified by the position vector

$$\mathbf{r}^* = x\mathbf{e}_1 + y\mathbf{e}_2 + \alpha(x,y)\mathbf{e}_3 \qquad (72)$$

and we specify the surface of the fluid by

$$\mathbf{r}^* = x\mathbf{e}_1 + y\mathbf{e}_2 + \beta(x,y,t)\mathbf{e}_3 \quad . \qquad (73)$$

In (72), α is a given function of x, y but β in (73) depends on x, y, t. At the surface (73) of the stream there is constant pressure, p_o, a constant normal surface tension, T. At the bed the (unknown) pressure, $\bar{p}$, depends on x, y and t. Thus, the normal pressure, p^*, at the top surface (73) is

$$p^* = p_o - q \quad ,$$

$$q = \frac{T\{(1+\beta_y^2)\beta_{xx} - 2\beta_x\beta_y\beta_{xy} + (1+\beta_x^2)\beta_{yy}\}}{(1+\beta_x^2+\beta_y^2)^{3/2}} \quad . \qquad (74)$$

At the bed (72) the normal velocity of the fluid is zero and the pressure, p^* takes the value

$$p^* = \bar{p}(x,y,t) \quad , \qquad (75)$$

where $\bar{p}$ is to be determined.

To proceed further, we recall the notation in (3), let the surface, $\xi = 0$, defined by (15) coincide with the surface, $\mathscr{S}$, and consider the three-dimensional region of space between the surfaces (72) and (73) occupied by the fluid. Any point in this three-dimensional region is then specified by

---

[‖] We use g^* (instead of g) for gravity, since the letter, g, is used for a different quantity in (3), (5) and elsewhere in the paper.

$$\underset{\sim}{r}^{*} = \underset{\sim}{r} + \theta^3\phi\underset{\sim}{e}_3 = x_1\underset{\sim}{e}_1 + y\underset{\sim}{e}_2 + (\psi + \theta^3\phi)\underset{\sim}{e}_3 \quad , \qquad (76)^{**}$$

where the surfaces, α and β, in (26) or (72) and (73) correspond to $\theta^3 = \xi_1$, $\theta^3 = \xi_2$, respectively. Also, x,y,ψ and ϕ in (76) are functions of θ^1,θ^2 and t and

$$\alpha = \psi + \xi_1\phi \quad , \quad \beta = \psi + \xi_2\phi \quad . \qquad (77)$$

Next, in order to obtain explicit values of $\gamma,\bar{k},k,\underset{\sim}{f}$ and ℓ in relation to the top and bottom surfaces of the fluid, we choose the surface, $\theta^3 = 0$, so that the center of mass of the three-dimensional fluid region under consideration always lies on this surface and we then identify this surface with the surface, $\mathcal{S}$, in the theory of Cosserat surface. Without loss in generality, we may choose $\xi_1 = -\tfrac{1}{2}$, $\xi_2 = +\tfrac{1}{2}$ (see Figure 2). This leads to the identification:

$$\gamma = \rho a^{\frac{1}{2}} = \int_{-\frac{1}{2}}^{\frac{1}{2}} \rho^{*} g^{\frac{1}{2}} d\theta^3 = \rho^{*}\phi \, \frac{\partial(x,y)}{\partial(\theta^1,\theta^2)} \quad ,$$

$$\bar{k} = \int_{-\frac{1}{2}}^{\frac{1}{2}} \rho^{*} g^{\frac{1}{2}} \theta^3 d\theta^3 = 0 \quad ,$$

$$\gamma k = \int_{-\frac{1}{2}}^{\frac{1}{2}} \rho^{*} g^{\frac{1}{2}} (\theta^3)^2 d\theta^2 = \frac{\overset{*}{\rho}}{12}\phi \, \frac{\partial(x,y)}{\partial(\theta^1,\theta^2)} \qquad (78)$$

where p^{*} is the three-dimensional mass density in (9) and the determinant g defined by $(3)_3$ is calculated from the approximation (21) so that

$$g^{\frac{1}{2}} = \phi \, \frac{\partial(x,y)}{\partial(\theta^1,\theta^2)} \quad . \qquad (79)$$

Substitution of (78) and the appropriate expressions for $\underset{\sim}{f}$ and $\underset{\sim}{\ell}$ into (57) to (59) results in the diferential equations of motion

$$\overset{*}{\rho}\phi\dot{u} = -p_x + (p_o - q)\beta_x = \bar{p}\alpha_x \quad ,$$

$$\rho^{*}\phi\dot{v} = -p_y + (p_o - q)\beta_y - \bar{p}\alpha_y \quad ,$$

$$\overset{*}{\rho}\phi\dot{\lambda} = q - p_o + \bar{p} - \rho^{*}g^{*}\phi \quad ,$$

$$\frac{1}{12}\,\rho^{*}\phi\dot{w} = \tfrac{1}{2}(q - p_o) - \tfrac{1}{2}\,\bar{p} + \frac{p}{\phi} \quad , \qquad (80)$$

where

$$p = p_o'\phi \quad . \qquad (81)$$

Moreover, since the bed of the stream is stationary, from (77) and $(70)_{3,4}$ we have

$$\dot{\alpha} = u\alpha_x + v\alpha_y = \dot{\psi} - \tfrac{1}{2}\,\dot{\phi} = \lambda - \tfrac{1}{2}\,w \quad . \qquad (82)$$

The above system of equations is independent of the remaining equations (58) which involve $\underset{\sim}{S}^{\alpha},\underset{\sim}{s}$. The fields, $\underset{\sim}{S}^{\alpha},\underset{\sim}{s}$, correspond to appropriate constraint responses for the restricted motion (51).

The questions of continuous dependence upon the initial data and uniqueness for solutions of initial boundary-value problems for a class of symmetric flows characterized by a special case of the system of nonlinear partial differential equations given by Green et al. (1974c) has been discussed by Green and Naghdi (1975). A similar procedure may be used to establish uniqueness for the more general system of equations (80).

For later reference, we consider here the reduction of the system of nonlinear differential equations (71) and (80) for unidirectional flow in the absence of surface tension, T. Without loss in generality, we set the ambient pressure, $p_o = 0$, and consider flows in the x-direction only. Then, with q = 0, from (71) and (80) we obtain

$$\phi_t + (\phi u)_x = 0 \quad ,$$

$$\rho^{*}\phi\dot{u} = -p_x - \bar{p}\alpha_x \quad ,$$

$$\overset{*}{\rho}\phi\dot{\lambda} = \bar{p} - \rho^{*}g^{*}\phi \quad ,$$

$$\frac{1}{12}\,\overset{*}{\rho}\phi\dot{w} = -\tfrac{1}{2}\,\bar{p} + \frac{p}{\phi} \quad . \qquad (83)$$

We may solve $(83)_{3,4}$ for $\bar{p}$ and p and obtain the expressions

$$\bar{p} = \overset{*}{\rho}\phi(\overset{*}{g} + \dot{\lambda}) \quad ,$$

$$p = \tfrac{1}{2}\,\overset{*}{\rho}\phi^2(g + \dot{\lambda} + \frac{1}{6}\,\dot{w}) \quad . \qquad (84)$$

Introduction of $(84)_{1,2}$ into $(83)_{1,2}$ yields a system of two partial differential equations in u and w but we do not record these here. A further simplification of these equations results for a horizontal bed. For a horizontal bottom α may be taken to be zero and $(77)_{1,2}$ and $(68)_{3,4}$ reduce to

$$\alpha = 0 \quad , \quad \beta = \phi \quad , \quad \psi = \tfrac{1}{2}\,\phi \quad , \quad \lambda = \tfrac{1}{2}\,w \quad . \qquad (85)$$

8. FURTHER REMARKS

The system of nonlinear differential equations (71) and $(80)_{1,2,3,4}$, which include the effects of gravity and surface tension, govern the two-dimensional motion of incompressible inviscid fluids for the propagation of fairly long waves in a stream of variable initial depth. They are derived here by a direct approach as consequences of the conservation laws (54) subject to the incompressibility condition (64). Upon specialization to unidirectional flow, the nonlinear differential equations (71) and (80) reduce to those for inviscid fluids over a bottom of variable initial depth given by Green and Naghdi (1976a, Sections 5-6), while the equations for two-dimensional flow over a horizontal bottom were derived earlier [Green et al. (1974c)].

The differential equations governing the motion of a viscous fluid sheet are discussed briefly by Green and Naghdi (1976a, Section 11) and a similar development can be given within the framework of the restricted theory of Section 6, but we do not consider this aspect of the subject here. The system of differential equations obtained in Section 6 is

---

[**] In (76) to (78), we have returned to the notation θ^3 instead of ξ introduced in (2).

valid for incompressible, inviscid, and homogeneous fluids. A more general derivation for propagation of fairly long waves in a nonhomogeneous stream of variable initial depth in which the mass density is allowed to vary with depth is contained in a recent paper of Green and Naghdi (1977).

In the case of incompressible inviscid fluid sheets, the nonlinear equations for wave propagation in water of variable depth can also be derived from the three-dimensional theory: the procedure involves the use of the (three-dimensional) equation for conservation of energy, the incompressibility condition, invariance requirements under superposed rigid body motions, along with a single approximation (21) for the position vector. Then, by (6) and (21), the approximation for the (three-dimensional) velocity field is given by

$$\underset{\sim}{v}^* = \underset{\sim}{v} + \theta^3 \underset{\sim}{w} \quad , \qquad (86)$$

where $\underset{\sim}{v}$ and $\underset{\sim}{w}$ in (86) have the same forms as those in (67). A derivation of this kind has been carried out by Green and Naghdi (1976b). It is important, however, to note that this derivation is limited to incompressible inviscid fluids which do not require constitutive equations.[††]

It is natural to ask what are the relationship and advantages (if any) between the above system of equations and those which are currently employed by other investigators. To provide a ready comparison, we list below from Whitham (1974) alternative forms of equations for water waves moving in the direction of a fixed x-axis for a stream of initial constant depth, h. Let the elevation of the stream be $h + \eta$. Then, for unidirectional flow and in terms of η and the horizontal velocity, u, we recall from Whitham (1974, pp. 460-463) the system of equations

$$\eta t + \{u(h + \eta)\}_x = 0 \quad ,$$

$$u_t + uu_x + g^*\eta_x + \frac{1}{3} c^2 h\eta_{xxx} = 0 \quad , \qquad (87)$$

and the pair of equations attributed to Boussinesq, namely

$$\dot{\eta} + (h + \eta)u_x = 0 \quad ,$$

$$\dot{u} + g^*\eta_x + \frac{1}{3} h\eta_{xtt} = 0 \quad , \qquad (88)$$

where the notations in (87) and (88) are the same as those in (70), g^* is the acceleration due to gravity introduced in Section 7 and $c^2 = g^*h$. Both systems of equations (87) and (88) allow for wave propagation in either direction along the x-axis. For waves moving along the positive x-direction only there is the Korteweg-deVries (1895) equation--hereafter referred to as the K.dV. equation--i.e.,

$$\eta_t + c(1 + \frac{3}{2}\,\frac{\eta}{h})\eta_x + \frac{1}{6} ch^2\eta_{xxx} = 0 \qquad (89)$$

or an equation due to Benjamin et al. (1972) given by

$$\eta_t + c(1 + \frac{3}{2}\,\frac{\eta}{h})\eta_x - \frac{1}{6} ch^2\eta_{xxt} = 0 \quad . \qquad (90)$$

As already remarked by Green and Naghdi (1977), it may immediately be verified that the set of equations (88) and (90) only have *steady state* solutions if η and u are both constants. Also, although the K.dV. Eq. (89) admits a solitary wave in which the velocity at infinity is zero and the stream there is at its undisturbed height, h, it does *not* admit a steady state solution with u constant and $\eta = 0$ at infinity. This fact is related to another property of (89) which is also shared by (88) and (90): the three sets of equations (88) to (90) are not invariant in form under a *constant* superposed rigid body motion of the whole fluid. To see this, suppose that a constant superposed rigid body translational velocity is imposed on the whole fluid so that the particles at the place, x, are displaced to x^+ at time, t^+, specified by

$$x^+ = x + at \quad , \quad t^+ = t + \bar{a} \quad , \qquad (91)$$

where a and $\bar{a}$ are constants. The variables that occur in the differential equations (87)-(90) are $\eta = \eta(x,t)$ and $u = u(x,t)$. Let $\eta^+ = \eta^+(x^+,t^+)$ and $u^+ = u^+(x^+,t^+)$ be the corresponding scalar quantities defined over the region of space occupied by the fluid after the imposition of the superposed rigid body motion $(91)_1$. Then, from $(68)_1$ and (8.6) we obtain

$$u(x,t) = u^+(x^+,t^+) - a$$

$$= u^+(x + at,\, t + \bar{a}) - a \quad . \qquad (92)$$

We expect the elevation, $h + \eta$, of the fluid to remain unaltered by superposed rigid body motions; and, since h remains unaltered also, this leads us to require that

$$\eta(x,t) = \eta^+(x^+,t^+) = \eta^+(x + at,\, t + \bar{a}) \quad . \qquad (93)$$

From (92) and (93), we calculate expressions of the type

$$\eta_t = \eta^+_{t^+} + a\eta^+_{x^+} \quad , \quad \eta_x = \eta^+_{x^+} \quad ,$$

$$\eta_{xtt} = \eta^+_{x^+t^+t^+} + 2a\eta^+_{x^+x^+t^+} + a^2\eta^+_{x^+x^+x^+} \quad ,$$

$$\dot{\eta} = \eta_t + u\eta_x = \eta^+_t + u^+\eta^+_{x^+} = \dot{\eta}^+ \quad , \qquad (94)$$

with similar results for u_t, u_x and $\dot{u}$ in terms of u^+ and their derivatives. It was noted by Green and Naghdi (1977) that if the independent variables, x, t, in (88) to (90) are changed to (91), the equations for u, η in terms of x^+, t^+ are different from those in terms of x,t and this was illustrated explicitly with reference to the K.dV. equation (89). Here, we consider the pair of equations $(88)_{1,2}$. After substituting (92)-(94), they become

---

[††] Recall that in the three-dimensional theory of incompressible inviscid fluids the stress vector is specified in terms of a pressure which is determined by the equations of motion and the boundary conditions.

$$\dot{\eta}^+ + (h+\eta^+)u^+_{x^+} = 0 \ ,$$

$$\dot{u}^+ + g^{*}\eta^+_{x^+} + \frac{1}{3} h\eta^+_{x^+t^+t^+}$$

$$= -2a\eta^+_{x^+x^+t^+} - a^2\eta^+_{x^+x^+x^+} \ . \qquad (95)$$

The first of (95) is of the same form as $(88)_1$ and hence invariant but clearly the second of (95) differs from $(88)_2$. This means that the character of the solutions of (88), (89) and (90) is substantially altered by superposing a *constant* rigid body translational velocity on the fluid, which is contrary to what happens if we use the full three-dimensional equations of motion for an inviscid fluid. On the other hand, the set of equations (87) is not subject to this drawback, and the equations do have useful steady state solutions. It may be argued that because of the nature of the approximation in obtaining (88) to (90) from the three-dimensional theory we should not expect these equations to be invariant under a superposed constant translational velocity, but this then leaves in doubt which version of any of the sets (88) to (90) are to be chosen as basic. The difficulty disappears if we linearize any of the above sets since the resulting equations are then invariant under a *small* superposed constant translational velocity, as we would expect.

From the above discussion, it might appear that the equations (87) may be preferable to any of (88) to (90), but arguments are put forward by Whitham (1974, p.462) to suggest that the system (88) is to be preferred to (87). Although considerable use has been made of some of the equations (87) to (90), it would seem that they all rest on a somewhat shaky physical foundation. By contrast, the system of equations (71) and (80) do not possess the undesirable features of the type noted above: they are properly invariant under superposed rigid body motions, admit general steady state solutions, and are free from anomalies mentioned earlier.

For the purpose of providing a more explicit comparison with the system of equations (87) to (90), we specialize the system of equations (83) to that for a horizontal bottom for which $(85)_{1,2,3,4}$ hold. Then, denoting again the elevation of the stream by $h + \eta$, the differential equations $(83)_{1,2}$ can be recorded in the form

$$\dot{\eta} + (h+\eta)u_x = 0 \ ,$$

$$\dot{u} + g^{*}\eta_x + \frac{1}{3} h\eta_{xtt} = R \ , \qquad (96)$$

where

$$R = -\frac{1}{3}\eta\eta_{xtt} - \frac{2}{3}\phi_x\phi_{tt}$$

$$-\frac{1}{3}\frac{1}{\phi}\left[\phi^2(2u\phi_{xt} + u^2\phi_{xx} + u_t\phi_x + uu_x\phi_x)\right]_x \ ,$$

$$\phi = h + \eta \ . \qquad (97)$$

Clearly if R on the right-hand side of $(96)_2$ can be neglected, then $(96)_{1,2}$ reduce to those of Boussinesq given by $(88)_{1,2}$. It should be emphasized, however, that the nonlinear equations $(96)_{1,2}$ are invariant under a constant superposed rigid body translation while $(88)_{1,2}$ are not.[‡‡] Within the scope of the nonlinear theory, it does not seem reasonable to neglect the quantity, R, in $(96)_2$ on the basis of either physical considerations or mathematical arguments. It may be, however, that in some special circumstances the solution of (88) is a good approximation to the solution of (96), but this is a different question than that discussed above. In this connection, it is worth noting that a solution to a system of differential equations, which results from neglecting certain terms in a more general system of equations, in general, will not be the same as a solution obtained by approximation from a corresponding solution of the more general system of equations.

We close this section by calling attention to some available evidence of the relevance and applicability of the direct formulation for fluid sheets. The system of equations (71) and (81), or a special case of it, has already been employed in some detailed studies of a number of two-dimensional problems of inviscid fluid sheets, as well as in some comparisons with known previous solutions on the subject. We mention here some of these studies and refer the reader to the papers cited for additional information: (a) the nonlinear differential equations admit a solitary wave solution [see Green et al. (1974c)] which is the same as that attributed by Lamb (1932, Section 252) to Boussinesq and Rayleigh; (b) this solitary wave solution, as well as appropriate jump conditions and certain results derived from the energy balance for an inviscid fluid sheet at constant temperature [Green and Naghdi (1976a, Appendix)], has been used by Caulk (1976) to discuss the flow of an inviscid incompressible fluid under a sluice gate; (c) the steady motion of a class of two-dimensional flows in a stream of finite depth in which the bed of the stream may change from one constant level to another, and the related problem of hydraulic jumps, both for homogeneous and nonhomogeneous incompressible fluids [Green and Naghdi (1976a, Section 7) and Green and Naghdi (1977)]; and (d) a class of exact solutions [Green and Naghdi (1976a, Section 9)] which characterize the main features of the time-dependent free surface flows in the three-dimensional theory of incompressible inviscid fluids [Longuet-Higgins (1972)].

ACKNOWLEDGMENT

The results reported here were obtained in the course of research supported by the U.S. Office of Naval Research under Contract N00014-76-C-0474, Project NR 062-534, with the University of California, Berkeley.

REFERENCES

Benjamin, T. B., J. L. Bona, and J. M. Mahony (1972). Model equations for nonlinear dispersive systems. *Phil. Trans. Royal Soc. Lond. A272*, 47.

Bogy, D. B. (1978). Use of one-dimensional Cosserat theory to study instability in a viscous liquid jet. *Phys. Fluids 21*, 190.

[‡‡] The difference between the two disappears, of course, upon linearization.

Caulk, D. A. (1976). On the problem of fluid flow under a sluice gate. *Int. J. Engng. Sci. 14*, 1115.

Caulk, D. A., and P. M. Naghdi (1978a). The influence of twist on the motion of straight ellipitcal jets. *Arch. Rational Mech. Anal.* (to appear) = *Report No. UCB/AM-77-5*, Office of Naval Research Contract N00014-76-C-0474, Project NR 062-534 (June 1977), Dept. of Mechanical Engineering, University of Calif., Berkeley.

Caulk, D. A., and P. M. Naghdi (1978b). The onset of breakup in inviscid and viscous jets, *Report No. UCB/AM-78-3*, Office of Naval Research Contract N00014-76-C-0474, Project NR 062-534 (July 1978), Dept. of Mechanical Engineering, University of Calif., Berkeley.

Chandrasekhar, S. (1961). *Hydrodynamic and Hydromagnetic Stability*. Oxford: Clarendon Press.

Cohen, H. (1966). A nonlinear theory of elastic directed curves. *Int. J. Engng. Sci. 4*, 511.

Cohen, H., and C. N. DeSilva (1966). Theory of directed surfaces. *J. Math. Phys. 7*, 960.

Cosserat, E. and F. (1909). *Théorie des corps déformables*. A. Hermann et Fils, Paris; also Theory of deformable bodies [transl. from original 1909 edition], NASA TTF-11, 561, Washington, D.C., 1968.

Duhem, P. (1893). Le potentiel thermodynamic et al pression hydrostatique. *Ann. Ecole Norm. 10*, 3; 187.

Ericksen, J. L., and C. Truesdell (1958). Exact theory of stress and strain in rods and shells. *Arch. Rational Mech. Anal. 1*, 295.

Green, A. E. (1975). Compressible fluid jets. *Arch. Rational Mech. Anal. 59*, 189.

Green, A. E. (1976). On the nonlinear behavior of fluid jets. *Int. J. Engng. Sci. 14*, 49.

Green, A. E. (1977). On the steady motion of jets with elliptical sections. *Acta Mechanica 26*, 171.

Green, A. E., and N. Laws (1966). A general theory of rods. *Proc. Royal Soc. Lond. A293*, 145.

Green, A. E., and N. Laws (1968). Ideal fluid jets, *Int. J. Engng. Sci. 6*, 317.

Green, A. E., and P. M. Naghdi (1974). On the derivation of shell theories by direct approach. *J. Appl. Mech. 41*, 173.

Green, A. E., and P. M. Naghdi (1975). Uniqueness and continuous dependence for water waves. *Acta Mechanica 23*, 297.

Green, A. E., and P. M. Naghdi (1976a). Directed fluid sheets, Proc. *Royal Soc. Lond. A347*, 447.

Green, A. E., and P. M. Naghdi (1976b). A derivation of equations for wave propagation in water of variable depth. *J. Fluid Mech. 78*, 237.

Green, A. E., and P. M. Naghdi (1977). Water waves in a nonhomogeneous incompressible fluid. *J. Appl. Mech. 44*, 523.

Green, A. E., P. M. Naghdi, and W. L. Wainwright (1965). A general theory of a Cosserat surface. *Arch. Rational Mech. Anal. 20*, 287.

Green, A. E., P. M. Naghdi, and M. L. Wenner (1974a). On the theory of rods. I. Derivations from the three-dimensional equations. *Proc. Royal Soc. Lond. A337*, 451.

Green, A. E., P. M. Naghdi, and M. L. Wenner (1974b). On the theory of rods. II. Developments by direct approach. *Proc. Royal Soc. Lond. A337*, 485.

Green, A. E., N. Laws, and P. M. Naghdi (1974c). On the theory of water waves. *Proc. Royal Soc. Lond. A338*, 43.

Korteweg, D. J., and G. deVries (1895). On the change of form of long waves advancing in a rectangular channel, and on a new type of long stationary waves. *Philosophical Magazine (Fifth Ser.) 39*, 422.

Lamb, H. (1932). *Hydrodynamics*, 6th edn. Cambridge University Press.

Longuet-Higgins, M. S. (1972). A class of exact, time-dependent, free surface flows. *J. Fluid Mech. 55*, 529.

Naghdi, P. M. (1972). The theory of shells and plates. S. Flügge's *Handbuch der Physik, VIa/2*, C. Truesdell, ed., Springer-Verlag, Berlin, 425-640.

Naghdi, P. M. (1974). Direct formulation of some two-dimensional theories of mechanics. *Proc. 7th U.S. National Congr. Appl. Mech.*, Amer. Soc. Mechanical Engineers, New York, N.Y., 3-21.

Naghdi, P. M. (1975). On the formulation of contact problems of shells and plates. *J. Elasticity 5*, 379.

Rayleigh, Lord (1879a). On the instability of jets. *Proc. Lond. Math. Soc. 10*, 4.

Rayleigh, Lord (1979b). On the capillary phenomena of jets. *Proc. Royal Soc. Lond. 29*, 71.

Weber, C. (1931). Zum Zerfall eines Flüssigkeitsstrahles, *ZAMM 11*, 136.

Whitham, G. B. (1974). *Linear and Nonlinear Waves*, John Wiley and Sons.

Discussion

G. L. CHAHINE

I would like to congratulate the author on his very fine work and to comment on his conclusion that the Rayleigh-Plesset equation represents fairly well the growth of bubbles attached to a wall. As is well-known, the Rayleigh-Plesset equation relates the growth and collapse of a spherical bubble, without relative motion with respect to the unbounded surrounding fluid, for a given variation of pressure far from it. It then seems really surprising that such an equation could describe so well the growth of the bubble on a blunt nose as shown in Figure 31. None of the requirements for the validity of the Rayleigh-Plesset equation are fulfilled:

a. the bubble is non-spherical, even if we agree that the shape in the figure plan is a portion of a circle,
b. presence of a wall,
c. shear flow around the bubble,
d. relative motion between the bubble and the fluid (as pointed out by the author).

Moreover, the presence of gas inside the bubble is not taken into account, while the gas behavior has been shown to be very important [Chahine (1974, 1976)]. We believe that the good agreement between experimental results and analytical computations shown in this paper is mainly due to:

a. the time of observation is too small compared to the hypothetical lifetime of the bubble. (For a bubble radius of 1.3 mm and an external pressure of 5,000 N/m^2, the Rayleigh time is about 0.7 ms and the lifetime is greater than 1.5 ms; say 10 times the observation time.)
b. in order to integrate numerically the Rayleigh-Plesset equation one needs two initial conditions: an initial radius and an initial growth rate. If R_0 and R_1 replace these initial conditions it is not surprising that the result deduced for R_2 differs only 4% from the experimental result.

Concerning Table 4, the calculated relatively small effect of surface tension and viscosity is in good agreement with previous asymptotic studies [Chahine (1976) and Poritsky (1952)].

REFERENCES

Chahine, G. L., (1974). Etude Asymptotique et Experimentale des Oscillations et du Collapse des Bulles de Cavitation. *ENSTA Report 042, CEDOCAR, MF 50831.*

Chahine, G. L., (1976). Etude Asymptotique du Comportment d'une Bulle de Cavitation dans un Champ de Pression Variable. *Jl. de Mecanique, 15 (2), pp. 287-306.*

Poritsky, H., (1952). The Collapse or Growth of a Spherical Bubble or Cavity in a Viscous Fluid. *Proceeding of the First U.S. National Congress in Applied Mechanics, ASME, pp. 813-821.*

Author's Reply

J. H. J. van der MEULEN

The author appreciates Dr. Chahine's comments and would like to point out that the principal aim of comparing the cavity growth on the blunt nose with theory was to show that the travelling bubble type of cavitation is more related to bubble dynamics than to boundary layer phenomena.

The surprising observation (Figure 31) that the shape of the attached, growing cavity is a spherical segment is, to a certain extent, consistent with the observation by Dr. Chahine (1977) that the growth of the lower part of a bubble below a free surface is not influenced by the presence of the free surface.

It seems most unlikely that the presence of gas originating from a small stream nucleus or from diffusion may have affected the growth of the cavity during the observation period. Oldenziel (1976) has shown that such effects can be neglected for explosive bubble growth.

REFERENCES

Chahine, G. L., (1977). Interaction between an Oscillating Bubble and a Free Surface. *J. Fluids Engng., Trans. ASME, 99, p. 709.*

Oldenziel, D. M., (1976). Gas Transport into a Cavitation Bubble during an Explosion. *LAHR Symp. on Two Phase Flow and Cavitation in Power Generation Systems. Grenoble, France.*

Discussion

R. LATORRE

Our lack of understanding of cavitation noise and its measurement technique is an area of recent concern and the authors' experiments and discussion will hopefully aid other researchers with these problems.

The correlation of cavitation noise and the observed cavitation is a complicated research topic. In my dissertation I am studying tip vortex cavitation noise and as a contribution to the authors' paper, I would like to present some illustrative

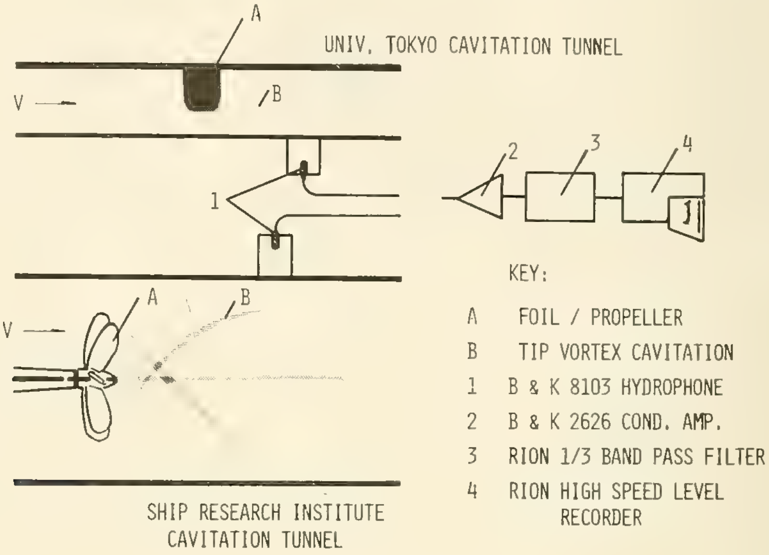
A
UNIV. TOKYO CAVITATION TUNNEL
V
B
1
2
3
4
KEY:
A FOIL / PROPELLER
B TIP VORTEX CAVITATION
1 B & K 8103 HYDROPHONE
2 B & K 2626 COND. AMP.
3 RION 1/3 BAND PASS FILTER
4 RION HIGH SPEED LEVEL RECORDER
V
A
B
SHIP RESEARCH INSTITUTE CAVITATION TUNNEL

FIGURE 1. Tip vortex cavitation noise measurement.

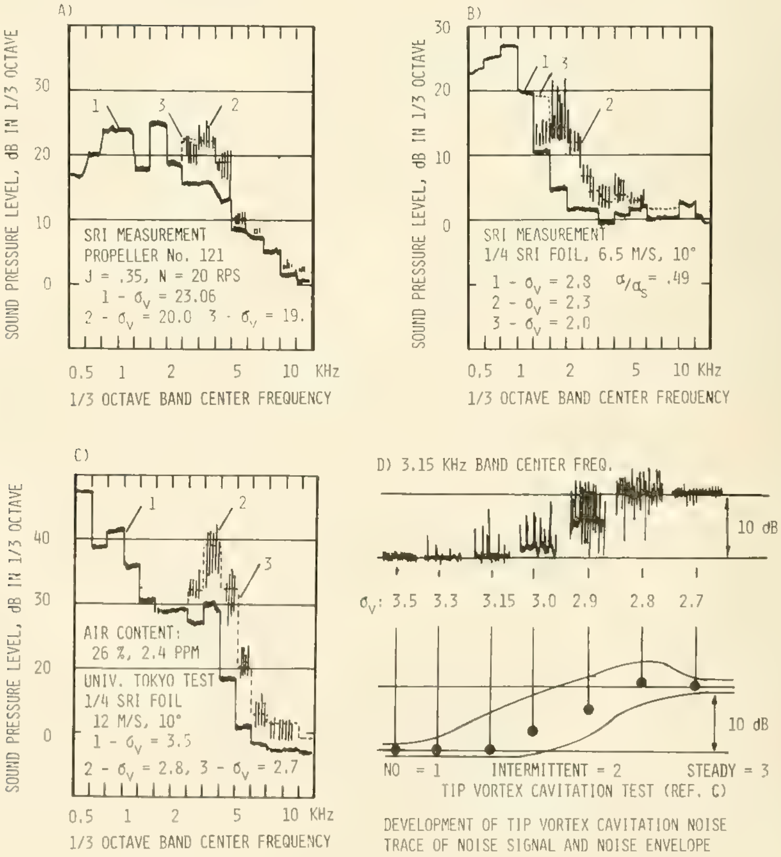

FIGURE 2. Tip vortex cavitation noise measurements of propeller and foil tests comparison of intermittent and steady tip vortex cavitation noise.

noise measurements made at the University of Tokyo's and the Ship Research Institute's (SRI) cavitation tunnel.

Figure 1 shows the measurement apparatus. The hydrophone was set in a 50 mm acrylic cup mounted on the tunnel's observation window and filled with water. The measurements were made in uniform flow at constant speed with the section pressure lowered, using propellers and foils. The propeller was SRI No. 121 (D = 250 mm, z = 6, area ratio = 0.8, constant P/D = 0.75). The foil (1/4 SRI Foil) was a scaled version of Dr. Ukon's (SRI) design using NACA 4412 wing section and a planform of $c(\eta) = c_0(1-\eta^2)^{\frac{1}{4}}$. The 1/4 SRI Foil had an aspect ratio of 3, semi-span = 50 mm, and base chord, c_0 = 40 mm.

The measurements are briefly illustrated in Figures 2, 3, and 4. In Figure 2 the noise spectrum and envelope of tip vortex cavitation noise is shown for SRI and Tokyo University tests. The intermittant tip vortex noise appears as spikes in the spectrum between 2 and 6.3 kHz, as denoted by "2" in this figure. Using the complete test record it is possible to construct the envelope shown in Figure 2D. The shifts in the frequency appear to be a function of both the low pressure vortex core and the condition of the water.

In an attempt to gain an understanding of the noise mechanism, additional experiments were performed. In Figure 3, the intermittant tip vortex noise signal at 6.3 kHz was used to trigger the camera shutter to photograph the intermittant tip vortex cavitation. It appeared that the noise mechanism is due to the pressure wave caused by the filling of the low pressure vortex core by dissolved gases.

To test this hypothesis of the tip vortex cavitation noise mechanism, air was injected from the 1/4 SRI Foil tip and the noise spectrum measured. Figure 4 shows the results of the initial tests illustrating a qualitative agreement in the actual tip vortex cavitation noise spectrum and the simulated tip vortex using air injection. At the time of writing, it has been possible to improve this technique and duplicate the intermittant "spikes" in the noise spectrum.

Thus by the experimental results a basis for understanding the low frequency aspects of tip vortex cavitation noise has become possible.

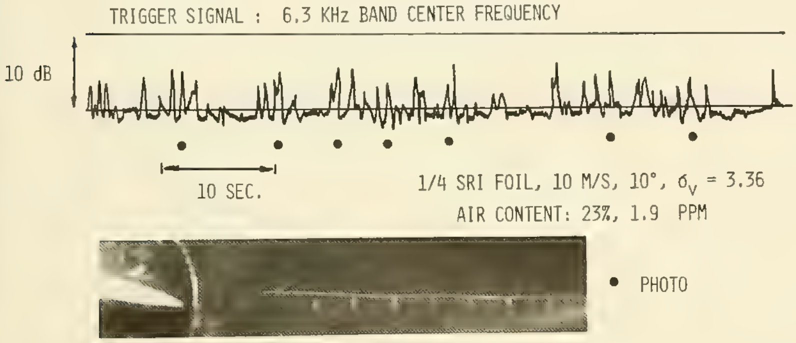

FIGURE 3. Intermittent tip vortex cavitation noise signal and photo.

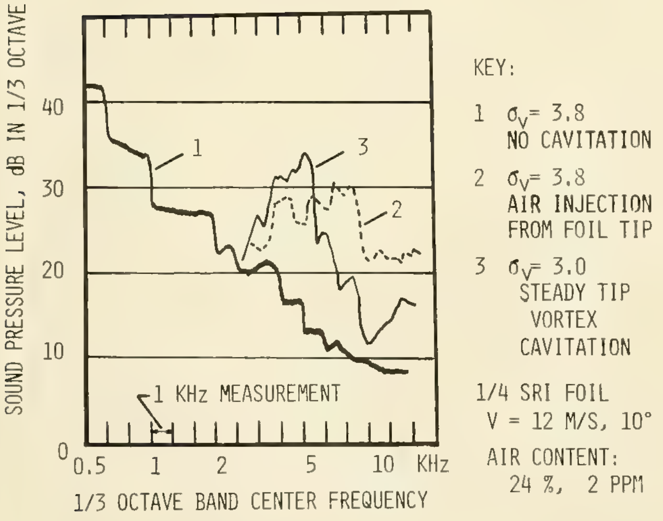

FIGURE 4. Comparison of tip vortex cavitation noise spectrum trace and simulated tip vortex using air injection.

Authors' Reply

GORAN BARK and WILLEM B. van BERLEKOM

It is very interesting to hear of this hypothesis concerning generation of noise by tip vortex cavitation. We have performed experiments with tip vortex cavitation at propellers and hydrofoils and found that intermittant tip vortex cavities were noisiest. However, we have not performed high speed filming or other more advanced attempts to study the real mechanisms involved in the volume fluctuations of the tip vortex cavity. In the case of bubble cavitation and unsteady sheet cavitation, which we have studied in more detail, we are of the opinion that the highest pulses are generated during the final part of a collapse, which often is rather symmetrical, and that filling the cavities with gas is of minor importance as a primary generation mechanism. However, some results indicate that this gas decreases the violence of the collapse.

Session VII

GEOPHYSICAL FLUID DYNAMICS

WALTER H. MUNK
Session Chairman
University of California, San Diego
La Jolla, California

The Boussinesq Regime for waves in a Gradually Varying Channel

John Wilder Miles
University of California
San Diego, California

ABSTRACT

The Boussinesq equations for gravity waves of amplitude $a(x)$ and characteristic length $\ell(x)$ in a gradually varying channel of breath $b(x)$ and depth $d(x)$ are derived from Hamilton's principle on the assumptions that $a/d \equiv \alpha << 1$, $(d/\ell)^2 = O(\alpha)$, $b'(x) = O(\alpha^{3/2} b/d)$ and $d'(x) = O(\alpha^{3/2})$ ($' \equiv d/dx$). The further assumption of unidirectional propagation then leads to the Korteweg-deVries equation for a gradually varying channel. It is shown that the latter equation admits two integral invariants. The second-order (in amplitude) invariant measures energy, as expected, but the first-order invariant measures mass divided by $b^{\frac{1}{2}} d^{\frac{1}{4}}$; accordingly, mass is conserved only if either the first-order invariant vanishes identically or $bd^{\frac{1}{2}}$ is constant, and only the former possibility appears to be consistent with conservation of energy. An approximate solution for a cnoidal wave, which conserves both energy and mass, is developed. The corresponding approximation for a solitary wave (which may be regarded as a limit of a cnoidal wave) does not conserve mass but nevertheless provides an approximation to the evolution of the amplitude, $a \propto b^{-2/3} d^{-1}$, that is in agreement with experiments for gradual decrease of depth or increase of breadth but not for decrease of breadth.

1. INTRODUCTION

The Boussinesq régime for gravity waves of amplitude *a* and characteristic length ℓ in water of depth d is characterized by

$$\alpha = a/d << 1, \quad \beta = (d/\ell)^2 << 1, \quad \beta = O(\alpha), \qquad (1a,b,c)$$

where α and β are measures of nonlinearity and dispersion, respectively, and (1c) refers to the asymptotic limit $\alpha \downarrow 0$. The assumptions of one-dimensional wave motion and uniform depth and the neglect of compressibility and viscosity then imply Boussinesq's equations for the free-surface displacement and the depth-averaged velocity, $\eta(x,t)$ and $u(x,t)$. The further assumption of undirectional propagation permits the elimination of u to obtain the Korteweg-deVries (KdV) equation for η. The classical derivations are given by Whitham (1974, §13.11). An alternative derivation, starting from the Luke-Whitham variational principle and using ξ, the velocity potential at the free surface, and η as dependent variables also has been given by Whitham (1967).

I consider here the generalization of the Boussinesq and KdV equations for a channel of gradually varying breadth and depth $b(x)$ and $d(x)$ and their approximate solution for slowly varying cnoidal and solitary waves. I begin (in Section 2) by deriving (what may be called) the Boussinesq channel equations directly from Hamilton's principle (to which the Luke-Whitham variational principle is equivalent in the present context) on the basis of (1) and the further assumptions (which imply *gradually varying*)

$$b'(x) = O(\alpha^{3/2} b/d), \quad d'(x) = O(\alpha^{3/2}) \qquad (2a,b)$$

I then (in Section 3) invoke the hypothesis of unidirectional propagation to obtain the KdV channel equation, which was developed originally by Shuto (1974) through a rather more involved procedure. I then go on to consider cnoidal waves in Section 4 and the solitary wave in Section 5 on the basis of the stronger assumptions

$$|b'| << \alpha^{3/2}(b/d), \quad |d'| << \alpha^{3/2} \qquad (3a,b)$$

A prominent feature of the KdV equation for a uniform channel is the existence of an infinite number of integral invariants (Whitham, 1974, §17.6). The KdV equation for a slowly varying channel admits only two such invariants, of first and second order in the amplitude; the latter measures energy, as expected, but the former measures mass only if $bd^{\frac{1}{2}} = \text{constant}$. This deficiency is presumably a consequence of the implicit neglect of the weak reflection that accompanies the gradual variation of the channel: the reflection coefficient for energy is second order in some appropriate measure of the channel variation and therefore has no cumulative effect, whereas that for mass is first order and does have a cumulative effect. The resulting difficulty may be avoided for a wave that is either periodic or of compact support simply by choosing a horizontal reference plane such that the mean value of the free-surface displacement vanishes identically (see Section 4), but the problem is more subtle for an aperiodic disturbance of unlimited extent such as a solitary wave (see Section 5) and remains unresolved.

The primary goal, at least for practical applications, of the analysis of waves in a gradually varying channel is the prediction of *a* as a function of b and d. Green's law, which neglects both nonlinearity and dispersion, predicts [Lamb (1932, §185)]

$$a \propto b^{-\frac{1}{2}} d^{-\frac{1}{4}} . \tag{4}$$

It is often used for practical shoaling calculations, and Shuto (1973) finds that $a \propto d^{-\frac{1}{4}}$ holds for solitary waves on relatively steep slopes for a/d as large as 2. On the other hand, the joint assumptions of Boussinesq similarity ($a/d \propto d^2/\ell^2$) and conservation of energy (which is proportional to $a^2 b\ell$) imply [Miles (1977a)]

$$a \propto b^{-2/3} d^{-1} . \tag{5}$$

Comparison with experiment (see Section 5) suggests that (5) should be valid for a shoaling or laterally diverging channel if $|\delta| < 0.1$, where

$$\delta = (3\alpha)^{-3/2}[2d(b'/b) + 9d'] , \tag{6}$$

but perhaps not for a laterally converging channel.

The present results also have implications for the approximate treatment of nonlinear wave propagation along the lines initiated by Whitham (1974, Ch. 8) in his treatment of shock-wave propagation and since applied to solitary waves [Miles (1977a)].

2. BOUSSINESQ CHANNEL EQUATIONS

The boundary-value problem for gravity waves in an ideal, homogeneous liquid may be deduced from Hamilton's principle in the form [Broer (1974), Miles (1977b)]

$$\delta\iint L\{\xi,\eta\}d\underset{\sim}{x}dt = 0, \quad L = \xi\eta_t - \frac{1}{2}\int_{d}^{\eta}(\nabla\phi)^2 dy - \frac{1}{2}g\eta^2, \tag{7a,b}$$

where $\underset{\sim}{x}$ and y are horizontal and vertical coordinates; $\delta(\underset{\sim}{x},t)$ and $\eta(\underset{\sim}{x},t)$ are the velocity potential at, and the displacement of, the free surface; $d\underset{\sim}{x}$ is an element of area in the $\underset{\sim}{x}$ space; $d(\underset{\sim}{x})$ is the quiescent depth; and the velocity potential $\phi(\underset{\sim}{x},y,t)$ is determined by

$$\nabla^2\phi = 0 \quad (-d < y < \eta) , \tag{8}$$

$$\phi_y + \nabla d\cdot\nabla\phi = 0 \quad (y = -d), \quad \phi = \xi \quad (y = \eta) . \tag{9a,b}$$

The solution of (8) and (9) is given by

$$\phi = \xi - y\nabla\cdot(d\nabla\xi) - \frac{1}{2}y^2\nabla^2\xi + O(\beta^2\xi) \tag{10}$$

where β is defined by (1b) with d and ℓ as scales of y and $\underset{\sim}{x}$. The corresponding approximation to the kinetic energy integral, after invoking $\eta = O(\alpha d)$, $d\nabla\xi = O(\beta^{\frac{1}{2}}\xi)$, $\beta = O(\alpha)$, (2), and $\nabla\cdot(A\nabla B) = \nabla A\cdot\nabla B + A\nabla^2 B$, is

$$\int_{-d}^{\eta}(\nabla\phi)^2 dy = (d+\eta)(\nabla\xi)^2 - \frac{1}{3}d^3(\nabla^2\xi)^2 + \frac{2}{3}\nabla\cdot[d^3(\nabla^2\xi)\nabla\xi] + O(\alpha^3 d^{-1}\xi^2) . \tag{11}$$

Substituting (11) into (7), invoking the further approximation that φ is independent of the transverse coordinate in a channel of slowly varying breadth b(x) and depth d(x), and integrating across the channel, we obtain

$$\delta\iint\left[\xi\eta_t - \frac{1}{2}(d+\eta)\xi_x^2 + \frac{1}{6}d^3\xi_{xx}^2 - \frac{1}{2}g\eta^2\right]bdxdt = 0. \tag{12}$$

The corresponding Euler-Lagrange equations,

$$\frac{1}{3}(bd^3\xi_{xx})_{xx} + [b(d+\eta)\xi_x]_x + b\eta_t = 0 \tag{13a}$$

and

$$\xi_t + \frac{1}{2}\xi_x^2 + g\eta = 0, \tag{13b}$$

are counterparts of the Boussinesq equations [cf. Whitham (1967)].

It is worth noting that the approximations to this point are consistent with conservation of both mass and energy:

$$\partial_t\int\eta bdx = 0, \quad \partial_t\int\left[\frac{1}{2}(d+\eta)\xi_x^2 - \frac{1}{6}d^3\xi_{xx}^2 + \frac{1}{2}g\eta^2\right]bdx = 0, \tag{14a,b}$$

where the integrals are over either (-∞,∞) or a periodic interval. The integral (14a) follows directly from the integration of (13a) with respect to x, subject to appropriate null or periodicity conditions at the end points. The integral (14b) may be similarly established or may be inferred (through Noether's theorem) from the invariance of the Lagrangian density in (12) under a translation of t; it is an exact invariant of (13), but it would be consistent with the antecedent approximations to approximate the specific energy in (14b) by $\frac{1}{2}(d\xi_x^2 + g\eta^2)$.

3. KORTEWEG-DEVRIES CHANNEL EQUATION

The Korteweg-deVries (KdV) equation for unidirectional wave propagation in a uniform channel may be deduced from the Boussinesq equations by assuming that ξ and η are slowly varying functions of t in a reference frame moving with the wave speed, c. It is expedient in the present context to choose x, rather than t, as the slow variable (since b and d are prescribed as slowly varying functions of x) and to introduce

$$s = \int\frac{dx}{c(x)} - t \quad (c^2 \equiv gd) \tag{15}$$

as a characteristic variable. The direction of propagation may be reversed by reversing the sign of t in (15).

The reduction of (13) on the hypothesis that $\eta_x = O(\alpha\eta_s)$ yields

$$\frac{1}{3}(d^2/c^3)\eta_{sss} + 3(cd)^{-1}\eta\eta_s + 2\eta_x + (\Lambda bc)\eta = 0, \qquad (16)$$

where

$$\Lambda(\ ) \equiv (d/dx)\log(\ ) \qquad (17)$$

(note that $\Lambda c = \frac{1}{2}\Lambda d$). Equation (16), which appears to have been derived originally by Shuto (1974), reduces to the KdV equation if b and d are constant.

The vertically averaged, horizontal velocity is given by

$$u = (g\eta/c)[1+O(a)], \qquad (18)$$

whilst the vertical velocity is $O(\alpha^{\frac{1}{2}}u)$. The mass, momentum, and energy of the wave therefore are given by

$$M = \rho bc\int_{-\infty}^{\infty}\eta ds,\ \mathcal{M} = \rho bcd\int_{-\infty}^{\infty} u ds = Mc,\ \mathcal{E} = \rho gbc\int_{-\infty}^{\infty}\eta^2 ds, \qquad (19a,b,c)$$

within $1+O(\alpha)$. The limits of integration may be replaced by $\pm\frac{1}{2}T$ for a wave of period T.

Multiplying (16) through by $\frac{1}{2}(bc)^{\frac{1}{2}}$ and $bc\eta$, respectively, and integrating over $-\infty < s < \infty$ on the assumption that η, η_s, and η_{ss} vanish in the limits, we obtain the integral invariants

$$I = (bc)^{\frac{1}{2}}\int_{-\infty}^{\infty}\eta ds,\ J = bc\int_{-\infty}^{\infty}\eta^2 ds. \qquad (20a,b)$$

It follows that $\mathcal{E} = \rho gJ$ is conserved. On the other hand,

$$M = \rho I(bc)^{\frac{1}{2}} \text{ and } \mathcal{M} = \rho I(bc^3)^{\frac{1}{2}} \qquad (21a,b)$$

so that, except for special combinations of b and d, M and $\mathcal{M}$ are conserved only if $\int_{-\infty}^{\infty}\eta ds = 0$. Non-conservation of momentum is acceptable in consequence of the horizontal thrust exerted on the fluid by the bottom and walls of the channel, but non-conservation of mass is generally unacceptable.

We remark that the neglect of both dispersion and nonlinearity, as represented by the first and second terms, respectively, in (16), yields Green's law, $(bc)^{\frac{1}{2}}\eta = f(s)$, where f is an arbitrary function of the characteristic coordinate, s.

4. SLOWLY VARYING CNOIDAL WAVE

Theory

Kinematical and scaling considerations suggest that an approximate solution of (16) for a wave of prescribed period

$$T \equiv 2\pi/\omega \equiv (L/g)^{\frac{1}{2}} \qquad (22)$$

be posited in the form

$$\eta(s,x) = a(x)N(\theta,x),\quad \theta = \omega s - \chi(x), \qquad (23a,b)$$

where θ and x are fast and slow variables, a(x) is a slowly varying amplitude, and $\chi(x)$ is a slowly varying phase shift. It also is expedient to introduce

$$\gamma(x) = 2(cd/a\omega)\chi'(x), \qquad (24a)$$

such that the phase speed of the wave is given by

$$\mathcal{C} = -\theta_t/\theta_x = c/[1-\tfrac{1}{2}\gamma(a/d] \doteq [g(d+\gamma a)]^{\frac{1}{2}}. \qquad (24b)$$

Conservation of mass and energy imply the constraints (see Section 3)

$$\langle N\rangle = 0,\quad a^2bcT\langle N^2\rangle = J, \qquad (25a,b)$$

where < > implies an average over a 2π interval of θ and J is the integral invariant obtained through the substitution of (23) into (20b).

A formal, asymptotic development of the description (23) may be obtained by expanding $N(\theta,x)$ and $\gamma(x)$ in powers of an appropriate measure of the slow variation of b and d and invoking (25a) and the requirement that the period of θ be 2π. The first approximation, which is obtained by substituting (23) into (16) and then neglecting all derivatives with respect to the slow variable x, corresponds to that for a cnoidal wave [Lamb (1932, §253)]. It may be placed in the form

$$N = \mathrm{cn}^2[(K/\pi)\theta|m] - \langle \mathrm{cn}^2\rangle,\ \langle \mathrm{cn}^2\rangle = [m-1+(E/K)]/m, \qquad (26a,b)$$

$$\gamma = [2-m-3(E/K)]/m,\ aL/d^2 = (16/3)mK^2 \equiv \mathcal{U}(m), \qquad (26c,d)$$

where $\mathrm{cn}(u|m)$ is an elliptic cosine of modulus $\sqrt{m}$ and K and E are complete elliptic integrals in the notation of Abramowitz and Stegun (1955), and $\mathcal{U}(m)$ is the local Ursell parameter. Substituting (26) into (25b), we obtain

$$JL^{3/2}/(bd^{9/2}) = \mathcal{U}^2\langle N^2\rangle \equiv \mathcal{F}(m), \qquad (27a)$$

where

$$\langle N^2\rangle = \langle \mathrm{cn}^4\rangle - \langle \mathrm{cn}^2\rangle^2 = [2(2-m)(E/K) - 3(E/K)^2 - (1-m)]/(3m^2) \qquad (27b)$$

and

$$\mathcal{F} = (4^4/3^3)K^2[2(2-m)EK - 3E^2 - (1-m)K^2]. \qquad (27c)$$

It follows from (27), which determines m(x), that m is constant if and only if $bd^{9/2}$ = constant, in which special case (23), (26), and (27) constitute an exact similarity solution of (16).

The results (26a) and (27a) provide a parametric relation between aL/d^2 and $JL^{3/2}/bd^{9/2}$ that may be graphically represented as a plot of log $\mathcal{F}$ vs log $\mathcal{U}$ [see Miles (1978b)]. The case of constant depth is especially simple in that the plot of log $\mathcal{F}$ vs log $\mathcal{U}$ is equivalent to -log b vs log a. The limiting relations

$$\mathcal{F} \to \frac{1}{8}\mathcal{U}^2,\ a \to (8J)^{\frac{1}{2}}b^{-\frac{1}{2}}(Ld)^{-\frac{1}{4}}\quad (\mathcal{U} \downarrow 0) \qquad (28a,b)$$

and

$$\mathcal{F} \sim (\tfrac{4}{3}\mathcal{U})^{3/2},\ a \sim \tfrac{3}{4}J^{2/3}b^{-2/3}d^{-1}\quad (\mathcal{U} \uparrow \infty) \qquad (29a,b)$$

intersect at $\mathcal{U} \doteq 150$ and provide rough approximations for $\mathcal{U} \lessgtr 150$.

The preceding calculation is a generalization of that of Svendsen and Brink-Kjaer (1972), who consider the one-dimensional (b = constant) shoaling problem; however, they replace $\theta + \omega t$ in (23b) by the equivalent of $[1 - \frac{1}{2}\gamma(a/d](x/c)$, which is clearly in error unless both b and d are constant.

The problem also is attacked by Shuto (1974), who allows for the variation of both b and d but arrives at a result (which he integrates numerically) that appears to be inconsistent with conservation of energy. However, his result is consistent with (28) in the limit $\mathcal{U} \downarrow 0$ and with (29) in the limit $\mathcal{U} \uparrow \infty$ or, more precisely, with the result obtained by neglecting only terms of exponentially small order in (27),

$$F \sim (\tfrac{4}{3}\mathcal{U})^{3/2}\{1 - 2(\tfrac{1}{3}\mathcal{U})^{-\frac{1}{2}}\} \quad (\mathcal{U} \uparrow \infty) , \tag{30}$$

which is in error by less than 1% for $\mathcal{U} > 70$. It therefore appears that Shuto's numerical results are not significantly in error (on the scale of his plots) over the entire range of $\mathcal{U}$.

Experiment

Shuto (1974) compares his results with his own experimental observations and with those of Iwagagi and Sakai (1969) for shoaling waves periods from 1.2 to 6 seconds on uniform slopes of 1/20 and 1/70. He concludes that linear surface-wave theory (which presumably accounts exactly for dispersion) is superior to his cnoidal-wave results for $\mathcal{U} < 30$ and conversely for $\mathcal{U} > 30$ and that the latter are good for a/d as large as 0.8.

5. SLOWLY VARYING SOLITARY WAVE

Theory

The slowly varying solitary wave

$$\eta = a\,\mathrm{sech}^2\left[\frac{(3ga)^{\frac{1}{2}}}{2d}\left(\int\frac{dx}{c} - t\right)\right], \quad c \doteq [g(d+a)]^{\frac{1}{2}}, \tag{31a,b}$$

$$a = \frac{3}{4}J^{2/3}b^{-2/3}d^{-1} , \tag{31c}$$

is obtained by letting $\mathcal{U} \uparrow \infty$ with $K\theta = O(1)$ in (26) and (27).* There is, however, a new difficulty: none of the integrals I, M, and $\mathcal{M}$ [see (20a) and (21a,b)], which now are proportional to $b^{1/6}d^{3/4}$, $b^{2/3}d$, and $b^{2/3}d^{3/2}$, respectively, is conserved except for special variations of b and d. [The failure of the condition $\langle N \rangle = 0$ in the limit $\mathcal{U} \uparrow \infty$ is a consequence of the loss of the displacement $-a\langle cn^2 \rangle \sim a/K$, which cancels the mean of $a\,cn^2(2K\theta)$ when integrated over $-K < 2K\theta < K$.] It follows that, except in the special case $bd^{9/2}$ = constant for which (31) is an exact solution of (16) and M and $\mathcal{M}$ vary like d^{-2} and $d^{-3/2}$, respectively, (31) cannot be a uniformly valid approximation to the solution of the KdV channel equation (16); instead, it is the first term in an inner expansion, which must be matched to an appropriate outer expansion.

Johnson (1973) obtains the next term in an inner expansion for b = constant and finds that it can be matched to an appropriate outer expansion if d is increasing in the direction of propagation (the solitary wave may undergo fission if d is decreasing); however, he does not obtain an explicit description of the oscillatory tail, nor does he allow for the possibility of expanding the slowly varying phase $\chi(x)$ as well as $N(\theta,x)$ [see (23)].

Ko and Kuehl (1978) have criticized Johnson for this latter omission and develop a joint expansion of (the equivalents of) N and χ. They conclude that the solitary wave ("soliton") experiences an *irreversible* energy loss in the sense that it does not re-establish itself if the channel gradually reverts to its initial, uniform breadth and depth. This may be, but the proper form of the inner expansion is to some extent a matter of expediency, and the ultimate validity of any particular expansion can be established (albeit heuristically) only through matching to a proper outer expansion. Ko and Kuehl appear to overlook the crucial role of matching, and, at least in this important respect, their results must be regarded as incomplete.

Johnson's results are readily generalized to allow for the variation of both b and d and reveal that

$$\delta = 2(3a/d)^{-3/2}d\Lambda(bd^{9/2}) = (3\alpha)^{-3/2}(2d\Lambda b + 9d') \tag{32}$$

is an appropriate measure of the slow variation of the channel (this same measure also is appropriate for a cnoidal wave for $\mathcal{U} \gtrsim 100$). The Boussinesq equations (13) and KdV equation (16) are based on the restriction $\delta = O(1)$ as $\alpha \downarrow 0$ [cf. (2)], whereas (26) and (31) are based on the stronger assumption $|\delta| \ll 1$ [cf. (3)]. Moreover, a consideration of the special case of linearly increasing breadth and constant depth [Miles (1978a)] suggests that the wave ultimately ceases to be solitary and evolves

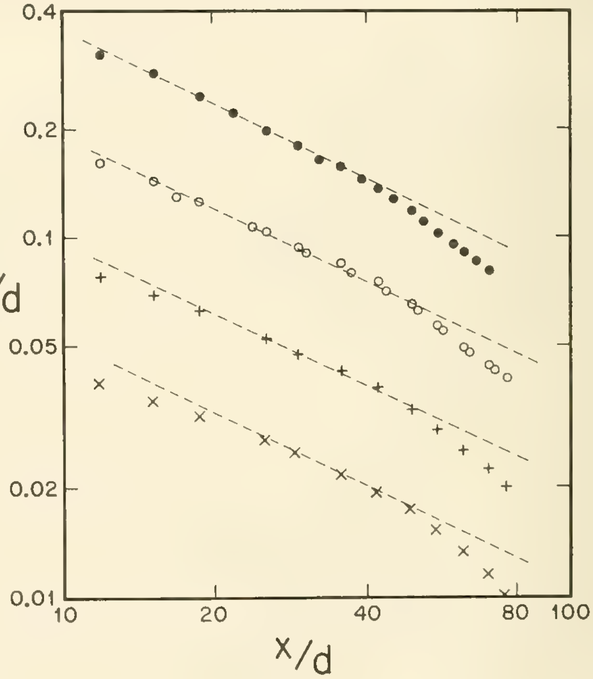

FIGURE 1. Decay of a solitary wave in a linearly expanding channel. The wave is propagating in the positive-x direction, where x is measured from the virtual origin at which b = 0, and enters the diverging channel (from an entry section of uniform width) at x/d ≑ 10. The amplitudes at the transition station are a/d = 0.05(×), 0.1(+), 0.2(o), and 0.4(•). The dashed lines have slopes of −2/3.

---

*The prediction that $a \propto b^{-2/3}d^{-1}$ appears to be due originally to Saeki, Takagi, and Ozaki (1971); see also Shuto (1973, 1974) and Miles (1977a).

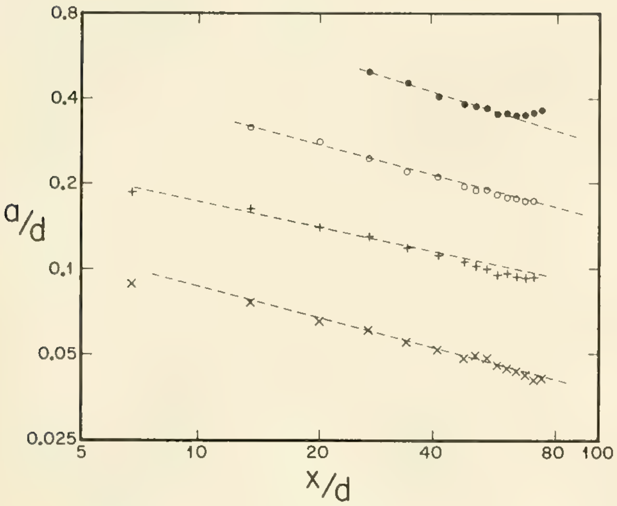

FIGURE 2. Growth of a solitary wave in a linearly contracting channel. The wave is propagating in the negative-x direction (right to left), where x is measured from the virtual origin at which b = 0, and enters the converging channel (from an entry section of uniform width) at x/d ÷ 94. The amplitudes at the transition station are a/d = 0.05(×), 0.1(+), 0.2(o), and 0.4(•); the corresponding slopes of the dashed lines are -0.39, -0.34, -0.41, and -0.42.

into a dispersive wave train for which the first peak closely approximates a solitary wave in shape but is followed by successive peaks of only gradually diminishing amplitude. There remains, however, the difficulty of nonconservation of mass, and the general problem of an aperiodic wave (in particular, an initially solitary wave) in a gradually varying channel is unresolved at this time.

Experiment

Shuto (1973) compares Green's law, $a \propto d^{-\frac{1}{4}}$, and the present prediction $a \propto d^{-1}$, with the experimental observations of Camfield and Street (1969) and Ippen and Kulin (1954) for shoaling of solitary waves on a uniform slope. He concludes that the range of validity of the "-1 power" law decreases with increasing slope and that the "¼ power" law holds for slopes in excess of 0.045 and a/d as large as 2.0. A more precise comparison can be made on the basis of (32), which reduces to

$$\delta = 9(3a/d)^{-3/2}d' \quad (b = \text{constant}) \qquad (33)$$

for a channel of constant breadth. The estimated critical values of δ, such that $a \propto d^{-1}$ or $d^{-\frac{1}{4}}$ provide better fits to the data for $\delta < \delta^*$ or $\delta > \delta^*$, respectively, are $\delta^* = 0.10$, 0.10, and 0.09 for slopes of .01, .02, and .03, and $a \propto d^{-1}$ is typically within the experimental scatter for $\delta < 0.01$.

Chang and Melville (unpublished) have recently measured a(x) in linearly diverging and converging channels. Their results for a diverging channel (Figure 1) tend to confirm the prediction $a \propto b^{-2/3}$ for initial values (at the transition from a uniform channel) of $0.05 \leq a/d \leq 0.2$ [the corresponding values of $\delta = 2(3\alpha)^{-3/2}(db'/b)$ are in the range (0.01, 0.07], although the decay ultimately exceeds this inviscid prediction--presumably in consequence of viscous or other dissipation -- and exceeds it after only a rather brief section for an initial value of a/d = 0.4. Their results for a converging channel (Figure 2) predict a growth that is roughly approximated by $a \propto b^{-0.4}$. Dissipation in the converging channel would tend to decrease the magnitude of the exponent, but why this decrease should be so much larger than the corresponding increase for the diverging channel is not clear at this time (intuition suggests that reflection could be more significant in a converging than in a diverging channel, but neither analytical nor experimental evidence is available to support this conjecture).

ACKNOWLEDGMENT

This work was partially supported by the Physical Oceanography Division, National Science Foundation, NSF Grant OCE74-23791, and by the Office of Naval Research under Contract N00014-76-C-0025. Most of the material in Sections 3 and 4 has been published elsewhere [Miles (1978b)] in slightly different form.

REFERENCES

Abramowitz, M., and I. Stegun (1965). *Handbook of Mathematical Functions*, Bureau of Standards, Washington, D. C.

Broer, L. J. F. (1974). On the Hamiltonian theory of surface waves. *Appl. Sci. Res. 30*, 430-446.

Camfield, F. E., and R. L. Street (1969). Shoaling of solitary waves on small slopes. *Proc. ASCE, Waterways and Harbors Div. 95*, 1-22.

Ippen, A., and G. Kulin (1954). The shoaling and breaking of the solitary wave. *Proc. 5th Coastal Engineering Conference*, 27-49.

Iwagaki, Y., and T. Sakai (1969). Studies on cnoidal waves (seventh report) - Experiments on wave shoaling. *Dis. Pre. Res. Inst. Annals, No. 12B*, Kyoto Univ., 569-583 [in Japanese; cited by Shuto (1974)].

Johnson, R. S. (1973). On the asymptotic solution of the Korteweg-deVries equation with slowly varying coefficients. *J. Fluid Mech. 60*, 813-824.

Ko, K., and H. H. Kuehl (1978). Korteweg-deVries soliton in a slowly varying medium. *Phys. Rev. Lett. 40*, 233-236.

Lamb, H. (1932). *Hydrodynamics*, Cambridge University Press.

Miles, J. W. (1977a). Note on a solitary wave in a slowly varying channel. *J. Fluid Mech. 80*, 149-152.

Miles, J. W. (1977b). On Hamilton's principle for surface waves. *J. Fluid Mech. 83*, 153-158.

Miles, J. W. (1977c). Diffraction of solitary waves. *ZAMP 28*, 889-902.

Miles, J. W. (1978a). An axisymmetric Boussinesq wave. *J. Fluid Mech. 84*, 181-192.

Miles, J. W. (1978b). On the Korteweg-deVries equation for a gradually varying channel. *J. Fluid Mech.* (sub judice).

Rayleigh, Lord (1876). On waves, *Phil. Mag. 1*, 257-279; *Papers 1*, 251-271.

Saeki, H., K. Takagi, and A. Ozaki (1971). Study on the transformation of the solitary wave (2). *Proc. 18th Conf. on Coastal Engg. in Japan*, 49-53 [in Japanese; cited by Shuto (1974)].

Shuto, N. (1973). Shoaling and deformation of nonlinear long waves. *Coastal Engineering in Japan 16*, 1-12.

Shuto, N. (1974). Nonlinear waves in a channel of variable section. *Coastal Engineering in Japan 17*, 1-12.

Svendsen, I. A., and O. Brink-Kjaer (1972). Shoaling of cnoidal waves. *Proc. 13th Coastal Engineering Conference (Vancouver 1*, 365-383.

Whitham, G. B. (1967). Variational methods and applications to water waves. *Proc. Roy. Soc. Lond. A 299*, 6-25.

Whitham, G. B. (1974). *Linear and nonlinear waves*, Wiley-Interscience, New York.

Study on Wind Waves as a Strongly Nonlinear Phenomenon

Yoshiaki Toba
Tohoku University
Sendai, Japan

ABSTRACT

Recent studies on wind waves in our laboratory, from a view point of strong nonlinearity of the wind waves, are reviewed. The main items are as follows. (1) It has been shown by experiments and theoretical analyses that the mechanism of initial generation of waves by the wind is the instability of shear flows of two-layer viscous fluids, air and water. It is a selective amplification of disturbances at the frequency of maximum growth rate. However, the transition of the initial wavelets to irregular wind waves including turbulence follows within several seconds [Kawai (1977)]. (2) Flow visualization studies of the internal flow pattern of wind waves show that the shearing stress of the wind is concentrated at the crest and windward face of individual waves, and a special area is formed where the surface wind drift, and consequently the vorticity is concentrated, causing the forced convection or the turbulent mode, which is the origin of the irregularity of wind waves [e.g., Toba et al. (1975); Okuda et al. (1977)]. (3) Statistical investigation of instantaneous individual waves in a wind-wave tunnel shows clearly the existence of similarity in the individual waves [Tokuda and Toba (1978)]. Namely, the energy spectrum, which is newly defined for the individual waves, is virtually equivalent to the traditional energy spectrum at the frequency range from 0.7- to 1.5-times the frequency of the energy maximum. However, the energy peaks which usually appear in the traditional spectrum at the higher harmonics of these dominant waves completely disappear. The apparent phase speed of individual waves, for each wind and fetch condition, is inversely proportional to the square root of their frequency, and is much larger than the phase speed of linear water waves. For the individual waves for each wind and fetch condition, there exists statistically a conspicuous relationship of the 3/2-power law [cf., Toba (1972, 1978a)] between the normalized wave height and period. Consistently with this and the phase speed relationships, the steepness of the individual waves is statistically constant. (4) Discussion is presented as to the possibility of approaching the above-mentioned characteristics of the individual waves from the similarity hypothesis and dimensional considerations. Self-adjustment of the individual waves to the local wind drift distribution is postulated to explain the 3/2-power relationships, which may be the basis of the possibility that the pure wind-wave field is represented by a single dimensionless parameter [Toba (1978a)]. (5) A new formulation is presented for the roughness parameter or the drag coefficient over the wind waves, incorporating the single dimensionless parameter of the wind-wave field. A physical interpretation of the form is given from the internal flow pattern of individual waves [Toba (1978b)].

1. INTRODUCTION

In a traditional model, the wind waves are treated as phenomena, expansible to component free water waves having weakly nonlinear interactions among waves of different wave numbers. However, detailed experimental studies on the actual conditions of wind waves produced in wind-wave tunnels, have shown that wind waves are much more strongly nonlinear phenomena, especially in their younger stages. This report presents a review of recent studies made in our laboratory, giving much emphasis to the strong nonlinearities which are inherent in wind waves.

2. INITIAL GENERATION OF WIND WAVES

The first topic starts with an approach from the process of the initial generation. The wind waves have long been assumed to be generated from a still water surface by the effect of pressure fluctuations.

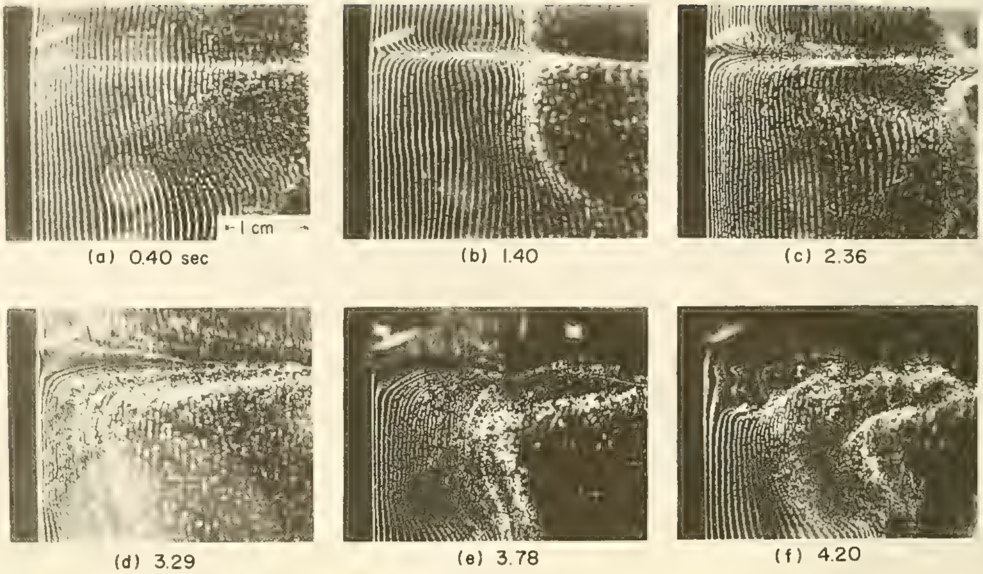

(a) 0.40 sec (b) 1.40 (c) 2.36

(d) 3.29 (e) 3.78 (f) 4.20

FIGURE 1. Flow visualization of the initial stage of the generation of wind waves by use of hydrogen bubble lines produced by the electrolysis of water. The photographs were taken from a viewpoint slightly below the air-water interface, so images reflected at the interface are seen in the upper 1/4 of each picture. The hydrogen bubble lines are produced near the left end as pulses of 0.002-s width at 0.04-s intervals in a very slow, uniform flow of water which was produced before the start of wind. The wind was 6.2 m/s blowing from left to right of each picture. The filmed time of each picture from the start of the wind is shown in seconds. The out-of-focus areas were caused by some fluctuation of the mean flow, for very shallow depth of the focus. In (e) are seen the initial wavelets, and in (f) is seen the onset of turbulent mode. [Cited from Okuda et al. (1976).]

A resonance mechanism for the initial generation proposed by Phillips (1957) and an instability mechanism for further growth proposed first by Miles (1957) have been referred to on every occasion. Valenzuela (1976) showed that the growth rate of waves in the gravity-capillary range, observed by Larson and Wright (1957) at the initial stage of the generation, agrees with the expected growth rate by the instability theory applied to a coupled shear flow of the air and the water.

Kawai (1977 and 1978) of our laboratory has arrived at the conclusion, by systematic experiments together with theoretical analyses, that the mechanism of generation of the initial wavelets is the instability in a two-layer shear flow of viscous fluid of air and the water, as a selective amplification of disturbances of the frequency at the maximum growth rate.

The experiments were carried out mainly by use of a wind-wave tunnel of 20 m length, 60 cm × 120 cm cross-section, containing water of 70 cm depth. After the sudden starting of wind on the still surface of water, a shear flow first develops in the uppermost thin layer of water, and several seconds later, regular, long-crested initial wavelets appears [Figure 1(e)]. His theoretical analysis of the shear flow instability of the two-layer viscous fluids, using the actual profile of the shear flow in water, shows that the system is unstable and there exists a frequency at which the growth rate, kC_i, is maximum (Figure 2). The frequency of kC_i-maximum does not necessarily coincide with that of C_r-minimum, or the minimum phase speed for the gravity-capillary wave. Three properties of the initial wavelets determined by the experiment, i.e., the frequency, the growth rate, and the phase speed are all virtually coincident with those of the theoretically predicted waves of the maximum growth rate as shown in the following.

Figure 3 shows an evolution of the spectrum calculated by the maximum entropy method, which may be applicable to nonstationary processes. Each spectrum represents an ensemble average of 8 runs. Wavelets of a constant frequency of about 15 Hz in this case grow as shown in the figure with a smooth spectrum. The peak then moves to a lower frequency side showing the evolution to irregular wind waves having the usual spectral form. In the stage of constant frequency, Figure 4 shows the agreement of the observed frequency of the initial wavelets with the theoretical frequency for the kC_i-maximum, as a function of the friction velocity of the air, u_*, but independent of the fetch. The frequency for the C_r-minimum is around 14 to 13 Hz, and does not coincide with the observed initial wavelets. Figure 5 shows the agreement in the phase speed, and Figure 6 the growth rate between the observed initial wavelets and the theoretical initial wavelets for kC_i-maximum.

Thus, Kawai's conclusion is that the generation of wind waves, whose initial stage is called initial wavelets, is caused by the selective amplification of small perturbations which inevitably occur in the flow by the instability of the two-layer viscous shear flow.

However, the duration of the exponential growth of the initial wavelets was limited to from 1 to 8 seconds in the experiments. The transition from the regular, long-crested initial wavelets to short-crested, irregular wind waves takes place in a very short time. The spectral peak, which has grown up with an approximately constant frequency, starts wandering at the transition, and then moves toward the lower frequency side with the energy increased in a general trend as seen in Figure 3, and also in Figure 7. The transition coincides with the onset of turbulence at the water surface as revealed in the next section.

3. INTERNAL FLOW PATTERN OF WIND WAVES — AN EXPERIMENTAL SUBSTANTIATION OF THE STRONGLY NONLINEAR PROCESSES

Irregularity is a character inherent in the wind waves. This has been demonstrated by detailed

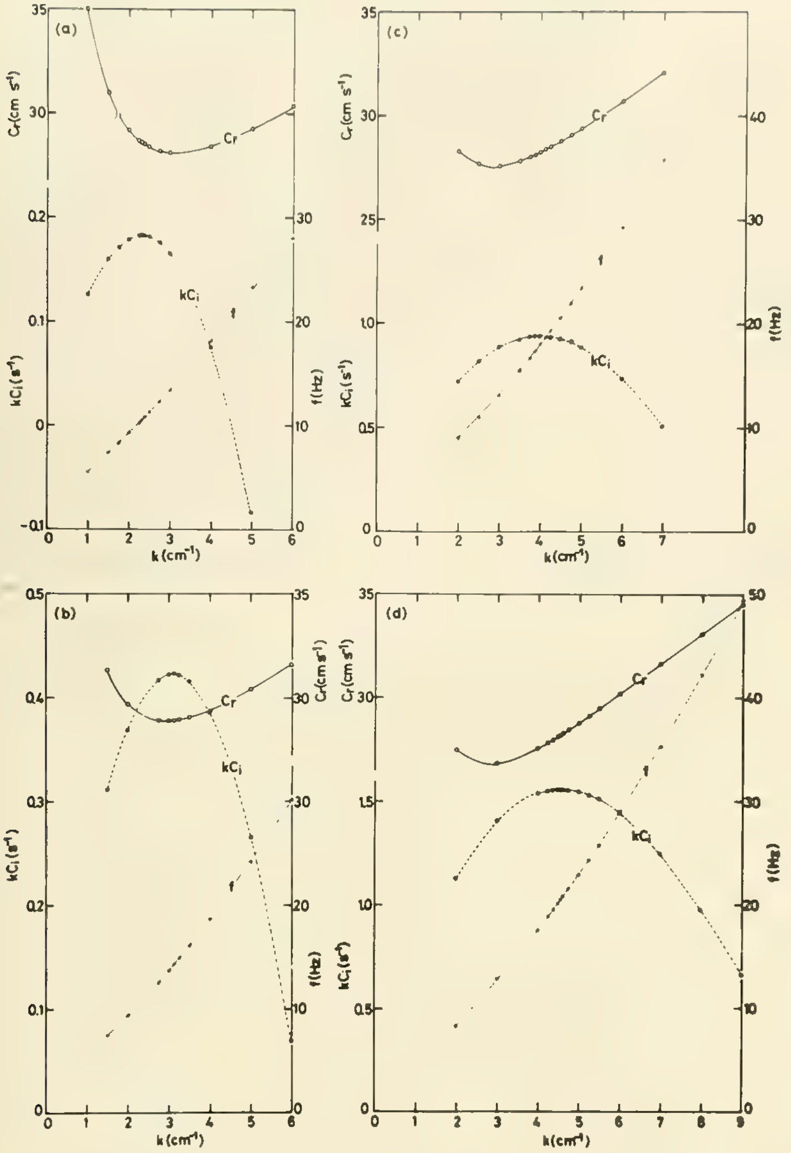

FIGURE 2. Theoretically obtained correlation of the amplification factor kC_i, the phase speed, C_r, and the frequency, f, to the wave number, k, in the instability of coupled shear flow of the air and the water, for four values of the friction velocity of the air u_* of (a) 13.6, (b) 17.0, (c) 21.4, (d) 24.8 cm/s. [Cited from Kawai (1977).]

studies of the internal flow pattern of wind waves by use of flow visualization techniques [Toba et al. (1975), Okuda et al. (1976, 1977) and Okuda (1977)].

Along the surface of individual undulations, hereafter called individual waves, there is a strong variation of the tangential stress exerted by the wind. The stress value determined locally from the distortion of hydrogen bubble lines, is several times greater than the average wind stress value at the windward face of the crest, and it is negligible at the lee side of the crest as shown in Figure 8 as an example. The concentration of the shearing stress results in the development of the local surface wind drift forming a special region under the crest where the strong vorticity is concentrated. The vorticity concentration causes the forced convection or turbulence, irrespective of whether or not the air entrainment, or the breaking in a usual sense occurs. As seen in Figure 9, small polystyrene particles of 0.99 specific gravity placed just beneath the water surface prior to the start of the wind, begin to disperse into the interior by the forced convection, coincidentally with the transition of the initial wavelets to the irregular wind waves. The main stage of the growth of wind waves thus seems to proceed as a strongly nonlinear processes.

4. COMPONENT WAVES AND INDIVIDUAL WAVES AS PHYSICAL MODEL OF WIND WAVES

Despite the fact that the wind waves are thus a strongly nonlinear phenomenon, they have been assumed as expansible to component waves, having phase speeds obeying the dispersion relation of free water waves, and weak wave-wave interactions have been considered.

Recently there have been some articles reporting that the phase speeds of component waves do not necessarily satisfy the dispersion relation, notably by Ramamonjiarisoa (1974) for the one dimensional case and Rikiishi (1978) for two-dimensional component waves. Rikiishi developed an experimental technique for the determination of the directional structure of the phase speed of component waves without pre-assuming the dispersion relation, and

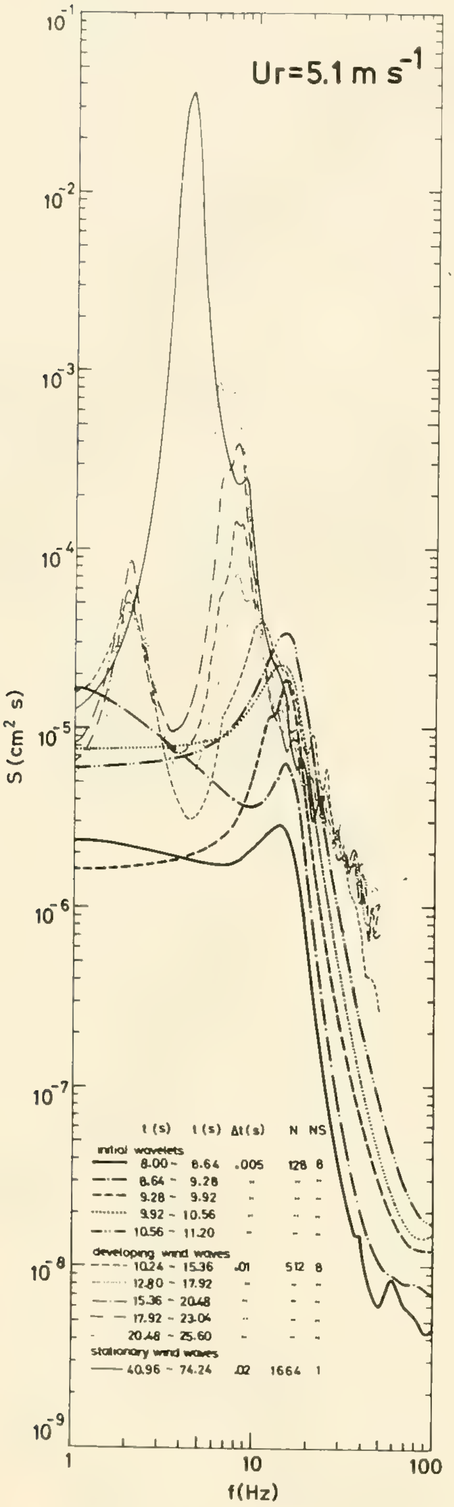

FIGURE 3. A sequence of spectra for the initial stage of the generation of wind waves, showing the growth of initial wavelets at a constant frequency of about 15 Hz, and the transition to irregular wind waves. The spectra were calculated by the Maximum Entropy Method, and each line represents an ensemble average of eight cases. The fetch was 8 m and the nominal wind speed was 5.1 m/s. [Cited from Kawai (1977).]

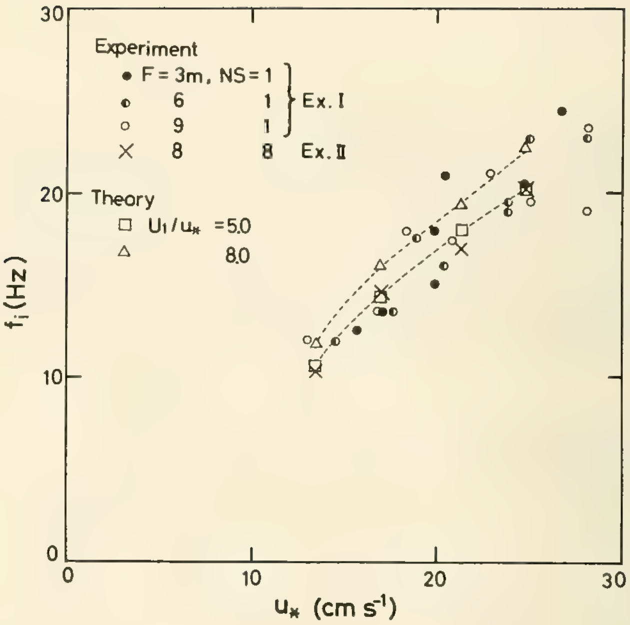

FIGURE 4. Observed theoretically predicted frequency of the initial wavelets, f_i, as a function of the friction velocity of air, u_*. Theoretical values are for the condition of the maximum growth rate, where U_1/u_* represents the dimensionless thickness of the viscous boundary layer of the air. [Cited from Kawai (1977).]

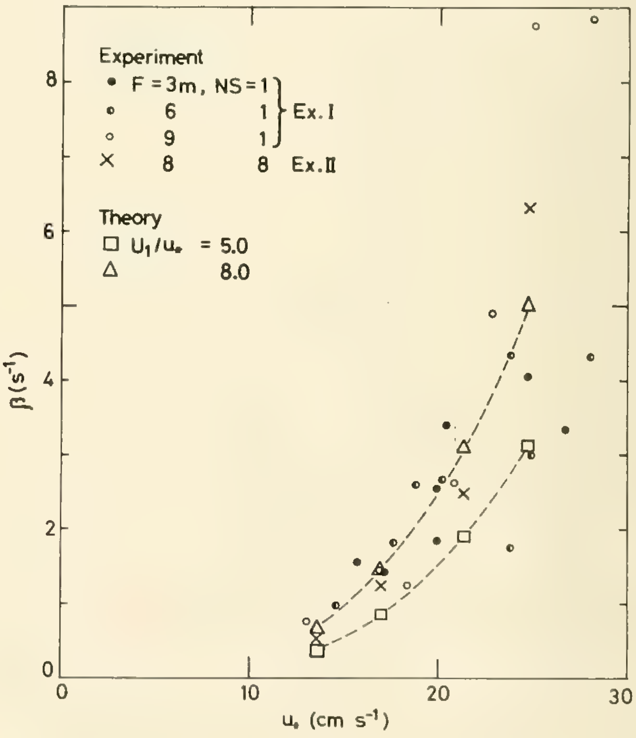

FIGURE 5. The growth rate of the initial wavelets, β, as a function of u_*. Theoretical values correspond to those for waves of the maximum growth rate. [Cited from Kawai (1977).]

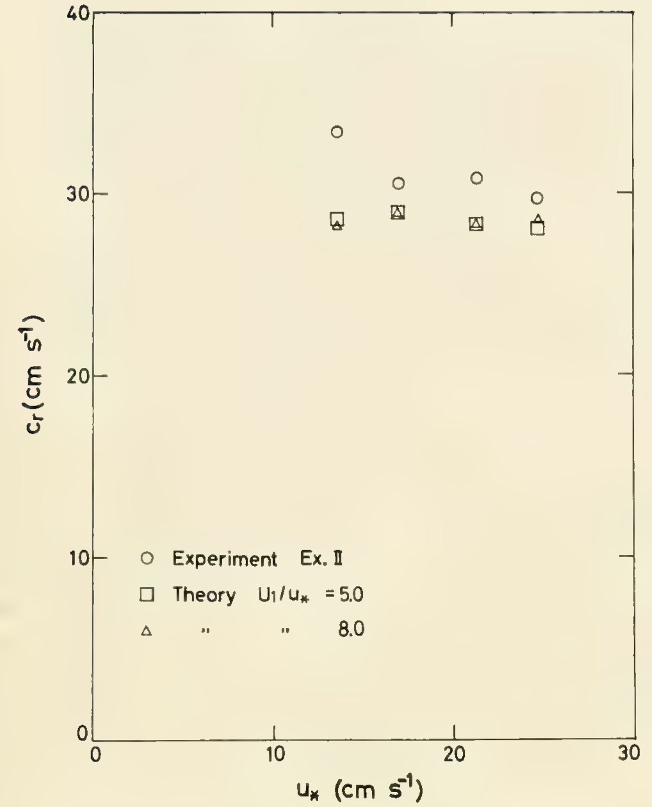

FIGURE 6. The phase speed of the initial wavelets C_r as a function of u_*. Theoretical values correspond to those for waves of the maximum growth rate. The theoretical values were calculated by use of the observed velocity profiles in the water at the critical time of the first appearance of the initial wavelets. The observed values for higher three wind speeds were determined at the critical time, whereas that for the lowest wind speed was determined about 3.5 s after the critical time because of the experimental difficulty, and this delay may presumably explain the observed higher value than the theoretical ones. [Cited from Kawai (1977).]

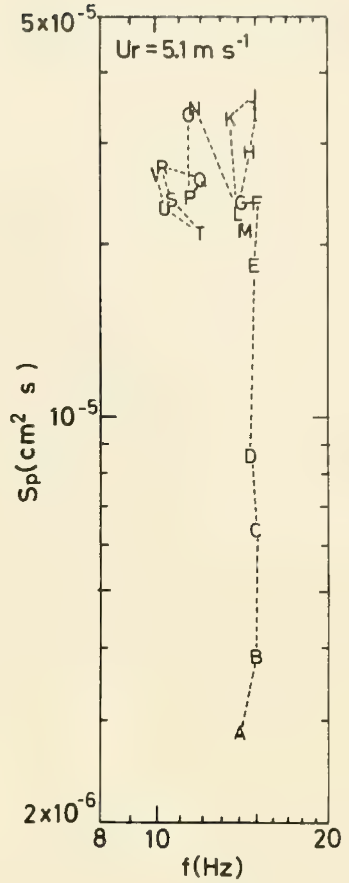

FIGURE 7. An example of minute inspection of the observed time series of the spectral peak for the initial stage of the generation of wind waves. The lapse of time is indicated in alphabetical order, the interval between successive points being 0.32 s. After the growth of regular initial wavelets at a constant frequency of about 15 Hz, the spectral peak shows an irregular motion corresponding to the transition to irregular wind waves. [Cited from Kawai (1977).]

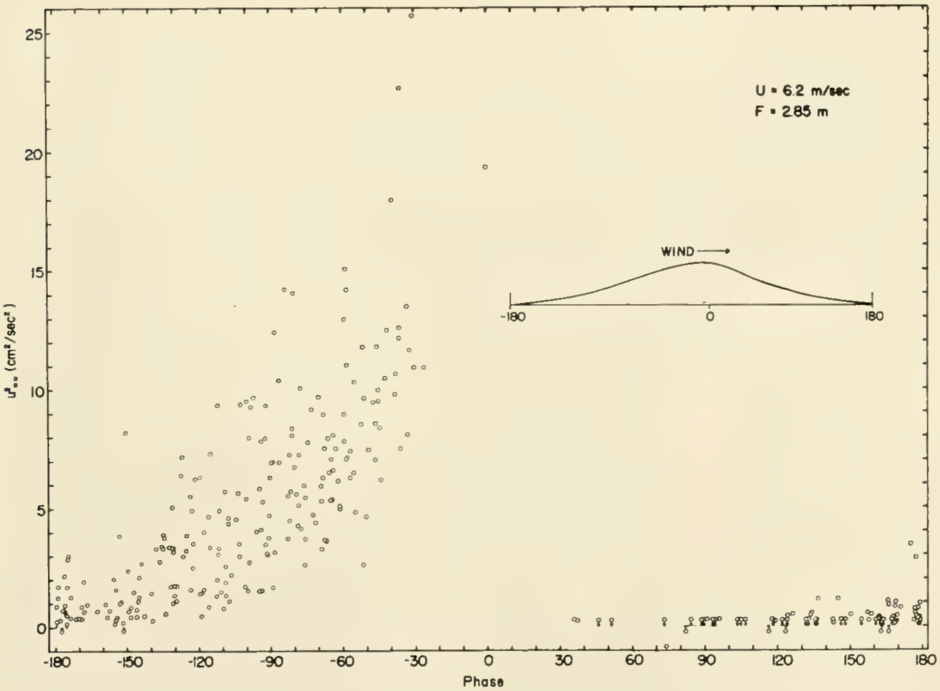

FIGURE 8. Observed values of the local shearing stress along the surface of representative wind waves. The abscissa is the phase relative to the peak point of the crest and the ordinate is expressed as the square of the friction velocity of the water. The wind speed was 6.2 m/s and the fetch was 2.85 m. [Cited from Okuda et al. (1977).]

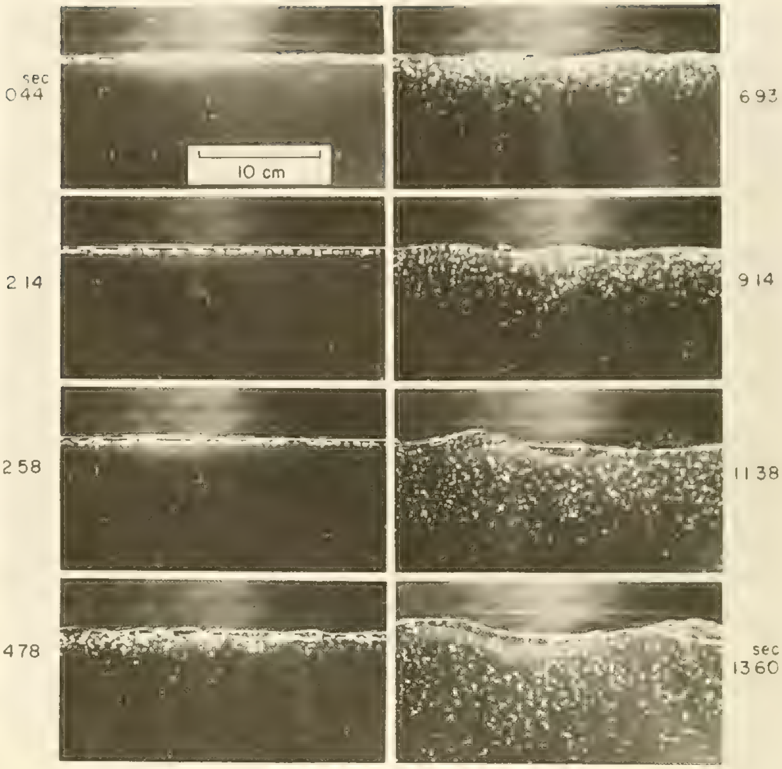

FIGURE 9. Flow visualization of the initial stage of the generation of wind waves by use of polystyrene particles which had a 2-mm diameter and the specific gravity of about 0.99, and which were placed just beneath the water surface prior to the start of the wind. The wind blows from the left to the right. The wind speed in the tunnel section was 8.6 m/s, and the fetch was 2.85 m. The time measured from the start of the wind is shown in seconds. In 2.58 s, initial wavelets may be recognized by streaks of light in the water, and some particles have already begun to disperse into the water. In 4.78 s, waves are already irregular wind waves and more particles are dispersed. In 13.6 s, particles are dispersed down to more than 10 cm, corresponding approximately to a half of the representative wave length. [Cited from Toba et al. (1975).]

found that the phase speed was virtually independent of the frequency, and had the same value as that of the waves of the spectral maximum, at respective fetches. These experimental results are interpreted as indicating that the assumption of wind waves as expansible to component free waves with weak nonlinearity is not necessarily appropriate for young growing wind waves.

On the other hand, since individual waves as instantaneous surface undulations have a specific shearing stress distribution, and a specific interval flow pattern, they may carry some factors as a physical element. We have examined, in a wind-wave tunnel of 15-cm width, energy density distributions for individual waves, as well as their phase speeds, and compared them with those obtained by usual component wave model for the same experimental data [Tokuda and Toba (1978)].*

First, a normalized energy spectrum for individual waves has been newly defined and calculated from the statistical distribution of two kinds of the individual waves: zero-crossing, trough-to-trough and all trough-to-trough on our wave records, as illustrated in Figure 10. The definition of the normalized individual-wave spectral density, θ_N, is

$$\theta_N(f_N) = \theta_i \Delta f/(\Delta f/f_p)E \qquad (1)$$

where

$$\theta_i \Delta f = \frac{1}{2}\,\frac{m_i T_i}{\Sigma m T}\left(\frac{\overline{H_i}}{2}\right)^2, \quad i = 1,2,\ldots\ldots,n+1$$

and where m_i is the number of individual waves of the period class, T_i, (frequency from f to $f + \Delta f$), $\Delta f = 1/(2n\Delta t)$, where we used $\Delta t = 0.02$ s, $n = 100$, and $\Delta f - 0.25$ Hz, and also

$$E = \sum_{i=1}^{n+1} \phi_i \Delta f$$

$$f_N = f/f_p$$

and where f_p is the frequency of the energy maximum.

Figure 10 shows the comparison. The A-spectrum is the normalized spectra by the traditional component wave model in which the secondary peak is seen at the normalized frequency of 2. The B-spectrum is for individual waves of zero-crossing, trough-to-trough, and the C-spectrum for all trough-to-trough on our wave records. In the main frequency range from 0.7 to 1.5, which is the value normalized by the peak frequency, the spectra are virtually equivalent with one another. The second peak at frequency of 2 in the A-spectrum completely disappears in the individual-wave spectra. The slope of these straight lines is f^{-9} for the high frequency side, and f^{9} for the low frequency side. The C-spectrum is considered to give a better representation of the high frequency side which is exactly on the f^{-9} line, and the B-spectrum represents the low frequency side better, which is more similar to the traditional A-spectrum. We may infer that much energy of the higher frequency part of traditional component waves, which is clearly shown as the energy at higher harmonics of the spectra, is a manifestation of the distorted shape of individual waves of the main frequency range, as was already suggested by Toba (1973).

Figure 11 shows the normalized phase speed of individual waves determined by two adjacent wave gauges. It is inversely proportional to the square root of the frequency, in contrast to the phase speed of linear waves which is inversely proportional to the frequency. In addition, the phase speed of the individual waves is much larger than that of linear waves as shown later. In the case of the phase speed of component waves of one-dimensional

---

*Tokuda, M., and Y. Toba (1978): Component waves and individual waves as physical model of wind waves. To be published.

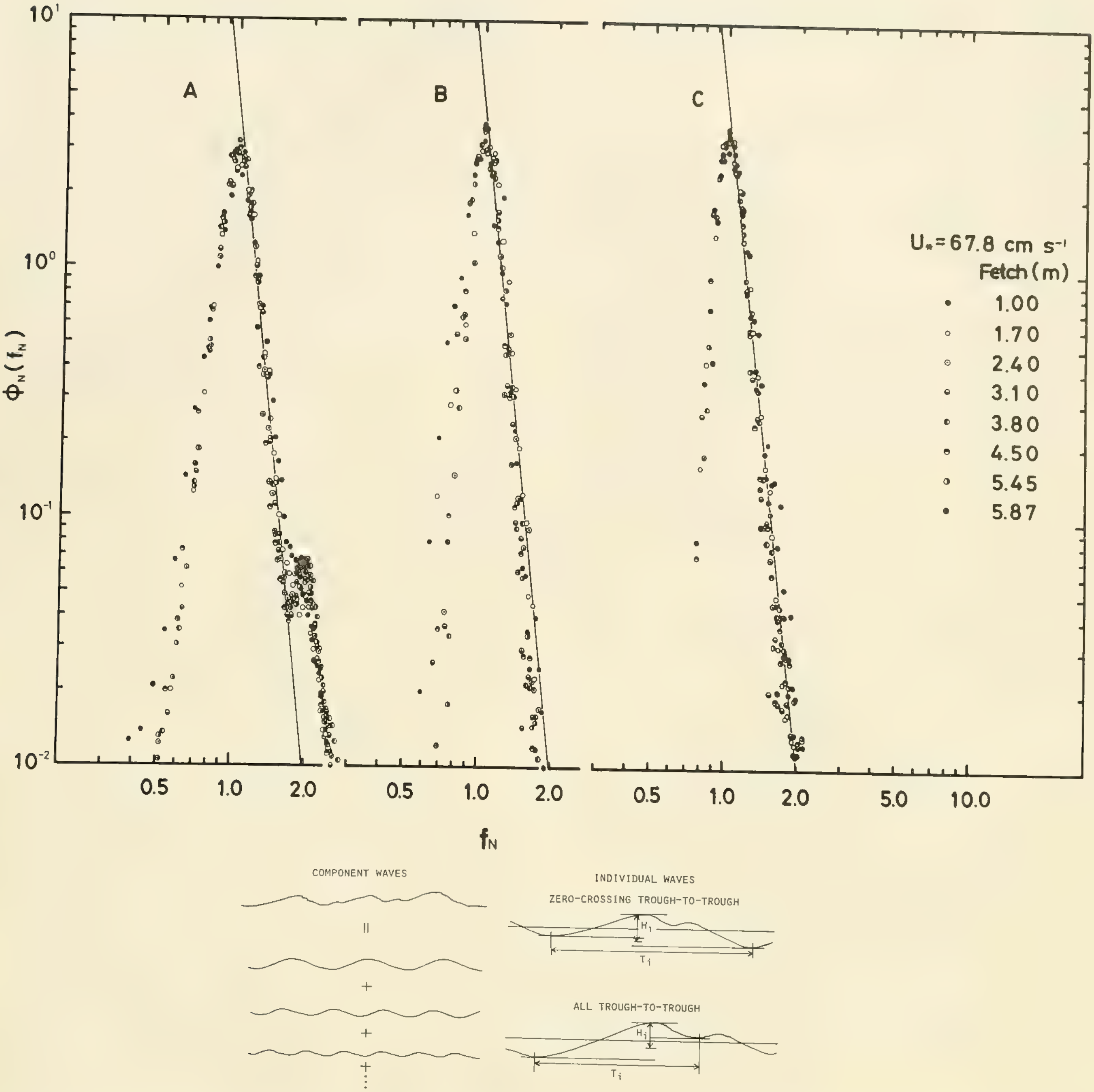

FIGURE 10. Comparison of three kinds of normalized energy spectra from the same wind-wave records in the wind wave tunnel. A: Traditional energy spectra by the component-wave model. B: Energy spectra for individual waves of zero-crossing trough-to-trough. C: Energy spectra for individual waves of all trough-to-trough. [Cited from Tokuda and Toba (1978).]

spectra, which was obtained from the cross-spectra of the records of two adjacent wave gauges (Figure 12), approximately the same phase speed is obtained in the before-mentioned main frequency range, where the coherence is close to unity. However, in the higher frequency range, it is virtually constant in agreement with Ramamonjiarisoa's 1974 measurement. The original values are shown in Figure 13, in which locations of the spectral peak are shown by arrows for the shortest and the longest fetches, respectively, and as the peak frequency moves to the left, the phase speed of the component waves becomes larger. In the figure, the full line shows the phase speed of linear waves. Figure 12 is the normalization of Figure 13, and Figure 14 shows an example of the comparison of phase speeds of component waves and individual waves. It should be noted that, as the distance of two wave gauges becomes wider, the range of high coherence becomes narrower, and the phase speed of component waves tends to be more uniform and obscure. However, it is at least evident that phase speeds for both component waves and individual waves have the same value near the peak frequency, and are inversely proportional to the square root of frequency, and much higher than the values of linear waves. It

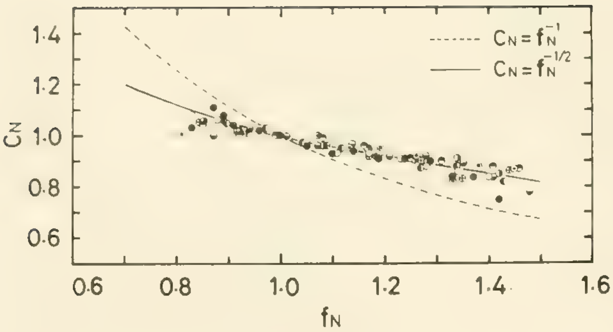

FIGURE 11. Phase speed distribution of individual waves (zero-crossing trough-to-trough), determined by a photographic method, and normalized by values for waves of maximum energy density. Dispersion relation for water waves are also entered by the dotted line. [Cited from Tokuda and Toba (1978).]

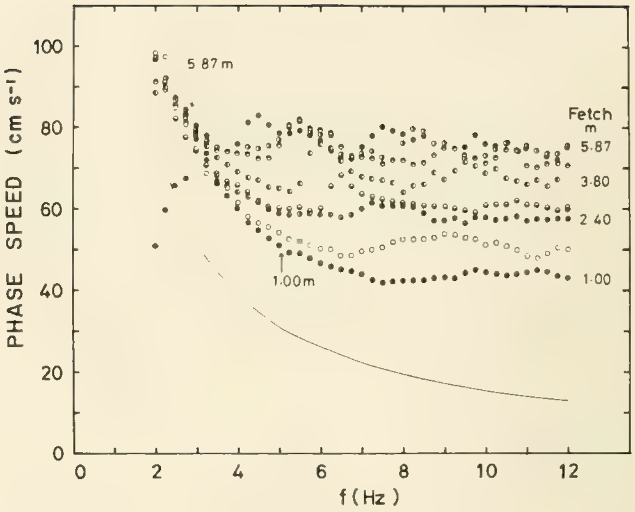

FIGURE 13. Original values of the phase speed distribution, for eight fetches, before the normalization shown in Figure 12. Peak frequencies for the shortest and the longest fetches are indicated by arrows, other cases being in between of these. The phase speed of linear water waves is indicated by the full line. [Cited from Tokuda and Toba (1978).]

is caused by the effect of the wind drift, which is concentrated near the crests.

Thus, by using appropriate normalization, we may express the energy distribution of physically substantial waves by the energy spectra of individual waves for some local frequency ranges, excluding false energy density. The above mentioned B-spectrum and C-spectrum are two examples of these. Further, we may reinterprete the traditional energy spectrum for the main frequency range as representing the energy distribution of individual waves, rather than the usual interpretation of a linear combination of small amplitudes of freely travelling component waves. In other words, the elementary physical substance of wind waves is rather in the individual waves, which have a specific distribution of local wind stress and flow pattern, and an apparent phase speed inversely proportional to the square root of the frequency.

Further, Figure 15 shows that, for the individual waves in the main frequency range for each wind and fetch condition, there exists a conspicuous statistical relation between normalized wave height and period, for significant waves which Toba (1972) proposed as the 3/2 power law:

$$H^* = BT^{*3/2} \qquad (2)$$

where $H^* \equiv gH/u_*^2$ and $T^* \equiv gT/u_*$ represents the dimensionless height and period, respectively, normalized by use of the acceleration of gravity g and the friction velocity of the air u_*. The figure shows the data for individual waves for various fetches. Except for very short fetches up to about 4 m, the factor of proportionality B is constant of about 0.045.

It should be noted that although the spectral form of wind waves in wind-wave tunnels is different from that in the sea as discussed, e.g., by Kawai et al. (1977), nevertheless the above power law holds for both cases, although the constant, B, is slightly different [cf, also Toba (1978a)]. Figure 16 shows another representation of the same relation: between the wave height and the frequency, normalized for those waves of maximum energy. The slope of the line is -3/2.

Consistently with this relation and the above-mentioned apparent phase speed, the steepness of the individual waves determined by a photographic method is approximately constant, statistically. It is

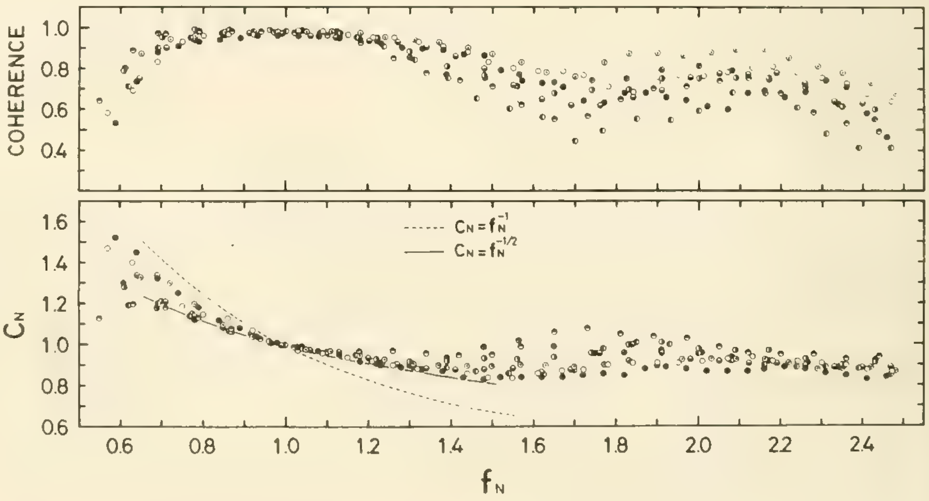

FIGURE 12. Phase speed distribution of one-dimensional component waves, obtained from the cross-spectra of records of adjacent two wave gauges, and normalized by values for waves of maximum energy density. The coherence of the cross-spectra is shown in the upper part. [Cited from Tokuda and Toba (1978).]

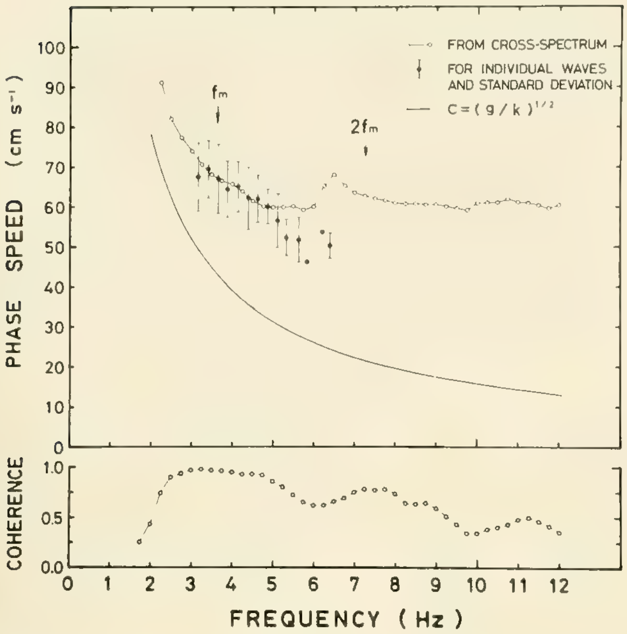

FIGURE 14. An example of the comparison of one-dimensional phase speeds of wind waves, determined from cross-spectra of records of two wave gauges, and determined for individual waves (zero-crossing trough-to-trough) together with the standard deviation, and the dispersion relation for water waves. At the bottom is shown the coherence of the cross-spectra. The f_m represents the frequency at the energy maximum. [Cited from Tokuda and Toba (1978).]

inferred that these facts strongly indicate the existence of similarity in the individual waves or in the field of wind waves, presumably as a result of the strong nonlinearity.

5. APPROACH BY SIMILARITY HYPOTHESIS AND DIMENSIONAL CONSIDERATION

In cases of strongly nonlinear processes, such as turbulence, it is hard to approach problems from the rigorous way of solving a closed system of equations. In these cases, some assumptions based on physical considerations are sometimes introduced to supplement the system of equations, to arrive at useful results. In the case of wind waves, it seems that an approach by the traditional model of component irrotational free waves with their weak interactions is not necessarily realistic as has been shown. There is another approach, in which a kind of similarity structure in the field of wind waves is assumed, and a regularity in gross structure is sought by invoking dimensional considerations. An example of this line of approach has been attempted as partly described in a paper by me [Toba (1978a)].

Since the local wind stress distribution along the surface of individual waves is as shown in Figure 7, the local wind drift is forced to be stronger near the crest and weaker near the trough. Water particles near the surface travel a longer distance when they are near the crest than when near the trough. On the other hand, water waves of finite amplitude cause the wave current, resulting from the difference between the foreward and the backward movements of the water particles. Some self-adjustment should occur for individual waves in such a manner than the forward and the backward movements by the waves are coincident with the difference in the local wind drift as to the phase. The wave current u_0 of the individual waves of amplitude, a, and angular frequency, σ, is now approximated by that of the second order Stokes wave:

$$u_0 = a^2\sigma^3/g$$

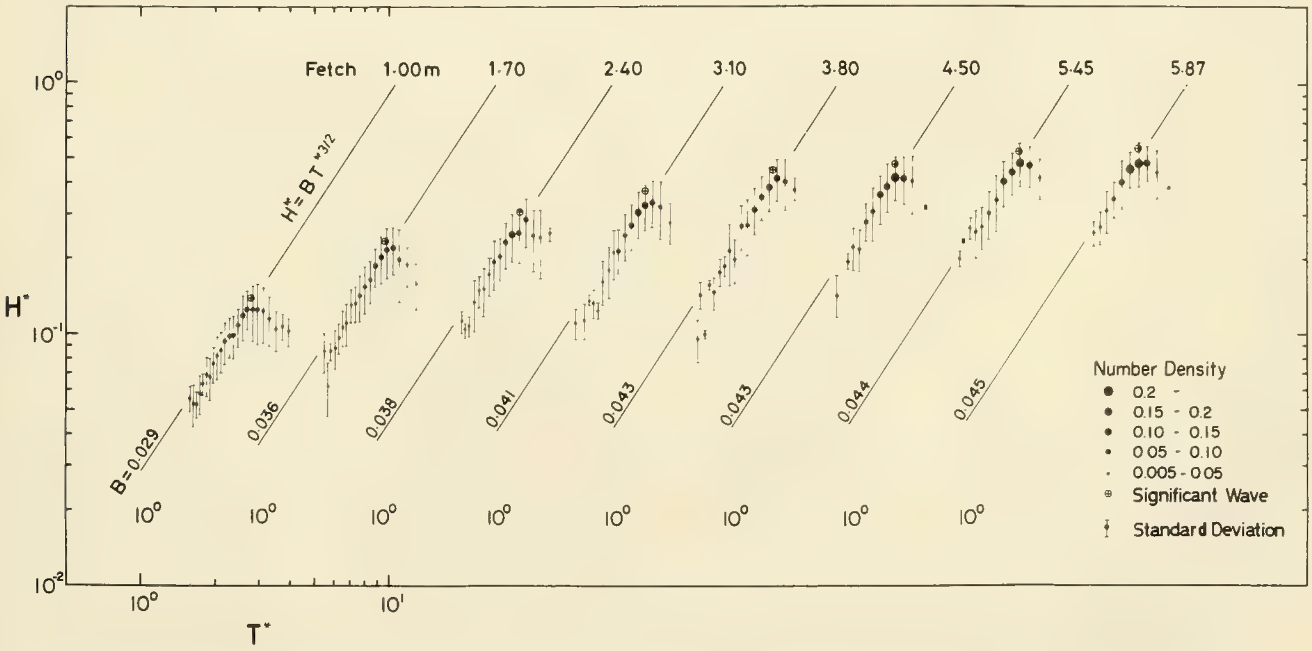

FIGURE 15. Examples showing that the main part of individual waves in the wind-wave tunnel (zero-crossing trough-to-trough) satisfies the 3/2 power law between the normalized wave height H* and the period T*. The u_* was 68 cm/s. [Cited from Tokuda and Toba (1978).]

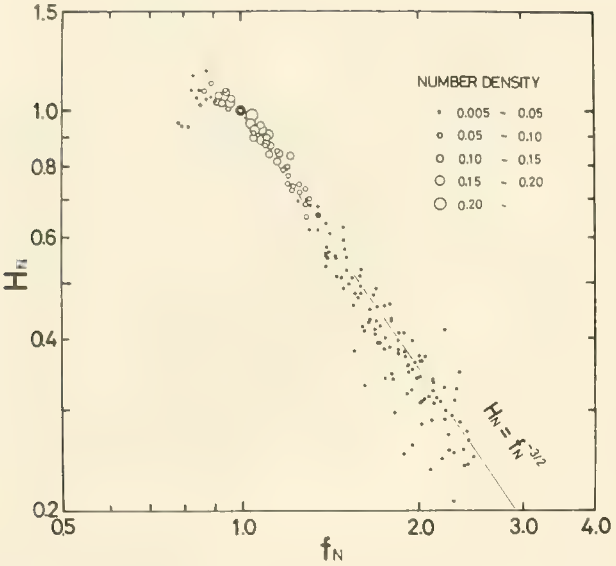

FIGURE 16. Another representation of the 3/2 power law for individual waves (all trough-to-trough). H_N and f_N represent the wave height and the frequency, respectively, normalized by values for waves of the maximum energy density. [Cited from Tokuda and Toba (1978).]

Since the difference in the local wind drift is caused by the mean wind stress, the self-adjustment is expressed by the condition that the wave current is proportional to u_*, namely,

$$a^2\sigma^3/gu_* = \text{constant} \tag{3}$$

This is transformed immediately to

$$H^* = B'\sigma^{*-3/2} \tag{4}$$

which is equivalent to (2), where $\sigma^* \equiv u_*\sigma/g$.

The condition of constant steepness may arise from the similarity requirement. The combination of the 3/2-power law relationship and the constant steepness condition leads to the apparent phase speed proportional to the square root of the frequency. These three relationships, which have been shown by the experiments to be satisfied by the individual waves, are self-consistent with one another, and may thus result from the strongly nonlinear effects.

The 3/2-power law makes it possible that the wind-wave field is represented by a single dimensionless parameter of the frequency at the energy maximum as discussed by Toba (1978a). One of the consequences of the above paper is that the growth of the wind wave field is expressed by the evolution of the dimensionless single parameter in a form of error function of the parameter itself, in which the value of the parameter approaches a final value as a simple stochastic process, irrespective of its initial conditons, through a rapid self-adjustment of the state.

6. WIND STRESS OVER WIND WAVES

The final topic of this paper concerns the expression of wind stress over wind waves. It has been pointed out on many occasions that the roughness length, or equivalently the drag coefficient of the water surface, depends not only on the wind speed but also on the state of the water surface. Various attempts have been made to obtain a functional form of the roughness length incorporating the state of wind waves or the wave breaking. However, in view of the complexity of the expressions, together with the wide scattering of data points, a simple dimensional formula by Charnock (1955) has been cited most frequently, but with various values of a constant of proportionality, although the formula contains only a parameter representing the wind field.

A dimensional consideration leads to an expression:

$$z_0{}^* = z_0{}^*(u_*{}^*, \sigma_m{}^*) \tag{5}$$

where $z_0{}^* \equiv z_0/\nu$ is the dimensionless roughness parameter, $u_*{}^* \equiv u_*{}^3/g\nu$ the dimensionless friction velocity representing the overall wind effect, and $\sigma_m{}^* \equiv u_*\sigma_m/g$ the single parameter representing the wind-wave field as stated in the previous section, where σ_m is the frequency at the energy maximum. Charnock's formula

$$z_0 = \beta u_*{}^2/g \tag{6}$$

is equivalent to

$$z_0{}^* = \beta u_*{}^* \tag{7}$$

which is a form of (5) in which $\sigma_m{}^*$ is disregarded. It is shown that another simple form for $z_0{}^*$, using symbols, σ and σ^*, instead of σ_m and $\sigma_m{}^*$ hereafter:

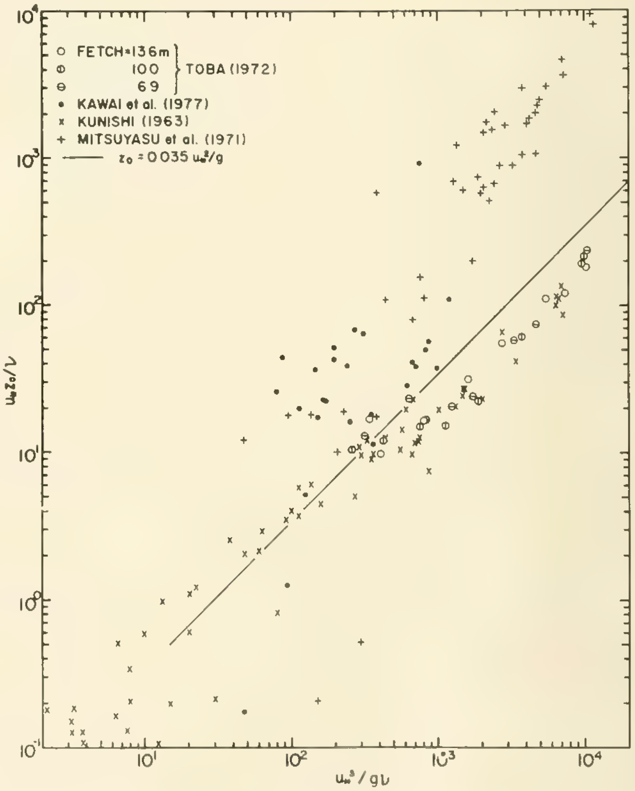

FIGURE 17. Data plots for the relationship (6) in a dimensionless form. Data by Toba (1972) and Kunishi (1963) are from wind-wave tunnel experiments, and data by Kawai et al. (1977) and Mitsuyasu et al. (1971) are from tower-station observations. [Cited from Toba (1978b).]

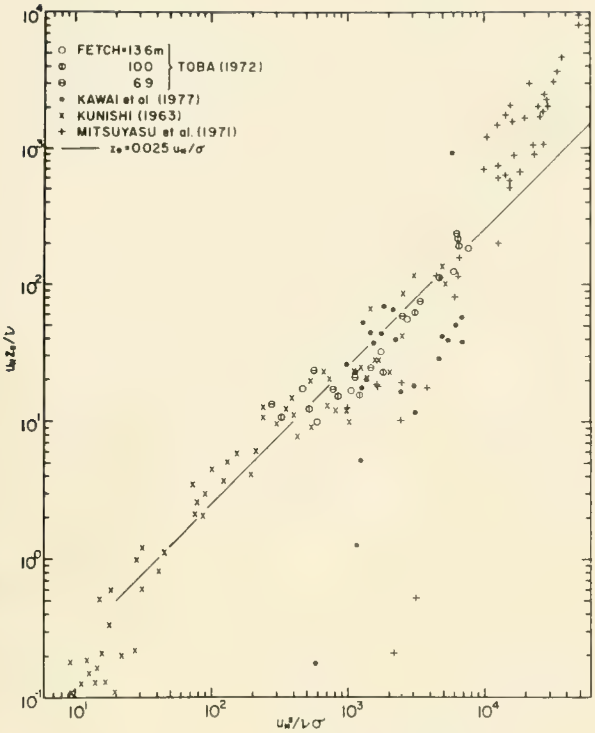

FIGURE 18. Data plots for the relationship (8) in a dimensionless form. The same data with Figure 17 is used. [Cited from Toba (1978b).]

$$z_0^* = \alpha u_*^*/\sigma^* = \alpha u_*^2/\nu\sigma, \quad \alpha = 0.025 \tag{8}$$

is a better representation [Toba (1978b)]*. In Figures 17 and 18 are shown plots of some available data in the forms of (6) and (8) including wind-wave tunnel experiments and field observations. It should be said that the new formula is better at least. It is seen from Figure 19 that the breaking of wind waves is also expressed as a function of the parameter, $u_*^2/\nu\sigma$, for data from the wind-wave tunnel and the sea. The ordinate is the percentage of the breaking crests among individual waves travelling through a fixed point, and it was determined by the same procedure for both cases. The breaking of wind waves occurs for the condition $u_*^2\ \nu\sigma \geq 10^3$.

Equation (8) corresponds to an elimination of g from the form of (5). In view of the recent recognition since Munk (1955) that the waves of high frequency components play a major role in the transfer of momentum from the wind to the sea, it seems rather unreasonable that Eq. (7) contains information only of energy containing waves as σ in the denominator. However, since $u_*^2/\nu = \tau/\mu = \partial u/\mu\eta$ represents the magnitude of the average wind stress, and $\sigma^{-1} \propto T$ is a measure of the integration time associated with individual waves, $u_*^2/\nu\sigma$ is interpreted as a measure of the accumulation of the shearing stress or the concentration of the vorticity at each crest of the individual waves, conveying the horizontal momentum transferred from the air into the interior of the water through forced convection, whether or not the waves are breaking, as stated in Section 3. As this effect increases, the total momentum transfer, as well as the probability of the occurrence of the breaking increases.

The form of (8) may be transformed to

$$z_0 = \beta' u_*^2/g, \quad \beta' = \alpha\, c/u_* \tag{9}$$

which may be interpreted as an extension of Charnock's formula (6) to include information of wind waves in the form of the wave age, c/u_*, where c is the phase speed of the dominant waves. Also, the drag coefficient, C_D, may be expressed from (8) as

$$C_D = \kappa^2/[\ \ln\ (z_{10}\sigma/\alpha u_*)]^{-2} \tag{10}$$

where κ is the von Kármán constant and z_{10} the reference height of 10 m. According to (10), C_D is more sensitive to the wind waves than to the wind speed.

7. SHORT SUMMARY

We may summarize the review paper as follows. First, the initial wavelets are generated by an instability of two-layer viscous shear flow of a type of instability that immediately transfers to three dimensional turbulence. Second, the main phase of the growth of wind waves is regarded as the consequent, strongly nonlinear processes. Third, the traditional component wave model is not necessarily realistic, and the elementary physical substance might better be treated by individual waves, especially for younger stages as observed in wind-wave tunnels. Fourth, the individual waves represent a conspicuous and characteristic similarity of structure, presumably as a result of the strong nonlinearities, and this may be the basis for the pure wind-wave field being represented by a single dimensionless parameter. Finally, a new stress formula over the wind-wave field is presented.

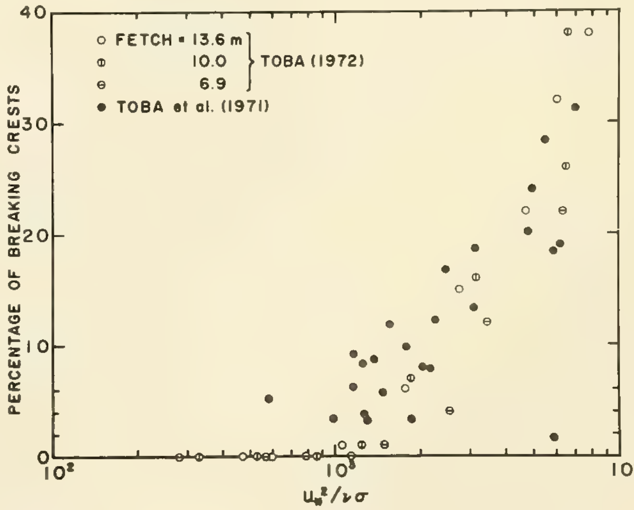

FIGURE 19. Percentage of breaking crests among individual waves traveling through a fixed point, may be expressed as a function of the same parameter with Figure 18. Toba et al. (1971) data are from tower station observations, which are common with data of Kawai et al. (1977) used in Figure 18. [Cited from Toba (1978b).]

---

*Toba, Y. (1978b). A formula of wind stress over wind waves. To be published.

ACKNOWLEDGMENTS

The author expresses many thanks to Messrs. M. Tokuda, K. Okuda, and Dr. S. Kawai of his laboratory for continuous cooperation and discussion, and to Professor H. Kunishi of Kyoto University, Professor K. Kajiura of University of Tokyo, Professor H. Mitsuyasu of Kyushu University, and Dr. N. Iwata of National Research Center for Disaster Prevention for valuable discussion and comments. He also thanks Mrs. F. Ishii for her continuous assistance.

REFERENCES

Charnock, H. (1955). Wind-stress on a water surface. *Quart. J. Roy. Met. Soc. 81,* 639.

Kawai, S. (1977). Study on the generation of wind waves. *Ph. D. Dissertation at Tohoku University,* 100 pp.

Kawai, S. (1978). Generation of initial wavelets by instability of a coupled shear flow and their evolution to wind waves. Submitted to *J. Fluid Mech.*

Kawai, S., K. Okada, and Y. Toba (1977). Support of the three-halves power law and the $gu_*\sigma^{-4}$ -spectral form for growing wind waves with field observational data. *J. Oceanogr. Soc. Japan 33,* 137.

Larson, T. R., and J. W. Wright (1975). Wind-generated gravity-capillary waves: Laboratory measurements of temporal growth rates using microwave backscatter. *J. Fluid Mech. 70,* 417.

Miles, J. W. (1957). On the generation of surface waves by shear flows. *J. Fluid Mech. 3,* 185.

Munk, W. H. (1955). Wind stress on water: an hypothesis. *Quart. J. Roy. Met. Soc. 81,* 320.

Okuda, J. (1977). Internal flow pattern of wind waves, *Proc. Nineth Symp. on Turbulence,* Inst. Space and Aeronautical Sci. Univ. Tokyo, June 1977, 54.

Okuda, K., S. Kawai, M. Tokuda, and Y. Toba (1976). Detailed observation of the wind-exerted surface flow by use of flow visualization methods. *J. Oceanogr. Soc. Japan 32,* 51.

Okuda, J., S. Kawai, and Y. Toba (1977). Measurement of skin friction distribution along the surface of wind waves. *J. Oceanogr. Soc. Japan 33,* 190.

Phillips, O. M. (1957). On the generation of waves by turbulent wind. *J. Fluid Mech. 2,* 417.

Ramamonjiarisoa, A. (1974). Contribution à l'étude de la structure statistique et des mécanismes de génération des vagues de vent, *Thèse à L'Université de Provence Le Grade de Docteur ès Sciences,* 160 pp.

Rikiishi, K. (1978). A new method for measuring the directional wave spectrum. Part II. Measurement of the directional spectrum and phase velocity of laboratory wind waves. *J. Phys. Oceanogr. 8,* 518.

Toba, Y. (1972). Local balance in the air-sea boundary processes, I. On the growth process of wind waves. *J. Oceanogr. Soc. Japan 28,* 109.

Toba, Y. (1973). Local balance in the air-sea boundary processes, III. On the spectrum of wind waves. *J. Oceanogr. Soc. Japan 29,* 209.

Toba, Y. (1978a). Stochastic form of the growth of wind waves in a single-parameter representation with physical implications. *J. Phys. Oceanogr. 8,* 494.

Toba, Y., M. Tokuda, K. Okuda, and S. Kawai (1975). Forced convection accompanying wind waves. *J. Oceanogr. Soc. Japan 31,* 192.

Valenzuela, G. R. (1976). The growth of gravity-capillary waves in a coupled shear flow. *J. Fluid Mech. 76,* 229.

Wilson, B. W. (1965). Numerical prediction of ocean waves in the North Atlantic for December, 1959. *Deut. Hydrogr. Z. 18,* 114.

An Interaction Mechanism between Large and Small Scales for Wind-Generated Water Waves

Marten Landahl,
Sheila Widnall,
and
Lennart Hultgren
Massachusetts Institute of Technology
Cambridge, Massachusetts

ABSTRACT

By aid of a non-linear two-scale analysis it is shown that large-scale water waves can experience growth due to spatial non-uniformities in the growth rate of the small-scale waves in the non-uniform wind field associated with the large-scale waves. The growth rate is shown to be proportional to the mean-square slope of the small-scale waves and their growth rates, but inversely proportional to the difference between the phase velocity of the large-scale wave and the group velocity of the small-scale waves. It is suggested that this mechanism can transfer wind energy to short gravity waves at a higher rate than the direct linear transfer mechanism of Miles (1962). The analysis also predicts that a large-scale wave moving against the wind will be damped by the action of the small-scale waves.

1. INTRODUCTION

The mechanism whereby wind generates water waves has long proven a difficult and challenging problem in theoretical fluid mechanics which has not yet been satisfactorily resolved. The simple linear mechanism of forcing by pressure fluctuations [Phillips (1957)] and by instability induced by the mean wind field [Miles (1957), 1962)] have been found inadequate to account for the high values of energy transfer from wind to waves observed for longer waves, both in the laboratory and in the open sea. For short waves in the capillary regime, laboratory experiments [Larson and Wright (1975)] have given good agreement between observed growth rates and Miles' instability theory, particularly when the surface drift velocity in the water is taken into account [Valenzuela (1976)]. For waves in the short gravity range, however, recent experiments by Plant and Wright (1977) give growth rates much in excess of that predicted by the instability theory with the discrepancy beginning at a wave length of about 10 cm and increasing with wave length. Open-sea measurements have also produced energy transfer rates for gravity waves which are much in excess of the values according to Miles. [See, for example, the recent review of Barnett and Kenyon (1975)].

In view of the failure of linear theory one is forced to look for nonlinear mechanisms for energy transfer. Nonlinear interaction between waves in the gravity range [Phillips (1966)] is a comparatively weak process (of third order in amplitude) which causes redistribution of the energy from waves of intermediate wave numbers to waves of lower and higher wave numbers. This could be effective for the eventual saturation of the spectrum but is unlikely to be strong enough to make a large change in the initial growth. A more tenable proposition is that the modification of the turbulence in the air by the wave induced velocity field could change the phase shift between surface elevation and the pressure so as to alter the energy transfer rate. This effect has been investigated by many authors [Manton (1972), Davies (1972), and Townsend (1972), among others] employing different turbulence models. These investigations point to the possibility that the modulation of the turbulence by the wind could have an important effect, but it is difficult to assess the adequacy of the postulated turbulence models employed.

An interesting possibility for transfer of energy to gravity waves is through nonlinear interaction with capillary waves which can draw energy from wind at a much higher rate than the longer waves. The interaction between short and long surface waves has been subject to a great deal of discussion in the literature. A train of short waves riding on a long wave becomes modulated by the orbital velocity field of the long wave so as to make their wave length smaller - and hence their amplitude greater - in the region near the crest of the long wave. Longuet-Higgins (1969) argued that the radiation stress then set up by the short-wave train would act to transfer momentum to the long wave. In particular, if the short wave were to reach an amplitude at the crest of the long wave high enough for breaking, it would give up all its momentum to the long wave. This maser-like mechanism was examined critically by Hasselman (1971) who showed that the change in potential energy in the surface layer due to Stokes' transport by the short waves would give a contribution to the energy transfer to the large waves which would exactly cancel that arising from Longuet-Higgins' momentum transfer term. Hasselman's analysis did not take into account any transfer due to modulation of surface wind stress or short wave growth rate, however. [This effect has been analysed by Valenzuela and Wright (1976)]. Also, his analysis concerned primarily gravity waves, for which resonant interaction between wave number triads only occurs to third order. For capillary-gravity waves, however, the dispersion relation allows resonant interaction at second order. Valenzuela and Laing (1972) have developed a theory for this, and Plant and Wright (1977) suggest that part of the measured excess growth rate in the low gravity wave range could be attributed to capillary-gravity resonant interaction. Benny (1976) has also shown that under certain conditions, a long gravity wave may grow in the presence of small scale capillary waves; the wind field was not included in his analysis.

The present paper reveals yet another possible mechanism for the transfer of energy from capillary to short gravity waves. The theory presented takes into account the effect of shear flow modulation on the local growth rate of the capillaries. It is found that this variation gives rise to a modulation of the Stokes' drift which is in phase with the long-wave surface slope and therefore makes possible an energy interchange with the long wave. It is found that the energy transfer rate due to this mechanism is positive for capillaries with a group velocity higher than the phase velocity of the long wave so that it can provide an increase in the long-wave growth for waves in the short gravity wave regime. For waves running against the wind the transfer rate is found to be negative, so that the presence of the capillaries would always increase the decay rate of the long waves.

2. INTERACTION BETWEEN LONG AND SHORT WAVES

We shall consider the situation depicted in Figure 1 with two-dimensional surface wave of small wave length, λ', riding on a large-scale wave of wave length, $\tilde{\lambda}$. An asymptotic analysis will be carried out under the assumption that

$$\varepsilon \equiv \lambda'/\tilde{\lambda} << 1 \qquad (1)$$

(Prime refers to the short and tilde to the long waves). The waves are excited by a wind field blowing over the water surface. Only the normal stress induced by the wind on the wavy surface is considered in this process, the effect of shear stresses being neglected. Of particular interest is whether the presence of the small-scale waves could change the growth rate of small-amplitude long waves.

To arrive at the simplest possible analysis, terms that are of higher order than linear in the long-wave slope are neglected. For the short waves, only quadratic and lower-order terms in the wave slope are retained. Further, it will be assumed that the flow in the water is irrotational, i.e., the effects of surface drift currents are neglected. This allows the use of potential-flow theory leading to the following boundary-value problem for the velocity potential Φ in deep water:

$$\nabla^2\Phi \equiv \Phi_{xx} + \Phi_{zz} = 0 \qquad (2)$$

with boundary conditions

$$\text{at } z = \zeta: \begin{cases} \Phi_z = \zeta_t + \Phi_x\zeta_x & (3) \\ \dfrac{P_W}{\rho} = -g\zeta - \Phi_t - \dfrac{1}{2}|\nabla\Phi|^2 + T\zeta_{xx}/(1+\zeta_x^2)^{3/2} & (4) \end{cases}$$

$$\text{at } z = -\infty: \quad \Phi = 0 \qquad (5)$$

Here, $\zeta = \zeta(x,t)$ is the surface deflection, P_w the surface pressure due to the wind, and T the surface tension. Since cubic terms are neglected throughout, the denominator in the last term of (4) will be set equal to unity henceforth. We now separate large and small scales by introducing into the equations of motion

$$\zeta = \tilde{\zeta} + \zeta' \qquad (6)$$

$$\Phi = \tilde{\Phi} + \Phi' \qquad (7)$$

$$P_W = \tilde{p}_W + p'_W \qquad (8)$$

For the boundary conditions it is useful first to transfer them to the surface of the large-scale motion, $z = \tilde{\zeta}$, by a Taylor series expansion. Thus,

$$\begin{aligned} \Phi_z(x,\zeta) &= \Phi_z(x,\tilde{\zeta}) + \zeta'\Phi_{zz}(x,\tilde{\zeta}) + \ldots \\ &\equiv \tilde{\Phi}_z(x,\tilde{\zeta}) + \Phi'_z(x,\tilde{\zeta}) + \zeta'(\tilde{\Phi}_{zz}(x,\tilde{\zeta}) \\ &\quad + \Phi'_{zz}(x,\tilde{\zeta})) + \ldots \end{aligned} \qquad (9)$$

etc. By neglecting terms involving triple and higher products one finds from (4) and (5) the following boundary conditions to be applied at $z = \tilde{\zeta}$:

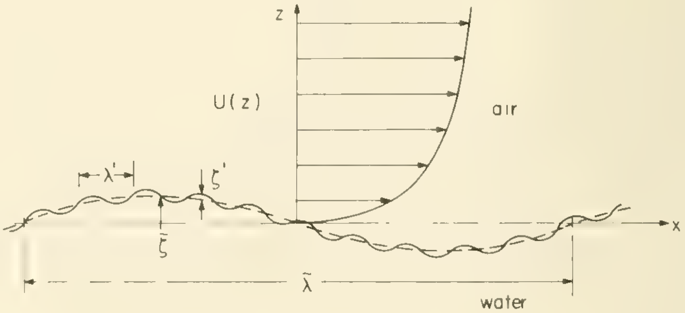

FIGURE 1. Long-wave short-wave interactions in a shear flow.

$$\tilde{\Phi}_z + \Phi'_z = \tilde{\zeta}_t + \zeta'_t + (\tilde{\Phi}_x + \Phi'_x)\tilde{\zeta}_x + \frac{\partial}{\partial x}[\zeta'(\tilde{\Phi}_x + \Phi'_x)] + \ldots \tag{10}$$

$$\frac{1}{\rho}(\tilde{p}_w + p'_w) = -g(\tilde{\zeta} + \zeta'_t) - (\tilde{\Phi}_t + \Phi'_t) - \zeta'(\tilde{\Phi}_{tz} + \Phi'_{tz}) - \frac{1}{2}[(\tilde{\Phi}_x + \Phi'_x)^2 + (\tilde{\Phi}_z + \Phi'_z)^2] + T(\tilde{\zeta}_{xx} + \zeta'_{xx}) + \ldots \tag{11}$$

In (11), $\tilde{P}_w$ is the surface pressure in the absence of the short waves and p'_w the additional surface pressure added due to the presence of the short waves. In deriving (10), partial use has been made of (2), which holds for $\tilde{\Phi}$ and Φ' separately. To arrive at equations for the long wave, (10) and (11) are averaged over the large scales. This is most conveniently done by taking the ensemble average of a large number of realizations differing only as to the phase of the short waves, which is assumed to be randomly distributed among the members of the ensemble. This procedure yields

$$\tilde{\Phi}_z = \tilde{\zeta}_t + \tilde{\Phi}_x\tilde{\zeta}_x + S'_x + \ldots \tag{12}$$

$$\frac{\tilde{P}_w}{\rho} = g\tilde{\zeta} - \tilde{\Phi}_t - \frac{1}{2}(\tilde{\Phi}^2_x + \tilde{\Phi}^2_x) + T\tilde{\zeta}_{xx} - \frac{1}{2}\frac{\partial^2}{\partial t^2}(\widetilde{\zeta'^2}) - \frac{1}{2}(\widetilde{\Phi'^2_x} - \widetilde{\Phi'^2_z}) + \ldots \tag{13}$$

at $z = \tilde{\zeta}$, where the tilde denotes the average over the large scales and

$$S' = \widetilde{\zeta'\Phi'_x} \tag{14}$$

is the Stokes' drift due to the small-scale motion. In deriving (13), use has been made of the linearized boundary conditions for the small scales, for example,

$$\widetilde{\zeta'\Phi'}_{tz} = \widetilde{\zeta'\zeta'}_{tt} + \ldots = \frac{\partial}{\partial t}(\widetilde{\zeta'\zeta'_t}) - \widetilde{\zeta'^2_t} + \ldots = \frac{1}{2}\frac{\partial^2}{\partial_t^2}(\widetilde{\zeta'^2}) - \widetilde{\Phi'^2_z} + \ldots \tag{15}$$

The long waves are to be determined as a solution of Laplace's equation

$$\nabla^2\tilde{\Phi} = 0 \tag{16}$$

subject to the boundary conditions (12) and (13) and the condition that disturbances vanish at large depths, i.e.,

$$\tilde{\Phi} = 0 \quad \text{for } z = -\infty \tag{17}$$

The corresponding boundary conditions for the short waves are obtained by subtracting those for the long waves from the full equations.

$$\Phi'_z = \zeta'_t + \Phi'_x\tilde{\zeta}_x + \tilde{\Phi}_x\zeta'_x + \zeta'\tilde{\Phi}_{xx} + \frac{\partial}{\partial x}(\zeta'\Phi'_x - \widetilde{\zeta'\Phi'_x}) + \ldots \tag{18}$$

$$\frac{P'_w}{\rho} = -(g + \tilde{\zeta}_{tt})\zeta' - \Phi'_t + T\zeta'_{xx} - \tilde{\Phi}_x\Phi'_x - \tilde{\Phi}_z\Phi'_z - \frac{1}{2}(\Phi'^2_x - \phi'^2_z - \widetilde{\phi'^2_x} + \widetilde{\phi'^2_z}) + \frac{1}{2}\frac{\partial^2}{\partial t^2}(\widetilde{\zeta'^2} - \zeta'^2) + \ldots. \tag{19}$$

both to be applied at $z = \tilde{\zeta}$. The last bracketed term of (18) and the last two of (19) will give rise to higher harmonics. Their contribution to the large-scale motion will be of higher order, and they can hence be neglected. In deriving (19), use was made of the linearized boundary conditions for the long waves. Thus, for example, the term $\tilde{\zeta}_{tt}\zeta'$ in (19) arises from replacing $\tilde{\Phi}_{tz}$ in (11) by $\tilde{\zeta}_{tt}$, which will give a negligible error to within the approximation employed.

Since the major aim of the analysis is to determine the lowest-order effect of the short waves on the growth rate of the long waves, it is sufficient to retain only linear terms. However, all terms linear in the large-scale motion which modulate the small-scale wave train must be retained. The long wave will be taken as a uniform, infinite wave train of wave number $\tilde{k} = 2\pi/\tilde{\lambda}$. Its phase velocity differs from the linearized value,

$$\tilde{c} = \sqrt{g/\tilde{k} + \tilde{k}T} \tag{20}$$

by terms proportional to the square of the small-scale wave slope, and by terms due to the wind, which are proportional to the density ratio between air and water both of which may be expected to be small. The short waves driven by the wind may also give rise to slow growth, or decay, of the large-scale waves. For the subsequent analysis, it is convenient to introduce the following nondimensional "slow" variables:

$$\xi = \tilde{k}(x - \tilde{c}t) \tag{21}$$

$$\tau = \tilde{k}\,\tilde{c}\,t \tag{22}$$

The solution for the long wave is sought in the form (real part always implied)

$$\tilde{\zeta} = \hat{\tilde{\zeta}}(\tau)e^{i\xi} \tag{23}$$

$$\tilde{\Phi} = \hat{\tilde{\Phi}}(\tau)e^{i\xi+\tilde{k}z} \tag{24}$$

The variation of the surface deflection and potential with the "slow" time, τ, allows for the effects of wind, and the presence of the short waves, to have a weak influence on the growth rate, and the phase (and consequently also the phase velocity) of the long waves. Without the wind and the short waves both $\hat{\tilde{\zeta}}$ and $\hat{\tilde{\Phi}}$ would be constants.

For the short-waves, on the other hand, both the phase velocity and wave number will vary slowly along the long wave because of the modulation by the latter. We therefore set

$$\zeta' = \hat{\zeta}'(\xi,\tau)e^{i\theta(x,t)} \tag{25}$$

$$\Phi' = \hat{\Phi}'(\xi,z',\tau)e^{i\theta(x,t)} \tag{26}$$

where θ is the phase,

$$k' = \theta_x \tag{27}$$

is the wave number,

$$\omega' = -\theta_t \tag{28}$$

is the frequency (measured in a fixed coordinate system), and

$$z' = k'(z - \tilde\zeta). \tag{29}$$

The assumption of a slowly varying wave train allows one to regard k' and ω' as functions of the "slow" variables, τ and ξ.

An approximate asymptotic solution for the short waves if sound by expansion in the small quantity

$$\varepsilon = \tilde k/k' \tag{30}$$

(That ε thus defined is a slowly varying quantity causes no special difficulty). Substitution of (25) - (29) into (18) and (19) and omission of all terms of order $|\zeta'|^2$, $|\tilde\zeta^2\zeta'|$, and higher, as well as of terms of order ε^2 and higher, gives the following boundary conditions for the small-scale motion to be satisfied at $z' = 0$:

$$\hat\Phi'_z = -i\hat\zeta'(c'-\tilde u) + \varepsilon\tilde u\hat\zeta'_\xi + \varepsilon\tilde c(\hat\zeta'_\tau - \hat\zeta'_\xi) + i\varepsilon k\tilde\zeta_\xi\hat\Phi'$$
$$+\dots \tag{31}$$

$$\frac{\hat p'_w}{\rho} = -(g + k'^2T)\hat\zeta' + ik'(c'-\tilde u)\hat\Phi'$$
$$+ i\varepsilon k'[i\tilde u\hat\Phi'_\xi + i\tilde c(\hat\Phi'_\tau - \hat\Phi'_\xi) + 2k'T\hat\zeta'_\xi + k'_\xi T\hat\zeta']$$
$$- k'\hat\Phi'_{z'}[\tilde w - \tilde k\tilde c(\tilde\zeta_\tau - \tilde\zeta_\xi)] + \dots \tag{32}$$

where

$$c' = \omega'/k' \tag{33}$$

$\tilde u$ and $\tilde w$ are the perturbation velocities, $\tilde\Phi_x$ and $\tilde\Phi_z$ respectively, of the large-scale-flow evaluated at $z = \tilde\zeta$ and p'_w is defined by

$$\frac{p'_w}{\rho} = \frac{1}{\rho}\hat p'_w e^{i\theta} \tag{34}$$

The terms neglected as being of higher order in ε include the term $\tilde\zeta_{tt}\hat\zeta'$ in (19), which expressed in the slow coordinates becomes

$$\varepsilon^2 k'^2 \hat\zeta' \left(\frac{\partial}{\partial\tau} - \frac{\partial}{\partial\xi}\right)^2 \tilde\zeta$$

and is hence negligible compared to the term $k'^2T\hat\zeta'$. For the long waves one finds similarly

$$\tilde\Phi_z \equiv \tilde w = \tilde k[\tilde c(\tilde\zeta_\tau - i\tilde\zeta) + S'_\xi] + \dots \tag{35}$$

$$\frac{\tilde p_w}{\rho} = -(g + \tilde k^2\ T)\ \tilde\zeta - \tilde k\tilde c(\tilde\Phi_\tau - i\tilde\Phi)$$
$$- \frac{1}{4}\tilde k^2\tilde c^2\left(\frac{\partial}{\partial\tau} - \frac{\partial}{\partial\xi}\right)^2 |\hat\zeta'|^2$$
$$- \frac{1}{4}k'^2[\,|i\hat\Phi' + \varepsilon\hat\Phi'_\xi|^2 - \Phi'_z|^2] + \dots \tag{36}$$

where

$$S' = \text{R.P.}\{\frac{k'}{2}\hat\zeta'^*(i\hat\Phi' + \varepsilon\hat\Phi'_\xi)\} \tag{37}$$

and the star denotes complex conjugate. The velocity potential must satisfy Laplace's equation. Substitution of (26)-(29) into (2) gives

$$k'^2(\hat\Phi'_{z'z'} - \hat\Phi') + i\varepsilon k'[\,k'_\xi\hat\Phi' + 2k'\hat\Phi'_\xi$$
$$+ 2(z'k'_\xi - \tilde\zeta_\xi k'^2)\hat\Phi'_{z'}]$$
$$+ 0(\varepsilon^2\hat\Phi') = 0 \tag{38}$$

This equation may be solved approximately by series expansion in ε. One finds in a straight-forward manner that

$$\hat\Phi' = e^{z'}\ \{[1 - i\varepsilon(\frac{z'^2}{2}\frac{k'_\xi}{k'} - k'z'\tilde\zeta_\xi)]\hat A - i\varepsilon z\hat A_\xi + 0(\varepsilon^2 A)\} \tag{39}$$

where $\hat A = \hat A(\xi,\tau)$ is to be determined by aid of the kinematic boundary condition (31). By substitution of (39) into (31) and expanding in powers of ε one finds

$$\hat A = -i(c'-\tilde u)\hat\zeta' + \varepsilon\{(c'\hat\zeta')_\xi + \tilde c(\hat\zeta'_\tau - \hat\zeta'_\xi)\}$$
$$+ 0(\varepsilon^2\hat\zeta') \tag{40}$$

Combination of (40) and (32) yields

$$\frac{\hat p'_w}{\rho} = -[g + k'^2T - k'(c'-\tilde u)^2]\hat\zeta' + i\varepsilon k'\{[\tilde c(c' - \tilde u)_\tau$$
$$+ (c'-\tilde u)\tilde u_\xi + (c'-\tilde c)(c' - \tilde u)_\xi + k'_\xi T]\hat\zeta'$$
$$+ 2\tilde c(c'-\tilde u)\hat\zeta'_\tau$$
$$+ [(c'-\tilde u)(c'-2\tilde c + \tilde u) + 2k'T]\hat\zeta'_\xi\ \} \tag{41}$$

The induced surface pressure due to the wind may be assumed to be related to the small-scale surface deflection in a quasilinear manner that takes into account the modulation of the wind field by the long waves. The following expression is chosen:

$$\frac{\hat p'_w}{\rho} = k'(c'-\tilde u)(\alpha' + i\beta')(1 - ak\tilde\zeta)\hat\zeta' \tag{42}$$

where α' and β' are aerodynamic coefficients (having the dimension of velocity) giving the in-phase and out-of-phase components, respectively, of the induced pressure. The modulation of the wind field due to the presence of the long waves is accounted for by the factor $(1 - a\tilde k\tilde\zeta)$. For long waves running with the wind and having a phase velocity less than the wind-speed, the air flow at the crest will slow down in the region below the matched layer where $U = \tilde c$, and the small-scale growth rate will thus be reduced in this region. Conversely, the air speed will increase over the troughs leading to an increased growth rate there. Hence, the coefficient, a, will be positive for such waves. For waves running against the wind, however, or for waves with $\tilde c$ greater than the wind speed, a will be negative. To determine the numerical value of a, one must carry out calculations based on the Orr-Sommerfeld equation. First the wind field modulation due to a long wave of small amplitude is calculated. Then, the pressure on the short waves is computed on the basis of quasilinear theory, whereafter the effect of wind field modulations may be extracted from the results. In Section 3, we derive the governing equations for the local growth rate for short waves in the modulated flow of the long waves. Numerical results for a are presented in Section 4.

Consistency of the two-scale expansion requires that the wind-induced growth rate is small, which is indeed the case, since it is proportional to the air-to-water density ratio. Accordingly, we shall set, formally,

$$\alpha' + i\beta' = \varepsilon(\bar{\alpha} + i\bar{\beta}) \qquad (43)$$

Substituting (42) and (43) into (41) and remembering that all the quantities involved are real, we find the following pair of relations:

$$g + k'^2T - k'(c'-\tilde{u})^2 + \varepsilon k'\bar{\alpha}(c'-\tilde{u})(1 - a\tilde{k}\tilde{\zeta}) = 0 \qquad (44)$$

$$\begin{aligned}[\tilde{c}(c'-\tilde{u})_\tau &+ (c'-\tilde{c})(c'-\tilde{u})_\xi + (c'-\tilde{u})\tilde{u}_\xi \\ &+ k'_\xi T - \bar{\beta}(c'-\tilde{u})(1 - a\tilde{k}\tilde{\zeta})]\hat{\zeta}' \\ &+ 2\tilde{c}(c'-\tilde{u})\hat{\zeta}'_\tau + [(c'-\tilde{u})(c'-2\tilde{c} + \tilde{u}) \\ &+ 2k'T]\hat{\zeta}'_\xi = 0 \end{aligned} \qquad (45)$$

From (44) it thus follows that

$$c' = \tilde{u} + \sqrt{g/k' + k'T} + 0(\varepsilon) \equiv \tilde{u} + v(k') - 0(\varepsilon) \qquad (46)$$

Inspection of (35) and (36) reveals that the long waves receive their growth both directly from wind pressure and indirectly from interaction with the short waves, the latter effect being proportional to the mean-square slope of the short waves. Thus, since the variation of long-wave parameters with time is small, little error is incurred by taking $\tilde{u}$ in (46) to be a function of ξ alone. Furthermore, the frequency of the short waves must then be constant in a coordinate system travelling with the long waves so that

$$k'(c' - \tilde{c}) = \omega'_0 \qquad (47)$$

which, together with (46) determines how the wave number for the short waves varies along the wave train. Differentiation of (47) gives

$$\frac{\partial k'}{\partial \xi} = -\frac{k'\tilde{u}_\xi}{c'_g - \tilde{c}} \qquad (48)$$

where c'_g is the group velocity,

$$c'_g = k'v_{k'} + v + \tilde{u} \qquad (49)$$

and where $v(k')$ is defined by (46). With the aid of (46)-(49), (45) may thus be written

$$\begin{aligned}2(c'-\tilde{u})[\tilde{c}\hat{\zeta}'_\tau + (c'_g - \tilde{c})\hat{\zeta}'_\xi] = \{&(c'-\tilde{u})\bar{\beta}(1 - a\tilde{k}\tilde{\zeta}) \\ &- (c'-\tilde{u})\tilde{u}_\xi + [(c'-\tilde{c})v_k' + T] \\ &k'\tilde{u}_\xi/(c'_g - \tilde{c})\}\hat{\zeta}\end{aligned} \qquad (50)$$

This equation may be readily solved by integration along the characteristic line

$$\tau = \tau_1 \ ; \quad d\xi/d\tau_1 = (c'_g - \tilde{c})/\tilde{c} \qquad (51)$$

Since only the terms which are linear in the large-scale perturbation are to be retained, one may ignore the variation of k' with ξ when carrying out this integration.

$$\begin{aligned}\hat{\zeta}^1 \simeq C \exp\{\frac{\bar{\beta}}{2\tilde{c}}\tau - \frac{a\tilde{k}}{2}\int^\xi \frac{\tilde{\beta}\tilde{\zeta}d\xi_1}{(c'_g-\tilde{c})} - \frac{\tilde{u}}{2(c'_g-\tilde{c})} \\ + \frac{k'\tilde{u}}{2v(c'_g-\tilde{c})^2}[(c' - \tilde{c})v_{k'} + T]\}\end{aligned} \qquad (52)$$

where C is a constant to be determined from the initial value of $\hat{\zeta}$. By inserting this expression into (37) one finds

$$\begin{aligned}S'_\xi = -\tilde{S}'^2 \Bigg[\frac{a\beta'\tilde{\zeta}v}{(c'_g-\tilde{c})} + \frac{\tilde{u}_\xi}{k'(c'_g-\tilde{c})}\{c'_g + c' - 2\tilde{u} \\ - \frac{k'}{(c'_g-\tilde{c})}[(c' - \tilde{c})v_{k'} + T]\}\Bigg]\end{aligned} \qquad (53)$$

where

$$\tilde{S}'^2 = \frac{1}{2}|k'\hat{\zeta}'|^2 \qquad (54)$$

is the mean-square slope of the short waves. (In Appendix A an alternative derivation, based on kinematic wave theory, is given.) In the second bracketed term $\tilde{u}$ may be expressed in terms of $\tilde{\zeta}$ by the use of the linearized expression

$$\tilde{u} = \tilde{k}\tilde{c}\tilde{\zeta} \qquad (55)$$

Thus, S'_ξ may be written

$$S'_\xi = A'\tilde{\zeta} + B'\tilde{\zeta}_\xi \qquad (56)$$

where (ignoring terms which are nonlinear in $\tilde{\zeta}$)

$$A' = -\tilde{S}'^2 \frac{a\beta' v}{(c'_g-\tilde{c})} \qquad (57)$$

$$\begin{aligned}B' = \varepsilon \frac{\hat{S}'^2\tilde{c}}{(c'_g-\tilde{c})}&\{-c'_g - c' + 2\tilde{u} \\ &+ \frac{k'}{(c'_g-\tilde{c})}[(c'-\tilde{c})v_k' + T]\}\end{aligned} \qquad (58)$$

The boundary conditions for the long waves may now be written. Substitution of the solution for the short waves, and (24), into (35) and (36), gives

$$\tilde{\Phi} = \tilde{c}(\tilde{\zeta}_\tau - i\tilde{\zeta}) + A'\tilde{\zeta} + iB'\tilde{\zeta} \qquad (59)$$

$$\frac{\tilde{P}_w}{\rho} = -(g + \tilde{k}^2T)\tilde{\zeta} - \tilde{k}\tilde{c}(\Phi_\tau - i\tilde{\Phi}) + 0(\varepsilon^2) \qquad (60)$$

For the wave-induced pressure an expression similar to (42) is used, namely

$$\frac{\tilde{P}_w}{\rho} = \tilde{k}\tilde{c}(\tilde{\alpha} + i\tilde{\beta})\tilde{\zeta} \qquad (61)$$

Substitution of this and (59) into (60) and separation into real and imaginary parts yields

$$0 = [g + \tilde{k}^2T - \tilde{k}\tilde{c}^2 - \tilde{k}\tilde{c}(B + \tilde{\alpha})]\tilde{\zeta} - \tilde{k}\tilde{c}^2\tilde{\zeta}_{\tau\tau} + \tilde{k}\tilde{c}\tilde{\zeta}_\tau \qquad (62)$$

$$(\tilde{\beta} - A')\tilde{\zeta} = (2\tilde{c} - B')\tilde{\zeta}_\tau \tag{63}$$

From (63) we find

$$\tilde{\zeta} = \tilde{\zeta}_0 \exp \int^{\tau} \frac{\tilde{\beta}-A'}{2\tilde{c}-B'}\, d\tau_1 \tag{64}$$

By use of this, $\tilde{\zeta}_\tau$ and $\tilde{\zeta}_{\tau\tau}$ may be expressed in terms of $\tilde{\xi}$ and an eigenvalue relation obtained by substitution into (62). This then gives

$$\tilde{c} = \sqrt{g/\tilde{k} + \tilde{k}T} \; + \ldots \tag{65}$$

with correction terms proportional to the mean square slope of the short waves and to the air-to-water density ratio, both of which are likely to be small corrections of little importance. The major result of the analysis is that given by (63), (64) namely that

$$\frac{d}{d\tau}(\ell n\tilde{\zeta}) = \frac{\tilde{\beta}-A'}{2\tilde{c}-B'} \simeq \frac{\tilde{\beta}}{2\tilde{c}} + \frac{a\beta' c'}{2\tilde{c}(c'_g-\tilde{c})}\, \tilde{S}'^2 \tag{66}$$

i.e., the growth of the long-wave amplitude is given by the sum of the growth due to direct action of pressures in the manner of Miles (1957, 1962) and the indirect growth due to the Stokes' transport by the growing short waves. The second term may be large compared to the first term, if c'_g is close to $\tilde{c}$. However, the analysis presented does not hold in the immediate neighborhood of $c'_g = \tilde{c}$ but a separate (and nonlinear) analysis is then required. For waves running against the wind, c', c'_g, and a will be negative, so that the presence of the short waves will always increase the decay rate of the long wave.

3. THE WIND-INDUCED GROWTH OF SHORT WAVES IN THE PRESENCE OF LONG WAVES

The perturbation equation governing the modification of short waves on the wind-water interface by the long-wave field is derived from the momentum equation by the procedure used to derive the Orr-Sommerfeld equation. Additional effects arise because the short waves see not only the mean wind field, $U(z)$, but long-wave fluctuations, $\tilde{u}$ and $\tilde{w}$. The large-scale field is governed by a linear equation, the small-scale field by an equation linear in u', w' which also contains terms linear in $\tilde{u}$ and $\tilde{w}$.

As in 2, we take the water to be inviscid and the flow potential but we consider the air to be viscous: with no surface current, and continuous tangential velocity between air and water, this corresponds to the limit $\mu_w \to \infty$, $\nu_w \to 0$ with μ_a and ν_a finite, justified by the large density ratio between water and air. Both fluids are taken to be incompressible.

We begin with the Navier-Stokes equations for two-dimensional flow in the air

$$\frac{\partial u}{\partial t} + u\frac{\partial u}{\partial x} + w\frac{\partial u}{\partial z} = -\frac{\partial p}{\partial x}\frac{1}{\rho} + \frac{1}{R}\nabla^2 u \tag{67}$$

$$\frac{\partial w}{\partial t} + u\frac{\partial w}{\partial x} + w\frac{\partial w}{\partial z} = -\frac{\partial p}{\partial z}\frac{1}{\rho} + \frac{1}{R}\nabla^2 w \tag{68}$$

where velocities are scaled to free stream velocity outside the boundary layer over the water, and lengths scaled to boundary-layer thickness δ ; R is the Reynolds number based on δ. (In Section 2, lengths were scaled to k', the short-scale wave number).

To derive the Orr-Sommerfeld equation, these equations are cross-differentiated and subtracted to eliminate the pressure. Some use is made of the continuity equation and the result is

$$\frac{\partial^2 u}{\partial z\partial t} - \frac{\partial^2 w}{\partial x\partial t} - u\nabla^2 w + w\nabla^2 u - \frac{1}{R}\nabla^2\frac{\partial u}{\partial z} + \frac{1}{R}\nabla^2\frac{\partial w}{\partial x} = 0 \tag{69}$$

The flow in the air is taken to be a horizontal shear flow plus two wave perturbations of disparate scales: the fast scale, x and t; and the slow scale, $\tilde{x} = \varepsilon x$, and $\tilde{t} = \varepsilon t$ where $\varepsilon = \tilde{k}/k'$. The variation with z is set by the shear profile and viscous effects and will be taken to be the same order for both wave fields. The long wave field is a function of $\tilde{x}, z$, and $\tilde{t}$ only; the short wave field is a function of x, z, and t and in addition will be influenced by the long scale waves so that

$$u = U(z) + \tilde{u}(\tilde{x},z,\tilde{t}) + u'(x,z,t;\tilde{x},\tilde{t})$$

$$w = \tilde{w}(\tilde{x},z,\hat{t}) + w'(x,z,t;\tilde{x},\tilde{t}) \tag{70}$$

The surface deflection is taken as

$$\zeta = \tilde{\zeta}\,(\tilde{x},\tilde{t}) + \zeta'(x,t;\tilde{x},\tilde{t})$$

The major effect of long waves in a parallel shear flow on the behavior of the short waves will come from changes in the local growth rate and convection velocities as well as an unsteady lifting of the small scale as the large waves pass. Therefore the small scales will be assumed to be of the form

$$w'(x,z,t;\tilde{x},\tilde{t}) = \hat{w}[z-\tilde{\zeta}(\tilde{x},\tilde{t})]e^{ik(x-ct)} = \hat{w}(z')e^{i\theta}$$

$$u'(x,z,t;\tilde{x},\tilde{t}) = \hat{u}[z-\tilde{\zeta}(\tilde{x},\tilde{t})]e^{ik(x-ct)} = \hat{u}(z')e^{i\theta} \tag{71}$$

where $z' = z-\zeta$ and $c = c(\tilde{x},\tilde{t})$. Changes in the wave number, k, are $O(\varepsilon\partial\tilde{u}/\partial\tilde{x})$; such terms will be ignored in this local analysis. For this assumed form of w' and u', the continuity equation becomes

$$\frac{\partial w'}{\partial z} + iku' - \varepsilon\frac{\partial u'}{\partial z}\frac{\partial\tilde{\zeta}}{\partial\tilde{x}} = 0 \tag{72}$$

which to lowest order becomes

$$\hat{u} = \frac{i}{k}\frac{d\hat{w}}{dz} + \frac{\varepsilon}{k^2}\tilde{\zeta}_{\tilde{x}}\frac{d^2\hat{w}}{dz^2} = \frac{i}{k}\frac{d\hat{w}}{dz} - \frac{\tilde{w}}{\tilde{c}}\frac{1}{k^2}\frac{d^2\hat{w}}{dz^2} \tag{73}$$

since $\varepsilon\tilde{\zeta}_{\tilde{x}} = -\tilde{w}/\tilde{c}$. The presence of $\tilde{\zeta}$ in the assumed form for w' and u' introduces several terms into the equation for the small scale. In addition, the velocity perturbations, $\tilde{u}$ and $\tilde{w}$, also appear.

The equation for the large scale is obtained by a phase average of (69) written with the assumed form (70) and (71). The non-linear coupling of the small-scale motions will not be included although the corresponding effects in the water are the main subject of this paper and are worked out in Section 2. We anticipate further work to complete the study of non-linear coupling in both the air and the water.

The large-scale motions are taken as

$$\tilde{u} = \hat{\tilde{u}}\, e^{j\tilde{k}(\tilde{x}-\tilde{c}\tilde{t})}; \quad \tilde{w} = \hat{\tilde{w}}\, e^{j\tilde{k}(\tilde{x}-\tilde{c}\tilde{t})} \tag{74}$$

with $\tilde{\zeta} = \hat{\tilde{\zeta}}\, e^{j\tilde{k}(\tilde{x}-\tilde{c}t)}$

To ease the process of working with products of wave perturbations, two distinct complex variables i and j are introduced.

Under these assumptions, the large-scale motions are governed by the linear homogeneous Orr-Sommerfeld equation

$$\hat{\tilde{w}}'''' - 2\tilde{k}^2\hat{\tilde{w}}'' + \tilde{k}^4\hat{\tilde{w}} - j\tilde{k}R((U-\tilde{c})(\hat{\tilde{w}}'' - \tilde{k}^2\hat{\tilde{w}}) - \hat{\tilde{w}}U'') = 0 \tag{75a}$$

and $\hat{\tilde{u}}$ is related to $\hat{\tilde{w}}$ through the continuity equation

$$\hat{\tilde{u}} = j\hat{\tilde{w}}'/\tilde{k} \tag{75b}$$

where from now on primes will denote derivatives with respect to z.

In the equation for the small scale, we will keep all terms linear in the small-scale perturbations including products of the small-scale and large-scale perturbations.

When the assumed form for the perturbations (71) is used in (69) together with the continuity equation (73) we obtain the following equation for the small scale

$$\begin{aligned}
&\hat{w}'''' - 2k^2\hat{w}'' + k^4\hat{w} - ikR[(U-c)(\hat{w}''-k^2\hat{w}) - \hat{w}U''] \\
&= R[\tilde{w}_a - \varepsilon\frac{\partial\tilde{\zeta}}{\partial\tilde{t}}](\hat{w}''' - k^2\hat{w}') + ikR\{(U'\tilde{\zeta} + \tilde{u})(\hat{w}''-k^2\hat{w}) \\
&\quad - ikR(\frac{\partial^2\tilde{u}}{\partial z^2} + U'''\tilde{\zeta})\hat{w} + \varepsilon R\frac{\partial\tilde{\zeta}}{\partial x}[(2k^2(U-c) + U'']\hat{w}' \\
&\quad - U(\hat{w}''' - k^2\hat{w}') + U'''\hat{w} - U'(\hat{w}'' - k^2\hat{w}')\} \\
&\quad \equiv r_2(\tilde{w},\hat{w},z)
\end{aligned} \tag{76}$$

where we have introduced the symbol $r_2(\tilde{w},\hat{w},z)$ for the right-hand side of (76). The various terms in (69) are worked out in Appendix C.

In deriving (76), terms of $0(\tilde{k}^2\tilde{\zeta})$ have been ignored, however terms such as $\partial^2\tilde{u}/\partial z^2$ in air have been kept since these can be large in a viscous flow. In terms of $0(\varepsilon\partial\tilde{\zeta}/\partial\tilde{x})$ a viscous correction has also been neglected since all other terms are proportional to R.

We are interested in the local equilibrium and more specifically the local growth rate of short waves in the modified wind-water field. Thus in the assumed form of solution for the short waves, for a given k the eigenvalue, c, will be a slowly varying function of space

$$c = c_o + c, (\tilde{x}) \tag{77}$$

where c_o is the eigenvalue of the short wave field in the presence of the wind shear field only; $c,(x)$ will be at most $0(\tilde{\zeta})$, the amplitude of the long wave.

Thus the governing equation for $\hat{w}$ is the Orr-Sommerfeld equation with additional terms arising from the long-wave perturbations. Some of these terms could be obtained directly by replacing U by $U + \tilde{u}$ in the Orr-Sommerfeld equation; additional terms come from the unsteady lifting and distortion of the small scale flow by the long waves.

The boundary conditions that are satisfied at the free water surface, $z = \tilde{\zeta} + \zeta'$, will now be derived for both the large and small scale motions. The first boundary condition is that the tangential velocity is continuous at the interface, $z' = \tilde{\zeta}'$,

$$U_T = u_a - w_a\frac{\partial\zeta}{\partial x} = u_w - w_w\frac{\partial\zeta}{\partial x}$$

Expanding the velocities from (70 and 71) in a Taylor series about $z' = 0$, and keeping terms linear in the large scale and small scales we obtain *for the large scale*

$$U'\hat{\tilde{\zeta}} + \hat{\tilde{u}}_a = \hat{\tilde{u}}_w \qquad \text{at } z = 0 \tag{78}$$

for the small scale [to $0(\tilde{k}\tilde{\zeta})$]

$$U'\zeta' + u' - u'_w = -\frac{\partial\tilde{u}}{\partial z}\zeta' \text{ at } z = 0 \tag{79}$$

The term $\partial\tilde{u}_w/\partial z = \tilde{k}\tilde{u}_w$ has been ignored in deriving (79) since it is $0(\tilde{k}^2\tilde{\zeta})$ and $d^2U/dz^2(o)$ has been taken to be zero.

Conditions (78 and 79) can be expressed in the vertical velocity, w' (and $\tilde{w}$), through use of the kinematic boundary condition; that the substantial derivative of the surface displacement function, $S(x,z,t)$, is zero for both the air and water flow at the interface, $S = 0$. That is, if $S(x,z,t) = z-\zeta'$, then $DS/Dt = 0$ at $S = 0$ $(z' = \zeta')$

where $\frac{D}{Dt} = \frac{\partial}{\partial t} + U(\zeta)\frac{\partial}{\partial x} + w(\zeta)\frac{\partial}{\partial x}$

Expanding the velocity field for both air and water about $z' = 0$, and again keeping terms linear in the large and small scales, we obtain in the long-wave limit *for the large scale*

$$\left.\begin{aligned}
&\text{for the air } \frac{\partial\tilde{\zeta}}{\partial\tilde{t}} - \tilde{w} = 0 \\
&\text{for the water } \frac{\partial\tilde{\zeta}}{\partial t} - \tilde{w} = 0
\end{aligned}\right\} \text{ at } z = 0$$

and for the small scale

for the air

$$ikc\tilde{\zeta} - [U'\tilde{\zeta} + \tilde{u}]ik\tilde{\zeta} - \varepsilon[U'\zeta' + u']\frac{\partial\tilde{\zeta}}{\partial\tilde{x}} + \hat{w} = 0$$

$$\text{at } z' = 0 \tag{80}$$

and for the water

$$ikc\hat{\zeta} - \tilde{u}_w ik\hat{\zeta} - \varepsilon\hat{u}_w\frac{\partial\tilde{\zeta}}{\partial\tilde{x}} + \hat{w}_w = 0 \quad \text{at } z' = 0$$

From (78) to (80) we see that

$$\left.\begin{aligned}
\hat{w} &= \hat{w}_w \\
\text{and} \qquad \tilde{w} &= \tilde{w}_w
\end{aligned}\right\} \text{ at } z' = 0$$

From (39) and (40), the velocities in the water at $z' = 0$ are related to the displacement $\tilde{\zeta}$ by the expressions

$$\hat{w}_w = -ik(c - \tilde{u})(1 + i\varepsilon\frac{\partial\tilde{\zeta}}{\partial\tilde{x}})\hat{\zeta}'$$

$$\hat{u}_w = k(c - \tilde{u}_w)(1 + i\varepsilon\frac{\partial\tilde{\zeta}}{\partial x})\hat{\zeta}' \tag{81}$$

$$\text{and} \qquad \hat{\zeta} = \frac{i\hat{w}_w}{kc}\left(1 + \frac{\tilde{u}}{c} + i\frac{\tilde{w}}{\tilde{c}}\right)$$

$$\text{where} \quad \varepsilon \frac{\partial \tilde{\zeta}}{\partial \tilde{x}} = -\frac{\tilde{w}}{\tilde{c}}$$

thus $\hat{u}_w = i\hat{w}_w$, as in fixed coordinates.

For the large scale motions,

$$\tilde{\zeta} = j\tilde{w}/\tilde{k}\tilde{c}$$

$$\text{and} \qquad \tilde{u}_w = j\tilde{w} \tag{82}$$

With (75b) and (82), condition (78) for the large scale motion becomes

$$U'\hat{\tilde{w}} + \tilde{c}\,\hat{\tilde{w}}' - \hat{\tilde{w}}\,\tilde{k}\,\tilde{c} = 0 \qquad \text{at } z = 0 \tag{83}$$

and with (73) and (81) condition (79) for the small scale motion [to $0(\tilde{k}\tilde{\zeta})$] becomes

$$U'\hat{w} + c\hat{w}' - \hat{w}kc = -\frac{\partial \tilde{u}}{\partial z}\hat{w} - \hat{w}\frac{dU}{dz}\left[\frac{\tilde{u}_w}{c} + i\frac{\tilde{w}}{\tilde{c}}\right]$$
$$- i\frac{c}{k}\hat{w}''\frac{\tilde{w}}{\tilde{c}} \equiv \gamma_{10}\,(\hat{w}) \text{ at } z = 0 \tag{84}$$

where we have introduced the symbol $\gamma_{10}(\hat{w})$ for the right hand side of (84).

The remaining boundary condition to be satisfied at $z = \zeta$ and then transferred to $z' = 0$, is the balance of pressure or more precisely of normal stress with surface tension

$$p_a - \sigma_{nn} = p_w + T\frac{\partial^2\zeta}{\partial x^2} \tag{85}$$

The viscous normal stress at $z = \zeta$ is given by

$$\sigma_{nn} = \frac{2}{R}\varepsilon_{nn} = \frac{2}{R}\frac{\partial w_n}{\partial n}$$

$$\text{where} \qquad w_n = w - u\frac{\partial \zeta}{\partial x} \text{ and } \frac{\partial}{\partial n} \simeq \frac{\partial}{\partial z} - \frac{\partial \zeta}{\partial x}\frac{\partial}{\partial x}$$

Because $\mu wU'_w(o) = \mu_a U'_a(o)$ in the limit $\mu_w \to \infty$ there is some cancellation in the stress condition and the final result for the large scale is $\hat{\tilde{\sigma}}_{nn} = 2\,\hat{\tilde{w}}'/R$.

For the small scale, all terms involving the large scale perturbations are negligible for $\tilde{k} << k'$ so that $\hat{\tilde{\sigma}}_{nn} = 2\,\hat{w}'/R$.

The pressure in the air at the surface, $z = \zeta$, is obtained by expanding the pressure about $z' = 0$.

$$p(\zeta) = p(o) + \zeta\frac{\partial p}{\partial z}(o) \tag{86}$$

where $p(o)$ and $\partial p/\partial z(o)$ are available from the momentum equation (67).

After considerable manipulation we obtain the following formula for $\hat{p}_a - \hat{\sigma}_{nn}$

$$ik[\hat{p}_a - \hat{\sigma}_{nn}] = p_a[-c\,\hat{u}' - \hat{w}U' + \frac{i}{Rk}(\hat{w}''' - 3k^2\hat{w}')$$
$$+ \left(\frac{dU}{dz}\hat{\zeta} + \tilde{u}\right)\hat{w}' - \hat{w}\frac{\partial \tilde{u}}{\partial z} + i\frac{\hat{w}'}{k}\frac{\partial \tilde{w}}{\partial z}$$
$$- \frac{\tilde{w}}{\tilde{c}}\left(2ikc\hat{w} + \frac{4\hat{w}''}{R} - 2\frac{k^2\hat{w}}{R} - ic\frac{\hat{w}''}{k}\right)] \tag{87}$$

We obtain $\hat{p}_w - k^2T\hat{\zeta}$ at $z' = \zeta'$ [to $0(\tilde{k}\tilde{\zeta})$] directly from (41)

$$\hat{p}_w - k^2T\hat{\zeta} = \rho_w[k(c - \tilde{u})^2 - (g + k^2T)]\hat{\zeta}' \tag{88}$$

Using (81) to rewrite (88) in terms of $\hat{w}$, introducing $s = \rho_a/\rho_w$ and using (84) to rewrite the group, $c\hat{w}' - U'\hat{w}$, we obtain the final form of the pressure boundary condition (85) to be satisfied at $z' = 0$.

$$\hat{w}[-k(1-s)c^2 + (g+k^2T)] + \frac{ic3}{R}sk\hat{w}' - \frac{isc}{Rk}\hat{w}'''$$
$$= \hat{w}[kc^2 - (g+k^2T)]\left(\frac{\tilde{u}_w}{c} + i\tilde{w}/\tilde{c}\right) - \hat{w}\,2c\tilde{u}_w$$
$$+ s\left(\tilde{u}_w\hat{w}'c + i\hat{w}'c\frac{\partial \tilde{w}_a}{\partial z}/k + c\hat{w}\,U'\left(\frac{\tilde{u}_w}{c} + \frac{i\tilde{w}}{\tilde{c}}\right)\right.$$
$$\left.+ \frac{ic^2}{k}\hat{w}''\frac{\tilde{w}}{\tilde{c}}\right) - s\frac{\tilde{w}}{\tilde{c}}\left(2ikc\hat{w} + \frac{4\hat{w}''}{R} - 2\frac{k^2\hat{w}}{R}\right) \equiv \gamma_{20}\,(\hat{w}) \tag{89}$$

We will introduce the variables p, Q, b, and γ_{20} and rewrite (89) as $P\hat{w} + Q\hat{w} + b\hat{w}''' = \gamma_{20}\,(w)$ where

$$P = [-k(1-s)c^2 + (g+k^2T)]$$

$$Q = \frac{ic3sk}{R}\,; \quad b = -isc/Rk$$

and $\gamma_{20}\,(\hat{w})$ is the right hand side of (89).

The corresponding boundary condition for the large scale is homogeneous and of the form

$$\tilde{P}\hat{\tilde{w}} + \tilde{Q}\hat{\tilde{w}}' + b\hat{\tilde{w}}''' = 0 \tag{90}$$

where

$$\tilde{P} = [-\tilde{k}(1-s)\tilde{c}^2 + (g+\tilde{k}^2T)]$$

$$\tilde{Q} = jc3s\tilde{k}/R; \quad \tilde{b} = -js\tilde{c}/R\tilde{k}$$

To summarize, the long waves satisfy the ordinary Orr-Sommerfeld equation (75) with the appropriate linear boundary conditions for a free water (83) and (90) plus $\hat{\tilde{w}}(\infty) = \hat{\tilde{w}}'(\infty) = \infty$. The resulting homogeneous eigenvalue problem is solved numerically to determine $\hat{\tilde{u}}$, $\hat{\tilde{w}}$, and $\tilde{c}$ for a given long wave amplitude, $\tilde{\zeta}$, wave number, k, and R.

The short waves satisfy a modified Orr-Sommerfeld equation, (75) with the effects of the long-wave perturbations appearing also in the boundary conditions (84) and (89).

To solve this short-wave local-equilibrium problem we resort to techniques that by now have become standard in stability theory for perturbed eigenvalue problems.

We assume that the short-wave solutions can be expanded about the perturbed solution (no long waves present) in the form

$$\hat{u} = \hat{u}_0 + \tilde{\zeta}\,\hat{u},$$

$$\hat{w} = \hat{w}_0 + \tilde{\zeta}\,w,$$

$$\hat{\tilde{\zeta}} = \hat{\tilde{\zeta}}_0 + \tilde{\zeta}\,\hat{\zeta}, \tag{91}$$

where $\tilde{\zeta}$ is the large wave amplitude. The eigenvalue, c, is also expanded

$$c = c_0 + \tilde{\zeta}\,c, \tag{91b}$$

For $\tilde{\zeta} = 0$ the problem of short-wave dynamics reduces to the ordinary Orr-Sommerfeld equation with free-surface boundary conditions.

$$\hat{w}_0'''' - 2k^2\hat{w}_0'' + k^4\hat{w}_0 - ikR[(U-c)(\hat{w}_0'' - k^2\hat{w}_0) - w_0U''] = 0$$

$$\left.\begin{aligned} & c_0\hat{w}_0' + (\frac{dU}{dz} - kc_0)\,\hat{w}_0 = 0 \\ & P\hat{w}_0 + Q\,\hat{w}_0' + b\,\hat{w}_0''' = 0 \end{aligned}\right\} \text{ at } z' = 0$$

$$\text{and} \qquad \hat{w}_0(\infty) = \hat{w}_0'(\infty) = 0 \tag{92}$$

The eigenvalue, c_0, which determines the growth rate of the short waves in the parallel shear flow, is determined by a numerical solution of these equations for a given k and R.

The equations governing the modification to the flow due to the long-wave perturbations are derived by using (91) in (76) and equating terms of $O(\tilde{\zeta})$.

In this operation the as-yet-unknown correction to the eigenvalue, c_1, will appear multiplying the lowest order solution, $\hat{w}_0$. The resulting problem for $\hat{w}_1$ is written

$$\hat{w}_1'''' - 2k^2\hat{w}_1'' + k^4\hat{w}_1 - ikR[(U-c_0)(\hat{w}_1'' - k^2\hat{w}_1) - w\,U'']$$

$$= c_1r_1(\hat{w},z) + r_2(\tilde{w},\hat{w},z) \tag{93}$$

where $r_1(\hat{w},z)$ and $r_2(\tilde{w},\hat{w},z)$ are known functions of the long-wave perturbation, $\tilde{w}(z)$, and the lowest-order short-wave perturbation, $w_0(z)$. From (84) and (91)

$$r_1(\hat{w},z) = -\,ikR(\hat{w}_0'' - k^2\hat{w}_0) \tag{94}$$

and $r_2(\tilde{w},\hat{w},z)$ is defined by (76) with the long wave perturbations normalized by $\tilde{\zeta}$.

The boundary conditions for $\hat{w}_1$ have homogeneous operations that are identical to those for $\hat{w}_0$ but the equations are non-homogeneous with terms that depend on $\hat{w}_0$, the long-wave perturbations, $\tilde{w}$, and the unknown correction to eigenvalue, c_1.

$$\left.\begin{aligned} & c_0\hat{w}_1' + (\frac{dU}{dz} - kc_0)\,\hat{w}_1 = \gamma_{11}\,c_1 + \gamma_{10}\,(\tilde{w},\hat{w}) \\ & P\hat{w}_1 + Q\,\hat{w}_1' + b\,\hat{w}_1''' = \gamma_{21}\,c_1 + \gamma_{20}\,(\tilde{w},\hat{w}_0) \end{aligned}\right\} \text{ at } z = 0 \tag{95}$$

$$\text{and} \quad \hat{w}_1(\infty) = \hat{w}_1'(\infty) = 0$$

where $\gamma_{10}\,(\hat{w})$ and $\gamma_{20}\,(\hat{w})$ are defined in equations (86) and (90) with the long wave perturbations normalized by $\tilde{\zeta}$

$$\text{and } \gamma_{11} = -\,\hat{w}_0' + k\hat{w}_0$$

$$\gamma_{21} = 2c_0k(1-s)\hat{w}_0 - ik3s/R\hat{w}_0' + is/kR\hat{w}_0'''$$

This problem is similar to that considered by Stuart (1960) and many others in later studies. In Stuart (1960) we have the problem

$$L(\hat{w}_1) = r(z)$$

$$\text{with} \quad \hat{w}_1(0) = \hat{w}_1'(0) = \hat{w}_1(\infty) = \hat{w}_1'(\infty) = 0 \tag{96}$$

where L is the Orr-Sommerfeld operator.

The solvability condition [Ince (1926) pg. 214] for this problem is

$$\int_0^\infty \hat{v}r\,dz = 0 \tag{97}$$

where $\hat{v}$ is the solution to the adjoint problem

$$\bar{L}(\hat{v}) = 0$$

$$\text{with} \qquad \hat{v}(0) = \hat{v}'(0) = \hat{v}(\infty) = \hat{v}'(\infty) = 0 \tag{98}$$

Condition (97) is then used to determine the modifications of the flow due to non-linearities.

The present problem differs from that in (96) - (98) in that the boundary conditions of (95) involve linear combinations of the derivatives of $\hat{w}_1$ at $z = 0$ and are non-homogeneous.

In Appendix B, we show that the adjoint boundary conditions that replace (98) in the determination of v are

$$\underline{\hat{v}}'(0) = \hat{v}'(\infty) = \hat{v}(\infty) = 0 \tag{99}$$

$$\text{and } [\beta - ikRcU' + \sigma(U'-kc)]\hat{v} + [U'-kc]\hat{v}'' + cv''' = 0 \quad \text{at } z = 0$$

where

$$\sigma = -\,[2k^2 + ikR(u-c)];\ \beta = \frac{c}{b}P - \frac{Q}{b}(U'-kc)$$

and the extended solvability condition for non-homogeneous boundary conditions is

$$\int_0^\infty rv\,dz = \int_0^\infty [c_1\,r_1\,(z_1) + r_2\,(z)]\hat{v}\,dz$$

$$= (\gamma_{11}c_1 + \gamma_{10})[\frac{v''}{c_0}(0) + (\frac{\sigma}{c_0} - \frac{Q}{bc_0})\hat{v}(0)]$$

$$+ (\gamma_{21}c_1 + \gamma_{20})[\frac{v}{b}(0)] \tag{100}$$

The solvability condition (100) is then used to determine c_1 and thus the correction to the local growth rate due to the presence of the long wave perturbations.

$$c_1 = -\,\frac{\gamma_{10}[\frac{\hat{v}''}{c_0}(0) + (\frac{\sigma}{c_0} - \frac{Q}{bc_0})\hat{v}(0)] + \gamma_{20}\frac{\hat{v}}{b}(0) - \int_0^\infty r_2(z)\hat{v}\,dz}{\gamma_{11}[\frac{\hat{v}''}{c_0}(0) + (\frac{\sigma}{c_0} - \frac{Q}{bc_0})\hat{v}(0)] + \gamma_{21}\frac{\hat{v}}{b}(0) - \int_0^\infty r_1(z)\hat{v}\,dz} \tag{101}$$

After c has been determined from (101), the normal stress on the small-scale waves in the water due to the air flow may be determined. The simplest approach is to use (88) and infer $\hat{p}_a - \sigma_{nn}$ directly from $\hat{p}_w$ using the momentum equation in the water (or Bernoulli's equation).

Retaining the terms linear in the large-scale quantities, we have

$$\hat{p}_a - \sigma_{nn} = \rho_w[+\,k\hat{\zeta}(c - \tilde{u}_w)^2 - (g + Tk^2)\hat{\zeta}] \tag{102}$$

where c is given by (91b) with c_1 from (101). The correction to the growth rate, c_1, is doubly complex in that it has both real and imaginary parts (c_r and c_i) that are in phase and out of phase with $\tilde{\zeta}$.

To complete the calculation of Section 2 for long-wave growth rate due to the non-uniformity of short-wave growth rate, we require the part of c_i that is in phase with $\tilde{\zeta}$. For the analysis of short waves, Section 2 uses an expression equivalent to

$$\grave{p}' - \sigma_{nn} \tilde{=} \rho_w k'(c' - \tilde{u})(\alpha' + i\beta')(1 - a\tilde{k}\tilde{\zeta})\hat{\zeta}' \quad (42)$$

where all quantities are real. This assumes that the real and imaginary part of c are modulated by the large scale in exactly the same proportions.

Thus by this assumption,

$$a\tilde{k}\tilde{y} = -2 \frac{(\tilde{\zeta}c_1 - \tilde{u}_w)}{\alpha + i\beta} \quad (103)$$

since

$$c_0 \simeq \sqrt{g/k+kT} + \frac{(\alpha+i\beta)}{2} \text{ and } c' \simeq c_0 + \tilde{u}$$

Should these assumptions not be exactly correct, a would have a small imaginary part, which will be ignored.

4. NUMERICAL RESULTS

We have carried out the calculations described in 3 using the Orr-Sommerfeld solver developed by Gustavsson (1977). This is an implicit method which uses an Adam's integration technique. One particularly attractive feature of the program is its variable step size. Thus it is possible with a reasonable number of points to have a fine mesh in the "wall" layer and other regions of high gradients and to coarsen the mesh as one moves out into the boundary layer. The programs and results will be more fully described in a subsequent publication. Only one set of calculations will be reported here.

The shear flow profile and its derivatives are modelled with continuous functions that approximate the mean profile of a turbulent boundary layer. Calculations were done at a friction velocity, $u\tau$, of 30 cm/sec; conditions were chosen so that the ratio, $u\tau/u_\infty$, was .05, a typical value for wind-tunnel experiments. Interaction between long waves of 100, 75, 50, 36, 20, and 16.5 cm with short waves of 2, 1, 0.75, and 0.6 cm were investigated. Although many interesting features of the flow can be investigated using this approach (such as the distortion of the mean profile as the large wave passes, and the variation of the wave speed, local growth rate, and amplitude of the short waves along the large waves), the only systematic investigation we have yet performed concerns the energy input to the large waves due to the modulation of the short-wave Stokes drift.

The linear temporal growth rate of wind-driven waves $\Omega_i = kc_i$ is of course a direct output of the calculations. Figure 2 shows $\Omega_i \sim \text{sec}^{-1}$ as a function of wave number, $k \sim \text{cm}^{-1}$, for $u_\tau = 30$ cm/sec. The growth rates we obtained are slightly higher than Miles's viscous calculations [Miles (1962)] but when we used his shear-flow profile, we obtain close agreement. For $u_\tau = 30$ cm/sec, all the waves we investigated were viscously dominated, that is, their critical layers were sufficiently close to the free surface to be essentially merged with the surface viscous layer. Thus, little insight to the behavior of these flows can be obtained from an inviscid model of the behavior of shear flows. The real part of the wave speed, c_r, also shown in Figure 2, differs very little from the free wave speed of gravity-capillary waves, c_0.

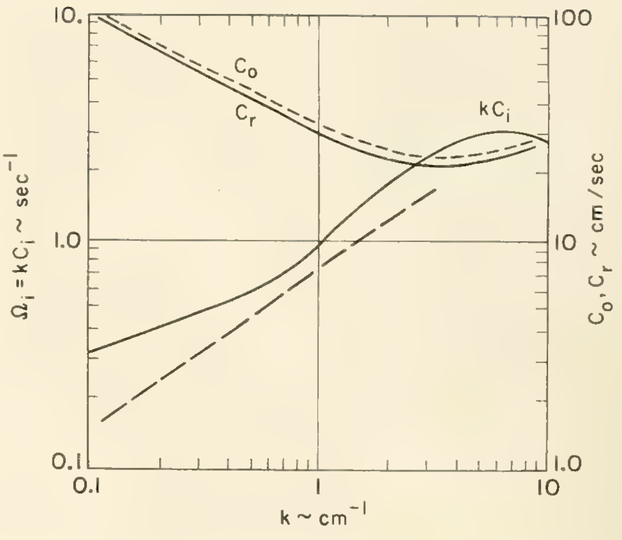

FIGURE 2. Linear temporal growth rate @ $u_\tau = 30$ cm/sec; ———, - - - - present calculations; — — present calculations with miles profile $U_1 = 5U^*$.

The energy input to the large waves from the small waves is given by (66). With $\tau = \tilde{k}\tilde{c}t$, and S'^2 from (54), the dimensional temporal growth rate of the large waves can be written

$$\frac{d\tilde{\zeta}_0}{dt} = \zeta_0 \left[\tilde{\Omega}_i + \frac{a\beta'}{4} \tilde{k} \frac{c'}{c'_g - \tilde{c}} k'^2 \hat{\zeta}^2\right] \quad (104)$$

where $\tilde{\Omega}_i$ is the linear growth rate $\tilde{\beta}\tilde{k}/2$. We define the coupling coefficient C as

$$C = \frac{-a\beta'\tilde{k}}{4} \quad (105)$$

where the minus sign is introduced because, contrary to our expectations, a turned out to be negative for the cases we investigated. Thus the growth of the large-wave amplitude is given by

$$\frac{d\tilde{\zeta}_0}{dt} = \zeta_0 \left[\Omega_i + \frac{C\ c'}{\tilde{c} - c'_g} |k'\hat{\zeta}'|^2\right] \quad (106)$$

Thus for C positive, an energy input to long waves comes from short waves whose group velocity, c'_g, is slightly less than the long wave phase velocity, $\tilde{c}$. The theory also predicts that long waves will decay if $c'_g > \tilde{c}$. Since waves satisfying this condition will be shorter capillary waves which will be more strongly damped by viscosity, we expect a net energy input to the large waves. Of course the theory does not hold at $\tilde{c} = c_g$ where non-linear interactions must be considered.

Numerical values of the coupling coefficient, C, are shown in Figure 3 as a function of $\tilde{\lambda}$ for various λ'. C is certainly O(1) having a maximum value of 3 at $\lambda' = 1$ cm. It is also a slowly varying function of $\tilde{\lambda}$. It has its maximum value about $\lambda' = 1$ cm which corresponds to the maximum in the linear growth rate for short waves for these conditions. It drops off more rapidly with decreasing wave length, λ', than does the linear growth rate, $\Omega_i(\lambda')$. The long-wave linear growth rate, Ω_i, is also shown for comparison; it is much smaller. Of course the interaction growth rate also involves $(k'\hat{\zeta}')^2$ of the short waves which would be typically 0.01 but the division by $\tilde{c}-c_g'$ would somewhat offset the effect of small slope. One calculation for an upstream travelling long wave verified that a was negative and energy was removed from the long wave by interaction with the short wave. We have not carried the calculations further to date.

Some idea of the wavelengths, involved in any practical application of these ideas can be seen from Figure 4 which shows the group velocity and phase velocities for gravity-capillary waves. The requirement for strong coupling is $\tilde{c} \approx c_g'$. We further note that waves shorter than say 0.3 cm are unlikely to be important in a viscous fluid. Thus short waves in the range 0.3 cm could interact with a 20 cm long wave in the manner we have discussed but waves longer than 20 cm would be unlikely to be affected.

Although the effects of surface drift are not yet included in our calculations, the range of affected long waves can be somewhat broadened by considering surface drift. Drift velocities are typically 5% of the wind velocity; this is the same order as the friction velocity which we have taken as $u_\tau = 0.05\ U_\infty$. If we assume that a surface layer will advect the short waves [Valuenzuela (1976)] but leave the phase velocity of the long waves unaffected (Valenzuela's calculations did not extend to long waves), we can consider a broader range of interaction possibilities, as sketched in Figure 4. For a group velocity augmented by a surface current of 30 cm/sec, interactions between a long wave of about 50 cm and waves longer than 0.3 cm become possible and a 20 cm wave may interact with waves of order 1.4 cm.

Experimental data in the range of wave lengths and friction velocities of interest for the interactions we have investigated here was presented by Plant and Wright (1977). Some of their results are reproduced in Figure 5, showing the temporal growth rate vs. wave number for several values of friction velocity. Of particular interest is that while the short-wave growth rate is accurately predicted by linear theory, there is a departure of theory and

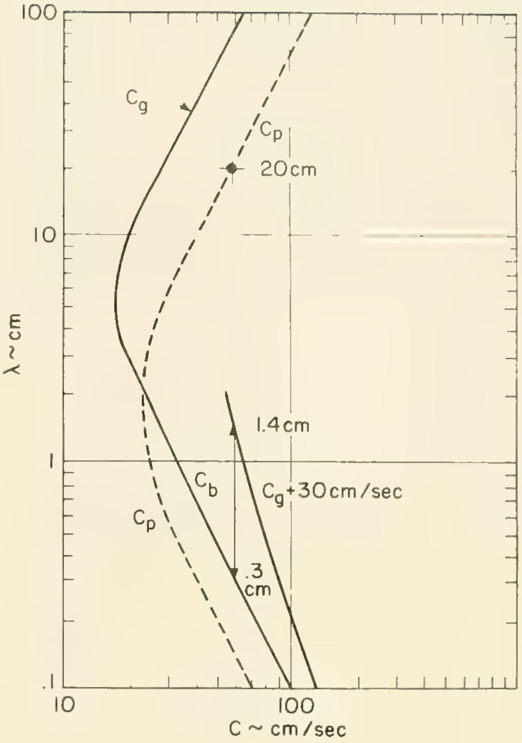

FIGURE 4. Group velocity and phase velocity for gravity-capillary waves.

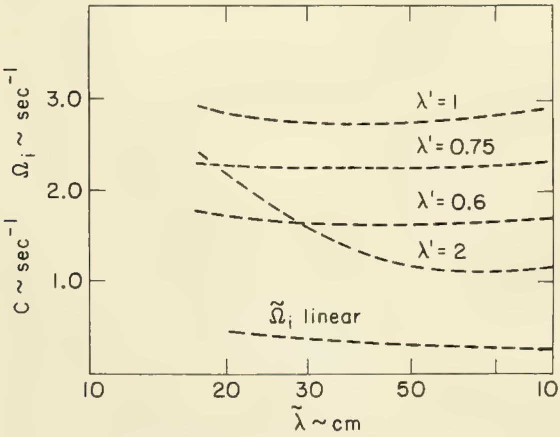

FIGURE 3. Coupling coefficients for long-wave and short-wave interaction; linear temporal growth rate Ω_i. u_τ = 30 cm/sec.

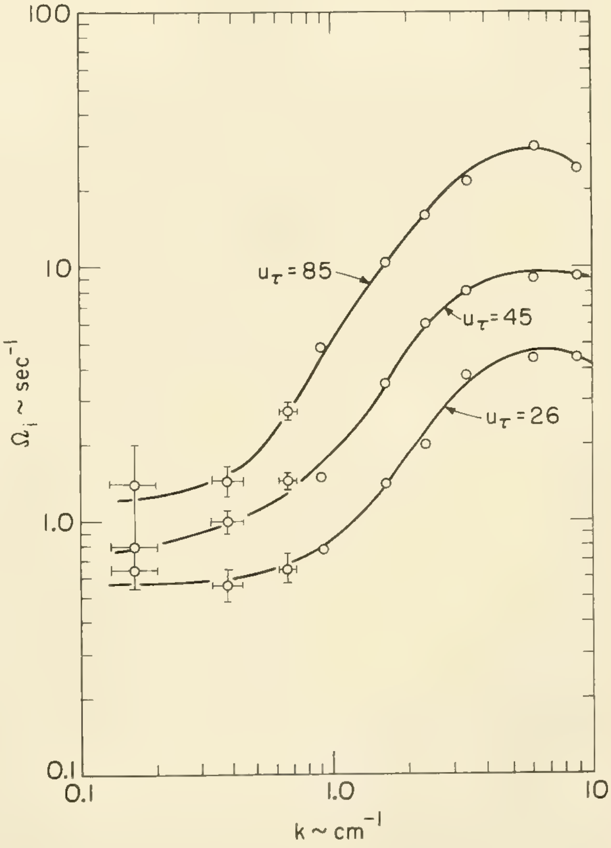

FIGURE 5. Measured temporal growth rates for various u_τ cm/sec; from Plant and Wright (1977).

experiment for waves longer than about 10 cm. This is close to the first possible long wave that can strongly interact with a short wave whose group velocity is equal to the long wave phase velocity.

Thus the results we have obtained to date indicate that the long waves can receive energy due to their interaction with wind driven short waves. The interaction mechanism we have investigated requires the presence of the wind and the variation of the short wave growth rate along the surface of the long wave due to changes in the local wind field caused by the passage of the long wave. Of course further work remains to be done to explore the full implications of these results, to complete the calculations and to make fuller comparison with experiment.

5. ACKNOWLEDGMENTS

This work was supported by the National Science Foundation under Grant ENG7617265. We acknowledge many stimulating discussions with our colleague, Professor E. Mollo-Christensen.

APPENDIX A.

DERIVATION OF STOKES' DRIFT MODULATION FROM KINEMATIC WAVE THEORY

Kinematic wave theory, modified to allow for small dissipation or growth due to energy interchange with the wind, gives the following conservation equation for the wave action density, A', of the train of short waves:

$$\frac{\partial A'}{\partial t} + \frac{\partial}{\partial x}(c'_g A') = 2\Omega'_i A' \qquad \text{(A.1)}$$

where Ω'_i is the temporal growth rate. The wave action density for waves on a current is given by [Bretherton and Garrett (1968)]

$$A' = E'/\Omega' \qquad \text{(A.2)}$$

where E' is the energy density and $\Omega' = k'(c' - \tilde{u})$ the frequency relative to the fluid at rest. By introduction of

$$E' = \frac{1}{2}k'(c' - \tilde{u})^2|\hat{\zeta}'|^2 = (c' - \tilde{u})S' \qquad \text{(A.3)}$$

(A.1) may be cast as a conservation equation for the Stokes' drift

$$\frac{\partial S'}{\partial t} + \frac{\partial}{\partial x}(c'_g S') = [\frac{1}{k'}(\frac{\partial k'}{\partial t} + c'_g \frac{\partial k'}{\partial x}) + 2\Omega'_i]S'$$

$$= (-\frac{\partial \tilde{u}}{\partial x} + 2\Omega'_i)S' \qquad \text{(A.4)}$$

With $\Omega'_i = k'\beta'(1-a\tilde{k}\tilde{\zeta})/2$ and expressed in the variables $\frac{1}{\tau}$ and ξ this takes the form

$$[\tilde{c}\frac{\partial}{\partial \tau} + (c'_g - \tilde{c})\frac{\partial}{\partial \xi}]\ell n\ S' = \bar{\beta}(1-a\tilde{k}\tilde{\zeta})$$

$$-\frac{\tilde{u}_\xi}{(c'-\tilde{u})}\{c'_g + c' - 2\tilde{u} - \frac{k'}{(c'_g-\tilde{c})}[c'-\tilde{c})v_{k'} + T]\} \qquad \text{(A.5)}$$

By neglecting the variation of the left-hand side with τ one finds from this

$$\frac{S'_\xi}{S'} = -\frac{\bar{\beta}a\tilde{k}\tilde{\zeta}}{(c'_g-\tilde{c})} - \frac{\tilde{u}_\xi}{(c'_g-\tilde{c})(c'-\tilde{u})}\{c'_g + c' - 2\tilde{u}$$

$$-\frac{k'}{(c'_g-\tilde{c})}[(c'-\tilde{c})v_{k'} + T]\} \qquad \text{(A.6)}$$

which, with $S' = (c-\tilde{u})\tilde{s}'^2/k'$, is found to agree with (53).

APPENDIX B.

THE EXTENDED SOLVABILITY CONDITION

We first determine the adjoint to the homogeneous problem for a shear flow over a water surface. This problem is written

$$L(w) = 0$$

$$\left.\begin{aligned} W_1 &= cw + (U' - kc)\,w' = 0 \\ W_2 &= Pw + Qw' + bw''' = 0 \\ w(\infty) &= w'(\infty) = 0 \end{aligned}\right\} \text{at } z = 0 \qquad \text{(B.1)}$$

where L is the Orr-Sommerfeld operator.

The adjoint to the Orr-Sommerfeld equation is [Sturart (1960)]

$$\bar{L}(v) = v'''' + \sigma v'' - 2ikRU'v' + [k^4 + ik^3R(U-c)]v = 0$$

where

$$\sigma = -2k^2 - ikR(U-c) \qquad \text{(B.2)}$$

From the Lagrange identity [Ince (1926) pp. 210, 214]

$$\int_0^\infty \{vL(w) - w\bar{L}(v)\}dz = P(w,v)\Big|_0^\infty$$

where P(w,v) is the bilinear concomitant. The boundary conditions on v that will complete the statement of the adjoint problem are found by the requirement that P(w,v) be zero at both end points. Since w and its derivatives are zero at $z = \infty$, this leaves the conditions on v to be found for $z = 0$. P(w,v) is written in bilinear form as

$$P(w,v) = \{v\ v'\ v''\ v'''\}\begin{bmatrix} ikRU' & \sigma & 0 & 1 \\ -\sigma & 0 & -1 & 0 \\ 0 & +1 & 0 & 0 \\ -1 & 0 & 0 & 0 \end{bmatrix}\begin{Bmatrix} w \\ w' \\ w'' \\ w''' \end{Bmatrix}$$

$$\equiv \underline{v}\cdot[U]\cdot\underline{w} \qquad \text{(B.3)}$$

The free surface boundary conditions for w may be written

$$\begin{bmatrix} v'-kc & c & 0 & 0 \\ P & Q & 0 & b \end{bmatrix} \begin{Bmatrix} w \\ w' \\ w'' \\ w''' \end{Bmatrix} = 0 \qquad \text{(B.4)}$$

(B.4) is an underdetermined set of equations that will yield two solution vectors with arbitrary coefficients. They are not unique and any linear combination will also be a solution. Two such solution vectors are

$$\underline{w}_1 = \{0,0,1,0\} \quad \text{and} \quad \underline{w}_2 = (-c, U'-kc, 0, \beta) \qquad \text{(B.5)}$$

where

$$\beta = -\,[Q(U'-kc)-cP]/b$$

We now enforce the requirement that $P(w,v)$ be zero. This requires that certain linear combinations of v, v', v'', v''' be zero and these are of course the required adjoint boundary conditions.

Consider the solution vector w_1. For $P(w,v)$ to be zero

$$P(w,v) = \underline{v} \cdot [U] \cdot \underline{w}_1 = \underline{v} \cdot \begin{Bmatrix} 0 \\ -1 \\ 0 \\ 0 \end{Bmatrix} = 0 \qquad \text{(B.6)}$$

This requires that

$$v' = 0 \qquad \text{(B.7)}$$

Consider the solution vector $\underline{w}_2$. For $P(w,v)$ to be zero,

$$P(w,v) = \underline{v} \cdot [U] \cdot \underline{w}_2 = \underline{v} \cdot \begin{Bmatrix} -icRU' + \sigma(U'-kc) + \beta \\ -c \\ U' - kc \\ c \end{Bmatrix} \qquad \text{(B.8)}$$

so that

$$[-icRU'k+\sigma(U'-kc) + \beta]v - c\sigma v' + (U'-kc)v''$$
$$+ c\, v''' = 0$$

Since $v' = 0$, this term may be eliminated from this relationship. Thus given

$$\left.\begin{aligned} W_1\ (w) &= cw' + (U' - kc)w = 0 \\ W_2\ (w) &= Pw + Qw' + bw''' = 0 \end{aligned}\right\} \text{at } z = 0 \qquad \text{(B.9)}$$

for $P(w,v)$ to be zero requires

$$V_1\ (v) = v' = 0$$

$$V_2\ (v) = [-ikcRU' + \sigma(U' - kc) + \beta]v + (U' - kc)v''$$
$$+ cv''' = 0 \text{ at } z = 0 \qquad \text{(B.10)}$$

It can be shown that if (B.9) and (B.10) are used to construct $P(w,v)$, the result is identically zero. Thus (B.10) are the boundary conditions for the adjoint problem.

The solvability condition for a problem of the form [Ince (1926)]

$$L(w) = r$$

$$W_i(w) = \gamma_i \qquad i = 1,n \qquad \text{(B.11)}$$

is that

$$\int_0^\infty vrdz = \gamma_1\ V_{2n} + \gamma_2\ V_{2n-1} + \ldots.. \qquad \text{(B.12)}$$

where the V_{2n}'s are determined such that $P(w,v) = W_1\ V_{2n} + W_2\ V_{2n-1} +\ldots$ and v is a solution of the adjoint system.

$$\bar{L}(v) = 0$$

$$V_i(v) = 0 \qquad i = 1,n \qquad \text{(B.13)}$$

For the present problem, only γ_1 and γ_2 are non-zero. By standard techniques, we have determined the additional linear combination of w and v,

$$W_3\ (w) = -\frac{w}{c}$$

$$W_4\ (w) = -\,w'' - \sigma w$$

$$V_3\ (v) = v/b$$

$$V_4\ (v) = v''/c + (\sigma/c - Q/bc)v \qquad \text{(B.14)}$$

such that the bilinear concomitant (B.3) may be written in the form

$$P(w,v) = W_1\ V_4 + W_2\ V_3 + W_3\ V_2 + W_4\ V_1$$

where W_1 and W_2 are the boundary conditions from (B.1) and V_1 and V_2 are the adjoint boundary conditions from (B.10).

Thus the solvability condition for non-homogeneous problem with non-homogeneous free water boundary conditions is

$$\int_0^\infty rvdz = \gamma_1\ V_4 + \gamma_2\ V_3 \qquad \text{(B.15)}$$

where

$$\left.\begin{aligned} V_4 &= v''/c + (\sigma/c - Q/bc)v \\ V_3 &= v/b \end{aligned}\right\} \text{at } z = 0$$

and v is a solution of the adjoint system

$$L(v) = 0$$

$$V_1(v(o)) = 0$$

$$V_2(v(0)) = 0$$

$$v(\infty) = v'(\infty) = 0 \qquad \text{(B.16)}$$

APPENDIX C.

In this section we give the expressions for the various terms in (69) for the assumed form of the small scale (71). The continuity equation (73) has been used to express u' in terms of w'.

The results are as follows

$$\frac{\partial^2 u}{\partial t\partial z} = \varepsilon \frac{\partial^2 \tilde{u}}{\partial \tilde{t}\partial z} + c\frac{\partial^2 w'}{\partial z^2} - \varepsilon \frac{i}{k} \frac{\partial^3 w}{\partial z^3}\frac{\partial \tilde{\zeta}}{\partial \tilde{t}} - \varepsilon \frac{ic}{k}\frac{\partial^3 w}{\partial z^3}\frac{\partial \tilde{\zeta}}{\partial x} \tag{C.1}$$

$$\frac{\partial^2 w}{\partial x\partial t} = \varepsilon^2 \frac{\partial^2 \tilde{w}}{\partial \tilde{x}\partial \tilde{t}} + k^2 c w' + i\varepsilon k c\frac{\partial w'}{\partial z}\frac{\partial \tilde{\zeta}}{\partial x} - i\varepsilon k \frac{\partial \tilde{\zeta}}{\partial \tilde{t}}\frac{\partial w'}{\partial z} \tag{C.2}$$

$$\nabla^2 w = \frac{\partial^2 w'}{\partial z^2} - k^2 w' - \varepsilon 2ik\frac{\partial w'}{\partial z}\frac{\partial \tilde{\zeta}}{\partial x} + \nabla^2 \tilde{w} \tag{C.3}$$

$$\nabla^2 u = \frac{i}{k}\frac{\partial^3 w'}{\partial z^3} - ik\frac{\partial w'}{\partial z} + \frac{\varepsilon}{k^2}\frac{\partial \tilde{\zeta}}{\partial \tilde{x}}\frac{\partial^4 w'}{\partial z^4} + \varepsilon\frac{\partial \tilde{\zeta}}{\partial x}\frac{\partial^2 w'}{\partial z^2}$$

$$+ \nabla^2 \tilde{u} + U'' + U'''\tilde{\zeta} \tag{C.4}$$

$$\frac{\partial}{\partial z}\nabla^2 u = \frac{i}{k}\frac{\partial^4 w}{\partial z^4} - ik\frac{\partial^2 w}{\partial z^2} + \frac{\varepsilon}{k^2}\frac{\partial \tilde{\zeta}}{\partial \tilde{x}}\frac{\partial^5 w}{\partial z^5} + \varepsilon\frac{\partial^3 w}{\partial z^3}\frac{\partial \tilde{\zeta}}{\partial x}$$

$$+ \frac{\partial}{\partial z}(\nabla^2 \tilde{u}) + U''' \tag{C.5}$$

$$\frac{\partial}{\partial x}\nabla^2 w = ik\left(\frac{\partial^2 w'}{\partial z^2} - k^2 w'\right) + \varepsilon 3k\frac{\partial w'}{\partial z}\frac{\partial \tilde{\zeta}}{\partial \tilde{x}} - \varepsilon\frac{\partial^3 w'}{\partial z^3}\frac{\partial \tilde{\zeta}}{\partial \tilde{x}}$$

$$+ \varepsilon\frac{\partial}{\partial \tilde{x}}\nabla^2 \tilde{w} \tag{C.6}$$

The equation for the small scale will contain coefficients involving the mean flow expressed as a function of z'.

$$U(z') = U(z) + U'(z)\,\tilde{\zeta}$$

and
$$U''(z') = U''(z) + U'''(z)\,\tilde{\zeta} \tag{C.7}$$

so that, for example, the term $u\nabla^2 w$, with only linear terms retained, becomes

$$u\nabla^2 w = U\nabla^2 \tilde{w} + [U + U'\tilde{\zeta} + \tilde{u}]\left[\frac{\partial^2 w'}{\partial z^2} - k^2 w'\right]$$

$$+ u'\nabla^2 \tilde{w} - \varepsilon 2ikU\frac{\partial \tilde{\zeta}}{\partial \tilde{x}}\frac{\partial w'}{\partial z} \tag{C.8}$$

and

$$w\nabla^2 u = \tilde{w}U'' + w'[U'' + U'''\tilde{\zeta}] + \tilde{w}\left[\frac{i}{k}\frac{\partial^3 w'}{\partial z^3} - ik\frac{\partial w'}{\partial z}\right]$$

$$+ w'\nabla^2 u \tag{C.9}$$

of these, $\nabla^2 \tilde{w}$ and $\partial^2 \tilde{u}/\partial x^2$ will be ignored.

The viscous term is manipulated as follows

$$\frac{1}{R}\left[\nabla^2\frac{\partial w}{\partial x} - \nabla^2\frac{\partial u}{\partial z}\right] = \frac{1}{R}\left[\nabla^2\frac{\partial \tilde{w}}{\partial x} - \nabla^2\frac{\partial \tilde{u}}{\partial z}\right]$$

$$+ \frac{1}{R}\left[ik\left(\frac{\partial^2 w'}{\partial z^2} - k^2 w'\right) - \frac{i}{k}\frac{\partial^4 w'}{\partial z^4} + ik\frac{\partial^2 w'}{\partial z^2}\right]$$

$$+ \frac{1}{R}\left[3k^2\frac{\partial w'}{\partial z} - 2\frac{\partial^3 w'}{\partial z^2} - \frac{1}{R^2}\frac{\partial^5 w'}{\partial z^5}\right] \tag{C.10}$$

The fifth derivative is obtained from the Orr-Sommerfeld equation. Some cancellation occurs among these terms to yield the final result (76).

REFERENCES

Benny, D. J. (1976). Significant interactions between small and large scale surface waves. *Studies in App. Math. 55,* 93.

Bretherton, F. P., and C.J.R. Garrett (1968). Wavetrains in inhomogeneous moving media. *Proc. Roy. Soc. A, 302,* 529.

Davis, R. E. (1972). On prediction of the turbulent flow over a wavy boundary. *J. Fluid Mech.* 52, 287.

Gustavsson, L. H. (1977). Private communication.

Hasselman, K. (1971). On the mass and momentum transfer between short gravity waves and larger scale motions. *J. Fluid Mech. 50,* 189.

Hinze, J. O. (1975). *Turbulence,* McGraw-Hill, New York.

Ince, E. L. (1926). *Ordinary Differential Equations,* Dover Publications, New York.

Larson, T. R., and J. W. Wright (1975). Wind-generated gravity-capillary waves: laboratory measurements of temporal growth rates using microwave backscatter. *J. Fluid Mech. 70,* 417.

Longuet-Higgins, M. S. (1969). A nonlinear mechanism for the generation of sea waves. *Proc. Roy. Soc. A, 311,* 737.

Manton, M. J. (1972). On the generation of sea waves by a turbulent wind. *Boundary Layer Meterology 2,* 348.

Miles, J. W. (1957). On the generation of waves by shear flow. *J. Fluid Mech. 3,* 185.

Miles, J. W. (1962). On the generation of surface waves by shear flow, Part 4. *J. Fluid Mech. 13,* 433.

Phillips, O. M. (1957). On the generation of waves by turbulent wind. *J. Fluid Mech. 2,* 417.

Phillips, O. M. (1960). On the dynamics of unsteady gravity waves of finite amplitude, Part 1. *J. Fluid Mech. 9,* 193.

Phillips, O. M. (1966). *The Dynamics of the Upper Ocean,* Cambridge University Press, 79-87.

Plant, W. J. and J. W. Wright (1977). Growth and equilibrium of short gravity waves in a wind-wave tank. *J. Fluid Mech. 82,* 767.

Stuart, J. T. (1960). On the non-linear mechanics of wave disturbances in stable and unstable parallel flows, Part 1. *J. Fluid Mech. 9,* 353.

Townsend, A. A. (1972). Flow in a deep turbulent boundary layer over a surface distorted by water waves. *J. Fluid Mech. 55,* 719.

Valenzuela, G. R. (1976). The growth of gravity-capillary waves in a coupled shear flow. *J. Fluid Mech. 76,* 229.

Valenzuela, G. R. and M. B. Laing (1972). Nonlinear energy transfer in gravity-capillary wave spectra, with applications. *J. Fluid Mech. 54,* 507.

Valenzuela, G. R. and J. W. Wright (1976). Growth of waves by modulated wind stress. *J. Geophysical Research 81,* 5795.

Preliminary Results of Some Stereophotographic Sorties Flown Over the Sea Surface

L. H. HOLTHUIJSEN
Delft University of Technology
The Netherlands

SYNOPSIS

Preliminary results are presented of a study which is concerned with the directional characteristics of wind generated waves. The basic approach adopted was to measure the actual sea surface elevation as a function of horizontal coordinates by means of stereophotogrammetric techniques. The surface representations thus obtained were Fourier transformed to estimate two-dimensional wave number spectra.

Basic considerations concerning the photogrammetrical process, the transformation rules and the statistical significance of the results are described. The required stereo photographs were obtained during photographic missions carried out in 1973 and 1976 off the island of Sylt (Germany) and off the coast of Holland. So far three two-dimensional spectra, each from a different flight, have been calculated. The sea and weather conditions during these flights are briefly stated. The wind direction in these flights was off-shore.

Frequency spectra computed from the observed wave number spectra are compared with an assumed frequency spectrum and an observed frequency spectrum. The agreement is reasonable but some discrepancy needs to be resolved. For two of the three observations the directional distribution of the wave energy is strongly asymmetrical around the wind direction. This asymmetry seems to correspond to asymmetry in the up-wind coast line.

From the observed spectra a directional spreading parameter has been computed as a function of wave number. The results in normalized form agree well with published data. The absolute values of the spreading parameter for two spectra are within 30% of the anticipated values. For the third spectrum the values were almost five times too large but a comparison in this case may not be proper. In one of the spectra some indications of bi-modality around the wind direction have been observed in the directional distribution function near the peak of the spectrum.

1. INTRODUCTION

Observations of the two-dimensional spectrum of wind generated waves are relatively few and are mostly based on methods with rather poor directional resolution. The techniques which are used for the observations may be based on such systems as a sparse wave gauge array [e.g., Panicker and Borgman (1970)] or a buoy capable of detecting directional characteristics of the sea surface [e.g., Longuet-Higgins et al. (1963)]. The few detailed observations which have been published were based on other techniques such as high-frequency radio-wave backscatter [e.g., Tyler et al. (1974)], analysis of the sea surface brightness [e.g., Stilwell (1969), Sugimori (1975)] or stereophotography [e.g., Cote et al. (1960)]. These provided information with a high directional resolution but the analysis of the results in terms of wave characteristics has not been very extensive.

The Delft University of Technology and the Ministry of Public Works in the Netherlands have developed a system based on stereophotography which monitors the instantaneous sea surface elevation as a function of horizontal coordinates. It has been used in this and other studies and it is anticipated that it will also be used in future studies of wave phenomena such as wave transformation in the surf zone or wave patterns around marine structures. The present study, which is a joint effort of the University and the Ministry, is aimed at observing and interpreting two-dimensional spectra of wind generated waves in a variety of atmospheric conditions. The study is primarily directed towards the evaluation of the shape characteristics of the directional energy distribution of the waves.

For this study a few hundred stereo pictures have been taken since 1973 and the analysis has just begun. The results reported here are preliminary in that the number of analyzed pictures is only a fraction of the total and in that the interpretation of these pictures has not as yet been completed. The spectra which are presented here were calculated from three sets of pictures, each containing ten stereo pairs. These sets were chosen on two bases. One is the photographic quality which was judged by photogrammetric experts, the other is the scientific interest. In this stage of the study it was felt that wave fields generated by off-shore winds would be of most interest because the boundary conditions are well defined. Also, results of past investigations of wave generation [Hasselmann et al. (1973), Hasselmann et al. (1976)] suggests that observations in these conditions may be extrapolated to more complex conditions.

The first set of pictures which was analyzed was taken in September 1973 during almost "ideal" offshore wind conditions in the area just west of the German island of Sylt. These observations were carried out in the framework of an international oceanographic project known as the Joint North Sea Wave Project (JONSWAP) which is concerned with the study of wave generation and prediction. A variety of articles directly related to JONSWAP has been published and more are being prepared for publication. Some references are: Hasselmann et al. (1973), Spiess (1975), Hasse et al. (1977), and Hühnerfuss et al (1978). The two other sets of pictures were taken in March and November 1976 in the area west of Holland near the town of Noordwijk, also in offshore wind conditions. Wave observations at sea level during the first and last flights are available and these have been used for comparison with the stereophotogrammetric results.

2. STEREOPHOTOGRAMMETRY OF THE SEA SURFACE

When an object is photographed from two slightly different positions, the imagery in the two pictures will also be slightly different. The differences depend upon the geometry of the object. By measuring the differences, the elevation of the surface relative to an arbitrary plane of reference can be determined. The conventional technique of analysis requires human interpretation of the pictures and complicated stereoscopic viewing devices. More advanced procedures, which have only recently been developed, use a computer to carry out a correlation between the images to arrive at the same results [e.g., Crawley (1975)].

In the conventional geodetic aerial survey the pictures are taken vertically in sequence from an airplane and the interval is chosen such that the pictures overlap in the area directly under the line of flight. An obvious condition is that the object does not change between exposures. In land survey this poses no problem since the ground surface does not move. The sea surface, however, changes very rapidly. To limit the distortions betweeen two successive pictures to an acceptable level, they should be taken within an interval of 1 - 5 ms. The airplane cannot possibly fly from one required point of photography to the other within this time lapse. The consequence is that not one but two cameras are needed which take the pictures "simultaneously," that is, within an interval of 1 - 5 ms and that two aircraft are needed to position the two cameras. Apart from these technical differences in obtaining the stereo pairs, the methods and procedures used in this study are standard in geodetic survey and they have been used in the past by various oceanographic investigators. A well publicized effort is the Stereo Wave Observation Project [SWOP, Cote et al. (1960)] and the present system is essentially a revised version of the system used in SWOP.

It will suffice here to comment only briefly on the operational system. Actually two independent systems were built. One is based on Hasselblad cameras and has been described in detail elsewhere [Holthuijsen et al. (1974)]. The other is an almost exact copy of that system except that the Hasselblad cameras were replaced by UMK cameras of Jenoptik which are superior in optical and metrical aspects. The Hasselblad system was used for observations in the area off Sylt and the UMK system was used in the area off the coast of Holland. Synchronization of the cameras was achieved by using a radio signal that triggered a command pulse which was manipulated electronically in such a way that it complied with the timing characteristics of the receiving camera. The synchronization error for the Hasselblad system was less than 1 ms for all of the analyzed stereo pairs and for the UMK system the synchronization error was less than 5 ms. To position the cameras two Alouette III helicopters were used. These helicopters had a drop-door over which the cameras could be mounted. The distance between the helicopters was estimated during the flight through a range finder which was imposed on the viewer of a third camera which looked from one helicopter to the other. It took a picture of the other helicopter every time the downward looking cameras were activiated. From these photographs the distance between the helicopters could be computed and the scale of photography could be determined.

The specification for the helicopter formation during a photographic sortie were largely based on photogrammetric requirements. Only the altitude was based on the anticipated sea state since the noise and resolution in the spectrum are directly related to the altitude of photography. The upper limit of the altitude was based on noise considerations. The standard deviation of the measurement error is estimated to be 0.03% of the altitude [Holthuijsen et al. (1973)]. Taking a noise to signal variance ratio of 1:10 as an acceptable upper limit, it can be shown that the altitude should be less than 1,000 times the standard deviation of the instantaneous sea surface elevation (or 250 times the significant wave height). The lower limit of the altitude is directly related to the resolution. If a resolution in the spectrum is required equivalent to ¼ of the peak wave number or better, it appears that for the Hasselblad system the altitude should be higher than 6.7 times the reciprocal of the peak wave number. For the UMK system the factor is 4.0. For most "young" sea states these upper and lower limits are not in conflict. The final choice of the altitude was confined to multiples of 250 ft for the pilot's convenience.

The size of the sea surface covered in stereo in one stereo pair is usually too small to produce sufficient data for a reliable estimate of the two-dimensional spectrum. To increase the amount of data more pictures were taken in sequence with a space interval sufficiently large to ensure photography of non-overlapping sea areas. The corresponding time interval between the exposures would be typically between 4 s and 20 s (depending on camera type, ground speed, and altitude). The photographic operation to obtain this sequence is called a sortie.

In principle, the pictures can be analyzed with recently developed, fully automated processes. The facilities, however, were not available for the present study and the conventional technique was used. In the three-dimensional space which is reproduced in the stereoscopic viewing devices a right-handed system of coordinates was defined with the y-axis in the direction of flight and the z-axis upward. During the analysis the sea surface was read at a square grid with spacing $\Delta x = \Delta y$, which was chosen such that aliasing in the spectrum would be limited to only a fraction of the total wave variance. For each stereo pair the analysis was carried out in a square field as large as possible and the elevations were determined relative to an arbitrary plane of reference. In the subsequent numerical analysis the linear trend was removed through a least-squares analysis. The fields obtained from a series of stereo pairs were initially arbitrary in shape but fairly close to a rectangle. Later they were clipped or extended to a square of one common size of $L_x \cdot L_y$ as required in the spectral analysis. Sections where no stereo information was available (mainly in the areas of extension) were filled with zeros.

3. TRANSFORMATION AND STATISTICAL SIGNIFICANCE

The sea surface data from the stereophotogrammetric analysis were Fourier transformed to estimate the two-dimensional wave number spectrum ($\vec{k}$-spectrum). To inspect the directional characteristics as a function of wave number, the $\vec{k}$-spectrum was transformed to the wave-number, direction space to produce the k,θ-spectrum. The $\vec{k}$-spectrum was also transformed to the frequency domain.

The $\vec{k}$-Spectrum

The definition adopted here for the two-dimensional wavenumber spectrum $E(\vec{k})$ is given by Eqs. 1, 2, and 3.

$$E(\vec{k}) = \lim_{A\to\infty} \left< \frac{H(\vec{k})}{A} \right> \qquad (1)$$

where

$$H(\vec{k}) = \left| \iint_{\vec{R}} h(\vec{x})\, e^{-i2\pi\vec{k}\cdot\vec{x}}\, d\vec{x} \right|^2 \qquad (2)$$

$$A = \iint_{\vec{R}} d\vec{x} \qquad (3)$$

and <> denotes ensemble averaging. Observations of $h(\vec{x})$ were available from the stereo analysis in a number of square fields and these fields were considered to be realizations of the ensemble. They were Fourier transformed with a multi-dimensional, multi-radix FFT procedure [Singleton (1969)] and the final estimates were obtained by averaging the results over the available realizations. The sea surface data were not tapered and the spectral estimates were not convolved; consequently the spectral estimates are "raw" estimates. In analogy with time series analysis [e.g., Bendat and Piersol (1971)] the reliability is represented by a χ^2-distribution with 2n degrees of freedom, where n is the number of fields. The resolution denoted by $\Delta k_x \cdot \Delta k_y$ is on the order of $(L_x \cdot L_y)^{-1}$.

The k,θ-Spectrum

The transformation of the $\vec{k}$-spectrum to the k,θ-spectrum is formally given by Eq. 4.

$$E(k,\theta) = E(\vec{k})\,|J_1| \qquad (4)$$

where k = magnitude of $\vec{k}$, θ = orientation of $\vec{k}$ and where the Jacobian $J_1 = k$. Computing the values of $E(k,\theta)$ at a regular grid in the k,θ-plane requires the estimation of $E(\vec{k})$ at corresponding values of $\vec{k}$. This was done by bi-linear interpolation of $E(\vec{k})$ at the proper values of $\vec{k}$ (see Figure 1).

The directional resolution can be estimated by considering the angular distance between two neighbouring, independent estimates of $E(\vec{k})$ on a circle in the $\vec{k}$-plane centred in $\vec{k} = \vec{0}$. On this circle with arbitrary radius, k, approximately $2\pi k/\Delta k$ independent estimates of $E(\vec{k})$ are available and the directional increment between these estimates in radians is $\Delta k/k$. This would be a fair approximation of the directional resolution if all pictures were oriented in the same direction. But actually the orientation is a random variable due to the helicopter motion during the sortie. The directional bandwidth to be added will be on the order of twice the standard deviation (σ_θ) of the helicopter yaw. The final expression for the directional resolution ($\Delta\theta$) is given in Eq. 5.

$$\Delta\theta \simeq \Delta k/k + 2\sigma_\theta \qquad (5)$$

The resolution in k will be on the order of the increment between estimates of $E(\vec{k})$ in the $\vec{k}$-plane which is $L_x^{-1} = L_y^{-1}$.

The reliability of the estimates of $E(k,\theta)$ can again be expressed in terms of a χ^2-distribution but the number of degrees of freedom is not uniformly distributed over the k,θ-plane. It constitutes an un-

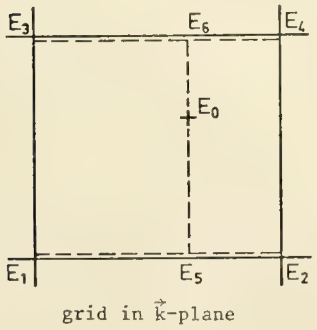

E is estimate of $E(\vec{k})$

E_5 linearly interpolated between E_1 and E_2

E_6 linearly interpolated between E_3 and E_4

E_0 linearly interpolated between E_5 and E_6

+ gridpoint in k,θ plane transformed to $\vec{k}$-plane

FIGURE 1. Bi-linear interpolation in the $\vec{k}$-plane.

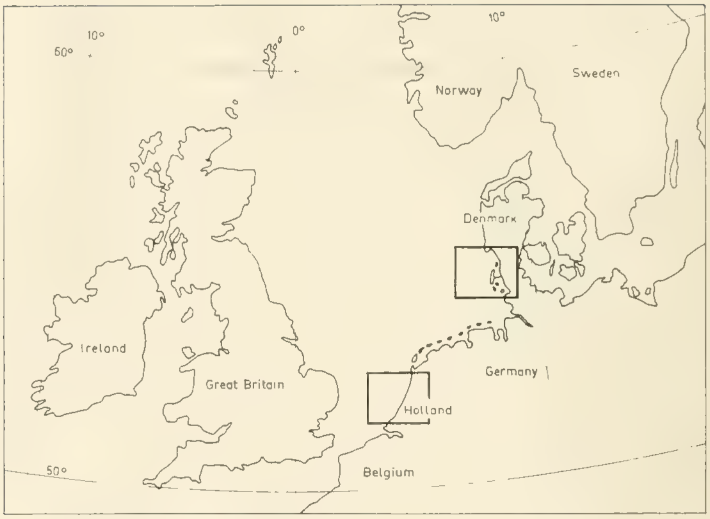

FIGURE 2. Sites of the field operations. The areas in the boxes are shown enlarged in Figures 3 and 4.

dulating function due to the fact that the estimated value of $E(k,\theta)$ is based on four values of $E(\vec{k})$ which are usually not equally weighted in the given interpolation technique. They are equally weighted only when a transformed gridpoint in the k,θ-plane coincides with the centre of a mesh in the $\vec{k}$-plane. In that case the number of degrees of freedom for $E(k,\theta)$ is four times the number of degrees of freedom for each individual estimate of $E(\vec{k})$. This is the upper extreme of the undulating function. The lower extreme occurs when a transformed k,θ gridpoint coincides with a gridpoint in the $\vec{k}$-plane. Then the number of degrees of freedom of the estimate of $E(k,\theta)$ is equal to the number of degrees of freedom of an individual estimate of $E(\vec{k})$. The values of the two extremes are 8n and 2n respectively.

The f-Spectrum

The f-spectrum is determined by integrating the f,θ-spectrum over the range $(0,\pi)$ and multiplying the result by two. The operation is given by Eq. 6.

$$E(f) = 2\int_0^\pi E(f,\theta)d\theta \qquad (6)$$

The f,θ-spectrum has been computed from the $\vec{k}$-spectrum. The relationship to transform from wave number vector to frequency is based on the linear dispersion relation for deep water corrected for currents. This expression and the transformation are given in Eqs. 7, 8, and 9.

$$f = (gk/2\pi)^{\frac{1}{2}} + \vec{k}.\vec{V} \qquad (7)$$

$$E(f,\theta) = E(\vec{k})\,|J_2| \qquad (8)$$

$$J_2 = [\tfrac{1}{2}\,(g/2\pi)^{\frac{1}{2}}k^{-3/2} + Vk^{-1}\cos\,(\theta_c - \theta)]^{-1} \qquad (9)$$

$\vec{V}$ is the current vector and V and θ_c are its magnitude and orientation. To determine the values of $E(\vec{k})$ the same procedure as described above was used. The resulting spectrum is the frequency spectrum as observed in a point stationary with respect to the sea bottom. This was done so as to be able to compare the results with measurements carried out with anchored buoys. Expressions for the approximate resolution (Δf) and number of degrees of freedom (N) are given by Eqs. 10 and 11.

$$\Delta f \simeq \frac{\partial f}{\partial k}\,\Delta k = \frac{1}{2\pi}\,c_g\Delta k \qquad (10)$$

$$N \simeq 8\,n\,\frac{\pi^2 f^2}{g}\,\frac{1}{\Delta k} \qquad (11)$$

4. DESCRIPTION OF THE SITES AND THE WEATHER CONDITIONS

Maps of the areas off Sylt and off Noordwijk and two bottom profiles are given in Figures 2, 3, 4 and 5. It may be noted that both areas are similar in general appearance but an important difference seems to be that the coast near Sylt recedes sharply North and South of the island and is strongly asymmetric with respect to the off-shore direction,

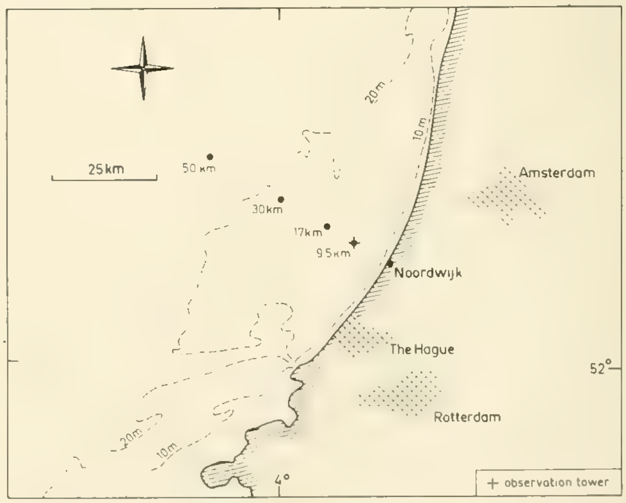

FIGURE 3. The area of observation off Noordwijk. Locations of observations indicated by dots.

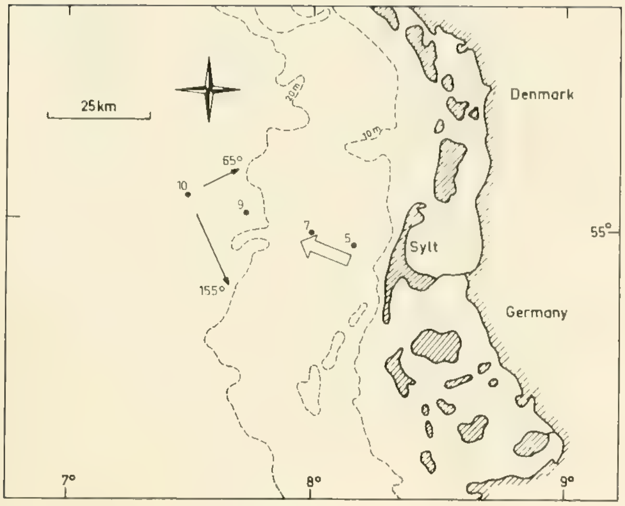

FIGURE 4. The area of observation off Sylt. Active wave monitoring stations and station of observation indicated by dots. Wind direction indicated by arrow.

whereas the coast near Noordwijk is more continuous and symmetric. For both sites the water is effectively deep for waves generated by an off-shore wind.

The sortie in the area west of Sylt was carried out during the field operations of JONSWAP in 1973, on September 18th, at 17:30 hr (local). Brümmer et al. (1974) describe the large scale weather features during the JONSWAP operations of 1973 and also give results of meteorological observations from ships, buoys, and balloons in the area. According to this information the windspeed and direction prior to the flight had been fairly constant for one day. Since the wind was almost perfectly off-shore the situation was classified as an "ideal" generation case. In the two hours prior to the flight the windspeed and direction at station 8 (see Figure 4), at 10 m elevation was approximately 13 m/s and 110° respectively. The direction is only a few degrees off the "ideal" off-shore direction of 107°.

The weather during this flight was poor for photographic operations and all pictures which were taken were under-exposed, in spite of the best possible photographic measures. Pictures were taken over six stations of JONSWAP, including active wave monitoring stations 5, 7 and 9 (see Figure 4). The frequency spectra observed at these stations are given in Figure 6 and they may be used for a direct comparison with the results of stereo observations over these stations. But in selecting the pictures for preliminary investigation preference was given to photographic quality rather than availability of ground-true information and it appeared that the best pictures were taken over station 10, which was otherwise inactive during the flight.

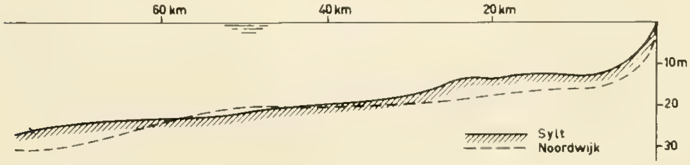

FIGURE 5. Bottom profiles off Sylt (direction 287°) and off Noordwijk (direction 300°).

The frequency spectrum at station 10 was estimated with a "hindcast" procedure based on the JONSWAP parameter relationships [Hasselmann et al. (1973)]. The "hindcast" was attempted for stations 5, 7, and 9 with the observed windspeed of 13 m/s but the results (Figure 6) were rather poor, although they seemed consistent with the statistical variation in the observations of JONSWAP. The agreement improved when a windspeed of 15 m/s was used (Figure 7). This was the windspeed estimated just prior to the flight. Since this fictitious windspeed produced more realistic results, in particular for station 9 which was the nearest to station 10, it was used for the "hindcast" at station 10. The resulting spectrum is given in Figure 8, the comparison with the stereophotographic results will be discussed in Section 5.

The second and third set of pictures to be analyzed were chosen from the pictures obtained in the area off Noordwijk. The main reason for selecting these pictures rather than the pictures taken off Sylt was that the results of the sortie just described indicated that the data were influenced by the asymmetry of the coastline of Sylt. The coast near Noordwijk is more symmetric for off-shore wind directions. The information on the atmospheric conditions during these flights was based on standard synoptical observations which were received through the office of the Royal Netherlands Meteorological Institute. In addition a cup-anemometer and a windcone were available at an observation tower located 9.5 km off-shore from Noordwijk (see Figure 3).

The second sortie (the sequence refers to the sequence of analysis, not the time sequence of the flights) was flown in off-shore wind conditions on November 12, 1976, at 13:05 hr (local). From the synoptical observations it was found that the wind was rather weak over the entire North Sea and the wind in the area of observation was mainly caused

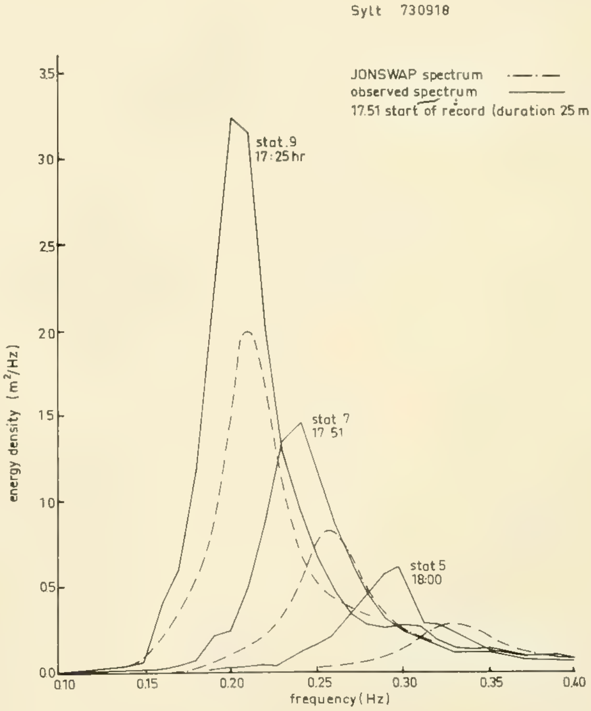

FIGURE 6. Observed frequency spectra at stations 5, 7, and 9 and corresponding JONSWAP spectra for U = 13 m/s.

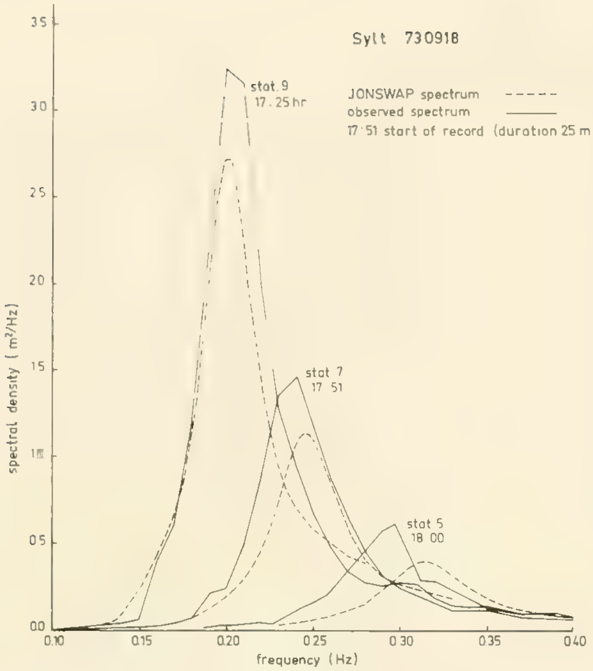

FIGURE 7. Observed frequency spectra at stations 5, 7, and 9 and corresponding JONSWAP spectra for U = 15 m/s.

by a weak and fairly large low pressure area over central France. Synoptical observations in the coastal region 25 km North and 8 km South of Noordwijk indicated windspeeds of 4.5 m/s and 4.0 m/s respectively and the wind directions of 100° and 160° respectively. The wind observation at the platform was carried out at 23 m above mean sea level. Averaged over the duration of the photographic operations (about 40 min.), the observed windspeed was 6.4 m/s and the directions just prior and just after the flight were approximately 140°. The "ideal" off-shore direction would have been 120°. To estimate the windspeed at 10 m elevation, the observed value was corrected. The correction for the bulk of the tower, is known from wind-tunnel tests, and the windspeed was extrapolated using a logarithmic wind-profile with a drag coefficient, $c_{10} = 1.5 \times 10^{-3}$. The resulting windspeed is 6.0 m/s. The corrections for the wind direction are marginal and well within the error of observation. During this flight pictures were taken over the observation tower and at locations 30 km and 50 km from the coast (see Figure 3). The pictures taken 30 km off-shore seemed to contain sufficient stereo information to obtain a relatively high directional resolution and these were chosen for preliminary investigation.

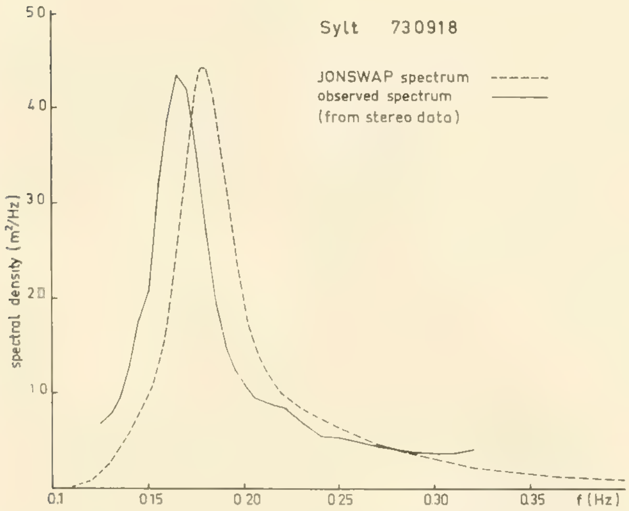

FIGURE 8. Spectrum inferred from stereo data and corresponding JONSWAP spectrum for U = 15 m/s.

Wave observations at sea level were available from a wave gauge at the observation tower and from an accelerometer buoy at the location 30 km off-shore. The spectrum of the buoy is given in Figure 9. It will be used for comparison with the stereo-photographic results. During the flight some swell coming from south-westerly directions was observed from the helicopters.

The third sortie was flown off Noordwijk on 23 March 1976 at 12:20 hr (local). The wind was rather weak over the entire North Sea and the direction varied from ENE off the Dutch coast to SSW off the Norwegian coast. This windfield was caused mainly by a fairly weak high pressure ridge over the North Sea and a low pressure area over central France. Synoptical observations at the same coastal stations as mentioned above indicated windspeeds of 11.0 m/s and 8.0 m/s respectively and wind directions of 80° and 70° respectively. The corrected wind speed and direction at the observation tower (averaged over 20 min.) were 8.3 m/s and 70°. Since the "ideal" off-shore wind direction would have been 120° the wind is slanting across the coast line at an angle of approximately 50°. Obviously this implies a strong asymmetry of the coast line with respect to the wind direction. Pictures were taken over the observation tower and at locations 17 km and 30 km off-shore. Since the pictures taken 17 km off-shore seemed to be the best, they were analyzed. Unfortunately no simultaneous wave observations in the area were available.

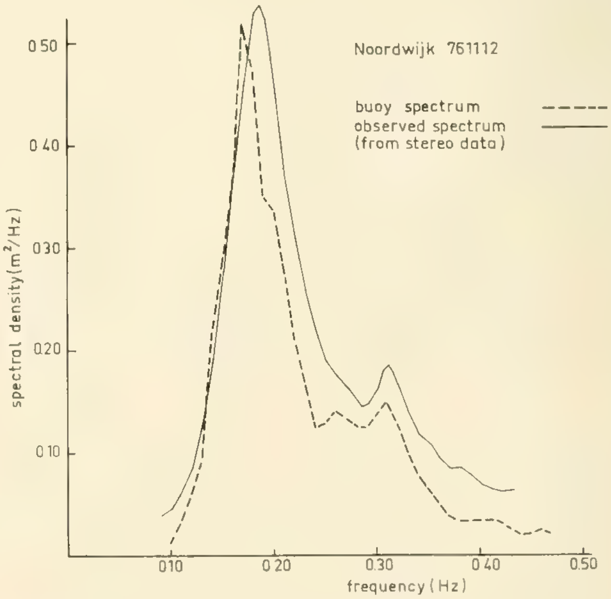

FIGURE 9. Spectrum inferred from stereo data and spectrum from buoy measurement.

TABLE 1 Photogrammetric parameters	Sylt Sept. 1973	Noordwijk Nov. 1976	Noordwijk March 1976
altitude of photography	1500 ft	500 ft	500 ft
orientation of helicopters relative to true North	110°	275°	310°
percentage of zeros added in stereo areas	4%	5%	2%
number of pictures accepted for stereo analysis	9	10	10
stereo area per picture	220x220 m^2	156x156 m^2	170x170 m^2
grid in $\vec{x}$-plane	5 x 5 m^2	3 x 3 m^2	2.5x2.5 m^2

5. RESULTS

The values of a number of parameters relevant to the photogrammetric process are given in Table 1. In view of the preceding paragraphs this table is largely self-explanatory but a few parameters will be discussed briefly.

The altitudes of photography are based on anticipated significant wave heights and peak wave numbers. These were estimated by substituting the windspeed and fetch in the JONSWAP parameter relationships [Hasselmann et al. (1973)]. For the sortie off Sylt the wind information was fairly good as it was based on ship observations in the area but for the sorties off Noordwijk this information was poorer, partly because no observations prior to the flights were available. The helicopters were flying directly into the wind during the sortie off Sylt. During the second and third sortie they were flying with the wind in the left respectively right rear quarter with 11° drift. Ten stereo pairs were taken in each sortie but one pair was rejected from the set taken off Sylt because it covered too small an area. Using the sea surface information from the stereophotogrammetric analysis the three $\vec{k}$-spectra were computed according to the procedures described in Section 3. The results are presented in the form of countour-line plots in Figures 10, 11, and 12. Some isolated regions in the $\vec{k}$-plane have been indicated where the spectra are thought to be seriously affected by noise. This noise is dealt with in the Appendix. Values of relevant spectral parameters are given in Table 2. For the determination of the directional resolution, σ_θ was estimated at 0.06 [c.f., Holthiujsen et al. (1974)].

On closer inspection of the contour-line plot of the spectrum of Sylt two wave fields can be identified: one coming from approximately 110° and one from approximately 155°. This is rather surprising because neither the wind conditions nor the ground-true information gave such indication. The swell in the second spectrum (off Noordwijk) coming from south-westerly directions was observed during the flight. It is well separated from the locally generated wind sea and it will be largely ignored in the following discussion. The peak of the third spectrum is, surprisingly, coming from Northerly directions rather than from Easterly directions, as may be antitipated from the wind direction.

Instead of the k, -spectra, the normalized directional distribution functions have been plotted in Figures 13, 14 and 15. The definition of these functions is given by Eqs. 12 and 13.

$$D(\theta;k) = \frac{E(k,\theta)}{\int_0^\pi E(k,\theta)d\theta} \qquad \text{for } 0 < \theta < \pi \qquad (12)$$

$$D(\theta;k) = 0 \qquad \text{for } \pi < \theta < 2\pi \qquad (13)$$

This seemed to be more illustrative than a contour-line plot of the k,θ-spectra, the normalized direc- primarily for the directional characteristics. An evaluation of these functions will be given in the next paragraph.

TABLE 2 Spectral parameters	Sylt Sept. 1973	Noordwijk Nov. 1976	Noordwijk March, 1976
resolution in $\vec{k}$-plane $[m^{-2}]$	$(220x220)^{-1}$	$(156x156)^{-1}$	$(170x170)^{-1}$
number of degrees of freedom	18	20	20
peak wave number (k_m) $[m^{-1}]$	0.0045	0.0641$^{(x)}$	0.0265
directional resolution			
at $k = k_m$	20°	13°	20°
$k = 2k_m$	13°	10°	13°
$k = 3k_m$	11°	-	11°

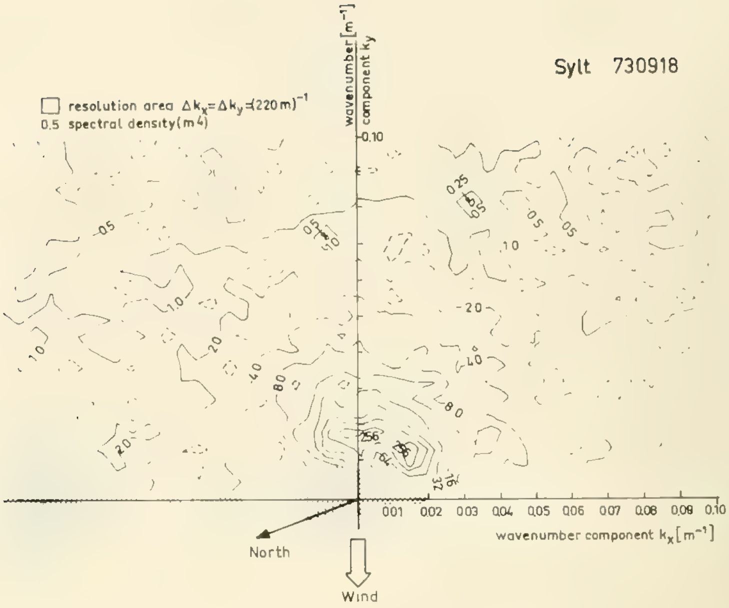

FIGURE 10. Contour-line plot of $\vec{k}$-spectrum off Sylt, Sept. 18th, 1973. Contour-line interval equivalent to factor 2. Minor variations are dashed, shaded areas seriously affected by noise. Orientation of positive k_y-axis 110°, k_x-axis 200° from true North. Wind direction 110°.

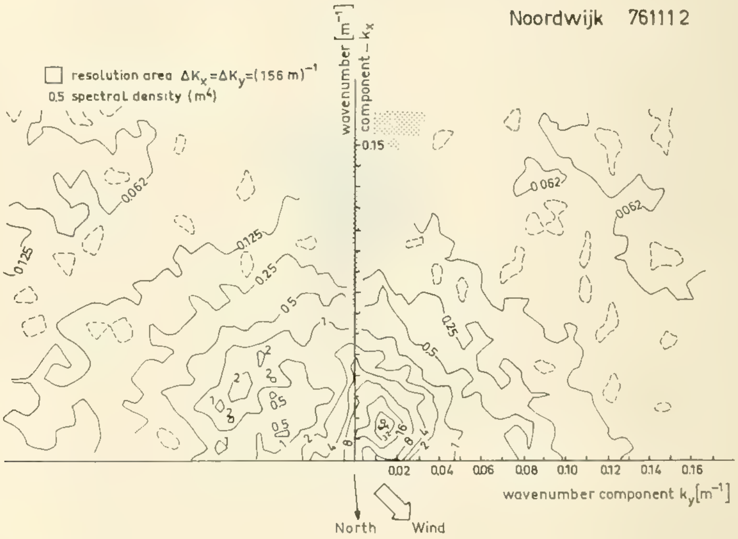

FIGURE 11. Contour-line plot of $\vec{k}$-spectrum off Noordwijk, Nov. 12th, 1976. Contour-line interval equivalent to factor 2. Minor variations are dashed, shaded areas seriously affected by noise. Orientation of k_y-axis 275°, negative k_x-axis 185° from true North. Wind direction 140°.

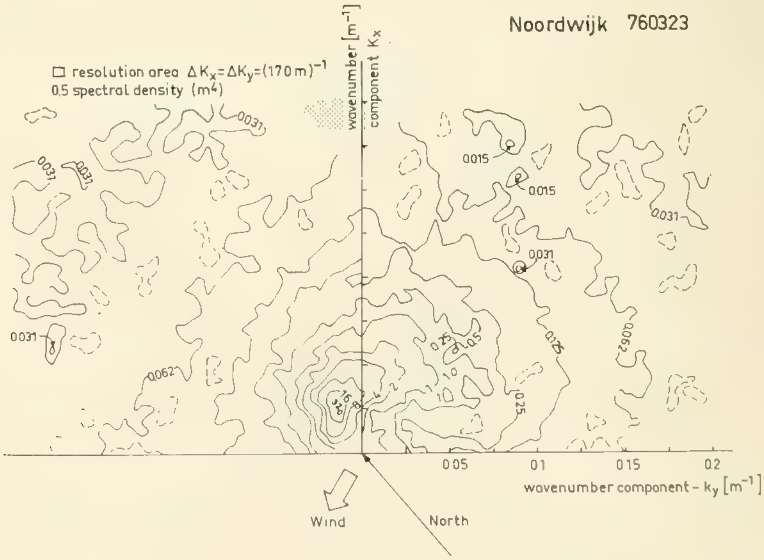

FIGURE 12. Contour-line plot of $\vec{k}$-spectrum off Noordwijk, March 23rd, 1976. Contour-line interval equivalent to factor 2. Minor variations are dashed, shaded area seriously affected by noise. Orientation of k_y-axis 310°, k_x-axis 40° from true North. Wind direction 70°.

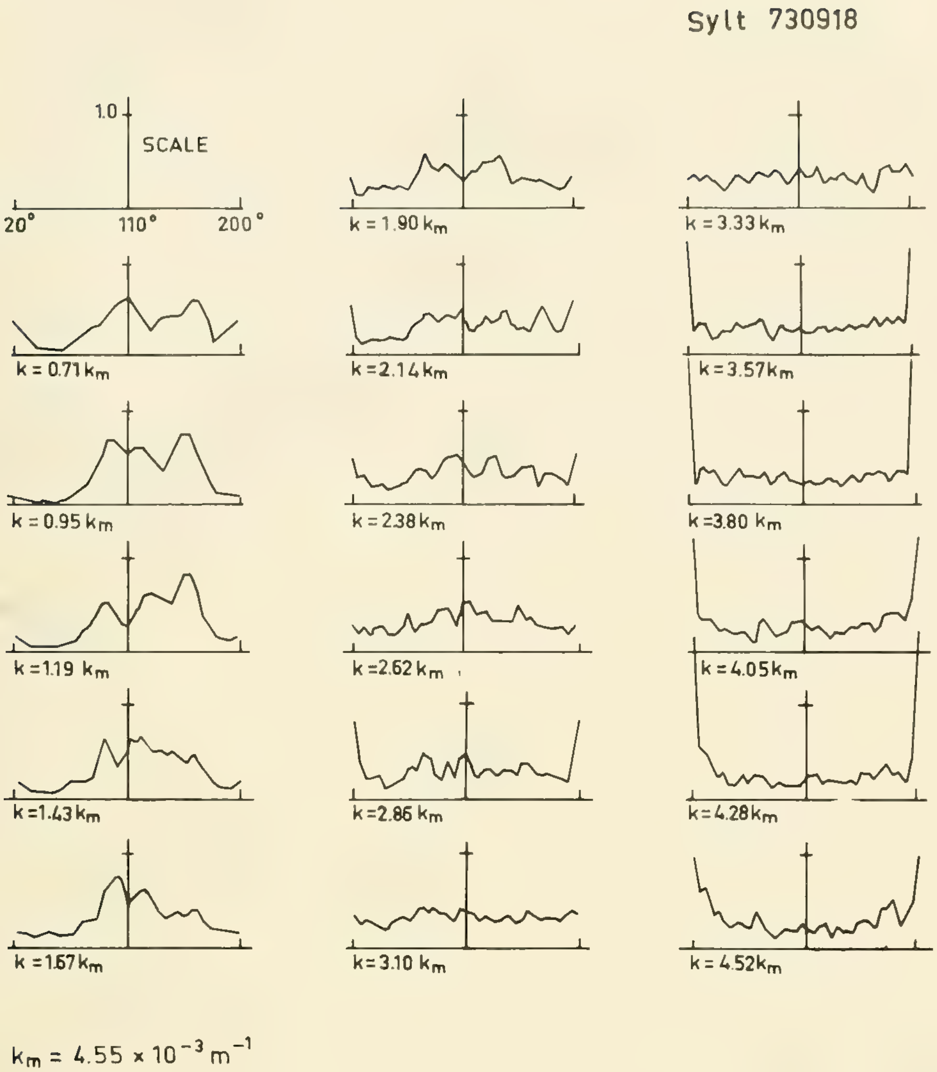

FIGURE 13. Normalized directional distribution functions of the $\vec{k}$-spectrum off Sylt, Sept. 18th, 1973. Directions are relative to true North.

The f-spectrum has been computed from the $\vec{k}$-spectrum according to the procedures described in Section 3. The result for the spectrum off Sylt is given in Figure 8 along with the corresponding JONSWAP spectrum. The resolution is about 0.02 Hz near the peakfrequency, which is 0.165 Hz, and 0.01 Hz at twice the peak frequency. The number of degrees of freedom for frequencies greater than 0.13 Hz is 250 or more. Considering the scatter in the original data set of JONSWAP and taking into account the resolution, it is concluded that the agreement between the two spectra is fair.

The frequency spectrum computed from the observed $\vec{k}$-spectrum of the second sortie is plotted in Figure 9 along with the frequency spectrum of the buoy. The resolution of the spectrum based on the stereo data is on the order of 0.02 Hz near the peak of the swell and 0.015 Hz near the peak of the locally generated wind sea. The number of degrees of freedom is 125 or more for frequencies greater than 0.10 Hz. For the spectrum of the buoy the resolution is about 0.02 Hz and the number of degrees of freedom is about 48.

The spectrum based on the stereo data seems to be shifted in energy density. This may have been caused by noise and to appreciate this influence the $\vec{k}$-spectrum was corrected. The noise was assumed to be uniformly distributed over the $\vec{k}$-plane and the variance was estimated at 0.002 m^2 (based on the anticipated measurement error of 0.03% of the altitude of photography, see Section 2). Accordingly a uniform noise level of 0.018 m^4 was subtracted from the $\vec{k}$-spectrum and the transformation was carried out again. The differences were marginal compared with the earlier results and the shift cannot be explained with the anticipated noise uniformly distributed over the $\vec{k}$-plane. Further investigation is needed to resolve the remaining discrepancy.

The frequency spectrum of the third sortie is given in Figure 16 but no attempt has been made to compare this spectrum with a "hindcasted" spectrum because the relatively simple relationships for off-shore wind situations cannot be applied.

6. DISCUSSION OF THE RESULTS

In the area off Sylt, where the wind was almost perfectly off-shore and fairly homogeneous and stationary, one would expect to find a frequency spectrum with a shape similar to the shape found earlier in JONSWAP. Finding a JONSWAP-type spectrum in the conditions off Noordwijk seems to be less

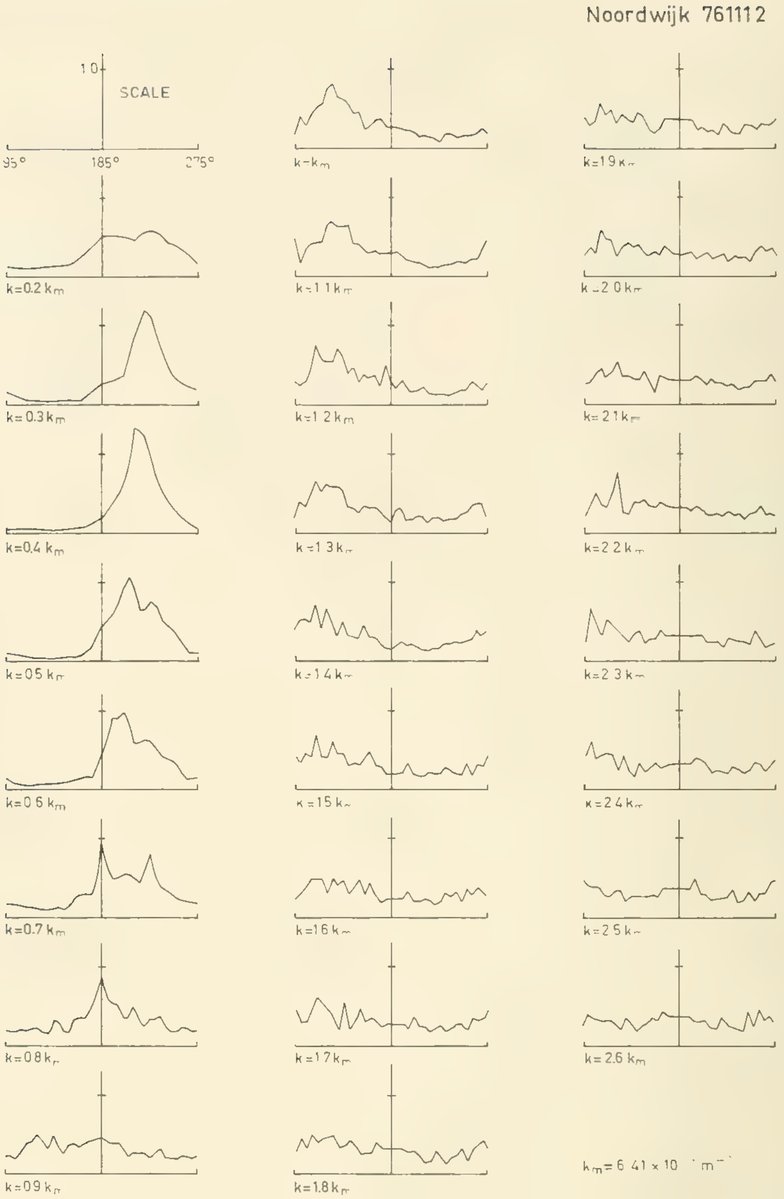

FIGURE 14. Normalized directional distribution functions of the $\vec{k}$-spectrum off Noordwijk, Nov. 12th, 1976. Directions are relative to true North. The peak wave number k_m is related to the locally generated wind sea.

likely because the differences between the wind observations at the coast and at the tower are fairly large and the wind may have varied between the point of observation and the coast. In particular for the slanting wind conditions it is obvious that a JONSWAP-type spectrum would not be found, due to the asymmetry in the coastline around the wind direction. On the other hand, non-linear interactions in the spectrum may produce a JONSWAP-type spectrum, in spite of the asymmetry and the variations in the windfield [Hasselmann, et al. (1976)]. From an inspection of Figure 8 it can be concluded that the frequency spectrum in the sortie off Sylt is indeed JONSWAP-like. The correspondence of the frequency spectra off Noordwijk with a JONSWAP-type spectrum has not yet been investigated.

For the $\vec{k}$-spectra of the first two sorties one would expect to find directional distribution functions having some kind of standard shape, symmetrical about the mean direction although some skewness may be expected in the observation off Noordwijk because the wind direction was not perfectly off-shore. For the third spectrum strong skewness may be anticipated due to the slanting position of the coastline.

These expectations seem to be far from reality in the $\vec{k}$-spectrum off Sylt. The directional distribution near the peak of the spectrum (see Figure 13) is distinctly asymmetric with respect to the wind direction with the highest peak at + 45° off the wind direction (155° from true North). It is highly improbable that the wave generation mechanism would build a directional distribution as strongly asymmetrical as this. An explanation for this unexpected observation can perhaps be found through a detailed study of the wind and wave fields, possibly using "hindcasting" procedures. But in the context of this paper one can only speculate on some possible causes. The source function is symmetrical, as is the radiative energy transfer, since bottom and current refraction is virtually non-existent. It seems then that the asymmetry stems from asymmetry in the wind field or in the boundary conditions. As for the wind field, a cursory inspection of the large scale weather maps revealed no asymmetry. As for the boundary conditions, the coast of Sylt, rather than the main-land coast was deemed to be relevant as upwind boundary. This was based on the expectation that the wave energy is propagating in a narrow angular sector around the wind direction [e.g., Hasselman et al, (1973)] and since the coast of Sylt is rather symmetric it should not cause asymmetry in the wave field. But the coast to the North and South of Sylt is strongly asymmetric. In fact, the distance to shore in the direction of 155° (the direction of the highest peak) is almost 2.5 times the distance to shore in the direction of 65° (the "symmetrical" direction, see Figure 4). If this asymmetry in the windward boundary is indeed the cause, then it seems that the "ideal" generation cases of JONSWAP may be contaminated to some degree by asymmetric boundary conditions. Still, relating this conclusion to the observed $\vec{k}$-spectrum is largely speculative as long as it is not substantiated with more data. In particular the shapes of the $\vec{k}$-spectra at locations closer to shore may give some clues.

The expectations regarding the directional distributions for the locally generated wind sea off Noordwijk in the second sortie seem to be more realistic, at least in an overall sense (Figure 14, for $k > k_m$). Any skewness is hard to identify through visual inspection of the plots due to the small scale variations in the functions. These probably stem from the statistical variability of the estimates. The swell peak ($k = 0.3\ k_m$ to $k = 0.6\ k_m$) is unimodal and covers a narrow angular sector with a half power width of about 35°.

The directional distribution functions of the spectrum in the third sortie seem to be strongly skewed for the lower wave numbers (Figure 15, $K \leq 2\ k_m$, say) but for higher wave numbers skewness is hard to identify visually. As for the main direction of the energy distribution, it varies almost monotonously from approximately 80° at higher wave

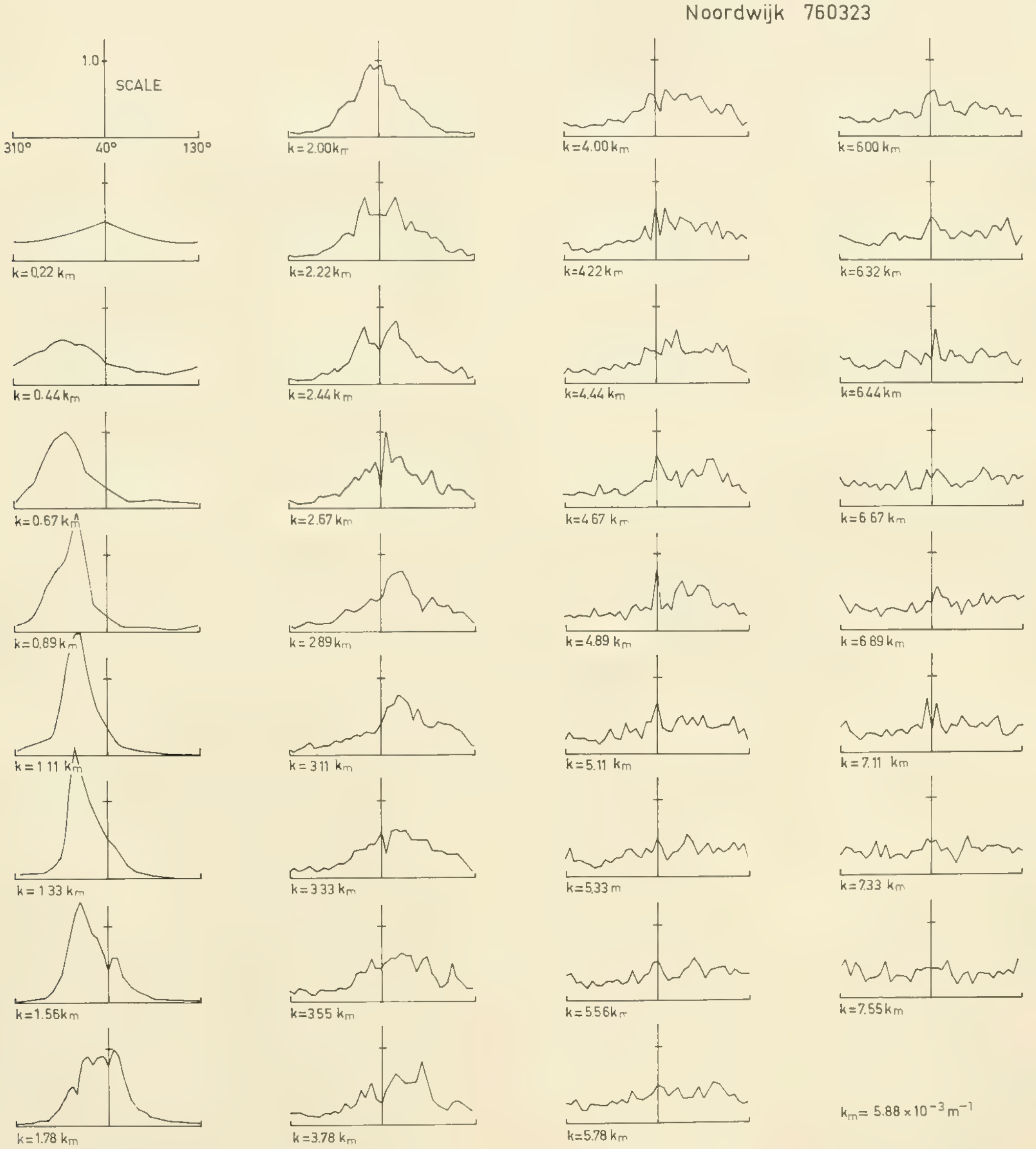

FIGURE 15. Normalized directional distribution functions of the $\vec{k}$-spectrum off Noordwijk, March 23rd, 1976. Directions are relative to true North.

numbers to about 0° for the lowest wave numbers (see also Figure 17). The energy of the higher wave numbers travels more or less in the wind direction but the main direction of the peak of the spectrum appears to be about 10° relative to true North; that is about 60° from the wind direction and almost parallel to the coast. This seems to be the most remarkable feature of this spectrum as one would expect to find a uniform main direction of 70°, considering the wind direction and the effects of non-linear interactions [Hasselmann et al. (1976)]. Again, as with the spectrum off Sylt, it is felt that the observed phenomenon is due to the asymmetry of the coastline around the wind direction.

To substantiate this preliminary conclusion qualitatively, a simplified "hindcasting" model was implemented for homogeneous, stationary wind fields, arbitrary coastlines, and deep water. In this model, which is basically the same as suggested by Seymour (1977), the wave components from different directions are decoupled. In this version the parameter relationships from JONSWAP [Hasselmann et al. (1973)] were taken and the suggestions of Mitsuyasu et al. (1975) were used for the directional distribution function. When applied to the situation of the first and third sortie it did produce two-dimensional f,θ-spectra which at least qualitatively agreed with the so far unexpected main directions in the observed $\vec{k}$-spectra.

This seems to be in contradiction with the conclusions of Hasselmann et al. (1976) that the shape of the spectrum is fairly insensitive to variations in the wind field due to the non-linear interactions in the spectrum. It should be noted however that the distance to the coast, in terms of wave lengths, seems to be rather short for the lower wave numbers in the two spectra so that non-linear interactions may not have been sufficiently effective to overcome the influence of the geometry of the coastline. For the higher wave numbers the distance to shore is relatively long and the non-linear interactions may have produced the observed directional distribution functions which indeed seem to be hardly affected by the asymmetry of the coastline. The observations therefore may still be consistent with the theory of non-linear interactions and the conclusions of Hasselmann et al. (1976) if the relevant space and time scales are considered.

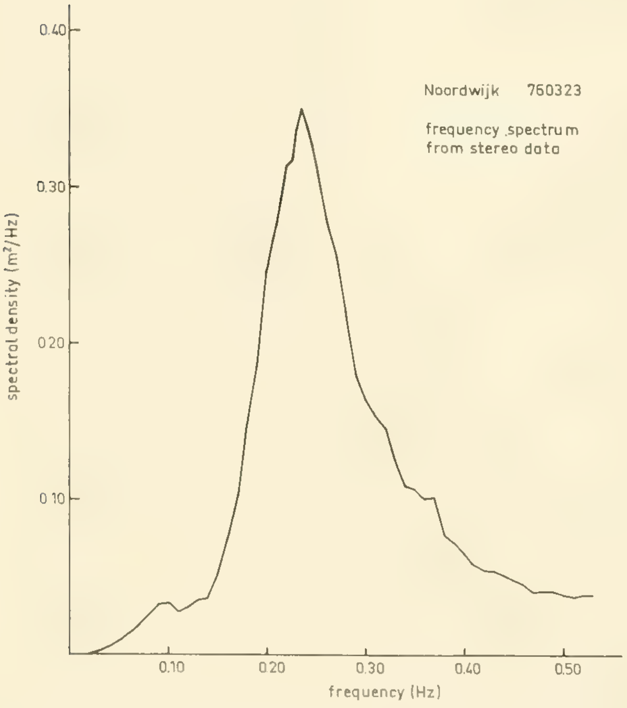

FIGURE 16. Spectrum inferred from stereo data of observation off Noordwijk, March 23rd, 1976.

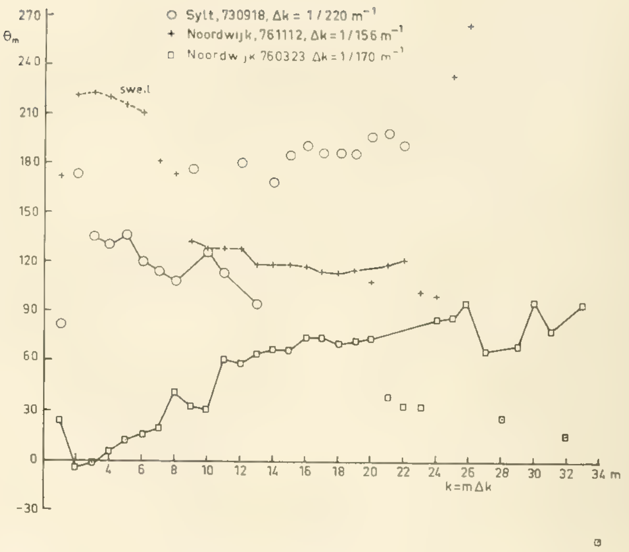

FIGURE 17. The mean direction of the waves relative to true North, as function of wave number.

In an "ideal" generation case the directional distribution of the wave energy is often approximated with a simple unimodal function. The observed situations are distinctly multi-modal, but one such function, given in Eq. 14, has been fitted to the data. This was done mainly to compare the results with the published data.

$$D(\theta) = \frac{1}{2\sqrt{\pi}} \frac{\Gamma(s + 1)}{\Gamma(s + \frac{1}{2})} \cos 2s \left(\frac{\theta - \theta_m}{2}\right) \qquad (14)$$

In this expression s is the spreading parameter and θ_m is the mean direction, both of which may vary with k. The values of θ_m and s have been computed using a least-squares technique. The results for θ_m as a function of wave number are given in Figure 15. Noise in the spectra (see Appendix) did influence these results and outliers had to be identified. As a criterion for acceptation, the rate of change of θ_m along the wave number axis has been chosen. An accepted value of θ_m should be within 30° of its neighboring values on the wave number axis.* This is equivalent to a rate of change of approximately 0.0024 m for the first sortie, 0.0033 m for the second sortie, and 0.0031 m for the third sortie. This allows for slow but significant variations in θ_m which is required, for instance, in the spectrum of the third sortie. The resulting set of accepted values of θ_m is also indicated in Figure 17. The values of s at the corresponding values of the wave number have been plotted in Figure 18 in a format suitable for a comparison with data published by Mitsuyasu et al. (1975).

---

*The value of 30° was chosen arbitrarily.

Mitsuyasu et al. (1975) presented results of a number of measurements (five) which were carried out with a cloverleaf buoy at several locations around the Japanese islands. The observed wave fields were generated by various types of wind fields, including on-shore and off-shore winds. It appears from the ratio of the wind speed to the phase speed of the peak frequency of these observations, that the state of development of the wave fields was rather advanced (the ratios ranging from 0.75 to 1.25). Based on the observed values of s, relationships in the frequency domain were suggested. The relevant expressions have been transformed here to the wave number domain to produce Eqs. 15 and 16.

$$\left.\begin{aligned} \tilde{s} &= \tilde{k}^{-1.25} && \text{for } \tilde{k} \geq 1 \\ \tilde{s} &= \tilde{k}^{2.5} && \text{for } \tilde{k} < 1 \end{aligned}\right\} \qquad (15)$$

$$s_m = 11.5\ (U/c_m)^{-2.5} \qquad (16)$$

where $\tilde{s} = s/s_m$ and $\tilde{k} = k/k_m$, s_m is the maximum value of s, k_m is the peak wave number, c_m is the phase speed of the peak wave number, and U is the wind speed. The data of Mitsuyasu et al. (1975) are probably obtained in situations where tidal currents were negligible and in the above transformation the deep water linear relationship between frequency and wave number was used.

Equations 15 and 16 are also plotted in Figure 18 and the agreement is fair, the scatter being on the same order of magnitude as the scatter in the data of Mitsuyasu et al. (1975). The values of s_m computed from the stereo data are 6.0 for the spectrum off Sylt, 5.0 for the first spectrum off Noordwijk. These are also in fair agreement with the values suggested by Mitsuyasu et al. (1975) which are 4.6 and 6.1 respectively. However, for the second spectrum off Noordwijk the observed value of s is 27.4 whereas the value following from expression 16 is 5.9. This is a very large discrepancy which is possibly due to the rather extreme asymmetry of the coastline around the wind direction where the suggestions of Mitsuyasu et al (1975) may not be applicable.

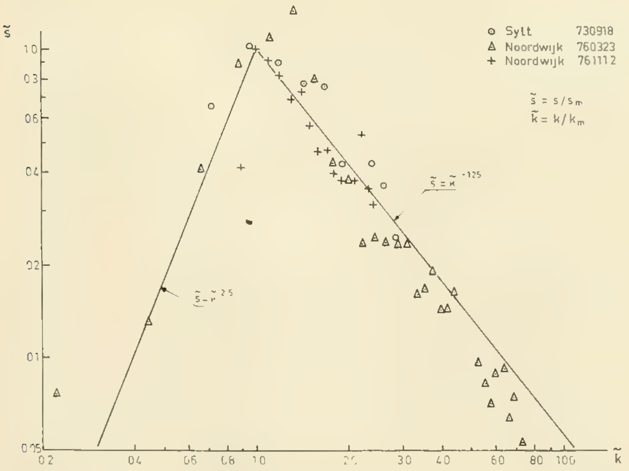

FIGURE 18. The normalized spreading parameter as a function of the normalized wave number.

The above discussion concerned rather overall-characteristics of the directional distributions. It is planned to investigate these functions more in detail. For instance, in the $\vec{k}$-spectrum off Sylt one aspect which will require closer study is the shape of the directional distribution near the peak of the spectrum in a sector around the wind direction. Two peaks at + and - 15° relative to the wind direction can be identified and this phenomenon seems to be "real" in the sense that the directional resolution seems sufficiently high (20°) to resolve these peaks in terms of statistical significance. The resonance theory of Phillips (1957) predicts a bimodal distribution for frequencies in the initial stage of development, but the components around the peak have passed that stage and there is no relation with this theory. More relevant seem to be the theory and calculations of Hasselmann (1963), Longuet-Higgins (1976), and Fox (1976) which produce a non-linear energy transfer in wave number space with two lobes towards the lower wave numbers and two lobes towards the higher wave numbers. Fox (1976) noted that this function resembles a "butterfly." Also the results of Tyler et al. (1976), who observed directional distributions of wind generated waves with high-frequency radio-wave backscatter, may be of interest since some of the distributions have a bimodal character around the mean direction.

7. CONCLUSIONS

Three, two-dimensional, wave number spectra have been computed from stereophotographic data obtained in off-shore wind conditions. The agreement with ground-true information is reasonable but some discrepancy needs to be resolved.

The directional distribution of the wave energy near the peak of the first spectrum is strongly asymmetric. In the third spectrum the main direction of the waves differs appreciably from the wind direction. It is speculated that these phenomena are due to asymmetry in the up-wind coastline. The directional distribution functions of the second spectrum are more symmetric and unimodal, at least in an overall sense.

A bimodality in a sector around the wind direction is observed near the peak of the first spectrum. This bimodality may be related to a multi-modal non-linear interaction in the spectrum.

The observed normalized directional spreading parameter as function of a normalized wave number is in fair agreement with published data. The absolute values are about 30% larger for the first spectrum and about 20% lower for the second spectrum. The values for the third spectrum are almost five times too large. This may be due to the rather extreme asymmetry of the coastline where a comparison with the published data may not be proper.

The results reported herein are preliminary. Additional analysis of available data is being carried out.

ACKNOWLEDGMENTS

The helicopters were provided by the Royal Netherlands Air Force and they were flown by the Search and Rescue team of Soesterberg airbase (the Netherlands). This is gratefully acknowledged. Considerable support in terms of logistics, groundtruth data, meteorological observations, etc. was received from colleagues in the framework of JONSWAP and this is greatly appreciated.

NOTATION

A	area of spatial integration
c_m	phase speed of component f_m
c_g	group velocity
$D(\theta)$	standard directional distribution function
$E(\vec{k})$	spectral density in k-space
$E(k,\theta)$	spectral density in k,θ-space
$E(f,\theta)$	spectral density in f,θ-space
$E(f)$	spectral density in f-space
f	frequency
g	acceleration due to gravity
h	instantaneous surface elevation
$H(\vec{k})$	Fourier transform of surface elevation
J	Jacobian
$\vec{k}$	wavenumber vector $\vec{k} = (k_x,k_y)$
k	wavenumber, modulus of wavenumber vector
k_m	wavenumber at peak of wavenumber vector spectrum of locally generated wind sea
L_x	dimension of area of analysis in x-direction
L_y	dimension of area of analysis in y-direction
N	number of degrees of freedom
n	number of transformations
$\vec{R}$	boundary of spatial integration
s	directional spreading parameter
s_m	maximum value of s
$\tilde{s}$	dimensionless spreading parameters s/s_m
U	windspeed at 10 m elevation
$\vec{V}$	tidal current vector
V	magnitude of $\vec{V}$
$\vec{x}$	place vector $\vec{x} = (x,y)$
x,y,z	spatial coordinates
Δ	increment
θ	direction, orientation of wavenumber vector
θ_c	orientation of tidal current
θ_m	mean direction
σ_θ	standard deviation of helicopter yaw

REFERENCES

Bendat, J. S., and A. G. Piersol (1971). *Random Data: Analysis and Measurement Procedures*, Wiley-Interscience, New York.

Brümmer, B., D. Heinrich, L. Krügermeyer, and D. Prüm (1974). The Large-Scale Weather Features over the North Sea during the JONSWAP II Experiment. *Berichte des Instituts für Radiometeorologie und Maritime Meteorologie, Universität Hamburg, Institut der Frauenhofer Gesellschaft, 24.*

Cote, L. J., J. O. Davis, W. Marks, R. J. McCough, E. Mehr, W. J. Pierson, J. F. Ropek, G. Stephenson, and R. Vetter (1960). The Directional Spectrum of a Wind-generated Sea as determined from Data obtained by the Stereo Wave Observation Project. *Meteorological Papers, 2,* No. 6, New York University.

Crawley, G. B. (1975). Automatic contouring on the Gestalt photomapper, testing and evaluation. *American Society of Photogrammetry, Workshop III,* San Antonio, Texas, U.S.A.

Fox, M. J. H. (1976). On the non-linear transfer of energy in the peak of a gravity-wave spectrum. II, *Proceedings Royal Society of London, A. 348,* 467.

Hasse, L., M. Grünewald, and D. E. Hasselmann (1977). Field observations of flow above the waves. Preprint from the *Proceedings of the NATO-Symposium on "Turbulent Fluxes through the Sea Surface, Wave Dynamics and Prediction,"* Bendol, to be published by Plenum Press (New York, London).

Hasselmann, K. (1963). On the non-linear energy transfer in a gravity-wave spectrum. Part 3. Evaluation of the energy flux and swell-sea interaction for a Neumann spectrum. *Journal of Fluid Mechanics, 15,* 385.

Hasselmann, K., R. P. Barnett, E. Bouws, H. Carlson, D. E. Cartwright, K. Enke, J. A. Ewing, H. Gienapp, D. E. Hasselmann, P. Krusemann, A. Meerburg, P. Muller, D. J. Olbers, K. Richter, W. Sell, and H. Walden (1973). Measurements of Wind-Wave Growth and Swell Decay during the Joint North Sea Wave Project (JONSWAP). *Ergänzungsheft zur Deutschen Hydrographischen Zeitschrift, Reihe A (8°),* No. 12.

Hasselmann, K., D. B. Ross, P. Müller, and W. Sell (1976). A parametric Wave Prediction Model. *Journal of Physical Oceanography, 6,* 2; 200.

Holthuijsen, L. H., M. Tienstra, and G. J. v.d. Vliet (1974). Stereophotography of the Sea Surface, an Experiment, *Proceedings of the International Symposium on Ocean Wave Measurement and Analysis, American Society of Civil Engineers,* 153.

Hühnerfuss, J., W. Alpers, and L. Jones (1978). Measurements at 13.9 GHz of the radar backscattering cross section of the North Sea covered with an artifical surface film to be published in *Radio Science.*

Longuet-Higgins, M. S., D. E. Cartwright, and N. D. Smith (1963). Observations of the directional spectrum of sea waves using the motions of a floating buoy. *Ocean Wave Spectra,* 111-132, Prentice Hall, Inc., New Jersey.

Longuet-Higgins, M. S. (1976). On the non-linear transfer of energy in the peak of a gravity-wave spectrum: a simplified model. *Proceedings Royal Society of London, A. 347,* 311.

Mitsuyasu, H., F. Tasai, T. Suhara, S. Mizuno, M. Ohkusu, T. Honda, and K. Rikiishi (1975). Observations of the Directional Spectrum of Ocean Waves Using a Cloverleaf Buoy. *Journal of Physical Oceanography, 5,* 750.

Panicker, N. N., and L. E. Borgman (1970). Directional Spectra from Wave Gage Arrays. *Proceedings of the 12th International Conference on Coastal Engineering,* Washington, D.C., p. 117.

Phillips, O. M. (1957). On the generation of waves by turbulent wind. *Journal of Fluid Mechanics, 2,* 417.

Singleton, R. C. (1960). An algorithm for computing the Mixed Radix Fast Fourier Transform, *IEEE Transactions on Audio and Electroacoustics, AU-17,* 2; 93.

Spiess, F. N. (1975). Joint North Sea Wave Project (JONSWAP) progress - an observer's report. *Report ONRL-C-8-75, Office of Naval Research,* London.

Seymour, R. J. (1977). Estimating wave generation on restricted fetches. Proceedings of the American Society of Civil Engineers. *Journal of the*

Waterway, Port, Coastal and Ocean Division, WW2, paper 12924, p. 251.

Stilwell, D. (1969). Directional Energy Spectra of the Sea from Photographs. *Journal of Geophysical Research, 74,* 8; 1974.

Sugimori, Y. (1975). A study of the application of the holographic method to the determination of the directional spectrum of ocean waves. *Deep-Sea Research, 22,* 339.

Tyler, G. L., C. C. Teague, R. H. Stewart, A. M. Peterson, W. H. Munk, and J. W. Joy (1974). Wave directional spectra from synthetic aperture observations of radio scatter. *Deep-Sea Research, 21,* 989.

APPENDIX

NOISE

Inspection of contour-line maps of the sea surface obtained from the observation off Sylt revealed a dome-shaped distortion. This distortion is probably caused by the fact that the pictures could not be positioned in the stereoscopic viewing devices with the accuracy normally obtained with high grade pictures. When this positioning is not optimal, a dome-shaped distortion is to be expected. Unfortunately the exact distortion cannot be determined, but in the $\vec{k}$-plane it seems to be well separated from the wave information (area No. 1 in Figure 19) and the data in this area was removed in the subsequent analysis.

The other noise-affected areas are related to a phenomenon introduced by the manner of scanning the pictures during the photogrammetrical process: the sea surface elevation at even-numbered lines (scanned in positive y-direction) is systematically slightly too low, while the elevation at odd-numbered lines (scanned in negative y-direction) are systematically slightly too high. This effect has been observed earlier in the analysis of stereo photos of regular waves generated in a hydraulic laboratory. The principal wave length and direction of this distortion correspond with the location of area No. 2 in Figure 19, which is the location of the Nyquist wavenumber in x-direction. This spectral information was removed from the spectra in the subsequent analysis. The noise in areas No. 3, 4, and 5 was labeled as such mainly because of the delta-type behavior of the directional distribution functions in these regions. It is probably due to variations in the error introduced by the scanning and possibly also by "leakage" from area No. 2. In the k-spectrum off Sylt this noise was not removed. In the k-spectrum off Noordwijk the noise in the indicated region in Figure 11 has been removed.

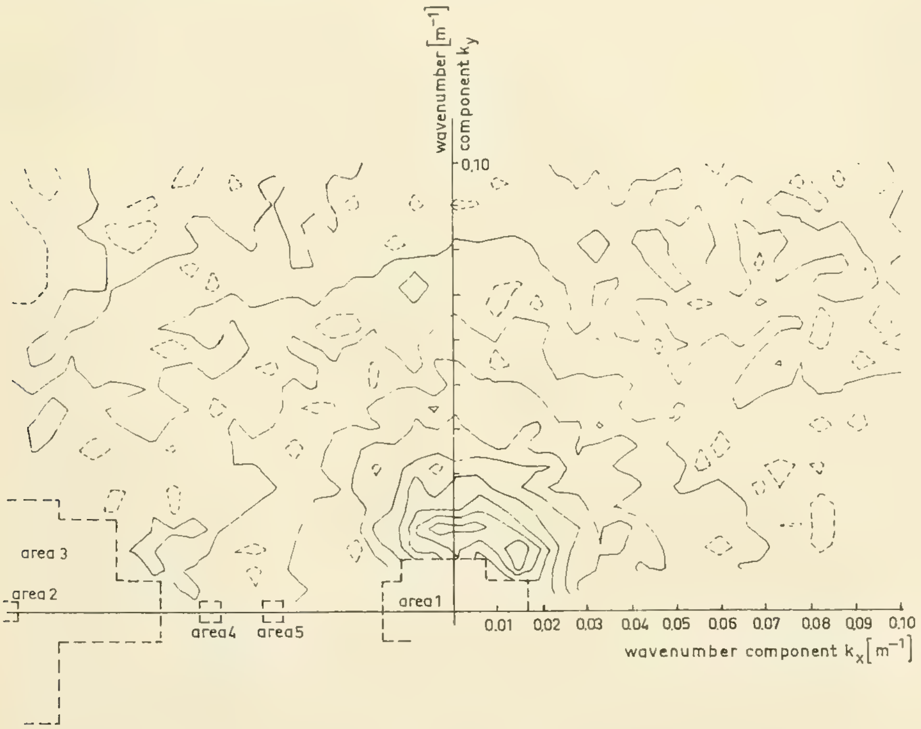

FIGURE 19. Location of noise in $\vec{k}$-plane.

Gerstner Edge Waves in a Stratified Fluid Rotating about a Vertical Axis

Erik Molo-Christensen
Massachusetts Institute of Technology
Cambridge, Massachusetts

ABSTRACT

An exact solution is obtained for edge waves along one inclined planar boundary in a fluid rotating about a vertical axis. The solution is based on a modification of Gerstner's rotational waves, and includes the effect of mean drift. The solution reduces to Yih's edge wave solution for zero rotation and to Pollard's rotational deep water Gerstner waves in rotating flow. Satellite observations of sea surface are shown which reveal patterns similar to those which would be generated by Gerstner edge waves.

1. INTRODUCTION

The early, exact solution by Gerstner (1802, see 1932, p. 419) was rediscovered by Rankine (1863), discussed by Lamb (1932), found to be valid for free surface waves in an arbitrarily stratified flow by Dubreil-Jacotin (1932), further modified to describe edge waves by Yih (1966), and free surface waves in a rotating flow by Pollard (1970). However, there has been a tendency to dismiss Gerstner waves as of limited applicability to phenomena in nature. As Lamb (1932) has pointed out, the generation of Gerstner, free surface waves by the application of surface stresses requires a certain mean vorticity distribution to exist in the fluid. It can be argued that in a nonrotating fluid of uniform density it is difficult to conceive how the required vorticity distribution can be established. However, in a stratified and rotating fluid, there are mechanisms capable of generating vorticity without viscous diffusion. In a stratified fluid, the baroclinic term, expressing the action of a pressure gradient normal to a density gradient in generating vorticity will be capable of establishing a horizontal vorticity field. In a rotating fluid, the effects of vortex stretching and compression can establish distributed vertical vorticity.

There, in a rotating stratified flow, waves similar to Gerstner waves are more likely to be encountered. In fact, the uniform flow, usually assumed as the mean flow on which small perturbation waves may ride, would be less likely to occur in a rotating stratified fluid. But the small perturbation solutions for waves, as well as exact, finite amplitude solutions, are all useful as approximate descriptions of real phenomena and actual observations.

If such solutions do not fit the exact circumstances, they can possibly serve as starting points for perturbation expansions. Furthermore, we may learn about some of the special features of finite amplitude exact wave solutions; there is a tendency to forget some of these facts when preoccupied with linear wave solutions.

In the following, I shall present a Lagrangian description of an edge wave field, point out where it differs from previous solutions, and develop the dispersion relation for the waves.

2. COORDINATE SYSTEMS AND DISPLACEMENT FIELD

Coordinate System

The waves propagate in the x - direction, normal to the plane of Figure 1. In the planes normal to the x - direction we define the $o\hat{y}\hat{z}$- coordinates, with $o\hat{z}$ vertical and the oyz-coordinates, with oy in the plane of the inclined boundary, inclined at an angle α with the vertical. The particle motion will be in planes parallel to xy.

While Yih (1966) could let the amplitude of particle motion decay with negative y-distance, and Pollard (1970), for deep water waves away from a side boundary, made the obvious and correct choice of letting the particle motion decay with decreasing vertical position; here I have to make a different choice. The amplitude of particle motion will decay along a direction - or, shown in Figure 1 as another coordinate system, ors.

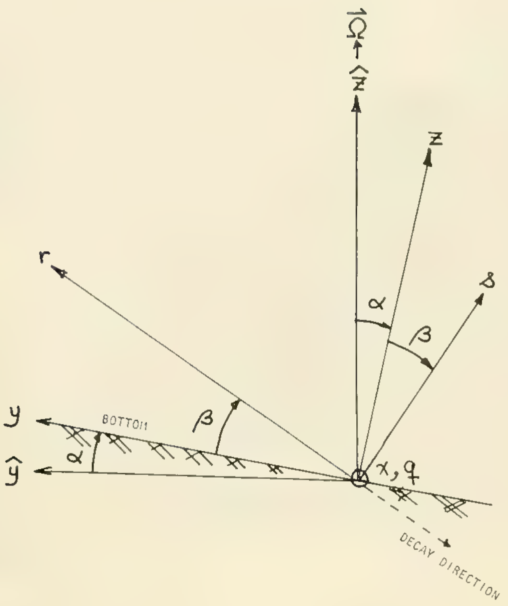

FIGURE 1. Coordinate system, looking along the direction of wave propagation, ox, and along the labeling coordinate direction, oq.

Displacement Field

Using labeling variables, q, r, s, to identify fluid particles, define the field of particle positions in terms of l, r, s and time, t, as follows:

$$x = q + Ut - a\,(\exp mr)\,\sin\,(kq - \sigma t) \qquad (1)$$

$$y = r\cos\beta - s\sin\beta$$

$$+\; a\,(\exp mr)\,\cos\,(kq - \sigma t) \qquad (2)$$

$$z = r\sin\beta + s\cos\beta \qquad (3)$$

for $\qquad r < R \leq 0$

U is a constant mean particle velocity in the x-direction, a is an oscillation amplitude parameter, m is an inverse decay distance measure, K is wavenumber and σ is the frequency of particle motion.

First consider the kinematics of wave motion, next find the condition for incompressibility before proceeding to apply dynamics to give the dispersion relation. A surface defined by letting r be a function of s will have waves that proceed in the x-direction. For example, a string (line) of particles defined by fixed values of r and s will have maxima in y-displacement at

$$kq - \sigma t = 2n\pi \qquad (4)$$

From Eq. 1, substituting for q from Eq. 4 gives the x-positions of crests to be at

$$x_{crest} = [2n\pi + (\sigma + Uk)t]/k \qquad (5)$$

The crests move at a speed of

$$c = (\sigma + Uk)k = \omega/k \qquad (6)$$

ω is the wave encounter frequency, and differs from the particle oscillation frequency by the Doppler shift, Uk.

Mass Conservation

The displacement field defined by Eqs. 1, 2, and 3 can be made to satisfy the requirement that the density of a fluid particle is independent of time by requiring that the Jacobian:

$$\partial(x,y,z)/\partial(q,r,s)$$

$$= 1 - a^2 km\,(\exp 2mr)\,\cos\beta$$

$$+\; (m\cos\beta - k)\,a(\exp mr)\,\cos\,(kq - \sigma t) \qquad (7)$$

is independent of time. This requires

$$k = m\cos\beta \qquad (8)$$

Now proceed to apply the momentum equations to calculate the pressure, which in turn will be set constant at the free surface.

3. PRESSURE FLUCTUATIONS

The momentum equation in Lagrangian variables gives, for the derivative of pressure with respect to the labeling variable q:

$$-p_q/\rho = (\ddot{x} + \dot{z}\,f\sin\alpha - \dot{y}\,f\cos\alpha)x_q$$

$$+\; (\ddot{y} + \dot{x}\,f\cos\alpha)y_q + (\ddot{z} - \dot{x}\,f\sin\alpha)z_q$$

$$+\; g\,\hat{z}_q \qquad (9)$$

The equations for the r and s-derivatives are similar. $f = 2\Omega$ is the angular velocity of rotation of the coordinate system, the angular velocity being vertical as mentioned before. Substituting for x, y, and z from Eqs. 1, 2, and 3 into Eq. 9, one obtains:

$$-p_q/\rho = [\sigma^2 - f\cos\alpha(\sigma + Uk)$$

$$-gk\sin\alpha]\,a\,(\exp mr)\,\sin\theta \qquad (10)$$

$$-p_r/\rho = -\,[\sigma^2 - f\,\sigma\cos\alpha]a^2\exp 2mr$$

$$+\; [-\sigma^2\cos\beta + f\,\sigma\cos(\alpha + \beta)$$

$$+\; fUm\cos\alpha + gm\sin\alpha]a(\exp mr)\,\cos\theta$$

$$+\; fU\cos\,(\alpha + \beta) + g\sin\,(\alpha + \beta) \qquad (11)$$

$$-p_S/\rho = [\sigma^2\sin\beta - f\,\sigma\sin\,(\alpha + \beta)]a(\exp mr)\,\cos\theta$$

$$-\; fU\sin\,(\alpha + \beta) + g\cos\,(\alpha + \beta) \qquad (12)$$

where $\theta = kg - \sigma t$ is the phase of particle oscillation.

At the free surface, which consists of particles with a specified relation between r and s, and with values of labeling variable, q, from − ∞ to + ∞, the pressure must be independent of q and t. This is satisfied, as can be seen from Eqs. 10, 11, and 12, if the pressure is independent of phase θ, and p_q, p_r, and p_s are independent of θ.

From Eq. 12, p_s is independent of θ when

$$\cot \beta = \frac{\sigma}{f \sin \alpha} - \cot \alpha \qquad (13)$$

Since α is given by the slope of the boundary, Eq. 13 gives β for a given σ and α. Equation 10 shows p_q to be independent of θ when

$$\sigma^2 - f \cos \alpha(\sigma + Uk) - g\, k \sin \alpha = 0 \qquad (14)$$

For a given value of σ, Eq. 14 yields k, and m is then found from Eqs. 8 and 13.

This leaves Eq. 11 unused, but it can be shown that the requirement that p_r be independent of θ is not independent of Eqs. 13 and 14. Equation 11 also shows that there will be a mean pressure gradient across the wave propagation direction, proportional to a^2. This is a nonlinear effect of the presence of waves.

4. DISCUSSION

The equivalent to a linear dispersion relation consists of Eqs. 8, 13, and 14, relating particle frequency, σ, decay direction angle, β, horizontal wavenumber, k, and decay parameter, m, with f, α, and U as parameters.

Note that the introduction of a mean drift velocity, U, has a now-trivial effect on dispersion, as can be seen from Eq. 14, where the effect is not a simple Doppler shift in frequency. The equations of rotating fluids are not invariant to Galilean transformations. Also note that the dispersion is independent of the amplitude parameter, a; this is an unexpected result for non-linear waves. But the amplitude of particle motion parallel to oy is really $a \exp[2mR(s)]$, where R is the value of r at the surface. Since m is found from the equations involved in determining dispersion, one cannot really claim that dispersion is independent of amplitude.

With the dependence on phase, θ, eliminated in Eqs. 10, 11, and 12 by satisfying the dispersion relations, one can see that the mean surface slope across the wave propagation direction will vary with wave amplitude and with y- position.

As pointed out by Dubreil-Jacotin (1932), and later by Yih (1966) the results are valid for a fluid of arbitrary stable density stratification.

The solutions given here can be further extended to replace the free surface by an interface between the given flow field and a homogeneous wave trapped fluid, giving the gravitational billows described elsewhere [Mollo-Christensen (1978)]. This will replace the acceleration of gravity, g, by $g' = g(\Delta\rho/\rho)$, where $\Delta\rho$ is the density difference between the two fluids and ρ the density of the lower fluid at the interface.

Similarly, the flow field at the off-shore or inside end may be bounded by a field of geostrophic billows or a combination of gravitational and geostrophic billows [see Mollo-Christensen (1978)].

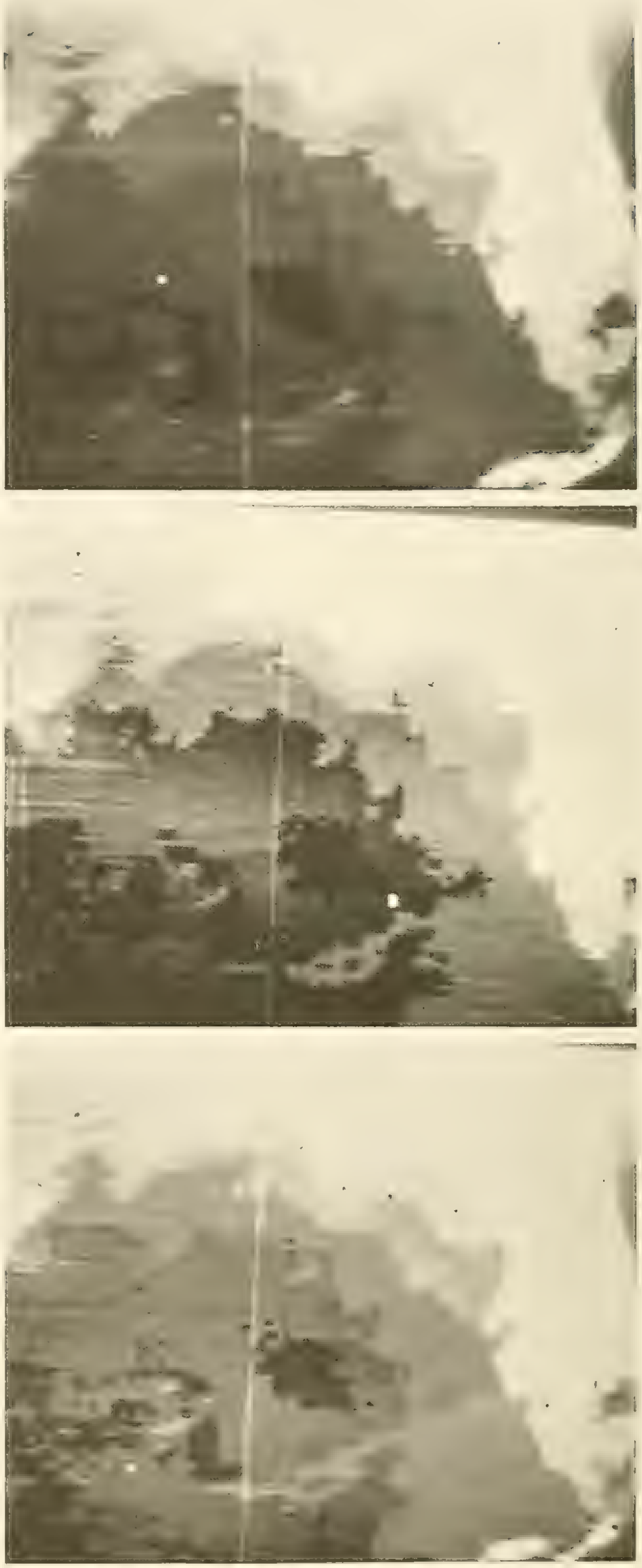

FIGURE 2. High-passed and contrast enhanced satellite infrared images from January 27, 1975, at 1600, 1700, and 1800 hrs., GMT. Florida on the right side, Gulf Coast on top.

5. SOME EXAMPLES OF OBSERVATIONS OF FINITE AMPLITUDE WAVES ALONG A SLOPING BOUNDARY

By processing satellite data on sea surface infrared emission one can see moving patterns of sea surface temperature in the Gulf of Mexico between the continental shelf edge and the coast.

A sequence of processed satellite images taken one hour apart is shown in Figure 2. Because the mean current, U, at the time of observation is not known, one cannot say whether these waves satisfy the dispersion relations for the kind of edge waves discussed here. All one can say at this point is that it appears possible to satisfy the dispersion relations given with wavelengths, bottom slopes, and currents of reasonable orders of magnitude, but one needs to refine the observations further before one can reach any definite conclusions.

6. CONCLUSIONS

Nonlinear edge waves of finite amplitude can have dispersion relations defined by a set of equations relating particle oscillation frequency, encounter frequency, wave number, and other parameters in a way that can be solved systematically if one starts by specifying a suitable wave variable, in the present case, frequency.

The observations which inspired the present analysis show Gerstner edge waves or possibly waves of a different kind; one cannot tell with the evidence now at hand.

ACKNOWLEDGMENT

The research reported here was supported by the Office of Naval Research under Contract No. N00014-76-C-0413. The observations cited were made with support from the Office of Naval Research under Contract No. N00014-75-C-0291. The satellite images were processed using the facilities of Air Force Geophysics Laboratory, Lincoln, Mass.

REFERENCES

Dubreil-Jacotin (1932). Sur les oudes de type permanente dans les liquides heterogenes. *Atti. Accad. Lincei. Rend. Cl. Sci. Fis. Mat. Nat., 6,* 15; 814-819.

Gerstner, F. (1802). Theorie der Wellen. *Abh. d. Königl. Böhmische Ges. d. Wissenschaften zu Prag für das Jahr 1802.*

Lamb, H. (1932). *Hydrodynamics,* 738 pp. Dover, New York, 1945.

Mollo-Christensen, E. (1978). Gravitational and geostrophic billows, some exact solutions. *J. Atmos. Sci.* To be published.

Pollard, R. T. (1970). Surface waves with rotation: an exact solution. *J. Geophys. Res., 75,* 5895-5898.

Rankine, W. J. M. (1863). On the exact form of waves near the surface of deep water. *Phil. Trans.,* 127-138.

Yih, C. -S. (1966). Note on edge waves in a stratified fluid. *J. Fluid Mech., 24,* 765-767.

The Origin of the Oceanic Microstructure

G. I. Barenblatt and A. S. Monin
P. P. Shirshov Institute of Oceanology
Moscow, USSR

ABSTRACT

Microstructure of hydrodynamical fields, a well-known phenomenon in the ocean, is attributed to the formation and development of turbulent spots generated due to the loss of stability or breaking of internal waves. Under some general assumptions the relations are obtained governing the development of turbulent spots at various stages of their evolution. It is shown that the longest and slowest stage of the extension of a turbulent spot is the final, viscous one. Simple self-similar laws of the extension of turbulent spots are obtained for this stage and compared with experiment. Long-standing turbulent layers of the "blini" shape, sharply bound by ambient non-turbulent stratified fluid, are identified with turbulent spots of the above-mentioned origin which are in the final viscous stage of their evolution. The relations are also obtained governing viscous intrusion of the bottom seawater into the body of the ocean.

1. INTRODUCTION

Under strongly stable stratification, turbulent mixing is inhibited due to large losses of the turbulent energy for the work against the buoyancy forces. Under natural conditions, therefore, turbulence cannot be present in the whole body of the fluid during rather long periods of time [Woods (1968), Monin et al. (1977), Federov (1976)]. In fact, it is concentrated only in separate turbulent layers having the shape of "blini," vertically quasi-homogeneous due to mixing, and separated by thin streaks with microjumps of temperature, electrical conductivity, sound velocity, salinity, density, refraction index, and other thermodynamic parameters of sea water sometimes accompanied by microjumps of flow velocity. Such thin-layered vertical structure, which is apparent from inhomogeneities ("steps") on the vertical profiles of density and other thermodynamic parameters (see schematic drawing in Figure 1) or even more sharply from multiple peaks on the profiles of vertical gradients of these parameters, is called *microstructure or fine structure* of hydrodynamical fields. Numerous measurements performed using the method of continuous vertical sounding in the cruises of the research vessels of the Institute of Oceanology, USSR Academy of Sciences, and research vessels of other countries showed that the microstructure exists always and everywhere in the World Ocean (the lack of microstructure may be expected only for the regions of macroconvection which occur rather seldom in the ocean, at least in the low and temperate latitudes).

Smoothing over the microstructural "steps" on the profile of a thermodynamic parameter, e.g., density or temperature, we obtain a smooth curve characterizing large-scale stratification of the ocean (gross-stratification). We have to emphasize that from the point of view of the Richardson criterion gross-stratification is nearly always stable - the Richardson number computed for it, Ri(z), as a rule, is essentially larger than its critical value, 1/4. How can the turbulence be generated under such conditions? Graphs of Ri(z), taking into account the "steps" of microstructure, show values of Ri < 1/4 in several layers of the microstructure - apparently in these very layers, at the moment of sounding, the generation of small-scale turbulence took place (in other layers where Ri > 1/4 turbulence decayed with time). The appropriate conditions for local generation of turbulence at stable gross-stratification may be created by internal waves. Indeed, in the field of internal waves in the regions near their crests and hollows the local values of the Richardson number can be reduced lower than the critical value, 1/4, and the turbulence spots would then be formed there. The internal waves can also break. For the turbulent spots formed after the breaking of internal waves, the formation is characteristic of continuous spectrum, i.e., of developed turbulence immediately

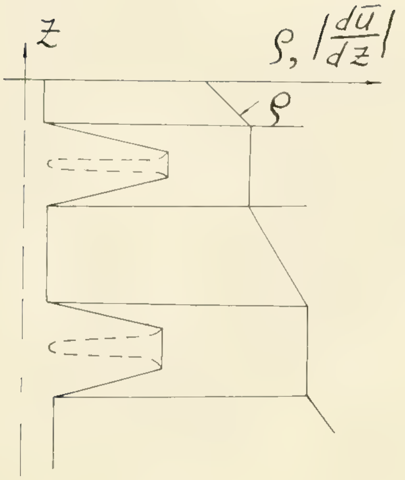

FIGURE 1. Schematic form of synchronous vertical distribution of density and shear in the ocean. The dashed line shows the shear distribution for intrusions.

after the breaking [Belyaev et al. (1975)].

The evolution of a newly-formed turbulent spot appears to be the following. The turbulent mixing makes the spot vertically quasi-homogeneous, therefore, within the spot the density of the water becomes uniform. For stable stratification, when the density grows with depth, the density in the upper half of the mixed spot is higher and in the lower half of the spot lower than at the same levels in ambient fluid. Therefore, under the action of the buoyancy forces, the upper half of the spot should go down and the lower half of the spot should rise to its middle level. Therefore, the spot should "collapse," simultaneously spreading and transforming itself into a thin "blin." The intrusion of such a "blin" into the body of surrounding stratified fluid creates in it a new layer of microstructure.

If the initial internal wave has a long period and wave length (e.g., internal waves with tide periods may be generated by tide forming forces and tides themselves) turbulent spots formed by this wave are large and corresponding turbulent layers are very thick. Internal waves of smaller periods and lengths may develop on these layers forming turbulent spots of smaller sizes and layers of microstructure of smaller thicknesses, etc.; internal waves of minimum periods and lengths, turbulent spots of minimum sizes and layers of microstructure of minimum thicknesses. Thus, the answer to the question "which came first, the chicken or the egg?" consists for this case in the indication of a cascade process "internal waves → turbulent spots → layers of microstructure → internal waves etc." This cascade process may lead to the formation of a quasi-steady spectrum of internal waves, intermittent turbulence, and layers of microstructure (although in real nature the action of some other processes influencing real spectra is possible, including storms and quasi-steady horizontal inhomogeneities of geographic and dynamic origin). The turbulent spots also take part in a rising cascade generated by local instabilities of available shear flows, breaking of surface waves, sinking of cooled fluid from the turbulized surface layer, etc. As distinct from the classical Kolmogorov cascade in non-stratified fluid, here, in passing from a larger scale to a smaller one, the energy is not preserved, being left in turbulent spots in the final stage of their evolution where internal waves do not generate. Thus, in stratified fluid turbulent spots of various scales are continuously generated and the process of their evolution is of considerable interest.

The first stages of the evolution of turbulent spots[*] where the radiation of internal waves takes place are rather short: by estimates of J. Wu (1969) and T. W. Kao (1976) they come to an end in a time interval of the order of several tens of N^{-1} (N is the Brunt-Väisälä frequency) after the beginning of the process. The final stage of the evolution of turbulent spots is much longer. This stage is much less known: in the paper of J. Wu (1969) concerning this stage it is mentioned only that viscosity is of significance at this stage and it is noted that the profile of the spot is preserved during this stage. The analysis presented here shows that the velocity of the extension of turbulent spots at the viscous stage is essentially lower than at the initial stages. It is our opinion that the "blini"-shaped turbulent structures are the intrusions of the turbulent spots of various scales into surrounding stratified fluid which are mainly at the final stage of their evolution.

Thus, let a turbulent spot (Figure 1) be formed in a stable continuously density-stratified (linearly for definiteness) fluid due to some reason (breaking of internal waves, local loss of stability of shear flow, penetration of denser fluid from the turbulent surface layer, etc.). The density of fluid within the turbulent spot due to mixing is uniform in contrast to an ambient continuously stratified fluid being in a state of rest or laminar motion. Certain potential energy is stored due to mixing in the turbulent spot, so the state of the mixed fluid-stratified environment system ceases to be in equilibrium. Mixed turbulent fluid starts to strike (Figure 2) into stratified non-turbulent fluid by tongues - "intrusions" which are formed at the level, $z = z_1$, (z is the vertical coordinate) where the density of stratified fluid is equal to the density of mixed fluid.

Potential energy, stored by the fluid at initial turbulization and mixing in the spot, dissipates during the intrusion of mixed fluid into stratified non-turbulent fluid. It is natural to consider three stages of the evolution of the spot:

(1) *Initial stage of free intrusion.* The motive force of the intrusion at this stage exceeds greatly the drag forces. The turbulent spot extends slightly but the internal waves are intensively formed by the spot.

(2) *Intermediate steady state.* The motive force at this stage is balanced mainly by form drag and wave drag due to radiation of internal waves by an extending turbulent spot. The acceleration of the tongue is negligible.

---

[*] The classification of stages of the evolution of the spot of mixed fluid in the continuously density-stratified fluid goes back to the fundamental work of J. Wu (1969) where the experimental investigation of the initial stages of this process was performed for the wake of circular initial cross-section. T. W. Kao (1976) performed semi-empirical theoretical investigation for the initial stages of the evolution of such wakes.

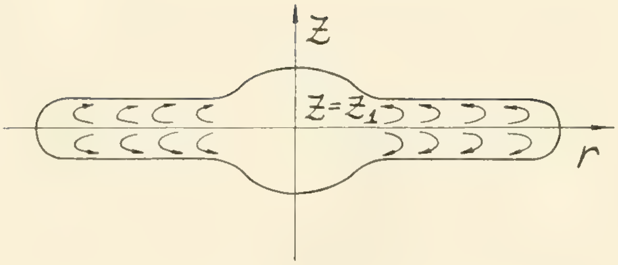

FIGURE 2. The intrusion of a turbulent spot into continuously stratified fluid.

(3) *Final viscous stage.* The motive force is balanced at this stage mainly by viscous drag.

Of course, between the first and second and the second and third stages there exist intermediate transitional periods. When the third stage comes to the end the spot is mixed due to diffusion with ambient fluid and disappears.

The turbulent motion inside of the intrusion tongue is supported by general shear stress together with eddy motions inside of the intrusion due to the difference of the velocities of the tongue and environmental non-turbulent fluid. The boundary of turbulent and non-turbulent fluid is sharp and if the thickness of the intrusion is not too small, the shear required for supporting the turbulence within the intrusion is not large.

Indeed, let us consider the equation of the balance of turbulent energy in a shear flow of stratified fluid neglecting, as usually, the viscous transfer term [Monin and Yaglom (1971)]

$$\partial_t \bar{E} + \partial_z \{\overline{w'E'} + \overline{p'w'}\} = -\overline{\rho w'}g - \bar{\rho}\bar{\varepsilon} - \bar{\rho}\,\overline{u'w'}\,\partial_z \bar{u} \qquad (1)$$

Here t is the time, E the turbulent energy of unit mass, ε the dissipation rate per unit mass, u the longitudinal and w the vertical velocity components, p the pressure. The flow is considered, for the estimates we need, as horizontally homogeneous and the Boussinesque approximation is accepted, i.e., the density variation is taken into account only if it is multiplied by very large factor - gravity acceleration g.

Let us accept for the terms of the equation of balance of turbulent energy, the Kolmogorov approximations [Monin and Yaglom (1971)]

$$\overline{w'E} + \overline{p'w'} = -\rho\ell\sqrt{\beta}\,\partial_z\beta$$

$$\overline{u'w'} = -\ell\sqrt{\beta}\,\partial_z\bar{u},\quad \bar{\varepsilon} = \gamma^4\beta^{3/2}/\ell \qquad (2)$$

Here $\beta = \bar{E}/\bar{\rho}$ is the mean turbulent energy per unit mass, ℓ the external turbulent scale. Thus, the equation of balance of turbulent energy takes the form

$$\partial_t\beta = \partial_z\ell\sqrt{\beta}\,\partial_z\beta - \overline{\rho w'}g/\bar{\rho} + \ell\sqrt{\beta}\,(\partial_x\bar{u})^2 - \gamma^4\beta^{3/2}/\ell \qquad (3)$$

The mathematical nature of sharp interface between the turbulent and the non-turbulent regions becomes completely transparent from this equation. In fact, Eq. (3) is a non-linear equation of heat conductivity type with heat inflow where the coefficient of transfer of turbulent energy equal to $\ell\sqrt{\beta}$ tends to zero with turbulent energy itself. For such equations under zero initial conditions the disturbed region, in contrast to the linear heat conductivity equation, is always finite; this explains (cf. below) mathematically the existence of a sharp interface between the turbulent and the non-turbulent regions.

It is important that, due to mixing following the generation of a turbulent spot, the losses of turbulent energy for the work of suspending a stratified fluid [the second term of the right-hand side of the Eq. (3)] disappear because the density within the spot becomes uniform. Furthermore, the first term of the right-hand side of (3) governs the diffusional transfer of turbulent energy within the mixed region and does not influence the averaged, through the spot, value of turbulent energy. Therefore, the decay of turbulent energy within the spot is governed by the balance of the two last terms of the right-hand side of the equation (3) representing generation and dissipation of turbulent energy, respectively.

It seems natural to accept that the external scale of turbulence ℓ, within a factor of the order of unity, coincides with the transverse size of the tongue of intrusion h; the constant γ by estimates has a value of about 0.5. Thus, the shear $\partial_z\bar{u} \sim \sqrt{\beta}/h$ is sufficient to support the turbulence within the spot at a steady level together with the state of mixing within the spot. If h has the value of tens of centimeters - one meter or more, then for the value $\sqrt{\beta} \sim 1$ cm/sec, characteristic of oceanic turbulence, the shear required for supporting steady turbulence is small. In thin layers it is large; therefore, the turbulence in thin layers decays rather quickly and the spot of mixed fluid exists during the time interval required only for the diffusional mixing of the spot with the ambient stratified fluid.

Furthermore, available experimental data show [J. Wu (1969)] that turbulent entrainment and the erosion of a turbulent spot may be neglected, starting from a very early stage of the evolution till rather late stages of this process. Therefore, we shall take the volume of turbulent spot constant at all stages of its collapse to be described.

For simplicity we shall further suppose that the initial form of a turbulent spot is symmetric in respect to the equilibrium plane where the densities of stratified fluid and mixed fluid coincide.

2. INITIAL STAGES OF THE EVOLUTION OF THE SPOT OF MIXED FLUID

At the first stage, free fall (lifting from below) of the particles of mixed fluid to the equilibrium plane takes place, followed by the spreading of fluid particles along this plane. Therefore, the rate of change of the area of horizontal projection, S, of a turbulent spot is proportional at this stage to the product of the actual area by the rate of fluid influx to the equilibrium plane. The latter quantity is equal to the product of the acceleration of free fall proportional to N^2 and time t. Thus, we obtain for the initial stage

$$dS/dt \sim SN^2t \qquad (4)$$

For small N^t we obtain by integration

$$(S - S_o)/S_o \sim N^2t^2 \qquad (5)$$

(S_o is the initial area of horizontal projection of the spot). Thus, at the first stage the characteristic size of the plan form of the turbulent spot, L, changes proportionally to the square of time

$$(L - L_o)/L_o \sim N^2t^2 \quad ; \quad dL/dt \sim L_oN^2t \qquad (6)$$

[for the wake, $S \sim L$, and the relation (6) follows from (5) in an elementary way; for the spot of the circular plan form, $S \sim L^2$, but at $(L - L_o) << L_o$, $L^2 - L_o{}^2 \sim 2\ (L - L_o)L_o$ and (6) follows again from (5)].

The relations of the type of (6) were obtained by J. Wu (1969) from the experimental investigation for a spot having the form of a cylinder with a horizontal axis; they were confirmed by some numerical investigations [see Kao (1976)]. Actually they were confirmed to be valid to $Nt \sim 2.5$.

At the intermediate stage the motive force of the intrusion is balanced by form drag and wave drag, thus, the velocity of the propagation of the intrusion tongue is governed by the parameter of stratification - Brunt-Väisälä frequency N - together with the actual height of the tongue, h, whence by dimensional considerations we obtain

$$dL/dt \sim Nh \qquad (7)$$

We see that at this stage the dependence of the velocity of the extension of the intrusion tongue is different for various geometries of the problem. In fact, the volume of the turbulent spot V is constant; for the cylindrical spot $h \sim V/LH$ (H is the longitudinal size of the spot) and $h \sim V/L^2$ for a spot of the circular plane form. Therefore, we obtain for the cylindrical spot

$$dL^2/dt \sim NV/H \quad , \quad L \sim \sqrt{NV(t - t_o)} \qquad (8)$$

(t_o is a conditional time moment of the beginning of the second stage), whereas for the spot of the circular plane form

$$dL^3/dt \sim NV \quad , \quad L \sim \sqrt[3]{NV(t - t_o)} \qquad (9)$$

The relations of the type (8) were obtained by J. Wu (1969) from the experimental data for collapse of a turbulent wake of initial circular cross-section. They were confirmed to be valid for $3 < Nt < 25$.

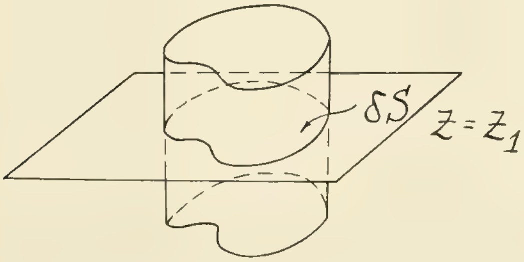

FIGURE 3. Elementary particle of the diffusion tongue.

3. FINAL, VISCOUS STAGE OF THE INTRUSION

Under accepted assumptions the equation of mass conservation for a mixed fluid takes the following form in hydraulic approximation.

$$\partial_t h + \text{div}\ (h\underset{\sim}{v}) = 0 \qquad (10)$$

Here $h(x,y,t)$ is the height of the intrusion tongue; x,y are the spatial horizontal coordinates, t is the time, $\underset{\sim}{v}$ is the velocity of fluid displacement averaged through the height of the tongue.

For the determination of the velocity, $\underset{\sim}{v}$, let us consider the system of forces acting on the cylindrical particle of the intrusion tongue leaning upon the area δS (Figure 3). The motive force of this particle is caused by the action of the gradient of redundant pressure, p, and spatial variation of the height of the tongue of intrusion

$$\underset{\sim}{Fm} = -\ \text{grad}(ph)\delta S \qquad (11)$$

Furthermore, the drag force per unit area of a particle surface due to the viscous character of the drag at the final stage of the intrusion under consideration is governed by the velocity, $\underset{\sim}{v}$, of the particle relative to ambient fluid, viscosity of the fluid, μ, and particle height, h. The dimensional considerations give the viscous drag force per unit area of particle surface proportional to $\mu v/h$. Therefore, the viscous drag force acting on the particle leaning upon the area, δS, is equal to

$$\underset{\sim}{Fr} = C\mu\underset{\sim}{v}\delta S/h \qquad (12)$$

where C is a constant, under given assumptions - a universal one. For estimating the constant, C, the well-known solution of the problem of viscous flow between flat plates may be used. This solution gives for the viscous drag the value $12\mu\underset{\sim}{v}\delta S/h$, whence $C = 12$. Equaling drag force to motive force (the inertia force, as at the second stage, is supposed to be a negligible one) we find

$$\underset{\sim}{v} = -\ h\,\text{grad}(ph)/C\mu \qquad (13)$$

To complete the statement of the problem we have to find the redundant pressure in the mixed fluid. In stratified fluids the density varies linearly with height. The intrusion tongue propagates symmetrically, thus, the equilibrium plane divides the height of the tongue in half. Let us denote by p_1 and ρ_1, correspondingly, the pressure and the density in stratified fluid at the level, $z = z_1$. Then, evidently, the pressure in the stratified fluid varies with depth following the relation

$$p = p_1 - \rho_1 g(z - z_1) + \rho_1 N^2(z - z_1)^2/2 \qquad (14)$$

Here, as before, N is the Brunt-Väisälä frequency $N^2 = ag$, g is the gravity acceleration, $a = (d\rho/dz)\rho_1$. Thus the pressure at the upper and the lower points of a vertical section of the tongue $z = z_1 \pm h/2$ are equal, respectively, to

$$p = p_1 - \rho_1 gh/2 + \rho_1 N^2h^2/8 \quad ;$$

$$p = p_1 + \rho_1 gh/2 + \rho_1 N^2h^2/8 \qquad (15)$$

because at the upper and the lower points the pressure in the tongue coincides with the pressure in ambient stratified fluid. Hence, the pressure within the tongue is distributed according to the hydrostatic law

$$p = p_1 - \rho_1 g(z - z_1) + \rho_1 N^2h^2/8 \qquad (16)$$

The pressure averaged over the section of the tongue is equal to

$$p_{ai} = p_1 + \rho_1 N^2h^2/8 \qquad (17)$$

The pressure averaged in the same way in the stratified fluid due to (14) is equal to

$$p_{ab} = p_1 + \rho_1 N^2h^2/24 \qquad (18)$$

Thus, the redundant pressure entering the expression of motive force of the intrusion tongue at a given vertical line is

$$p = p_{ai} - p_{ab} = \rho_1 N^2h^2/12 \qquad (19)$$

The relations (13) and (19) give

$$\underset{\sim}{v} = - \frac{\rho_1 N^2}{12C\mu} h\,\mathrm{grad}(h^3) = - \frac{\rho_1 N^2}{4C\mu} h^3\mathrm{grad}(h) \qquad (20)$$

Putting this expression into the equation of mass conservation of mixed fluid (10) we obtain for h a non-linear equation of the heat conductivity type

$$\partial_t h - n\Delta h^5 = 0 \;, \; n = \rho_1 N^2/20C\mu = N^2/20C\nu \qquad (21)$$

Here Δ is the Laplace operator, ν the kinematic viscosity of the fluid. In particular, for one-dimensional motions Eq. (21) takes the form

$$\partial_t h - n\partial^2_{xx} h^5 = 0 \qquad (22)$$

$$\partial_t h - n(1/r)\partial_r r\partial_r h^5 = 0 \qquad (23)$$

for the plane and the axisymmetrical cases, respectively. Here x is the horizontal Cartesian coordinate, r the horizontal polar radius.

4. SELF-SIMILAR ASYMPTOTIC LAWS OF TURBULENT SPOT EXTENSION AT THE VISCOUS STAGE

We neglected turbulent entrainment and the erosion of a turbulent region; therefore, the volume of the turbulent mixed region is considered to be constant and equal to the initial volume of the turbulent spot. It stands to reason that this assumption at the viscous stage is valid for sufficiently high stratification only. If the characteristic dimensions of the plane form of a turbulent spot are nearly equal, it is natural to expect that the extension of the intrusion starts already to be axisymmetric at the end of the intermediate stage and deliberately is axisymmetric at the viscous stage. Hence, Eq. (23) may be applied for its description. Thus, the condition of conservation of the volume of a turbulent spot takes the form

$$2\pi \int_0^\infty rh(r,t)\,dr = V \equiv \mathrm{Const} \qquad (24)$$

The asymptotic stage of the spreading of the spot is of primary interest when the plane size of the intrusion exceeds the corresponding initial size of the turbulent spot. At this stage the details of the initial distribution h(r,0) cease to be essential and for an asymptotic description of the viscous stage of the intrusion the initial distribution may be represented in the form of an instantaneous point source

$$h(r,t_1) \equiv 0 \;(r \neq 0),\; 2\pi \int_0^\infty rh(r,t_1)\,dr = V \qquad (25)$$

Here, t_1 is the conditional time moment of the beginning of the viscous stage.

The solutions of such type for non-linear heat conductivity equations with the power-type non-linearity to which Eqs. (22, 23) belong were considered in the papers of Ya. B. Zel'dovich, A. S. Kompaneets, and one of the present authors [see Barenblatt et al. (1972)]. In our case the solution depends on the quantities $t - t_1$, n, V, r. The dimensional considerations show that it is a self similar one:

$$h = \left\{\frac{V}{2\pi n(t - t_1)}\right\}^{1/5} f(\zeta)$$

$$\zeta = r[V^4 n(t - t_1)/16\pi^4]^{-1/10} \qquad (26)$$

Putting (26) into Eq. (23) and integrating the ordinary differential equation obtained for the function, $f(\zeta)$, we find

$$f(\zeta) = \begin{cases} \left(\frac{10^{1/5}}{6}\right)^{1/4} \left(1 - \frac{\zeta^2}{\zeta_0^{\,2}}\right)^{1/4}, & 0 \le \zeta \le \zeta_0 \\ 0, \; \zeta \ge \zeta_0 = 10^{3/5}/2 \simeq 2 & \end{cases} \qquad (27)$$

Thus, at each moment of time the intrusion tongue stretches for a finite distance: this is (cf. Section 1) the peculiar feature of non-linearity distinguishing the equation of intrusion from the linear equation of heat conductivity. The edge of the intrusion propagates following the law

$$r_0(t) = 2(V^4 n(t - t_1)/16\pi^4)^{1/10} \qquad (28)$$

The form of the intrusion tongue represented by the curve 1 in Figure 4 also is peculiar: the thickness of the tongue changes slowly to the very edge where it comes abruptly to naught. The maximum spot thickness, $h_0(t) = h(0,t)$, also changes very slowly with time

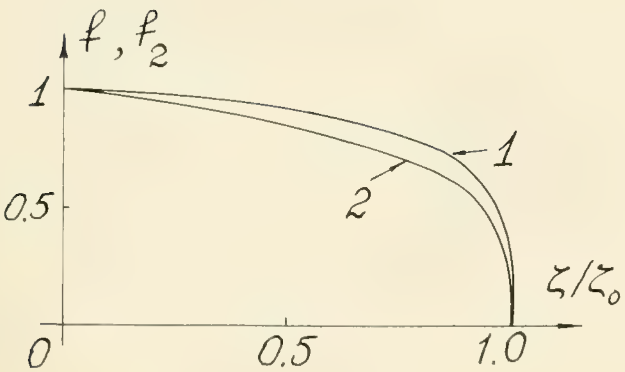

FIGURE 4. The distribution of thickness along an intrusion.

$$h_o(t) = \left(\frac{10^{1/5}}{6}\right)^{1/4} \left(\frac{V}{2\pi n(t - t_1)}\right)^{1/5} \qquad (29)$$

Equation (28) seems very simple and accessible for experimental confirmation: confirmation of this equation will give some confidence in the validity of the model proposed here. The experimental checking of Eq. (28) was performed by A. G. Zatsepin, K. N. Federov, S. I. Voropaev, and A. M. Pavlov. They used the following scheme for the experiment (Figure 5). An open plexiglass tank having the form of a rectangular parallelepiped contained a stable, temperature-stratified fluid. A hollow cylindrical tube was introduced from above under the surface of the fluid. The fluid in the tube was mixed and then the tube was raised, leaving in its place a spot of mixed fluid which immediately started penetrating the ambient stratified fluid. The observations, photo- and movie camera, were performed using a shadow device. The experiment allowed one to observe clearly the two last stages of spot evolution; the spot extension at the viscous stage is represented in Figure 6. The mixed fluid volume in the spot was fixed for all experiments, as well as the kinematic viscosity of the fluid and the diameter of the tube. Therefore, if Eq. (28) is correct, the experimental data in the coordinates $\ell g[2r_o(t)/D]$, $\ell g[N\ (t - t_1)]$ had to fall on a single straight line with the slope 0.1. This is confirmed by the graph of Figure 6 where the slope of the solid straight line is 0.1 and $t_1 = -10$ sec. Thus, the law of one tenth Eq. (28) for the viscous extension of a spot was confirmed by the experiments of A. G. Zatsepin, K. N. Federov, S. I. Voropaev, and A. M. Pavlov with a satisfactory accuracy.

Analogously, in the case when the form of the turbulent spot is close to the cylinder with a horizontal axis Eq. (22) for the height of the intrusion tongue will hold, where x is the horizontal coordinate normal to the axis of the spot. The condition of conservation of the volume of the spot of mixed fluid takes, for this case, the form

$$H \int_{-\infty}^{\infty} h(x,t)dx = V \equiv \text{Const} \qquad (30)$$

where H is the longitudinal size of the cylindrical spot. The initial conditions corresponding to the asymptotic solution of the instantaneous point source type may be written in the form

$$h(x,t_1) \equiv 0\ (x \neq 0), \quad H \int_{-\infty}^{\infty} h(x,t_1)dx = V \qquad (31)$$

and the asymptotic solution itself due to the same reasons, as before, may be represented in the form

$$h = \left\{\frac{V^2}{4n(t - t_1)H^2}\right\}^{1/6} f_1(\zeta)$$

$$\zeta = x[V^4 n(t - t_1)/16H^4]^{-1/6}$$

$$f_1 = \begin{cases} A(1 - \zeta^2/\zeta_o^{\,2})^{1/4}, & 0 \leq \zeta \leq \zeta_o \\ 0, & \zeta \geq \zeta_o = (15)^{1/6}\left[\dfrac{2\Gamma(5/4)\Gamma(1/2)}{\Gamma(7/4)}\right]^{2/3} \approx 3.6 \\ A = (\zeta_o^{\,2}/15)^{1/4} \approx 0.97 \end{cases} \qquad (32)$$

so that the leading edge of the intrusion, $x = x_o(t)$, propagates according to the law

$$x_o(t) = \zeta_o[V^4 n(t - t_1)/16H^4]^{1/6} \qquad (33)$$

while the maximum thickness of the intrusion, $h_o(t) = h(o,t)$, decays with time according to

$$h_o t(t) = 0.97(V^2/4H^2 n(t - t_1))^{1/6} \qquad (34)$$

Thus, in both cases a strong deceleration of the extension of intrusion was characteristic for a turbulent spot in the transition to the viscous stage. Indeed, at the free intrusion stage the extension of a turbulent spot is proportional to the

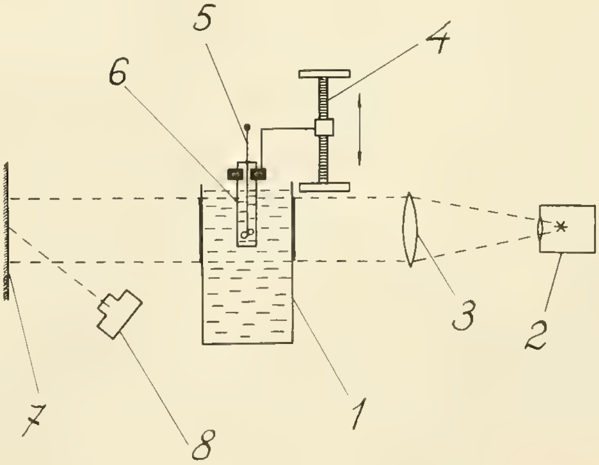

FIGURE 5. The scheme of the experimental checking of the law of viscous extension of a spot of mixed fluid. 1) The tank, 2) Point light source with collimator, 3) Lens, 4) Vertical elevator with electromotor, 5) Mixer, 6) Tube, 7) Screen, 8) Movie camera.

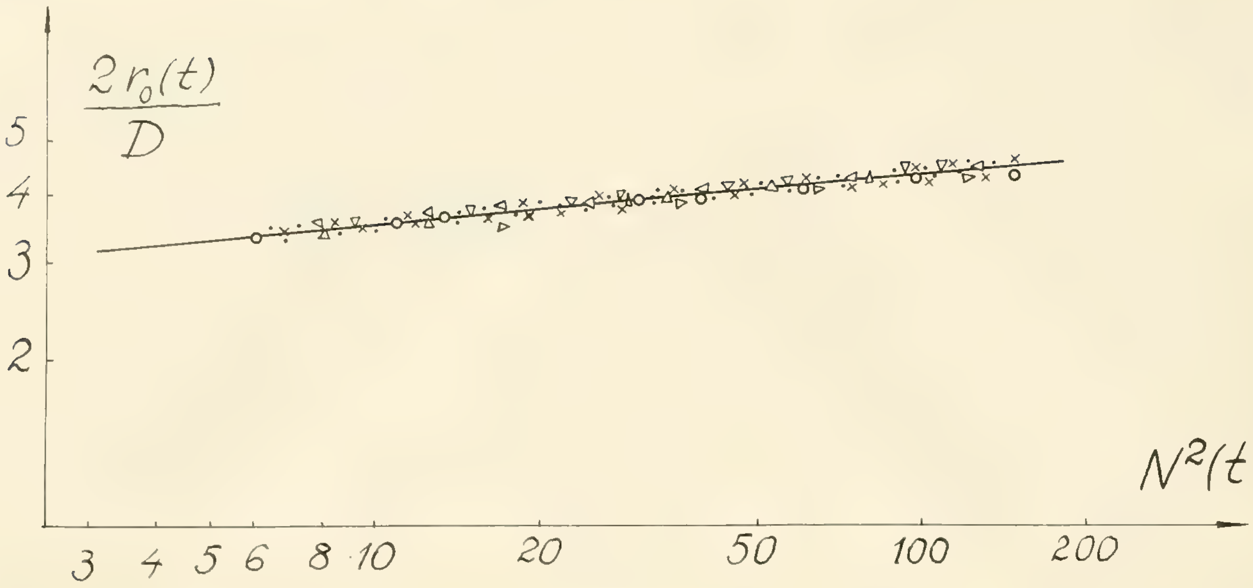

FIGURE 6. The one tenth law as confirmed by laboratory experiments of A. G. Zatsepin, K. N. Fedorov, S. I. Voropaev, and A. M. Pavlov.

● — $N = 0.63\ \mathrm{sec}^{-1}$
× — $N = 1.00\ \mathrm{sec}^{-1}$
△▽◁▷ — $N = 0.58\ \mathrm{sec}^{-1}$

square of time; at the intermediate stage it is proportional to the square root of time for a cylindrical spot and to the cube root of time for an axisymmetric spot. At the viscous stage the extension is proportional to time; to one sixth in the case of a cylindrical spot and to one tenth in the case of an axisymmetric spot. Thus the extension of the spot is sharply decelerated at the viscous stage in comparison with the initial stages.

It seems plausible to us that the "blini" shaped regions of constant density and temperature observed in the ocean are turbulent spots of various scales generated by the loss of stability or breaking of internal waves, local instability of shear flows, penetration of cooled turbulized fluid from the turbulized surface layer, etc. which are mainly in the last, viscous stage of their evolution. Note that along with the states in which turbulence is preserved within the spot, the states are possible and apparently rather frequent, especially for spots of small scales, in which turbulence within the spot has disappeared but the fluid remains mixed and homogeneous. This assumption is supported qualitatively by some data of simultaneous measurements of vertical distributions of density and velocity gradient [Federov (1976)]. These distributions have the form presented by solid lines in Figure 1. Indeed, if the regions of constant density are intrusions, then the shear should increase near their boundaries compared to ambient fluid (cf., Figure 2). However, in this case the shear should be reduced near the central line of intrusion (dashed line in Figure 1). It is plausible that the resolution in these measurements was not sufficient to observe this shear reduction.

5. THE INTRUSION OF BOTTOM SEA WATER INTO THE BODY OF THE OCEAN

The intrusion of mixed fluid into a continuously stratified medium is widely distributed in nature; it is of interest from the point of view of the evolution of turbulent spots in stratified fluid. A characteristic example - the intrusion of the bottom Mediterranean water into the body of the Atlantic (Figure 7). The bottom water descends through the Straits of Gibraltar down the continental slope and enters the body of the ocean in an intermediate layer where the density of the ocean water is equal to its own density. The intrusion of the bottom water of the Red Sea into the body of the Indian Ocean is completely analogous. The intrusion of bottom water is a slow process and we may assume that for its description, Eq. (22), corresponding to a pure viscous mechanism of the intrusion drag, is valid.

The intrusion of bottom sea water into the body of the ocean goes by separate portions [Federov (1976)] and it is possible to assume that, at the beginning of the intrusion of a new portion, the bottom fluid that intruded earlier is carried sufficiently far away so that the initial condition holds

$$h(x,0) \equiv 0 \quad (x > 0) \qquad (35)$$

Here h, as before, is the height of the intrusion tongue, x the horizontal coordinate in the direction of intrusion from its origin. Let us suppose that

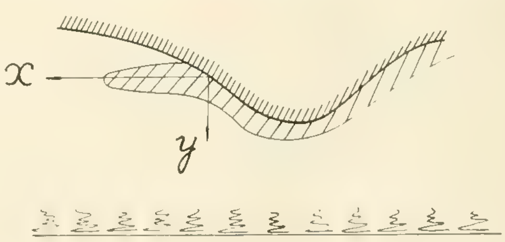

FIGURE 7. The intrusion of sea bottom water into the body of the ocean.

the height of the bottom water layer at the origin of intrusion does not depend on time:

$$h(o,t) \equiv h_o = \mathrm{Const} \qquad (36)$$

The solution of Eq. (22) under conditions (35) and (36) is also self-similar and has the form

$$h = h_o f_2(\zeta), \quad \zeta = x/\sqrt{nh_o^4 t} \qquad (37)$$

where the function $f_2(\zeta)$ which satisfies the equation

$$\frac{d^2 f_2^5}{d\zeta^2} + \frac{1}{2}\zeta\frac{df_2}{d\zeta} = 0 \qquad (38)$$

under the conditions

$$f_2(0) = 1 \quad , \quad f_1(\infty) = 0 \qquad (39)$$

is continuous and has a continuous derivative $df_2^5/d\zeta$ (the last requirement follows from the continuity of the flow of bottom fluid). The solution, $f_2(\zeta)$, is represented in Figure 4 (curve 2). It is also different from zero only in a finite interval $0 \leq \zeta \leq \zeta_0 \approx 1.66$, so that the leading edge of the intrusion $x_0(t)$ propagates as

$$x_o(t) = \zeta_o\sqrt{nh_o^4 t} \qquad (40)$$

REFERENCES

Woods, J. D. (1968). Wave-induced shear instability in the summer thermocline. *J. Fluid Mech. 32,* 791.

Monin, A. S., V. M. Kamenkovich, and V. G. Kort (1977). *Variability of the ocean.* J. Wiley.

Federov, K. N. (1976). *Fine thermohaline structure of oceanic waters.* Gidrometeoizdat, Leningrad.

Belyaev, V. S., I. D. Lozovatsky, and R. V. Ozmidov (1975). On the relation between the small-scale turbulence parameters and the local stratification conditions in the ocean. *Izv. AN SSR, Ser. Physics of Atmosphere and Ocean II,* 718.

Wu Jin (1969). Mixed region collapse with internal wave generation in a density stratified medium. *J. Fluid Mech. 35,* 531.

Kao, T. W. (1976). Principal stage of wake collapse in a stratified fluid: two-dimensional theory. *Physics of Fluids 19,* 1071.

Monin, A. S., A. M. Yaglom (1971). *Statistical hydromechanics. Part I.* The MIT Press.

Barenblatt, G. I., V. M. Entov, and V. M. Ryzhik (1972). *Theory of non-steady filtration of liquid and gas.* Nedra, Moscow.

Session VIII

GEOPHYSICAL FLUID DYNAMICS

LOUIS N. HOWARD
Session Chairman
Massachusetts Institute of Technology
Cambridge, Massachusetts

The Rise of a Strong Inversion Caused by Heating at the Ground

Robert R. Long and Lakshmi H. Kantha
The Johns Hopkins University
Baltimore, Maryland

ABSTRACT

A theory is offered for the rise of a strong inversion in the atmosphere caused by heating at the ground. The heating, specified by the buoyancy flux, q_1, near the ground, causes turbulence in a growing layer of depth, D, above the ground with an inversion or interfacial layer of thickness, h, separating the mixed layer from the non-turbulent air above. There is a buoyancy jump, Δb, across the interfacial layer and the air above the inversion has a buoyancy gradient, N^2.

The lower surface of the inversion layer rises (at a speed, $u_e = dD/dt$) because of two processes. One is related to the mean temperature rise of the mixed layer which, in the present model, leaves h + D unaffected but which causes the interfacial thickness, h, to decrease and therefore D to increase at a rate proportional to $\hat{Ri}^{-1}$, where $\hat{Ri} = D\Delta b/w_*^2$ is the Richardson number and $w_* \equiv (q_1 D)^{1/3}$ is the convective velocity typical of the rms velocities in the main portion of the mixed layer. The second process, increasing both h and D, is the erosion of the stable fluid by the turbulence in the mixed layer and the intermittent turbulence in the interfacial layer. This causes D to increase at a rate proportional to $\hat{Ri}^{-7/4}$. The total effect is contained in the equation

$$\frac{u_e}{w_*} = a\hat{Ri}^{-1} + c\hat{Ri}^{-7/4}$$

where a and c are universal constants. Other results are presented, notably the ratio, $|q_2/q_1|$, where q_2 is the (negative) buoyancy flux near the level z = D. This ratio decreases with increase of stability as observed in experiments of Willis and Deardorff. $|q_2/q_1| \sim \hat{Ri}^{-3/4}$.

1. INTRODUCTION

When the sun rises and begins to heat the ground, the atmosphere is normally in a stable state (potential temperature increases with height). If we neglect the effect of mean wind for the moment, the heating creates instability and turbulence near the ground and a mixed layer of depth, D, appears, capped by an inversion. This phenomenon is called penetrative convection. The potential temperature of the mixed layer is nearly constant with height except very close to the ground, where a superadiabatic lapse rate exists in a thin layer, and just below the inversion base where there is weak stability. The inversion base rises because of two processes. The first is heating alone which tends to decrease the thickness, h, of the inversion layer, (IL), and so increase D. The second is the entrainment effect of the turbulent eddies just below the inversion base. We do not have a detailed understanding of this erosion process but laboratory experiments with mechanical stirring [Moore and Long (1971), Linden (1973)] suggest that the eddies in the mixed layer deflect the IL upward storing potential energy. When this is released by downward motion, a portion of the lighter fluid in the IL is ejected into the homogeneous layer where it is carried away by the turbulent eddies, leaving the lower surface of the IL sharp again.

If there is no mean wind, the energy for the turbulence comes from the energy flux divergence term and from the buoyancy flux term in the energy equation, where $q = -\overline{w'b'}$ is the buoyancy flux*. When there is a mean wind, as is usual in the atmosphere, the shear yields another energy source. This serves to increase the turbulence energy and thus to increase the entrainment effect through greater agitation of the IL. In addition, the shear may cause Kelvin-Helmholtz instability and consequent wave breaking at the interface and thereby enhance erosion.

On the other hand, the effect of shear should be negligible if the mixed layer depth is much greater than the Monin-Obukhov length, $L = -u_*^3/q_1$, [Monin and Yaglom (1971, p. 427)] where u_* is the friction velocity. Thus $(-L/D)^{1/3}$ is proportional to the ratio, u_*/w_*, of the turbulent velocity in the mixed layer associated with shear to the turbulent velocity associated with convection, $w_* = (q_1 D)^{1/3}$. The shear effect becomes less important as this ratio decreases. Lenschow (1970, 1974) presents aircraft measurements, which appear to confirm the unimportance of energy production by the shear for the turbulence near the inversion if $|L/D|$ is small enough.

---

* Buoyancy in an incompressible fluid is defined as $b = g(\rho - \rho_0)/\rho_0$ where g is gravity, ρ is density and ρ_0 is a representative density. In the atmosphere, ρ and ρ_0 are potential densities. We may also write $b = g(\theta - \theta_0)/\theta_0$ where θ is a potential temperature.

The purpose of this paper is to construct a theory for the rise of an inversion in the atmosphere neglecting the effect of shear. The analysis is similar in some respects to that in a recent paper by the first author, [Long (1977b), hereinafter referred to as MISF] in which a theory is developed for turbulence in a stably stratified liquid, as for example in the experiments of Rouse and Dodu (1955), Turner (1968), Wolanski (1972), Linden (1973), Crapper and Linden (1974), Linden (1975), Thompson and Turner (1975), Wolanski and Brush (1975), and Hopfinger and Toly (1976). In these experiments a stably stratified fluid is agitated by a grid oscillating up and down near the bottom of the vessel (Figure 1). A growing mixed layer of depth, D, appears in the lower portion of the fluid separated from the non-turbulent fluid above, in which the buoyancy gradient is given, by an IL of thickness, h. Observations indicate that the lower mixed layer has a very weak mean buoyancy gradient. The buoyancy difference across the IL is relatively large and is denoted by Δb.

As indicated by the experiments of Thompson and Turner and Hopfinger and Toly, and derived by the first author in a recent paper [Long (1977a)], the turbulence generated by the grid in a *homogeneous* fluid is nearly isotropic, and if u is the rms velocity and ℓ is the integral length scale, the quantity, $u\ell$ (proportional to eddy viscosity), is constant with height. When there is stratification, the mixed layer is nearly homogeneous and $u\ell = K$ is again constant near the grid [Hopfinger and Toly (1976)]. Since ℓ is proportional to the depth, D, the velocity, $u_1 \equiv K/D$, is characteristic of the turbulent velocities in the mixed layer. The quantity, K, may be taken to be characteristic of the "action" of the energy source (grid).

On the basis of observations, experimenters have proposed that the entrainment velocity $u_e = dD/dt$ is expressible in the form

$$\frac{u_e}{fS} \sim Ri^{*-3/2} \quad , \quad Ri^* = \frac{D\Delta b}{f^2S^2} \qquad (1)$$

where Ri^* is the overall Richardson number, f is the frequency, and S is the stroke of the grid. The measurements correspond to large values of Ri^* so that attention is confined to the usual situation in nature in which the Richardson number is large. In terms of the "action" K of the grid, another Richardson number is

$$\hat{Ri} = \frac{D\Delta b}{u_1^2} \quad , \quad u_1 = K/D \qquad (2)$$

This is very similar to the number $Ri = \ell\Delta b/u^2$ proposed by Turner (1973), where ℓ and u are the integral length scale and rms velocity measured at the level z = D in a *homogeneous* fluid agitated by the same grid at the same grid frequency and stroke.

In MISF and in the present paper, the role of the IL separating the mixed layer from the non-turbulent fluid above is essential. This contrasts with earlier theories in which h is neglected despite experimental evidence [Linden (1975)] that h is proportional to D and is not particularly small ($h/D \cong 1/4$). Observations [for example, Wolanski and Brush (1975)] indicate that the IL with its large density gradient is typified by wave motion. Wolanski and Brush found that the frequency of disturbances in this layer was proportional to the Brunt-Väisälä frequency $(\Delta b/h)^{\frac{1}{2}}$ although numerically one order of magnitude smaller. Certainly turbulence of some kind exists in the IL and since the density gradient there is strong rather than weak as in the mixed layer, it is reasonable to assume that the turbulence in the IL is intermittent and that this intermittent, weak turbulence transfers the buoyancy in the layer. In MISF the intermittency factor decreases with increase of stability so that for the large Richardson numbers of the asymptotic theory the layer is, for the most part, in laminar wave motion with occasional breaking waves in the interior and at the lower surface of the interface.

Similar ideas may be applied to the present problem in which the turbulence in the mixed layer is caused by heating at the lower surface. The principal differences are the effect of heating in causing h to decrease and D to increase, and the differences in the sources of turbulence kinetic energy. The energy equation is

$$0 = -\frac{\partial}{\partial z}\left[\overline{w'\left(\frac{p'}{\rho_0} + \frac{u'^2 + v'^2 + w'^2}{2}\right)}\right] - \overline{w'b'} - \varepsilon \quad (3)$$

where the first term is the energy flux divergence; u', v', w' are the instantaneous velocities, p' is the pressure, ρ_0 is a reference density, $q = -\overline{w'b'}$ is the buoyancy flux, and ε is the energy dissipation. In the present problem the buoyancy flux term, $-\overline{w'b'}$, is of basic importance and corresponds to the conversion of potential energy to kinetic energy. This effect is missing of course, in the case of mechanical stirring in a homogeneous fluid.

Equation (3) omits the local time rate-of-change of kinetic energy although, in fact, the inversion is rising and conditions are therefore unsteady. With respect to the mixed layer, the kinetic energy

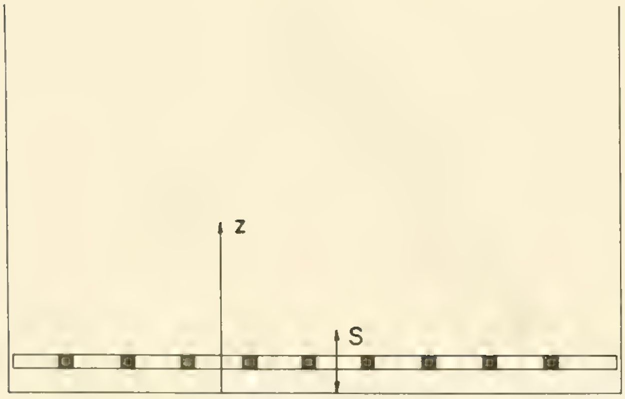

FIGURE 1. Oscillating grid experiment. (S = stroke of the grid.)

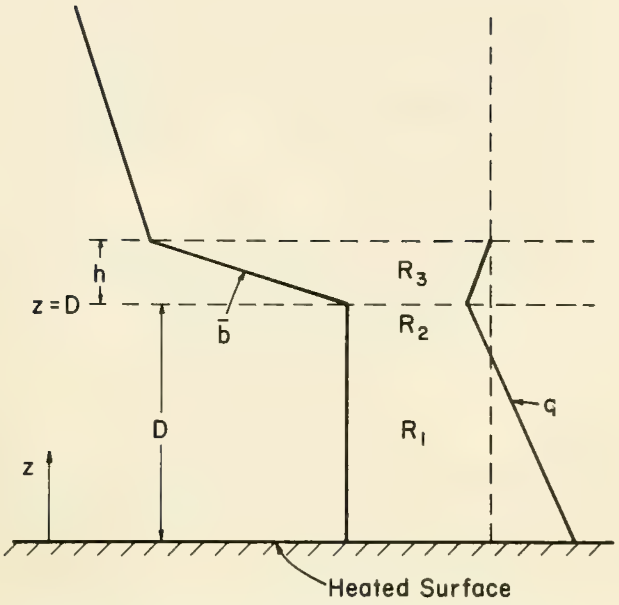

FIGURE 2. Model of entrainment at an interface by heating from below. The curve on the left is the mean buoyancy, b, with an assumed linear profile above the interfacial layer. The curve for buoyancy flux, q, is on the right. The superadiabatic layer near z = 0 is not shown.

is proportional to the square of the convective velocity, $(q_1D)^{2/3}$, so that the ratio of the time rate-of-change term to the other terms in Eq. (3) is $u_e/w_\star$. This ratio is of order one if the convective motions are spreading upward at a speed, u_e, in initial conditions of *neutral stability*. Even a fairly weak inversion will cause a great slowdown and $u_e/w_\star$ will be small. Similar remarks apply to the IL and we are assured that the time dependence is negligible in the stable conditions of the paper, although it has received some attention in considerations of the real atmosphere [Zilitinkevich (1975)].

We may conclude this introduction with reference to work on penetrative convection in the atmosphere and oceans including atmospheric observations: Lettau and Davidson (1957), Ball (1960), Veronis (1963), Izumi (1964), Summers (1965), Deardorff (1967), Kraus and Turner (1967), Lilly (1968), Deardorff (1972), Betts (1973), Carson (1973), Stull (1973), Tennekes (1973a,b, and 1975), Adrian (1975), Farmer (1975), Zilitinkevich (1975), Kuo & Sun (1976), Stull (1976a,b,c), and Zeman and Tennekes (1977). Related experiments have been run by Deardorff, Willis, and Lilly (1969), Willis and Deardorff (1974), and Hedit (1977). A second-order closure model has been given by Zeman and Lumley (1977). More recent field observations have been made by Kaimal, et al. (1976). Mixed layer deepening in the upper layers of the ocean, which is almost always associated with wind stirring has been discussed by Niiler and Kraus (1977).

2. RELATION OF FLUXES TO THE BUOYANCY JUMP AND TO MIXING LAYER AND INTERFACIAL LAYER THICKNESSES

In the theory of the paper we ignore rotation, radiative heating, water vapor, and horizontal variations of mean quantities. The model is shown in Figure 2 which contains curves for the mean buoyancy and buoyancy flux. The mean buoyancy curve above the IL is assumed to be linear with buoyancy gradient N^2. In one case we assume that $N^2 = 0$ so that the inversion rises and weakens, eventually disappearing. When $N^2 \neq 0$ we assume that the air was at rest with uniform buoyancy gradient when heating began. Then the inversion strength increases with time. Since the theory of this paper is concerned with very stable conditions, the solutions hold for large values of the Richardson number.

The buoyancy flux curve is derived below from the assumed buoyancy distribution. The latter is assumed to be linear in the IL (region R_3). This is an excellent approximation* in certain circumstances at least, for example in the mechanical stirring experiments of Wolanski and Brush (1975). Observations in the mixed layer [Willis and Deardorff (1974)] indicate that there is very little mean buoyancy variation in this layer except for some indication of a stable mean gradient near the heated plate. If we ignore these gradients for the moment, the equation

$$\frac{\partial \bar{b}}{\partial t} = \frac{\partial q}{\partial z} \tag{4}$$

indicates that q is a linear function of z. In fact, experiments show that q is nearly linear [Willis and Deardorff (1974)] so that the neglect of mean buoyancy variations in the mixed layer in the model of Figure 2 seems reasonable. The lower surface is heated and the buoyancy flux $q = -\overline{w'b'}$ (proportional to the heat flux) is held constant at the lower surface where it is denoted by q_1. The mean buoyancy in the mixed layer is

$$\bar{b}_m = b_{00} = N^2(D + h) + \Delta b \tag{5}$$

where Δb is the buoyancy jump across the interfacial layer and b_{00} is constant equal to the buoyancy at the surface if the linear gradient above is extrapolated down to the surface. Integrating (4) over the mixed layer, we get the flux, q_2, just below the IL. It is

$$q_2 = q_1 + D\frac{d\Delta b}{dt} - N^2 D \frac{d}{dt}(D + h) \tag{6}$$

On physical grounds q_2 must be negative (Figure 2) and this is confirmed by laboratory measurements [Willis and Deardorff (1974)]. In the IL, the mean buoyancy is

$$\bar{b} = \Delta b - \frac{\Delta b}{h}(z - D) + b_{00} - N^2(D = h) \tag{7}$$

Integrating (4), we get the flux at a given level in the interfacial layer

$$q_3 = q_2 + \frac{d\Delta b}{dt}\left(\zeta - \frac{\zeta^2}{2h}\right) + \Delta b\left(\frac{\zeta^2}{2h^2}\frac{dh}{dt} + \frac{\zeta}{h}\frac{dD}{dt}\right)$$
$$- N^2\zeta\left(\frac{dD}{dt} + \frac{dh}{dt}\right) \tag{8}$$

where $\zeta = z - D$. At $z = D + h$, the buoyancy flux is zero so that

---

*Even when the approximation is only fair, the error in assuming a linear profile is small. We discuss this in Section 6.

$$q_2 = -\Delta b \frac{dD}{dt} - \frac{d}{dt}\left(\frac{h}{2}\ \Delta b\right) + N^2 h\left(\frac{dD}{dt} + \frac{dh}{dt}\right) \quad (9)$$

Using (6) we get

$$q_1 = -\frac{d}{dt}\left[(D + \tfrac{1}{2}h)\ \Delta b - \tfrac{1}{2}N^2(D + h)^2\right] \quad (10)$$

The integral of (10) is

$$(D + \tfrac{1}{2}h)\ \Delta b - \tfrac{1}{2}N^2(D + h)^2 = V_0^2 - q_1 t \quad (11)$$

where

$$V_0^2 = (D_0 + \tfrac{1}{2}h_0)\ \Delta b_0 - \tfrac{1}{2}N^2(D_0 + h_0)^2 \quad (12)$$

and the zero subscript denotes values at $t = 0$. Tennekes (1973b) obtained (11) and (12) with h and h_0 missing. As we have indicated, the interfacial layer thickness h plays an important role in the theory of this paper. The time $t_0 \equiv V_0^2/q_1$ is the time for an initial buoyancy difference to disappear when the upper air has a uniform potential temperature [Tennekes (1973b)].

3. THE INTERFACIAL LAYER (REGION R_3)

According to the discussion in Section 1, the IL in our model is turbulent with intermittency factor, I_3, defined here as the ratio of the volume in turbulent motion to the whole volume*. Much of the layer is in wave motion in which all of the components of the fluid velocity are of the same order, i.e., the ratios w_3/u_3, w_3/v_3 are independent of the Richardson number. The intermittent turbulence is caused by the intermittent breaking of these waves. Since the wave amplitude is of the order of the wave length when the wave breaks, we should have $u_3 \sim v_3 \sim w_3$ initially in the breaking waves as well and we assume this. Of course the "homogeneous" fluid in the breaking patch will tend to flatten out and the vertical velocities in the patch will decrease relatively as time goes on. In our model we ignore the patch after a time of order $(h/\Delta b)^{\frac{1}{2}}$ and consider that the local heat transfer has already been accomplished. In actual fact this transfer is accomplished by the spreading of the patch over a larger time interval and the ultimate transfer by molecular processes. Since buoyancy flux occurs only in the turbulent portions of this layer, we get, at any level in the IL,

$$q_3 = -B_1 u_3 b_3 I_3 \quad (13)$$

where b_3 is the rms buoyancy fluctuation in the interfacial layer. B_1 is a universal constant† but b_3, u_3, and I_3 may vary with height. The turbulence is certainly strongly influenced by buoyancy in this layer so that kinetic and available potential energies [Long (1977d)] are of the same order not only in the waves but in the turbulent patches, i.e.,

$$u_3^2 = B_2 \delta_3 b_3 = B_3 \delta_3^2 \frac{\Delta b}{h} \quad (14)$$

where δ_3 is the order of the size of the disturbances and because of the tendency for conservation of buoyancy, we assume b_3 is proportional to $\delta_3(\Delta b/h)$. Using (14), Eq. (13) becomes

$$q_3 = -\frac{B_3^{\frac{1}{2}} B_1}{B_2} u_3^2 \left(\frac{\Delta b}{h}\right)^{\frac{1}{2}} I_3 \quad (15)$$

Let us now find the dissipation. This occurs only in the turbulent patches and we assume that the local dissipation $\varepsilon_p = f(u_3, \delta_3, b_3)$. Since $u_3^2 \sim b_3\delta_3$, we get $\varepsilon_p \sim u_3^3/\delta_3$ and

$$\varepsilon_3 = I_3 \frac{B_4 u_3^3}{\delta_3} = B_4 B_3^{\frac{1}{2}} u_3^2 \left(\frac{\Delta b}{h}\right)^{\frac{1}{2}} I_3 \quad (16)$$

Equations (15) and (16) show that $\varepsilon_3 \sim q_3$. *Since these are both dissipative, it follows that they are of the order of the energy flux divergence.* At the upper boundary of the IL, the kinetic energy of the waves has been so reduced by losses to potential energy and dissipation, that there can no longer be wave breaking and turbulence. Thus h is the depth of penetration of the turbulence. At the height $z = D + h$, the energy flux is too weak to support turbulence so that it has apparently decreased to a value well below that at the bottom of the IL. Therefore, the increment in energy flux over the IL is proportional to the value at the bottom of the IL. Integrating Eq. (3) between levels in the layer near the upper and lower surface, we find that $\bar{q}_3 h$ is of the order of the energy flux just below the inversion where $\bar{q}_3$ is the average buoyancy flux in R_3. Since the interface is being distorted by the vertical motions (inducing pressure fluctuations), the energy flux should be proportional to $\overline{w_2' p_2'}/\rho_0 \sim w_2^3$ in R_2. We may write

$$\bar{q}_3 h = -A_2 w_2^3 \quad (17)$$

Equation (17) has a form superficially similar to that proposed by others in a number of papers [for example Long (1975), Zeman and Tennekes (1977)] on the basis of assumptions about the size of terms in the mixed layer. In present notation, these authors propose $q_2 D \sim w_*^3$ and this leads rather directly to the Ri^{-1} law for the entrainment. Equation (17) is really quite different. If the upper fluid is homogeneous, A_2 should be a universal constant. However, when the upper layer is stratified, losses of energy may occur by wave radiation and A_2 may then be a function of $s = N^2/(\Delta b/h)$.

Using (6), (8), (14), (15), (17), we get

$$-\frac{A_2 w_2^3}{h} = D\frac{d\Delta b}{dt} + \frac{h}{3}\frac{d\Delta b}{dt} + \frac{\Delta b}{6}\frac{dh}{dt} + \frac{1}{2}\Delta b\frac{dD}{dt}$$

$$+ q_1 - N^2(D + \tfrac{1}{2}h)\frac{d}{dt}(D + h) \quad (18)$$

---

*The introduction of intermittency may result in confusion if one inadvertently thinks of the IL as a surface or even as a layer with thickness of the order of the amplitude of the wave disturbances. The latter is not excluded as a possibility in this section but, in fact, as we see in Eq. (26) the wave amplitude is much smaller than the thickness of the IL so that I is *not* the ratio of the times that a fixed point is in the upper (non-turbulent) and lower (turbulent) fluid.

†We use symbols B_1, B_2,... to denote universal constants. Later, "constants" arise which, at first glance at least, may be functions of $s = N^2/(\Delta b/h)$, i.e., the ratio of the stabilities of the upper "quiescent" layer and the interfacial layer. We denote these "constants" by $A_1, A_2, \ldots$.

$$\delta_2 = B_3^{-\frac{1}{2}} \left(\frac{h}{\Delta b}\right)^{\frac{1}{2}} w_2 \qquad (19)$$

$$\frac{B_3^{\frac{1}{2}} B_1}{B_2} I_2 w_2^2 \left(\frac{\Delta b}{h}\right)^{\frac{1}{2}} = -D \frac{d\Delta b}{dt} + N^2 D \frac{d}{dt} (D + h) - q_1 \qquad (20)$$

where the subscript "2" denotes values at a level just above $z = D$. Equation (19), which follows from Eq. (18), is consistent with the assumption that the pressure fluctuations in eddies in region R_2 of frequency w_2/δ_2 of order of the natural frequency $(\Delta b/h)^{\frac{1}{2}}$ are generating the breaking waves by resonance.

4. TURBULENCE IN THE MIXED LAYER

According to (17) the vertical turbulence velocity in R_2 is related to the average buoyancy flux in the interfacial layer. The latter is related to the entrainment velocity so that it is essential to relate w_2 to turbulence in the main portion of the mixing layer, or to $w_* \equiv (q_1 D)^{1/3}$. This is often called the convective velocity. A great deal of confusion has arisen regarding this problem because of two explicit or implicit assumptions often made: (1) that the turbulence near the interface is quasi-isotropic, i.e., $u_2 \sim v_2 \sim w_2$, and (2) that $w_2 \sim w_*$. We will try to show that both of these assumptions are incorrect[*].

In laboratory experiments with mechanical mixing, measurements indicate that the mean buoyancy gradient in the mixed layer is very weak and, in fact, approaches zero as the Richardson number increases [Wolanski (1972)]. Instantaneously, the lower surface of the interfacial layer is very sharp (perhaps a discontinuity for infinite Reynolds numbers!). This surface is agitated by the disturbances of the mixed layer so that the *mean* buoyancy curve varies continuously, although rapidly in the region, R_2. It seems quite safe, however, to neglect effects of buoyancy on the turbulence of the instantaneous mixed layer. Let us do this tentatively although we will return to this point later. Since, for the highly stable conditions of this paper, the interface disturbances will be very small, the inversion will act like a 'rigid lid' with slip[†] and the turbulence will be similar to turbulence between a rigid heated plate at $z = 0$ and a rigid plate a $z = D$. The first question to face, then, is the nature of the turbulence at some level $\zeta = D - z$ near the upper "plate." To do this, we first consider the findings in two recent papers by Hunt (1977) and Hunt and Graham (1977) regarding the distorting effect of a rigid plane on homogeneous turbulence. The corresponding laboratory experiment is produced by passing air through a grid in a wind tunnel. The rigid plane is a moving belt along one wall of the wind tunnel with speed equal to the mean wind. This serves to eliminate the shear near the wall and the corresponding energy source. The wall causes two boundary layers (Figure 3). One is a very thin viscous layer of thickness δ_v near the wall in which all three components of velocity go to zero, and the other, called a source layer of thickness δ_s, extends from the viscous layer to a level at which the disturbing effects of the wall are negligible. The vertical velocity must decrease throughout the source layer because it is very small at the top of the viscous layer, but there is no obvious reason for a decrease of the horizontal velocity components in the source layer. This is confirmed by experiment and by the mathematical analysis by Hunt and Graham who derive the following results of interest in the present problem: The rms vertical velocity in the lower portions of the source layer is $w_2 = B(\varepsilon\zeta)^{1/3}$, where B is a universal constant and ε is the dissipation function far from the wall, and the rms horizontal velocities are of the same order as those far from the wall although somewhat larger. It is useful to obtain these and other results more intuitively.

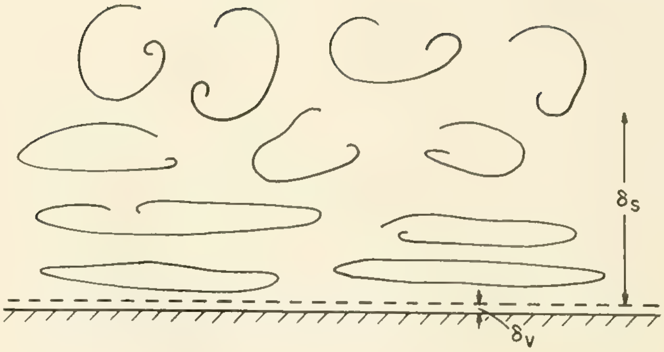

FIGURE 3. Turbulence near a wall.

In a recent paper, the first author [Long (1977c)] has shown that turbulence at high Reynolds number in a wind tunnel far from a wall is determined completely by two quantities, K and $\bar{u}/x$, where K is a quantity of dimensions L^2T^{-1} characteristic of the grid and proportional to $u\ell$. $\bar{u}$ is the mean velocity and x is distance downstream from the grid (or more accurately from a virtual energy source replacing the grid). For example, the dissipation function far from the wall is $\varepsilon \sim K\bar{u}^2/x^2$, the rms velocity is $u \sim (K\bar{u}/x)^{\frac{1}{2}}$, and the integral length scale is $\ell \sim (Kx/\bar{u})^{\frac{1}{2}}$.

Obviously the source layer thickness is $\delta_s \sim \ell$ [Hunt (1977)] and the dissipation in the source layer is

$$\varepsilon_s = \varepsilon f \left(\frac{\zeta \bar{u}^{\frac{1}{2}}}{K^{\frac{1}{2}} x^{\frac{1}{2}}} \right) \qquad (21)$$

Just outside of the viscous layer, ε_s is ε_{s0}, or

$$\varepsilon_{s0} = \varepsilon f \left(\frac{\delta_v \bar{u}^{\frac{1}{2}}}{K^{\frac{1}{2}} x^{\frac{1}{2}}} \right) \qquad (22)$$

As $\nu \to 0$, $\delta_v \to 0$, and, since ε_{s0} must be independent of viscosity for high Reynolds number turbulence, $\varepsilon_{s0} \sim \varepsilon$.

At small ζ, eddies of length much less than ζ will not feel the distorting effect of the surface and will be isotropic. Eddies of length much greater than ζ will feel the surface very strongly and will be strongly flattened. Eddies of length of order $\zeta << \ell$ will feel the surface but will remain quasi-isotropic. From the equation of continuity the large flattened eddies of horizontal dimensions D yield vertical velocities of order $u_1\zeta/D \sim K\zeta/D^2$. The quasi-isotropic eddies are much smaller and for high Reynolds numbers will lie in the inertial subrange. They will have a spectrum function

---

[*] We mean by $A \sim B$ that A/B is finite and non-zero in the limit as $Ri \to \infty$.

[†] This is the opinion also of Zeman and Tennekes (1977).

$$E_1(k) \sim \varepsilon_{s0}^{\frac{2}{3}} k^{-\frac{5}{3}} , \quad k \sim \zeta^{-1} \tag{23}$$

where k is the wave number so that the contribution to the vertical velocity is $\varepsilon_{s0}^{1/3}\zeta^{1/3}$. This is much larger than the contribution from the flattened eddies so that $w_s \sim \varepsilon_{s0}^{1/3}\zeta^{1/3}$ or $w_s \sim \varepsilon^{1/3}\zeta^{1/3}$, as derived rigorously by Hunt and Graham (1977).

In the mixing experiments the surface at $z = D$ is not rigid but is agitated by disturbances of amplitude δ_2. Assuming that eddies of this size are in the inertial subrange, we get vertical velocities of order $\varepsilon^{1/3}\delta_2^{1/3}$ and again these, rather than the eddies of size D, contribute most to the rms. Then $w_2 \sim \varepsilon^{1/3}\delta_2{}^{1/3}$. Since $\varepsilon \sim K^3/D^4$, we get, as in MISF,

$$\frac{w_2^3 D^4}{\delta_2 K^3} = B_6 \tag{24}$$

The problem of the present paper is somewhat more complicated but the distorting effect of the interface should be the same since the buoyancy variations in the mixed layer are very small. The air in the main portion of the mixed layer has velocities of order $(q_1 D)^{1/3}$ rather than K/D and in R_2 the buoyancy flux is similar to that in the case of mechanical stirring. Equation (24) takes the form

$$\frac{w_2^3}{\delta_2} = B_{11} q_1 \tag{25}$$

This result, together with (19), implies $w_2 \sim w_\star \hat{Ri}^{-\frac{1}{4}}(h/D)^{\frac{1}{4}}$, where $\hat{Ri} = D\Delta b/w_\star^2$, and differs fundamentally from that of Tennekes (1973b) who assumed $w_2 \sim w_*$ by arbitrarily equating the buoyancy flux and the energy flux divergence. Tennekes has acknowledged [Zeman and Tennekes (1977)] the inadequacy of this assumption.

The drop-off of w as the interface is approached is revealed in the data of Willis and Deardorff (1974). As shown by Hunt and Graham (1977), the total kinetic energy is the same near the distorting surface as it is far away so that the horizontal components of rms velocity should increase toward the interface. There is an indication of this also in the data of Willis and Deardorff.

It is also interesting that we may predict the same type of behavior near the *lower heated surface*. In fact, earlier data of Deardorff and Willis (1967) as well as the more recent data of Willis and Deardorff (1974) show that the vertical velocity near the heated plate increases with height, roughly in accordance with similarity theory [Prandtl (1932)], but that the horizontal velocity decreases with height. Thus, it is possible to apply similarity theory to obtain the vertical component, w, but not to obtain the horizontal components, u and v. The dimensional analysis for the horizontal components at large Rayleigh number must include D as well as q_1 and z no matter how small the ratio, z/D! There are experimental indications that the classical arguments of "localness" are also incorrect in problems of turbulent shear flow [Tritton (1977, p. 283)].

Using (25), the relations in (18)-(20) and the expression for w_2 are

$$\delta_2 = B_3^{-\frac{3}{4}} B_{11}^{\frac{1}{2}} q_1^{\frac{1}{2}} \left(\frac{h}{\Delta b}\right)^{\frac{3}{4}} \tag{26}$$

$$w_2 = B_{11}^{\frac{1}{2}} B_3^{-\frac{1}{4}} q_1^{\frac{1}{2}} \left(\frac{h}{\Delta b}\right)^{\frac{1}{4}} \tag{27}$$

$$\frac{B_1}{B_2} B_{11} q_1 I_2 = - D \frac{d\Delta b}{dt} + N^2 D \frac{d}{dt} (D + h) - q_1 \tag{28}$$

$$\frac{-\alpha_2 q_1^{\frac{3}{2}}}{h^{\frac{1}{4}}(\Delta b)^{\frac{3}{4}}} = q_1 + \left(D + \frac{h}{3}\right)\frac{d\Delta b}{dt} + \frac{\Delta b}{6}\frac{dh}{dt} + \frac{1}{2}\Delta b \frac{dD}{dt}$$

$$- N^2 (D + \tfrac{1}{2} h) \frac{d}{dt} (D + h) \tag{29}$$

where $\alpha_2 = A_2 B_{11}^{\frac{3}{2}}/B_3^{\frac{3}{4}}$.

5. DIFFERENTIAL EQUATIONS

Equation (29) is a single differential equation in three unknowns, D, h, Δb. Let us now seek additional information. The quantity, u_3^3/δ_3, is the dissipation in the turbulent patches in the interfacial layer. We have seen that it is independent of $\hat{Ri}$ in the lower portions of the layer. Obviously it will vary continuously with ζ (now defined as z - D) in the layer and, to the first order, will remain independent of Ri although it may vary with the quantity $s = N^2 h/\Delta b$ when the upper fluid has a linear buoyancy field. We may therefore write

$$\frac{u_3^3}{\delta_3} - q_1 \varphi\left(\frac{\zeta}{D}, s\right) \tag{30}$$

or using (14)

$$u_3^3 = B_3^{-\frac{3}{4}} q_1^{\frac{3}{2}} \left(\frac{h}{\Delta b}\right)^{\frac{3}{4}} \varphi_1\left(\frac{\zeta}{D}, s\right) \tag{31}$$

We may obtain another expression for u_3^3 by integrating the energy equation over the interfacial layer. We have already seen that $|\varepsilon_3| \sim |q_3|$ and assuming that the energy flux is proportional to u_3^3 in this layer*, we have from the energy equation

$$\frac{\partial u_3^3}{\partial \zeta} = B_{12} q_3 \tag{32}$$

Using (8) and integrating, we get

$$u_3^3 = w_2^3 + B_{12} \left[q_2 \zeta + \frac{d\Delta b}{dt}\left(\frac{\zeta^2}{2} - \frac{\zeta^3}{6h}\right) \right.$$

$$+ \Delta b \left(\frac{\zeta^3}{6h^2}\frac{dh}{dt} + \frac{\zeta^2}{2h}\frac{dD}{dt}\right)$$

$$\left. - N^2 \frac{\zeta^2}{2}\frac{d}{dt}(D + h) \right] \tag{33}$$

---

*We have seen that the energy flux at the bottom of the layer is proportional to u_{30}^3. To the first order it should be proportional to u_3^3 in the rest of the layer, i.e., independent of $\hat{Ri}$.

Comparing (31) and (33) and using (27), we get

$$\varphi_1\left(\frac{\zeta}{D},s\right) = B_{11}^{\frac{3}{2}} - A_3\frac{\zeta}{D} + A_4\frac{\zeta^2}{D^2} + A_5\frac{\zeta^3}{D^3} \tag{34}$$

where[†] A_3, A_4, and A_5 may depend on s. Equating coefficients in (34) we get (29) again and the following

$$q_1 + D\frac{d\Delta b}{dt} - N^2 D\frac{d}{dt}(D+h) = -\alpha_3\frac{q_1^{\frac{3}{2}}h^{\frac{3}{4}}}{D(\Delta b)^{\frac{3}{4}}} \tag{35}$$

$$\frac{D}{2}\frac{d\Delta b}{dt} + \frac{\Delta b}{2h}D\frac{dD}{dt} - \frac{N^2 D}{2}\frac{d}{dt}(D+h) = \alpha_4\frac{q_1^{\frac{3}{2}}h^{\frac{3}{4}}}{D(\Delta b)^{\frac{3}{4}}} \tag{36}$$

$$-\frac{D^2}{6h}\frac{d\Delta b}{dt} + \frac{D^2\Delta b}{6h^2}\frac{dh}{dt} = \alpha_5\frac{q_1^{\frac{3}{2}}h^{\frac{3}{4}}}{D(\Delta b)^{\frac{3}{4}}} \tag{37}$$

where $\alpha_i = A_i/B_{12}B_3^{3/4}$ $(i = 3,4,5)$. Equations (35)-(37), (29), and (11) are five equations in the three unknowns. They determine the solution to the first order for large $\hat{R}i$, although we must make sure that all equations are satisfied to that order. In this regard, if we use (35)-(37), (29), and the derivative of (11), i.e., (10), we may consider these as five homogeneous linear, algebraic equations in five unknowns $d\Delta b/dt$, dD/dt, dh/dt, q_1, and $q_1^{3/2}h^{3/4}/D(\Delta b)^{3/4}$. The determinant of these equations vanishes and we satisfy compatibility.

6. HOMOGENEOUS CASE (N = 0)

If N = 0, the upper fluid is homogeneous and (11) becomes

$$(D + \tfrac{1}{2}h)\Delta b = V_0^2 - q_1 t \tag{38}$$

where V_0^2 is a constant related to initial conditions. We use (35) and (38) to eliminate Δb in (29), (36), and (37). We get

$$\frac{d}{dt}(\Delta b) = -\frac{q_1}{D} - \alpha_3\frac{q_1^{\frac{3}{2}}h^{\frac{3}{4}}}{D^2}\frac{(D+\frac{1}{2}h)^{\frac{3}{4}}}{(V_0^2 - q_1 t)^{\frac{3}{4}}} \tag{39}$$

$$\frac{dh}{dt} + \frac{q_1 h}{D}\frac{(D+\frac{1}{2}h)}{(V_0^2 - q_1 t)} + \left(\alpha_3 - 6\alpha_5\frac{h}{D}\right)\frac{q_1^{\frac{3}{2}}h^{\frac{7}{4}}}{D^2}\frac{(D+\frac{1}{2}h)^{\frac{7}{4}}}{(V_0^2 - q_1 t)^{\frac{7}{4}}} = 0 \tag{40}$$

$$\frac{dD}{dt} - q_1\frac{h}{D}\frac{(D+\frac{1}{2}h)}{(V_0^2 - q_1 t)} - (\alpha_3 + 2\alpha_4)\frac{q_1^{\frac{3}{2}}h^{\frac{7}{4}}}{D^2}\frac{(D+\frac{1}{2}h)^{\frac{7}{4}}}{(V_0^2 - q_1 t)^{\frac{7}{4}}} = 0 \tag{41}$$

$$3\frac{dD}{dt} + \frac{dh}{dt} - 2q_1\frac{h}{D}\frac{(D+\frac{1}{2}h)}{(V_0^2 - q_1 t)} + \left[6\alpha_2\frac{D^2}{h^2} - 6\alpha_3\frac{D}{h} - 2\alpha_3\right]\frac{q_1^{\frac{3}{2}}h^{\frac{7}{4}}(D+\frac{1}{2}h)^{\frac{7}{4}}}{D^2(V_0^2 - q_1 t)^{\frac{7}{4}}} = 0 \tag{42}$$

Two effects occur in (40) and (41). We may separate them by adding the two equations. We get

$$\frac{d}{dt}(D+h) = \left(2\alpha_4 + 6\alpha_5\frac{h}{D}\right)\frac{q_1^{\frac{3}{2}}h^{\frac{7}{4}}}{D^2}\left(\frac{D+\frac{1}{2}h}{V_0^2 - q_1 t}\right)^{\frac{7}{4}} \tag{43}$$

The term on the right of (43) expresses the upward motion of the boundary between (intermittently) turbulent and non-turbulent fluid due to turbulence in the interfacial layer causing entrainment of the upper, non-turbulent fluid. On the other hand, the second terms in (40) and (41) express the upward motion of the boundary between fully turbulent and intermittently turbulent fluid (and the consequent decrease of h) due to heating alone. This contribution to the entrainment velocity is proportional to the interfacial thickness, h, and disappears when the common approximation is made that h = 0.

Let us find an approximate solution to (40)-(42). If we let D_0 and h_0 be the values of D and h at t = 0, we make the following definitions:

$$\frac{h_0}{D_0} = a\ ,\quad \frac{h}{D_0} = h_1\ ,\quad \frac{D}{D_0} = D_1\ ,$$

$$\frac{q_1^{\frac{2}{3}}D_0^{\frac{2}{3}}}{V_0^2} = \delta\ ,\quad \frac{q_1^{\frac{1}{3}}t}{D_0^{\frac{2}{3}}} = \tau \tag{44}$$

Then equations (40)-(42) may be written

$$\frac{dh_1}{d\tau} + \frac{h_1}{D_1}\frac{(D_1 + \frac{1}{2}h_1)}{(1-\delta\tau)}\delta + \left(\alpha_3 - 6\alpha_5\frac{h_1}{D_1}\right)\frac{h_1^{\frac{7}{4}}(D_1 + \frac{1}{2}h_1)^{\frac{7}{4}}\delta^{\frac{7}{4}}}{D_1^2(1-\delta\tau)^{\frac{7}{4}}} = 0 \tag{45}$$

$$\frac{dD_1}{d\tau} - \frac{h_1}{D_1}\frac{(D_1 + \frac{1}{2}h_1)}{(1-\delta\tau)}\delta - (\alpha_3 + 2\alpha_4)\frac{h_1^{\frac{7}{4}}(D_1 + \frac{1}{2}h_1)^{\frac{7}{4}}\delta^{\frac{7}{4}}}{D_1^2(1-\delta\tau)^{\frac{7}{4}}} = 0 \tag{46}$$

[†] For arbitrary $\hat{R}i$, the quantities A_i may depend on $\hat{R}i$. As $\hat{R}i \to \infty$, however, A_i will approach "constants" which may, of course, be zero.

$$\left(6\alpha_2 \frac{D_1^2}{h_1^2} - 6\alpha_3 \frac{D_1}{h_1} + 6\alpha_4 + 6\alpha_5 \frac{h_1}{D_1}\right)$$

$$\frac{h_1^{\frac{7}{4}}(D_1 + \frac{1}{2}h_1)^{\frac{7}{4}}\delta^{\frac{7}{4}}}{D_1^2(1 - \alpha\tau)^{\frac{7}{4}}} = 0 \qquad (47)$$

Solutions are of the form

$$\frac{h}{h_0} = 1 - (1 + \tfrac{1}{2}a)\frac{q_1 t}{v_0^2}$$

$$- (\alpha_3 - 6\alpha_5 a)\, a^{\frac{3}{4}} (1 + \frac{1}{2}a)^{\frac{7}{4}} \frac{q_1^{\frac{3}{2}} D_0^{\frac{1}{2}} t}{V_0^{\frac{7}{2}}}$$

$$+ \frac{1}{8} a(2 + a)^2 \frac{q_1^2 t^2}{V_0^4} + \ldots \qquad (48)$$

$$\frac{D}{D_0} = 1 + a(1 + \tfrac{1}{2}a)\frac{q_1 t}{v_0^2}$$

$$+ (\alpha_3 + 2\alpha_4) a^{\frac{7}{4}} (1 + \frac{1}{2}a)^{\frac{7}{4}} \frac{q_1^{\frac{3}{2}} D_0^{\frac{1}{2}} t}{V_0^{\frac{7}{2}}}$$

$$- \frac{1}{8} a^2(2 + a)^2 \frac{q_1^2 t^2}{V_0^4} + \ldots \qquad (49)$$

$$\frac{D_0 \Delta b}{V_0^2} = \frac{2}{2 + a} - \frac{q_1 t}{V_0^2}$$

$$- \left(\frac{\alpha_3}{2} + 2\alpha_4 + 3\alpha_5 a\right) a^{\frac{7}{4}}\left(1 + \frac{a}{2}\right)^{-\frac{1}{4}} \frac{q_1^{\frac{3}{2}} D_0^{\frac{1}{2}} t}{V_0^{\frac{7}{2}}}$$

$$+ \frac{a(2 + a)}{4} \frac{q_1^2 t^2}{V_0^4} + \ldots \qquad (50)$$

where h_0 and D_0 are related by the equation

$$6\alpha_2 - 6\alpha_3 a + 6\alpha_4 a^2 + 6\alpha_5 a^3 = 0 \qquad (51)$$

The entrainment velocity, $u_e = dD/dt$, may be expressed in terms of the Richardson number, $\hat{Ri} = D\Delta b/w_*^2$, by using

$$\delta(1 + \frac{1}{2}a) \approx \hat{Ri}^{-1} + \ldots$$

we get

$$\frac{u_e}{w_*} = a\hat{Ri}^{-1} + c\hat{Ri}^{-\frac{7}{4}} + \ldots, \quad c = (\alpha_3 + 2\alpha_4)a^{\frac{7}{4}} \qquad (52)$$

The first term is of the same form as the non-dimensional entrainment velocity of Tennekes (1973) but, as already pointed out, the derivation and physical mechanism are very different. It is easy to trace the error in (52) arising from the simplification of Section 2 that the IL has a linear buoyancy field. The error is proportional to $(u_e/w_*) ab_e/\Delta b$ where b_e is the maximum difference between the actual buoyancy in the IL and the assumed buoyancy. Since a is 1/6 or so and $b_e/\Delta b$ is fairly small, this error is negligible. Notice also that the theory concerns strongly stable conditions so that (52) does not apply in the limit as $\hat{Ri} \to 0$. As $\hat{Ri}$ tends to order one u_e becomes of order w_* as one would expect.

The ratio q_2/q_1 is of interest. Using (6), we get

$$\frac{q_2}{q_1} = 1 + \frac{D}{q_1}\frac{d\Delta b}{dt} \qquad (53)$$

Using (50) and (52), we get

$$\left|\frac{q_2}{q_1}\right| = \gamma\hat{Ri}^{-\frac{3}{4}}, \quad \gamma = \frac{a^{\frac{7}{4}}}{(1 + \frac{1}{2}a)^{\frac{1}{4}}}\left(\frac{\alpha_3}{2} + 2\alpha_4 + 3\alpha_5 a\right) \qquad (54)$$

The expressions (26)-(28) are

$$\frac{w_2}{w_*} = \frac{B_{11}}{B_3^{\frac{1}{4}}} a^{\frac{1}{4}}\hat{Ri}^{-\frac{1}{4}}, \quad \frac{\delta_2}{h} = \frac{B_{11}^{\frac{1}{2}}}{B_3^{\frac{3}{4}} a^{\frac{3}{4}}} \hat{Ri}^{-\frac{3}{4}},$$

$$I_2 = \frac{B_2}{B_1 B_{11}} \gamma\hat{Ri}^{-\frac{3}{4}} \qquad (55)$$

These relations are identical to those in MISF. The result that the disturbances in the IL are small compared to the thickness of the IL is contrary to speculation [Stull (1973) and Zeman and Tennekes (1977)] that h is the depth of penetration of the eddies into the stable region.

7. LINEAR BUOYANCY FIELD IN THE UPPER LAYER ($N \neq 0$).

We consider initial conditions in which the fluid is at rest initially with a linear buoyancy field, so that D, h, Δb are zero at $t = 0$. Equation (11) becomes

$$(D + \frac{1}{2}h)\Delta b = \frac{N^2}{2}(D + h)^2 = -q_1 t \qquad (56)$$

Equations (56), (29), and (35)-(37) determine the problem. The approximate solutions* are

---

*The solutions, as throughout the paper, are for strong stability, which implies here that Nt is large. Then $s \to 1$, and $\alpha_2, \alpha_3, \alpha_4, \alpha_5$ are independent of s.

$$D = \frac{(2q_1t)^{\frac{1}{2}}}{N} + \frac{(2q_1)^{\frac{1}{2}}b_1}{N^{\frac{3}{2}}} ,$$

$$h = (2q_1t)^{\frac{1}{2}}\frac{a}{N} + \frac{(2q_1)^{\frac{1}{2}}b_2}{N^{\frac{3}{2}}}$$

$$\Delta b = (2q_1t)^{\frac{1}{2}}aN + (2q_1)^{\frac{1}{2}}b_3N^{\frac{1}{2}} \qquad (57)$$

where

$$a = -1 + \left(1 + \frac{\alpha_3}{\alpha_4}\right)^{\frac{1}{2}} , \quad \frac{b_1}{\alpha_4} = \frac{a(a+2)}{2^{\frac{1}{2}}} , \quad \frac{\alpha_5}{\alpha_4} = \frac{1}{3}$$

$$\frac{\alpha_2}{\alpha_4} = a^2(1 + \frac{2}{3}a) , \quad \frac{b_3 - b_2}{\alpha_4} = 2^{\frac{1}{2}}a \qquad (58)$$

Using the relationship

$$Nt = \frac{\hat{Ri}^{\frac{3}{2}}}{2a^{\frac{3}{2}}}\left[1 - \frac{3a^{\frac{3}{4}}}{2^{\frac{1}{2}}}\left(\frac{b_1}{3} + \frac{b_3}{a}\right)\hat{Ri}^{-\frac{3}{4}}\right] \qquad (59)$$

we obtain for the entrainment velocity

$$\frac{u_e}{w_*} = a\hat{Ri}^{-1} + 2^{\frac{1}{2}}b_3a^{\frac{3}{4}}\hat{Ri}^{-\frac{7}{4}} \qquad (60)$$

The ratio of fluxes is

$$\left|\frac{q_2}{q_1}\right| = 2^{\frac{1}{2}}b_1a^{\frac{3}{4}}\hat{Ri}^{-\frac{3}{4}} \qquad (61)$$

Notice that $\Delta b/h \to N^2$ as $t \to \infty$ so that the IL becomes indistinguishable from the upper layer as the turbulence in it weakens (becomes more intermittent). This contrasts with MISF in which the stability in the IL is several times larger than the stability in the upper fluid. Notice also that $s \to 1$ implies $\alpha_2 \ldots \alpha_5$ are universal constants. More accurately,

$$\frac{\Delta b}{hN^2} = 1 + \alpha_4\left(\frac{2}{Nt}\right)^{\frac{1}{2}} \qquad (62)$$

We see from (32) that $\alpha_4 > 0$ so that the buoyancy gradient in the IL is more stable than in the air above. These results suggest that an interfacial layer will be difficult to identify when there is a stable buoyancy gradient aloft. This is certainly the case in the experiments of Deardorff, Willis, and Lilly (1969) and Willis and Deardorff (1974).

8. DISCUSSION

We have already contrasted the theory of this paper with that of Tennekes (1973). He obtains

$$\frac{u_e}{w_*} = a_1\hat{Ri}^{-1} \qquad (63)$$

which has the same form as the first term in (52) or (60). The present theory should not, however, be regarded as an extension or modification of the Tennekes' theory because, as we have noted in several places, the two theories differ fundamentally. This is also evident in the difference in the nature of the two constants of proportionality for the $\hat{Ri}^{-1}$ term in the two theories. The a_1 in (63) may be identified physically as the ratio $|q_2/q_1|$ which is a universal constant in the Tennekes' theory. The constant, a, in (52) or (60), however, is a universal constant equal to the asymptotic value of the ratio of the inversion layer thickness to the thickness of the mixed layer. Tennekes assumed a value of 0.2 or so for a_1 and it is a coincidence that this is also a reasonable choice for a.

We may attempt to estimate the constants in the expressions

$$\frac{u_e}{w_*} = a\hat{Ri}^{-1} + c\hat{Ri}^{-\frac{7}{4}} , \quad \frac{q_2}{q_1} = \gamma\hat{Ri}^{-\frac{3}{4}} \qquad (64)$$

using the data of Willis and Deardorff (1974)*. Approximate estimates for the two cases:

S1: $D \cong 58$ cm, $h \cong 9$ cm, $\Delta T \cong 1.7°C$,
$\Delta b \cong 0.39$ cm/sec^2, $Q_0 \cong 0.18°C$ cm/sec,
$w_* \cong 1.3$ cm/sec, $\hat{Ri} \cong 13.5$, $a \cong 0.16$,
$c = 1.09$, $\gamma \equiv 1.61$
S2: $D \cong 55$cm, $h = 8.5$ cm, $\Delta T \cong 3°C$,
$\Delta b \cong 0.69$ cm/sec^2, $Q_0 \cong 0.22°C$ cm/sec,
$w_* \cong 1.4$ cm/sec, $\hat{Ri} \cong 20$, $a \cong 0.15$,
$c = 1.05$, $\gamma = 1.05$

We may also attempt to compare with atmospheric data. For example, using the 1200 observation on Day 33 for the Wangara data, [Zeman and Tennekes (1977)], we obtain

$D \cong 1.1\ 10^5$cm, $h \cong 2 \times 10^4$ cm, $\Delta\theta \cong 4°C$,
$\Delta b \cong 13$ cm/sec^2, $Q_0 \cong 20°C$ cm/sec,
$w_* \cong 194$ cm/sec, $\hat{Ri} = 38$, $a \cong 0.2$, $c \cong 2.2$

These computations indicate that the two terms in the expression for u_e in Eq. (64) are roughly similar in magnitude for atmospheric and laboratory conditions.

It is interesting to compare the theory of the erosion of a linear buoyancy field with a numerical experiment of Zeman and Lumley (1977) using a second-order closure model. The numerical calculation began from an initial instant, t_0, at which time $D = D_0$, $w_* = w_{*0} = (q_1D_0)^{1/3}$. The present theory at time $t_1 = t - t_0$ is

$$\frac{D}{D_0} = 1 + \frac{\tau}{S_0} + \ldots, \quad S_0 = N^2D_0^2/w_{*0}^2, \quad \tau = \frac{t_1w_{*0}}{D_0} \qquad (65)$$

where we have assumed that $(t_0N)^{\frac{1}{2}}$ is large. The numerical curves [Figure 1 of the paper of Zeman and Lumley] are nearly linear after τ exceeds 2 or so although, as (57) would indicate, D/D_0 increases somewhat more slowly after considerable time. The

---

*Supplemented by information in a personal communication from Dr. Willis.

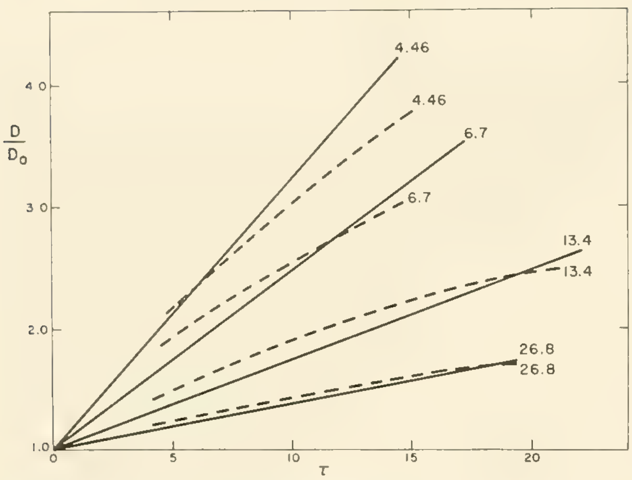

FIGURE 4. Comparison of present theory and numerical experiment of Zeman and Tennekes (1977). The curves correspond to values of S_o in (65).

most important comparison, however, is that the curves of Zeman and Lumley for various S_0 collapse rather well when plotted against τ/S_0 instead of τ as in Figure 1 of Zeman and Lumley. Conversely, we may reproduce Figure 1 of Zeman and Lumley together with plots of D/D_0 in (65) for the same values of S_0 chosen by Zeman and Lumley. This is shown in Figure 4. The agreement is good, especially at large stabilities where the approximation in (65) should be best. This indicates that the two models have some similar features.

ACKNOWLEDGMENT

This research was supported by the National Science Foundation under Grant Nos. ATM76-22284, ATM76-04050, and OCE76-18887, and by the Office of Naval Research, Fluid Dynamics, under Contract No. N00014-75-C-0805.

REFERENCES.

Adrian, R. J. (1975). Turbulent convection in water over ice. *J. Fluid Mech. 69*, 753.

Ball, F. K. (1960). Control of inversion height by surface heating. *Quart. J. Roy. Met. Soc. 86*, 483.

Betts, A. K. (1973). Non-precipitating cumulus convection and its parameterization. *Quart. J. Roy. Met. Soc. 99*, 178.

Carson, D. J. (1973). The development of a dry, inversion-capped convectively unstable boundary layer. *Quart. J. Roy. Met. Soc. 99*, 450.

Crapper, P. F., and P. F. Linden (1974). The structure of turbulent density interfaces. *J. Fluid Mech. 65*, 45.

Deardorff, J. W. (1967). Empirical dependence of the eddy coefficient for heat upon stability above the lowest 50 m. *J. Appl. Meteor. 6*, 631.

Deardorff, J. W. (1972). Parameterization of the planetary boundary layer for use in general circulation models. *Mon. Wea. Rev. 100*, 73.

Deardorff, J. W., G. E. Willis, and D. K. Lilly (1969). Laboratory investigation of non-steady penetrative convection. *J. Fluid Mech. 35*, 7.

Farmer, D. M. (1975). Penetrative convection in the absence of mean shear. *Quart. J. Roy. Met. Soc. 101*, 869.

Heidt, F. -D. (1977). Comparison of laboratory experiments on penetrative convection with measurements in nature. *Heat Transfer and Turbulent Buoyant Convection, 1*. D. Spalding and N. Afgan, ed., 199-210.

Hopfinger, E. J. and J. A. Toly (1976). Spatially decaying turbulence and its relation to mixing across density interfaces. *J. Fluid Mech. 78*, 155.

Hunt, J. C. R. (1977). A review of the theory of rapidly distorted turbulent flows and its applications. *XII Biennial Fluid Dynamics Symposium*, Poland.

Hunt, J. C. R., and J. M. R. Graham (1977). Free stream turbulence near plane boundaries. *J. Fluid Mech.* (In press).

Izumi, T. (1964). Evolution of temperature and velocity profiles during a breakdown of a nocturnal inversion and a low level jet. *J. Appl. Meteor. 3*, 70.

Kaimal, J. C., J. C. Wyngaard, D. A. Haugen, O. R. Cote, Y. Izumi, S. J. Caughey, and C. J. Readings (1976). Turbulence structure in the convective boundary layer. *J. Atmos. Sci. 33*, 2152.

Kraus, E. B., and J. S. Turner (1967). A one-dimensional model of the seasonal thermocline. Part II. The general theory and its consequences. *Tellus 19*, 98.

Kuo, H. L., and W. Y. Sun (1976). Convection in the lower atmosphere and its effects. *J. Atmos. Sci. 33*, 21.

Lenschow, D. H. (1970). Airplane measurements of planetary boundary layer structure. *J. Appl. Meteor. 9*, 874.

Lenschow, D. H. (1974). Model of the height variation of the turbulence kinetic energy budget in the unstable planetary boundary layer. *J. Atmos. Sci. 31*, 465.

Lettau, H. H., and B. Davidson (1957). *Exploring the Atmosphere's First Mile., Vols. 1* and *2*. Pergamon Press, New York.

Lilly, D. K. (1968). Models of cloud-topped mixed layers under a strong inversion. *Quart. J. Roy. Meteor. Soc. 94*, 292.

Linden, P. F. (1973). The interaction of a vortex ring with a sharp density interface: a model for turbulent entrainment. *J. Fluid Mech. 60*, 467.

Linden, P. F. (1975). The deepening of a mixed layer in a stratified fluid. *J. Fluid Mech. 71*, 385.

Long, R. R. (1975). The influence of shear on mixing across density interfaces. *J. Fluid Mech. 70*, 305.

Long, R. R. (1977a). A theory of turbulence in a homogeneous fluid induced by an oscillating grid. Submitted to *Physics of Fluids*.

Long, R. R. (1977b). A theory of mixing in a stably stratified fluid. Submitted to *Physics of Fluids*.

Long, R. R. (1977c). The decay of turbulence. Submitted to *Physics of Fluids*.

Long, R. R. (1977d). Some aspects of turbulence in geophysical systems. *Advances in Applied Mechanics 17*, 1.

Monin, A. S. and A. M. Yaglom (1971). *Statistical Fluid Mechanics: Mechanics of Turbulence 1*. The MIT press., Mass.

Moore, M. J., and R. R. Long (1971). An experimental investigation of turbulent stratified shearing flow. *J. Fluid Mech. 49*, 635.

Niiler, P. P., and E. B. Kraus (1977). One-dimensional models of the upper ocean. *Modelling and Prediction of the Upper Layers of the Ocean*, E. B. Kraus, ed., Pergamon Press, Oxford, England, pp. 143-172.

Prandtl, L. (1932). Meteorlogische Andwendungen der Strömungslehre. *Beitr. Phys. fr. Atmos. 19*, 188.

Rouse, H. and J. Dodu (1955). Turbulent diffusion across a density discontinuity. *Houille Blanche 10*, 405.

Stull, R. B.(1973). Inversion rise model based on penetrative convection. *J. Atmos. Sci. 30*, 1092.

Stull, R. B. (1976a). The energetics of entrainment across a density interface. *J. Atmos. Sci. 33*, 1260.

Stull, R. B. (1976b). Mixed-layer depth model based on turbulent energetics. *J. Atmos. Sci. 33*, 1268.

Stull, R. B. (1976c). Internal gravity waves generated by penetrative convection. *J. Atmos. Sci. 33*, 1279.

Summers, P. W. (1965). An urban heat island model: Its role in air pollution problems with special application to Montreal. *Proc. First Canadian Conf. Micrometeorology*, Toronto, Atmos. Environ. Service.

Tennekes, H. (1973a). Similarity laws and scale relations in planetary boundary layers. *Workshop on Micrometeorology*, D. A. Haugen, ed., AMS, Boston.

Tennekes, H. (1973b). A model for the dynamics of inversion above a convective boundary layer. *J. Atmos. Sci. 30*, 558.

Tennekes, H. (1975). Reply (to Zilitinkevich, S. S.). *J. Atmos. Sci. 32*, 992.

Thompson, S. M., and J. S. Turner (1975). Mixing across an interface due to turbulence generated by an oscillating grid. *J. Fluid Mech. 67*, 349.

Tritton, D. J. (1977). *Physical Fluid Dynamics*, Van Nostrand Reinhold, New York.

Turner, J. S. (1968). The influence of molecular diffusivity on turbulent entrainment across a density interface. *J. Fluid Mech. 33*, 639.

Turner, J. S. (1973). *Buoyancy Effects in Fluids*, Chapter 9, Cambridge Univ. Press.

Veronis, G. (1963). Penetrative convection. *Astrophys. J. 137*, 641.

Willis, G. F., and J. W. Deardorff (1974). A laboratory model of the unstable planetary boundary layer. *J. Atmos. Sci. 31*, 1297.

Wolanski, E. J. (1972). *Turbulent entrainment across stable density-stratified liquids and suspensions.* Ph.D. Thesis, The Johns Hopkins Univ., Baltimore, Md.

Wolanski, E. J., and L. M. Brush (1975). Turbulent entrainment across stable density step structures. *Tellus 27*, 259.

Zeman, O. and J. L. Lumley (1977). A second-order model for buoyancy driven mixed layers. *Heat Transfer and Turbulent Buoyant Convection, Vol. 1*, D. Spalding and N. Afgan, ed., pp. 65-76.

Zeman, O., and H. Tennekes (1977). Parameterization of the turbulent energy budget at the top of the daytime atmospheric boundary layer. *J. Atmos. Sci. 34*, 111.

Zilitinkevich, S. S. (1975). Comments on 'A Model for the Dynamics of the Inversion above a Convective Boundary Layer.' *J. Atmos Sci. 32*, 991.

Laboratory Models of Double-Diffusive Processes in the Ocean

J. Stewart Turner
Australian National University
Canberra, Australia

ABSTRACT

There is now good observational evidence to support the ideas that double-diffusive processes, i.e., those for which the differential diffusion of heat and salt are important, can affect the rates of vertical transport of these properties in the ocean, and are responsible for the formation of certain types of microstructure. Much of our detailed understanding of these effects has come from related laboratory experiments, but new phenomena are still being discovered which are as yet untested by direct measurements in the ocean. It is the purpose of this paper first to review the background to this subject, and then to describe the more recent experiments which suggest further double-diffusive effects likely to be significant in various oceanographic contexts.

A convenient laboratory technique has been to use two solutes (commonly salt and sugar) to model the T-S variations; some of these experiments with closer diffusivities are in fact directly relevant to the ocean. When more than two diffusing components are present it has been shown that even small differences in molecular diffusivity can significantly affect the relative rates of transfer of solutes through an interface, and this should be considered more carefully in geochemical studies. Strong double-diffusive layering is often associated with large horizontal gradients of T and S, and related effects have been studied in our laboratory in three different geometries: the circulation produced by a block of ice in a salinity gradient; a line source of one fluid intruding at its own density level into a gradient with different properties; and the spreading across a frontal surface separating two fluids having the same vertical density but different T-S structures.

1. INTRODUCTION

It is past the stage when the relevance of double-diffusive effects has to be justified *ab initio* to an audience of oceanographers. Over the last few years, there have been many observations of fine-structure and microstructure in the deep ocean which can only be explained in these terms. Wherever there is a systematic association between T and S variations, with both properties increasing or decreasing together (so that their effect on the density is in opposite senses), then it is clear that the difference in molecular diffusivities for heat and salt can affect the vertical structure and the transports of the two properties. It is not then sufficient to base predictions of mixing on the net density distribution alone.

Our understanding of these processes has been greatly influenced by related laboratory experiments [see Turner (1973, 1974)]. Much of the detailed work has concentrated on the properties of sharp interfaces separating relatively well-mixed layers: it has been shown that when there are compensating T-S gradients, a smoothly stratified water column typically breaks up into a series of steps, and molecular processes must be more important across such interfaces. Once layers have formed there remains little doubt that the coupled transports can be estimated using the laboratory results. It is much less certain, however, that the processes of formation of layers have always been adequately modelled in the laboratory, where most of the experiments have been one-dimensional in form.

More recent experiments [Turner and Chen (1974), Huppert and Turner (1978), Turner (1978)] have begun to explore a variety of two-dimensional effects, and it is these which will be given most attention in the verbal presentation of this paper. It should be admitted right at the beginning that these experiments are still largely qualitative, and that much more remains to be done, but already they suggest new explanations of some existing observations in the ocean, and allow us to predict what might be measurable in future work.

2. ONE-DIMENSIONAL PROCESSES

Formation of Layers from a Gradient

For completeness, the fundamental physics of the double-diffusive convection will be outlined briefly by referring to the simpler early experiments. The review of one-dimensional experiments will then be brought up to date and specific oceanographic examples of these processes will also be described.

The necessary conditions for double-diffusive convection to occur in a fluid are firstly that there should be two or more components having different molecular diffusivities, and secondly that these components should make compensating contributions to the density. It is remarkable that under these conditions strong convective motions can arise even when the net density distribution increases downwards. The overall density is 'statically stable' in this sense in all the cases described here. Motions are nevertheless generated since the action of molecular diffusion, at different rates for the two components, makes it possible to release the potential energy in the component which is heavy at the top. This can drive convection in relatively well-mixed layers, while the second (stably distributed) component preserves the density difference across the interfaces separating them.

There are two cases to be considered, depending on the relation between the diffusivities and the density gradients, i.e., on whether the driving energy comes from the component having the higher or lower diffusivity. The simplest example of the former is a linear stable salinity gradient, heated from below. An unstratified tank would overturn from top to bottom, but because of the stabilizing salinity gradient only a thin temperature boundary layer is formed at first, which breaks down through an overstable oscillation [Shirtcliffe (1967)] to form a shallow convecting layer. This layer grows by incorporating fluid from the gradient above it, in such a way that the steps of S and T are nearly compensating, and there is no discontinuity of density, only of density gradient.

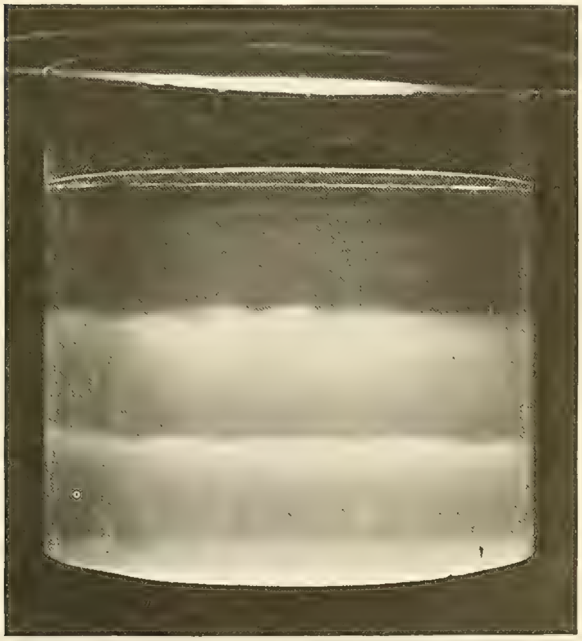

FIGURE 1. Layering produced from an initially smooth salinity gradient by heating from below. Three well-mixed layers are marked by fluorescein dye, lit from the top. (Tank diameter, 300mm.)

When the thermal boundary layer ahead of the convecting region reaches a critical Rayleigh number, it too becomes unstable. A second layer then forms above, and eventually many other layers form in succession (See Figure 1). The vertical scale of these layers increases as the heating rate is increased, and decreases with larger salinity gradients. Turner (1968) has shown that the first layer stops growing when

$$d_C = D\,B^{3/4}\,N_S^{-2} \qquad (1)$$

Here d_C is the critical depth, D is a dimensional constant which depends on the critical Rayleigh number and the molecular properties, $B = -g\alpha F_T/\rho C$ is the imposed buoyancy flux corresponding to a heat flux F_T (α being the coefficient of expansion and C the specific heat), and $N_S = [(g/\rho)\ (d\rho/dz)]^{\frac{1}{2}}$ is the initial buoyancy frequency of the stabilizing salinity distribution. The criterion for the formation of further layers is currently being studied by Huppert and Linden (personal communication).

A device which has proved very helpful in eliminating uncontrolled sidewall heat losses (as well as providing results directly relevant to the ocean) is to carry out experiments with two solutes, say sucrose and sodium chloride solutions, instead of salt and heat. Essentially the same phenomena can be observed, although the diffusivities are much more nearly equal (the ratio $\tau = \kappa_S/\kappa_T$, where κ_T denotes the larger and κ_S the smaller diffusivity in each case, is about 1/3 for sugar and salt, compared with $\approx 10^{-2}$ for salt and heat).

Linden (1976) has in this way extended the "heated gradient" experiments to study the case where there is a destabilizing salt (T) gradient partially compensating the stabilizing sugar (S) gradient in the interior. He has shown, both theoretically and experimentally, that during the formation of layers the relative contributions of the energy provided by the boundary flux, and that released in the interior, change systematically with the ratio of the vertical T and S gradients. In the limit where these gradients become equal, all the energy comes from the destabilizing component in the interior, and the ultimate layer depth is finite and proportional to $N_S^{-\frac{1}{2}}$ (where N_S is the buoyancy frequency corresponding to the stabilizing component).

Once layers and interfaces have formed, it is important to understand what governs the fluxes of S and T across them. For this purpose two or more layers can be set up directly, and the interfaces examined using a variety of optical techniques. For example, Figure 2 is a shadowgraph picture of a very sharp interface formed between a layer of salt solution above a layer of sugar solution, which is equivalent to colder fresh water above hot salty water. Note that salt is here the analogue of heat,

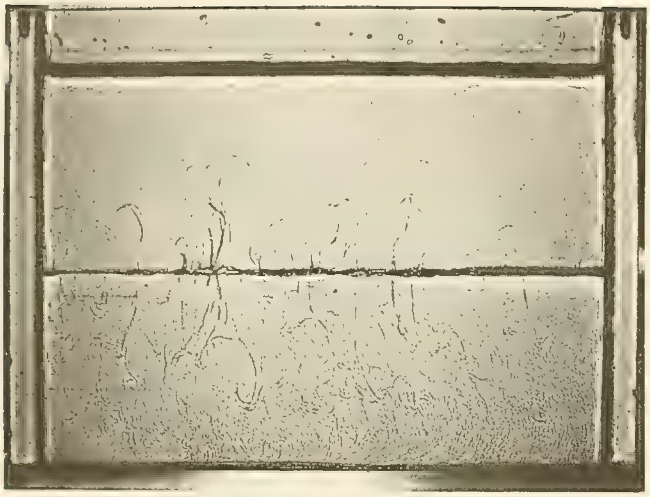

FIGURE 2. Shadowgraph picture of a sharp "diffusive" interface, formed between a layer of salt solution above a denser sugar solution. Note the convective plumes each side of the interface, evidence of strong interfacial transports. (Scale: the tank is 150mm. wide.)

and sugar the analogue of salt, since in each case the convection is maintained, and the interface kept sharp, by the more rapid vertical transfer of the faster diffusing component. Such interfaces have been called "diffusive interfaces", for reasons which will become clearer in the following section.

Fluxes through Diffusive Interfaces

Quantitative laboratory measurements have been made of the S and T fluxes across the interface between a hot salty layer below a cold fresh layer, and they have been interpreted in terms of an extension of well-known results for simple thermal convection at high Rayleigh number. Explicitly, Turner (1965), Crapper (1975), and Marmorino and Caldwell (1976) have shown that the heat flux αF_T (in density units) is described by

$$\alpha F_T = A_1 \ (\alpha \Delta T)^{4/3} \tag{2}$$

where A_1 has the dimensions of velocity. For a specified pair of diffusing substances, A_1 is a function of the density ratio $R_\rho = \beta\Delta S/\alpha\Delta T$, where β is the corresponding "coefficient of expansion" relating salinity to density differences. The deviation of A_1 from the constant A obtained using solid boundaries, with a heat flux but no salt flux, is a measure of the effect of ΔS on F_T. When R_ρ is less than about 2, $A_1 > A$ due to the increased mobility of the interface, and when $R_\rho > 2$, A_1 falls progressively below A as R_ρ increases and more energy is used to transport salt across the interface. The empirical form

$$A_1/A = 3.8 \ (\beta\Delta S/\alpha\Delta T)^{-2} \tag{3}$$

[Huppert (1971)] provides a good fit to the observations over the whole of the measured range $1.3 < R_\rho < 7$.

The salt flux also depends systematically on R_ρ, and has the same dependence on ΔT as does the heat flux. Thus the ratio of salt to heat fluxes (both expressed in density units) should be a function of R_ρ alone for given diffusing substances:

$$\beta F_S/\alpha F_T = f_*(\beta\Delta S/\alpha\Delta T) \tag{4}$$

The results reproduced in Figure 3 support this relation, and they also reveal the striking feature that the flux ratio is substantially constant (≈0.15) for $2 < R_\rho < 7$. [The more recent experiments of Marmorino and Caldwell (1976) suggest that the flux ratio can be as high as 0.4 with much smaller heat fluxes, but the reason for this discrepancy is not yet resolved]. Experiments by Shirtcliffe (1973), using a layer of salt solution above sugar solution, have shown a much stronger dependence of F_T on R_ρ than (3), but again a constant flux ratio, the measured value (for NaCl and sucrose) being $\beta F_S/\alpha F_T \approx 0.60$. Note that the flux ratio must always be <1, for energetic reasons: the increase in potential energy of the driven component must always be less than that released by the component providing the energy. This implies that the density difference between two layers must always increase as a result of a double-diffusive transport between them.

Direct measurements through the interface in Shirtcliffe's experiment suggest that this has a diffusive core, in which the transport is entirely molecular, and which is bounded above and below by unstable boundary layers. The "thermal burst" model of Howard (1964) has recently been extended to this two-component case by Linden and Shirtcliffe (1978), to predict both the fluxes and flux ratios. The constant range of flux ratio can be explained in the following way. Boundary layers of both T and S grow by diffusion to thicknesses proportional to $\kappa_T^{1/2}$ and $\kappa_S^{1/2}$, and then both break away intermittently. If only the statically unstable part at the edge of the double boundary layer is removed (such that $\alpha\Delta T = \beta\Delta S$), then the fluxes will be in the ratio $\tau^{1/2}$, in reasonable agreement with the laboratory results for the two values of τ used. Linden (1974a) has given a mechanistic argument to explain the increase of flux ratio at lower values of R_ρ, which he attributes to the direct entrainment of both properties across the interface.

It is worth noting in passing that Huppert (1971)

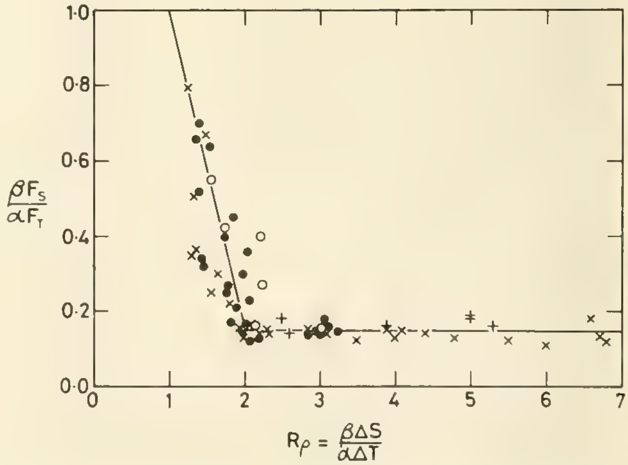

FIGURE 3. The ratio of the fluxes of salt and heat (in density units) across an interface between a layer of hot, salty water below colder, fresh water, plotted as a function of the density ratio R_ρ. [From Turner (1965).]

has shown theoretically that an intermediate layer, or series of layers, is stable if the overall S and T differences lie in the range where the flux ratio is constant, and unstable if the flux ratio varies with R_ρ. Observations of stable layers in the ocean seem to be consistent with this criterion. The merging of layers by this and other mechanisms has been studied experimentally by Linden (1976).

Some measurements have also been made in the case where several solutes with different diffusivities, κ_x, are driven across an interface by heating from below. Turner, Shirtcliffe, and Brewer (1970) showed that the individual eddy-transport coefficients can be different, and suggested that they are proportional to $\kappa_x^{\frac{1}{2}}$. More recent work by Griffiths (personal communication) predicts theoretically that the ratios of transports of pairs of solutes should be proportional to $\tau^{\frac{1}{2}}$ at low solute-heat density ratios, and to τ at higher ratios. His much more accurate and extensive experiments show an even larger variation, for reasons which are still unexplained. These results are potentially of great importance for the interpretation of geochemical data, as will be discussed further below.

Observations of Diffusive Interfaces

There are now many observations of layering in the ocean which can unambiguously be associated with "diffusive" interfaces, and where a one-dimensional interpretation seems appropriate. The regularity of the steps and the systematic increase of both S and T with depth serves to distinguish these from layers produced in other ways (by internal wave breaking, for example). Neal et al. (1969) and Neshyba et al. (1971) have observed layers about 5 m thick, underneath a drifting ice island in the Arctic where cold fresh melt water overlies warm salty water. A common observation in Norwegian fjords is that cold fresh water, formed by melting snow, can often form a thin layer on top of warmer seawater, with an interface which remains extremely sharp, and thickens much less rapidly than expected. This is due to double-diffusive convection driven by the heat flux from below, which will stir the layers on each side of the interface (independently of any wind stirring at the surface) and thus keep the interface sharpened.

There are also fresh-water lakes in various parts of the world which have become stratified in the past by the intrusion of sea water. Some of these are heated at the bottom by solar radiation, and convectively mixed layers separated by diffusive interfaces are formed. A particularly well-documented example is Lake Vanda in the Antarctic [Hoare (1968), Shirtcliffe and Calhaem (1968)]. Since these lakes are not complicated by horizontal advection processes, Huppert and Turner (1972) were able to use the Lake Vanda data to show that the one-dimensional laboratory result (3) can be applied quantitatively to comparable large-scale motions.

Other striking examples are the multiple steps observed in a lake in the East African Rift zone, which is heated geothermally by the injection of hot saline water at the bottom [Newman (1976)], and the layers of hot salty water found at the bottom of various Deeps in the Red Sea [Degens and Ross (1969)]. These layers are nearly saturated with salts of geothermal origin, including a high proportion of heavy metals, and are of special interest because of the potential commerical value of the associated thick sediments. [Another related application, to the genesis of ore deposits on the sea floor, has recently been proposed by Turner and Gustafson (1978)].

The existence of many components in these layers raises another question which should be explored more systematically in the oceanic context. Griffiths' laboratory measurements mentioned above indicate that different solutes are transferred across diffusive interfaces at different rates, depending on their molecular diffusivities. The "mixing rate" for a tracer is thus not necessarily a good indicator of the transport of a major component if interfaces are important. In the absence of definite knowledge of the mixing mechanisms which have operated between the sources and the sampling point, the assumption that all components are mixed simultaneously (i.e., that a single "eddy diffusivity" should be used) seems likely to lead to large errors, and even to gross misinterpretations of geochemical data.

Double-diffusive processes can also be important in other systems besides aqueous solutions. A situation of oceanographic interest arises if liquid natural gas (LNG) or some other liquid gas spills (following a tanker accident for instance) onto the sea surface [Fay and MacKenzie (1972)]. The liquid quickly evaporates to form a layer of cold gas, predominantly methane, which would be lighter than the air above it except that it is much colder. Since methane, and also water vapour picked up from the sea surface, have larger diffusivities than heat in air, double-diffusive effects can again be important in this gaseous system. The driving energy comes from the distribution of methane and water vapour, so the interface is "diffusive". The limited observations available suggest that the top of such a layer is very sharp, and its rate of spread vertically small, which is consistent with a self-stabilizing double-diffusive transport across the interface. Another application, to explain the phenomenon of "rollover" in LNG storage tanks, will not be described in detail here, but it too depends on double-diffusive effects, this time in the liquified gas [see Sarsten (1972)].

Salt Fingers and Related Phenomena

We now turn to the second type of double-diffusive convection, that for which the driving energy is derived from the component having the *lower* molecular diffusivity. Though this is associated with the very different phenomenon of "salt fingers", there are many similarities between it and the "diffusive" case already presented, and these will be emphasized in the following discussion.

When a small amount of hot salty water is poured on top of cooler fresh water, long narrow convection cells or "salt fingers" rapidly form. These motions were first predicted by Stern (1960) [and see Stern (1975) for a more up to date account of the theoretical work]. They are sustained by the slower horizontal diffusion of salt relative to heat, which permits the release of the potential energy in the salt field. Again, fingers may be produced using two solutes with much closer diffusivities, and when there are strong contrasts of properties, the fingers are confined to an interface. Figure 4

FIGURE 4. Shadowgraph of a thickened "finger" interface, formed between a layer of sugar solution on top of salt solution. (Scale: the tank is 150mm. wide.)

shows a shadowgraph picture of such an interface between a layer of sugar solution (S) above heavier salt solution (T). This is bounded by sharp edges, where the fingers break down and feed an unstable buoyancy flux into the convecting layers on either side.

Finger interfaces between two such layers have been shown to thicken linearly in time [Stern and Turner (1969), Linden (1973)]. They have also been observed in plan by Shirtcliffe and Turner (1970) who showed that the convection cells have a square cross section, with upward and downward motions alternating in a close-packed array. The initial stability of an interface has been examined quantitatively by Huppert and Manins (1973). When a layer of S is placed on a layer of T, the sharp boundary thickens by diffusion; the condition for formation of fingers depends on the magnitude of the gradients and the ratio of diffusivities, τ, and is related to the overall differences by

$$\beta\Delta S/\alpha\Delta T > \tau\sqrt{\tau} \ . \qquad (5)$$

These results can be extended to three components, as can the earlier linear stability theories [Griffiths (1978)]. For heat and salt, (5) shows that fingers should form with very small destabilizing salinity differences, and suggests that they will be ubiquitous phenomena in the ocean.

Our confidence in applying these results on a geophysical scale has recently been increased greatly by the direct observations of fingers (using an optical method) by Williams (1974, 1975) under conditions close to those predicted by Linden (1973) on the basis of laboratory results. Magnell (1976) has also measured horizontal conductivity variations with the right scale (≈2cm.) to support this interpretation.

As mentioned above, there is not as big a difference between the "diffusive" and "finger" cases as there appears to be when we simply compare the interfaces illustrated in Figures 2 and 4. Layers can be produced from a smooth gradient in the latter case too, by supplying a flux of S at the edge of a gradient of T; this was first demonstrated, using a sugar flux above a salt gradient, by Stern and Turner (1969). When viewed on the scale of the convecting layers, there is in fact a close correspondence between the two systems. The inequality of diffusivities results in an unstable buoyancy flux across statically stable interfaces in both cases, and this maintains convection above and below. Only the mechanism of interfacial transport differs, and it is here that the detailed structure of the interface enters. Across a finger interface the buoyancy flux is dominated by the destabilizing component, S, and salt is transported faster than heat, whereas the opposite holds a diffusive interface.

Corresponding laboratory measurements of the two coupled fluxes have been made for finger interfaces. Again there is a strong dependence on the density ratio across the interface, and the ratio of heat to salt fluxes is constant over a considerable range. Turner (1967) has shown in the heat salt case that the salt flux is about 50 times as large at $R_\rho{}^* = \alpha\Delta T/\beta\Delta S \to 1$ as it would be if the same salinity difference were maintained at solid boundaries, and falls slowly as $R_\rho{}^*$ increases. He also obtained a value for the flux ratio $\alpha F_T/\beta F_S = 0.56$ over the range $2 < R_\rho{}^* < 10$. Linden (1973) has made direct observations of the structure of salt fingers and the velocity in them that support these estimates of the salt flux. His estimate of the flux ratio was much lower, but recent experiments in our laboratory have supported the earlier value. These new experiments have concentrated on achieving as small a value of $R_\rho{}^*$ as possible, but measurements in the "variable" range of flux ratio are still elusive. This range could, however, be of great importance in the ocean, where $R_\rho{}^*$ is often close to unity.

It is also of interest to mention the experiments of Linden (1974b) who applied a shear across a salt-finger interface. He showed that a steady shear has little effect on the fluxes, though it changes the fingers into two-dimensional sheets aligned down shear. Unsteady shears (i.e., stirring on both sides of the interface) can, on the other hand, rapidly disrupt the interface, and actually decrease the salt flux.

There are now many examples of layering in the ocean which are consistent with the "fingering" process. These are observed in situations where both the mean salinity and the temperature decrease with increasing depth, and often occur under warm salt intrusions of one water mass into another. The first observations were made by Tait and Howe (1968, 1971) under the Mediterranean outflow, and a good summary of other measurements is to be found in Fedorov (1976). For reasons which will be discussed more fully in later sections, it is difficult to find cases where one can be sure that the *formation* of layers bounded by finger interfaces has been the result of one-dimensional processes, strictly analogous to those studied in the laboratory. Once layers have formed, however, the effects of the fluxes through the finger interfaces between them *can* properly be discussed in these terms, and two practical examples will be given.

The first arises in the context of sewage disposal in the sea. Fischer (1971) has discussed the case where effluent, which can be regarded for this purpose as nearly fresh (though polluted) water, is ejected from a pipe laid along the bottom, and rises as a line plume into sea water which is stratified in temperature. Careful design of the outfall ensures that the effluent, diluted with many times its volume of cold sea water, will spread out in a layer below the thermocline. But this layer will remain colder and fresher than the water above it, so the salt finger mechanism can cause it to thicken vertically, and even extend to the surface. A related case, in which the environmental effects could be even more serious, arises in the disposal of effluent from a desalination plant. Suppose that the brine from which water has been evaporated, and the heated water from the cooling plant, are mixed together to be disposed of as a single effluent. This hot, salty water will have about the same density as the original sea water - according to the precise design conditions, it can be slightly heavier or slightly lighter. If it is made heavier, and forms a layer along the bottom, a diffusive interface will be formed, and the coupled transports will tend to increase the density difference and thus keep the layer distinct. If it is put in at the surface, or at an intermediate level in a gradient, fingers will form, and there will be more rapid vertical mixing. One thing is certain: the rate of mixing cannot be determined using only the net density distribution and leaving out of account the double-diffusive effects.

3. TWO-DIMENSIONAL EFFECTS

Side-wall Heating and Related Processes

It became clear in early laboratory experiments on double-diffusive convection that layers will readily form from a salt gradient in another way, if it is heated from the side. This effect was studied systematically by Thorpe, Hutt, and Soulsby (1969) and by Chen, Briggs, and Wirtz (1971), and their results can be summarized as follows. The thermal boundary layer at a heated vertical wall grows by conduction and begins to rise. Salt is lifted to a level where the net density is close to that in the interior; then fluid flows out away from the wall, producing a series of layers that form simultaneously at all levels and grow inwards from the boundary. The layer thickness is close to the length-scale

$$\ell = \frac{\alpha \Delta T}{\beta dS/dz} \qquad (6)$$

which is the height to which a fluid element with temperature difference ΔT would rise in the initial salinity gradient.

The stability problem corresponding to sidewall heating of a wide container has not been solved, though Stern (1967) has shown theoretically how lateral gradients could lead to the generation of layers. Thorpe, Hutt, and Soulsby (1969) have analyzed the simpler case of a fluid containing compensating linear horizontal gradients of S and T, contained in a narrow vertical slot and Hart (1971) improved their analysis; both theories predict slightly inclined cells extending right across the gap, with a spacing in fair agreement with the measurements.

Similar layers are formed when the salinity as well as the temperature of the vertical boundary does not match that in the interior, for example when a block of ice is inserted into a salinity gradient and allowed to melt. A qualitative experiment of this kind was reported by Turner (1975), but interest in the process has increased recently, because of the application to melting icebergs. Huppert and Turner (1978) have carried out a more extensive set of experiments with this problem in mind.

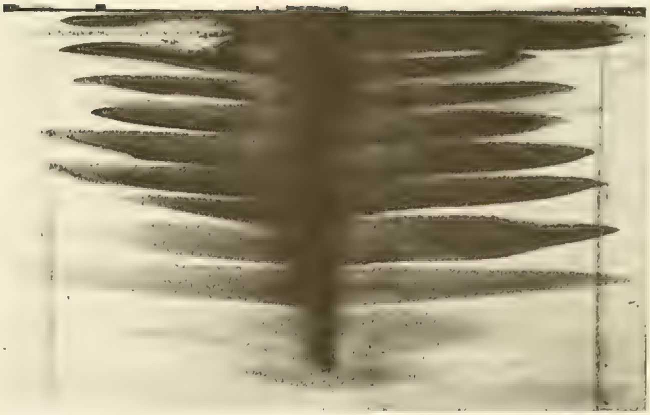

FIGURE 5. Showing the tilted layers formed by inserting a block of ice into salt-stratified water at room temperature. Fluorescein was frozen into the ice, and was illuminated from the side, so that the spread of the dye indicates the distribution of the melt water. (Negative print.)

An understanding of the melting of icebergs could be important in various contexts. Several groups are currently examining the feasibility of towing icebergs to their coasts and melting them to provide fresh water, but there are many unsolved scientific and engineering problems [see, for example, Bader (1977)]. It has been proposed that fresh water could be obtained by building a shallow pen round a grounded iceberg, allowing the melt water to collect in this, and siphoning it off the surface. On the other hand Neshyba (1977) has suggested that the melt water produced by icebergs would mix with the surrounding sea water, and could thus be effective in lifting water and nutrients from deeper layers to the surface, where it would increase biological production.

Huppert and Turner's (1978) experiments have shown, however, that neither idea is likely to be valid, because of the neglect of the stable salinity gradient which exists in the upper layers of the oceans where icebergs are found. As demonstrated in Figure 5, the presence of horizontal S and T differences then produces a regular series of tilted convecting layers, which feed most of the meltwater into the interior; very little rises to the surface. A more detailed analysis of the experiments is continuing. At present it appears that for a cooled sidewall the layer depths are similar whether melting is occurring or not, and that they are not described simply by (6) but depend more weakly on the initial salinity gradient. Another phenomenon which deserves more careful study is the series of grooves and ridges produced by non-uniform melting associated with the circulation in the layers (see Figure 6).

Sloping Boundaries

Phenomena analogous to those described above can be observed in systems containing smooth gradients of more slowly diffusing solutes. The essential physical feature of the heated sidewall process is

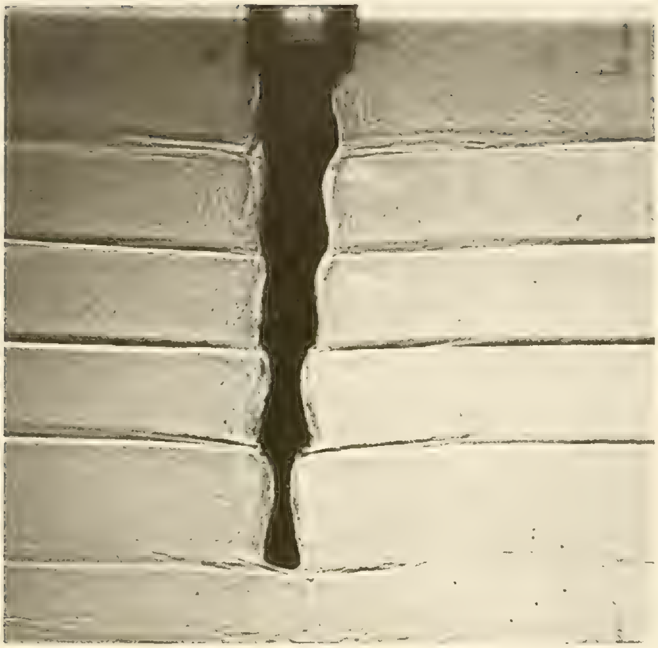

FIGURE 6. Shadowgraph photograph of a melting ice-block in a salinity gradient. Note the regularly spaced scallops and ridges, caused by uneven melting associated with the convection in layers.

that the boundary conditions (on temperature or salinity or both) do not match the conditions in the interior. In tanks containing opposing gradients of two components, with say a maximum salt concentration at the top falling linearly to zero at the bottom, and a maximum (slightly larger) sugar concentration at the bottom falling to zero at the top, the same kind of instability can be produced in another way. With vertical side walls, the surfaces of constant concentration are normal to the boundaries, and the no-flux boundary condition is automatically satisfied. But when an inclined boundary is inserted, diffusion will distort the surfaces of constant concentration away from the horizontal, so that they become normal to the boundary. Density anomalies are produced which tend to drive flows along the wall; these cannot remain steady, but instead turn out into the interior and produce a series of layers.

This process was first investigated experimentally by Turner and Chen (1974), with the initial stratification in the "diffusive" sense. A prominent feature of the intruding layers is the local reversal of gradients in the extending "noses", where fingers are prominent. In the later stages of that experiment, the advancing noses have become independent of the mechanism which produced them, and this suggested the systematic study of double-diffusive sources in various environments which is pursued below. Linden and Weber (1977) have investigated layer formation in the "finger" case; they have also discussed the instability of the boundary layer at the sloping wall, and the criteria determining the layer depths. In the limit where the opposing gradients are nearly equal, the characteristic vertical lengthscale depends mostly on the initial vertical distributions of S and T, and little on the mechanism triggering the instability.

A different effect of sloping boundaries should be mentioned here. In a two-layer system, in which the layer depths vary because one wall of the containing vessel is inclined, large-scale quasi-horizontal motions can be set up even when the buoyancy flux across the horizontal interface is uniform. This effect is a purely geometrical consequence of the sloping boundary. The net result of the double-diffusive transports across the interface is to provide an unstable buoyancy flux which makes the bottom layer heavier. A given flux produces more rapid density changes in shallower regions where there is less dilution, and this sets up a circulation in the sense which includes a flow down the slope. Gill and Turner (1969) have shown that this flow can reverse the relative gradients of the two components, for example, giving rise to salt fingers at the bottom of a tank originally stratified in the diffusive sense. They have also suggested an application to the formation of bottom water near the Antarctic continent. Similar effects have been observed by Turner and Chen (1974) when a sloping interface, rather than a solid sloping boundary, produces the non-uniformity of depth, and this too can have implications for the formation of bottom water in deeper water.

Double-diffusive Intrusions

The experiments described in the two preceding sections have recognized the importance of horizontal gradients, but they still have not dealt with the common situation where fluid with one set of T-S properties intrudes into another having different properties. This question has recently been addressed by Turner (1978), using sources of sugar and salt solutions released into gradients of various kinds.

The basic intrusion process with which other phenomena can be compared is the two-dimensional flow of a uniform fluid at its own density level into a linear gradient set up using the same property. Figure 7 shows the behaviour of a (dyed) source of salt solution released into a salinity gradient. This is what we might intuitively expect: the intruding fluid just displaces its surroundings upwards and downwards, and is kept confined to a horizontal layer by the denisty gradient. Detailed studies of this process have been reported by Maxworthy (1972), Manins (1976), and Imberger, Thompson, and Fandry (1976). Note praticularly the "upstream wake" effect, leading to a considerable disturbance of the environment ahead of the advancing nose.

When the source of salt is replaced by sugar solution (S), while the same salinity gradient (T) is retained in the environment, the behaviour is very different. (It is worth keeping in mind throughout the following, the analogous situation with temperature and salinity: this corresponds to the intrusions of a layer of warmer, saltier water into a stable temperature gradient). As shown in Figure 8, there is strong vertical convection near the source: this is produced by a mechanism which also occurs with a uniform ambient fluid close to the same density as that injected. The more rapid diffusion of T relative to S across the plume boundary causes it to become heavier, and its immediate surroundings lighter, than the fluid at the level of the source. The vertical spread is limited by the stratification, and "noses" begin to spread out at levels above and below the

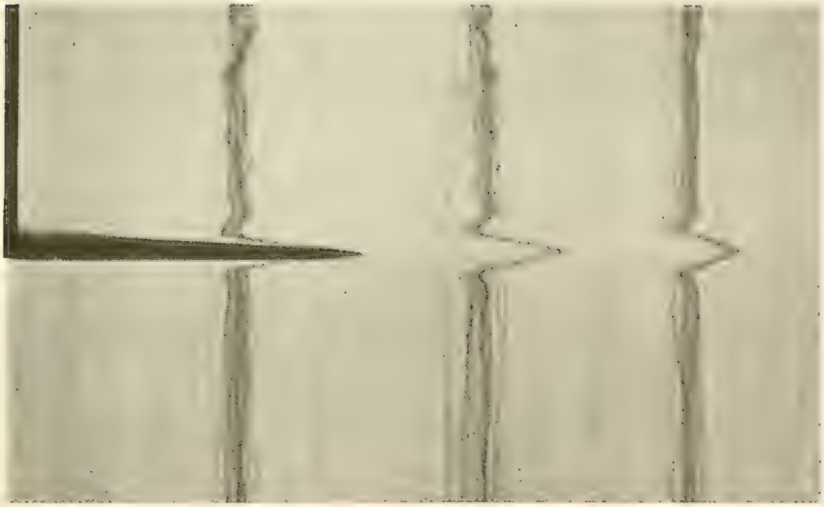

FIGURE 7. The intrusion of dyed salt solution into a salinity gradient at its own density level. The distorted dye streaks show that the fluid in the environment begins to flow well ahead of the advancing fluid. (The region shown is about 400mm. wide.)

source. The process of vertical convection continues, and further layers appear as the layers first formed extend away from the source. The total volume of fluid affected by mixing is many times that of the input, showing that the intrusions are overtaking and incorporating the environment, rather than just displacing it as in the experiment of Figure 7. The implication for the ocean is, of course, that large scale intrusions will tend to break up into thinner noses and layers, as is indeed observed.

Each individual nose as it spreads contains an excess of S relative to its environment, so that conditions are favourable for the formation of a diffusive interface above and fingers below, as can be seen in Figure 8. This also implies that there will be a local decrease with depth or an inversion of T through each layer, and that the density gradient above such an intrusion will be greater than that below. These features have been demonstrated in oceanic data by Howe and Tait (1972), Gregg (1975), and Gargett (1976).

Note too the slight upward tilt of each layer as it extends, which can be interpreted as follows. Above and below an intrusion, the net density differences are small and the double-diffusive fluxes therefore large. The one-dimensional laboratory observations indicate that the transports across a finger interface (both in the sugar-salt and salt-heat case) are larger than those across a comparable diffusive interface. Thus the flux of positive buoyance through the fingers from below can exceed the negative flux from above, so a layer becomes lighter and rises across isopycnals as it advances away from the source. There is also a systematic shear flow associated with the inclined layers, and both these features would seem worth looking for when observations are made of oceanic finestructure in the future.

The interpretation of the layer slope in terms of the differences in fluxes across the two interfaces is supported by experiments carried out in the inverse sense. With a source of salt solution (T) flowing at its own density level into a gradient of sugar solution (S), the behaviour is as shown in Figure 9. Vertical convection near the source is again followed by the spread of noses at various levels, but now with diffusive interfaces below and fingers above, corresponding to the excess of T in the noses relative to their S environment. There is a systematic downward tilt as the noses advance, due again to the dominance of the buoyancy flux at the finger interfaces, which now causes the layers to become heavier as they extend. The sense of the internal shear is also consistent with this picture: the motion is inclined slightly down and away from the source at the bottom of the

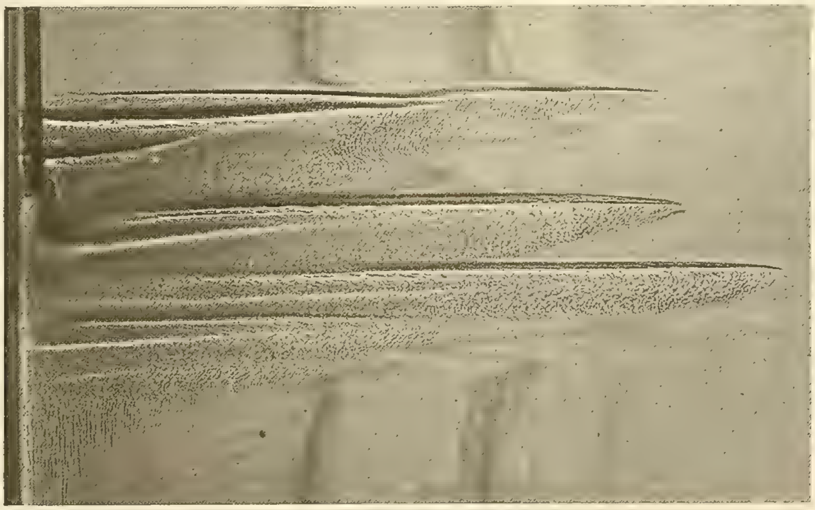

FIGURE 8. The flow produced by releasing sugar solution at its own density level into a salinity gradient. Strong vertical convection occurs, followed by intrusion at several levels. The density gradient and flow-rate, and the scale of the photograph, are approximately the same as for Figure 7.

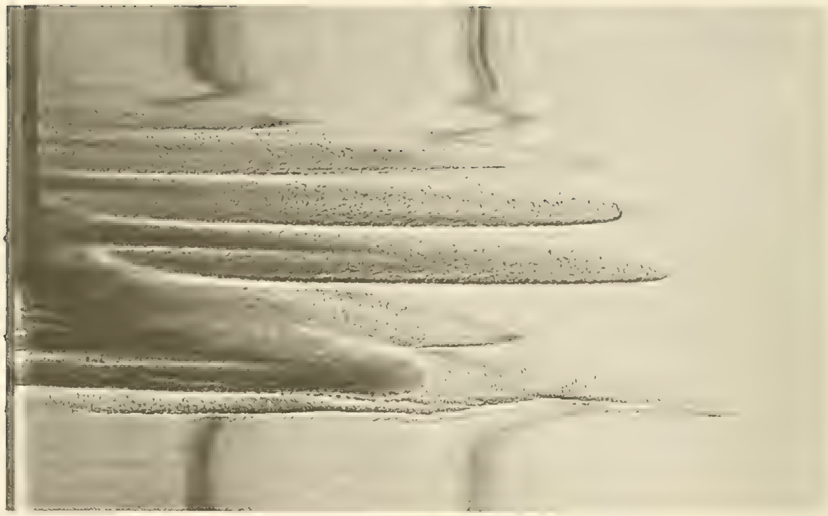

FIGURE 9. The flow produced by releasing salt solution into a gradient of sugar solution, using conditions comparable with, but the inverse of those shown in Figure 8.

fingers and above the diffusive interfaces, indicating again that there is an increase in density due to the continuing flux in the fingers.

Two other features of the laboratory observations which have important implications for the ocean should also be mentioned. The most rapid formation of layers in the series of experiments reported by Turner (1978) occurred when the tank was stratified in the "finger" sense, and the fingers were allowed to run down towards a marginally stable state. When source fluid was introduced, layers formed more rapidly and regularly than before, because of the potential energy already available in the ambient fluid. This implies that "reactivation" of layers in a region where they have previously formed will proceed more quickly than the original layering process. It suggests that the patches of strong layers, under the Mediterranean outflow into the Atlantic for example, are associated with the arrival of a fresh pulse of intruding fluid. The second related observation is that the further stage of overturning to produce nearly uniformly-mixed layers, bounded above and below by finger interfaces is also more likely to be reached near the source of the intruding water. The relationship between the two types of layering has been demonstrated directly in the measurements of Gregg (1975), which show that inversions of intrusive origin can in the course of time break down to form well-mixed layers.

Layer Formation at Fronts

An important geometry which merits separate study is a discontinuity of T-S properties over a vertical or inclined surface, i.e., a front. The motions produced when an inclined boundary is inserted into a fluid stratified with opposing gradients (Section 3) have some of the required features, but the presence of the solid wall is clearly undesirable.

Fronts can be set up in the laboratory in several ways. Large horizontal T and S gradients can, for example, be produced just by pouring fluid with contrasting properties into one end of a stratified tank at several levels, or by stirring it in throughout the depth. A somewhat more controllable method is to insert a vertical barrier in a previously stratified tank, to introduce the extra fluid on one side of it, and allow the disturbances to die away before removing the barrier. This technique has been used in the experiment shown in Figure 10. It is difficult to get the two vertical gradients exactly matched, and so when the barrier is removed internal waves are set up, which soon die away, leaving the isopycnals horizontal but the front distorted. The initial state illustrated in Figure 10a is completely determined by the readjustment of the density field, but note that diffusive interfaces have already developed in the sense to be expected with an excess of S on the left. At a later stage (Figure 10b) the frontal surface is spread out horizontally by the interleaving of inclined layers, the scale of which is unrelated to that of the initial adjustment, and which are driven entirely by the local density anomalies produced by double-diffusive transports.

A more sophisticated version of this experiment is currently being studied by Ruddick (personal communication). He has set up identical vertical density distributions on two sides of a barrier, using sugar (S) in one half and salt (T) in the other. When the barrier is withdrawn, there is some small scale mixing, but virtually no larger scale distortion. A series of regular, interleaving layers then develops, with a spacing and speed of advance which are systematically related to the horizontal property differences.

There are now many measurements which support the view that the prominence and strength of layering in the ocean are related to the magnitude of the horizontal gradients of properties. To cite just two examples: profiles across the Antarctic polar front [Gordon et al. (1977)] reveal inversions which decrease in strength with increasing distance away from the front. Coastal fronts between colder fresh water on a continental shelf and warmer salty water offshore also exhibit strong interleaving [Voorhis, Webb, and Millard (1976)].

A general conclusion which can already be drawn from the laboratory experiments described in this section is that the formation and propagation of interleaving double-diffusive layers is a self-driven process, sustained by *local* density anomalies due to double-diffusive transports. Once a series of noses and layers has formed, the changes of T and S within them can be described in terms of the one-dimensional (vertical) transport processes previously studied. It should eventually be possible

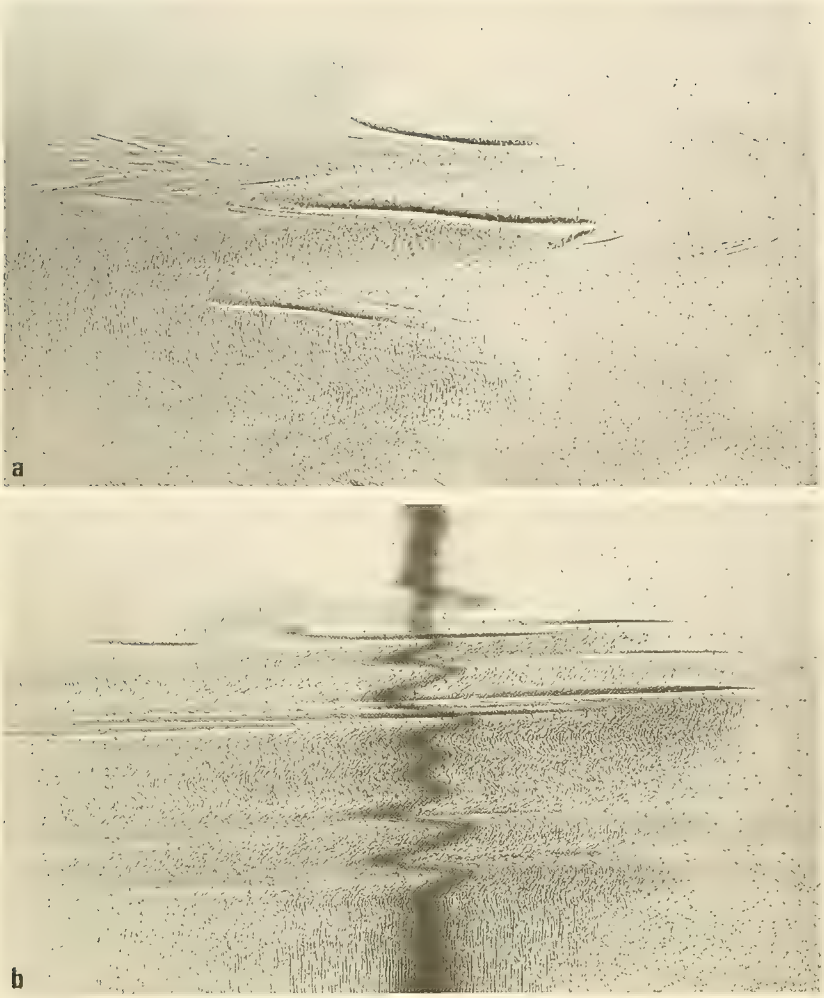

FIGURE 10. Showing the spread of a front, formed by withdrawing a barrier from the center of an experimental tank. The initial state corresponded to "run down" fingers, with extra (dyed) sugar solution mixed in at the left.
Upper: 2-1/2 mins. after barrier was removed, showing intrusions formed by the density adjustment.
Lower: 65 mins. after barrier removed, showing the smaller scale motions driven by double-diffusive processes across the frontal region.

[Joyce (1977)] to parameterize the effective increase in the horizontal diffusion of T and S, produced by interleaving, in terms of the horizontal gradients and these quasi-vertical fluxes.

ACKNOWLEDGMENT

I am grateful to R. Wylde-Browne for his assistance with many of the recent experiments described here, and particularly with the photography. Discussions with R. W. Griffiths and B. R. Ruddick about their current work have been very stimulating.

REFERENCES

Bader, H. (1977). A critical look at the iceberg project. *First International Conference on Iceberg Utilization,* Iowa State University.

Chen, C. F., D. G. Briggs and R. A. Wirtz (1971). Stability of thermal convection in a salinity gradient due to lateral heating. *Int. J. Heat and Mass Trans. 14,* 57-65.

Crapper, P. F. (1975). Measurements across a diffusive interface. *Deep-Sea Res. 22,* 537-545.

Degens, E. T, and D. A. Ross (eds.) (1969). *Hot brines and recent heavy metal deposits in the Red Sea.* Berlin: Springer-Verlag.

Fay, J. A., and J. J. MacKenzie (1972). Cold cargo. *Environment 14,* 21-29.

Fedorov, K. N. (1976). *The thermohaline finestructure of the ocean.* Gidrometeoizdat, Leningrad.

Fischer, H. B. (1971). The dilution of an undersea sewage cloud by salt fingers. *Water Research 5,* 909-915.

Gargett, A. E. (1976). An investigation of the occurrence of oceanic turbulence with respect to finestructure. *J. Phys. Oceanog. 6,* 139-156.

Gill, A. E., and J. S. Turner (1969). Some new ideas about the formation of Antarctic bottom water. *Nature 224,* 1287-1288.

Gregg, M. C. (1975). Microstructure and intrusions in the California current. *J. Phys. Oceanog. 5,* 253-278.

Griffiths, R. W. (1978). The influence of a third diffusing component upon the onset of convection. *J. Fluid Mech.* (in the press)

Gordon, A. L., D. T. Georgi, and H. W. Taylor (1977). Antarctic polar front zone in the western Scotia Sea - summer 1975. *J. Phys. Oceanog. 7,* 309-328.

Hart, J. E. (1971). On sideways diffusive instability. *J. Fluid Mech. 49,* 279-288.

Hoare, R. A. (1968). Thermohaline convection in Lake Vanda, Antarctica. *J. Geophys. Res. 73,* 607-612.

Howard, L. N. (1964). Convection at high Rayleigh number. *Proc. eleventh Int. Congress Applied*

Mechanics, Münich (ed. H. Görtler), 1109-1115. Berlin: Springer-Verlag.

Howe, M. R., and R. I. Tait (1972). The role of temperature inversions in the mixing processes of the deep ocean. *Deep-Sea Res. 19,* 781-791.

Huppert, H. E. (1971). On the stability of a series of double-diffusive layers. *Deep-Sea Res. 18,* 1005-1021.

Huppert, H. E., and P. C. Manins (1973). Limiting conditions for salt-fingering at an interface. *Deep-Sea Res. 20,* 315-323.

Huppert, H. E., and J. S. Turner (1972). Double-diffusive convection and its implications for the temperature and salinity structure of the ocean and Lake Vanda. *J. Phys. Oceanog. 2,* 456-461.

Huppert, H. E., and J. S. Turner (1978). On melting icebergs. *Nature 271,* 46-48.

Imberger, J., R. Thompson, and C. Fandry (1976). Selective withdrawal from a finite rectangular tank. *J. Fluid Mech. 78,* 489-512.

Joyce, T. M. (1977). A note on the lateral mixing of water masses. *J. Phys. Oceanog. 7,* 626-629.

Linden, P. F. (1973). On the structure of salt fingers. *Deep-Sea Res. 20,* 325-340.

Linden, P. F. (1974a). A note on the transport across a diffusive interface. *Deep-Sea Res. 21,* 283-287.

Linden, P. F. (1974b). Salt fingers in a steady shear flow. *Geophys. Fluid Dynam. 6,* 1-27.

Linden, P. F. (1976). The formation and destruction of fine-structure by double-diffusive processes. *Deep-Sea Res. 23,* 895-908.

Linden, P. F., and T. G. L. Shirtcliffe (1978). The diffusive interface in double-diffusive convection. *J. Fluid Mech.* (in the press)

Linden, P. F., and J. E. Weber (1977). The formation of layers in a double-diffusive system with a sloping boundary. *J. Fluid Mech. 81,* 757-774.

Magnell, B. (1976). Salt fingers observed in the Mediterranean outflow region (34°N, 11°W) using a towed sensor. *J. Phys. Oceanog. 6,* 511-523.

Manins, P. C. (1976). Intrusion into a stratified fluid. *J. Fluid Mech. 74,* 547-560.

Marmorino, G. O., and D. R. Caldwell (1976). Equilibrium heat and salt transport through a diffusive thermohaline interface. *Deep-Sea Res. 23,* 59-68.

Neal, V. T., S. Neshyba, and W. Denner (1969). Thermal stratification in the Arctic Ocean. *Science 166,* 373-374.

Neshyba, S. (1977). Upwelling by icebergs. *Nature 267,* 507-508.

Neshyba, S., V. T. Neal, and W. Denner (1971). Temperature and conductivity measurements under Ice Island T-3. *J. Geophys. Res. 76,* 8107-8120.

Newman, F. C. (1976). Temperature steps in Lake Kivu: a bottom heated saline lake. *J. Phys. Oceanog. 6,* 157-163.

Sarsten, J. A. (1972). LNG stratification and rollover. *Pipeline and Gas Journal.* Sept. 1972, 37-39.

Shirtcliffe, T. G. L. (1967). Thermosolutal convection: observation of an overstable mode. *Nature, 213,* 489-490.

Shirtcliffe, T. G. L. (1973). Transport and profile measurements of the diffusive interface in double-diffusive convection with similar diffusivities. *J. Fluid Mech. 57,* 27-43.

Shirtcliffe, T. G. L., and I. M. Calhaem (1968). Measurements of temperature and electrical conductivity in Lake Vanda, Victoria Land, Antarctica. *N. Z. J. Geol. Geophys. 11,* 976-981.

Shirtcliffe, T. G. L., and J. S. Turner (1970). Observations of the cell structure of salt fingers. *J. Fluid Mech. 41,* 707-719.

Stern, M. E. (1960). The 'salt fountain' and thermohaline convection. *Tellus 12,* 172-175.

Stern, M. E. (1967). Lateral mixing of water masses. *Deep-Sea Res. 14,* 747-753.

Stern, M. E. (1969). Collective instability of salt fingers. *J. Fluid Mech. 35,* 209-218.

Stern, M. E. (1975). *Ocean circulation physics.* Academic Press, pp. 246.

Stern, M. E., and J. S. Turner (1969). Salt fingers and convecting layers. *Deep-Sea Res. 16,* 497-511.

Tait, R. I., and M. R. Howe (1968). Some observations of thermohaline stratification in the deep ocean. *Deep-Sea Res. 15,* 275-280.

Tait, R. I., and M. R. Howe (1971). Thermohaline staircase. *Nature, 231,* 178-179.

Thorpe, S. A., P. K. Hutt, and R. Soulsby (1969). The effect of horizontal gradients on thermohaline convection. *J. Fluid Mech. 38,* 375-400.

Turner, J. S. (1965). The coupled turbulent transports of salt and heat across a sharp density interace. *Int. J. Heat and Mass Trans. 8,* 759-767.

Turner, J. S. (1967). Salt fingers across a density interface. *Deep-Sea Res. 14,* 599-611.

Turner, J. S. (1968). The behaviour of a stable salinity gradient heated from below. *J. Fluid Mech. 33,* 183-200.

Turner, J. S. (1973). *Buoyancy effects in fluids.* Cambridge University Press, 367 pp.

Turner, J. S. (1974). Double-diffusive phenomena. *Ann. Rev. Fluid Mech. 6,* 37-56.

Turner, J. S. (1975). Laboratory experiments on double-diffusive instabilities. *Adv. Chem. Phys. 32,* 135-149.

Turner, J. S. (1978). Double-diffusive intrusions into a density gradient. *J. Geophys. Res.* (in the press)

Turner, J. S., and C. F. Chen (1974). Two-dimensional effects in double-diffusive convection. *J. Fluid Mech. 63,* 577-592.

Turner, J. S., and L. B. Gustafson (1978). The flow of hot, saline solutions from vents in the sea floor - some implications for exhalative sulfide deposits. *Econ. Geol.* (in the press)

Turner, J. S., T. G. L. Shirtcliffe, and P. G. Brewer (1970). Elemental variations of transport coefficients across density interfaces in multiple-diffusive systems. *Nature 228,* 1083-1084.

Voorhis, A. D., D. C. Webb, and R. C. Millard (1976). Current structure and mixing in the shelf-slope water front south of New England. *J. Geophys. Res. 81,* 3695-3708.

Williams, A. J. (1974). Salt fingers observed in the Mediterranean out-flow. *Science 185,* 941-943.

Williams, A. J. (1975). Images of ocean microstructure. *Deep-Sea Res. 22,* 811-829.

Buoyant Plumes in a Transverse Wind

Chia-Shun Yih
The University of Michigan
Ann Arbor, Michigan

ABSTRACT

With the rise in energy needs and the consequent proliferation of cooling towers (not to mention smoke stacks) on the one hand, and society's enchanced concern with the environment on the other, the study of buoyant plumes caused by heat sources in a transverse wind has become important. Buoyant plumes may also occur in the ocean, such as when a deeply submerged heat source moves horizontally in it. The fluid mechanics involved in buoyant plumes is very nearly the same, be they atmospheric or submarine.

In this paper a similarity solution for turbulent buoyant plumes due to a point heat source in a transverse wind is presented. By a set of transformations the mathematical dimension of the problem is reduced from 3 to 2. Analytical solutions for the first and second approximations are obtained for the temperature and velocity fields. The solution exhibits the often observed pair of longitudinal counter-rotating vortices. As a result of buoyancy, the point of highest temperature and the "eyes" of the vortices at any section normal to the wind direction continuously rise as the longitudinal distance from the heat source increases.

1. INTRODUCTION

As industry expands and energy needs rise, the buoyant plumes caused by ever-increasing cooling towers and smoke stacks have become an important concern for societies anxious to protect their environment. Much effort has been expanded on the so-called numerical modeling of the phenomenon of plumes both in the United States and in Europe. In most of the numerical studies, the eddy viscosity is assumed constant, and its value is chosen to make the results agree with whatever gross observations are available. The power of modern computers has made it possible to obtain numerical solutions for partial differential equations with very irregular data, such as wind and temperature profiles in the atmosphere. On the other hand, one can only carry out a number of these special solutions, and while the power of the computer makes computation possible it also makes the intermediate steps so opaque that one can only have faith in the accuracy of the results and the correctness of the programing; and one can attempt to interpret the results and understand the phenomenon only at the very end, when numerical results are available. One can hardly see, for example, the effects of changing one single parameter of the problem, without giving that parameter several values and going to the computer again and again. It is in view of this condition that even people most concerned with the immediate applicability of calculated results desire a certain measure of transparency in the analysis of the phenomenon.

At the same time systematic and detailed experiments on buoyant plumes in transverse winds, with temperature and velocity measurements, are lacking. This being so, it seems that an analytical solution of the problem is most desirable and timely, even if it must of necessity be constructed by assuming certain quantities (such as the turbulence level in the plume) on the basis of whatever related experimental results are available. The assumed quantities (or quantity) will appear in the analysis as unspecified coefficients (or coefficient, as in this analysis), to be determined by experiments later. In the present work only one coefficient related to the turbulence level is left unspecified, to be determined by future experiments. But the probable range in which it lies is given.

The solution is based on a set of transformations that reduces the mathematical dimension of the phenomenon from 3 to 2 is thus characterized by the striking feature of similarity between cross sections normal to the wind direction. The laws of decay of the temperature and velocity fields are given in simple, explicit terms. Thus, apart from the quantitative predictions that this analysis is intended to furnish, I hope that the general features of the solution will be found especially useful.

2. THE DIFFERENTIAL EQUATIONS

The two basic assumptions underlying the analysis are that the longitudinal velocity component in the direction of the wind is constant and that an eddy viscosity, ε, is constant in any cross section normal to the wind direction. It can be shown that the first assumption ceases to be true only at stages of approximations later than those arrived at in the present analysis, and its violation is therefore not very important. The second assumption mentioned above has been made in all analytic solutions for turbulent jets and plumes, according to Prandtl's simplified theory. These solutions are well known. See, for example, the paper by Yih (1977) on turbulent plumes for the latest application of that theory. One feels reassured that for a calculation of the mean temperature and velocity fields, this theory can again be used.

We shall take the direction of the wind to be the direction of increasing x, and the z direction to be vertically upward. The y direction will then be a horizontal direction transverse to the x direction. In general ε depends on x, y, and z. But it has been repeatedly shown before in other studies of jets and plumes that in their core, ε can be taken as constant at a constant value of x, and that only at their outer edges does the nonuniformity in the y-z plane introduce some errors in the calculated mean quantities. (Very far away from the jets and plumes the value of ε is immaterial for the determination of the temperature and velocity distributions). Accepting these outer-edge errors, which are fairly small, we shall take ε to be a function of x only, apart from the parameters of the problem to be defined later. We note that if an eddy viscosity is used to determine the velocity distribution in turbulent flow in a circular pipe, Laufer's (1953) measurements show that in the core, that is, away from the narrow region near the pipe wall, ε is nearly constant.

The equations of motion are then, with subscripts denoting partial differentiations,

$$Uv_x + vv_y + wv_z = -\frac{1}{\rho}p_y + \varepsilon(v_{yy} + v_{zz}), \qquad (1)$$

$$Uw_x + vw_y + ww_z = -\frac{1}{\rho}p_z - g\theta + \varepsilon(w_{yy} + w_{zz}), \qquad (2)$$

in which U is the wind velocity, assumed constant, v and w are the velocity components in the directions of increasing y and z, respectively, ρ is the density, p is the pressure, and g is the gravitational acceleration. The variable θ is defined by

$$\theta = \frac{\Delta\rho}{\rho}, \qquad (3)$$

where $\Delta\rho$ is the variation of the density from the ambient density ρ, assumed constant. Thus the Boussinesq approximation has been used in Eqs. (1) and (2). Since θ is small and the pressure variation in the plume, though important for determination of the flow field, is unimportant in the determination of $\Delta\rho$ from the temperature variation by the equation of state, θ can also be written, by virtue of the equation of state of ideal gases.

$$\theta = -\frac{\Delta T}{T},$$

where ΔT is the temperature variation and T the ambient temperature. For a liquid, the relationship between $\Delta\rho$ and ΔT is still linear if θ is small, and the constant of proportionality is determined by the property of the liquid.

We shall assume the eddy viscoity for heat diffusion to be the same as that for momentum diffusion. This may not be strictly true, for the turbulent Prandtl number may be slightly different from 1. The effect of this difference, if any, is not of great importance in our attempt to determine the mean temperature and velocity fields. The equation for heat diffusion can then be written in the form

$$U\theta_x + v\theta_y + w\theta_z = \varepsilon(\theta_{yy} + \theta_{zz}). \qquad (4)$$

Longitudinal diffusion of heat or of momentum is ignored in Eq. (1), (2), and (4). This is justified in the same way as in other works that use the boundary-layer theory.

The equation of continuity is, since the longitudinal velocity component is assumed constant,

$$v_y + w_z = 0. \qquad (5)$$

The heat source, located at the origin, is measured by the quantity

$$G = -\int_{-\infty}^{\infty}\int_{-\infty}^{\infty} U\theta dydz. \qquad (6)$$

Note that solid boundaries are assumed to be far away from the source, so that their effects are negligible. Equations (1), (2), (4), (5), and (6), with appropriate boundary conditions, govern the phenomenon under investigation.

The equation of continuity (5) allows the use of a stream function ψ in terms of which v and w can be expressed:

$$v = \psi_z, \qquad w = -\psi_y. \qquad (7)$$

By cross-differentiation of Eqs. (1) and (2), we obtain the vorticity equation

$$U\hat{\xi}_x + v\hat{\xi}_y + w\hat{\xi}_z = \varepsilon(\hat{\xi}_{yy} + \hat{\xi}_{zz}) - g\theta_y, \qquad (8)$$

in which $\hat{\xi}$ is the x component of the vorticity and is given by

$$\hat{\xi} = w_y - v_z = -(\psi_{yy} + \psi_{zz}). \qquad (9)$$

3. THE FORM OF THE EDDY VISCOSITY

We assume the terms in Eqs. (1) or (2) or (4) to be of the same order of magnitude. In particular, this means that the diffusive and the convective terms are of the same order of magnitude in any of these equations. It also means that in Eq. (2) the buoyancy term is of the same order of magnitude as the convective and diffusive terms for w. This assumption underlies all existing analytical studies of jets and plumes and can be regarded as amply justified.

Comparing the first and last terms in Eq. (2), then, we have

$$\varepsilon \sim \frac{U\ell_z^2}{\ell_x}, \tag{10}$$

in which ℓ_x and ℓ_z are the length scales for the x and z directions. Comparing the first term in Eq. (2) with the term $g\theta$, we have

$$\theta \sim \frac{Uw}{g\ell_x}, \tag{11}$$

where θ and w stand for the magnitudes of θ and w, rather than θ and w rigorously, as they do also in the following proportionalities. Equation (6) gives, further,

$$\theta \sim \frac{G}{U\ell_z^2}, \tag{12}$$

if we take ℓ_y and ℓ_z to be equal. From proportionalities (11) and (12) we have, after some rearrangement,

$$w\ell_z \sim \frac{gG\ell_x}{U^2\ell_z}. \tag{13}$$

But surely

$$\varepsilon \sim w\ell_z. \tag{14}$$

Hence

$$\varepsilon \sim \frac{gG\ell_x}{U^2\ell_z}. \tag{15}$$

From proportionalities (10) and (15) we have

$$\ell_z^3 \sim \frac{gG}{U^3}\ell_x^2 = \frac{gG}{U^3}x^2, \tag{16}$$

since the ℓ_x, the scale of x, is just x. Thus (12), (13), (14), and (16) give

$$\ell_z \sim x^{2/3}, \quad \varepsilon \sim x^{1/3}, \quad w \sim x^{-1/3}, \quad \theta \sim x^{-4/3}.$$

These results are unaffected when other comparisons are made between terms in either Eq. (1), (2), (4), or (5).

From porportionalities (15) and (16) we have

$$\varepsilon = \frac{\alpha}{U}(g^2G^2x)^{1/3}, \tag{17}$$

where α is a dimensionless constant to be determined experimentally or estimated from known values of ε in similar phenomena. We shall leave it free throughout our analysis. Equation (17) gives the form of ε to be used in this paper.

It seems strange at first sight that ε should vary inversely as U. I believe that the interpretation of $\varepsilon \sim U^{-1}$ is that ε increases with the time that is required for the wind to travel a unit distance in the x direction, because turbulence needs time to develop.

4. THE TRANSFORMATIONS AND THE DIFFERENTIAL SYSTEM TO BE SOLVED

The transformations to be used to obtain similarity solutions are already suggested by (12), (13), and (16) and are

$$\theta = -\frac{U}{3\alpha}\left(\frac{G}{g^2}\right)^{1/3} x^{-4/3} h(\eta,\zeta), \tag{18}$$

$$(v,w) = \frac{1}{3\alpha}\left(\frac{Gg}{x}\right)^{1/3}(V,W), \tag{19}$$

$$(\eta,\zeta) = \frac{U}{(3\alpha)^{1/2}}(Ggx^2)^{-1/3}(y,z). \tag{20}$$

Then the equation of continuity (5) becomes

$$V_\eta + W_\zeta = 0,$$

and Eqs. (7) become

$$V = \Psi_\zeta, \qquad W = -\Psi_\eta, \tag{21}$$

in which Ψ is the dimensionless stream function related to ψ by

$$\psi = \frac{1}{(3\alpha)^{1/2}U}(G^2g^2x)^{1/3}\Psi(\eta,\zeta). \tag{22}$$

Equation (9) now takes the form

$$\xi = W_\eta - V_\zeta = -(\Psi_{\eta\eta} + \Psi_{\zeta\zeta}), \tag{23}$$

where ξ is the dimensionless vorticity component in the x direction.

With the transformations (18), (19), and (20), Eq. (4) becomes

$$Lh = \lambda(Vh_\eta + Wh_\zeta), \tag{24}$$

where L is the linear operator defined by

$$L = \frac{\partial^2}{\partial\eta^2} + \frac{\partial^2}{\partial\zeta^2} + 2\eta\frac{\partial}{\partial\eta} + 2\zeta\frac{\partial}{\partial\zeta} + 4, \tag{25}$$

and

$$\lambda = (3\alpha^3)^{-1/2}. \tag{26}$$

Equation (8) now has the form

$$(L - 1)\xi = -h_\eta + \lambda(V\xi_\eta + W\xi_\zeta). \tag{27}$$

Equations (23), (24), and (27) are the final equations governing the dynamics of the plume in a transverse wind. They are to be solved with the boundary conditions

(i) $h_\eta = 0, \quad \xi = 0, \quad \Psi = 0, \quad \text{and } \Psi_{\eta\eta} = 0 \text{ at } \eta = 0.$

(ii) $h = 0, \quad \xi = 0, \quad \Psi = 0 \text{ at } \eta = \pm\infty \text{ or } \zeta = \pm\infty.$

Boundary conditions (i) correspond to symmetry with respect to the ζ axis, and conditions (ii) ensure that there is no temperature variation and no velocity components v and w at infinity. The integral relation (6) now takes the form

$$\int_{-\infty}^{\infty}\int_{-\infty}^{\infty} h\,d\eta\,d\zeta = 1, \tag{28}$$

The mathematical problem is now completely specified.

5. THE METHOD OF SOLUTION

The mathematical problem just formulated can be solved numerically once λ is known. But considerable effort is required for this solution, since there are three second-order partial differential equations to be solved, two of which are nonlinear. It is true that computers can deal with nonlinearities, but the domain is infinite, and some estimate has to be made of how far to go in the numerical computation. Furthermore the integral condition (28) can only be imposed after the computations are done for h, and this makes the computation very cumbersome.

For arbitrarily large values of λ an analytical solution is extremely difficult because the nonlinearities present formidable difficulties. We shall attempt a power-series solution of the form

$$\left.\begin{aligned} h &= h_0 + \lambda h_1 + \lambda^2 h_2 + \ldots, \\ \xi &= \xi_0 + \lambda\xi_1 + \lambda^2\xi_2 + \ldots, \\ \Psi &= \Psi_0 + \lambda\Psi_1 + \lambda^2\Psi_2 + \ldots \end{aligned}\right\} \tag{29}$$

The success or failure of this approach depends not only on the value of λ, but also on the magnitudes of h_1/h_0, h_2/h_1, etc. Thus we need to make an estimate of the range of λ, and we have to find out how fast h_n, ξ_n, and Ψ_n decrease as n increases. Furthermore, even the estimate of λ cannot be made without knowing the magnitudes of Ψ_0. It turns out that a reasonable estimate of λ is

$$30 < \lambda < 50.$$

Using Eq. (29), we shall show in the following sections that h_1/h_0, ξ_1/ξ_0, and Ψ_1/Ψ_0 are all of the order of 10^{-2}. Thus, if $\lambda = 30$, stopping at the second approximation, that is, at the terms with the first power in λ, would introduce an error of about 10%, if we assume, as we evidently can, that the ratio 10^{-2} would apply to $(h_{n+1})/h_n$ etc. for n equal and greater than 1. If $\lambda = 50$ this error would be about 25 to 30 percent, and it would be necessary to go to at least the λ^2 terms to reduce the error to less than 15%.

We shall delay the presentation of the estimate of λ until later and shall proceed with the solution according to the approach in Eq. (29). In awaiting the experimental determination of λ, we shall carry out the solution to the second approximation.

6. THE FIRST APPROXIMATION

The first approximation is governed by the equations

$$Lh_0 = 0, \tag{30}$$

$$(L - 1)\,\xi_0 = -h_{0_\eta}, \tag{31}$$

$$\Psi_{0_{\eta\eta}} + \Psi_{0_{\zeta\zeta}} = -\xi_0, \tag{32}$$

with the boundary conditions (i) and (ii) stated before, which we need not repeat here.

The solution of Eq. (30) is

$$h_0 = Ce^{-(\eta^2 + \zeta^2)},$$

and application of the integral condition (28) on h_0 gives the value $1/\pi$ for C, so that

$$h_0 = \frac{1}{\pi} e^{-r^2}, \tag{33}$$

where

$$r^2 = \eta^2 + \zeta^2.$$

Then the solution of Eq. (31) is

$$\xi_0 = -\frac{2}{3\pi}\eta e^{-r^2} = -\frac{2}{3\pi}\cos\theta \cdot re^{-r^2},$$

where

$$\theta = \tan^{-1}\frac{\zeta}{\eta}.$$

Given ξ_0, Eq. (32) can be easily integrated by separation of the variables r and θ. The result is

$$\Psi_0 = -\frac{\cos\theta}{6\pi r}(1 - e^{-r^2}). \tag{34}$$

The isotherms given by Eq. (32) are just concentric circles. But the streamlines given by Eq. (34) are already interesting. They are shown in Figure 1, which shows two very prominent vortices, with the vorticity pointing in the x direction. Thus the first approximation already shows the prominent features of the flow pattern in any plane normal to the x axis. Note that both the flow pattern and the temperature field are symmetric

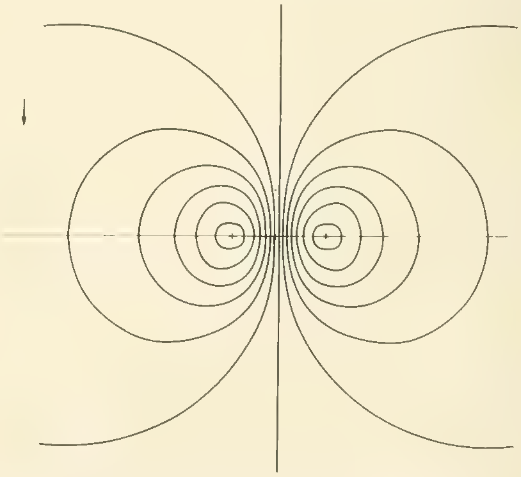

FIGURE 1. Flow pattern from the first approximation. The horizontal axis is the η axis, the vertical axis the ζ axis, and the arrow indicates the direction of the gravitational acceleration. The value of $6\pi\Psi_0$ is zero on the ζ axis. It increases toward the left and decreases toward the right. The increments (or decrements) are all 0.1.

with respect to the ζ axis, and that both h_0 and Ψ_0 vanish at infinity, as desired.

The maximum vorticity is 0.09 and is at the point

$$\eta = 1/\sqrt{2}\,, \quad \zeta = 0,$$

at which both V and W are zero. The maximum vertical velocity is $1/6\pi$ and is at the origin. The maximum absolute value of Ψ_0 is $0.63817/6\pi$, which occurs at $\theta = 0$ or π, $r = 1.1225$.

7. THE SECOND APPROXIMATION

The equation for h_1 is

$$Lh_1 = V_0 h_{0\eta} + W_0 h_{0\zeta}, \tag{35}$$

where V_0 and W_0 are the velocity components from the first approximation. The right-hand side of Eq. (35) can be written in polar coordinates as

$$\frac{1}{r}\,\frac{\partial}{\partial\theta}\Psi_0 \cdot \frac{dh_0}{dr}\,.$$

Hence Eq. (35) can be written as

$$Lh_1 = -\,\frac{\sin\theta}{3\pi^2 r}\,e^{-r^2}\,(1 - e^{-r^2}),$$

where L, in its polar-coordinate form, is

$$L = \frac{\partial^2}{\partial r^2} + \frac{1}{r}\frac{\partial}{\partial r} + \frac{1}{r^2}\frac{\partial^2}{\partial\theta^2} + 2r\,\frac{\partial}{\partial r} + 4.$$

Writing

$$h_1 = \frac{\sin\theta}{3\pi^2}\,H_1\,(r), \tag{36}$$

we have

$$L_1 H_1 = -\,\frac{e^{-r^2}}{r}\,(1 - e^{-r^2}), \tag{37}$$

if we write L_n for L with the operator $\partial^2/\partial\theta^2$ in L replaced by $-n^2$.

To solve Eq. (37), we let

$$H_1 = r^{-1}f, \tag{38}$$

so that Eq. (37) becomes

$$f'' + \left(2r - \frac{1}{r}\right)\,f' + 2f = -e^{-r^2}\,(1 - e^{-r^2}). \tag{39}$$

Then we approximate the right-hand side of this equation by

$$-r^2e^{-r^2}\,\left(1 - \frac{r^2}{2} + \frac{r^4}{6} - \frac{r^6}{24} + \frac{r^8}{240}\right)\,. \tag{40}$$

The greatest error occurs at $r = 1.8$, but it is less than 6.5% of the maximum value of the quantity approximated. Up to $r = 1.2$ the approximation is excellent. It is expected that the local errors around $r = 1.8$ will be diffused out when Eq. (39) is integrated and will introduce negligible errors in the result. After (40) is substituted into Eq. (39), the latter is solved by repeated use of the following formula for various values of n:

$$\left[\frac{d^2}{dr^2} + \left(2r - \frac{1}{r}\right)\frac{d}{dr} + 2\right]\,\left(r^n e^{-r^2}\right)$$
$$= r^{n-2}[n(n-2) - 2(n-1)r^2]e^{-r^2}.$$

The result for f is put into Eq. (38), and we have

$$H_1 = r\,\left(\frac{193}{630} - \frac{61}{1260}\,r^2 + \frac{11}{1260}\,r^4 - \frac{5}{3024}\,r^6 + \frac{1}{4320}\,r^8\right)\,e^{-r^2}. \tag{41}$$

The function H_1 is tabulated in Table 1. A look at h_1 given by Eq. (36) then reveals that the temperature is increased in the upper half of the η-ζ plane and decreased in the lower-half plane, making the isotherms more widely spaced in the upper-half plane and more crowded in the lower-half plane.

The tabulated values of H_1 show a very smooth variation of H_1 with r, verifying the expectation that the local irregular variation of (40) is diffused away when Eq. (39) is solved with (40) replacing its right-hand side.

The next step is to solve

$$(L - 1)\xi_1 = -h_{1\eta} + V_0\xi_{0\eta} + W_0\xi_{0\zeta}. \tag{42}$$

A simplification is possible before we attempt to solve Eq. (42). Differentiating Eq. (35), we have

$$(L + 2)h_{1\eta} = V_0 h_{0\eta\eta} + W_0 h_{0\eta\zeta} + V_{0\eta}h_{0\eta}$$
$$+ W_{0\eta}h_{0\zeta}. \tag{43}$$

Let

$$\xi_1 = \frac{h_{1\eta}}{3} + q. \tag{44}$$

Then Eq. (42) becomes

$$(L - 1)q + (L + 2)\,\frac{h_{1\eta}}{3} = \frac{1}{3}\,(V_0 h_{0\eta\eta} + W_0 h_{0\eta\zeta}), \tag{45}$$

since

$$\xi_0 = \frac{1}{3}\,h_{0\eta}.$$

By virtue of (43), Eq. (45) becomes

$$(L - 1)q = -\,\frac{1}{3}\,(V_{0\eta}h_{0\eta} + W_{0\eta}h_{0\zeta}). \tag{46}$$

But

$$V_{0\eta} = (\Psi_0)_{\zeta\eta}, \quad W_{0\eta} = -(\Psi_0)_{\eta\eta},$$

so that $\Psi_{0\eta}$ is a stream function for the fictitious velocity field $(V_{0\eta}, W_{0\eta})$, and we can write Eq. (46) as

TABLE 1 Values of H_1, S, and F; for $r > 4$, $-100F = 5.04\ r^{-2}$

r	0.1	0.2	0.3	0.4	0.5	0.6	0.7	0.8	0.9	1.0
$100H_1$	3.03	5.85	8.28	10.19	11.48	12.14	12.20	11.75	10.89	9.76
-100S	0.25	0.97	2.06	3.39	4.80	6.12	7.23	8.00	8.41	8.43
-100F	0.03	0.11	0.24	0.41	0.60	0.80	1.00	1.17	1.32	1.44
r	1.1	1.2	1.3	1.4	1.5	1.6	1.7	1.8	1.9	2.0
$100H_1$	8.47	7.13	5.84	4.65	3.62	2.74	2.04	1.48	1.06	0.75
-100S	8.11	7.51	6.70	5.79	4.83	3.91	3.07	2.34	1.73	1.25
-100F	1.52	1.56	1.57	1.55	1.51	1.45	1.38	1.30	1.22	1.13
r	2.1	2.2	2.3	2.4	2.5	2.6	2.7	2.8	2.9	3.0
$100H_1$	0.53	0.38	0.27	0.19	0.14	0.11	0.08	0.06	0.05	0.03
-100S	0.88	0.61	0.42	0.29	0.20	0.14	0.11	0.08	0.06	0.05
-100F	1.05	0.98	0.90	0.84	0.78	0.73	0.68	0.63	0.59	0.56
r	3.1	3.2	3.3	3.4	3.5	3.6	3.7	3.8	3.9	4.0
$100H_1$	0.02	0.02	0.01	0.01	0.01	0.00				
-100S	0.04	0.03	0.02	0.02	0.01	0.01	0.01	0.00		
-100F	0.52	0.49	0.46	0.44	0.41	0.39	0.37	0.35	0.33	0.32

$$(L - 1)q = -\frac{1}{3r}\frac{\partial}{\partial\theta}\Psi_{0\eta}\cdot\frac{dh_0}{dr}.$$

Remembering that

$$\frac{\partial}{\partial\eta} = -\frac{\sin\theta}{r}\frac{\partial}{\partial\theta} + \cos\theta\,\frac{\partial}{\partial r},$$

and with Ψ_0 and h_0 given by Eqs. (34) and (32), we have, finally,

$$(L - 1)q = \frac{2}{9\pi^2}\sin 2\theta\left[e^{-r^2}\left(1 + \frac{1}{r^2}\right) - \frac{1}{r^2}\right]e^{-r^2}. \qquad (47)$$

To solve this, let

$$q = \frac{2}{9\pi^2}\sin 2\theta\cdot r^{-2}k.$$

Then Eq. (47) becomes

$$\hat{L}k \equiv k'' + \left(2r - \frac{3}{r}\right)k' - k = e^{-r^2}[e^{-r^2}(r^2 + 1) - 1], \qquad (48)$$

where $\hat{L}$ is the linear operator defined by (48). It is advantageous to write the right-hand side of (48) as

$$e^{-2r^2}\left(r^2 + \frac{7}{8}\right) - \frac{7}{8}e^{-r^2} + \frac{1}{8}e^{-r^2}(e^{-r^2} - 1), \qquad (49)$$

for

$$\hat{L}\left(\frac{1}{8}e^{-2r^2} - \frac{7}{24}e^{-r^2}\right) = e^{-2r^2}\left(r^2 + \frac{7}{8}\right) - \frac{7}{8}e^{-r^2},$$

and the last member of (49) can be approximated by one eighth of (40). By repeated use of the formula

$$\hat{L}(r^n e^{-r^2}) = r^{n-2}[n(n - 4) - (2n - 3)r^2]e^{-r^2}$$

for various values of n, we can then find the solution for (48), and the final result for q is

$$q = \frac{2}{9\pi^2}\sin 2\theta\cdot Q, \qquad (50)$$

with

$$Q = \frac{1}{8r^2}e^{-r^2}(e^{-r^2} - 1) - e^{-r^2}\left(-\frac{1}{8} + \frac{116}{9945}r^2 - \frac{133}{95472}r^4 - \frac{11}{42432}r^6 - \frac{1}{32640}r^8\right). \qquad (51)$$

With h_1 given by (36) and (41) and therefore with $h_{1\eta}$ known, (44), (50), and (51) give

$$\xi_1 = \frac{1}{9\pi^2} \sin 2\theta \cdot S(r), \tag{52}$$

where

$$S(r) = e^{-r^2} \left[\frac{1}{4r^2} (e^{-r^2} - 1) + \frac{1}{4} - \frac{105283}{278460} r^2 + \frac{114713}{1670760} r^4 - \frac{3517}{247520} r^6 + \frac{181}{68544} r^8 - \frac{1}{4320} r^{10} \right]. \tag{53}$$

The values of $S(r)$ are tabulated in Table 1, from which it can be seen that the maximum absolute value of S occurs at about $r = 0.95$ and is about 0.847. Since S is negative throughout, inspection of Eq. (52) shows that the maximum value of ξ_1 is at

$$r = 0.95, \qquad \theta = \frac{3\pi}{4},$$

and its minimum value (negative) at

$$r = 0.95, \qquad \theta = \frac{\pi}{4}.$$

The effect of S is to reduce the strenths of the vorticity for the lower-half plane, but to augment them in the upper-half plane, thus to raise the eyes of the vortices.

Finally, Ψ_1 is to be found from

$$\Psi_{1\eta\eta} + \Psi_{1\zeta\zeta} = \left(\frac{\partial^2}{\partial r^2} + \frac{1}{r}\frac{\partial}{\partial r} + \frac{1}{r^2}\frac{\partial^2}{\partial \theta^2} \right) \Psi_1 = -\xi_1.$$

Let

$$\Psi_1 = \frac{\sin 2\theta}{9\pi^2} F(r). \tag{54}$$

Then

$$F'' + \frac{1}{r} F' - \frac{4}{r^2} F = -S(r).$$

Two integrations by the method of variation of parameters (since a complimentary solution of F is simply r^2) gives, with due regard for the boundary conditions,

$$F = -r^2 \int_\infty^r \left[r^{-5} \int_0^r r^3 S dr \right] dr$$

$$= \frac{1}{4} \left[r^{-2} \int_0^r r^3 S dr - r^2 \int_\infty^r r^{-1} S dr \right], \tag{55}$$

which is given in Table 1 also. The calculations for the second approximation have now been accomplished.

8. ESTIMATE OF λ

The terms involving ε in Eq. (2) have their origin in the Reynolds stress terms

$$\frac{\partial}{\partial y} (v'w') \text{ and } \frac{\partial}{\partial z} (w'^2),$$

where the primes indicate turbulent quantities. The terms were originally on the left-hand side of Eq. (2). The nonlinear terms on the left-hand side of Eq. (2) can be written as

$$\frac{\partial}{\partial y} (vw) + \frac{\partial}{\partial z} (w^2).$$

Thus the ratio of

$$\frac{\partial}{\partial z} (w^2) \text{ and } \frac{\partial}{\partial z} (w'^2)$$

is the ratio of

$$\frac{\partial}{\partial z} (w^2) \text{ and } -\varepsilon w_{zz},$$

and this ratio has the magnitude of

$$-\lambda W^2/W_\zeta .$$

The magnitude of W_0 is $1/6\pi$, and the magnitude of $W_{0\zeta}$ is $0.267/3\pi$, which is the maximum value of $W_{0\zeta}$ along the η axis. Thus, approximately,

$$\frac{\lambda}{0.267(12\pi)} = \frac{1}{s}, \tag{56}$$

where s is the square of w'/w. The convection in the bent plume is like the convection in a two-dimensional plume, since the plume is bent by the wind to a nearly horizontal position. The measurements of Kotsovinos (1977) for the plane plume give the value 0.2 to s. This is considered by some people to be too high. But for the problem under investigation s may be even higher, because any swaying or deformation of the vortices would contribute a good deal to turbulence. Thus using 0.2 for s in Eq. (56) would *overestimate* λ. Using 0.2 for s, we obtain from Eq. (2)

$$\lambda = 48.5.$$

This is probably too high. My estimate of λ is that it is somewhere in the range

$$30 < \lambda < 40.$$

The value 30 for λ corresponds to a value of 0.34 for s.

Let us now see what errors would be committed for h, Ψ, and ξ by stopping at the second approximation. For $\lambda = 30$, the errors (in ratio of the

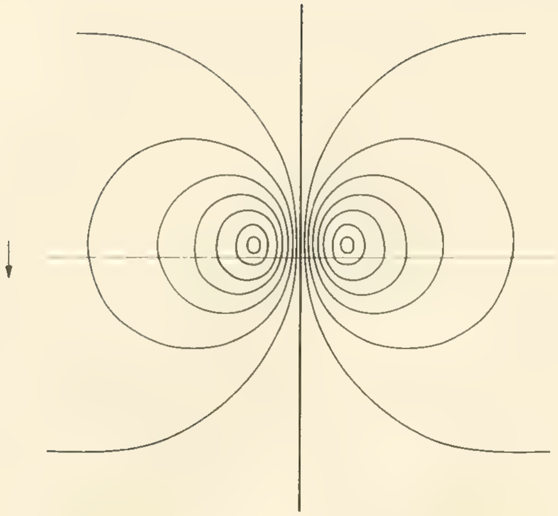

FIGURE 2. Flow pattern from the second approximation. The η axis is horizontal and the ζ axis vertical. The arrow indicates the direction of the gravitational acceleration. The value of $6\pi\Psi$ is, starting from the ζ axis and going to the curves on the right, respectively, 0, -0.1, -0.2, -0.3, -0.4, -0.5, -0.6, and -0.65. The values of $6\pi\Psi$ on the curves to the left of the ζ axis have corresponding absolute values but are positive.

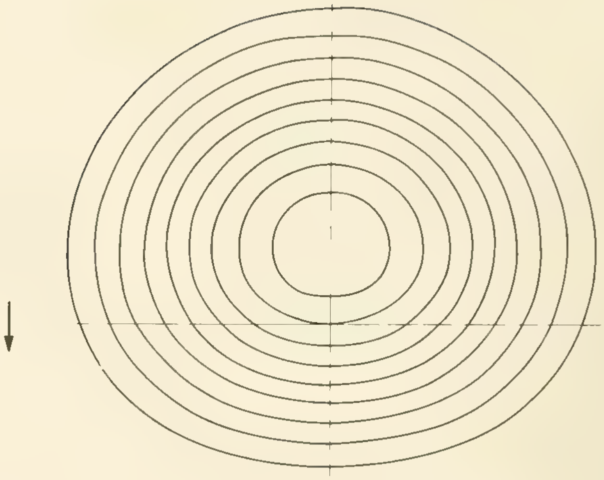

FIGURE 3. Isotherms from the second approximation. The η axis is horizontal and the ζ axis vertical. The arrow indicates the direction of the gravitational acceleration. The value of πh is 1.1 on the smallest closed curve and 0.3 on the outermost curve. The increments are 0.1.

estimated* maximum value of the terms neglected to the maximum value of the computed quantity) are, respectively, less than 15%, 3%, and 10%. For $\lambda = 40$ these percentage errors are, respectively, 25%, 5%, and 18%. The most interesting thing to note is that Ψ is the most accurately calculated quantity. Figure 2 shows the flow pattern in a plane normal to the x axis, and Figure 3 shows the isotherms therein, all for $\lambda = 30$. The flow pattern in Figure 2 can be regarded as sufficiently accurate to be representative of the actual flow pattern in a plane normal to the x axis. As expected, the hottest point and the "eyes" of the vortices occur at positive values of ζ. That is to say, the plume rises according to the $x^{2/3}$ law. After the present work was done, I found that this law had recently been verified experimentally by Wright (1977), although he did not measure the detailed velocity and temperature distributions in the plume.

If later measurements show λ is larger than 30, higher approximations would be necessary.

9. DISCUSSION

It is perhaps surprising that the analysis shows that the results in dimensionless terms are independent of the parameter Gg^2/U^5. The explanation is that the velocity (v,w) far downwind from the heat source becomes vanishingly small, and whatever the value of U, the transverse wind is asymptotically *always strong*.

Near the heat source the flow indeed depends very much on the magnitude of U. The plume may rise high in a weak wind before being bent sufficiently for the present theory to apply. In using the present theory it is always necessary to determine a virtual position for the heat source, which for small value of U can be considerably higher than its actual position.

ACKNOWLEDGMENT

This work was partially supported by the Office of Naval Research. The subject of this work was suggested to me by my friend Dr. Michel Hug, Director of the Department of Equipment, Electricity of France, through Mr. F. Boulot of the National Hydraulics Laboratory at Chatou, France, during my brief sojourn there in the summer of 1977. Their interest in this work, as well as the interest of Dr. A. Daubert, director of that laboratory, is very much appreciated. The work, begun at Chatou, was substantially improved and finished during the tenure of my Humboldt Award, at the University of Karlsruhe. To the Humboldt Foundation and my Karlsruhe hosts I should like to express my sincere appreciation.

REFERENCES

Kotsovinos, N. E. (1977). Plane turbulent buoyant jets. Part 2. Turbulence structure. *J. Fluid Mech. 81*, 45-62 (see P. 52, Figure 7).

Laufer, J. (1953). The structure of turbulence in fully developed pipe flow. *NACA Tech. Note 2954*.

Wright, S. J. (1977). *Report KH-R-36, Keck Laboratory, California Institute of Technology*.

Yih, C.-S. (1977). Turbulent buoyant plumes. *Phys. Fluids 20*, 1234-1237.

---

*On the basis that h_1/h_0 and $(h_{n+1})/h_n$ are of the same order of magnitude and that the same is true for Ψ and ξ.

APPENDIX: THE EFFECT OF NEGLECTING THE PRESSURE GRADIENT IN CALCULATIONS FOR THE CONVECTION PLUME IN A TRANSVERSE WIND

J. P. Benqué
Electricité de France
Chatou, France

In many previous studies on jets and plumes, the pressure distribution in the jets or plumes is assumed hydrostatic, so that if the body-force term in the equation of motion is written in the form $-g\Delta\rho$, where $\Delta\rho$ is the difference between the local density and the ambient density, the pressure gradient can be neglected in the equations of motion. If, further, the flow is two dimensional or axisymmetric, only the equation of motion for the vertical velocity component is then needed. After that velocity component is determined, the equation of continuity can be used to determine the other velocity component.

In the preceding paper by Yih, the assumption that the x component of the velocity is constant leaves only two other velocity components to be determined, and it is tempting to adopt the usual procedure of neglecting the pressure gradient. Yih has resisted that temptation. But it is useful to see what effects such a neglect would have on the flow and to determine whether in the problem treated by Yih such a neglect is allowable. This Appendix is devoted to this question.

If the pressure distribution is assumed hydrostatic and the usual procedure is followed, one will drop Eq. (1) and retain Eq. (2), with the first term on its right-hand side dropped. [Equation numbers in Yih's paper are retained.] Equations (3) to (7) will remain but (8) and (9) will not be needed.

Following Yih's development and using his notation, then, we have, as the dimensionless equations to solve, (24) and

$$(L - 3)W = -h + \lambda(VW_\eta + WW_\zeta). \qquad (A.1)$$

Using the λ-series (29), we have again (33) for the solution of h_0. The equation for W_0, obtained from (A.1), however, is now

$$(L - 3)W_0 = -h_0. \qquad (A.2)$$

The solution of this equation, satisfying all the boundary conditions for W stated in Yih's paper, is

$$W_0 = \frac{1}{3\pi} e^{-r^2} = \frac{1}{3\pi} e^{-\eta^2-\zeta^2}. \qquad (A.3)$$

Although it can be readily verified that Eq. (A.3) satisfies Eq. (A.2), it is not obvious that Eq. (A.3) is the unique solution. We shall show in the following that it indeed is the unique solution. The complementary solution W_{0c} of Eq. (A.2) satisfies

$$(L - 3)W_{0c} = 0 \qquad (A.4)$$

and must be even in both η and ζ. Let

$$W_{0c} = f(\eta)g(\zeta),$$

where the f is in no manner the same as the f in Eq. (38) of Yih's paper, we have

$$f'' + 2\eta f' + af = 0, \qquad (A.5)$$

$$g'' + 2\zeta g' + bg = 0, \qquad (A.6)$$

where

$$a + b = 1. \qquad (A.7)$$

Now let

$$f(\eta) = e^{-\eta^2/2}\beta(\eta). \qquad (A.8)$$

Then Eq. (A.5) becomes

$$\beta'' - (\eta^2 + b)\beta = 0. \qquad (A.9)$$

Similarly, if we let

$$g(\zeta) = e^{-\zeta^2/2}\gamma(\zeta).$$

Then

$$\gamma'' - (\zeta^2 + a)\gamma = 0. \qquad (A.10)$$

Because of Eq. (A.7), a or b must be positive. Let b be positive. (The argument is strictly similar if a is positive.) Because of the symmetry with respect to the ζ axis,

$$\beta'(0) = 0.$$

Then Eq. (A.9) shows that β will approach infinity as η^2 approaches infinity, if $\beta(0)$ is not zero. [If $\beta(0) = 0$ then $\beta = 0$ throughout.] To see how $f(\eta)$ behaves at infinity, it is necessary to see how $\beta(\eta)$ behaves asymptotically. A simple calculation shows that the two solutions of Eq. (A.9) behave, for large values of η^2, like

$$\exp\left[-\int_0^\eta (\eta^2 - a - 2)^{\frac{1}{2}} d\eta\right] \quad \text{and} \quad \exp\left[\int_0^\eta (\eta^2 - a)^{\frac{1}{2}} d\eta\right].$$

As we have seen, β must contain the second solution since β approaches infinity as $\eta^2 \to \infty$. Using the second solution as the dominant term (a constant multiplier being understood), and recalling that

$$(\eta^2 - a)^{\frac{1}{2}} = \eta - \frac{a}{2\eta} + 0\left(\frac{1}{\eta^2}\right),$$

we see from Eq. (A.8) that for large η^2

$$f(\eta) \sim |\eta|^{-a/2}, \qquad (A.11)$$

which can be seen to satisfy Eq. (A.5) asymptotically. If a is negative, (A.11) shows that $f(\eta)$, and therefore W_{0c}, cannot satisfy the condition on W_0 at infinity. If a is positive, it must be less than 1, because of (A.7) and because b is positive. Then if W_0 contains W_{0c},

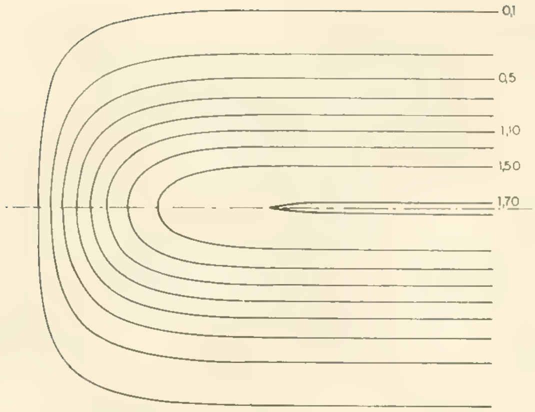

FIGURE A.1. Flow pattern for (V_1W_1). $\Delta 6\pi\Psi_1 = 0.2$.

$$I = \int_{-\infty}^{\infty}\int_{-\infty}^{\infty} W_0 d\eta d\zeta = \infty. \qquad \text{(A.12)}$$

But this cannot be true, because integration of (A.2), by parts if necessary, gives

$$-3I = -\int_{-\infty}^{\infty}\int_{-\infty}^{\infty} h_0 d\eta d\zeta = -1,$$

so that

$$I = \frac{1}{3}.$$

Hence W cannot contain a multiple of W_{0c}, and Eq. (A.3) is the unique solution.

Then the equation of continuity gives

$$V_0 = \frac{2}{3\pi}\int_0^{\eta} \zeta e^{-(\eta^2 + \zeta^2)} d\eta, \qquad \text{(A.13)}$$

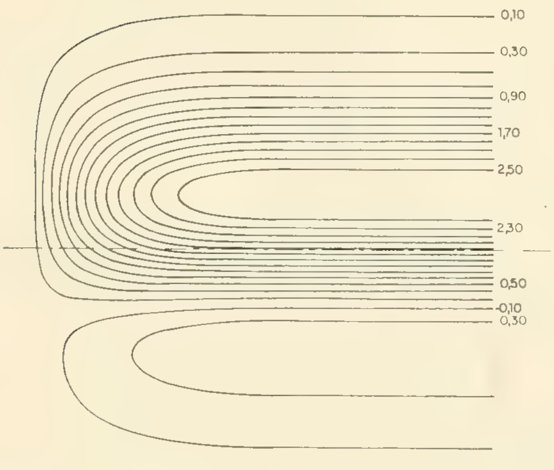

FIGURE A.2. Flow pattern for $(V_0 + \lambda V_1, W_0 + \lambda W_1)$. $\Delta 6\pi\Psi = 0.2$.

which shows that at $|\eta| = \infty$, V_0 does not vanish. We must then, if we adopt the procedure of neglecting the pressure gradient, not demand that V_0 vanish at infinity, but instead demand

$$\frac{\partial V_0}{\partial \eta} = 0 \text{ at } |\eta| = \infty . \qquad \text{(A.14)}$$

This boundary condition for V_0 must, for consistency, be demanded of V, i.e., of V_1, V_2, etc., as we proceed to higher and higher approximations.

In this connection we can also see that it is not possible to add a multiple of W_{0c} to the W_0 given by Eq. (A.3) to make V_0 vanish at infinity. For, in order to make V_0 vanish at infinity, the only possibility is to add to the W_0 given by Eq. (A.3) a multiple of

$$W_{0c} = e^{-\zeta^2} f(\eta), \qquad \text{(A.15)}$$

where f satisfies

$$f'' + 2\eta f' - f = 0.$$

That means

$$a = -1,$$

and Eq. (A.11) gives

$$f(\eta) \sim |\eta|^{\frac{1}{2}},$$

which makes W_{0c}, and therefore W_0 if it contains W_{0c}, infinite at $|\eta| = \infty$. Any other dependence of W_0 on ζ than $\exp(-\zeta^2)$ would, of course, not make V_0 vanish at infinity, for the part of V_0 that arises from W_{0c} would not be able to cancel out Eq. (A.13) at $|\eta| = \infty$.

Hence W_0 and V_0 are uniquely given by Eqs. (A.3) and (A.13). Using them in

$$Lh_1 = V_0 h_{0_\eta} + W_0 h_{0_\zeta}, \qquad \text{(A.16)}$$

and

$$(L - 3)W_1 = -h_1 + V_0 W_{0\eta} + W_0 W_{0_\zeta}, \qquad \text{(A.17)}$$

we find that

$$W_1 = \frac{h_1}{3} . \qquad \text{(A.18)}$$

I have computed h_1 numerically from Eq. (A.16) and the boundary conditions, and therefore W_1. The velocity component, V_1, is then found from the equation of continuity. The flow pattern corresponding to (V_1,W_1) is given in Figure A.1, where the streamlines are shown, with $\Psi_1 = 0$ on the ζ axis and $\Delta 6\pi\Psi_1 = 0.2$.

Then the flow field for

$$V = V_0 + \lambda V_1 \text{ and } W = W_0 + \lambda W_1$$

is shown in Figure A.2, with $\lambda = 30$, where the $\Delta 6\pi\Psi = 0.2$.

It is clear that the "streamlines" do not close to form closed eddies, as in the figures of Yih's paper. Thus the effect of the pressure gradient cannot be neglected in the problem studied by Yih.

In past studies of jets and plumes, where the pressure gradient has been successfully neglected, the velocity component other than the one retained is one order of magnitude smaller than the one retained. Thus the equation of motion for it can be neglected together with the gradient of (the dynamic part of) the pressure, and the flow pattern can be determined from the equation of continuity once the principal component of the velocity is determined. Such is not the case in the problem under discussion here, and therefore for this problem it is necessary to retain the pressure gradient, as Yih has done.

Internal Waves

O. M. Phillips
Johns Hopkins University
Baltimore, Maryland

ABSTRACT

It has become evident in the past few years that the wave-number, frequency spectrum of deep ocean oscillations has a remarkably consistent form close to that which would be expected for statistical equilibrium among the modes under wave-wave resonant interactions. The energy sources that maintain deep oceanic internal waves are, however, not well understood.

In the vicinity of the thermocline, the energy density (per unit mass) of internal wave activity is generally much greater than in the ocean depths. Relatively high frequency internal waves, generated in a variety of ways, are to a first approximation, trapped in this region. Disturbances whose frequencies are less than N_d, the deep stability frequency, do however radiate downwards effectively. Also, groups of high frequency, low mode waves generate second order mean perturbations to the thermocline structure, and if the *group* frequency is less than N_d, again energy radiates down. The flux of energy into the deep ocean is illustrated first in a simple model in which a sharp pycnocline lies over uniformly weakly stratified water. The more general problem involving an arbitrary stratification is formulated and some preliminary asymptotic solutions are presented.

1. INTRODUCTION

During the last 10 years or so, a variety of new and ingeneous oceanographic observations has been made on the structure of internal waves fluctuations in the ocean. Twelve years ago, in the first edition of *The Dynamics of the Upper Ocean,* I was forced to write that in view of the difficulty and expense involved in the systematic study of oceanic internal waves, "those (measurements) that do exist are correspondingly rare and valuable." The present situation is gratifyingly different. Deep oceanic observations of internal waves are no longer rare, but they remain valuable; Cairns (1975), Katz (1975), Gould, Simmons, and Wunsch (1974), and a number of others have provided different kinds of observations from which a consistent pattern is emerging. It appears that the deep oceanic internal wave spectrum has a remarkably universal form close to that specified by the Garrett-Munk (1975) spectrum, though why this is so cannot yet, I think, be asserted with confidence. McComas' (1975) calculations on resonant wave-wave interactions indicate that the Garrett-Munk spectrum is close to what one would expect in a state of statistical equilibrium under the balance of these interactions. On the other hand, there are indications, such as the occurrence of sporadic, isolated patches of turbulence in the stably stratified regions of the ocean which suggest that local instabilities may be limiting the wave spectral density.

Soviet investigations, such as those of Brekhovskikh et al. (1975) have concentrated on the low mode structure in the thermocline region whose energy density (per unit mass) exceeds, usually by an order of magnitude, that of the deep oceanic internal waves. The characteristic frequencies are also about an order of magnitude higher. The calculations of Watson, West, and Cohen (1975) among others indicate that the lowest modes are generated quite rapidly by interactions among surface wave components; a number of studies along these lines are described in the useful review by Thorpe (1975) and by the present author (1977). The upper ocean is certainly the site of considerable dynamical activity, but how much of it is radiated downwards to provide a source for those motions encountered in the deeper, less strongly stratified region below? According to the usual linear analysis, the low mode, relatively high frequency waves are trapped to the strongly stratified thermocline region; only the low frequency high modes have structure that can penetrate great depth.

Yet the description of deep oceanic motions as a linear superposition of high modes may make little sense. A linear mode can itself be considered the superposition of two disturbance trains, one propagating downwards and the other upwards with reflections either at the bottom or at a region where the buoyancy (or stability) frequency N drops below the wave frequency. McComas' calculations indicate that the non-linear interaction time of such components at the spectral densities found in the deep ocean, is remarkably short, only a few wave periods in many wave cases. Accordingly, a train of waves generated, say, near the thermocline will in actuality have little opportunity to travel to the bottom, reflect upwards, and combine with a downwards travelling wave to produce a 'mode' as usually conceived. More realistic would be the view of disturbances generated in the more active thermocline region, radiated downwards but being 'scrambled' by wave-wave interactions into a more diffuse spectral background.

This contribution is concerned with some aspects of the energy flux downwards from high frequency, low mode internal waves at the thermocline. If the internal wave frequency is greater than the stability frequency N_d below the thermocline, the waves are of course trapped to the thermocline region. However, as their frequency decreases below N_d, they become 'leaky' and their energy radiates rapidly downwards as the simple analysis of the next section will demonstrate. Yet, if Brekhofskikh et al.(1975) measurements are at all typical, most of the energy of the low mode internal waves in the thermocline region is at frequencies considerably above N_d; indeed, in view of the efficiency with which such low frequency energy is propagated downwards, we would not expect to find much energy at these frequencies in the main thermocline. However, one possible link is suggested by the work of McIntyre (1973) who showed that groups of internal waves in a fluid of constant frequency N, confined between horizontal boundaries, produce second order 'mean' motions, modulated as are the wave groups. There is no reason to believe that these second order disturbances are confined only to the particularly simple case that he considered, and indeed in Section 3 it is shown that they are not. High frequency internal waves, occurring in groups and trapped within the main thermocline, produce second order low frequency disturbances; if the *group* frequency is less than N_d, their energy is radiated downwards at the group frequency.

The results presented here are preliminary but intended to provoke consideration of this mechanism as a source of oceanic internal waves. The simplest case of a sharp thermocline overlying a deep, uniformly stratified region is described in some detail. The more realistic (and complicated) case with a general distribution of N(z) can be considered by asymptotic methods and these results will be described elsewhere.

2. RADIATION DOWNWARDS--A "LEAKY MODE"

Consider the following experiment: a laboratory tank (Figure 1) is stratified with a layer of uniform density lying over a density jump $\delta\rho$ below which the fluid is uniformly stratified, with $N^2 = (-\rho^{-1} g\, \partial\rho/\partial z)$ = constant. A wave-maker at the end of the tank generates a periodic disturbance with (real) frequency n. What are the characteristics of the motion induced?

It is, I think intuitively evident that if $n > N$ an interfacial wave mode will propagate. The structure of the mode below the pycnocline will be influenced by the stratification but at these high frequencies, no internal waves can be supported in the lower layer and the interfacial wave will propagate without loss. If, however, $n < N$, internal waves induced in the lower region by the interfacial disturbance can carry energy downwards so that the interfacial wave will attenuate. The question is: how rapidly does this occur?

A linear analyses suffices. Suppose the pycnocline displacement is represented by the real part of $\zeta = a \exp i(kx - nt)$, where n is real and k may be real or complex. Above the pycnocline at $z = 0$, the motion is irrotational with $u = \nabla\phi$ and $\nabla^2\phi = 0$. In the uniformly stratified region below, the vertical velocity component, w, obeys the internal wave equation

$$\frac{\partial^2}{\partial t^2} \nabla^2 w + N^2 \nabla_h^{\,2} w = 0 \quad , \tag{1}$$

where $\nabla_h^{\,2}$ is the horizontal Laplacian operator, $\partial^2/\partial x^2$ in this two-dimensional problem. At the upper free surface at $z = d$, $w = 0$ to sufficient accuracy; at the pycnocline the vertical displacement and the pressure must both be continuous and as $z \rightarrow -\infty$, the disturbance must either die away or represent internal waves with an energy flux downwards.

In the upper region, the solution for ϕ is readily found to be

$$\phi = \frac{ina}{k} \frac{\cosh k(z - d)}{\sinh kd} \exp i(kx - nt) \quad , \tag{2}$$

while in the lower layer, if

$$w = - ina \exp\left[\kappa z + i(kx - nt)\right] \quad , \tag{3}$$

(which satisfies the condition of continuity of w at $z = 0$), then substitution into (1) requires that

$$(\kappa/k)^2 = 1 - (N/n)^2 \quad . \tag{4}$$

Note that since n is real, κ/k is either purely real (if $n \geq N$) or purely imaginary (if $n < N$).

The dispersional relation is obtained from the condition that the pressure be continuous at $z = \zeta$. In the upper region of density ρ,

$$p_\zeta = - \rho g \zeta - \left.\frac{\partial\phi}{\partial t}\right|_\zeta \quad ,$$

$$= - \rho a\left[g + (n^2/k) \coth kd\right] \exp i(kx - nt) \quad , \tag{5}$$

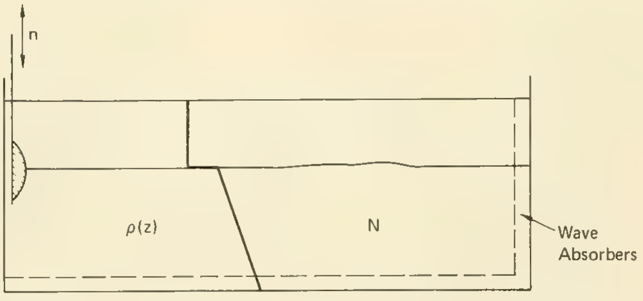

FIGURE 1. Tank stratified with a layer of uniform density over a density jump below which the fluid is uniformly stratified.

to the first order in the wave amplitude. In the lower region, where the density is $\rho + \delta\rho - \rho N^2 z/g$, the horizontal pressure gradient

$$\frac{\partial p}{\partial x} = -(\rho + \delta\rho)\frac{\partial u}{\partial t}, \qquad \text{to the lowest order,}$$

$$= i(\rho + \delta\rho) a n^2 (\kappa/k) \exp i(kx - nt)$$

at $z = 0$ from (3), so that

$$p_0 = (\rho + \delta\rho) a n^2 (\kappa/k^2) \exp i(kx - nt)$$

At $z = \zeta$, below the pycnocline,

$$p_\zeta = -(\rho + \delta\rho) a (g - n^2\kappa/k^2) \exp i(kx - nt) \qquad (6)$$

From (5) and (6) it follows that

$$n^2 = \frac{(\delta\rho/\rho) gk}{\coth kd + (\kappa/k)} = \frac{bk}{\coth kd + (\kappa/k)}, \qquad (7)$$

to the Boussinesq approximation, when $\delta\rho/\rho \ll 1$, and where b is the contrast in buoyancy across the pycnocline.

For high frequency oscillations, when $n \geq N$, equation (4) shows that κ/k is real and less than unity; from (7) k is real and the waves propagate without attenuation. The additional restoring forces provided by the stratification below do however increase the wave frequency for given k and b above the value for an unstratified lower layer by the ratio

$$[\coth kd + 1] / [\coth kd + (1 - N^2/n^2)^{\frac{1}{2}}],$$

The case when $n < N$ is algebraically simplest when $|kd| \to \infty$. In view of the upper boundary conditions, the real part of $k > 0$, while from (4)

$$\frac{\kappa}{k} = \pm i\left(1 - \frac{N^2}{n^2}\right)^{\frac{1}{2}} = \pm i \tan\theta, \qquad (8)$$

where $n = N\cos\theta$. From (7)

$$k = (n^2/b)(1 \pm i\tan\theta) \quad . \qquad (9)$$

Since the interfacial waves attenuate in the positive x-direction as energy leaks downwards, the positive sign in (9) is relevant and the vertical wave-number

$$\kappa = ik\tan\theta,$$

$$= (n^2/b)(-\tan^2\theta + i\tan\theta) \quad . \qquad (10)$$

The motion of the pycnocline is therefore represented by

$$\zeta = a\exp\left(-\frac{n^2 x}{b}\tan\theta\right)\exp i\left(\frac{n^2 x}{b} - nt\right),$$

$$= \alpha(x)\exp i\left(\frac{n^2 x}{b} - nt\right), \qquad (11)$$

where

$$\alpha(x) = a\exp\left(-\frac{n^2 x}{b}\tan\theta\right).$$

The ratio of the spatial attenuation rate to the wave-number is simply $\tan\theta = (N^2/n^2 - 1)^{\frac{1}{2}}$; when n is significantly less than N the attenuation distance is short as the energy leaks downwards very effectively.

Expressions for the motion in the upper and lower regions can be written down simply. In the lower layer energy flows along the characteristics $\xi = x\cos\theta + z\sin\theta = \text{const.}$, and the distribution of vertical velocity is

$$w = -ina\exp\left(-\frac{n^2\sin\theta}{b\cos^2\theta}\xi\right)\exp i\left(\frac{n^2}{b\cos\theta}\xi - nt\right),$$

$$= -in\alpha_1(\xi)\exp i\left(\frac{n^2\xi}{b\cos\theta} - nt\right), \qquad (12)$$

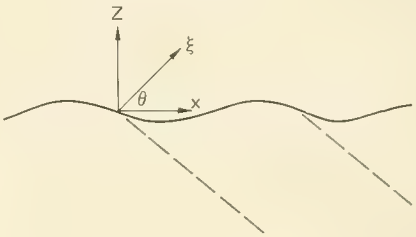

where $\alpha_1(\xi)$ is the amplitude of the interfacial wave at the point where the characteristic intersects the pycnocline. The horizontal component of the velocity field in the lower layer is $u = -w\tan\theta$, since the motion here consists of alternate layers sliding relative to one another along the characteristic surface inclined at an angle θ to the vertical. The pressure fluctuation can be found most simply from the horizontal momentum equation:

$$p = -\alpha_1(\xi) b\sin\theta(\sin\theta + i\cos\theta)\exp i\left(\frac{n^2\xi}{b\cos\theta} - nt\right). \qquad (13)$$

The vertical energy flux is therefore

$$E_z = -\tfrac{1}{2} n\alpha_1^2(\xi) b\sin\theta\cos\theta,$$

and the total energy flux, directed downwards along the characteristics $\xi = \text{const}$ is

$$E = \tfrac{1}{2} n\alpha_1^2(\xi) b\sin\theta \quad . \qquad (14)$$

In the upper region, the fluctuations in pressure are found from (2):

$$p = -\frac{\partial\phi}{\partial t} = \frac{n^2 a}{k}\exp[-kz + i(kx - nt)],$$

when $kd \gg 1$, whose real part, in view of (9) and (12) reduces to

$$p_r = -\alpha(x + z\cot\theta) b(\cos^2\theta\cos\chi + \cos\theta\sin\theta\sin\chi), \qquad (15)$$

where

$$\chi = \frac{n^2}{b}(x - z\tan\theta) - nt,$$

The real part of the horizontal velocity field is likewise

$$u_r = (\partial\phi/\partial x)_r = -\, n\alpha(x + z\cot\theta)\cos\chi \quad ,$$

so that the horizontal energy flux in the upper layer

$$\mathcal{E}_x = \int_0^\infty \overline{up}\ \alpha z = \frac{a^2b^2\cos^2\theta}{4n} \exp\left\{-\frac{2n^2}{b}\, x\tan\theta\right\}, \quad (16)$$

the horizontal divergence of which

$$\frac{\partial \mathcal{E}x}{\partial x} = -\, \tfrac{1}{2} n\alpha^2(x)b\, \sin\theta\cos\theta \quad (17)$$

provides for the radiative flux in the lower layer.

This simple example illustrates the way that energy can be radiated downwards by the low frequency perturbations produced by groups of high frequency waves, but they have a deeper theoretical interest. Gaster (1977) has pointed out that if the dispersion relation for waves involves complex wave-numbers or frequencies, the usual kinematic definition of group velocity may not be correct, and a simple calculation shows that the solution is an example of this failure. Here the wave-numbers are complex as the energy leaks into the lower layer, but the energy flux is not at the rate represented by the local energy density, $n^2\alpha_1{}^2/2\ \cos^2\theta$, times the ordinary group velocity $\nabla_k\omega = c\tan\theta = (b/n)\sin\theta$. The correct interpretation of these situations will be considered elsewhere.

3. ENERGY RADIATION DOWNWARDS FROM GROUPS OF INTERFACIAL WAVES

To illustrate the way in which groups of internal waves produce 'mean,' second order disturbances locked to the wave group, let us consider the same basic stratification as in the previous section, with fluid of depth d and constant density lying over a buoyancy jump b below which the stability frequency N is constant. Suppose that interfacial waves with frequency $n > N$ are maintained by high frequency forcing f from the upper layer, perhaps by the surface wave-wave interactions described by Watson, West, and Cohen (1976). If the internal wave amplitude is characterised by a and the wave-number by k, then, to order $\mathcal{E}^2 = (ak)^2$, the condition or continuity of pressure across the interface can be expressed as

$$\Delta\left(\frac{\partial u}{\partial t}\right) - b\,\frac{\partial\zeta}{\partial x} + f = -\Delta\left(\zeta\,\frac{\partial^2 u}{\partial z\zeta t} + \underset{\sim}{u}\cdot\nabla u\right) \quad , \quad (18)$$

at $z = 0$, where $\Delta(\ ) = (\ )_+ - (\ )_-$, the difference across the density jumps. Since

$$\dot{\zeta} = w_\zeta - \underset{\sim}{u}_\zeta \cdot \nabla\zeta = w_0 + \zeta\,\frac{\partial w}{\partial z}\Big|_0 - u_0\,\frac{\partial\zeta}{\partial x} \,,$$

$$= w_0 - \frac{\partial}{\partial x}(u_0\zeta) \quad , \quad (19)$$

to order $\mathcal{E}^2$, where the suffixes, ζ and 0, represent quantities measured at $z = \zeta, 0$, then the condition that ζ be continuous across the interface assumes the form

$$\Delta w = \Delta\left[\frac{\partial}{\partial x}(u\zeta)\right] \quad \text{at } z = 0 \quad . \quad (20)$$

Finally, in the lower layer,

$$\frac{\partial^2}{\partial t^2}\nabla^2 w + N^2\,\frac{\partial^2 w}{\partial x^2} = Q \quad , \quad (21)$$

where the non-linear terms

$$Q = \frac{\partial^3}{\partial x\partial z\partial t}(\underset{\sim}{u}\cdot\nabla u)$$

$$-\,\frac{\partial^2}{\partial x^2}\left(\underset{\sim}{u}\cdot\nabla b + \frac{\partial}{\partial t}(u\cdot\nabla w)\right) \quad . \quad (22)$$

Variations in energy density of the primary waves will propagate with the group velocity, c_g; let us therefore average these equations at points fixed with respect to the wave groups but over random phases of the waves themselves, a process represented by brackets [ ]. The averaged interfacial conditions are then, to order $\mathcal{E}^2 = (ak)^2$,

$$\Delta\left[\frac{\partial u}{\partial t}\right] - b\,\frac{\partial}{\partial x}[\zeta] = -\Delta\left[\zeta\,\frac{\partial^2 u}{\partial z\partial t} + \underset{\sim}{u}\cdot\nabla u\right] , \quad (23)$$

$$\Delta\,[w] = \Delta\left[\frac{\partial}{\partial x}(u\zeta)\right] , \quad (24)$$

both at $z = 0$, and

$$[\dot{\zeta}] = [w] - \frac{\partial}{\partial x}[u\zeta] \quad , \quad (25)$$

also at $z = 0$. The averaged field equation for the lower layer follows similarly from (21) and (22).

The linear fluctuating internal wave motion is as given in the previous section when $n > N$; through the non-linear terms on the right of (23)-(25), this forces a second order mean disturbance $[\zeta]$, $[w]$, etc., that moves with the velocity of the wave groups. The pycnocline disturbance can be represented as

$$\zeta = \tfrac{1}{2}a\{\cos(k'x - n't) + \cos(k''x - n''t)\} \quad .$$

The form of the forcing functions is simplest when the pycnocline depth is such that $kd \gg 1$, and it is found that (23) reduces to

$$\Delta\left[\frac{\partial u}{\partial x}\right] - b\,\frac{\partial}{\partial x}[\zeta]$$

$$= -\,\tfrac{1}{4}\, a^2 nkk_g\left\{1 - \left(\frac{\kappa}{k}\right)^2\right\}$$

$$(c_g + \tfrac{1}{2}c)\,\mathrm{Sin}\ k_g\,(x - c_g t)$$

$$\{1 + O(ak,\ n_g^2/n^2)\} \,,$$

$$= -\,\tfrac{1}{4}\, a^2 k_g N^2\left(\frac{c_g}{c} + \frac{1}{2}\right)\sin k_g(x - c_g t) \quad , \quad (26)$$

where $k_g = k' - k''$, $n_g = n' - n''$, and c_g represent the wave-number, frequency, and velocity of the groups. Similarly, from (24)

$$\Delta\ [w] = \frac{1}{8} a^2 n\ k_g \left(1 + \frac{\kappa}{k}\right) \sin \chi\ , \tag{27}$$

where $\chi = k_g(x - c_g t)$ and from (25)

$$[\dot{\zeta}] = [w]_+ - \frac{1}{8} a^2 n k_g \sin \chi\ ,$$

$$= [w]_- + \frac{1}{8} a^2 n k_g (\kappa/k) \sin \chi\ , \tag{28}$$

where $[\ ]_+$ and $[\ ]_-$ represent averages taken just above and below the discontinuity in density.

These matching conditions to be applied as $z = 0$ involve the non-linear forcing provided by the wave groups. The field equations are, however, linear to this order. Above the pycnocline, when $d > z > 0$, we have Laplace's equation for the averaged velocity

$$\nabla^2\ [\phi] = 0\ , \tag{29}$$

while in the averaged internal wave equation (21) for $z < 0$, the non-linear terms are smaller by at least $(n_g/n)^2 \ll 1$ than those in the matching conditions, since they involve two horizontal derivatives (or one x and one t derivative) of averaged second order quantities. Accordingly, to sufficient accuracy,

$$\frac{\partial^2}{\partial t^2} \nabla^2 [w] + N^2 \frac{\partial^2}{\partial x^2} [w] = 0\ , \quad z < 0\ . \tag{30}$$

Since the length of the wave groups is large compared with the wavelength of the interfacial waves, $k_g \ll k$ and it is consistent to assume that $k_g d \ll 1$, even though $kd \gg 1$. Furthermore $n/N \ll 1$ while $N_g N = 0(1)$. Under these conditions the solutions for the mean pycnocline displacement and the low frequency internal waves radiated downwards are found to be

$$[\zeta] \triangleq - \frac{a^2 n c_g}{bd} \cos k_g (x - c_g t)\ , \tag{31}$$

$$[w] \triangleq - \frac{1}{8} a^2 n k_g (2 + \frac{\kappa}{k}) \cos\ (k_g x + \kappa_g z - n_g t)\ , \tag{32}$$

where

$$\kappa_g = k_g \left(\frac{N^2}{n_g{}^2} - 1\right)^{\frac{1}{2}} \tag{33}$$

is the vertical wave-number of the radiated field. The horizontal velocity component in the internal wave motion below the pycnocline

$$[u] = [w] \tan \psi\ ,$$

where $\cos \psi = n_g/N$ and the energy density (twice the kinetic energy density) is

$$E = \rho \left(\overline{[u]^2} + \overline{[w]^2}\right),$$

$$= \frac{\rho a^4 k_g{}^2 n^2 N^2}{128 n^2_g} \left(2 + \frac{\kappa}{k}\right)^2\ ,$$

$$\triangleq \frac{9 \rho a^4 n^2 N^2}{128 c_g{}^2}\ , \tag{34}$$

since $n/N \gg 1$ and $\kappa/k \simeq 1$. The vertical component of the group velocity of the radiated waves is $c_g \cos \psi \sin \psi$ where c_g is the group of the interfacial waves, so that the vertical energy flux is

$$\bar{E}_2 = (9/128)\ a^4 n^2 N k_g \left(1 - \frac{n^2 g}{N^2}\right)^{\frac{1}{2}}. \tag{35}$$

Although this representation of the density distribution by a discontinuity at the pycnocline, followed by a uniform stratification below, is a gross simplification of typical oceanic conditions, it is of interest to examine the order of magnitude of the vertical energy flux that might be generated in this way. If the interfacial wave amplitude is 10 m at a frequency of 5 c.p.h., having groups 1 km in length and if N = 2 c.p.h., the downwards energy flux is about 2 erg/cm^2 sec., which is of the same order as the 5 erg/cm^2 sec. estimated by Garrett and Munk (1972) for the rate of energy dissipation from internal waves by sheer instability. This correspondence is sufficiently close to encourage a more detailed study with N(z) arbitrary, the results of which will be presented elsewhere.

ACKNOWLEDGMENT

This work was supported by the Fluid Dynamics Branch of the Office of Naval Research under contract NR 062-245.

REFERENCES

Brekhovskikhk, L. M., K. V. Konjaev, K. D. Sabinin, and A. N. Serikov (1975). Short period internal waves in the sea. *J. Geophys. Res.*, *80*, 856-64.

Cairns, J. L. (1975). Internal wave measurements from a midwater float. *J. Geophys. Res.*, *80*, 299-306.

Garrett, C., and W. H. Munk (1972). Space-time scales of internal waves. *J. Geophys. Fluid Dyn.*, *3*, 225-64.

Garrett, C., and W. H. Munk (1975). Space-time scales of internal waves: a progress report. *J. Geophys. Res.*, *80*, 291-7.

Gaster, M. (1977). On the application of ray mathematics to nonconservative systems. *Geofluid-dynamical wave mathematics*, *Appl. Math. Gp.*, U. Washington, 61-6.

Gould, W. J., W. J. Schmitz, and C. Wunsch (1974). Preliminary field results of a mid-ocean dynamics experiment (MODE-0). *Deep-sea Res.*, *21*, 911-32.

Katz, E. J. (1975). Tow spectra from MODE. *J. Geophys. Res.*, *80*, 1163-7.

McComas, C. H., and F. P. Bretherton (1977). Resonant interaction of oceanic internal waves. *J. Geophys. Res.*, *82*, 1397-1412.

McIntyre, M. E. (1973). Mean motions and impulse of a guided internal wave packet. *J. Fluid Mech.*, *60*, 801-11.

Phillips, O. M. (1977). *Dynamics of the Upper Ocean* 2nd ed., Cambridge University Press.

Thorpe, S. A. (1975). The excitation, dissipation and interaction of internal waves in the deep ocean. *J. Geophys. Res.*, *80*, 328-38.

Watson, K. M., B. West, and B. I. Cohen (1976). Coupling of surface and internal gravity waves: a Hamiltonian model. *J. Fluid Mech.*, *77*, 185-208.

Breaking Internal Waves in Shear Flow

S. S. Thorpe
Institute of Oceanographic Sciences,
Wormley, United Kingdom

ABSTRACT

During and following periods of strong winds, the Richardson number (the square of the ratio of the Brunt-Väisälä frequency to the shear) in the thermocline is of order unity, and the shear becomes an important factor in determining the properties of internal gravity waves. These properties are discussed and the shape and breaking of waves in a shear flow is investigated in laboratory experiments. These experiments show that the waves may break at their crests or their troughs depending on the sign of a certain vector scalar product. An analogy between surface waves and interfacial waves is invoked to account for this behaviour. Breaking is observed to occur by particles of fluid moving forward more rapidly than the wave crest advances, leading to gravitational instability. The effect of breaking in the ocean will not only enhance diffusion rates, but it will modify the directional spectrum of the internal waves.

Although many acoustic backscatter observations from ships reveal clearly the presence of internal waves in the ocean seasonal thermocline, very few have been published which appear to show signs of their breaking. This is surprising in view of the clear and not infrequent evidence of 'breaking events' in the equivalent acoustic or Doppler radar measurements in the atmosphere. Our knowledge of internal wave breaking in the ocean still rests almost entirely on the direct observations by divers using dye in the Mediterranean thermocline [Woods (1968)]. The present towed, moored, or dropped instruments give inadequate information on the nature or structure of the intermittent mixing events in the ocean to be certain of their cause, or even of the scales of motion which contribute most to diffusion across density surfaces in spite of its great importance to the prediction of the thermocline structure of the upper ocean.

It is against this background of poorly known dynamical structures that this paper is presented. One aim is to describe the patterns which accompany wave breaking, for without a knowledge of such patterns it is difficult to design the appropriate experiment to detect wave breaking or, conversely, to correctly identify the processes involved once observations are available.

It would be naive to ignore the effect of wind in a description of breaking waves on the surface of the sea in deep water [see, for example, Phillips and Banner (1974)]. (Wave breaking on a beach is a different matter). It is similarly inappropriate to ignore the effect of mean shear on internal waves in the seasonal thermocline, since the Richardson number there is low, especially during, and following, storms [Halpern (1974)]. Internal gravity waves can exist and propagate in a shear flow just as they can when a mean flow is absent. These waves belong to a group which Banks, Drazin, and Zaturska (1976) have classified as 'modified' (-by shear) 'internal gravity waves'. They may sometimes coexist with a set of wavelike disturbances which grow in amplitude (the 'unstable wave solutions' of the Taylor-Goldstein equation) and which may eventually lead to turbulence (Figure 1). It is known however that (for steady mean flows) the latter solution corresponding to Kelvin-Helmholtz instability (K-H.I) only exists if the Richardson number, Ri, in the flow is somewhere less than a quarter [Miles (1961), Howard (1961)] and even then in some flows an unstable solution may not exist. One way in which internal gravity waves may break is by themselves causing or augmenting a mean shear to induce regions of such low Ri that small-scale disturbances may grow as K-H.I and generate turbulence. It appears that Woods' (1968) billows were generated in this way, and similar structures in Loch Ness [Thorpe, Hall, Taylor, and Allen (1976)] may have a like cause. It is however known that internal waves may break in quite a different way, by what has been termed 'convective instability' [Orlanski and Bryan (1969)]. This form of instability becomes much more likely in the presence of a mean shear.

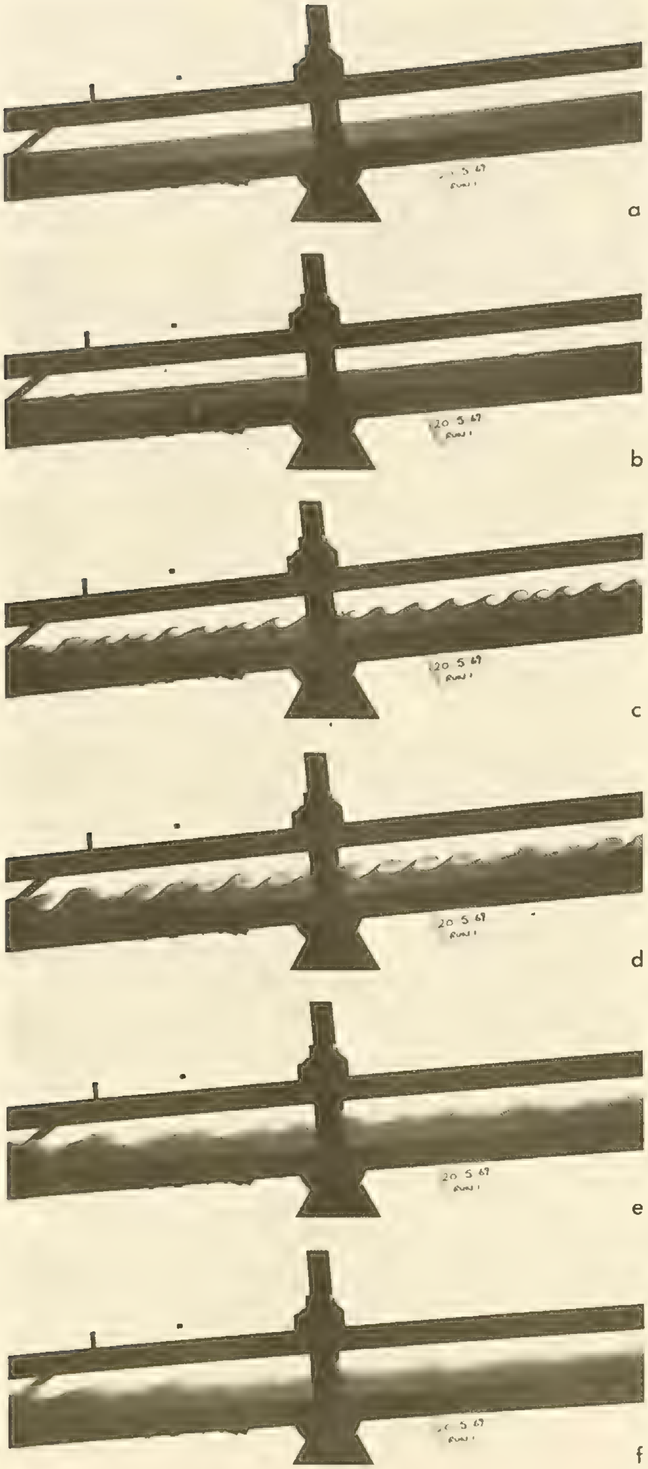

FIGURE 1. The development of Kelvin Helmholtz Instability (K-H.I) in a stratified shear flow [from Thorpe (1971)].

Shear affects internal gravity waves in several ways. Perhaps the most important concern the wave speed. Bell (1974) has shown that for any wave mode, the phase speed, c, is a decreasing function of wavenumber, k, which, for waves moving faster than the mean flow at any level, tends to $k^{-1}N_{max} + U_{max}$ as k increases indefinitely, where N_{max} is of the Brunt-Väisälä frequency, N, and U_{max} the maximum mean flow. (A similar result holds for waves travelling more slowly than the mean flow.) This result reduces to the well-known property, $\sigma < N_{max}$, of internal waves in the absence of shear [Groen (1948)] where $\sigma = ck$ is the wave frequency relative to the mean flow. It implies that even in a shear flow the wave frequency is less than N_{max} provided the waves are viewed in frame of reference which moves forward at the speed, U_{max}. Banks et al. showed further that, at least for simple mean flow profiles, the speed of waves of a given mode and wavenumber tends to U_{max} (from above) as Ri decreases. We see a consequence of this result later.

The vertical structure of internal waves is also changed by shear. Figure 2 shows how the distribution of the amplitude of a small amplitude wave of given k varies with z as the shear increases for (a) plane Couette flow of a fluid with constant N and (b) hyperbolic tangent profiles of mean speed and density. The profiles are distorted as Ri decreases with the largest amplitudes displaced towards the level at which the mean speed in the direction of wave propagation is greatest. We shall find it convenient to distinguish these cases by the sign of $\chi \equiv \underline{c}.\underline{g} \times \underline{\Omega}$ where $\underline{\Omega}$ is the mean flow vorticity and $\underline{c}$ the phase speed of the waves in a frame of reference in which the depth averaged mean flow is zero. Positive U_0 in Figure 2 corresponds to $\chi > 0$, and conversely.

The shape of waves in a fluid with density and velocity distributed as tanh z (corresponding to Figure 2b) is shown in Figure 3 for (a) backward relative motion in the upper layer, $\chi < 0$, (b) no shear, (c) forward motion in the upper layer, $\chi > 0$. The waves in (b) and (c) have narrower crests than troughs, whilst the waves in (a) have wide crests and narrow troughs.

This second-order effect is not unexpected. It may easily be shown [Thorpe (1974, Appendix C)] that interfacial waves (see Figure 4) which move forward with the speed of the upper layer (the limit, as we have seen, towards which the phase speed of the internal waves tends as Ri decreases) have *exactly* the same shape as have surface waves on a fluid of depth equal to the lower layer. Conversely those moving at the speed of the lower layer have the shape of surface waves on a fluid of depth equal to the upper layer, *but inverted*. This is just the trend shown in Figure 3. The limiting form of the surface wave is one with a sharp apex of 120°. Such an angle can exist in a two-layer flow only in the cases we have considered where the wave speed is the same as the flow in one of the two layers. Otherwise there is a relative flow around the apex in the upper (or lower) fluid leading to a singularity of infinite flow in the irrotational fluid. In general, some other limiting profile must appear, although it is likely to tend in a continuous way towards the limiting sharp apex profile. Recent work on breaking surface waves [Cokelet (1977)] cannot be applied even in the special case for the analogy is valid only for steady waves.

Experiments, however, [Thorpe (1968)] demonstrate how internal waves break in a shear flow. Figure 5 shows wave breaking for $\chi > 0$. A jet of fluid moves forward (that is faster than the waves advance) from the wave crest above the level of the mean

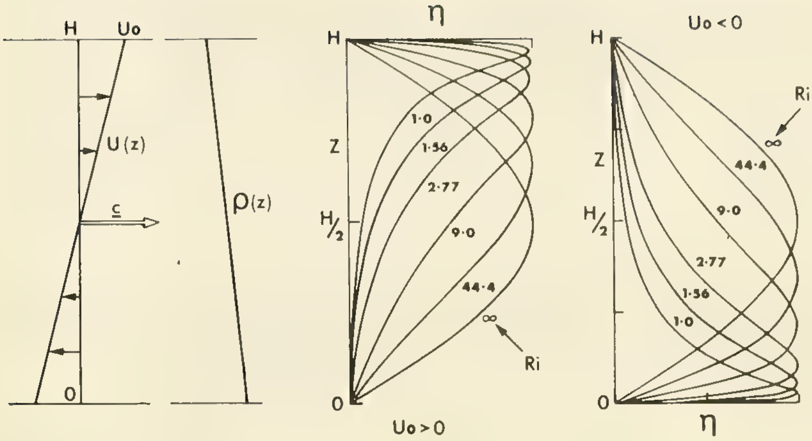

FIGURE 2. The amplitude of the displacement of lines of constant density in internal waves of the first mode with wave number $k = \pi/H$ calculated from linear theory (i.e., from the Taylor-Goldstein equation) at various Richardson numbers (as labelled) in

(a) Couette flow, $U = U_0(2z/H - 1)$, with constant density gradient. U_0 is positive for the left hand set of curves and negative for the right hand set.

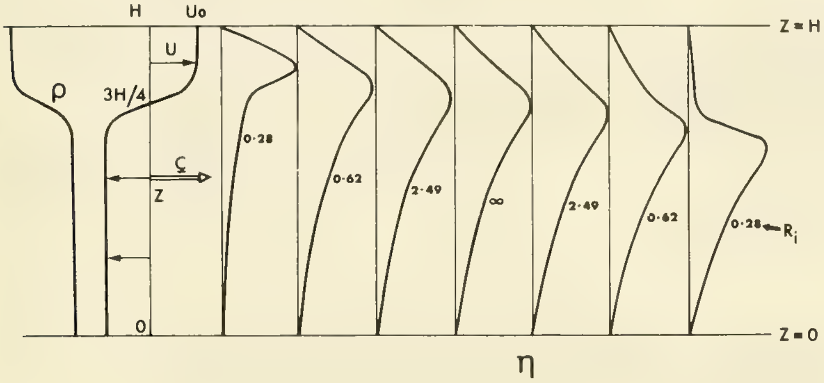

(b) Hyperbolic tangent profiles, $U = U_0 \tanh y$ and density $\rho = \rho_0(1 - \Delta \tanh y)$ where $y = 20z/H - 15$. U_0 is positive for the first three curves at the left, zero for $Ri = \infty$ and negative for the three curves on the right. The value of Ri marked on these curves is the minimum mean flow value at $z = 3H/4$.

interface where we saw in Figure 2 that the displacement was concentrated, and, in Figure 3, where the curvature was greatest. The fluid particles move forward (at speed C_p) more rapidly than the wave advances and this leads to a layered structure with a region of slightly denser fluid overlying less dense fluid with the potential consequence of gravitational instability. Similar 'forward' breaking occurs at the wave troughs when $\chi < 0$. The experiments demonstrate clearly the difference between K-H.I of the mean flow (seen in Figure 5j) and the convective instability of the waves. In the former the wave-like disturbances grow, extracting energy from the mean flow, whilst in the latter the waves do not grow in amplitude and lose energy as a consequence of instability.

The condition for convective instability to occur ($C_p = c$) has been used in a calculation to produce the stability diagrams of Figure 6. These are appropriate only to a particular wavelength and show the wave slope at which instability will occur for a given Ri. The Couette flow (Figure 6a) is stable in the absence of waves for all $Ri > 0$, but the hyperbolic tangent profile (Figure 6b) is unstable at $Ri = 0.25$ and the dashed lines show the value $Ri = 0.25$ at the interface marking the boundary at which K-H.I will occur in a quasi steady flow. These diagrams demonstrate how shear greatly reduces the wave slope at which convective instability sets in, a partial consequence of the trend of the phase speed toward U_{max} and hence a reduction of the wave particle speed necessary to promote net speeds, C_p, which exceed the phase speed. The nonlinear terms are also very important however, the finite amplitude change in the phase speed being as important as other non-linear effects.

We may press the analogy between interfacial internal waves in a shear flow and surface waves further. The shape of surface gravity waves (narrower crests than troughs) and their habit of breaking forwards at the crests seems universal, in that it is independent of water depth, being observed and (where theory is available) predicted for both shallow and deep water waves. The internal waves observed in the experiments have similar properties, accepting that the profile is inverted with respect to the surface waves if $\chi < 0$, even though they are not strictly interfacial waves or moving at the speed of one of the layers. This suggests that the shape and breaking, by convective overturn, of long first mode internal waves on a relatively narrow interface between two uniform layers follow the pattern observed in the experiments, *independent of the depths of the layers*, provided that the Richardson number of the mean flow in the interfacial region is small.

Figure 6b is not symmetrical, a consequence of the asymmetry introduced by having unequal layer thicknesses above and below the interface. Translated to a situation in which wind is driving a flow above a shallow thermocline, the diagram implies that internal waves travelling with the wind ($\chi > 0$) will break at a greater amplitude (or later if the shear flow is increasing) then waves of the same length travelling against the wind. This result also follows from our analogy with surface waves since, for a given wavelength, surface waves of limiting (120° apex) amplitude in deep water (corresponding to the forward moving, $\chi > 0$, internal gravity waves) are higher than waves in shallow water (which correspond to the backward moving waves). Waves moving across the flow will

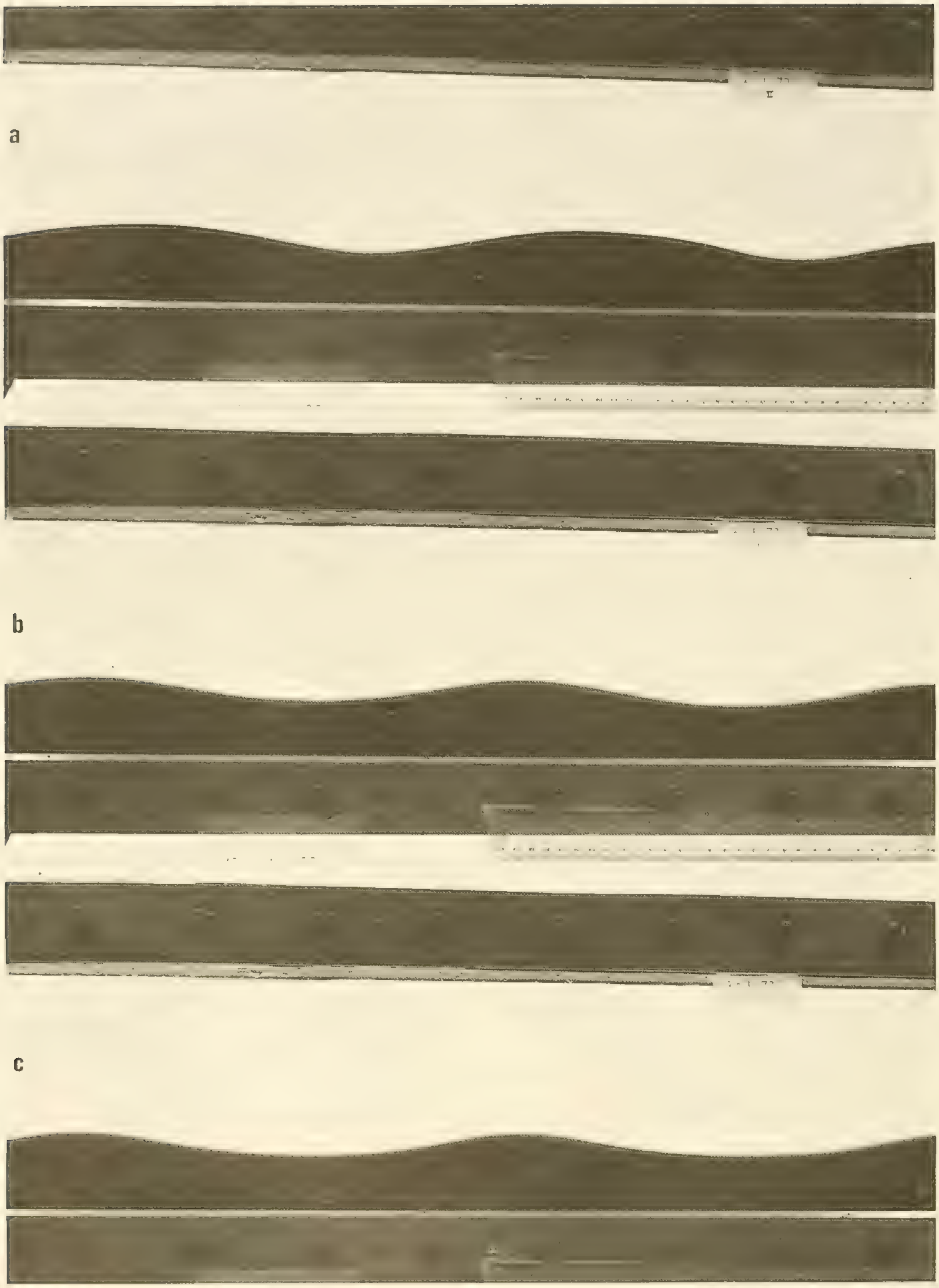

FIGURE 3. Internal waves in a shear flow with profiles of U and ρ similar to those of Figure 2(b), except that the interface is at $z = H/4$ and the mean, depth averaged, flow is zero. The waves propagate to the left and in (a) the mean flow in the upper layer is to the right, lower to the left ($\chi<0$), in (b) there is no mean flow, whilst in (c) the mean flow in the upper layer is to the right and in the lower layer to the left ($\chi > 0$).

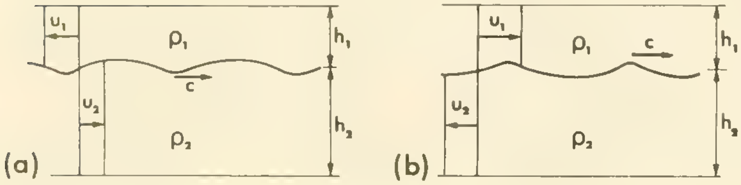

FIGURE 4. Interfacial waves in a two-layer fluid. In (a) the phase speed of the waves, c, is equal to the speed of the lower layer, U_2. The wave shape is identical to that of surface waves on a layer of depth h_1, but inverted. (This corresponds to $\chi < 0$). In (b), $c = U_1$, and the wave shape is identical to that of surface waves on a layer of depth h_2.

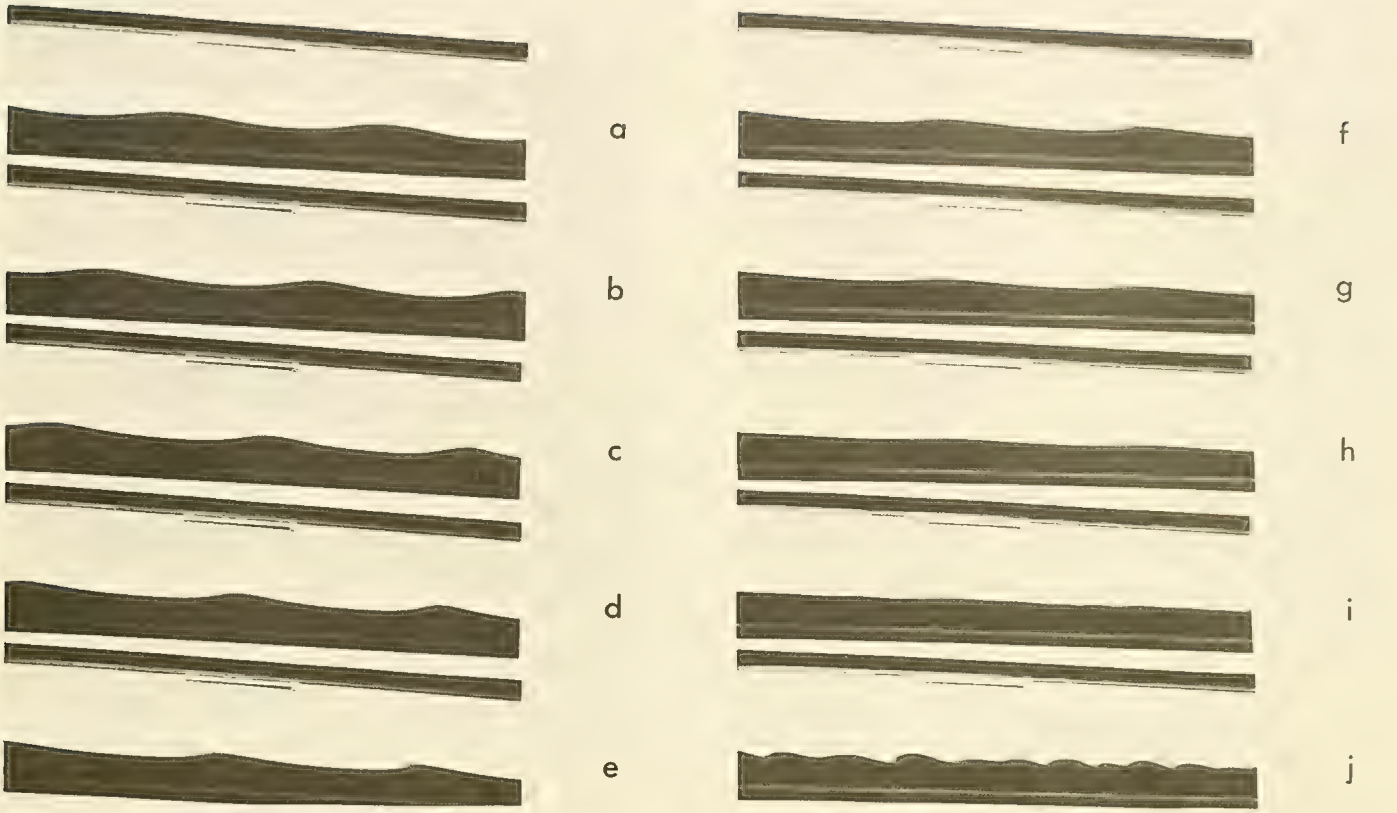

FIGURE 5. The onset of wave breaking for $\chi > 0$. The waves are moving to the left. The mean Richardson number at the interface in the accelerating flow is approximately (a) 2.5 (b) 0.73 (c) 0.36 (d) 0.25 (e) 0.18 (f) 0.14 (g) 0.11 (h) 0.09 (i) 0.07 (j) 0.06 [from Thorpe (1968)]. Convective overturn is seen to begin at (c) and K-H.I at (i). The instability is not seen at the critical value of Ri because of the time needed for growth in the accelerating flow.

not be unaffected by it. This process may be important in producing asymmetric directional wave spectra in the seasonal thermocline.

In practice of course unidirectional flows and long trains of internal waves do not occur in the ocean. The component of the mean flow velocity normal to the direction of wave propagation appears to play no part in the breaking or dynamics of the waves, and the results should be valid for long crested waves even in (Ekman) spiral flows. A periodic shear flow applied to a wave, as when one internal wave moves through another, may produce locally the conditions for convective overturn of the kind we have described. The final stages of the experiments of Keulegan and Carpenter (1961) or Davis and Acrivos (1967) illustrate this process. In these experiments a short second mode wave is driven by resonant interaction from a long first mode wave, itself generated by a wavemaker. The shorter wave eventually breaks in the shear field of the longer first mode wave.

Flow acceleration accompanies both the periodic flows in a wave field and the motion of the upper layers of the ocean during periods of wind forcing. In the experiments shown here breaking was induced by allowing the flow to accelerate uniformly. It was discovered that the energy of the fluctuating wave components was reduced very rapidly as a result of this acceleration. The consequent Reynolds stress working on the mean velocity gradient transferred energy to the mean flow. This interaction may have important consequences on the development of the seasonal thermocline during

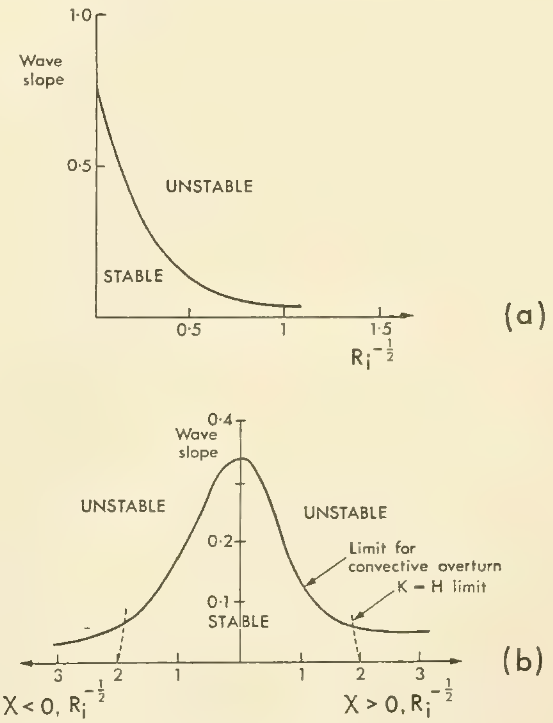

FIGURE 6. Stability diagrams corresponding to the waves described in Figure 2, based on a calculation extended to third order (Thorpe, 1968). (a) Couette flow (b) Hyperbolic tangent profiles.

periods of wind forcing and the acceleration of the mixing layer, but they are beyond the scope of this paper.

It seems likely that in the seasonal thermocline short internal waves may break predominantly by convective overturn whilst the longer are more prone to K-H.I, but the balance of effects is not known. The importance of non-linearities in determining the condition of convective overturn and the unknown structure of the density and velocity fields make the problem difficult to resolve theoretically, and some effort is being directed towards an observational, and hence empirical, solution using small arrays of thermistors with rapid response times, and sensitive CTDs.

REFERENCES

Banks, W. H. H., P. G. Drazin, and M. B. Zaturska (1976). On the normal modes of parallel flow of inviscid stratified fluid. *J. Fluid Mech. 75,* 149.

Bell, T. H. (1974). Effects of shear on the properties of internal gravity wave modes. *Dt. Hydrogr. Z. 27,* 57.

Cokelet, E. D. (1977). Breaking waves. *Nature 267,* 769.

Davis, R. E, and A. Acrivos (1967). The stability of oscillating internal waves. *J. Fluid Mech. 30,* 723.

Groen, P. (1948). Two fundamental theorems on gravity waves in inhomogeneous incompressible fluids. *Physica 14,* 294.

Halpern, D. (1974). Observations of the deepening of the wind-mixed layer in the Northeast Pacific Ocean. *J. Phys. Oceanog. 4,* 454.

Howard, L. N. (1961). Note on a paper by John W. Miles. *J. Fluid Mech. 10,* 509.

Keulegan, G. H., and L. H. Carpenter (1961). An experimental study of internal progressive oscillatory waves. *Nat. Bur. Stand. Rep. No. 7319.*

Miles, J. W. (1961). On the stability of heterogeneous shear flows. *J. Fluid Mech. 10,* 496.

Orlanski, I., and K. Bryan (1969). Formation of the thermocline step structure by large amplitude internal gravity waves. *J. Geophys. Res. 74,* 6975.

Phillips, O. M., and M. L. Banner (1974). Wave breaking in the presence of wind drift and swell. *J. Fluid Mech. 66,* 625.

Thorpe, S. A. (1971). Experiments on the instability of stratified shear flows: miscible fluids. *J. Fluid Mech. 46,* 299.

Thorpe, S. A. (1974). Near-resonant forcing in a shallow two-layer fluid: a model for the internal surge in Loch Ness? *J. Fluid Mech. 63,* 509.

Thorpe, S. A., A. J. Hall, C. Taylor, and J. Allen (1977). Billows in Loch Ness. *Deep-Sea Res. 24,* 371.

Thorpe, S. A. (1978). On the shape and breaking of finite amplitude internal gravity waves in a shear flow. *J. Fluid Mech. 85,* 7.

Woods, J. D. (1968). Wave-induced shear instability in the summer thermocline. *J. Fluid Mech. 32,* 791.

List of Participants

Allan J. Acosta, California Institute of Technology, Pasadena, USA
Bruce H. Adee, University of Washington, Seattle, USA
Jose A. Alaez, Canal de Experiencias Hidrodinamicas, Madrid, Spain
Klaus Albrecht, Institut fur Hydroakustik, Ottobrunn, Federal Republic of Germany
Vladimir K. Ankudinov, Hydronautics, Inc., Laurel, USA
Robert E. Apfel, Yale University, New Haven, USA
Roger E. A. Arndt, University of Minnesota, Minneapolis, USA
Glenn M. Ashe, U. S. Coast Guard, Washington, USA
Daniel G. Bagnell, U. S. Coast Guard, Washington, USA
Kwang-June Bai, David Taylor Naval Ship R & D Center, Bethesda, USA
Ignacio Baquerizo Briones, Spanish Society of Naval Architects, Madrid, Spain
Goran B. R. Bark, Swedish State Shipbuilding Experimental Tank, Goteborg, Sweden
Steven J. Barker, University of California, Los Angeles, USA
Franco C. Bau, Cantieri Navali Riuniti, Genoa, Italy
Robert F. Beck, University of Michigan, Ann Arbor, USA
Michael L. Billet, Pennsylvania State University, State College, USA
William K. Blake, David Taylor Naval Ship R & D Center, Bethesda, USA
Christian Bratu, Institut Francais Du Petrole, Rueil-Malmaison, France
John P. Breslin, Stevens Institute of Technology, Hoboken, USA
Neal G. Brower, Johns Hopkins University, Baltimore, USA
Samuel H. Brown, David Taylor Naval Ship R & D Center, Bethesda, USA
Donald R. Burklew, Operations Research, Inc., Silver Spring, USA
Otto Bussemaker, Schottel-Nederland B. V., The Hague, Netherlands
Ben J. Cagle, Office of Naval Research, Pasadena, USA
Nicholas Caracostas, Advanced Marine Enterprises, Inc., Washington, USA
George F. Carrier, Harvard University, Cambridge, USA
F. Sherman Cauldwell, Naval Ship Engineering Center, Washington, USA
Tuncer Cebeci, Douglas Aircraft Company, Long Beach, USA
Georges L. Chahine, Ecole Nationale Superieure de Techniques Avancees, Paris, France
Ming-Shun Chang, David Taylor Naval Ship R & D Center, Bethesda, USA
Richard B. Chapman, Science Applications, Inc., San Diego, USA
Howard A. Chatterton, U. S. Coast Guard, Washington, USA
Michael A. Chaszeyka, Office of Naval Research, Chicago, USA
Henry M. Cheng, Office of the Chief of Naval Operations, Washington, USA
Teresa Chereskin, Massachusetts Institute of Technology, Cambridge, USA
George H. Christoph, Sun Shipbuilding & Dry Dock Company, Chester, USA
Allen T. Chwang, California Institute of Technology, Pasadena, USA
David W. Coder, David Taylor Naval Ship R & D Center, Bethesda, USA
E. N. Comstock, Naval Ship Engineering Center, Washington, USA
Genevieve Comte-Bellot, Ecole Centrale de Lyon, Ecully, France
Reilley E. Conrad, Naval Ship Engineering Center, Washington, USA
Ralph D. Cooper, Office of Naval Research, Washington, USA
Bruce D. Cox, David Taylor Naval Ship R & D Center, Bethesda, USA

William E. Cummins, David Taylor Naval Ship R & D Center, Bethesda, USA
Douglas J. Dahmer, David Taylor Naval Ship R & D Center, Bethesda, USA
Tore G. Dalvag, AB Karlstads Mekaniska Werkstad, Kristinehamn, Sweden
Stephen H. Davis, John Hopkins University, Baltimore, USA
Charles W. Dawson, David Taylor Naval Ship R & D Center, Bethesda, USA
William G. Day, Jr., David Taylor Naval Ship R & D Center, Bethesda, USA
Jean-Francois M. Demanche, Bassin d'Essais des Carenes, Paris, France
Jean-Claude Dern, Bassin d'Essais des Carenes, Paris, France
William K. Dewar, Woods Hole Oceanographic Institution, Woods Hole, USA
Warren C. Dietz, U. S. Coast Guard, Washington, USA
Richard C. DiPrima, Rensselaer Polytechnic Institute, Troy, USA
Jan M. Dirkzwager, Ministry of Defence, The Hague, Netherlands
Stanley W. Doroff, Office of Naval Research, Washington, USA
Phillip Eisenberg, Hydronautics, Inc., Laurel, USA
N. M. El-Hady, Virginia Polytechnic Institute, Blacksburg, USA
J. W. English, National Maritime Institute, Feltham, England
Robert Falls, Maritime Administration, Washington, USA
Hermann F. Fasel, University of Stuttgart, Stuttgart, Federal Republic of Germany
Archibald M. Ferguson, University of Glasgow, Glasgow, Scotland
Peter D. Fitzgerald, Exxon International, Florham Park, USA
Francois N. Frenkiel, David Taylor Naval Ship R & D Center, Bethesda, USA
Daniel H. Fruman, Laboratoire d'Aerodynamique, Orsay, France
Donald Fuhs, David Taylor Naval Ship R & D Center, Bethesda, USA
Michael Gaster, National Maritime Institute, Middlesex, England
Edward M. Gates, University of Alberta, Edmonton, Canada
Carl Gazley, Jr., The Rand Corporation, Santa Monica, USA
William K. George, State University of New York, Buffalo, USA
Robert K. Geiger, Office of Naval Research, Washington, USA
Douglas L. Gile, Boulder, USA
Alex Goodman, Hydronautics, Inc., Laurel, USA
Stephan At. Goranov, Bulgarian Ship Hydrodynamics Center, Varna, Bulgaria
Paul S. Granville, David Taylor Naval Ship R & D Center, Bethesda, USA
Richard A. Griffiths, U. S. Coast Guard, Washington, USA
William L. Haberman, Rockville, USA
Jacques B. Halder, David Taylor Naval Ship R & D Center, Bethesda, USA
Francis R. Hama, Princeton University, Princeton, USA
Henry J. Haussling, David Taylor Naval Ship R & D Center, Bethesda, USA
Grant E. Hearn, British Ship Research Association, Wallsend, England
Harold I. Heaton, Johns Hopkins University, Applied Physics Laboratory, Laurel, USA
Isom H. Herron, Howard University, Washington, USA
Leo H. Holthuijsen, Delft University of Technology, Delft, Netherlands
Max G. A. Honkanen, Engineering Company M. G. Honkanen, Helsinki, Finland
Louis N. Howard, Massachusetts Institute of Technology, Cambridge, USA
Chun-Che Hsu, Hydronautics, Inc., Laurel, USA
Thomas T. Huang, David Taylor Naval Ship R & D Center, Bethesda, USA
Lee M. Hunt, National Academy of Sciences-National Research Council, Washington, USA
Stephen J. Hunter, Admiralty Marine Technology Establishment, Haslar, England
Erling Huse, Ship Research Institute of Norway, Trondheim, Norway
Takao Inui, University of Tokyo, Tokyo, Japan
Shunichi Ishida, Ishikawajima-Harima Heavy Industries Co., Ltd., Yokohama, Japan
Gerald S. Janowitz, North Carolina State University, Raleigh, USA
Stuart D. Jessup, David Taylor Naval Ship R & D Center, Bethesda, USA
Bruce Johnson, U. S. Naval Academy, Annapolis, USA
Virgil E. Johnson, Hydronautics, Inc., Laurel, USA
Francois J. Jouaillec, French Ministry of Defence, Paris, France
Peter Numa Joubert, University of Melbourne, Melbourne, Australia
Vijay K. Jyoti, Dominion Engineering Works, Ltd., Montreal, Canada
Lakshmi H. Kantha, Johns Hopkins University, Baltimore, USA
Paul Kaplan, Oceanics, Inc., Plainview, USA
George M. Kapsilis, M. Rosenblatt & Son, Inc., Gaithersburg, USA
Hiroharu Kato, University of Tokyo, Tokyo, Japan
R. G. Keane, Jr., Naval Ship Engineering Center, Washington, USA
Andreas P. Keller, Technical University of Munich, Munich, Federal Republic of Germany
Colen G. Kennell, Naval Ship Engineering Center, Washington, USA
Philip S. Klebanoff, National Bureau of Standards Washington, USA
Leslie S. G. Kovasznay, Johns Hopkins University, Baltimore, USA
Ruby E. Krishnamurti, Florida State University, Tallahassee, USA
Gert Kuiper, Netherlands Ship Model Basin, Wageningen, Netherlands
Jurgen H. Kux, University of Hamburg, Hamburg, West Germany
Louis Landweber, University of Iowa, Iowa City, USA
Arie J. W. Lap, Royal Netherlands Naval College, Dan Helder, Netherlands
Jochen Lauden, Hamburgische Shiffbau-Versuchsanstalt, Hamburg, Federal Republic of Germany
George K. Lea, National Science Foundation, Washington, USA
Yves Lecoffre, Alsthom Atlantique, Grenoble Cedex, France
Choung M. Lee, David Taylor Naval Ship R & D Center, Bethesda, USA
Yu-Tai Lee, University of Iowa, Iowa City, USA

Lennox J. Leggat, Defence Research Establishment Atlantic, Nova Scotia, Canada
Spiros G. Lekoudis, Lockheed-Georgia Company, Marietta, USA
John A. LeRoy, Australian Naval Attache Office, Washington, USA
Wen-Chin Lin, David Taylor Naval Ship R & D Center, Bethesda, USA
Robert R. Long, Johns Hopkins University, Baltimore, USA
Hans J. Lugt, David Taylor Naval Ship R & D Center, Bethesda, USA
Justin McCarthy, David Taylor Naval Ship R & D Center, Bethesda, USA
John M. Macha, Texas A & M University, College Station, USA
Leslie Mack, California Institute of Technology, Pasadena, USA
Toshio Maeda, Mitsubishi Heavy Industries, Ltd., Kobe, Japan
Allen H. Magnuson, Virginia Polytechnic Institute, Blacksburg, USA
Robert W. Manning, Naval Sea Systems Command, Washington, USA
Chiang C. Mei, Massachusetts Institute of Technology, Cambridge, USA
Kenneth R. Meldahl, The Boeing Company, Seattle, USA
John W. Miles, University of California, San Diego, USA
Robert J. Mindak, Office of Naval Research, Washington, USA
Erik Mollo-Christensen, Massachusetts Institute of Technology, Cambridge, USA
Vincent Monacella, David Taylor Naval Ship R & D Center, Bethesda, USA
Alan W. Moore, Admiralty Marine Technology Establishment, Teddington, England
David D. Moran, David Taylor Naval Ship R & D Center, Bethesda, USA
William B. Morgan, David Taylor Naval Ship R & D Center, Bethesda, USA
Kazuhiro Mori, Hiroshima University, Hiroshima, Japan
Parma Mungur, Lockheed-Georgia Company, Marietta, USA
Walter H. Munk, University of California, San Diego, USA
Hitoshi Murai, Tohoku University, Sendai, Japan
Paul M. Naghdi, University of California, Berkeley, USA
Ali H. Nayfeh, Virginia Polytechnic Institute, Blacksburg, USA
J. Nicholas Newman, Massachusetts Institute of Technology, Cambridge, USA
Francis Noblesse, Massachusetts Institute of Technology, Cambridge, USA
David J. Norton, Texas A & M University, College Station, USA
John A. Norton, Bird-Johnson Company, Walpole, USA
John F. O'Dea, David Taylor Naval Ship R & D Center, Bethesda, USA
Denis C. O'Neill, Ministry of Defence, Bath, England
Marinus W. C. Oosterveld, Netherlands Ship Model Basin, Wageningen, Netherlands
Blaine R. Parkin, Pennsylvania State University, State College, USA
Virendra C. Patel, University of Iowa, Iowa City, USA
Mariano Perez, Canal de Experiencias Hidrodinamicas, Madrid, Spain
Gonzalo Perez Gomez, Spanish Society of Naval Architects, Madrid, Spain
Frank B. Peterson, David Taylor Naval Ship R & D Center, Bethesda, USA
Owen M. Phillips, Johns Hopkins University, Baltimore, USA
Ennio Piantini, Ministero Difesa Marina, Rome, Italy
Pao C. Pien, David Taylor Naval Ship R & D Center, Bethesda, USA
Leonard J. Pietrafesa, North Carolina State University, Raleigh, USA
Gregory Platzer, David Taylor Naval Ship R & D Center, Bethesda, USA
Allen Plotkin, University of Maryland, College Park, USA
Alan Powell, David Taylor Naval Ship R & D Center, Bethesda, USA
Jaakko V. Pylkkanen, Helsinki University of Technology, Helsinki, Finland
Arthur M. Reed, David Taylor Ship R & D Center, Bethesda, USA
Sidney R. Reed, Office of Naval Research, Washington, USA
Bernd Remmers, Kempf & Remmers, Hamburg, Federal Republic of Germany
Eli Reshotko, Case Western Reserve University, Cleveland, USA
Wolfgang Reuter, Naval Ship Engineering Center, Washington, USA
M. B. Ricketts, David Taylor Naval Ship R & D Center, Bethesda, USA
Joel C. W. Rogers, Johns Hopkins University, Applied Physics Laboratory, Laurel, USA
Richard R. Rojas, Naval Research Laboratory, Washington, USA
Olle G. A. Rutgersson, Swedish State Shipbuilding Experimental Tank, Goteborg, Sweden
Manley St. Denis, U. S. Naval Academy, Annapolis, USA
Nils Salvesen, David Taylor Naval Ship R & D Center, Bethesda, USA
Geert H. Schmidt. University of Technology, Delft, Netherlands
Michael Schmiechen, VWS Berlin Model Basin, Berlin, Federal Republic of Germany
Joanna W. Schot, David Taylor Naval Ship R & D Center, USA
Paul Sclavounous, Massachusetts Institute of Technology, Cambridge, USA
Carl A. Scragg, Science Applications Inc., San Diego, USA
Som D. Sharma, Massachusetts Institute of Technology, Cambridge, USA
Young T. Shen, David Taylor Naval Ship R & D Center, Bethesda, USA
Vincent G. Sigillito, Johns Hopkins University, Applied Physics Laboratory, Laurel, USA
Leslie Sinclair, Stone Manganese Marine Ltd., London, England
Olav H. Slaattelid, Ship Research Institute of Norway, Trondheim, Norway
Neill S. Smith, Naval Coastal Systems Center, Panama City, USA
J. A. Sparenberg, University of Groningen, Groningen, Netherlands
Nicholas R. Stark, Beltsville, USA
Frank X. Stora, U. S. Army, Fort Belvoir, USA

Albert M. Sturrman, Royal Netherlands Navy, The Hague, Netherlands
Ming-Yang Su, U. S. Navy, NORDA, Bay St. Louis, USA
Hiraku Tanaka, Ship Research Institution, Tokyo, Japan
Stephen A. Thorpe, Institute of Oceanographic Sciences, Surrey, England
Yoshiaki Toba, Tohoku University, Sendai, Japan
Ernest O. Tuck, University of Adelaide, Adelaide, Australia
Marshall P. Tulin, Hydronautics, Inc., Laurel, USA
Ka-Kit Tung, Dynatech, Torrance, USA
J. Stewart Turner, Australian National University, Canberra, Australia
Willem van Berlekom, Swedish State Shipbuilding Experimental Tank, Goteborg, Sweden
Jan D. van Manen, Netherlands Ship Model Basin, Wageningen, Netherlands
Pieter van Oossanen, Netherlands Ship Model Basin, Wageningen, Netherlands
Jan van der Meulen, Netherlands Ship Model Basin, Wageningen, Netherlands
Christian von Kerczek, David Taylor Naval Ship R & D Center, Bethesda, USA
Alice Vucinic, Rijeka University, Rijeka, Yugoslavia
Nicholas Vytlacil, Westinghouse Electric Corp., Annapolis, USA
David A. Walden, U. S. Coast Guard, Washington, USA
Lawrence W. Ward, Webb Institute of Naval Architecture, Glen Cove, USA
Richard M. Wargelin, U. S. Navy, Suitland, USA
John V. Wehausen, University of California, Berkeley, USA
Michael A. Weissman, Flow Industries, Inc., Kent, USA
Ernst-August Weitendorf, University of Hamburg, Hamburg, Federal Republic of Germany
John R. Weske, University of Maryland, College Park, USA
Robert E. Whitehead, Office of Naval Research, Washington, USA
Sheila Widnall, Massachusetts Institute of Technology, Cambridge, USA
Karl Wieghardt, University of Hamburg, Hamburg, Federal Republic of Germany
Colin B. Wills, Admiralty Marine Technology Establishment, Haslar, England
Theodore Y. Wu, California Institute of Technology, Pasadena, USA
Chia-Shun Yih, University of Michigan, Ann Arbor, USA
Bohyun Yim, David Taylor Naval Ship R & D Center, Bethesda, USA
Hajime Yuasa, Mitsui Engineering & Shipbuilding Co., Ltd., Tokyo, Japan
P. Richard Zarda, David Taylor Naval Ship R & D Center, Bethesda, USA

PREVIOUS BOOKS IN THE NAVAL HYDRODYNAMICS SERIES

"First Symposium on Naval Hydrodynamics." National Academy of Science-Nation Research Council, Publication 515, 1957. Washington, D. C.; PB133732.

"Second Symposium on Naval Hydrodynamics: Hydrodynamic Noise and Cavity Flow," Office of Naval Research, Department of the Navy, ACR-38, 1958; PB157668.

"Third Symposium on Naval Hydrodynamics: High Performance Ships," Office of Naval Research, Department of the Navy, ACR-65, 1960; AD430729.

"Fourth Symposium on Naval Hydrodynamics: Propulsion and Hydroelasticity," Office of Naval Research, Department of the Navy, ACR-92, 1962; AD447732.

"The Collected Papers of Sir Thomas Havelock on Hydrodynamics," Office of Naval Research, Department of the Navy, ACR-103, 1963; AD623589.

"Fifth Symposium on Naval Hydrodynamics: Ship Motions and Drag Reduction," Office of Naval Research, Department of the Navy, ACR-112, 1964; AD640539.

"Sixth Symposium on Naval Hydrodynamics: Physics of Fluids, Maneuverability and Ocean Platforms, Ocean Waves, and Ship-Generated Waves and Wave Resistance," Office of Naval Research, Department of the Navy, ACR-136, 1966; AD676079.

"Seventh Symposium on Naval Hydrodynamics: Unsteady Propeller Forces, Fundamental Hydrodynamics, Unconventional Propulsion," Office of Naval Research, Department of the Navy, DR-148, 1968; AD721180.

"Eighth Symposium on Naval Hydrodynamics: Hydrodynamics in the Ocean Environment," Office of Naval Research, Department of the Navy, ACR-179, 1970; AD748721.

"Ninth Symposium on Naval Hydrodynamics: Unconventional Ships, Ocean Engineering, Frontier Problems," Office of Naval Research, Department of the Navy, ACR-203, 1972; Two Volumes; Vol. 1, ADA-010505; Vol 2, ADA010506.

"Tenth Symposium on Naval Hydrodynamics: Hydrodynamics for Safety, Fundamental Hydrodynamics," Office of Naval Research, Department of the Navy, ACR-204, 1974; ADA022379.

"Eleventh Symposium on Naval Hydrodynamics: Unsteady Hydrodynamics of Marine Vehicles," Office of Naval Research, Department of the Navy. Also available from Mechanical Engineering Publications Limited, London and New York.

NOTE: The above books are avilable on microfilm and microfiche from the National Technical Information Service, U. S. Department of Commerce, Springfield, Virginia 22151. Some early issues are also available in paper copies. The catalog numbers, as of the date of this issue, are shown for each book.

ISBN 0-309-02896-5